SPRINGER NATURE
Reference

Xing Lu
Takeshi Akasaka
Zdeněk Slanina
Editors

Handbook of Fullerene Science and Technology

Springer

Handbook of Fullerene Science and Technology

Xing Lu • Takeshi Akasaka • Zdeněk Slanina
Editors

Handbook of Fullerene Science and Technology

With 755 Figures and 21 Tables

Springer

Editors
Xing Lu
Huazhong University of Science and Technology
Wuhan, Hubei, China

Zdeněk Slanina
Huazhong University of Science and Technology
Wuhan, Hubei, China

Takeshi Akasaka
University of Tsukuba
Tsukuba, Ibaraki, Japan

ISBN 978-981-16-8993-2 ISBN 978-981-16-8994-9 (eBook)
https://doi.org/10.1007/978-981-16-8994-9

This Springer imprint is published by the registered company Springer Nature Singapore Pte Ltd.
The registered company address is: 152 Beach Road, #21-01/04 Gateway East, Singapore 189721, Singapore

Dedicated to Professors Robert F. Curl Jr., Sir Harold Kroto, and Richard E. Smalley for their pioneering work of discovering fullerenes.

Preface

Fullerenes, with typical members of C_{60} and C_{70} and a tremendous number of derivatives, emerged as the third and the only soluble, molecular form of carbon allotrope and triggered the huge development of novel carbon materials, such as carbon nanotubes, graphene, and graphyne. During the past three decades, both the fundamental research and the applications of fullerenes have progressed dramatically with many commercial fullerene products available on the market. As a consequence, this Handbook aims to give a comprehensive scientific summary of fullerene science and technology covering both the fundamental research and the future applications, which may serve as a textbook for young students and fresh researchers who are interested in the field of fullerenes.

There are seven parts in this Handbook, with 29 chapters, all contributed by groups of active scientists. Regarding the history of fullerenes, Prof. Krätschmer shares the initial attempt to produce interstellar-like graphitic grains and the discovery of arc-discharge method for bulk generation of fullerenes which open the door for extensive research into the structure, chemistry, properties, and applications of fullerenes. The following part edited by Prof. Slanina reviews the molecular structures of fullerene from the perspectives of practical generation of fullerenes by Profs. Stevenson and Sakurai et al. and structural characteristics and stabilities of fullerene molecules, including the unexpected findings of fullerenes violating the isolated-pentagon rule and structural connection of fullerenes with carbon nanotubes and graphene in chapters by Profs. Jin, Slanina, Tan, Lu, and their coworkers; then nanocarbon/porphyrin conjugates for photon and charge managements are reviewed by Prof. Guldi et al. Based on the structures of pristine fullerenes, the interest of chemists is undoubtedly the chemical properties which are summarized in the next part edited by Prof. Akasaka. It starts with an overview of the chemical reactivity and addition patterns by Prof. Li and ends with theoretical considerations of fullerene reactivity by Prof. Yang and coauthors. Attention in this part is given to respective reactions, namely, addition reactions, radical reactions, electrochemical reactions, metal complexation, and transition metal salt-catalyzed reactions, presented by Profs. Yamada, Maeda, Gao, Pan, and Wang et al., respectively. After the discovery of C_{60}, the concept of encapsulating isolated atoms within fullerene cages was verified. Advancing of this concept is marked by the preparation of a collection of endofullerenes containing not only metallic species but also single nonmetal atom

(s)/molecule(s) (N, H_2O, etc.) or even a lithium ion. The part on endofullerenes edited by Prof. Akasaka first describes the classification, preparation, structures, properties, and chemical reactions of endohedral metallofullerenes in the chapters by Profs. Lu, Chen, Yang, and Li, and then two special kinds of endofullerenes that encapsulate single nitrogen atom or an isolated lithium ion are reviewed by groups of Profs. Porfyrakis and Matsuo, respectively. Going beyond single molecules of fullerenes, the assembly of fullerenes and metallofullerenes into nanostructures through supramolecular chemistry is contributed by Profs. Wakahara and Haino and coauthors in the following part. Given the unique spherical structures and novel properties of fullerenes, various applications of fullerenes and their derivatives have been demonstrated. The potentials of photovoltaics, antiviral and anticancer agents, photodynamic therapy, soft materials, and superconductivity are discussed by Profs. Matsuo, Ohe, Yamakoshi, Tashiro, Tanigaki, and their coworkers, respectively. Despite the remarkable achievements in the fullerene field, the fundamental formation mechanism of fullerene remains an open question. In the last part, Profs. Crichton and Zhang survey the continuous efforts of the fullerene community devoted to this intriguing yet vital puzzle.

Considering the extent and expansion of fullerenes, it is clear that our volume focusing on the whole picture cannot cover every aspect of fullerenes. Certain topics such as endofullerenes containing single molecules (H_2O_2, HF, etc.) and their applications as single-molecule magnets or in lubricants and cosmetics are not included in this Handbook; however, we may refer to some excellent reviews available elsewhere. Nevertheless, in spite of its limitations, the Handbook should (temporarily) offer the most comprehensive and up-to-date survey of fullerene science. As Tai T'ung wrote in History of Chinese Writing in the thirteenth century: "Were I to await perfection, my book would never be finished."

Wuhan, China — Xing Lu
Tsukuba, Japan — Takeshi Akasaka
Wuhan, China — Zdeněk Slanina
October 2022

Contents

About the Editors

Xing Lu is a full professor in Huazhong University of Science and Technology. He received his Ph.D. from Peking University (2004), and then he worked as a COE postdoctoral researcher in Nagoya University, Japan. During 2006–2013, he was a Senior Scientist in the University of Tsukuba, Japan. He is the recipient of the Ambassador Award from Chinese Embassy in Japan (2009), the Osawa Award from Fullerenes and Nanotubes Research Society of Japan (2011), and the National Science Fund for Distinguished Young Scholars (2019). His research interests lie in the rational design and facile generation of novel hybrid carbon materials with applications in energy storage and conversion. He has published more than 180 peer-reviewed papers in international journals with ~40 in Journal of The American Chemical Society and Angewandte Chemie International Edition.

Takeshi Akasaka was born in Kyoto. He received his Ph.D. degree from University of Tsukuba, Japan, in 1979. After working as a postdoctoral fellow at Brookhaven National Laboratory, he returned to the University of Tsukuba in 1981. In 1996, he began work at Niigata University as a professor. During 2001–2013, he was a professor at the TARA Center and Department of Chemistry, University of Tsukuba. After his retirement from the University of Tsukuba in 2013, he was appointed a senior researcher at the Foundation for Advancement of International Science (FAIS) and a professor emeritus of the University of Tsukuba. He received the Chemical Society of Japan Award for Creative Work (2000), the Commendation of Science

and Technology (Research Category) from the Ministry of Education, Culture, Sports, Science and Technology of Japan in 2011, and the Chemical Society of Japan Award for 2013. His research interests include the chemistry of nanocarbons.

Zdeněk Slanina was born in the former Czechoslovakia. He received his M.A. degree from Charles University in Prague and Ph.D. from the (former) Czechoslovak Academy of Sciences where he was also employed between 1971 and 1991, up to the principal-senior-scientist level. After the fullerene-era beginning, he has been active in computational research and teaching at various fullerene research centers like Hokkaido University, Sapporo; Max-Planck Institute for Chemistry, Mainz; University of Arizona, Tucson; Institute for Molecular Science, Okazaki; University of Tsukuba; and Huazhong University of Science and Technology, Wuhan.

Contributors

Ludwik Adamowicz Department of Chemistry and Biochemistry, University of Arizona, Tucson, AZ, USA

Takeshi Akasaka University of Tsukuba, Tsukuba, Ibaraki, Japan

Ning Chen College of Chemistry, Chemical Engineering and Materials Science, Soochow University, Suzhou, Jiangsu, P. R. China

Muqing Chen Hefei National Laboratory for Physical Science at Microscale, CAS Key Laboratory of Materials for Energy Conversion, Department of Materials Science and Engineering, University of Science and Technology of China, Hefei, China

Zuo-Chang Chen State Key Laboratory for Physical Chemistry of Solid Surfaces, and Department of Chemistry, College of Chemistry and Chemical Engineering, Xiamen University, Xiamen, China

Ryan A. Crichton Department of Chemistry and Chemical Biology, Rutgers, The State University of New Jersey, Piscataway, NJ, USA

Xiang Gao Adare Pharma Solutions, Philadelphia, PA, USA

Xiaojiao Gu School of Materials Science and Engineering, Hebei University of Technology, Tianjin, China

Dirk M. Guldi Department of Chemistry and Pharmacy, Interdisciplinary Center for Molecular Materials, Friedrich-Alexander University of Erlangen-Nürnberg, Erlangen, Germany

Takeharu Haino Graduate School of Advanced Science and Engineering, Hiroshima University, Hiroshima, Japan

Takehiro Hirao Graduate School of Advanced Science and Engineering, Hiroshima University, Hiroshima, Japan

Yajing Hu State Key Laboratory of Materials Processing and Die and Mould Technology, School of Materials Science and Engineering, Huazhong University of Science and Technology, Wuhan, People's Republic of China

Xiaole Jiang Hefei National Laboratory for Physical Science at Microscale, CAS Key Laboratory of Materials for Energy Conversion, Department of Materials Science and Engineering, University of Science and Technology of China, Hefei, China

Meihe Jin College of Chemistry, Chemical Engineering and Materials Science, Soochow University, Suzhou, Jiangsu, P. R. China

Peng Jin School of Materials Science and Engineering, Hebei University of Technology, Tianjin, China

Ramandeep Kaur Department of Chemistry and Pharmacy, Interdisciplinary Center for Molecular Materials, Friedrich-Alexander University of Erlangen-Nürnberg, Erlangen, Germany

Wolfgang Krätschmer Max-Planck-Institut für Kernphysik, Heidelberg, Germany

Fa-Bao Li School of Chemistry and Chemical Engineering, Hubei University, Wuhan, Hubei, China

Fang-Fang Li State Key Laboratory of Materials Processing and Die and Mould Technology, School of Materials Science and Engineering, Huazhong University of Science and Technology, Wuhan, People's Republic of China

Mengyang Li Ministry of Education Key Laboratory for Non-Equilibrium Synthesis and Modulation of Condensed Matter, School of Physics, Xi'an Jiaotong University, Xi'an, Shaanxi, China

Xiaomeng Li College of Chemistry, Chemical Engineering and Materials Science, Soochow University, Suzhou, Jiangsu, P. R. China

H.-S. Lin Department of Mechanical Engineering, School of Engineering, The University of Tokyo, Tokyo, Japan

Department of Chemical System Engineering, Graduate School of Engineering, Nagoya University, Nagoya, Japan

Qing-Song Liu Hefei National Laboratory for Physical Sciences at Microscale and Department of Chemistry, University of Science and Technology of China, Hefei, China

Wen-Qiang Lu Hefei National Laboratory for Physical Sciences at Microscale and Department of Chemistry, University of Science and Technology of China, Hefei, China

Xing Lu Huazhong University of Science and Technology, Wuhan, Hubei, China

Y. Ma Hefei National Laboratory for Physical Sciences at the Microscale, University of Science and Technology of China, Hefei, Anhui, P. R. China

Yutaka Maeda Tokyo Gakugei University, Koganei, Tokyo, Japan

Tadahiko Mashino Faculty of Pharmacy, Keio University, Tokyo, Japan

Y. Matsuo Department of Mechanical Engineering, School of Engineering, The University of Tokyo, Tokyo, Japan

Department of Chemical System Engineering, Graduate School of Engineering, Nagoya University, Nagoya, Japan

Arjun Menon Department of Chemistry and Pharmacy, Interdisciplinary Center for Molecular Materials, Friedrich-Alexander University of Erlangen-Nürnberg, Erlangen, Germany

Kun'ichi Miyazawa Department of Industrial Chemistry, Faculty of Engineering, Tokyo University of Science, Tokyo, Japan

Shigeru Nagase Kyoto University, Kyoto, Japan

Hironobu Nakazawa Division of Applied Chemistry, Graduate School of Engineering, Osaka University, Suita, Osaka, Japan

Tomoyuki Ohe Faculty of Pharmacy, Keio University, Tokyo, Japan

Changwang Pan College of Chemistry and Chemical Engineering, Jinggangshan University, Ji'an, Jiangxi, China

Kyriakos Porfyrakis School of Engineering, University of Greenwich, Kent, UK

Hidehiro Sakurai Division of Applied Chemistry, Graduate School of Engineering, Osaka University, Suita, Osaka, Japan

Innovative Catalysis Science Division, Institute for Open and Transdisciplinary Research Initiatives (ICS-OTRI), Osaka University, Suita, Osaka, Japan

Wangqiang Shen School of Materials Science and Engineering, Huazhong University of Science and Technology, Wuhan, Hubei, China

Zdeněk Slanina Huazhong University of Science and Technology, Wuhan, Hubei, China

Steven Stevenson Department of Chemistry, Purdue University Fort Wayne, Fort Wayne, IN, USA

Yuan-Zhi Tan State Key Laboratory for Physical Chemistry of Solid Surfaces, and Department of Chemistry, College of Chemistry and Chemical Engineering, Xiamen University, Xiamen, China

Katsumi Tanigaki Beijing Academy of Quantum Information Sciences (BAQIS), Beijing, China

Advanced Institute of Materials Research, Tohoku University, Sendai, Japan

Kentaro Tashiro International Center for Materials Nanoarchitectonics (MANA), National Institute for Materials Science (NIMS), Tsukuba, Japan

Xinyue Tian School of Materials Science and Engineering, Huazhong University of Science and Technology, Wuhan, Hubei, China

Filip Uhlík Department of Physical and Macromolecular Chemistry, Faculty of Science, Charles University, Prague, Czech Republic

Takatsugu Wakahara Research Center for Functional Materials, National Institute for Materials Science, Ibaraki, Japan

Guan-Wu Wang Hefei National Laboratory for Physical Sciences at Microscale and Department of Chemistry, University of Science and Technology of China, Hefei, China

Su-Yuan Xie State Key Laboratory for Physical Chemistry of Solid Surfaces, and Department of Chemistry, College of Chemistry and Chemical Engineering, Xiamen University, Xiamen, China

Michio Yamada Tokyo Gakugei University, Koganei, Tokyo, Japan

Yoko Yamakoshi Laboratorium für Organische Chemie, ETH Zürich, Zürich, Switzerland

Shangfeng Yang Hefei National Laboratory for Physical Science at Microscale, CAS Key Laboratory of Materials for Energy Conversion, Department of Materials Science and Engineering, University of Science and Technology of China, Hefei, China

Tao Yang Ministry of Education Key Laboratory for Non-Equilibrium Synthesis and Modulation of Condensed Matter, School of Physics, Xi'an Jiaotong University, Xi'an, Shaanxi, China

Pengwei Yu School of Materials Science and Engineering, Huazhong University of Science and Technology, Wuhan, Hubei, China

Jianyuan Zhang Department of Chemistry and Chemical Biology, Rutgers, The State University of New Jersey, Piscataway, NJ, USA

Pei Zhao Ministry of Education Key Laboratory for Non-Equilibrium Synthesis and Modulation of Condensed Matter, School of Physics, Xi'an Jiaotong University, Xi'an, Shaanxi, China

Shen Zhou School of Chemistry and Chemical Engineering, South China University of Technology, Guangzhou, China

College of Aerospace Science and Engineering, National University of Defence Technology, Changsha, China

Jiaxin Zhuang College of Chemistry, Chemical Engineering and Materials Science, Soochow University, Suzhou, Jiangsu, P. R. China

Part I

History and Nomenclature of Fullerenes

Our Road to Fullerenes: A Personal Account

1

Wolfgang Krätschmer

Dedicated to Donald R. Huffman and to the memory of Ahmed El Goresy (1934–2019)

Contents

Abstract

Carbon is the most abundant condensable element in space. Our attempts to produce interstellar-like graphitic grains unexpectedly led to the discovery of a method for fullerene production in bulk amounts. These works opened the door for an entirely new branch of materials research and carbon chemistry. Recently, fullerenes were also detected in interstellar space. Presented are the various phases and steps of our work which with intermissions lasted from 1983 to 1990. In the beginning there were unexplained UV absorptions in the soot samples we had produced, and the endpoint was marked by the extraction of fullerenes in crystalline form and in form of coated films from just these samples.

Keywords

Fullerite · Fullerene generator · Interstellar particle scattering and absorption · Graphite rods · Carbon molecules · Carbon evaporator · Isotope replacement

W. Krätschmer (✉)
Max-Planck-Institut für Kernphysik, Heidelberg, Germany
e-mail: kraetschmer@mpi-hd.mpg.de

X. Lu et al. (eds.), *Handbook of Fullerene Science and Technology*,
https://doi.org/10.1007/978-981-16-8994-9_19

Introduction

Our institute is surrounded by forest and located outside the Heidelberg downtown area. I had the privilege to stay there for most of my scientific carrier, and now, as retired guest researcher, I can still keep an office there. One may wonder why an institute for nuclear physics can work on such remote topics, as e.g. interstellar matter. This was the idea of the founding director of our institute, Wolfgang Gentner (1906–1980) who in the late 1960s established besides the nuclear physics also a department which conducted research on meteorites, interplanetary dust (by space-borne experiments), and atmospheric composition. When in 1976 a young American professor gave a lecture at our place on the physics of interstellar grains, the directors apparently were such impressed that they decided to extend the already existing interplanetary dust research. A new group headed by me should perform laboratory studies in order to better understand the composition of interstellar dust. The young professor was Don Huffman and his lecture marked the beginning of our acquaintance. In 1977 I spend about 8 months in his "Solid-State-Astrophysics" lab in Tucson, Arizona, to learn the basic techniques and methods [1].

In general, interstellar grains are much too far away to ever be studied directly. What, however, is possible is the study of their optical spectra in emission or absorption. These data are provided by observational astronomy. To give a feeling about interstellar grains, some numbers may be helpful: Typical grain sizes are in the 10–100 nm range and densities in the order of 1000 per km^3. These figures can change dramatically depending on whether one considers diffuse or dense molecular clouds. For laboratory work, the task would be to produce interstellar-like material, disperse this material into tiny particles, and measure their spectra – usually in absorption. Alternatively, one can measure the dielectric functions of the interstellar-like material and calculate (e.g. by Mie theory or other methods) how particles of a suitable size would absorb. If possible, one should try both approaches. Measurements on dispersed particles are of course extremely difficult to make. The interstellar grains are likely to be well separated from each other – a feature which is important for the optical properties of the particle system as a whole. In the time of concern, such conditions were difficult to meet in the lab. However, with modern particle trapping techniques and laser spectroscopic means, these difficulties may be overcome in the future. The final goal of the laboratory work is to obtain spectra which reproduce the astronomical absorption peaks as close as possible in wavelength position, width, and relative intensity.

Donald Huffman in Heidelberg

Our and other Max Planck Institutes in Germany applied for a Humboldt fellowship for Don Huffman which was granted. In 1982–1983 he could take a sabbatical in our institute with the option to spend also some time in the Max Planck Institute for solid-state research in Stuttgart. As working programme we decided to study the spectra of graphitic soot in order to check how far these particles can explain the

rather intense interstellar absorption at 220 nm. More precisely, the central position of that feature is at 217 nm (see, e.g., [2]). For particle production, we used a carbon evaporator which originally served for sample preparation for a transmission electron microscope. The evaporator (see Fig. 1) consisted of a bell jar in which a vacuum could be generated and in which tipped graphite electrodes could be evaporated by resistive heating, i.e. by running a high current through the electrodes. Rather than in vacuum, as required for coating carbon films, we filled the bell jar with helium and evaporated the graphite rods electrodes under several torr (1 torr corresponds to about 133 Pa) helium pressure. This procedure is well established: The evaporating carbon atoms and molecules collide with the rare gas atoms and cool such that at a certain distance from the graphite electrodes, a supersaturated carbon vapour forms and spontaneous nucleation into small (about 100 nm diameter) particles occurs. Helium as quenching gas guarantees that no chemistry takes place

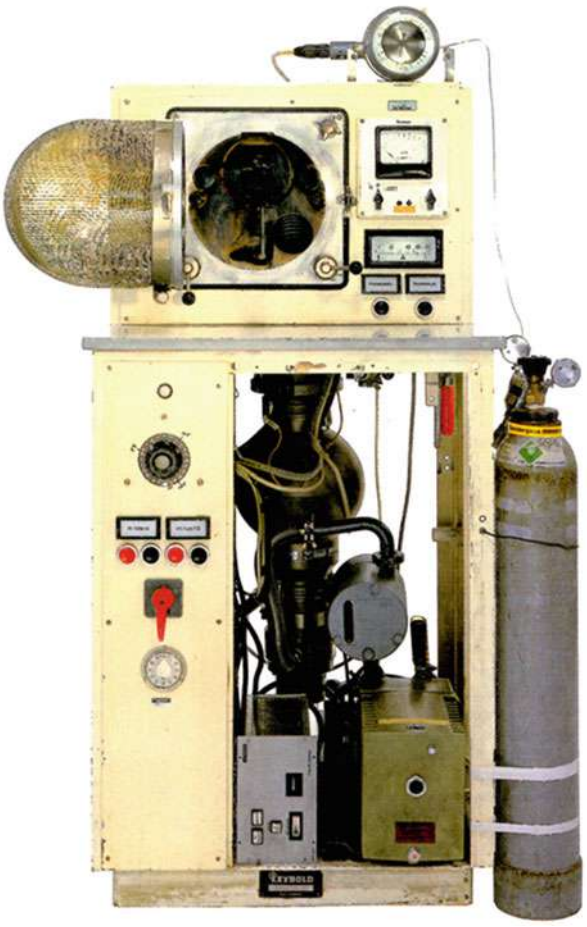

Fig. 1 The carbon evaporator we used for soot production. The apparatus is now on display at the "Deutsche Museum" in Bonn (Germany). The picture is reproduced from the museum's catalogue (with permission).

which would alter the graphitic nature of the grains. These particles float in the convection stream of the helium and deposit on the inside of the bell jar or on quartz glass slides which can serve as targets for optical (UV-VIS) examination. Naturally, in the deposited soot, the particles are sticking together – a serious handicap, as stated before. The clumping leads to clusters which in size may become larger than the wavelength of light. In such case scattering becomes significant. The absorption (actually the extinction) develops a continuum steeply rising towards shorter wavelengths, and the particle-related absorption peak develops a wing towards longer wavelengths. It is thus rather difficult to judge from the measured absorption of the clumped particles to that of a dispersed system of grains as it presumably exists in interstellar space. To avoid clumping, we produced carbon vapour molecules under vacuum and co-deposited these together with an excess of argon on a cryogenic substrate (i.e. applied the matrix isolation technique), in the hope that the carbon molecules would by diffusion and coalescence within the frozen argon form isolated particles. This approach failed but we entered the exciting field of spectroscopy of linear carbon molecules, which was pioneered by William Weltner several years earlier [3]. For our research, molecular carbon species were of considerable interest since they may be responsible for producing the so-called diffuse interstellar bands (or DIBs for short) [4]. DIBs are broad absorptions occurring in interstellar clouds in the UV, Visible, and NIR (see, e.g., [5]). The carriers of these features so far remain unknown (however, see below). Returning to the 220 nm interstellar absorption, since our research some encouraging experimental progress has been reported in matrix-isolating carbon grains [6]; however to my knowledge, so far no convincing explanation has been given in terms other than "graphitic" particles. Maybe, fullerene-related graphitic onions would provide a better analogue for these grains.

Besides worrying about particle isolation, there was another effect which caught our attention. Occasionally, we observed three additional absorption humps in the broad and usually smooth spectrum of our graphitic particle samples. At that time we didn't know under which conditions these "camel hump" spectra (as we called them in our lab jargon) could be produced regularly – we used low helium pressures (about 10 torr) in order to keep the particle sizes small. The experimental situation is shown schematically (i.e. suppressing most of the background produced by scattering) in the spectra depicted in Fig. 2. In Stuttgart, Huffman obtained Raman spectra of these samples, which looked strange: A small peak existed in between the two major Raman features of graphite at 1350 and 1600 cm^{-1} (that peak much later turned out to be the main Raman feature of C_{60}). The IR spectra showed nothing suspicious; we at that time used a dry air purged grating spectrometer equipped with a thermocouple detector – an instrument just not sensitive enough. Don and I discussed where these occasionally occurring absorptions may come from. He speculated that some form of distorted or intercalated graphite may be responsible, while I preferred as explanation that the small particles with their large surface area had trapped some contamination, e.g. diffusion pump oil, and this produced the absorptions. We in fact occasionally had problems when by accident air ventilated through the hot diffusion pump and a cloud of smoke entered the bell jar.

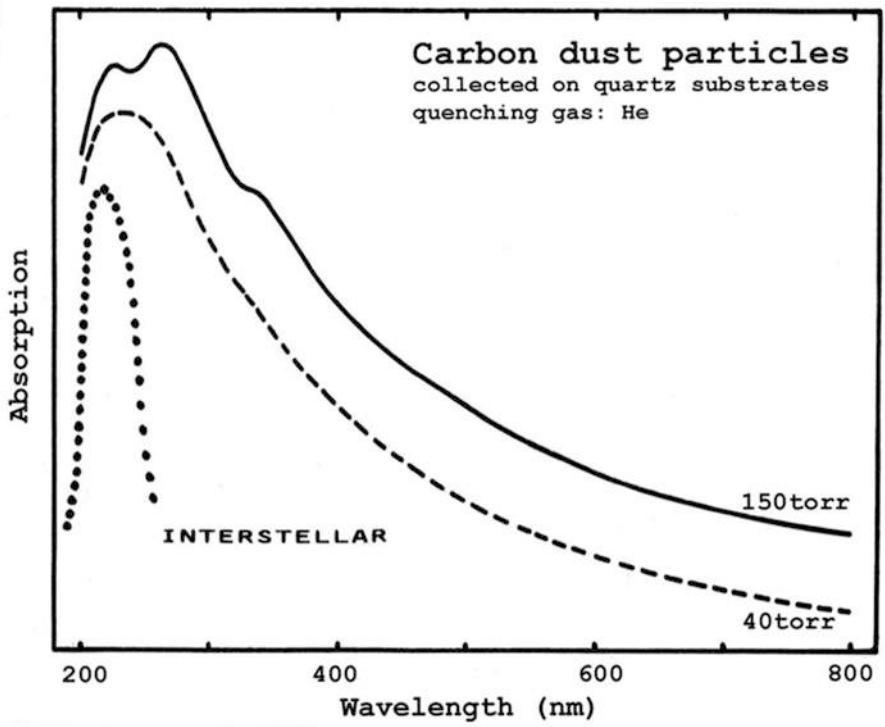

Fig. 2 Schematic representation of the interstellar 220 nm absorption feature and the absorption spectra of soot produced at different helium quenching gas pressures. Compared to the interstellar absorption, notice the much larger width of the soot spectra which is caused by a scattering background, and further notice the occurrence of additional absorption structures in the soot spectra taken at high pressure. These turned out to originate mainly from C_{60}

In 1984 at the third ISSIPC conference which took place in the west part of the still divided Berlin, we prepared two posters. One concerned our spectroscopy of carbon molecules [7] and the other our results on graphitic particles. The officials of the conference were not happy with our soot paper and discouraged us in publishing these data in the proceedings – and in fact they remained unpublished. One highlight of the conference I still remember: Andrew Kaldor from the Exxon research labs showed a then "state-of-the-art" time-of-flight mass spectrum (TOF-MS) of laser ablated carbon clusters which for the first time showed clusters up to more than 100 carbon atoms [8]. I was deeply impressed and – of course, as probably everybody at that time – didn't notice the suspicious overabundance of C_{60} and C_{70} in that spectrum. We were fighting to understand small carbon molecules such as C_3, C_4, or C_6 which we had matrix-isolated. Such huge species like C_{30}-C_{100} were completely out of our scope. I couldn't believe that I would have ever to deal with these.

C_{60} Buckminsterfullerene

In the following years, I worked on the spectroscopy of silicates and ices along with that of matrix-isolated carbon species. Ices, in particular solid H_2O, NH_3, CO_2, CO, and their mixtures, are interesting for the IR astronomy of dense and thus cold molecular clouds. These works were carried out in collaboration with Roger Knacke from the University of New York at Stony Brook. With the promise to get our old IR spectrometer replaced by a "state-of-the-art" evacuable Fourier transform (FT) instrument, I also participated in ESA's Infrared Space Observatory (ISO) project. ISO was a helium-cooled satellite dedicated for IR astronomy. This project turned out to be quite successful and provided a lot of data within its about 2-year lifetime. My task was to use the FT spectrometer to perform high-precision measurements on the transmission of IR optical components, as, e.g. on filters and polarisers of ISOPHOT, an instrument onboard of ISO. These data had to be taken at liquid helium temperatures. In the time remaining, I of course could use the instrument for my own research.

In 1985, Kroto, Smalley, Curl, and co-workers – in their famous experiment at Rice University – studied the mass spectra of carbon clusters similar to what had been done already by the Exxon group. However, the Rice researchers discovered the striking significance of C_{60} and speculated that this species must be very special and may exhibit a soccer ball structure [9]. Most remarkably, Harry Kroto who initiated this experiment was interested in learning about carbon-bearing molecules as they occur in space. One may conclude that C_{60} and the fullerenes are by-products of the research on interstellar matter! Needless to say that C_{60} with its assumed soccer ball structure became rather popular, last but not least by the entertaining lectures given by Harry Kroto. The problem, however, was that the structure remained hypothesis – though rather plausible – but there was no clear poof.

After this seminal work, it didn't took very long that when I met Don at conferences or at other occasions, he reminded me on the strange soot spectra we had obtained in Heidelberg. He suspected that the "camel" features may originate from C_{60}. "What else could it be" he argued. I thought this to be very far-fetched – has the evaporation of carbon in inert atmospheres been carried out by dozens of researchers before in the past and not the slightest indication of something peculiar was ever reported. In late summer of 1988 at a conference in California, Don again tried to persuade me to resume. Back in Heidelberg, it came to pass that a student approached me. His name was Bernd Wagner. He was studying physics and wanted to see how a research institute like ours looks from the inside. He volunteered for 2 weeks in my lab. This was a lucky incident: I asked him to carry out the soot experiments again and to play with the production parameters, e.g. the graphite electrode diameters, heating rates, and helium pressure. After he got familiar with the old carbon evaporator, he played with the helium pressure, and we observed that in samples produced at high pressure, i.e. in the range around 100 torr, the "camel" absorption became rather pronounced and appeared reproducible.

The greatest surprise came when we measured IR absorption of the high-pressure samples in our new FT spectrometer: On a continuum, there were several quite

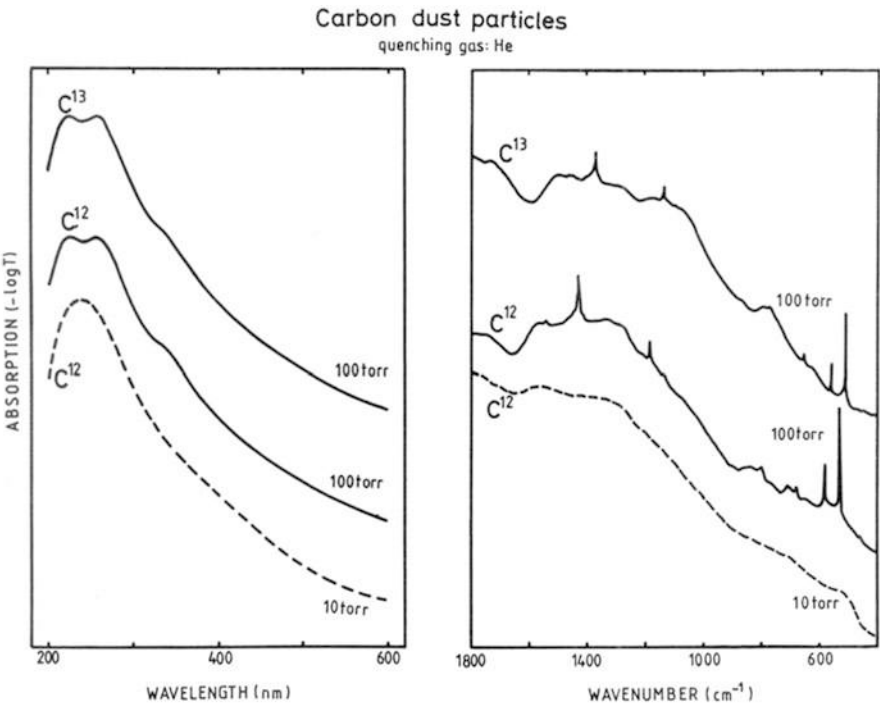

Fig. 3 UV-VIS and IR spectra of soot produced at higher and lower pressures. The left side spectra were taken by evaporating C^{12} (i.e. natural carbon) and the right by evaporating C^{13} (99% enriched) graphite. Notice the occurrence of just four IR absorptions (which is indicative for soccer ball structured C_{60}), and further notice the displacement of the IR absorptions of C^{13} produced C_{60} towards lower frequencies, corresponding to the higher atomic mass. The much weaker IR absorptions are from trace amounts of C_{70}. The background in the spectra originates from soot particle absorption and scattering

narrow absorption lines, of which four lines were particularly prominent, at 1492, 1183, 577, and 528 cm^{-1}. This pattern (see Fig. 3) was unequivocally the signature of the soccer ball C_{60} as predicted by theory. I still remember my feeling at this moment: I was surprised and shocked at the same time! It was just too good to be true. Can C_{60} be produced so easily – and more worrying: Why this hasn't been found before? In any event, it almost looked as if Don would be right.

Fullerite

Now I faced the problem how to prove that the absorptions really are from C_{60}. At around this time, the sensational "cold fusion" story went through the media, and the scientific community became reluctant to accept more "sensations." In view of the fact that organic chemists with their sophisticated methods had failed to synthesise

C_{60}, our production method was sensational simple. The easiest way would have been to check the samples by mass spectroscopy, but I thought this would not work. Not alone that we hadn't a suitable mass spectrometer at hand, but how to evaporate and ionise the sooty material? I found the best method to proceed would be a pure spectroscopic test: In case one deals with a pure carbon species and would replace all the ^{12}C carbon atoms in that molecule (natural composition 99% ^{12}C) by ^{13}C, then the IR eigenfrequencies should shift by a ratio equal to the square root of 12/13. In case the peaks would originate from a compound involving other elements besides carbon, the shift would be different. As a further precaution against contamination, I decided to add an oil filter to the rough pump, to replace the diffusion pump by a turbo pump, and to increase the size of the liquid nitrogen cold trap at the baffle valve.

Fortunately, at that time, a PhD student came and I asked him to improve the vacuum system and to perform the isotope exchange experiment for his thesis work. The student's name was Konstantinos Fostiropoulos. He replaced the vacuum system and we found that the IR absorptions remained unaffected. This encouraged me to report our finding at a conference on interstellar dust held from September 8–13, 1989, in Capri. With this report we wanted to establish our priority in case we really had produced C_{60} [10]. On the other hand, I didn't want that a large number of researchers would jump on this and eventually scoop us. The conference in Capri was relatively small and was joined exclusively by astronomers and interstellar dust researchers. I thus thought the risk would be quite small that our finding would leak into a larger community. However, Mike Jura, an attending astronomer, right away reported our work to Harry Kroto to whom he was acquainted. I didn't know that, but we learned later that Harry and his student Jon Hare soon started to work to reproduce our results. The race was on but fortunately we so far were in a leading position.

To come back to the isotope replacement: The required commercial ^{13}C powder (99% purity) we could borrow from colleagues of the department. We soon realised that the main technical problem was to produce electrode rods from the ^{13}C powder material which were sufficiently rigid not to crumble away when pressed together for electrical contact. Not without reason the ^{13}C container stated: "amorphous carbon" implying that this powder cannot easily be converted into graphite. Kosta, as Fostiropoulos liked to be called, constructed a die by which the powder could be compressed inside a thick-walled quartz tube and simultaneously heated by running a current through two tantal rod electrodes between which the powder was enclosed. The die could be evacuated, and the body weight turned out to be sufficient for exerting the required pressure. A few, relatively stable 3 mm diameter rods could be produced in this way and could also be successfully evaporated. The UV-VIS and IR spectra of both kinds of the produced carbon soot are depicted in Fig. 3.

I still remember the excited outcry of Kosta when he examined the IR spectra for the first time: The displacement was there and had just the proper amount. Furthermore, we also carried out partial isotopic replacements. In the IR this didn't yield a fence-like pattern of isotopomeric sup-peaks, but just a broadening of each of the absorption features. Thus the absorbing species must be a fairly big carbon molecule

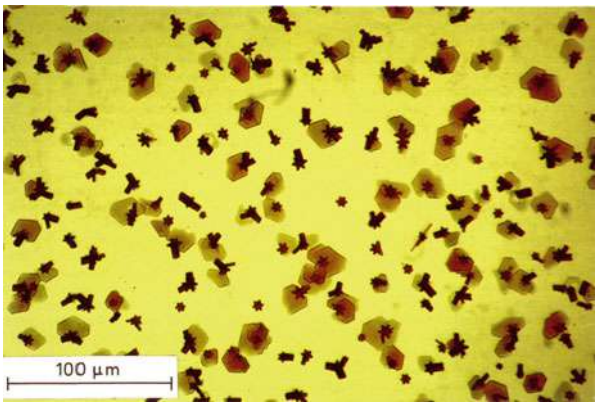

Fig. 4 Microscopic picture of crystals of C_{60} (with traces of C_{70}), obtained by drying a benzene solution of the fullerenes on a glass slide. The picture was taken in transmitted light

– again, all was pointing towards C_{60}. We submitted our results to Chem. Phys. Letters for publication [11]. After acceptance of that paper, I sent preprints to colleagues from whom I did know that they may be interested. With the present work, I thought, our task would be finished: C_{60}, as a kind of "noble soot," should remain buried in the regular soot and never be recovered from there. How wrong I was! But again we had good luck. In response to our preprint, I received a letter by Werner Schmidt, a chemist working on polycyclic aromatic hydrocarbons (PAHs), whom I happened to know, who congratulated us for our finding and gave us an advice how to separate C_{60} from the soot. He suggested that according to his experience with similar large PAHs, C_{60} should sublime at about 500 °C and be soluble in trichlorobenzene. Both approaches worked – we however took ordinary benzene. It was the beginning of May 1990 that we had the material in our hand in the form of coated films and as tiny crystals as shown in Fig. 4. The crystals we decided to be called "fullerite."

A New Form of Solid Carbon

In the following, we tried to co-ordinate our efforts in Heidelberg and Tucson. Don and his student Lowell Lamb should care for characterising the solid by X-ray diffraction, and we concentrated on the optical properties. Both parties were also seeking for a convincing mass spectrum of fullerite. The later task turned out to be more difficult than expected. Laser desorption MS was not standard at that time and the commonly used electron ionisation sources couldn't be heated high enough to evaporate and ionise fullerenes. Fortunately, there was an ion sputter source TOF-MS in our department which was the prototype of an instrument planned for the in situ analysis of cometary dust in a space mission. With this instrument, our samples showed a clear peak at 720 amu (C_{60}) and a smaller at 840 amu (C_{70}) – similar to the already well-known mass pattern of fullerenes as observed by Kroto, Smalley, and co-workers. Occasionally, the spectrum also showed fragmentation of C_{60} into lower

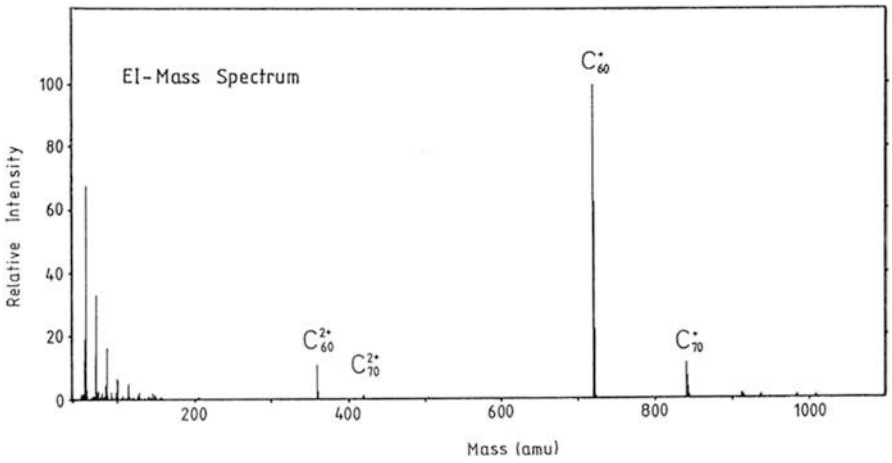

Fig. 5 Mass spectrum of one of our fullerene samples, obtained by electron ionisation of the fullerene vapour. Notice the intense C_{60} peak at 720 amu with its isotopic C^{13} splitting. The other peaks come from C_{70} and the doubly charged species

even masses, a phenomenon also known from previous MS works. Furthermore, the C_{60} peak exhibited a sub-structure of ^{13}C isotopomeres in a proportion consistent with a 60 carbon atom species. At about the same time, the Tucson team obtained an electron impact ionisation MS of much better quality showing no fragmentation (similar to a mass spectrum of our samples, obtained later by Helmut Schwarz and co-workers from the TU Berlin, shown in Fig. 5). The researchers in Tucson who made the measurements did allow using that spectrum only under the provision that they become co-authors. This we couldn't accept. We hoped the paper would be accepted without explicit showing a mass spectrum.

The X-ray diffraction pattern of the crystal material could be indexed by assuming a hexagonal lattice, i.e. hcp, one of the two possible closest packing of spheres. With the indexing, however, we faced some difficulties which we interpreted by the absence of long-range crystal order. One has to realise that our crystals were far from pure C_{60}: First, there was an about 10% admixture of C_{70}, and second, the solvent was embedded into the structure. This may explain why later researchers working with purified C_{60} fullerites obtained an fcc close packing structure. The curious fact that in both kinds of indexing (hcp and fcc), some diffraction peaks were missing could be explained much later by the hollow shell geometry of C_{60} [12]. Our electron diffraction data confirmed the X-ray results, both leading to a C_{60} nearest neighbour distance of 10.2 angstrom. This implies for fullerite a slightly shorter extended π-system as for graphite.

The UV-VIS and IR absorptions of fullerite didn't reproduce any of the astronomical inter- or circumstellar features known at that time. Quite recently, however, the IR emissions of C_{60} have been observed by space-borne telescopes in some planetary nebulae, making C_{60} the largest interstellar molecule so far detected [13].

We finally did write a paper in which we presented all our findings and we agreed to submit the manuscript to Nature. Don was writing most of the text in his rather

readable style and agreed to be the corresponding author. Of course, there was always the fear that we may become scooped. Jon Hare had written a letter in which he told that he could reproduce our results – but how far he progressed beyond that he didn't say and we didn't know. Independently, and unknown to us Don Bethune and Gerard Meijer from the IBM research centre in Almaden were also on our tracks. Five years after discovery, the production of C_{60} as substance was in the air!

Despite this I went into vacations during August since all experimental data were at hand – I thought. However, when I returned, Don was very nervous: The reviewers demanded a mass spectrum! As I mentioned, we had such spectrum but couldn't use it for copyright reasons and so we had to use the inferior mass spectrum obtained in our department. In a rush we provided that spectrum, and the reviewers – Harry Kroto and Bob Curl as it turned out later – were happy and we were very much relieved. The publication date in Nature was scheduled for end of September 1990 [14].

The news of our success leaked through the community. Rick Smalley had contacted Don and Don asked me to announce our discovery on occasion of the fifth ISSPIC conference held in Konstanz, Germany. For this purpose Rick promised me 5 minutes of his lecture which was scheduled for the morning of September 12, 1990. I still remember going to the lecture hall by bus, very nervous, and delivering my announcement. When I finished there was a long moment of silence. Then Rick slowly rose from his seat and started clapping his hands. The audience took the opportunity to do the same. In retrospect I think this was one of the most rewarding moments of my career.

Since this section concerns new forms of carbon, it should be mentioned that other forms besides diamond, graphite, and fullerenes (i.e. closed cage carbon structures including nanotubes) may exist. A colleague of mine in the institute, the mineralogist Ahmed El Goresy, many years ago reported a finding he made in the meteor impact crater located in Nördlingen (Germany). His sample consisted of tiny pieces of heavily shocked graphite, which contained a metallic shining carbon phase. The lattice parameters of this phase could be determined and were found to be entirely different from that of graphite [15]. The small sample size and the poorness of the analytical techniques of that time did not allow the atomic structure of the phase to be determined. Attempts were made by some researchers to relate this phase to the so-called carbynes, i.e. structures based on sp-carbon chains. But these remained inconclusive. Reports on solids apparently based on carbyne structures nevertheless occasionally surface the literature here and there, suggesting that the carbon system may still contain some surprises.

Epilogue

Our discovery earned a lot of recognition, in particular among chemists. In bewilderment it was recognised that it were physicists who were "harvesting in their gardens." An enormous boost of fullerene research happened when Robert Haddon and co-workers from the Bell research labs discovered the superconductivity of

fullerides (i.e. the compound K_3C_{60}) [16]. Now also the large community of solid-state physicists joined the enthusiasm about C_{60}. Initially, there was a large demand for samples but soon researchers could make fullerenes by their own. The carbon evaporators used for this purpose became called "fullerene generators." Our old carbon evaporator was taken for display into the "Deutsche Museum" in Bonn. Also, already existing or newly founded chemical companies produced fullerenes commercially by using essentially our technique. Probably, lots of patents were filed in this field. Don and I also had filed a patent on the production method, which not only was challenged by a similar later patent by Rick Smalley but also made Fostiropoulos very upset because he felt himself and his contribution not appropriately recognised. Books were written about the story of fullerene discovery and in 1992 BBC made an exciting science movie about this topic [17]. After a few years, it became more and more silent about fullerenes and the carbon nanotubes took over the leading position in carbon science. It became almost forgotten that Sumio Iijima, who is regarded as discoverer of nanotubes, harvested his first multi-walled nanotubes from the electrodes of a fullerene generator. Then, fairly late in the fullerene saga, for their discovery, Bob Curl, Harry Kroto, and Rick Smalley earned the Nobel Prize in Chemistry in 1996. Recently and better timed, A. Geim und K. Novoselov got the Nobel Prize in Physics for the preparation and characterisation of graphene layers. Apparently, the story of graphitic carbon and its many phases is not over yet.

The late Harry Kroto was a strong believer that many of the so far unexplained interstellar absorptions originate from C_{60}. In an interview shown in the BBC movie [17], he was asked whether C_{60} may be the carrier of the mysterious diffuse interstellar bands (DIBs) which I mentioned above. The interviewer challenged Harry by stressing that so far no C_{60} absorption features in the DIB range have been found. Harry emphatically replied: "They are wrong!" With that somewhat surprising statement the movie ends. About 20 years later, it turned out that rather than the neutral species, the C_{60}^+ ion indeed shows absorptions which coincide with some of the DIB features [18]. After all, Harry was right and could still enjoy the fulfilment of his prediction.

References

1. Huffman DR (1977) Adv Phys 26:129
2. Draine BT (2003) Annu Rev Astron Astrophys 41:241
3. Weltner W Jr, Walsh PN, Angell CL (1964) J Chem Phys 40:1299
4. Krätschmer W (1986) Astrophys Space Sci 128:93
5. Herbig E (1975) Astrophys J 196:129
6. Schnaiter M, Mutschke H, Henning T, Lindackers D, Strecker M, Roth P (1996) Astrophys J 464:L187
7. Krätschmer W, Sorg N, Huffman DR (1985) Surf Sci 156:814
8. Rohlfing EA, Cox DM, Kaldor A (1984) J Chem Phys 81:3322
9. Kroto HW, Heath JR, O'Brien SC, Curl RF, Smalley RE (1985) Nature 318:162
10. Krätschmer W, Fostiropoulos K, Huffman DR (1990) In: Bussoletti E, Vittone AA (eds) Dusty objects in the universe. Kluwer, Dordrecht
11. Krätschmer W, Fostiropoulos K, Huffman DR (1990) Chem Phys Lett 170:167

12. Fischer JE, Heiney PA, McGhie AR, Romanow WJ, Denenstein AM, McCauley JP, Smith AB III (1991) Science 252:1288
13. Cami J, Bernard-Salas J, Peeters E, Malek SE (2010) Science 329:1180
14. Krätschmer W, Lamb LD, Fostiropoulos K, Huffman DR (1990) Nature 347:354
15. El Goresy A, Donnay G (1968) Science 161:363
16. Hebard AF, Rosseinsky MJ, Haddon RC, Murphy DW, Glarum ST, Palstra TTM, Ramirez AP, Kortan AR (1991) Nature 350:600
17. BBC Horizon "Molecules with Sunglasses" 1992
18. Campbell EK, Holz M, Gerlich D, Maier JP (2015) Nature 523:322

Part II

Molecular Structures of Fullerenes

Preparation, Extraction/Isolation from Soot, and Solubility of Fullerenes

2

Steven Stevenson

Contents

Abstract

The goal of this chapter is an overview of various methods used to prepare and extract fullerenes. With limits on cited references, this chapter cannot be a comprehensive review. We begin with a historical discussion surrounding their serendipitous discovery. Next, we introduce a variety of production methods, with each approach having its unique advantages and disadvantages. Regardless of the chosen synthesis, the generated soot represents a complex mixture of nanomaterials ranging from amorphous carbon to fullerenes to metallofullerenes,

S. Stevenson (✉)
Department of Chemistry, Purdue University Fort Wayne, Fort Wayne, IN, USA
e-mail: stevenss@pfw.edu

X. Lu et al. (eds.), *Handbook of Fullerene Science and Technology*,
https://doi.org/10.1007/978-981-16-8994-9_20

if metal is added to the plasma. During fullerene formation, the coproduction of structural isomers further complicates subsequent purification efforts. For this reason, the second half of this chapter describes efforts to simplify the complexity of soot extract based on some aspect of selectivity. Strategies to obtain specific types of fullerenes and metallofullerenes include soot extraction with selective solvents, solubility differences for fractional crystallization, electrochemical methods, and chemical derivatization to isolate otherwise unstable species. Further details describing the purification, characterization, and application development of fullerenes and metallofullerenes are located in other chapters. Herein, we primarily discuss key and seminal works – with a time line beginning with the birth of fullerene-containing soot, to the advent of new methods of synthesis, and concluding with strategies to selectively extract these carbon structures of wondrous molecular architectures that are fullerenes and endohedral metallofullerenes.

Keywords

Synthesis · Preparation · Soot · Extraction · Isolation · Purification · Separation · Solubility · Fullerene · Metallofullerene

Introduction

Carbon clusters have long fascinated a diverse array of scientists for many decades. With fields of expertise ranging from chemists to engineers, researchers continue their quest for application development, e.g., catalysis and combustion. In astronomy, astrophysicists seek to understand the role of small carbon clusters spectroscopically located in carbon stars and comet tails. Indeed, early studies on carbon cluster formation ultimately lead to the discovery of C_{60} buckminsterfullerene. Note the serendipitous synthesis of fullerenes has its roots in fundamental research. Even to the present day, these carbon-cage clusters, their formation, fundamental science, and application development, still intrigue scientists. This is true even as new forms of carbon emerge.

The common allotropes of carbon (e.g., graphite and diamond) are well known for centuries. In contrast, the fullerene time line begins more recently, with seminal studies originating only since the 1980s. It is during this decade that fullerenes are *experimentally* synthesized and discovered. Fullerenes are born, along with the intriguing idea that metals can be trapped inside their carbon cages to produce a new class of molecules, i.e., metallofullerenes [1, 2].

The breakthrough for empty-cage production occurs in 1990, when Krätschmer and Huffman publish their landmark synthesis of fullerenes [3]. Still used in many labs today, the electric arc method immediately opens the floodgates of sample availability for C_{60} and C_{70} fullerenes. With macroscopic quantities of purified C_{60} finally in the hands of researchers, the number of fullerene publications skyrockets in the 1990s. This paradigm shift away from laser vaporization and toward the electric

arc allows for many long-awaited experiments with fullerenes. Note the 5-year time lapse (1985–1990) between the microgram quantities prepared from the laser vaporization method (1985) [2] to the arrival and invention of Krätschmer and Huffman's (K-H) [3] electric arc synthesis. In retrospect, this electric arc technique becomes a primary production method for making kilogram quantities of fullerene soot. It is the arc-reactor that produces the gram-scale quantities of C_{60} purified and disseminated during the 1990s and beyond.

During the early 1990s, a key question emerges. Can fullerenes be synthesized only from a laser source or an electric arc? Intuitively, one envisions other approaches to vaporize a carbon source while under a reduced pressure environment in the presence of helium or argon. Between 1990 and 2020, other attempts to produce fullerenes are reported, and we briefly discuss them below. Although far less common, these alternative strategies include their formation from solar energy, radio-frequency furnace, CVD, and combustion. On a side note, the 1990s also represents the arrival of carbon nanotubes. More recently, the rapid rise of graphene-based materials and research has emerged. Other chapters focus on these alternative forms of carbon, e.g., nanotubes and graphene.

Regardless of which fullerene is desired, the fundamental hurdle to overcome is the production and isolation of macroscopic quantities of purified and pristine samples. Shown in Fig. 1, the bottommost levels demonstrate a critical requirement prior to subsequent experiments, application development, and sales. All levels of the pyramid revert to a foundational need to produce the carbon-based material. In the case of fullerenes and metallofullerenes, the first step is their production. Once formed, the second stage is an effective way to extract the desired species from a complex mixture of nanomaterials embedded within the collected soot.

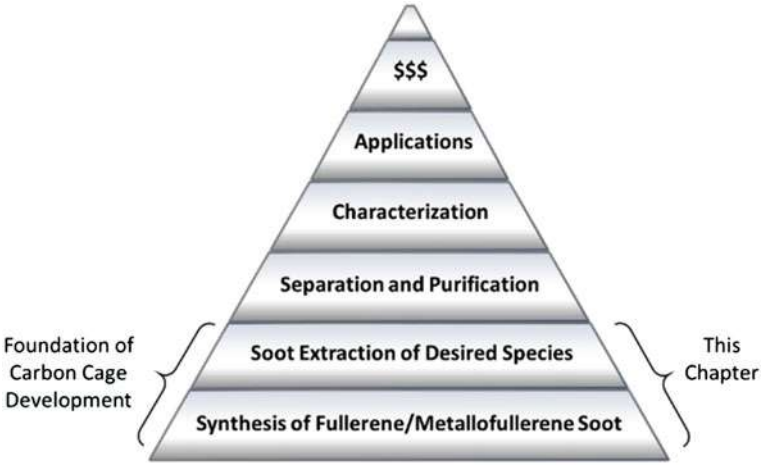

Fig. 1 Foundational importance of soot preparation and extraction

We conclude this fullerene chapter with several strategies for their extraction and isolation. Our discussion includes selective methods based on differences in solubility, electrochemistry, and reactivity. More recently, the chemical stabilization of otherwise reactive species in soot now permits the discovery and structural characterization of novel carbon cages – with and without encapsulated metal clusters.

Discussion

Preparation Methods for Fullerenes/Metallofullerenes

Laser Synthesis

Many fullerene reviews begin with the landmark paper of Kroto, Curl, and Smalley et al. [2] in 1985. This is certainly logical because the discovery of fullerenes dates back to their seminal publication in *Nature* [2]. However, in this chapter we begin 1 year earlier with the 1984 work of Rohlfing et al. [4] Although less discussed, it is historically noteworthy because this research group at Exxon also uses the laser vaporization of a carbon substrate. In doing so, they generate and analyze a supersonic beam of carbon clusters. Shown in Fig. 2 is the mass spectrum obtained downstream from the laser vaporization of a graphite rod located within the throat of a high-pressure pulsed nozzle [4]. Their experimental data suggests that two types of carbon clusters are generated. First, they observe a family of *smaller* size clusters with an odd number of atoms for carbon clusters C_n, $1 < n < 30$. The authors also create an even number of carbon atoms for a second family of *larger* carbon clusters, C_{2n}, $20 < n < 90$. Rohlfing et al. [4] discuss these two bimodal distributions. [Note their mass spectrum exhibits a spike at m/z of 720, which is later shown by the Smalley group in 1985 to be C_{60} fullerene.] Because this is 1984 and *before* the discovery of fullerenes, Rohlfing et al. [4] speculate a possible structure for those even numbered clusters to be a form of carbon that is crystalline. Specifically, they propose a "carbyne" form of carbon that consists of C_2 units possessing alternating short (triple) carbon-carbon bonds alternating with longer (single) carbon-carbon bonds [4]. Today, with 2020 hindsight, it appears that Rohlfing et al. [4] do indeed produce C_{60} fullerene earlier in 1984 by the laser vaporization of graphite. However, they do not correctly assign the $m/z = 720$ species as buckminsterfullerene in their publication.

Just 1 year later (1985), Smalley's collaborative team with Kroto and Curl report in *Nature* [2] their experimental findings. Shown in Fig. 3 is a schematic diagram of their laser vaporization chamber at Rice University. Using a focused pulsed laser and vaporizing carbon from the surface of a rotating graphite disk into a helium stream, they successfully obtain this landmark mass spectrum. They also observe a preferential formation of molecules corresponding to the carbon cluster peaks of C_{60} and C_{70}. For larger carbon clusters, they notice adjacent peaks being separated by

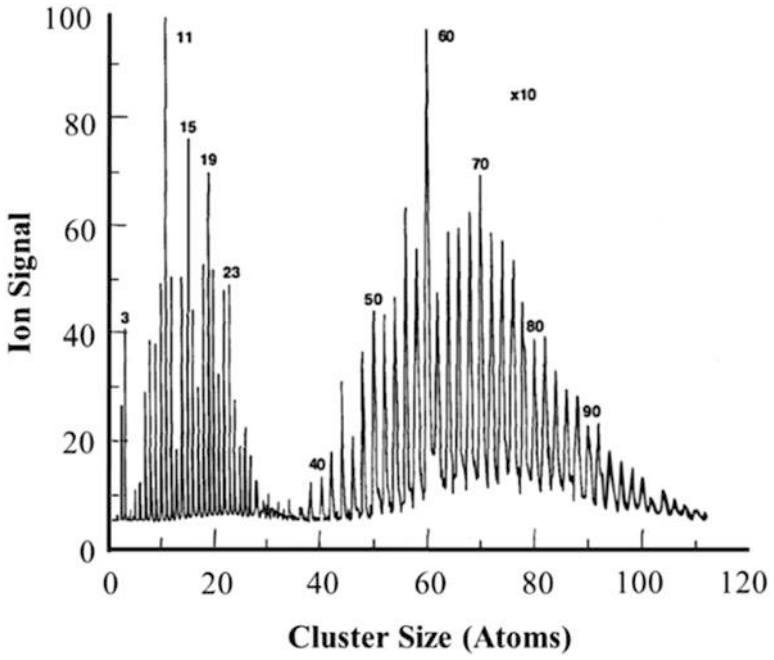

Fig. 2 Time of flight (positive ion) mass spectrum for carbon clusters produced via laser vaporization at Exxon in 1984. (Used with permission from Rohlfing et al. [4])

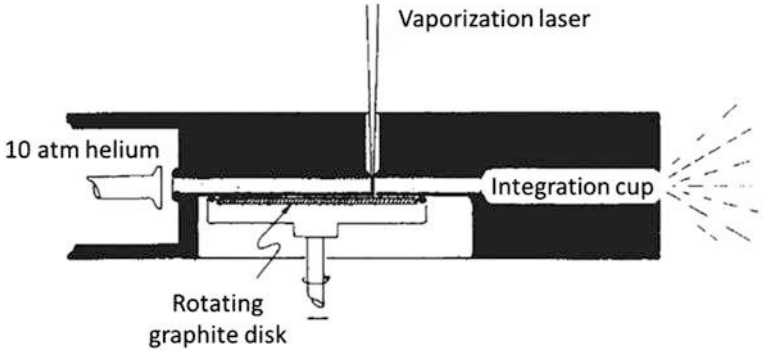

Fig. 3 Schematic showing the laser vaporization of graphite to generate carbon cluster beams. (Used with permission from Kroto et al. [2])

repeating increments of two carbon units (m/z = 24) to form the higher fullerenes (e.g., C_{76}, C_{78}, C_{84}, C_{90}, etc.) [2]. The field of fullerenes is born (Fig. 4). [The following decade, Kroto, Curl, and Smalley will receive the Nobel Prize.]

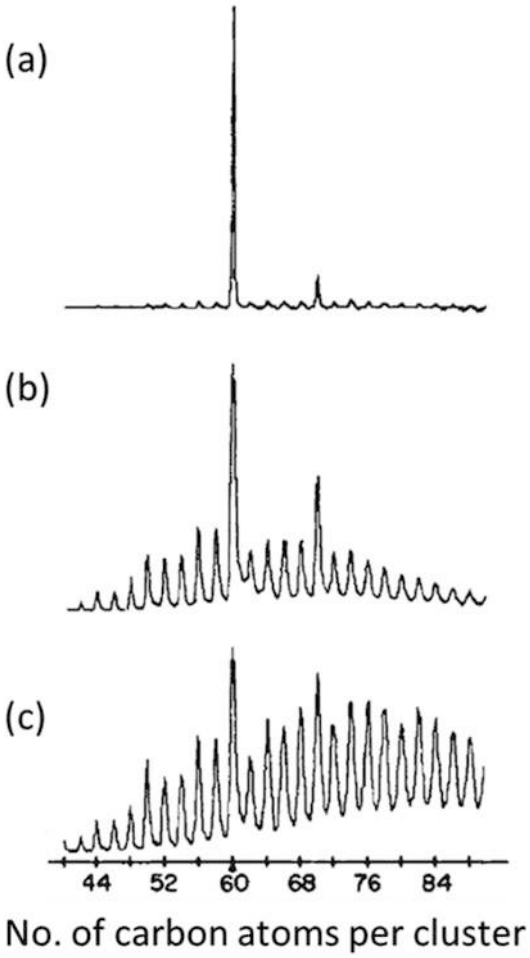

Fig. 4 Time-of-flight mass spectra of carbon clusters obtained under various pressures and collisions with helium. Mass spectral conditions (**a**) maximize cluster thermalization and cluster-cluster reactions, (**b**) utilize 760 torr of helium at the graphitic target, and (**c**) with a much lower He pressure of less than 10 torr. (Used with permission from Kroto et al. [2])

A short time later, also in 1985, Heath et al. [1] report the first experimental evidence suggesting the formation of metallofullerenes. For their laser vaporization experiments, a pulsed supersonic nozzle and lanthanum-impregnated graphite disk are used as the source of carbon and metal. The corresponding mass spectral data in Fig. 5 demonstrate the complex mixture often created when soot mixtures contain both empty-cage fullerenes and metallofullerenes [1]. A separate chapter describes their separation with HPLC stationary phases (e.g., PYE, PBB, and BuckyPrep-M) and nonchromatographic methods (e.g., Lewis acids, and selective reactivity with amines and cyclopentadiene).

Electric Arc-Synthesis

From 1985 to 1990, it is increasingly clear that fullerenes do indeed exist. Multiple labs working independently reproducibly synthesize and characterize their presence

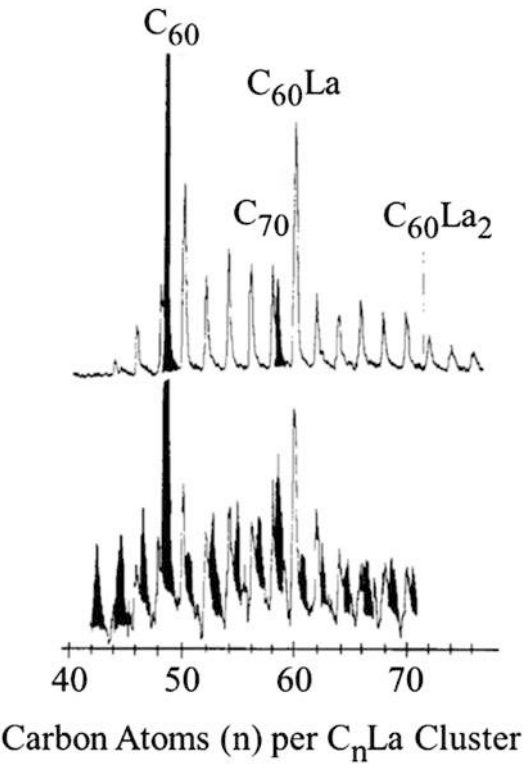

Fig. 5 TOF mass spectrum empty-cage fullerenes (shaded in black) along with coproduced La metallofullerenes (unshaded peaks). (Used with permission from Heath et al. [1])

with mass spectrometry. During this period, scientists seek to increase fullerene production from micrograms to milligrams. The problem with the laser approach used during the 1980s is the woefully small amount of soot and insufficient amounts of extractable fullerenes. Although interest is rising, research groups are in desperate need of a better way to produce soot and fullerenes. Without a paradigm shift in fullerene synthesis, many anticipated experiments are not possible without macroscopic amounts of purified C_{60} and C_{70} samples.

This historical background explains the excitement and large impact of Krätschmer-Huffman's new method to prepare fullerenes [3, 5]. The arrival of their electric arc production means that, for the first time, gram quantities of soot and fullerenes are possible. Their arc approach is inexpensive and versatile enough to accommodate a variety of chamber designs. Further, this electric arc process is later adapted to produce empty-cage fullerenes, endohedral metallofullerenes, and nanotubes.

Now it is important to discuss two key works [3, 5] published in 1990 by the research team of Krätschmer and Huffman. In May, we are introduced to the vaporization of graphite rods by their resistive heating in the presence of a quenching gas [5]. The resulting "carbon smoke particles" are collected on substrates and analyzed. By comparing C-12- and C-13-labeled samples prepared from their arc

synthesis, the authors obtain and utilize infrared and ultraviolet absorption spectra to provide experimental evidence for an all-carbon, icosahedral C_{60} molecule [5]. A key finding is the agreement of their experimental number of bands with theory – all of which support a symmetrical, soccer-ball-shaped structure of C_{60}. Note the last sentence of their paper would be foreshadowing of the future. They accurately predict their K-H arc method would permit bulk quantities of extractable fullerenes from soot [5]. With the passage of time, their concluding remark is correct. Total 30 years later, we are in the pandemic year of 2020, and their electric arc method is still a popular and globally used method to synthesize carbon nanomaterials.

In their second paper (September, 1990), the Krätschmer and Huffman collaboration publish their often cited *Nature* work "*Solid C_{60}: a new form of carbon*" [3]. Specific details emerge of the synthesis, separation, and characterization of macroscopic quantities of isolated C_{60}. Special to this paper is the experimental detail provided with their new electric arc approach. They discuss resistively heating and vaporizing carbon rods under reduced pressures of 100 torr of He buffer gas [3]. Gram quantities of soot-containing fullerenes are extracted with an aromatic solvent (benzene). We see other solvents, e.g., carbon disulfide and carbon tetrachloride, that also dissolve and remove fullerenes from the soot matrix. As an alternative to solvent extraction, Krätschmer and Huffman also discuss sublimation as an alternative to not only remove fullerenes from soot, but also as a way to prepare thin films of C_{60}-coated surfaces [3]. Indeed, these coatings are characterized by IR and UV-vis spectroscopy.

Many people cite this reference primarily as the first electric arc process [3] invented to produce fullerenes. This is true, but the paper also lays the groundwork for future studies on soot extraction. This work also contains some of the first experimental characterization of C_{60} – all of which are possible because their arc-process permits the first large quantities of purified C_{60} [3]. Indeed, dating 30 years back in time to this seminal paper, Krätschmer and Huffman could isolate 100 mg of C_{60} in only 1 day [3]. Similar to their earlier 1990 paper [5], the authors conclude this second paper [3] by predicting the impact of their electric arc discovery. Their last sentence accurately predicts the opening of doors to fundamental studies and application development of fullerenes – all made possible by their 1990 discovery [3].

This paper *experimentally* settles the great 5-year debate (1985–1990) of scientists arguing over the structure of C_{60}. During that period, not everyone is fully convinced of the soccer ball structure of C_{60} fullerene. Today's generation of carbon nanomaterial scientists is well aware of the Krätschmer-Huffman discovery of the electric arc process for fullerene synthesis. Lost sometimes in the present day, though, is recognition of their pioneering, characterization efforts that *experimentally* supported C_{60}'s I_h structure [3].

By December of 1990, Smalley et al. [6] successfully isolate gram quantities of C_{60} using the electric arc reactor shown in Fig. 6. Specific parameters emerge to optimize its synthesis. Helium bleed rates of 1 sccm, 100 torr of pressure inside the reactor, 100–200 amps of current, and rms voltages of 10–20 volts are used [6]. Using this design, 10 g per hour of soot is produced. For extraction, the

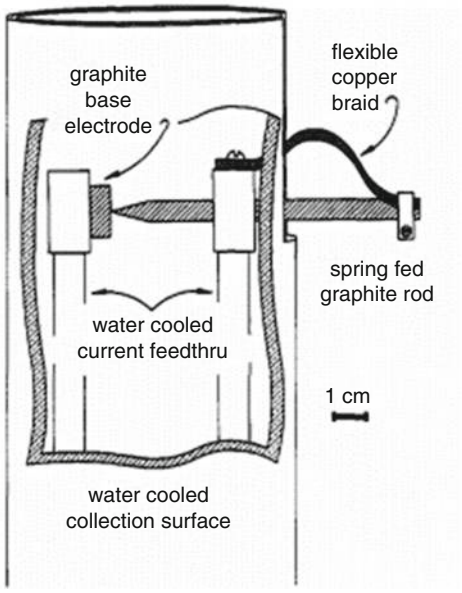

Fig. 6 Electric arc production of fullerenes in 1990. (Used with permission from Haufler et al. [6])

authors use a different extraction approach than Krätschmer and Huffman. Rather, Smalley's group uses boiling toluene in a Soxhlet extraction for 3 h to yield approximately 10% extractable fullerenes from soot [6]. Their fullerene-to-soot ratio is comparable to percent yields of many electric arc reactors currently in use.

Also in this paper are the first experimental reactions with C_{60} [6]. Electrochemical characterization is thus added to the emerging palette of seminal characterization of C_{60} in 1990. The authors use a Birch reduction to produce $C_{60}H_{36}$, with dehydrogenation to bare C_{60} via treatment with DDQ reagent [6]. Upon doing so, they accomplish a reversible reaction with C_{60}. This is the birth of functionalization chemistry on the surface of fullerene cages. The derivatization of empty-cage fullerenes and endohedral metallofullerenes is discussed in other chapters. Indeed, Smalley prognosticated the impact of their reactivity findings when he predicts a rich chemistry of chemical derivatization on the outer surface of fullerenes [6]. In terms of the interior of the cavity, Smalley also suggests the ability to fine-tune the electronic and optical properties of a fullerene upon its encapsulation of metal atoms [6]. Looking back with 20/20 hindsight from the year 2020, we witness the true fruition of their predictions. Thousands upon thousands of fullerene papers have appeared in the literature in those two predicted research areas, i.e., exohedral functionalization and endohedral encapsulation.

Simultaneous to Smalley's paper and published as sequential articles in *J. Phys. Chem.* is the contribution of Ajie et al. [7] Krätschmer and Huffman are also on this paper, along with the UCLA group of Rubin and Whetten [7]. In this work, the soluble fullerene extractable yield is increased to 14% by optimizing their reactor

parameters, e.g., current, rod diameter, graphite source, helium pressure, and choice of soot extraction [7].

In summary, 1990 is arguably the greatest year for fullerenes as defined by the number of discoveries and their long-reaching impact. From 1991 to 2020, we see the electric arc method successfully adapt to produce fullerenes, metallofullerenes, nanotubes, and a rich diversity of other carbonaceous nanomaterials.

Before moving to the next topic, let us discuss one of the published figures in Smalley's paper [6]. There is an FT-ICR mass spectrum of $[C_{60}U]^+$ ions generated from their laser vaporization of a graphite disk impregnated with UCl_3 [6]. Why is this important? This suggests that Smalley recognized that the production method of the future would not be a laser synthesis – but rather from the electric arc method. Why? First, the amount of laser-generated fullerenes is only trace quantities on the order of micrograms to milligrams of fullerene material. The electric arc, just in its first year (1990), is already making gram quantities. Second, there is no reason to believe that the electric arc approach could not also use metal-impregnated graphite as a metallofullerene source. Indeed, Smalley's last sentence of his discussion section correctly predicts that the Krätschmer-Huffman production would be amenable to making metallofullerenes [6]. In his writing, Smalley anticipates the forthcoming explosion of research in the area of fullerenes (exterior cage surface) and metallofullerenes (interior cage cavity) because of the K-H electric arc discovery.

Solar Power

Whereas the electric arc process is rightfully lauded for its ability to synthesize large quantities of soot, several issues arise during efforts to increase fullerene production. Attempts to vaporize graphite rods of increasing diameter in the arc process do not scale up appropriately. Moreover, the photochemical destruction of freshly formed fullerenes inside the reactor becomes a problem due to intense radiation emanating from the arc-plasma.

For this reason, scientists begin to explore a bright idea to make fullerenes – a solar generation approach. To mitigate the deleterious effects of arc-radiation, Chibante et al. [8] introduce in 1993 the experimental synthesis of fullerenes using solar power. The authors note two primary advantages of the solar method: (1) avoiding high intensity UV radiation associated with the arc-method and (2) delaying the clustering of carbon vapor until a darker region of the generator is reached. To demonstrate a solar-based fullerene synthesis, the authors utilize a solar flux of 800–900 W/m^2. Argon gas is used as the carrier gas with a reduced pressure of 50 torr. Vaporization of carbon is achieved with focused sunlight onto the tip of a 0.4 mm diameter graphite rod. This initial demonstration, performed at a test site in El Paso, Texas, by the Smalley group is described as the "Solar 1" fullerene generation apparatus [8].

Almost simultaneously in 1993, another research group working at the National Renewable Energy Laboratory (NREL) also demonstrates the

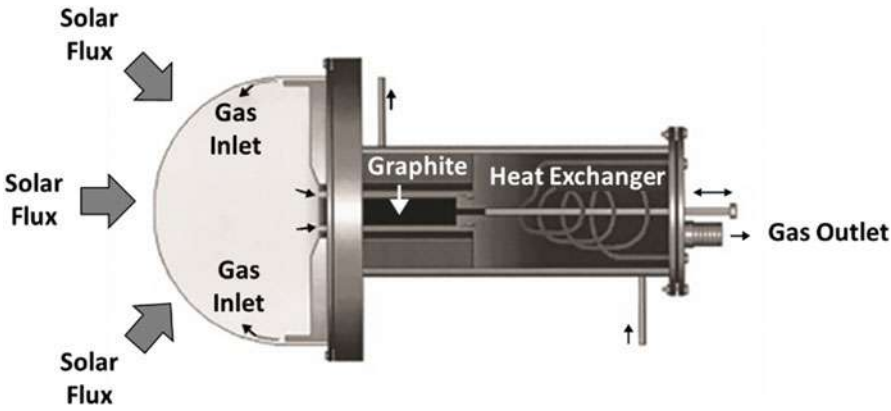

Fig. 7 Solar reactor for fullerene synthesis. (Used with permission from Flamant et al. [10])

successful synthesis of fullerenes using solar power. In their production, Fields et al. [9] use a more powerful solar furnace which delivers up to 10 kW of concentrated sunlight. Peak fluxes on the graphite target are measured at 1200 W/cm^2. They also use argon gas with a reduced pressure of 50 torr. The difference between these two experiments is the NREL team uses a more powerful flux of concentrated beam at the graphite target. Neither the vaporization rate nor fullerene yields are indicated in the paper.

By the mid-1990s, several key questions still linger. How scalable is this solar method? What is the maximum percent yield of fullerenes that can be extracted from solar generated soot? What are the upper limits of optimized production of soot per day? What are the effects of increasing solar power on fullerene production? In 2004, Flamant et al. [10] address these questions. They create an optimal solar reactor specifically designed to maximize fullerene synthesis. At the Centre Nationale de Recherche Scientifique (CNRS), they use a 1 MW solar furnace as the source of graphite vaporization [10]. Of special note is their iterative leveraging of experimental data and numerical simulations. Their models account for detailed processes such as heat transfer and chemical reaction kinetics. They report the vaporization of carbon becomes significant only at temperatures beyond 3400 K [10]. An optimal diameter of the graphite target would be 22 cm, with an output of 80–150 g of soot per hour with an effective power of 325 kW [10]. Their solar apparatus for fullerene synthesis is shown in Fig. 7.

Combustion and Flame Method

As early as 1991 [11], the feasibility of fullerene production in sooting flames is evaluated at MIT. In their seminal work, Johnson et al. [11] demonstrate C_{60} and C_{70} fullerene formation with a flame approach. Using the combustion and condensation of hydrocarbons, they report the influence of pressure (20 torr),

temperature (1800 K), ratio of carbon/oxygen (0.995), and the residence time of carbon in the flame. Optimization of these parameters yields 3 g of fullerenes per kilogram of fuel carbon [11].

In relation to the historical time line of the electric arc, this new combustion approach [11] with flames shows promise as early as 1991, just 1 year after the arrival of the K-H electric arc synthesis in 1990 [3, 5]. A seldom-discussed finding of the flame method is the flexibility of the operator to tune the ratio of C_{70} and C_{60} fullerenes [11]. By adjusting experimental conditions, one can vary the C_{70}/C_{60} ratio over a wide range from 0.26 to 5.7. This "tunability" of fullerene production is a key finding in terms of their formation. The authors also observe and discuss differences in the formation mechanisms of fullerenes in comparison to soot [11]. For example, the highest fullerene yields do not occur with the most heavily sooting flames. Rather, the yield of fullerenes increases with (1) decreasing pressure or (2) increasing temperature [11].

Five years later, in 1996, the MIT team publishes another key paper on the combustion approach with benzene, oxygen, and argon flames [12]. A key difference with this latter work is their objective to study *higher* fullerenes. Of particular interest is their formation, extraction, and HPLC separation. They target fullerenes beyond C_{60} and C_{70}. Rather, they pursue the feasibility of making and isolating larger cage structures, e.g., C_{76}, C_{78}, C_{84}, C_{90}, and C_{96} [12]. Therein, they emphasize the importance of solvent selection for extracting these less-known, higher fullerenes. As such, they develop an approach of sequential extraction with multiple solvents to achieve an efficient removal from soot [12].

In their earlier 1991 paper, Howard et al. [11] envision scaling up the flame method for a large-scale fullerene synthesis. Their prediction becomes a reality 13 years later when industry invests in their commercial production. In 2004, Frontier Carbon Corporation (established in Japan in December 2001 as a joint venture by Mitsubishi) and TDA Research publish their combustion synthesis that will produce fullerenes at an incredible scale of tons per year [13]. This transition of fullerene production from university labs to the industrial setting mitigates the decade's long dependence on individual academic groups for sample collaborations. Rather, a commercial source would produce and sell them at affordable cost. In doing so, industry would remove the long-standing sample availability problem that had lingered for two decades (1985–2004).

Technical breakthroughs in flame-based technology, inexpensive hydrocarbons, and a continuous-flame synthesis are successfully achieved with this commercialization [13]. Upon optimization of experimental parameters, soot obtained from the flame method can achieve a quite high percentage of 20% fullerene content. The authors emphasize the importance of other industrial processes beyond solely the cost of feedstock [13]. To offer fullerenes at affordable price also requires industrial advances in extraction, separation, and purification processes. A detailed study of experimental parameters is published a year later in 2005 [14]. A diagram of their flame synthesis is shown in Fig. 8 [14].

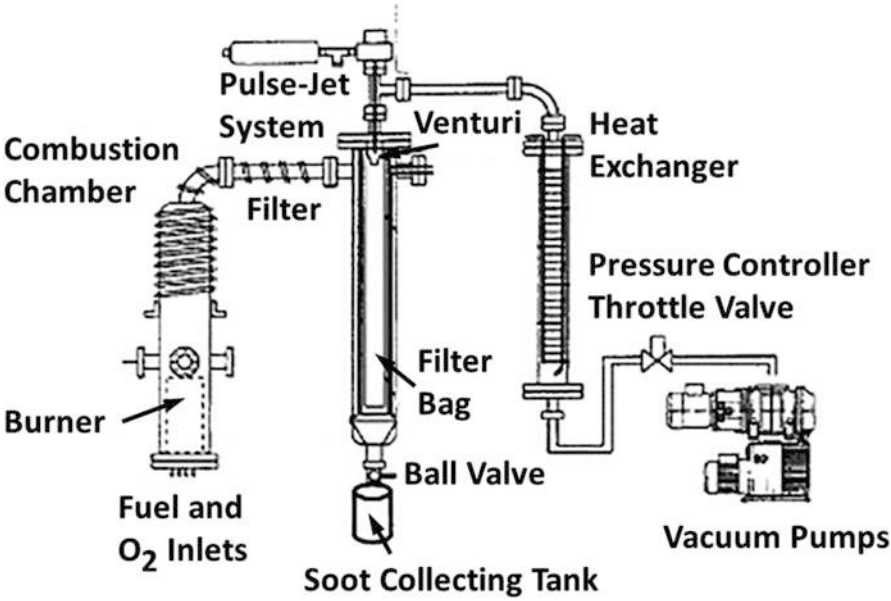

Fig. 8 Combustion synthesis under reduced pressure and pilot scale apparatus or making tons of fullerenes. (Used with permission from Takehara et al. [14])

Radio-Frequency (RF) Furnace

Other creative approaches for making fullerenes exist. Two decades after metallofullerenes are produced in the laboratory from the laser vaporization and electric arc methods, Krokos produces empty-cage fullerenes and Sc metallofullerenes (e.g., $Sc_4C_2@C_{80}$) from a plasma-coupled radio frequency furnace [15]. Shown in Fig. 9, the fullerene and metallofullerene formation zone occurs just beyond the carbon evaporation region. The source of nitrogen for the unexpected and simultaneous synthesis of $Sc_3N@C_{68}$ and $Sc_3N@C_{80}$ originates from partial decomposition of the boron nitride shield at high temperatures [15]. To this date, the RF furnace method of producing endohedrals is rarely used. Lower temperature methods, such as the RF approach, are more amenable to metals possessing lower first ionization energies (e.g., La, Eu). In contrast, the electric arc approach appears better-suited for endohedral metals possessing higher ionization energies (e.g., Y, Sc) [15].

Because the arc process establishes itself as a viable method for fullerene synthesis, alternative production approaches compare their efficiencies with the electric arc. Marković et al. [16] analyze the fullerene production made from RF discharge methods. Similarities between RF and electric arc processes include their kinetic model of fullerene formation. The fullerene yield is dependent on the carbon concentration, velocity of the plasma flame, and the rotational temperatures of C_2

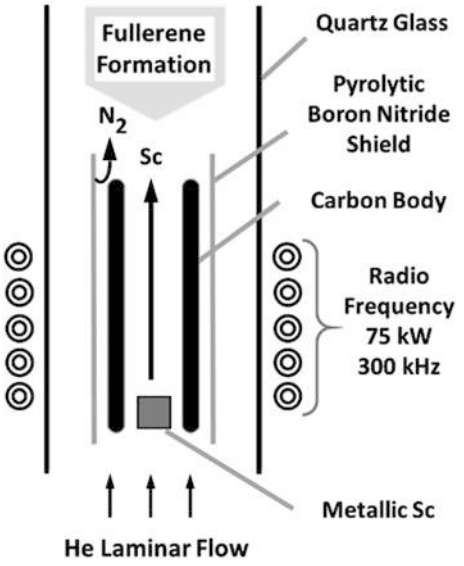

Fig. 9 Fullerene synthesis using the RF furnace. (Used with permission from Krokos [15])

radicals. Their study indicates the fullerene yield is high for either method, but with the caveat of a mean rotational temperature of C_2 radicals needing to be higher than 3000 K. However, a significant difference between these approaches is a larger zone of fullerene formation associated with the RF discharge technique.

Extraction and Isolation of Fullerene/Metallofullerenes from Soot

Regardless of the chosen production method, one must still extract the fullerenes. The composition of soot is a complex mixture of amorphous carbon by-products. Fullerenes are a minor component of soot. The soluble portion, i.e., fullerene and metallofullerenes, obtained from a typical arc generator is typically only 5–15%, by mass. Of the extracted fullerenes, 85–95% of this soluble material is a C_{60}/C_{70} mixture. The remaining 5–15% of soluble fullerenes is higher fullerenes (e.g., C_{76}–C_{150}). The process of soot extraction often uses an organic solvent, many of which are aromatic solvents or carbon disulfide.

A typical soot extract contains a range of fullerenes with different carbon sizes and shapes. Multiple structural isomers are present for higher fullerenes (e.g., C_{78}, C_{80}, C_{82}, and C_{84}). In such extracts, 50–100 unique fullerene isomers can complicate purification efforts. These complex mixtures often represent a separation nightmare. For a given fullerene, finding unique retention times without coeluting and contaminating fullerenes can require multiple HPLC stationary phases and tedious fraction collection.

Selective Solubility

Initial soot extractions dating to the early 1990s often utilize aromatic solvents. A primary objective at that time is demonstrating that fullerenes (i.e., C_{60} and C_{70}) are successfully made from a particular production technique. In Krätschmer and Huffman's seminal paper [3], they use benzene to remove fullerenes from soot. Alternative solvents for soot extraction include carbon disulfide and carbon tetrachloride [3]. This early work lays the foundation for other research groups, such as those from Diederich and Ruoff, who strategically use higher boiling point solvents, (e.g., trimethylbenzene and trichlorobenzene) to selectively extract giant fullerenes from soot [17–19]. For large metallofullerene cages above 100 atoms, the use of trichlorobenzene is used recently (2016) by Cai et al. [20] in the extraction process of isolating $La_2C_2@C_{102}$ and $La_2@C_2@C_{104}$. This work also provides a perspective on the top-down formation mechanism of fullerenes [20].

Revisiting the historic year of 1990, the Smalley group introduces the Soxhlet extraction of fullerenes from soot with boiling toluene [6]. Since the dawn of the fullerene era, scientists are already exploring a variety of extraction conditions. In 1992, Shinohara et al. [21] seek solvents best suited for extracting the higher fullerenes. Shifting focus beyond the more common C_{60} and C_{70}, they look for answers to the following questions: What are the upper limits of carbon cage size? What solvents are best suited for extracting higher fullerenes? By using the scheme shown in Fig. 10, the authors demonstrate the idea of selective solvent extraction based on solubility differences [21].

In their initial step, Shinohara et al. [21] use benzene as a preliminary step to preferentially extract the usual C_{60} and C_{70} that dominate fullerene product distributions. To the depleted soot, the authors introduce a second solvent, quinolone, to extract higher fullerenes. Additional use of quinolone permits the extraction of carbon cages up to C_{500} [21]. In doing so, they demonstrate the need for different solvents to customize the extraction process for giant fullerene sizes.

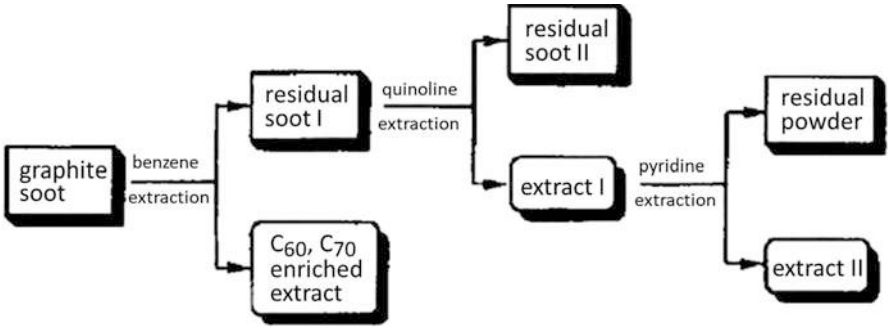

Fig. 10 Strategic sequence of benzene, quinoline, and pyridine for extracting higher fullerene cages from soot. (Used with permission from Shinohara et al. [21])

When the arc-synthesis of metallofullerenes emerges in the early 1990s, endohedral soot extractions and empty-cage fullerenes initially use similar solvents. Because the stability of endohedrals is not well-understood during these early years, anaerobic extractions are used to safeguard against metallofullerene degradation from O_2 present in air. This is why in 1992, Bandow et al. [22] report the extraction of La endohedral soot with the commonly used solvent, toluene, but with anaerobic sampling and extraction under nitrogen flow. In this manner, they successfully extract La@C_{76}, La@C_{82}, and other La@$_{2n}$ species in order to obtain a multiplicity of octets in their EPR spectra [22]. They experimentally confirm the air-sensitivity of La endohedrals by noting the decrease in EPR signal intensity upon exposure to air.

A few years later, Ding et al. [23] publish in 1996 an efficient method using DMF as the solvent of choice for metallofullerenes. With a selective extraction and under a N_2 atmosphere, they obtain enriched samples (5–15%) of Ce@C_{2n} endohedrals [23]. They note that DMF strongly discriminates against C_{60}, C_{70}, and higher empty-cage fullerenes. Subsequent HPLC of DMF-enriched endohedrals permits a facile, one-step HPLC isolation of metallofullerenes.

In 1997, Sun et al. [24] develop a high-yield extraction of metallofullerenes from soot using pyridine as a solvent at high pressure and elevated temperatures. In their study of a range of lanthanide-based metallofullerenes, they suggest encapsulated metals with the lower +2 oxidation states are especially difficult to extract. This phenomenon is in contrast to +3 lanthanides. Based on mass spectral evidence, they establish a relationship between the endohedral yield obtained after soot extraction versus the metals' oxidation state and ionic radii [24].

Six years later in 2002, Sun et al. [25] perform soot extraction studies at elevated temperatures. In their work, Gd@C_{82}, Tb@C_{82}, and Sm@C_{82} are isolated using a high-heat extraction with DMF solvent, all while under a nitrogen atmosphere [25]. Also in 2002, Lian et al. [26] use DMF in the extraction of La-based endohedrals, which are made in the arc-process from an La-Ni_2 alloy. The authors suggest that Ni may have a catalytic role in selectively synthesizing metallofullerenes [26]. In 2002, the Gu group use DMF to extract arc-generated soot prepared from Sm_2Co and $GdNi_2$ alloys [27]. The use of transition metal catalysts, in combination with DMF, leads to purified Sm@C_{82} and Gd@C_{82} endohedrals [27]. Two years later, the Gu group [28] expand their use of selective solvents and create a multistage extraction using carbon disulfide, DMF, pyridine, and aniline. This multisolvent approach permits enriched samples of divalent and trivalent metallofullerenes, such as Yb-, Ca-, Gd-, and Tb-encapsulated atoms [28].

Solvent-Free Extraction

Some extractions of fullerene-containing soot during the 1990s avoid solvents altogether. Thermal based approaches use temperature and sublimation to achieve selective separations of fullerene and metallofullerenes. For example,

Yeretzian et al. [29] obtain a gradient sublimation of La-based endohedrals in 1993 using this approach.

Another interesting approach is introduced in 2008 by Angeli et al. [30], who extract arc-generated soot with molten 9-methylanthracene. Their ultimate goal is to selectively react and remove empty-cage fullerenes. This method provides samples enriched in metallofullerenes [30]. The strategy in this approach is based on metallic nitride metallofullerenes remaining as unreacted species with the simultaneous removal of empty-cage fullerenes as their anthracene derivatives. This approach is categorized as a reaction-based, selective extraction method capable of isolating and purifying samples of $Lu_3N@C_{80}$ and $Sc_3N@C_{80}$ [30].

Electrochemical Extraction

Diener and Alford [31] open the door in 1998 to the extraction of small band gap fullerenes. This is a significant achievement because scientists are puzzled about the absence of *extractable* fullerenes between C_{70} and C_{76}. In their *Nature* paper, intermolecular bonds are broken using electrochemical reduction to release the anions of these otherwise insoluble fullerenes [31]. With electrochemical extraction, C_{74} is reduced and rendered as a soluble anion for its subsequent isolation and characterization. Likewise, the chemical oxidation of Gd-metallofullerenes permits the extraction of $Gd@C_{60}$ and $Gd@C_{74}$ [31]. Either approach permits the study of very low band gap fullerenes such as C_{74} – with or without encapsulation of a gadolinium atom.

Four years later in 2002, the selective reduction of endohedrals in soot is demonstrated for $Gd@C_{82}$ and $Gd_2@C_{80}$. Sun et al. [32] show the extractability of otherwise insoluble $M@C_{60}$ and $M@C_{70}$ (M = Gd and Y) [32]. The significance of electrochemical extraction is permitting the study of new fullerene species that previously could be neither isolated nor characterized. Soon thereafter in 2004, Tsuchiya et al. [33] leverage the reduction of metallofullerenes into an isolation method for $La@C_{82}$. Two years later in 2016, these two approaches (i.e., DMF extraction and subsequent chemical oxidation) are combined when Tsuchiya et al. report the isolation scheme shown in Fig. 11 [34].

The 2005 work by Lu et al. [35] is significant because it combines a variety of advances in soot production, extraction, and separation areas – all directed toward the isolation of $Gd_2@C_{80}$. Specifically, they use an Al-Ni alloy in the electric arc to maximize the abundance of $Gd_2@C_{80}$ in soot [35]. In their next step, they determine an optimal ratio of toluene and THF to obtain a highly purified sample of $Gd_2@C_{80}$ of higher than 95% yield [35]. This is a noteworthy accomplishment to isolate an endohedral in great purity without being fully dependent on HPLC separations and fraction collection.

For a different type of metallofullerene, Céron et al. [36] successfully demonstrate in 2013 a selective oxidation with acetylferrocenium to separate I_h and D_{5h} isomers of $Sc_3N@C_{80}$. This work by Echegoyen's group is a great achievement

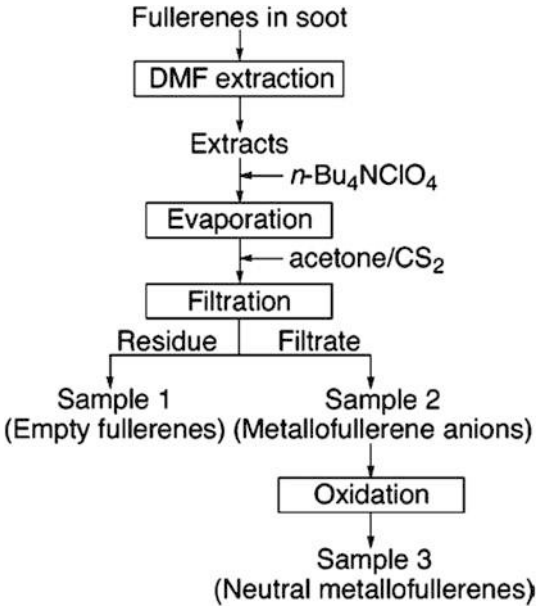

Fig. 11 Selective extraction of fullerene soot with DMF and subsequent chemical oxidation to separate different types of fullerenes. (Used with permission from Tsuchiya et al. [34])

given the difficult HPLC separation and chromatographic challenge of resolving these two structural isomers.

Chemical Stabilization

Despite the passage of 15 years since the arrival of macroscopic quantities of fullerene soot in 1990 [3, 5], scientists still know little information about the "missing" fullerenes. As an example, refer to the peaks of La@C_{60}, La@C_{70}, and La@C_{82} that appear in the mass spectra of the 1991 paper from Smalley's research group [1]. In contrast, when the electric arc method is used to generate soot that is extracted with toluene, La@C_{82} is easily detected in mass spectra. Where are these missing fullerenes La@C_{60} and La@C_{70} produced from the laser method? Clearly, the product distribution of soot extracts is different and depends on which technique, i.e., electric or laser method, is used in their synthesis.

In a key work, Nikawa et al. [37], from the team of Akasaka and Nagase, discover that endohedral "missing" fullerene cages can be stabilized by their reaction with dichlorophenyl radicals produced during their soot extraction with trichlorobenzene. Once derivatized, these functionalized "missing" cages can then be extracted, purified, and characterized. As such, it becomes possible to identify their carbon cages and symmetries. These derivatives are amenable to X-ray crystallographic analysis, as reported for La@C_{74} (2005) [37], La@C_{72} (2006) [38], and La@C_{80}

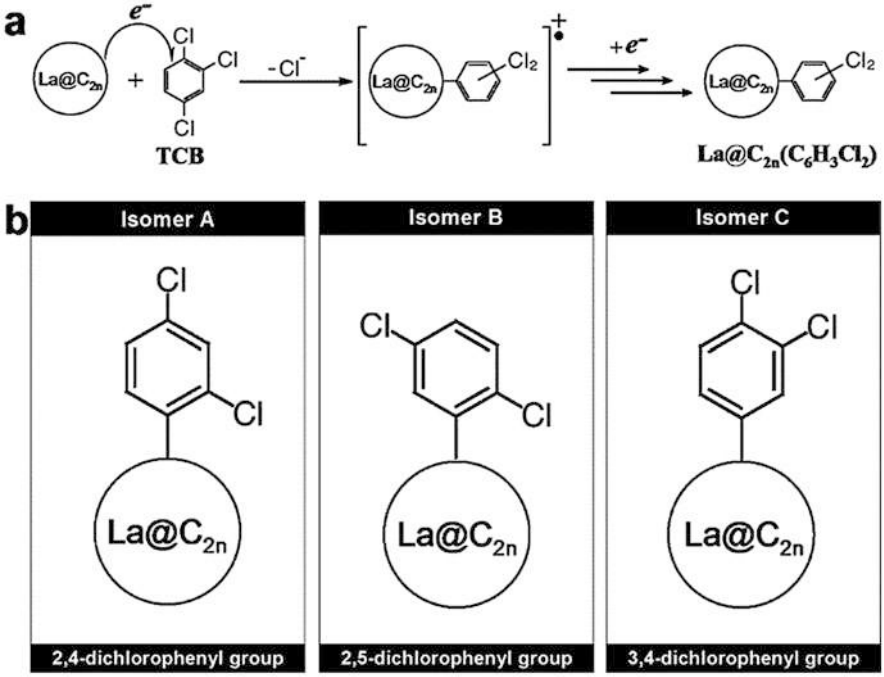

Fig. 12 (**a**) reaction of La@C_{2n} with dichlorophenyl radicals during the soot extraction process and (**b**) possible structural isomers after derivatization. (Used with permission from Akasaka et al. [41])

(2009) [39]. From this trifecta of JACS papers, these missing cages are assigned as endohedral cages with symmetries of C_{74} (D_{3h}) [37], C_{72} (D_{6d}) [38], and C_{80} (C_{2v}) [39], respectively. This derivatization and stabilization approach is used a year later by Akasaka et al. [40] in the characterization and discovery of an unprecedented isomer of La@C_{3v}(7)-C_{82} obtained after chemical attack at a triple-hexagon junction. An illustration showing the dichlorophenyl reaction scheme and possible isomers is shown in Fig. 12 [41].

Another intriguing example of stabilizing fullerenes and endohedrals is the cage functionalization with CF_3 groups. By adding polytetrafluoroethene (PTFE) to the arc-discharge chamber, Wang et al. [42] from the Shinohara group in 2013 successfully prepare a series of stabile trifluoromethylated products of Y@C_{60}, Y@C_{70}, Y@C_{72}, and Y@C_{74}. By extracting and isolating these species as stable derivatives, it is possible to characterize these rare and unconventional metallofullerenes. Just published in 2018 by Yamada et al. [43] is a well-written and detailed review discussing ways to salvage, process, and characterize reactive fullerenes from soot by using this approach of exohedral derivatization, stabilization, isolation, and characterization.

Host-Guest Complexation and Extraction

The concept of host-guest complexation is also useful for selectively extracting and studying less common fullerenes and metallofullerenes, which otherwise are present in soot in trace quantities. In 2004, Shoji et al. [44] demonstrate that cyclodimeric zinc porphyrins exhibit a preference for complexation with higher empty-cage fullerenes. In 2014, the Shinohara group [45] report a selective extraction approach for endohedrals based on a size-selective complexation of metallofullerenes with cycloparaphenylene (CPP). Nakanashi et al. [45] are able to purify $Gd@C_{82}$ based on the high affinity of CPP for $M@C_{82}$ and $M_2@C_{82}$ endohedrals.

Selective extraction of endohedrals is recently demonstrated by the Echegoyen group [46] in their purification of actinide-based metallofullerenes. In those experiments, soot extracts containing uranium-based metallofullerenes exhibit a selective host-guest interaction with supramolecular nanocapsules. In doing so, $Sc_2CU@C_{80}$ and $U_2@C_{80}$ can be purified with this approach [46]. This example represents the powerful approach of selectively extracting, enriching the abundance, and isolating endohedrals present in trace amounts in soot extracts.

Another creative example of performing chemical reactions on soot is the work of Sarina et al. [47] from the Balch group. In their approach, 2-aminoethanol is used as a reagent to preferentially react and remove empty-cage fullerenes from soot by rendering their derivatives water soluble [47]. Remaining in chlorobenzene solution as unreacted metallofullerenes, Y, Lu, Dy, Tb, and Gd-based endohedrals are hydrophobic and reside in the organic layer. Water-soluble fullerene derivatives are removed in the aqueous layer. As such, they obtain highly enriched samples of metallofullerenes. This approach is useful for isolating metallic nitride fullerenes, e.g., $Sc_3N@C_{80}$, and also less common metallofullerenes of Y, Lu, Dy, Tb, and Gd endohedrals [47].

Solubility Studies

Solubility Measurements

A key paper addressing fullerene solubility is published by Ruoff et al. in 1993 [48]. This detailed study measures the room temperature solubility of C_{60} in an impressively large number of 47 solvents. The concentration of soluble C_{60} varies widely from only 0.01 mg/ml (methanol) to upward of 50 mg/ml (chloronaphthalene) [48]. Upon comparing the diversity of polar and nonpolar solvents, the authors conclude there is no single solvent parameter that fully predicts the fullerene solubility. Rather, a combination of factors influences a solvent's ability to dissolve C_{60}. Specifically, they look at variables such as index of refraction, dielectric constant, molecular volume, Hildebrand solubility parameter, and nucleophilic strength of the solvent [48].

The effect on the solubility of C_{60} as related to the number of methyl groups on the benzene ring is also investigated by Ruoff et al. [48] The increased methylation

of benzene results in higher solubilities of C_{60}. The trend for C_{60} solubility is 1.7 mg/ml (benzene), 2.8 mg/ml (toluene), and 5.2 mg/ml (xylenes). Likewise for halogenated benzene, the solubility of C_{60} improves with increasing chlorination as observed in the following trend: 1.7 mg/ml (benzene), 7.0 mg/ml (chlorobenzene), and 27 mg/ml (*o*-dichlorobenzene) [48]. However, the solubility of C_{60} in 1,2,4-trichlorobenzene decreases to 8.5 mg/ml – despite the increased number of chlorine substituents. The highest solubilities for C_{60} are achieved with functionalized naphthalenes as seen with 1-methylnaphthalene (33 mg/ml), dimethylnaphthalene (36 mg/ml), 1-phenylnaphthalene (50 mg/ml), and 1-chloronaphthalene (51 mg/ml) [48]. Note the elevated temperatures associated with these high boiling point solvents. This is an important factor in solvent selection for soot extraction. For this reason, popular solvents for soot extraction for empty-cage fullerene soot are often those with lower boiling points, e.g., carbon disulfide, toluene, and xylene. These solvents represent a compromise between having an acceptable solubility versus their ease of removal during rotary evaporation. As discussed above, the extraction of metallofullerenes from soot can include more polar solvents such as DMF.

Purification of Fullerenes Using Selective Solubility

Efforts to isolate C_{60} and C_{70} fullerenes based on their physical properties emerge in the early 1990s. Even then, the following question soon arises. Are solubility differences between C_{60}, C_{70}, and higher fullerenes sufficiently different to permit their purification? In 1994, Zhou et al. [49] describe the gram scale separation of C_{60} and C_{70} using solubility and fractional crystallization. In doing so, they isolate C_{60} and C_{70} at purity levels of >99.5% and 98%, respectively. Particularly useful solvents described in detail are carbon disulfide and *o*-xylene [49]. An advantage of their solubility approach is avoiding HPLC in the purification process. Indeed, they nonchromatographically isolate 100 g of C_{60} and 10 g of C_{70}. This is an impressive amount of material in 1994 [49].

Three years later, 1,3-diphenylacetone is used in 1997 by Doome et al. [50] to purify C_{60} using a fractional crystallization approach. This solvent is not commonly used to dissolve fullerenes due, in part, to its lower solubilities of 1.40 mg/ml for C_{60} and 2.20 mg/ml for C_{70}. The temperature dependence of C_{60} and C_{70} solubility in 1,3-diphenylacetone is shown in Fig. 13. As noted by the authors, 1,3-diphenylacetone is a solid at room temperature with its melting point of 33 °C. However, the 2% ethanol impurity results in their diphenylacetone reagent being a liquid at room temperature [50]. Advantages of their C_{60} purification approach are twofold. First, the method is low cost by avoiding the high cost of HPLC instrumentation, waste and repurchase of mobile phases, and custom-made stationary phase specifically designed for fullerene separations. Second, their fractional crystallization approach has minimal losses of material since fullerenes remaining after the purification process are recovered from the mother liquor [50].

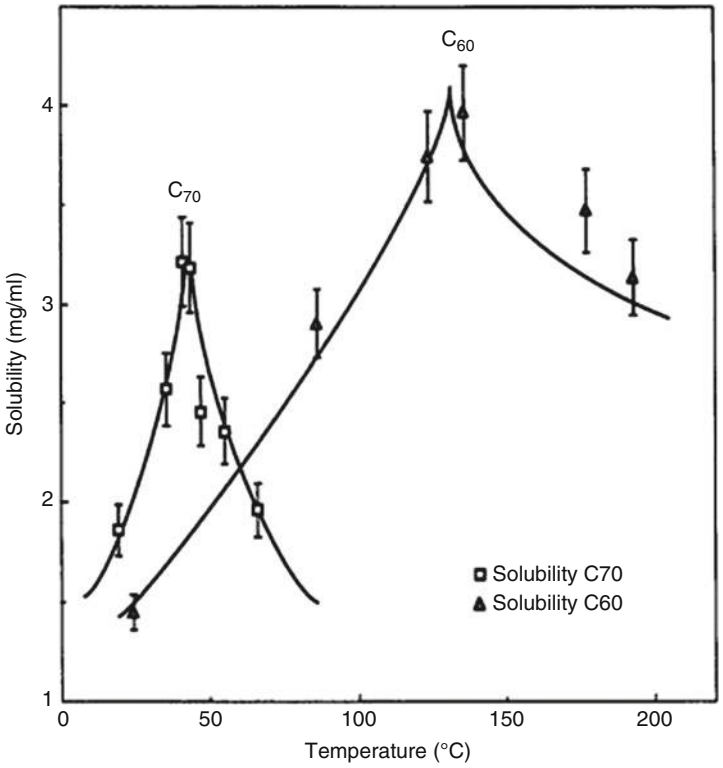

Fig. 13 Temperature dependence and selective solubility of C_{60} and C_{70} in 1,3-diphenylacetone. (Used with permission from Doome et al. [50])

As a demonstration, Doome et al. [50] begin with a soot extraction using toluene. The composition of starting material is 84% C_{60}, 15% C_{70}, and 1% higher fullerenes. After just one fractional crystallization experiment with 1,3-diphenylacetone, the purity of C_{60} increases from 84.3% to 95.3%. Two additional crystallization steps improve the C_{60} purity to 97.7% and 99.5%, respectively [50].

Concluding Remarks

In conclusion, this chapter represents a balance between early and recent work. We blend the pioneering research of fullerenes in their first decade (1985–1995) with modern findings of the twenty-first century. With limits on the number of cited references, a comprehensive discussion of all papers related to fullerene production, extraction, and solubility is impossible. Indeed, the objective of this chapter is not a detailed review, but rather a broad overview. A goal of this writing is helping the reader to place modern findings into a historical context with the seminal work discussed herein.

Cross-References

- ▶ Connecting Fullerenes with Carbon Nanotubes and Graphene
- ▶ Formation Mechanism of Fullerenes/Metallofullerenes
- ▶ Preparation of Endohedral Metallofullerenes

Acknowledgments The author acknowledges funding from the National Science Foundation grant 1856461.

References

1. Heath JR, O'Brien SC, Zhang Q, Liu Y, Curl RF, Kroto HW et al (1985) Lanthanum complexes of spheroidal carbon shells. J Am Chem Soc 107(25):7779–7780
2. Kroto HW, Heath JR, O'Brien SC, Curl RF, Smalley RE (1985) C60: buckminsterfullerene. Nature 318(6042):162–163
3. Kratschmer W, Lamb LD, Fostiropoulos K, Huffman DR (1990) Solid C60 – a new form of carbon. Nature 347(6291):354–358
4. Rohlfing EA, Cox DM, Kaldor A (1984) Production and characterization of supersonic carbon cluster beams. J Chem Phys 81(7):3322–3330
5. Kratschmer W, Fostiropoulos K, Huffman DR (1990) The infrared and ultraviolet-absorption spectra of laboratory-produced carbon dust – evidence for the presence of the C60 molecule. Chem Phys Lett 170(2–3):167–170
6. Haufler RE, Conceicao J, Chibante LPF, Chai Y, Byrne NE, Flanagan S et al (1990) Efficient production of C60 (buckminsterfullerene), C60H36, and the solvated buckide ion. J Phys Chem 94(24):8634–8636
7. Ajie H, Alvarez MM, Anz SJ, Beck RD, Diederich F, Fostiropoulos K et al (1990) Characterization of the soluble all-carbon molecules C60 and C70. J Phys Chem 94(24): 8630–8633
8. Chibante LPF, Thess A, Alford JM, Diener MD, Smalley RE (1993) Solar generation of the fullerenes. J Phys Chem 97(34):8696–8700
9. Fields CL, Pitts JR, Hale MJ, Bingham C, Lewandowski A, King DE (1993) Formation of fullerenes in highly concentrated solar flux. J Phys Chem 97(34):8701–8702
10. Flamant G, Robert JF, Marty S, Gineste JM, Giral J, Rivoire B et al (2004) Solar reactor scaling up: the fullerene synthesis case study. Energy 29(5–6):801–809
11. Howard JB, McKinnon JT, Makarovsky Y, Lafleur AL, Johnson ME (1991) Fullerenes C60 and C70 in flames. Nature 352(6331):139–141
12. Richter H, Labrocca AJ, Grieco WJ, Taghizadeh K, Lafleur AL, Howard JB (1997) Generation of higher fullerenes in flames. J Phys Chem B 101(9):1556–1560
13. Murayama H, Tomonoh S, Alford JM, Karpuk ME (2004) Fullerene production in tons and more: from science to industry. Fuller Nanotub Car N 12(1–2):1–9
14. Takehara H, Fujiwara M, Arikawa M, Diener MD, Alford JM (2005) Experimental study of industrial scale fullerene production by combustion synthesis. Carbon 43(2):311–319
15. Krokos E (2010) Plasma coupled radio frequency furnace: the synthesis, separation, and elucidation of the elusive Sc4C82 fullerene. J Phys Chem C 114(17):7626–7630
16. Markovic Z, Todorovic-Markovic B, Mohai I, Farkas Z, Kovats E, Szepvolgyi J et al (2007) Comparative process analysis of fullerene production by the arc and the radio-frequency discharge methods. J Nanosci Nanotechnol 7(4–5):1357–1369
17. Diederich F, Ettl R, Rubin Y, Whetten RL, Beck R, Alvarez M et al (1991) The higher fullerenes: isolation and characterization of C76, C84, C90, C94, and C70O, an oxide of D5h-C70. Science 252(5005):548–551

18. Smart C, Eldridge B, Reuter W, Zimmerman JA, Creasy WR, Rivera N et al (1992) Extraction of giant fullerene molecules, and their subsequent solvation in low boiling-point solvents. Chem Phys Lett 188(3–4):171–176
19. Creasy WR, Zimmerman JA, Ruoff RS (1993) Fullerene molecular-weight distributions in graphite soot extractions measured by laser desorption Fourier-transform mass spectrometry. J Phys Chem 97(5):973–979
20. Cai WT, Li FF, Bao LPA, Xie YP, Lu X (2016) Isolation and crystallographic characterization of La2C2@C-5(574)-C-102 and La2C2@C-2(816)-C-104: evidence for the top-down formation mechanism of fullerenes. J Am Chem Soc 138(20):6670–6675
21. Shinohara H, Sato H, Saito Y, Izuoka A, Sugawara T, Ito H et al (1992) Extraction and mass spectroscopic characterization of giant fullerenes up to C500. Rapid Commun Mass Sp 6(7): 413–416
22. Bandow S, Kitagawa H, Mitani T, Inokuchi H, Saito Y, Yamaguchi H et al (1992) Anaerobic sampling and characterization of lanthanofullerenes: extraction of LaC76 and other LaC2n. J Phys Chem 96(24):9609–9612
23. Ding JQ, Yang SH (1996) Efficient N,N-dimethylformamide extraction of endohedral metallofullerenes for HPLC purification. Chem Mater 8(12):2824–2827
24. Sun DY, Liu ZY, Guo XH, Xu WG, Liu SY (1997) High-yield extraction of endohedral rare-earth fullerenes. J Phys Chem B 101(20):3927–3930
25. Sun BY, Feng L, Shi ZJ, Gu ZN (2002) Improved extraction of metallofullerenes with DMF at high temperature. Carbon 40(9):1591–1595
26. Lian YF, Yang SF, Yang SH (2002) Revisiting the preparation of La@C-82 (I and II) and La-2@C-80: efficient production of the "minor" isomer La@C-82 (II). J Phys Chem B 106(12): 3112–3117
27. Sun BY, Li MX, Luo HX, Shi ZJ, Gu ZN (2002) Electrochemical properties of metallofullerenes and their anions. Electrochim Acta 47(21):3545–3549
28. Lian YF, Shi ZJ, Zhou XH, Gu ZN (2004) Different extraction behaviors between divalent and trivalent endohedral metallofullerenes. Chem Mater 16(9):1704–1714
29. Yeretzian C, Wiley JB, Holczer K, Su T, Nguyen S, Kaner RB et al (1993) Partial separation of fullerenes by gradient sublimation. J Phys Chem 97(39):10097–10101
30. Angeli CD, Cai T, Duchamp JC, Reid JE, Singer ES, Gibson HW et al (2008) Purification of trimetallic nitride templated endohedral metallofullerenes by a chemical reaction of congeners with eutectic 9-methylanthracene. Chem Mater 20(15):4993–4997
31. Diener MD, Alford JM (1998) Isolation and properties of small-bandgap fullerenes. Nature 393(6686):668–671
32. Sun BY, Gu ZN (2002) Solvent-dependent anion studies on enrichment of metallofullerene. Chem Lett 12:1164–1165
33. Tsuchiya T, Wakahara T, Shirakura S, Maeda Y, Akasaka T, Kobayashi K et al (2004) Reduction of endohedral metallofullerenes: a convenient method for isolation. Chem Mater 16(22): 4343–4346
34. Tsuchiya T, Wakahara T, Lian YF, Maeda Y, Akasaka T, Kato T et al (2006) Selective extraction and purification of endohedral metallofullerene from carbon soot. J Phys Chem B 110(45): 22517–22520
35. Lu X, Li HJ, Sun BY, Shi ZJ, Gu ZN (2005) Selective reduction and extraction of Gd@C82 and Gd2@C80 from soot and the chemical reaction of their anions. Carbon 43(7):1546–1549
36. Ceron MR, Li FF, Echegoyen L (2013) An efficient method to separate Sc3N@C80 Ih and D5h isomers and Sc3N@C78 by selective oxidation with acetylferrocenium Fe(COCH3C5H4)Cp +. Chem Eur J 19(23):7410–7415
37. Nikawa H, Kikuchi T, Wakahara T, Nakahodo T, Tsuchiya T, Rahman GMA et al (2005) Missing metallofullerene La@C74. J Am Chem Soc 127(27):9684–9685
38. Wakahara T, Nikawa H, Kikuchi T, Nakahodo T, Rahman GMA, Tsuchiya T et al (2006) La@C72 having a non-IPR carbon cage. J Am Chem Soc 128(44):14228–14229

39. Nikawa H, Yamada T, Cao BP, Mizorogi N, Slanina Z, Tsuchiya T et al (2009) Missing metallofullerene with C80 cage. J Am Chem Soc 131(31):10950–10954
40. Akasaka T, Lu X, Kuga H, Nikawa H, Mizorogi N, Slanina Z et al (2010) Dichlorophenyl derivatives of La@C3v(7)-C82: endohedral metal induced localization of pyramidalization and spin on a triple-hexagon junction. Angew Chem Int Edit 49(50):9715–9719
41. Akasaka T, Lu X (2012) Structural and electronic properties of endohedral metallofullerenes. Chem Rec 12(2):256–269
42. Wang ZY, Nakanishi Y, Noda S, Niwa H, Zhang JY, Kitaura R et al (2013) Missing small-bandgap metallofullerenes: their isolation and electronic properties. Angew Chem Int Edit 52(45):11770–11774
43. Yamada M, Akasaka T, Nagase S (2018) Salvaging reactive fullerenes from soot by exohedral derivatization. Angew Chem Int Edit 57(41):13394–13405
44. Shoji Y, Tashiro K, Aida T (2004) Selective extraction of higher fullerenes using cyclic dimers of zinc porphyrins. J Am Chem Soc 126(21):6570–6571
45. Nakanishi Y, Omachi H, Matsuura S, Miyata Y, Kitaura R, Segawa Y et al (2014) Size-selective complexation and extraction of endohedral metallofullerenes with cycloparaphenylene. Angew Chem Int Edit 53(12):3102–3106
46. Fuertes-Espinosa C, Gomez-Torres A, Morales-Martinez R, Rodriguez-Fortea A, Garcia-Simon C, Gandara F et al (2018) Purification of uranium-based endohedral metallofullerenes (EMFs) by selective supramolecular encapsulation and release. Angew Chem Int Edit 57(35): 11294–11299
47. Sarina EA, Mercado BQ, Franco JU, Thompson CJ, Easterling ML, Olmstead MM et al (2015) 2-Aminoethanol extraction as a method for purifying Sc3N@C-80 and for differentiating classes of endohedral fullerenes on the basis of reactivity. Chem Eur J 21(47):17035–17043
48. Ruoff RS, Tse DS, Malhotra R, Lorents DC (1993) Solubility of C60 in a variety of solvents. J Phys Chem 97(13):3379–3383
49. Zhou XH, Gu ZN, Wu YQ, Sun YL, Jin ZX, Xiong Y et al (1994) Separation of C60 and C70 fullerenes in gram quantities by fractional crystallization. Carbon 32(5):935–937
50. Doome RJ, Fonseca A, Richter H, Nagy JB, Thiry PA, Lucas AA (1997) Purification of C60 by fractional crystallization. J Phys Chem Solids 58(11):1839–1843

Total Synthesis of C_{60}

3

Hidehiro Sakurai and Hironobu Nakazawa

Contents

Abstract

More than 30 years have passed since the discovery of C_{60}, yet its appeal has not faded. Just as a mountaineer climbs a mountain because "there is a mountain there," it is natural for a synthetic chemist to challenge the "total synthesis" of such an exciting and beautiful molecule. Conventionally, two approaches have been investigated through the step-by-step flask reactions; synthesis of carbon cage molecules and the bottom-up approach from the buckybowls, bowl-shaped partial structure of fullerenes. In particular, two pristine frameworks of

H. Sakurai (✉)
Division of Applied Chemistry, Graduate School of Engineering, Osaka University, Suita, Osaka, Japan

Innovative Catalysis Science Division, Institute for Open and Transdisciplinary Research Initiatives (ICS-OTRI), Osaka University, Suita, Osaka, Japan
e-mail: hsakurai@chem.eng.osaka-u.ac.jp

H. Nakazawa
Division of Applied Chemistry, Graduate School of Engineering, Osaka University, Suita, Osaka, Japan
e-mail: h.nakazawa@chem.eng.osaka-u.ac.jp

X. Lu et al. (eds.), *Handbook of Fullerene Science and Technology*,
https://doi.org/10.1007/978-981-16-8994-9_21

buckybowl, corannulene and sumanene, have been intensively studied. The first chemical synthesis of C_{60} was achieved by flash vacuum pyrolysis, thanks to the careful design of a precursor of C_{60} which should consist of 60 carbons and should be a planar development diagram. Recent progress of metal surface reactions realized the quantitative synthesis of C_{60} and the related artificial azafullerene, and even the selective growth of SWCNTs with a single chirality on Pt (111) surface. Although the traditional bottom-up synthesis of C_{60} using the flask reactions has not been achieved, yet the required pieces for the total synthesis of C_{60} starting from sumanene are finally in place. The total synthesis route to C_{60} from sumanene by the convergent synthesis concept might be more promising because of the wide variety of the available reactions and derivatives, and the ease of introducing the sp^3 carbons at the appropriate positions for the construction of the three-dimensional structure.

Keywords

Bottom-up approach · Carbon allotrope · Carbon cage · Buckybowl · Corannulene · Sumanene · Convergent synthesis · Flash vacuum pyrolysis · Metal surface reaction

Introduction

Suddenly, C_{60} appeared in front of us as "the most beautiful molecule." [1] Although Prof. Osawa had predicted it [2], it immediately attracted many scientists when it appeared as an actual molecule. The impact can be observed in the many nicknames of C_{60}. The name "fullerene" derived from Buckminster Fuller's famous architecture and the nickname "buckyball" have become popular.

C_{60} impacted a wide range of fields, from fundamental physicists and astronomers to researchers at the forefront of materials science, and, of course, synthetic organic chemists were among them. Just as a mountaineer climbs a mountain because "there is a mountain there," it is natural for a synthetic chemist to challenge the "total synthesis" of an exciting molecule if there is one. The history of the conquest of many monsters with complicated structures, such as Woodward's series of outstanding achievements, reveals the motivations of synthetic chemists. The intriguing targets are not only natural products but also structurally unique molecules, such as cubane.

C_{60} has two crucial implications for synthetic organic chemistry. First, C_{60} is a steric allotrope of the sp^2 carbon, which means that it has the properties of a completely new "aromatic compound." C_{60} behaves like an organic compound (in fact, once functionalized at any position, it immediately becomes an organic compound!). In other words, the chemistry of aromatic compounds was expanding in an unprecedented three-dimensional manner. Therefore, modifying these symmetrical molecules as desired and developing new functions became a real challenge for synthetic organic chemists. Another was the simple question of how to

"synthesize" this beautiful molecule, which, unlike many natural products and bioactive molecules, has no "functional groups" to serve as a stepping-stone for synthesis. How can we synthesize a "smooth-faced" molecule without a "functional group," and how can we "distort" the intrinsically planar sp^2 carbon skeleton into a spherical shape?

In this chapter, we focus on the history of the total synthesis of C_{60}. The preparative method of C_{60} at the laboratory level had already been established by the arc discharge method at an early stage of the C_{60} research history. Moreover, industrially the combustion method has been used for producing C_{60} in large quantities. Therefore, it is difficult to find the merit in procuring C_{60} through organic synthetic methods at the industrial level. In addition, as will be discussed later, the synthesis of C_{60} has been achieved using "non-classical" techniques such as flash vacuum pyrolysis (FVP) and surface reaction on metal surfaces. Unfortunately, the so-called classical "total synthesis" of C_{60} through a step-by-step process using flask reactions has not yet been achieved. However, we believe that the total synthesis of C_{60} is still meaningful, even if it is practically meaningless. This is because of the desire to conquer the synthesis itself and because we think that the research process contains various discoveries. Indeed, the chemistry of buckybowls, partial bowl-shaped structures of buckyballs, such as corannulene and sumanene, which are the mainstays of C_{60} bottom-up synthesis, ought to establish a large research field on its own [3].

We turned it down once when we were asked to write this review because our attempt at the bottom-up synthesis of C_{60} is still on the way. However, we finally decided to accept the invitation to write because I wanted to describe with looking into the future, including the intermediate stage. Therefore, the readers might feel strange due to some examples that seem not directly related to the C_{60} synthesis, but we hope you will forgive us if we consider them a stepping-stone for the future.

This chapter does not include a discussion of the route of the formation of C_{60}, especially in the gas phase, as it has already been introduced in many reviews. Indeed, several pathways for generating C_{60} have been discussed including the pentagon road, the fullerene road, ring coalescence, and the shrinking hot giant model. Just as the optimal route for the total synthesis of natural products is very often quite different from the biosynthetic pathway, there is likely another optimal route for the total synthesis of C_{60}. We would like to introduce four different synthetic approaches to C_{60}: (1) carbon cage synthesis, (2) the bottom-up approach from buckybowls, (3) the FVP approach, and (4) synthesis on a metal surface.

Approaches by Carbon Cage Synthesis

C_{60} had a significant impact as a novel "carbon allotrope" with a definite molecular weight. Before the discovery of C_{60}, the existence of small carbons was proven spectroscopically, such as in the interstellar medium. Still, at the same time, it had been thought to exist only in extreme environments [4]. Despite the theoretical predictions made by Osawa [2], most researchers might not imagine that a giant

carbon cluster like C_{60} would suddenly appear in a tremendously stable form. This finding has dramatically stimulated research on organic chemical approaches to producing a new family of carbon allotropes. Organic chemists can construct carbon flameworks in a wide variety of three-dimensional structures using a mixture of sp^3, sp^2, and sp-hybridized carbon atoms. For example, "graphyne" is one of the artificial carbon allotropes possessing a sheet structure composed of sp^2 and sp carbons [5]. By constructing such a structure in three dimensions, a wide variety of carbon allotropes can be generated one after another through organic synthesis! The C_{60} synthesis must exist as an extension of this idea. The retrosynthesis of C_{60} involves constructing a three-dimensional caged structure with 60 carbons, which leads to a thermodynamically stable C_{60}. Reports of the generation of C_{60} from cyclocarbons support this approach [6]. Rubin and Tobe mainly led this carbon cage synthesis approach [7].

Based on the D_{6h} symmetry, what kinds of precursors were considered? By combining the benzene ring with alkynes, intermediates such as **1**, **2**, and **3** were envisioned. For example, **3** was expected to be easily converted to C_{60} according to I_h symmetry via an electrocyclic reaction, as shown in Fig. 1. However, the synthesis of a distorted carbon-carbon triple bond compound with a steric structure is essentially challenging. Rubin et al. used two different alkyne-alkyne coupling reactions to synthesize a cyclophane derivative $C_{60}H_{18}$ (**4**) bent at the double bond in the middle. However, **4** was not a rigid D_{3h} structure but a distorted chiral structure, and was unstable in the crystal state. Indeed, the peak derived from C_{60} was hardly observed under MALDI-TOF MS conditions, indicating that the expected isomerization had not proceeded. This might be due to the flexible ethylene tether and

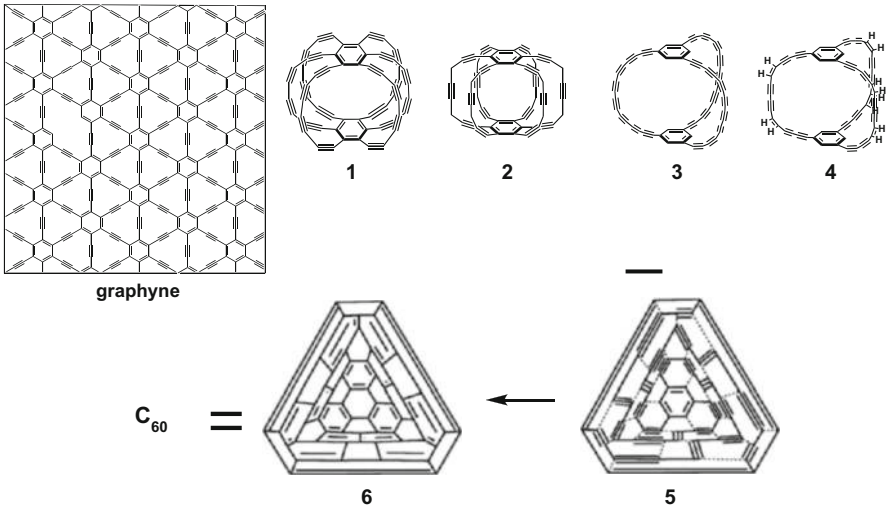

Fig. 1 Structures of graphyne and carbon cage approach

predominance of Bergman cyclization [8]. Therefore, the same group decided to use squaric acid derivatives as a more rigid structure. The cyclobutenedione unit derived from this derivative is known to generate an alkyne upon CO elimination, which is a reliable reaction for the formation of distorted carbon-carbon triple bonds. In the MALDI-TOF MS of the compound **12** ($C_{50}H_6(CO)_{12}$), a significant number of C_{60}^+ and $C_{60}H_6^+$ peaks were observed due to the skeletal change caused by the cleavage of the cyclobutanedione moiety, leading to the formation of C_{60}. Unfortunately, however, the formation of C_{60} was not confirmed by laser irradiation into a THF dilute solution of **5**, and the bulk synthesis of C_{60} has not been successful [9] (Scheme 1).

Tobe et al. also independently succeeded in the synthesis of a precursor (**17**) possessing a propellatriene unit as a bending site (masked alkyne) moiety. A C_{60}^+ peak was observed in the positive mode of MALDI-TOF MS from **6** [10] (Scheme 2).

On the other hand, the approach based on the D_{5h} symmetry, which is different from the D_{6h} symmetry, is also worth considering. Bunz et al. investigated the synthesis of C_{60} from precursor **20**, starting from bis(pentaethynyl)-cyclopentadienylmetallocene. The interesting point of this approach is that metal complexes serve as templates to force the two five-membered rings to be spatially close to each other. Furthermore, when this method is successful, the metal is likely to be encapsulated in the fullerene cage; this is called a bottom-up synthesis of metallofullerenes. However, at present, this approach has not been accomplished [7] (Fig. 2).

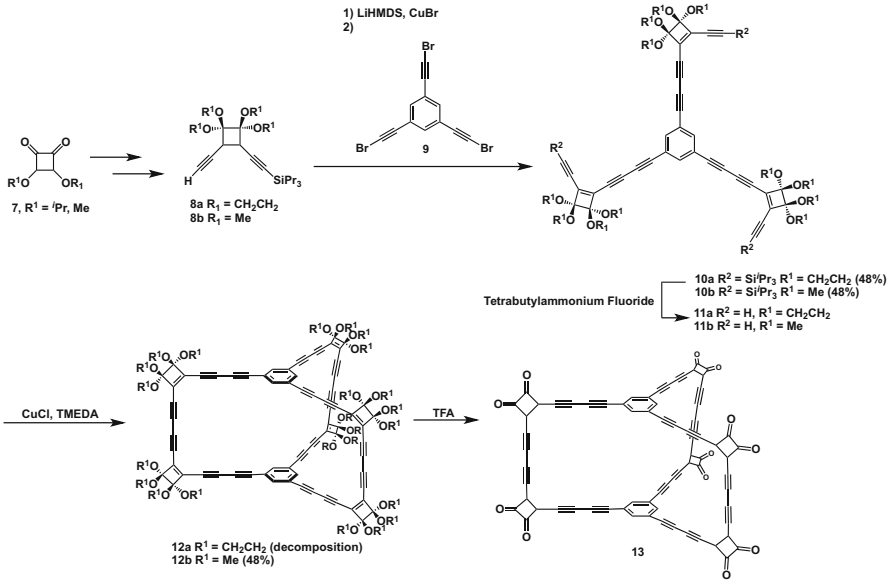

Scheme 1 Rubin's approach through **12**

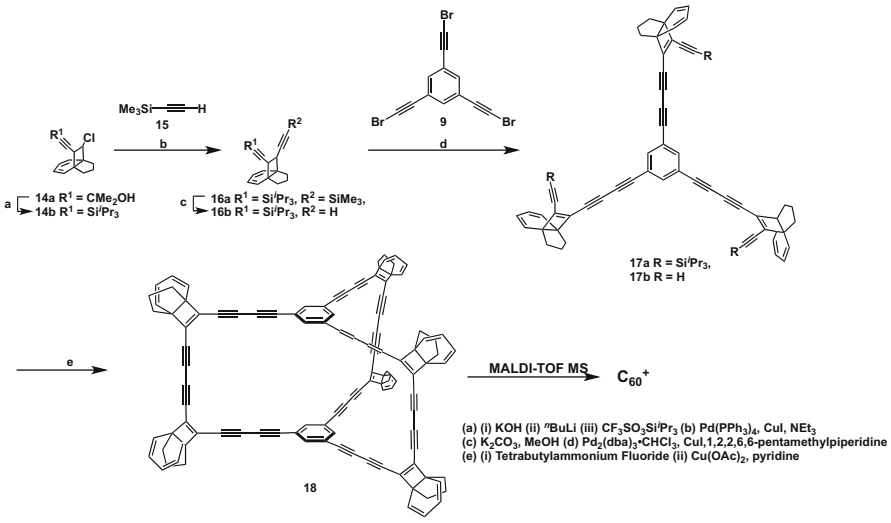

Scheme 2 Tobe's approach through **17**

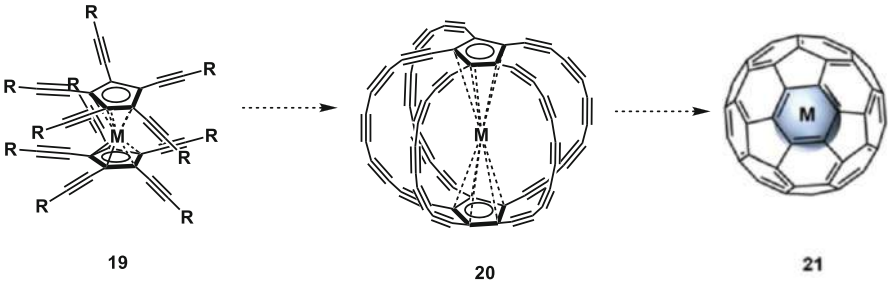

Fig. 2 Bunz's metallocene approach

Bottom-Up Synthesis Approach from Buckybowls

As mentioned in the introduction, many organic chemists went into a frenzy after the publication of C_{60}. Physical organic chemistry and material scientists welcomed C_{60} as an unprecedented three-dimensional aromatic compound. Chemistry utilizing C_{60} as an utterly discrete cage to trap atoms and small molecules was also promoted. In all of these fields, synthetic organic chemists have played a significant role. And, of course, there were many organic chemists who tried to synthesize C_{60} itself using the so-called classical synthetic organic approach.

The structure of C_{60} is a so-called truncated icosahedron consisting of 20 hexagons and 12 pentagons. According to Euler's law, constructing a three-dimensional aromatic system is equivalent to the insertion of pentagons into the hexagonal

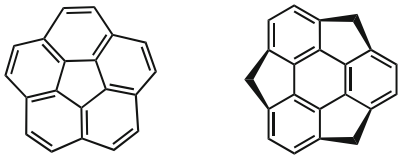

22 23

Fig. 3 Structures of corannulene (**22**) and sumanene (**23**)

network. When a total of six pentagons are introduced, the network becomes a nanotube (hemisphere) structure, and when 12 pentagons are introduced, the network closes and becomes a fullerene (in fact, nanotube and fullerene structures can be formed even when ring structures other than five-membered rings are introduced) [11]. In C_{60}, pentagons are the most densely arranged while satisfying the so-called IPR (isolated pentagon rule), which means that hexagons surround all pentagons in C_{60} on all sides, and the sides of all hexagons face three pentagons and three hexagons alternately.

Therefore, a symmetry-preserving synthetic route from a molecule consisting of two skeletons, hexagons, and pentagons makes sense when considering the synthesis of such a highly symmetrical compound. The above idea led to a bucky "bowl," indicating a bowl-shaped partial structure of fullerenes. By definition, a buckybowl consists of hexagons and 1–11 pentagons. As mentioned earlier, the buckybowls with six pentagons correspond to a hemispherical structure of fullerenes and serve as the caps of single-wall carbon nanotubes (SWCNTs). Among an infinite number of buckybowl flameworks, including those that do not satisfy the IPR rule, two pristine structures of buckybowls are considered: corannulene (**22**) and sumanene (**23**) (Fig. 3). Corannulene is a five-fold symmetric molecule with a pentagon at its center surrounded by five hexagons, while sumanene is a three-fold symmetric molecule with a hexagon at its center surrounded by three hexagons and three pentagons. Mehta et al. have discussed the pathway of a bottom-up construction of C_{60} starting from corannulene and sumanene to maintain symmetry (Fig. 4) [12]. We will discuss the attempted bottom-up synthesis starting from these two buckybowls as follows.

Synthesis of Corannulene (22)

Corannulene (**22**) is the smallest of the buckybowls. The only corannulene has a curved bowl structure with a single five-membered ring. This is because five benzene rings fully surround the five-membered ring. In fact, the chemistry of corannulene started much earlier than the discovery of fullerenes, and its first synthesis was achieved by Barth and Lawton in 1966 (Scheme 3) [13]. The motivation of corannulene chemistry seems to be an extension of the chemistry of radialene or circulene. The method of corannulene synthesis used in the 1960s highlights the difficulty of synthesizing distorted aromatic compounds. It requires 17 steps,

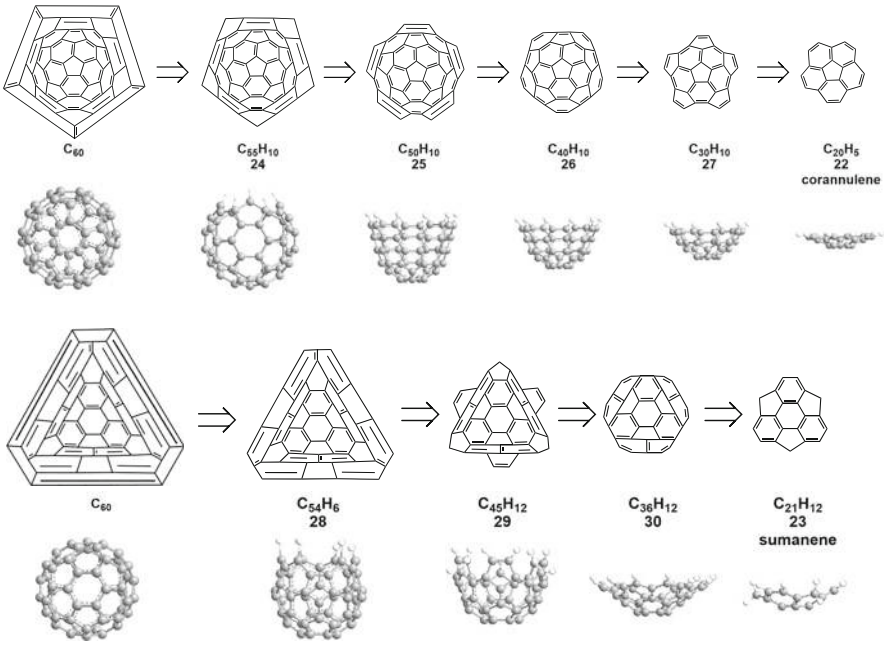

Fig. 4 Mehta's retrosynthetic analysis of C_{60} synthesis from corannulene (**22**) and sumanene (**23**)

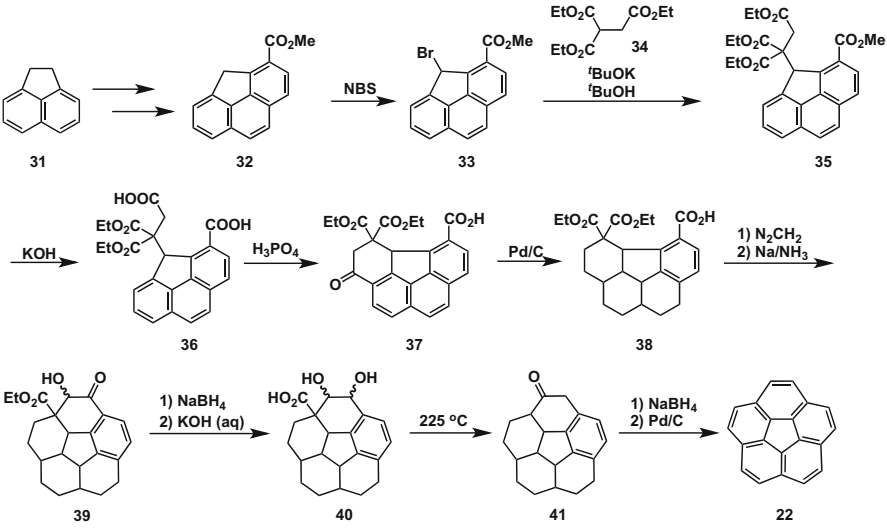

Scheme 3 The first synthesis of corannulene (**22**) by Barth and Lawton in 1966

beginning with acenaphthene (**31**) as a starting material. Moreover, before the acyloin condensation used in the final six-membered ring construction, two of the three benzene rings that have already been installed should be hydrogenated and

converted to the three-dimensional sp^3 carbon frameworks (from **37** to **38**). There is only one aromatic ring left in the total of six fused skeletons (**39**) (five six-membered rings and one five-membered ring) completed after the condensation reaction and the synthesis of the first corannulene (**22**) was achieved by thorough oxidative aromatization of a total of four cyclohexane rings. Such a long and winding route indicates how difficult it is to construct a three-dimensional framework using a planar sp^2 carbon structure. Understandably, very few researchers followed up on the synthesis of corannulene, which required such a long procedure, and corannulene became a virtually "forgotten" compound.

It was the discovery of C_{60} that brought corannulene back into the limelight, with its newfound value as a "buckybowl." However, as long as such a multistep synthesis is required, research will not progress. In 1991/1992, a breakthrough in the synthesis of corannulene occurred when L. Scott's group [14] and J. Siegel's group [15] independently reported the FVP method for the short-step synthesis of corannulene (Scheme 4). Although the pyrolysis method provides enough energy to overcome the distortion caused by the bowl, precise control of the reaction pathway is usually tricky. They succeeded in obtaining corannulene directly from readily prepared planar aromatic compound derivatives (**44**, **47**) in good yields through radical coupling reactions and/or carbene C-H insertion reactions, which are relatively selective and reliable even in thermal reactions. The impact of these two reports on the synthesis of FVPs was extremely high. Since then, research on corannulene has exploded, as it is the only buckybowl that is relatively easy to obtain. Subsequently, Scott's group actively pursued the synthesis of buckybowl derivatives using the FVP method and provided numerous derivatives [16]. Mehta group and Sygula/Rabideau group also contributed significantly to enlarge the applicability of FVP approach to the buckybowl synthesis.

On the other hand, Siegel's group pursued sequential synthesis without FVP, especially the method available for bulk synthesis, and finally completed the kilogram-scale process [17] (Scheme 5). This achievement is crucial because corannulene has gone from being a purely academic compound to a "material" that can be commercialized industrially. Now many companies deal with

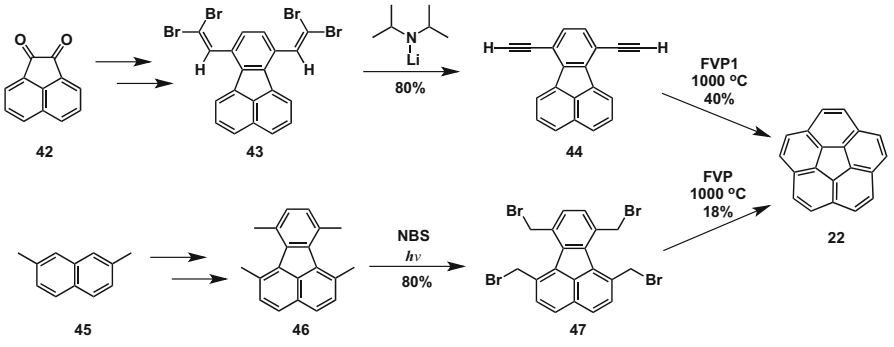

Scheme 4 Scott and Siegel's FVP synthesis of **22** in 1991–1992

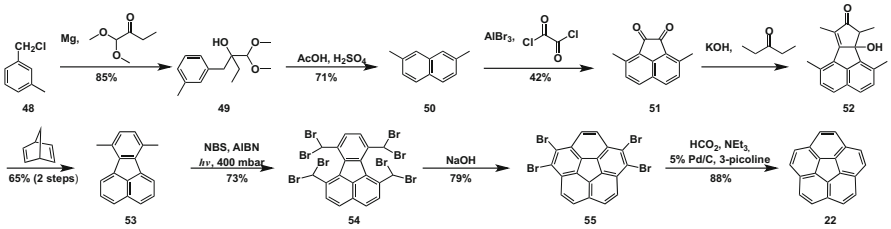

Scheme 5 Siegel's kilogram synthesis of **22**

corannulene, and indeed, the number of papers about corannulene is rapidly increasing.

Derivatization of Corannulene

Since corannulene possesses only one pentagon in the center, 5 more pentagons need to be introduced for the cap structure of the SWCNT (hemisphere), and 11 pentagons for the synthesis of fullerene. In particular, to limit the discussion to the synthesis of C_{60}, it is essential to synthesize a C_{30} skeleton with five fused five-membered rings (**27** in Fig. 4) simultaneously introduced to the corannulene skeleton. To elongate the framework, it is necessary to introduce the functional groups at the periphery. In corannulene, the whole periphery is surrounded by benzene rings, so aromatic electrophilic substitution reactions might be the main methods for introducing the functional groups. The perchlorination (all ten-position chlorination) of the periphery of corannulene was achieved relatively early [18], and many deca-substituted corannulenes have been synthesized through the substitution reaction including the cross-coupling reactions. Taking advantage of the low reactivity of the *ortho* and *peri* positions for substituted corannulenes, it is also possible to synthesize C_5-symmetric penta-substituted corannulenes. In addition to chlorination, borylation [19], which is more convenient for Suzuki-Miyaura cross coupling, was achieved (Scheme 6).

However, it is not so easy to introduce five-membered rings from **22** at the appropriate positions. Wu et al. succeeded in constructing up to two additional five-membered rings using organometallic approaches (Scheme 7) [20]. An interesting point of his method is that, unlike FVP, five-membered rings with an active methylene group can be directly introduced. Under FVP conditions (the first sumanene synthesis trial is a typical example in Scheme 9), susceptible functions or atoms cannot survive, leading to decomposition or further reactions. Therefore, the products of the FVP method must be covered with an aromatic ring on their periphery. However, when the active methylene unit remains at the periphery as in **60**, it is advantageous for subsequent chemical modification.

Scott et al. have successfully synthesized various buckybowls using FVP. Even in their early work, they achieved buckybowls with one, two, and even three

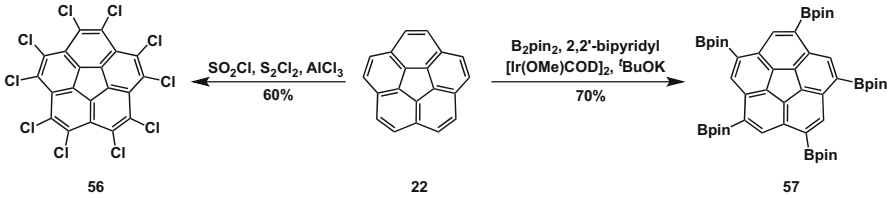

Scheme 6 Examples of *deca*-substitution and C_5-symmetric *penta*-substitution of **22**

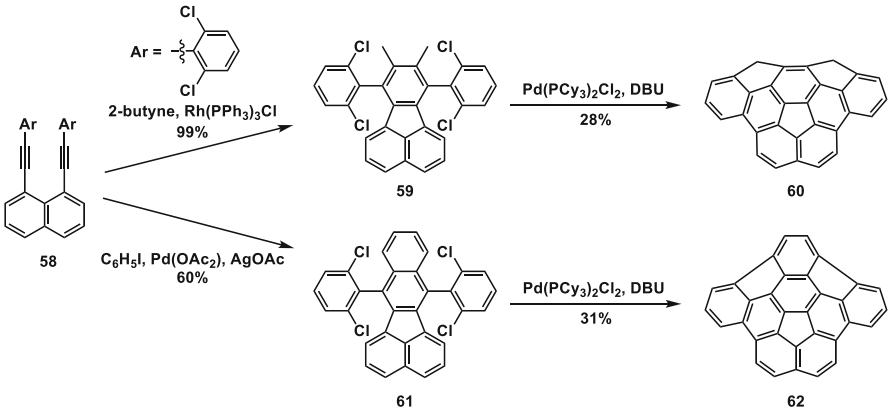

Scheme 7 Wu's organometallic approach for the buckybowl construction

additional pentagons introduced from **22** at the appropriate positions [16]. At last, in 2012, they completed synthesizing a hemispherical structure **25**, a capped structure of SWCNT (Scheme 8) [21]. **25** is highly significant as the very first example of the bottom-up synthesis of the smallest (5,5) SWCNT. Moreover, it should be noted that **25** possesses an armchair-type peripheral structure, which opens up the possibility of pure chemical synthesis of SWCNTs by repeating the Diels-Alder-type reaction.

However, it is not so reasonable to consider **25** as a precursor of C_{60}. Since **25** is the cap structure of SWCNTs, it is composed entirely of sp^2 hybridized carbons and is rigid. Moreover, **25** already consists of 50 carbons; thus, only the remaining ten carbons must be introduced into the armchair periphery. The framework needs to be bent inward all at once toward a closed structure, including six-time five-membered ring formation processes. In reality, such a bending process might be impossible with all sp^2-carbon molecules due to their planar nature. In fact, it is a common and general problem for the entire bottom-up synthesis approach, after this hemispheric structure, to narrow the framework toward a "closed structure."

To avoid the above problem and achieve the total synthesis of fullerenes, we need to consider the concept of "convergent synthesis," i.e., the independent synthesis of two hemispherical buckybowls, which are eventually woven together to form a

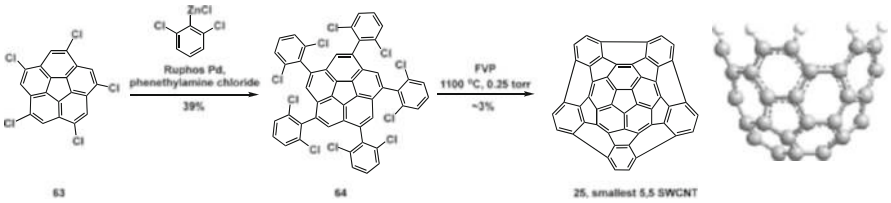

Scheme 8 The first bottom-up synthesis of a cap structure of (5,5)-SWCNT (**25**)

fullerene. This concept of convergent synthesis is commonly accepted in the synthesis of gigantic molecules, such as the total synthesis of natural products. It should be particularly potent in pursuing relatively large fullerene synthesis because there is less restriction on the skeleton at the connection between the two hemispherical buckybowls (i.e., a consecutive six-membered ring structure such as acene can be introduced). In addition, if we can successfully design a pathway for introducing five-membered rings during the connection process, we may not even need to preinstall six five-membered rings in two buckybowls. However, in the C_{60} skeleton, in which the five-membered rings are packed tightly together while satisfying the IPR rule, there is no structural "room" at the connection. Therefore, in reality, the dimerization of C_{30} molecule **27** achieves the C_{60} synthesis through the convergent synthesis method starting from corannulene.

As mentioned above, the synthesis of **27** has not yet been achieved (indeed, it would be challenging due to its highly distorted structure and the presence of highly active five-membered rings at the periphery). In contrast, a computational study on the possibility of the dimerization of **27** was reported by Méndez and coworkers [22]. **27** has an armchair-like peripheral structure similar to that of **25**, with five distorted five-membered rings protruding. Therefore, **25** is expected to have high activity against Diels-Alder-type reactions. In fact, a Diels-Alder reaction can be envisioned in which the cyclopentene moiety is a dienophile, and the quinodimethane structure generated via the two cyclopentane rings is a diene (Fig. 5a). If the reaction proceeds formally at five sites (although all must proceed with the desired stereoselectivity), formation occurs of a total of ten carbon-carbon bonds, resulting in a $C_{60}H_{20}$ molecule (**65**). **65** is just a belt of hydrogen left at the suture of the two hemispheres, and although **65** itself has not yet been reported, it will probably form C_{60} with the release of ten molecules of H_2 without any problems. For dimerization, both one-step and stepwise mechanisms have been calculated. The one-step reaction may not proceed because its maximum energy barrier is above 7 eV. On the other hand, in the stepwise mechanism, the highest barrier was involved in the first D-A reaction with two carbon-carbon bond formations at about 4 eV (Fig. 5b). However, once the desired concave-type intermediate was generated, further bond formation and products including **65** were expected to proceed in an ergogenic manner. Although 4 eV is still an extremely high-energy barrier to achieve in a conventional flask reaction, it may not be impossible with the use of particular conditions, such as laser-assisted synthesis.

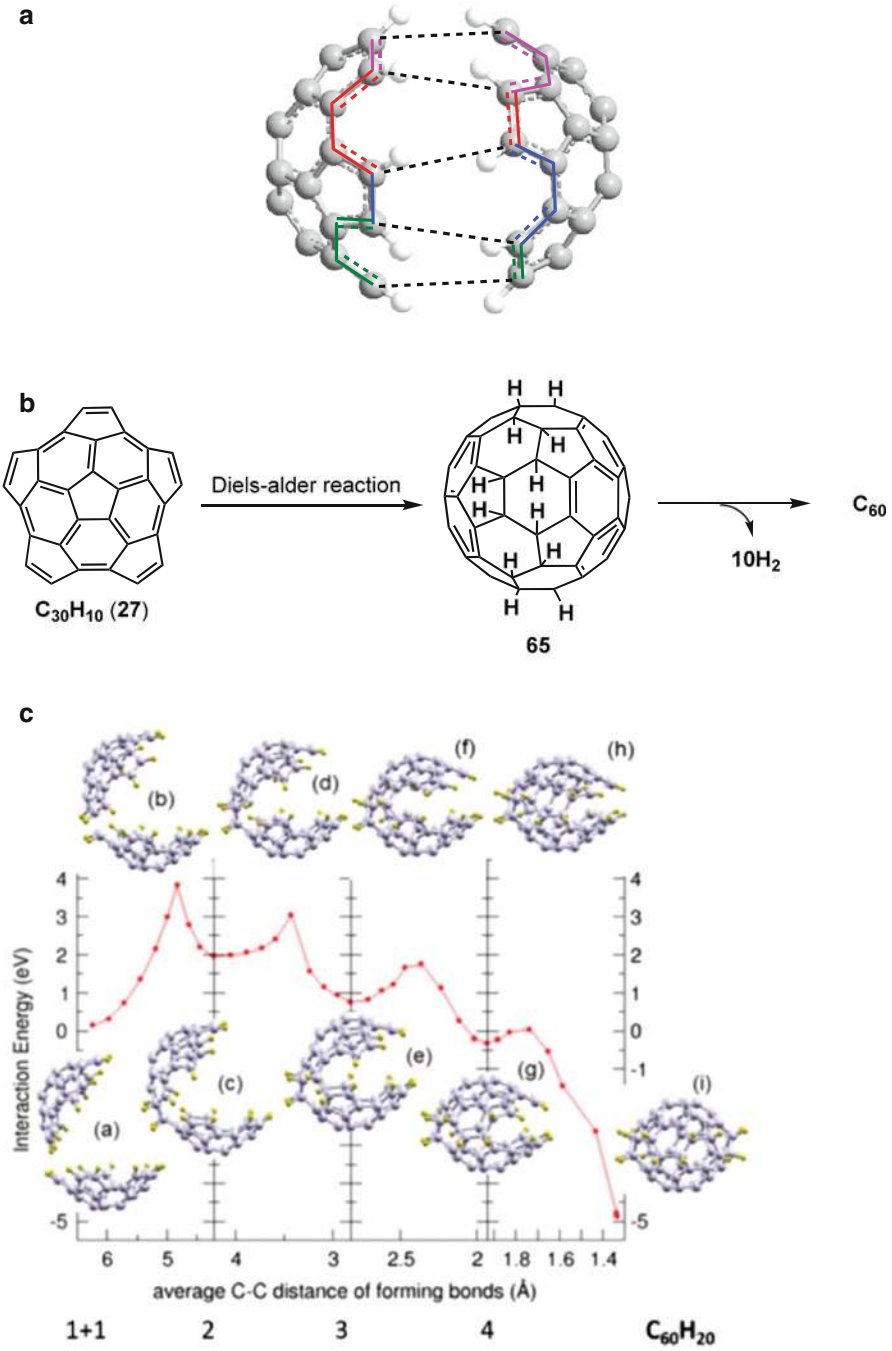

Fig. 5 Convergent approach to C_{60}. (**a**) Dimerization model of **27**. (**b**) Possible scheme to C_{60}. (**c**) Energy diagram by calculation with permission from Royal Society of Chemistry

Synthesis of Sumanene (23)

Sumanene (**23**) is a fused structure of three hexagons and three pentagons to a central benzene ring and is another pristine structure of buckybowls with three-fold symmetry. Unlike corannulene, **23** was newly proposed after the discovery of C_{60} by Mehta et al.'s retrosynthetic analysis as shown in Scheme 1 (hence the Sanskrit-derived name given by Prof. Mahta). The characteristic feature of **23** is the presence of three reactive benzylic methylenes at its periphery. Since many variations of functionalization via this benzylic position are expected, **23** is fascinating from the viewpoint of synthetic organic chemistry. On the other hand, when viewed as a novel aromatic compound, **23** has the iso-structure as triphenylene with four benzene rings. Therefore, its photochemical and electrochemical properties may not be so different from those of triphenylene. Nevertheless, in comparison with corannulene that has only one pentagon, sumanene, with three pentagons, is more distorted, to such an extent that the depth of the bowl is expected to be about 1.11 angstroms compared to 0.89 angstroms for corannulene, making the synthesis even more difficult. In fact, Mehta et al. reported in 1993 that their attempt to synthesize **23** using FVP from a precursor with a triphenylene skeleton was unsuccessful [23] (Scheme 9). Under FVP conditions, one or two five-membered rings were constructed, but not the third one, sumanene itself. Unlike corannulene, FVP in the attempt at sumanene synthesis was carried out under milder conditions because the decomposition at the susceptible benzylic positions is likely to proceed under harsh conditions. The result that FVP, the principal method for buckybowl synthesis at that time, was essentially unavailable was quite depressing and stalled the chemistry of sumanene. Therefore, we should consider ways other than FVP to achieve the synthesis of sumanene.

Sumanene was first synthesized in 2003, more than a decade after Scott and Siegel achieved the practical synthesis of corannulene by FVP [24]. Sakurai, Daiko, and Hirao did not use FVP; instead, they developed a stepwise chemical synthesis (Scheme 10). Starting from readily available norbornadiene, they completed the synthesis of **23** in only three to four steps: cyclotrimerization of norbornadiene, tandem ring opening-ring closing olefin metathesis (ROM-RCM), and oxidative aromatization. For more details and the history of this sumanene synthesis, please refer to the recently published accounts [25]. If we may emphasize one point, the key to the success of this synthesis is the presence of the sp^3 carbon. Using the intrinsic three-dimensionality of the sp^3 carbon to first construct a bowl structure and finally acquire aromaticity by oxidation is a universal concept in the chemical synthesis of highly strained molecules, as seen in the first synthesis of corannulene by Barth and Lawton [13]. It should be mentioned that sumanene is also commercially available, although it is limited to some regions.

Derivatization of Sumanene

There are three major reaction sites in sumanene (**23**): benzylic carbon, aromatic carbon, and internal carbon. However, only the first two, which are relevant to C_{60}

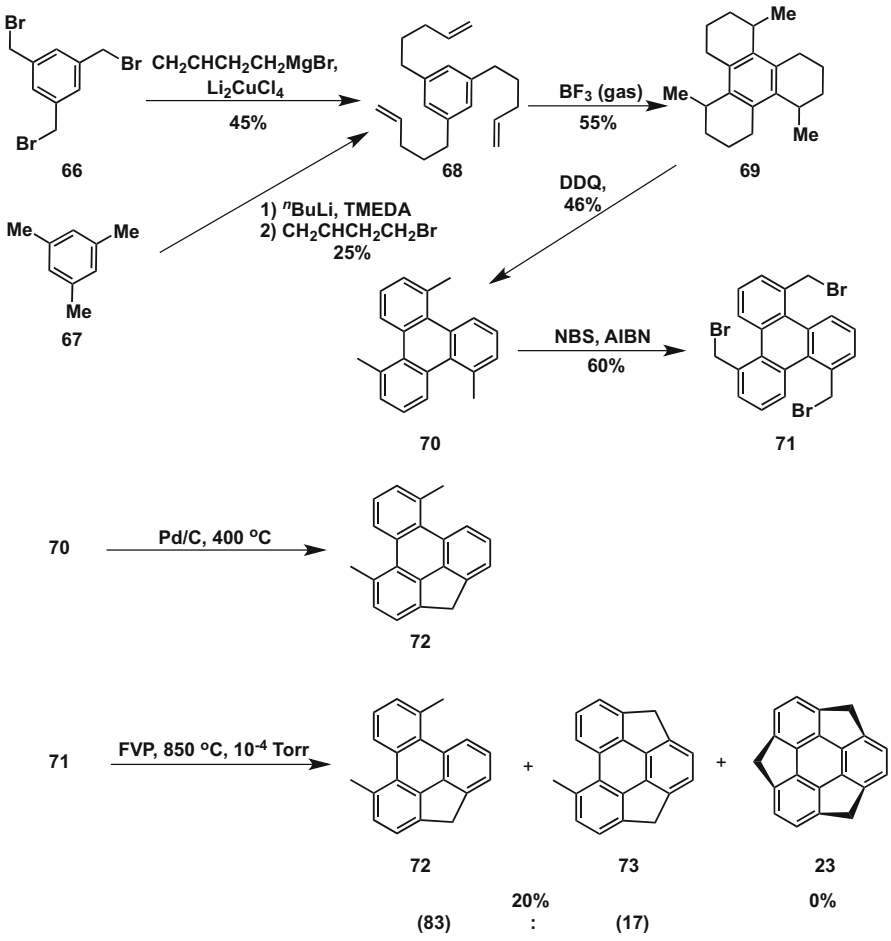

Scheme 9 Mehta's attempt to synthesize **23** by FVP

synthesis, will be discussed in detail here. Before we get into that, we need to add some comments on the synthesis with FVP. We have already mentioned that the synthesis of **9** with Mehta's FVP was unsuccessful because **23** has three reactive benzylic positions at the periphery, and under FVP conditions, further reactions would proceed [23]. Indeed, FVP can provide more distorted buckybowls and even C_{60}, as discussed in section "FVP Approach." In other words, the FVP approach is affordable as long as there is no active substituent, such as a benzylic position at the periphery. Among several FVP syntheses of molecules with the sumanene fragment reported previously, the most famous example is the synthesis of the hemifullerene C_{30} molecule (**83**) by Rabideau et al. (Scheme 11) [26]. Starting from a compound derived from truxene (**80**), they have successfully synthesized **21**, which is a substructure of C_{60} containing a sumanene skeleton (thus named hemifullerene),

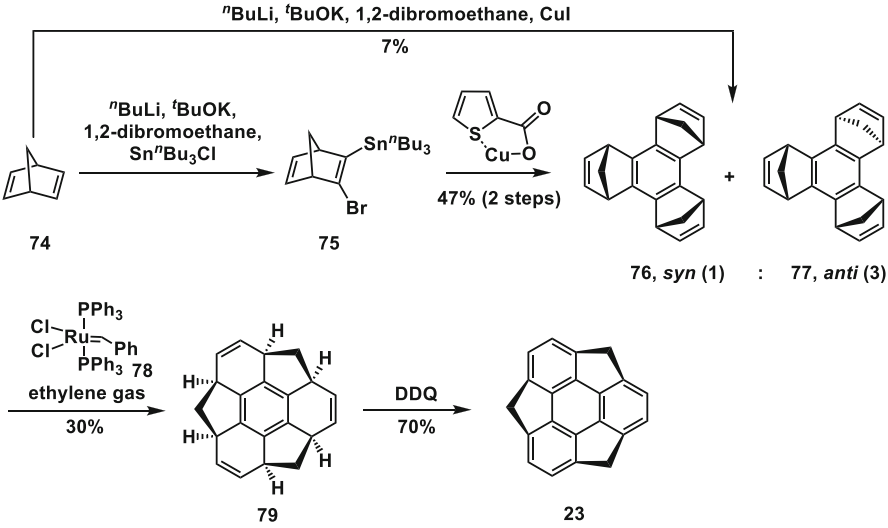

Scheme 10 The first synthesis of sumanene (**23**)

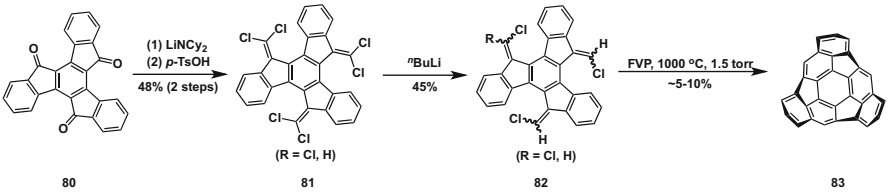

Scheme 11 Hemifurrelene (**83**) synthesis by FVP

by FVP. FVP accelerates the bond formation between the outer aromatic rings in this pathway, cleverly avoiding the exposure of the free benzyl positions. On the other hand, there will be significant limitations on further functionalization when the whole periphery consists of aromatic rings. In principle, the dimerization of **83** will give C_{60}. However, since **83** involves only three pentagons, the zipping-up process must be very tough: The process requires the simultaneous construction of six pentagons.

Let us return to the topic of sumanene derivatization. Since the benzylic position of sumanene is an isostructure of that of fluorene, their reactivities might resemble each other. However, there are two main differences in their reactivity. One is that the three benzylic positions interact with each other through the triphenylene moiety, which affects the reactivity of the remaining sites as the reaction progresses. A typical example is the oxygenation of **9** at the benzylic positions (Scheme 11) [27]. Oxosumanenes are valuable precursors for further functionalization at the benzylic positions. The corresponding monooxo- (**84**) or trioxo- (**86**) sumanenes can be prepared by changing the conditions for Ru-catalyzed oxidation; however,

dioxosumanene (**85**), which is supposed to be formed as an intermediate between **84** and **86**, is scarcely obtained. Indeed, the calculated values of pKa (in THF) of the benzylic acidity reveal that the benzylic acidity of **85** (20.0) is much larger than that of the malonic acid esters (26.2), while the acidity of the benzylic acidity of **23** and **84** is 30.9 and 25.6, respectively. Therefore, it is difficult to terminate the oxidation at **24** formation under the Ru-catalyzed reaction conditions. Such a perturbation between the three benzylic positions of sumanene may not cause serious interference in the synthetic route in a triply symmetrical manner, as in the C_{60} synthesis. Still, it can sometimes be a problem when an unsymmetrical synthetic pathway needs to be considered (Scheme 12).

Another difference between sumanene and fluorene in their benzylic positions is that, unlike planar fluorene, the two protons on the benzyl position of the curved sumanene are in a diastereotopic relationship, and the inside (*endo*) proton and outside (*exo*) proton of the bowl have different reactivities. Such a difference in reactivity is significant in constructing a three-dimensional structure. As shown in the synthesis of **23** [24] (or the first synthesis of **22** [13]), introducing the sp^3 carbon is critical in the bottom-up synthesis to ensure stereogenicity. In this respect, it makes sense to use the sp^3 carbon in the benzylic position of sumanene as a stepping-stone for the three-dimensional construction, which must be superior to the compounds at the periphery that are completely aromatized.

So how different are the reactivities of these two diastereotopic protons? In 2005, Sakurai et al. reported that mono-, di-, and tri-anions are selectively generated at the benzylic positions of **9**, and from trianion intermediate, treatment of Me_3SiCl gave the tris(trimethylsilyl)sumanene (**87**) as the first example as a benzyl-substituted derivative (Scheme 13) [28]. The geometry of TMS groups was exclusively exo, in this particular case, the stereosectivity can be explained by a simple steric hindrance. Subsequently, some substituents have been found to be introduced endo-selectively such as OH groups [29]. Moreover, both of the two xylyl groups in bis(2,6-Xylyl) sumanene are endo-selective with 100% selectivity, despite being sterically bulky [29, 30].

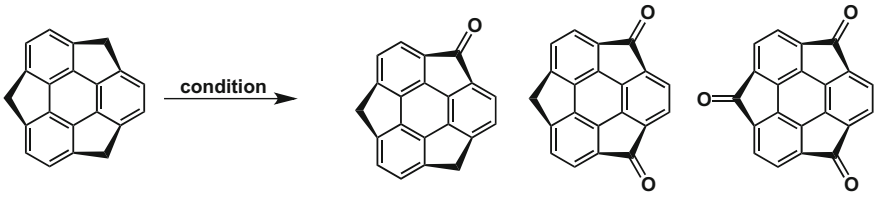

		23	84	85	86
condition a	$RuCl_3$, 70% ^{t}BuOOH aq pyridine		0%	0%	73%
condition b	Phosphotungstic acid 70% ^{t}BuOOH aq pyridine		51%	< 1%	10%

Scheme 12 Ru-catalyzed oxygenation of **23**

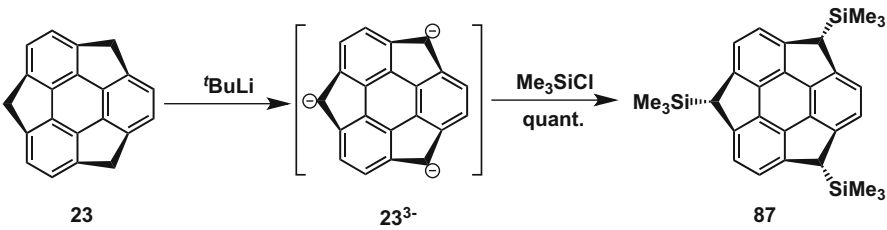

Scheme 13 *Exo*-selective trimethylsilylation of 23

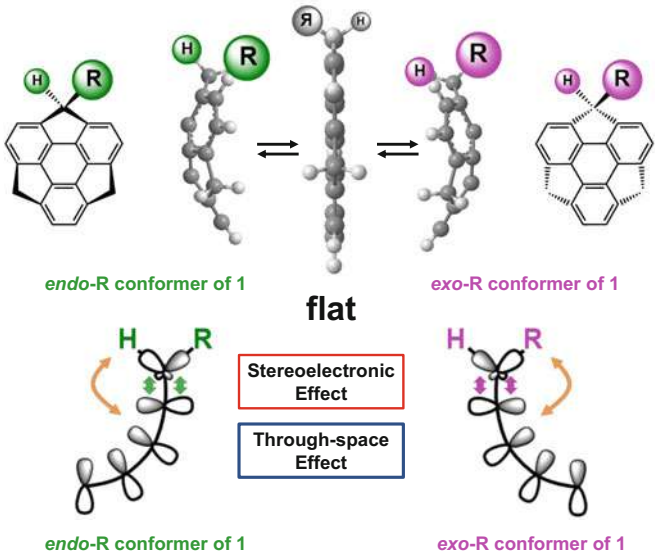

Fig. 6 Stereoelectronic effect at the benzylic position of **23**

One of the characteristics of buckybowls, such as sumanene, is the "bowl-to-bowl inversion" motion, in which the concave and convex surfaces of the bowl are inverted. Since the bowl inversion barrier in sumanene is approximately 20 kcal/mol, the bowl is slowly inverted even at room temperature [24]. Therefore, the endo−/exo-selectivity of substituents can be translated to each thermodynamic stability. The stereoelectronic effect explains the above selectivity well [29]. The hyperconjugation effect of a curved pi surface differs between the concave and the convex faces. It was experimentally and theoretically confirmed that the substituent with the more significant stereoelectric effect faces the exo-side. This guideline will provide an excellent hint for future three-dimensional construction starting from sumanene [29] (Fig. 6).

As crucial as the stereoselective introduction of functional groups into the benzyl position is the possibility of extending the conjugation from this benzyl position. As shown above, anions are easily generated at the benzylic positions of **23** by strong

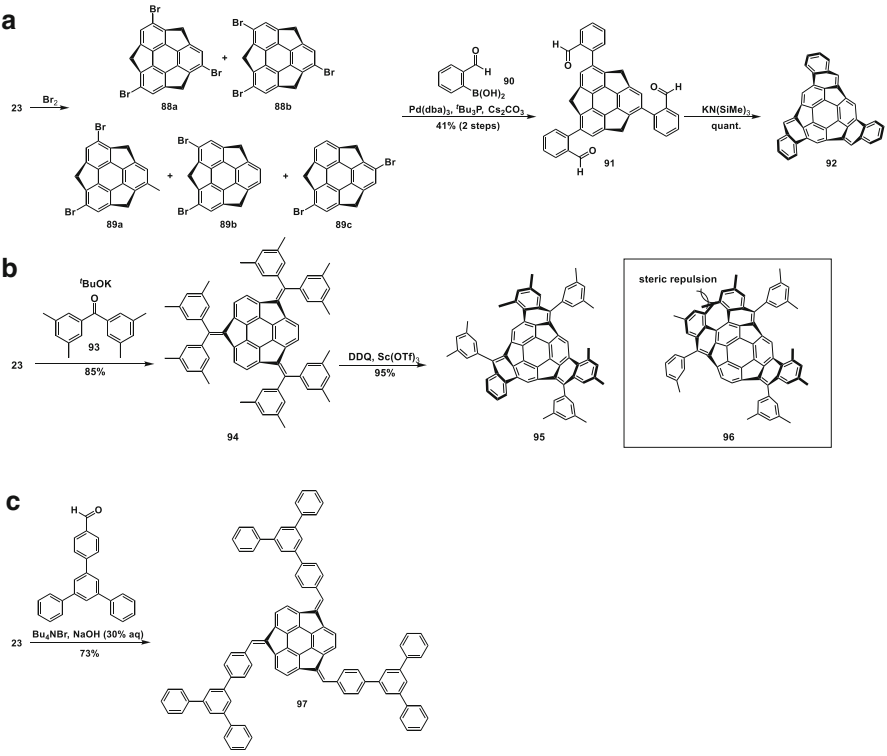

Scheme 14 Examples of conjugation extension at the benzylic position of 23

bases [28]; therefore, condensation reactions with carbonyl compounds such as aldehydes take place to yield the corresponding conjugated molecules [31]. When the substituents with formyl groups are introduced at the aromatic positions (**91**), intramolecular condensation can be carried out to yield the fused compound (**92**) (the family structure as Sygula's hemifurrelene) (Scheme 14a) [32]. Furthermore, by performing the condensation reaction first, followed by the oxidative cyclization-aromatization under equilibrium conditions, it is possible to selectively synthesize C_3 symmetric molecules (**95**) without prior separation of positional isomers (Scheme 14b) [33]. Recently, a highly conjugated molecule with terphenyl units (**97**) was synthesized that exhibited the exclusive cesium cation response in emission quenching (Scheme 14c) [34].

To introduce various functional groups, we need to have many variations in the transformation reactions. In addition to reactions via carbanions, reactions via carbonyls are also important. In addition, it has recently been reported that carbenes (**99**) can also be generated from the corresponding diazo derivative (**98**). From **98**, tetrasubstituted olefins (**100**) have been introduced in reactions with thiocarbonyl compounds (Scheme 14) [35] (Scheme 15).

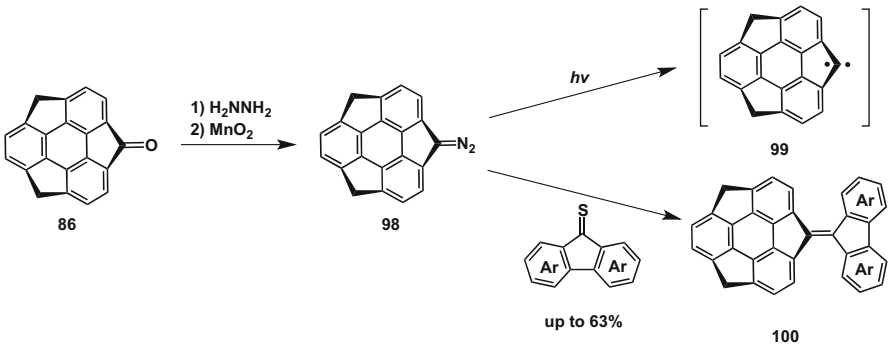

Scheme 15 Carbene formation at the benzylic position and further functionalization

On the other hand, the functionalization of sumanene's aromatic ring is more complicated than that of corannulene. All aromatic peripheries of sumanene correspond to the substitution of an alkyl group in the ortho position. In addition, in terms of bond alternation, the less reactive carbons are on the periphery. Furthermore, it is difficult to introduce substituents in a regioselective manner because the five-membered ring is bridged between neighboring aromatic rings, making perturbation by substituent effects difficult. Indeed, electrophilic substitution of sumanene results in a mixture of positional isomers, and the C_3-symmetrical form is not only low yielding but also difficult to separate and purify (Scheme 16a) [36]. In order to selectively prepare the C_3-symmetric derivatives, it is more practical to change the starting material itself and synthesize it by a different route. Asymmetric synthesis of C_3-symmetric trimethylsumanene (**107**) (Scheme 16b) [37] and a couple of tri-substituted sumanenes (**39**) (Scheme 16c) [38] have been achieved using the syn-selective cyclotrimerization catalyzed by Pd nanoclusters so far. However, longer steps are required. Therefore, the synthesis of poly-substituted compounds on sumanene aromatic rings has not progressed for a long time.

A synthetic method for the hexabromosumanene (**113**) overcame the stagnation [39]. Since halides are the principal substituent for further conversion to functional groups, their synthesis must have been investigated. However, it was probably overlooked due to their extremely low solubility. In fact, **113** is only scarcely soluble in heated *o*-dichlorobenzene and is even difficult to identify by NMR due to its poor solubility. Once prepared, it was easily isolated and purified by recrystallization. We worried that subsequent reactions might be challenging due to the low solubility, but luckily, we can manage them very smoothly by the careful choice of reaction conditions. In particular, the applicability of Suzuki-Miyaura coupling was very effective (Scheme 16) [39]. A variety of aromatic functional groups, including the usual phenyl group, can be introduced with six substitutions, and the resulting compounds generally have improved solubility. Indeed, the construction of supramolecular structures such as hydrogen-bonded network structures with nonplanar sheet structures [40], MOFs with spherical isolated spaces [41], and liquid crystal systems [42] has been reported from the hexasubstituted sumanene derivatives obtained in this way (Scheme 17).

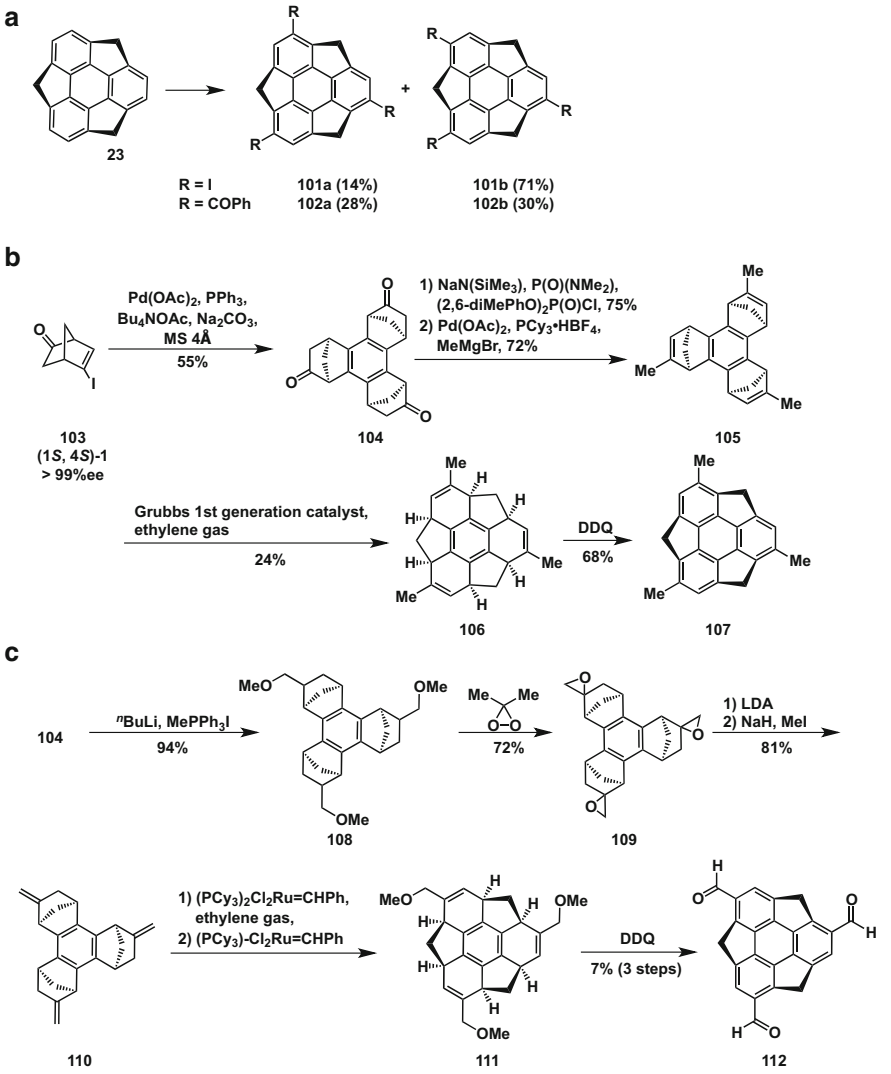

Scheme 16 Examples of *tri*-substitution of **23** at the aromatic position

As described above, we can say that the required pieces for the total synthesis of C_{60} starting from sumanene are finally in place. We believe that the total synthesis route to C_{60} from sumanene might be more promising because of the wide variety of the available reactions and derivatives, and the ease of introducing the sp^3 carbons at the appropriate positions for the construction of the three-dimensional structure.

Finally, we want to discuss the requirements for a C_{60} synthesis from sumanene. Just as in the discussion in the corannulene section, a convergent synthesis must be more promising. It is desirable to dimerize the C_{30} unit and, if possible, to possess six pentagons already to achieve the convergent synthesis. In particular, it is highly

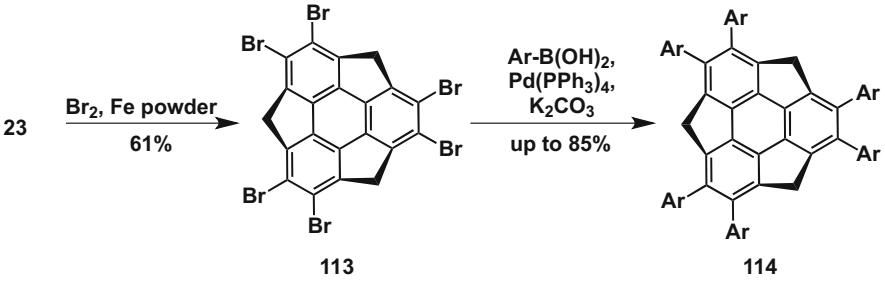

Scheme 17 *Hexa*-substitution of **23** through hexabromo derivative (**113**)

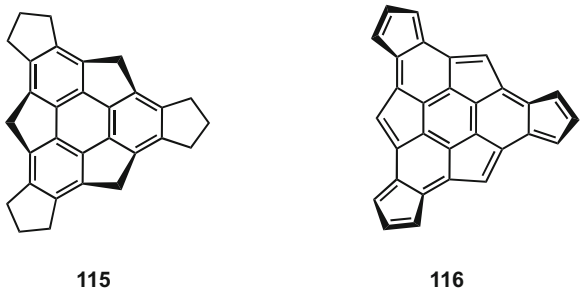

Fig. 7 C_{30} units (**115**, **116**) from sumanene framework for convergent synthesis

advantageous to use only the six-membered ring formation processes in the final zip-up process, which can proceed in a planar geometry reaction. A hemispherical molecule that satisfies the above requirements will have the structure of **115** (Fig. 7). In this structure, the six five-membered rings have few fused sites and are bare at the periphery. Therefore, although the bowl curvature is still shallow and the subsequent ring condensation reaction might be difficult, more versatile synthetic routes will be available with a significant number of sp^3 carbons to achieve the ring closure direction. Rabideau previously proposed six potential hemifurrelene structures, and among them, **116** seems to be the most energetically disfavored structure rather than other hemifurrelene structures like **83** [26]. However, they limited their discussion to fully conjugated molecules. Indeed, we do not need such a limitation. Rather, it is more advantageous for synthetic chemistry to aggressively use the sp^3 carbon!

FVP Approach

In the section on bottom-up synthesis, we mentioned that FVP could be a powerful tool for synthesizing highly strained but thermodynamically stable compounds such as buckybowls. Initially, Smally et al. found C_{60} in the chemical species that multiply when the carbon clusters produced by laser evaporation of graphite are cooled. In the arc discharge and combustion methods that have become the mainstream methods

for synthesizing C_{60} since then, C_{60} is preferentially generated when (to put it crudely) carbon clusters of a specific size in a high-energy state are generated and then reduced to thermodynamically stable chemical species. For example, Chuvilin et al. reported the details of the formation process of C_{60} by arc discharge from graphene bilayers [43]. In fact, the production of C_{60} is not so harrowing as long as the corresponding high-energy carbon clusters are generated, as C_{60} exists in India ink and space. The same is true under FVP conditions. For example, even when small molecules such as naphthalene are exposed to FVP conditions, the formation of C_{60} is confirmed, albeit the yield is small. Although it is undoubtedly detected, it is probably too much to be called a synthesis.

Scott et al. attempted to synthesize C_{60} through the FVP method by harnessing the advantage that FVP shows high selectivity for relatively reliable reactions, such as radical reactions and carbene insertion reactions [44] (Scheme 18). They carefully designed a precursor of C_{60} (**119**), which should consist of 60 carbons and should be a planar development diagram. The precursor was prepared from the truxene derivative (**118**) (as you can see in the later section, this framework becomes the standard for the C_{60} precursor). As a result, from an almost planar structure (in reality, it is helically twisted) as a starting material, they can detect a significant amount of C_{60}! This method is absolutely different from the previous method of "spontaneously promoting" the formation of C_{60} from carbon clusters, where C_{60} was generated bottom up through the targeted bond formation. Therefore, we now recognize that this is the first "chemical synthesis" of C_{60} [44].

It would be difficult to discuss the structure of the intermediates during the FVP process, but let us try to analyze the key to success (Fig. 8). First, the isomerization associated with bond rotation is avoided throughout the structure of the compound. Additionally, since it is a three-fold symmetric molecule, it is simple to obtain the desired structure if the same type of reaction proceeds in three different locations. Assuming that the compound is zipped up in a bottom-up manner, the first reaction of bowl formation can be presumed to be the formation of a six-membered ring by an electrocyclic reaction of triene, followed by dehydrogenation, which is a reasonably reliable reaction in FVP. The next step is considered to be more difficult because it involves the formation of a five-membered ring in three places at the same timing.

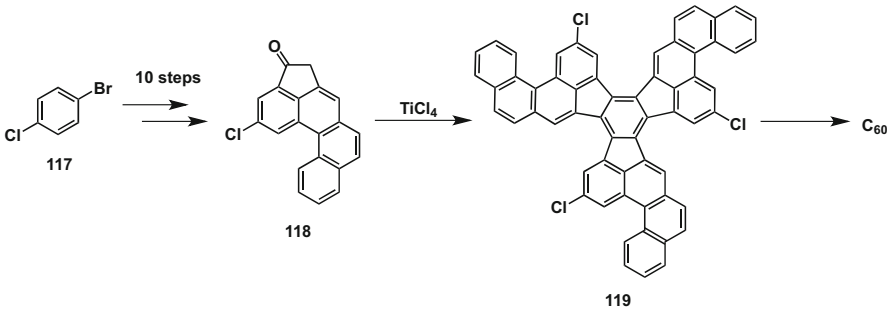

Scheme 18 Chemical synthesis of C_{60} by FVP method

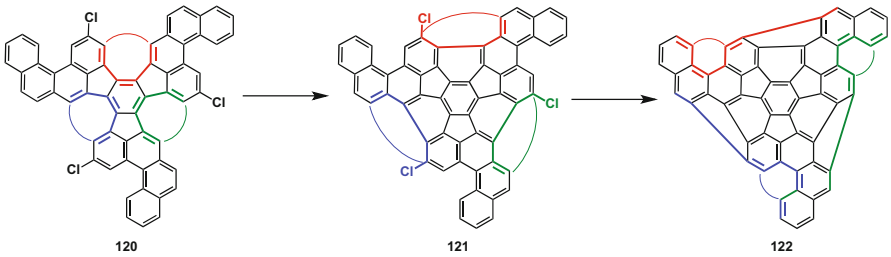

Fig. 8 Possible construction route under FVP

The introduction of chlorine at the reaction point contributes to the acceleration of the reaction. In addition, three more five-membered ring formation sites have already been introduced into the molecule.

Unfortunately, C_{60} synthesis by FVP is insufficient in terms of efficiency, with a few percent yield. However, it is undisputed that this study is an epoch-making one in that it is the first time that C_{60} has been produced in a bottom-up manner. In contrast, the previous generation of C_{60} in FVP, arc discharge, combustion, and in nature were all top-down processes. (Of course, this kind of physical method may be formally classified as bottom-up synthesis, but here I will call the chemical synthesis approach bottom-up synthesis.)

Synthesis on Metal Surfaces

The application of metal surfaces in synthetic organic chemistry has recently made rapid progress. In particular, the effect is remarkable in the field of aromatic compound synthesis.

Planar compounds containing benzene rings have excellent compatibility with metal surfaces. The metal surface functions as a template – not to mention graphene, a leading material of 2D materials. Most of these carbon-carbon skeleton-forming reactions between benzene rings are catalyzed by transition metals, including cross-coupling reactions such as Suzuki-Miyaura coupling, Ullmann coupling between two aryl halides, and even dehydrogenative coupling between two C-H bonds (or so-called cyclodehydrogenation). In other words, the metal surface itself works as a catalyst. In addition, many reactions useful for aromatic ring formation, such as electrocyclic reactions, are expected to be accelerated by the adsorbed species on the metal surface. On the other hand, on-surface reactions are often observed by electron microscopy, and the effect of electron beams and currents on accelerating these reactions must be taken into account.

In 2008, the first C_{60} synthesis on a metal surface was achieved by Otero and Biddau [45]. They used $C_{60}H_{30}$ (**123**) as a precursor to C_{60}, which has the same topologically favorable truxene framework as the molecule used by Scott et al. If dehydrogenative coupling is performed at the desired position, it can be assembled directly into C_{60} (without the need for rearrangement reaction). Moreover, there must

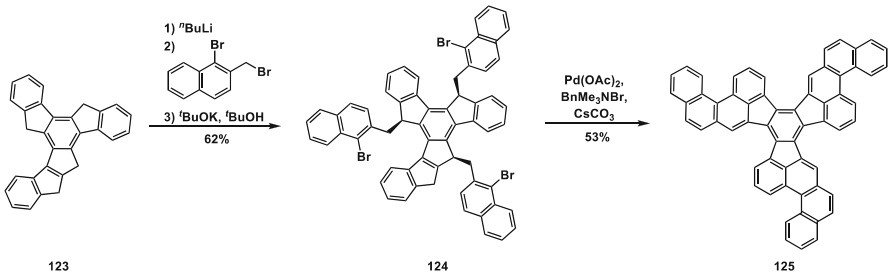

Scheme 19 C_{60} formation on Pt(111)

be no isomer formation pathway caused by bond rotation, etc. during the process. STM was used to observe the chemical transformation process. When **123** was adsorbed on a Pt(111) surface, the three wings of **123** were visible and observed as a triangular image with a length of 2.2 nm and a height of 0.14 nm. When annealed at 750 K, all these triangular images were converted to circular images, and the diameter was reduced to 1.5 nm, while the height was increased to 0.38 nm. This image is very similar to that of C_{60}, which has been observed previously, suggesting that the expected zip-up reaction proceeds in almost a 100% yield (Scheme 19). Mass spectrometric analysis of the decomposition products during annealing showed only hydrogen, suggesting that only dehydrogenative coupling proceeded and that no side reaction involving the decomposition of carbon-carbon bonds occurred. On the other hand, this phenomenon hardly proceeded on the Au(111) surface, indicating that the catalytic effect on the Pt(111) surface plays a critical role.

This achievement had a tremendous impact not only on the quantitative formation of C_{60} from planar-like precursors on metal surfaces but also on subsequent research in the following two senses.

The first is that they have shown that it is possible to synthesize fullerenes other than C_{60} if a topologically reasonable precursor can be designed. In the same paper, they demonstrated the synthesis of heterofullerene $C_{57}N_3$ (**124**) [45]. The heterofullerenes, in which some of the carbon atoms of C_{60} are replaced by other elements, are extremely interesting both structurally and electronically, by analogy with other doped carbon materials. However, it is difficult to introduce these heteroatoms in a targeted position and a targeted amount using a physical, top-down approach; therefore, a chemical process is indispensable. In fact, synthetic methods have been established only for very few cases, such as $C_{59}N$, which can be derived from C_{60}. Otero and Biddau et al. synthesized the indole-based trimer $C_{57}H_{33}N_3$ (**47**), which has nearly the same skeleton as the **123**. They performed the same experiments and observed almost the same images and changes after annealing, strongly suggesting the formation of a new heterofullerene **47** (Fig. 9). The existence and electronic state of nitrogen atoms were confirmed by X-ray photoelectron spectroscopy (XPS). The N_{1p} peak intensity did not change significantly before and after annealing, and two peaks corresponding to the N atom in the graphite sheet and the N atom interacting with Pt were observed. Of course, the materials obtained

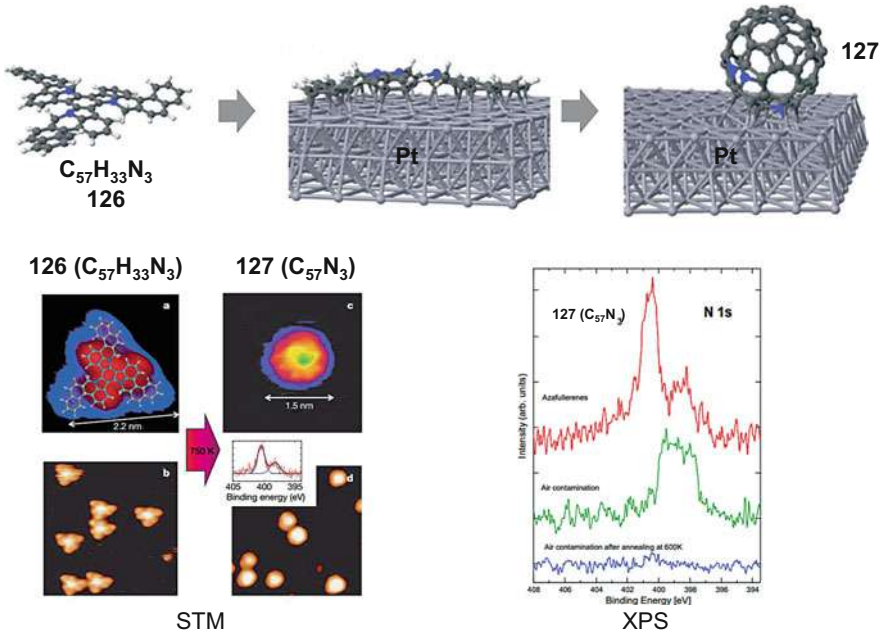

Fig. 9 Observation of $C_{57}N_3$ formation with permission from Nature Publishing Group

in this experiment were observed only when they were strongly adsorbed and stabilized on the Pt(111) surface. Someone may assert a need to prove the formation of the molecule only when it was isolated (in hand), and was confirmed spectroscopically such as through NMR and even X-ray crystal structure analysis data. Indeed, formation of C_{60} in this experiment was confirmed by laser desorption-ionization time-of-flight mass spectrometry; unfortunately, however, **124** was not confirmed due to its strong interaction with Pt(111). However, at the very least, this work is significant in that it shows that if a reasonable precursor is synthesized, the corresponding fullerene can be produced in an almost 100% yield (or should we call it probability?).

The second point is that, unlike FVP, they can also examine chemical species that we might call intermediates by tuning the operation temperature. They observed that dehydrogenative coupling does not proceed below 400 K but starts around 500 K. In addition, an unsymmetrical image of the structure is observed around 400–600 K, suggesting that a partial cyclization reaction is in progress. As in Scott's C_{60} synthesis by FVP, the first cyclization is considered the formation of three six-membered rings in the interior. According to the calculations, the formation of the next three five-membered rings is expected to have the highest energy barrier. However, it is still about 0.3 eV, which is not a problem under the present conditions. At this energy state, the carbon skeleton is relatively free to isomerize, but once these three five-membered rings are formed, it is expected that the rest of the process will lead to the formation of stable C_{60} (Fig. 10). And these intermediates are expected to

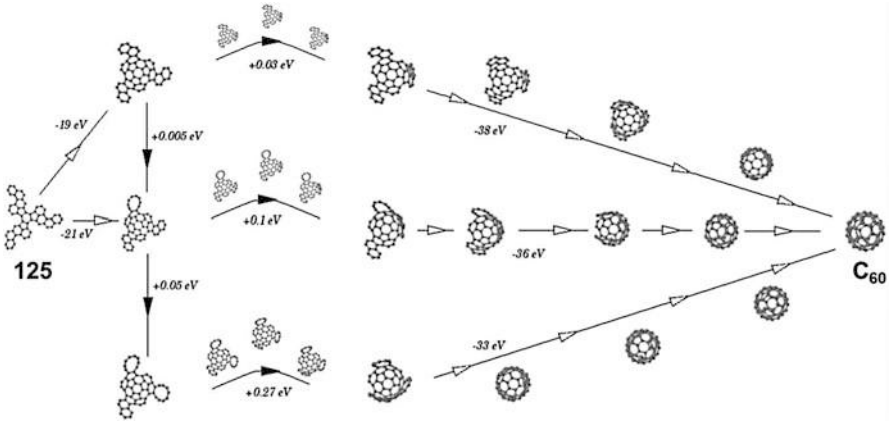

Fig. 10 Calculated pathways for the formation of C_{60} on Pt(111) with permission from Nature Publishing Group

produce chemical species that have undergone C-H activation by Pt, i.e., the edge of the bowl has been adsorbed onto Pt [45].

Such a metal surface–adsorbed buckybowl species resembles a proposed model for the elongation species and the catalytic site of single-wall carbon nanotubes (SWCNT). In other words, this method presents the possibility of realizing the single-chirality synthesis of SWCNT (which is even more important for material science than C_{60} synthesis). The physical properties of SWCNTs, including electrical conductivity, vary depending on their chirality. Carbon nanotubes are usually obtained as a mixture of various chirality, but if pure SWCNTs with a single chirality can be obtained, it is expected to improve their physical properties and the reproducibility of their performance. Since SWCNTs are generated by the epitaxial growth of sp^2 carbon layers on the surface of the metal (nanoparticle) catalysts, the synthesis of carbon nanotubes with a single chirality requires the use of a seed molecule whose chirality has already been determined and from which carbon nanotubes can be grown without isomerization. In this case, the seed molecule is either a hemispherical (with six pentagons) buckybowl or a carbon nanobelt that does not undergo bond rotation. In terms of the versatility of synthetic routes, the approach of buckybowl synthesis, in which the pentagons are spatially arranged in six appropriate positions, is higher. Still, in practice, as mentioned earlier, there is only one example of a complete hemispherical buckybowl synthesis achieved.

Reactions on a metal surface can sequentially catalyze both the formation of hemispherical buckybowls and the epitaxial growth. In 2014, Amsharov and Fasel et al. reported the first example of the selective growth of (6,6)SWCNTs on a Pt(111) surface [46]. In this case, the precursor must have a structure that allows for the continuous construction of hexagons without ring closure after the formation of six pentagons. In contrast, the carbon source should be supplied and the elongation reaction should be catalyzed on Pt. The precursor $C_{96}H_{54}$ (**125**) shown in Fig. 11 was

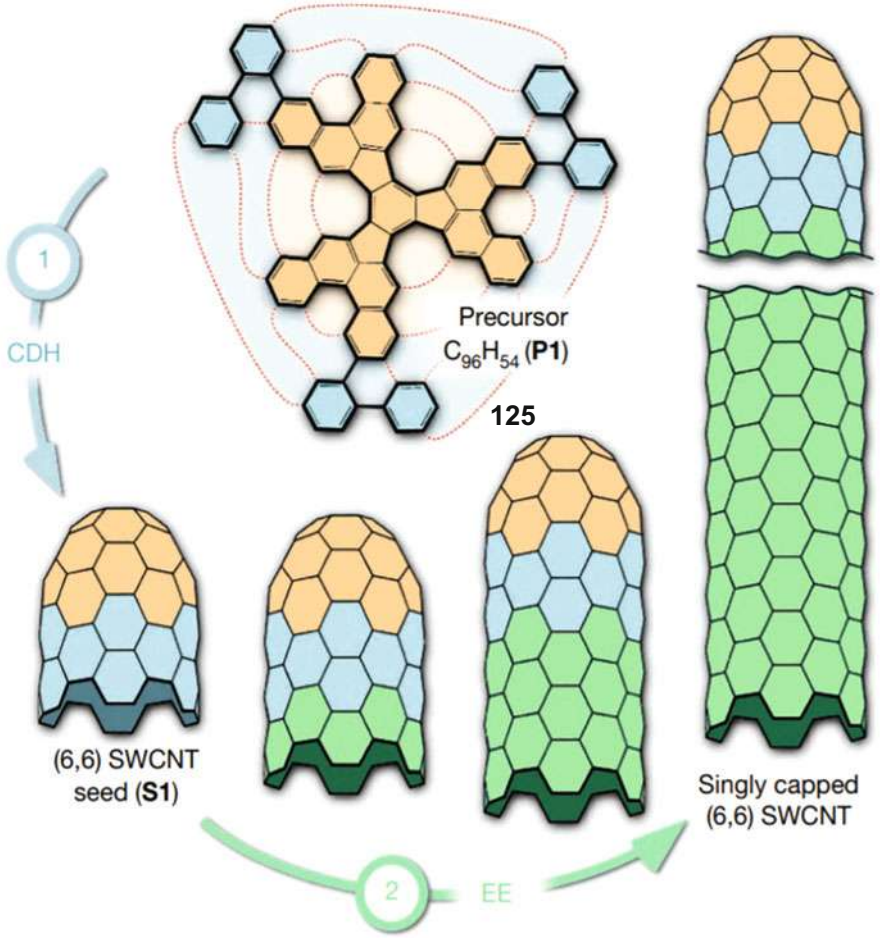

Fig. 11 Pt(111) surface-catalyzed singly capped (6,6) SWCNT formation with permission from Nature Publishing Group

designed, synthesized, fixed on Pt(111), and annealed at 770 K under vacuum. In this stage, cyclodehydrogenation (CDH: the same as dehydrogenative coupling) constructs the hemispherical structure adsorbed on Pt. In C_{60} synthesis, once the ring is built up to the hemisphere, the downhill reaction can proceed toward the thermodynamically most stable C_{60} backbone structure using the 60 carbon atoms available in the field. However, in SWCNT formation, it is necessary to prevent such a ring closure to the fullerene and form the "guide" part required for tube structure elongation before epitaxial elongation. So, inevitably, the structure of the precursor becomes huge (96 carbons), and therefore, isomers due to bond rotation exist. In the case of **125**, there are three free-rotating bonds, so a total of four different isomers are immobilized on Pt. In metal surface reactions, the initial structure is fundamental,

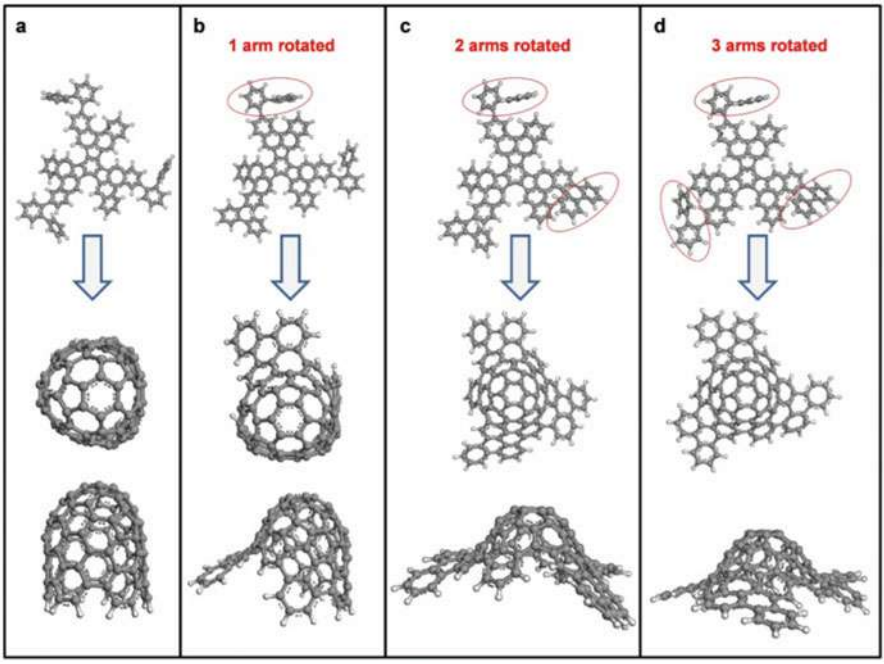

Fig. 12 Only one isomer can "survive" among four isomers with permission from Nature Publishing Group

and only adsorbed molecules with a topologically reasonable structure will "survive" in the hemispherical structure. In contrast, the remaining molecules will not assemble into a hemisphere and become dead end (Fig. 12). In other words, in this system, the cap structure of SWCNTs with (6,6) chirality was selectively synthesized, or perhaps it is more accurate to say that the form remained in the survival race. In any case, only the cap structure consistent with (6,6)SWCNTs is generated on the surface at the annealing stage. When epitaxial growth occurs using EtOH (actually ethylene obtained from the decomposition of ethanol) as feedstock, the resulting CNTs are confirmed to be highly pure (6,6)SWCNTs by Raman spectra. Another factor that makes this survival race possible is Pt(111) as a catalyst. The catalysts for SWCNTs are metal nanoparticles, and the size and shape of the particles also determine the chirality of the SWCNTs. However, since Pt(111) is not a catalyst for the epitaxial growth of SWCNTs, SWCNTs do not spontaneously form at other positions but only at the part where the cap structure is generated, resulting in less efficient but chirality-selective CNTs.

While this paper is exceptionally groundbreaking in that it enables the chirality-selective growth of SWCNTs, it also shows that in practice there are still many hurdles to overcome in synthesizing SWCNTs of arbitrary single chirality using this technique. The most important reason is the design of precursors to preassemble a relatively long CNT cap structure with some graphene walls. There are only three free-rotating bonds

in **125**, yet there are four positional isomers on the metal surface, and CNTs cannot grow from mismatched isomers. Alternatively, if another chirality can be generated from the rotational isomers, the single chirality itself will no longer be realized.

In reactions on metal surfaces, the most crucial observation method is the electron microscopy technique. Recent advances in electron microscopy technology have made it possible to observe and "visualize" phenomena at the "single-molecule" level. This is essentially different in meaning from what we have observed of populations by spectra in solution. However, the scanning probe technology used in the above examples has a limitation with observation speed, especially in terms of in situ observation. Nakamura, Harano, and their colleagues have been working on developing SMART-EM, a technique and measurement method to bring TEM to atomic resolution, which enables faster measurement. This technology has also made it possible to "visualize" the formation process of C_{60} [47].

The SMART-EM method is usually necessary to place the molecule in a cage such as an SWCNT to observe a single molecule. The $C_{60}H_{30}$ molecule **123**, however, was able to be measured on a graphene monolayer (GML). On the Pt (111) surface, Pt worked as the catalytic center for various reactions, and the reactions were activated by heating. It is known that aromatic carbons (or hydrocarbons), such as graphene, can also catalyze the electrocyclic reaction and cyclodehydrogenation, which are indispensable for C_{60} formation. In the case of TEM, the electron beam dose contributes to the activation of the chemical reactions. Lungrrich et al. succeeded in determining the structural changes in a single molecule of **123** by videorecording the structural changes upon electron irradiation and comparing them with simulation calculations. On Pt(111), **123** adsorbed closer to a flat surface with a wider Pi surface due to physisorption. In contrast, on GML, chemisorption progressed, probably forming a carbon-carbon bond in the form of impingement at the armchair position. When observed under accelerating voltage conditions of 315 K and 80 kV, an intermediate structure was observed, which was eventually converted into a spherical material, confirmed to be C_{60}. The structures of the intermediates were also predicted from the image analysis, and it is easy to imagine that the initial process is still the same as in other systems, where the inner six-membered ring formation is followed by an electrocyclic reaction/dehydrogenation, and then the final zip-up to C_{60} (Fig. 13).

Although the activation of the Pt(111) surface catalyzed by heat and that of the GML surface catalyzed by electron beam are different, the reactions are principally the same. However, the impact of visualizing the reaction process in the form of a movie was significant, and it is expected to provide substantial hints for the bottom-up synthesis of C_{60} and related substances in the future, not only for surface reactions.

Summary

More than 30 years have passed since the discovery of C_{60}, yet its appeal has not faded. As mentioned in the introduction, nowadays, C_{60} is readily available both as an inexpensive mixture and as a reasonably pure reagent, thanks to advances in

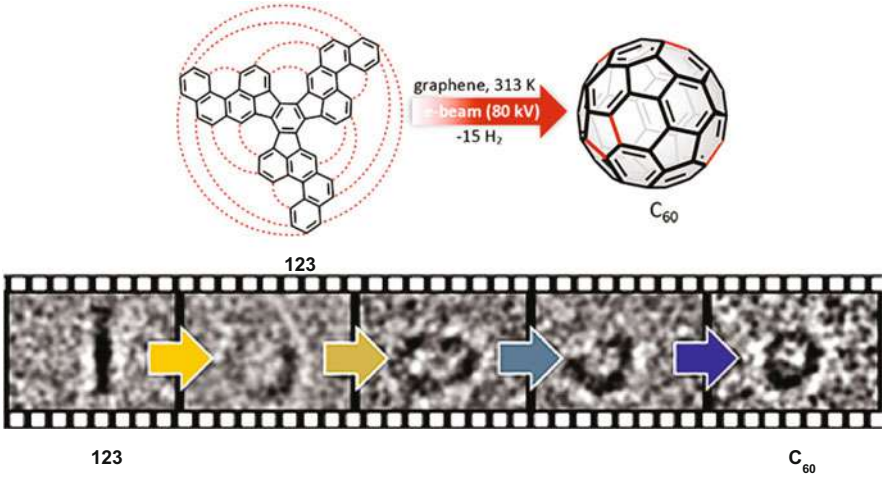

Fig. 13 Visualization of C_{60} formation from **123** by SMART-EM method with permission from American Chemical Society

synthetic techniques, such as the arc discharge method at the laboratory level and the combustion method, which is already commercially available. Therefore, a total synthesis of C_{60} through organic synthesis may not be so significant, at least for industrial technology. However, the 2011 report estimated the total energy consumption of C_{60} production by the combustion method to be close to 106.9 GJ/kg due to the extremely high cost of separation and purification [48]. Therefore, if an innovative means for the selective synthesis of C_{60} is realized, its value will be purely scientific as well as having a significant impact on the industry.

Synthetic organic chemistry continues to make steady progress day by day. From the viewpoint of researchers in other fields, organic chemistry always deals with the same types of reactions, with minor changes over the years. Still, even if the same types of reactions are carried out, innovations are being produced one after another that evolve from basic research using stoichiometric reactions as a beginning to catalytic reactions, to green processes, and finally to mass product processes. Therefore, synthetic techniques available in the 1980s, when C_{60} was discovered, were tremendously different than those available today. Similarly, even if a reaction is only at the fundamental research level, there are many possibilities that it will evolve into a process that can apply to large quantities in 30 years.

So, what do we expect in the future for each approach to C_{60} synthesis described here? The carbon cage approach described in the introduction was initially motivated by fundamental research on carbon allotropes. From the synthetic point of view, it is also very challenging. Since we have scarcely seen papers in the generation following Rubin and Tobe aiming at the synthesis of C_{60} using a similar approach, perhaps the synthesis of C_{60} utilizing this method may not be realistic. However, let us look at the field of physical organic chemistry. The impact of the discovery of C_{60}, which expanded the concept of aromaticity from two dimension to

three dimension, is still significant, and various unique three-dimensional pi-system molecules other than C_{60} have been constructed. Especially in the last decade, many previously imagined molecules have been synthesized, and the speed of progress has been remarkable. Due to the limitation of the number of citations, we should regret not introducing each of the leading players in this field. Still, I will just cite the concept of "global aromaticity" [49]. In any case, the chemistry of three-dimensional pi-conjugates is undoubtedly one of the hottest topics in modern synthetic organic chemistry and physical organic chemistry.

Chemical reactions on metal surfaces constitute another significant recent advances. As mentioned in section "Synthesis on Metal Surfaces," combined with measurement and visualization techniques, this field also produces chemistry that has never been "seen" before. It is worth noting that single-molecule observation is possible, and ultimately, it is 100% or 0% whether the molecule does or does not perform the desired reaction. Therefore, if the molecule is designed for the purpose, a 100% yield reaction is feasible. On the other hand, if there is still some "ambiguity" in the reactants, such as bond rotations, as explained in the SWCNT synthesis, the selectivity of the reaction can be recognized by tracing the fate of each molecule. Indeed, even if the reaction process itself was 100%, the isolation/generation process is essential for the overall production. The current most prominent problem in using metal surface reactions as a real production process is probably the isolation process. In particular, **123** has not been successfully isolated, only characterized by spectroscopic methods such as XPS, due to its strong interaction with the Pt(111) surface and the susceptible nature of **123**.

However, again, the speed of innovation in chemistry is sufficiently fast that if metal surface reactions are genuinely needed, technological innovation toward mass production will indeed occur. Just because it is not possible now does not mean that it will not be possible in the future. Perhaps the most outstanding merit of metal surface reactions is in predicting the structure of the products accurately. We look forward to the day when future innovations will make pure C_{60} synthesis more advantageous than the separation and purification process from combustion methods. By that time, it should be possible to synthesize various artificially designed fullerenes by metal surface reactions.

Finally, we would like to mention the bottom-up synthesis from buckybowls. We have already mentioned that buckybowls themselves have already been established as a significant research field because they exhibit various unique properties derived from their curved bowl structure. Therefore, the motivation to synthesize fullerenes and SWCNTs with single chirality using the buckybowls as seed molecules may not be as compelling as when it started. However, as in other fields, the chemistry of buckybowls is progressing day by day. Just looking back at the evolution of the synthesis of corannulene, we can see that it has evolved from the first synthesis in 1966 to the FVP synthesis (there are many other contributors besides Scott and Siegel, but I could not cite them), to Siegel's kilogram synthesis, and to a more practical level of availability. The synthesis of sumanene has also evolved to a more reasonable level of availability. The principal route of sumanene synthesis has not changed since 2003, but it has been improved and continues to evolve in terms of yield and scalability.

Now, we need to reconsider paying attention to the possibility of the total synthesis of C_{60}. In particular, "convergent synthesis," as mentioned in the main text, is vital as a basic concept of total synthesis. Of course, the most efficient way to use the convergent process is to dimerize the same molecule with high symmetry. In the case of corannulene, **22** is the equivalent. However, **22** is highly strained and has a structure with five reactive isolated double bonds protruding from the surface. Therefore, as a practical matter, the $C_{30}H_{20}$ molecule in which these isolated double bonds are hydrogenated may be the target. On the other hand, the corresponding C_{30} molecule in sumanene is **116**, but this molecule itself is structurally unstable and unrealistic. Thus, the reduced $C_{30}H_{24}$ (**115**) has the isostructure as triphenylene in the aromatic ring site, and thanks to the sp^3 carbon, **115** is not so sterically distorted. Since a wide variety of reactions can be used, it is assumed to be a more promising intermediate.

The key to the success of bottom-up synthesis is introducing the sp^3 carbon at the target position in the target stereoselectivity to ensure three-dimensionality. In this sense, the route starting from sumanene, which can stereoselectively modify the sp^3 carbon at the benzylic position, seems to have more significant potential. However, although it was not described here, molecules with large strains such as buckybowls often exhibit unexpected reactivity. Even seemingly simple reactions are not always straightforward. This is one of the most exciting aspects of total synthesis.

References

1. Aldersay-Williams H (1997) The most beautiful molecule: the discovery of the buckyball. Wiley
2. Osawa E (1970) Hyperaromaticity Kagaku 25:854–863
3. Saito M, Shinokubo H, Sakurai H (2018) Figuration of bowl-shaped π-conjugated molecules: properties and functions. Mater Chem Front 2:635–661
4. Weltner W Jr, van Zee RJ (1989) Carbon molecules, ions and clusters. Chem Rev 89:1713–1747
5. Haley MM, Brand SC, Pak JJ (1997) Carbon networks based on Dehydrobenzoannulenes: synthesis of Graphdiyne substructures. Angew Chem Int Ed Engl 36:836–838
6. von Helden G, Gotts NG, Bowers MT (1993) Experimental evidence for the formation of fullerenes by collisional heating of carbon rings in the gas phase. Nature 363:60–63
7. Bunz UHF, Rubin Y, Tobe Y (1999) Polyethynylated cyclic π-systems: scaffoldings for novel two and three-dimensional carbon networks. Chem Soc Rev 28:107–119
8. Rubin Y, Parker TC, Khan SI, Holliman CL, McElvany SW (1996) Precursors to endohedral metal fullerene complexes: synthesis and x-ray structure of a flexible acetylenic cyclophane $C_{60}H_{18}$. J Am Chem Soc 118:5308–5309
9. Rubin Y, Parker TC, Pastor SJ, Jalisatgi S, Boulle C, Wilkins CL (1998) Acetylenic cyclophanes as fullerene precursors: formation of $C_{60}H_6$ and C_{60} by laser desorption mass spectrometry of $C_{60}H_6(CO)_{12}$. Angew Chem Int Ed 37:1226–1229
10. Baughman RH, Eckhardt H (1987) Structure-property predictions for new planar forms of carbon: layered phases containing sp^2 and *sp* atoms. J Chem Phys 87:6687
11. Sugai T, Sakurai H (2017) Two-way correspondence between carbon nanotubes and caps: development of a numerical algorithm and a tool for organic cap synthesis. Carbon 116:678–685
12. Sastry GN, Jemmis ED, Mehta G, Shar SR (1993) Synthetic strategies towards C_{60}. Molecular mechanics and MNDO study on sumanene and related structures. J Chem Soc Perkin Trans 2: 1867–1871

13. Barth W, Lawton RG (1966) Dibenzo[ghi,mno]fluoranthene. J Am Chem Soc 88:380–381
14. Scott LT, Hashemi MM, Bratcher MS (1992) Corannulene bowl-to-bowl inversion is rapid as room temperature. J Am Chem Soc 114:1920–1921
15. Borchardt A, Fuchicello A, Kilway KV, Baldridge KK, Siegel JS (1992) Synthesis and dynamics of the corannulene nucleus 114:1921–1923
16. Tsefrikas VM, Scott LT (2006) Geodesic polyarenes by flash vacuum pyrolysis. Chem Rev 106: 4868–4884
17. Butterfield AM, Gilomen B, Siegel JS (2012) Kilogram-scale production of corannulene. Org Process Res Dev 16:664–676
18. Seiders TJ, Baldridge KK, Elliott EL, Grube GH, Siegel JS (1999) Synthesis and quantum mechanical structure of *sym*-Pentamethylcorannulene and Decamethylcorannulene. J Am Chem Soc 121:7439–7440
19. Eliseeva MN, Scott LT (2012) Pushing the Ir-catalyzed C–H polyborylation of aromatic compounds to maximum capacity by exploiting reversibility. J Am Chem Soc 134:15169–15172
20. Wu TC, Hsin HJ, Kuo MY, Li CH, Wu YT (2011) Synthesis and structural analysis of a highly curved buckybowl containing corannulene and sumanene fragments. J Am Chem Soc 133: 16319–16321
21. Scott TL, Jackson EA, Zhang Q, Steinberg BD, Bancu M, Li B (2012) A short, rigid, structurally pure carbon nanotube by stepwise chemical synthesis. J Am Chem Soc 134: 107–110
22. Richaud A, López MJ, Mojica M, Alonso JA, Méndez F (2020) Dimerization of pentacyclopentacorannulene $C_{30}H_{10}$ as a strategy to produce $C_{60}H_{20}$ as a precursor for C_{60}. RSC Adv 10:3689–3693
23. Mehta G, Shah SR, Ravikumar K (1993) Towards the design of tricyclopenta[def,jkl,pqr] triphenylene ("sumanene"): a "bowl-shaped" hydrocarbon featuring a structural motif present in C_{60} (buckminsterfullerene). J Chem Soc Chem Commun 1006–1007
24. Sakurai H, Daiko T, Hirao T (2003) A synthesis of sumanene, a fullerene fragment. Science 301:1878
25. Sakurai H (2021) The dawn of sumanene chemistry: my personal history with π-figuration. Bull Chem Soc Jpn 94:1579–1587
26. Abdourazak AH, Marcinow Z, Sygula A, Sygula R, Rabideau PW (1995) Buckybowls. 2. Toward the total synthesis of buckminsterfullerene (C_{60}): benz[5,6]-as-indaceno[3,2,1,8,7-mnopqr]indeno[4,3,2,1-cdef]chrysene. J Am Chem Soc 117:6410–6411
27. Amaya T, Hifumi M, Okada M, Shimizu Y, Moriuchi T, Segawa K, Ando Y, Hirao T (2011) Synthesis of oxosumanenes through benzylic oxidation. J Org Chem 76:8049–8052
28. Sakurai H, Daiko T, Sakane T, Amaya T, Hirao T (2005) Structural elucidation of sumanene and generation of its benzylic anions. J Am Chem Soc 127:11580–11581
29. Higashibayashi S, Onogi S, Srivastava K, Sastry GN, Wu YT, Sakurai H (2013) Stereoelectronic effect of curved aromatic structure favouring the unexpected *endo* conformation of benzylic substituted sumanene. Angew Chem Int Ed 52:7314–7316
30. Chen JJ, Onogi S, Hsieh YC, Hsiao CC, Higashibayashi S, Sakurai H, Wu YT (2012) Palladium-catalyzed Arylation of methylene-bridged Polyarenes: synthesis and structures of 9-Arylfluorene derivatives. Adv Synth Catal 354:1551–1558
31. Amaya T, Mori K, Wu HL, Ishida S, Nakamura J, Murata K, Hirao T (2007) Synthesis and characterization of π-extended bowl-shaped π-conjugated molecules. Chem Commun 1902–1904
32. Amaya T, Nakata T, Hirao T (2009) Synthesis of highly strained π-bowls from Sumanene. J Am Chem Soc 131:10810–10811
33. Amaya T, Ito T, Hirao T (2015) Construction of a hemifurrelene skelton: a regioselective intramolecular oxidative cyclization. Angew Chem Int Ed 54:5483–5487
34. Kasprzak A, Sakurai H (2021) Disaggregation of a sumanene-containing fluorescent probe towards highly sensitive and specific detection of caesium cations. Chem Commun 57:343–346
35. Yakiyama Y, Wang Y, Hatano S, Abe M, Sakurai H (2019) Generation of "sumanenylidene": a ground-state triplet carbene on a curved π-conjugated periphery. Chem Asian J 14:1844–1848

36. Shrestha BB, Karanjit S, Panda G, Higashibayashi S, Sakurai H (2013) Synthesis of substituted sumanenes by aromatic electrophilic substitution reactions. Chem Lett 42:386–388
37. Higashibayashi S, Sakurai H (2008) Asymmetric synthesis of a chiral buckybowl, trimethylsumanene. J Am Chem Soc 130:8592–8593
38. Higashibayashi S, Nasir Baig RB, Morita Y, Sakurai H (2012) Selective synthesis of C_3 symmetric functionalized sumanenes. Chem Lett 41:84–86
39. Toda H, Yakiyama Y, Shoji Y, Ishiwari F, Fukushima T, Sakurai H (2017) 2,3,5,6,8,9-Hexabromosumanene: synthesis and its application to Suzuki-Miyaura cross-coupling. Chem Lett 46:1368–1371
40. Hisaki I, Toda H, Sato H, Tohnai N, Sakurai H (2017) Hydrogen-bonded hexagonal buckybowl network. Angew Chem Int Ed 56:15294–15298
41. Yakiyama Y, Hasegawa T, Sakurai H (2019) Formation of large confined spherical space with small aperture using flexible hexa-substituted sumanene. J Am Chem Soc 141:18099–18103
42. Shoji Y, Kajitani T, Ishiwari F, Ding Q, Sato H, Anetai H, Akutagawa T, Sakurai H, Fukushima T (2017) Hexathioalkyl sumanenes: an electron-donating buckybowl as a building block for supramolecular materials. Chem Sci 8:8405–8410
43. Chuvilin A, Kaiser U, Bichoutskaia E, Besley NA, Khlobystov AN (2010) Direct transformation of graphene to fullerene. Nat Chem 2:450–453
44. Scott LT, Boorum MM, McMahon BJ, Hagen S, Mack J, Blank J, Wagner H, de Meijere A (2002) Rational chemical synthesis of C_{60}. Science 295:1500–1503
45. Otero G, Biddau G, Sánchez-Sánchez C, Caillard R, López MF, Rogero C, Palomares FJ, Cabelllo N, Basanta MA, Ortega J, Méndez J, Echavarren AM, Pérez R, Gómez-Lor B, Martín-Gago JA (2008) Fullerenes from aromatic precursors by surface-catalyzed cyclodehydrogenation. Nature 454:865–868
46. Sanchez-Valencia JR, Dienel T, Gröning O, Shorubaiko I, Mueller A, Jansen M, Amsharov K, Ruffieux P, Fasel R (2014) Controlled synthesis of single-chirality carbon nanotubes. Nature 512:61–64
47. Lungerich D, Hoelzel H, Harano K, Jux N, Yu K, Amsharov NE (2021) A singular molecule-to-molecule transformation on video: the bottom-up synthesis of fullerene C_{60} from truxene derivative $C_{60}H_{30}$. ACS Nano. https://doi.org/10.1021/acsnano.1c02222
48. Anctil A, Babbitt CW, Raffaelle RP, Landi BJ (2011) Material and energy intensity of fullerene production. Environ Sci Techonol 45:2353–2359
49. Rickhaus M, Jirasek M, Tejerina L, Gotfredsen H, Peeks MD, Haver R, Jiang HW, Claridge TDW, Anderson HL (2020) Nat Chem 12:235–241

Structural Characteristics of Fullerenes

4

Peng Jin and Xiaojiao Gu

Contents

Abstract

Fullerenes, exemplified by the famous C_{60}, all feature alluring closed cage-shaped structures composed of pentagons and hexagons. They are pure carbon clusters and also the molecular form of element carbon. Getting familiar with the structural characteristics of pristine fullerenes is essential for further understanding their properties. In this chapter, various important aspects regarding the fullerene structures are presented, including the fullerene polyhedra, fullerene duals, fullerene graphs, spiral algorithm, naming schemes, steric strain, cage stability, point-group symmetry, cage isomerization and cage interconversion, etc. Important rules such as the isolated pentagon rule and $2(N + 1)^2$ rule of spherical aromaticity are introduced. Then the detailed structural characteristics of a series of representative members in the big fullerene family are selectively

P. Jin (✉) · X. Gu
School of Materials Science and Engineering, Hebei University of Technology, Tianjin, China

X. Lu et al. (eds.), *Handbook of Fullerene Science and Technology*,
https://doi.org/10.1007/978-981-16-8994-9_22

shown. The involved cage size ranges from the smallest C_{20} to the supergiant C_{540}. Some studies from both the experimental and theoretical sides are reviewed. Besides, different fullerene derivatives (endohedral and exohedral forms, heterofullerenes) and nonclassical fullerenes containing square or heptagon are also briefly mentioned. The illustrated various cage structures will present the readers a beautiful fullerene world.

Keywords

Fullerene · Cage structure · Carbon cluster · Isomer · Isolated pentagon rule

Introduction

Fullerenes are the pure carbon clusters featuring aesthetically pleasant, fully closed, empty cage structures. They are the molecular form of elemental carbon. Fullerenes are usually named as C_{2n} ($2n \geq 20$ and $\neq 22$) with the even number of carbon framework atoms ranging from dozens to hundreds. In the formed fullerene polyhedron, each vertex is a carbon atom, each edge is a single or double bond, and each face is a pentagonal or hexagonal ring. According to the Euler's theorem, a convex polyhedron should have the sum of the numbers of vertices and faces equal to that of edges plus two. Thus, as a trivalent polyhedron, classical fullerene (C_{2n}) contains $2n$ vertices (atoms), $3n$ edges (skeletal bonds), and $n + 2$ faces (pentagonal/hexagonal rings). Further calculations reveal that it should have constant 12 pentagonal rings and n-10 hexagonal rings to obtain the required $2n$ vertices. Therefore, the number of hexagonal rings determines the size of a fullerene. The smallest fullerene is the dodecahedral I_h-C_{20} (i.e., $n = 10$) without any hexagon, whereas the archetypal I_h-C_{60} first discovered in 1985 holds 20 hexagonal rings (Fig. 1) [1]. However, it is

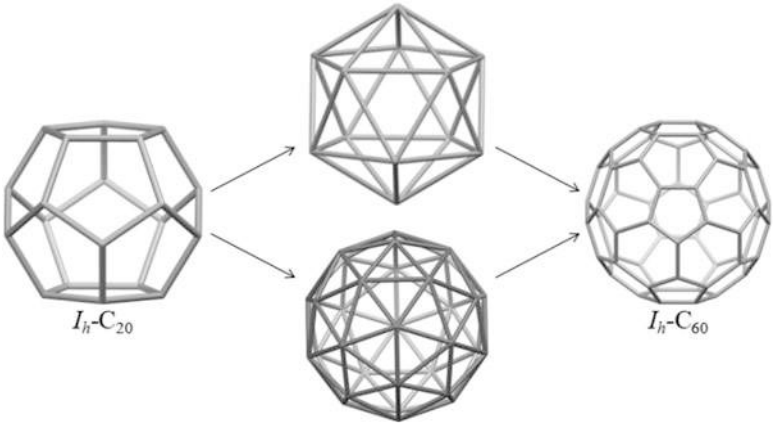

Fig. 1 The polyhedron structures of I_h-C_{20} and I_h-C_{60} and the transformation from the former to the latter

impossible to construct a 22-vertex polyhedron using 12 pentagons and 1 hexagon. C_{22} thus cannot form a fullerene structure.

Different from the one-dimensional (1D) carbon nanotubes, two-dimensional (2D) graphenes and three-dimensional (3D) diamonds, fullerenes have a unique zero-dimensional (0D) graphitic cage structure belonging to both molecules and clusters. The element carbon has the electronic configuration of $1s^2 2s^2 2p^2$. Its four valence orbitals (2s, $2p_x$, $2p_y$, $2p_z$) occupied by four electrons participate in the chemical bonding. It assumes sp^2 and sp^3 hybridization states in graphite and diamond, respectively. By comparison, the hybridization of all the carbon atoms on the fullerene surface is between sp^2 and sp^3, and sometimes approximately sp^2 though the surface is generally not as planar as that of graphite. Each carbon atom forms three carbon-carbon σ bonds with its three neighbors, and the three bonds are not coplanar. The remaining radial orbital (usually a hybrid orbital of 2s and 2p) and one electron contribute to the formation of delocalized π bonds on the surface. They have large and small orbital lobes toward the outer surface and inner cavity, respectively. The cage surface of I_h-C_{60} is thus covered by the sea of 60 π electrons with a spacious cavity enclosed by the all-carbon shell.

Structure Generation

The 3D fullerene polyhedron can be easily transformed to a 2D Schlegel diagram by stretching a chosen face (either pentagon or hexagon) outward and flatting the whole cage onto a plane with all the bonds kept unbroken (Fig. 2). The bonding connectivity becomes much clearer though the rings are somewhat deformed. After drawing such a planar fullerene graph, a fullerene surface can be unwound to become a spiral strip composed of continuous pentagonal and hexagonal rings based on the rule proposed by Fowler and Manolopoulos [2]. Then, according to the 1D spiral sequence which records the relative positions of all rings along the path, any cage isomer can be assigned and easily identified by a unique spiral code. For example, the ring spiral (12 integers) of I_h-C_{60} is 1 7 9 11 13 15 18 20 22 24 26 32, showing the

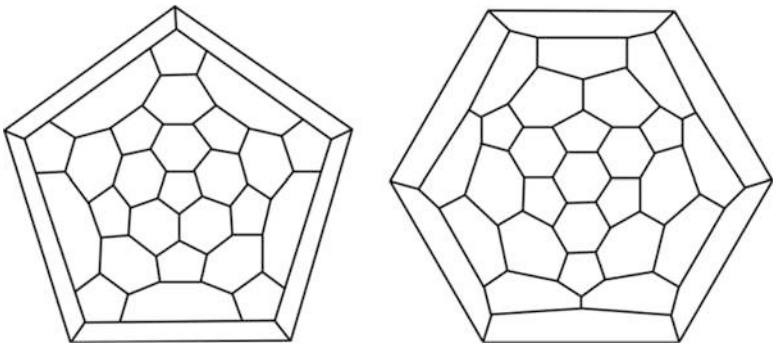

Fig. 2 Schlegel diagrams of I_h-C_{60}

positions of all the 12 pentagons in the spiral code. Inversely, the corresponding spiral code can be first generated mathematically and then used to (re)construct the whole 3D cage, namely there is a one-to-one relationship between a specific fullerene structure and its spiral code. The spiral algorithm can deal with the low-symmetry structures very well. The smallest fullerene without spiral was pointed out as C_{380}. It grasps the key connectivity relationship of bonds, the fundamental difference between various fullerenes. It is easily programmed, and thus widely used in practice.

To show the fullerene structure, both the 3D cage model and 2D Schlegel diagram are frequently used in the literature. The former can be easily plotted by inputting the coordinates of all the carbon atoms to the graphics software. However, it often needs more views to present all the faces. The latter can show all the atom (point), ring (face) and bond connectivity (line) information in a single graph, but lack of the stereo cage characteristics. The two diagrams can be interconverted manually or by using simple code.

By using the spiral algorithm, one can systematically generate and enumerate all the topologically possible fullerene isomers for a given cage size (reliable for the cage smaller than C_{380}, where isomers without a spiral appear) regardless of whether an isomer really exists or obeys some rules. The isomer generation is exhaustive, and the isomer numbers can be enormous. The carbon cages with sizes less than C_{60} and larger than C_{70} are often called small and higher fullerenes, respectively. Those consisting of 100 and more carbon atoms are also called giant fullerenes. For higher fullerenes, some limitations are required to selectively generate certain isomer structures to save the CPU time and storage space of computer. The number of fullerene isomers grows quickly with the increased cage size. For example, according to the spiral algorithm, C_{20} has one classical isomer, C_{40} has 40, C_{60} has 1812, and C_{80} has 31,924 when the enantiomers are neglected (Table 1).

Fullerene Dual

Fullerene dual is formed if one interchanges all the vertices and faces of a fullerene polyhedron. The fullerene dual is a deltahedron containing only triangular faces. It is easy to reconstruct a fullerene structure from its dual because each triangular face of the dual corresponds to a unique vertex of the fullerene. For the five Platonic solids, cube and octahedron, dodecahedron and icosahedron are well-known dual pairs, and tetrahedron is its own dual. Thus, I_h-C_{60} can be built from I_h-C_{20} by first making the dual of dodecahedral C_{20}, and then truncating all the 12 vertices of obtained icosahedral dual (Fig. 1). Alternatively, the leapfrog transformation can also be used: first cap all the faces of C_{20} to get a deltahedron with 32 vertices, and then take its dual to generate I_h-C_{60}. The operation will generate new fullerene three times as large as the original one with the fullerene symmetry remained intact.

Table 1 Total number of C_{2n} fullerene isomers found by the spiral algorithm (enantiomers are excluded). The ranges of the isomer no. are also separately given for the IPR and non-IPR members

$2n$	All isomer	IPR	Isomer no. range	Non-IPR	Isomer no. range
20	1	0	–	1	#1
24	1	0	–	1	#1
26	1	0	–	1	#1
28	2	0	–	2	#1, #2
30	3	0	–	3	#1–#3
32	6	0	–	6	#1–#6
34	6	0	–	6	#1–#6
36	15	0	–	15	#1–#15
38	17	0	–	17	#1–#17
40	40	0	–	40	#1–#40
42	45	0	–	45	#1–#45
44	89	0	–	89	#1–#89
46	116	0	–	116	#1–#116
48	199	0	–	199	#1–#119
50	271	0	–	271	#1–#271
52	437	0	–	437	#1–#437
54	580	0	–	580	#1–#580
56	924	0	–	924	#1–#924
58	1205	0	–	1205	#1–#1205
60	1812	1	#1812	1811	#1–#1811
62	2385	0	–	2385	#1–#2385
64	3465	0	–	3465	#1–#3465
66	4478	0	–	4478	#1–#4478
68	6332	0	–	6332	#1–#6332
70	8149	1	#8149	8148	#1–#8148
72	11,190	1	#11,190	11,189	#1–#11,189
74	14,246	1	#14,246	14,245	#1–#14,245
76	19,151	2	#19,150, #19,151	19,149	#1–#19,149
78	24,109	5	#24,105–#24,109	24,104	#1–#24,104
80	31,924	7	#31,918–#31,924	31,917	#1–#31,917
82	39,718	9	#39,710–#39,718	39,709	#1–#39,709
84	51,592	24	#51,569–#51,592	51,568	#1–#51,568
86	63,761	19	#63,743–#63,761	63,742	#1–#63,742
88	81,738	35	#81,704–#81,738	81,703	#1–#81,703
90	99,918	46	#99,873–#99,918	99,872	#1–#99,872
92	126,409	86	#126,324–#126,409	126,323	#1–#126,323
94	153,493	134	#153,360–#153,493	153,359	#1–#153,359
96	191,839	187	#191,653–#191,839	191,652	#1–#191,652
98	231,017	259	#230,759–#231,017	230,758	#1–#230,758
100	285,913	450	#285,464–#285,913	285,463	#1–#285,463

Cage Symmetry

For a fullerene polyhedron, its all possible symmetries can be easily deduced. A vertex could have the C_{3v}, C_3, C_s, or C_1 site symmetry, corresponding to the presence of both threefold rotational axis and three mirror planes, only the rotational axis, only a mirror plane and none of both, respectively. An edge midpoint could have C_{2v}, C_2, C_s, or C_1 site symmetry, corresponding to the presence of both twofold rotational axis and two mirror planes, only the rotational axis, only a mirror plane, or none. Similarly, a pentagon face center could have C_{5v}, C_5, C_s, or C_1 site symmetry and a hexagon face center could have C_{6v}, C_6, C_{3v}, C_3, C_{2v}, C_2, C_s, or C_1 site symmetry. Accordingly, a total of 36 point groups may be assigned to the fullerene. However, the presence of a C_5 or C_6 rotational axis requires a twofold rotational axis perpendicular to them to fulfill the cage closure. As a result, C_5, C_{5v}, C_{5h}, S_{10} and C_6, C_{6v}, C_{6h}, S_{12} could only exist as subgroups of fivefold dihedral/icosahedral groups and sixfold dihedral groups, respectively. Table 2 summarizes all the possible 28 point groups a fullerene cage could have. The cage shapes range from the highest symmetric one (I_h) to the completely asymmetric one (C_1). The fullerenes belonging to a pure rotational point group (I, T, D_6, D_5, D_3, D_2, C_3, C_2, C_1) are chiral. Those missing multiple rotational axes, improper rotational axes, or a center of inversion (C_{3v}, C_3, C_{2v}, C_2, C_s, C_1) are polar with permanent dipole moments. The high cage symmetry of fullerenes makes them easy to form molecular crystals.

Table 2 Allowed 28 point-group symmetries of fullerenes and their immediate subgroups. The groups showing chiral or polar are also marked

Point group	Group order	subgroups	Point group	Group order	subgroups
I_h	120	I, T_h, D_{5d}, D_{3d}	D_{2h}	8	C_{2v}, C_{2h}, D_2
I (chiral)	60	T, D_5, D_3	D_{2d}	8	C_{2v}, D_2, S_4
T_d	24	T, D_{2d}, C_{3v}	D_2(chiral)	4	C_2
T_h	24	T, D_{2h}, S_6	S_6	6	C_3, C_i
T(chiral)	12	D_2, C_3	S_4	4	C_2
D_{6h}	24	D_{3d}, D_{3h}, D_6, D_{2h}	C_{3h}	6	C_3, C_s
D_{6d}	24	D_6, D_{2d}	C_{3v}(polar)	6	C_3, C_s
D_6(chiral)	12	D_3, D_2	C_3(chiral) (polar)	3	C_1
D_{5h}	20	D_5, C_{2v}	C_{2h}	4	C_2, C_s, C_i
D_{5d}	20	D_5, C_{2h}	C_{2v}(polar)	4	C_2, C_s
D_5(chiral)	10	C_2	C_2(chiral) (polar)	2	C_1
D_{3h}	12	C_{3v}, C_{3h}, D_3, C_{2v}	C_s(polar)	2	C_1
D_{3d}	12	C_{3v}, D_3, S_6, C_{2h}	C_i	2	C_1
D_3(chiral)	6	C_3, C_2	C_1(chiral) (polar)	1	none

Structural Stability

The number of isomers for a fullerene is growing rapidly with the increased cage size. It is important to disclose the relationship between their structural characteristics and thermodynamic stability to rationalize, for example, why only I_h-C_{60} can be obtained among all the possible 1812 C_{60} isomers. The excellent stability of fullerenes can be understood by their rigid closed-cage structures which avoid the possible presence of any unstable dangling edge bond. The strain energy introduced by closing the finite carbon sheet can be effectively overcome by the bonding energy released during the cage closure. The hexagonal rings in fullerenes inherit the stability of the hexagons in graphite. The presence of pentagon, which is absent in the graphite, brings the critical curvature required by the cage formation. However, the possible occurrence of fused pentagon pairs (Fig. 3) in fullerenes will bring not only the strong local pyramidalization and large strain energy, but also the anti-aromatic pentalene structure with 8π electrons. In general, more pentagon fusions result in increased instability. Thus, the observed empty fullerenes mostly obey the well-known isolated pentagon rule (IPR) [3] which states that all the pentagons in the stable fullerene must be separated by the hexagons. Fullerenes obeying and violating the rule are often called IPR and non-IPR fullerenes, respectively. The spherical characteristics of IPR fullerenes can optimize the distribution of steric strain to achieve high structural stability. Fowler et al. further proposed the pentagon adjacency penalty rule (PAPR) [4] to underscore that the energy increase owing to the presence of every pentagon adjacency is about 10–20 kcal/mol. Both IPR and PAPR are based on the structural characteristics of fullerenes. By using these simple rules, the relative stability between cage isomers can be qualitatively established accordingly based on the number of fused pentagons: the fewer, the better. All the fullerenes smaller than C_{60} inevitably have fused pentagons. PAPR is then very useful for these non-IPR isomers, and low-lying ones can be easily identified to be those having less fused pentagons. I_h-C_{60} is the smallest fullerene member which obeys the IPR, and D_{5h}-C_{70} is the next one with a larger cage size. Thus, it is understandable that why both of them were first discovered in the early experiments and produced with high yield. As a matter of fact, the pristine fullerenes successfully observed by now basically all follow the IPR.

According to the symmetry, fullerenes have different types of inequivalent carbon atoms, namely they have distinct environments on the cage surface. The carbon atoms exhibit various rehybridization deviating away from the ideal sp^2, namely, slightly pyramidalized, leading to different local strains on the different regions of cage surface. This difference should lead to diverse "local" chemical reactivities. Assuming the three σ orbitals are all strictly along their respective carbon-carbon bonds, the direction of π-orbital axis vector (POAV) [5] which makes equal angles to the three σ bonds, can be easily calculated for each cage carbon (Fig. 4). The local strain of any cage surface carbon can then be quantitatively evaluated by calculating the corresponding pyramidal angle (angle between the π orbital and its three adjacent C-C bonds minus 90.0°). The method is simple and only needs the input of atomic coordinates of a fullerene molecule. Usually, the larger the pyramidal angle,

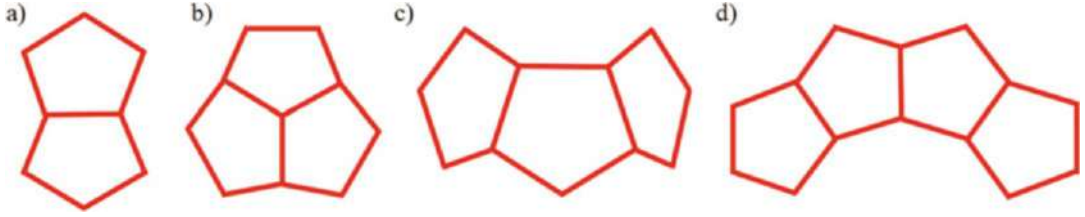

Fig. 3 Four typical configurations of fused pentagons in the non-IPR fullerenes. (**a**) double fused pentagons; (**b**) triple directly fused pentagons; (**c**) triple sequentially fused pentagons; (**d**) quadruple sequentially fused pentagons

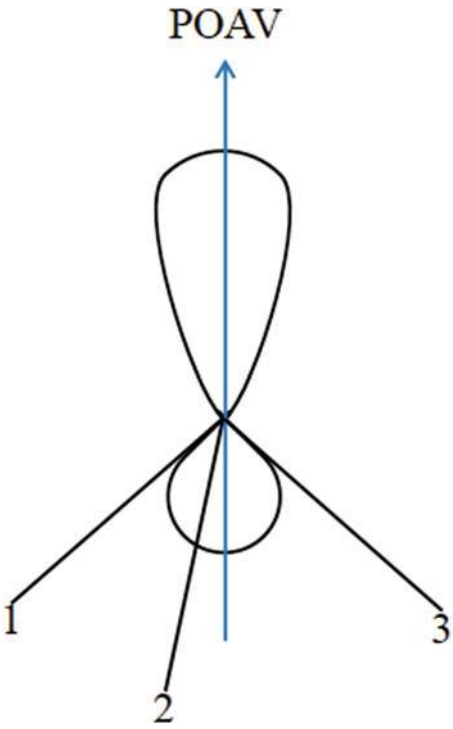

Fig. 4 Definition of the π-orbital axis vector of a cage carbon with regards to its three neighbors

the higher the reactivity of the site due to the easier transformation to higher sp^3 hybridization state. It also indicates serious deviation from the stable planar graphite structures. The carbon atoms at the fused pentagon region all have the largest pyramidal angles and they thus exhibit high reactivity. Owing to the local curvature, the π orbital overlaps between neighboring cage carbons are lower than in planar graphite. The triple-hexagon junctions are the least pyramidalized cage carbons, usually corresponding to lower chemical reactivity.

Naming Schemes

Different isomers of the same cage size may exhibit rather different cage shapes and bonding connectivities. To simply identify a particular carbon cage from its enormous number of isomers, a fullerene can be named using the highest point group symmetry of the cage together with its isomer sequence number in the lexicographically ordered list of spirals in parenthesis, plus C_{2n} at the end showing the cage size. For instance, I_h(1812)-C_{60} is the well-known C_{60} fullerene because it is the last member among all the 1812 topologically possible isomers of C_{60}. D_{5h}(31923)-C_{80} and I_h(31924)-C_{80} denote the isomer with Nos. of 31,923 and 31,924 of the C_{80} fullerene, respectively. For the fullerene of any cage size, the number of its IPR

isomers is always much smaller than the non-IPR ones. Such difference in member numbers rapidly becomes much larger with the increased carbon atom count. For example, C_{60} has one IPR isomer and 1811 non-IPR ones, and C_{70} has one IPR isomer and 8148 non-IPR ones, whereas C_{80} has only seven IPR members but as many as 31,917 non-IPR counterparts. By comparison, the number of all the small C_{2n} fullerenes ($20 \leq 2n < 60$) is only 3958 (all are non-IPR). Therefore, in most cases, for convenience, an IPR fullerene is assigned a simpler isomer serial number, considering only its order among all the IPR isomers. Also note that all the IPR isomers of a fullerene appear at the end of the isomer numbering, namely they have the highest isomer serial numbers according to the spiral algorithm. Thus, $D_{5h}(6)$-C_{80} and $I_h(7)$-C_{80} are often employed to represent the above two C_{80} isomers because they are the sixth and seventh IPR isomers, respectively. Besides, the nomenclature without serial isomer numbers such as I_h-C_{60}, D_{5h}-C_{70}, D_{6d}-C_{72}, D_{3h}-C_{74}, D_2-C_{76}, and T_d-C_{76} are often used for simplicity because they have only one or two IPR isomers. The mixed usage of both numbering schemes can be found in the literature with the simplified one for IPR isomers and the complete one for both IPR and non-IPR ones.

Cage Isomerization and Interconversion

Fullerene isomerization may occur and different cage isomers could interconvert with energetically unfavorable isomers gradually evolving to the favorable ones. Stone-Wales (SW) rearrangement [6] describes an important nondestructive cage isomerization mechanism. Typically, a 90° rotation of the central C-C bond of a pyracylene patch leads to the interchanged positions of the pentagons and hexagons (Fig. 5). The simple SW rotation relationship between isomer topologies suggests the possible presence of interisomeric equilibrium at high temperatures for fullerene synthesis.

The conversion between fullerenes may also occur with the simultaneous extrusion or insertion of two carbon atoms, namely, a C_2 fragment, from the carbon framework (Fig. 6). For a C_{2n} cage, the two processes are reverse and result in the cage shrinkage and cage expansion to generate smaller C_{2n-2} and larger C_{2n+2},

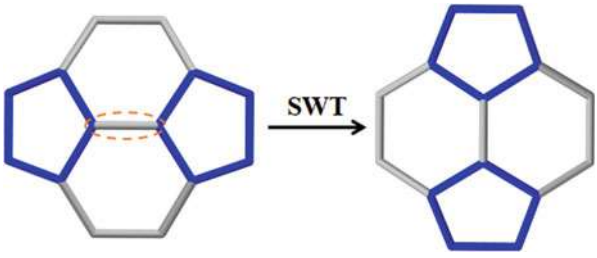

Fig. 5 Stone-Wales (SW) rearrangement in a pyracylene substructure of cage. The rotated bond is highlighted by dashed circle

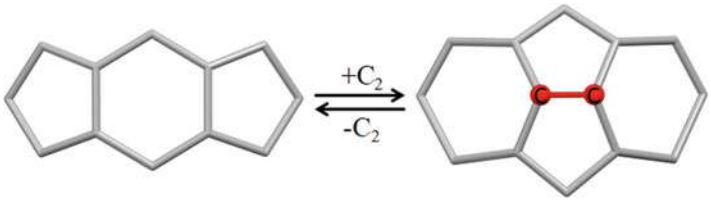

Fig. 6 C_2 insertion and extrusion

respectively. The corresponding growth mechanisms are top-down and bottom-up, respectively. The involved cages thus hold closely related structural characteristics.

Electronic Structure and Aromaticity

The stability of fullerenes is not only the thermodynamic stability determined by the total energy; the kinetic stability is also critical which is closely related to the molecular orbitals and their energy levels. The most important molecular orbitals are the highest occupied molecular orbital (HOMO) and lowest unoccupied molecular orbital (LUMO). The energy gap between them, namely, the HOMO-LUMO gap is usually employed to evaluate the kinetic stability of the system: the larger, the better. Large HOMO-LUMO gap indicates that it is difficult for the electrons on the HOMO to jump to the high LUMO. For example, $I_h(7)$-C_{80} has a fourfold degenerated HOMO but occupied by only two electrons (i.e., Jahn-Teller situation). It thus tends to accept six electrons to achieve a large HOMO-LUMO gap.

The open-shell and closed-shell electron configurations correspond to the situations with unpaired and fully paired electrons on the molecular orbitals, respectively. The fullerene cage could distort and loses the ideal highest symmetry. If the electronic structure calculations with the maximal symmetry group suggest a spatially degenerate ground state, the open-shell fullerene will undergo the first-order Jahn-Teller distortion, which lowers the symmetry to some subgroup to resolve the degeneracy problem. The second-order Jahn-Teller distortion may also occur when a fullerene has a rather small HOMO-LUMO gap and the product of their orbital symmetries match one of the normal modes of vibration.

Sometimes, the fullerene stability can be understood by the concept of aromaticity. The spherical aromaticity is described by the $2(N + 1)^2$ rule [7] which states that the fullerenes with π electrons of 2, 8, 18, 32, 50, 72, etc. are highly aromatic due to their fully filled π valence shells. It is an important extension of the Hückel's $4N + 2$ π-electron rule for the cyclic annulenes. In practice, as a very simple and efficient method to evaluate aromaticity, nucleus-independent chemical shifts (NICS) [8] are often computed at the cage centers of the optimized fullerene molecules. A more negative NICS value indicates more aromatic characteristics of the whole cage, whereas a positive and near-zero one suggest antiaromatic and nonaromatic, respectively.

Structural Characterization

The exact structures of fullerenes are usually determined in experiments by using the infrared (IR), Raman, UV-vis, ^{13}C nuclear magnetic resonance (NMR) spectra, and X-ray crystallography. The ^{13}C NMR can only give the information of molecular symmetry but not the definitive cage connectivity. Theoretical calculations based on the density functional theory (DFT) are thus frequently carried out to help characterize the possible structure of a prepared fullerene by analyzing the relative stabilities of different possible isomer candidates and comparing their simulated spectra (e.g., ^{13}C NMR) to the observed one. Note that the relative stability of isomers may be affected by the temperature (entropy) effect and also the intrinsic error bar of the DFT calculations. The relative energy order is also dependent on the chosen functional method. Thus, the isomers with relative energies of several kcal/mol higher than the global minimum on the potential energy surface may be also possible. The similar structures of different isomers may lead to their close retention times during the high performance liquid chromatography (HPLC) separation. The powerful X-ray crystallographic studies can unambiguously determine the isomeric structure. They are often applied to the co-crystals (e.g., with metal porphyrinates) or exohedral derivatives of fullerenes due to their ordered positions in the crystals compared to the mobility (rotation or libration) of pristine ones.

Fullerene Derivatization

By forming the close carbon shell of fullerene, the whole space is separated into two regions: inside the cage and outside the cage. For the "inside part," fullerenes generally feature spacious cavity of various sizes. For example, the diameter of the I_h-C_{60} cage is about 7.1 Å. They can thus serve as ideal hosts and are able to encapsulate exotic atoms, ions, molecules, and even clusters to form different kinds of endohedral fullerenes [9]. Among such host-guest systems, the formation of endohedral metallofullerenes can greatly affect the thermodynamic stability of parent cage due to the substantial metal-to-cage charge transfer and coordination interactions. As a result, a large number of otherwise labile fullerene isomers including many non-IPR members have been achieved by this means and greatly enrich the feasible fullerene structures. As a special case, multiple-layered nested (onion-like) fullerenes can also be formed by encapsulating fullerenes inside fullerenes. Interestingly, the closed cage walls of fullerenes can be opened with some single/double bonds broken by chemical methods. Then some small molecules such as H_2, H_2O, HF, and CH_4 can be put into the inner space through the hole, followed by the chemical cage closing to prohibit the escape of the trapped species. Endohedral fullerenes such as $H_2@C_{60}$, $H_2O@C_{60}$ and $CH_4@C_{60}$ have been successfully obtained via such molecular surgery. On the other hand, for the "outside part," the cage surface can be chemically functionalized by different addition reactions to achieve various exohedral fullerene adducts. In addition, they can form heterofullerenes such as $C_{59}N$ by substituting a cage carbon atom with nitrogen as well.

The endohedral azafullerenes and the exohedral modification of endohedral fullerenes are also hot topics in the fullerene field. All these systems are rather important fullerene derivatives with novel electronic structures and physicochemical properties different from the pristine fullerenes, promising their many potential applications.

Nonclassical Fullerenes

Nonclassical fullerenes represent the carbon cages bearing rings other than the traditional pentagonal and hexagonal rings. For example, the fullerene structures containing a quadrilateral or a heptagonal ring could start to appear at the cage sizes of C_{22} and C_{30}, respectively. According to the Euler's theorem, one extra heptagonal ring needs an additional pentagonal ring, and the number of hexagons correspondingly decreases by two. With 13 pentagons, the possibly increased pentagon adjacencies bring additional local strain and thus introduce instability to the cage structure. However, the heptagon introduces negative curvature and its presence could also help release the steric strain of adjacent pentagons. On the other hand, the inclusion of a highly strained square will increase the system energy, but its presence also leads to decreased pentagon number from 12 to 10, which then may lower the energy due to the fewer fused pentagons. Thus, the energetic stability of nonclassical fullerenes is much complicated to be predicted than classical ones and jointly determined by many nuanced effects. Interestingly, such nonclassical fullerenes may compete with the classical fullerenes at small size ranges, and need more attention in the future studies.

Example Structures of Fullerenes

In this section, the structural characteristics of a series of representative empty fullerenes (C_{20}–C_{110}) are introduced in the order of increased cage sizes. All the cage structures smaller than C_{70} except I_h-C_{60} are non-IPR, whereas for the fullerenes of size $\geq C_{70}$, the IPR isomers are mainly discussed. For the sake of uniformity, the carbon atom shared by one pentagon and two hexagons is denoted as [5,6,6] carbon. IPR fullerenes can have [5,6,6] or [6,6,6] (shared by three hexagons) carbons. Non-IPR cages can have additional [5,5,6] (shared by two pentagons and one hexagon) or [5,5,5] (shared by three pentagons) carbon type. With similar definitions, IPR fullerenes have [5,6] (shared between one pentagon and one hexagon) and [6,6] (shared between two hexagons) bonds, whereas non-IPR ones also have [5,5] (shared by two pentagons) bond.

As the smallest possible fullerene, C_{20} only has one non-IPR cage isomer bearing the high I_h point group symmetry (Fig. 1). Its dodecahedral structure is purely composed of 12 pentagonal rings and free of any hexagonal ring. The ideal NMR pattern is 1×20 (number of distinct peaks $\times$ intensity) corresponding to the sole [5,5,5] carbon type. It has 12 faces and 30 [5,5] bonds due to the complete distribution of fused pentagons on the whole cage surface. The steric strain of cage

is thus rather high and the molecule is very unstable and moreover undergoes a Jahn-Teller distortion. It cannot form under the normal condition for carbon cluster growth, and the alternative macrocyclic structure is more favored in gas phase. The chemical synthesis of its perhydrogenated derivative $C_{20}H_{20}$, pentagonal dodecahedrane, is even earlier than the discovery of fullerenes. Later, the yield of $C_{20}H_{20}$ is greatly improved via the pagodane→dodecahedrane route. Significantly, C_{20} was successfully produced by the gas-phase debromination of the bromine-substituted $C_{20}H_{20}$ derivative in 2000 [10]. The successful production of I_h-C_{20} demonstrates that a fullerene structure can be obtained from a suitable precursor besides the conventional graphite evaporation process.

C_{24} has one non-IPR isomer of D_{6d} symmetry. It bears two extra hexagonal rings compared to the C_{20}, and is the first "real" fullerene containing both pentagons and hexagons, strictly in line with the definition of classical fullerene. It has 14 faces and 36 bonds (24 [5,5] bonds and 12 [5,6] bonds). The two hexagons reside at two poles of the cage and along the C_6 rotary axis with all the 12 pentagons evenly situated between them, resulting in a drum-like cage structure (Fig. 7). Its NMR pattern is 2×12 corresponding to the presence of 12 [5,5,5] and 12 [5,5,6] carbons.

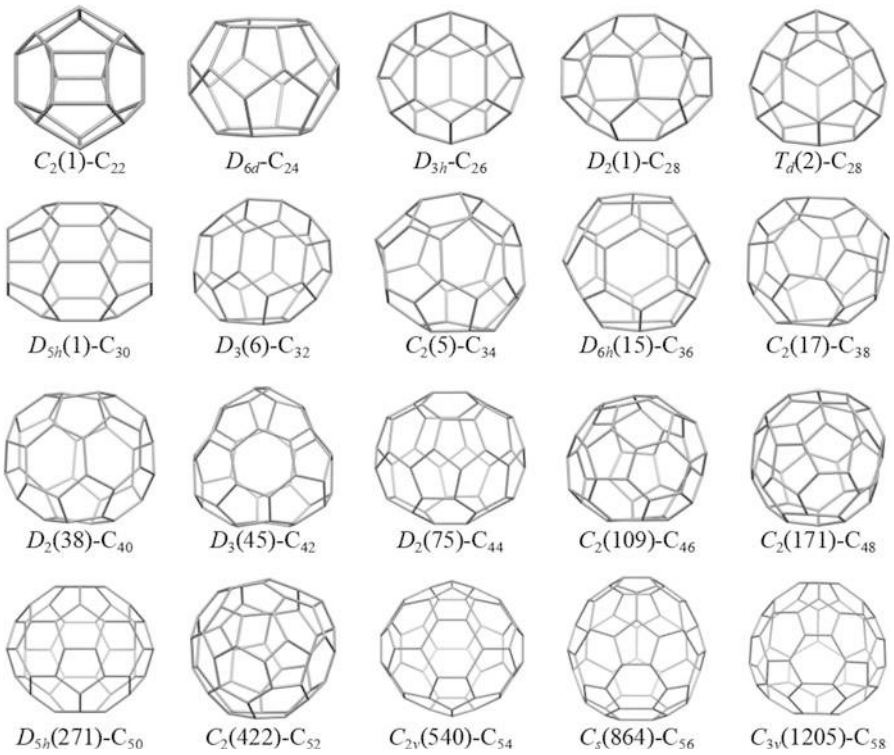

Fig. 7 Structures of selected small fullerenes. A nonclassical C_{22} cage with a four-membered ring is also given

C_{26} also has only one non-IPR isomer in the D_{3h} symmetry. It has two sets of triple directly fused pentagons (Fig. 3) at the two poles and along the C_3 axis. The three hexagonal rings are located at the waist and separated from each other by a pair of fused pentagons. There are 15 faces, 21 [5,5] bonds, and 18 [5,6] bonds in the cage framework. The NMR pattern is [1 × 2, 2 × 6, 1 × 12], corresponding to four types of [5,5,5] or [5,5,6] carbons.

The presence of two or more fullerene isomers occurs when the cage size reaches C_{28}. C_{28} has two non-IPR isomers with D_2 and T_d symmetry (ordered according to their relative positions in spiral list). They both have 4 hexagons, 16 faces, and 42 bonds in total. D_2-C_{28} has 20 [5,5] bonds, 20 [5,6] bonds, and 2 [6,6] bonds, which stems from the first occurrence of fused hexagons. T_d-C_{28} has 18 [5,5] bonds and 24 [5,6] bonds. It has four special [5,5,5] vertexes with large pyramidal angle, each of which is along a C_3 axis. It ($^5A_2$ state) has been theoretically suggested as the smallest stable fullerene [11]. Their NMR patterns are [7 × 4] and [1 × 4, 2 × 12], respectively, where the former also corresponds to four new [5,6,6] carbons besides the aforementioned [5,5,5] and [5,5,6] ones.

C_{30} has three non-IPR isomers with D_{5h}, C_{2v}, and C_{2v} symmetry, respectively. Each isomer has five hexagons and 17 faces in total. The D_{5h} isomer has an intriguing short nanotube-like shape with all the pentagons at the two poles (six in each group) and all the five hexagons are fused together and form a belt around the waist. They have 45 bonds with at least 17 [5,5] bonds. Their NMR patterns are 3 × 10, [3 × 2, 6 × 4] and [5 × 2, 5 × 4], respectively.

C_{32} has six non-IPR isomers with C_2, D_2, D_{3d}, C_2, D_{3h}, and D_3 symmetry, respectively. They all have 6 hexagons, 18 faces, 48 bonds with at least 15 [5,5] bonds. As a representative, Fig. 7 depicts the structure of $D_3(6)$-C_{32} isomer, whose six hexagons are separated into three groups of double fused hexagons and isolated by pentagons. Their NMR patterns are [16 × 2], [8 × 4], [1 × 2, 1 × 6, 2 × 12], [16 × 2], [1 × 2, 3 × 6, 1 × 12], and [1 × 2, 5 × 6], respectively. C_{32} has relatively high abundance in small fullerenes. The good stability may be possible because it obeys the $2(N+1)^2$ rule ($N = 3$) of spherical aromaticity [7].

C_{34} has six non-IPR isomers with C_2, C_s, C_s, C_2, C_2, and C_{3v} symmetry, respectively. They have seven hexagons, 19 faces, 51 bonds, and at least 14 [5,5] bonds. Their NMR patterns are [17 × 2], [6 × 1, 14 × 2], [6 × 1, 14 × 2], [17 × 2], [17 × 2], and [1 × 1, 3 × 3, 4 × 6], respectively. The cage structure of $C_2(5)$-C_{34} is selectively shown in Fig. 7.

C_{36} has 15 non-IPR isomers, and they have C_2, D_2, C_1, C_s, D_2, D_{2d}, C_1, C_s, C_{2v}, C_2, C_2, C_2, D_{3h}, D_{2d}, and D_{6h} symmetry, respectively. All of them hold 8 hexagons, 20 faces, 54 bonds, and at least 12 [5,5] bonds. C_{36} is unstable and could undergo polymerization or form hydrogenated derivatives such as $C_{36}H_6$. The solid form of C_{36} was synthesized by the arc-discharge method, and the molecule has the D_{6h} symmetry as indicated by the solid-state ^{13}C NMR spectrum (two peaks at 146.1 and 137.5 ppm with a relative intensity ratio of 2:1) [12]. The electron-diffraction patterns reveal that the obtained C_{36} solid has a intermolecular distance of about 1.7 Å, suggesting the presence of covalent bonding between adjacent C_{36} molecules.

C_{38} has 17 non-IPR isomers, with C_2, D_{3h}, C_1, C_1, C_1, C_2, C_1, C_1, D_3, C_2, C_1, C_{2v}, C_2, C_1, C_{2v}, C_{3v}, and C_2 symmetry in sequence. There are nine hexagons, 21 faces, and at least 11 [5,5] bonds among all the 57 bonds. Figure 7 gives the structure of $C_2(17)$-C_{38} (NMR pattern: 19 × 2), which contains a linear chain of 12 fused pentagons and has been predicted to have the lowest relative energy [13].

C_{40} has as many as 40 non-IPR isomers with molecular symmetries of 8 C_1, 14 C_2, 2 C_{2v}, 1 C_3, 1 C_{3v}, 7 C_s, 3 D_2, 1 D_{2h}, 2 D_{5d}, and 1 T_d. They have 10 hexagons, 22 faces and at least 10 [5,5] bonds in the total 60 bonds. The cage structure of the low-energy $D_2(38)$-C_{40} is given in Fig. 7 (NMR pattern: 10 × 4) [14]. It features two linear chains each composed of six fused pentagons.

C_{42} has 45 non-IPR isomers: 23 C_1, 11 C_2, 4 C_{2v}, 6 C_s, and 1 D_3. They have 11 hexagons, 23 faces, and at least 9 [5,5] bonds among 63 bonds. As an example, the low-lying $D_3(45)$-C_{42} features two hexagons residing at the two poles along the C_3 axis (Fig. 7, NMR pattern: 7 × 6). It is noteworthy that the number of asymmetric isomers (C_1) increases quickly and is more than half (51%) for C_{42}. They become the majority in the following larger fullerenes.

C_{44} has 89 non-IPR isomers: 42 C_1, 22 C_2, 3 C_{2v}, 7 C_s, 6 D_2, 2 D_3, 2 D_{3h}, 3 D_{3d}, 1 T, and 1 S_4. They have 12 hexagons, 24 faces, and at least 8 [5,5] bonds in total 66 bonds. The structure of lowest-energy $D_2(75)$-C_{44} is selectively drawn (Fig. 7, NMR pattern: 11 × 4). It bears two linear chains, and each contains four fused pentagons.

C_{46} has 116 non-IPR isomers: 69 C_1, 22 C_2, 4 C_{2v}, 19 C_s, and 2 C_3. They have 13 hexagons, 25 faces, and at least 8 [5,5] bonds among 69 bonds. Figure 7 shows the cage structure of $C_2(109)$-C_{46} (NMR pattern: 23 × 2). It also features two linear chains linked from four fused pentagons.

C_{48} has 199 non-IPR isomers: 117 C_1, 52 C_2, 3 C_{2v}, 1 C_{2h}, 16 C_s, 5 D_2, 2 D_{2h}, 1 D_3, and 2 D_{6d}. They have 14 hexagons, 26 faces, and at least 7 [5,5] bonds among 72 bonds. Figure 7 gives the structure of $C_2(171)$-C_{48} (NMR pattern: 24 × 2), and it has one four-pentagon chain and two three-pentagon chains.

C_{50} has 271 non-IPR isomers: 195 C_1, 37 C_2, 6 C_{2v}, 2 C_3, 1 C_{3v}, 25 C_s, 2 D_3, 1 D_{3h}, and 2 D_{5h}. They have 15 hexagons, 27 faces, and at least 5 [5,5] bonds among 75 bonds. One isomer was successfully obtained in experiments by forming the $C_{50}Cl_{10}$ derivative in 2004 [15]. According to the ^{13}C NMR spectrum (four peaks at 161.5, 146.6, 143.0, and 88.7 ppm) and DFT calculations, the obtained isomer should be $D_{5h}(271)$ which has five pairs of fused pentagons surrounding the cage equator and one pentagon at each pole. The ten chlorine atoms are attached to the five [5,5] bonds, resulting in a belt of sp^3-hybridized carbons (88.7 ppm NMR signal) surrounding the equator, and the whole molecule thus seems like Saturn. Such an intriguing structure was confirmed recently by single-crystal X-ray diffraction [16]. C_{50} is (after C_{20} and C_{36}) another observed empty fullerene with fused pentagon pairs. The released strain of fused pentagons via such chemical functionalization has helped achieve a large number of non-IPR fullerenes [17–19].

C_{52} has 437 non-IPR isomers: 307 C_1, 78 C_2, 3 C_{2v}, 3 C_3, 2 C_{3v}, 1 C_{2h}, 26 C_s, 9 D_2, 2 D_{2h}, 5 D_{2d}, and 1 T. They have 16 hexagons, 28 faces, and at least 5 [5,5]

bonds among the 78 bonds. The low-lying C_2(422)-C_{52} isomer is selectively depicted (Fig. 7), and it has two sets of triple sequentially fused pentagons.

C_{54} has 580 non-IPR isomers: 470 C_1, 62 C_2, 8 C_{2v}, 38 C_s, 1 D_3, and 1 D_{3h}. They have 17 hexagons, 29 faces, and at least four [5,5] bonds among the 81 bonds. Theoretical calculations reveal that the lowest-energy one is the C_{2v}(540) isomer because it bears the least number (four) of [5,5] bonds. The isomer has two sets of triple sequentially fused pentagons at two sides of the cage, each of which thus contains two [5,5] bonds. Consistent with the favorable thermodynamic stability, its $C_{54}Cl_8$ derivative has been successfully obtained in experiments, and X-ray crystallographic analyses reveal that only six of the eight chlorine atoms are attached to the [5,5] bond carbon atoms [20].

C_{56} has 924 non-IPR isomers: 700 C_1, 135 C_2, 2 C_{2h}, 49 C_s, 1 C_i, 13 C_{2v}, 3 C_3, 10 D_2, 1 D_{2h}, 1 D_{2d}, 6 D_3, 2 D_{3d}, and 1 T_d. They have 18 hexagons, 30 faces, and at least four [5,5] bonds among the 84 bonds. The three low-lying C_s(864), C_{2v}(913) and D_2(916) isomers, with the least number (four) of [5,5] bonds, can be obtained as chlorinated derivatives: C_s(864)-$C_{56}Cl_{12}$, C_{2v}(913)-$C_{56}Cl_{10}$, and D_2(916)-$C_{56}Cl_{12}$, respectively [20]. The latter two species both have four pairs of double fused pentagons, whereas the former one has two pairs of double fused pentagons and one set of triple sequentially fused pentagons (Fig. 3). Interestingly, the three C_{56} isomers can be interconverted by the SW rearrangement: D_2(916) → C_s(864) → C_{2v}(913), implying their close relationship during the fullerene formation process. The chlorination-promoted skeletal transformation has been reviewed very recently, and often involves the SW rotation and/or C_2 loss [21].

More than 1000 cage isomers appear when carbon count is 58. C_{58} has 1205 non-IPR isomers: 1037 C_1, 98 C_2, 6 C_{2v}, 4 C_3, 2 C_{3v}, and 58 C_s. They have 19 hexagons, 31 faces, and at least three [5,5] bonds among the 87 bonds. The lowest-energy one is the C_{3v}(1205) isomer with the least number (three) of [5,5] bonds on the three pairs of double fused pentagons (Fig. 7). However, classical C_{58} has not been synthesized thus far. Two stable C_{58} derivatives containing an unusual heptagonal ring ($C_{58}F_{18}$ and $C_{58}F_{17}CF_3$) have been obtained by losing a C_2 unit (from a [5,6] bond) from the fluorinated C_{60} and characterized by mass spectrometry and ^{19}F NMR measurements. This case indicates the chemical derivatization such as halogenation under harsh conditions can induce the cage shrinkage.

The above data show that the number of [5,5] bonds gradually decreases with the increased carbon count because the additional rings are all hexagons. The [5,5] bond finally disappears in one isomer of C_{60}, forming the first IPR fullerene.

C_{60} has 1812 isomers: 1508 C_1, 189 C_2, 9 C_{2v}, 67 C_s, 4 C_{2h}, 1 C_{3v}, 19 D_2, 1 D_{2h}, 4 D_{2d}, 3 D_3, 2 S_4, and 1 I_h. They have 20 hexagons, 32 faces and 90 bonds. Only one isomer, I_h(1812)-C_{60}, obeys the IPR (Fig. 1). It has the highest yield among all the fullerenes. Its every pentagon is surrounded by five hexagons, and each hexagon is surrounded by three pentagons and three hexagons. An icosahedron with a truncated vertex can form a pentagon. C_{60} is thus a truncated icosahedron generated by removing all the 12 vertexes to obtain the 12 pentagons. I_h-C_{60} bears a spherical structure perfectly resembling a soccerball (though it is much smaller), and it is also called buckyball or soccerene. From the point of view of the valence bond theory,

each carbon atom in C_{60} forms two C–C [5,6] single bonds and one C=C [6,6] double bond with the three neighbors. The two types of covalent bonds appear alternatively. Thus, it has many resonance forms with all the bonds saturated. The bond lengths of the single and double bonds are 1.45 and 1.38 Å, respectively. Each pentagon thus has five [5,6] edges, and each hexagon has three [5,6] and three [6,6] edges. The single to double bond ratio in fullerenes is 2:1. C_{60} thus has 60 single bonds and 30 double bonds among the total 90 carbon-carbon bonds. The double bond nature of [6,6] bond renders its higher chemical reactivity. I_h-C_{60} has one type of [5,6,6] carbon atoms due to the high point group of symmetry (the highest one in molecules). Its ^{13}C NMR spectrum thus exhibits only one line at 143 ppm (NMR pattern: 1×60).

Among the 1811 non-IPR isomers, their high local strain and local antiaromatic character cause higher relative energy, unfavorable for experimental production. It is noteworthy that two low-lying non-IPR isomers $C_s(1804)$ and $C_{2v}(1809)$ can be obtained in the form of their chlorinated derivatives: $C_s(1804)$-$C_{60}Cl_{12}$ and $C_{2v}(1809)$-$C_{60}Cl_8$, or trifluoromethyl derivatives $C_{2v}(1809)$-$C_{60}(CF_3)_n$ ($n = 10$, 12, 14, 16). According to the single crystal data, they have three and two pairs of double fused pentagons, respectively. Notably, they can interconvert with I_h-C_{60} via the SW rearrangement: $C_s(1804) \rightarrow C_{2v}(1809) \rightarrow I_h(1812)$, suggesting that they are two key intermediates towards the final formation of I_h-C_{60} (Fig. 8). The

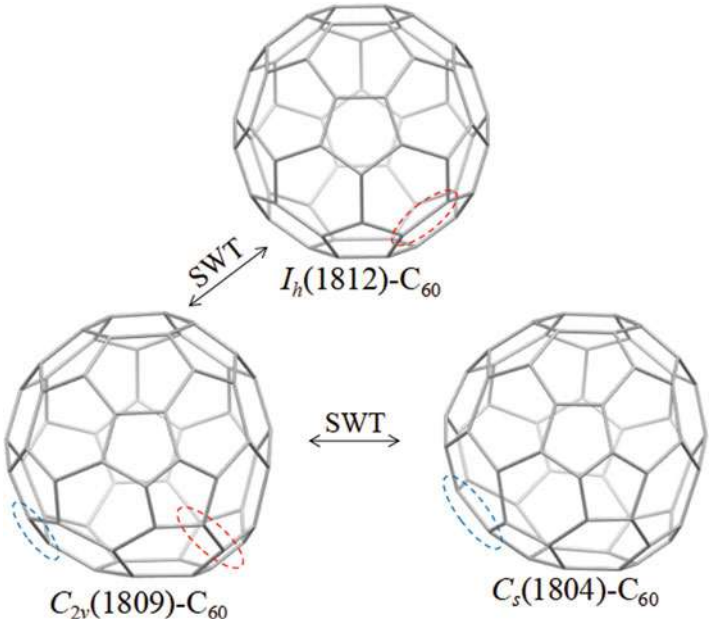

Fig. 8 Interconversion of C_{60} cage isomers through the SW transformation. The rotated C_2 units are highlighted by dashed circles

trifluoromethylation of fullerenes is a very important derivatization method, and a recent nice review summarizes the progress of perfluoroalkylfullerenes [22].

Within the cage size range of C_{62}–C_{68}, no IPR isomers are possible. Their structures have at least two energetically unfavorable fusions of pentagons.

C_{62} has 2385 topological non-IPR isomers: 2135 C_1, 142 C_2, 16 C_{2v}, 80 C_s, 4 C_3, 1 C_{3h}, 1 C_{3v}, 4 D_3, and 2 D_{3h}. They have 21 hexagons, 33 faces, and 93 bonds, and at least three [5,5] bonds. Formally, it can be obtained by the direct C_2 insertion to the C_{60} framework. Indeed, three stable $C_{62}Ar_2$(Ar = 4-Me-C_6H_4, 2-Py, 3,5-$(MeO)_2C_6H_3$) derivatives were successfully produced via a one-pot synthesis containing a series of tandem reactions [23]. They all feature a C_{2v}-symmetric C_{62} cage with a tetragonal ring formed from the insertion of a C_2 unit into two adjacent 5,6-ring junctions of I_h-C_{60}. The X-ray structure of C_{62}(4-Me-$C_6H_4)_2$ reveals that the two *p*-tolyl groups are attached to the two carbon atoms belonging to the four-membered ring, which is surrounded by four hexagons. The high local strain of the cyclobutene ring is thus effectively released. Figure 9 shows the structure of a classical C_2(2378)-C_{62} isomer.

C_{64} has 3465 non-IPR cage isomers: 2990 C_1, 316 C_2, 118 C_s, 2 C_i, 4 C_{2v}, 4 C_{2h}, 8 C_3, 4 C_{3v}, 17 D_2, 1 D_{2h}, and 1 D_{2d}. They have 22 hexagons, 34 faces, 96 bonds, and at least three [5,5] bonds. Among them, C_{3v}(1911)-C_{64} has been synthesized and isolated as hydrogenated derivative ($C_{64}H_4$) by introducing methane in the arc-discharge fullerene production process [24]. A series of spectroscopic measurements (^{13}C NMR, IR and UV-vis) and DFT calculations reveal that it has a set of unique triple directly fused pentagons (Fig. 9), and all the four hydrogen atoms are attached to the four carbon atoms shared within the fused pentagons. Two years later, its chlorinated derivative $C_{64}Cl_4$ was also reported, and X-ray characterization confirmed that it has a similar pineapple-like structure with all the chlorine atoms added to the fused edges of the pentagons, just like the pineapple leaves [16]. Afterwards, its octachlorinated derivative was also reported [25].

C_{66} has 4478 non-IPR isomers: 4134 C_1, 211 C_2, 18 C_{2v}, 1 C_{3v}, 112 C_s, and 2 D_3. They have 23 hexagons, 35 faces, 99 bonds and at least two [5,5] bonds. Among them, C_s(4169)-C_{66} and C_{2v}(4348)-C_{66} were successfully produced via their chlorinated derivatives C_s(4169)-$C_{66}Cl_6$, C_s(4169)-$C_{66}Cl_{10}$, C_{2v}(4348)-$C_{66}Cl_{10}$, and characterized by X-ray diffraction [20, 26]. C_s(4169)-C_{66} bears a triply sequentially fused pentagons, whereas C_{2v}(4348)-C_{66} has two pairs of double fused pentagons. Recently, an unusual C_{2v}-symmetric hydrofullerene $C_{66}H_4$ containing two heptagons and two pairs of fused pentagons was successfully synthesized, and it features four hydrogen atoms attached to the two [5,5] bonds [27].

C_{68} is the largest fullerene which only contains non-IPR isomers without any IPR counterparts. It has 6332 isomers: 5714 C_1, 411 C_2, 5 C_3, 21 C_{2v}, 7 C_{2h}, 1 C_{3h}, 122 C_s, 28 D_2, 2 D_{2d}, 2 D_{2h}, 10 D_3, 3 D_{3d}, 1 D_{3h}, 1 T, 1 T_d, 2 S_4, and 1 S_6. They have 24 hexagons, 36 faces, 102 bonds and at least two [5,5] bonds. C_s(6094)-C_{68} has been captured as its $C_{68}Cl_8$ derivative by in situ chlorination though it is not the energetically most favorable isomer [28]. The single-crystal X-ray analysis revealed that it has two pairs of double fused pentagons, and is the first experimentally

Fig. 9 Structures of selected medium and higher fullerenes

reported antiaromatic fullerene as indicated by the DFT calculations. Recent theoretical study further indicates that it should have an open-shell triplet ground state.

There are 8149 possible C_{70} isomers: 7634 C_1, 300 C_2, 14 C_{2v}, 8 C_3, 5 C_{3v}, 186 C_s, and 2 D_{5h}. They have 25 hexagons, 37 faces and 105 bonds. D_{5h}(8149)-C_{70} is the second IPR fullerene after I_h-C_{60} with high structural stability and high yield. D_{5h}-C_{70} can be seen as a lengthened I_h-C_{60} or shortened carbon nanotube, namely, a key bridge between the two carbon forms. It is the smallest IPR fullerene with condensed hexagons, which are located at its cage equator. It has five NMR lines (3×10, 2×20) due to the presence of five types of inequivalent carbon atoms. The carbon atoms at the two poles exhibit the highest strain, whereas those at the equator have the lowest strain due to the low curvature. Thus, the polar carbon atoms have higher chemical reactivity. It has eight types of inequivalent bonds (four single and four double bonds). Besides D_{5h}-C_{70}, a non-IPR isomer C_2(8064)-C_{70} has been obtained as the corresponding $C_{70}Cl_{10}$ derivative as well [29]. It has an irregular, chiral structure with two pairs of double fused pentagons according to the single crystal X-ray diffraction analysis (Fig. 9). It can convert to D_{5h}-C_{70} via a heptagon-containing intermediate and two steps of SW transformation. Interestingly, a novel $C_{70}Cl_6$ structure with two symmetric heptagons and 14 pentagons in the cage was recently reported [30].

All the following species are higher fullerenes with cage sizes larger than C_{70}. For each cage size, more than 10,000 classical fullerene isomers are possible. There are 11,190 cage isomers of C_{72}: 10304 C_1, 619 C_2, 190 C_s, 3 C_i, 1 C_3, 26 C_{2v}, 7 C_{2h}, 1 C_{3v}, 24 D_2, 3 D_3, 5 D_{2h}, 4 D_{2d}, 1 D_6, and 2 D_{6d}. They have 26 hexagons, 38 faces and 108 bonds. D_{6d}(11190)-C_{72} is the IPR fullerene, and the sole one among various C_{72} isomers. However, theoretical calculations reveal that it is much higher in energy than the lowest-lying C_{2v}(11188)-C_{72} non-IPR isomer bearing one pair of double fused pentagons (Fig. 9) [31]. Thus, C_{2v}(11188)-C_{72} is a very special non-IPR isomer and holds energy even lower than its IPR counterpart. As evidence of its stability, it was synthesized as the C_{2v}(11188)-$C_{72}Cl_4$ derivative, and has an intriguing pineapple-like structure as characterized by the X-ray crystallography [32]. The four chlorine atoms are covalently linked to the fused pentagons and resemble the leaves.

C_{74} has 14,246 cage isomers: 13557 C_1, 414 C_2, 237 C_s, 18 C_{2v}, 9 C_3, 1 C_{3v}, 1 C_{3h}, 6 D_3, and 3 D_{3h}. They have 27 hexagons, 39 faces, and 111 bonds. Among them only D_{3h}(14246)-C_{74} obeys the IPR (Fig. 9). This isomer can be obtained as fluorinated or trifluoromethyl derivatives. Recently, the non-IPR C_1(14049)-C_{74} isomer (Fig. 9) with one pair of double fused pentagons has also been successfully synthesized and X-ray characterized as the $C_{74}Cl_{10}$ derivative [33]. The two isomers can interconvert via single step of SW transformation.

C_{76} has 19,151 cage candidates: 18005 C_1, 800 C_2, 246 C_s, 14 C_{2v}, 11 C_{2h}, 14 C_3, 5 C_{3v}, 2 C_i, 45 D_2, 3 D_{2d}, 1 T, 1 T_d, and 4 S_4. They have 28 hexagons, 40 faces and 114 bonds. When reaching C_{76}, fullerenes start to have more than one IPR isomer, and it is convenient to adopt the short name for IPR isomer (Table 1). There are two IPR isomers for C_{76}: D_2(1)-C_{76} and T_d(2)-C_{76} (Fig. 9). D_2-C_{76} features an intriguing chiral structure, namely it has two enantiomers. It was first characterized in the form

of $C_{76}Cl_{18}$ by single-crystal X-ray analysis [34]. Recently, its many trifluoromethylated derivatives were successfully obtained and characterized. It is the smallest chiral IPR fullerene. It exhibits 19 NMR lines of equal intensity. Interestingly, its reaction with excess $SbCl_5$ affords the chlorinated product $C_{76}Cl_{24}$ with a rather different non-IPR C_2(18917) isomeric cage containing five pairs of double fused pentagons and exhibiting a flattened lens-like shape (Fig. 9) [35]. Such a dramatic IPR-to-non-IPR structural transformation during a chemical reaction is unprecedented. These two cages can be interconnected by seven steps of SW rearrangements.

C_{78} has 24,109 isomers: 23197 C_1, 557 C_2, 312 C_s, 35 C_{2v}, 2 C_3, 3 D_3, and 3 D_{3h}. They have 29 hexagons, 41 faces and 117 bonds. C_{78} has many favorable isomers in the experiments due to their similar energetic stability. There are five IPR ones: D_3(1), C_{2v}(2), C_{2v}(3), D_{3h}(4), and D_{3h}(5). All these isomers have been characterized as trifluoromethyl or chlorinated derivatives, completing the first multi-membered fullerene isomeric group. Figure 9 shows the structure of the D_3(1)-C_{78} isomer.

C_{80} has 31,924 topological isomers: 30280 C_1, 1146 C_2, 371 C_s, 28 C_{2v}, 15 C_3, 2 C_{3v}, 16 C_{2h}, 5 C_i, 39 D_2, 12 D_3, 2 D_{3h}, 2 D_{3d}, 2 D_{5h}, 2 D_{5d}, 1 S_4, and 1 I_h. They have 30 hexagons, 42 faces, and 120 bonds. C_{80} has seven IPR isomers, and they have D_{5d}, D_2, C_{2v}, D_3, C_{2v}, D_{5h}, and I_h symmetry. Note that C_{80} is the first fullerene after C_{60} to have an IPR isomer with the high I_h symmetry, though I_h(7)-C_{80} is unstable and undergoes a Jahn-Teller distortion. Among them, the energetically more stable D_{5d}(1) and D_2(2) isomers were first characterized by the ^{13}C NMR spectra. D_{5d}(1) features an ellipsoidal shape with an aspect ratio of about 1.3 (Fig. 9), and can be generated by first dissecting I_h-C_{60} into two C_{30} hemispheres, and then adding two C_{10} rings successively to the equator to combine them. D_2(2) is a chiral isomer, and its $C_{80}Cl_{12}$, $C_{80}(CF_3)_{12}$, and $C_{80}Cl_{28}$ derivatives have been reported and structurally characterized by X-ray diffraction. Interestingly, the former two share the same addition pattern though the addends differ in size. The structure of C_{2v}(5)-C_{80} was also determined by the ^{19}F NMR measurement on its $(CF_3)_{12}$ adduct.

C_{82} has 39,718 topologically possible isomers: 38548 C_1, 742 C_2, 380 C_s, 28 C_{2v}, 15 C_3, and 5 C_{3v}. They have 31 hexagons, 43 faces and 123 bonds. There are nine IPR ones: C_2(1), C_s(2), C_2(3), C_s(4), C_2(5), C_s(6), C_{3v}(7), C_{3v}(8), and C_{2v}(9). According to the theoretical calculations, C_2(3)-C_{82} is the thermodynamically most stable one [36]. Its structure was characterized by ^{13}C NMR spectrum and X-ray diffraction on the single crystals of its C_2(3)-$C_{82}(CF_3)_{12,18}$ derivatives. Interestingly, its chlorination by $SbCl_5$ can covert the cage to the non-IPR C_1(39173)-C_{82} with one pair of fused pentagons through two steps of SW transformation. It is the only non-IPR C_{82} synthesized thus far. The chloride C_s(4)-$C_{82}Cl_{20}$ was successfully synthesized by the chlorination of C_s(4)-C_{82} with VCl_4 and characterized by single-crystal X-ray diffraction. In addition, C_2(5)-$C_{82}(CF_3)_{12}$ was also produced and characterized by ^{19}F NMR.

When the carbon count increases to 84, fullerenes have more than 50,000 topologically possible isomers and more than ten IPR isomers. C_{84} is relatively abundant among higher fullerenes. It has 24 IPR structures among the 51,592 possible isomers: D_2(1), C_2(2), C_s(3), D_{2d}(4), D_2(5), C_{2v}(6), C_{2v}(7), C_2(8), C_2(9),

C_s(10), C_2(11), C_1(12), C_2(13), C_s(14), C_s(15), C_s(16), C_{2v}(17), C_{2v}(18), D_{3d}(19), T_d(20), D_2(21), D_2(22), D_{2d}(23), and D_{6h}(24). All isomeric structures have 32 hexagons, 44 faces and 126 bonds. It is the smallest fullerene that has an IPR cage without symmetry (C_1). The lowest-energy ones are the major D_2(22)-C_{84} and D_{2d}(23)-C_{84} isomers, both of which have the highest yield with relative ratio of 2: 1 according to the ^{13}C NMR measurement. The exact structure of D_{2d}(23)-C_{84} has been unambiguously determined from the single crystal X-ray diffraction of $C_{84}Ir(CO)Cl(PPh_3)_2$ [37]. Later, the minor D_{3d}(19) and D_{6h}(24) isomers were also synthesized as a mixture (abundance ratio of 2: 3) from the arc-burned soot of Gd-doped composite rods and characterized by ^{13}C NMR and UV-vis-NIR spectra. The structures of several other isomers have been obtained via the exohedral functionalization.

C_{86} has 19 IPR isomers within the 63,761 classical isomers: C_1(1), C_2(2), C_2(3), C_2(4), C_1(5), C_2(6), C_1(7), C_s(8), C_{2v}(9), C_{2v}(10), C_1(11), C_1(12), C_1(13), C_2(14), C_s(15), C_s(16), C_2(17), C_3(18), and D_3(19). They have 33 hexagons, 45 faces and 129 bonds. C_2(17)-C_{86} is the lowest-energy one with large HOMO-LUMO gap, closely followed by C_s(16)-C_{86}. Both structures have been determined by the ^{13}C NMR spectra, and exhibit 43 peaks with equal intensity and full-intensity peaks: half-intensity of 40:6, respectively. They can also be obtained as chlorinated derivatives such as C_s(16)-$C_{86}Cl_{16}$ and C_2(17)-$C_{86}Cl_{18,20,22}$ or trifluoromethyl ones [38].

C_{88} has 35 IPR isomers among the 81,738 classical fullerene structures: D_2(1), C_1(2), C_2(3), C_s(4), C_{2v}(5), C_1(6), C_2(7), C_s(8), C_s(9), C_{2v}(10), C_1(11), C_1(12), C_1(13), C_s(14), C_1(15), C_s(16), C_s(17), C_1(18), C_s(19), C_2(20), C_1(21), C_{2v}(22), C_s(23), C_s(24), C_2(25), C_1(26), C_2(27), C_2(28), C_1(29), C_1(30), C_s(31), C_s(32), C_2(33), T(34), and D_2(35). They have 34 hexagons, 46 faces, and 132 bonds. Among them, C_s(17) is the lowest-energy one (Fig. 9), closely followed by C_2(7) and C_2(33). C_s(17) has the full-intensity peak: half-intensity peak of 42:4 in the ^{13}C NMR spectrum, whereas C_2(7) and C_2(33) each exhibits 44 NMR peaks with equal intensity. The three major isomers have been characterized as chloro and trifluoromethyl derivatives. The high-temperature chlorination of an unstable C_2(3)-C_{88} precursor causes it to undergo two C_2 losses and two SW rearrangements to yield a novel nonclassical, non-IPR isomer $C_{84}Cl_{30}$ bearing two heptagons and two quartets of sequentially fused pentagons (Fig. 3) [39].

C_{90} has 46 IPR isomers among 99,918 classical isomers: D_{5h}(1), C_{2v}(2), C_1(3), C_2(4), C_s(5), C_2(6), C_1(7), C_2(8), C_1(9), C_s(10), C_1(11), C_2(12), C_{2v}(13), C_1(14), C_1(15), C_{2v}(16), C_s(17), C_2(18), C_2(19), C_1(20), C_1(21), C_1(22), C_2(23), C_1(24), C_{2v}(25), C_1(26), C_1(27), C_2(28), C_1(29), C_1(30), C_2(31), C_1(32), C_s(33), C_s(34), C_s(35), C_{2v}(36), C_2(37), C_1(38), C_{2v}(39), C_2(40), C_2(41), C_2(42), C_2(43), C_2(44), C_2(45), and C_{2v}(46). They have 35 hexagons, 47 faces, and 135 bonds. Among them, C_2(45) is the lowest-energy one, followed by C_{2v}(46) and C_s(35). The cage connectivity of C_1(32)-C_{90} was obtained by the ^{19}F NMR spectrum of $C_{90}(CF_3)_{12}$. C_{2v}(46) and C_s(34) present as the major and minor isomers of the $C_{90}Cl_{32}$ derivatives from chlorination of C_{90} by excess $SbCl_5$. C_{2v}(46) has one hexagon surrounded by six adjacent hexagons, and C_s(34) has three such hexagons. D_{5h}(1)-C_{90} has a capped nanotubular structure according to its co-crystal with Ni^{II}(OEP)

(OEP = 2,3,7,8,12,13,17,18-octaethylporphyrin dianion) [40] or its CS_2 crystalline solvate (Fig. 9). Its chloro derivatives $C_{90}Cl_{10,12}$ were later synthesized. It can be obtained by dissecting I_h-C_{60}, then rotating one half by 36°, and inserting 30 carbon atoms. It only has six types of carbon atoms and ten types of C-C bonds due to the high D_{5h} symmetry. The two $C_1(30)$-C_{90} and $C_1(32)$-C_{90} isomers among the total 16 asymmetric IPR cages were then characterized using the same co-crystallization method. The exact structures of $C_1(30)$-, $C_s(35)$- and $C_2(45)$-C_{90} were also obtained from the single crystals of the $C_1(30)$-$C_{90}(CF_3)_{14,18}$, $C_s(35)$-$C_{90}(CF_3)_{14,16,18}$, and $C_2(45)$-C_{90} $(CF_3)_{16,18}$ adducts, respectively. Single-crystal X-ray structures of six C_{90} chlorides, $C_2(28)$-C_{90}, $C_1(30)$-C_{90}, $C_1(32)$-C_{90}, $C_s(34)$-C_{90}, $C_s(35)$-C_{90}, and $C_{2v}(46)$-C_{90} were also reported. Importantly, except $D_{5h}(1)$, most of these isomers are interconnected by one or two steps of pyracylene SW transformation. Interestingly, the chlorination of $C_2(28)$-C_{90} at high temperature results in cage shrinkage by losing a C_2 unit and formation of a non-classical cage containing a heptagon flanked by two pairs of fused pentagons, $C_{88}Cl_{22,24}$ [41].

When the carbon count becomes 92, more than 100,000 classical isomers and more than 50 IPR isomers appear. C_{92} has 86 IPR isomers among all 126,409 classical isomers: 38 C_1, 26 C_2, 1 C_3, 8 C_s, 2 C_{2v}, 4 D_2, 5 D_3, 1 D_{2h}, and 1 T. They have 36 hexagons, 48 faces and 138 bonds. The early ^{13}C NMR spectra of C_{92} isomeric mixture suggest the coexistence of four isomers with D_2 or C_2 symmetry. The structure of $D_2(82)$ isomer was determined by its $D_2(82)$-$C_{92}(CF_3)_{16}$ trifluoromethyl derivative (alternative $D_2(81)$ may also exist) [42]. The asymmetric $C_1(38)$ isomer was also characterized by synthesizing its $C_1(38)$-$C_{92}(CF_3)_{14,16}$ and $C_1(38)$-$C_{92}Cl_{18,20,22}$ derivatives. The presence of the IPR $C_2(23)$-C_{92}, $C_2(26)$-C_{92}, and $C_1(50)$-C_{92} were also demonstrated via the chlorination of C_{92} and isomer reconstruction.

C_{94} has 134 IPR isomers among the 153,493 classical isomers: 89 C_1, 26 C_2, 2 C_{2v}, 3 C_3, 13 C_s, and 1 C_{3v}. They have 37 hexagons, 49 faces, and 141 bonds. It is hard to determine their structures by ^{13}C NMR due to the small quantities and coexistence of multiple isomers. The $C_2(61)$ isomer (Fig. 9) was first structurally determined via its $C_2(61)$-$C_{94}(CF_3)_{20}$ derivative, and later also by the synthesis of $C_2(61)$-$C_{94}Cl_{20}$. It has an egg-like cage shape. In addition, by trifluoromethylation and chlorination, $C_1(34)$-$C_{94}Cl_{14}$, $C_s(42)$-$C_{94}(CF_3)_{16}$, $C_2(43)$-$C_{94}(CF_3)_{18}$, and $C_2(133)$-$C_{94}Cl_{22}$ were also obtained to characterize the exact cage structures of respective parent fullerenes. The $C_1(34)$-C_{94}, $C_s(42)$-C_{94}, and $C_2(43)$-C_{94} isomers all have a similar group of four pentagons closely arranged and interconnected by C−C bonds, leading to their common pear-like cage structure. The three isomers are interrelated by two steps of SW rearrangements, whereas $C_2(61)$ and $C_2(133)$ are related by four steps.

C_{96} has 187 IPR isomers from the total 191,839 classical isomers: 108 C_1, 43 C_2, 3 C_{2v}, 1 C_{3v}, 14 C_s, 8 D_2, 1 D_{2d}, 1 D_{2h}, 3 D_3, 1 D_{3d}, 1 D_{3h}, 2 D_{6d} and 1 D_{6h}. They have 38 hexagons, 50 faces and 144 bonds. $C_2(181)$ and $D_2(183)$ have the lowest energy. The structure of $C_1(145)$-C_{96} was determined from its $(C_2F_5)_{12}$ or Cl_{22} adduct. $D_{3d}(3)$-C_{96} and $C_2(181)$-C_{96} were characterized by the co-crystal with Ni^{II}(OEP) [43]. $D_{3d}(3)$-C_{96} has an oblong nanotube-like structure with the C_3 axis passing

through the two hexagons at two ends (Fig. 9). It has 10 types of carbon atoms and 15 types of C-C bonds. By comparison, C_2(181)-C_{96} has a more spherical shape with some sides slightly flattened. Besides, the C_1(144)-$C_{96}Cl_{22}$, C_2(176)-$C_{96}Cl_{22}$ (or C_2(176)C_{96}-$(CF_3)_{18}$) and D_2(183)-$C_{96}Cl_{24}$ derivatives were also reported to clarify their parent cage structures. Later, the single crystal of C_1(175)-$C_{96}Cl_{20}$ was obtained, and the presence of C_1(114)-C_{96} and C_2(80)-C_{96} was also proposed by deducing from the cage shrinkage (via one and two C_2 losses, respectively) to yield the experimentally observed nonclassical $C_{94}Cl_{28}$ (one heptagon) and $C_{92}Cl_{32}$ (two heptagons) chlorides, respectively. Similar structural reconstruction was also applied for another nonclassical C_{96} isomer (obtained as $C_{96}Cl_{20}$ single crystal) containing 3 heptagons and 15 pentagons. It was considered to be formed from the chlorination of C_2(18)-C_{100} with VCl_4 and $SbCl_5$. The C_{100} should undergo two C_2 losses and one step of SW transformation to generate this unconventional cage. Recently, the chloro derivatives C_2(127)-$C_{96}Cl_{26}$, C_1(129)-$C_{96}Cl_{24}$, C_1(143)-$C_{96}Cl_{24}$, C_1(144)-$C_{96}Cl_{18,24}$, and C_s(146)-$C_{96}Cl_{22}$ [44], and the single crystals of trifluoromethyl derivatives C_1(94)-$C_{96}(CF_3)_{18,20}$, C_2(181)-$C_{96}(CF_3)_{18,20}$, and C_2(182)-$C_{96}(CF_3)_{18}$ [45] were all continually obtained to further extend the IPR structures of C_{96}. Among the reported 15 isomers, only D_{3d}(3)-C_{96} cannot transform to any other isomer by the pyracylene-type SW rearrangements.

C_{98} has 259 IPR isomers among all 231,017 topologically possible classical isomers: 169 C_1, 49 C_2, 3 C_3, 30 C_s, 5 C_{2v}, and 3 D_3. They have 39 hexagons, 51 faces and 147 bonds. Among them, recent theoretical studies pointed out that the lowest-energy one is C_2(248)-C_{98} (Fig. 9) though it is almost isoenergetic with several other isomers [36]. C_2(248)-C_{98} and C_1(116)-C_{98} were first isolated in 2016 as their chlorides, C_2(248)-$C_{98}Cl_{22}$ (C_2(248)-$C_{98}Cl_{24,26}$ also reported later) and C_1(116)-$C_{98}Cl_{20}$. The two isomers have eight common pentagon positions and are interconnected by at least five steps of SW rearrangements. Several other isomers C_s(107)-C_{98}, C_1(109)-C_{98}, and C_s(120)-C_{98} are also characterized as the chloro derivatives such as: C_s(107)-$C_{98}Cl_{20}$, C_1(109)-$C_{98}Cl_{22}$, and C_s(120)-$C_{98}Cl_{18,22}$ (C_s(111)-C_{98} derivatives may also exist). Very recently, C_2(248)-C_{98}, C_1(116)-C_{98}, C_s(120)-C_{98}, C_s(110)-C_{98}, and C_s(111)-C_{98} are all isolated as trifluoromethyl fullerenes [46, 47].

The giant fullerene C_{100} has 450 IPR isomers in the total 285,913 possible classical isomers: 336 C_1, 62 C_2, 3 C_3, 31 C_s, 5 C_{2v}, 9 D_2, 1 D_{2d}, 1 D_5, 1 D_{5d}, and 1 *T*. They have 40 hexagons, 52 faces, and 150 bonds. D_2(449) is the lowest-energy one with C_1(425) and C_2(442) almost isoenergetic. D_{5d}(1)-C_{100} was successfully prepared and characterized in the form of D_{5d}(1)-$C_{100}Cl_{12}$ adduct, and recently in its 2DPC cocrystal (DPC = decapyrrylcorannulene) [48]. It has an elongated nanotube-like structure with all the 12 pentagons residing at the 2 poles (6 for each) of the cage (Fig. 10). The central pentagon of each end is along the C_5 axis and surrounded by five pentagons, resembling that of I_h-C_{60} and D_{5h}-C_{70}. It can be formally constructed from I_h-C_{60} by inserting four layers of ten carbon atoms after dissecting C_{60} into two halves. Though higher in energy, the rather unstable D_{5d}(1)-C_{100} cannot transform to other IPR isomers via SW transformation, and it can thus survive during the annealing process of fullerene synthesis. In addition, the structures of C_2(18)-C_{100},

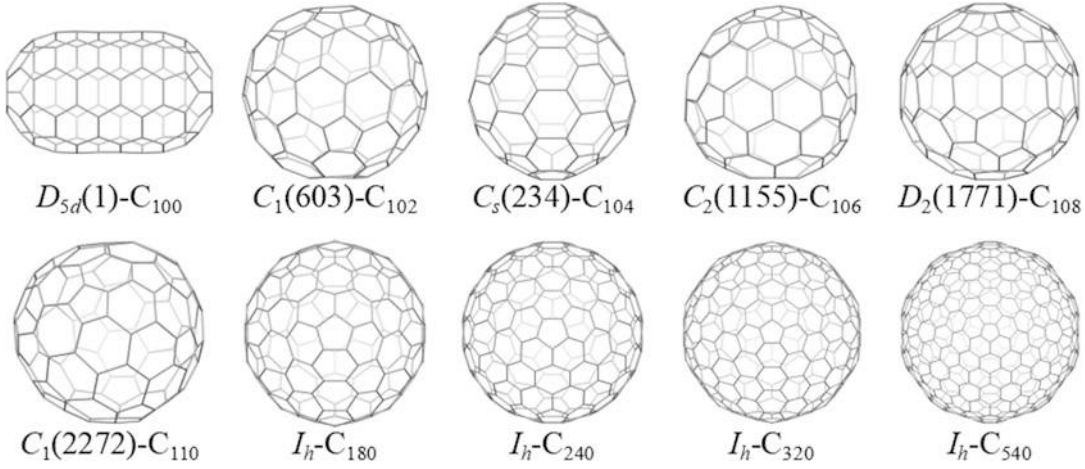

Fig. 10 Structures of some giant fullerenes

C_1(425)-C_{100}, and C_{2v}(417)-C_{100} are all captured as various chloro derivatives: C_2(18)-$C_{100}Cl_{28,30}$, C_1(425)-$C_{100}Cl_{22}$, and C_{2v}(417)-$C_{100}Cl_{28}$. C_{2v}(417)-$C_{100}Cl_{28}$ undergoes chlorination-promoted skeletal transformation via the C_2 loss (a [5,6] bond) to a nonclassical $C_{98}Cl_{26}$ bearing a heptagon. The possible presence of C_1(382)-C_{100} which could transform (via single SW rotation) to two isolated non-classical one-heptagon-containing $C_{100}Cl_{18,22}$ was also proposed.

C_{102} has 616 IPR isomers among all 341,658 possible classical isomers: 488 C_1, 73 C_2, 44 C_s, 8 C_{2v}, 1 C_{3v}, and 2 D_3. They have 41 hexagons, 53 faces, and 153 bonds. C_1(603)-C_{102} (Fig. 10) is the lowest-energy one according to the DFT calculations. However, the non-IPR C_1(283794)-C_{102} with two pairs of fused pentagons was first characterized via the $C_{102}Cl_{20}$ adduct. It was theoretically suggested to be generated from the C_1(19)-C_{102} isomer via two steps of SW rotations though this IPR isomer is much higher in energy than C_1(603)-C_{102}. The C_1(603)-$C_{102}Cl_{18,20}$ adducts were recently obtained to verify the cage connectivity of this lowest-lying IPR isomer.

C_{104} has 823 IPR isomers: 644 C_1, 123 C_2, 1 C_3, 26 C_s, 8 C_{2v}, 11 D_2, 2 D_{2h}, 2 D_{2d}, 4 D_3, 1 D_{3d}, and 1 D_{3h}. They have 42 hexagons, 54 faces, and 156 bonds. DFT calculations reveal that C_s(234) is the lowest-energy one, and its structure (Fig. 10) was confirmed via the single crystals of C_s(234)-$C_{104}Cl_{16–22}$ derivatives. The chloro derivatives of C_1(258)-$C_{104}Cl_{16}$, D_2(812)-$C_{104}Cl_{12,24}$, and C_2(811)-$C_{104}Cl_{24,28}$ were obtained to characterize the cage structures of these isomers. The isomers have a short nanotube-like shape with the pentagons distributed on two sides (six in each group) of the cages. The region between the pentagon groups contains several domains of annulated hexagons, leading to flattened cage surface.

C_{106} has 1233 IPR isomers: 1054 C_1, 105 C_2, 54 C_s, 8 C_{2v}, 9 C_3, and 3 C_{3v}. They have 43 hexagons, 55 faces, and 159 bonds. C_s(331) is the lowest-energy one. The chloro derivative C_2(1155)-$C_{106}Cl_{24}$ was reported to determine the structure of C_2(1155)-C_{106} isomer [49]. It is slightly flattened because of the pyrene and coronene structures on the poles of the cage. C_2(1155)-$C_{106}Cl_{24}$ was cocrystallized with a non-classical $C_{104}Cl_{24}$ derivative containing a heptagon in the cage isomer, which may exist in the fullerene soot.

C_{108} has 1799 IPR isomers: 1479 C_1, 201 C_2, 72 C_s, 9 C_{2v}, 3 C_{2h}, 1 C_{3v}, 21 D_2, 5 D_{2d}, 1 D_{2h}, 2 D_3, 2 D_{3h}, 1 D_{3d}, 1 D_{6h}, and 1 S_4. They have 44 hexagons, 56 faces, and 162 bonds. D_2(1771) is the lowest-energy one. Its structure was determined via the formation of D_2(1771)-$C_{108}Cl_{12}$ [49]. The cage is slightly flattened due to the presence of several coronene units close to the poles (Fig. 10). This is the largest pristine cage with determined structure.

Among all its 713,319 possible classical isomers, C_{110} has 2355 IPR members: 2111 C_1, 168 C_2, 4 C_3, 56 C_s, 8 C_{2v}, 6 D_3, 1 D_5, and 1 D_{5h}. They have 45 hexagons, 57 faces, and 165 bonds. DFT calculations suggest that C_1(2272)-C_{110} is the lowest-energy one [36]. Other two isomers with similar energies within 1 kcal/mol are C_{2v}(1262) and C_1(2293). For more information of giant fullerenes, a very nice review regarding their synthesis, separation, and structural elucidation published very recently is a must-read [50]. Besides, supergiant fullerenes such as icosahedral C_{180}, C_{240}, C_{320}, and C_{540} are also frequently studied mainly by theory (Fig. 10). The

quick developments of computer hardware and software have made it feasible to compute very large fullerenes consisting of hundreds of carbon atoms within reasonable time to reveal their novel structural features and various properties. The synthesis and characterization of more giant fullerenes, though rather challenging, are highly desirable to further enrich the renowned fullerene family.

Conclusions

This chapter introduces the basic structural characteristics of fullerenes and important rules governing their stabilities. The combination of simple building blocks of 12 pentagons and different numbers of hexagons has established such an amazing world of pure carbon clusters. They cover a rather wide size range and include numerous isomers exhibiting diverse cage shapes. Their roomier internal cavities and large cage surfaces promise rich endohedral/exohedral derivatives, which not only stabilize the otherwise labile isomeric forms but also bring novel properties with many practical applications. Though the synthesis and characterization of fullerenes have made great progress in last decades, the reported structures are still the tip of the iceberg. Undoubtedly, more new fullerene members including the classical IPR and non-IPR isomers as well as the nonclassical ones will be continually achieved in the near future, and keep all of us refreshed.

Cross-References

- ▶ Connecting Fullerenes with Carbon Nanotubes and Graphene
- ▶ Fullerenes Violating the Isolated Pentagon Rule
- ▶ Theoretical Predictions of Fullerene Stabilities

References

1. Kroto HW, Heath JR, O'Brien SC, Curl RF, Smalley RE (1985) C_{60}: buckminsterfullerene. Nature 318:162–163
2. Fowler PW, Manolopoulos DE (1995) An atlas of fullerenes. Oxford University Press, Oxford, UK
3. Kroto HW (1987) The stability of the fullerenes C_n, with n = 24, 28, 32, 36, 50, 60 and 70. Nature 329:529–531
4. Campbell EEB, Fowler PW, Mitchell D, Zerbetto F (1996) Increasing cost of pentagon adjacency for larger fullerenes. Chem Phys Lett 250:544–548
5. Haddon RC (1988) π-Electrons in three dimensional. Acc Chem Res 21:243–249
6. Stone AJ, Wales DJ (1986) Theoretical studies of icosahedral C_{60} and some related species. Chem Phys Lett 128:501–503
7. Hirsch A, Chen Z, Jiao H (2000) Spherical aromaticity in I_h symmetrical fullerenes: the $2(N+1)^2$ rule. Angew Chem Int Ed 39:3915–3917

8. von Schleyer PR, Maerker C, Dransfeld A, Jiao H, van Hommes NJRE (1996) Nucleus-independent chemical shifts: a simple and efficient aromaticity probe. J Am Chem Soc 118: 6317–6318
9. Popov AA, Yang S, Dunsch L (2013) Endohedral fullerenes. Chem Rev 113:5989–6113
10. Prinzbach H, Weiler A, Landenberger P, Wahl F, Wörth J, Scott LT, Gelmont M, Olevano D, Issendorff BV (2000) Gas-phase production and photoelectron spectroscopy of the smallest fullerene, C_{20}. Nature 407:60–63
11. Martin JML (1996) C_{28}: the smallest stable fullerene? Chem Phys Lett 255:1–6
12. Piskoti C, Yarger J, Zettl A (1998) C_{36}, a new carbon solid. Nature 393:771–774
13. Sun G, Nicklaus MC, Xie RH (2005) Structure, stability, and NMR properties of lower fullerenes C_{38}–C_{50} and azafullerene $C_{44}N_6$. J Phys Chem A 109:4617–4622
14. Shao N, Gao Y, Zeng XC (2007) Search for lowest-energy fullerenes 2: C_{38} to C_{80} and C_{112} to C_{120}. J Phys Chem C 111:17671–17677
15. Xie SY, Gao F, Lu X, Huang RB, Wang CR, Zhang X, Liu ML, Deng SL, Zheng LS (2004) Capturing the labile fullerene [50] as $C_{50}Cl_{10}$. Science 304:699
16. Han X, Zhou SJ, Tan YZ, Wu X, Gao F, Liao ZJ, Huang RB, Feng YQ, Lu X, Xie S, Zheng LS (2008) Crystal structures of Saturn-like $C_{50}Cl_{10}$ and pineapple-shaped $C_{64}Cl_4$: geometric implications of double- and triple-pentagon-fused chlorofullerenes. Angew Chem Int Ed 47: 5340–5343
17. Tan YZ, Xie SY, Huang RB, Zheng LS (2009) The stabilization of fused-pentagon fullerene molecules. Nat Chem 1:450–460
18. Yamada M, Akasaka T, Nagase S (2018) Salvaging reactive fullerenes from soot by exohedral derivatization. Angew Chem Int Ed 57:13394–13405
19. Guan R, Chen M, Jin F, Yang S (2020) Strain release of fused pentagons in fullerene cages by chemical functionalization. Angew Chem Int Ed 59:1048–1073
20. Tan YZ, Li J, Zhu F, Han X, Jiang WS, Huang RB, Zheng Z, Qian ZZ, Chen RT, Liao ZJ, Xie SY, Lu X, Zheng LS (2010) Chlorofullerenes featuring triple sequentially fused pentagons. Nat Chem 2:269–273
21. Yang S, Ioffe IN, Troyanov SI (2019) Chlorination-promoted skeletal transformations of fullerenes. Acc Chem Res 52:1783–1792
22. Boltalina OV, Popov AA, Kuvychko IV, Shustova NB, Strauss SH (2015) Perfluoroalkyl-fullerenes. Chem Rev 115:1051–1105
23. Qian W, Chuang SC, Amador RB, Jarrosson T, Sander M, Pieniazek S, Khan SI, Rubin Y (2003) Synthesis of stable derivatives of C_{62}: the first nonclassical fullerene incorporating a four-membered ring. J Am Chem Soc 125:2066–2067
24. Wang CR, Shi ZQ, Wan LJ, Lu X, Dunsch L, Shu CY, Tang YL, Shinohara H (2006) $C_{64}H_4$: production, isolation, and structural characterizations of a stable unconventional fulleride. J Am Chem Soc 128:6605–6610
25. Shan GJ, Tan YZ, Zhou T, Zou XM, Li BW, Xue C, Chu CX, Xie SY, Huang RB, Zhen LS (2012) $C_{64}Cl_8$: a strain-relief pattern to stabilize fullerenes containing triple directly fused pentagons. Chem Asian J 7:2036–2039
26. Gao CL, Li X, Tan YZ, Wu XZ, Zhang Q, Xie SY, Huang RB (2014) Synthesis of long-sought C_{66} with exohedral stabilization. Angew Chem Int Ed 53:7853–7855
27. Tian HR, Chen MM, Wang K, Chen ZC, Fu CY, Zhang Q, Li SH, Deng SL, Yao YR, Xie SY, Huang RB, Zheng LS (2019) An unconventional hydrofullerene $C_{66}H_4$ with symmetric heptagons retrieved in low-pressure combustion. J Am Chem Soc 141:6651–6657
28. Amsharov KY, Ziegler K, Mueller A, Jansen M (2012) Capturing the antiaromatic (#6094)C_{68} carbon cage in the radio-frequency furnace. Chem Eur J 18:9289–9293
29. Tan YZ, Li J, Du MY, Lin SC, Xie SY, Lu X, Huang RB, Zheng LS (2013) Exohedrally stabilized C_{70} isomer with adjacent pentagons characterized by crystallography. Chem Sci 4: 2967–2970
30. Zhong YY, Chen ZC, Du P, Cui CH, Tian HR, Shi XM, Deng SL, Gao F, Zhang Q, Gao CL, Zhang X, Xie SY, Huang RB, Zheng LS (2019) Double negatively curved C_{70} growth through a heptagon-involving pathway. Angew Chem Int Ed 58:14095–14099

31. Slanina Z, Ishimura K, Kobayashi K, Nagase S (2004) C_{72} isomers: the IPR-satisfying cage is disfavored by both energy and entropy. Chem Phys Lett 384:114–118
32. Tan YZ, Zhou T, Bao J, Shan GJ, Xie SY, Huang RB, Zheng LS (2010) $C_{72}Cl_4$: a pristine fullerene with favorable pentagon-adjacent structure. J Am Chem Soc 132:17102–17104
33. Gao CL, Abella L, Tan YZ, Wu XZ, Rodriguez-Fortea A, Poblet JM, Xie SY, Huang RB, Zheng LS (2016) Capturing the fused-pentagon C_{74} by stepwise chlorination. Inorg Chem 55:6861–6865
34. Simeonov KS, Amsharov KY, Jansen M (2007) Connectivity of the chiral D_2-symmetric isomer of C_{76} through a crystal-structure determination of $C_{76}Cl_{18}.TiCl_4$. Angew Chem Int Ed 46: 8419–8421
35. Ioffe IN, Goryunkov AA, Tamm NB, Sidorov LN, Kemnitz E, Troyanov SI (2009) Fusing pentagons in a fullerene cage by chlorination: IPR D_2-C_{76} rearranges into non-IPR $C_{76}Cl_{24}$. Angew Chem Int Ed 48:5904–5907
36. Shao N, Gao Y, Yoo S, An W, Zeng XC (2006) Search for lowest-energy fullerenes: C_{98} to C_{110}. J Phys Chem A 110:7672–7676
37. Balch AL, Ginwalla AS, Lee JW, Noll BC, Olmstead MM (2002) Partial separation and structural characterization of C_{84} isomers by crystallization of (.eta.2-C_{84})Ir(CO)Cl(P$(C_6H_5)_3)_2$. J Am Chem Soc 116:2227–2228
38. Yang S, Wei T, Troyanov SI (2014) Chlorination of two isomers of C_{86} fullerene: molecular structures of $C_{86}(16)Cl_{16}$, $C_{86}(17)Cl_{18}$, $C_{86}(17)Cl_{20}$, and $C_{86}(17)Cl_{22}$. Chem Eur J 20:14198–14200
39. Jin F, Yang S, Kemnitz E, Troyanov SI (2017) Skeletal transformation of a classical fullerene C_{88} into a nonclassical fullerene chloride $C_{84}Cl_{30}$ bearing quaternary sequentially fused pentagons. J Am Chem Soc 139:4651–4654
40. Yang H, Beavers CM, Wang Z, Jiang A, Liu Z, Jin H, Mercado BQ, Olmstead MM, Balch AL (2010) Isolation of a small carbon nanotube: the surprising appearance of $D_{5h}(1)$-C_{90}. Angew Chem Int Ed 49:886–890
41. Ioffe IN, Mazaleva ON, Sidorov LN, Yang S, Wei T, Kemnitz E, Troyanov SI (2013) Cage shrinkage of fullerene via a C_2 loss: from IPR $C_{90}(28)Cl_{24}$ to nonclassical, heptagon-containing $C_{88}Cl_{22/24}$. Inorg Chem 52:13821–13823
42. Troyanov SI, Tamm NB (2009) Cage connectivities of $C_{88}(33)$ and $C_{92}(82)$ fullerenes captured as trifluoromethyl derivatives, $C_{88}(CF_3)_{18}$ and $C_{92}(CF_3)_{16}$. Chem Commun 40:6035
43. Yang H, Jin H, Che Y, Hong B, Liu Z, Gharamaleki JA, Olmstead MM, Balch AL (2012) Isolation of four isomers of C_{96} and crystallographic characterization of nanotubular $D_{3d}(3)$-C_{96} and the somewhat flat-sided sphere $C_2(181)$-C_{96}. Chem Eur J 18:2792–2796
44. Tamm NB, Guan R, Yang S, Troyanov SI (2020) New isolated-pentagon-rule isomers of fullerene C_{96} captured as chloro derivatives. Eur J Inorg Chem 2020:2092–2095
45. Tamm NB, Guan R, Yang S, Sidorov LN, Troyanov SI (2020) Three isolated-pentagon-rule isomers of C_{96} fullerene isolated as trifluoromethyl derivatives. Inorg Chem 59:17866–17869
46. Tamm NB, Guan R, Yang S, Troyanov SI (2020) Trifluoromethyl derivatives of elusive fullerene C_{98}. Chem Eur J 26:616–619
47. Tamm NB, Troyanov SI (2021) Two isolated-pentagon-rule isomers $C_{98}(110)$ and $C_{98}(111)$ isolated as trifluoromethylfullerenes $C_{98}(CF_3)_{22}$. Inorg Chem 60:18625–18628
48. Koenig RM, Tian HR, Seeler TL, Tepper KR, Franklin HM, Chen ZC, Xie SY, Stevenson S (2020) Fullertubes: cylindrical carbon with half-fullerene end-caps and tubular graphene belts, their chemical enrichment, crystallography of pristine C_{90}-$D_{5h}(1)$ and C_{100}-$D_{5d}(1)$ fullertubes, and isolation of C_{108}, C_{120}, C_{132}, and C_{156} cages of unknown structures. J Am Chem Soc 142: 15614–15623
49. Wang S, Yang S, Kemnitz E, Troyanov SI (2016) New giant fullerenes identified as chloro derivatives: isolated-pentagon-rule $C_{108}(1771)Cl_{12}$ and $C_{106}(1155)Cl_{24}$ as well as nonclassical $C_{104}Cl_{24}$. Inorg Chem 55:5741–5743
50. Wang S, Chang Q, Zhang G, Li F, Wang X, Yang S, Troyanov SI (2020) Structural studies of giant empty and endohedral fullerenes. Front Chem 8:607712

Theoretical Predictions of Fullerene Stabilities

5

Zdeněk Slanina, Filip Uhlík, and Ludwik Adamowicz

Contents

Z. Slanina (✉)
Huazhong University of Science and Technology, Wuhan, Hubei, China
e-mail: zdeneks@email.arizona.edu

F. Uhlík
Department of Physical and Macromolecular Chemistry, Faculty of Science, Charles University, Prague, Czech Republic
e-mail: filip.uhlik@natur.cuni.cz

L. Adamowicz
Department of Chemistry and Biochemistry, University of Arizona, Tucson, AZ, USA
e-mail: ludwik@email.arizona.edu

X. Lu et al. (eds.), *Handbook of Fullerene Science and Technology*,
https://doi.org/10.1007/978-981-16-8994-9_23

Abstract

This chapter deals with computational and theoretical support to fullerene/nanocarbon research needed for interpretations, rationalizations, and generalizations of experimental results. In particular, predictions of various nanocarbon stabilities, or even populations, based on quantum-chemical and statistical-mechanical methods, are surveyed. The calculations are, with respect to high temperatures in fullerene electric-arc syntheses, frequently based on the Gibbs energy. Considerable thermal effects on the relative isomeric and nonisomeric populations thus revealed in the theoretical treatments originate, on molecular level, in a complex interplay between rotational, vibrational, electronic, relative potential-energy, symmetry, and chirality factors. The considered treatments are built upon a presumption of the (inter-isomeric) thermodynamic equilibrium; however, some kinetic and catalytic aspects are also included. The survey is focused on empty fullerenes, metallofullerenes, clusterfullerenes, and nonmetal endohedrals. The covered quantum-chemical treatments are the semiempirical, *ab initio* Hartree-Fock, density-functional theory, and perturbation approaches. The calculations have already yielded a reasonable computation-observation agreement for the isomeric systems with empty C_{76} till C_{96} cages, and mostly also when applied to metallofullerenes. This relatively large tested set supports the belief in still wider applicability of the Gibbs-energy calculations to basically all classes of nanocarbons. This chapter is complementary to this volume chapter Theoretical Prediction of Fullerene Reactivity.

Keywords

Fullerenes · Metallofullerenes · Clusterfullerenes · Isomeric and nonisomeric relative stabilities · Gibbs-energy evaluations · DFT and *ab initio* calculations · Kinetic control and catalysis

Introduction

Empty fullerenes, as polyhedral cage compounds built exclusively from carbon atoms, were for the first time reported in the gas phase by Kroto et al. [1] in 1985 though large carbon clusters without any structural elucidation were observed [2] 1 year earlier. Then, fullerenes in crystalline form were prepared by Krätschmer et al. [3] in 1990 [4]. Metal-containing forms of fullerenes, known as metallofullerenes, were for the first time observed in the gas phase by Heath et al. [5] – also still in 1985. A tremendous volume of observed and calculated data has been accumulated since then; for reviews, see [6–9]. In addition to spheroidal fullerene cages, other objects [6] especially elongated cylindrical bodies known as nanotubes, as well as nanocones and peapods, have been studied extensively, in particular as they could be applied, for example, in molecular electronics and quantum computing. Fullerenes and metallofullerenes have also been vigorously treated [7–11] by theoretical and computational techniques. As experimental characterization of nanocarbons is

frequently based on ^{13}C NMR and other spectroscopies, computational support is essential for a more reliable structural clarification. Given the complexity of the fullerenic structures, calculations have supplied, from the early days of fullerene science, a useful support for a deeper insight into various observed systems, their characteristics, and phenomena.

Fullerenes themselves are [11] polyhedral cages containing only carbon atoms arranged into five- and six-membered rings, or pentagons and hexagons, while quasi-fullerenes contain also other types of polygons (such as squares or heptagons). Prehistory of fullerenes can be traced back [4, 11] to mass-spectrometric observations of carbon aggregates or clusters up to C_{15} by Hahn and coworkers in the 1940s, later on expanded up to C_{33}. Nevertheless, there could be a little help from that time theoretical chemistry. Although the Hückel molecular-orbital (HMO) method was available, computational hardware was very modest, and symmetry reductions of the eigenvalue problem were not developed. Experimental studies of carbon vapor in the 1950s and 1960s could receive [12, 13] a bit better computational support; however, only small species were observed at that time. In 1965, Schultz [14] carried out the very first, pioneering computational stability evaluations for – in the present terms – fullerene or pseudofullerene derivatives, and then a stability reasoning by Ōsawa [15] on the pristine C_{60} itself followed in 1971. Schultz [14] selected cage hydrocarbons (he called polyhedranes) based on Platonic or Archimedean polyhedra, including $C_{60}H_{60}$ – fully hydrogenated fullerene C_{60}. His 55-year-old predictions based only on a very simple molecular mechanics reasonably agree with the present day advanced quantum-chemical calculations [16]. They both point out the well-known synthetic hydrocarbon dodecahedrane $C_{20}H_{20}$ as the most stable while $C_{60}H_{60}$ is the third (the second most stable is a yet hypothetical truncated octahedrane $C_{24}H_{24}$). They all are computed as more stable than another synthetic polyhedrane cubane C_8H_8. However, the Schultz pioneering work has almost entirely been ignored by fullerene historians. When C_{60} was discovered [1], computations could readily produce applicable supporting data, including its predicted IR spectrum [17] that was actually soon of some use in the C_{60} identification [3].

Studies of C_{60} and higher fullerenes have widely been based on the so-called isolated pentagon rule (IPR) – especially stable fullerenes should have all pentagons surrounded just by hexagons. Even such IPR cages can be quite numerous; nevertheless, their equilibrium mixtures have been computed in agreement with experiments for C_{76}–C_{96}. A similar isomeric interplay has also been studied for smaller fullerene systems such as C_{32} or C_{36} (though the IPR pattern cannot exist below C_{60}). Moreover, isomeric metallofullerenes can also coexist [18, 19] in several isomeric forms as well (out of truly numerous such known cases), for example, $Ca@C_{72}$, $Ca@C_{74}$, $Ca@C_{82}$, $La@C_{82}$, $Tm@C_{82}$, $Sc_2@C_{76}$, $Ti_2@C_{80}$, $Sc_2@C_{84}$, $Ti_2@C_{84}$, and very many other species (though violations of the IPR pattern are more likely here, and well known). Isomeric sets are obviously also possible for derivatives of fullerenes or nanotubes. Although the inter-isomeric relative energies are important for such systems, they alone cannot predict the relative stabilities or populations of the isomers. Owing to high temperatures, entropy contributions can in fact even overcompensate the enthalpy terms. Hence, the enthalpy-entropy interplay represents [16] an essential issue for nanocarbon systems. Fullerene research has

from its early days developed in a close theory-experiment cooperation, indeed, frequently being supported by truly large-scale computations. Several fullerene overviews are available; however, the computations themselves are still reviewed rather rarely. This survey is thus devoted to the theoretical predictions of fullerene stabilities mostly within the thermodynamic equilibrium. However, this overview cannot present a comprehensive list of all relevant papers (owing to a tight editorial reference limit – actually set originally to just around 50 references), and therefore it refers for more complete reference listings also to some previous computational reviews [7–11, 16].

Energetics and Thermodynamics of Nanocarbons

The present quantum-chemical calculations of fullerenes [10, 11] can still start from the optimized geometries obtained with some of several semiempirical methods such as MNDO, AM1, PM3, SAM1, and PM6. The optimized geometries are further refined with more sophisticated *ab initio* Hartree-Fock Self-Consistent-Field (HF SCF), or density-functional theory (DFT) approaches. The geometry optimizations produce stationary points on the particular potential energy hypersurface, i.e., the points with the first derivatives of the potential energy with respect to nuclear coordinates equal to zero. The first derivatives of the potential energy are nowadays customarily calculated from the analytical formulas. Various *ab initio* computational procedures are mostly applied using Gaussian or Spartan program packages. The so-called stability of the SCF wave function can be an issue for some fullerenic structures. The wave function stability concerns a situation when the obtained wave function does not exhibit the lowest possible variational energy, so that it must be reoptimized and replaced. Here, the stability, or possibly reoptimization, is related to the SCF expansion coefficients (not to nuclear coordinates). The wave function-stability test is essential though it can be quite demanding on computational resources. The geometry optimizations should be followed by harmonic vibrational analysis (with an optional frequency scaling for some methods and applications) in order to check the types of localized stationary points. The harmonic vibrational analysis employs the second derivatives of potential energy, also typically evaluated from the analytical formulas at present. Using the vibrational analysis, we can distinguish between local energy minima important for thermodynamic stabilities, transition states (activated complexes) important for reaction kinetics, and higher saddle points (enabling interconversion between lower saddle points). The stationary points other than local energy minima exhibit one or more imaginary vibrational frequencies. The harmonic vibrational analysis offers simulations of IR or Raman spectra, too. The anharmonic corrections can in principle be also calculated; however, they are based on numerical differentiation of the second derivatives of potential energy, which is a task demanding computer time.

More recently, evaluations of nanocarbon energetics, for a very few first systems, have been performed with still more sophisticated quantum-chemical methods

beyond HF SCF or DFT levels. In particular, the energetics can further be refined using the second order Møller-Plesset (MP2) perturbation treatment with all electrons (full, FU) or for the frozen core (FC) option. Yet, more advanced approach nowadays already applicable to nanocarbons is represented by a combination of the MP2 and DFT treatments known as B2PLYP(D) technique. There are already instructive examples where such perturbation MP2 type approaches improved agreement of the calculations with the observed nanocarbon data.

The Relative Populations of Isomeric Nanocarbons

As already mentioned, the inter-isomeric relative energies alone cannot predict the relative stabilities, or better say relative populations, of the isomers. Owing to high temperatures, the enthalpy-entropy interplay [16] is to be respected accordingly with fullerenic systems. The relative populations of m isomers (of any kind) in their equilibrium mixture can be expressed as their mole fractions, w_i, using the isomeric partition functions q_i. In the terms of q_i and the ground-state energy changes $\Delta H^o_{0,i}$, the mole fractions are given by a compact formula [20]:

$$w_i = \frac{q_i \, exp\left[-\Delta H^o_{0,i}/(RT)\right]}{\sum_{j=1}^{m} q_j \, exp\left[-\Delta H^o_{0,i}/(RT)\right]}, \tag{1}$$

where R stands for the gas constant and T for the absolute temperature. Equation (1) is – under the conditions of the inter-isomeric thermodynamic equilibrium – a rigorous formula. However, the partition functions are to be practically constructed within the rigid-rotor and harmonic-oscillator (RRHO) approximation as anharmonic corrections can presently be evaluated only rarely – and for simple systems, not for fullerenes. The partition functions q_i reflect the rotational, vibrational, electronic, symmetry, and chirality contributions [translational contributions cancel out exactly in Eq. (1)]. However, the (mono-)metallofullerene relative-stability treatment according to Eq. (1) can further be improved [18, 19] by a modified approach to the description of the encapsulate motions (i.e., still somewhat beyond the simple RRHO approach). It is reasonable to expect that if the encapsulate is relatively free to move within the cage (which is documented by the NMR spectra [21]), then, at sufficiently high temperatures, its behavior in different cages will bring about the same contribution to the partition functions. The contributions would then cancel out in Eq. (1). This simplification is called [18, 19] free, fluctuating, or floating encapsulate model (FEM). In the FEM model, the three lowest vibrational frequencies, belonging to the encapsulate motions, should be removed (to which the vibrational partition function is otherwise especially sensitive). Moreover, symmetries of the cages should be treated as the highest topologically possible (which reflects the averaging effect of the large amplitude motions of the encapsulate as observed [21] in the ^{13}C NMR spectra).

Let us mention in addition that if the partition functions are neglected in Eq. (1) and the vibrational zero-point energy is moreover ignored in the $\Delta H^{o}_{0,i}$ terms (so that we deal with the relative potential-energy terms $\Delta E_{r,i}$), the simple Boltzmann factors (quite commonly used for population estimates outside the fullerene field) are obtained:

$$w_i' = \frac{exp\left[-\Delta E^{o}_{r,i}/(RT)\right]}{\sum_{j=1}^{m} q_j \, exp\left[-\Delta E^{o}_{r,i}/(RT)\right]}. \tag{2}$$

Clearly, there is no reference to entropy contributions in simple Eq. (2). Obviously, the simple Boltzmann factors w_i' (in contrast to the properly evaluated mole fractions w_i from Eq. (1)) can never cross with a temperature change (in other words – they do not allow for any stability interchange), and thus, they are of limited applicability only.

The Relative Stabilities of Nonisomeric Nanocarbons

It is of interest to analyze [12, 16, 22, 23] also the behavior of the enthalpy terms (and actually even of other thermodynamic terms, too) for carbon aggregates C_n with variable carbon content n, i.e., for nonisomeric aggregates. Some useful features can in fact be obtained from a purely geometrical, topological reasoning.

Fullerenes C_n are cages (mostly) built from three-coordinated (sp^2) carbon atoms arranged into two types of rings, pentagons, and hexagons. However, all polyhedra (more precisely, all convex polyhedra) have to obey [11] Euler's classical polyhedral theorem:

$$V + F = E + 2 \tag{3}$$

where V denotes the number of vertexes (i.e., atoms $V = n$), F number of faces (rings), and E number of edges (bonds). However, if only pentagons and hexagons are allowed for fullerenes, their numbers n_5 and n_6 give the total count of faces:

$$F = n_5 + n_6. \tag{4}$$

Moreover, all carbon atoms in fullerenes are to be three-coordinated, so that it must hold for the number of edges:

$$E = \frac{3V}{2} \tag{5}$$

as each bond is accounted twice (if counting is carried out across all atoms). In addition, we can also count the bonds while going systematically through rings (though each bond would again be counted twice):

$$E = \frac{5n_5 + 6n_6}{2}. \tag{6}$$

Hence:

$$V = \frac{5n_5 + 6n_6}{3}. \tag{7}$$

Euler's theorem gives:

$$V + F = \frac{3V}{2} + 2. \tag{8}$$

One can thus get for the ring counts:

$$n_5 + n_6 = \frac{5n_5 + 6n_6}{6} + 2 \tag{9}$$

which can immediately be simplified to a surprising general finding:

$$n_5 = 12. \tag{10}$$

In other words, owing to purely topological reasons, in any conventional fullerene C_n, the number of five-membered rings must be equal to 12. The number of six-membered rings is variable; however, Eq. (7) gives a relationship to the number of carbon atoms:

$$n_6 = \frac{n - 20}{2}. \tag{11}$$

According to Eq. (11), the smallest possible fullerene (i.e., for $n_6 = 0$) has the stoichiometry C_{20}. As there are always 12 pentagons, then the smallest IPR cage should have 12 × 5 carbon atoms – known as truncated icosahedron or buckminsterfullerene C_{60}. Findings (10) and (11) are actually quite general – they are valid for any polyhedral nanocarbon species as long as it is built from just five- and six-membered rings (e.g., also for closed nanotubes).

The above topological analysis can also be applied to polyhedra built just from four- and six-membered rings. This structural pattern is important for boron-nitrogen analogues [23] of fullerenes such as $B_{12}N_{12}$, $B_{28}N_{28}$, $B_{36}N_{36}$, and $B_{36}N_{24}$. Let us consider now cages built only from squares (the word square means here a four-membered ring rather than a rectangle with equal sides) with altogether n_4 squares and n_6 hexagons, so that the number of rings or faces F of the polyhedron is $F = n_4 + n_6$, and let us consider altogether V three-coordinated atoms or vertices as above. Then, the total number of bonds or edges (E) in the cage is $3V/2$, where the factor of 2 again prevents a double counting of each bond. The number of bonds can be counted not through atoms but through the rings; then another expression, $(4n_4 + 6n_6)/2$, is obtained and thus:

$$4n_4 + 6n_6 = 3V. \tag{12}$$

Let us apply now the Euler's polyhedral formula from Eq. (3), $V + F = E + 2$, and implement in it what we already derived for F and E:

$$V + n_4 + n_6 = \frac{3}{2}V + 2. \tag{13}$$

If we eliminate V by combining Eqs. (12) and (13), we end up with formulas:

$$n_4 = 6 \tag{14}$$

$$n_6 = \frac{V}{2} - 4. \tag{15}$$

This result means that in each polyhedron built from four- and six-membered rings, and three- coordinated atoms, the number of the four-membered rings will always be six. It is obvious from Eq. (15) that the smallest possible number of atoms is eight (then one has only six squares and no hexagons, i.e., one of the five regular solids, a cube – if all atoms are equivalent). There is still another unique case in the series, namely for $V = 24$, when we deal (for equivalent atoms) with one of the 13 semi-regular polyhedrons, truncated octahedron, and thus with the real squares and regular hexagons. Similar to the isolated pentagon rule, we can introduce a concept of the isolated squares. As we deal with six squares we cannot meet the requirement with less than 24 atoms. However, in the truncated octahedron indeed, there is no junction of two squares so that it is the smallest square/hexagon polyhedron with the isolated-square property.

As a third useful case, we can consider [24] four-, five-, six-, and seven-membered rings: n_4 squares, n_5 pentagons, n_6 hexagons, and n_7 heptagons, number of faces $F = n_4 + n_5 + n_6 + n_7$. Again, as we deal with V three-coordinated atoms, the total number of bonds E in the cage is $3V/2$. The number of bonds can similarly be counted through the rings so that we have another expression, $(4n_4 + 5n_5 + 6n_6 + 7n_7)/2$:

$$4n_4 + 5n_5 + 6n_6 + 7n_7 = 3V. \tag{16}$$

Euler's polyhedral formula gives:

$$V + n_4 + n_5 + n_6 + n_7 = \frac{3}{2}V + 2. \tag{17}$$

Finally, combining Eqs. (16) and (17), we end up [24] with the formula:

$$2n_4 + n_5 - n_7 = 12, \tag{18}$$

Interestingly, the number of hexagons does not appear in Eq. (18). If $n_4 = n_7 = 0$, the equation is obviously reduced to the 12 pentagons. If $n_5 = n_7 = 0$, it is reduced to the six squares. In particular, Eq. (18) says that a removal of two pentagons could be

compensated by an increase of the four-membered rings by one, etc. This step can in some convenient cases (obviously connected pentagons) result in a decrease of energy as shown [24] for C_{32} cages.

Let us move now from the pure fullerene topology to energetics. It has been customary that the semiempirical quantum-chemical methods primarily produce the heats of formation at room temperature (instead at the absolute zero temperature). In the case of the carbon aggregates C_n in the gas phase, the heats of formation at room temperature $\Delta H^o_{f,298}$ belong to the thermochemical processes:

$$n\mathrm{C(s)} = \mathrm{C}_n(g). \tag{19}$$

In our connections, however, it is more convenient to deal with formal, unified, or normalized processes:

$$\mathrm{C\,(s)} = \frac{1}{n}\mathrm{C}_n(g) \tag{20}$$

that always start from the identical amount of carbon atoms and thus allow for direct comparisons. The enthalpy changes for the unified processes are the relative heats of formation $\Delta H^o_{f,298}/n$.

There is a relatively smooth, decreasing dependency [12, 16, 22, 23] of the calculated relative heats of formation $\Delta H^o_{f,298}/n$ on the number of atoms n in carbon clusters (Fig. 1). In fact, the finding can readily be rationalized qualitatively, using

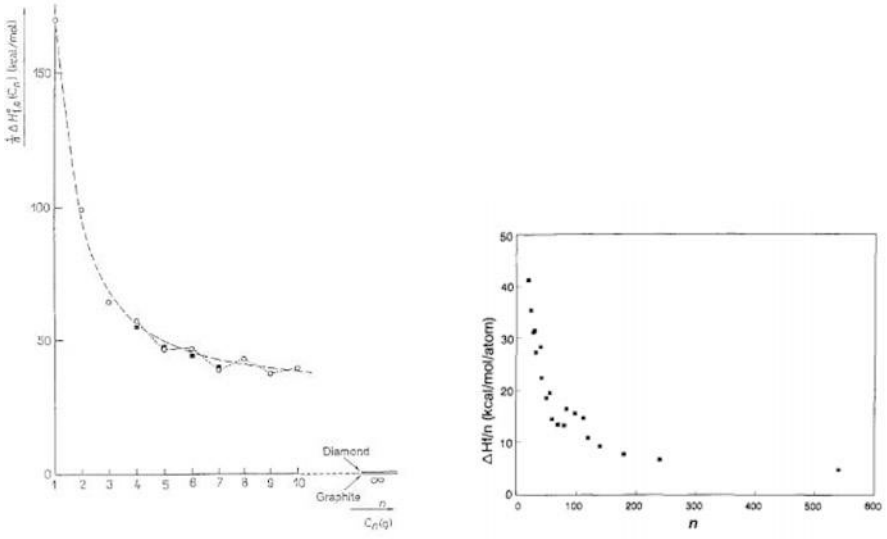

Fig. 1 Relative heats of formation $\frac{1}{n}\Delta H^o_{f,298}$ for small carbon clusters C_n (MINDO/2 [22]) and for fullerenes (MNDO [23])

the above topological analysis. For simplicity, let us consider just the IPR fullerenes C_n (non-IPR isomers would be placed somewhat higher in Fig. 1). For the IPR fullerenes, we deal with just two types of bonds – 5/6 (between pentagons and hexagons) and 6/6 (shared by two hexagons). Let us suppose that these two types of bonds can be represented by some uniform dissociation energies, $H_{5/6}$ and $H_{6/6}$ (taken as positive numbers); then we can straightforwardly write for the C_n atomization heat ΔH_{at} (i.e., defined here as a positive enthalpy change connected with dissociation into atoms):

$$\Delta H_{at} = 60H_{5/6} + \left(\frac{3n}{2} - 60\right)H_{6/6} \tag{21}$$

as an IPR fullerene C_n always has 60 5/6 bonds (it comes from the 12 isolated pentagons), while the number of the 6/6 bonds according to Eq. (5) is $\frac{3n}{2} - 60$. The relative atomization heat $\Delta H_{at}/n$ is linked to the process:

$$\frac{1}{n}\mathrm{C}_n(g) = \mathrm{C(g)} \tag{22}$$

The atomization and formation heats for carbon aggregates are related by the heat of vaporization of carbon, ΔH_{vap}. More specifically (as a production of a species from atoms should be connected with an energy release, i.e., an energy gain), the reversal process:

$$\mathrm{C(g)} = \frac{1}{n}\mathrm{C}_n(g) \tag{23}$$

is connected with the (negative) enthalpy change of $-\Delta H_{at}/n$. Combining Eq. (20) and Eq. (23) with the evaporation of carbon leads to the following expression:

$$\frac{\Delta H_f^o}{n} = -\frac{\Delta H_{at}}{n} + \Delta H_{vap}. \tag{24}$$

Thus, after using the bond-energy terms:

$$\frac{\Delta H_f^o}{n} = -\frac{3}{2}H_{6/6} + \Delta H_{vap} + \frac{60}{n}\left(H_{6/6} - H_{5/6}\right). \tag{25}$$

This functional dependency can be expressed as:

$$\frac{\Delta H_f^o}{n} = A + \frac{B}{n}, \tag{26}$$

where B is a positive constant, A is a relatively small number, and hence Eq. (26) indeed gives a smoothly decreasing curve known [12, 16, 22, 23] from various quantum-chemical computations.

However, it is still not the end of stability reasoning. From such a curve, one cannot yet see a particular stability of C_{60} or C_{70} – any larger fullerene than those two would seem like an energetically better option. Thus, a still more complex description of the fullerene synthesis is needed. In the first place, even if we treat the problem from the thermodynamic point of view, pressure terms should be taken into account [16, 25]. For example, the equilibrium constant $K_{60/70}$ for a (rather hypothetical, formal) interconversion equilibrium between the two clusters expressed in the partial pressures p_i gives:

$$K_{60/70} = \frac{p_{70}^{6/7}}{p_{60}} = \frac{(1 - x_{60})^{6/7}}{x_{60}} P^{-1/7}, \tag{27}$$

where P stands for the total pressure of the two clusters and x_{60} is the mole fraction of buckminsterfullerene. At some sufficiently high pressures, C_{70} could be even more populated [16] than C_{60}, but at the conditions of a saturated carbon vapor the stability order is reversed in favor of C_{60} so that an agreement with observation is obtained. In order to model the interplay of nonisomeric carbon clusters C_n, saturated carbon vapor was simulated [16, 25] simply as a mixture of just seven representative clusters, namely with $n = 1, 2, 3, 4, 5, 60$, and 70. The simulation employs equilibrium constants for the cluster formation derived from quantum-chemical calculations. The calculations of the equilibrium constants are the moment where the entropic parts are added so that the Gibbs-energy level is reached. The scheme is actually pressure dependent. Clearly enough, the pressure does not reflect the He pressure used in the synthesis but the carbon-vapor pressure itself (difficult to be measured – after all, it is always covered by the He pressure). At very low pressures around the saturated carbon-vapor pressure, the scheme gives [16, 25] the correct order of the relative populations of C_{60} and C_{70}. If we increase the pressure to very high, unrealistic values like 1 atm, we can reverse the order. The scheme is quite sensitive to the heats of formation. Moreover, we would have to select some representative values of temperature and pressure for fullerene synthesis. As there is a considerable temperature gradient in the chamber, we could expect (in parts of the synthetic chamber) actually a supersaturated carbon vapor.

Clearly enough, the isomeric-population stability problem is much better understood at present than the relative stabilities of nonisomeric carbon clusters, partly because the former task has been given considerably higher attention. Still, this pressure reasoning allows for a qualitative rationalization of the observed populations of nonisomeric fullerenes, and there are even some interesting more general results already available for the nonisomeric situation, too. This is especially true for a (quite general) temperature increase of the clustering degree under the saturation conditions [26]. While the equilibrium constants for cluster formation decrease with temperature, the saturated pressure increases. It is just the competition between these two terms which decides the final temperature behavior. This saturation-pressure-based temperature increase of cluster formation is an interesting feature of fullerene synthesis, useful for its understanding.

Enumeration of Fullerene Cages

Enumerations and generations of fullerene structures represent an important step in their computational studies. The enumerations are basically geometrical or algebraic treatments [20] (or graph-theory applications). Enumeration results in the works of Fowler and Manolopoulos [27, 28] as well as from other groups [11, 29] have indeed been applied to structure elucidation and calculations of various numerous fullerenic systems. It has been obvious from the very early days that $n = 60$ or 70 cannot be just singular isolated stability islands and, moreover, that for a selected carbon content actually several isomeric forms can *a priori* be expected, too. Interestingly, the concept of Goldberg polyhedra developed earlier in mathematics also allows [11, 28, 29] for a systematic generation of icosahedral fullerene cages. Goldberg polyhedra [11, 28] have $20 \times (b^2 + bc + c^2)$ atoms, where b and c are nonnegative integers. If $b = c$ or $bc = 0$, the point group of symmetry is I_h, otherwise it is only its rotational subgroup I (though it is customary to call both of them as icosahedral symmetry). In particular, C_{60} emerges for the choice $b = c = 1$; other I_h symmetry cases are, for example, $n = 20$, 80, 180, 240, 320, 500, 540, etc. However, applicability of the algebraic treatment does not end here as it can predict which of the Goldberg structures has closed electronic shell (singlet state) at the HMO level. The key parameter is $(b–c)$. If it is divisible by 3, the cluster has a multiple of 60 atoms and it has an electronic closed shell. Otherwise, it has $(60 \times n + 20)$ atoms, it has electronic open shell (i.e., triplet electronic state), and the Jahn-Teller distortion is to be expected, leading to a reduction of both symmetry and orbital degeneracy, thus bringing a lower stability. Hence, the electronic closed shells free of the Jahn-Teller distortion are predicted, for example, for $n = 60$, 180, 240, 420, 540, etc., cages in the class of Goldberg polyhedra.

There are several other (in fact, quite early recognized [27–40]) useful concepts like the so-called Stone-Wales transformation [31], i.e., a process for fullerene isomerizations, rearrangements of the rings in the original icosahedral C_{60} or other cages (pairwise interchange of two pentagons and two hexagons, also called pyracylene transformation). It involves movement of two atoms and requires two bonds be broken. It is not necessarily a convenient kinetic process as it is thermally (but not photochemically) forbidden. Nevertheless, it allows for a formal stepwise, systematic (topological) generation of various isomeric cages. The Stone-Wales transformations were, for example, applied to a topological analysis of C_{84} IPR structures, and it was demonstrated [28] that the isomerizations would decompose into two disjoint families, two disconnected isomerizations maps (i.e., not every two fullerene isomers can be linked by a series of the Stone-Wales isomerizations).

The leapfrog transformation represents [28] another useful method for the classification of fullerene cages. It works with a topological concept called dual. Two polyhedra are duals if the vertices of one correspond to the face-centers of the other (e.g., cube and octahedron are duals). The duals of fullerene cages have triangular faces and five- and six-coordinated vertices (for example, there are such topological links between fullerenes and boron hydrides). The leapfrog transformation consists of two steps: (i) Each face in a fullerene is capped by a central atom (becoming a pentagonal or hexagonal pyramid), and then (ii) take the dual of the triangular

polyhedron created in (i). The result is again a fullerene cage but with three times as many atoms; nevertheless, both fullerene cages belong to the same symmetry group. The transformation also allows for a formulation [28] of $60 + 6 \times k$ stability rule (k is zero or any integer greater than 1).

The enumeration of the IPR structures of fullerenes represents a particularly useful outcome of the topological approaches. The key concept in the enumerations is a two-dimensional representation of fullerenes by their ring spiral [28, 29]. It should be noticed that at least smaller fullerenes could be peeled like an orange – each face, after the first, borders its immediate predecessor, so that the sequence of the rings comes off the cage in a single continuous spiral. It was not obvious if this is true for any cage regardless its dimension. In fact, the single spiral is not always possible, as a counterexample is known [30], namely a fullerene with 380 atoms. It is the smallest tetrahedral fullerene (T symmetry) without a spiral. It is not clear, however, whether this is the smallest possible unspirable fullerene of any symmetry. The C_{380} structure looks more like a giant tetrahedron than a sphere, and this is apparently important for its unspiralability (there are four symmetry equivalent sets of three fused pentagons at the vertices of the giant tetrahedron). Hence, the enumeration algorithm based on the ring spirals is a rather practical, heuristic tool, not exact in mathematical sense. But it should fail only in regions which are not really topical, at least at present. Moreover, the spiral algorithm also produces a systematic serial numbering of the cages [28, 29] which is rather frequently used for fullerene-cage nomenclature.

The basic idea is that the bonding topology can be reconstructed from the sequence of the rings in the spiral. Thus, all possible C_n fullerene graphs can be generated by considering all the ways in which 12 pentagons and $\left(\frac{n}{2} - 10\right)$ hexagons in the spiral can in principle be combined:

$$S_n = \frac{\left(\frac{n}{2} + 2\right)!}{12! \times \left(\frac{n}{2} - 10\right)!}. \tag{28}$$

However, the correspondence between ring spirals and distinct fullerenes turns out to be many-one. A spiral can be started in a number of possible ways; this problem is to be overcome by a uniqueness test. Moreover, not every spiral generated can be closed (incidentally, no fullerene cage is possible for C_{22}). The uniqueness test could, for example, be based on the eigenvalues of the topological adjacency matrix (basically, the HMO matrix). Therefore, a term of spectrally distinct fullerene isomers is then considered [11, 27], i.e., the spectrum of the eigenvalues or of the energies of the HMO matrix. In fact, the HMO matrix was historically for the first time used with fullerenes by Bochvar and Gal'pern [39] in 1973, namely for C_{20} and C_{60}. The adjacency matrix also allows [28, 29] for the application of topological stability indicators. Moreover, the eigenvectors of topological adjacency matrices are useful for the generation of the Cartesian coordinates of the atoms in a cage. The spirals can be lexicographically coded with a sequence of digits 5 (pentagon) and 6 (hexagon), organized into one number. The spiral that has such number with the lowest value is called a canonical spiral. The spiral codes can further be simplified by

writing just the (12) numbers of the pentagon positions in the spiral, taking the pentagon sequence simply as a number, and again organizing such pentagon-based sequences by their numerical values. The only IPR isomer of C_{60}, for example, comes in this lexicographic convention as the last cage with serial number of 1812 (IPR cages come at the end as in the IPR structures all pentagons are separated). The list of the 12 pentagon positions [28] (or face spiral pentagon index [29]) for the IPR isomer (numbered as 1812 and with symmetry I_h) is as follows: 1 7 9 11 13 15 18 20 22 24 26 32. The non-IPR isomer just below it (numbered 1811 and with symmetry D_3) has the pentagon-position list: 1 2 9 12 16 17 19 22 24 25 29 30. The final serial number (together with point group of symmetry) can serve in a fullerene-cage nomenclature, for example, I_h(1812)-C_{60} for buckminsterfullerene, or D_{5h}(8149)-C_{70} for the only IPR isomer of C_{70}.

The total number of spectrally distinct C_n fullerene isomers increases very rapidly with the carbon content n. In particular, it has been established that the number of spectrally distinct C_{60} isomers is 1812. However, this number has its own interesting case history. First, Manolopoulos et al. [32] reported 1760 isomers. But Liu et al. [33] arrived at 1790 isomers using an independent algorithm (they believed it was owing to the fact that the spiral algorithm produces a lower bound to the correct value). Finally, both groups developed their computer programs further and arrived at the present common value of 1812. For example, with $n = 50$, 40, 30, and 20, the computed [28] total numbers of isomers read 271, 40, 3, and 1, respectively. However, we should realize that this concerns only the pentagon/hexagon rings, no other cycles have been considered, and a chiral pair is essentially considered as one isomer. Moreover, there is not necessarily a one-to-one correspondence between topologically generated structures and local energy minima on a potential hypersurface. The actually computed structure can be a transition state, the particular stationary point may not exist at all, or there may be more than one conformer with the required connectivity [34].

Incidentally, the odd-numbered cages were left aside in the enumerations (not because they do not exist) but because they cannot be built from three-coordinated atoms only. We can consider two-, three-, and four-coordinated atoms in a cage, p two-coordinated atoms and q four-coordinated. If we still allow only pentagons and hexagons, we can get [35] from Euler's formula the number of pentagons, n_5:

$$n_5 = -2p + 2q + 12, \tag{29}$$

which of course reduces to 12 pentagons if $p = q = 0$. For example, if we allow for just one two-coordinated carbon atom in the odd-numbered cages, and for pentagons/hexagons only, the number of pentagons is reduced [35] to ten. If we allow for two tetra-coordinated and one two-coordinated carbon(s), the number of pentagons is again uniform, however, increases [35] to 14. An extension of the IPR concept and generalized enumerations could be built along the line. Decorated fullerenes represent an even more exotic by-product [36], but there is an unexpected experimental basis for it as cages built from water molecules and kept by hydrogen bonds could recently be observed. Formally, from any fullerene, we can derive the related

hydrogen-bonded cage. Clearly enough, as for n water molecules, we have $\frac{3n}{2}$ bonds in the cage; $\frac{n}{2}$ H atoms cannot be involved in the hydrogen bonds and must direct outwardly (or even possibly inside the cage).

Among all possible isomers, the IPR structures are particularly important as high stability candidates. The requirement of isolated pentagons can be readily implemented [28] into the spiral algorithm. First, of all possible spirals (cf. Eq. (28)), we can immediately eliminate those with at least one pentagon/pentagon junction. This is of course not sufficient as we still have to eliminate in cage-building treatment the spirals with the secondarily generated pentagon/pentagon junctions. One should realize that there cannot be an IPR structure for $n < 60$. It is obvious as we always have 12 pentagons, and 12 isolated pentagons just represent $12 \times 5 = 60$ carbon atoms. Indeed, the smallest possible IPR fullerene is buckminsterfullerene C_{60}. The second smallest IPR fullerene appears at $n = 70$, but still it is a unique structure as well as for $n = 72$ and 74. After this threshold, the picture becomes more diversified [28] as, for example, for $n = 76$, 78, 80, 82, 84, 86, 88, and 90 there are 2, 5, 7, 9, 24, 19, 35, and 46 IPR structures, respectively (N.B. – it is not necessarily a monotonous series – for $n = 86$, the number drops to 19).

A different enumeration procedure by Liu et al. [33] generates cages ring by ring in all possible ways starting from a seed, e.g., a single pentagon. In each step, it searches for unsaturated vertices of degree two and then adds a segment to the two unsaturated vertices in order to create a ring. Again, in order to identify distinct cages, it is necessary to eliminate redundant occurrences (it is done via a graph-isomorphism testing program).

From the purely mathematical point of view, some enumeration problems can be treated by Polya's theorem though it is not necessarily the most practical tool for a particular situation. Balasubramanian [37] applied the theorem to various substituted fullerenes. For example, for the derivatives [37] $C_{60}X_n$, the numbers of isomers are 37, 577, and 1971076398255692 for n equal to 2, 3, and 30, respectively (the optical isomers can be distinguished or treated as one species, for example, there are 14 chiral pairs among the $C_{60}X_2$ isomers).

There has also been interest in the HMO-related aspects of fullerene cages (which started even before establishing the fullerene research) as it is frequently useful to start from this simple model before applying more sophisticated approaches. Interestingly enough, the HMO orbital energies of C_{60} are available in analytic form so that its HMO characteristic polynomial can be expressed [38] in the following condensed form:

$$(x+3)(x+1)^9(x-2)^4\left(x^2+x-3\right)^5\left(x^2-3x+1\right)^3\left(x^2-x-1\right)^5 \\ \left(x^2-x-4\right)^4\left(x^4+3x^3-2x^2-7x+1\right)^3 \tag{30}$$

(note the factor 9 with the root -1; it is a coincidence of fourfold and fivefold degeneracy). The highest occupied MO (HOMO) is five times, the lowest unoccupied (LUMO) three times degenerated. The HOMO is fully filled with electrons which avoids the Jahn-Teller distortion and serves [39] as a first computational

argument for its stability (in contrast to C_{20} with a Jahn-Teller symmetry reduction [40]). Similarly, the high symmetry of C_{60} brings [17] ample degeneracies in vibrational spectra – the symmetry representation $\Gamma_{C_{60}}$ of the 174 vibrational modes of C_{60} reads:

$$\Gamma_{C_{60}} = 2A_g + A_u + 3T_{1g} + 4T_{2g} + 4T_{1u} + 5T_{2u} + 6G_u + 6G_g + 8H_g + 7H_u, \quad (31)$$

where *A*, *T*, *G*, and *H* denote onefold, threefold, fourfold, and fivefold degenerate modes, respectively (so that we have $3 \times 1 + 16 \times 3 + 12 \times 4 + 15 \times 5 = 174 = 60 \times 3 - 6$). The high symmetry creates only 46 distinct vibrational frequencies, 4 of them (T_{1u}) active in the IR and 10 of them (A_g, H_g) in the Raman spectra. Such a strong symmetry simplification of spectra is rare and was useful [3] for the C_{60} identification.

Relative Populations of Isomeric Empty Fullerenes

Small carbon clusters have frequently been studied [41] by both experimental and theoretical techniques. Ion-chromatography observations by von Helden [42] showed that starting from about $n = 7$, cyclic rings always exist in addition to the linear forms. Cyclic structures were, for example, computed [11, 41, 43] for C_6–C_{13}. C_{11} should be the first species for which the cyclic structure becomes dominant. A similar transition from cyclic to polyhedral species was expected around $n = 45$. The linear and cyclic (rhombic, bicyclic) C_4 isomers were especially frequently computed. Newer energy evaluations suggest [41, 43] only a small energy separation between the two forms. Then, the entropy contributions are important and in fact lead to the linear species prevalence at higher temperatures in agreement with ion chromatography. A similar enthalpy-entropy interplay is calculated for C_6, too. Isomers of C_6 were also employed [44] in testing anharmonicity effects on the calculated isomeric populations. At the MP2 = FC/6-31G* level, the molar fraction at 2000 K of the prevailing isomer was 95.2% and 96.0% in the harmonic and anharmonic treatment, respectively, thus supporting the expected ample cancellation in Eq. (1).

As ion-chromatography has pointed out the existence of polyhedral structures already around C_{30}, isomeric populations for smaller fullerenes have also been treated [24, 40]. The relative populations of larger isomeric (mostly IPR) cages are however studied primarily [16] – at present from C_{72} to C_{98}. A few computational examples for fullerenic isomeric mixtures evaluated according to the master Eq. (1) follow (in all the illustration, the general computer program [45] for the determination of composition and thermodynamics of the ideal gas-phase equilibrium isomeric mixtures was employed).

Actually, C_{72} and C_{74} are the only species among C_{60}–C_{96} not isolated yet. A low solubility [46] in conventional solvents may be one of possible reasons for the difficulties. Hence, as C_{72} could only be recorded in gas phase, its structure is

unknown from experiments. There is just one IPR-satisfying structure for C_{72}, namely with D_{6d} symmetry. However, a non-IPR (i.e., IPR-violating) structure with one pentagon-pentagon junction is a few kcal/mol lower in energy than the IPR cage. Hence, the C_{72} system was calculated [47] at DFT level in a more detailed way. The geometry optimizations were carried out [47] using the B3LYP/3-21G treatment. In the optimized B3LYP/3-21G geometries, the harmonic vibrational analysis was carried out, and also the B3LYP/6-31G* separation energies were evaluated. The electronic excitation energies were evaluated by the ZINDO method. The following structures were considered (Fig. 2): the IPR cage (a), two non-IPR cages with one pentagon-pentagon junction (b) and (c), a structure with one heptagon (d), a cage with two heptagons (e), and two structures each with two pentagon/pentagon junctions (f) and (g). The (c) structure of C_{2v} symmetry with just one pentagon/pentagon fusion represents the lowest energy isomer. Figure 3 presents the DFT-computed temperature development of the relative concentrations of the seven C_{72} isomers in a high temperature region. The lowest energy structure (c) is the most populated species at any temperature. On the other hand, the IPR structure (a) is always negligible.

However, the next case, C_{74}, is different. Wan et al. [48] suggested that it could be extracted by convenient solvents. This suggestion prompted DFT calculations [49] that treated a set of six isomers, five of them being non-IPR species. The sole C_{74} IPR isomer exhibits D_{3h} symmetry; in spiral coding comes as D_{3h}(14246)-C_{74} (a simpler numbering $1/D_{3h}$ is also used [49]). Then, three isomers are non-IPR cages with one pair of connected pentagons, while the remaining two species contain (in addition to the fused pentagon/pentagon pair) also one heptagon (Fig. 4). It turns out that the IPR D_{3h} species has not only favorable enthalpy but also entropy term, and thus, all the remaining isomers can act as minor species at best (Fig. 5). A specific consideration should be done [49] for the electronic partition function q_{el} in C_{74} owing to considerably low-lying triplet states. The electronic partition function can be based either on both singlet and triplet electronic excited states or just on singlet electronic excited states. It can be argued [49] that the singlet-only approach could produce more realistic results. The basic reason is that it could be expected that the fullerene triplet species, after condensation in the form of soot, will in the end polymerize and form insoluble solids. Hence, if the triplet-state isomers can be removed by such mechanism during the condensation, only the singlet-state isomers will keep their high-temperature concentration ratios, and those should be the observed values found in the soot.

There are seven [50, 51] IPR C_{80} structures. The C_{80} IPR isomers have conventionally been coded by letters **A**–**G** (Fig. 6). Of the seven IPR C_{80} structures, the species **B** exhibits a high topological symmetry I_h; however, it is subjected to a Jahn-Teller distortion. The SAM1 calculations predict [51] the **C** isomer (D_{5d} symmetry) as the system's ground state, being followed by the **A** species of D_2 symmetry. However, also for the C_{80} isomers, the presence of low-lying triplet states is pointed out [52] so that again a special approach to the electronic partition function q_{el} should be applied. Figure 7 shows that the singlet-only approach to q_{el} actually gives

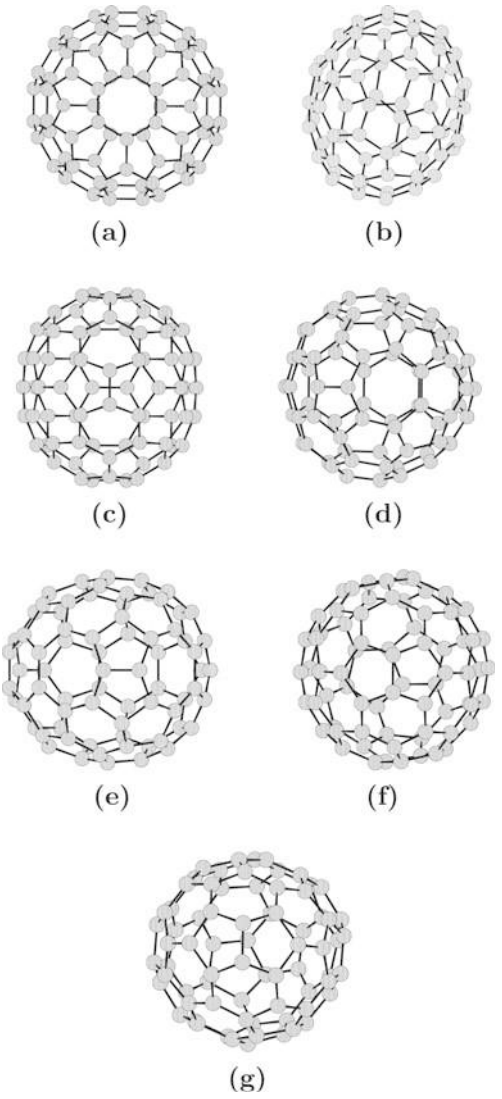

Fig. 2 B3LYP/3-21G optimized structures [47] of C72 isomers: (**a**) IPR, (**b**) 5/5 pair, (**c**) 5/5 pair, (**d**) seven-membered ring, (**e**) two seven-membered rings, (**f**) two 5/5 pairs, (**g**) two 5/5 pairs

[51] a better agreement with observations as the **A** (D_2) cage is produced in larger amounts than a minor isomer, the *C* (D_{5d}) species. Interestingly, entropic contributions cause a population interchange between the **A** and **C** isomers. Moreover, the energetics was further calculated [51] at the advanced MP2 = FC/6-31G* level though with a simplified frozen core (FC) option. In the MP2 = FC/6-31G* approach, the **A** species (D_2) is lower in energy than the **C** isomer (D_{5d}) so that the final population prediction in Fig. 8 gives still better agreement between theory and experiment.

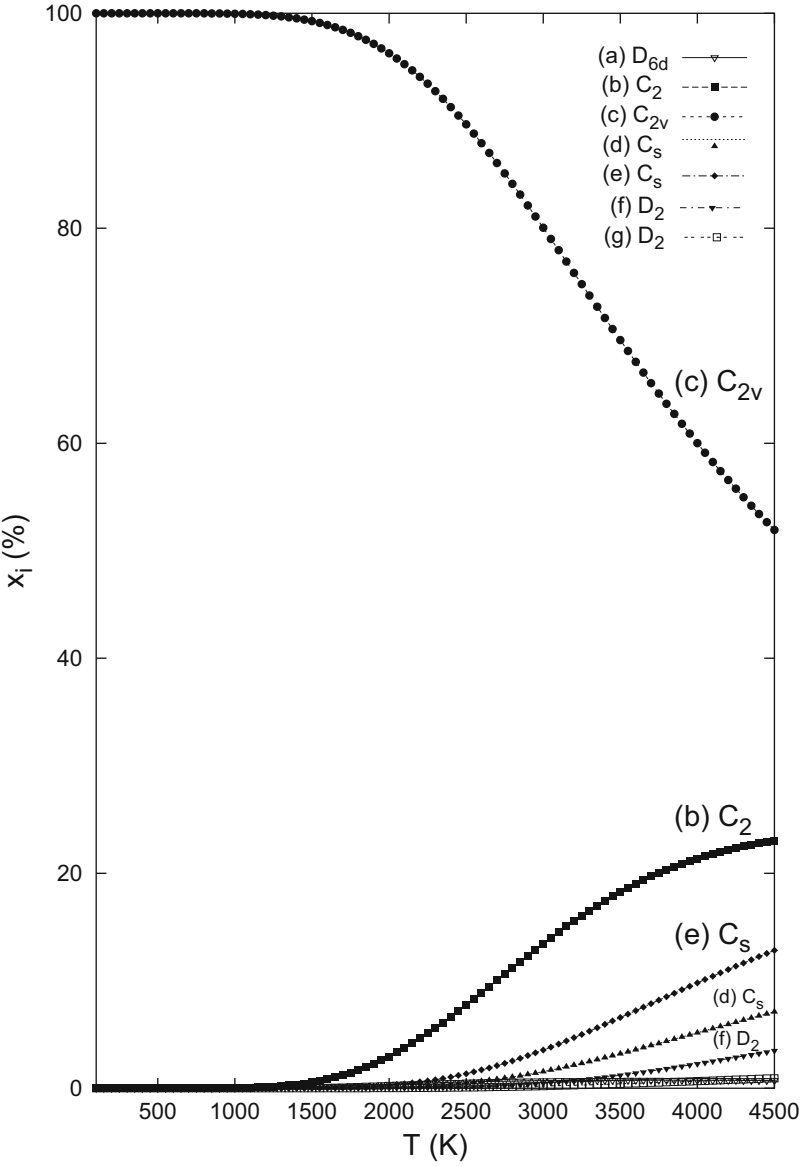

Fig. 3 Relative concentrations[361] of the C_{72} isomers [47] based on the B3LYP/6-31G* energetics and the B3LYP/3-21G & ZINDO entropy

The intuitive reasoning on the electronic partition function q_{el} can be given in a more formal way [51] as follows. Let us consider a set of altogether x isomeric fullerene cages – the first n of them being in singlet and the next $x - n$ in triplet electronic states. Here, we shall not follow the conventional, practical approach to

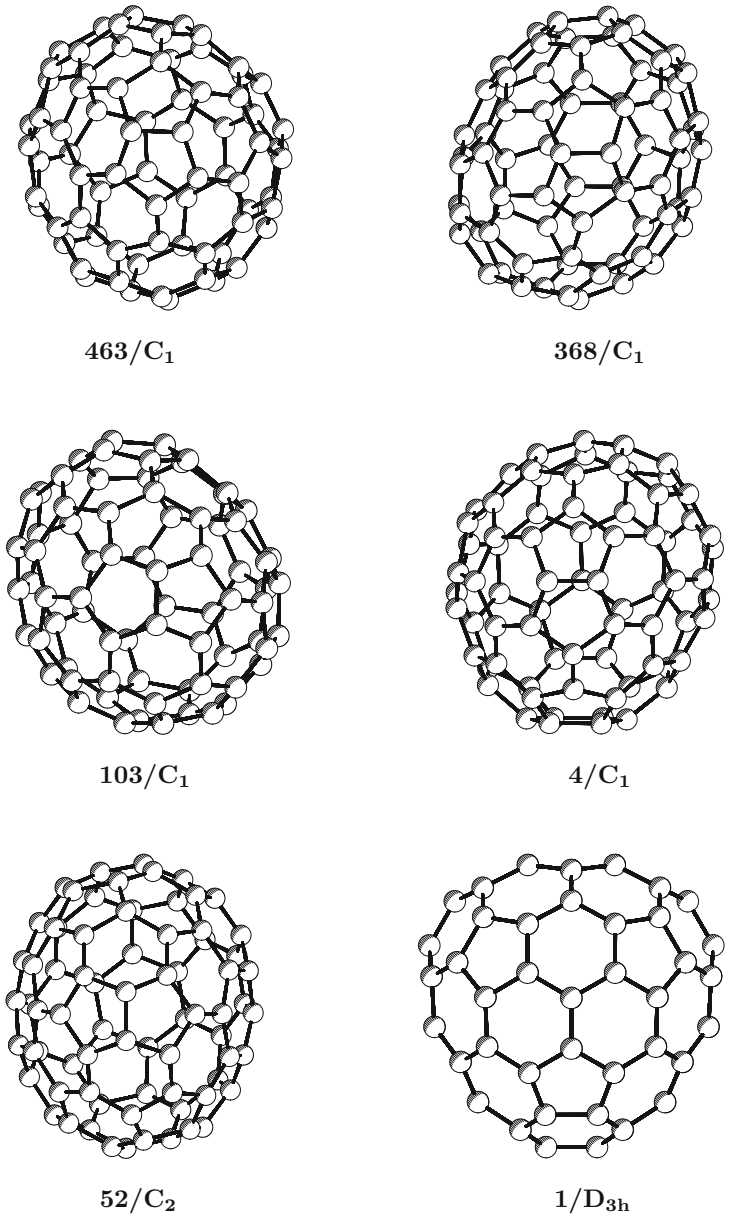

Fig. 4 B3LYP/3-21G optimized structures [49] of C_{74} isomers

the higher electronic states normally applied with Eq. (1), i.e., the identification of the rotational and vibrational levels of any excited electronic state with those of the respective electronic ground state. With this differentiation, every of the higher

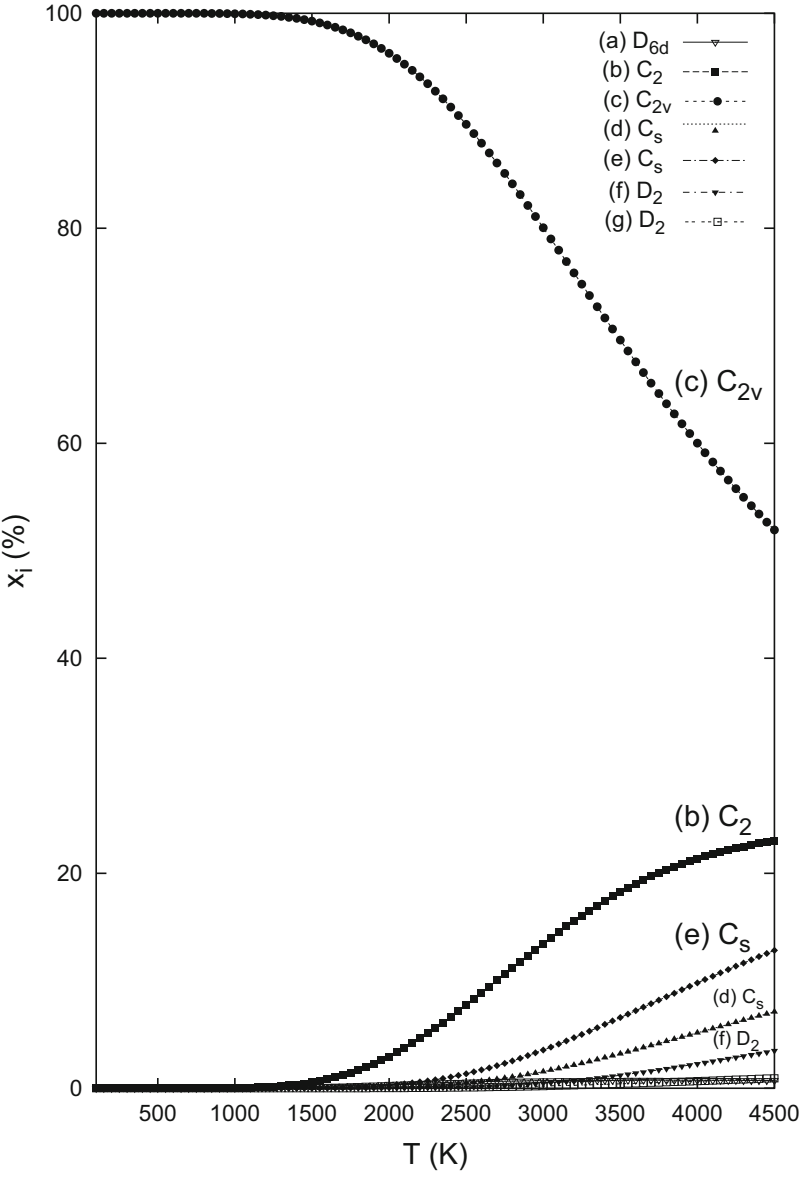

Fig. 5 Relative concentrations of the C_{74} isomers based [49] on the B3LYP/6-31G* energetics and the B3LYP/3-21G & ZINDO entropy; only singlet electronic excited states are included into the partition functions

electronic states is now taken as a particular isomer of its own. Their gas-phase equilibrium mole fractions $w_i^{(x)}$ are according to Eq. (1) given:

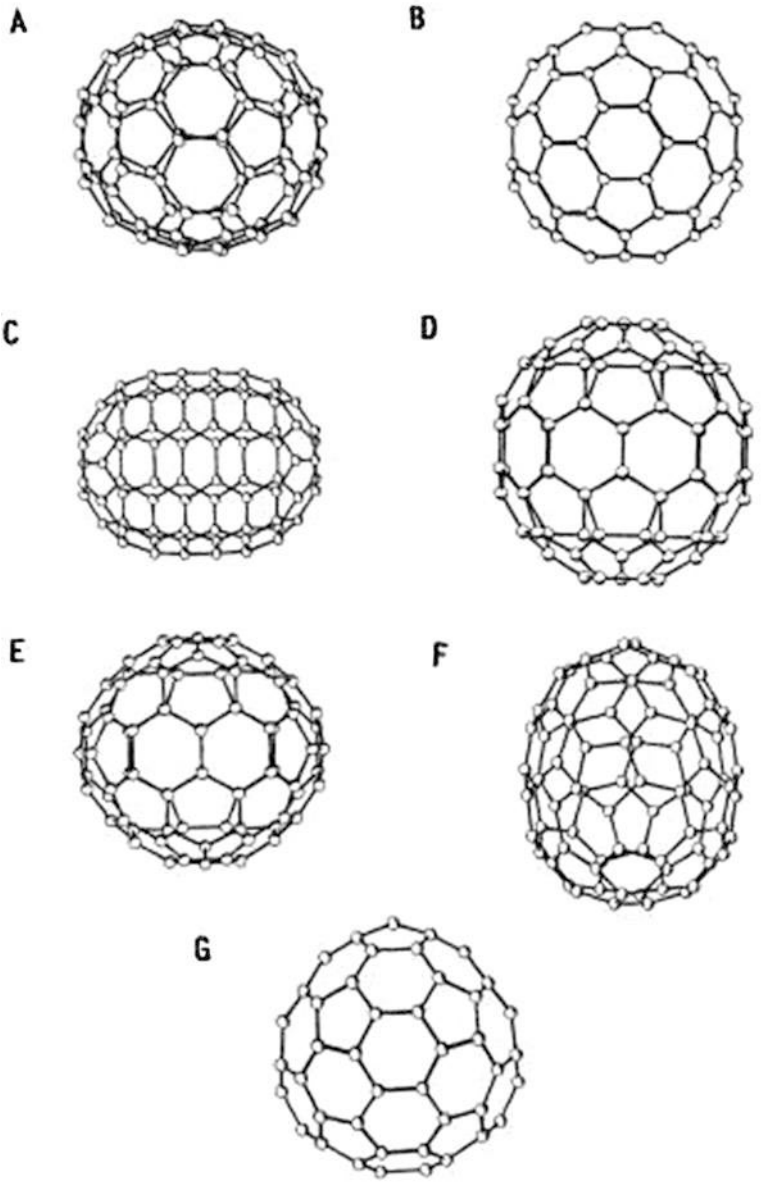

Fig. 6 The AM1 optimized IPR structures [50] of C_{80}

$$w_i^{(x)} = \frac{q_i \, exp\left[-\Delta H^o_{0,i}/(RT)\right]}{\sum_{j=1}^{x} q_j \, exp\left[-\Delta H^o_{0,i}/(RT)\right]}. \tag{32}$$

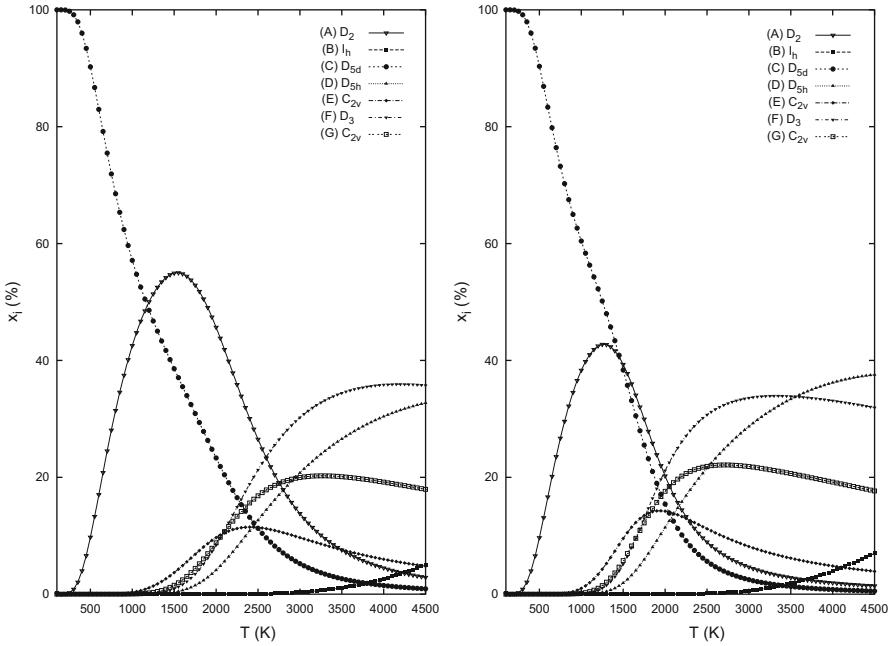

Fig. 7 Mole fractions x_i of seven IPR isomers of C_{80} [51] from the SAM1 data and q_{el} with the singlet (left) and the singlet and triplet excitation energies (right)

As we are concerned only with the inter-isomeric equilibrium, the mole fractions should still satisfy:

$$\sum_{i=1}^{x} w_i^{(x)} = 1. \tag{33}$$

If the equilibrium gas-phase isomeric mixture is cooled down and condenses, the high-temperature gas-phase mole fractions are effectively frozen. If the triplet-state isomers can be removed by some mechanism (polymerization) during the condensation, the singlet-state isomers should still keep their high-temperature concentration ratios. However, in order to avoid a formal artifact:

$$\sum_{i=1}^{n} w_i^{(x)} = p, \tag{34}$$

one should rescale the mole fractions into:

$$w_i^{(n)} = \frac{1}{p} w_i^{(x)}, (i = 1, \ldots, n). \tag{35}$$

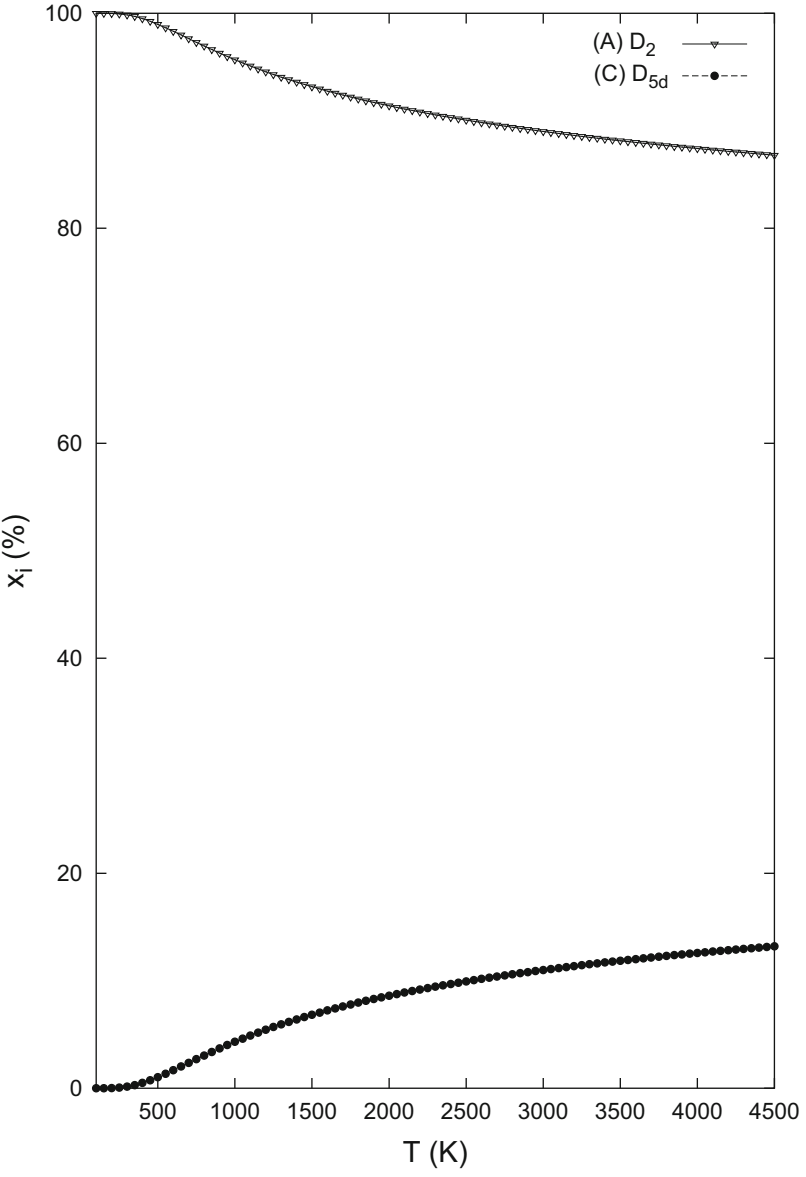

Fig. 8 Mole fractions x_i of the two observed IPR isomers of C_{80}, **A** (D_2) and **C** (D_{5d}), based [51] on the DFT data and q_{el} with the singlet excitation energies, however, using the MP2 = FC/6-31G*// B3LYP/6-31G* separation energy

Molar fractions (35) are the terms that should be found by an analysis of the soot in this case. Moreover, it can (perhaps somewhat surprisingly) be shown that they can actually be derived from Eq. (1) just considering the singlet states only:

$$w_i^{(n)} = \frac{q_i \exp\left[-\Delta H_{0,i}^o/(RT)\right]}{\sum_{j=1}^{n} q_j \exp\left[-\Delta H_{0,i}^o/(RT)\right]}. \tag{36}$$

To prove this, one should replace p in (35) by (34), then express $w_i^{(x)}$ by (32) and cancel out the common term $\sum_{j=1}^{x} q_j \exp\left[-\Delta H_{0,i}^o/(RT)\right]$. This result suggests that we can indeed limit the calculations only to the isomers in the singlet electronic states as long as we are interested in comparison with the observed concentration ratios derived from the condensed-phase products. In a similar way, it can be shown that the ratio of molar fractions between two particular isomers does not change after the addition (removal) of some other isomers to the set. More generally, it gives some rationalization for the limitation of the geometry optimizations and vibrational treatments just to the species in the singlet ground states when studying empty-fullerene stabilities.

The complete set of 19 isolated-pentagon-rule species of C_{86} represents another interesting fullerenic isomeric system, actually calculated [53, 54] already a quarter of century ago, namely by the SAM1 semiempirical method as well as other approaches. The computations consistently point out the species $C_2(17)$-C_{86} (Fig. 9) as the lowest-energy species in the IPR C_{86} set (the spiral numbering [28]). However, the $C_2(17)$-C_{86} population exhibits a rather fast temperature decrease while another species, $C_s(16)$-C_{86}, reaches its temperature maximum of 17.5% at a temperature of 1503 K (the $C_2(17)$-C_{86} population at this temperature amounts to 50.9%). Interestingly, experimental results [55] suggest that a representative temperature for fullerene synthesis should be expected around or above 1500 K. Later on, the two C_{86} cages, previously calculated [53, 54] as the most

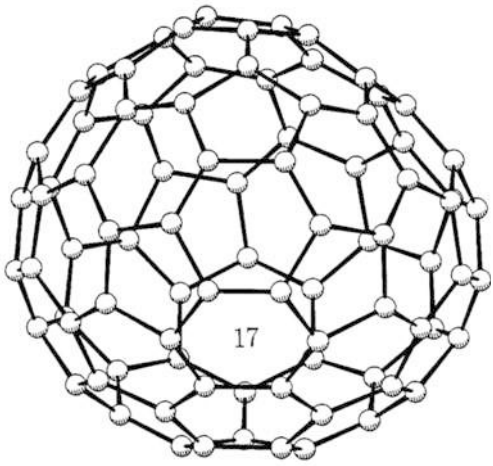

Fig. 9 The SAM1 optimized lowest-energy isomer [54] of C_{86}, viz. $C_2(17)$-C_{86}

populated at the relevant temperatures [55], were isolated [56, 57] indeed, thus producing an encouraging calculation-observation agreement.

As no IPR cages are possible below C_{60}, the calculations of C_{32} considered [24] cages built from four-, five-, six-, and seven-membered rings. Altogether 199 cages were optimized using semiempirical quantum-chemical methods (AM1, PM3, SAM1). The energetics was further checked with *ab initio* HF/3-21G calculations and also by density functional theory at the B3LYP/6- 31G* level. All five levels of theory suggest a D_{4d} cage (two squares, eight pentagons, and eight hexagons) as the lowest-energy structure. The thermodynamic treatment points out five cages significantly populated at high temperatures. Moreover, at very high temperatures, the structure lowest in energy is not the most abundant isomer. There are just six conventional fullerenes C_{32}, built exclusively from pentagons and hexagons; however, only two of them show significant populations at high temperatures. The remaining three relatively stable cages contain at least one four-membered ring. On the other hand, no structure with a heptagon shows a significant population at high temperatures. The study [24] thus suggests that in the non-IPR region below C_{60}, the *quasi*-fullerene cages with four-membered rings can in some cases be more important than the conventional fullerenes built from pentagons and hexagons only.

Stabilities of Metallofullerenes

The relative populations of the individual empty cages do not directly imply a stability order for metallofullerenes created by metal encapsulations into the empty cages. The reason is rooted in the charge transfer from the encapsulated metal atom to the cage – the transferred charge may roughly correspond to the encapsulated atom chemical valence (however, quantum-chemical calculations basically give the amount of transferred charge as nonintegral numbers). Such substantial charge transfer can considerably change the cage energy order. Hence, for metallofullerenes, the populations of the related charged cages are obviously more relevant than those of the neutral empty species. This interplay can, for example, be illustrated [58] on $La_2@C_{80}$. As mentioned above, there are seven C_{80} IPR cages, the energy-highest empty species being the icosahedral structure (I_h symmetry). The icosahedral cage actually undergoes a Jahn-Teller distortion as it has a fourfold degenerate HOMO, partially filled with just two electrons (owing to the Jahn-Teller effect, the cage symmetry can in fact be reduced from I_h to D_2, depending on the applied method). However, upon the encapsulation of two La atoms, the cage gets the remaining six electrons in order to fill completely its HOMO (and to avoid the Jahn-Teller effect). Moreover, $La_2@C_{80}$ derived from the icosahedral C_{80} cage is actually the lowest-energy isomer, and it was indeed isolated [21] as the most populated $La_2@C_{80}$ species. Hence, in the calculations of relative populations of isomeric metallofullerenes, one has to start from scratch – from the properly charged empty cages in order to obtain a first stability guess.

Relative Populations of Isomeric Metallofullerenes

The relative-population evaluations according to Eq. (1) have actually been performed for numerous metallofullerenes such as Ca@C_{72}, Ca@C_{74}, Ca@C_{82}, La@C_{82}, and other endohedrals of current interest (for surveys, see [18, 19, 58]). Let us start with Ca@C_{72} as the first illustrative example. Ca@C_{72} was isolated [48], and recently even its second isomer [59]; however, their structures were not determined. Five isomers were considered [60] in Ca@C_{72} stability calculations (Fig. 10). The endohedral Ca@C_{72} species created by Ca encapsulation into the sole IPR cage is labeled by (a). The other three Ca@C_{72} isomers are derived from two non-IPR C_{72} cages (b) and (c), and from a C_{72} structure even with one heptagon (d). Finally, there is also a species with two heptagons (e). The computations [60] were performed in the 3-21G basis set for C atoms and a dz basis and the effective core potential (ECP) on Ca combined with the B3LYP functional (B3LYP/3-21G~dz). The electronic excitation energies were evaluated by means of time-dependent (TD) DFT response theory at the B3LYP/3-21G~dz level. Figure 11 shows the RRHO and FEM temperature developments [60] of the relative populations of the five Ca@C_{72} isomers in a high-temperature region. At a low temperature, the molar fractions of the (c) and (b) structures are interchanged, and beyond the point, the (b) structure is always somewhat more populated.

In contrast to the Ca@C_{72} system, Ca@C_{74} was not only isolated [48], but also its structure was clarified [61]. According to the ^{13}C NMR spectra recorded [61] by Kodama et al., Ca@C_{74} exhibits D_{3h} symmetry of its cage. There is only one IPR structure possible [62] for C_{74}, and the sole C_{74} IPR cage has D_{3h} symmetry. In fact, a set of altogether six Ca@C_{74} isomers was submitted [62] to the stability computations. It has turned out, in agreement with the observation, that the endohedral with the IPR cage has not only favorable enthalpy but also entropy term, and thus, all the remaining isomers can act as minor species at best (Fig. 12). A similar IPR-cage dominance operates, for example, in the Eu@C_{74} system, too. At a representative temperature of 1500 K, the FEM evaluation yields [63] 93.7, 5.1, and 1.2% for the $1/D_{3h}$, $4/C_1$, and $103/C_1$ Eu@C_{74} isomers, respectively.

The third illustrative system, Ca@C_{82}, exhibits the richest isomerism among the Ca endohedrals. Xu et al. isolated [64] four isomers of Ca@C_{82} and labeled the isomers (I), (II), (III), and (IV). Kodama et al. measured [65] the ^{13}C NMR spectra and assigned the symmetry of isomers (I), (II), (III), and (IV) as C_s, C_{3v}, C_2, and C_{2v}, respectively. The Ca@C_{82} species were of course computed [66], too, and the C_{2v} structure found as the lowest-energy isomer. There are still three other low-energy species – C_s, C_2, and C_{3v}. Interestingly, there are some reductions of their symmetry during the geometry optimizations: C_{3v}(b) → C_s, C_{2v} → C_s, C_2(a) → C_1, C_2(b) → C_1, C_s(b) → C_1. Figure 13 presents the calculated temperature development [66] of the relative populations of the nine Ca@C_{82} IPR isomers in the FEM treatment (the enthalpy part is from the B3LYP/6-31G*//B3LYP/3-21G~dz calculations, and the entropy part is evaluated at the B3LYP/3-21G~dz level). Incidentally, the FEM approach is in a better agreement with the available observed relative populations compared to the conventional RRHO approach. The observed yields

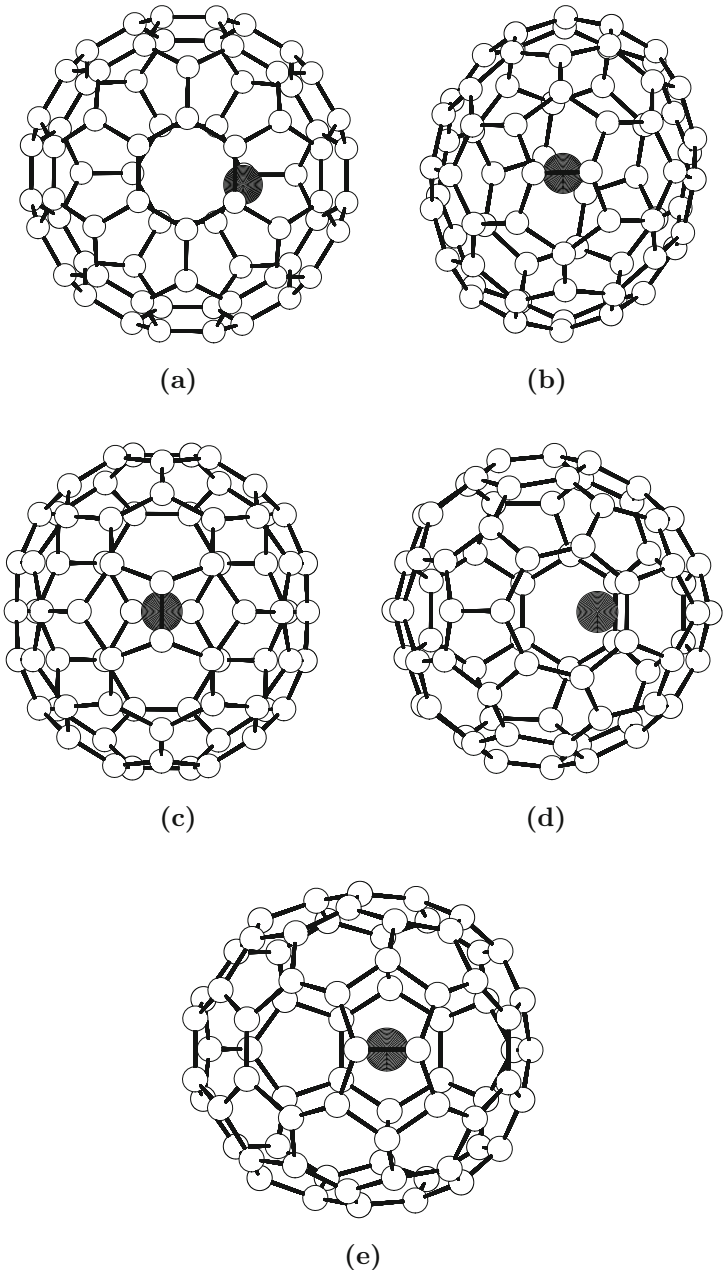

Fig. 10 B3LYP/3-21G~dz optimized structures [60] of $Ca@C_{72}$ isomers: (**a**) IPR; (**b**) 5/5 pair; (**c**) 5/5 pair; (**d**) seven-membered ring; and (**e**) two seven-membered rings

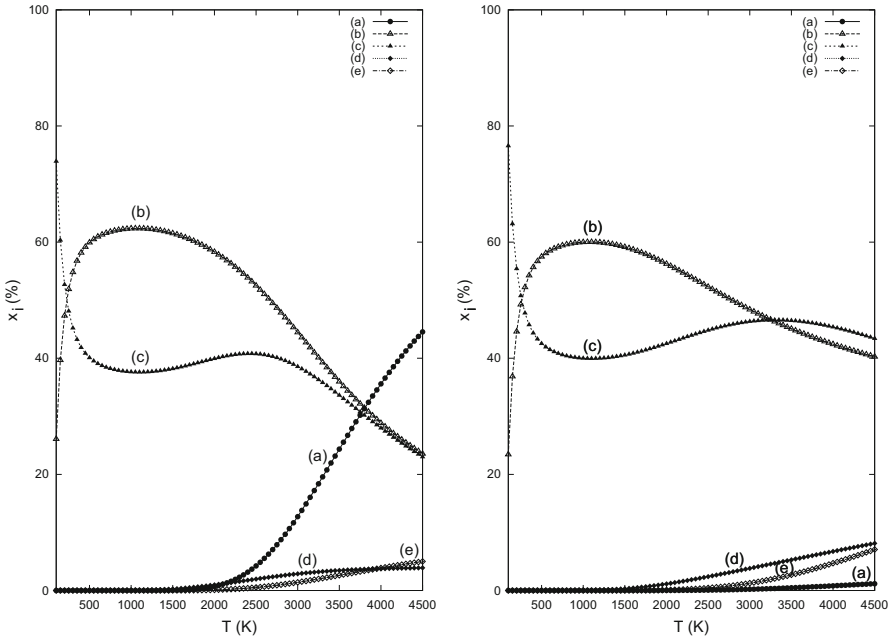

Fig. 11 Relative populations [60] of the Ca@C_{72} isomers based on the B3LYP/6-31G* energetics and the B3LYP/3-21G~dz entropy, using the RRHO (left) and FEM (right) treatment

[65] of the Ca@C_{82} isomers were nearly equal except for the considerably less-produced C_{3v} species (the HPLC chromatograms [64] can possibly indicate somewhat larger production differences). The FEM treatment basically reproduces the observed relative populations of the four Ca@C_{82} isomers.

Let us also mention the La@C_{82} isomeric set (which is electronic open-shell system). Structures of two of its isomers were clarified [67] using ^{13}C NMR spectra of their monoanions generated electrochemically. The major isomer was thus assigned C_{2v} symmetry and the minor species C_s. The findings differ from the Ca@C_{82} isomeric system with four known isomers. Calculations [68] pointed out just three IPR cages with a sufficiently low energy of La endohedrals: C_{2v}, C_{3v}(b), and C_s(c). The fourth energy-lowest La endohedral species, C_2(a), is actually already rather high in energy to be significant in experiment. A partial agreement with experiment can be achieved [68] for temperatures from about 1000 K to 1300 K using the RRHO treatment. However, a really good agreement with the observations is reached with the FEM approach. Incidentally, there is still one important aspect to be considered. The fullerene and metallofullerene production is likely not always close to the inter-isomeric equilibrium. This factor may be relevant to the La@C_{82} case. Lian et al. reported [69] a Ni-catalyzed production of La@C_{82} with a considerably variable isomeric ratio, thus suggesting a possible kinetic control.

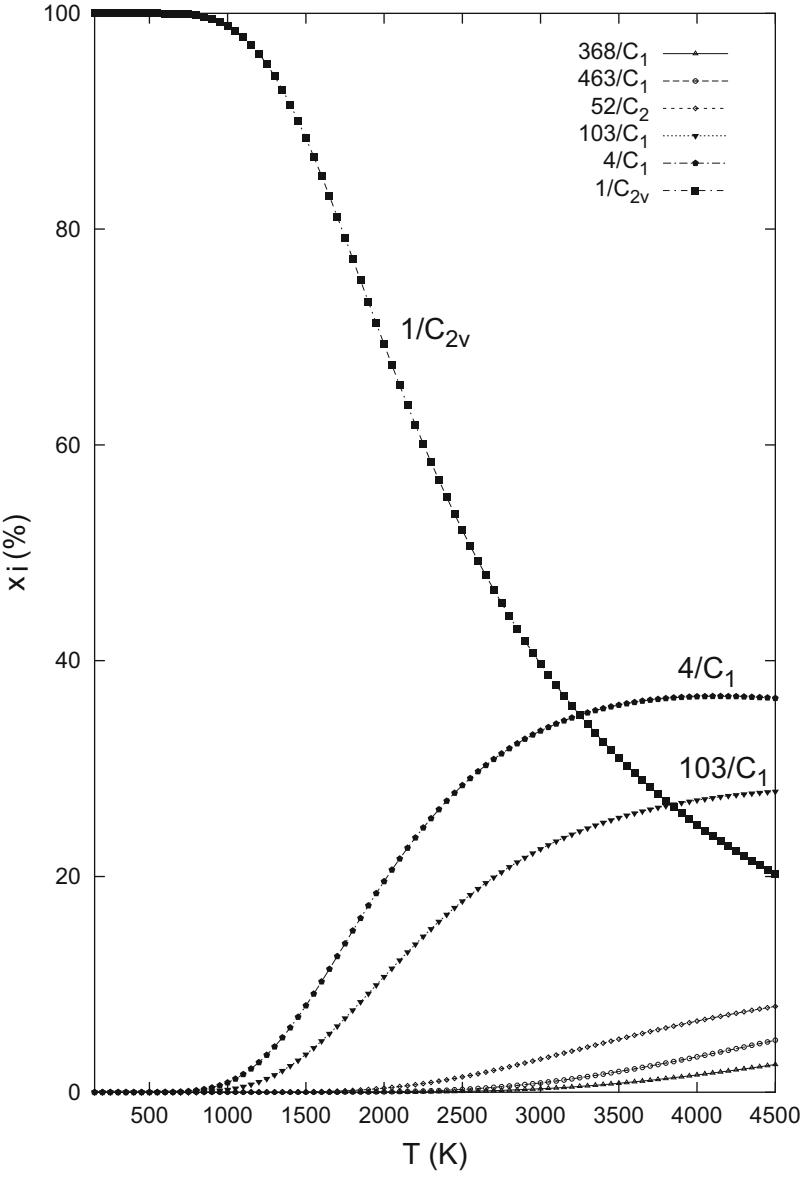

Fig. 12 Relative populations [62] of the Ca@C_{74} isomers based on the B3LYP/6-31G* energetics and the B3LYP/3-21G~dz entropy, using the FEM treatment

Very recently, relative populations of the IPR isomers of Ce@C_{82} were calculated [70] with the advanced B2PLYPD/6-31G*~SDD energetics and the B3LYP/3-21G~SDD entropic term. In agreement with observation [71], the Ce@C_{2v} (9)-C_{82} (major isomer) and Ce@C_s (*c*; 6)-C_{82} (minor isomer) endohedrals (Fig. 14) are

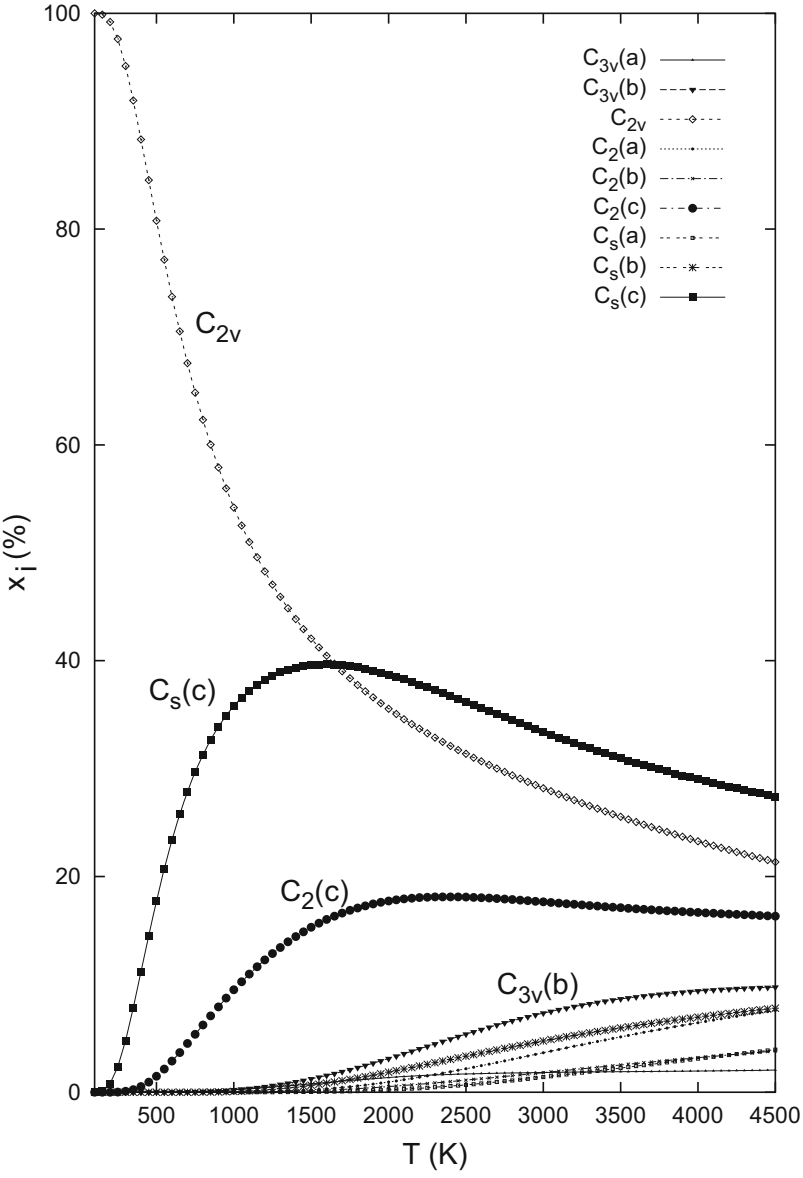

Fig. 13 Relative concentrations of the Ca@C_{82} isomers based [66] on the B3LYP/6-31G* energetics and the B3LYP/3-21G~dz entropy, using the FEM treatment

the most populated species. At very low temperatures, the structure lowest in the $\Delta H^o_{0,i}$ scale must be prevailing, i.e., the Ce@C_{2v} (9)-C_{82} isomer. However, the second (C_{3v} (*b*); 8) and third (C_s(*c*); 6) energy-lowest species exhibit rather fast increase of their relative concentrations. Moreover, the Ce@C_s(*c*; 6)-C_{82} isomer becomes soon

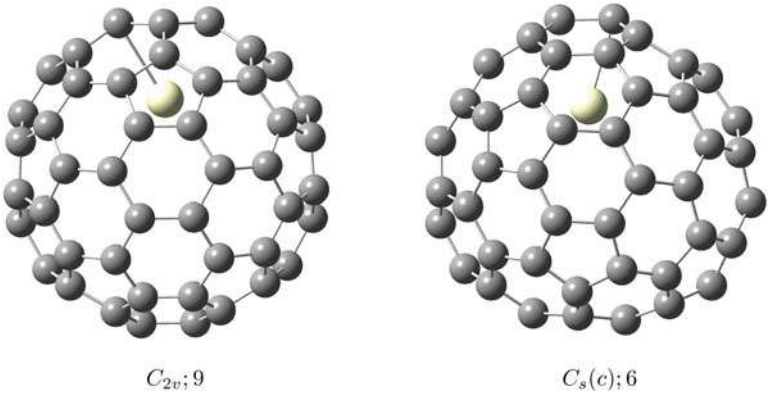

Fig. 14 The B3LYP/6-31G*~SDD optimized structures [70] of the two most populated Ce@C_{82} isomers (the shortest Ce-C contact is indicated by a link)

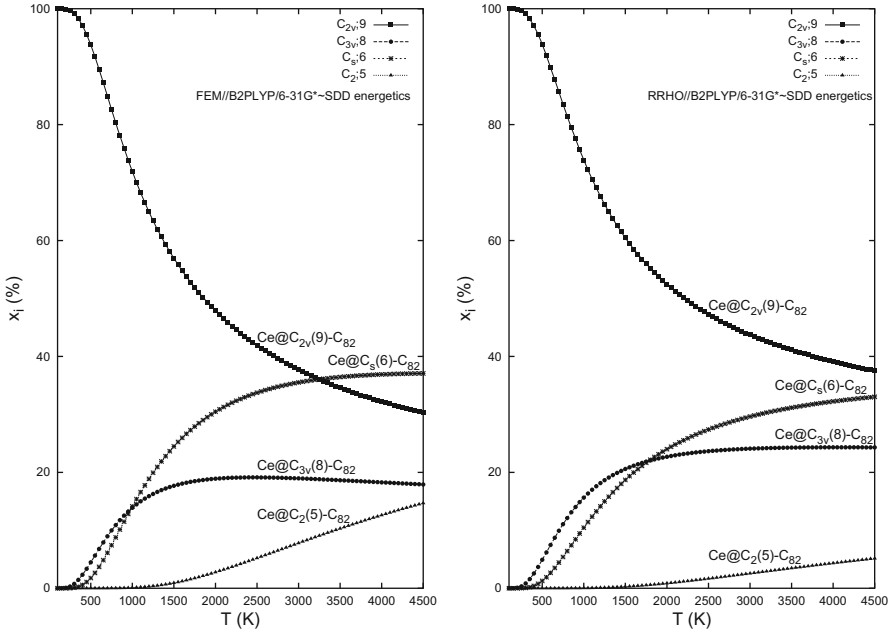

Fig. 15 The relative populations of the Ce@C_{82} isomers [70] based on the advanced FEM (left) and conventional RRHO treatment (right) with the B3LYP/3-21G~SDD entropy and B2PLYPD/6-31G*~SDD energetics

more populated than the Ce@C_{3v}(*b*; 8)-C_{82} endohedral, especially so in the FEM approach (Fig. 15). Their observed ratio is in the FEM computational treatment reached at a temperature of about 1225 K. Again, there may be the factor that observations can depend on the applied metal sources [69, 72]. Another issue is

the solubility of different isomers in the applied extraction solvents – they can hardly be exactly the same (as it nevertheless has to be tacitly supposed when comparing the results from the computational treatment of the isomeric relative populations with observed data).

The B3LYP/3-21G~SDD computed Mulliken atomic charges [70] on Ce in Ce@C_{82} are close to 2.5. This result points out that quantum-chemical calculations, as mentioned previously, usually give the amount of transferred charge as nonintegral numbers. The Mulliken-charge evaluation at the B3LYP/3-21G~SDD level deserves a more general comment. The Mulliken charges from the 3-21G~SDD basis, in contrast to the, e.g., 6-31G*~SDD level, are known [73] to give a good agreement with the observed charges [74] for metallofullerenes. Moreover, there are general methodological arguments [75] why larger basis sets should not be used with the Mulliken charges as they can sometimes produce truly unreasonable values. In fact, it is not possible to uniquely define charges on individual atoms. Instead, there are numerous other definitions in addition to the (most common) Mulliken charges, and each of them contains an element of arbitrariness. However, it is not really possible to say generally which approach provides the best atomic charges. Each offers distinct advantages and each suffers from disadvantages. A unique universal definition which would satisfy all requirements is in fact rather unlikely to be ever constructed. Thus, the choice ultimately rests with applicability for a particular situation. With metallofullerenes, it seems rational to operate such computational approaches that can reasonably reproduce charge terms derived from observations – so, e.g., for La@C_{82} a value [74] close to +3 on the metal.

Relative Stabilities of Nonisomeric Metallofullerenes

Similarly like for pristine fullerenes, more general stability problems related to metallofullerenes can also be considered, namely relative stabilities of clusters with different stoichiometries, i.e., nonisomeric species. In contrast to the already mentioned example with empty C_{60} and C_{70}, metal presence has to be respected here accordingly, too. Let us consider [18, 19] a series of metallofullerenes X@C_n with one common fixed cage C_n and variable encapsulated metals X:

$$\mathrm{X(g)} + \mathrm{C}_n\mathrm{(g)} = X@\mathrm{C}_n\mathrm{(g)}. \tag{37}$$

The encapsulation process is thermodynamically characterized by the standard changes of, for example, enthalpy $\Delta H^o_{X@C_n}$ the Gibbs energy $\Delta G^o_{X@C_n}$. An illustration [19] is presented here on a series Mg@C_{74}, Ca@C_{74}, Sr@C_{74}, and Ba@C_{74} with the potential-energy changes computed at the B3LYP/6-31G*~dz level and the entropy part at the B3LYP/3-21G~dz level. The equilibrium composition of the reaction mixture for a particular metal is controlled by the encapsulation equilibrium constants $K_{X@C_n,p}$:

$$K_{X@C_n,p} = \frac{p_{\mathrm{X@C_n}}}{p_{\mathrm{X}} p_{\mathrm{C_n}}}, \tag{38}$$

expressed in the terms of partial pressures of the components. The encapsulation equilibrium constant is in the usual way interrelated with the standard encapsulation Gibbs energy change:

$$\Delta G^{o}_{X@C_n} = -RT\, ln\, K_{X@C_n,p}. \tag{39}$$

Moreover, temperature dependency of the encapsulation equilibrium constant $K_{X@C_n,p}$ is then described by the general van't Hoff equation:

$$\frac{d\, ln\, K_{X@C_n,p}}{dT} = \frac{\Delta H^{o}_{X@C_n}}{RT^2} \tag{40}$$

where the $\Delta H^{o}_{X@C_n}$ term is typically negative for the encapsulation processes so that the encapsulation equilibrium constants decrease with increasing temperature. Let us further suppose that the metal pressure p_X is actually close to the respective saturated metal pressure $p_{X,sat}$, known from experiment, so that we can deal with a special case of clustering under saturation conditions [76]. While the saturated pressures $p_{X,sat}$ for various metals are available [77] from observations, the partial pressure of C_n is a less clear term (or more elusive, though p_{C_n} should exhibit a temperature maximum and then vanish). As already noted, the computed equilibrium constants $K_{X@C_n,p}$ have to exhibit a temperature decrease with respect to the van't Hoff eq. (40) which however does not necessarily mean a yield decrease with increasing temperature as the metal-saturated pressure increases relatively fast. To clarify the temperature interplay, let us consider the combined $p_{X,sat}K_{X@C_n,p}$ term:

$$p_{X@C_n} \sim p_{X,sat}K_{X@C_n,p}, \tag{41}$$

that directly controls the partial pressures of various $X@C_n$ species in an endohedral series, based on one common C_n fullerene. We can even consider a (hypothetical or model) experimental situation when all the considered metals are present in the reaction chamber. Then, we get a different, more varied temperature dependency. The considered $\Xi = p_{X,sat}K_{X@C_n,p}$ term can indeed be frequently (though not necessarily) increasing with temperature:

$$\frac{d\Xi}{dT} = \frac{d\left(p_{X,sat}K_{X@C_n,p}\right)}{dT} > 0. \tag{42}$$

The temperature dependency of the saturated pressure is related to the heats of vaporization of the considered metals:

$$\frac{d\, ln\, p_{X,sat}}{dT} = \frac{\Delta H_{X,vap}}{RT^2} \tag{43}$$

and consequently:

$$\frac{d\Xi}{dT} = \frac{p_{X,sat}K_{X@C_n,p}}{RT^2}\left[\Delta H_{X,vap} + \Delta H^o_{X@C_n}\right]. \tag{44}$$

If $\Delta H_{X,vap} > \left|\Delta H^o_{X@C_n}\right|$, the $p_{X,sat}K_{X@C_n,p}$ stability factor increases with temperature. In fact, while for Ca@C_{74} the $p_{X,sat}K_{X@C_{74},p}$ term increases [19, 78] with temperature, it is about constant for Sr@C_{74}, and it decreases with temperature for Ba@C_{74}. However, it is more convenient to deal with the relative term $\frac{p_{X,sat}K_{X@C_{74},p}}{p_{Ba,sat}K_{Ba@C_{74},p}}$. The computed values [78] of the relative quotient in the series Ca@C_{74}, Sr@C_{74}, and Ba@C_{74} at a temperature of 1500 K are 4.3×10^{-5}, 5.3×10^{-3}, and 1.0, respectively, and at 2000 K they read 9.9×10^{-4}, 0.030, and 1.0, respectively. Incidentally, the calculated stability proportions do correlate [78] with qualitative abundances known from observations. For Ba@C_{74}, even microcrystals could be prepared so that a diffraction study was possible, while for Sr@C_{74} at least various spectra could be recorded in solution, and Ca@C_{74} was studied only by NMR spectroscopy (while Mg@C_{74} was never observed yet). Generally speaking, under some experimental arrangements, undersaturated or perhaps even supersaturated metal vapors are also possible (for example, it is likely in ion-bombardment production technique [79]).

The series of the metallofullerene X@C_n formations with one common cage C_n introduced in Eq. (37) allows for another interesting stability conclusion. Three purely formal reaction steps can be considered for our illustrative series Mg@C_{74}, Ca@C_{74}, Sr@C_{74}, and Ba@C_{74} (with the encapsulated metals in a uniform dication state [78] according to the Mulliken atomic charges): (i) double-ionization of the free metal, (ii) double negative charging of the empty cage, and (iii) placing the metal dication into the dianionic cage. The (ii) energy is identical for all members of the series, and the (iii) terms should be similar as they are controlled by electrostatics. Incidentally, the feature that the stabilization of metallofullerenes is mostly electrostatic can be supported [80] using the topological concept of "atoms in molecules" (AIM) which indeed shows that the metal-cage interactions form ionic (and not covalent) bonds. Hence, the free-metal ionization potentials should actually represent a critical yield-controlling factor. In other words, the computed relative potential-energy changes upon encapsulation $\delta_{rel}\Delta E$, and the relative observed ionization potentials (into the relevant charge state) of the free atoms $\delta_{rel}IP$ should (according to the above three-step analysis) be correlated:

$$\delta_{rel}\Delta E \sim \delta_{rel}IP. \tag{45}$$

This interesting relationship is tested in Fig. 16 that uses both the observed second and first ionization potentials of the free metals and correlates them with the MPWB1K/6-31G*~dz calculated [19, 78] relative potential-energy changes upon encapsulation $\delta_{rel}\Delta E$ in the series Mg@C_{74}, Ca@C_{74}, Sr@C_{74}, and Ba@C_{74}. Although for this reaction series both the observed second and first ionization potentials are presented, the second IP ionization potentials should obviously be more relevant according to the computed [78] Mulliken charges. Incidentally, step

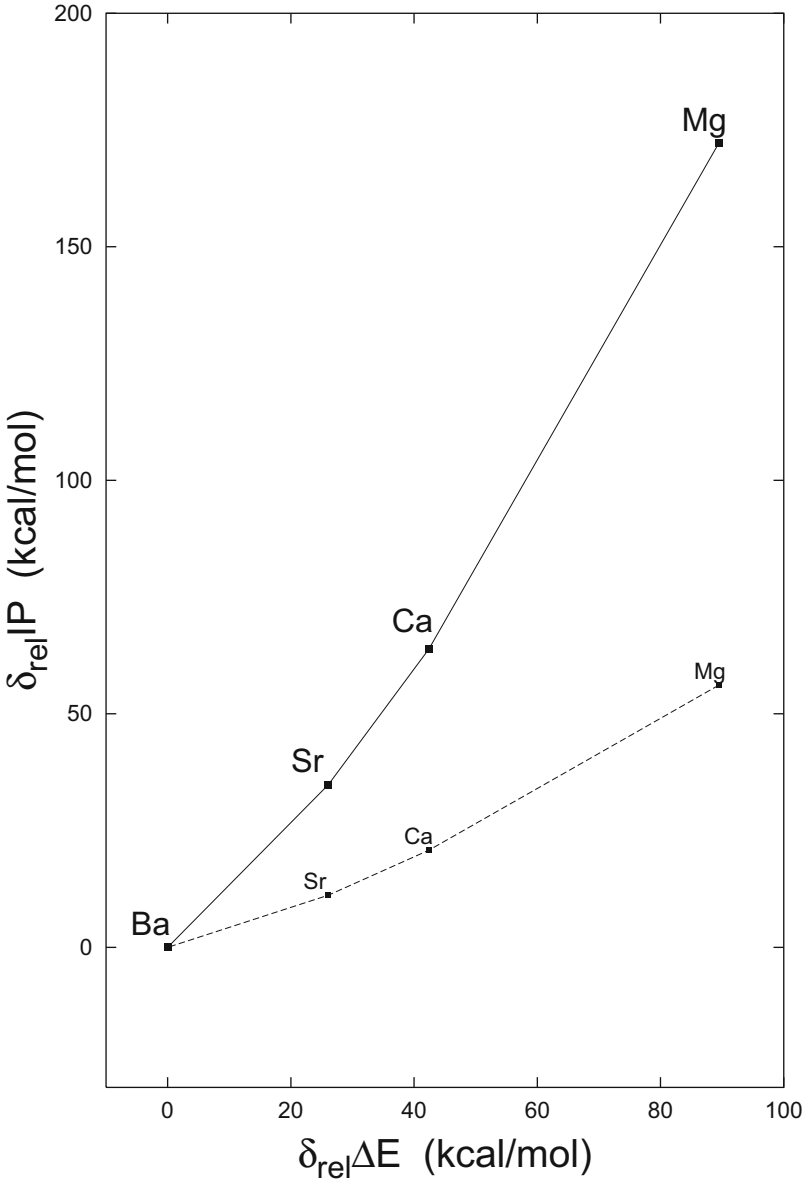

Fig. 16 The computed [19, 78] MPWB1K/6-31G*~dz relative potential-energy changes upon encapsulation $\delta_{rel}\Delta E$ and the observed relative ionization potentials (IP) of the free atoms $\delta_{rel}IP$ for the series Mg@C_{74}, Ca@C_{74}, Sr@C_{74}, and Ba@C_{74} (solid line – the second IP, dashed line – the first IP)

(ii) in the above decomposition scheme (charging the cage to the same charge state) requires just the metal charges to be about the same in the reaction series (not to be equal to some preselected number – like the charge of 2 above). As another example,

the B3LYP/6-31+G*~dz calculated [19, 81] relative potential-energy changes for the Z@C_{82} series (Z = Al, Sc, Y, and La) are plotted against the observed free-atom relative ionization potentials in Fig. 17. The expected correlation works well in both reaction series, indeed. Similarly, the B3LYP/SDD computed relative potential-

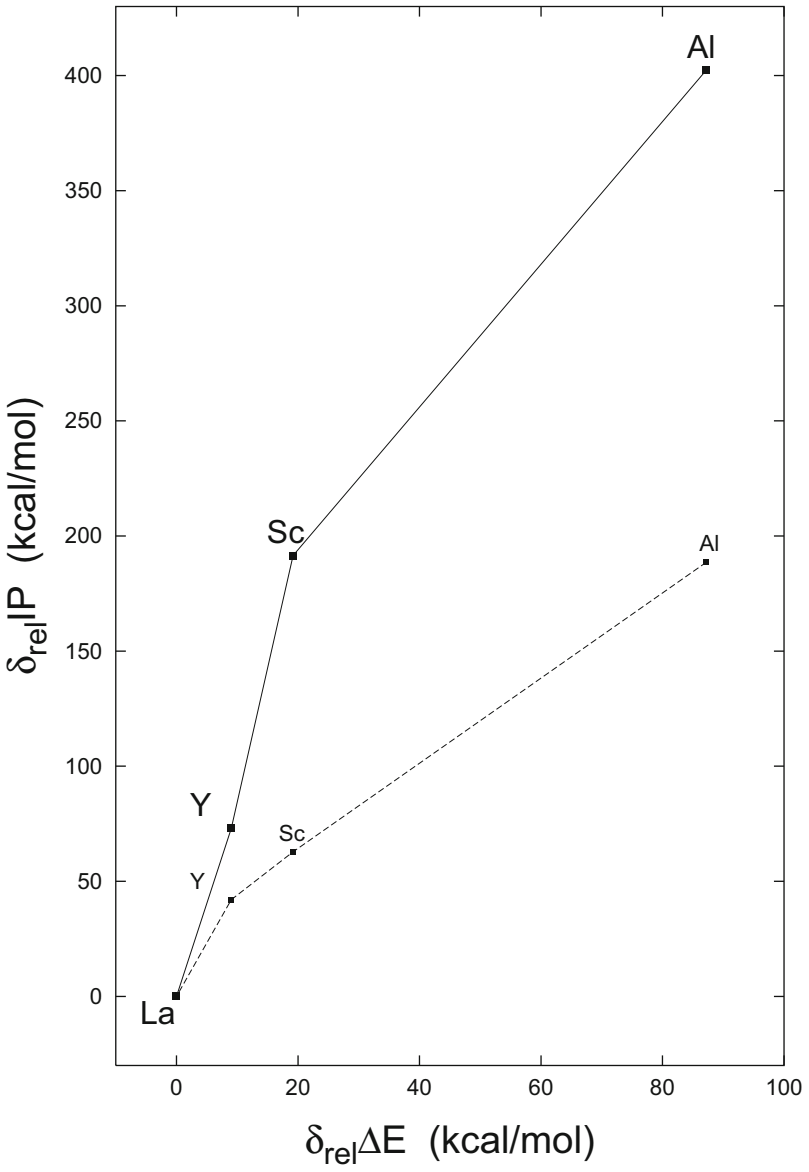

Fig. 17 The computed [19, 81] B3LYP/6-31+G*~dz & BSSE relative potential-energy changes upon encapsulation $\delta_{rel}\Delta E$ and the observed relative ionization potentials (IP) of the free atoms $\delta_{rel}IP$ for Z@C_{82}, Z = Al, Sc, Y, and La (solid line – third IP, dashed line – second IP)

energy changes in the lanthanide encapsulation L@C_{74} (L: La-Lu) correlate [19] with the observed free atom-relative ionization potentials. However, the last-mentioned correlation is not particularly good – the uniformity condition for the metal charges is not really obeyed in the L@C_{74} series. For example, the B3LYP/3-21G~CEP Mulliken charge on L in L@C_{74} equals [19] to 3.03, 1.67, and 1.35 for La@C_{74}, Yb@C_{74}, and Lu@C_{74}, respectively. In fact, such a correlation should operate for any homologous reaction series of metal encapsulations, i.e., for encapsulations into any type of a common carbon nanostructure. Moreover, this sort of reasoning could in the end explain the fullerene-encapsulation stability islands known throughout the periodic system.

Stabilities of Nonmetal Endohedrals

Recently, the encapsulations inside the fullerene cages have been extended from metal atoms to nonmetals and even to their small molecules. N_2@C_{60} and N_2@C_{70} were first such nonmetal endohedrals, namely prepared [82] by heating under high pressure. Out of 2000 C_{60} molecules, about one was observed to incorporate N_2. The nitrogen molecule-containing endohedrals were present even after several-hours heating at 500 K. N_2@C_{60} was also found [83] in the chromatographic separation after the nitrogen-ion implantation into C_{60}. In fact, this ion bombardment is primarily used for the N@C_{60} production [84] though with very low yields. Complexes of fullerenes with rare gas atoms [85] represent another family of nonmetallic endohedrals. More recently, molecular hydrogen and even a water molecule were placed inside open-cage fullerenes, further on closed synthetically. The synthetic approach [86] has so far culminated with the production of C_{70} with the encapsulated water dimer.

Such fullerene encapsulations of nonmetals have obviously been computed, too. For example, the lowest-energy N_2@C_{60} structure found [87] has the N_2 unit oriented toward a pair of parallel pentagons so that the complex exhibits D_{5d} symmetry. Such a minimum energy structure was also computed [88] for NH_3@C_{60}. With N_2@C_{60} [87], the MP2 = FC/6-31G* encapsulation energies before and after the basis set superposition error (BSSE) correction are equal to −17.5 kcal/mol and −9.28 kcal/mol, respectively. The BSSE-corrected MP2 = FC/6-31G* value for NH_3@C_{60} is [88] −5.23 kcal/mol. Once the corresponding entropy change ΔS_T^o is evaluated, one can deal with the thermodynamics controlling Gibbs-energy term ΔG_T^o. Using the partition functions from the DFT calculations and the enthalpy terms derived from the BSSE-corrected MP2 = FC/6-31G* stabilization energy, the ΔG_T^o standard changes for productions of N_2@C_{60} and NH_3@C_{60} at room temperature [87, 88] read −2.64 and 1.53 kcal/mol, respectively.

Calculations have also been performed for water dimer and trimer encapsulations, in particular into the D_2(22)-C_{84} cage [89, 90]. For example, when the encapsulation energy for the cyclic water-trimer encapsulation into D_2(22)-C_{84} is computed at the M06-2X/6-31++G** level with the BSSE correction, it is found that the trimer storage in C_{84} yields the potential-energy gain of 10.4 kcal/mol. The encapsulated

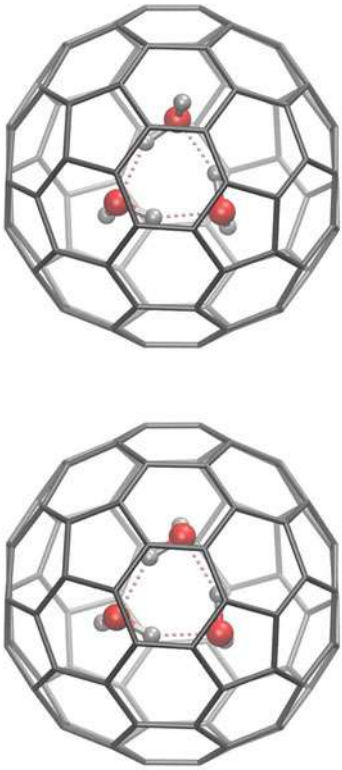

Fig. 18 The M06-2X/6-31++G** optimized structures [90] of $(H_2O)_3@D_2(22)$-C_{84}: top – *trans*-organization of H atoms not involved in the hydrogen bonds (C_1 species), bottom – *cis*-organization (C_3 species)

trimer can have two different forms (Fig. 18), either the conformation known for the free gas-phase water trimer (*trans*, C_1 symmetry) or the arrangement with the three non-hydrogen-bonded H atoms on the same side of the O–O–O plane (*cis*, C_3 symmetry). The latter endohedral isomer is calculated [90] as lower in the potential energy by 0.071 kcal/mol and forms about 57% of their equilibrium mixture at room temperature (Fig. 19).

Stabilities of Clusterfullerenes

A large family of endohedrals encapsulating three metals and one nitrogen atom has been produced and studied after the discovery [91] of $Sc_3N@C_{80}$, presently employing cages from C_{68} to C_{96}. Such species belong to so-called clusterfullerenes [92] (or metalloheterofullerenes). An illustrative example can be presented using the very recent calculations [93] of the two observed $Lu_3N@C_{80}$ isomers, experimentally well known. Namely, they are produced by encapsulation into the C_{80} IPR cages with I_h and D_{5h} symmetries (Fig. 20). The calculations are based on the B3LYP/6-31G*~SDD approach. However, the inter-isomeric energetics is further

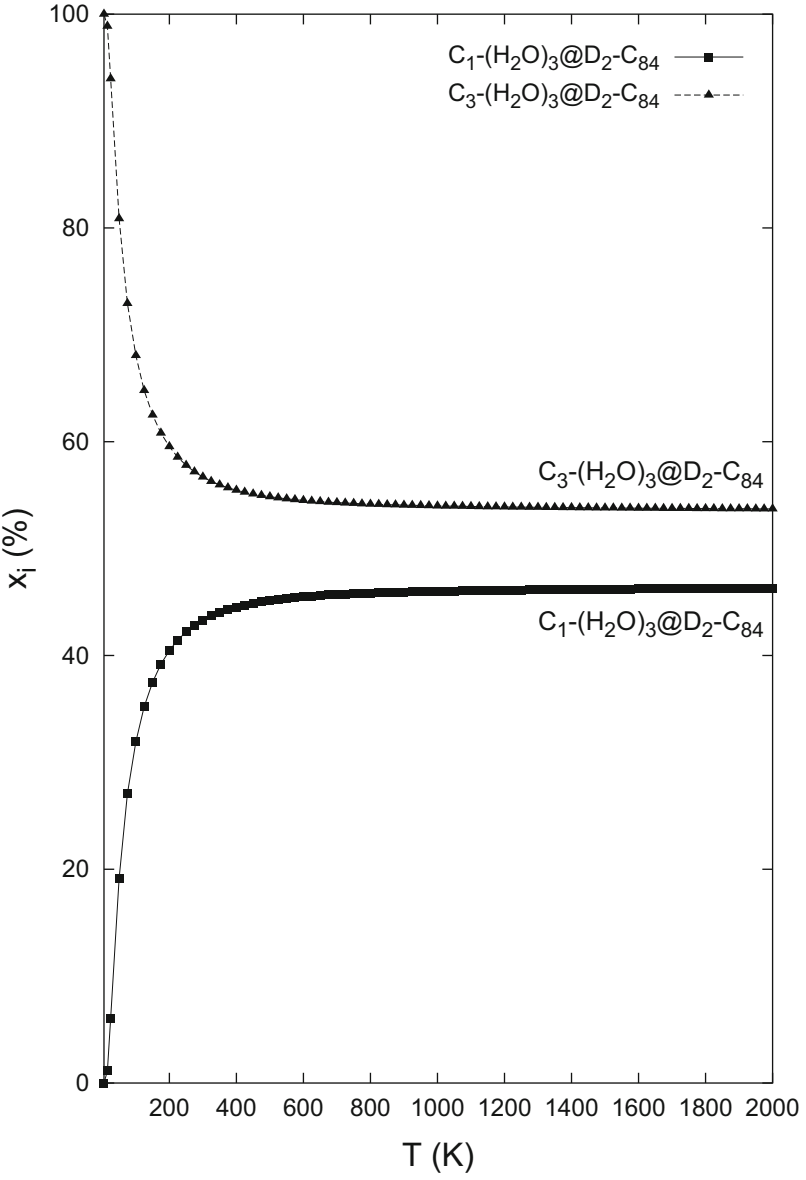

Fig. 19 Relative concentrations of the $(H_2O)_3@D_2(22)$-C_{84} isomers computed [90] at the M06-2X/6-31++G** level

refined with the MP2 = FU/6-31G*~SDD technique which places the D_{5h} endohedral higher in the potential energy by 16.9 kcal/mol. The isomeric populations are evaluated (Fig. 21) using both the RRHO and FEM treatments; however, only the FEM results are in a reasonable agreement with the observed isomeric ratios [94].

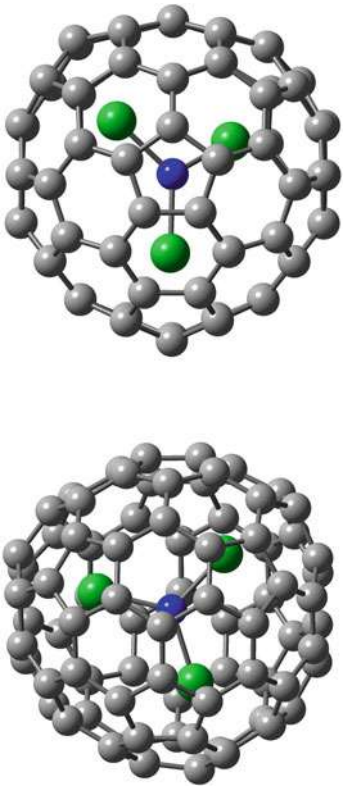

Fig. 20 The B3LYP/6-31G*~SDD optimized structures [93] of $Lu_3N@I_h(7)$-C_{80} (bottom) and $Lu_3N@D_{5h}(6)$-C_{80}

Cage symmetry plays an important role with the $Lu_3N@C_{80}$ isomers. The optimized structures of $Lu_3N@D_{5h}(6)$-C_{80} and $Lu_3N@I_h(7)$-C_{80} exhibit no imaginary frequency so that they are local energy minima; however, they both possess C_1 static symmetry. As the Lu_3N unit is not compatible with a fivefold axis of symmetry, the $Lu_3N@C_{80}$ endohedrals cannot anyhow have the high I_h or D_{5h} symmetries of the original pristine C_{80} cages. However, three-dimensional rotational motions of the encapsulates in the cages (or at least large-amplitude oscillations) recover the dynamic symmetry, simplifying [21] the NMR patterns at room temperature. So, the observed ^{13}C NMR spectra should be as simple as would be for the pristine C_{80} cages with the I_h or D_{5h} topological symmetry. In other words – fast, isotropic motions of encapsulates inside the cages yield a time-averaged equalizing environment on the NMR timescale. Moreover, in the FEM treatment, the symmetries of the endohedrals should be treated as the highest (topological) symmetries for the empty cages. Thus, the FEM treatment respects the averaging effects, and we deal with just the dynamic I_h and D_{5h} and not static C_1 symmetries (incidentally, the FEM treatment also removes the chirality feature in this case). Obviously, the change in symmetry is rather profound and its consequences for the relative stabilities are

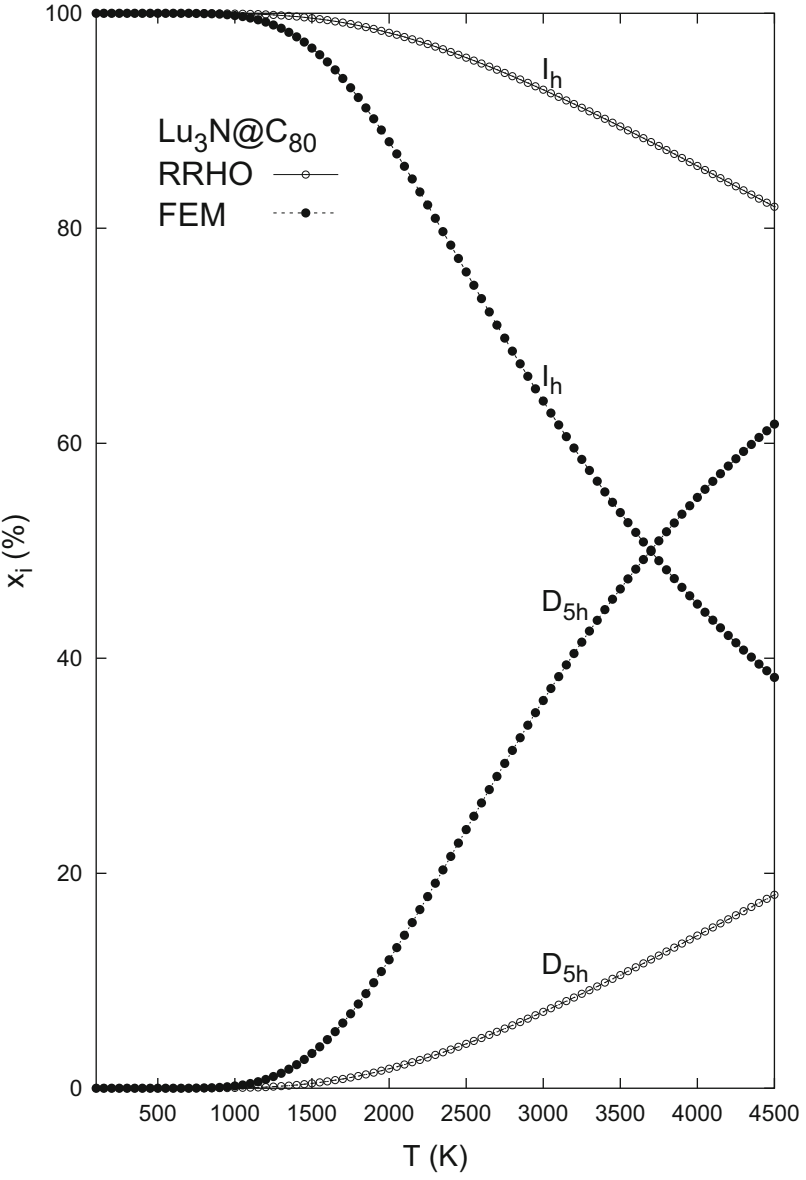

Fig. 21 Relative concentrations [93] of the $Lu_3N@C_{80}$ isomers, based on the MP2=FU/6-31G*~SDD energetics and the B3LYP/6-31G*~SDD entropy, evaluated with the conventional RRHO (o) and the more advanced FEM (•) treatment

substantial. Interestingly, some quantum-chemical packages still wrongly produce the symmetry number for C_{60} as 1 instead of the correct value [93] of 60 (which would imply, for example, a substantial change in an equilibrium constant by a huge factor of 60), a similar omission also exists with the chirality effects (factor of 2).

Another interesting class of metalloheterofullerenes encapsulates sulfur instead of nitrogen, for example [95, 96] $Sc_2S@C_{82}$ and $Y_2S@C_{82}$. Their relative production yields can also be predicted [97] by computations though the evaluation scheme is more complex. Let us start with a presumption that the diatomic species XS exists as a significant template in the hot-gas phase so that we can consider an encapsulation process:

$$X(g) + XS(g) + C_n(g) = X_2S@C_n(g); \quad K_{X_2S@C_n,p} = \frac{p_{X_2S@C_n}}{p_X p_{XS} p_{C_n}}, \tag{46}$$

characterized by its encapsulation equilibrium constant $K_{X_2S@C_n,p}$ expressed in the terms of partial pressures of the components. The encapsulation equilibrium constant is interrelated with the standard encapsulation Gibbs-energy change $\Delta G^o_{X_2S@C_n}$:

$$\Delta G^o_{X_2S@C_n} = -RT\, ln\, K_{X_2S@C_n,p}. \tag{47}$$

Moreover, the XS template formation is described by another equilibrium constant, $K_{XS,p}$:

$$X(g) + S(g) = XS(g); \quad K_{XS,p} = \frac{p_{XS}}{p_X p_S}. \tag{48}$$

In the terms from Eqs. (46) and (48), the $X_2S@C_n$ metallofullerene yield is given:

$$p_{X_2S@C_n} = p_X p_{XS} p_{C_n} K_{X_2S@C_n,p} = p_X^2 p_S p_{C_n} K_{XS,p} K_{X_2S@C_n,p}. \tag{49}$$

Let us suppose again that the metal pressure p_X is actually close to the respective saturated metal pressure $p_{X,sat}$:

$$p_X \approx p_{X,sat}. \tag{50}$$

Then, the yield ratio r for two different metals, X and Y, is simply given by:

$$r = \frac{p_{X_2S@C_n}}{p_{Y_2S@C_n}} = \frac{p^2_{X,sat} K_{XS,p} K_{X_2S@C_n,p}}{p^2_{Y,Sat} K_{YS,p} K_{Y_2S@C_n,p}}. \tag{51}$$

Again, while the observed saturated pressures $p_{X,sat}$ for various metals are known [77], the partial pressure of C_n would be a less clear term. Similarly, the p_S partial pressure is also not well defined as sulfur is likely already above its critical temperature at the metallofullerene-synthesis conditions so that its saturated pressure cannot be applied. However, the convenient canceling-out of the two terms can actually be derived in a rigorous form. In order to observe the relative populations in a metallofullerene series, one can again think of an experiment where all the considered metals are simultaneously placed in the electric-arc chamber. This experiment would obviously create the same conditions for every member of the series. Moreover, the terms p_{C_n} and p_S in Eq. (49) will in this (thought) experiment be really common for all the members of the series, and thus,

it can be canceled out, indeed. Hence, we can consider just the combined $p_{X,sat}^2 K_{XS,p} K_{X_2S@C_n,p}$ terms as the useful governing expressions. The terms were evaluated [97] for encapsulations in the $C_s(6)$ and $C_{3v}(8)$ C_{82} IPR cages. The yield of $Sc_2S@C_{82}$ was always calculated considerably higher than that of $Y_2S@C_{82}$ which is in agreement with the available observations [95, 96]. The $Sc_2S@C_{82}$ production has in fact a double-advantage: higher gain in encapsulation potential energy and higher saturated metal pressure.

Interestingly, other formation schemes could however be considered as well, for example, processes with the encapsulated atoms in free state:

$$2X\,(g) + S\,(g) + C_n(g) = X_2S@C_n(g); K'_{X_2S@C_n,p} = \frac{p_{X_2S@C_n}}{p_X^2 p_S p_{C_n}}, \tag{52}$$

The $X_2S@C_n$ metallofullerene yield is then:

$$p_{X_2S@C_n} = p_X^2 p_S p_{C_n} K'_{X_2S@C_n,p}. \tag{53}$$

If the metal pressures are close to saturation, Eq. (50), the relative yields for two different metals, X and Y, become:

$$\frac{p_{X_2S@C_n}}{p_{Y_2S@C_n}} = \frac{p_{X,sat}^2 K'_{X_2S@C_n,p}}{p_{Y,sat}^2 K'_{Y_2S@C_n,p}} \tag{54}$$

Here, $p_{X,sat}^2 K'_{X_2S@C_n,p}$ should be the useful evaluation term within the scheme. It should be realized that Eqs. (51) and (54) are equivalent as:

$$K_{XS,p} K_{X_2S@C_n,p} = \frac{p_{XS}}{p_X p_S} \frac{p_{X_2S@C_n}}{p_X p_{XS} p_{C_n}} = \frac{p_{X_2S@C_n}}{p_X^2 p_S p_{C_n}} = K'_{X_2S@C_n,p}. \tag{55}$$

Moreover, yet another scheme could explicitly deal with the X_2S species:

$$X_2S(g) + C_n(g) = X_2S@C_n(g); \quad K''_{X_2S@C_n,p} = \frac{p_{X_2S@C_n}}{p_{X_2S} p_{C_n}}, \tag{56}$$

where the X_2S template formation is described by the equilibrium constant:

$$2X(g) + S(g) = X_2S(g); \quad K_{X_2,S,p} = \frac{p_{X_2S}}{p_X^2 p_S}. \tag{57}$$

The $X_2S@C_n$ metallofullerene yield is now:

$$p_{X_2S@C_n} = p_{X_2S} p_{C_n} K''_{X_2S@C_n,p} = p_X^2 p_S p_{C_n} K_{X_2S,p} K'_{X_2S@C_n,p}. \tag{58}$$

With the presumption (50) of saturation, we get for two different metals:

$$\frac{p_{X_2S@C_n}}{p_{Y_2S@C_n}} = \frac{p_{X,sat}^2 K_{X_2S,p} K''_{X_2S@C_n,p}}{p_{Y,sat}^2 K_{Y_2S,p} K''_{Y_2S@C_n,p}}, \tag{59}$$

So that $p_{X,sat}^2 K_{X_2S,p} K''_{X_2S@C_n,p}$ are the useful evaluation terms in this case. However, the equivalency works again as:

$$K_{X_2S,p} K''_{X_2S@C_n,p} = \frac{p_{X_2S}}{p_X^2 p_S} \frac{p_{X_2S@C_n}}{p_{X_2S} p_{C_n}} = \frac{p_{X_2S@C_n}}{p_X^2 p_S p_{C_n}} = K'_{X_2S@C_n,p}. \tag{60}$$

Still, the encapsulation energetics computed for different schemes can, owing to numerical reasons, have a different level of accuracy. Moreover, the calculations in different schemes can give information on template populations as a byproduct.

The Sc_2O unit is another interesting encapsulate. Recently, population ratio for two such C_{78}-based heterometallofullerenes was observed [98], namely $Sc_2O@C_{78}(C_{2v}/3)$: $Sc_2O@C_{78}(D_{3h}/5) = 3{:}1$, and quantum-chemical calculations [99] tried to reproduce it. However, the DFT approaches consistently place [99] the $C_{2v}/3$ species higher in energy than the $D_{3h}/5$ isomer. Still, in the more advanced MP2 perturbation calculations, the $C_{2v}/3$ endohedral is lower in energy. This distinct difference is obviously felt in the temperature development of the isomeric relative populations presented in Fig. 22. With the M06-2X/6-311+G*~SDD energetics and FEM treatment, it is not possible to get the observed ratio $Sc_2O@C_{78}(C_{2v}/3)$: $Sc_2O@C_{78}(D_{3h}/5) = 3{:}1$ at any considered temperature. As can be expected, if the conventional RRHO approach is used, the agreement with the observed ratio is even worse. It is true that the entropic contributions can sometimes overcompensate unfavorable energetics; however, this interesting control does not operate here. Nevertheless, an agreement with the observed ratio can be achieved using the MP2-computed interisomeric energy. As can be seen in Fig. 22, the MP2 = FU/3-21G~SDD energetics (with the FEM treatment), for example, at 1750 K, gives the relative concentrations $Sc_2O@C_{78}(C_{2v}/3)$: $Sc_2O@C_{78}(D_{3h}/5) = 75.3{:}24.7$, i.e., in the ratio known from the experiment [98].

Clusterfullerene $Y_2C_2@C_1(1660)-C_{108}$ is one of the largest endohedral species computed [100] by now. In agreement with experiment, the Y_2C_2 encapsulate in the optimized endohedral has a near-linear structure. The computed Wiberg bond index for the encapsulate CC bond comes as 2.59, 2.61, and 2.32 at the B3LYP/3-21G~SDD, M06-2X/3-21G~SDD, and MP2 = FU/3-21G~SDD level, respectively. The encapsulation enthalpy ΔH_0^o (i.e., after addition of the zero-point vibrational energy to the encapsulation potential-energy change ΔE_{pot}) connected with the formal thermodynamic process:

$$2\mathrm{Y(g)} + 2\mathrm{C(g)} + C_1(1660) - \mathrm{C_{108}(g)} = \mathrm{Y_2C_2@}C_1(1660)-\mathrm{C_{108}(g)} \tag{61}$$

refined by the inclusion of the basis set superposition error (BSSE/CP5) and steric correction amounts to −469, −467, and −462 kcal/mol at the B3LYP/

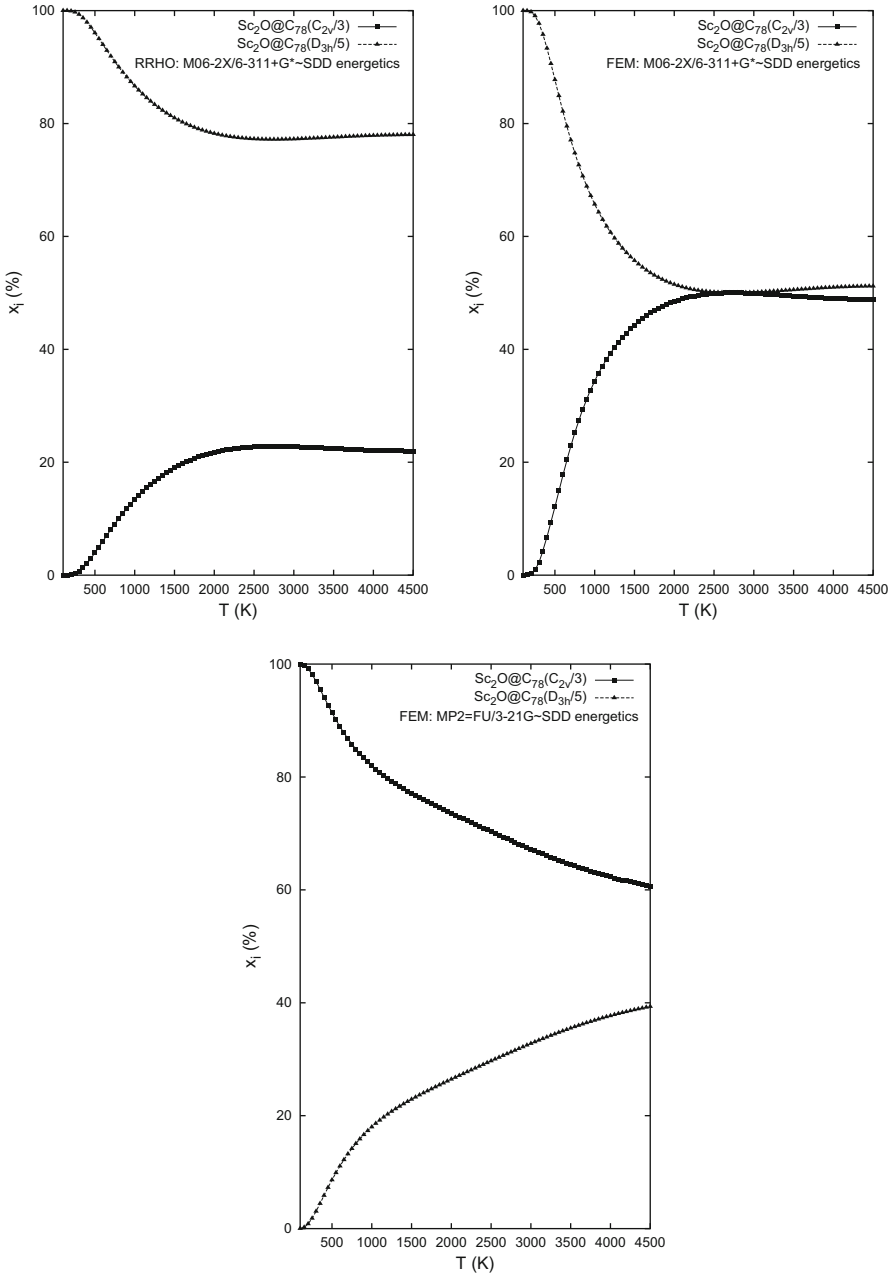

Fig. 22 Calculated [99] relative concentrations for the observed $Sc_2O@C_{78}$ isomers evaluated with the M06-2X/6-311+G*~SDD energetics and the M06-2X/6-311G*~SDD entropy in the RRHO (top left) or FEM (top right) treatment, while the MP2 = FU/3-21G~SDD energetics and the M06-2X/6-311G*~SDD entropy within the FEM approach (bottom) give the temperature development consistent with the observation

6-31G*~SDD, B3LYP/6-31+G*~SDD, and MP2 = FU/3-21G~SDD levels, respectively. It should be mentioned that the study [100] actually supplies a comparison between the DFT approach and the more advanced MP2 treatment for the presently largest system. The zero-point energy correction in fact turns out to be relatively small in this case owing to a convenient cancellation – the mere ΔE_{pot} term, for example, with the B3LYP/6-31G*~SDD method, equals to −474 kcal/mol. For comparison – the La atom encapsulation [81] into the C_{82} cage calculated at, for example, the B3LYP/6-31+G*~LanL2DZ level with the BSSE and steric correction gives the energy gain of some −111 kcal/mol. The sizeable encapsulation energy in the $Y_2C_2@C_1(1660)-C_{108}$ case is in part linked to the formation of a near-triple CC bond (the observed CC bond energy in C_2H_2 is 228.8 ± 0.7 kcal/mol [101]). Incidentally, average carbon-carbon bond dissociation energies for fullerenes were evaluated [102] as 112 kcal/mol for 6/6 type bond and 105 kcal/mol for 5/6 type, while a term of only 60 kcal/mol was assigned to 5/5 type bond. Very recently, another considerable encapsulation energy [103] is reported, namely for $Ti_3C_3@C_{80}$. The relative encapsulation potential energy per one atom of the encapsulate $\Delta E_{pot}/6$ for $Ti_3C_3@C_{80}$ at the B3LYP/6-31G*~SDD level with the BSSE and steric correction amounts to −136.4 kcal/mol/atom. The related $\Delta E_{pot}/4$ term for $Y_2C_2@C_1(1660)-C_{108}$ is equal to −118.5 kcal/mol/atom, i.e., the relative energy gain is larger in the $Ti_3C_3@C_{80}$ case by some 18 kcal/mol/atom.

A special instance of relative stabilities of nonisomeric endohedrals is the case of one type of metal Y encapsulated into one common cage C_n, yielding a series $Y_x@C_n$, i.e., stepwise [104] metal encapsulation:

$$\mathrm{xY(g)} + \mathrm{C}_n\mathrm{(g)} = \mathrm{Y_x@C}_n\mathrm{(g)}. \tag{62}$$

The equilibrium composition of the reaction mixture introduced by Eq. (62) is controlled by the encapsulation equilibrium constants $K_{Y_x@C_n,p}$:

$$K_{Y_x@C_n,p} = \frac{p_{Y_x@C_n}}{p_Y^x p_{C_n}}, \tag{63}$$

expressed in the terms of partial pressures of the components. The encapsulation equilibrium constants are interrelated with the standard encapsulation Gibbs-energy changes $\Delta G^o_{Y_x@C_n}$:

$$\Delta G^o_{Y_x@C_n} = -RT\, ln\, K_{Y_x@C_n,p}. \tag{64}$$

Temperature dependency of the equilibrium constant $K_{Y_x@C_n,p}$ is again described by the van't Hoff equation:

$$\frac{dlnK_{Y_x@C_n,p}}{dT} = \frac{\Delta H^o_{Y_x@C_n}}{RT^2} \tag{65}$$

where the standard encapsulation enthalpy change $\Delta H^{o}_{Y_x@C_n}$ term is typically negative so that the encapsulation equilibrium constants decrease with increasing temperature.

Let us again suppose that the metal pressure p_Y is actually close to the respective saturated metal pressure $p_{Y,sat}$. As already mentioned, the computed equilibrium constants $K_{Y_x@C_n,p}$ have to show a temperature decrease with respect to the van't Hoff eq. (65). However, if we consider the combined $p^{x}_{Y,sat}K_{Y_x@C_n,p}$ terms:

$$p_{Y_x@C_n} \sim p^{x}_{Y,sat}K_{Y_x@C_n,p}, \tag{66}$$

that directly control the partial pressures of the $Y_x@C_n$ encapsulates in an encapsulation series (based on one common C_n fullerene), we get a different picture. The considered $p^{x}_{Y,sat}K_{X@C_n,p}$ term can frequently (though not necessarily) be increasing with temperature so that a temperature enhancement of metallofullerene formation in the electric-arc technique would again be possible. This type of relative stabilities of nonisomeric clusterfullerenes can be demonstrated [104] on $Li@C_{60}$, $Li_2@C_{60}$, and $Li_3@C_{60}$ (Fig. 23), using [104] the MPWB1K density functional. For all three members of the series, the $p^{x}_{Y,sat}K_{Y_x@C_n,p}$ quotient indeed increases with temperature. Moreover, the computed equilibrium thermodynamics shows that $Li_2@C_{60}$ is at least by two orders of magnitude less populated than $Li@C_{60}$ when the saturated Li vapor is considered, while for $Li_3@C_{60}$ it is at least by four orders of magnitude less compared to $Li@C_{60}$. The calculated relative stabilities [104] correspond to the available experimental findings.

In connection with the $Li@C_{60}$ species, one peculiar computational problem was experienced, namely the so-called spin contamination [105], which is however rather common in calculations of electronic open-shell fullerenic systems. In addition to the MPWB1K density functional [104], the HF/3-21G and B3LYP/3-21G approaches were [105] also applied to the $Li_x@C_{60}$ species, more specifically the unrestricted treatments (like UHF/3-21G or UB3LYP/3-21G) if a species was an electronic open shell case (radical). The UHF approach can be faster than restricted open-shell treatment; however, it can be seriously influenced by the spin contamination. The spin contamination was present in the $Li_x@C_{60}$ set with its values higher than a recommended threshold. The spin contamination is measured by the expectation value for the $<S^2>$ term that should be equal to $S(S + 1)$ (i.e., singlet: $S = 0 \rightarrow <S^2> = 0$, doublet: $S = 1/2 \rightarrow <S^2> = 0.75$, triplet: $S = 1 \rightarrow <S^2> = 2$, and so on). As long as the deviations from the theoretical value are smaller than 10%, the unrestricted results are considered applicable. In contrast to the UHF/3-21G method, the requirement was well satisfied [105] in the UB3LYP/3-21G calculations as the $<S^2>$ expectation value amounted even before annihilation to 0.7552 and 0.7546 for $Li@C_{60}$ and $Li_3@C_{60}$, respectively, i.e., less than 1% higher than the exact value. Unfortunately, the spin-contamination issue is rather frequent with fullerenic species. In order to avoid it, one can change [106] the applied DFT functional as well as the basis set, or try to drop to the UHF level. Actually, there is also the restricted open-shell method (like ROB3LYP) which is (exactly) free of

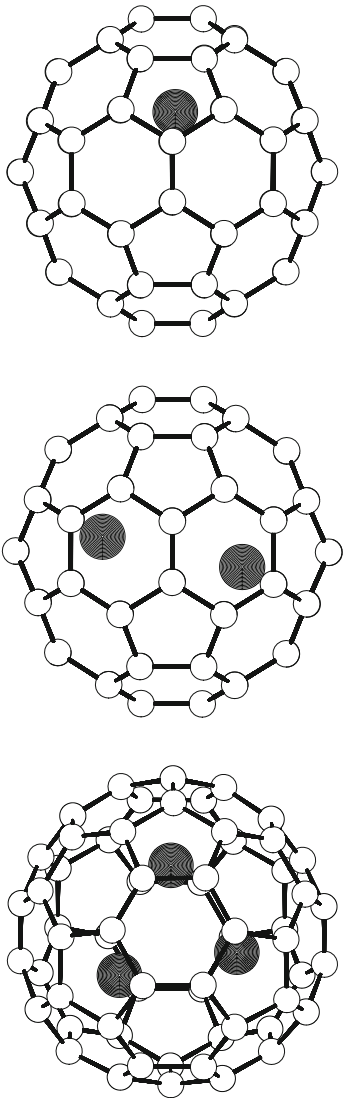

Fig. 23 MPWB1K/3-21G optimized structures [104] of $Li_x@C_{60}$

the spin contamination. However, the restricted open-shell method can exhibit a poor SCF convergence for larger systems like metallofullerenes. There is also a possibility to try more sophisticated (but also more demanding on computational resources) B2PLYP(D) techniques [70].

We can move to a still more general task, viz. encapsulation [107] of a variable number of metal atoms into different but isomeric cages. Recently, a new member of the lanthanum-containing metallofullerene family was isolated [108] and its

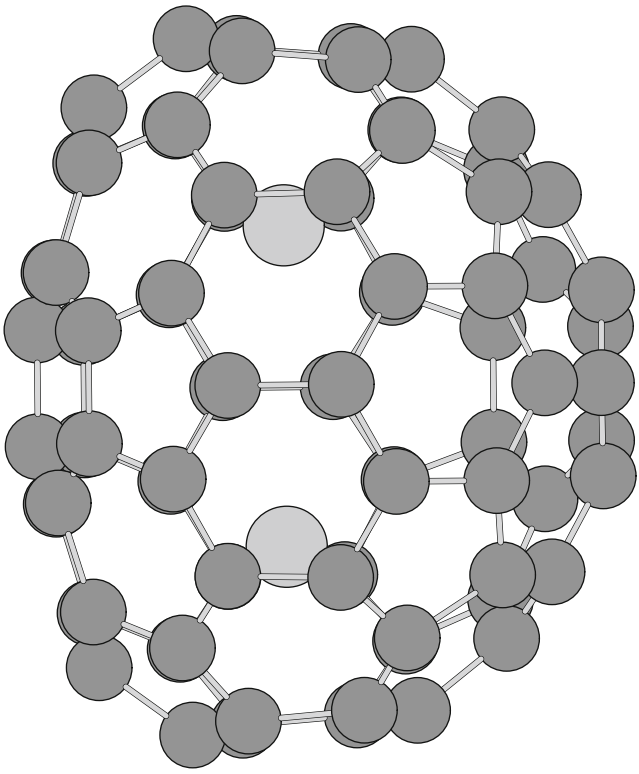

Fig. 24 The B3LYP/3-21G~LanL2DZ optimized [107] structure of $La_2@C_{76}$ (C_s) (i.e., $La_2@C_{76}(C_s,17490)$)

structure determined from X-ray-crystallographic analysis, namely $La_2@C_{76}(C_s,17490)$, even with two pairs of connected pentagons, hence violating the IPR rule (Fig. 24). In order to explain the interesting observation, a computational treatment was suggested [107] for evaluations of the relative populations of nonisomeric metallofullerenes. As a comparative reference structure, the most stable $La@C_{76}$ isomer is selected – the IPR-$C_{76}(T_d)$-cage-based endohedral $La@C_{76}(T_d)$. With this treatment, it is found that in the relevant temperature region, the $La_2@C_{76}(C_s,17490)$ species should be considerably more populated compared to $La@C_{76}(T_d)$.

Let us consider two encapsulation thermodynamic equilibria (metal X is encapsulated into two different but isomeric cages $C_n(A)$ and $C_n(B)$ while the number of the encapsulated metal atoms is not the same):

$$2X(g) + nC(g) = X_2@C_n(A;g), \tag{67}$$

$$X(g) + nC(g) = X@C_n(B;g) \tag{68}$$

with the encapsulation equilibrium constants $\left(K_{X_i@C_n(Z),p}\right)$:

$$K_{X_2@C_n(A),p} = \frac{p_{X_2@C_n(A)}}{p_X^2 p_C^n}, \tag{69}$$

$$K_{X@C_n(B),p} = \frac{p_{X@C_n(B)}}{p_X p_C^n}, \tag{70}$$

expressed in the terms of partial pressures of the reaction components. Division of Eq. (69) by Eq. (70) basically yields the population ratio we are interested in:

$$\frac{p_{X_2@C_n(A)}}{p_{X@C_n(B)}} = p_X \frac{K_{X_2@C_n(A),p}}{K_{X@C_n(B),p}}. \tag{71}$$

The ratio of the equilibrium constants in the right side of Eq. (71) is actually equal to the equilibrium constant $K_{X/B/A,p}$ for process (72) so that Eq. (71) can be expressed in a more compact form (73):

$$\mathrm{X(g)} + \mathrm{X@C}_n(B;\mathrm{g}) = \mathrm{X}_2\mathrm{@C}_n(A;\mathrm{g}) \tag{72}$$

$$\frac{p_{X_2@C_n(A)}}{p_{X@C_n(B)}} = p_X K_{X/B/A,p}. \tag{73}$$

If we suppose that the metal partial pressure p_X is actually close to its saturated pressure known $p_{X,sat}$ from observations, the final formula for the relative populations reads:

$$\frac{p_{X_2@C_n(A)}}{p_{X@C_n(B)}} = p_{X,sat} K_{X/B/A,p}. \tag{74}$$

The energetics for reactions (67) and (68) was evaluated [107] with the M06-2X functional in the 6-31G*~SDD and 6-311G*~SDD basis sets. The BSSE calculations (owing to convergence problems) were carried out in a simpler B3LYP/6-311G*~LanL2DZ approach. The BSSE correction for process (72) is rather small – at the M06-2X/6-31G*~SDD//M06-2X/3-21G~SDD level, the potential-energy change for reaction (72) amounts to −138.38 and −140.16 kcal/mol with and without the BSSE term, respectively. In all studied cases, the $La_2@C_{76}(C_s)$ population is considerably higher compared to the $La@C_{76}(T_d)$ one which agrees with the observations. It should be mentioned that one can also deal with the mass ratio instead of the partial-pressure ratio in Eq. (74). Their conversion is related through the molecular masses of the species involved. For example, it can be demonstrated for the partial-pressure ratio p_i/p_j (using the state equation of the ideal gas) that it is converted to the mass ratio m_i/m_j with multiplication by the related molecular-mass ratio M_i/M_j. The last mentioned conversion factor for the pair of $La_2@C_{76}(C_s)$ and $La@C_{76}(T_d)$ in Eq. (74) is however relatively close to one (and, obviously, it is exactly equal to one for an isomeric pair). This computational treatment of the relative populations of nonisomeric metallofullerenes with isomeric cages and

variable number of the same encapsulated metal atom(s) could be further applied to similar systems, like La@C_{80} versus La_2@C_{80}.

Stabilities of Nanocarbon Derivatives

The above examples of the various possible types of relative-stability calculations are not exhaustive. Fullerene and metallofullerene cages with their X-ray crystallographic analysis already available have an important role as they enable direct tests of computations. However, extraction-solvent-produced metallofullerene derivatives represent a special subgroup that needs a more complex treatment. For example, an extraction of La-metallofullerenes from soot using 1,2,4-trichlorobenzene produces [109] not pristine but solvent-derivatized metallofullerenes, namely La@C_{80}-$C_6H_3Cl_2$ and La@C_{82}-$C_6H_3Cl_2$ with X-ray proven $C_{80}(C_{2v};3)$ and $C_{82}(C_{3v};7)$ cages, respectively. In order to explain the discovery, a two-step computational treatment [109] is needed. The first step deals with the high-temperature gas-phase formation of the pristine (underivatized) endohedrals such as La@$C_{80}(C_{2v};3)$ and La@$C_{80}(C_{2v};5)$. The second step treats the reaction with the solvent that produces their La@C_{80}-$C_6H_3Cl_2$ derivatives. In order to have a more reliable description of the thermodynamic terms, the Gibbs-free energies are evaluated at representative temperatures of 1500 and 298.15 K for the first and second step, respectively. Although the underivatized La@$C_{80}(C_{2v};5)$ species is lower in energy, the derivatization changes the energy order so that after the derivatization the La@$C_{80}(C_{2v};3)$ isomer should prevail in the solution as follows from the coupled two-level stability evaluations. First, La@$C_{80}(C_{2v};3)$ and La@$C_{80}(C_{2v};5)$ are formed in the hot gas phase (representative [55] temperature $T_1 = 1500$ K), being characterized by an encapsulation equilibrium constant:

$$\mathrm{La(g)} + \mathrm{C_{80}(i;g)} = \mathrm{La@C_{80}(i;g)};\quad K_{1,i} = K_{La@C_{80}(i),p} = \frac{p_{\mathrm{La@C_{80}(i)}}}{p_{\mathrm{La}} p_{\mathrm{C_{80}(i)}}}. \tag{75}$$

Then, the soot is placed in solution at room temperature ($T_2 = 298.15$ K) and reacts with the solvent (76), and the formed derivative is dissolved and isolated, being characterized by a derivatization equilibrium constant (77):

$$\mathrm{La@C_{80}(i;s)} + \mathrm{C_6H_3Cl_3(sl)} = \mathrm{La@C_{80}(i)} - \mathrm{C_6H_3Cl_2(sl)} + 1/2\mathrm{Cl_2(sl)}; \tag{76}$$

$$K_{2,i} = \frac{c_{La@C_{80}(i)-C_6H_3Cl_2} c_{Cl_2}^{1/2}}{c_{La@C_{80}(i)} c_{C_6H_3Cl_3}}. \tag{77}$$

Our interest aims at the final concentration ratio between derivatized La@$C_{80}(C_{2i};3)$ and La@$C_{80}(C_{2v};5)$ labeled now simply by (**3**) and (**5**), respectively:

$$c\,(\mathbf{3}) : c\,(\mathbf{5}) = \frac{c_{La@C_{80}(\mathbf{3})-C_6H_3Cl_2}}{c_{La@C_{80}(\mathbf{5})-C_6H_3CL_2}} \tag{78}$$

which can be expressed with the equilibrium constants as:

$$c(\mathbf{3}) : c(\mathbf{5}) = \frac{K_{1,\mathbf{3}}(T_1)K_{2,\mathbf{3}}(T_2)}{K_{1,\mathbf{5}}(T_1)K_{2,\mathbf{5}}(T_2)}. \tag{79}$$

Interestingly, the solvent in the left and the second product in the right side cancel out in this expression. Eq. (79) can also be expressed in the Gibbs-energy terms:

$$c(\mathbf{3}) : c(\mathbf{5}) = \exp\left(-\frac{\Delta\Delta G_{1,\mathbf{3}-\mathbf{5}}}{RT_1}\right) exp\left(-\frac{\Delta\Delta G_{2,\mathbf{3}-\mathbf{5}}}{RT_2}\right). \tag{80}$$

In an approximation, it can be simplified by using mere enthalpy terms:

$$c(\mathbf{3}) : c(\mathbf{5}) \approx \exp\left(-\frac{\Delta\Delta H_{1,\mathbf{3}-\mathbf{5}}}{RT_1}\right) \exp\left(-\frac{\Delta\Delta H_{2,\mathbf{3}-\mathbf{5}}}{RT_2}\right). \tag{81}$$

It may seem that the two enthalpy terms could partly cancel out mutually; however, there is a difference in the temperatures T_1, T_2. Consequently, the factor $-\frac{\Delta\Delta H_{2,3-5}}{RT_2}$ is (if signs are ignored) several times larger than $-\frac{\Delta\Delta H_{1,3-5}}{RT_1}$.

Figure 25 shows [109] that in the gas phase, the La@C_{80}(C_{2v};3) isomer represents only a minor species while La@C_{80}(C_{2v};5) is the prevailing product in the high-temperature synthetic region. However, if the comprehensive stability treatment according to Eq. (80) is performed at the B3LYP/6-31G*~SDD//B3LYP/3-21G~SDD level, it turns out that the $\frac{La@C_{80}(C_{2v};3)-C_6H_3Cl_2}{La@C_{80}(C_{2v};5)-C_6H_3Cl_2}$ concentration ratio in solution should be equal to about 67.2 (if simplified Eq. (81) is used, the ratio comes as 89.7) so that agreement with observation is achieved. Let us add that the pure (nonreactive) solvent effect is rather negligible here as according to the SCRF IPCM model the energy separation between both isomers is estimated [109] to be changed by about 0.2 kcal/mol upon transfer from gas phase to solution.

Another recent example of calculated populations for nanocarbon derivatives can be supplied [110, 111] with a conjugate of dimetallofullerene $La_2@C_{80}$ and dodecafluoro-subphthalocyanine with summary formula $C_{113}H_{10}BF_{12}La_2N_7O$, F_{12}SubPc-$La_2@C_{80}$, studied as potentially promising materials for molecular photovoltaics. The calculated nanocarbon system is one of the largest of its type computationally treated so far. The conjugate can be synthesized [110] via Prato reaction. The reaction produces a pyrrolidine ring at a cage C–C bond between five- and six-membered rings or between two six-membered rings. However, the major isomer of the F_{12}SubPc-$La_2@C_{80}$ conjugate exhibits [110] bridging over the cage C–C bond between five- and six-membered rings (Fig. 26). Four rotameric isomers can still be distinguished for the major species, depending on the location of the nitrogen of the pyrrolidine ring and the dodecafluoro-SubPc moiety with respect to the five- and six-membered rings belonging to the bridged-over C–C bond. In fact, in the energy-lowest rotamer, the two fragments are inclined toward the five-membered ring – here called F_{12}SubPc-$La_2@C_{80}$(A) (Fig. 26). In the second energy-lowest

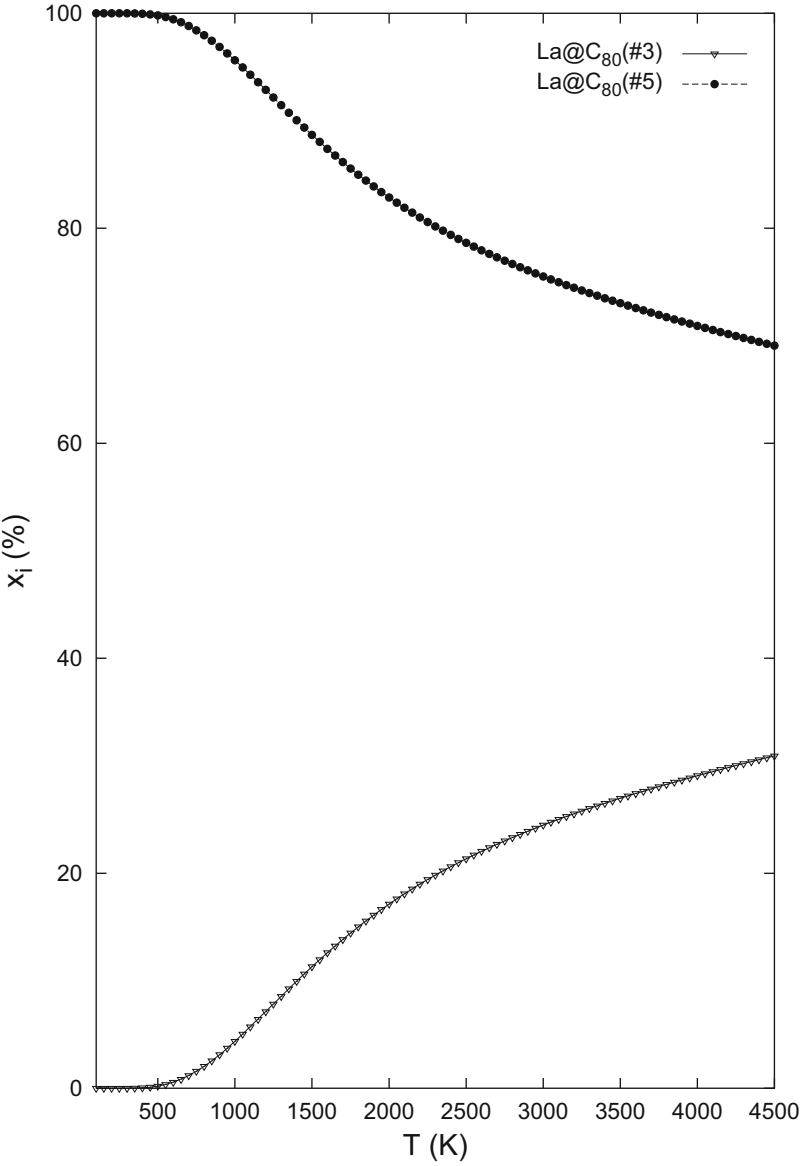

Fig. 25 Relative concentrations [109] of two C_{2v} La@C_{80} isomers computed with the B3LYP/6-31G*~SDD energetics, B3LYP/3-21G~la entropy, and the FEM treatment

rotamer, F_{12}SubPc-La_2@C_{80}(B), the two fragments are inclined toward the six-membered ring (Fig. 26). The remaining two rotamers are rather high in energy compared to the lowest-energy stereoisomer, for example, more than 6 kcal/mol at

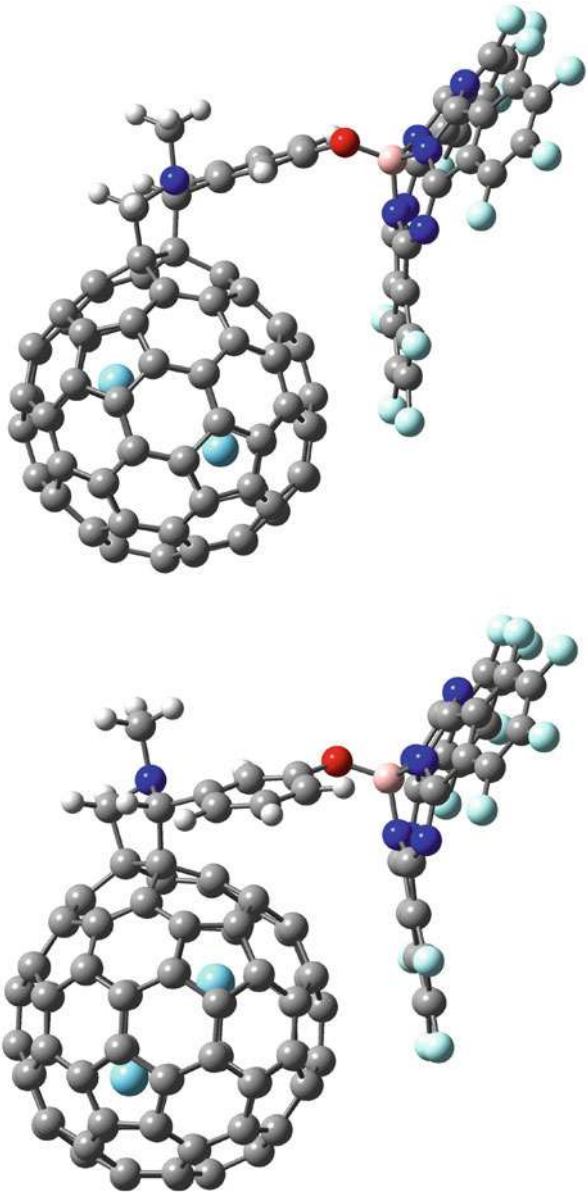

Fig. 26 The M06-2X/3-21G~SDD optimized structure [111] of F_{12}SubPc-La_2@C_{80}(A) (bottom – moieties above pentagon) and F_{12}SubPc-La_2@C_{80}(B) (top – moieties above hexagon); summary formula $C_{113}H_{10}BF_{12}La_2N_7O$

the M06-2X/6-31G*~SDD level [110]. In particular, the standard thermodynamic terms for the isomerization equilibrium:

$$F_{12}\text{SubPc} - La_2@C_{80}(B)(g) = F_{12}\text{SubPc} - La_2@C_{80}(A)(g), \qquad (82)$$

were evaluated, namely the standard reaction change in the potential energy ΔE, enthalpy ΔH_T^o, entropy ΔS_T^o, Gibbs energy ΔG_T^o, and also the equilibrium constant $K_{p,T}$ at temperature T:

$$K_{p,T} = \frac{p_{F_{12}SubPc-La_2@C_{80}(A)}}{p_{F_{12}SubPc-La_2@C_{80}(B)}} = p_a/p_B, \tag{83}$$

where p_i stands for the partial pressures of the rotamers in their equilibrium mixture. Interestingly, the reaction potential energy change ΔE amounts to -1.596 kcal/mol while the related enthalpy reaction change at the absolute zero temperature ΔH_0^o is equal to -2.08 kcal/mol, the latter term acting in the statistical-mechanical expression for the isomerization equilibrium constant $K_{p,T}$:

$$K_{p,T} = \frac{q_A}{q_B} \exp\left(-\frac{\Delta H_0^o}{RT}\right), \tag{84}$$

where R is the gas constant and q_i denote the rotameric partition functions. The temperature behavior of the isomerization equilibrium constant $K_{p,T}$ is again described by the van't Hoff equation. As the ΔH_T^o term is negative, the isomerization equilibrium constant $K_{p,T}$ decreases with temperature and therefore also the population ratio of the two isomers, $K_{p,T} = p_A/p_B$. Two particular temperatures were considered – room temperature and the normal boiling point of toluene used [110] in the Prato reaction. The calculated population ratio $K_{p,T} = p_A/p_B$ shows that the rotamer F_{12}SubPc-La_2@C_{80}(A) should be in comparison with the F_{12}SubPc-La_2@C_{80}(B) rotamer more than 20 and ten times more populated at room temperature and in boiling toluene, respectively.

The vibrational frequencies represent input for the vibrational partition function. The M06-2X/3-21G~SDD IR-vibrational spectra for both rotamers are shown in Fig. 27 (though evaluated in the harmonic approximation and, moreover, for free, gas-phase species). They exhibit numerous very low frequencies that belong to various torsional motions, some of them including motions of the La atoms inside the cage. Some torsion motions could for the thermodynamic evaluations be described using the partition function for internal rotation instead for harmonic vibration. However, given the spectral similarities, an ample cancellation would anyhow operate in Eq. (1).

Kinetic Control

Although this chapter deals with the thermodynamic stabilities, in some situations, experimental findings can be explained only by kinetic control. Historically, fullerene oxides were the first observed fullerene compounds, and they have naturally attracted attention of both experiment and theory [112]. With the mono-oxide $C_{60}O$, two structures are in particular considered, originated in bridging over a 5/6 or 6/6 bond (i.e., the bond shared by a pentagon-hexagon pair and by two hexagons,

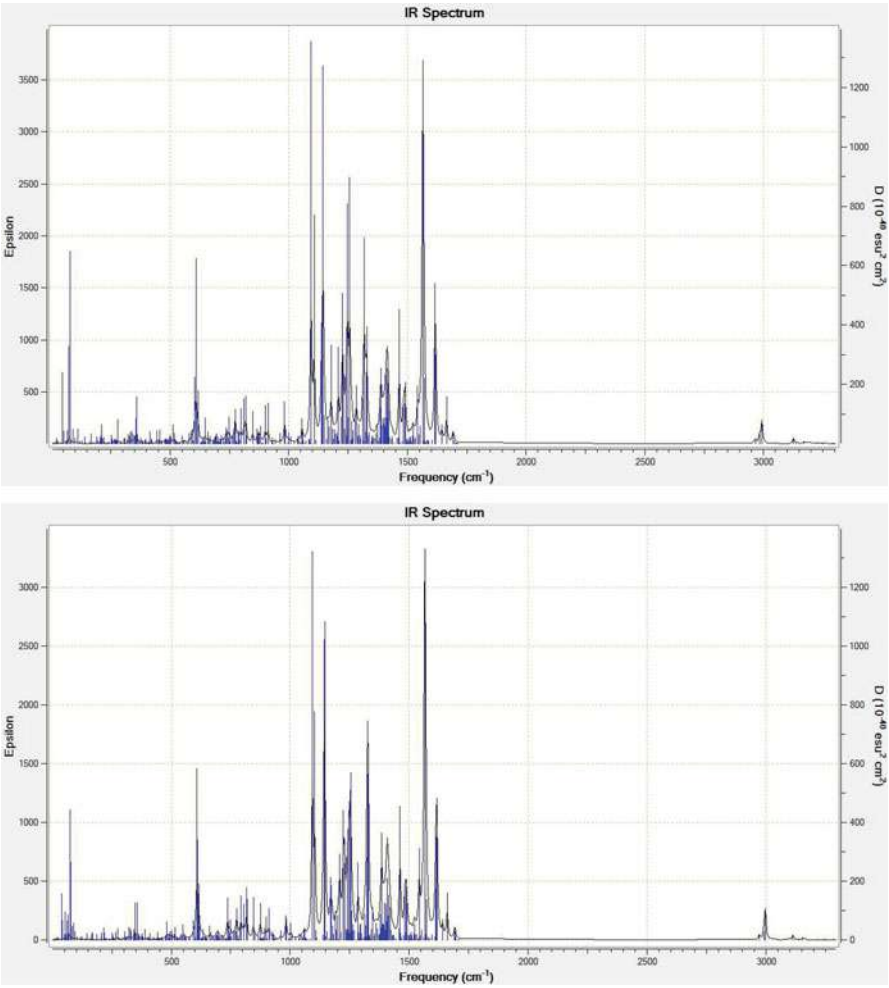

Fig. 27 The M06-2X/3-21G~SDD IR-vibrational spectrum [111] of F_{12}SubPc-$La_2@C_{80}$(A) (bottom) and F_{12}SubPc-$La_2@C_{80}$(B) (top)

respectively) in the pristine C_{60}, i.e., 5/6 or 6/6 isomeric oxides. However, the $C_{60}O$ isomeric thermodynamic stability is consistently calculated [112] in a disagreement with observations. The ground state or the lowest-energy isomer in the C_{60} system is calculated (almost regardless of what kind of method is applied) as the 5/6 species, while in the experiment only the 6/6 structure could be observed. The theory-experiment disagreement could not be explained through temperature (i.e., entropy) factors. The problem becomes even more serious with $C_{60}O_2$. In experiment, only 6/6 6/6 structures were reported; however, in computations [112], the higher thermodynamic stability of the 5/6 mono-oxide is still conserved even with di-oxides. Consequently, the thermodynamic-stability computations are unable to identify the

computed most-populated isomer with the observed 6/6 6/6 species as among the computed bridged structures a 5/6 5/6 isomer is the lowest in energy. The disturbing problem is successfully explained [112] as a possible kinetic control of the relative stabilities. Similar type of stability reasoning is also available [112] for monooxides of the two most abundant isomers of C_{84} (D_2 and D_{2d}). Their full geometry optimizations and also vibrational harmonic analyses were performed at semiempirical PM3 quantum-chemical level, not only for local energy minima but also for related activated complexes (Fig. 28). The located activated complexes are rather of ketoform. The vibrational eigenvector associated with the imaginary frequency represents in one direction a motion toward the dissociation of the C–O bond. In the opposite direction, it leads to a formation of the second C–O bond and thus to the bridging. However, such kinetic computations within the activated-complex theory are considerably more demanding and, thus, still quite rare compared to the grossly prevailing thermodynamic-stability calculations at present.

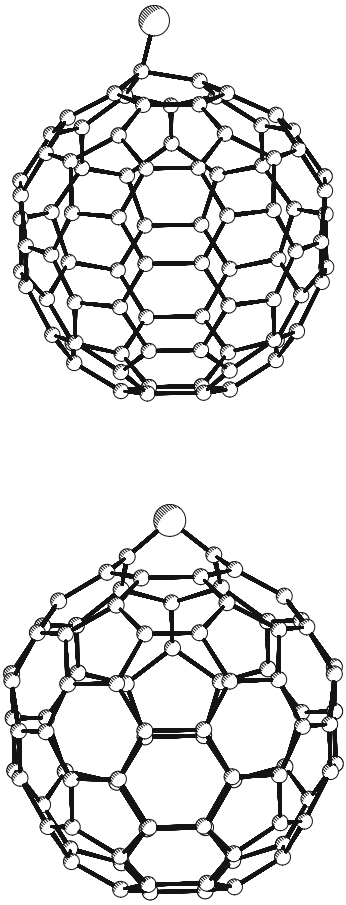

Fig. 28 $C_{84}O$ – addition to the longest C–C bond of D_{2d} C_{84}: PM3 optimized [112] minimum-energy structure and activated complex (top)

Kinetic control is closely related to catalytic aspects that come into consideration with the Stone-Wales isomerizations [31] in order to achieve the inter-isomeric equilibrium. An autocatalysis by free carbon atoms was considered by Eggen et al. [113]. As graphite always contains small amounts of various chemical elements, moreover, N_2 and O_2 also come as an impurity in the inert gas used in the fullerene synthesis, and even some metals can originate from the electric-arc wires; a larger-scale computational study was carried out [114] in order to evaluate their possible catalytic effects. The computations were performed with both semiempirical (AM1, PM3, and SAM1) and DFT (B3LYP/6-31G*) methods. The catalytic agents were represented [114] by free elements, neutral or charged, and acted on a model bowl-shaped fragment $C_{34}H_{12}$. In all computed cases, the catalyzed activation barrier was lowered compared to the uncatalyzed reaction. The kinetic barriers for the catalyzed rearrangements increase in the following order: N, H, O, P, S, B, Cl, C, F, Li, Se, Fe, Hg, Zn, Si, Sn, Ge, Mg, and Al. Nitrogen atoms were pointed out as especially potent catalytic agents. At the PM3-computational level, the isomerization kinetic barrier is reduced to 46, 26, and 82 kcal/mol for the N^+, N, and N^- species, respectively. If the activation barriers are recomputed at the B3LYP/6-31G*//PM3 level, they are changed to 18, 25, and 77 kcal/mol for the N^+, N, and N^- species, respectively. As small amounts of nitrogen (as well as of other elements) are available virtually in fullerene synthesis of any kind, the study [114] offers a computational support for kinetic feasibility of the Stone-Wales fullerene transformation.

In order to have some standard for comparison, we tried [115] to suggest some reasonable value for $\Delta E_1^{\neq}$ such that the Stone-Wales rearrangement will be a kinetically feasible process. Thermodynamic formulation of transition state (activated complex) theory expresses a rate constant k in terms of the activation entropy $\Delta S_T^{\neq}$ and the activation enthalpy $\Delta H_T^{\neq}$:

$$k = \frac{k_B T}{h} \exp\left[\Delta S_T^{\neq}/R\right] \exp\left[-\Delta H_T^{\neq}/(RT)\right]. \tag{85}$$

If we now neglect the entropy part, temperature changes in the enthalpy part, and the contribution of the zero-point motions into it, we get:

$$k = \frac{k_B T}{h} \exp\left[\Delta E_1^{\neq}/(RT)\right]. \tag{86}$$

Finally, the reaction half-life $\tau_{1/2}$ for a unimolecular reaction is given by (if the reverse rate process is not considered, though it cannot be negligible):

$$\tau_{1/2} = \frac{ln\,2}{k}. \tag{87}$$

For the sake of an illustration, let us select a rather arbitrary half-life of 1 s for a general unimolecular process. Of course, it is a rather arbitrary value and some shorter time, for example [116], 0.001 s, could be considered as well. In addition, not only we do not know what a reasonable half-time should be, but also we do not know

what is actually a typical temperature in fullerene synthesis. If we, for example, consider temperatures 1000 and 1500 K, the selected half-life of 1 second requires the activation energy of 61.7 and 93.7 kcal/mol, respectively. If we now combine this simple reasoning with the lowest activation barrier found by Eggen et al. [113], we could place a reasonable value for the $\Delta E_1^{\neq}$ term somewhere around 60 kcal/mol. It is interesting to note that the master equation approach of Walsh and Wales [116] would require temperatures 1900–2300 K to get expected predictions (in fact, their density-functional tight-binding potential barrier may be underestimated). Clearly enough, we are just treating the first step of a nonconcerted mechanism, and there must be moreover many such subsequent nonconcerted mechanisms. Let us also mention that the evaluation of such multistep reaction schemes represents a problem of its own, actually leading to time-dependent reaction parameters [117, 118]. There is still another important factor – condensation of the produced C_{60}. This heterogeneous kinetics/thermodynamics perpetually removes C_{60} from the reaction zone. This transport into a cold condensed phase effectively prevents any decomposition of C_{60} and simultaneously disturbs conditions in the gas phase in a convenient direction (a relatively high sublimation/condensation temperature of C_{60} indeed helps the transfer into the condensed phase). Only if we combine all such numerous partial steps into one reaction superscheme, we could evaluate its performance for C_{60} production.

The fullerene yield in the electric-arc synthetic technique clearly depends [3] on the helium (or other inert gas) pressure, and the factor could also be related [119] to the fullerene annealing process facilitated by the Stone-Wales isomerizations [31]. The isomerization can actually be viewed via the Lindemann-Hinshelwood mechanism [120, 121] (also called the Lindemann-Christiansen mechanism [122], further developed in the RRKM theory [123]) for thermal unimolecular reactions transforming a species A into B with the participation of an inert general molecule M:

$$A + M \rightleftharpoons A^* + M;\ A^* \rightarrow B. \tag{88}$$

In Eq. (88), A^* is an A molecule that gets from the collision with M enough vibrational energy (so-called energized molecule) to isomerize to B. It turns out that an effective rate constant for isomerization of A into B actually increases with increasing inert-molecule pressure (reaching a saturation in high-pressure limit, however before the limit, the reciprocal of the effective rate constant is a linear function of the reciprocal of the inert-molecule pressure). In a rather formal way, one could even consider the inert-gas presence as a kind of catalytic action on the Stone-Wales isomerizations, too (though it is just one piece in a pretty complex story of fullerene formation).

Another example of catalysis, actually more complex, is available [98] with the $Sc_2O@C_{78}$ isomeric system. The $Sc_2O@C_{78}$ (C_{2v}/3) and $Sc_2O@C_{78}$ (D_{3h}/5) isomers can be interconverted via a single-step Stone-Wales transformation. A complex of Sc atom exohedrally attached to $Sc_2O@C_{78}$ can considerably reduce the kinetic barrier for the Stone-Wales transformation. According to the M06-2X/3-21G~SDD treatment, the catalyzed kinetic barrier is 73.1 kcal/mol (the imaginary frequency of the activated complex is $262i$ cm^{-1} where $i = \sqrt{-1}$) while without the exohedral

catalytic agent the barrier amounts to 145.5 kcal/mol. Such significant catalytic reduction of the kinetic barrier should facilitate the Stone-Wales transformation at fullerene-formation temperatures, indeed.

More detailed description of various steps in fullerene and metallofullerene formations can be supplied by quantum-mechanical molecular dynamics based on tight-binding approximation [124, 125]. This advanced approach can side by side study nanocarbon systems with and without helium presence, showing, for example, that He atoms accelerate the formation of five- and six-membered rings. On the other hand, even purely topological, mechanistic reasoning with cage-interconversion maps can point out [126–128] important cages, too.

Conclusions

This survey presents the ongoing productive interaction between calculations and observations in fullerene research that allows for a deeper insight into the experimental facts. In studies of fullerenes and metallofullerenes, the mutual experiment-theory interaction is indeed essential, given the complexity of the systems. The considerable thermal effects on the relative isomeric and nonisomeric populations revealed by the quantum-chemical and statistical-mechanical computations originate in a complex interplay between rotational, vibrational, electronic, symmetry, and chirality factors as well as potential-energy terms. Some of the features would never be seen if only energetics is considered (while entropy is neglected). The treatment is however built upon the (tacit) presumption of the (inter-isomeric) thermodynamic equilibrium. We can hardly know directly to which degree this presumption is satisfied in a particular situation. There are some cases [129] with indications that the system can be outside thermodynamic equilibrium. On the other hand, the thermodynamic-equilibrium treatment has already produced a reasonable computation-observation agreement for the isomeric systems with empty C_{76} till C_{96} cages, and mostly when applied to metallofullerenes. This relatively large tested set supports the belief in a still wider applicability of the equilibrium treatment. In addition to a possible kinetic control in some situations, there are also issues [130] with the solubility of different isomers in the applied extraction solvents – they can hardly be exactly the same (as it is, nevertheless, supposed without saying when comparing the results from the computational treatment of the isomeric relative populations with observed data).

There are also some more methodological aspects of the combined computational treatment that should further be studied – especially anharmonicity of vibrations, motions of encapsulates in cages, and reliability of inter-isomeric energetics. As for the energy evaluations with nanocarbon systems, a Pauling point [131] (i.e., choice of treatments in which errors from the basis set and from the applied method itself mutually compensate so that they produce a correct answer) has not been established yet. However, more advanced approaches, beyond the DFT methods, like B2PLYP-(D) techniques [70, 132–135], have successfully been tested. Motions of encapsulates in clusterfullerenes, e.g., recent systems [136–141], as well as representations

of symmetry [93, 142–145] can serve as examples of other issues which would deserve further efforts. Very recently, metallofullerenes with encapsulated actinides [146–153] have also been observed and calculated. Although this chapter focuses on the calculated thermodynamic stabilities of nanocarbons, it is likely that in some systems the observed stability picture is created by a cooperation of both thermodynamic and kinetic factors. This could be the case even for C_{60} – its spheroidal shape can contribute [29, 154] to both thermodynamic and kinetic stability. Such combined thermodynamic/kinetic calculations are still nearly prohibited by their demands on computational resources. Moreover, for a complete picture, photochemical kinetics and kinetics of charged species should also be considered though such aspects are presently still ignored entirely. Further developments are ahead for various nanocarbon forms, three decades after the first public exposure of the fullerene cages in the solid form (namely [4] at the 5th International Symposium on Small Particles and Inorganic Clusters, ISSPIC, in Konstanz) – that time commented by their discoverers [155] with a kind of surprise: "Fullerene molecules must belong to a very frequently overlooked molecular species".

Cross-References

► Theoretical Prediction of Fullerene Reactivity

Acknowledgments The reported research has been supported by the NSFC (21171061 & 51472095), the Program for Changjiang Scholars and Innovative Research Team in University (IRT1014); by the Czech Science Foundation/GACR (P208/10/1724); by the Charles University Centre of Advanced Materials/CUCAM (CZ.02.1.01/0.0/0.0/15-003/0000417); and by the MetaCentrum (LM2010005) and CERIT-SC (CZ.1.05/3.2.00/08.0144) computing facilities. An initial phase of the research line was supported by the Alexander von Humboldt-Stiftung and the Max-Planck-Institut fur Chemie (Otto-Hahn-Institut).

References

1. Kroto HW, Heath JR, O'Brien SC, Curl RF, Smalley RE (1985) C_{60}: buckminsterfullerene. Nature 318:162–163
2. Rohlfing EA, Cox DM, Kaldor A (1984) Production and characterization of supersonic carbon cluster beams. J Chem Phys 81:3322–3330
3. Krätschmer W, Lamb LD, Fostiropoulos K, Huffman DR (1990) Solid C_{60}: a new form of carbon. Nature 347:354–358
4. Slanina Z (2001) ISSPIC-5 in Konstanz in 1990: announcements of the C_{60} preparation and its structure confirmation. Int J Hist Eth Natur Sci Technol Med NTM 9:41–46
5. Heath JR, O'Brien SC, Zhang Q, Liu Y, Curl RF, Kroto HW, Tittel FK, Smalley RE (1985) Lanthanum complexes of spheroidal carbon shells. J Am Chem Soc 107:7779–7780
6. Kroto HW, Allaf AW, Balm SP (1991) C_{60}: buckminsterfullerene. Chem Rev 91:1213–1235
7. Rodríguez-Fortea A, Balch AL, Poblet JM (2011) Endohedral metallofullerenes: a unique host-guest association. Chem Soc Rev 40:3551–3563
8. Popov AA, Yang S, Dunsch L (2013) Endohedral fullerenes. Chem Rev 113:5989–6113

9. Slanina Z, Uhlík F, Lee S-L, Akasaka T, Nagase S (2012) Stability computations for fullerenes and metallofullerenes. In: D'Souza F, Kadish KM (eds) Handbook of carbon Nano materials, Vol. 4. Materials and fundamental applications. World Scientific, Singapore, pp 381–429
10. Cioslowski J (1993) Ab initio calculations on large molecules: methodology and applications. Rev Comput Chem 4:1–33
11. Slanina Z, Lee S-L, Yu C-H (1996) Computations in treating fullerenes and carbon aggregates. Rev Comput Chem 8:1–62
12. Slanina Z (1975) Remark on the present applicability of quantum chemistry to the calculations of equilibrium and rate constants of chemical reactions. Radiochem Radioanal Lett 22:291–298
13. Slanina Z, Zahradnik R (1977) MINDO/2 study of equilibrium carbon vapor. J Phys Chem 81: 2252–2257
14. Schultz HP (1965) Topological organic chemistry. Polyhedranes and prismanes. J Org Chem 30:1361–1364
15. Ōsawa E (1970) Superaromaticity. Kagaku 25:854–863; Chem. Abstr. 74, 75698v (1971)
16. Slanina Z, Zhao X, Uhlík F, Lee S-L, Adamowicz L (2004) Computing enthalpy-entropy interplay for isomeric fullerenes. Int J Quantum Chem 99:640–653
17. Slanina Z, Rudziński JM, Togasi M, Ōsawa E (1989) Quantum-chemically supported vibrational analysis of giant molecules: the C_{60} and C_{70} clusters. J Mol Struct (THEOCHEM) 202: 169–176
18. Slanina Z, Lee S-L, Uhlik F, Adamowicz L, Nagase S (2007) Computing relative stabilities of metallofullerenes by Gibbs energy treatments. Theor Chem Accounts 117:315–322
19. Slanina Z, Uhlík F, Lee S-L, Adamowicz L, Akasaka T, Nagase S (2011) Calculations of metallofullerene yields. J Comput Theor Nanosci 8:2233–2239
20. Slanina Z (1986) Contemporary theory of chemical isomerism. Kluwer Academic Publishers, Dordrecht
21. Akasaka T, Nagase S, Kobayashi K, Wälchli M, Yamamoto K, Funasaka H, Kako M, Hoshino T, Erata T (1997) ^{13}C and ^{139}La NMR studies of $La_2@C_{80}$: first evidence for circular motion of metal atoms in endohedral dimetallofullerenes. Angew Chem Intl Ed Engl 36:1643–1645
22. Slanina Z (1974) Ph.D. thesis. Czech Academy of Science, Prague
23. Sun M-L, Slanina Z, Lee S-L (1995) Square/hexagon route towards the boron-nitrogen clusters. Chem Phys Lett 233:279–283
24. Zhao X, Slanina Z, Ozawa M, Osawa E, Deota P, Tanabe K (2000) C_{32}: computations of low-energy cages with four-membered rings. Fuller Sci Technol 8:595–613
25. Slanina Z, Zhao X, Kurita N, Gotoh H, Uhlik F, Rudziński JM, Lee KH, Adamowicz L (2001) Computing the relative gas-phase populations of C_{60} and C_{70}: beyond the traditional $\Delta H^o_{f,298}$ scale. J Mol Graphics Mod 19:216–221
26. Slanina Z (2003) Clusters in a saturated vapor: pressure-based temperature enhancement of the cluster fraction. Z Phys Chem 217:1119–1125
27. Manolopoulos DE, Fowler PW (1992) Molecular graphs, point groups, and fullerenes. J Chem Phys 96:7603–7614
28. Fowler PW, Manolopoulos DE (1995) An atlas of fullerenes. Clarendon Press, Oxford
29. Schwerdtfeger P, Wirz LN, Avery J (2015) The topology of fullerenes. WIREs Comput Mol Sci 5:96–145
30. Manolopoulos DE, Fowler PW (1993) A fullerene without a spiral. Chem Phys Lett 204:1–7
31. Stone AJ, Wales DJ (1986) Topological theoretical studies of icosahedral C_{60} and some related species. Chem Phys Lett 128:501–503
32. Manolopoulos DE, May JC, Down SE (1991) Theoretical studies of the fullerenes – C_{34} to C_{70}. Chem Phys Lett 181:105–111
33. Liu X, Klein DJ, Seitz WA, Schmalz TG (1991) Sixty-atom carbon cages. J Comput Chem 12: 1265–1269
34. Slanina Z, Uhlík F, Sheu J-H, Lee S-L, Adamowicz L, Nagase S (2008) Stabilities of fullerenes: illustration on C_{80}. MATCH Commun Math Comput Chem 59:225–238

35. Sun M-L, Slanina Z, Lee S-L (1995) AM1 computations on C_{59}: significant eight- and nine-membered rings. Fuller Sci Technol 3:627–639
36. Fowler PW, Quinn CM, Redmond DB (1991) Decorated fullerenes and model structures for water clusters. J Chem Phys 95:7678–7681
37. Balasubramanian K (1991) Enumeration of isomers of polysubstituted C_{60} and application to NMR. Chem Phys Lett 182:257–262
38. Brendsdal E, Cyvin SJ, Cyvin BN, Brunvoll J, Klein DJ, Seitz WA (1990) Buckminsterfullerene, Part C: Hückel energy levels. In: Hargittai I (ed) Quasicrystals, networks, and molecules of fivefold symmetry. VCH Pub, New York, pp 265–276
39. Bochvar DA, Gal'pern EG (1973) Hypothetical systems: carbododecahedron, s-icosahedron, and carbo-s-icosahedron. Dokl Akad Nauk SSSR 209:610–612
40. Slanina Z, Adamowicz L (1993) One-, two- and three-dimensional structures of C_{20}. Fuller Sci Technol 1:1–9
41. van Orden A, Saykally RJ (1998) Small carbon clusters: spectroscopy, structure, and energetics. Chem Rev 98:2313–2357
42. von Helden G, Kemper PR, Gotts NG, Bowers MT (1993) Isomers of small carbon cluster anions – linear chains with up to 20 atoms. Science 259:1300–1302
43. Slanina Z, Adamowicz L, François J-P, Ōsawa E (1998) Fullerenes & other carbon aggregates and the diffuse interstellar bands. In: Vigasin AA, Slanina Z (eds) Molecular complexes in Earth's, planetary, cometary, and interstellar atmospheres. World Scientific, Singapore, pp 133–176
44. Slanina Z, Uhlík F, Lee S-L, Adamowicz L, Nagase S (2006) Computations of endohedral fullerenes: the Gibbs energy treatment. J Comput Meth Sci Eng 6:243–250
45. Slanina Z (1989) A program for determination of composition and thermodynamics of the ideal gas-phase equilibrium isomeric mixtures. Comput Chem 13:305–311
46. Kato H, Taninaka A, Sugai T, Shinohara H (2003) Structure of a missing-caged metallofullerene: $La_2@C_{72}$. J Am Chem Soc 125:7782–7783
47. Slanina Z, Ishimura K, Kobayashi K, Nagase S (2004) C_{72} isomers: the IPR-satisfying cage is disfavored by both energy and entropy. Chem Phys Lett 384:114–118
48. Wan TSM, Zhang HW, Nakane T, Xu ZD, Inakuma M, Shinohara H, Kobayashi K, Nagase S (1998) Production, isolation, and electronic properties of missing fullerenes: $Ca@C_{72}$ and $Ca@C_{74}$. J Am Chem Soc 120:6806–6807
49. Slanina Z, Uhlík F, Zhao X, Adamowicz L, Nagase S (2007) Relative stabilities of C_{74} isomers. Fulleren Nanotub Carb Nanostruct 15:195–205
50. Sun M-L, Slanina Z, Lee S-L, Uhlík F, Adamowicz L (1995) AM1 computations on seven isolated-pentagon-rule isomers of C_{80}. Chem Phys Lett 246:66–72
51. Slanina Z, Lee S-L, Uhlík F, Adamowicz L, Nagase S (2006) Excited electronic states and relative stabilities of C_{80} isomers. Int J Quantum Chem 106:2222–2228
52. Furche F, Ahlrichs R (2001) Fullerene C_{80}: are there still more isomers? J Chem Phys 114: 10362–10367
53. Slanina Z, Lee S-L, Yoshida M, Ōsawa E (1996) Computations on nineteen isolated-pentagon-rule isomers of C_{86}. Chem Phys 209:13–18
54. Slanina Z, Lee S-L, Adamowicz L (1997) C_{80}, C_{86}, C_{88}, Semiempirical and ab initio SCF calculations. Int J Quantum Chem 63:529–535
55. Cross RJ, Saunders M (2005) Transmutation of fullerenes. J Am Chem Soc 127:3044–3047
56. Wang Z, Yang H, Jiang A, Liu Z, Olmstead MM, Balch AL (2010) Structural similarities in C_s(16)-C_{86} and C_2(17)-C_{86}. Chem Commun 46:5262–5264
57. Chen C-H, Lin D-Y, Yeh W-Y (2014) Regiospecific coordination of Re_3 clusters with the sumanene type hexagons on endohedral metallofullerenes and higher fullerenes that provides an efficient separation method. Chem Eur J 20:5768–5775
58. Kobayashi K, Nagase S (2002) Structures and electronic properties of endohedral metallofullerenes; theory and experiment. In: Akasaka T, Nagase S (eds) Endofullerenes – a new family of carbon clusters. Kluwer Academic Publishers, Dordrecht, pp 99–119

59. Ichikawa T, Kodama T, Suzuki S, Fujii R, Nishikawa H, Ikemoto I, Kikuchi K, Achiba Y (2004) Isolation characterization of a new isomer of Ca@C_{72}. Chem Lett 33:1008–1009
60. Slanina Z, Kobayashi K, Nagase S (2003) Ca@C_{72} IPR and non-IPR structures: computed temperature development of their relative concentrations. Chem Phys Lett 372:810–814
61. Kodama T, Fujii R, Miyake Y, Suzuki S, Nishikawa H, Ikemoto I, Kikuchi K, Achiba Y (2003) ^{13}C NMR study of Ca@C74: cage structure and dynamics of a Ca atom inside the cage. In: Guldi DM, Kamat PV, D'Souza F (eds) Fullerenes, Vol. 13: fullerenes and nanotubes: the building blocks of next generation Nanodevices. The Electrochemical Society, Pennington, pp 548–551
62. Slanina Z, Kobayashi K, Nagase S (2004) Ca@C_{74} isomers: relative concentrations at higher temperatures. Chem Phys 301:153–157
63. Uhlík F, Slanina Z, Lee S-L, Adamowicz L, Nagase S (2013) Stability calculations for Eu@C_{74} isomers. Int J Quantum Chem 113:729–733
64. Xu ZD, Nakane T, Shinohara H (1996) Production and isolation of Ca@C_{82} (I-IV) and Ca@C_{84} (I,II) metallofullerenes. J Am Chem Soc 118:11309–11310
65. Kodama T, Fujii R, Miyake Y, Sakaguchi K, Nishikawa H, Ikemoto I, Kikuchi K, Achiba Y (2003) Structural study of four Ca@C_{82} isomers by ^{13}C NMR spectroscopy Chem. Phys Lett 377:197–200
66. Slanina Z, Kobayashi K, Nagase S (2004) Ca@C_{82} isomers: computed temperature dependency of relative concentrations. J Chem Phys 120:3397–3400
67. Akasaka T, Wakahara T, Nagase S, Kobayashi K, Waelchli M, Yamamoto K, Kondo M, Shirakura S, Maeda Y, Kato T, Kako M, Nakadaira Y, Gao X, van Caemelbecke E, Kadish KM (2001) Structural determination of the La@C_{82} isomer. J Phys Chem B 105:2971–2974
68. Slanina Z, Kobayashi K, Nagase S (2004) Computed temperature development of the relative stabilities of La@C_{82} isomers. Chem Phys Lett 388:74–78
69. Lian YF, Yang SF, Yang SH (2002) Revisiting the preparation of La@C_{82} (I and II) and La_2@C_{80}: efficient production of the "minor" isomer La@C_{82} (II). J Phys Chem B 106:3112–3117
70. Slanina Z, Uhlík F, Akasaka T, Lu X, Adamowicz L (2019) Computational modeling of the Ce@C_{82} metallofullerene isomeric composition. ECS J Solid State Sci Technol 8:M118–M121
71. Shibata K, Rikiishi Y, Hosokawa T, Haruyama Y, Kubozono Y, Kashino S, Uruga T, Fujiwara A, Kitagawa H, Takano T, Iwasa Y (2003) Structural and electronic properties of Ce@C_{82}. Phys Rev B 68:094104-1–094104-7
72. Yang H, Yu M, Jin H, Liu Z, Yao M, Liu B, Olmstead MM, Balch AL (2012) Isolation of three isomers of Sm@C84 and X-ray crystallographic characterization of Sm@D_{3d}(19)-C_{84} and Sm@C_2(13)-C_{84}. J Am Chem Soc 134:5331–5338
73. Slanina Z, Uhlík F, Nagase S, Akasaka T, Adamowicz L, Lu X (2017) Eu@C_{72}: computed comparable populations of two non-IPR isomers. Molecules 22:1053-1–1053-8
74. Takata M, Nishibori E, Sakata M, Shinohara H (2002) Charge density level structures of endohedral metallofullerenes determined by synchrotron radiation powder method. New Diam Front Carb Technol 12:271–286
75. Jensen F (2017) Introduction to computational chemistry. Wiley, Chichester, p 319
76. Slanina Z (2004) Temperature development of mono- and hetero-clustering in saturated vapors. J Clust Sci 15:3–11
77. Alcock CB, Itkin VP, Horrigan MK (1984) Vapor pressure equations for the metallic elements: 298-2500 K. Can Metallurg Quart 23:309–313
78. Slanina Z, Uhlík F, Nagase S (2007) Computational evaluation of the relative production yields in the X@C_{74} series (X = Ca, Sr, Ba). Chem Phys Lett 440:259–262
79. Gromov A, Krawez N, Lassesson A, Ostrovskii DI, Campbell EEB (2002) Optical properties of endohedral Li@C_{60}. Curr App Phys 2:51–55
80. Kobayashi K, Nagase S (1999) Bonding features in endohedral metallofullerenes. Topological analysis of the electron density distribution. Chem Phys Lett 302:312–316

81. Slanina Z, Uhlík F, Lee S-L, Adamowicz L, Akasaka T, Nagase S (2011) Computed stabilities in metallofullerene series: Al@C_{82}, Sc@C_{82}, Y@C_{82}, and La@C_{82}. Int J Quant Chem 111: 2712–2718
82. Peres T, Cao BP, Cui WD, Khong A, Cross RJ, Saunders M, Lifshitz C (2001) Some new diatomic molecule containing endohedral fullerenes. Int J Mass Spectr 210:241–247
83. Suetsuna T, Dragoe N, Harneit W, Weidinger A, Shimotani H, Ito S, Takagi H, Kitazawa K (2002) Separation of N_2@C_{60} and N@C_{60}. Chem Eur J 8:5079–5083
84. Knapp C, Dinse K-P, Pietzak B, Waiblinger M, Weidinger A (1997) Fourier transform EPR study of N@C_{60} in solution. Chem Phys Lett 272:433–437
85. Saunders M, Jiménez-Vázquez HA, Cross RJ, Poreda RJ (1993) Stable compounds of helium and Neon: He@C_{60} and Ne@C_{60}. Science 259:1428–1430
86. Zhang R, Murata M, Aharen T, Wakamiya A, Shimoaka T, Hasegawa T, Murata Y (2016) Synthesis of a distinct water dimer inside fullerene C_{70}. Nature Chem 8:435–441
87. Slanina Z, Nagase S (2006) A computational characterization of N_2@C_{60}. Mol Phys 104: 3167–3171
88. Slanina Z, Uhlík F, Adamowicz L, Nagase S (2005) Computing fullerene encapsulation of non-metallic molecules: N_2@C_{60} and NH_3@C_{60}. Mol Simul 31:801–806
89. Slanina Z, Uhlík F, Nagase S, Lu X, Akasaka T, Adamowicz L (2016) Computed relative populations of D_2(22)-C_{84} endohedrals with encapsulated monomeric and dimeric water. ChemPhysChem 17:1109–1111
90. Slanina Z, Uhlík F, Nagase S, Akasaka T, Lu X, Adamowicz L (2018) Cyclic water-trimer encapsulation into D_2(22)-C_{84} fullerene. Chem Phys Lett 695:245–248
91. Stevenson S, Rice G, Glass T, Harich K, Cromer F, Jordan MR, Craft J, Hadju E, Bible R, Olmstead MM, Maitra K, Fisher AJ, Balch AL, Dorn HC (1999) Small-bandgap endohedral metallofullerenes in high yield and purity. Nature 401:55–57
92. Yang S, Liu F, Chen C, Jiao M, Wei T (2011) Fullerenes encaging metal clusters – cluster-fullerenes. Chem Commun 47:11822–11839
93. Slanina Z, Uhlík F, Feng L, Akasaka T, Lu X, Adamowicz L (2019) Calculations of the Lu_3N@C_{80} two-isomer equilibrium. Fulleren Nanotub Carb Nanostruct 27:382–386
94. Shen W-Q, Bao L-P, Hu S-F, Gao X-J, Xie Y-P, Gao X-F, Huang W-H, Lu X (2018) Isolation and crystallographic characterization of Lu_3N@C_{2n} (2n = 80–88): cage selection by cluster size. Chem Eur J 24:16692–16698
95. Dunsch L, Yang SF, Zhang L, Svitova A, Oswald S, Popov AA (2010) Metal sulfide in a C_{82} fullerene cage: a new form of endohedral clusterfullerenes. J Am Chem Soc 132:5413–5421
96. Mercado BQ, Chen N, Rodriguez-Fortea A, Mackey MA, Stevenson S, Echegoyen L, Poblet JM, Olmstead MM, Balch AL (2011) The shape of the Sc-2(mu(2)-S) unit trapped in C_{82}: crystallographic, computational, and electrochemical studies of the isomers, Sc-2(mu(2)-S) @C-s(6)-C-82 and Sc-2(mu(2)-S)@C-3v(8)-C-82. J Am Chem Soc 133:6752–6760
97. Slanina Z, Uhlík F, Lee S-L, Mizorogi N, Akasaka T, Adamowicz L (2011) Calculated relative yields for Sc_2S@C_{82} and Y_2S@C_{82}. Theor Chem Accounts 130:549–554
98. Hao Y, Tang Q, Li X, Zhang M, Wan Y, Feng L, Chen N, Slanina Z, Adamowicz L, Uhlík F (2016) Isomeric Sc_2O@C_{78} related by a single-step Stone-Wales transformation: key links in an unprecedented fullerene formation pathway. Inorg Chem 55:11354–11361
99. Slanina Z, Uhlík F, Feng L, Adamowicz L (2017) Sc_2O@C_{78}: calculations of the yield ratio for two observed isomers. Fulleren Nanotub Carb Nanostruct 25:124–127
100. Slanina Z, Uhlík F, Pan C, Akasaka T, Lu X, Adamowicz L (2018) Computed stabilization for a giant fullerene endohedral: Y_2C_2@C_1(1660)-C_{108}. Chem Phys Lett 710:147–149
101. Ervin KM, Gronert S, Barlow SE, Gilles MK, Harrison AG, Bierbaum VM, DePuy CH, Lineberger WC, Ellison GB (1990) Bond strengths of ethylene and acetylene. J Am Chem Soc 112:5750–5759
102. Slanina Z, Ōsawa E (1997) Average bond dissociation energies of fullerene. Fuller Sci Technol 5:167–175

103. Yu P, Shen W, Bao L, Pan C, Slanina Z, Lu X (2019) Trapping an unprecedented Ti_3C_3 unit inside the icosahedral C_{80} fullerene: a crystallographic survey. Chem Sci 10:10925–10930
104. Slanina Z, Uhlík F, Lee S-L, Adamowicz L, Nagase S (2008) MPWB1K calculations of stepwise encapsulations: $Li_x@C_{60}$. Chem Phys Lett 463:121–123
105. Slanina Z, Uhlík F, Lee S-L, Adamowicz L, Nagase S (2007) Alkali-metal clusters encapsulated into fullerenes: computations on $Li_x@C_{60}$. J Comput Meth Sci Eng 7:541–547
106. Mardirossiana N, Head-Gordon M (2017) Thirty years of density functional theory in computational chemistry: an overview and extensive assessment of 200 density functionals. Mol Phys 115:2315–2372
107. Slanina Z, Uhlík F, Lee S-L, Wang B-C, Adamowicz L, Suzuki M, Haranaka M, Feng L, Lu X, Nagase S, Akasaka T (2014) Towards relative populations of non-isomeric metallofullerenes: $La@C_{76}(T_d)$ vs. $La_2@C_{76}(C_s,17490)$. Fulleren Nanotub Carb Nanostruct 22:299–306
108. Suzuki M, Mizorogi N, Yang T, Uhlik F, Slanina Z, Zhao X, Yamada M, Maeda Y, Hasegawa T, Nagase S, Lu X, Akasaka T (2013) $La_2@C_s(17490)$-C_{76}: a new non-IPR dimetallic metallofullerene featuring unexpectedly weak metal-Pentalene interactions. Chem Eur J 19:17125–17130
109. Slanina Z, Uhlík F, Lee S-L, Adamowicz L, Kurihara H, Nikawa H, Lu X, Yamada M, Nagase S, Akasaka T (2014) Computations on metallofullerenes derivatized during extraction: $La@C_{80}$-$C_6H_3C_{12}$ and $La@C_{82}$-$C_6H_3Cl_2$. Fulleren Nanotub Carb Nanostruct 22:173–181
110. Feng L, Rudolf M, Trukhina O, Slanina Z, Uhlík F, Lu X, Torres T, Guldi DM, Akasaka T (2015) Tuning intramolecular electron and energy transfer processes in novel conjugates of $La_2@C_{80}$ and electron accepting subphthalocyanines. Chem Commun 51:330–333
111. Slanina Z, Uhlík F, Feng L, Akasaka T, Lu X, Adamowicz L (2020) Rotameric isomers of $La_2@C_{80}$ & dodecafluoro-subphthalocyanine conjugate: computational characterization. ECS J Solid State Sci Technol 9:061014
112. Slanina Z, Uhlík F, Juha L, Tanabe K, Adamowicz L, Ōsawa E (2004) Computations on $C_{84}O$: thermodynamic, kinetic and photochemical stability. J Mol Struct (Theochem) 684:129–133
113. Eggen BR, Heggie MI, Jungnickel G, Latham CD, Jones R, Briddon PR (1996) Autocatalysis during fullerene growth. Science 272:87–90
114. Slanina Z, Zhao X, Uhlík F, Ozawa M, Ōsawa E (2000) Computational modelling of the metal and other elemental catalysis in the Stone-Wales fullerene rearrangements. J Organomet Chem 599:57–61
115. Slanina Z, Zhao X, Ozawa M, Adamowicz L, Ōsawa E (2000) Computational evaluations of the elemental-catalytical effects on the kinetics of the Stone-Wales isomerizations. In: Kamat PV, Guldi DM, Kadish KM (eds) Recent advances in the chemistry and physics of fullerenes and related materials: vol. 10 – Chemistry and physics of fullerenes and carbon nanomaterials. The Electrochemical Society, Pennington, pp 129–141
116. Walsh TR, Wales DJ (1998) Relaxation dynamics of C_{60}. J Chem Phys 109:6691–6700
117. Slanina Z (1982) Sequential isomerism of activated complexes and comparisons of theoretical and observed data: a general case of a unimolecular process with one intermediate. Z Phys Chem (Wiesbaden) 132:41–54
118. Slanina Z (1983) Sequential isomerism of activated complexes: interfering versus non-interfering intermediate. Int J Quantum Chem 23:1553–1561
119. Ōsawa E, Ueno H, Yoshida M, Slanina Z, Zhao X, Nishiyama M, Saito H (1998) Combined topological and energy analysis of the annealing process in fullerene formation. Stone-Wales interconversion pathways among IPR isomers of higher fullerenes. J Chem Soc Perkin Trans 2: 943–950
120. Lindemann FA (1922) Discussion on the radiation theory of chemical action. Trans Faraday Soc 17:598–599
121. Hinshelwood CN (1926) On the theory of unimolecular reactions. Proc Roy Soc London A 113:230–233
122. Bao JL, Zhang X, Truhlar DG (2016) Predicting pressure-dependent unimolecular rate constants using variational transition state theory with multidimensional tunneling combined

with system-specific quantum RRK theory: a definitive test for fluoroform dissociation. Phys Chem Chem Phys 18:16659–16670
123. Levine RD (2005) Molecular reaction dynamics. Cambridge University Press, Cambridge, pp 215–224
124. Irle S, Zheng G, Wang Z, Morokuma K (2006) The C_{60} formation puzzle solved: QM/MD simulations reveal the shrinking hot giant road of the dynamic fullerene self-assembly mechanism. J Phys Chem B 110:1453114545
125. Deng Q, Heine T, Irle S, Popov AA (2016) Self-assembly of endohedral metallofullerenes: a decisive role of cooling gas and metalcarbon bonding. Nanoscale 8:3796–3808
126. Bao L, Yu P, Pan C, Shen W, Lu X (2019) Crystallographic identification of Eu@C_{2n} (2n = 88, 86 and 84): completing a transformation map for existing metallofullerenes. Chem Sci 10: 2153–2158
127. Feng L, Hao YJ, Liu AL, Slanina Z (2019) Trapping metallic oxide clusters inside fullerene cages. Acc Chem Res 52:1802–1811
128. Cai W, Alvarado J, Metta-Magaña A, Chen N, Echegoyen L (2020) Interconversions between uranium mono-metallofullerenes: mechanistic implications and role of asymmetric cages. J Am Chem Soc 142:1311213119
129. Abella L, Mulet-Gas M, Rodriguez-Fortea A, Poblet JM (2016) $La_3N@C_{92}$: an endohedral metallofullerene governed by kinetic factors? Inorg Chem 55:3302–3306
130. Maeda Y, Tsuchiya T, Kikuchi T, Nikawa H, Yang T, Zhao X, Slanina Z, Suzuki M, Yamada M, Lian Y, Nagase S, Lu X, Akasaka T (2016) Effective derivatization and extraction of insoluble missing lanthanum metallofullerenes La@C_{2n} (n = 36–38) with iodobenzene. Carbon 98:67–73
131. Ulusoy IS, Wilson AK (2019) Slater and Gaussian basis functions and computation of molecular integrals. In: Blinder SM, House JE (eds) Mathematical physics in theoretical chemistry. Elsevier, Amsterdam, p 43
132. Schwabe T, Grimme S (2007) Double-hybrid density functionals with long-range dispersion corrections: higher accuracy and extended applicability. Phys Chem Chem Phys 9:3397–3406
133. Menon AS, Radom L (2008) Consequences of spin contamination in unrestricted calculations on open-shell species: effect of Hartree-Fock and Mpller-Plesset contributions in hybrid and double-hybrid density functional theory approaches. J Phys Chem A 112:13225–13230
134. Slanina Z, Uhlík F, Bao L, Akasaka T, Lu X, Adamowicz L (2019) Calculated relative populations for the Eu@C_{82} isomers. Chem Phys Lett 726:29–33
135. Slanina Z, Uhlík F, Bao L, Akasaka T, Lu X, Adamowicz L (2020) Eu@C_{86} isomers: calculated relative populations. Fulleren Nanotub Carb Nanostruct 28:565–570
136. Zhao S, Zhao P, Cai W, Bao L, Chen M, Xie Y, Zhao X, Lu X (2017) Stabilization of giant fullerenes C_2(41)-C_{90}, D_3(85)-C_{92}, C_1(132)-C_{94}, C_2(157)-C_{69}, and C_1(175)-C_{98} by encapsulation of a large La_2C_2 cluster: the importance of cluster-cage matching. J Am Chem Soc 139: 4724–4728
137. Zhao R, Yuan K, Zhao S, Zhao X, Ehara M (2017) Quantum chemical insight into La_2C_{96}: metal carbide fullerene $La_2C_2@C_{94}$ versus dimetallofullerene $La_2@C_{96}$. Inorg Chem 56: 11883–11890
138. Li Q-Z, Zheng J-J, He L, Nagase S, Zhao X (2018) La-La bonded dimetallofullerenes $[La_2@C_{2n}]^-$: species for stabilizing C_{2n} ($2n$ = 92–96) besides $La_2C_2@C_{2n}$. Phys Chem Chem Phys 20:14671–14678
139. Hu SF, Shen WQ, Zhao P, Xu T, Slanina Z, Ehara M, Zhao X, Xie YP, Akasaka T, Lu X (2019) Crystallographic characterization of $Er_2C_2@C_2$(43)-C_{90}, $Er_2C_2@C_2$(40)-C_{90}, $Er_2C_2@C_2$(44)-C_{90}, and $Er_2C_2@C_4$(21)-C_{90}: the role of cage-shape on cluster configuration. Nanoscale 11:17319–17326
140. Liu FP, Spree L, Krylov DS, Velkos G, Avdoshenko SM, Popov AA (2019) Single-electron lanthanide-lanthanide bonds inside fullerenes toward robust redox-active molecular magnets. Acc Chem Res 52:2981–2993

141. Slanina Z, Uhlík F, Bao LP, Akasaka T, Lu X, Adamowicz L (2020) Calculated relative populations for the Eu@C_{84} isomers. Fulleren Nanotub Carb Nanostruct 29:144–148
142. Slanina Z (1989) Some aspects of mathematical chemistry of equilibrium and rate processes: steps towards a completely non-empirical computer design of syntheses. J Mol Struct (THEOCHEM) 185:217–228
143. Slanina Z, Uhlík F, Nagase S, Akasaka T, Adamowicz L, Lu X (2017) A computational characterization of CO@C_{60}. Fulleren Nanotub Carb Nanostruct 25:624–629
144. Slanina Z, Uhlík F, Feng L, Adamowicz L (2016) Evaluation of the relative stabilities of two non-IPR isomers of Sm@C_{76}. Fulleren Nanotub Carb Nanostruct 24:339–344
145. Yu YL, Slanina Z, Wang F, Yang Y, Lian YF, Uhlík F, Xin BF, Feng L (2020) Ho_2O@D_3 (85)-C_{92}: highly stretched cluster dictated by a giant cage and unexplored isomerization. Inorg Chem 59:11020–11027
146. Popov AA (2017) Synthesis and molecular structures of endohedral fullerenes. In: Popov AA (ed) Endohedral fullerenes: electron transfer and spin. Springer, Cham, pp 1–34
147. Slanina Z, Uhlík F, Adamowicz L, Akasaka T, Nagase S, Lu X (2017) Stability issues in computational screening of carbon nanostructures: illustrations on La endohedrals. Mol Simul 43:1472–1479
148. Wang Y, Morales-Martínez R, Zhang X, Yang W, Wang Y, Rodriguez-Fortea A, Poblet JM, Feng L, Wang S, Chen N (2017) Unique four-electron metal-to-cage charge transfer of Th to a C_{82} fullerene cage: complete structural characterization of Th@C_{3v} (8)-C_{82}. J Am Chem Soc 139:5110–5116
149. Cai WT, Abella L, Zhuang JX, Zhang XX, Feng L, Wang YF, Morales-Martinez R, Esper R, Boero M, Metta-Magana A, Rodriguez-Fortea A, Poblet JM, Echegoyen L, Chen N (2018) Synthesis and characterization of non-isolated-pentagon-rule actinide endohedral metallofullerenes U@C_1(17418)-C_{76}, U@C_1(28324)-C_{80}, and Th@C_1(28324)-C_{80}: low-symmetry cage selection directed by a tetravalent ion. J Am Chem Soc 140:18039–18050
150. Wang YF, Morales-Martínez R, Cai WT, Zhuang JX, Yang W, Echegoyen L, Poblet JM, Rodríguez-Fortea A, Chen N (2019) Th@C_1(11)-C_{86}: an actinide encapsulated in an unexpected C_{86} fullerene cage. Chem Commun 55:9271–9274
151. Cai W, Chen C-H, Chen N, Echegoyen L (2019) Fullerenes as nanocontainers that stabilize unique actinide species inside: structures, formation, and reactivity. Acc Chem Res 52:1824–1833
152. Zhao Y-X, Li M-Y, Zhao P, Ehara M, Zhao X (2019) New insight into U@C_{80}: missing U@D_3(31921)-C_{80} and nuanced enantiomers of U@C_1(28324)-C_{80}. Inorg Chem 58: 141591416
153. Hao D, Yang L, Wei Z, Hou Q, Li L, Jin P (2020) U_2O@C_{76}: non-isolated-pentagon-rule cages prevail with the U_2O configuration determined by cage shape and dominated by multicenter bonds. Inorg Chem 59:70397048
154. Sure R, Hansen A, Schwerdtfeger P, Grimme S (2017) Comprehensive theoretical study of all 1812 C_{60} isomers. Phys Chem Chem Phys 19:14296–14305
155. Huffman D, Krätschmer W (1990) Solid C_{60} – how we found it. MRS Proc 206:601–610

Fullerenes Violating the Isolated Pentagon Rule

6

Zuo-Chang Chen, Yuan-Zhi Tan, and Su-Yuan Xie

Contents

Abstract

Fullerenes are cage-shaped carbon clusters. Compared with the vast number of theoretically possible fullerene isomers, only quite a few of them were obtained experimentally. It is due to the constraint of the isolated pentagon rule (IPR), which states that the fullerenes with isolated pentagons are stable, otherwise they are instable. The adjacent pentagons have unfavorable antiaromaticity and local strain. In terms of endohedral and exohedral derivatization, fullerenes with adjacent pentagons can be stabilized. Following these stabilization principles, the synthetic routes to non-IPR fullerenes nowadays include the metal-doped arc discharge, chlorine or hydrogen-involved arc discharge, low-pressure combustion, chlorine-involved radio frequency furnace, and postfunctionalization-promoted cage transformation. Based on these methods, more than 60 members of non-IPR fullerenes were synthesized and characterized from C_{20} to C_{102}. These non-IPR fullerenes are vital for understanding the mechanism of fullerene for-

Z.-C. Chen · Y.-Z. Tan (✉) · S.-Y. Xie
State Key Laboratory for Physical Chemistry of Solid Surfaces, and Department of Chemistry, College of Chemistry and Chemical Engineering, Xiamen University, Xiamen, China
e-mail: yuanzhi_tan@xmu.edu.cn

X. Lu et al. (eds.), *Handbook of Fullerene Science and Technology*,
https://doi.org/10.1007/978-981-16-8994-9_5

mation, but also provide novel basic building blocks for fullerene materials. Based on the structures of prepared non-IPR fullerenes, the stabilization of fused pentagons was well understood, which can guide the synthesis of non-IPR fullerenes in the future. After the decades of research, the non-IPR fullerenes have been a hot field in the fullerene science.

Keywords

Fused pentagons-stabilization · Derivatization · Chlorination · Hydrogenation · Endofullerene · Aromaticity

Introduction

Fullerenes are closed cage-like carbon clusters composed of sp^2-hybridized carbon atoms [1]. Each carbon atom on the fullerene carbon cage forms three C–C bonds with three other adjacent carbon atoms, which results in a cage-shaped carbon skeleton. This carbon–carbon bonding makes the carbon skeleton of the fullerene forming a polyhedron. Each carbon atom is on the vertex of the polyhedron, the C–C bonds are the edges of the polyhedron, and the formed carbon rings are the faces of the polyhedron. Euler's theorem can mathematically describe the relationship between the number of vertices (V), edges (E), and faces (F) of a polyhedron: $V + F = E + 2$. If a fullerene (C_{2n}) is composed of hexagons and pentagons only, it must have 12 pentagons and (n-10) hexagons, according to the Euler's theorem.

Although the carbon rings of fullerene are usually hexagons and pentagons, with the development of fullerene research, fullerenes containing tetragon or heptagon have also been discovered and prepared. At present, fullerenes composed of only hexagons and pentagons are called as classical fullerenes, whereas fullerenes with tetragon or heptagon are classified as nonclassical fullerenes. Incorporating heptagon or tetragon will change the number of pentagons in the fullerene cage. For example, one heptagon in the carbon skeleton of fullerene requires one addition pentagon in the cage. Namely, the fullerenes containing one heptagon have 13 pentagons. On the other hand, addition of one tetragon to the cage will decrease by two. Up to date, most of fullerenes belong to the classical fullerenes; however, more and more fullerenes containing heptagons were discovered recently.

It is easy to see that there is a large number of isomers for a fullerene with a given number of carbon atoms [2] (Table 1), due to the different arrangements of carbon rings. The arrangement between pentagons was found to be of great impact. As early as 1987, Kroto, one of the discoverers of fullerenes, pointed out that when there were adjacent pentagons (Fig. 1) on the fullerene cage, the strain of the fullerene carbon cage increased, making the fullerene instable [3]. This is called as the "isolated pentagon rule" (IPR). Subsequent theoretical studies manifested that the adjacent-pentagon structure was antiaromatic and therefore fullerenes containing adjacent pentagons were very active and difficult to obtain experimentally [4–7].

Table 1 The number of IPR and non-IPR fullerene (C_n) isomers ($20 \leq n \leq 100$)

n	Non-IPR	IPR	n	Non-IPR	IPR
20	1	0	62	2385	0
24	1	0	64	3465	0
26	1	0	66	4478	0
28	2	0	68	6332	0
30	3	0	70	8148	1
32	6	0	72	11,189	1
34	6	0	74	14,245	1
36	15	0	76	19,149	2
38	17	0	78	24,104	5
40	40	0	80	31,917	7
42	45	0	82	39,710	9
44	89	0	84	51,568	24
46	116	0	86	63,742	19
48	199	0	88	81,703	35
50	271	0	90	99,872	46
52	437	0	92	126,323	86
54	580	0	94	153,359	134
56	924	0	96	191,652	187
58	1205	0	98	230,758	259
60	1811	1	100	285,463	450

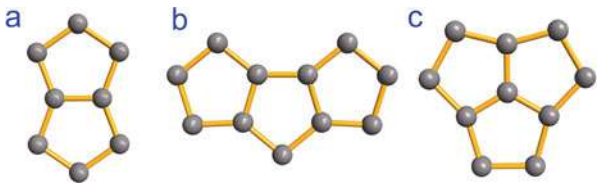

Fig. 1 Structures of fused pentagons containing 2–3 pentagons. (**a**) Double fused pentagons (DFP). (**b**) Triple sequentially fused pentagons (TSFP). (**c**) Triple directly fused pentagons (TDFP)

Then, the IPR was used as a very simple empirical structural rule to classify the stability of fullerenes. The fullerenes with isolated pentagons are stable, otherwise they are instable. Accordingly, fullerenes can be divided into two categories: fullerenes with isolated pentagons (IPR fullerenes) and fullerenes with fused pentagons (non-IPR fullerenes). The synthesis of these instable non-IPR fullerenes was a great challenge for chemists and 15 years after the discovery of fullerene, the first non-IPR fullerenes were synthesized [8, 9]. Significant progress has been made in the synthesis and isolation of non-IPR fullerenes in the last two decades [10–18]. A series of non-IPR fullerenes have been successfully synthesized and isolated by means of endohedral and exohedral stabilization strategies.

Nomenclature of Fullerene Carbon Cages

For fullerenes (C_n), there are a lot of structural isomers owing to the different arrangement of pentagons and hexagons in the carbon cage and the number of isomers increases sharply as the carbon number (n) increases (Table 1). Therefore, it is necessary to distinguish these isomers by an effective nomenclature, especially for the studies of non-IPR fullerenes, which generally have complex carbon connection and low molecular symmetry. In 1995, Fowler and Manolopoulos developed a widely accepted nomenclature: the spiral algorithm [2]. This algorithm provides a unique way to label fullerene isomers composed of hexagons and pentagons. Then cage structure of isomers can be assigned one-to-one correspondence with the numbers given by the spiral algorithm. In this chapter, when naming isomers of fullerene C_n, its isomer numbers in the spiral algorithm are added as the superscript before C_n. For example, the spiral number of famous IPR I_h-C_{60} is 1812, then it can be represented exclusively by $^{\#1812}C_{60}$. The fullerene isomers containing heptagons are represented as C_n(NCx), x is the number of heptagons, in this chapter.

Endohedral Stabilization of Non-IPR Fullerenes

As early as the 1990s, there were theoretical calculations that indicated that reactive non-IPR fullerenes could be stabilized by intramolecular electron transfer from embedded metal atoms to external carbon cages. The first experimental synthesis of non-IPR fullerenes succeeded in 2000 [8, 9].

Generally, the carbon cages of endohedral fullerenes are considered to be negatively charged due to the charge transfer from the encapsulated metal atoms. Consequently, the stability of endofullerene depends on the stability of its charged cage anions rather than the stability of the neutral cages. Poblet et al. proposed a simple rule to discriminate and predict the most suitable carbon cages for endofullerenes [19]. Taking $Sc_3N@^{\#6140}C_{68}$ as an example [9, 20], its stability relies on the energy gap between the LUMO+3 and LUMO+4 orbital of its carbon cage instead of the HOMO-LUMO gap (Fig. 2). LUMO+3 and LUMO+4 correspond to the third and fourth lowest unoccupied molecular orbitals, respectively. That is based on the assumption of complete transferring all six electrons from the HOMOs of the encapsulated metal nitride cluster to the corresponding LUMOs of the carbon cage. Although the calculated molecular orbital energies of $^{\#6140}C_{68}$ are not exactly the same as those of $Sc_3N@^{\#6140}C_{68}$, the HOMO-LUMO gap of $Sc_3N@^{\#6140}C_{68}$ can be simply estimated from the LUMO+3 and LUMO+4 energy gaps of $^{\#6140}C_{68}$. Based on the blueprint above, Popov et al. used DFT calculations to search the possible fullerene isomers for endohedral encapsulation, theoretically investigated $M_3N@C_n$ with 68–98 carbons [21], and found that some C_n^{6-} anions and their corresponding $M_3N@C_n$ n were non-IPR and more stable than their IPR counterparts, with cage sizes up to C_{84}.

Poblet's rule can be applied to the endofullerenes encapsulating metal atoms or metal carbides as well. The encapsulated cluster transfers the electrons to the host fullerene and the number of transferred electrons depends on the encapsulated

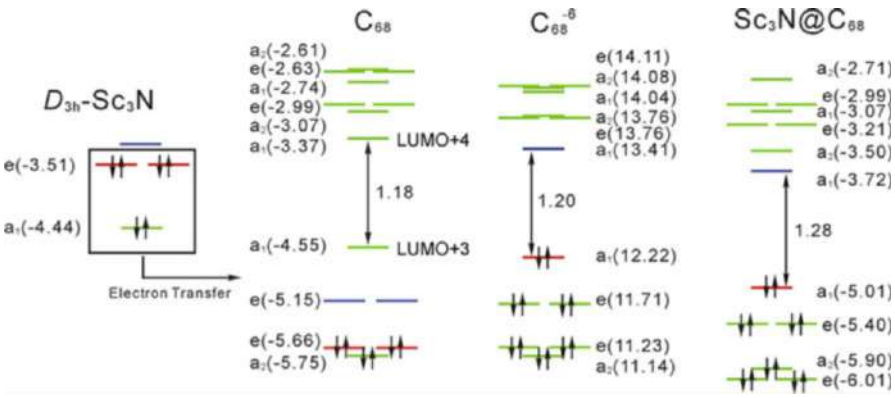

Fig. 2 Molecular orbitals of $Sc_3N@^{\#6140}C_{68}$, $^{\#6140}C_{68}$, and $^{\#6140}C_{68}{}^{6-}$. Six electrons on the three HOMOs of Sc_3N on the left are transferred to the three LUMOs of the $^{\#6140}C_{68}$ carbon cage to form the $^{\#6140}C_{68}{}^{6-}$ anion. The figure clearly shows that the HOMO-LUMO energy gaps of $^{\#6140}C_{68}{}^{6-}$ and $Sc_3N@^{\#6140}C_{68}$ are very similar and also consistent with the energy gap of $^{\#6140}C_{68}$'s LUMO+3 and LUMO+4

clusters. For example, for $Ca@C_n$, two electrons are transferred from calcium atom to C_n cage, and thus the stability of $Ca@C_n$ depends on the (LUMO)-(LUMO+1) energy gap of C_n [22]; while for the endofullerenes encapsulating M_2C_2 cluster, four electrons are transferred from the M_2C_2 cluster to the cage and thus the stability of $M_2C_2@C_n$ is determined by the gap between (LUMO+2) and (LUMO+3) [23, 24].

The Poblet's rule considered the electron transfer between the encapsulated cluster and the carbon cage host, without considering the geometrical factors of the inner cluster and the cage. The cage geometry is another important factor in determining the stability of endofullerenes. First, in principle, those cages with small cavities cannot encapsulate large clusters. For example, no M_3N encapsulated complex of C_{60} was observed so far, although C_{60} also has a (LUMO+3)-(LUMO+4) energy gap greater than 1 eV, which satisfies the Poblet's rule. To date, the smallest endofullerene containing M_3N cluster is C_{68}, which is attributed to the large size of M_3N cluster. Second, the geometries of both the encapsulated clusters and the cage are deformed by multiple interactions with each other. For example, the inner M_3N clusters were deformed from the usual triangular pyramid shape to the planar triangular configuration due to the interaction between the inner cluster and the host carbon cage [25, 26]. In addition, the structure of the outer carbon cage changes due to the embedded clusters. For example, for $M_3N@C_{78}$, the most stable carbon cage changes from D_{5h}-$^{\#24109}C_{78}$, which satisfies the IPR rule, to C_2-$^{\#22010}C_{78}$ with two pairs of DFPs, when the inner cluster changes from small Sc_3N to large Gd_3N [27–31].

The mechanism for endohedral stabilization of non-IPR fullerenes is mostly the same as that of IPR endofullerenes, but due to the existence of adjacent pentagons, the encapsulated metal atoms were found to be favorable to bind at these sites [32, 33]. Owing to the strong coordination between metal atoms and fused pentagon units, the metal atoms cannot move in the cage in most cases of non-IPR

endofullerenes, significantly different from the cases of IPR endofullerenes. The coordination between metal atoms and fused pentagons can greatly deform the geometry of inner cluster. For example, in the case of $Sc_3N@^{\#7854}C_{70}$ and $DySc_2N@^{\#17490}C_{76}$ [34, 35], the M–N–M bond angle is greatly deviated from 120°. This strong coordination was considered to be comparable with that of cyclopentadiene's organometallic coordination compounds [36].

Exohedral Stabilization of Non-IPR Fullerenes

Compared with their IPR analogues [37], non-IPR fullerenes have higher chemical reactivity due to adjacent pentagons, which are easy to bond to other chemical species. Therefore, non-IPR fullerenes are ready to form the derivatives by addition reaction at the fused pentagons and consequentially are stabilized as exohedral derivatives. As early as 1993, the experiments in gas phase proved that small fullerenes (C_n, $n < 60$), which are inevitably non-IPR, could be reduced by n-butane in the gas phase to form hydrogenated products. That gave the first experimental hint that the hydrogenation can be used to stabilize the highly active non-IPR fullerenes [38, 39]. But experimentally unambiguous synthesis and characterization of non-IPR fullerenes by exohedral derivatization was not successful until 2004. The synthesis and characterization of $C_{50}Cl_{10}$ in 2004 opens a new strategy for the synthesis and stabilization of non-IPR fullerenes [40, 41].

Because the sp^2-hybridized carbon atoms are more inclined to form a planar triangular geometry, the curvature of the spherical fullerene inevitably causes the surface strain. This strain can be reflected by the π-orbital axis vector (POAV) pyramidalization angle of the corresponding carbon atom [42]. For sp^2-hybridized carbon atom, the POAV angle (θ_p) can be defined as $\theta_{\sigma\pi}$-90°, $\theta_{\sigma\pi}$ corresponds to the average of the angles between the π orbital of sp^2-hybridized carbon atom and its three adjacent C–C bonds (Fig. 3). The same concept of θ_p can be extended to sp^3-hybridized carbon atoms to describe the degree to which it deviates from the sp^3-hybridized tetrahedral configuration (Fig. 3). Then it can be used to represent the local strain of sp^3-hybridized carbon atoms. θ_p for sp^3-hybridized carbon atoms was defined as the average of the angles between the C–X bond (X is the atom added to a carbon atom during exohedral derivatization) (Fig. 3) and its three adjacent C–C bonds minus 109.47°, the ideal bond angle of the tetrahedral configuration.

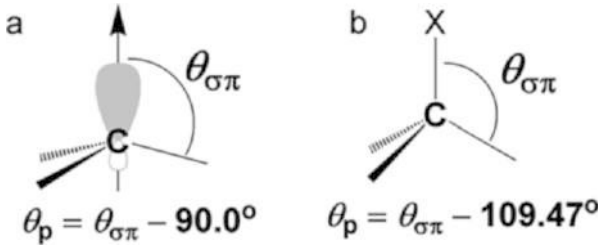

Fig. 3 Scheme of the θ_p for sp^2-hybridized carbon atom (**a**) and sp^3-hybridized carbon atom (**b**)

Graphene sheet has a perfectly planar structure with zero θ_p. The θ_p of spherical C_{60} is 11.64°. For non-IPR fullerenes, the θ_p at the fused pentagon sites is generally as high as 16°, indicating its larger local curvature. That is to say, the angle of the π orbital for the carbon atoms at fused pentagon sites is about 106°, which is quite close to the ideal bond angle of 109.47° for the tetrahedral configuration of sp^3 hybridized carbon atoms. Therefore, the carbon atoms at the fused pentagon sites are more likely to bond with other atoms or groups, transforming its hybridization from sp^2 to sp^3 [4, 5, 39]. After that, the local strain can be released, thereby stabilizing the non-IPR fullerenes. This "strain-relief" principle was verified by the synthesized exohedral derivatives of non-IPR fullerenes, in which the θ_p of carbon atoms at fused pentagon sites was greatly reduced after derivatization.

On the other hand, passivation of fused pentagons can be explained by Hückel's rule [5]. The fused pentagon unit has an 8π electronic state, which is antiaromatic according to Hückel's rule. Non-IPR fullerenes tend to reduce this antiaromatic electronic structure [43, 44]. In addition to the "strain release" principle, the aromaticity of the sp^2-hybridized carbon skeleton remaining after derivatization gives the additional stability for the exohedral derivatives of non-IPR fullerenes. This was summarized as the "local aromaticity" principle for the exohedral stabilization. Taking the structure of $^{\#1809}C_{60}Cl_8$ as an example [45] (the non-IPR isomer of IPR $^{\#1812}C_{60}$ containing two pairs of DFPs), besides the four chlorine atoms bonded to the fused pentagon sites, the other four chlorine atoms are bonded to para-positions of fused pentagon sites. These chlorinated carbon atoms form a sp^3-hybridized chain, dividing the carbon cage into two aromatic fragments, C_{10} and C_{42}. This "local aromaticity" principle was also found in the other reported exohedral derivatives of non-IPR fullerenes, and also useful for the exohedral derivatives of IPR fullerenes [46–49]. This stabilization from local aromaticity enhances the stability of exohedral non-IPR fullerene derivatives [10, 50] and can also account for the site-selective reactivity during the exohedral derivatization of fullerenes.

According to the principles of "strain-relief" and "local aromaticity," many possible structures of non-IPR fullerenes stabilized by exohedral derivatization can be constructed and predicted theoretically. As early as 1993, Kroto et al. [39] predicted a series of small fullerene hydrides (C_n, n = 20, 24, 28, 32, 36, and 50), among which the predicted hydrogenated C_{50} was identical to $C_{50}H_{10}$ synthesized by low-pressure combustion method [51] and similar to that of $C_{50}Cl_{10}$ [40]. There are also a lot of theoretical calculations recently reporting the structures and properties of exohedral derivatives for non-IPR fullerenes [52–67], especially those with carbon numbers between 60 and 70. The structures of these predicted fullerene derivatives are generally based on the most energetically stable fullerene isomers.

Structures of Synthesized Non-IPR Fullerenes

In the following, the representative synthesized and characterized non-IPR fullerenes so far were presented (with increasing number of carbon atoms) in Table 2. In general, the smallest non-IPR fullerene obtained so far is C_{20}, and the largest non-IPR fullerene is C_{102}.

Table 2 Summary of representative non-IPR fullerenes

Cage	Structure captured	Symmetry of parent cage/ derivative	Fused pentagons	Synthetic approach	References
C_{20}	$C_{20}H_{20}$			Organic synthesis	Ref. [68–70]
C_{50}	$^{\#271}C_{50}Cl_{10}$	D_{5d}/D_{5d}	5 DFPs	Arc discharge in the presence of CCl_4	Ref. [40, 41]
	$^{\#271}C_{50}H_{10}$	D_{5d}/D_{5d}	5 DFPs	Low-pressure combustion	Ref. [51]
C_{54}	$^{\#540}C_{54}Cl_8$	C_{2v}/C_2	2 TSFPs	Arc discharge in the presence of CCl_4	Ref. [79]
C_{56}	$^{\#864}C_{56}Cl_{12}$	C_s/C_1	1 TSFPs; 2 DFPs	Arc discharge in the presence of CCl_4	Ref. [79]
	$^{\#913}C_{56}Cl_{10}$	C_{2v}/C_{2v}	4 DFPs		Ref. [80]
	$^{\#916}C_{56}Cl_{12}$	D_2/C_1	4 DFPs		Ref. [81, 82]
C_{58}	$C_{58}(NC1)F_{17}CF_3$	C_s/C_s	2 TSFPs	Fluorination of I_h-C_{60} at 550 °C	Ref. [83]
	$C_{58}(NC1)F_{18}$	C_s/C_1	2 TSFPs		
C_{60}	$^{\#1804}C_{60}Cl_{12}$	C_s/C_s	3 DFPs	Arc discharge in the presence of CCl_4	Ref. [45]
	$^{\#1809}C_{60}Cl_8$	C_{2v}/C_{2v}	2 DFPs		
	$^{\#1809}C_{60}H_8$	C_{2v}/C_s	2 DFPs	Low-pressure combustion	Ref. [84]
	$^{\#1794}C_{60}Cl_{20}$	D_5/D_5	5 DFPs	Chlorination on I_h-C_{60} with $SbCl_5$ at 420–440 °C	Ref. [85]
	$^{\#1805}C_{60}Cl_{24}$	D_{2d}/D_{2d}	4 DFPs		Ref. [85]
	$^{\#1809}C_{60}Cl_{16}$	C_{2v}/C_s	2 DFPs		Ref. [87]
	$^{\#1810}C_{60}Cl_{20}$	D_{2h}/D_{2h}	4 DFPs		Ref. [88]
	$^{\#1810}C_{60}Cl_{24}$	D_{2h}/D_{2h}	4 DFPs		Ref. [85]
	$^{\#1807}C_{60}(CF_3)_{12}$	C_2/C_2	4 DFPs	Further high-temperature trifluoromethylation on the chlorinated mixture	Ref. [87]
	$^{\#1809}C_{60}(CF_3)_{10}$	C_{2v}/C_1	2 DFPs		Ref. [85, 86]
	$^{\#1809}C_{60}(CF_3)_{12}$	C_{2v}/C_1	2 DFPs		Ref. [86]
	$^{\#1809}C_{60}(CF_3)_{14}$	C_{2v}/C_1	2 DFPs		Ref. [85, 86]
	$^{\#1809}C_{60}(CF_3)_{16}$	C_{2v}/C_1	2 DFPs		Ref. [86]
	$^{\#1810}C_{60}(CF_3)_{14}$	D_{2h}/C_1	4 DFPs		Ref. [88]
	$C_{60}(NC1)(CF_3)_{15}F$	C_s/C_1	1 TDFPs; 2 DFPs		Ref. [85]

C_{62}	$C_{62}(4\text{-}MeC_6H_4)_2$	C_{2v}/C_1	0 DFPs	Organic synthesis based on I_h-C_{60}	Ref. [89, 90]
C_{64}	$^{\#1911}C_{64}H_4$	C_{3v}/C_{3v}	1 TDFPs	Arc discharge in the presence of CH_4 and low-pressure combustion	Ref. [91, 92]
	$^{\#1911}C_{64}Cl_4$	C_{3v}/C_{3v}	1 TDFPs	Arc discharge in the presence of CCl_4	Ref. [41]
	$^{\#1911}C_{64}Cl_8$	C_{3v}/C_s	1 TDFPs		
C_{66}	$Sc_2@^{\#4059}C_{66}$	C_{2v}/C_{2v}	2 TSFPs	Arc discharge with metal-doped graphite electrodes	Ref. [8, 93]
	$C_{66}(NC2)H_4$	C_{2v}/C_{2v}	2 DFPs	Low-pressure combustion	Ref. [95]
	$^{\#4169}C_{66}Cl_6$	C_s/C_1	1 TSFPs	Arc discharge in the presence of CCl_4	Ref. [79]
	$^{\#4169}C_{66}Cl_{10}$	C_s/C_1	1 TSFPs		Ref. [79]
	$^{\#4348}C_{66}Cl_{10}$	C_{2v}/C_s	2 DFPs		Ref. [94]
C_{68}	$C_{68}(NC1)Cl_6$	C_1/C_1	2 DFPs	Arc discharge in the presence of CCl_4	Ref. [97]
	$^{\#6094}C_{68}Cl_8$	C_s/C_s	2 DFPs		Ref. [98]
	$Sc_3N@^{\#6140}C_{68}$	D_3/D_3	3 DFPs	Arc discharge with graphite electrodes packed with Sc_3O_2 in an atmosphere of helium and N_2	Ref. [9, 101]
	$C_{68}(NC3)Cl_{26}(OH)_2$	C_1/C_1	2 TSFPs; 3 DFPs	High-temperature (440 °C) chlorination of D_{5d}-C_{70} with $SbCl_5$	Ref. [100]
	$C_{68}(NC3)Cl_{25}(OH)_3$	C_1/C_1	2 TSFPs; 3 DFPs		
C_{70}	$C_{70}(NC2)Cl_6$	C_s/C_s	2 DFPs	Arc discharge in the presence of CCl_4	Ref. [104]
	$^{\#8064}C_{70}Cl_{10}$	C_2/C_1	2 DFPs		Ref. [103]
	$Sc_2O@^{\#7892}C_{70}$	C_2/C_2	2 DFPs	Arc discharge with graphite electrodes packed with Sc_2O_3	Ref. [105]
	$^{\#8111}C_{70}Cl_6$	C_s/C_s	2 DFPs	High-temperature (440 °C) chlorination of D_{5d}-C_{70} with $SbCl_5$ and further dechlorination at 450 °C	Ref. [108]
	$^{\#8111}C_{70}Cl_8$	C_s/C_s	2 DFPs		
	$^{\#8005}C_{70}Cl_{26}$	C_1/C_1	2 DFPs	High-temperature (440 °C) chlorination of D_{5d}-C_{70} with $SbCl_5$	Ref. [107]
C_{72}	$^{\#11188}C_{72}Cl_4$	C_{2v}/C_2	1 DFPs	Arc discharge in the presence of CCl_4	Ref. [110, 111]
	$La@^{\#10612}C_{72}C_6H_3Cl_2$	C_2/C_1	1 DFPs		Ref. [113]
	$La_2@^{\#10611}C_{72}(Ad)$	D_2/C_1	2 DFPs		Ref. [114]

(continued)

Table 2 (continued)

Cage	Structure captured	Symmetry of parent cage/ derivative	Fused pentagons	Synthetic approach	References
				Arc discharge with graphite electrodes packed with La/graphite composite under He flow conditions and modified by photolytic reaction	
	$Sc_2S@^{\#10528}C_{72}$	C_s/C_s	2 DFPs	Arc discharge with Sc-doped graphite electrodes using a mixture of helium and SO_2 atmosphere	Ref. [115]
	$Sc_2C_2@^{\#10528}C_{72}$	C_s/C_s	2 DFPs	Arc discharge with graphite electrodes packed with Sc/Ni_2 alloy	Ref. [116]
C_{74}	$^{\#14049}C_{74}Cl_{10}$	C_1/C_1	1 DFPs	Arc discharge in the presence of CCl_4	Ref. [117]
	$Ho_2O@^{\#13333}C_{74}$	C_2/C_1	2 DFPs	Arc discharge with graphite electrodes packed with Ho_2O_3 and Cu in a He/CO_2 atmosphere	Ref. [118]
C_{76}	$La_2@^{\#17490}C_{76}$	C_s/C_s	2 DFPs	Arc discharge with graphite electrodes packed with $La_2O_3/U_3O_8/ThO_2/Tb_4O_7/Y_2O_3/SmNi_2$	Ref. [119]
	$U@^{\#17418}C_{76}$	C_1/C_1	1 DFPs		Ref. [122]
	$TbNC@^{\#19138}C_{76}$	C_{2v}/C_1	1 DFPs		Ref. [120]
	$YNC@^{\#19138}C_{76}$	C_{2v}/C_1	1 DFPs		Ref. [120]
	$Sm@^{\#19138}C_{76}$	C_{2v}/C_{2v}	1 DFPs		Ref. [121]
	$^{\#18917}C_{76}Cl_{24}$	C_2/C_2	5 DFPs	Chlorination of D_2-C_{76} with $SbCl_5$ at 340 °C for 4–5 days	Ref. [123]
	$^{\#18387}C_{76}Cl_{30}$	C_1/C_1	4 DFPs		Ref. [124]
	$C_{76}(NC3)Cl_{24}$	C_1/C_1	1 TDFPs; 1 quaternary sequentially fused pentagons, 3 DFPs	Chlorination of IPR C_{78} isomers with $SbCl_5$ at 350 °C for 6 weeks	Ref. [126]
	$C_{76}(NC2)(CF_3)_{14}$	C_1/C_1	2 TSFPs; 3 DFPs	Trifluoromethylation of $C_{76}Cl_n$ with gaseous CF_3I at 450 °C	Ref. [125]
	$C_{76}(NC2)(CF_3)_{14}F_2$	C_1/C_1	2 TSFPs; 3 DFPs		
	$C_{76}(NC2)(CF_3)_{16}F_6$	C_1/C_1	2 TSFPs; 3 DFPs		
C_{78}	$^{\#23863}C_{78}Cl_7OOCH_2C_6H_5$	C_1/C_1	1 DFPs	Arc discharge in the presence of CCl_4	Ref. [127]
	$Gd_3N@^{\#22010}C_{78}$	C_2/C_1	2 DFPs	Arc discharge with graphite electrodes packed with Gd_2O_3	Ref. [31]

	$C_{78}(NC2)Cl_{24}$	C_2/C_2	6 DFPs	Chlorination of IPR C_{78} with $SbCl_5$ at 350 °C for 6 weeks	Ref. [126]
C_{80}	$LaSc_2N@C_{80}(NC1)$	C_s/C_s	2 DFPs	Arc discharge with graphite electrodes that contained La_2O_3, Sc_2O_3, and guanidine thiocyanate/U_3O_8/ThO_2/Lu_2O_3	Ref. [131]
	$U@^{\#28324}C_{80}$	C_1/C_1	1 DFPs		Ref. [122]
	$Th@^{\#28324}C_{80}$	C_1/C_1	1 DFPs		Ref. [122]
	$Lu_2O@^{\#31876}C_{80}$	C_1/C_1	1 DFPs		Ref. [132]
C_{82}	$Gd_3N@^{\#39663}C_{82}$	C_s/C_s	1 DFPs	Arc discharge with graphite electrodes packed with Gd_2O_3	Ref. [133]
	$C_{82}(NC2)Cl_{30}$	C_s/C_s	2 DFPs	Chlorination of C_{86} with VCl_4 for 4–12 weeks at 340–360 °C	Ref. [138]
	$^{\#39173}C_{82}Cl_{28}$	C_1/C_1	1 DFPs		
C_{84}	$Gd_3N@^{\#51365}C_{84}$	C_s/C_s	1 DFPs	Arc discharge with graphite electrodes packed with Gd_2O_3/Tb_4O_7 and Fe_xN/Tm_2O_3 and Fe_xN in a He–N_2 atmosphere	Ref. [134]
	$Tb_3N@^{\#51365}C_{84}$	C_s/C_s	1 DFPs		Ref. [152]
	$Tm_3N@^{\#51365}C_{84}$	C_s/C_s	1 DFPs		Ref. [134]
	$Gd_2C_2@^{\#51383}C_{84}$	C_1/C_1	1 DFPs	Arc discharge with graphite electrodes packed with Gd_2O_3	Ref. [136]
	$C_{84}(NC1)Cl_{30}$	C_s/C_s	2 DFPs	Chlorination of C_{86} with VCl_4 for 4 weeks at 340 °C	Ref. [138]
	$C_{84}(NC2)Cl_{30}$	C_1/C_1	2 quaternary sequentially fused pentagons; 2 DFPs	High-temperature chlorination of C_2-$C_{88}(3)$ with VCl_4/$SbCl_5$	Ref. [140]
	$C_{84}(NC2)Cl_{26}$	C_1/C_1	1 TDFPs; 2 DFPs	Chlorination of C_2-$C_{88}(33)$ with VCl_4 at 340–360 °C for 1–6 weeks	Ref. [141]
	$C_{84}(NC2)Cl_{26}$	C_2/C_2	4 DFPs		
C_{86}	$C_{86}(NC1)Cl_{26}$	C_1/C_1	2 DFPs	Chlorination of C_2-$C_{88}(33)$ with VCl_4 at 340–360 °C for 1–6 weeks	Ref. [141]
	$C_{86}(NC1)Cl_{24}$	C_1/C_1	1 TSFPs; 1 DFPs		
C_{88}	$Sc_2C_2@C_{88}(NC1)$	C_s/C_1	1 DFPs	Arc discharge with graphite electrodes packed with Sc_2O_3	Ref. [137]
	$C_{88}(NC1)Cl_{22}$	C_1/C_1	2 DFPs	Chlorination of C_2-$C_{90}(28)$ with VCl_4 at 340–360 °C for 1–6 weeks	Ref. [142]
	$C_{88}(NC1)Cl_{24}$	C_1/C_1	2 DFPs		
C_{90}	$C_{90}(NC1)Cl_{24}$	C_1/C_1	2 DFPs		Ref. [143]

(continued)

Table 2 (continued)

Cage	Structure captured	Symmetry of parent cage/ derivative	Fused pentagons	Synthetic approach	References
	$^{\#86239}C_{90}Cl_{26}$	C_2/C_2	2 DFPs	Chlorination of C_{92} isomers with VCl_4 or VCl_4/ $SbCl_5$ mixture at 350–360 °C for several months	
C_{92}	$C_{92}(NC2)Cl_{32}$	C_1/C_1	4 DFPs	Chlorination of C_{96} isomers with an excess of VCl_4 plus a drop of $SbCl_5$ at 340–360 °C for 1–4 weeks	Ref. [144]
C_{94}	$C_{94}(NC1)Cl_{22}$	C_1/C_1	1 TSFPs; 3 DFPs	Chlorination of C_{96} isomers with an excess of VCl_4 plus a drop of $SbCl_5$ at 340–360 °C for 1–4 weeks	Ref. [147]
	$C_{94}(NC1)Cl_{28}$	C_1/C_1	2 DFPs	Chlorination of C_{100} isomers with an excess of VCl_4 plus a drop of $SbCl_5$ at 350 °C for 4 weeks	Ref. [146]
C_{96}	$^{\#185115}C_{96}Cl_{28}$	C_1/C_1	2 DFPs	Chlorination of C_{102} isomers with an excess of VCl_4 plus a drop of $SbCl_5$ at 350–360 °C for 8–10 days	Ref. [150]
	$C_{96}(NC3)Cl_{20}$	C_1/C_1	1 TSFPs; 1 TDFPs; 3 DFPs	Chlorination of C_{100} isomers with an excess of VCl_4 plus a drop of $SbCl_5$ at 350–360 °C for 4 weeks	Ref. [148]
C_{98}	$C_{98}(NC1)Cl_{26}$	C_1/C_1	2 DFPs	Chlorination of C_{100} isomers with an excess of VCl_4 plus a drop of $SbCl_5$ at 350–360 °C for 1–12 weeks	Ref. [149]
	$C_{98}(NC2)Cl_{26}$	C_1/C_1	1 TDFPs; 1 DFPs	Chlorination of C_{102} isomer with an excess of VCl_4 plus a drop of $SbCl_5$ at 350–360 °C for 8–10 days	Ref. [150]
C_{102}	$^{\#283794}C_{102}Cl_{20}$	C_1/C_1	2 DFPs	Chlorination of C_{102} isomers with an excess of VCl_4 plus a drop of $SbCl_5$ at 350–360 °C for 8–10 days	Ref. [150]

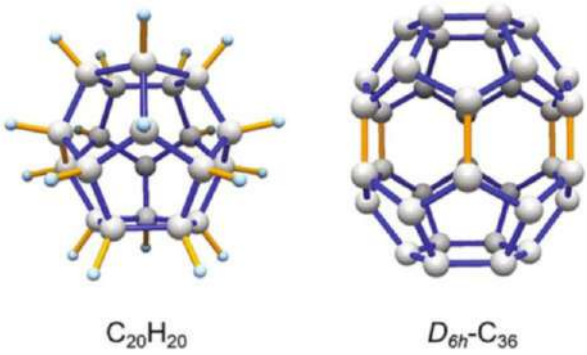

Fig. 4 Molecular structures of $C_{20}H_{20}$ and D_{6h}-C_{36}. Fused pentagons are highlighted in blue

C_{20}. C_{20} is the smallest classical fullerene in theory, which consists solely of pentagons. C_{20} was first synthesized as $C_{20}H_{20}$ (Fig. 4) by multi-steps of organic reactions from cyclopentadiene in 1982, earlier than the discovery of C_{60} and the emergence of fullerene chemistry [68–70]. The synthesis of $C_{20}H_{20}$ was simplified by the "isodrin-pagodane-dodecahedrane" route in a higher yield in the subsequent studies [71, 72]. To produce the pristine C_{20}, the $C_{20}H_{20}$ was brominated to produce $C_{20}H_nBr_{14-n}$ (n = 0, 1, 2, 3), which could undergo debromination under laser ablation and finally result in the formation of bare C_{20} in gas phase. The formed bare C_{20} was studied in situ by the photoelectron spectroscopy, which suggested fullerene-like structure of formed C_{20} [73]. Another C_{20} derivative ($C_{20}Cl_{16}$) was synthesized by chlorination of $C_{20}H_{20}$ [74]. However, under the fullerene formation conditions, such as arc-discharge, laser ablation of graphite, the carbon clusters with 20 carbon atoms generally are considered to be cyclic or bowl shaped.

C_{36}. Carbon solid C_{36} (Fig. 4) was synthesized in a helium-environment arc discharge experiment from graphite, isolated and characterized [75]. The crystal structure of C_{36} was not obtained in experiment, and the captured C_{36} was assigned to be D_{6h}-C_{36} by solid-state NMR measurements. The signal of 438 in time-of-flight mass spectrum indicated that the C_{36} would be derivatized as $C_{36}H_6$. Moreover, the electron-diffraction pattern of the C_{36} microcrystal showed that strong covalent interaction exists between C_{36} molecules because of 1.7 Å intermolecular distance. Theoretical studies also proved that C_{36} was unstable, but it should be stabilized by self-polymerization or exohedral derivatization. In addition, $C_{36}H_6O$ was also observed and characterized by mass spectra [76, 77].

C_{50}. D_{5h}-$^{\#271}C_{50}$ is the first small fullerene synthesized in clustering process and unambiguously characterized [40]. D_{5h}-$^{\#271}C_{50}$ was captured as $^{\#271}C_{50}Cl_{10}$ (Fig. 5), which was first characterized by NMR spectroscopy and mass spectra. Four distinct signals located at 161.5, 146.6, 143.0, and 88.7 ppm were present in ^{13}C NMR measurement of $^{\#271}C_{50}Cl_{10}$, which indicated it had a molecular symmetry of D_{5h}, the same as the parent D_{5h}-$^{\#271}C_{50}$. Mass spectrum and theoretical simulations confirmed the molecular structure as $^{\#271}C_{50}Cl_{10}$. $^{\#271}C_{50}$ is not the most stable one of all 271 C_{50} isomers, but according to the $2(N + 1)^2$ electron counting rule for

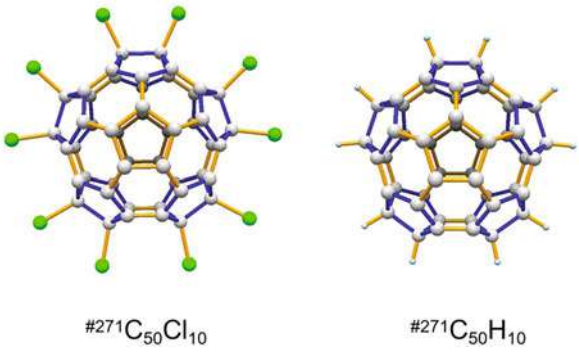

Fig. 5 Molecular structures of $^{\#271}C_{50}Cl_{10}$ and $^{\#271}C_{50}H_{10}$. Fused pentagons are highlighted in blue

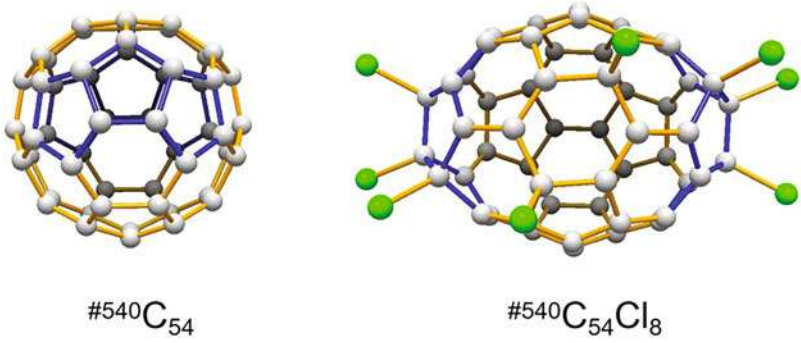

Fig. 6 Molecular structures of C_{2v}-$^{\#540}C_{54}$ and $^{\#540}C_{54}Cl_8$. Fused pentagons are highlighted in blue

spherical molecules, $^{\#271}C_{50}$ is expected be highly aromatic with a completely filled electron shell [78]. Even though, owning to the high strain from DFPs, pristine $^{\#271}C_{50}$ could not survive as its pristine form and finally captured as $^{\#271}C_{50}Cl_{10}$. The further single-crystal X-ray diffraction (SCXRD) analysis of $^{\#271}C_{50}Cl_{10}$ was provided in the subsequent studies [41], which clearly revealed its Saturn-like molecular structure. On the other hand, $^{\#271}C_{50}$ was first predicted to be stabilized by hydrogenation and captured as $^{\#271}C_{50}H_{10}$ [39]. After nearly 20 years, the hydrofullerene $^{\#271}C_{50}H_{10}$ (Fig. 5) was finally synthesized by the low-pressure combustion [51]. The structure of $^{\#271}C_{50}H_{10}$ was characterized by ^{13}C and ^{1}H NMR spectroscopy, which revealed the same cage symmetry and addition pattern as $^{\#271}C_{50}Cl_{10}$. Further investigations indicated $^{\#271}C_{50}Cl_{10}$ had the better redox reversibility and electronic accepting ability, suggesting its potential as the acceptor in organic solar cells.

C_{54}. $^{\#540}C_{54}$ is the only captured C_{54} isomer among all 580 classical isomers [79]. $^{\#540}C_{54}$ was predicted as the most stable C_{54} cage by theoretical calculation, but it is still so unstable that exohedral derivatization is needed. $^{\#540}C_{54}$ was also synthesized by the chorine-involved arc-discharge and captured as $^{\#540}C_{54}Cl_8$ (Fig. 6), similar with the synthesis of $^{\#271}C_{50}Cl_{10}$. The structure of $^{\#540}C_{54}Cl_8$ was clearly

characterized by SCXRD. Notably, the pentagons in $^{\#540}C_{54}Cl_8$ form the TFSP motifs, different from the case of $^{\#271}C_{50}$. Two pairs of TSFP motifs were found in $^{\#540}C_{54}Cl_8$. Interestingly, only three chlorine atoms were bonded on a TSFP motif, which indicated not all the carbon atoms at the fused pentagon sites should be capped with exohedral groups.

C_{56}. Three C_{56} isomers (C_{2v}-$^{\#913}C_{56}$, C_s-$^{\#864}C_{56}$, and D_2-$^{\#916}C_{56}$) are obtained experimentally so far [79–82] (Fig. 7). The first C_{56} isomer experimentally isolated was C_{2v}-$^{\#913}C_{56}$, synthesized as $^{\#913}C_{56}Cl_{10}$ using chlorine-involved arc discharge reactor [80]. The structure of $^{\#913}C_{56}Cl_{10}$ was characterized by SCXRD, showing four pairs of DFPs. In addition to the eight chlorines bonded at the fused-pentagon sites, two chlorines were added at the para-position of fused-pentagon sites. Consequently, a belt of the sp^3 hybridized carbon atoms cuts the fullerene cage into two aromatic fragments, thus satisfying the "local-aromaticity" principle. Notably, before the synthesis and characterization of $^{\#913}C_{56}Cl_{10}$, the same chlorofullerene was theoretically predicted [57]. After $^{\#913}C_{56}Cl_{10}$, $^{\#864}C_{56}Cl_{12}$ was also synthesized by chlorine-involved arc discharge and reported in 2010 [79]. Different from $^{\#913}C_{56}Cl_{10}$, $^{\#864}C_{56}Cl_{12}$ has one TSFP and two DFPs. In consistent with chlorination of $^{\#540}C_{54}$, the four fused pentagon sites in TSFP in $^{\#864}C_{56}Cl_{12}$ bonded to three chlorines, remaining one site unsaturated. The POAV analysis indicated the θ_p of remained fused pentagon site was decreased from 16.2° to 9.9°, which is comparable to that of IPR $^{\#1812}C_{60}$. It clearly shows the strain relief in $^{\#864}C_{56}Cl_{12}$ after chlorination. The last C_{56} isomer reported is $^{\#916}C_{56}$, which was also captured as the chlorofullerene, $^{\#916}C_{56}Cl_{12}$. $^{\#916}C_{56}Cl_{12}$ was synthesized by Jansen and co-workers using chlorine-involved radio frequency furnace and by Xie and co-works using chlorine-involved arc discharge reactor [81, 82]. Both groups reported $^{\#916}C_{56}Cl_{12}$ almost at the same time and obtained the structure of $^{\#916}C_{56}Cl_{12}$ by SCXRD. Among the C_{56} isomers, these three captured isomers $^{\#864}C_{56}$, $^{\#913}C_{56}$, and $^{\#916}C_{56}$ are the most stable ones, according to the theoretical

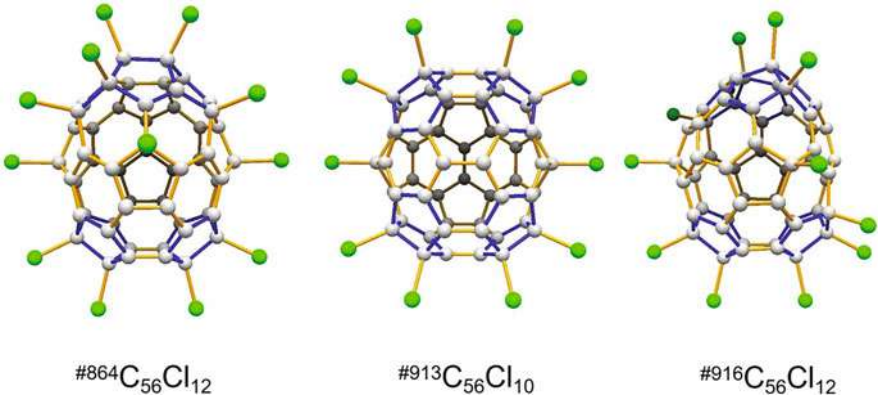

Fig. 7 Molecular structures of $^{\#864}C_{56}Cl_{12}$, $^{\#913}C_{56}Cl_{10}$, and $^{\#916}C_{56}Cl_{12}$. Fused pentagons are highlighted in blue

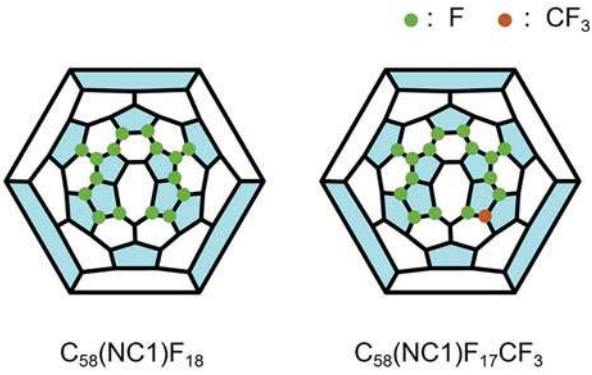

Fig. 8 Schlegel diagrams of $C_{58}(NC1)F_{18}$ and $C_{58}(NC1)F_{17}CF_3$. Pentagons are highlighted in blue

energy calculations. Although structure connections show that $^{\#913}C_{56}$ and $^{\#916}C_{56}$ can be transformed into $^{\#864}C_{56}$ by only one step of Stone-Wales transformation, the experimental evidence for that isomerization still lacks.

C_{58}. Only one C_{58} isomer is characterized in experiment up till now [83] (Fig. 8). This heptagon-containing C_{58} was synthesized in a top-down approach by fluorination of IPR $^{\#1812}C_{60}$ at 550 °C by Taylor and co-workers, which opened the avenue of postfunctionalization-promoted cage transformation. Two stable products, $C_{58}(NC1)F_{18}$ and $C_{58}(NC1)F_{17}CF_3$, were characterized by ^{19}F NMR spectroscopy. Comparing to the IPR $^{\#1812}C_{60}$, it is believed that a C_2 junction between pentagon and hexagon was removed during fluorination. Notably, this C_{58} is the first heptagon-containing fullerene experimentally synthesized.

C_{60}. For more than two decades, IPR I_h-$^{\#1812}C_{60}$ was the sole C_{60} species experimentally available, because the rest isomers of C_{60} contain fused pentagon units and are consequentially instable under ambient conditions. In 2008, two I_h-symmetry-breaking C_{60} isomers (C_{2v}-$^{\#1809}C_{60}$ and C_s-$^{\#1804}C_{60}$) were reported (Fig. 9) [45]. These two C_{60} isomers were formed in arc-discharge reactor, stabilized as $^{\#1809}C_{60}Cl_8$ and $^{\#1804}C_{60}Cl_{12}$, along with the formation of IPR $^{\#1812}C_{60}$. There are two pairs of DFPs in $^{\#1809}C_{60}$ while $^{\#1804}C_{60}$ owns three pairs. These DFPs were stabilized by chlorination, transforming the hybridization from sp^2 to sp^3, which released the unfavorable strain of fused pentagons. In addition to the chlorines at the fused pentagon sites, the additional chlorines were added to fullerene cage. Similar to other chlorofullerenes, the belt of sp^3 carbon atoms separated the fullerene cage into aromatic domains, which gave the local aromaticity to $^{\#1809}C_{60}Cl_8$ and $^{\#1804}C_{60}Cl_{12}$. Structurally, C_{2v}-$^{\#1809}C_{60}$ can link both IPR $^{\#1812}C_{60}$ and C_s-$^{\#1804}C_{60}$ through one step of Stone-Wales transformation. Despite the $^{\#1809}C_{60}$ and $^{\#1804}C_{60}$ are more unstable than the most famous I_h-$^{\#1812}C_{60}$, their chlorinated derivatives own larger HOMO-LUMO gaps.

$^{\#1809}C_{60}$ was also synthesized in low-pressure combustion, stabilized as $^{\#1809}C_{60}H_8$ (Fig. 9) [84]. Owing to different addition pattern of hydrogenation from chlorination, the molecular symmetry of $^{\#1809}C_{60}H_8$ was decreased to C_s,

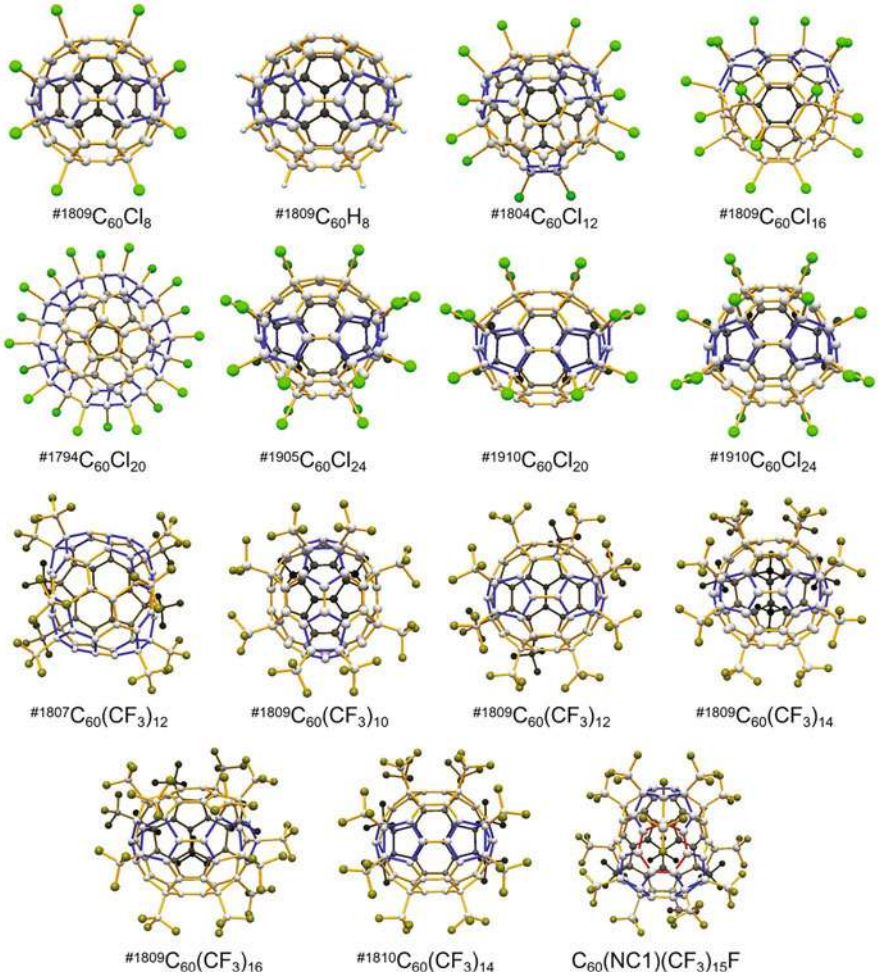

Fig. 9 Molecular structures of C_{60} derivatives with fused pentagons. Fused pentagons and heptagon are highlighted in blue and red, respectively

compared with the C_{2v} symmetry of pristine $^{\#1809}C_{60}$ and $^{\#1809}C_{60}Cl_8$. In addition, three classical non-IPR C_{60} isomers, captured as $^{\#1794}C_{60}Cl_{20}$, $^{\#1805}C_{60}Cl_{24}$, $^{\#1809}C_{60}Cl_{16}$, and $^{\#1810}C_{60}Cl_{24}$ (Fig. 9), were also synthesized using the postfunctionalization-promoted cage transformation by reacting I_h-$^{\#1812}C_{60}$ with $SbCl_5$ at 420–440 °C in the sealed ampoule [85]. Further trifluoromethylation of the chlorinated mixtures afforded $^{\#1807}C_{60}(CF_3)_{12}$, $^{\#1809}C_{60}(CF_3)_n$ (n = 10, 12, 14, 16), and a nonclassical $C_{60}(NC1)(CF_3)_{15}F$ [86–88]. $^{\#1794}C_{60}$, $^{\#1805}C_{60}$, $^{\#1807}C_{60}$, and $^{\#1810}C_{60}$ have four, four, four, and five pairs of DFPs, respectively. Remarkably, $C_{60}(NC1)$ in $C_{60}(NC1)(CF_3)_{15}F$ contains one heptagon surrounded by two DFPs and one TDFP (Fig. 9), which represents the first heptagon-containing C_{60} isomer

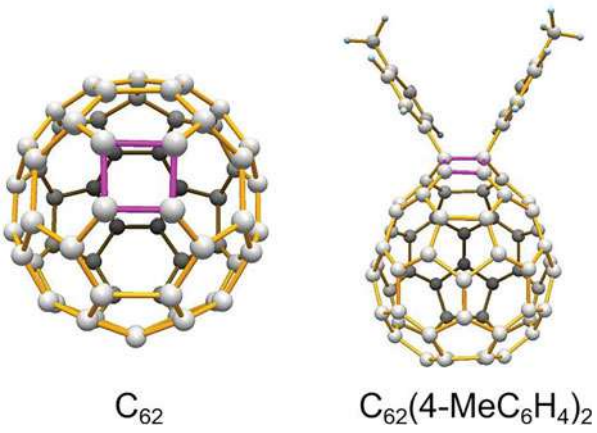

Fig. 10 Molecular structures of C_{62} and $C_{62}(4\text{-}MeC_6H_4)_2$

[85]. Different from the chlorinated non-IPR C_{60} isomer captured in clustering processes, the chlorinated non-IPR C_{60} formed by postfunctionalization-promoted cage transformation are highly derivatized, owing to the harsh reaction conditions. Further reduction of these highly chlorinated non-IPR C_{60}s could provide a way to access non-IPR fullerenes in large quantity, taking advantage of feasible availability of parent I_h-$^{\#1812}C_{60}$.

C_{62}. Same with C_{58}, C_{62} has not been isolated from clustering system as yet. But opposite to C_{58}, the formation of C_{62} requires a C_2 insertion basing on IPR I_h-$^{\#1812}C_{60}$. By multi-steps of organic reactions, a four-membered ring was built, yielding $C_{62}X_2$ (Fig. 10) (X = H, 4-MeC_6H_4, 2-Py,3,5-$(MeO)_2C_6H_3$) [89, 90]. According to the cage structure of C_{62}, the introduction of four-membered ring eliminates two pentagons but gains two hexagons, compared with IPR I_h-$^{\#1812}C_{60}$. Although the synthesis of such nonclassical C_{62} cuts no ice with the mechanism of fullerene formation, the crystal structure of $C_{62}(4\text{-}MeC_6H_4)_2$ still provides a good example for the stabilization of four-membered ring. $C_{62}X_2$ is the only case of fullerene containing four-membered ring.

C_{64}. $^{\#1911}C_{64}$ was the only isomer of C_{64} synthesized and characterized. It was stabilized as both chlorofullerene and hydrofullerene, in a form of $^{\#1911}C_{64}H_4$, $^{\#1911}C_{64}Cl_4$, and $^{\#1911}C_{64}Cl_8$ [41, 91, 92] (Fig. 11). In 2006, $^{\#1911}C_{64}H_4$ was first synthesized in a methane-involved arc discharge reactor. The structure of $^{\#1911}C_{64}H_4$ was characterized by mass spectra, ^{13}C, ^{1}H, and 2D-HMQC NMR spectroscopy, IR spectroscopy. Combined with DFT calculations, the structure of $^{\#1911}C_{64}H_4$ was unambiguously determined. $^{\#1911}C_{64}H_4$ has triple directly fused pentagons and the four fused pentagon sites of which was bonded to four hydrogens. Later, the low-pressure combustion is also proved to be a promising macroscopic synthesis route for $^{\#1911}C_{64}H_4$ in 2010. $^{\#1911}C_{64}$ is the first captured cage with TDFP, and it is more unstable than many other C_{64} isomers theoretically. As the $^{\#1911}C_{64}$ can be treated as a "Y" shape C_4 cluster inserting on a hexagon of I_h-C_{60} cage structurally, the formation of $^{\#1911}C_{64}$ hints that the insertion of C_4 units into fullerene cage could

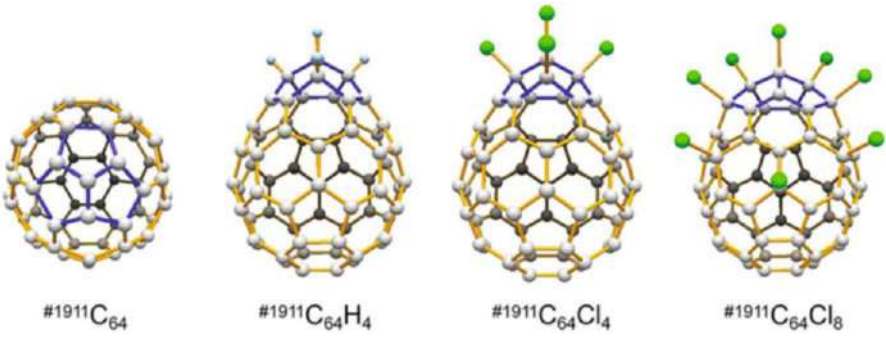

Fig. 11 Molecular structures of $^{\#1911}C_{64}$, $^{\#1911}C_{64}H_4$, $^{\#1911}C_{64}Cl_4$, and $^{\#1911}C_{64}Cl_8$

be a possible route for fullerene growth. Besides, the chlorine stabilized $^{\#1911}C_{64}$ was also reported as $^{\#1911}C_{64}Cl_4$ and $^{\#1911}C_{64}Cl_8$. Both $^{\#1911}C_{64}Cl_4$ and $^{\#1911}C_{64}Cl_8$ were validated by SCXRD. They shared the same fullerene cage, but different chlorination pattern. $^{\#1911}C_{64}Cl_4$ has the same cage and substitution pattern with $^{\#1911}C_{64}H_4$, whereas, in $^{\#1911}C_{64}Cl_8$, one of the four carbon atoms at the fusion sites in triple directly fused pentagon motif stays unsaturated, which is stabilized by forming the aromatic benzenoid fragment (Fig. 11). The formation of $^{\#1911}C_{64}Cl_4$ and $^{\#1911}C_{64}Cl_8$ exemplifies the strain-relief and local aromaticity principles for the stabilization of non-IPR fullerenes.

C_{66}. Four C_{66} isomers have been characterized so far (Fig. 12). Three of them are classical isomers (C_{2v}-$^{\#4059}C_{66}$, C_s-$^{\#4169}C_{66}$, and C_{2v}-$^{\#4348}C_{66}$) which were captured by metal encapsulation and chlorination, while the rest nonclassical C_s-C_{66}(NC2) was obtained by hydrogenation [8, 79, 93–95]. $^{\#4169}C_{66}Cl_6$, $^{\#4169}C_{66}Cl_{10}$, and $^{\#4348}C_{66}Cl_{10}$ were synthesized in the chlorine-involved arc discharge using CCl_4 as the chlorine source. $^{\#4169}C_{66}Cl_6$ and $^{\#4169}C_{66}Cl_{10}$ share the same carbon cage, which had a set of TSFP (Fig. 12). Similar with other fullerenes containing TSFP, three out of four fused pentagon sites were added with chlorine, while the rest one stayed unsaturated. They demonstrated the unique chlorination pattern of TSFP. Chlorination processes of $^{\#4169}C_{66}$ to $^{\#4169}C_{66}Cl_6$ and $^{\#4169}C_{66}Cl_{10}$ were well illustrated by theoretical simulations, revealing a step-wise chlorination mechanism. In the chlorine-involved arc discharge, $^{\#4348}C_{66}$ was also synthesized and captured as chlorofullerene $^{\#4348}C_{66}Cl_{10}$. $^{\#4348}C_{66}Cl_{10}$ has two pairs of DFPs and the same fullerene cage of previously assigned $Sc_2@^{\#4348}C_{66}$, which was later corrected and reassigned as $Sc_2@^{\#4059}C_{66}$. Up to date, the non-IPR fullerenes stabilized by exohedral derivatization have different cages from those stabilized by endohedral encapsulation, which hints the different formation mechanism between hollow fullerenes and endofullerenes.

In the low-pressure combustion system, a $C_{66}(NC2)H_4$ was obtained and characterized by SCXRD [95]. The structure of $C_{66}(NC2)H_4$ owns two heptagons and two pairs of DFPs. $C_{66}(NC2)H_4$ was the first heptagon-containing fullerene found in low-pressure combustion, which suggested the heptagons were also the fundamental building block in addition to hexagons and pentagons in combustion.

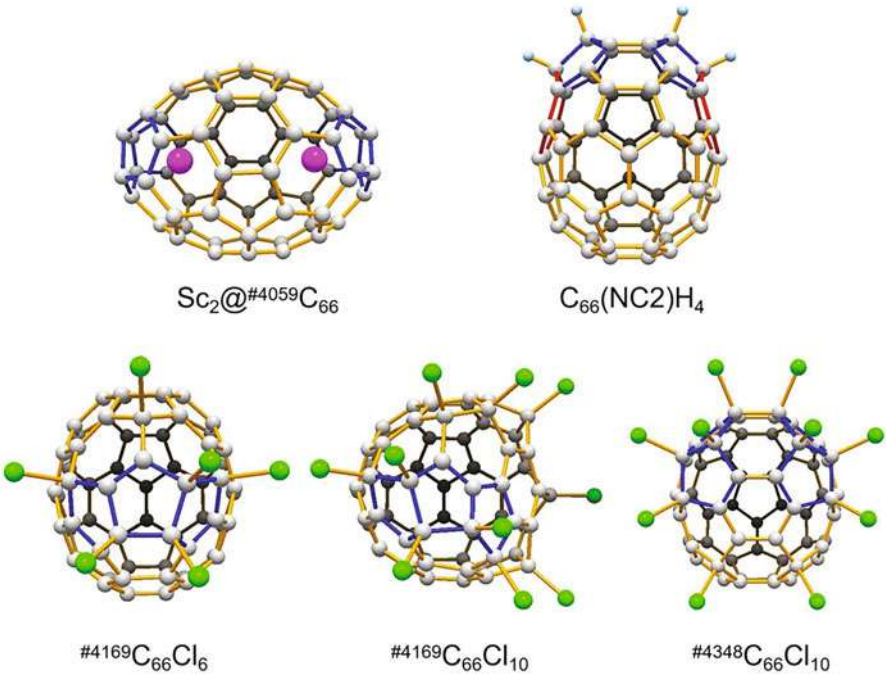

Fig. 12 Molecular structures of $Sc_2@^{\#4059}C_{66}$, $C_{66}(NC2)H_4$, $^{\#4169}C_{66}Cl_6$, $^{\#4169}C_{66}Cl_{10}$, and $^{\#4348}C_{66}Cl_{10}$. Fused pentagons and heptagon are highlighted in blue and red, respectively

Owning the geometrical match, fullerenes with small carbon numbers are too small to encapsulate large clusters. Starting from C_{66}, non-IPR fullerenes are able to be stabilized and synthesized by endohedral derivatization. $Sc_2@C_{66}$ was reported as the first non-IPR fullerene in 2000 and still the smallest endofullerene characterized. The synthesis and isolation of $Sc_2@C_{66}$ opened the experimental field of non-IPR fullerenes. Because C_{66} has no isomer satisfying the IPR rule, the cage of $Sc_2@C_{66}$ inevitably has fused pentagons. According to the ^{13}C NMR spectra and a synchrotron X-ray powder diffraction study in combination with maximum entropy method/Rietveld analysis, the cage structure of $Sc_2@C_{66}$ was first assigned as $^{\#4348}C_{66}$. Following this work, DFT calculations [96] rechecked the structure of $Sc_2@C_{66}$ and found $Sc_2@^{\#4059}C_{66}$, containing two TSFP was the most stable isomer rather than the reported $Sc_2@^{\#4348}C_{66}$. Notably, $^{\#4059}C_{66}$ and $^{\#4348}C_{66}$ have the same cage symmetry, C_{2v}, therefore $Sc_2@^{\#4059}C_{66}$ fits the original ^{13}C NMR spectrum as well. In 2014, Akasaka and co-workers repeated the synthesis of $Sc_2@C_{66}$ and final definitively assign it as $Sc_2@^{\#4059}C_{66}$ in terms of SCXRD and 2D INADEQUATE NMR spectroscopy [93]. Different from previously assigned $^{\#4348}C_{66}$, $Sc_2@^{\#4059}C_{66}$ have two sets of TSFP (Fig. 12), which are stabilized by the coordination with Sc atoms. $Sc_2@^{\#4059}C_{66}$ is the only endofullerene containing triple fused pentagons isolated up to date [93].

C_{68}. Two C_{68} isomers (C_{68}(NC1) and C_s-$^{\#6094}C_{68}$) were synthesized by chlorine-involved clustering process [97, 98] (Fig. 13). C_{68}(NC1) was verified to be formed in a bottom-up fashion by ^{13}C-labelled experiments and stabilized by six chlorines in situ. Chlorines were bonded on the intersection of the heptagon and fused pentagons to relief the cage strain. $^{\#6094}C_{68}$ was also synthesized through a bottom-up way by the radio-frequency furnace containing CCl_4. The crystal structure of its chlorinated derivative was characterized as $^{\#6094}C_{68}Cl_8$. Despite both $^{\#6094}C_{68}$ and the most stable $^{\#6290}C_{68}$ have two pairs of DFPs, $^{\#6094}C_{68}$ has an energy 17.4 kcal/mol higher [99]. Meanwhile, local aromaticity of $^{\#6094}C_{68}Cl_8$ was investigated by NICS values theoretically, revealing addition stabilization effects.

Two derivatives of C_{68} were synthesized by high-temperature (440 °C) chlorination of D_{5d}-C_{70} with $SbCl_5$ as $C_{68}(NC3)Cl_{26}(OH)_2$ and $C_{68}(NC3)Cl_{25}(OH)_3$ by chlorination-promoted cage transformation (Fig. 13). This nonclassical C_{68}(NC3) contains 3 heptagons and 15 pentagons arranged in DFPs and TSFPs [100]. This work demonstrated the ability of chlorination at high temperature transform C_{70} into smaller fullerene.

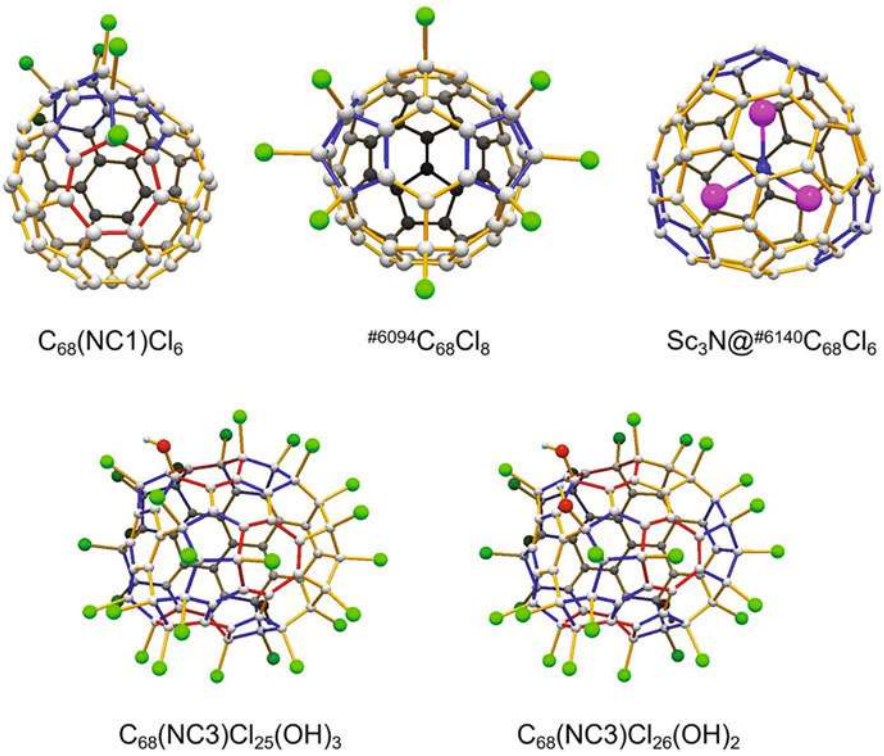

Fig. 13 Molecular structures of C_{68} isomers. Fused pentagons and heptagon are highlighted in blue and red, respectively

C_{68} can be also stabilized by endohedral derivatization (Fig. 13). $Sc_3N@D_3$-$^{\#6140}C_{68}$ was reported in 2000 [9] as the first non-IPR fullerenes together with $Sc_2@C_{66}$. It was characterized by mass spectra and NMR spectroscopy and its structure was finally confirmed in 2003 by SCXRD [101]. $Sc_3N@D_3$-$^{\#6140}C_{68}$ has three pairs of DFPs, which coordinated with three Sc atoms of Sc_3N cluster. Notably the number of fused pentagon pairs in $Sc_3N@D_3$-$^{\#6140}C_{68}$ is still the largest among the endofullerenes, which could due to the limited number of encapsulated metal atoms in the endofullerenes. It opens the question whether the non-IPR fullerene containing more than three pairs of fused pentagons can be stabilized by encapsulation of metal atoms or metal clusters. $Sc_2C_2@C_{2v}$-$^{\#6073}C_{68}$ was also synthesized, isolated, and characterized experimentally [23]. The cage structure of $Sc_2C_2@C_{2v}$-$^{\#6073}C_{68}$ was assigned by ^{13}C NMR spectroscopy in combination with DFT calculations. However, due to lacking of SCXRD data, the controversy of whether it is $Sc_2C_2@C_{68}$ or $Sc_2@C_{70}$ still exists [102].

C_{70}. Two reported C_{70} (C_2-$^{\#8064}C_{70}$ and C_s-C_{70}(NC2)) with fused pentagons have been synthesized (Fig. 14) so far in the arc discharge in the presence of CCl_4. $^{\#8064}C_{70}$ has two pairs of DFPs and was chlorinated as $^{\#8064}C_{70}Cl_{10}$. Serving as the only reported classical isomer of D_{5h}-C_{70} in exohedral derivatization, $^{\#8064}C_{70}$ provides an helpful experimental linker for the formation mechanism of fullerene [103]. The double negatively curved C_{70}(NC2) was captured and chlorinated as $C_{70}(NC2)Cl_6$. A heptagon-involved pathway from $^{\#4169}C_{66}$ to C_{70}(NC2) with direct-

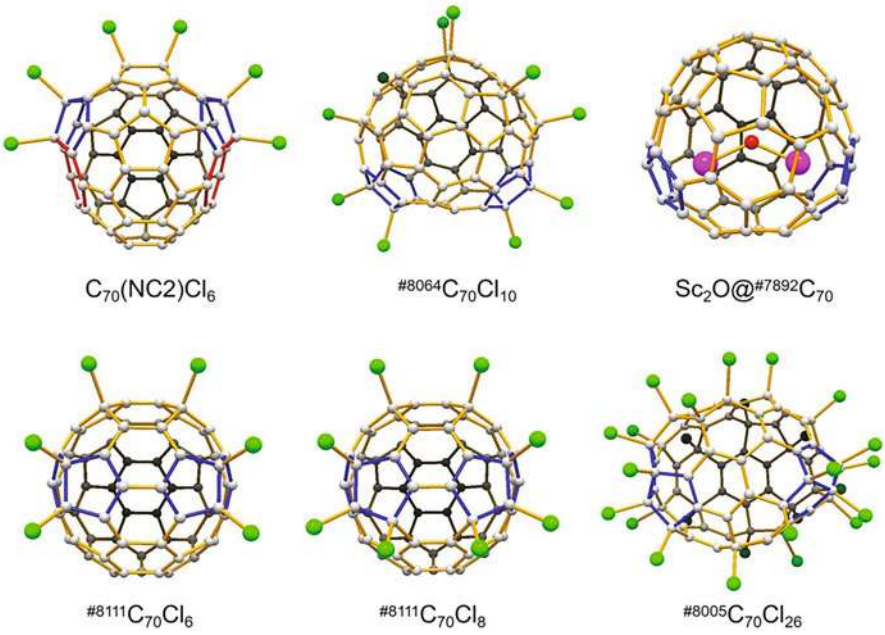

Fig. 14 Molecular structures of C_{70} isomers. Fused pentagons and heptagon are highlighted in blue and red, respectively

C_2-insertions via C_{68}(NC1) was proposed theoretically and showed low energy barriers, which was in line with the bottom-up fashion proved by ^{13}C-labelled experiments. Further analysis shows that chlorination at the intersection of a heptagon and two adjacent pentagons can reduce θ_p and greatly enlarge the HOMO-LUMO gap [104].

Another non-IPR C_2-$^{\#7892}C_{70}$ was synthesized by encapsulating Sc_2O metal cluster inside as $Sc_2O@^{\#7892}C_{70}$ (Fig. 14) and its structure was revealed by SCXRD [105]. Furthermore, $Sc_3N@^{\#7854}C_{70}$ and $Sc_2S@^{\#7892}C_{70}$ were synthesized and well characterized, but without SCXRD data [34, 106]. Postfunctionalization-promoted cage transformation of IPR D_{5d}-C_{70} using $SbCl_5$ at 440 °C and 450 °C produced two non-IPR $^{\#8111}C_{70}Cl_{6/8}$ and $^{\#8005}C_{70}Cl_{26}$, respectively. $^{\#8111}C_{70}Cl_{6/8}$ and $^{\#8005}C_{70}Cl_{26}$ (Fig. 14) were characterized by SCXRD and both of them have two pairs of DFPs [107, 108]. The cage transformation based on IPR D_{5h}-C_{70} by chlorination also showed the potential to provide the non-IPR C_{70} cage in large quantity, although the harsh reaction conditions and toxic chlorination agents were required.

C_{72}. $^{\#11188}C_{72}$ is a special cage with fused pentagons violating the "universal" IPR rule for fullerenes because $^{\#11188}C_{72}$ is more stable than its IPR-following cage D_{6h}-C_{72} [109] thermodynamically. By introducing CCl_4 to the carbon arc plasma in situ, $^{\#11188}C_{72}Cl_4$ was synthesized and determined by SCXRD (Fig. 15) [110, 111]. APCI mass spectrometric measurements at different furnace temperatures indicated the facile dechlorination of $^{\#11188}C_{72}Cl_4$ and the possible stability of bare $^{\#11188}C_{72}$ at appropriate temperature. However, local strain caused by the double adjacent pentagons motif still hinders $^{\#11188}C_{72}$ obtained in pristine form under the ambient conditions.

The first C_{72} endofullerene was stabilized as $La_2@C_{72}$ in 2003, and the cage structure was finally characterized as non-IPR D_2-$^{\#10611}C_{72}$ in 2008 by functionalized with an adamantylidene carbine (Fig. 15) [112, 113]. Another non-IPR isomer $^{\#10612}C_{72}$ was obtained and characterized by SCXRD as $La@^{\#10612}C_{72}$ with an external $C_6H_3Cl_2$ group (Fig. 15), which showed the interesting case combining the endohedral and exohedral stabilization [114]. Moreover, C_s-$^{\#10528}C_{72}$ was synthesized and stabilized by encapsulation of Sc_2S and Sc_2C_2 clusters. Both of them were clearly characterized by SCXRD [115, 116]. As shown, the shape of non-IPR fullerene host $^{\#10528}C_{72}$ matches well with the angular shape of the encapsulated Sc_2S and Sc_2C_2 cluster, in comparison with egg-shaped $La@^{\#10612}C_{72}$ and D_2-$^{\#10611}C_{72}$ (Fig. 15), which clearly showed the geometrical matching between inner cluster and host fullerene.

C_{74}. The first exohedral derivative of non-IPR C_{74} was reported in 2016, stabilized as $^{\#14049}C_{74}Cl_{10}$ [117] (Fig. 16). Capping with ten chlorines, $^{\#14049}C_{74}Cl_{10}$ was synthesized and isolated in chlorine-involved arc-discharge reactor. The structural characterization of $^{\#14049}C_{74}Cl_{10}$ was achieved by SCXRD, showing a cage structure with one DFP units. Chlorination process of $^{\#14049}C_{74}$ was simulated in a step-wise mechanism. Moreover, $^{\#14049}C_{74}$ was also suggested to be formed by two steps of C_2-insertions on D_{5d}-C_{70} through the known $^{\#11188}C_{72}$, based on their structures. The other non-IPR C_{74} is captured by endohedral stabilization as $Ho_2O@^{\#13333}C_{74}$ (Fig. 16) [118]. The SCXRD data showed that the angle of Ho−O−Ho cluster is

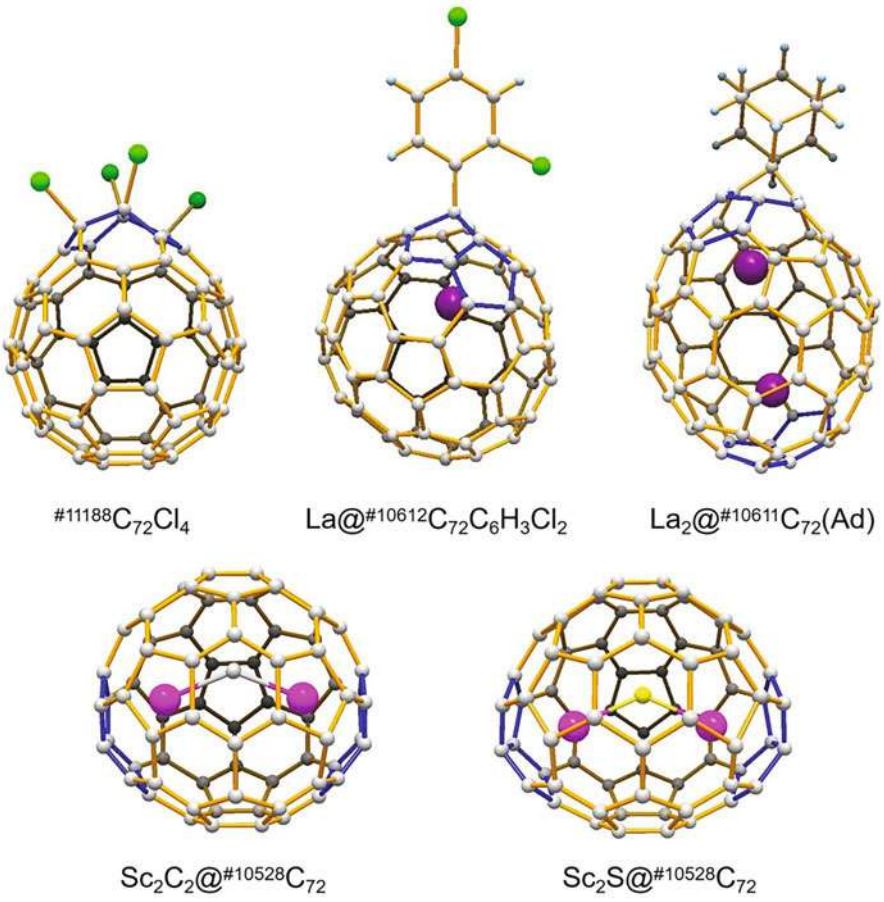

Fig. 15 Molecular structures of $^{\#11188}C_{72}Cl_4$, La@$^{\#10612}C_{72}C_6H_3Cl_2$, La_2@$^{\#10611}C_{72}$(Ad), Sc_2S@$^{\#10528}C_{72}$, and Sc_2C_2@$^{\#10528}C_{72}$. Fused pentagons are highlighted in blue

larger than 170°, much larger than typical angle of free M-O-M cluster. Two pairs of DFPs in $^{\#13333}C_{74}$ show the clear coordination to Ho atoms, which responses to the stabilization of fused pentagons and deformed shape of encapsulated Ho_2O cluster.

C_{76}. C_s-$^{\#17490}C_{76}$ was first reported as $DySc_2N$@$^{\#17490}C_{76}$ predicted by theoretical calculation [35] and the SCXRD of La_2@$^{\#17490}C_{76}$ (Fig. 17) revealed the cage structure experimentally [119]. $DySc_2N$@$^{\#17490}C_{76}$ and La_2@$^{\#17490}C_{76}$ shared the same cage but had completely different types of encapsulated clusters. The reason accounting for this is that their cage has the same electronic structure $(^{\#17490}C_{76})^{6-}$, due to both $DySc_2N$ and La_2 donate six electrons to the cage. The second non-IPR cage C_{2v}-$^{\#19138}C_{76}$ (Fig. 17) was stabilized as TbNC@$^{\#19138}C_{76}$, YNC@$^{\#19138}C_{76}$, and Sm@$^{\#19138}C_{76}$ [120, 121], the cage of which accepted two electrons from the inner clusters and formed the same $(^{\#17418}C_{76})^{2-}$ anion. Another isolated C_{76}

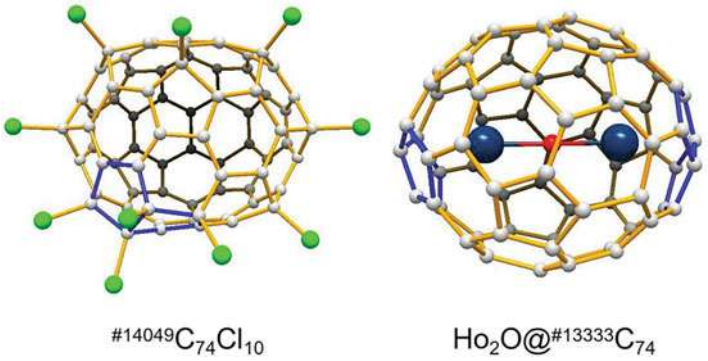

Fig. 16 Molecular structures of $^{\#14049}C_{74}Cl_{10}$ and $Ho_2O@^{\#13333}C_{74}$. Fused pentagons are highlighted in blue

endofullerene is $U@^{\#17418}C_{76}$ (Fig. 17), in which U atom donated four electrons to the fullerene host [122]. Two pairs of DFPs were found in C_s-$^{\#17490}C_{76}$ while only one pair exists in $^{\#19138}C_{76}$ and $^{\#17418}C_{76}$. These isolated endofullerenes isomers of C_{76} demonstrated the number of electron transferred from the inner cluster can directly determine the cage structure of the fullerene host.

Non-IPR $^{\#18917}C_{76}Cl_{24}$ and $^{\#18387}C_{76}Cl_{30}$ (Fig. 17) were synthesized by chlorination-promoted transformation of IPR D_2-C_{76} with $SbCl_5$ [123, 124], which is the initial case of chlorination-promoted cage transformation. Nonclassical $C_{76}(NC2)(CF_3)_nF_m$ (n/m = 14/0, 14/2, 16/6) was then synthesized by further trifluoromethylation of the chlorination products of IPR D_2-C_{76} [125]. Moreover, a new C_{76} cage with three heptagons (Fig. 17) was synthesized by chlorination-promoted cage transformation of IPR C_{78} isomers [126], during which a C_2 unit was lost.

C_{78}. At present, $^{\#23863}C_{78}$ is the largest non-IPR hollow cage obtained in clustering systems (Fig. 18). Eight exohedral derivatization sites were capped with seven -Cl groups and one $-OOCH_2C_6H_5$ group [127]. Despite many non-IPR C_{78} endofullerenes were reported and characterized by spectroscopies and DFT calculations, such as $Y_3N@^{\#22010}C_{78}$ and $DySc_2N@^{\#24109}C_{78}$ [128, 129], the only one characterized by SCXRD is $Gd_3N@^{\#22010}C_{78}$ [130] (Fig. 18). $Gd_3N@^{\#22010}C_{78}$ was synthesized by Gd_2O_3 doped carbon arc discharge under helium and nitrogen atmosphere. A nonclassical C_{78} with two heptagons (Fig. 18) was produced in the chlorination-promoted transformation of IPR C_{78} isomers. As shown in the structure obtained by SCXRD, this $C_{78}(NC2)Cl_{24}$ contains as many as six pairs of DFPs [125].

C_{80}. Although $Sc_3N@I_h(7)$-C_{80} is one of the most famous endofullerenes with relative high yield, the first C_{80} with fused pentagons has not be synthesized and isolated until 2015. The heptagon-containing $LaSc_2N@C_{80}(NC1)$ (Fig. 19) was characterized by SCXRD [131], showing a heptagon fused with two pairs of DFPs. Another non-IPR C_{80} cage was stabilized as $(C_1$-$^{\#28324}C_{80})^{4-}$ with single

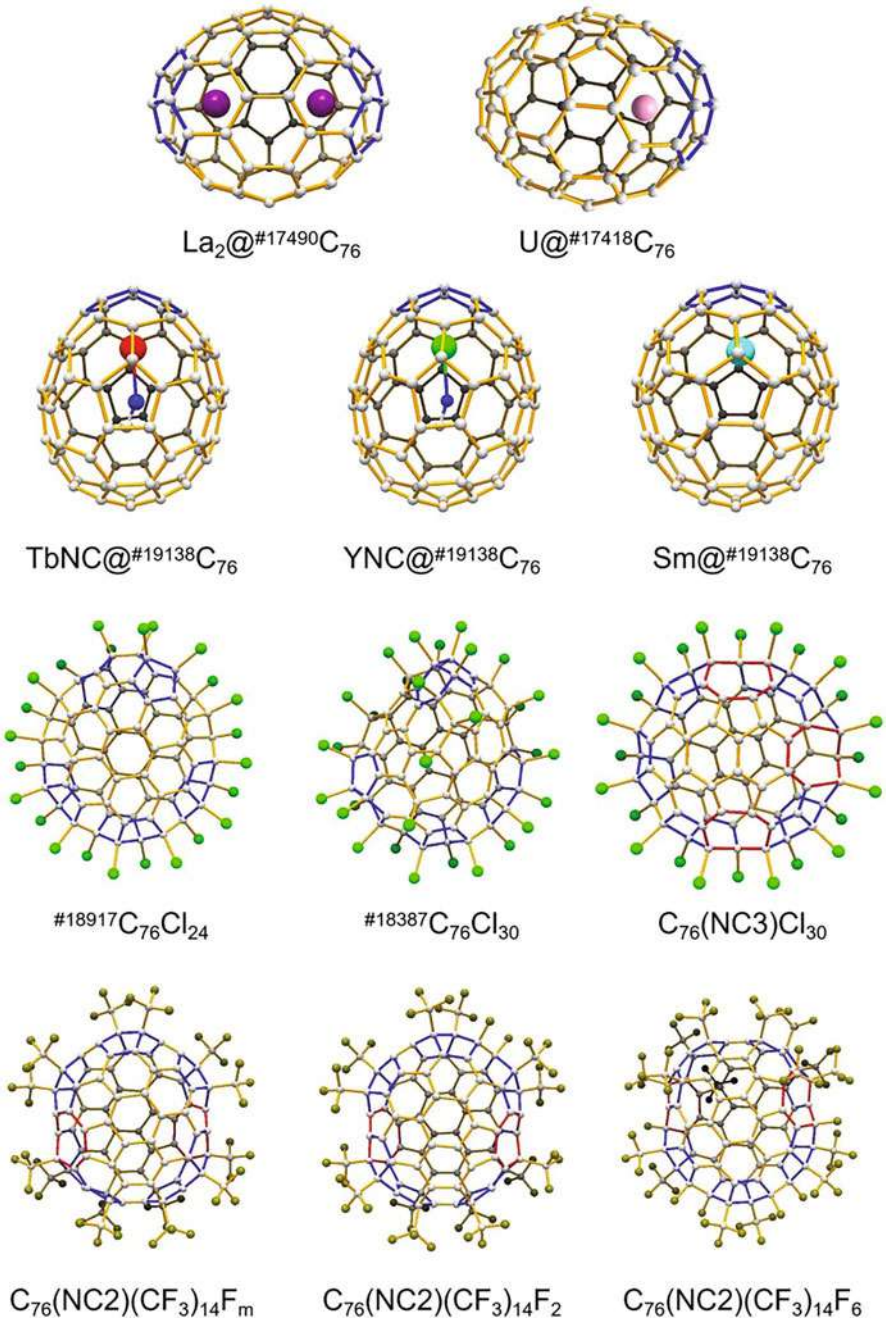

Fig. 17 Molecular structures of C_{76} isomers with fused pentagons. Fused pentagons and heptagon are highlighted in blue and red, respectively

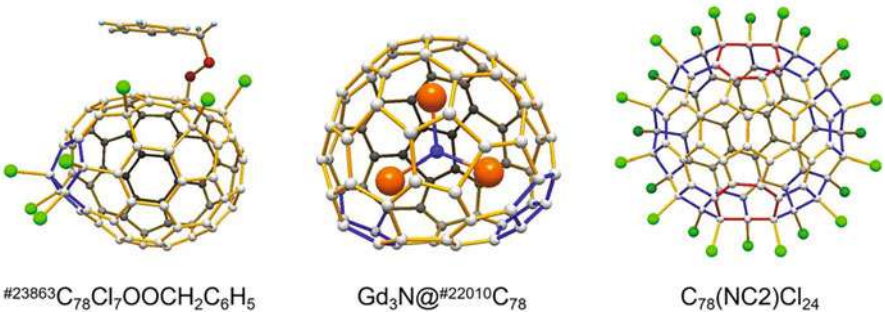

Fig. 18 Molecular structures of C_{78} isomers with fused pentagons. Fused pentagons and heptagon are highlighted in blue and red, respectively

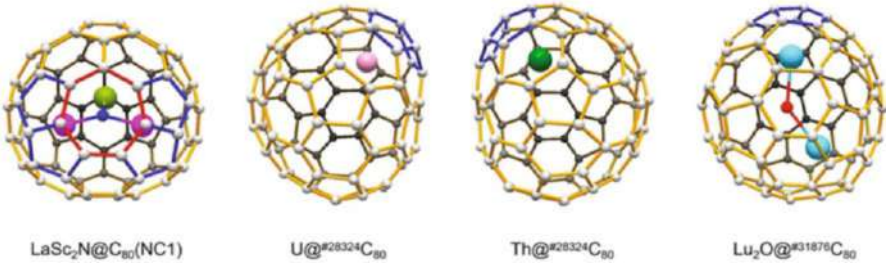

Fig. 19 Molecular structures of C_{80} isomers with fused pentagons. Fused pentagons are highlighted in blue

U^{4+} and Th^{4+} ion inside (Fig. 19), respectively. The formation of $U@^{\#28324}C_{80}$ was suggested to consist of two steps of C_2 insertions on the captured $U@^{\#17418}C_{76}$, topologically [122]. Although the cage cavity of $^{\#28324}C_{80}$ is quite large, the encapsulated U^{4+} or Th^{4+} ion preferred to be close to the DFP unit according to the SCXRD structure. In addition, $Lu_2O@^{\#31876}C_{80}$ and $Lu_2O@C_{2v}(5)$-C_{80} were successfully isolated and unambiguously assigned by X-ray crystallography (Fig. 19). Although $^{\#31876}C_{80}$ is a non-IPR cage with a DFP, $Lu_2O@^{\#31876}C_{80}$ was calculated to be more stable than the IPR $Lu_2O@C_{2v}(5)$-C_{80} with larger HOMO-LUMO gap and lower energy [132].

C_{82}-C_{90}. Higher fullerenes with fused pentagons captured in experiments could be classified into two categories in terms of their synthetic strategies, encapsulation of metal and chlorination-promoted cage transformation. $Gd_3N@^{\#39663}C_{82}$ is the only non-IPR C_{82} isolated from the products of vaporizing graphite rod packed with Gd_2O_3 in He/N_2 atmosphere in an arc-discharge reactor [133]. A pair of fused pentagons was found in $^{\#39663}C_{82}$ and coordinated to Gd^{3+} ion (Fig. 20). C_s-$^{\#51365}C_{84}$ was stabilized by $(M_3N)^{6+}$ (M = Tb, Gd, Tm) clusters while C_s-$^{\#51383}C_{84}$ encapsulated a $(Gd_2C_2)^{4+}$ cluster (Fig. 20). Both of them own a DFP unit [134–136]. These cases also demonstrated the cage selection by the electron transfer from inner cluster, as the showed cases of C_{76} endofullerenes [119–122].

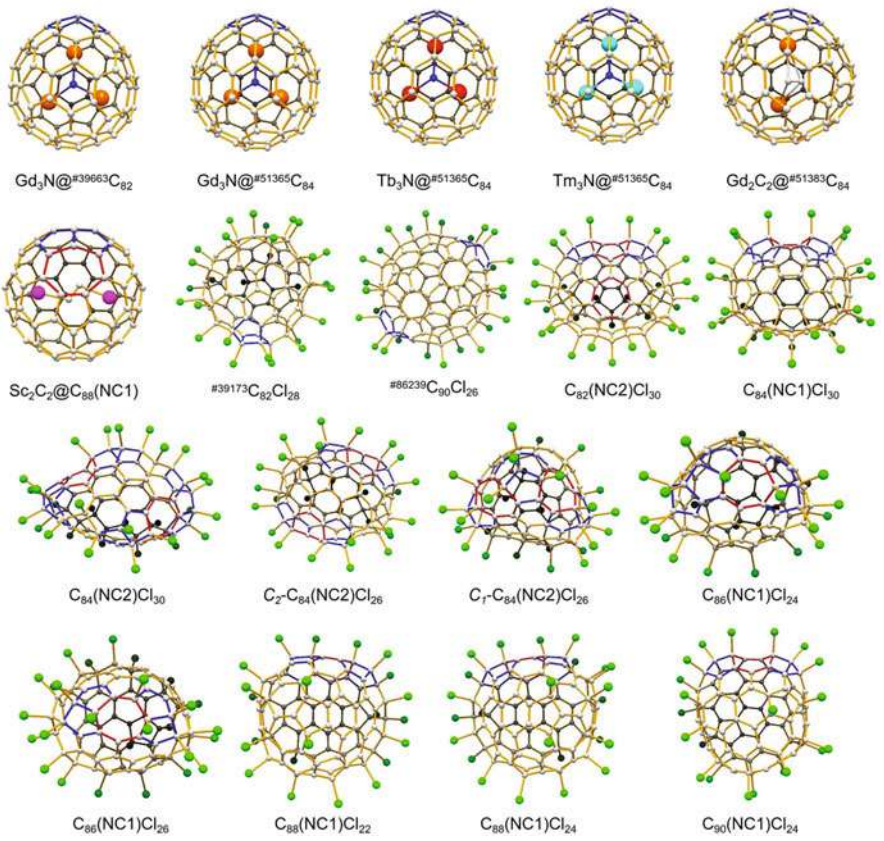

Fig. 20 Molecular structures of C_{82}, C_{84}, C_{86}, C_{88}, and C_{90} isomers with fused pentagons. Fused pentagons and heptagon are highlighted in blue and red, respectively

Particularly, $^{\#51383}C_{84}$ was regarded as a vital link in a top-down route through C_2 extrusion. On the contrary, the largest endofullerene with fused pentagons characterized by SCXRD is $Sc_2C_2@C_{88}(NC1)$ (Fig. 20). It was suggested as the link in a bottom-up growth mechanism by inserting a C_2 unit on the captured $Sc_2C_2@C_{2v}(9)$-C_{86} [137].

On the other hand, chlorination-promoted cage transformation of IPR fullerenes into non-IPR ones have been proven to be the most feasible way to access non-IPR fullerenes with carbon number larger than C_{82}. More than ten chlorinated fullerenes with fused pentagons and heptagon were synthesized and characterized (Fig. 20), including C_s-$C_{82}(NC2)Cl_{30}$, C_s-$C_{84}(NC1)Cl_{30}$, C_2-$C_{84}(NC2)Cl_{30}$, C_1-$C_{84}(NC2)Cl_{26}$, C_2-$C_{84}(NC2)Cl_{26}$, C_1-$C_{86}(NC1)Cl_{26}$, C_1-$C_{86}(NC1)Cl_{24}$, C_1-$C_{88}(NC1)Cl_{22}$, C_1-$C_{88}(NC1)Cl_{24}$, $C_{90}(NC1)Cl_{24}$, and so on [138–143]. Beyond that, the captured $^{\#39173}C_{82}Cl_{28}$ and $^{\#86239}C_{90}Cl_{26}$ are the classical fullerenes with only one DFP [143, 144].

Larger than C_{92}. Non-IPR fullerenes larger than C_{92} characterized experimentally were all produced by postfunctionalization-promoted cage transformation

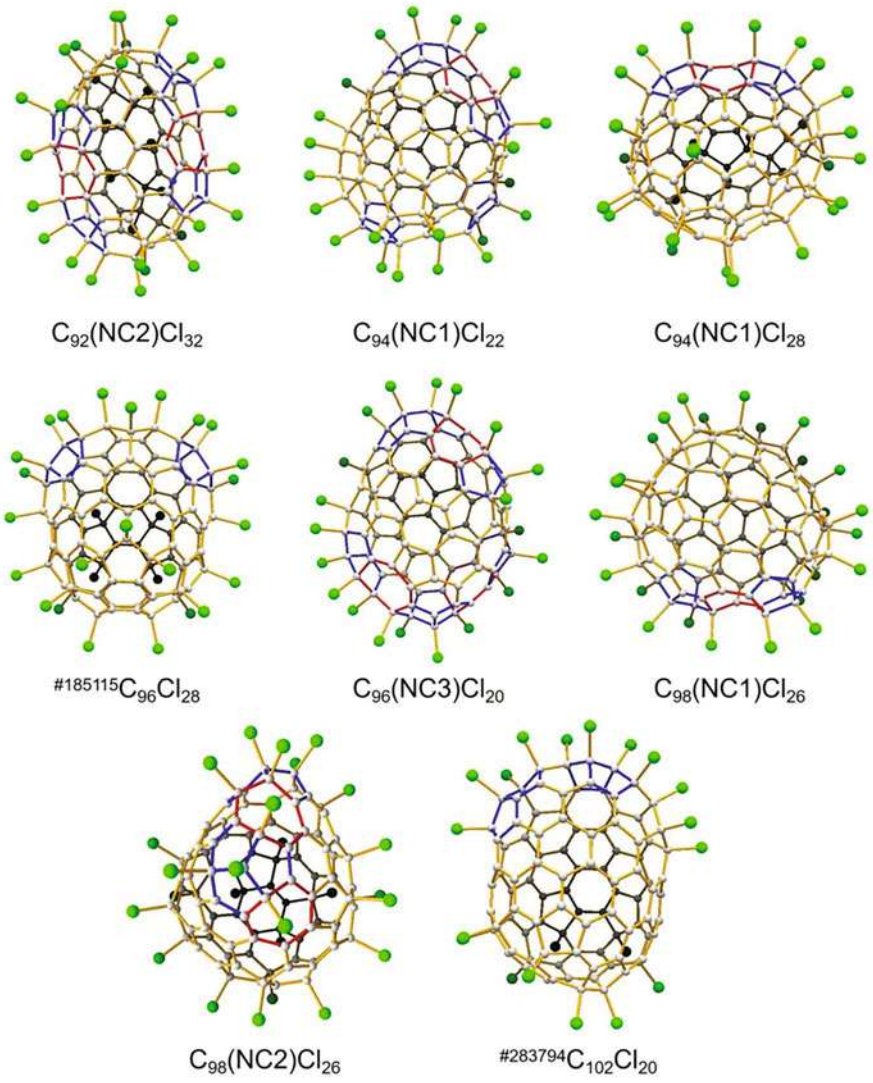

Fig. 21 Molecular structures of C_{92}, C_{94}, C_{96}, C_{98}, and C_{102} isomers with fused pentagons. Fused pentagons and heptagon are highlighted in blue and red, respectively

so far. C_1-C_{92}(NC2)Cl_{32}, C_1-C_{94}(NC1)Cl_{28}, C_1-C_{94}(NC1)Cl_{22}, $^{\#185115}C_{96}Cl_{28}$, C_1-C_{96}(NC3)Cl_{20}, C_1-C_{98}(NC1)Cl_{26}, C_1-C_{98}(NC2)Cl_{26}, and $^{\#283794}C_{102}Cl_{20}$ (Fig. 21) were all synthesized by chlorination-promoted cage transformation on corresponding IPR fullerenes with VCl_4 and $SbCl_5$ at 340–360 °C [145–151]. Based on structures of these large non-IPR chlorofullerenes, it can be proposed the large higher fullerenes intended to lose C_2 unit during the cage transformation and consequentially the heptagon-containing non-classic isomers were formed.

If this feasible C_2 excursion could also be prevalent for giant fullerenes in the clustering processes, such as arc-discharge and combustion, remains an open question.

Conclusion and Outlook

Through more than two decades of research, the synthesis and characterization of non-IPR fullerenes have made great progress. At present, more than 60 different non-IPR cages (Table 2) have been unambiguously characterized, which greatly enriched the fullerene family. Non-IPR fullerenes nowadays become an important category of fullerenes. The discovery of these non-IPR fullerenes provides indispensable structural evidence for understanding the formation and growth mechanism of fullerenes. They are also expected to provide molecular cornerstones for the development of fullerene materials. In terms of the growth and capture of carbon clusters in situ using arc-discharge or combustion or radio-frequency plasma, the non-IPR fullerenes can be synthesized and obtained by exohedral or endohedral stabilization. The endohedral stabilization of non-IPR fullerenes relies on the charge transfer from encapsulated atom (clusters) to the cage and coordination between metal and fused-pentagon units. For the exohedral stabilization, the principles of "strain release" and "local aromaticity" were proposed, and widely recognized in the exohedral derivatives of non-IPR fullerenes. In addition to the clustering process, postfunctionalization-promoted cage transformation provided alternative strategy to achieve non-IPR fullerene derivatives. The stabilization of non-IPR fullerene derivatives obtained by cage transformation can also be rationalized by the "strain-relief" and "local aromaticity" principles.

Although great advances have been achieved, many directions remain to be studied in the field of non-IPR fullerenes. Structurally, non-IPR fullerenes obtained in ambient conditions were all stabilized by encapsulation of atom(clusters) or exohedral groups. The pristine non-IPR fullerenes that can be separated and characterized under ambient conditions are still a topic to be broken through. The size of carbon cages characterized to date is larger than C_{50}, except the organically synthesized $C_{20}H_{20}$. Fullerenes smaller than C_{50} inevitably contain multiple fused pentagons, which have great cage strain and low π conjugation. Could these fullerenes be synthesized and characterized in the future? For giant higher fullerenes, their carbon skeleton can have smaller $\boldsymbol{\theta}_p$ and curvature, and thus the fused pentagons embedded in these giant fullerenes could have reduced strain. Combined with the stabilization of the extended π conjugation in giant fullerenes, could the fused pentagons in some giant fullerenes become stable enough to survive as the pristine form without exohedral or endohedral derivatization?

On the potential applications of non-IPR fullerene, although some non-IPR fullerenes have shown intriguing electronic and optical properties and have promising potentials in photovoltaics and electronics, the preparation yields of non-IPR fullerenes are low and require tedious and complex HPLC separation. It is still difficult to obtain non-IPR fullerenes in gram scale, which greatly hinders the studies

on the applications of non-IPR fullerenes. Although postfunctionalization-promoted cage transformation based on commercially available IPR C_{60} and C_{70} could offer a potential way to access the non-IPR C_{60} and C_{70} in large quantity, postfunctionalization-promoted cage transformation requires highly toxic and corrosive metal chlorides and harsh reaction conditions, high pressure, and temperature. The amplification of the reaction scale of postfunctionalization-promoted cage transformation is still technically difficult. More importantly, the non-IPR fullerenes prepared by postfunctionalization-promoted cage transformation are highly functionalized and lose most electronic and optical characteristics of fullerenes. In the future, decreasing the degree of functionalization for these non-IPR fullerene derivatives and restoring their spherical conjugation may offer a feasible source of non-IPR fullerenes for the material researches.

The research of non-IPR fullerenes have brought many novel and surprise structures to the field of fullerene, which were not imaged two decades ago. These novel fullerenes greatly enriched the structural toolbox of fullerenes. Nowadays study on non-IPR fullerenes has become one of the most important fields of fullerene research. It is believed that non-IPR fullerenes will give us more surprises in the future, both structurally and functionally.

Cross-References

- ▶ Preparation, Extraction/Isolation from Soot, and Solubility of Fullerenes
- ▶ Structural Characteristics of Fullerenes
- ▶ Structures and Properties of Endohedral Metallofullerenes

References

1. Kroto HW, Heath JR, O'Brien SC, Curl RF, Smalley RE (1985) C_{60}: buckminsterfullerene. Nature 318:162–163
2. Fowler PW, Manolopoulos DE (1995) An atlas of fullerenes. Oxford University Press, Oxford
3. Kroto HW (1987) The stability of the fullerenes C_n, with n=24, 28, 32, 36, 50, 60 and 70. Nature 329:529–531
4. Schmalz TG, Seitz WA, Klein DJ, Hite GE (1986) Sixty-carbon-atom carbon cages. Chem Phys Lett 130:203–207
5. Schmalz TG, Seitz WA, Klein DJ, Hite GE (1988) Elemental carbon cages. J Am Chem Soc 110:1113–1127
6. Haddon RC (1987) Pyramidalization: geometrical interpretation of the pi-orbital axis vector in three dimensions. J Phys Chem 91:3719–3720
7. Haddon RC (1988) P-electrons in three dimensiona. Acc Chem Res 21:243–249
8. Wang CR et al (2000) Materials science – C_{66} fullerene encaging a scandium dimer. Nature 408:426–427
9. Stevenson S et al (2000) A stable non-classical metallofullerene family. Nature 408:427–428
10. Tan YZ, Xie SY, Huang RB, Zheng LS (2009) The stabilization of fused-pentagon fullerene molecules. Nat Chem 1:450–460
11. Lu X, Feng L, Akasaka T, Nagase S (2012) Current status and future developments of endohedral metallofullerenes. Chem Soc Rev 41:7723–7760

12. Popov AA, Yang S, Dunsch L (2013) Endohedral fullerenes. Chem Rev 113:5989–6113
13. Yang S, Wei T, Jin F (2017) When metal clusters meet carbon cages: endohedral clusterfullerenes. Chem Soc Rev 46:5005–5058
14. Yamada M, Akasaka T, Nagase S (2018) Salvaging reactive fullerenes from soot by exohedral derivatization. Angew Chem Int Ed 57:13394–13405
15. Jin P, Li Y, Magagula S, Chen Z (2019) Exohedral functionalization of endohedral metallofullerenes: interplay between inside and outside. Coord Chem Rev 388:406–439
16. Yang S, Ioffe IN, Troyanov SI (2019) Chlorination-promoted skeletal transformations of fullerenes. Acc Chem Res 52:1783–1792
17. Yao Y, Xie S (2019) Structures and progress of carbon clusters. Progr Chem 31:50–62
18. Guan R, Chen M, Jin F, Yang S (2020) Strain release of fused pentagons in fullerene cages by chemical functionalization. Angew Chem Int Ed 59:1048–1073
19. Campanera JM, Bo C, Poblet JM (2005) General rule for the stabilization of fullerene cages encapsulating trimetallic nitride templates. Angew Chem Int Ed 44:7230–7233
20. Yang S, Rapta P, Dunsch L (2007) The spin state of a charged non-IPR fullerene: the stable radical cation of $Sc_3N@C_{68}$. Chem Commun 2:189–191
21. Popov AA, Dunsch L (2007) Structure, stability, and cluster-cage interactions in nitride clusterfullerenes $M_3N@C_{2n}$ (M = Sc, Y; 2n=68–98): a density functional theory study. J Am Chem Soc 129:11835–11849
22. Nagase S, Kobayashi K, Akasaka T (1999) Unconventional cage structures of endohedral metallofullerenes. Theochem J Mol Struct 461–462:97–104
23. Shi ZQ, Wu X, Wang CR, Lu X, Shinohara H (2006) Isolation and characterization of $Sc_2C_2@C_{68}$: a metal-carbide endofullerene with a non-IPR carbon cage. Angew Chem Int Ed 45:2107–2111
24. Iiduka Y et al (2005) Structural determination of metallofullerene Sc_3C_{82} revisited: a surprising finding. J Am Chem Soc 127:12500–12501
25. Dunsch L, Yang S (2007) Endohedral clusterfullerenes-playing with cluster and cage sizes. Phys Chem Chem Phys 9:3067–3081
26. Dunsch L, Yang S (2007) Metal nitride cluster fullerenes: their current state and future prospects. Small 3:1298–1320
27. Olmstead MM et al (2001) Isolation and structural characterization of the endohedral fullerene $Sc_3N@C_{78}$. Angew Chem Int Ed 40:1223–1225
28. Cai T et al (2007) $Sc_3N@C_{78}$: encapsulated cluster regiocontrol of adduct docking on an ellipsoidal metallofullerene sphere. J Am Chem Soc 129:10795–10800
29. Popov AA, Krause M, Yang S, Wong J, Dunsch L (2007) C_{78} cage isomerism defined by trimetallic nitride cluster size: a computational and vibrational spectroscopic study. J Phys Chem B 111:3363–3369
30. Osuna S, Swart M, Sola M (2009) The Diels-Alder reaction on endohedral $Y_3N@C_{78}$: the importance of the fullerene strain energy. J Am Chem Soc 131:129–139
31. Beavers CM, Chaur MN, Olmstead MM, Echegoyen L, Balch AL (2009) Large metal ions in a relatively small fullerene cage: the structure of $Gd_3N@C_2$(22010)-C_{78} departs from the isolated pentagon rule. J Am Chem Soc 131:11519–11524
32. Akasaka T et al (1997) ^{13}C and ^{139}La NMR studies of $La_2@C_{80}$: first evidence for circular motion of metal atoms in endohedral dimetallofullerenes. Angew Chem Int Ed Engl 36: 1643–1645
33. Stevenson S et al (1999) Small-bandgap endohedral metallofullerenes in high yield and purity. Nature 401:55–57
34. Yang SF, Popov AA, Dunsch L (2007) Violating the isolated pentagon rule (IPR): the endohedral non-IPR cage of $Sc_3N@C_{70}$. Angew Chem Int Ed 46:1256–1259
35. Yang S, Popov AA, Dunsch L (2007) The role of an asymmetric nitride cluster on a fullerene cage: the non-IPR endohedral $DySc_2N@C_{76}$. J Phys Chem B 111:13659–13663
36. Summerscales OT (2006) The organometallic chemistry of pentalene. Coord Chem Rev 250: 1122
37. Hirsch A, Brettreich M (2005) Fullerenes: chemistry and reactions. Wiley-VCH Verlag GmbH & Co. KGaA, London

38. Petrie S, Bohme DK (1993) Enhanced reactivity of fullerene cations containing adjacent pentagons. Nature 365:426–429
39. Kroto HW, Walton DRM (1993) Stable derivatives of small fullerenes. Chem Phys Lett 214: 353–356
40. Xie SY et al (2004) Capturing the labile fullerene[50] as $C_{50}Cl_{10}$. Science 304:699–699
41. Han X et al (2008) Crystal structures of saturn-like $C_{50}Cl_{10}$ and pineapple-shaped $C_{64}Cl_4$: geometric implications of double- and triple-pentagon-fused chlorofullerenes. Angew Chem Int Ed 47:5340–5343
42. Haddon RC (1993) Chemistry of the fullerenes: the manifestation of strain in a class of continuous aromatic molecules. Science 261:1545–1550
43. Aihara, J.-i. (1995) Bond resonance energy and verification of the isolated pentagon rule. J Am Chem Soc 117:4130–4136
44. Aihara J-I, Oe S, Yoshida M, Osawa E (1996) Further test of the isolated pentagon rule: thermodynamic and kinetic stabilities of C_{84} fullerene isomers. J Comput Chem 17:1387–1394
45. Tan YZ et al (2008) Two I_h-symmetry-breaking C_{60} isomers stabilized by chlorination. Nat Mater 7:790–794
46. Taylor R (2000) Surprises, serendipity, and symmetry in fullerene chemistry. Synlett 6: 776–793
47. Taylor R (2004) Why fluorinate fullerenes? J Fluor Chem 125:359–368
48. Simeonov KS, Amsharov KY, Jansen M (2009) $C_{80}Cl_{12}$: a chlorine derivative of the chiral D_2-C_{80} isomer – empirical rationale of halogen-atom addition pattern. Chem Eur J 15:1812–1815
49. Simeonov KS, Amsharov KY, Jansen M (2007) Connectivity of the chiral D_2-symmetric isomer of C_{76} through a crystal-structure determination of $C_{76}Cl_{18}TiCl_4$. Angew Chem Int Ed 46:8419–8421
50. Hirsch A, Chen Z, Jiao H (2000) Spherical aromaticity in I_h symmetrical fullerenes: the 2(N+1)2 rule. Angew Chem Int Ed 39:3915–3917
51. Chen J-H et al (2012) Combustion synthesis and electrochemical properties of the small hydrofullerene C50H10. Chem Eur J 18:3408–3415
52. Lu X, Chen ZF (2005) Curved p-conjugation, aromaticity, and the related chemistry of small fullerenes ($<C_{60}$) and single-walled carbon nanotubes. Chem Rev 105:3643–3696
53. Chen DL, Tian WQ, Feng JK, Sun CC (2007) Structures, stabilities, and electronic and optical properties of C_{52} fullerene, ions, and metallofullerenes. J Chem Phys 126:074313
54. Sun L, Chang Y, Tang S, Wang R (2008) Theoretical studies on structures and stabilities of C_2-$C_{52}X_2$ (X=H, F, and Cl) isomers. Chem Phys Lett 464:113–117
55. Alcami M, Sanchez G, Diaz-Tendero S, Wang Y, Martin F (2007) Structural patterns in fullerenes showing adjacent pentagons: C_{20} to C_{72}. J Nanosci Nanotechnol 7:1329–1338
56. Gao X, Zhao Y (2007) The way of stabilizing non-IPR fullerenes and structural elucidation of $C_{54}Cl_8$. J Comput Chem 28:795–801
57. Chen DL, Tian WQ, Feng JK, Sun CC (2007) Structures and electronic properties of $C_{56}Cl_8$ and $C_{56}Cl_{10}$ fullerene compounds. ChemPhysChem 8:2386–2390
58. Chen D-L, Tian WQ, Feng J-K, Sun C-C (2008) Theoretical investigation of C_{56} fullerene isomers and related compounds. J Chem Phys 128:044318/044311-044318/044317
59. Chen DL, Tian WQ, Feng JK, Sun CC (2007) Structures, stabilities, and electronic and optical properties of C_{58} fullerene isomers, ions, and metallofullerenes. ChemPhysChem 8: 1029–1036
60. Ayuela A et al (1996) C_{62}: theoretical evidence for a nonclassical fullerene with a heptagonal ring. J Phys Chem 100:15634–15636
61. Cui Y-H, Chen D-L, Tian WQ, Feng J-K (2007) Structures, stabilities, and electronic and optical properties of C_{62} fullerene isomers. J Phys Chem A 111:7933–7939
62. Sun LL, Tang SW, Chang YF, Wang ZL, Wang RS (2008) Searching for stable hept-$C_{62}X_2$ (X = F, Cl, and Br): structures and stabilities of heptagon-containing C_{62} halogenated derivatives. J Comput Chem 29:2631–2635
63. Cui Y-H, Tian WQ, Feng J-K, Chen D-L (2008) Structures, stabilities, electronic, and optical properties of C_{64} fullerene isomers, anions (C2-64 and C4-64), metallofullerene $Sc_2@C_{64}$, and $Sc_2C_2@C_{64}$. J Comput Chem 29:2623–2630

64. Gan L-H et al (2011) Geometrical and electronic rules in fullerene-based compounds. Chem Asian J 6:1304–1314
65. Song X, Li X, Qi J (2018) Theoretical studies on the structural and spectral properties of two specific C-54 isomers and the chlorinated species C54Cl8. RSC Adv 8:32731–32739
66. Mao R, Wang Z, Song X, Chen W-K, Qi J (2021) Structural and spectral properties of a nonclassical C-66 isomer with its hydrogenated derivative C66H4 in theory. ACS Omega 6: 27101–27111
67. Song X, Mao R, Wang Z, Qi J (2021) Structural and spectral properties of a non-classical C-58 isomer and its fluorinated derivatives in theory. RSC Adv 11:1472–1481
68. Paquette LA (1982) Dodecahedrane – the chemical transliteration of Plato's universe (A review). Proc Natl Acad Sci U S A 79:4495–4500
69. Paquette LA, Ternansky RJ, Balogh DW (1982) A strategy for the synthesis of mono-substituted dodecahedrane and the isolation of an isododecahedrane. J Am Chem Soc 104: 4502–4503
70. Ternansky RJ, Balogh DW, Paquette LA (1982) Dodecahedrane. J Am Chem Soc 104: 4503–4504
71. Wahl F, Woerth J, Prinzbach H (1993) The pagodane route to dodecahedranes: improved access to the $C_{20}H_{20}$ framework as well as partial and total functionalization. Does C_{20} fullerene exist? Angew Chem Int Ed Engl 32:1722–1726
72. Prinzbach H, Weber K (1994) From insecticide to Plato's universe – the pagodane route to dodecahedranes: new routes and new targets. Angew Chem Int Ed Engl 33:2239–2257
73. Prinzbach H et al (2000) Gas-phase production and photoelectron spectroscopy of the smallest fullerene, C_{20}. Nature 407:60–63
74. Wahl F et al (2006) Towards perfunctionalized dodecahedranes – en route to C_{20} fullerene. Chem Eur J 12:6255–6267
75. Piskoti C, Yarger J, Zettl A (1998) C_{36}, a new carbon solid. Nature 393:771–774
76. Koshio A, Inakuma M, Wang ZW, Sugai T, Shinohara H (2000) In situ laser-furnace TOF mass spectrometry of C_{36} and the large-scale production by arc-discharge. J Phys Chem B 104: 7908–7913
77. Koshio A, Inakuma M, Sugai T, Shinohara H (2000) A preparative scale synthesis of C_{36} by high-temperature laser-vaporization: purification and identification of $C_{36}H_6$ and $C_{36}H_6O$. J Am Chem Soc 122:398–399
78. Lu X et al (2004) Properties of fullerene[50] and D_{5h} decachlorofullerene[50]: a computational study. J Am Chem Soc 126:14871–14878
79. Tan YZ et al (2010) Chlorofullerenes featuring triple sequentially fused pentagons. Nat Chem 2:269–273
80. Tan YZ et al (2008) An entrant of smaller fullerene: C_{56} captured by chlorines and aigned in linear chains. J Am Chem Soc 130:15240–15241
81. Ziegler K, Mueller A, Amsharov KY, Jansen M (2011) Capturing the most-stable C_{56} fullerene cage by in situ chlorination. Chem Asian J 6:2412–2418
82. Zhou T et al (2011) Retrieving the most prevalent small fullerene C_{56}. Chem Eur J 17: 8529–8532
83. Troshin PA et al (2005) Isolation of two seven-membered ring C_{58} fullerene derivatives: $C_{58}F_{17}CF_3$ and $C_{58}F_{18}$. Science 309:278–281
84. Weng QH et al (2010) Simple combustion production and characterization of octahydro 60 fullerene with a non-IPR C-60 cage. J Am Chem Soc 132:15093–15095
85. Brotsman VA et al (2018) Rebuilding C60: chlorination-promoted transformations of the buckminsterfullerene into pentagon-fused C60 derivatives. Inorg Chem 57:8325–8331
86. Tamm NB, Markov VY, Troyanov SI (2021) Trifluoromethyl derivatives of pentagon-fused C60: 1809C60(CF3)n (n = 10, 12, 14, 16). Dalton Trans 50:5765–5769
87. Vysochanskaya ON, Brotsman VA, Goryunkov AA, Feiler CG, Troyanov SI (2020) Fused-pentagon isomers of C60 fullerene isolated as chloro and trifluoromethyl derivatives. Chem Eur J 26:2338–2341

88. Tamm NB, Brotsman VA, Sidorov LN, Troyanov SI (2021) Chloro- and trifluoromethyl derivatives of a pentagon-fused C-60:(C60Cl24)-C-1810, (C60Cl20)-C-1810, and C-1810(60)(CF3)(14). Inorg Chem 60:6991–6993
89. Qian WY et al (2000) C_{62}, a non-classical fullereneincorporating a four-membered ring. J Am Chem Soc 122:8333–8334
90. Qian W et al (2003) Synthesis of stable derivatives of C_{62}: the first nonclassical fullerene incorporating a four-membered ring. J Am Chem Soc 125:2066–2067
91. Wang CR et al (2006) $C_{64}H_4$: production, isolation, and structural characterizations of a stable unconventional fulleride. J Am Chem Soc 128:6605–6610
92. Gao ZY et al (2010) Synthesis of C3v – #1911C64H4 using a low-pressure benzene/oxygen diffusion flame: another pathway toward non-IPR fullerenes. Combust Flame 157:966–969
93. Yamada M et al (2014) Sc2@C66 revisited: an endohedral fullerene with scandium ions nestled within two unsaturated linear Triquinanes. J Am Chem Soc 136:7611–7614
94. Gao C-L et al (2014) Synthesis of long-sought C66 with exohedral stabilization. Angew Chem Int Ed 53:7853–7855
95. Tian H-R et al (2019) An unconventional hydrofullerene C66H4 with symmetric heptagons retrieved in low-pressure combustion. J Am Chem Soc 141:6651–6657
96. Kobayashi K, Nagase S (2002) A stable unconventional structure of Sc-2@C-66 found by density functional calculations. Chem Phys Lett 362:373–379
97. Tan YZ et al (2011) Carbon arc production of heptagon-containing fullerene[68]. Nat Commun 2:1431–1436
98. Amsharov KY, Ziegler K, Mueller A, Jansen M (2012) Capturing the antiaromatic #6094C_{68} carbon cage in the radio-frequency furnace. Chem Eur J 18:9289–9293
99. Chen D-L, Tian WQ, Feng J-K, Sun C-C (2008) C68 fullerene isomers, anions, and their metallofullerenes: charge-stabilizing different isomers. ChemPhysChem 9:454–461
100. Brotsman VA, Ioffe IN, Troyanov SI (2022) Crippling the C70 fullerene: non-classical C68Cl26(OH)2 and C68Cl25(OH)3 with three heptagons and only fused pentagons via chlorination-promoted skeletal transformations. Chem Commun 58:6918–6921
101. Olmstead MM et al (2003) $Sc_3N@C_{68}$: folded pentalene coordination in an endohedral fullerene that does not obey the isolated pentagon rule. Angew Chem Int Ed 42:900–903
102. Zheng H, Zhao X, Wang WW, Yang T, Nagase S (2012) Sc-2@C-70 rather than Sc2C2@C-68: density functional theory characterization of metallofullerene Sc2C70. J Chem Phys 137:014308
103. Tan YZ et al (2013) Exohedrally stabilized C-70 isomer with adjacent pentagons characterized by crystallography. Chem Sci 4:2967–2970
104. Zhong Y-Y et al (2019) Double negatively curved C70 growth through a heptagon-involving pathway. Angew Chem Int Ed 58:14095–14099
105. Feng L et al (2016) Endohedrally stabilized C70 isomer with fused pentagons characterized by crystallography. Dalton Trans 45:8142–8148
106. Chen N et al (2013) Sc2S@C2(7892)–C70: a metallic sulfide cluster inside a non-IPR C70 cage. Chem Sci 4:180–186
107. Brotsman VA, Kemnitz E, Troyanov SI (2019) Fused-pentagon C70Cl26 obtained via chlorination-promoted Stone–Wales cage transformations of C70. Chem Commun 55: 13378–13381
108. Tamm NB, Brotsman VA, Markov VY, Troyanov SI (2020) Fused-pentagon C70Cl6 and C70Cl8 obtained via chlorination-promoted skeletal transformation of IPR C70. Inorg Chem 59:10400–10403
109. Slanina Z, Ishimura K, Kobayashi K, Nagase S (2004) C_{72} isomers: the IPR-satisfying cage is disfavored by both energy and entropy. Chem Phys Lett 384:114–118
110. Tan YZ et al (2010) $C_{72}Cl_4$: a pristine fullerene with favorable pentagon-adjacent structure. J Am Chem Soc 132:17102–17104
111. Ziegler K, Mueller A, Amsharov KY, Jansen M (2010) Disclosure of the elusive C_{2v}-C_{72} carbon cage. J Am Chem Soc 132:17099–17101

112. Kato H, Taninaka A, Sugai T, Shinohara H (2003) Structure of a missing-caged metallofullerene: $La_2@C_{72}$. J Am Chem Soc 125:7782–7783
113. Lu X et al (2008) Chemical understanding of a non-IPR metallofullerene: stabilization of encaged metals on fused-pentagon bonds in $La_2@C_{72}$. J Am Chem Soc 130:9129–9136
114. Wakahara T et al (2006) $La@C_{72}$ having a non-IPR carbon cage. J Am Chem Soc 128: 14228–14229
115. Chen N et al (2012) Sc2S@Cs(10528)-C72: a Dimetallic Sulfide endohedral fullerene with a non isolated pentagon rule cage. J Am Chem Soc J Am Chem Soc 134:7851–7860
116. Feng Y et al (2013) Structural and electronic studies of metal carbide clusterfullerene Sc2C2@Cs–C72. Nanoscale 5:6704–6707
117. Gao C-L et al (2016) Capturing the fused-pentagon C-74 by stepwise chlorination. Inorg Chem 55:6861–6865
118. Liu A et al (2019) Ho2O@C74: Ho2O cluster expands within a small non-IPR fullerene cage of C2(13333)-C74. Inorg Chem 58:4774–4781
119. Suzuki M et al (2013) La2@Cs(17 490)-C76: a new non-IPR dimetallic metallofullerene featuring unexpectedly weak metal–pentalene interactions. Chem Eur J 19:17125–17130
120. Liu F et al (2017) Mononuclear clusterfullerene single-molecule magnet containing strained fused-pentagons stabilized by a nearly linear metal cyanide cluster. Angew Chem Int Ed 56: 1830–1834
121. Hao Y et al (2015) Sm@C2v(19138)-C76: a non-IPR cage stabilized by a divalent metal ion. Inorg Chem 54:4243–4248
122. Cai W et al (2018) Synthesis and characterization of non-isolated-pentagon-rule actinide endohedral metallofullerenes U@C1(17418)-C76, U@C1(28324)-C80, and Th@C1(28324)-C80: low-symmetry cage selection directed by a tetravalent ion. J Am Chem Soc 140: 18039–18050
123. Ioffe IN et al (2009) Fusing pentagons in a fullerene cage by chlorination: IPR D_2-C_{76} rearranges into non-IPR $C_{76}Cl_{24}$. Angew Chem Int Ed 48:5904–5907
124. Sudarkova SM, Mazaleva ON, Konoplev-Esgenburg RA, Troyanov SI, Ioffe IN (2018) Versatility of chlorination-promoted skeletal transformation pathways in C76 fullerene. Dalton Trans 47:4554–4559
125. Tamm NB, Brotsman VA, Markov VY, Kemnitz E, Troyanov SI (2018) Chlorination-promoted skeletal transformation of IPR C76 discovered via trifluoromethylation under the formation of non-IPR C76(CF3)nFm. Dalton Trans 47:6898–6902
126. Brotsman VA, Ignat'eva DV, Troyanov SI (2017) Chlorination-promoted transformation of isolated pentagon rule C78 into fused-pentagons- and heptagons-containing fullerenes. Chem Asian J 12:2379–2382
127. Tan YZ et al (2010) Pentagon-fused hollow fullerene in C_{78} family retrieved by chlorination. J Am Chem Soc 132:12648–12652
128. Zhang J et al (2013) Enhanced dipole moments in trimetallic nitride template endohedral metallofullerenes with the pentalene motif. J Am Chem Soc 135:3351–3354
129. Wei T et al (2015) An expanded family of dysprosium–scandium mixed-metal nitride clusterfullerenes: the role of the lanthanide metal on the carbon cage size distribution. Chem Eur J 21:5750–5759
130. Beavers CM, Chaur MN, Olmstead MM, Echegoyen L, Balch AL (2009) Large metal ions in a relatively small fullerene cage: the structure of Gd3N@C-2(22010)-C-78 departs from the isolated pentagon rule. J Am Chem Soc 131:11519–11524
131. Zhang Y et al (2015) Synthesis and structure of LaSc2N@Cs(hept)-C80 with one heptagon and thirteen pentagons. Angew Chem Int Ed 54:495–499
132. Yu P et al (2022) An unprecedented C80 cage that violates the isolated pentagon rule. Inorg Chem Front 9:2264–2270
133. Mercado BQ et al (2008) Is the isolated pentagon rule merely a suggestion for endohedral fullerenes? The structure of a second egg-shaped endohedral fullerene-Gd_3N @ C_s(39663)-C_{82}. J Am Chem Soc 130:7854–7855

134. Zuo T et al (2008) New egg-shaped fullerenes: non-isolated pentagon structures of Tm3N@Cs (51 365)-C84 and Gd3N@Cs(51 365)-C84. Chem Commun 9:1067–1069
135. Beavers CM et al (2006) Tb3N@C-84: an improbable, egg-shaped endohedral fullerene that violates the isolated pentagon rule. J Am Chem Soc 128:11352–11353
136. Zhang J et al (2013) A missing link in the transformation from asymmetric to symmetric metallofullerene cages implies a top-down fullerene formation mechanism. Nat Chem 5: 880–885
137. Chen C-H et al (2016) Zigzag Sc2C2 carbide cluster inside a [88]fullerene cage with one heptagon, Sc2C2@Cs(hept)-C88: a kinetically trapped fullerene formed by C2 insertion? J Am Chem Soc 138:13030–13037
138. Wei T, Yang S, Kemnitz E, Troyanov SI (2015) Two successive C2 losses from C86 fullerene upon chlorination with the formation of non-classical C84Cl30 and C82Cl30. Chem Asian J 10:559–562
139. Ioffe IN et al (2010) Chlorination of C_{86} to $C_{84}Cl_{32}$ with nonclassical heptagon-containing fullerene cage formed by cage shrinkage. Angew Chem Int Ed 49:4784–4787
140. Jin F, Yang S, Kemnitz E, Troyanov SI (2017) Skeletal transformation of a classical fullerene C88 into a nonclassical fullerene chloride C84Cl30 bearing quaternary sequentially fused pentagons. J Am Chem Soc 139:4651–4654
141. Yang S, Wei T, Scheurell K, Kemnitz E, Troyanov SI (2015) Chlorination-promoted skeletal-cage transformations of C88 fullerene by C2 losses and a C-C bond rotation. Chem Eur J 21: 15138–15141
142. Ioffe IN et al (2013) Cage shrinkage of fullerene via a C2 loss: from IPR C90(28)Cl24 to nonclassical, heptagon-containing C88Cl22/24. Inorg Chem 52:13821–13823
143. Guan R, Jin F, Yang S, Tamm NB, Troyanov SI (2019) Stable C92(26) and C92(38) as well as unstable C92(50) and C92(23) isolated-pentagon-rule isomers as revealed by chlorination of C92 fullerene. Inorg Chem 58:5393–5396
144. Ioffe IN et al (2012) Skeletal transformation of isolated pentagon rule (IPR) fullerene C82 into non-IPR C82Cl28 with notably low activation barriers. Inorg Chem 51:11226–11228
145. Tamm NB, Guan R, Yang S, Kemnitz E, Troyanov SI (2019) Chlorination-promoted cage transformation of IPR C92 discovered via trifluoromethylation under formation of non-classical C92(NC)(CF3)22. Chem Asian J 14:2108–2111
146. Yang S et al (2014) Structures of chlorinated fullerenes, IPR C96Cl20 and non-classical C94Cl28 and C92Cl32: evidence of the existence of three new isomers of C96. Chem Asian J 9:3102–3105
147. Ioffe IN et al (2015) C100 is converted into C94Cl22 by three chlorination-promoted C2 losses under formation and elimination of cage heptagons. Chem Eur J 21:4904–4907
148. Yang S, Wang S, Kemnitz E, Troyanov SI (2014) Chlorination of IPR C100 fullerene affords unconventional C96Cl20 with a nonclassical cage containing three heptagons. Angew Chem Int Ed 53:2460–2463
149. Wang S, Yang S, Kemnitz E, Troyanov SI (2016) New isolated-pentagon-rule and skeletally transformed isomers of C100 fullerene identified by structure elucidation of their chloro derivatives. Angew Chem Int Ed 55:3451–3454
150. Mazaleva ON et al (2018) Experimental and theoretical approach to variable chlorination-promoted skeletal transformations in fullerenes: the case of C102. Inorg Chem 57:4222–4225
151. Yang S et al (2013) The first structural confirmation of a C102 fullerene as C102Cl20 containing a non-IPR carbon cage. Chem Commun 49:7944–7946
152. Beavers CM et al (2006) $Tb_3N@C_{84}$: an improbable, egg-shaped endohedral fullerene that violates the isolated pentagon rule. J Am Chem Soc 128:11352–11353

Merging Carbon Nanostructures with Porphyrins

7

Arjun Menon, Ramandeep Kaur, and Dirk M. Guldi

Contents

Abstract

In this contribution, we highlight the most important work in the field of photon and charge management, focusing on electron donor-acceptor conjugates and/or systems built around porphyrins, on the one hand, and 0D, 1D, and 2D nanocarbons, on the other hand. Photons in these conjugates/systems are managed by the porphyrins, while the 0D, 1D, and 2D nanocarbons serve as the electro-active component, which allow the charges to be managed. Going beyond the highlighted examples with the characterization of photon and charge management, we emphasize photovoltaics and photocatalysis to convert and store energy.

Keywords

Charge management · Nanocarbons · Porphyrins · Photon management · Solar energy conversion

A. Menon · R. Kaur · D. M. Guldi (✉)
Department of Chemistry and Pharmacy, Interdisciplinary Center for Molecular Materials, Friedrich-Alexander University of Erlangen-Nürnberg, Erlangen, Germany
e-mail: arjun.menon.puthiyedath@fau.de; ramandeep.kaur@fau.de; dirk.guldi@fau.de

X. Lu et al. (eds.), *Handbook of Fullerene Science and Technology*,
https://doi.org/10.1007/978-981-16-8994-9_24

Introduction

Plants, algae, and even some microorganisms all perform photosynthesis. It is based on the use of light energy to produce sugars from carbon dioxide and water. A sophisticated synergy of photon and charge management is, however, required. Artificial photosynthesis attempts to replicate the natural processes of photosynthesis by converting sunlight as a practically unlimited and sustainable source of energy and making high-energy chemicals to store energy. A far-reaching challenge in artificial photosynthesis is to use cheap and environmentally friendly materials [1–3].

Nature provides the perfect blueprint for an optimized photon and charge management [4–7]. With focus on photon management, it is light-harvesting within an array of proteins, carotenoids, and chlorophylls that enables unidirectional transfer of light energy in light-harvesting complexes. Important is hereby that the absorption spectra of the individual building blocks are not overlapping. As a consequence, they broaden the range of light that is absorbed and that sets up the ways and means to panchromaticity. Panchromaticity is one of the many down-conversion scenarios as the thermodynamic driving force must be negative to render the energy transfer unidirectional and feasible.

Marcus theory of charge transfer stands out as the dominant theory to describe charge management in chemistry [8]. It treats the rate constants of charge transfer as a parabolic dependence on the free energy changes of the reaction. It sheds light onto the control over the efficiency and kinetics of charge management in the form of charge separation versus charge recombination. Important are, on one hand, the electronic coupling (V) between electron donor and acceptor and, on the other hand, the reorganization energies (λ). They both regulate the absolute rate constants. Notable, the rate constant first increases with increasing thermodynamic driving force ($-\Delta G^{\circ}$). This range of the bell-shape relationship is generally referred to as the Marcus *normal* region. Once the driving force is of the same magnitude as the reorganization energy, the reaction rate reaches a maximum. From here on, the highly exothermic region of the parabola is entered. This range of the bell-shape relationship is generally referred to as the Marcus *inverted* region. Any additional increase of $-\Delta G^{\circ}$ results in an actual slowdown of the reaction rate. In charge management, a thermodynamically driven charge separation should yield a highly energetic radical ion pair. Large energy gaps should ensure dynamics that are deeply shifted into the Marcus *inverted* region, where the limiting and energy wasting charge recombination are slowed down.

Fullerenes, single-walled carbon nanotubes (SWCNTs), and carbon nanodots (CNDs) are some of the most promising materials with enormous potential for high-performance applications based on their unprecedented electronic, optical, mechanical, and chemical properties [9–18]. Solar energy conversion, in general, and optoelectronics, in particular, are important fields of use. At the same time, they are ideal targets for investigating fundamental chemical and physical questions such as shape- and charge-dependent binding and release of molecules, charge transport in confined spaces, and superior sensing of supramolecular interactions. On one hand, probing charge transfer with fullerenes has led to fundamental insights and

major advances in understanding charge transport phenomena. Using fullerenes as molecular electron acceptors has, for example, shed light onto the role of linkers and bridges in molecular charge transfer systems as a means to mediate charge transport. On the other hand, significant breakthroughs have been made with one-dimensional (1D) and two-dimensional (2D) carbon allotropes regarding their functionalization and charge-management manipulation. In particular, SWCNTs and CNDs give rise to amphoteric charge transfer properties that are tunable by covalent as well as non-covalent functionalization [19–32]. The recent past has shown that advanced carbon allotropes play a central role in optoelectronic devices [33, 34]. To this end, their charge-management properties are central, and each of them possesses their own undeniable advantages.

Amorphous Carbon Structures

Carbon Nanodots (CNDs)

Under the generic term "CND," there are many examples of luminescent, colloidal, and carbon materials synthesized in solution. In contrast to the well-defined 0D hollow fullerenes and endohedral fullerenes, on the one hand, and 1D SWCNTs, on the other hand, the exact structural characteristics of CNDs still present great difficulties. Strictly speaking, CND is a nanocarbon with a (partially) amorphous structure and high heteroatom content. Much of our own work focuses on the synthesis of CND under pressure, for which citric acid and urea are used as cheap and bio-based precursors. However, CND devices are of increasing interest: they are readily available, non-toxic, and specifically designed for use with carbon nanomaterials. In particular, CNDs for electron transfer reduction and oxidation have been successfully tested in studies. Among the many unusual properties of CNDs, their luminescence stands out perhaps as the most striking optical characteristic [35–41].

Covalent Porphyrin Conjugates

In CND–H_2P conjugates (**1**), strong intramolecular charge-transfer interactions were observed both in the ground and excited states in 1:1 H_2O/THF solutions (Fig. 1) [42]. The H_2P Soret-band absorptions were found to be broadened and red-shifted by about 30 nm compared to the H_2P reference, while the Q-band absorptions were red-shifted from 518, 555, 581, and 636 nm to 523, 556, 597, and 650 nm, respectively. In addition, the CND-centered absorptions in the CND–H_2P conjugate (**1**) were blue-shifted by 6 nm compared with the bare CND absorptions. These results indicated strong electronic interactions between CND and H_2P already in the ground state. These were favored by their spatial proximity, which stems from their covalent linkage. Transfer of these interactions to the excited state resulted in 50% quenching of CND fluorescence and 80% quenching of H_2P fluorescence in the CND–H_2P conjugate (**1**) compared with the individual constituents. The red-shift of the H_2P fluorescence by 6 nm was striking. The effective excited-state electronic interaction within the conjugate provided rich excited-state activity. On one hand, an

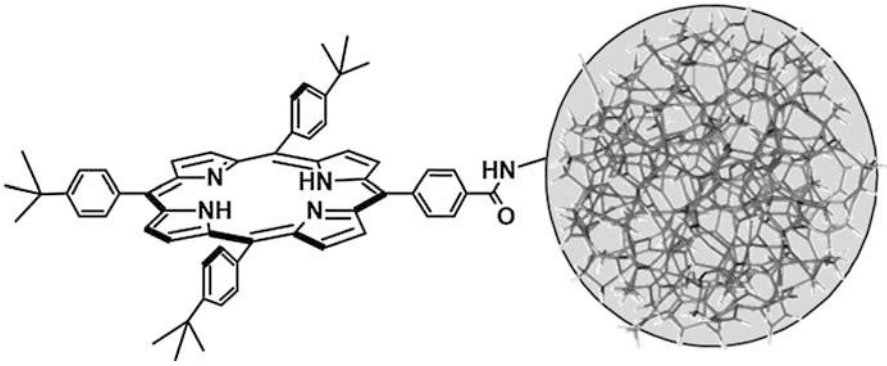

Fig. 1 Representative porphyrin conjugate featuring 2D CNDs: CND–H_2P (**1**) with an electron-accepting CND and a light-harvesting/electron-donating free-base porphyrin (H_2P). In H_2O/THF (1:1 v/v), charge separation and bi-phasic recombination are $>1 \times 10^{12}$ and 1.59×10^{11}/4.44×10^{9} s^{-1}, respectively

intramolecular energy transfer process was accompanied by selective excitation of CND at 300 nm, resulting in significant H_2P fluorescence. On the other hand, selective H_2P excitation at 422 nm initiated the intramolecular ultrafast electron transfer from H_2P to CNDs. This resulted in a charge-separated state that recombined bi-phasically with rate constants of 1.59×10^{11} and 4.44×10^{9} s^{-1} to restore the ground state.

Non-covalent Porphyrin Systems

Here, a diverse series of neutral, positively charged, and negatively charged H_2P/ZnP-based CND systems were investigated (Fig. 2) [43]. The ground state interactions between CNDs and H_2P/ZnP were corroborated by means of spectrophotometric absorption titration assays. In the case of CND•H_2P^{4+} (**2**)/CND•ZnP^{4+} (**3**), the Soret-band absorptions of the H_2P^{4+}/ZnP^{4+} were found to be attenuated and red-shifted in comparison with what was seen in the references. In contrast, no shifts were observed for CND•H_2P^{4-} (**4**)/CND•ZnP^{4-} (**5**) and CND•H_2P (**6**)/CND•ZnP (**7**) systems. For the bulky, positively charged porphyrin-based CND systems, CND•H_2P^{8+} (**8**)/CND•ZnP^{8+} (**9**), an intermediate scenario was found in the form of slightly decreased and red-shifted Soret-band absorption features of H_2P^{8+}/ZnP^{8+} with respect to the references. These results pointed to stronger ground state interaction between H_2P^{4+}/ZnP^{4+} and CNDs than for H_2P/ZnP and H_2P^{8+}/ZnP^{8+}. Turning to excited-state interactions for all CND•porphyrin systems, the observed trend was well in line with the steady-state absorption assays. The porphyrin-centered fluorescence features were 90%, and 40% quenched for CND•H_2P^{4+} (**2**)/CND•ZnP^{4+} (**3**) and CND•H_2P^{8+} (**8**)/CND•ZnP^{8+} (**9**) conjugates, respectively. For the CND•H_2P (**6**)/CND•ZnP (**7**) systems, very subtle porphyrin-centered quenching was noted. The complimentary use of spectroelectrochemical and transient absorption measurements substantiated the formation of the one-electron oxidized form of the porphyrins and the one-electron reduced form of the CNDs

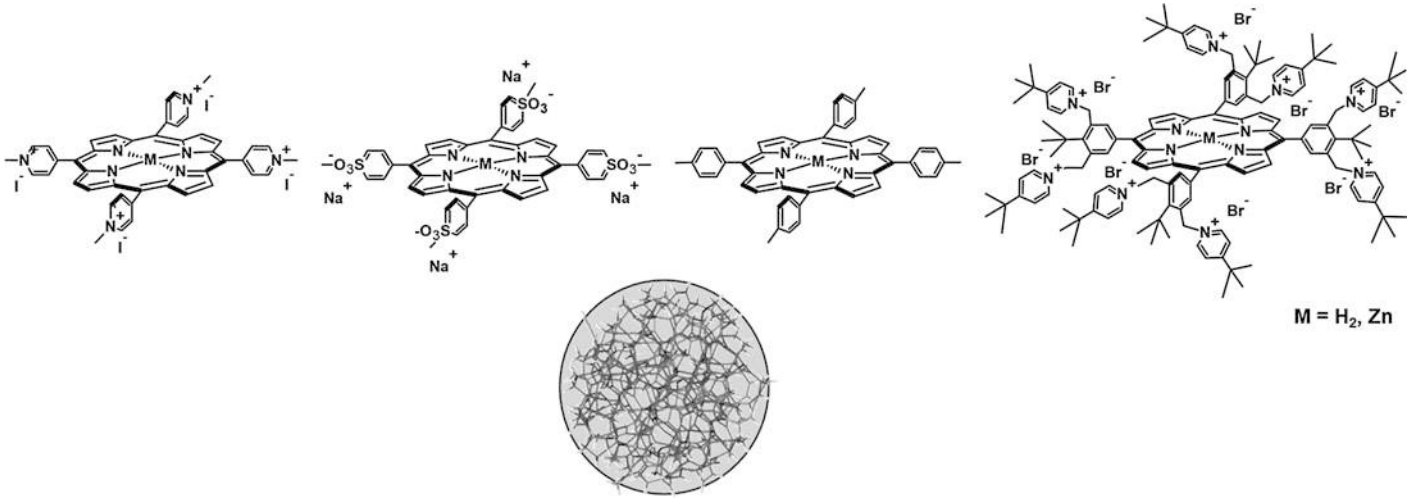

Fig. 2 Representative porphyrin systems featuring 2D CNDs: CND•H_2P^{4+} (**2**)/CND•ZnP^{4+} (**3**) with an electron-accepting CND and light-harvesting/electron-donating positively charged free-base/zinc (II) porphyrin (H_2P^{4+}/ZnP^{4+}) on the left, CND•H_2P^{4-} (**4**)/CND•ZnP^{4-} (**5**) with an electron-accepting CND and light-harvesting/electron-donating negatively charged free-base/zinc (II) porphyrin (H_2P^{4-}/ZnP^{4-}) in the center left, CND•H_2P (**6**)/CND•ZnP (**7**) with an electron-accepting CND and light-harvesting/electron-donating neutral free-base/zinc (II) porphyrin (H_2P/ZnP) in center right, and CND•H_2P^{8+} (**8**)/CND•ZnP^{8+} (**9**) with an electron-accepting CND and light-harvesting/electron-donating bulky positively charged free-base/zinc (II) porphyrin (H_2P^{8+}/ZnP^{8+}) on the right. In methanol, the charge recombination is 2.89×10^{10} s^{-1} (CND•H_2P^{4+} (**2**)), 2.70×10^{10} s^{-1} (CND•ZnP^{4+} (**3**)), 2.68×10^{10} s^{-1} (CND•H_2P^{8+} (**8**)), and 6.02×10^{10} s^{-1} (CND•ZnP^{8+} (**9**))

after photoexcitation. The rate constants of the charge-separated states were 2.89×10^{10}, 2.70×10^{10}, 2.68×10^{10}, and 6.02×10^{10} s^{-1} in the case of CND•H_2P^{4+} (**2**), CND•ZnP^{4+} (**3**), CND•H_2P^{8+} (**8**), and CND•ZnP^{8+} (**9**), respectively. Notably, no charge separation was found in the case of CND•H_2P^{4-} (**4**)/CND•ZnP^{4-} (**5**) and CND•H_2P (**6**)/CND•ZnP (**7**) systems.

Crystalline Carbon Structures

Fullerenes

The 0D structure of empty fullerenes, ever since their discovery in 1985, have enriched the palette of carbon chemistry and have stimulated interest in exploring their properties as an important building block in the fields of nanoscience [9, 44]. Fullerenes are made of alternating hexagons and pentagons of $sp^{2.278}$-hybridized carbon atoms and which feature a diameter of 7.8 Å for C_{60} [45–47]. In order to synthesize gram quantities of empty fullerenes, especially pure and single isomers in the case of the most abundant C_{60} and C_{70}, arc discharge with graphite electrodes is the method of choice. Fullerenes possess extraordinary electron-accepting properties, which were predicted theoretically and confirmed experimentally. Owing to this property, integration of fullerenes into electron-donor-acceptor systems has resulted in noteworthy advances in the areas of light-induced electron transfer chemistry and solar energy conversion. Remarkable is the small reorganization energy and the ability to delocalize electrons, which have rendered fullerenes unique for inter- and intramolecular electron transfer processes. In essence, multifaceted work has demonstrated that empty fullerenes function predominantly as electron acceptors when integrated together with (metallo)porphyrins into energy conversion and storage units [10, 11, 48, 49].

Porphyrinoid systems, particularly metalloporphyrinoids, with their rich and extensive absorption in the entire visible region of the solar spectrum, are particularly promising as integrative building blocks with enhanced absorption cross sections. Over the past two and a half decades, they have emerged as light-harvesting building blocks in the construction of molecular architectures. Their high electron excitation energy, typically above 2.0 eV, powers a strong exergonic electron transfer and intercedes the conversion between light and chemical/electrical energy [50–53]. Another important feature of porphyrins is the highly delocalized π-electron system. When electrons are accepted or donated, this delocalization leads to minimal structural changes during electron transfer. Rich redox properties render porphyrins and porphyrin analogous as essential components in important biological electron transport systems including photosynthesis and respiration [49, 54].

Covalent Porphyrin Conjugates

Pioneering work in the view of covalently linking porphyrins/metalloporphyrin and fullerene covers the examples reported by Gust et al. and Imahori et al., employing either bicyclic or amide linkers [55, 56]. These were the landmarks towards

designing molecular artificial reaction centers incorporated with a molecular motif, which was not restricted to the components known from the natural photosynthesis. Investigation into the photoinduced charge-transfer events disclosed a significant stabilization of charge-separated state relative to the conjugates with quinone as electron acceptor. This evoked the synthesis of a plethora of (metallo)porphyrin- and fullerene-based electron donor-acceptor conjugates. On a general note, it is important to mention that confirmations about the electron transfer from ZnP to fullerene in the following reported studies are derived from the characteristic transients associated with the one-electron oxidized form of ZnP and the one-electron reduced form of C_{60}, obtained in pump-probe experiments. In the visible region, transients around 415 nm and broad features in the 600–700 nm region confirm the $ZnP^{\bullet+}$ formation. In the NIR region, benchmark transients around 1000–1100 nm confirm the $C_{60}^{\bullet-}$, and 1350–1400 nm confirm the $C_{70}^{\bullet-}$ formation [57–58].

Herein, we wish to highlight the evolution of the porphyrin-fullerene conjugates over the past 25 years, as a function of electronic-coupling strength, π-conjugation length, and advanced understanding of the charge-transfer mechanism in the light of Marcus theory, which could be imparted to enhance the design of the systems subsequently. Furthermore, over time, methods to analyze and determine the rate constants and underlying mechanism for the electron-donor acceptor systems have advanced. Most of the early reported protocols were based on following the kinetics by multi-exponential decay analysis. This analysis over the past 10 years has been complemented by global-target analyses of the time-resolved data using any relevant software.

Early studies on intramolecular electron transfer in short-distanced C_{60}-porphyrin conjugates involved the two π-electron systems in van Waals contacts or in close proximity due to the type of linker. In this regard, the two examples shown here, reported by Gust et al., involved two different approaches of covalently linking fullerenes to porphyrins: H_2P and ZnP. The first system, namely, C_{60}–H_2P (**10**) and C_{60}–ZnP (**11**), is based on the direct attachment of the porphyrin at its meso-position to C_{60} [60] – Fig. 3 – and the second system, namely, C_{60}–H_2P (**12**) and C_{60}–ZnP (**13**), features a bicyclic linkage between the porphyrin and C_{60} [61] – Fig. 4 In C_{60}–H_2P (**10**), the center-center distance is 9.9 Å and in C_{60}–H_2P (**12**) due to the folded conformation 6.7 Å. Comparing the photophysical properties of C_{60}–H_2P (**10**) and C_{60}–H_2P (**12**) indicated that the electronic coupling is stronger in C_{60}–H_2P (**12**) than in C_{60}–H_2P (**10**), despite the 5 versus 3 single bonds between the two π-systems. What is, however, important is the shorter distance.

For both systems, time-resolved studies suggested that the first singlet excited state of the porphyrin decayed by a combination of electron and energy transfer to generate $C_{60}^{\bullet-}$–$ZnP^{\bullet+}$/$C_{60}^{\bullet-}$–$H_2P^{\bullet+}$ and $^{1*}C_{60}$–ZnP/$^{1*}C_{60}$–H_2P, respectively. Singlet excited-state energy transfer in C_{60}–H_2P (**12**) occurred in 1.4×10^{11} s^{-1} in toluene solution, whereas the time constant for the comparable process in C_{60}–H_2P (**10**) is 4.5×10^{10} s^{-1}. In C_{60}–H_2P (**10**), photoinduced electron transfer from $^{1*}C_{60}$–H_2P to form $C_{60}^{\bullet-}$–$H_2P^{\bullet+}$ occurs in benzonitrile with a free energy change of −0.16 eV and a rate constant of 1.3×10^{10} s^{-1}. In C_{60}–H_2P (**10**), photoinduced electron transfer from C_{60}–$^{1*}H_2P$ to yield $C_{60}^{\bullet-}$–$H_2P^{\bullet+}$ followed in the same solvent with a free

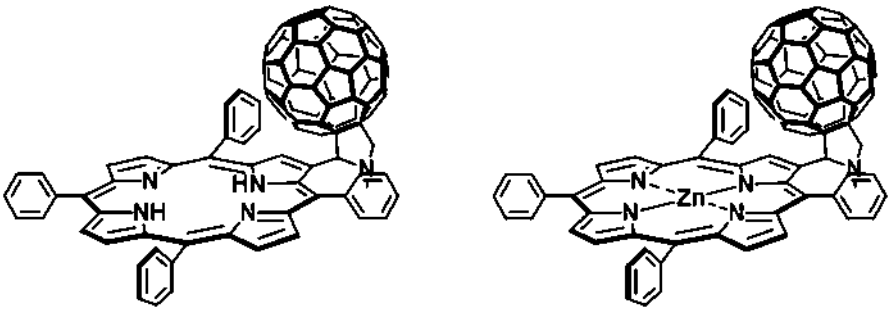

Fig. 3 Representative porphyrin conjugates featuring 0D C_{60}: C_{60}–H_2P (**10**) with an electron-accepting empty fullerene (C_{60}) and a light-harvesting/electron-donating free-base porphyrin (H_2P) on the left and C_{60}–ZnP (**11**) with an electron-accepting empty fullerene (C_{60}) and a light-harvesting/electron-donating zinc (II) porphyrin (ZnP) on the right. In benzonitrile, the charge recombination is 3.4×10^9 s^{-1} (C_{60}–H_2P (**10**))/2.0×10^{10} s^{-1} (C_{60}–ZnP (**11**))

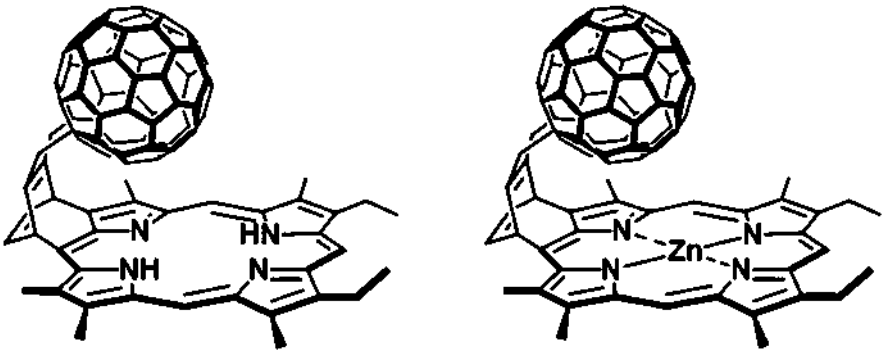

Fig. 4 Representative porphyrin conjugates featuring 0D C_{60}: C_{60}–H_2P (**12**) with an electron-accepting empty fullerene (C_{60}) and a light-harvesting/electron-donating free-base porphyrin (H_2P) on the left and C_{60}–ZnP (**13**) with an electron-accepting empty fullerene (C_{60}) and a light-harvesting/electron-donating zinc (II) porphyrin (ZnP) on the right. In benzonitrile, the charge recombination is $>2 \times 10^{11}$ s^{-1} for both C_{60}–H_2P (**12**) and C_{60}–ZnP (**13**)

energy change of −0.32 eV and a rate constant of 1.8×10^{11} s^{-1}. Most importantly, the charge recombination for the pyrrole-linked C_{60}–H_2P (**10**) and C_{60}–ZnP (**11**), which occurred with a rate constant of 3.4×10^9 ($C_{60}^{\bullet-}$–$H_2P^{\bullet+}$ − 1.58 eV) and 2.0×10^{10} s^{-1} ($C_{60}^{\bullet-}$–$ZnP^{\bullet+}$ − 1.38 eV) in benzonitrile, respectively, pointed towards a considerable deceleration of this process versus charge separation. An important consideration implies that the 200 mV higher oxidation potential of the $H_2P^{\bullet+}/H_2P$ couple relative to that of $ZnP^{\bullet+}/ZnP$ would allow storing a larger fraction of the excited-state energy as chemical potential in the charge-separated state. Slower charge separation and charge recombination in the C_{60}–H_2P versus the C_{60}–ZnP conjugates were logical consequences that stemmed from the energy-gap variation. These results were important in signifying the importance of incorporating

fullerenes, solvent polarity, $H_2P^{\bullet+}/H_2P$ versus $ZnP^{\bullet+}/ZnP$ redox couple, and free energy change of underlying processes on the dynamics of photoinduced processes in the conjugates. Additionally, it underlined the consistency with theory of occurrence of charge recombination in the Marcus inverted region due to its structural rigidity and small reorganization energy [55, 60, 61].

Other examples involving short-range charge transfer, designed by employing the strategy of π-π stacking in C_{60}–ZnP conjugate (**14**), employed a trans-2 addition pattern to enforce a close proximity between the electron donor and acceptor [62] – Fig. 5. In comparison with the abovementioned systems, even shorter separation of 3.0 Å guaranteed that an intramolecular charge separation dominates over the competing energy transfer and succeeds in virtually any solvent. The rapid formation and decay of the one-electron oxidized form of ZnP between 670 and 680 nm and the one-electron reduced form of C_{60} around 900 nm in toluene affirmed the charge separation and charge recombination processes, respectively. A systematic change in the polarity of the solvent, for example, from non-polar toluene to polar benzonitrile allowed changes in the free energy to vary over a wide range. Obviously, at lower thermodynamic driving forces, that is, higher dielectric constants, a significant acceleration of the charge recombination rate was observed, which confirms our working hypothesis. To illustrate this, the rate, at which charge recombination took place, was varied over a wide range, that is, from 1.6×10^9 s^{-1} in toluene to 2.6×10^{10} s^{-1} in benzonitrile. Most importantly, the correlation between rate constants and thermodynamic driving forces results in a parabolic dependence, from which an experimental reorganization energy of 0.86 eV was derived. Moreover, the electron delocalization in C_{60} given by its large three-dimensional π-system led to the conclusion that the reorganization energy in the C_{60}–ZnP systems is not subject to large changes in solvent polarity when switching, for example, from

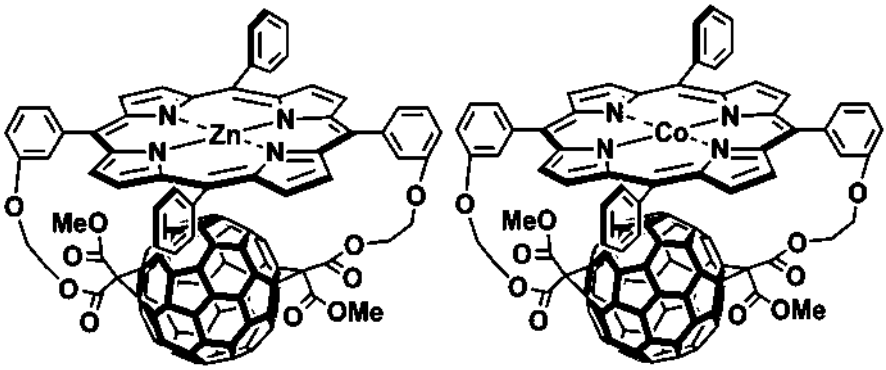

Fig. 5 Representative porphyrin conjugates featuring 0D C_{60}: C_{60}–ZnP (**14**) with an electron-accepting empty fullerene (C_{60}) and a light-harvesting/electron-donating zinc (II) porphyrin (ZnP) on the left and C_{60}–CoP (**15**) with an electron-accepting empty fullerene (C_{60}) and a light-harvesting/electron-donating cobalt (II) porphyrin (CoP) on the right. In THF, charge separation and recombination are $>4.3 \times 10^{10}$ s^{-1} (C_{60}–ZnP (**14**)/5.5×10^{10} s^{-1} (C_{60}–CoP (**15**)) and 2.5×10^9 s^{-1} (C_{60}–ZnP (**14**))/4.3×10^9 s^{-1} (C_{60}–CoP (**15**)), respectively

toluene and THF to benzonitrile. Therefore, it is reasonable to assume that the rearrangement energies of the C_{60}–ZnP conjugate in different solvents are comparable.

Additionally, a series of different metalloporphyrins (MP) bearing manganese(III), iron(III), cobalt (II), nickel(II), and copper(II) were investigated [63]. A key feature of all these C_{60}–MP conjugates was the van der Waals distance separating the electron-donating metalloporphyrin from the electron-accepting C_{60} in the excited state. To overcome the rapid deactivation of excited states in metalloporphyrins, the π-π-stacking motif proved to be an important tool. It was found that the lifetime of the charge-separated state, which is generated quickly and efficiently, depends on the solvent polarity and the type of metal.

It is also very important to point out that around the same time in the late twentieth century, when Gust et al. synthesized and reported on the photophysical properties of porphyrin-fullerene conjugates, Imahori et al. designed different porphyrin-fullerene conjugates. In these conjugates, C_{60} was covalently linked to a meso-porphyrin aryl ring at the para-position via an amide bond. The cyclohexene unit in the spacers provided the overall rigidity [64, 65] – Fig. 6. For the C_{60}–ZnP (**16**) conjugate, formation of the charge-separated state was observed in THF with a driving force of −0.67 eV at a rate constant of 9.0×10^9 s^{-1}, followed by a slower charge recombination with a rate constant of 2.0×10^9 s^{-1}. Later on, Guldi and Imahori et al. successfully demonstrated fascinating photophysical properties for a variety of C_{60}–ZnP and C_{60}–H_2P conjugates based on a similar design. However, the amide linkage was reversed, and cyclohexene was replaced by pyrrolidinone to link C_{60} with the porphyrin [66]. Photophysical studies on these conjugates provided insights into charge stabilization as a result of implementation of changes in the design. This encompassed linear arrays, in which a systematic variation of the spatial distance, separating the electron donor (ZnP) from the electron acceptor (C_{60}) by about 11.9 Å (R_{ee}) in C_{60}–ZnP conjugate (**17**), but persevering the overall free energy changes (for instance, in polar solvents) with rate constants as low as 3.7×10^5 s^{-1} in deoxygenated THF [66–68]. Comparing this value to the rate of ~10^9 s^{-1} in **14** and **15** based on close proximity between ZnP and C_{60}, this approach was a success as it assisted in increasing the lifetime of the charge-separated state by a factor of 7000. In several publications, the group provided thorough photophysical investigations by employing the same architecture and addressed multiple factors, which could influence the underlying mechanism and as a result the lifetimes of the charge-separated states, induced upon photoexcitation in a variety of fullerene-porphyrin conjugates [10, 48, 54].

In order to discuss the next results, we need to introduce the strategy to separate charges over large distances and, in turn, to achieve long-lived charge-separated states reaching into the micro or even millisecond regimes. In this regard, early work involved combining several redox-active building blocks with porphyrins and fullerene in order to promote a cascade of short-range, fast, and efficient electron transfer.

The leading examples by Guldi et al., which documented promising photophysical results, were based on combining redox-active Fc, ZnP, H_2P, and C_{60} in

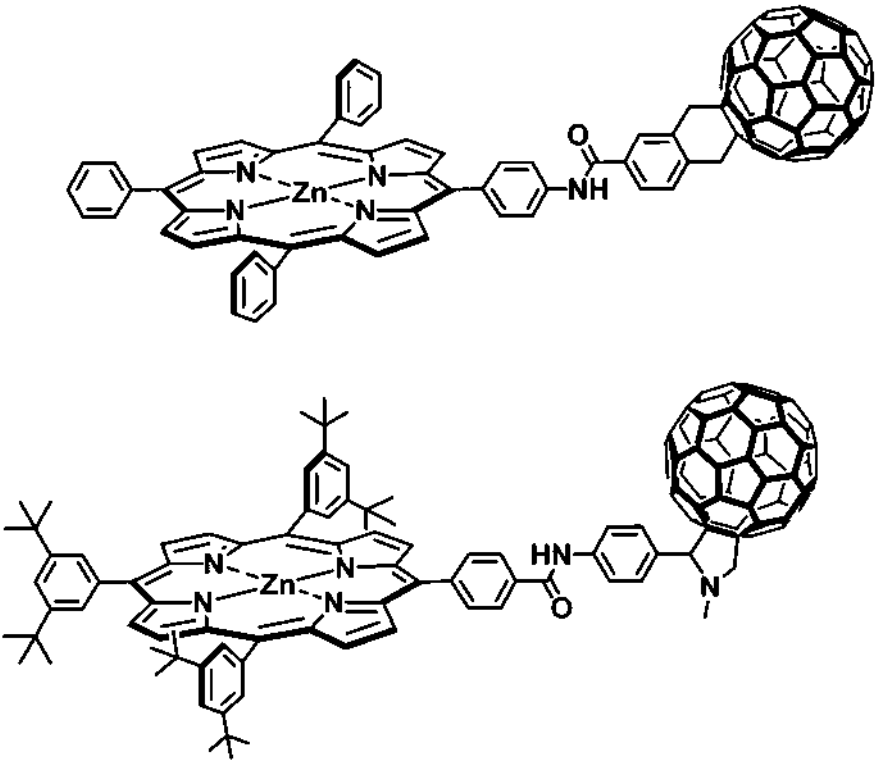

Fig. 6 Representative porphyrin conjugates featuring 0D C_{60}: (C_{60}–ZnP)s with an electron-accepting empty fullerene (C_{60}) and a light-harvesting/electron-donating zinc (II) porphyrin (ZnP) linked by a amide-based spacer (**16**) on the top and a reversed amide-based spacer (**17**) on the bottom. In THF, charge separation and recombination are 9.0×10^9 s^{-1} (C_{60}–ZnP (**16**))/ 1.3×10^{10} s^{-1} (C_{60}–ZnP (**17**)) and 2.0×10^{10} s^{-1} (C_{60}–ZnP (**16**))/3.7×10^5 s^{-1} (C_{60}–ZnP (**17**)), respectively. In benzonitrile, charge separation and recombination are 1.1×10^{10} and 1.3×10^6 s^{-1} (C_{60}–ZnP (**17**)), respectively

the form of linear-shaped conjugates of types: C_{60}–H_2P–ZnP, C_{60}–ZnP–Fc, C_{60}–H_2P–Fc [67–69]. Another sophisticated example reported by Gust et al. also involved the combination of ZnP, H_2P, and C_{60}, but in a branched rather than linear fashion, documenting a cascade of efficient light-harvesting and electron-transfer processes in C_{60}–H_2P–ZnP–$(ZnP)_3$ conjugates [70].

Our focus here lies on the linear arrays as benchmark electron donor-acceptor conjugates. In C_{60}–H_2P–ZnP (**18**), ZnP performs as an antenna that transfers its singlet excited-state energy to that of the lower lying H_2P [69, 71] – Fig. 7. In polar benzonitrile, this energy transfer is followed by a sequential electron transfer yielding $C_{60}^{\bullet-}$–$H_2P^{\bullet+}$–ZnP and subsequently via charge-shift $C_{60}^{\bullet-}$–H_2P–$ZnP^{\bullet+}$. Considering the overall efficiency of 40% for (i) funneling light from the antenna ZnP to H_2P, (ii) charge injection into C_{60}, and (iii) charge-shift, this artificial reaction center reproduces the natural system very well. The rate constant of charge recombination

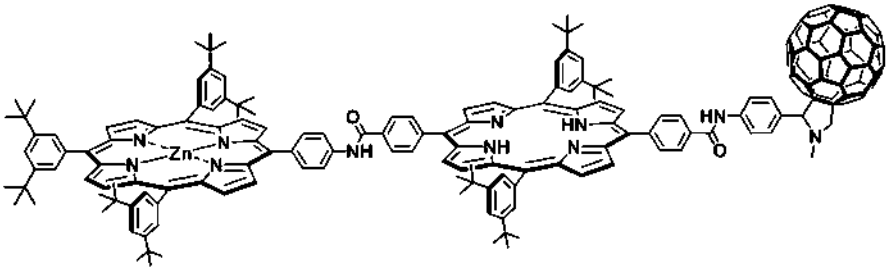

Fig. 7 Representative porphyrin conjugates featuring 0D C_{60}: (C_{60}–H_2P–ZnP) (**18**) with an electron-accepting empty fullerene (C_{60}), a light-harvesting/electron-donating/energy transductor zinc (II) porphyrin (ZnP), and a light-harvesting/electron-donating free-base porphyrin (H_2P) linked via amide-based spacer. In benzonitrile, the charge recombination for $C_{60}^{\bullet-}$–$H_2P^{\bullet+}$–ZnP and $C_{60}^{\bullet-}$–H_2P–$ZnP^{\bullet+}$are 1.3×10^7 s^{-1} and 4.7×10^4 (C_{60}–H_2P–ZnP) (**18**), respectively

for $C_{60}^{\bullet-}$–H_2P–$ZnP^{\bullet+}$ in the different media correlates well with the polarity: 2.9×10^4 s^{-1} (THF), 4.7×10^4 s^{-1} (benzonitrile), 5.0×10^4 s^{-1} (DMF). Since the driving force of charge recombination decreases even in C_{60}–H_2P–ZnP with increasing solvent polarity, the observed trend suggests that the associated rate constants are in the "inverted region" of the Marcus curve [71].

The function of C_{60}–H_2P–Fc (**19**) and C_{60}–ZnP–Fc (**20**), on the other hand, – Fig. 8 – is a lot simpler and limited to two consecutive electron transfers with ZnP and H_2P as primary electron donor to afford $C_{60}^{\bullet-}$–ZnP–$Fc^{\bullet+}$ and C_{60}–$H_2P^{\bullet-}$–$Fc^{\bullet+}$, respectively. In Ar-saturated benzonitrile, the final charge-separated state undergoes charge recombination, however, considerably faster than observed for $C_{60}^{\bullet-}$–H_2P–$ZnP^{\bullet+}$ (4.8×10^4 s^{-1}). The actual rate constants are 1.3×10^5 s^{-1} ($C_{60}^{\bullet-}$–ZnP–$Fc^{\bullet+}$) and 1.2×10^5 s^{-1} ($C_{60}^{\bullet-}$–H_2P–$Fc^{\bullet+}$). Taking into account the similarity in molecular structure and separation (R_{ee} = 30.3 Å), the different thermodynamics must be responsible for this intrinsic behavior. In fact, variation of the driving force by comparing, for example, THF with DMF led to a confirmation that due to the large reorganization energy associated with $Fc^{\bullet+}$, the dynamics within the $Fc^{\bullet+}$/$C_{60}^{\bullet-}$ couples are located in the "normal region" of the Marcus curve [67].

This approach was further extended by combining C_{60}–H_2P–ZnP and C_{60}–ZnP–Fc into an integrated single system, C_{60}–H_2P–ZnP–Fc (**21**). Later in order to enhance the efficiency by increasing the excited-state energy of the electron donor from 1.89 to 2.04 eV, replacement of H_2P by ZnP yielded C_{60}–ZnP–ZnP–Fc (**22**) – Fig. 9. Through these conjugates, a large-distanced separation of charges over a distance of 50 Å as a product of multi-step energy transduction and electron transfer was accomplished. This example features so far the longest lifetime ever reported with 0.38 and 1.6 s in C_{60}–H_2P–ZnP–Fc (**21**) and C_{60}–ZnP–ZnP–Fc (**22**), respectively. This value is also comparable to the lifetime (~ 1 s) of the radical ion pair in bacterial photosynthetic reaction centers [72].

Some important parameters were derived from these linear arrays as a function of the electron donor-acceptor distance. The reorganization energy increases from C_{60}–ZnP (**17**) and C_{60}–H_2P–ZnP (**18**) to C_{60}–H_2P–ZnP–Fc (**21**) with values ranging from

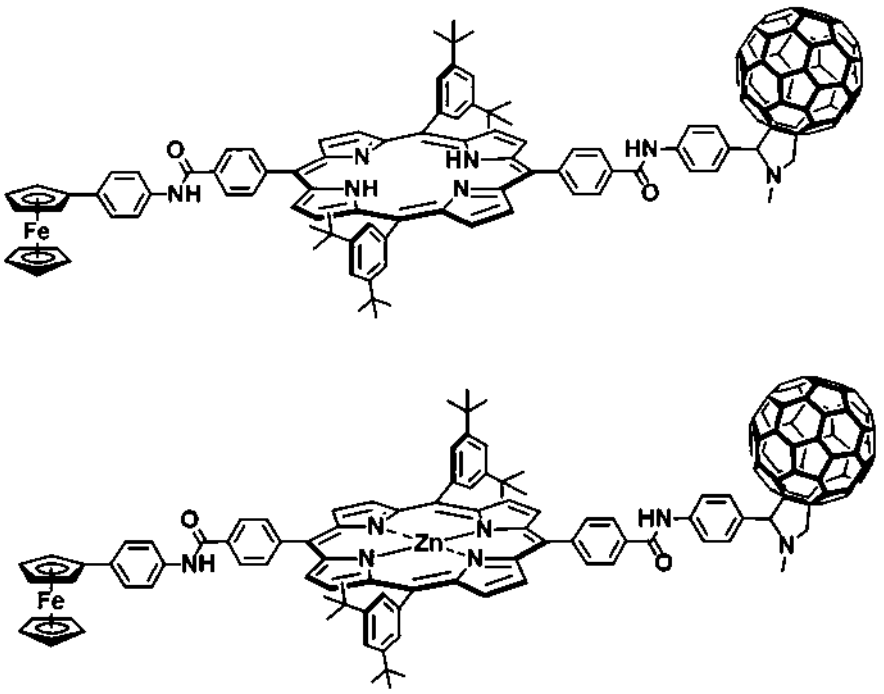

Fig. 8 Representative porphyrin conjugates featuring 0D C_{60}: (C_{60}–H_2P–Fc) (**19**) with an electron-accepting empty fullerene (C_{60}), a light-harvesting/electron-donating free-base (II) porphyrin (H_2P) on the top, and (C_{60}–ZnP–Fc) (**20**) with an electron-accepting empty fullerene (C_{60}), a light-harvesting/electron-donating zinc (II) porphyrin (ZnP), and an electron-donating ferrocene (Fc) on the bottom. In benzonitrile, charge recombination is 1.25×10^5 s^{-1} for $C_{60}^{\bullet-}$–H_2P–$Fc^{\bullet+}$ (C_{60}–H_2P–Fc) (**19**)/1.3×10^5 s^{-1} for $C_{60}^{\bullet-}$–ZnP–$Fc^{\bullet+}$ (C_{60}–ZnP–Fc) (**20**), respectively

0.66 to 1.32 eV. Furthermore, the electronic coupling was calculated to be as small as 5.6×10^{-5} cm^{-1}. Another very important parameter, the attenuation factor, was also derived from the distance dependence of rate constants of C_{60}–H_2P–ZnP–Fc (**21**) (50 Å), C_{60}–H_2P–ZnP (**18**) (30 Å), and C_{60}–ZnP (**17**) (12 Å). A rather high value of 0.60 $Å^{-1}$ was obtained [67, 69, 71, 72].

Another strategy, which facilitates long-distance electron transfer in porphyrin-fullerene systems, is the implementation of molecular bridges as a coupling medium. It is well documented that not only the electronic coupling but also the attenuation factor is a function of electronic structure and overall architecture of the molecular bridge. The quality of a linker functioning as the molecular bridge is determined from the following equation:

$$k_{ET} = k_0 e^{-R_{DA}\beta}$$

where k_0 is the kinetic pre-factor, R_{DA} represents the electron donor-acceptor distance, and β is the attenuation factor, which depends on the intrinsic electronic

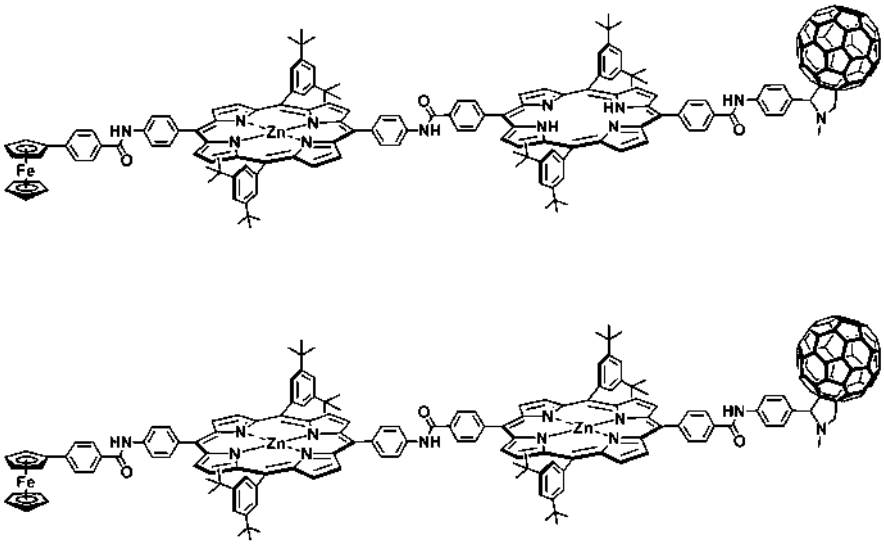

Fig. 9 Representative porphyrin conjugates featuring 0D C_{60}: (C_{60}–H_2P–ZnP–Fc) (**21**) with an electron-accepting empty fullerene (C_{60}), a light-harvesting/electron-donating/energy transductor zinc (II) porphyrin (ZnP), a light-harvesting/electron-donating free-base porphyrin (H_2P), and an electron-donating ferrocene (Fc) on the top and (C_{60}–ZnP–ZnP–Fc) (**22**) with an electron-accepting empty fullerene (C_{60}), a light-harvesting/electron-donating/energy transductor zinc (II) porphyrin (ZnP), and an electron-donating ferrocene (Fc) on the bottom, linked via amide-based spacer. In benzonitrile, charge recombination is $<10^2$ s^{-1} for $C_{60}^{\bullet-}$–H_2P–ZnP–$Fc^{\bullet+}$/$C_{60}^{\bullet-}$–ZnP–ZnP–$Fc^{\bullet+}$ (C_{60}–H_2P–ZnP–Fc) (**21**)/(C_{60}–H_2P–ZnP–Fc) (**22**)

properties of the bridge. Much effort has been devoted to design bridges that facilitate long-range electron transfer reactions with the smallest attenuation factor possible [73, 74]. In this context, π-conjugated oligomers were interesting candidates, which led to the investigations of C_{60} and ZnP connected by alkynes, *p*-phenyleneethylenes (o*p*PE), fluorenes (oFl), and *p*-phenylenevinylenes (o*p*PV) – Fig. 10. The electronic coupling decreased monotonically with distance throughout the series: from 415 to 39 cm^{-1}. Likewise, the reorganization energies exhibited differences. They described a fundamental distance dependence, where they first drop from 0.82 eV at 3.0 Å to 0.5 eV at 6.18 Å and after that they steadily increase to 0.66 eV at 11.9 Å [74].

As a leading example, molecular o*p*PV bridges, which span electron donor-acceptor distances of up to 38.7 Å, exhibited attenuation factors as low as 0.01 $Å^{-1}$. However, the reorganization energy was distance invariant between 24.9 and 38.7 Å with 0.72 eV. A major setback of the aforementioned π-conjugated oligomers was the rotation around the single bonds, which connect the individual phenyl units [75]. It caused a deviation from planarity along the oligomer chain. To this end, the most intriguing contribution came from carbon-bridged oligo-*p*-phenylenevinylene (Co*p*PV) bridges – Fig. 10. Their rigid structure

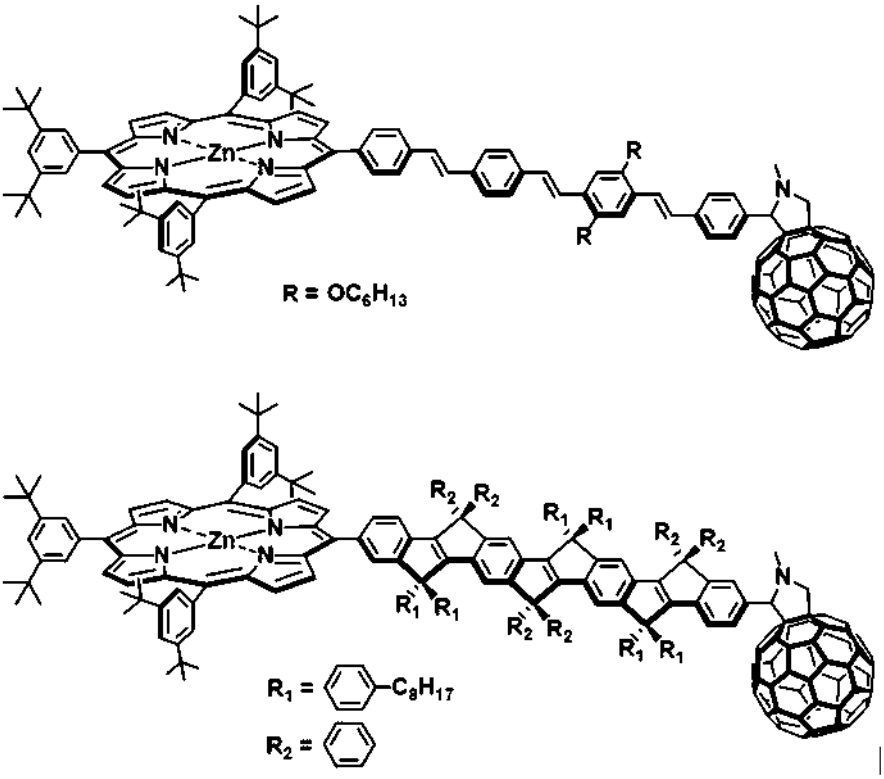

Fig. 10 Representative porphyrin conjugates featuring 0D C_{60}: (C_{60}–ZnP)s with an electron-accepting empty fullerene (C_{60}) and a light-harvesting/electron-donating zinc (II) porphyrin (ZnP) linked by a molecular (o*p*PV)$_3$ bridge (**23**) on the top and a molecular (Co*p*PV)$_3$ bridge (**24**) on the bottom. In THF, charge separation and recombination are 4.5×10^9 s^{-1} (C_{60}–(o*p*PV)$_3$–ZnP (**23**))/7.1×10^{10} s^{-1} (C_{60}– (Co*p*PV)$_3$–ZnP (**24**)) and 1.2×10^6 s^{-1} (C_{60}–(o*p*PV)$_3$–ZnP (**23**))/5.9×10^9 s^{-1} (C_{60}–(Co*p*PV)$_3$–ZnP (**24**)), respectively

ruled out any deviation from planarity along the oligomer chain [76, 77]. Both, the electronic coupling element and the reorganization energy, relative to a comparable molecular o*p*PV bridge, were enhanced due to the flatness of the molecular Co*p*PV bridge with values of 39 cm^{-1} and 0.89 eV, respectively [76].

A similar approach in combining C_{60}, ZnP, and Fc to produce a series of C_{60}–ZnP–Fc conjugates was recently revisited, but by shifting the focus towards beta-substitution of the porphyrin and implementation of molecular bridges between all constituents – Fig. 11. The distance of separation between ZnP/Fc and C_{60}/ZnP was systematically varied via implementation of *p*-phenylene-acetylene/acetylene bridges of different lengths to gain control over shuttling of electrons or holes [78]. As a result, rates for charge-transfer events lead to the formation of the different charge-separated states, that is, C_{60}–ZnP$^{\bullet-}$–Fc$^{\bullet+}$, $C_{60}{}^{\bullet-}$–ZnP$^{\bullet+}$–Fc, and $C_{60}{}^{\bullet-}$–ZnP–Fc$^{\bullet+}$.

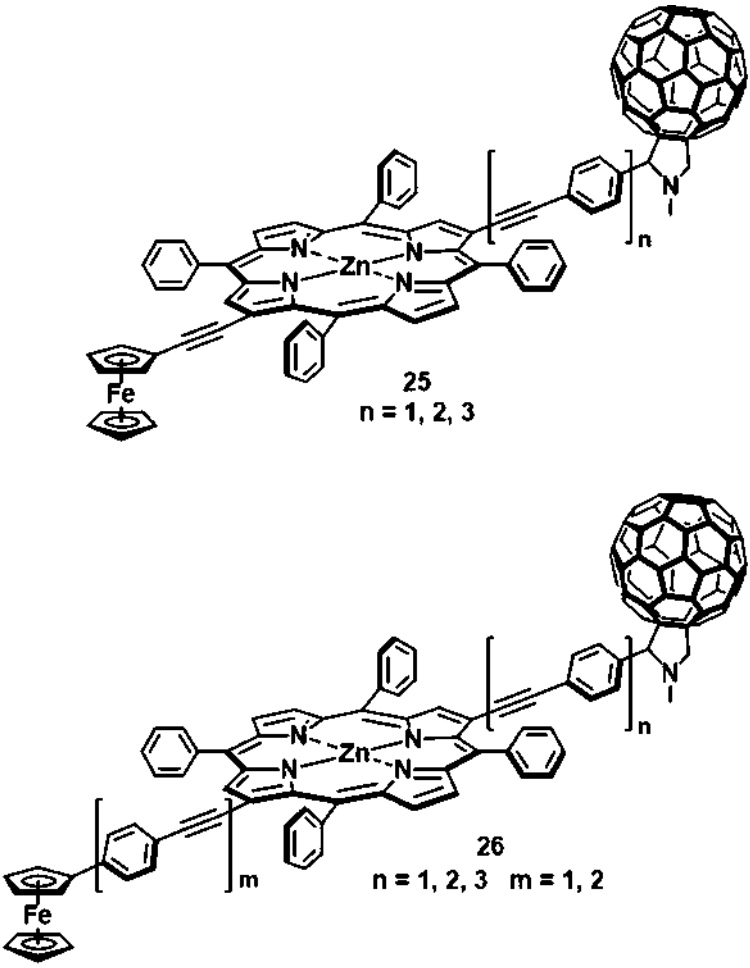

Fig. 11 Representative porphyrin conjugates featuring 0D C_{60}: (C_{60}–ZnP–Fc) (**25**; $n = 1,2,3$) with an electron-accepting empty fullerene (C_{60}), a light-harvesting/electron-accepting/electron-donating zinc (II) porphyrin (ZnP), and an electron-donating ferrocene (Fc), with later linked via acetylene bridge on the top, and (C_{60}–ZnP–Fc) (**26**; $n = 1,2,3$ and $m = 2$) with an electron-accepting empty fullerene (C_{60}), a light-harvesting/electron-accepting/electron-donating zinc (II) porphyrin (ZnP), and an electron-donating ferrocene (Fc), with later linked via phenylene-acetylene bridge on the bottom. In benzonitrile, charge recombination for $C_{60}^{\bullet-}$–$ZnP^{\bullet+}$–Fc and $C_{60}^{\bullet-}$–ZnP–$Fc^{\bullet+}$ are 1.10×10^9 and 2.90×10^5 s^{-1}, respectively (C_{60}–ZnP–Fc (**26**; n = 2, and m = 2))

Charge recombination was studied as an interplay of changes in the reorganization energy, damping factor of the molecular bridges, and variation in the solvent polarity.

The systematic distance variation between C_{60}/ZnP and ZnP/Fc results into a rather inefficient population of $C_{60}^{\bullet-}$–ZnP–$Fc^{\bullet+}$ via charge-shift reaction from

$C_{60}^{\bullet-}$–$ZnP^{\bullet+}$–Fc. The reason behind this was the weak electronic coupling between ZnP and C_{60} with the increased length of the molecular bridge. This caused a considerable deceleration of the charge separation to generate $C_{60}^{\bullet-}$–$ZnP^{\bullet+}$–Fc in the first place. This bottleneck was overcome by reducing the separation in the Fc/C_{60} couple. In turn, an efficient population of $C_{60}^{\bullet-}$–ZnP–$Fc^{\bullet+}$ was observed with a lifetime of the charge-separated state in the microsecond regime. Furthermore, the short- and long-range damping factors were determined. For example, the charge recombination $C_{60}^{\bullet-}$–$ZnP^{\bullet+}$–Fc and charge-shift kinetics of $C_{60}^{\bullet-}$–$ZnP^{\bullet+}$–Fc and C_{60}–$ZnP^{\bullet-}$–$Fc^{\bullet+}$ to yield the $C_{60}^{\bullet-}$–ZnP–$Fc^{\bullet+}$ were analyzed as a function of distance. The corresponding values were 0.17 $Å^{-1}$ for the phenylene-acetylene bridge and 0.13 $Å^{-1}$ and 0.097 $Å^{-1}$ for the acetylene-phenylene bridges. With the employment of molecular bridges of variable lengths in the multicomponent electron donor-acceptor conjugates, two aspects were covered: a relay of photoinduced processes along the well-designed redox gradient and modulation of electronic coupling strength between different redox couples as function of distance and type of bridge.

Non-covalent Porphyrin Systems

A multifaceted control over the separation, angular relationships, electronic coupling, and incorporation of the photo- and redox-active motifs within the scaffolds of electron donor-acceptor assemblies is an elegant, yet challenging, task. Meaningful insights have been borrowed from the organization-principle in action in the bacterial photosynthetic reaction centers, which feature the role of non-covalent interactions in keeping the different components embedded into a protein matrix. Notably, the biomimetic methodologies, such as hydrogen bonding, electron donor-acceptor complexation, Coulomb interactions, π-π stacking, and metal-ligand interactions, guarantee a tool to engineer and achieve a variety of electron donor-acceptor assemblies with well-defined architectures, featuring directionality and selectivity. Depending on the types of interactions and composition of electron donor-acceptor assemblies, the electronic coupling and, therefore, the electron transfer rates can be modulated [69, 79].

An obvious approach, drawing its motivation from the abovementioned short-range conjugates, would be to study association between fullerenes and porphyrins via π-π stacking to construct supramolecular assemblies. The attraction of the curved π-surface of fullerene to the flat π-surface of porphyrins was recognized in the solid-state molecular packing of a crystal structure containing a covalent fullerene-porphyrin conjugate in a protocol by Reed et al. Notably, the 2.75 Å approach of a fullerene carbon atom to the center of the neighboring porphyrin plane was shorter than the separations of common π-π interactions [80]. Soon after, reports on co-crystal formation between fullerenes and a variety of porphyrins and metalloporphyrins followed. To enable association between porphyrins and fullerenes to organize into assemblies held by π-π interactions in the solution phase, creative designs like porphyrin jaws, or cyclic porphyrin dimers, were documented [81, 82]. By following the changes in the characteristic porphyrin features, binding constants as high as 6.7×10^5 M^{-1} for the bicyclic dimer were realized – Fig. 12.

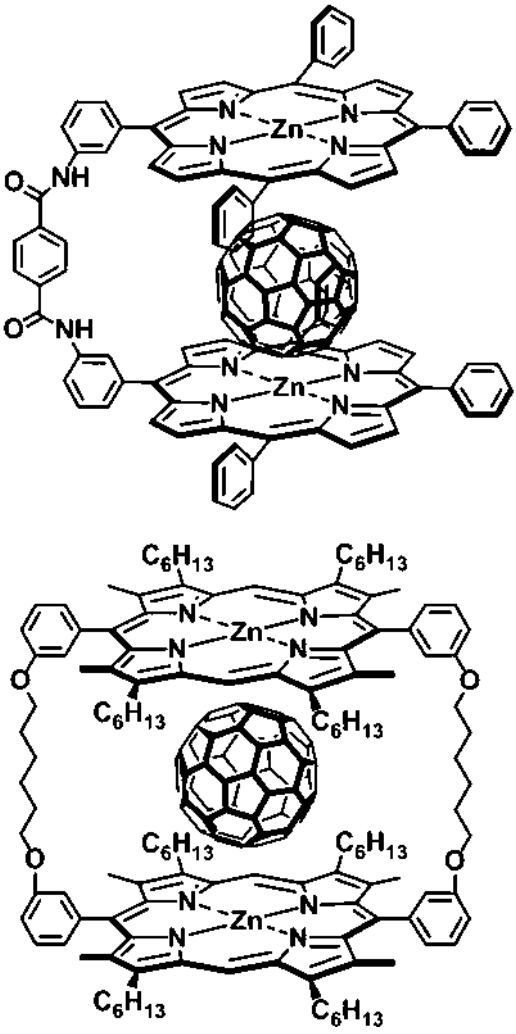

Fig. 12 Representative porphyrin systems featuring 0D C_{60}: C_{60}•$(ZnP)_2$ (**27**) with an electron-accepting C_{60} and a light-harvesting/electron-donating zinc (II) porphyrin on the top and C_{60}•$(ZnP)_2$ (**28**) with an electron-accepting C_{60} and a light-harvesting/electron-donating zinc (II) porphyrin on the bottom

Metal-ligand coordination constitutes another promising approach for obtaining electron donor-acceptor systems. The first demonstration was presented in the form of a C_{60}-pyridine•ZnP complex – Fig. 13. In this, the reversible coordination of a pyridine-functionalized fullerene ligand (C_{60}-pyridine) to the square-planar zinc center was documented simultaneously by three different research teams [69, 83]. The progression of the C_{60}-pyridine•ZnP (**29**) formation was monitored by the red-shifts in the Q-band transitions and the observance of clear isosbestic points, which assisted in determining the binding constants of approximately 5×10^3 M^{-1}. In a chain of events, which were triggered by light, the excited electron donor activates a rapidly occurring electron transfer to the electron-

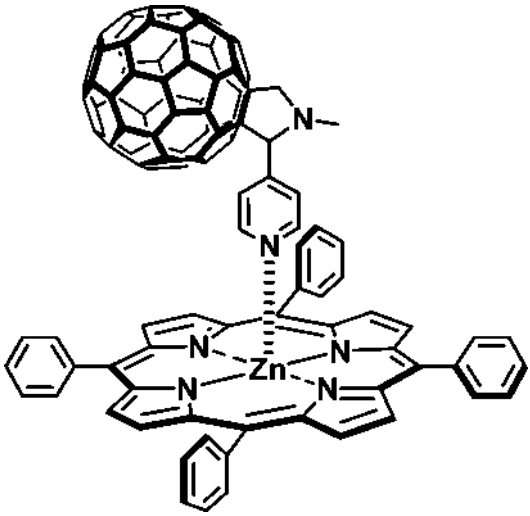

Fig. 13 Representative porphyrin systems featuring 0D C_{60}: C_{60}-pyridine•ZnP (**29**) with an electron-accepting C_{60}-pyridine and a light-harvesting/electron-donating zinc (II) porphyrin (ZnP). In THF and benzonitrile, the charge recombination is $>10^6\ s^{-1}$ (C_{60}-pyridine•ZnP (**29**))

accepting C_{60}. The weak equilibrium between dissociation and association of the "metal-pyridine" bond facilitated then, in the final step of the sequence, the crucial breakup of the charge-separated state, before the competing charge recombination starts to become a restriction. ($C_{60}^{\bullet-}$/$ZnP^{\bullet+}$) lives for tens of microseconds in THF and benzonitrile, and any processes, as they may take place, are exclusively governed by an intermolecular diffusion. In stark contrast, in covalently linked electron donor-acceptor conjugates, fast charge recombination prevails, limiting the lifetime of the charge-separated state to a few nanoseconds – vide supra [83].

In another novel study, metal-ligand axial coordination of the C_{60}-pyridine to ZnP was presented in combination with probing of proximity effects by employing tail on-off approach – Fig. 14. The results of steady-state and time-resolved fluorescence revealed that the charge separation rates and efficiency in the "tail-off" versus "tail-on" differed, which suggested the presence of some through-space interactions between the singlet excited state of ZnP and C_{60} in the "tail-off" form. Charge separation from the singlet excited state of ZnP was ascertained from the rise of the one-electron reduced form of C_{60} over $>5 \times 10^7\ s^{-1}$. Additionally, a long-lived charge-separated state with a rate of charge recombination of about $10^6\ s^{-1}$ was also observed in C_{60}-pyridine•ZnP (**30**) complex [84].

The aforementioned metal-ligand interactions between ZnP and C_{60} have also been expanded and explored in an assembly, which involved the two molecular binding motifs designed suitably to facilitate a two-point metal-ligand coordination. It involved a host featuring BF_2-chelated azadipyrromethane (azaBODIPY) covalently linked to two porphyrins – Fig. 15. C_{60}-$(pyridine)_2$ featuring two pyridines was used as a guest. The two binding constants for the complex C_{60}-$(pyridine)_2$•$(ZnP)_2$ (**31**) were as high as $1.85 \times 10^5\ M^{-1}$. A control over energy versus electron transfer was demonstrated in the absence versus presence of C_{60}, respectively. In the

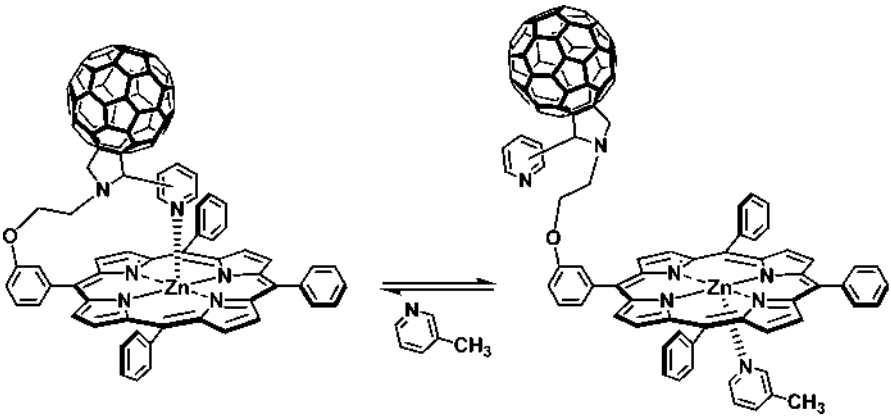

Fig. 14 Representative porphyrin systems featuring 0D C_{60}: C_{60}-pyridine•ZnP (**30**) with an electron-accepting C_{60}-pyridine and a light-harvesting/electron-donating zinc (II) porphyrin (ZnP). In benzonitrile charge recombination is ~10^6 s^{-1} (C_{60}-pyridine•ZnP (**30**))

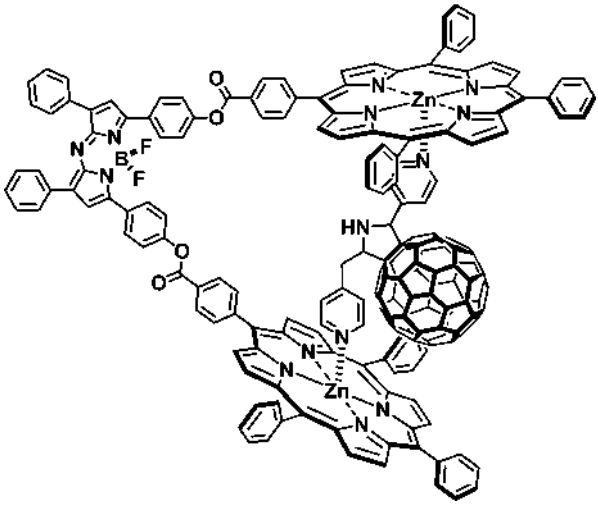

Fig. 15 Representative porphyrin systems featuring 0D C_{60}: C_{60}-$(pyridine)_2$•$(ZnP)_2$ (**31**) with an electron-accepting C_{60}-$(pyridine)_2$ and a light-harvesting/electron-donating zinc (II) porphyrin (ZnP). In benzonitrile, the charge recombination is 1.8×10^8 s^{-1} (C_{60}-$(pyridine)_2$•$(ZnP)_2$ (**31**))

absence of C_{60}, an energy transfer from the singlet excited state of ZnP to azaBODIPY was witnessed. In the presence of C_{60}, electron transfer dominates between the closely packed porphyrins and C_{60} [85].

Likewise, hydrogen bonding is also a powerful tool to construct self-assembled system. After documenting exceptionally strong communication in hydrogen-bonded C_{60}•porphyrin systems via a two-point amidinium-carboxylate salt bridge, efforts were directed to establish multiple-hydrogen bonding. It transcended into a promising approach to achieve even further stable complexes. In this context, Hamilton receptor-based hydrogen bonding motif (**32**) – Fig. 16 – was introduced

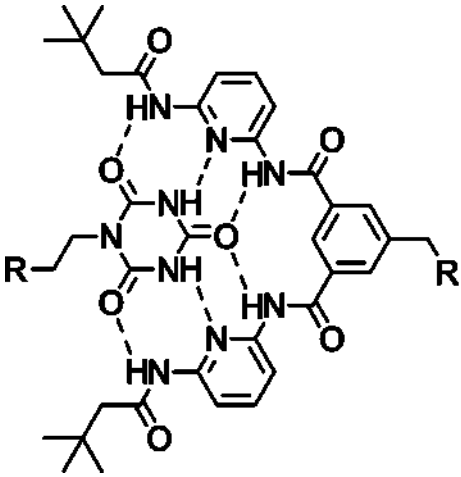

Fig. 16 Representative system featuring hydrogen bonding motif: cyanuric acid derivative and a Hamilton receptor (**32**)

in work in the late 1990s and early 2000s, in solution and later on in dye-sensitized solar cells. The composition of a cyanuric acid terminus and the malonate addend provided strong and highly directional association with binding constants that range in apolar solvents such as dichloromethane and toluene between 10^3 and 10^6 M^{-1}. The use of the Hamilton receptor in combination with a cyanuric acid motif is at times cumbersome due to its poor solubility. This hurdle was overcome by means of a variety of dendritic termini at the second malonate branch of C_{60} [86].

In an effort towards strengthening the binding between (metallo)porphyrins and C_{60}, the combination of different supramolecular binding motifs, so-called cooperative binding, was applied. In this term, the guanidinium bis-ZnP tweezers and C_{60} were investigated – Fig. 17. The approach to merge π-π interactions and hydrogen bonds is a viable strategy as it resulted in exceptionally high binding constant of 10^6 M^{-1}. Importantly, photoexcitation of C_{60}•$(ZnP)_2$ (**33**) generated a nanosecond-lived charge-separated state [87].

However, one aspect, which has been covered rather moderately, is to investigate the role of the molecular bridge in such non-covalent systems and, in turn, its impact on the electronic coupling and electron transfer rates as a function of molecular bridge length. In this context, we present a description of photophysical properties documented for the two recently published C_{60}•porphyrin systems, based on hydrogen-bond and metal-ligand interactions, respectively.

The role of molecular bridge and its attenuation factor was investigated in C_{60}•ZnP systems, C_{60}a-d•ZnP (**34–37**), held together by hydrogen bonding: a benzoate carrying C_{60} and an amidinium-substituted ZnP to afford an amidinium-carboxylate salt bridge – Fig. 18. In order to account for the impact of the distance between electron donor and acceptor, p-phenylene oligomers were incorporated. The number of phenylenes in the bridges were varied from one all the way to five leading to distances from 18 to 36.2 Å. From the ground- and excited-state assays in toluene,

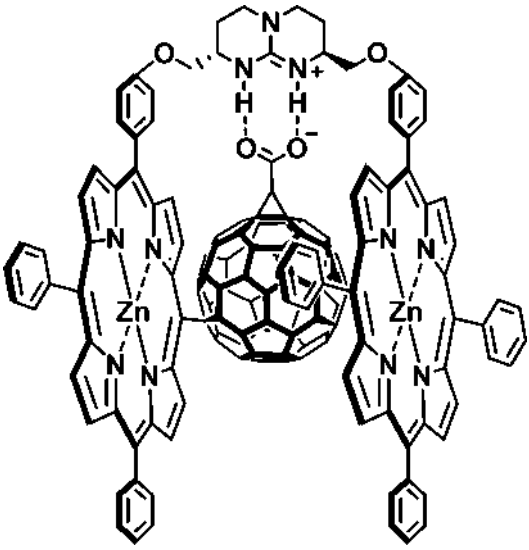

Fig. 17 Representative porphyrin systems featuring 0D C_{60}: C_{60}•$(ZnP)_2$ (**33**) with an electron-accepting C_{60} and a light-harvesting/electron-donating zinc (II) porphyrin (ZnP). In THF, the charge recombination is 5.5×10^6 s^{-1} (C_{60}•$(ZnP)_2$ (**33**))

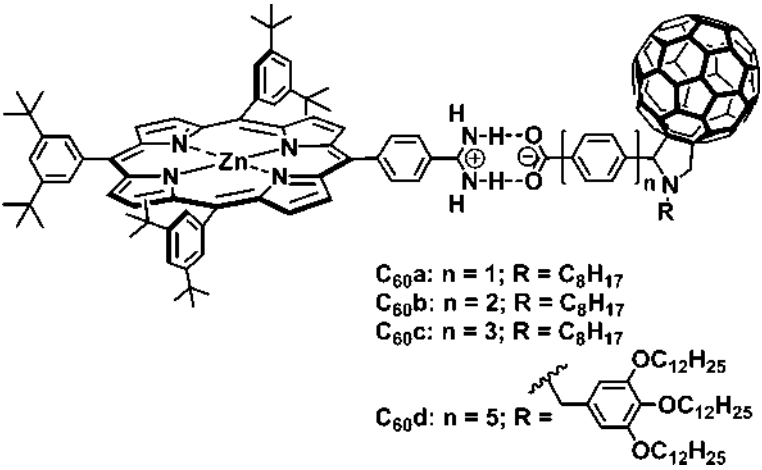

Fig. 18 Representative porphyrin systems featuring 0D C_{60}: C_{60}a•ZnP (**34**) with an electron-accepting C_{60}a and a light-harvesting/electron-donating zinc (II) porphyrin ZnP, C_{60}b•ZnP (**35**) with an electron-accepting C_{60}b and a light-harvesting/electron-donating zinc (II) porphyrin ZnP, C_{60}c•ZnP (**36**) with an electron-accepting C_{60}c and a light-harvesting/electron-donating zinc (II) porphyrin ZnP, and C_{60}d•ZnP (**37**) with an electron-accepting C_{60}d and a light-harvesting/electron-donating zinc (II) porphyrin (ZnP). In chlorobenzene, the charge recombination is 1.3×10^9 s^{-1} (C_{60}a•ZnP (**34**)), 1.0×10^9 s^{-1} (C_{60}b•ZnP (**35**)), 8.7×10^8 s^{-1} (C_{60}c•ZnP (**36**)), and 6.0×10^8 s^{-1} (C_{60}d•ZnP (**37**))

where the concentration of C_{60} was varied relative to a constant ZnP concentration, strong interactions were corroborated. The results from absorption assays provided indication for the formation of charge-transfer state only in the case of the closest spatial proximity. Interestingly, the fluorescence quenching depends strongly on the bridge length. The binding constants determined from ZnP fluorescence quenching ranged from 2.4×10^6 to 1.2×10^5 M^{-1} for the shortest and the longest separation, respectively [88].

In time-resolved absorption spectra recorded in chlorobenzene, the same ZnP singlet excited-state features were discernible at early times. Notable is that the transient features were the same, but the corresponding lifetimes differed substantially. It was concluded that photoexcitation of ZnP was followed by an intramolecular electron transfer to afford a charge-separated state. The charge separation rates were deduced as 7.9×10^{10}, 6.4×10^{10}, 3.7×10^{10}, and 2.4×10^{10} s^{-1}, whereas the charge recombination rates were 1.3×10^9, 1.0×10^9, 8.7×10^8, and 6.0×10^8 s^{-1}, as the electron donor-acceptor separation was gradually increased from C_{60}a-d, therefore in the complexes C_{60}a•ZnP (**34**), C_{60}b•ZnP (**35**), C_{60}c•ZnP (**36**), and C_{60}d•ZnP (**37**), respectively. Plotting the electron transfer rate constants versus electron donor-acceptor afforded a β value of 0.07 ± 0.01 $Å^{-1}$. Especially for p-phenylene oligomers, such low β values were attributed to induction of co-planarization between the adjacent phenylenes by the hydrogen bonds [88].

Another example, designed on similar grounds, involved metal-ligand interactions between porphyrins and fullerenes. Formation of the metal-ligand coordinate bond is facilitated by functionalization of C_{60} with pyridine (C_{60}-pyridine), whose lone pair undergoes axial coordination with ZnP. Within the realm of this approach, electronic communication between porphyrins and fullerenes was studied as a function of electron donor strength, electron donor-acceptor separation, solvent polarity, and temperature [89]. The strength of the electron-donating ZnP was modulated by functionalization of the four meso-position with 4-((1,3-dithiol-2-ylidene)methyl)phenyl. Three different C_{60}s, that is, C_{60}-pyridine, C_{60}Ph-pyridine, and $C_{60}(Ph)_2$-pyridine, served as electron acceptors – Fig. 19. The number of phenyls were increased all the way to two to induce a distance dependence on the dynamics. Binding constants were fit to be in the order of 10^5 M^{-1}. Importantly, the dynamics of the electron transfer exhibited a dependence on the bridge length. As a matter of fact, charge separation rates in chlorobenzene were 2.4×10^{11}, 2.8×10^{10}, and 1.0×10^9 s^{-1} for the complexes C_{60}Ph-pyridine•ZnP (**38**), $C_{60}(Ph)_2$-pyridine•ZnP (**39**), and $C_{60}(Ph)_3$-pyridine•ZnP (**40**), respectively, whereas the charge recombination rates were 1.8×10^9, 7.4×10^7, and 3.5×10^6 s^{-1}.

Marcus theory was used to determine the total reorganization energies and electronic couplings. Values of 0.92 ± 0.01, 0.88 ± 0.01, and 0.92 ± 0.03 eV evolved for C_{60}-pyridine-, C_{60}Ph-pyridine-, and $C_{60}(Ph)_2$-pyridine-based systems, respectively. These values are particularly large, when compared to covalently linked electron donor-acceptor conjugates. A rather strong distance dependence was

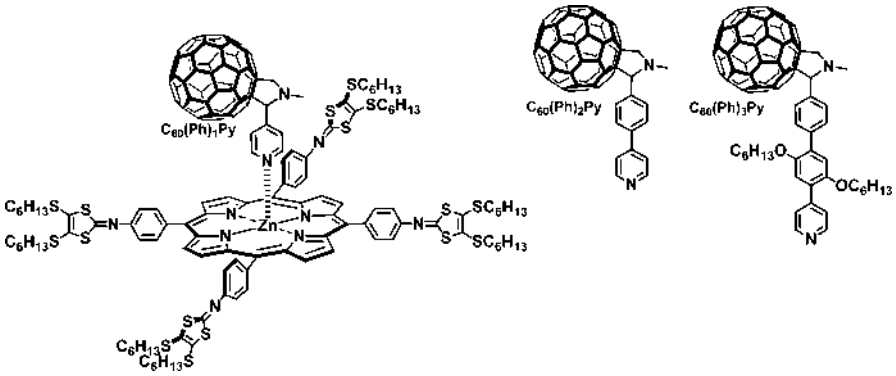

Fig. 19 Representative porphyrin systems featuring 0D C_{60}: C_{60}Ph-pyridine•ZnP (**38**) with an electron-accepting C_{60} and a light-harvesting/electron-donating zinc (II) porphyrin (ZnP) on the left, $C_{60}(Ph)_2$-pyridine•ZnP (**39**) with an electron-accepting C_{60} and a light-harvesting/electron-donating zinc (II) porphyrin (ZnP) in the center, and $C_{60}(Ph)_3$-pyridine•ZnP (**40**) with an electron-accepting C_{60} and a light-harvesting/electron-donating zinc (II) porphyrin (ZnP) on the right. In chlorobenzene, the charge recombination is $1.8 \times 10^9\ s^{-1}$ (C_{60}Ph-pyridine•ZnP (**38**)), $7.4 \times 10^7\ s^{-1}$ ($C_{60}(Ph)_2$-pyridine•ZnP (**39**)), and $3.5 \times 10^6\ s^{-1}$ ($C_{60}(Ph)_3$-pyridine•ZnP (**40**))

obtained for electronic couplings, ranging from as high as $80.52 \pm 13.86\ cm^{-1}$ to as low as $6.88 \pm 2.44\ cm^{-1}$. Additionally, temperature-dependent transient absorption measurements suggested a super-exchange versus hopping mechanism of electron transfer [89].

In another molecular system, [10]CPP was incorporated as the new building block to encapsulate fullerenes, with a notion to investigate electronic communication between ZnP and encapsulated fullerene. To accomplish this, the strong concave-convex π-π interactions between cycloparaphenylene, namely, [10] CPP, and C_{60} were taken advantage of [90]. The design of the ZnP–[10] CPP conjugate involved the functionalization of ZnP with [10] CPP via biphenyl-ethynylene bridge. In contrast to the aforementioned examples, the distance between ZnP and fullerene was fixed by employing [10] CPP to bind different fullerenes – Fig. 20. At the focal point was the electronic communication between ZnP and a range of fullerenes with different electron-acceptor strength: C_{60}, PCBM, $(C_{60})_2$, and C_{70}. The binding strength was determined from the titration assays for the different fullerenes. Overall, extraordinarily high association constants were determined for C_{60}•ZnP–[10] CPP (**41**) with $(1.6 \pm 0.1) \times 10^6\ M^{-1}$ and for $(C_{60})_2$•ZnP–[10]CPP (**43**) with $(4.7 \pm 0.1) \times 10^6/(1.9 \pm 0.05) \times 10^6\ M^{-1}$. From the transient absorption spectroscopy, the mechanism, by which the charge-separated states were formed and decayed, was elucidated. Only subtle changes were, however, observed. The lifetimes of the charge-separated states were fit to lie in the range of $0.25–0.33 \times 10^9\ s^{-1}$. An interesting observation was made for the $(C_{60})_2$, for which depending on the relative the rate of charge recombination differed [91].

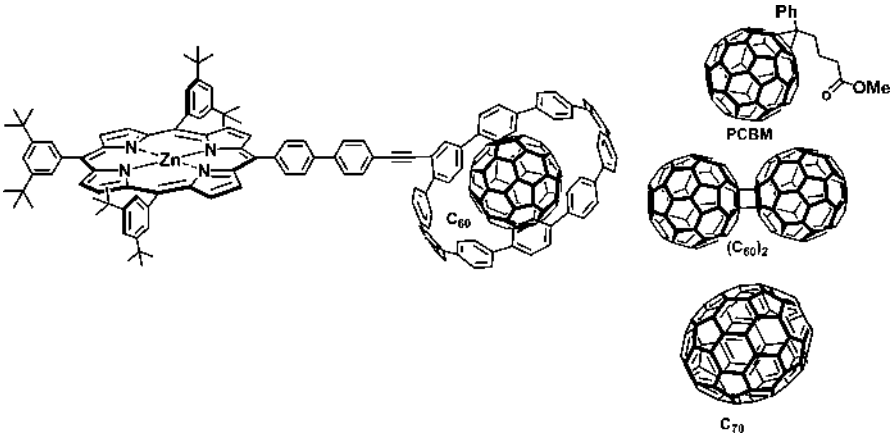

Fig. 20 Representative porphyrin systems featuring 0D C_{60}: C_{60}•ZnP–[10] CPP (**41**) with an electron-accepting C_{60} and a light-harvesting/electron-donating zinc (II) porphyrin (ZnP) on the left, PCBM•ZnP–[10] CPP (**42**) with an electron-accepting PCBM and a light-harvesting/electron-donating zinc (II) porphyrin (ZnP) on the top right, $(C_{60})_2$•ZnP–[10] CPP (**43**) with an electron-accepting $(C_{60})_2$ and a light-harvesting/electron-donating zinc (II) porphyrin (ZnP) on the middle right, and C_{70}•ZnP–[10] CPP (**44**) with an electron-accepting C_{70} and a light-harvesting/electron-donating zinc (II) porphyrin (ZnP) on the bottom middle right. In benzonitrile charge recombination is 2.3×10^8 s^{-1} (C_{60}•ZnP–[10]CPP (**41**)), 2.8×10^8 s^{-1} (PCBM•ZnP–[10]CPP (**42**)), 1.8×10^6 s^{-1} ((C_{60})$_2$•ZnP–[10]CPP (**43**)), and 2.6×10^8 s^{-1} (C_{70}•ZnP–[10]CPP (**44**))

Endohedral (Metallo)fullerenes

The versatility of empty fullerenes as a building block for the construction of electron donor-acceptor conjugates stimulated scientists to explore enclosing of additional atoms, ions, or even clusters into their interior. Such fullerenes are referred to as endohedral fullerenes (EMFs). Doping empty fullerenes with electropositive metals has been demonstrated in an arc generator to yield EMFs. To this date, their production and purification are widely established despite their overall low yields and the large number of isomers. They retain the spherical structure but possess a modified π-system and novel chemical/physical properties, which have never been seen for empty fullerenes. Most important is the strong influence of the endohedral atoms, ions, or even clusters on the nature of EMFs. Therefore, it provides a way to control the molecular properties by altering the endohedral composition [12, 14, 92].

In this context, noteworthy studies were reported with EMFs of different types, namely, mono-metallofullerenes, di-metallofullerenes, trimetallic nitride fullerenes, etc. In 2008, a ferrocenylpyrrolidine adduct of $Sc_3N@I_h$-C_{80} was reported as the first covalent electron donor-acceptor conjugate along with the documentation of photophysical properties by time-resolved transient absorption spectroscopy, confirming photoinduced electron transfer between ferrocene and the fullerene. Later, several intriguing electron donor-acceptor architectures, based on variously functionalized porphyrins and EMFs, were reported. Incorporation of different metal species

enabled, for the first time, insights into intramolecular electron transfer processes. In principle, an unlimited access towards EMF-based multi-functional material is of great interest for emerging applications [12, 14, 92].

Covalent Porphyrin Conjugates

A molecular switching behavior was documented, in a pioneering investigation with the $Ce_2@I_h$-C_{80}–ZnP conjugate (**45**) – Fig. 21. In particular, depending on the polarity of the medium, $Ce_2@I_h$-C_{80} (**45**) underwent either reductive electron transfer in non-polar media or oxidative electron transfer in polar media with lifetimes of ca. 0.8 ps and 0.4–0.7 ps, respectively. The formation of one-electron reduced form of $Ce_2@I_h$-C_{80} was confirmed from the transients observed in the near-infrared between 900 and 1200 nm, while the transient for one-electron oxidized form of $Ce_2@I_h$-C_{80} was observed around 850 nm. The non-adiabatic formation of $(Ce_2@I_h\text{-}C_{80})^{\bullet-}$–$ZnP^{\bullet+}$ was favored despite the flexible 2-oxyethyl butyrate spacer, the short distance, and the higher strength in the electronic coupling between C_{80}/ZnP and $[Ce_2]^{6+}$/ZnP. A closer look revealed the reduction of $[Ce_2]^{6+}$ and not that of C_{80}. This electron transfer mechanism with rate constants up to 2.4×10^8 s^{-1} dominated in non-polar media such as toluene and THF. In stark contrast was the behavior in polar media. In benzonitrile or DMF, the otherwise endergonic level $(Ce_2@I_h\text{-}C_{80})^{\bullet+}$–$ZnP^{\bullet-}$, which is 2.3 eV in non-polar media with respect to the singlet excited state of ZnP (2.1 eV), was stabilized by 0.3 eV. This, in turn, drove its formation with

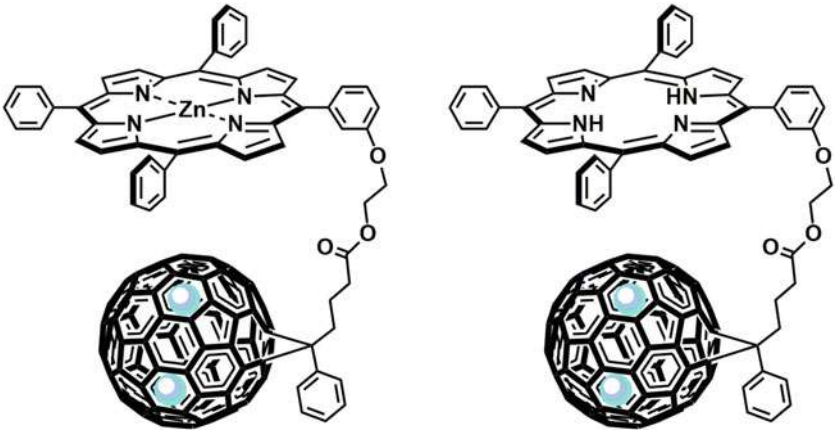

Fig. 21 Representative porphyrin conjugates featuring 0D EMFs: $Ce_2@I_h$-C_{80}–ZnP (**45**) (Ce^{3+}s are shown in cyan) with an electron-accepting EMF ($Ce_2@I_h$-C_{80}) and a light-harvesting/electron-donating zinc (II) porphyrin (ZnP) in non-polar solvents or an electron-donating EMF ($Ce_2@I_h$-C_{80}) and a light-harvesting/electron-accepting zinc (II) porphyrin (ZnP) in non-polar solvents on the left and $Ce_2@I_h$-C_{80}–H_2P (**46**) (Ce^{3+}s are shown in cyan) with an electron-accepting EMF ($Ce_2@I_h$-C_{80}) and a light-harvesting/electron-donating free-base porphyrin (H_2P) on the right. In THF, charge separation and recombination are 1.3×10^{12} s^{-1} ($Ce_2@I_h$-C_{80}–ZnP (**45**))/5.4×10^{10} s^{-1} ($Ce_2@I_h$-C_{80}–H_2P (**46**)) and 2.4×10^8 s^{-1} ($Ce_2@I_h$-C_{80}–ZnP (**45**))/> 5.4×10^{10} s^{-1} ($Ce_2@I_h$-C_{80}–H_2P (**46**)), respectively

subsequent charge recombination to afford $^{3*}(Ce_2@I_h\text{-}C_{80})$–ZnP. For the charge recombination of $(Ce_2@I_h\text{-}C_{80})^{\bullet+}$–$ZnP^{\bullet-}$ in benzonitrile and DMF, the rate constants were 1.8×10^{10} and 8.6×10^{9} s^{-1}, respectively [93].

For the analogous conjugates with H_2P, that is, $Ce_2@I_h\text{-}C_{80}$–H_2P (**46**), intriguingly, the electron transfer mechanism was documented to have a rather character. This was in contrast to the investigation with $Ce_2@I_h\text{-}C_{80}$–ZnP (**45**). The reason for which was the H_2P singlet excited state (1.90 eV), which is 0.2 eV lower in energy than the ZnP singlet excited state (2.10 eV). This in turn provided less thermodynamic driving forces for the oxidative pathway. The $(Ce_2@I_h\text{-}C_{80})^{\bullet-}$–$H_2P^{\bullet+}$ lifetime could not be determined in this case for it was shorter than its formation [94].

In another important study, a comparative investigation of two electron donor-acceptor conjugates using isoelectronic EMFs based on an I_h-C_{80} cage, with different types of endohedral guests, $(La_2)^{6+}$ versus $(Sc_3N)^{6+}$ – Fig. 22, was carried out [95]. In $La_2@I_h\text{-}C_{80}$–ZnP (**47**) and $Sc_3N@I_h\text{-}C_{80}$–ZnP (**48**), the excited-state electron-donating ZnPs were linked via 2-oxyethyl butyrate spacers. Even though the combined studies of crystallography and NMR indicated a common (6,6)-open addition pattern, a subtly different conformations came into highlight from the structural characterization, that is, rigid and comparatively flexible structure for $La_2@I_h\text{-}C_{80}$–ZnP (**47**) and $Sc_3N@I_h\text{-}C_{80}$–ZnP (**48**), respectively. In addition, from the electrochemical measurements, stronger interactions between I_h-C_{80} and ZnP in $La_2@I_h\text{-}C_{80}$–ZnP (**47**) was implied. DFT calculations also supported this observation, which suggested that in the lowest energy confirmation for $La_2@I_h\text{-}C_{80}$–ZnP,

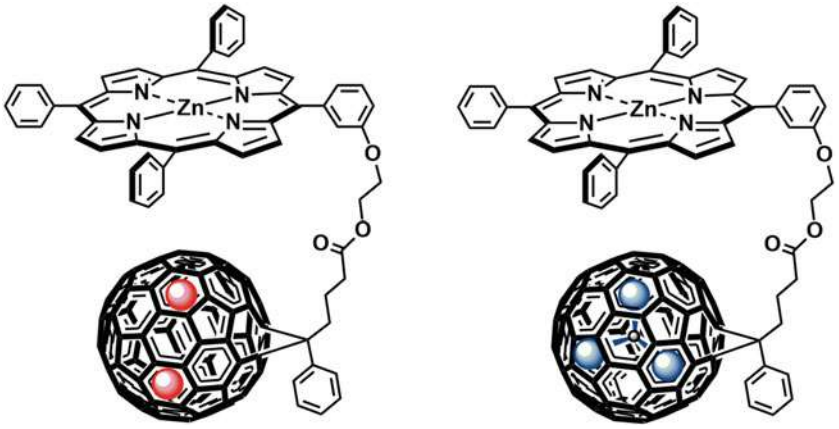

Fig. 22 Representative porphyrin conjugates featuring 0D EMFs: $La_2@I_h\text{-}C_{80}$–ZnP (**47**) (La^{3+}s are shown in red) with an electron-accepting EMF ($La_2@I_h\text{-}C_{80}$) and a light-harvesting/electron-donating zinc (II) porphyrin (ZnP) in non-polar solvents or an electron-donating EMF ($La_2@I_h\text{-}C_{80}$) and a light-harvesting/electron-accepting zinc (II) porphyrin (ZnP) in non-polar solvents on the left and $Sc_3N@I_h\text{-}C_{80}$–ZnP (**48**) (Sc_3N^{6+} is shown in blue) with an electron-accepting EMF ($Sc_3N@I_h\text{-}C_{80}$) and a light-harvesting/electron-donating zinc (II) porphyrin (ZnP) on the right. In THF, charge separation and recombination are 1.0×10^{12} s^{-1} ($La_2@I_h\text{-}C_{80}$–ZnP (**47**))/1.0×10^{11} s^{-1} ($Sc_3N@I_h\text{-}C_{80}$–ZnP (**48**); toluene) and 5.8×10^{9} s^{-1} ($La_2@I_h\text{-}C_{80}$–ZnP (**47**))/2.3×10^{10} s^{-1} ($Sc_3N@I_h\text{-}C_{80}$–ZnP (**48**); toluene), respectively

$La_2@I_h$-C_{80} and ZnP assume van der Waals distances. Owing to these subtle changes, the duality of charge separation properties, that is, reductive and oxidative electron transfer, with solvent polarity was observed in the excited state for $La_2@I_h$-C_{80} similar to the finding described for $Ce_2@I_h$-C_{80} – vide supra [93, 95]. In contrast to $Ce_2@I_h$-C_{80}–ZnP (**45**), reductive charge transfer was limited to the reduction of I_h-C_{80} without revealing any evidence for any occurring $[La_2]^{6+}$ reduction. Lifetimes of 230 ps in toluene and 170 ps in THF are notably shorter than the 4100 ps found upon $[Ce_2]^{6+}$ reduction in $Ce_2@I_h$-C_{80}–ZnP. In the case of $Sc_3N@I_h$-C_{80}–ZnP (**48**), the oxidative pathway was closed; regardless of the solvent polarity, $(Sc_3N\ @I_h$-$C_{80})^{\bullet-}$–$ZnP^{\bullet+}$ evolved as the sole product of charge separation.

As an extension to the aforementioned, the electron transfer events were investigated between ZnP as electron donor and $Sc_3N@I_h$–C_{80} as electron acceptor over larger distances with center-to-center distances of up to 45 Å – Fig. 23. The quenched fluorescence quantum yields of $Sc_3N@I_h$-C_{80}–ZnP and the nature of the excited-state deactivation from transient absorption spectroscopy delivered the conclusive evidence of charge separation over transduction of energy transfer from ZnP (2.1 eV) to $Sc_3N@I_h$-C_{80} (1.5 eV). Kinetic analysis established the evolution of $(Sc_3N@I_h$-$C_{80})^{\bullet-}$–$ZnP^{\bullet+}$ with a driving force of 0.63 eV. In terms of charge

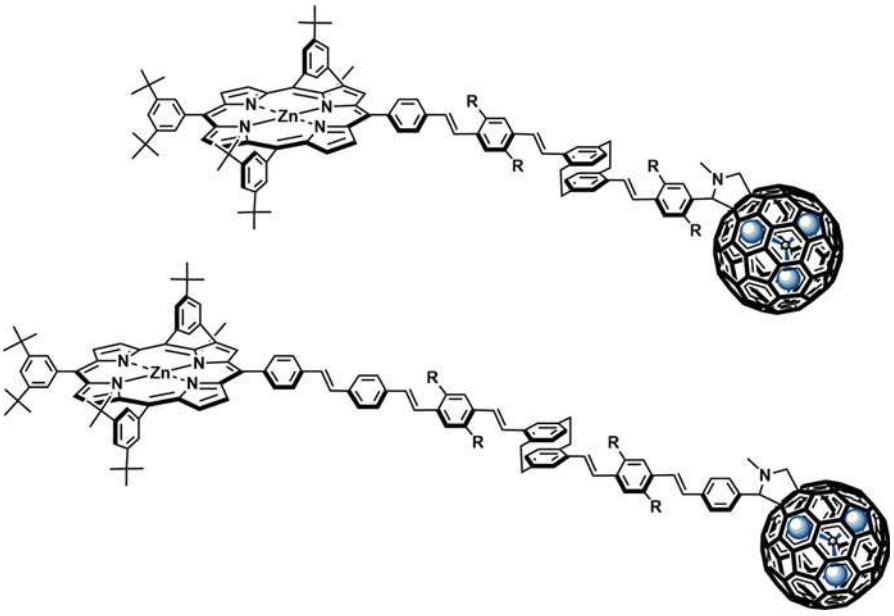

Fig. 23 Representative porphyrin conjugates featuring 0D EMFs: $Sc_3N@I_h$-C_{80}–ZnP (**49**) (Sc_3N^{6+} is shown in blue) with an electron-accepting EMF ($Sc_3N@I_h$-C_{80}) and a light-harvesting/electron-donating zinc (II) porphyrin (ZnP) on the top and $Sc_3N@I_h$-C_{80}–ZnP (**50**) (Sc_3N^{6+} is shown in blue) with an electron-accepting EMF ($Sc_3N@I_h$-C_{80}) and a light-harvesting/electron-donating zinc (II) porphyrin (ZnP) on the bottom (R = $-C_8H_{17}$). In THF, the charge recombination is $1.0 \times 10^6\ s^{-1}$ ($Sc_3N@I_h$-C_{80}–ZnP (**49**))/$6.6 \times 10^5\ s^{-1}$ ($Sc_3N@I_h$-C_{80}–ZnP (**50**))

recombination for $(Sc_3N@I_h\text{-}C_{80})^{\bullet-}$–$ZnP^{\bullet+}$ in THF and benzonitrile at electron donor-acceptor distances of 33 and 45 Å in $Sc_3N@I_h$-C_{80}–ZnP (**49**) and $Sc_3N@I_h$-C_{80}–ZnP (**50**), respectively, the lifetimes were fit to be in the 1–3 μs regime [96].

In conclusion, different from the reductive electron transfer reactivity of empty fullerenes – vide supra – has been our full-fledged investigations on EMFs: depending on the nature of the (metallo)porphyrins, on one hand, and the solvent polarity, on the other hand, electrons have been transferred both ways to either reduce or oxidize EMFs. This clearly stands out in the area of charge transfer with empty fullerenes. The ability of EMFs to trap charges in their interior is unique, for example, reducing $[Ce_2]^{6+}$, since it enables stabilizing the charge-separated states by a factor of about 40 and 100, relative to the reduction of I_h-C_{80} in $La_2@I_h$-C_{80}–ZnP (**49**) and $Sc_3N@I_h$-C_{80}–ZnP (**50**), respectively. What poses a real drawback is the low triplet excited-state energies of EMFs, as it governs the charge recombination to afford the triplet excited state rather than the ground state. In other words, the underlying driving forces are placed close to the Marcus *top* region, and, in turn, the rate constants are maximal. In order to bypass the aforementioned, one possible way is trapping the charges reductively at the endohedral atoms, ions, or even clusters. However, this comes at the cost of weak electronic coupling, which opens deactivation channels that compete with the charge separation.

Non-covalent Porphyrins

A study on the non-covalent system formation between EMFs ($La@C_{2v}$-C_{82} and $La_2@I_h$-C_{80}) and porphyrins was presented by comparing their photophysical properties to that of C_{60} and the porphyrin. In this context, C_{60}-pyridine and the corresponding lanthanum metallofullerene derivatives, with an open-shell and closed-shell electronic configuration, $La@C_{2v}$-C_{82}-pyridine and $La@I_h$-C_{80}-pyridine, respectively, featuring a pyridyl group were utilized, to facilitate metal-ligand coordination with ZnP. This, in turn, rendered coordinative electron-donor/acceptor arrays – Fig. 24. By following the progression of complexation in all three systems, the binding constants were determined, which ranged from $K_{assoc} = 8.70 \times 10^3$ to 2.40×10^4 M^{-1}. Steady-state as well as time-resolved photophysical techniques revealed that the electron transfer dominates the deactivation of the excited state in all three systems, namely, C_{60}-pyridine•ZnP (**51**), $La@C_{2v}$-C_{82}-pyridine•ZnP (**52**), and $La_2@I_h$-C_{80}-pyridine•ZnP (**53**). Importantly, the choice of the fullerene/metallofullerene assisted in controlling the charge separation kinetics (10^{10} s^{-1}) and the charge recombination kinetics (10^8 s^{-1}), whereas the binding constants are only marginally impacted. Owing to the lowest reduction potential of $La@C_{2v}$-C_{82} and the resultant largest driving force for charge separation in $La@C_{2v}$-C_{82}-pyridine•ZnP (**52**), the fastest charge separation was determined to occur in $La@C_{2v}$-C_{82}-pyridine•ZnP (**52**). Whereas due to fact that the SOMO of $[La_2@I_h\text{-}C_{80}]^{\bullet-}$ is localized between the encapsulated La^{3+} atoms, any intermolecular overlap with $ZnP^{\bullet+}$ for $La_2@I_h$-C_{80}-pyridine•ZnP (**53**) is supposed to be small, which results in the inhibition of charge recombination. As a consequence, the slowest charge recombination was found in $La_2@I_h$-C_{80}-pyridine•ZnP (**53**) [97].

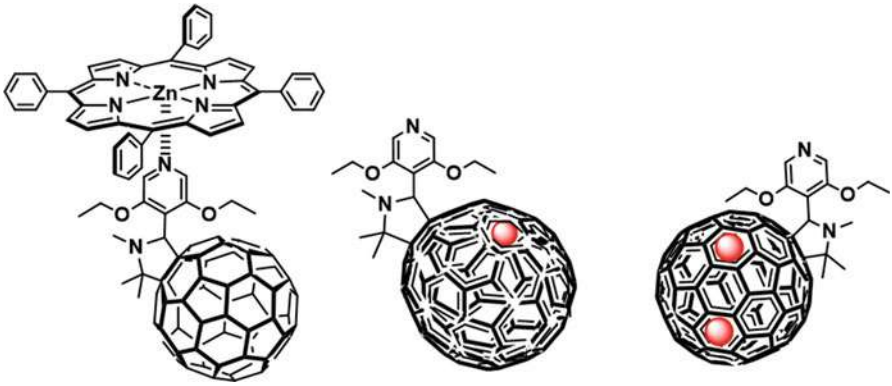

Fig. 24 Representative porphyrin conjugates featuring 0D EMFs: C_{60}-pyridine•ZnP (**51**) with an electron-accepting C_{60}-pyridine and a light-harvesting/electron-donating zinc (II) porphyrin (ZnP) on the left, La@C_{2v}-C_{82}-pyridine•ZnP (**52**) with an electron-accepting La@C_{2v}-C_{82}-pyridine and a light-harvesting/electron-donating zinc (II) porphyrin (ZnP) in the center, and La_2@I_h-C_{80}-pyridine•ZnP (**53**) with an electron-accepting La_2@I_h-C_{80}-pyridine and a light-harvesting/electron-donating zinc (II) porphyrin (ZnP) on the right. In toluene, the charge recombination is 5.8×10^8 s^{-1} (C_{60}-pyridine•ZnP (**51**)), 6.5×10^8 s^{-1} (La@C_{2v}-C_{82}-pyridine•ZnP (**52**)), and 4.6×10^8 s^{-1} (La_2@I_h-C_{80}-pyridine•ZnP (**53**))

Single-Walled Carbon Nanotubes (SWCNTs)

Extending the delocalized structure of the ($sp^{2.278}$)-hybridized carbon atoms into empty 0D and EMF fullerenes over 1D by introducing additional carbon hexagons allowed for the 1D SWCNTs. Conceptually, 1D SWCNTs improve delocalization and charge transfer in a way that empty 0D fullerenes and EMFs would never be able to do. SWCNTs have unique electronic, mechanical, and optical properties. Most notably, SWCNTs are either semiconductors with a small band gap or metals with conductance that reach ballistic dimensions. But the synthesis of SWCNT results in heterogeneous products in terms of chirality, diameter, and length. Multiple structural defects go hand in hand with the presence of catalytic particles and the fact that SWCNTs bundle. In summary, the synthesis, classification, and individualization of SWCNTs are great challenges for future applications. Several techniques emphasize the fact that SWCNT semiconductors are inherently p-doped and, in turn, donate electrons instead of receiving them. Only these properties are noted for SWCNTs, which are de-bundled, individualized, and stabilized, often in solution. They are generally not very soluble in many environments. Large SWCNT bundles originate from attractive interactions such as π-π stacking and the London dispersion forces. Over the past 15 years, a large number of studies on the covalent and non-covalent functionalization of SWCNTs by various porphyrins have been reported [98–106].

Covalent Porphyrin Conjugates

Covalent modification provides a firmer anchoring of the functional entity. In other words, covalent attachment generally produces modified materials with improved

stability. In one such method, ZnP functionalized at three meso-positions with triphenylamine entities as an electron donor was attached to SWCNTs at the remaining meso-positions (Fig. 25) [107]. The SWCNT–ZnP conjugate (**54**) was synthesized by a Sonogashira coupling under microwave irradiation conditions. The advantages of the covalent approach are counterbalanced by the defects or detrimental disruption of the π-conjugated backbone of the SWCNT, which strongly affects the optical and electronic properties. In Raman spectra, the intensity of D-mode provides insights into the level of covalent functionalization. The downshifts noted in the G-, D-, and 2D-modes confirm n-type doping in the form of charge-transfer interactions between ZnP and SWCNTs. In general, strong electronic communication between ZnPs and SWCNTs in the ground state was confirmed by broadened and significantly red-shifted absorption features of SWCNT–ZnP conjugate (**54**) relative to what was seen for pristine SWCNTs. In addition, the presence of ZnP fluorescence quenching in the conjugate suggests the occurrence of excited-state events such as electron transfer and/or energy transfer. Furthermore, the polarity of the solvent is likely to play a role in the fluorescence quenching mechanism. In SWCNT–ZnP (**54**), the fluorescence quenching, which was weaker in non-polar solvents than in polar solvents, suggests electron transfer rather than energy transfer as the main quenching mechanism in the SWCNT–ZnP conjugate (**54**). The formation of a charge-separated state after photoexcitation of ZnP, which is immobilized onto SWCNTs, corroborates the presence of one-electron oxidized form of ZnP ($ZnP^{\bullet+}$) and one-electron reduced form of SWCNTs ($SWCNT^{\bullet-}$). It is important to note that, due to the competitive process of charge separation, the recovery of the excitonic maxima in the conjugate was much faster compared to pristine SWCNTs. The corresponding rate constants for the SWCNT–ZnP conjugate (**54**) and pristine SWCNTs are 2.0×10^{11} and 3.03×10^{10} s^{-1}, respectively.

A similar trend was also observed for other SWCNT–ZnP conjugates, where ZnP was covalently grafted onto the sidewalls of SWCNT through a direct addition of

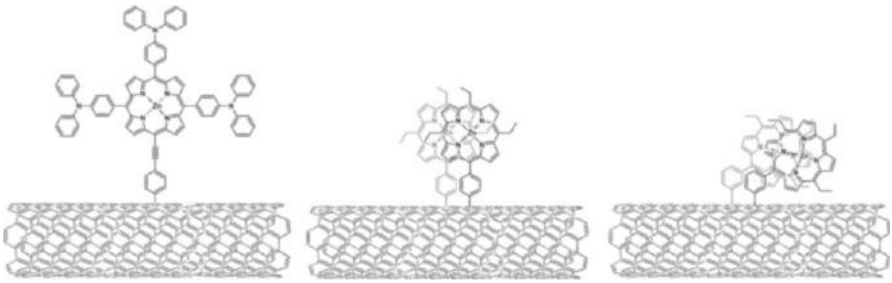

Fig. 25 Representative porphyrin conjugates featuring 1D SWCNTs: SWCNT–ZnP (**54**) with an electron-accepting SWCNT and a light-harvesting/electron-donating zinc (II) porphyrin (ZnP), on the left; SWCNT–ZnP (**55**) with an electron-accepting SWCNT and a light-harvesting/electron-donating zinc (II) porphyrin (ZnP), in the center; and SWCNT–ZnP (**56**) with an electron-accepting SWCNT and a light-harvesting/electron-donating zinc (II) porphyrin (ZnP), on the right. In THF, charge recombination is 2.0×10^{11} s^{-1} (SWCNT–ZnP (**54**)). In DMF, charge recombination is 4.2×10^{10} s^{-1} (SWCNT–ZnP (**55**))/2.0×10^{10} s^{-1} (SWCNT–ZnP (**56**))

aryl radical with a meta- or para-phenylene linkers (Fig. 25) [108]. In particular, the rate constants were much longer due to the weaker electronic coupling through the meta-linkage (SWCNT–ZnP (**56**); 2.04×10^{10} s^{-1}) than the para-linkage (SWCNT–ZnP (**55**); 4.17×10^{10} s^{-1}).

Next, our focus was on a different class of SWCNT–$(H_2P)_4$ conjugates (**57**): a series of SWCNTs functionalized with polyamidoamine dendrimers with four H_2Ps linked to the periphery of the dendrimers (Fig. 26) [109]. The absorption spectra of SWCNT–$(H_2P)_4$ conjugate (**57**) confirmed the presence of both SWCNT and H_2P. Furthermore, Raman spectra substantiated the covalent functionalization between SWCNTs and $(H_2P)_x$ with the presence of an increased D-band in the SWCNT–$(H_2P)_4$ conjugate (**57**) relative to pristine SWCNTs. It should be noted that the D-band was not affected by the dendrimer formation. Turning to fluorescence spectroscopy of SWCNT–$(H_2P)_4$ (**57**), a significant fluorescence quenching of the H_2P-centered features corroborated the excited-state interactions between SWCNT and $(H_2P)_4$. The respective fluorescence kinetics provided evidence for two components, that is, a short-lived (0.04 ± 0.01 ns) and a long-lived (8.6 ± 1.2 ns) component. The latter resembles that of pristine H_2P (9.5 ± 0.5 ns) implying a lack of interaction between H_2Ps and SWCNTs. A possible explanation is the dendritic structure of $(H_2P)_4$. Finally, transient absorption spectroscopy revealed

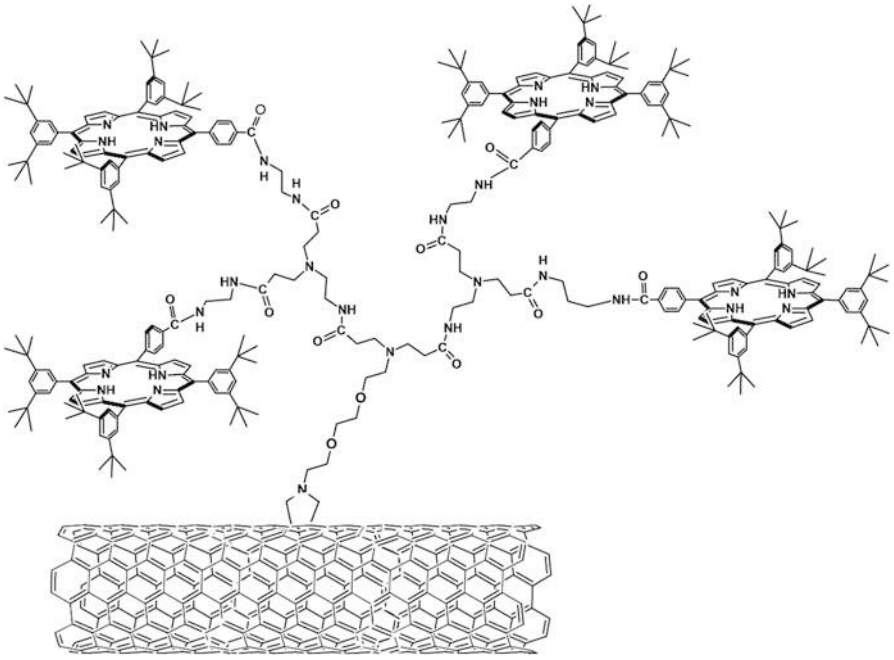

Fig. 26 Representative porphyrin conjugates featuring 1D SWCNTs: SWCNT–$(H_2P)_4$ (**57**) with an electron-accepting SWCNT and a light-harvesting/electron-donating free-base porphyrin (H_2P). In THF, the charge separation and recombination are 1.5×10^{10} and 2.9×10^{6} s^{-1}, respectively

the nature of the excited species. SWCNT–$(H_2P)_4$ (**57**) is subject to fast charge separation (1.5×10^{10} s^{-1}) after photoexcitation of H_2P to yield $(H_2P)_4^{\bullet+}$ and $SWCNT^{\bullet-}$, which was verified by the presence of the respective fingerprint absorption features. Importantly, the rapid decay of the H_2P singlet excited state was linked to an intra-conjugate electron-transfer process.

In previous works, which referred to the SWCNT–H_2P conjugate (**58**) with a single H_2P and not with four H_2Ps per linker, the same trends were established (Fig. 27) [110]. The weaker H_2P absorption, due to less H_2P, made the investigation very difficult. For example, the presence of SWCNTs slightly modified the dynamics of the excited state and/or the lifetime in the SWCNT–H_2P conjugate (**58**): fluorescence lifetime of 10.4 ± 0.5 ns for H_2P. For the SWCNT–H_2P conjugate (**58**), the corresponding lifetime was 5.2 ± 0.5 ns. However, the transient absorption measurements that were carried out using the SWCNT–H_2P (**58**) gave a characteristic absorption of the oxidized form of one-electron H_2P that accompanies the 2.0×10^{10} s^{-1} decay in the singlet excited state of H_2P.

At last, the light shed on the properties of two different SWCNT–ZnP conjugates (Fig. 28) [111]. In SWCNT–ZnP (**59**), one ZnP per functional group was attached to SWCNT, whereas in the case of SWCNT–dend–ZnP (**60**), a first-generation dendron bearing two ZnPs was attached to the SWCNT. The functionalization of SWCNTs with a porphyrin dendron was introduced via click chemistry. In Raman spectra of SWCNT–ZnP (**59**) and SWCNT–dend–ZnP (**60**), a significant increase in the relative intensity of the D-band was observed compared to pristine SWCNTs,

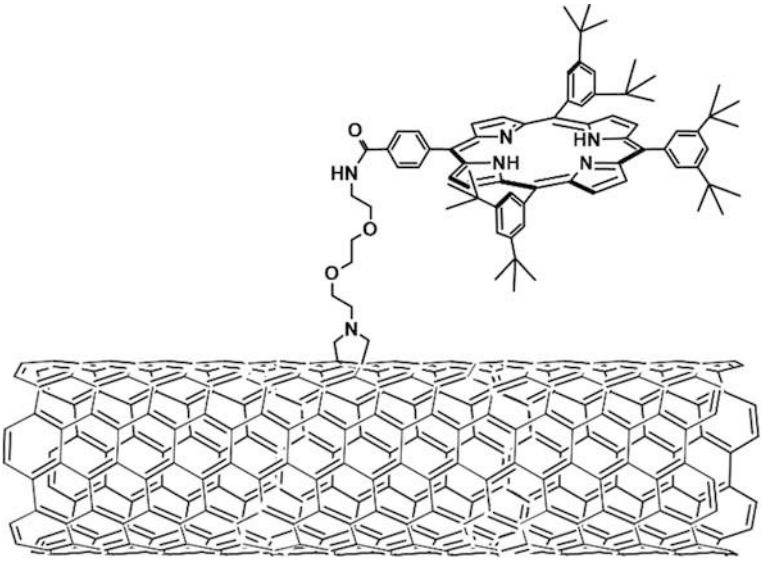

Fig. 27 Representative porphyrin conjugates featuring 1D SWCNTs: SWCNT–H_2P (**58**) with an electron-accepting SWCNT and a light-harvesting/electron-donating free-base porphyrin (H_2P). In THF, the charge recombination is 2.0×10^{10} s^{-1}

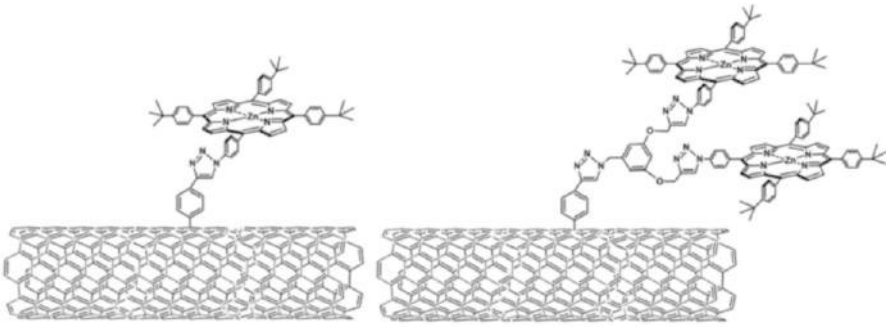

Fig. 28 Representative porphyrin conjugates featuring 1D SWCNTs: SWCNT–ZnP (**59**) with an electron-accepting SWCNT and a light-harvesting/electron-donating zinc (II) porphyrin (ZnP) on the left and SWCNT–dend–ZnP (**60**) with an electron-accepting SWCNT and a light-harvesting/electron-donating zinc (II) porphyrin (ZnP) on the right. In DMF, the charge recombination is $1.2 \times 10^9\ s^{-1}$ (SWCNT–ZnP (**59**))/$5.0 \times 10^9\ s^{-1}$ (SWCNT–dend–ZnP (**60**))

indicating the successful covalent functionalization between SWCNT and ZnP. Ground-state interactions between SWCNT and ZnP were confirmed by means of absorption spectroscopy, in which the ratio of ZnP-centered features in SWCNT–ZnP (**59**) and SWCNT–dend–ZnP (**60**) was ~1:2 relative to the pristine SWCNT absorption. The excited-state charge transfer was corroborated by strong fluorescence quenching and fast excited-state decay of ZnP in SWCNT–ZnP (**59**) and SWCNT–dend–ZnP (**60**). Important were transient absorption measurements, which revealed that the photoexcitation of ZnP in SWCN–ZnP (**59**) and SWCNT–dend–ZnP (**60**) was followed by a rapid charge separation. The rate constant of charge-separated states in SWCNT–ZnP (**59**) ($1.2 \times 10^9\ s^{-1}$) and SWCNT–dend–ZnP (**60**) ($5.0 \times 10^9\ s^{-1}$) was marginally affected by the presence of different spacers that link ZnPs to the SWCNTs.

Non-covalent Porphyrin Systems

In this work, a new class of three different SWCNT•ZnP systems were investigated (Fig. 29) [112]. All three ZnPs were substituted with conjugated linkers at the β-pyrrolic position. The formation of SWCNT•ZnP (**61**), SWCNT•ZnP (**62**), and SWCNT•ZnP (**63**) was solely driven by π-π interactions. Steady-state absorption and fluorescence measurements showed appreciable electronic interactions between ZnPs and SWCNTs in the ground state. This was present by the broadened and red-shifted ZnP-centered absorptions, on one hand, and blue-shifted SWCNT-centered absorptions, on the other hand. A redistribution of charge density in the ground state from ZnPs to SWCNTs was supported by the hidden ZnP absorption in the presence of SWCNTs and ground-state n-type doping of SWCNTs in the presence of ZnPs. Evidence for the excited-state electron transfer came from a significant fluorescence quenching and a shortening of the singlet excited-state lifetimes in the presence of SWCNTs. The ultrafast electronic process in the ZnPs, once immobilized onto SWCNTs, started with the formation of excited states, which

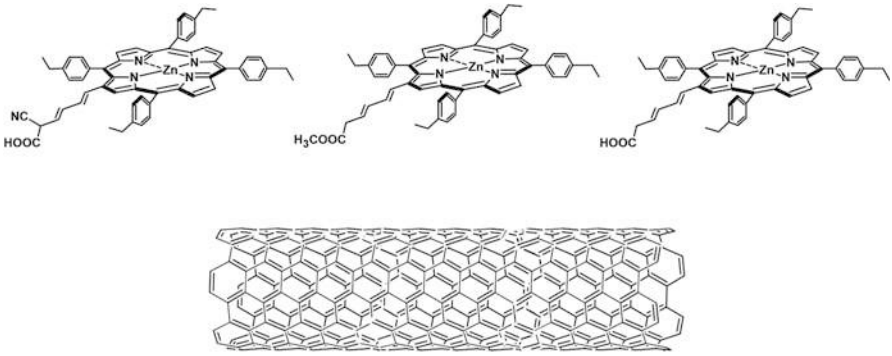

Fig. 29 Representative porphyrin systems featuring 1D SWCNTs: SWCNT•ZnP (**61**) with an electron-accepting SWCNT and a light-harvesting/electron-donating zinc (II) porphyrin (ZnP) on the left, SWCNT•ZnP (**62**) with an electron-accepting SWCNT and a light-harvesting/electron-donating zinc (II) porphyrin (ZnP) in the center, and SWCNT•ZnP (**63**) with an electron-accepting SWCNT and a light-harvesting/electron-donating zinc (II) porphyrin (ZnP) on the right. In 2 propanol, the charge recombination is 2.08×10^{10} s^{-1} (SWCNT•ZnP (**61**)), 2.38×10^{10} s^{-1} (SWCNT•ZnP (**62**)), and 1.25×10^{10} s^{-1} (SWCNT•ZnP (**63**))

decay to the ground state via the intermediate population of a fully charge-separated state after ZnP photoexcitation. Formation of the one-electron oxidized form of ZnP ($ZnP^{\bullet+}$) as a result of interactions with SWCNTs was supported by spectroelectrochemistry. The charge-separated state in SWCNT•ZnP (**61**), SWCNT•ZnP (**62**), and SWCNT•ZnP (**63**) recombined with rate constants of 2.08×10^{10}, 2.38×10^{10}, and 1.25×10^{10} s^{-1}, respectively, to restore the ground state.

Next, the focus was shifted to doubly fused pyrenylporphyrin-based SWCNT systems (Fig. 30) [113]. Here, two pyrene groups were fused at the meso- and β-positions of the porphyrin. Absorption spectra prompted to sizeable ground-state electronic communication between this ZnP and SWCNTs in the form of broadened and red-shifted ZnP-centered features in the visible region and blue-shifted SWCNT-centered features in the NIR region. Turning to fluorescence spectroscopy of SWCNT•ZnP (**64**), a significant fluorescence quenching of the ZnP-centered characteristics was interpreted in terms of energy or electron transfer from ZnP to SWCNTs. Finally, transient absorption spectroscopy confirmed that the fluorescence quenching results from ultrafast electron transfer events from the photoexcited ZnP to SWCNTs (3.85×10^{12} s^{-1}) followed by fast charge recombination on a picosecond time scale.

In $ZnP(Pyr)_4$, four pyrenes were linked to ZnP to enhance π-π interactions with SWCNTs (Fig. 31) [114]. The absorption spectra of SWCNT•$ZnP(Pyr)_4$ (**65**) present broadened and slightly red-shifted ZnP-centered features as evidence for mutual interactions between them in the ground state. The efficient ZnP-centered fluorescence quenching found in SWCNT•$ZnP(Pyr)_4$ (**65**) mirrors this with strong excited-state interactions. Possible quenching mechanism involved either energy or electron transfer from photoexcited $ZnP(Pyr)_4$ to SWCNTs. The presence of both $ZnP^{\bullet+}$ at

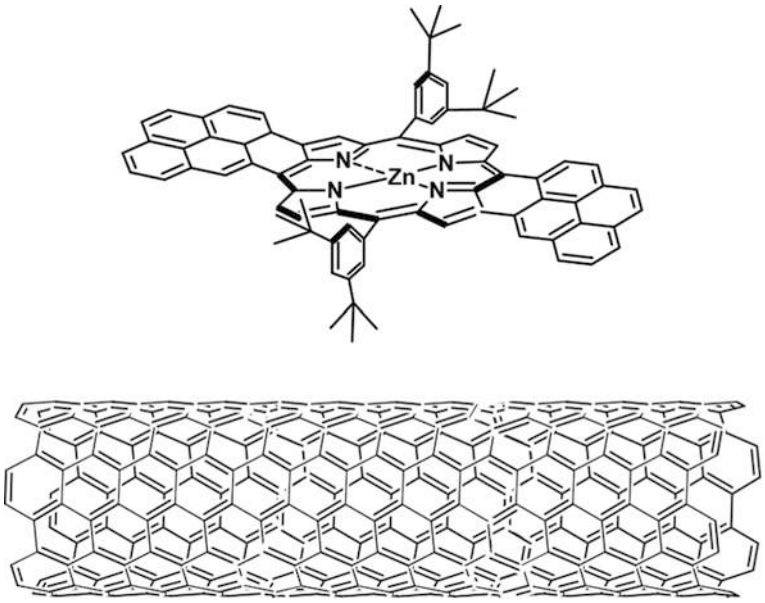

Fig. 30 Representative porphyrin systems featuring 1D SWCNTs: SWCNT•ZnP (**64**) with an electron-accepting SWCNT and a light-harvesting/electron-donating zinc (II) porphyrin (ZnP). In DMF, the charge separation is 3.85×10^{12} s^{-1}

680 nm and $SWCNT^{\bullet -}$ at 1400 nm in the transient spectra of SWCNT•ZnP(Pyr)$_4$ (**65**) confirmed the formation of charge-separated state. Hereby, the charge recombination in SWCNT•ZnP(Pyr)$_4$ (**65**) occurred with a rate constant of 5.55×10^9 s^{-1}.

In SWCNT•Pyr^+•H_2P^{8-} (**66**) and SWCNT•Pyr^+•ZnP^{8-} (**67**), the trimethylammonium head groups of pyrene were used as electrostatic anchors to link H_2P^{8-}/ZnP^{8-} and immobilize them onto the surface of SWCNTs by means of π-π interaction (Fig. 32) [115]. Absorption spectroscopy revealed red-shifted porphyrin and pyrene-centered features in SWCNT•Pyr^+•H_2P^{8-} (**66**) and SWCNT•Pyr^+•ZnP^{8-} (**67**) compared to their references. This pointed to notable electronic interaction between the individual components in the ground state. The excited-state electron transfer event from photoexcited H_2P^{8-}/ZnP^{8-} to SWCNTs was corroborated by static fluorescence quenching, which occurred in SWCNT•Pyr^+•H_2P^{8-} (**66**) and SWCNT•Pyr^+•ZnP^{8-} (**67**), and the formation of the one-electron oxidized form of H_2P^{8-}/ZnP^{8-} and the one-electron reduced form of SWCNTs. The rate constant of the charge-separated state was around 2.5×10^6 s^{-1}.

A very similar motive was used in four different non-covalent systems: SWCNT•Pyr^+•H_2P^{4-} (**68**), SWCNT•Pyr^+•ZnP^{4-} (**69**), SWCNT•Pyr^-•H_2P^{4+} (**70**), and SWCNT•Pyr^-•ZnP^{4+} (**71**) – Fig. 33 [116]. Importantly, π-π interactions were employed to immobilized negatively or positively charged pyrenes (Pyr^+ and Pyr^-) onto pristine SWCNTs followed by ion-pairing interactions with oppositely charged porphyrins (H_2P^{4-}, ZnP^{4-}, H_2P^{4+}, and ZnP^{4+}). The rate constants of 3.12×10^9,

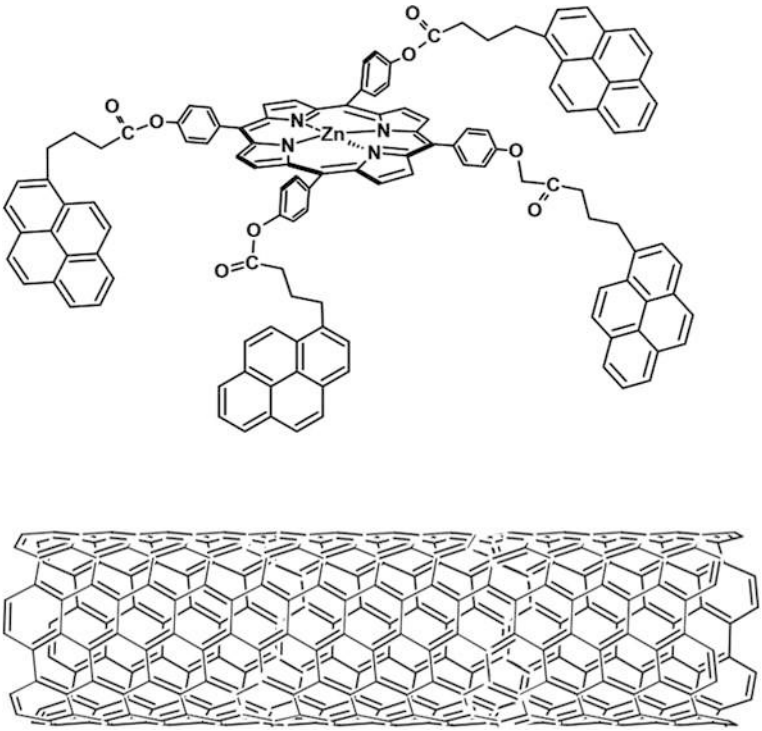

Fig. 31 Representative porphyrin systems featuring 1D SWCNTs: SWCNT•ZnP(Pyr)$_4$ (**65**) with an electron-accepting SWCNT and a light-harvesting/electron-donating four pyrene-linked zinc (II) porphyrin (ZnP(Pyr)$_4$). In DMF, the charge recombination is 5.55×10^9 s^{-1}

7.14×10^9, 3.85×10^9, and 9.09×10^9 s^{-1} reflect the charge recombination in SWCNT•Pyr$^+$•H_2P^{4-} (**68**), SWCNT•Pyr$^+$•ZnP^{4--} (**69**), SWCNT•Pyr$^-$•H_2P^{4+} (**70**), and SWCNT•Pyr$^-$•ZnP^{4+} (**71**), respectively.

In another study, pyrenes featuring an alky ammonium head group (Pyr$^+$) self-assembled by using ammonium ion-crown ether interactions with ZnPs that contain four ([18]-crown-6)s (ZnPCrown$_4$) were used to build up step by step the SWCNT•(Pyr$^+$)$_4$•ZnPCrown$_4$ (**72**) – Fig. 34 [117]. Once again, Pyr$^+$ π-π stacked onto SWCNTs. From steady-state absorption and fluorescence measurements, electronic communication was concluded. For example, broadened absorption features along with an efficient fluorescence quenching were noted when compared with the corresponding references. Electron transfer from photoexcited ZnPCrown$_4$ to SWCNTs was confirmed in a series of time-resolved experiments with focus on fluorescence and transient absorption. In particular, a marked decrease in the singlet excited-state lifetime of ZnPCrown$_4$ in SWCNT•(Pyr$^+$)$_4$•ZnPCrown$_4$ (**72**) went hand in hand with the formation of a charge-separated state. This SWCNT$^{\bullet-}$•(Pyr$^+$)$_4$•-ZnPCrown$_4$ charge-separated state was subject to a remarkable charge stabilization to led to a rate constant of about 1.0×10^7 s^{-1}.

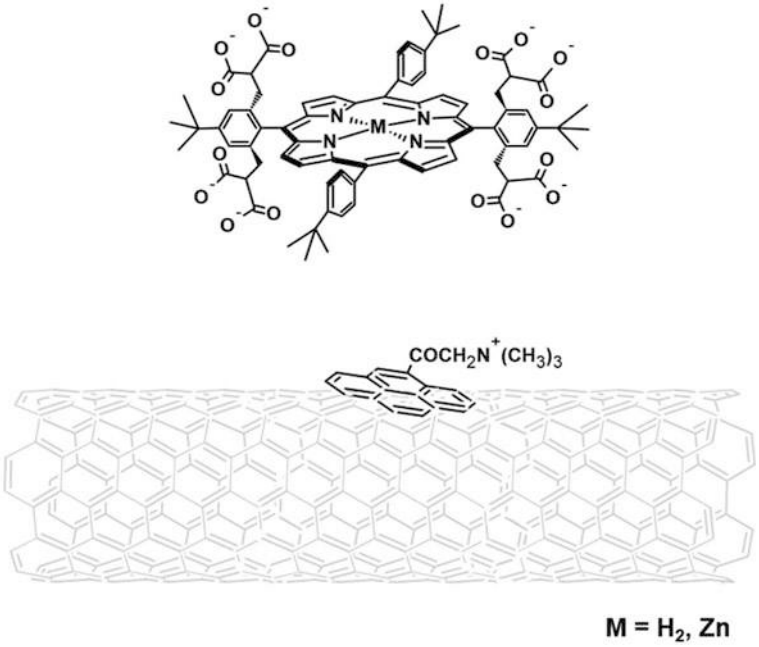

Fig. 32 Representative porphyrin systems featuring 1D SWCNTs: SWCNT•Pyr^{+}•H_2P^{8-} (**66**)/ZnP^{8-} (**67**) with an electron-accepting SWCNT•Pyr^{+} and a light-harvesting/electron-donating negatively charged free-base/zinc (II) porphyrin (H_2P^{8-}/ZnP^{8-}). In D_2O, the charge recombination is 2.5×10^6 s^{-1}

Conclusions

Years of pioneering research in 0D, 1D, and 2D nanocarbons have led to significant breakthroughs in promising energy materials. At the forefront of effective energy conversion and storage devices are the electron-accepting nature of 0D empty fullerenes, the electron-accepting/electron-donating nature of 0D EMFs, the electron-accepting/electron-donating nature of 1D SWCNTs, and the electron-accepting/electron-donating nature of 2D CNDs. But it took a transdisciplinary methodology to realize its full potential. Our transdisciplinarity in the field of photon and charge management has always been based on synergies arising from synthetic chemistry, characterization, theory and modeling, and prototype devices. But a prototype is only a proof of concept; it is not a proof of product. It takes a lot of effort, planning, and experience to get from a prototype that has been used to test the idea/general design and has proven that the ideas are applicable to production and getting the prototype to a place where it can be commercialized.

The extensive fullerene research over two and half decades have brought a wealth of information regarding electron transfer chemistry. Through the profound understanding of interactions between electron-donating (metallo)porphyrins – the key

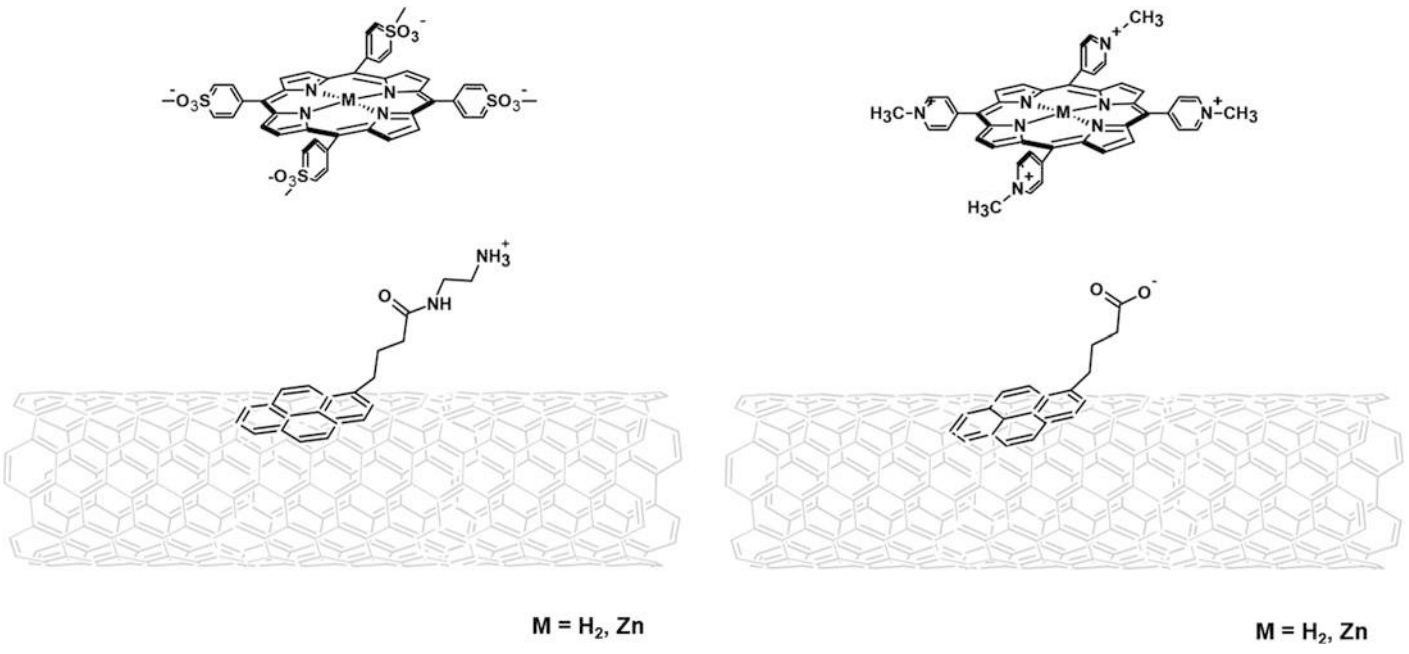

Fig. 33 Representative porphyrin systems featuring 1D SWCNTs: SWCNT•Pyr^{+}•H_2P^{4-} (**68**)/ZnP^{4-} (**69**) with an electron-accepting SWCNT•Pyr^{+} and a light-harvesting/electron-donating negatively charged free-base/zinc (II) porphyrin (H_2P^{4-}/ZnP^{4-}) on the left and SWCNT•Pyr^{-}•H_2P^{4+}(**70**)/ZnP^{4+} (**71**) with an electron-accepting SWCNT•Pyr^{-} and a light-harvesting/electron-donating positively charged free-base/zinc (II) porphyrin (H_2P^{4+}/ZnP^{4+}) on the right. In DMF, the charge recombination is 3.12×10^9 (SWCNT•Pyr^{+}•H_2P^{4-} (**68**)), 7.14×10^9 (SWCNT•Pyr^{+}•ZnP^{4-} (**69**)), 3.85×10^9 (SWCNT•Pyr^{-}•H_2P^{4+} (**70**)), and 9.09×10^9 s^{-1}(SWCNT•Pyr^{-}•ZnP^{4+} (**71**))

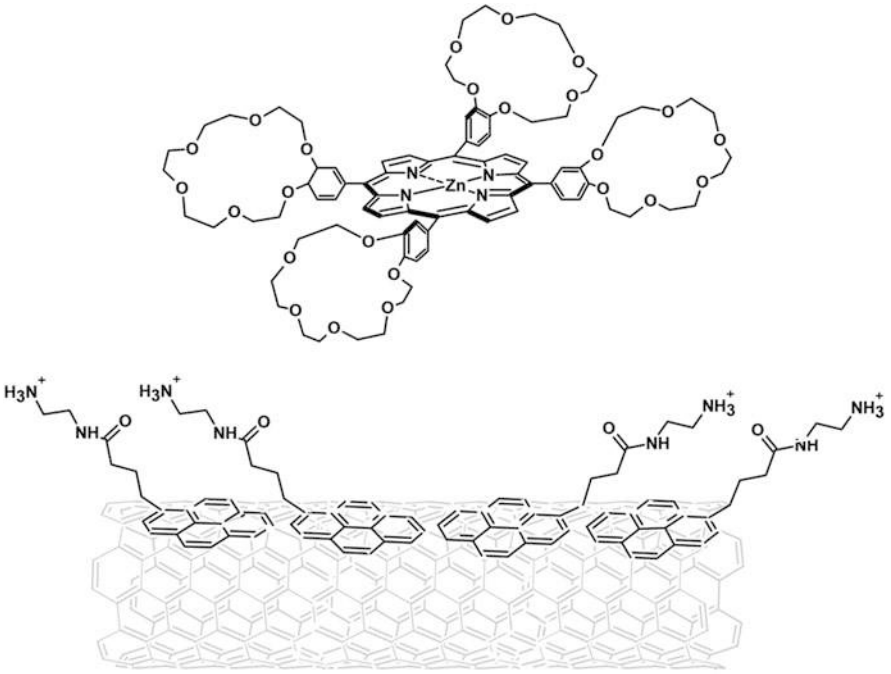

Fig. 34 Representative porphyrin systems featuring 1D SWCNTs: SWCNT•$(Pyr^{+})_4$•$ZnPCrown_4$ (**72**) with an electron-accepting SWCNT•$(Pyr^{+})_4$ and a light-harvesting/electron-donating ([18]-crown-6)s zinc (II) porphyrin ($ZnPCrown_4$). In DMF, the charge recombination is $1.0 \times 10^7\ s^{-1}$

player – and electron-accepting fullerenes, more profitable designs of organic photovoltaics featuring organic semiconductors rather than (metallo)porphyrins have been achieved. An immense body of work has been performed on fullerene-based systems. Most notable is to fine-tune and optimize the characteristics of artificial photosynthetic systems. Here, efficient light harvesting is linked to the generation of long-lived radical ion pair states as the product of energy as well as electron transfer. Still, we believe that there is "plenty of room" for further explorations in the context of enhanced photon and charge management.

From our point of view, future challenges in this field will be to use nearly defect-free and individualized/stabilized 1D SWCNTs to embellish them with suitable light harvesters, electron donors, or electron acceptors. This would be part of a concept that allows, on the one hand, the storage of single charges and, on the other hand, the accumulation of multiple charges, that is, either electrons or holes, in 1D SWCNTs. Equally important is the unidirectional mediation of the latter to catalytically active centers. All of this would be necessary to drive, for example, solar fuel formation. In general, photon and charge management is key for many applications such as photocatalysis, photosensitization, or photosensitization. In fact, the good water solubility, low toxicity, and low-cost nature of CNDs make photocatalysis one of the most interesting applications. Exploring and understanding the basic

charge-transfer properties could lead to crucial improvements in, for example, photocatalytic processes using CNDs as photosensitizers and/or catalytic centers.

References

1. Deisenhofer J, Norris JR (1993) The photosynthetic reaction center, 1st edn. Academic, San Diego
2. Collings AF, Critchley C (2005) Artificial photosynthesis: from basic biology to industrial application. Wiley-VCH, Weinheim
3. Balzani V (2001) Electron transfer in chemistry, vol 1. Wiley-VCH, Weinheim
4. Wasielewski MR (1992) Photoinduced electron transfer in supramolecular systems for artificial photosynthesis. Chem Rev 92:435–461
5. Gust D, Moore TA, Moore AL et al (1993) Molecular mimicry of photosynthetic energy and electron transfer. Acc Chem Res 26:198–205
6. Mattes SL, Farid S et al (1984) Exciplexes and electron transfer reactions. Science 226: 917–921
7. Roth HD (1990) In: Mattay J (ed) A brief history of photoinduced electron transfer and related reactions in photoinduced electron transfer, vol 156. Springer, Berlin, p 1
8. Marcus RA (1993) Electron transfer reactions in chemistry: theory and experiment. Angew Chem Int Ed 32:1111–1121
9. Kroto HW, Allaf AW, Balm SP et al (1991) C_{60}: buckminsterfullerene. Chem Rev 91: 1213–1235. https://doi.org/10.1021/cr00006a005
10. Bracher PJ, Schuster DI (2002) Electron transfer in functionalized fullerenes. In: Guldi DM, Martin N (eds) Fullerenes: from synthesis to optoelectronic properties. Kluwer Academic Publishers, Dordrecht, pp 163–212
11. Guldi DM (1997) Electron transfer to buckminsterfullerenes and functionalized fullerene derivatives in aqueous and protic media, as studied by radiolytic techniques. Res Chem Intermed 23:653–673
12. Popov AA, Yang S, Dunsch L et al (2013) Endohedral fullerenes. Chem Rev 113:5989–6113
13. Prato M (1997) [60]Fullerene chemistry for materials science applications. J Mater Chem 7: 1097–1109
14. Rudolf M, Kirner SV, Guldi DM et al (2016) A multicomponent molecular approach to artificial photosynthesis-the role of fullerenes and endohedral metallofullerenes. Chem Soc Rev 45:612–630
15. Scott LT (2004) Methods for the chemical synthesis of fullerenes. Angew Chem Int Ed 43: 4994–5007
16. Akasaka T, Nagase S (2002) Endofullerenes: A new family of carbon clusters, 1st edn. Kluwer Academic Publishers, Dordrecht
17. Dresselhaus MS, Dresselhaus G, Avouris P (2001) Carbon nanotubes: synthesis, structure, properties and applications, 1st edn. Springer-Verlag, Berlin
18. Lim SYY, Shen W, Gao Z et al (2015) Carbon quantum dots and their applications. Chem Soc Rev 44:362–381
19. Strauss V, Roth A, Sekita M, Guldi DM et al (2016) Efficient energy-conversion materials for the future: understanding and tailoring charge-transfer processes in carbon nanostructures. Chem 1:531–556
20. Cadranel A, Margraf JT, Strauss V, Clark T, Guldi DM et al (2019) Carbon nanodots for charge-transfer processes. Acc Chem Res 52:955–963
21. Ogunro OO, Wang XQ et al (2010) Charge transfer in the non-covalent functionalization of carbon nanotubes. New J Chem 34:1084–1088
22. Meng L, Fu C, Lu Q et al (2009) Advanced technology for functionalization of carbon nanotubes. Prog Nat Sci 19:801–810

23. Strauss V, Margraf JT, Dirian K, Syrgiannis Z, Prato M, Wessendorf C, Hirsch A, Clark T, Guldi DM et al (2015) Carbon nanodots: supramolecular electron donor-acceptor hybrids featuring perylenediimides. Angew Chem Int Ed 54:8292–8297
24. Xiao L, Sun H et al (2018) Novel properties and applications of carbon nanodots. Nanoscale Horiz 3:565–597
25. Ferrer-Ruiz A, Scharl T, Haines P, Rodriguez-Perez L, Cadranel A, Herranz MA, Guldi DM, Martin N et al (2018) Exploring tetrathiafulvalene-carbon nanodots conjugates in charge transfer reactions. Angew Chem Int Ed 57:1001–1005
26. Cacioppo M, Scharl T, Dordevic L, Cadranel A, Arcudi F, Guldi DM, Prato M et al (2020) Symmetry-breaking charge-transfer chromophore interactions supported by carbon nanodots. Angew Chem Int Ed 132:12879–12884
27. Strauss V, Margraf JT, Clark T, Guldi DM et al (2015) A carbon-carbon hybrid-immobilizing carbon nanodots onto carbon nanotubes. Chem Sci 6:6878–6885
28. Strauss V, Margraf JT, Dolle C, Butz B, Nacken TJ, Walter J, Bauer W, Peukert W, Spiecker E, Clark T, Guldi DM et al (2014) Carbon nanodots: toward a comprehensive understanding of their photoluminescence. J Am Chem Soc 136:17308–17316
29. Menon A, Slominskii YL, Joseph J, Dimitriev OP, Guldi DM et al (2020) Reversible charge transfer with single-walled carbon nanotubes upon harvesting the low energy part of the solar spectrum. Small 16:1906745
30. Sgobba V, Guldi DM et al (2009) Carbon nanotubes – electronic/electrochemical properties and application for nanoelectronics and photonics. Chem Soc Rev 38:165–184
31. Menon A, Papadopoulos I, Harreiß C, Mora-Fuentes JP, Cortizo-Lacalle D, Mateo-Alonso A, Spiecke E, Guldi DM et al (2020) Collecting up to 115% of singlet-fission products by single walled carbon nanotubes. ACS Nano 14:8875–8886
32. Dyke CA, Tour JM et al (2004) Covalent functionalization of single-walled carbon nanotubes for materials applications. J Am Chem Soc 108:11151–11159
33. Hirsch A (2010) The era of carbon allotropes. Nat Mater 9:868–871
34. Yap SHK, Chan KK, Tjin SC, Yong KT et al (2020) Carbon allotrope-based optical fibers for environmental and biological sensing: a review. Sensors (Basel) 20:2046
35. Li H, Kang Z, Liu Y, Lee ST et al (2012) Carbon nanodots: synthesis, properties and applications. J Mater Chem 22:24230–24253
36. Li Z, Wang L, Li Y, Feng Y, Feng W et al (2019) Frontiers in carbon dots: design, properties and applications. Mater Chem Front 3:2571–2601
37. Liu ML, Chen BB, Li CM, Huang CZ et al (2019) Carbon dots: synthesis, formation mechanism, fluorescence origin and sensing applications. Green Chem 21:449–471
38. Carbonaro CM, Corpino R, Salis M, Mocci F, Thakkar SV, Olla C, Ricci PC et al (2019) On the emission properties of carbon dots: reviewing data and discussing models. C 5:60
39. Sciortino A, Cannizzo A, Messina F et al (2018) Carbon nanodots: a review-from the current understanding of the fundamental photophysics to the full control of the optical response. C 4:67
40. De B, Karak N et al (2017) Recent progress in carbon dot-metal based nanohybrids for photochemical and electrochemical applications. J Mater Chem A 5:1826–1859
41. Yu H, Shi R, Zhao Y, Waterhouse GIN, Wu LZ, Tung CH, Zhang T et al (2016) Smart utilization of carbon dots in semiconductor photocatalysis. Adv Mater 28:9454–9477
42. Arcudi F, Strauss V, Dordevic L, Cadranel A, Guldi DM, Prato M et al (2017) Porphyrin antennas on carbon nanodots: excited state energy and electron transduction. Angew Chem Int Ed 56:12097–12101
43. Cadranel A, Strauss V, Margraf JT, Winterfeld KA, Vogl C, Đorđevic L, Arcudi F, Hoelzel H, Jux N, Prato M, Guldi DM et al (2018) Screening supramolecular interactions between carbon nanodots and porphyrins. J Am Chem Soc 140:904–907
44. Kroto HW, Heath JR, Brien SC, Curl RF, Smalley RE et al (1985) C_{60}: buckminster fullerene. Nature 318:1985–1986

45. Kroto HW (1987) The stability of the fullerenes C_n, with n = 24, 28, 32, 36, 50, 60 and 70. Nature 329:529–531
46. Hirsch A, Chen Z, Jiao H et al (2000) Spherical aromaticity in I_h symmetrical fullerenes. Angew Chem Int Ed 39:3915–3917
47. Krätschmer W, Lamb LD, Fostiropoulos K, Huffman DR et al (1990) Solid C_{60}: a new form of carbon. Nature 347:354–358
48. Guldi DM, Fukuzumi S (2002) The small reorganization energy of fullerenes. In: Guldi DM, Martin N (eds) Fullerenes: from synthesis to optoelectronic properties. Kluwer Academic Publishers, pp 237–265
49. Gust D, Moore TA, Moore AL et al (2001) Mimicking photosynthetic solar energy transduction. Acc Chem Res 34:40–48
50. Lin VS, DiMagno SG, Therien MJ et al (1994) Highly conjugated, acetylenyl bridged porphyrins: new models for light-harvesting antenna systems. Science 264:1105–1111
51. Nappa M, Valentine JS et al (1978) The influence of axial ligands on metalloporphyrin visible absorption spectra. Complexes of tetraphenylporphinatozinc. J Am Chem Soc 100:5075–5080
52. Goldberg PK, Pundsack TJ, Splan KE et al (2011) Photophysical investigation of neutral and diprotonated free-base bis(arylethynyl)porphyrins. J Phys Chem A 115:10452–10460
53. Kuo MC, Li LA, Yen WN, Lo SS, Lee CW, Yeh CY et al (2007) New synthesis of zinc tetrakis (arylethynyl)porphyrins and substituent effects on their redox chemistry. Dalt Trans 14:1433–1439
54. Imahori H (2004) Porphyrin – fullerene linked systems as artificial photosynthetic mimics. Org Biomol Chem 2:1425–1433
55. Gust D, Moore TA et al (1997) Fullerenes pigments linked to pigments. Res Chem Intermed 23:621–651
56. Imahori H, Hagiwara K, Akiyama T, Aoki M, Taniguchi S, Okada T, Shirakawa M, Sakata Y et al (1996) The small reorganization energy of C_{60} in electron transfer. Chem Phys Lett 263:545–550
57. Bracher PJ, Schuster DI et al (2002) Electron transfer in functionalized fullerenes, pp 163–212
58. Lawson DR, Feldheim DL, Foss CA, Dorhout PK, Elliott CM, Martin CR, Parkinson B et al (1992) Near-IR absorption spectra for the buckminsterfullerene anions: an experimental and theoretical study. J Electrochem Soc 139:L68–L71
59. Lawson DR, Feldheim DL, Foss CA, Dorhout PK, Elliott CM, Martin CR, Parkinson B et al (1992) Near-IR absorption spectra for the C_{70} fullerene anions. J Phys Chem 96:7175–7177
60. Kuciauskas D, Lin S, Seely GR, Moore AL, Moore TA, Gust D, Drovetskaya T, Reed CA, Boyd PDW et al (1996) Energy and photoinduced electron transfer in porphyrin-fullerene dyads. J Phys Chem 100:15926–15932
61. Liddell PA, Sumida JP, Macpherson AN, Noss L, Seely GR, Clark KN, Moore AL, Moore TA, Gust D et al (1994) Preparation and photophysical studies of porphyrin-C_{60} dyads. Photochem Photobiol 60:537–541
62. Guldi DM, Luo C, Prato M, Dietel E, Hirsch A et al (2000) Charge-transfer in a π-stacked fullerene porphyrin dyad: evidence for back electron transfer in the "Marcus-inverted" region. Chem Commun 5:373–374
63. Sutton LR, Scheloske M, Pirner KS, Hirsch A, Guldi DM, Gisselbrecht J-P et al (2004) Unexpected change in charge transfer behavior in a cobalt(II) porphyrin−fullerene conjugate that stabilizes radical ion pair states. J Am Chem Soc 126:10370–10381
64. Imahori H, Hagiwara K, Akiyama T, Taniguchi S, Okada T, Sakata Y et al (1995) Synthesis and photophysical property of porphyrin-linked fullerene. Chem Lett 24:265–266
65. Imahori H, Hagiwara K, Aoki M, Akiyama T, Taniguchi S, Okada T, Shirakawa M, Sakata Y et al (1996) Linkage and solvent dependence of photoinduced electron transfer in zincporphyrin-C_{60} dyads. J Am Chem Soc 118:11771–11782
66. Imahori H, El-Khouly ME, Fujitsuka M, Ito O, Sakata Y, Fukuzumi S et al (2001) Solvent dependence of charge separation and charge recombination rates in porphyrin-fullerene dyad. J Phys Chem A 105:325–332

67. Imahori H, Tamaki K, Guldi DM, Luo C, Fujitsuka M, Ito O, Sakata Y, Fukuzumi S et al (2001) Modulating charge separation and charge recombination dynamics in porphyrin – fullerene linked dyads and triads: marcus-normal versus inverted region. J Am Chem Soc 123:2607–2617
68. Imahori H, Yamada H, Guldi DM, Endo Y, Shimomura A, Kundu S, Yamada K, Okada T, Sakata Y, Fukuzumi S et al (2002) Comparison of reorganization energies for intra- and intermolecular electron transfer. Angew Chem Int Ed 41:2344–2347
69. Guldi DM (2002) Fullerene-porphyrin architectures; photosynthetic antenna and reaction center models. Chem Soc Rev 31:22–36
70. Kuciauskas D, Liddell PA, Lin S, Johnson TE, Weghorn SJ, Lindsey JS, Moore AL, Moore TA, Gust D et al (1999) An artificial photosynthetic antenna-reaction center complex. J Am Chem Soc 121:8604–8614
71. Luo C, Guldi DM, Imahori H, Tamaki K, Sakata Y et al (2000) Sequential energy and electron transfer in an artificial reaction center: formation of a long-lived charge-separated state. J Am Chem Soc 122:6535–6551
72. Imahori H, Guldi DM, Tamaki K, Yoshida Y, Luo C, Sakata Y, Fukuzumi S et al (2001) Charge separation in a novel artificial photosynthetic reaction center lives 380 ms. J Am Chem Soc 123:6617–6628
73. Gilbert M, Albinsson B et al (2015) Photoinduced charge and energy transfer in molecular wires. Chem Soc Rev 44:845–862
74. Schubert C, Margraf JT, Clark T, Guldi DM et al (2015) Molecular wires – impact of π-conjugation and implementation of molecular bottlenecks. Chem Soc Rev 44:988–998
75. de la Torre G, Giacalone F, Segura JL, Martín N, Guldi DM et al (2005) Electronic communication through π-conjugated wires in covalently linked porphyrin/C_{60} ensembles. Chem Eur J 11:1267–1280
76. Sukegawa J, Schubert C, Zhu X, Tsuji H, Guldi DM, Nakamura E et al (2014) Electron transfer through rigid organic molecular wires enhanced by electronic and electron–vibration coupling. Nat Chem 6:899–905
77. Yzambart G, Zieleniewska A, Bauroth S, Clark T, Bryce MR, Guldi DM et al (2017) Charge-gating dibenzothiophene – S, S – dioxide bridges in electron donor – bridge – acceptor conjugates. J Phys Chem C 121:13557–13569
78. Kaur R, Possanza F, Limosani F, Bauroth S, Zanoni R, Clark T, Arrigoni G, Tagliatesta P, Guldi DM et al (2020) Understanding and controlling short- and long-range electron/charge-transfer processes in electron donor-acceptor conjugates. J Am Chem Soc 142:7898–7911
79. Zieleniewska A, Lodermeyer F, Roth A, Guldi DM et al (2018) Fullerenes-how 25 years of charge transfer chemistry have shaped our understanding of (interfacial) interactions. Chem Soc Rev 47:702–714
80. Boyd PDW, Reed CA et al (2005) Fullerene−porphyrin constructs. Acc Chem Res 38: 235–242
81. Sun D, Tham FS, Reed CA, Chaker L, Boyd PDW et al (2002) Supramolecular fullerene-porphyrin chemistry. Fullerene complexation by metalated "jaws porphyrin" hosts. J Am Chem Soc 124:6604–6612
82. Tashiro K, Aida T, Zheng JY, Kinbara K, Saigo K, Sakamoto S, Yamaguchi K et al (1999) A cyclic dimer of metalloporphyrin forms a highly stable inclusion complex with C_{60}. J Am Chem Soc 121:9477–9478
83. Da Ros T, Prato M, Guldi DM, Ruzzi M, Pasimeni L et al (2001) Efficient charge separation in porphyrin-fullerene-ligand complexes. Chem A Eur J 7:816–827
84. D'Souza F, Deviprasad GR, El-Khouly ME, Fujitsuka M, Ito O et al (2001) Probing the donor-acceptor proximity on the physicochemical properties of porphyrin-fullerene dyads: "tail-on" and "tail-off" binding approach. J Am Chem Soc 123:5277–5284
85. D'Souza F, Amin AN, El-Khouly ME, Subbaiyan NK, Zandler ME, Fukuzumi S et al (2012) Control over photoinduced energy and electron transfer in supramolecular polyads of

covalently linked azaBODIPY-bisporphyrin "molecular clip" hosting fullerene. J Am Chem Soc 134:654–664
86. Wessendorf F, Gnichwitz J-F, Sarova GH, Hager K, Hartnagel U, Guldi DM, Hirsch A et al (2007) Implementation of a hamiliton-receptor-based hydrogen-bonding motif toward a new electron donor−acceptor prototype: electron versus energy transfer. J Am Chem Soc 129: 16057–16071
87. Calderon RMK, Valero J, Grimm B, De Mendoza J, Guldi DM et al (2014) Enhancing molecular recognition in electron donor-acceptor hybrids via cooperativity. J Am Chem Soc 136:11436–11443
88. Vela S, Bauroth S, Atienza C, Molina-Ontoria A, Guldi DM, Martín N et al (2016) Determining the attenuation factor in molecular wires featuring covalent and noncovalent Tectons. Angew Chem 128:15300–15304
89. Wang B, Bauroth S, Saha A, Chen M, Clark T, Lu X, Guldi DM et al (2019) Tuning electron transfer in supramolecular nano-architectures made of fullerenes and porphyrins. Nanoscale 11:10782–10790
90. Leonhardt EJ, Jasti R et al (2019) Emerging applications of carbon nanohoops. Nat Rev Chem 3:672–686
91. Xu Y, Wang B, Kaur R, Minameyer MB, Bothe M, Drewello T, Guldi DM, von Delius M et al (2018) A supramolecular [10]CPP junction enables efficient electron transfer in modular porphyrin–[10]CPP⊃fullerene complexes. Angew Chem Int Ed 57:11549–11553
92. Yamada M, Akasaka T, Nagase S et al (2010) Endohedral metal atoms in pristine and functionalized fullerene cages. Acc Chem Res 43:92–102
93. Guldi DM, Feng L, Radhakrishnan SG, Nikawa H, Yamada M, Mizorogi N, Tsuchiya T, Akasaka T, Nagase S, Herranz MA, Martín N et al (2010) A molecular $Ce_2@I_h$-C_{80} switch – unprecedented oxidative pathway in photoinduced charge transfer reactivity. J Am Chem Soc 132:9078–9086
94. Rudolf M, Feng L, Slanina Z, Wang W, Nagase S, Akasaka T, Guldi DM et al (2016) Strong electronic coupling and electron transfer in a $Ce_2@I_h$-C_{80}–H_2P electron donor acceptor conjugate. Nanoscale 8:13257–13262
95. Feng L, Radhakrishnan SG, Mizorogi N, Slanina Z, Nikawa H, Tsuchiya T, Akaksaka T, Nagase S, Martín N, Guldi DM et al (2011) Synthesis and charge-transfer chemistry of $La_2@I_h$-C_{80}/$Sc_3N@I_h$-C_{80}−zinc porphyrin conjugates: impact of endohedral cluster. J Am Chem Soc 133:7608–7618
96. Wolfrum S, Pinzon JR, Molina-Ontario A, Gouloumis A, Martín N, Echegoyen L, Guldi DM et al (2011) Utilization of $Sc_3N@C_{80}$ in long-range charge transfer reactions. Chem Commun 47:2270–2272
97. Tsuchiya T, Rudolf M, Wolfrum S, Radhakrishnan SG, Aoyama R, Yokosawa Y, Oshima A, Akasaka T, Nagase S, Guldi DM et al (2013) Coordinative interactions between porphyrins and C_{60}, $La@C_{82}$, and $La_2@C_{80}$. Chem A Eur J 19:558–565
98. Langa F, Gomez-Escalonilla MJ, de la Cruz P et al (2007) Carbon nanotubes and porphyrins: an exciting combination for optoelectronic devices. J Porphyrins Phthalocyanines 11:348–358
99. Wang A, Ye J, Humphrey MG, Zhang C et al (2018) Graphene and carbon-nanotube nanohybrids covalently functionalized by porphyrins and phthalocyanines for optoelectronic properties. Adv Mater 30:1705704
100. Baskaran D, Mays JW, Zhang XP, Bratcher MS et al (2005) Carbon nanotubes with covalently linked porphyrin antennae: photoinduced electron transfer. J Am Chem Soc 127:6916–6917
101. Hijazi I, Khedhiri K, Campidelli S et al (2018) Grafting of porphyrin oligomers on single-walled carbon nanotubes by hay coupling. Org Biomol Chem 16:6767–6772
102. Chen J, Collier CP et al (2005) Noncovalent functionalization of single-walled carbon nanotubes with water-soluble porphyrins. J Phys Chem B 109:7605–7609
103. Girek B, Sliwa W et al (2015) Hybrids of cationic porphyrin with nanocarbons. J Incl Phenom Macrocycl Chem 82:283–300

104. Murakami H, Nomura T, Nakashima N et al (2003) Noncovalent porphyrin functionalized single-walled carbon nanotubes in solution and the formation of porphyrin-nanotube nanocomposites. Chem Phys Lett 378:481–485
105. Roquelet C, Langlois B, Vialla F, Garrot D, Lauret JS, Voisin C et al (2013) Light harvesting with non covalent carbon nanotube/porphyrin compounds. Chem Phys 413:45–54
106. Dirian K, Herranz MA, Katsukis G, Malig J, Rodriguez-Perez L, Romero-Nieto C, Strauss V, Martin N, Guldi DM et al (2013) Low dimensional nanocarbons – chemistry and energy/electron transfer reactions. Chem Sci 4:4335–4353
107. Arellano LM, Barrejon M, Gobeze HB, Gomez-Escalonilla MJ, Fierro JLG, D'Souza F, Langa F et al (2017) Charge stabilizing tris(triphenylamine)-zinc porphyrin-carbon nanotube hybrids: synthesis, characterization and excited state charge transfer studies. Nanoscale 9:7551–7558
108. Baek J, Umeyama T, Mizuno S, Tkachenko NV, Imahori H et al (2018) Photophysical properties of porphyrin dimer-single walled carbon nanotube linked systems. J Phys Chem C 122:13285–13293
109. Campidelli S, Sooambar C, Diz EL, Ehli C, Guldi DM et al (2006) Dendrimer-functionalized single-wall carbon nanotubes: synthesis, characterization, and photoinduced electron transfer. J Am Chem Soc 128:12544–12552
110. Ehli C, Campidelli S, Brunetti FG, Prato M, Guldi DM et al (2007) Single-wall carbon nanotube porphyrin nanoconjugates. J Porphyrins Phthalocyanines 11:442–447
111. Palacin T, Khanh HL, Jousselme B, Jegou P, Filoramo A, Ehli C, Guldi DM, Campidelli S et al (2009) Efficient functionalization of carbon nanotubes with porphyrin dendrons via click chemistry. J Am Chem Soc 131:15394–15402
112. Menon A, Münich PW, Wagner P, Officer DL, Guldi DM et al (2021) Amphiphilic zinc porphyrin single walled carbon nanotube hybrids: efficient formation and excited states charge transfer studies. Small. https://doi.org/10.1002/smll.202005648
113. Zhong Q, Diev VV, Roberts ST, Antunez PD, Brutchey RL, Bradforth SE, Thompson ME et al (2013) Fused porphyrin-single-walled carbon nanotube hybrids: efficient formation and photophysical characterization. ACS Nano 7:3466–3475
114. D'Souza F, Sandanayaka ASD, Ito O et al (2010) SWNT-based supramolecular nanoarchitectures with photosensitizing donor and acceptor molecules. J Phys Chem Lett 1:2586–2593
115. Guldi DM, Rahman GMA, Jux N, Tagmatarchis N, Prato M et al (2004) Integrating single-wall carbon nanotubes into donor-acceptor nanohybrids. Angew Chem Int Ed 43:5526–5530
116. Das SK, Subbaiyan NK, D'Souza F, Sandanayaka ASD, Hasobe T, Ito O et al (2011) Photoinduced processes of the supramolecularly functionalized semi-conductive SWCNTs with porphyrins via ion-pairing interactions. Energy Environ Sci 4:707–716
117. D'Souza F, Chitta R, Sandanayaka ASD, Subbaiyan NK, D'Souza L, Araki Y, Ito O et al (2007) Self-assembled single walled carbon nanotube: zinc-porphyrin hybrids through ammonium ion-crown ether interaction: construction and electron transfer. Chem Eur J 13:8277–8284

Connecting Fullerenes with Carbon Nanotubes and Graphene

8

Xing Lu

Contents

Abstract

Novel carbon allotropes such as fullerene, carbon nanotube (CNT), graphene, and graphyne have attracted intensive attention from the scientific community. Except graphyne which contains sp- and sp^3-hybridyzed carbon atoms, the other three elemental carbon materials consist of merely sp^2-hybridyzed carbon atoms, and thus they show some similarities in structures and even properties to some extent. This chapter gives a brief summary of the recent results regarding the mutual transformation among these sp^2-hybridyzed carbon allotropes, namely, the structural identification of giant fullerenes that provides hints to the formation process or mechanical deformation of CNTs, and the interconversion between fullerenes and graphene deduced from crystallographic results of typical fullerene cages.

Keywords

Fullerene · Carbon nanotube · Graphene · Graphyne · Transformation · Formation mechanism · Carbon allotrope

X. Lu (✉)
Huazhong University of Science and Technology, Wuhan, Hubei, China
e-mail: lux@hust.edu.cn

X. Lu et al. (eds.), *Handbook of Fullerene Science and Technology*,
https://doi.org/10.1007/978-981-16-8994-9_8

Introduction

The emergence of fullerenes has opened a wide avenue for human beings to enter an unprecedented realm of pure-carbon materials [1], such as the later-discovered carbon nanotubes (CNTs) [2] and graphene [3]. In particular, graphene represents as the first stable two-dimensional materials that has been isolated artificially and was awarded the Nobel Prize in Physics in 2010, following the Nobel Prize in Chemistry in 1996 of fullerenes.

Fullerenes and Carbon Nanotubes

In fact, all these newly emerged carbon allotropes, such as fullerenes, carbon nanotubes, and graphene, consist of merely sp^2-hybirdized carbon atoms, and their structural similarities are rather evident. As illustrated in Fig. 1 the molecular structures of C_{60}, C_{70}, C_{80}, and C_{90}-fullerenes tend to grow along the long axis to display a tubular appearance, and thus tubular higher fullerenes are viewed as capped CNTs with definite molecular structures [4]. Thus, it enables us to characterize the structural aspects of short CNTs by using the reliable and accurate methods such as single-crystal X-ray crystallography and solution nuclear magnetic resonance.

Two compounds, namely, $La_2@D_5(450)$-C_{100} and $La_2C_2@D_5(450)$-C_{100} which bear the same cage structure but different endohedral moieties, have been isolated and structurally determined with single-crystal X-ray crystallography [5]. In fact, the $D_5(450)$-C_{100} cage can be viewed as a short (10,0)-zigzag CNT consisting of two bands of ten continuously linked hexagons with two caps in the two ends. Detailed analyses of their molecular structures reveal unexpectedly that the long axis of $La_2@D_5(450)$-C_{100} is anomalously shorter than that of $La_2C_2@D_5(450)$-C_{100} although the latter encapsulates a larger La_2C_2 cluster inside (Fig. 2). More interestingly, it is discovered for the first time that the cage deformation has mainly occurred at the two bands of continuous hexagons (highlighted in yellow in Fig. 2), whereas

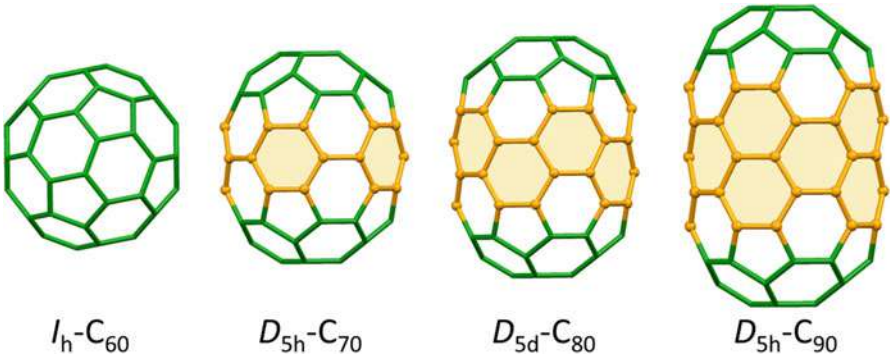

Fig. 1 Molecular structures of C_{60}–C_{90} showing their tubular appearances. The flat region consisting of merely hexagonal rings is highlighted in yellow

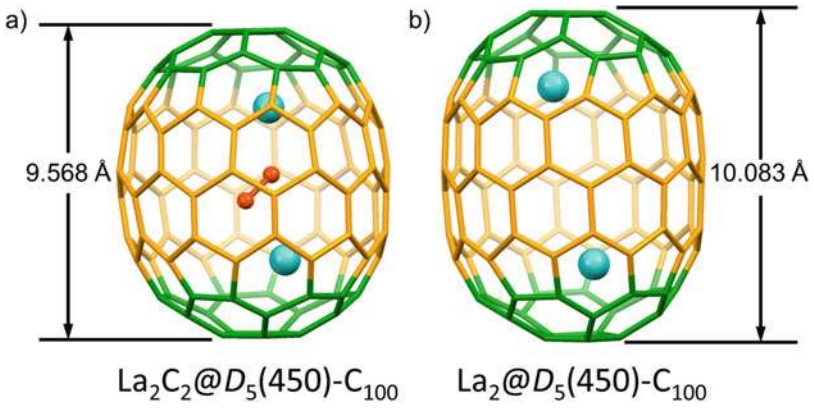

Fig. 2 X-ray structures of $La_2@D_5(450)$-C_{100} and $La_2C_2@D5(450)$-C_{100} showing anomalous compression of the tubular cage occurring mainly on the two bands of ten continuously linked hexagons which are highlighted in yellow

the two caps of the cage with pentagonal carbon rings are rather stiff to suffer from obvious deformation. Considering the different electronic structures of these two compounds, one may conclude that the deformation is mainly caused by the electron transfer from the internal metallic species to the cage, namely, 6 for $La_2@D_5(450)$-C_{100} versus 4 for $La_2C_2@D_5(450)$-C_{100}. Thus, a speculation that electronic reduction may also result in the elongation of CNTs and oxidation may shorten them seems instructive for the future works utilizing CNTs as electronic transistors or devices [6].

In addition, structural elucidation of giant metallofullerenes may also provide valuable information of the formation mechanism of CNTs. For instance, a defective cage $C_2(816)$-C_{104} (obtained as $La_2C_2@C_2(816)$-C_{104}) can transform into the other three ideal tubular cages reported so far, namely, $D_5(450)$-C_{100}, $C_s(574)$-C_{102}, and $D_{3d}(822)$-C_{104}, all encapsulating a La_2C_2 cluster, via well-defined routes (Fig. 3), revealing possible transformation routes of short CNTs at the molecular level [7].

Fullerenes and Graphene: Structural Transformation Mechanism

Meanwhile, the interconversion between fullerenes and graphene has also been reported. In 2010, Chuvilin and coworkers observed the transformation of a piece of graphene sheet into a fullerene sphere under electron beam irradiation [8]. Though the exact molecular structure (e.g., cage size and symmetry) of the resultant fullerene cage is not clear, this result demonstrates the possibility of graphene transforming to fullerene. Considering the differences between the flat structure of graphene and the curved fullerene cages, it is reasonable to speculate that the interconversion between them faces high energy barriers and is thus scarcely observed [9].

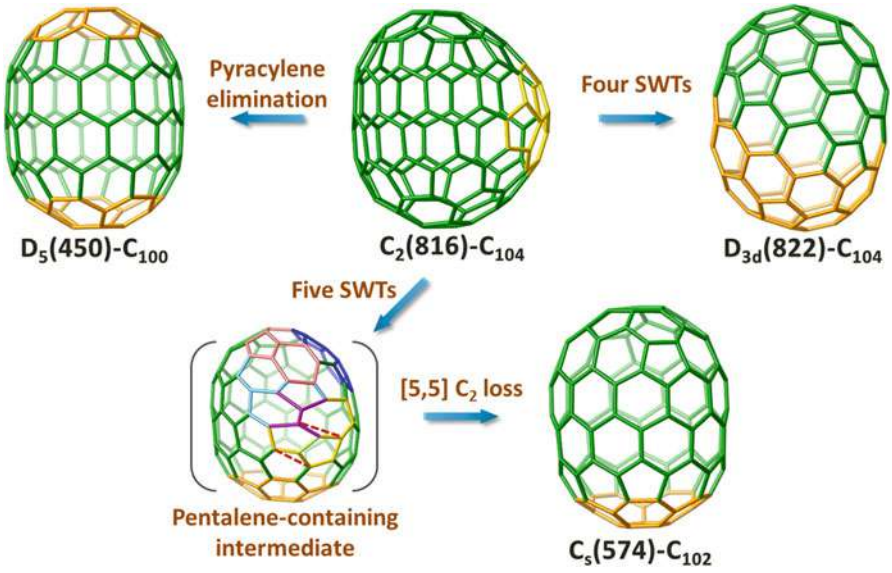

Fig. 3 Transformation from a defective cage $C_2(816)$-C_{104} to the other three ideal cages identified so far: $D_5(450)$-C_{100}, $C_s(574)$-C_{102}, and $D_{3d}(822)$-C_{104}

Alternatively, crystal structural analysis of typical fullerene cages may provide valuable information that may link fullerenes with graphene. A recent report describing a rather complete transformation map of existing metallofullerene-isomers has been advanced which covers more than 97% of the known structures of identified metallofullerenes with a cage size ranging from C_{74} to C_{86} [10]. Interestingly, topological analysis of the top compound in the map, namely, Eu@$C_2(27)$-C_{88}, reveals a direct connection with a graphene nanoribbon (Fig. 4). From the energetic point of view, it seems that the curved fullerene cages are less stable than the flat graphene structure so that energy gain is necessary to make graphene transform to fullerenes [11].

Moreover, considering the different structural features among the novel carbon allotropes, especially the pentagonal carbon rings in fullerene frameworks which bring high curvature to the spherical molecules but are absent from the tubular CNTs and the flat graphene, the chemical properties of fullerenes are in principle rather reactive [12]. Indeed, the effective methods for the functionalization of fullerenes are sometimes not possible to be adopted directly to modify CNTs and graphene, and accordingly, harsher experimental conditions are generally necessary for the functionalization of the latter two carbon allotropes [13].

A recent report on the utilization of hybrid materials consisting of fullerene C_{60} and CNTs as efficient multiple electrocatalysts is of special interest. By simply attaching fullerene molecules onto the surface of CNTs, Dai and coworkers have obtained metal-free, pH universal, and multifunctional electrochemical catalysts with excellent catalytic properties for oxygen reduction reaction, oxygen evolution

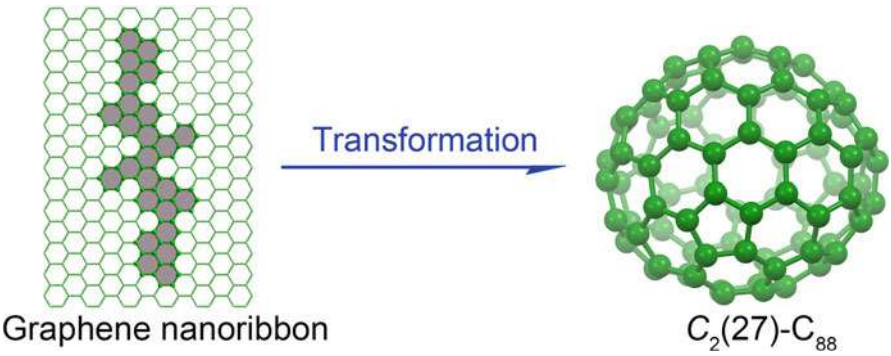

Fig. 4 Topological connection between a graphene nanoribbon and $C_2(27)$-C_{88} which is revealed as an ancestral compound of a series of existing metallofullerene cages ranging from C_{86} to C_{74}

reaction, and hydrogen evolution reaction [14]. Future works may demonstrate clearly the mechanism for the catalytic processes, in particular the interactions between fullerene molecules and CNTs which certainly account for the excellent catalytic performances. Moreover, recent results have revealed that the pentagon defects in carbon structures are important for their catalytic activities in electrochemical processes [15]. Accordingly, future works utilizing fullerenes as carbon precursors or directly as catalysts may find a solution to high-efficient water-splitting and/or metal-air batteries.

The emergence of graphyne, a kind of novel carbon allotrope containing sp- and sp^3-hybridized carbon atoms, has opened a wide avenue to future developments of carbon materials [16]. It is thus expected that new carbon-based allotropes and useful materials are to be discovered in the near future, and unprecedented structures and properties are expected.

References

1. Kroto HW, Heath JR, O'Brien SC, Curl RF, Smalley RE (1985) Nature 318:162–163
2. Iijima S (1991) Nature 354:56–58
3. Novoselov KS, Geim AK, Morozov SV, Jiang D, Zhang Y, Dubonos SV, Grigorieva IV, Firsov AA (2004) Science 306:666–669
4. Lu X, Akasaka T, Nagase S (2012) Angew Chem Int Ed 51:2812–2814
5. Cai W, Bao L, Hill JP, Zhao S, Xie Y, Akasaka T, Lu X (2015) J Am Chem Soc 137:10292–10296
6. Joselevich E (2004) Angew Chem Int Ed 43:2992–2994
7. Cai W, Li FF, Bao L, Xie Y, Lu X (2016) J Am Chem Soc 138:6670–6675
8. Chuvilin A, Kaiser U, Bichoutskaia E, Besley NA, Khlobystov NA (2010) Nat Chem 2:450–453
9. Lozovik Y, Popov AM (1997) Phys Usp 40:717–7787
10. Bao LP, Yu PY, Pan CW, Shen WQ, Lu X (2019) Chem Sci 10:2153–2158
11. Pichler T (2007) Nat Mater 6:332–333
12. Georgakilas V, Perman JA, Tucek J, Zboril R (2010) Chem Rev 115:4744–4822

13. Liao L, Peng HL, Liu ZF (2014) J Am Chem Soc 136:12194–12200
14. Gao R, Dai Q, Du F, Yan D, Dai L (2019) J Am Chem Soc 141:11658–11666
15. Zhu J, Huang Y, Mei W, Zhao C, Zhang C, Zhang J, Amiinu IS, Mu S (2019) Angew Chem Int Ed 58:3859–3864
16. Zhang S, Liu H, Huang C, Cui G, Li Y (2015) Chem Comm 51:1834–1837

Part III

Chemical Properties of Fullerenes and Metallofullerenes

Chemical Reactivity and Addition Pattern on C_{60} and C_{70}

9

Fa-Bao Li

Contents

Abstract

Fullerenes are a class of three-dimensional all-carbon hollow molecules incorporating conjugated π systems. The important principle to determine the stability of fullerene cages is the isolated pentagon rule (IPR). The chemical reactivity of fullerenes is similar to that of a fairly localized, electron-deficient polyolefin. Chemical modification of fullerenes is generally classified into exohedral modification and skeletal modification. Exohedral modification affords fullerene derivatives with one or several addends covalently linked to the spherical carbon framework. The main reactions are cycloadditions, radical additions, and nucleophilic additions. Skeletal modification produces open-cage fullerenes or heterofullerenes. Open-cage fullerenes usually refer to fullerene derivatives with more than one σ-bond scission and significantly disturbed π system. Heterofullerenes are those in which one or more carbons are replaced by other non-carbon atoms such as nitrogen. The addition pattern of exohedral modification on fullerenes is generally divided into monoaddition and multiaddition. In the case of monoaddition, C_{60} has only two possible isomers, including 1,2- and 1,4-additions, but for C_{70}, there are eight possible isomers, including the predominant 1,2- and 5,6-additions. As for multiaddition, low regioselectivity is generally observed and complex regioisomers are easily formed. Fullerene derivatives have displayed

F.-B. Li (✉)
School of Chemistry and Chemical Engineering, Hubei University, Wuhan, Hubei, China
e-mail: lfb0615@hubu.edu.cn

X. Lu et al. (eds.), *Handbook of Fullerene Science and Technology*,
https://doi.org/10.1007/978-981-16-8994-9_32

promising applications in many fields including material science, biological medicine, and nanotechnology due to their outstanding properties.

Keywords

Fullerenes · Exohedral modification · Skeletal modification · Open-cage fullerenes · Heterofullerenes · Chemical reactivity · Addition pattern

Introduction

Fullerenes are a kind of unique three-dimensional all-carbon hollow molecules with conjugated π systems, and have attracted extensive attention among the scientific community over the past three decades. Each fullerene C_n ($n \geq 20$ with the exception of $n = 22$) is composed of even number of carbon atoms with three connected vertices, which represents a closed cage structure with 12 pentagons and $(n - 20)/2$ hexagons (Euler's theorem). The number of fullerene isomers in topological structure is huge, and increases geometrically with the increase of n size. However, only a small part of them can exist stably in air. Kroto et al. proposed that all stable fullerenes had pentagons isolated by hexagons (Fig. 1a), that is, the stability of an all-carbon fullerene without any chemical modification is controlled by the isolated pentagon rule (IPR), because the presence of fused-pentagons (Fig. 1b) leads to local strain enhancement and stability reduction [1]. The proposed IPR has now been well recognized and widely applied to determine the stability of caged fullerenes composed of hexagons and pentagons.

Although fullerenes had been observed experimentally by the mass spectroscopic studies of pulsed laser vaporization of graphite in 1985 [2], this method could not provide enough fullerenes for further scientific research. A major breakthrough in the preparation of fullerenes occurred in 1990, when a macroscopic amount of fullerenes became available by resistive heating of graphite in a 100 torr inert helium atmosphere [3]. The crude product of graphite evaporation is soot containing various

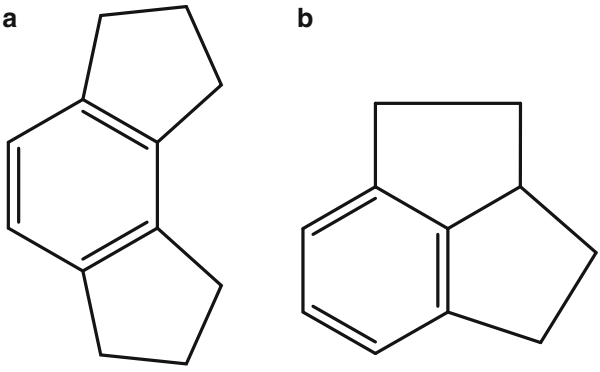

Fig. 1 Favorable (**a**) and unfavorable (**b**) structures in caged fullerenes

closed carbon structures (fullerene content ~5%). Fullerenes can be separated from soot by extraction with organic solvents such as toluene and chloroform. Subsequent column chromatography yields [60]fullerene (abbreviated as C_{60}) and [70]fullerene (abbreviated as C_{70}), which are magenta and port-wine red solutions in either benzene or toluene, respectively.

The macroscopic manufacturing of fullerenes provides an unprecedented opportunity to develop an interesting "three-dimensional" chemistry of all-carbon molecules. Among these formed fullerenes, C_{60} is the dominant species, and C_{70} is also obtained in relatively large quantities. C_{60} (Fig. 2a) is one of the most widely studied carbon clusters with a truncated icosahedral (I_h) spherical structure of 20 hexagons and 12 pentagons, in which all carbon atoms are equivalent. Its structure has two bond lengths, and the 6:6 bonds (between two hexagons, 0.140 nm) can be regarded as "double bonds," which are shorter than the 6:5 bonds (between a hexagon and a pentagon, 0.145 nm) [4]. The double bond character of the 6:6 bonds tends to take place addition reactions on this bond, which is the basis of most of the chemistry of C_{60}. The delocalization of electrons in C_{60} cage is relatively weak, so it is not a very "aromatic" molecule. This discovery has an important influence on its reactivity and addition pattern. C_{70} (Fig. 2b) is a kiwi-like ellipsoid molecule composed of 25 hexagons and 12 pentagons with a D_{5h} symmetry. Its structure is similar to that of C_{60}, but it contains an additional equatorial band composed of 10 carbon atoms and eight bonds with a length of 0.137–0.146 nm.

Classical spectroscopic techniques, such as mass spectrometry (MS), nuclear magnetic resonance (NMR), Fourier transform infrared (FT-IR), ultraviolet visible (UV-vis), and Raman spectroscopy, are commonly used to characterize the structures of C_{60} and C_{70}. In their mass spectra, C_{60} and C_{70} show strong peaks at m/z 720 and 840, respectively. In ^{13}C NMR spectra, C_{60} exhibits a peak at 142.7 ppm, and C_{70}

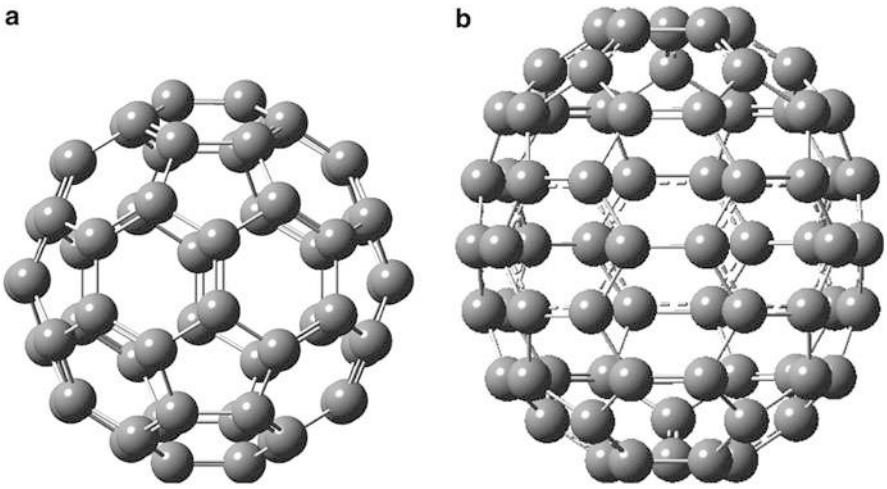

Fig. 2 Structures of (**a**) C_{60} and (**b**) C_{70}

gives five signals at 150.1, 147.5, 146.8, 144.8, and 130.3 ppm. In IR spectra, C_{60} displays four characteristic absorption peaks at 528, 577, 1183, and 1429 cm^{-1}, while C_{70} shows 12 peaks at 458, 536, 566, 578, 642, 674, 795, 1087, 1133, 1414, 1431, and 1461 cm^{-1} due to its lower symmetry. In UV-vis spectra, C_{60} shows three strong absorption peaks at 213, 257, and 329 nm, and a weak absorption at 404 nm, while C_{70} gives two main peaks at 214 and 236 nm, and four minor peaks at 331, 360, 378, and 468 nm. In addition, the 1,2- and 1,4-adducts of C_{60} show diagnostic absorptions at around 430 and 448 nm, respectively. As for Raman spectra, there are 10 and 27 Raman bands in C_{60} and C_{70}, respectively. In addition, single crystal X-ray analysis has also been used to provide definitive structural features of fullerenes and their derivatives when large enough crystals can be grown.

The room temperature solubility of pure C_{60} in approximately 150 solvents has been determined [5, 6]. It was found that the solubility of C_{60} covers a wide range from 0.01 mg/mL in methanol to 51.68 mg/mL in 1-chloronaphthalene. The solubilities of C_{60} in common solvents such as CS_2, toluene, chlorobenzene, 1,2-dichlorobenzene, trichloromethane, and hexane are 7.9, 2.8, 6.4, 27, 0.32, and 0.04 mg/ml, respectively. The solubility of C_{70} in 70 solvents has also been measured [6], but the solubility of C_{70} is lower than that of C_{60}. The water solubilities of C_{60} and C_{70} can be increased greatly by the introducing of hydrophilic groups such as hydroxyl group on the fullerene cage.

The heats of formation of C_{60} and C_{70} are about 10.2 and 9.7 kcal mol^{-1} per C-atom, respectively, indicating that C_{70} is more stable than C_{60}, resulting in a lower reactivity. Fullerenes have strong electron affinities (2.65 and 2.73 eV for C_{60} and C_{70}, respectively). The electron affinities can be increased by electron-withdrawing addends. For example, the value of $C_{60}F_{48}$ is 4.06 ev. The electron affinities are also manifest in fullerenes having energetically low-lying lowest unoccupied molecular orbitals (LUMO). They are thus easy to be reduced and can accept electrons reversibly under electrochemical conditions (up to six in the case of C_{60}).

Chemical Modification of Fullerenes

On the basis of the above-mentioned properties of fullerenes described in the Introduction, chemical modification has been carried out on those isolated fullerenes, primarily on C_{60}, much less on C_{70}. Investigations indicate that some structural properties of fullerenes can largely govern their chemical behaviors. Taking C_{60} as an example, its molecular structure displays three characteristic properties. Firstly, the arrangement of all the double bonds at the junctions of two hexagons (6–6 double bonds) and all the single bonds at the junctions of a hexagon and a pentagon (5–6 single bonds) is the most stable structure. Secondly, the highly pyramided sp^2 carbon atoms in spherical C_{60} result in the generation of a large amount of strain energy within the molecule. Thirdly, the low lying triply degenerate LUMO and fivefold degenerate HOMO of C_{60} make it easy to be reduced, but difficult to be oxidized. Similar properties can also be observed for C_{70}. Based on these properties, three

rules of reactivity can be deduced. Firstly, the addition of electron-rich species on the 6–6 double bonds of fullerenes, especially for cycloaddition, radical addition, and nucleophilic addition, has become the main reactions due to the similar reactivity of fullerenes and electron-deficient polyolefins. Secondly, the formation of saturated sp^3 hybridized carbon atoms in the fullerene framework is more favorable thermodynamically as a result of the release of strain in fullerene cage by addition reactions. However, new type of strain such as spatial repulsion of adducts are to build up increasingly, and thus a high degree of addition reactions will be precluded. Thirdly, 1,2-addition (addition on a 6–6 double bond) is the exclusive mode for typical cycloadditions and the preferred mode for additions of sterically undemanding addends because the regiochemistry of addition reactions is controlled by the minimization of 5–6 double bonds within the fullerene skeleton. As for the addition of bulkier segregated addends, 1,4-addition mode may occur simultaneously or exclusively for C_{60} to avoid the great steric interactions.

Generally speaking, chemical modification of fullerenes mainly refers to the exohedral modification and skeletal modification. Exohedral modification affords fullerene derivatives with one or several addends covalently linked to the spherical carbon framework. Skeletal modification yields open-cage fullerenes or heterofullerenes. The addition pattern of exohedral modification on fullerenes is generally classified into two categories, namely, monoaddition and multiaddition. In the case of monoaddition, there are only two possible isomers comprising 1,2- and 1,4-addition for C_{60}, yet eight possible isomers including the predominant 1,2- and 5,6-addition for C_{70}. As for multiaddition, low regioselectivity is generally observed and complex regioisomers are easily formed.

Exohedral Modification

The majority of exohedral modifications of fullerenes includes cycloadditions, radical additions, nucleophilic additions, dimerization reactions, transition-metal-catalyzed/promoted reactions, aldehyde/amine-participated reactions, asymmetric synthesis, retro-cycloaddition reactions, mechanochemical reactions, halogenation, hydrogenation, hydroxylation, additions of organocopper reagents**,** additions of peroxides, additions of amines, and so on.

Monoaddition Reactions

Cycloadditions

Cycloadditions are one of the most studied fullerene reactions because they can give fullerene products that are usually single and relatively easy to separate and purify [7]. Almost any functional group can be covalently connected to fullerenes by cycloadditions with appropriate adducts. Representative cycloadditions include [2+1], [2+2], [3+2] and [4+2] cycloadditions. Since there are so many different kinds of cycloadditions, only a few typical examples will be described in this section.

[2+1] Cycloadditions [2+1] Cycloadditions are one of the most commonly used methods for the annelation of three membered carbo- or heterocyclic fragments to the fullerene molecule to produce methanofullerenes, epiminofullerenes, and oxafullerenes. The synthetic methods for methanofullerenes are generally classified in three major groups, that is, addition-elimination of stabilized carbanions (Bingel reaction) [8], addition of in situ generated carbenes to fullerenes [9], and thermal addition of diazo compounds followed by thermolysis or photolysis of the resulting intermediates [10]. Intriguingly, when a large steric bulk of *N*-heterocylic carbene (NHC) was employed to react with C_{60}, a thermally stable zwitterionic Lewis acid-base adduct that is connected via a C-C single bond was formed in place of the expected methanofullerene [11]. Epiminofullerenes are usually prepared by the cycloadditions of fullerenes with nitrenes, which are most commonly generated in situ via thermal decomposition of azides [12]. Oxafullerenes are commonly formed by liquid-phase oxidation processes of fullerenes with different oxidants [13], such as photooxygenation with oxygen, oxidation with dimethyldioxirane, hydrogen peroxide, *m*-chloroperoxybenzoic acid (*m*-CPBA), and ozone. Fig. 3 shows the basic structures of oxa-[60]fullerene, epimino-[60]fullerene, and methano-[60]fullerene.

It is worth mentioning that the corresponding oxafullerenes, epiminofullerenes, and methanofullerenes in which the oxygen, nitrogen, and carbon atoms insert into 6–5 bonds of a fullerene can also be obtained by different synthetic procedures, respectively. Fullerene adducts with such structures are known as oxahomofullerenes (oxafulleroids), azahomofullerenes (azafulleroids) [14], and homofullerenes (fulleroids), respectively. Fig. 4 shows the basic structures of oxahomo-[60]fullerene, azahomo-[60]fullerene, and homo-[60]fullerenes. In addition, azahomofullerenes can be used as the starting materials to prepare open-cage fullerenes and azafullerenes. This will be noted in the section titled "Skeletal Modification."

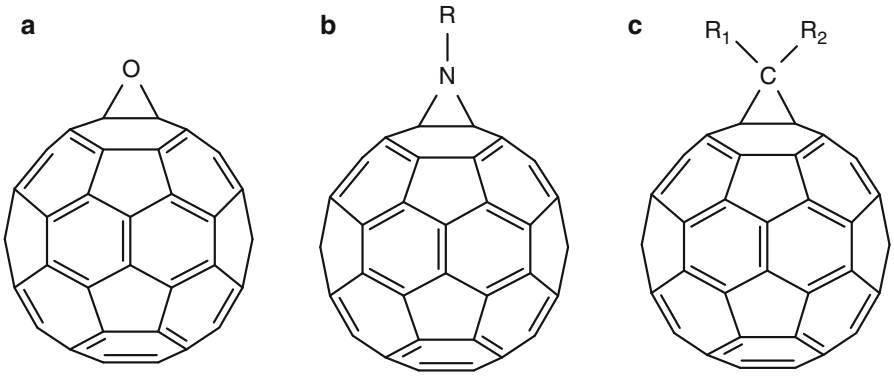

Fig. 3 Basic structures of (**a**) oxa-, (**b**) epimino-, and (**c**) methano-[60]fullerenes

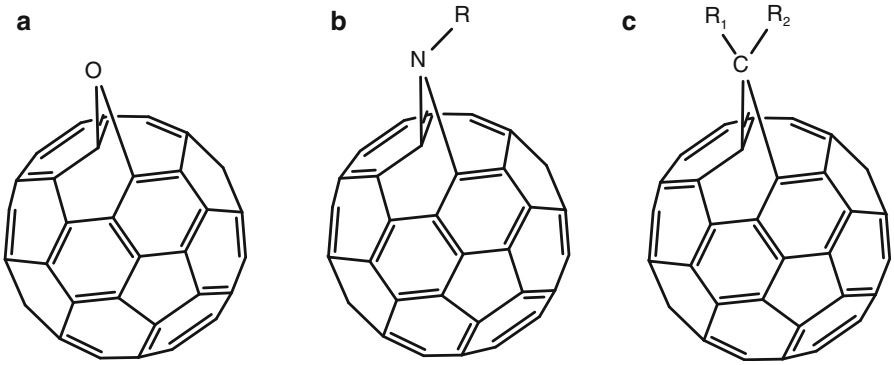

Fig. 4 Basic structures of (**a**) oxahomo-, (**b**) azahomo-, and (**c**) homo-[60]fullerenes

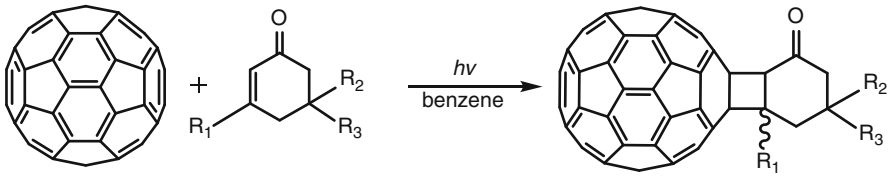

Scheme 1 Addition of cyclic enones to C_{60}

[2+2] Cycloadditions [2+2] Cycloadditions can be used for annelation of fullerenes with cyclobutane or cyclobutene fragments by photochemical irradiation and/or thermal reactions with cyclic enones, acyclic enones, ketenes, alkynes, benzynes, alkenes, and cumulenes [7]. A representative example is photocycloaddition of cyclic enones to C_{60} (Scheme 1). In addition, [2+2] cycloaddition reactions have also been utilized for the preparation of fullerene dimers in which two fullerene cages are linked by two C-C bonds. A typical example involves the dimerization of two C_{60} molecules by formal [2+2] cycloaddition to produce C_{120}. This will be described in the section titled "Dimerization Reactions."

[3+2] Cycloadditions [3+2] Cycloadditions of various 1,3-dipoles with fullerenes are one of the most promising procedures for annelation of five-membered heterocyclic fragments to the fullerene molecule. A wide range of fullerene-fused heterocycles such as fullerotriazolines, fulleropyrazolines, fulleropyrrolidines, fulleropyrrolines, fullerodihydrofurans, fullerenopyrazolines, fullerenoisoxazolines, fullerotetrahydrofuran, fullerotetrahydrothiophenes, fulleroxazolidines, fulleroisothiazolidines, and fullero-2-imino-1,3-thiazolidines have been prepared by the above strategy [7]. Fig. 5 shows the general form of these derivatives from C_{60}. In addition, the transition-metal salt-promoted [3+2] cycloaddition to fullerenes has

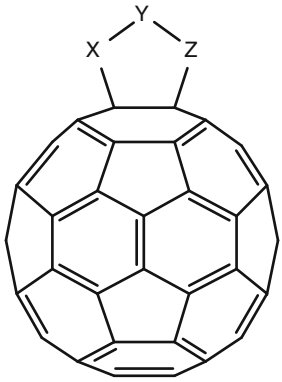

X	Y	Z
O	N	C
O	C	N
C	N	C
N	N	C
C	S	N
N	C	S
C	O	C
C	S	C
C	C	O
N	N	N

Fig. 5 Various heterocyclic derivatives generated by [3+2] cycloadditions

also been developed to afford novel fullerene-fused heterocyclic compounds such as fullerene-fused lactones, fullerene-fused boronic esters, oxazolidinofullerenes/thiazolidinofullerenes, and fullerene-fused 1,3-dioxolanes. This will be described in detail in the section titled "Transition-Metal-Catalyzed/Promoted Reactions."

Among the known fullerene-fused five-membered heterocycles, fulleropyrrolidines (Scheme 2) are the most widely studied heterocyclic fullerenes. Generally speaking, fulleropyrrolidines were synthesized by two main strategies, that is, the best-known Prato reaction together with the newly developed reaction based on aldehydes and amines. The in situ generated azomethine ylides by thermal ring opening of aziridines [15], thermal condensation of aldehydes and amines [16], or decarboxylation of immonium salts derived from condensation of α-amino acids with aldehydes/ketones (Prato reaction) [15] play a crucial role in the successful preparation of fulleropyrrolidines.

[4+2] Cycloadditions Diels-Alder reactions are one of the first studied fullerene reactions and are often utilized to prepare fullerene-fused six-membered carbo- or heterocyclic compounds by [4+2] cycloadditions in which the [6,6]-double bonds of fullerenes always act as dienophiles and are liable to react with different dienes including carbodienes and heterodienes to produce fullerene cycloadducts [7]. Shown in Fig. 6 are the representative cycloadducts obtained by [4+2] cycloadditions of C_{60} with anthracene, cyclopentadiene, and 2,3-dimethylene-1,4-dioxane, respectively.

It should be pointed out that many [4+2] cycloaddition products can also be formed by the reactions of fullerenes with in situ generated dienes. For example, *o*-quinodimethanes as carbodienes can be obtained by the reaction of 1,2-bis (bromomethyl)benzene with KI, the thermolysis of benzocyclobutenes, and the thermal extrusion of sulfur dioxide from either benzosulfolanes or benzosultines,

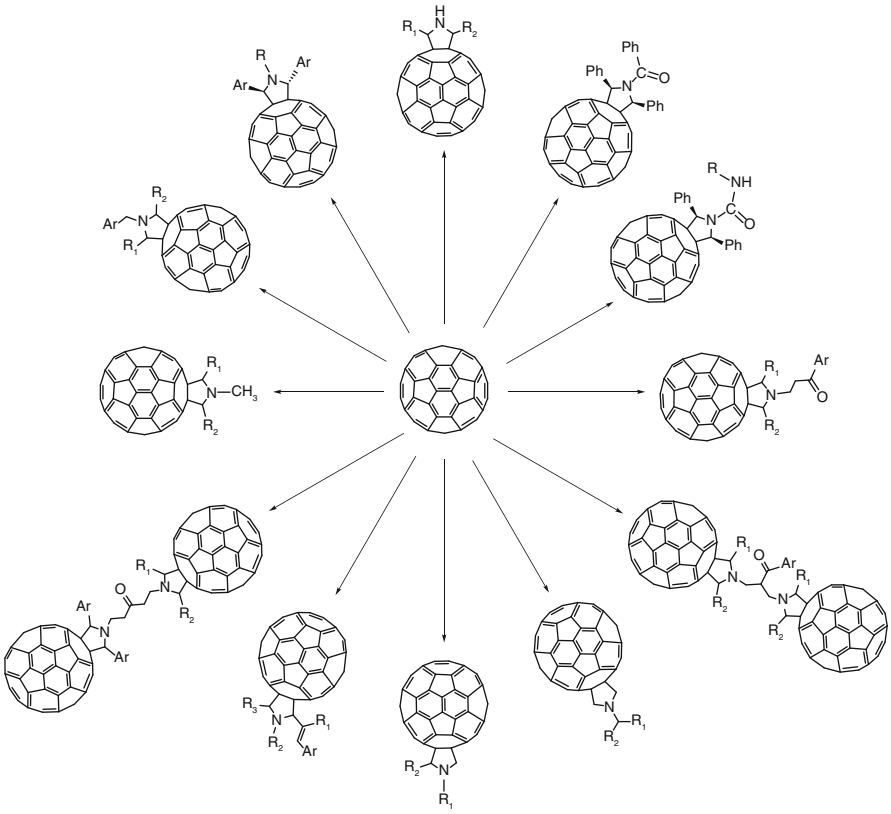

Scheme 2 Preparation of pyrrolidino[60]fullerene based on aldehydes/amines

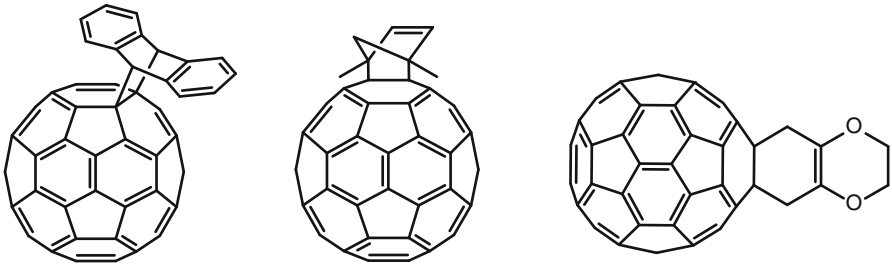

Fig. 6 Representative cycloadducts of C_{60} produced by [4+2] cycloadditions

respectively (Fig. 7a–d). As for heterodienes, azadienes, oxadienes, and thiadienes can be generated by decarboxylation of 1,3-benzoxazin-2-one derivatives and thermolysis of *o*-aminobenzyl alcohols, *o*-hydroxybenzyl alcohol, or benzothietanes (Fig. 7e–h). Some representative cycloadducts of this kind are shown in Fig. 8.

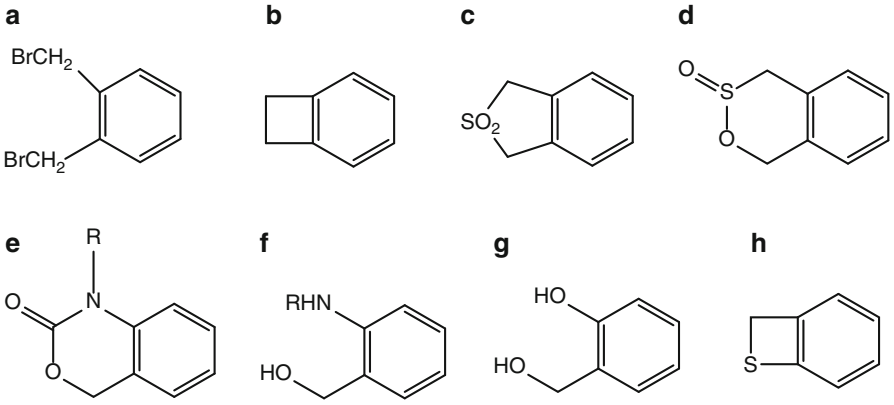

Fig. 7 Typical precursors employed for the preparation of [4+2] cycloadducts of fullerenes

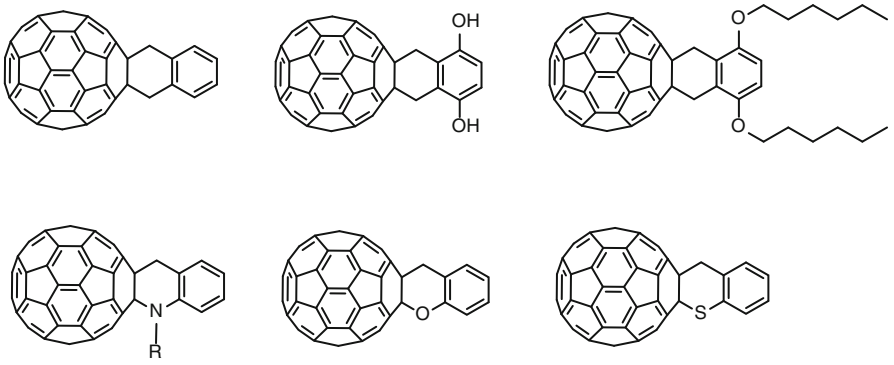

Fig. 8 Some [4+2] cycloaddition products from in situ generated dienes

Radical Additions

Due to the high radical scavenging activity that fullerenes exhibit by virtue of their high electron affinity (ca. 2.7–2.8 eV), the conjugated double bonds of fullerenes can be readily attacked by radical species. Radical reactions were among the first investigated fullerene reactions and continue to be an important methodology to functionalize fullerenes [17]. Typically, there are three forms of fullerenes that take part in radical reactions: (i) neutral fullerenes (i.e., C_{60}). Reactions of neutral C_{60} with *C*-centered radicals were among the first radical reactions to be studied in fullerene chemistry. Other radicals such as *Si*-centered radicals, *O*-centered radicals, *S*-centered radicals, *P*-centered radicals, *N*-centered radicals, *Sn*-centered radicals, *Re*-centered radicals, *Hg*-centered radicals, *Cr*-centered radicals, *Mo*-centered radicals, hydrogen radicals, and halogen radicals were also employed to functionalize fullerenes; (ii) fullerene radical anions (i.e., $C_{60}^{\bullet -}$) or radical cations (i.e., $C_{60}^{\bullet +}$). Fullerene radical anions were usually generated via a single electron transfer from

electron donors during the addition of amines/diamines, alkyl halides, and ketene silyl acetals to fullerenes. Fullerene radical anions can also be formed by one- and two-electron reduction of fullerenes with NADH (nicotinamide adenine dinucleotide, reduced) and NAD (nicotinamide adenine dinucleotide) dimer analogues or by the reactions of fullerenes with cyclopropyl-substituted olefins. As for fullerene radical cations, their formation is readily achieved by treatment of ground state fullerenes with powerful oxidizing reagents such as SbF_5/SO_2ClF, $SbCl_5$, concentrated and fuming sulfuric acids, magic acid (FSO_3H, SbF_5), or a mixture of fuming sulfuric acid and SO_2ClF; (iii) fullerene radical derivatives (i.e., $RC_{60}^{\bullet}$), which are commonly produced by nucleophilic addition followed by oxidation of the primarily formed fullerenyl anions (i.e., RC_{60}^{-}).

In most cases, multiple addition is liable to occur when pristine fullerenes react with radicals, yielding a mixture of many and hardly separable products. The facile addition of up to 11 phenyl groups, 15 benzyl groups, and 34 methyl groups to the C_{60} core has been previously singled out as the first landmark example of the radical reactivity of fullerenes. Under appropriately controlled conditions, much fewer products such as $C_{60}(R_FOH)$, $C_{60}(R_FCO_3H)$, $C_{60}(R_F)H$, R_FC_{60}-$C_{60}R_F$, 1,2- and 1,16-silyl adducts, and perfluoroalkyl fullerene derivatives can be separated and characterized by the radical reactions of fullerenes with diacyl peroxides (Scheme 3), R_FI/Bu_4SnH, $R_FI/(R_3Sn)_2$, phenylpolysilanes, silver(I) trifluoroacetate, trifluoroiodomethane, K_2PtF_6, and pentafluoroiodoethane.

In contrast to the traditional peroxide- or light-initiated processes, transition-metal-salt-mediated radical additions of fullerenes can proceed well under mild conditions and can produce a large number of novel mono-addition fullerene derivatives [17]. Various transition metal salts including mostly TBADT [$(n\text{–}Bu_4N)_4W_{10}O_{32}$], $Mn(OAc)_3{\cdot}2H_2O$, $Fe(ClO_4)_3$, $Pb(OAc)_4$, $Cu(OAc)_2{\cdot}H_2O$, and $CoCl_2$dppe [dppe=bis-(diphenylphosphino)ethane] have been utilized as promoters to initiate radical reactions of fullerenes to afford a large variety of fullerene adducts with a well-defined structure. This will be described in detail in the section titled "Transition-Metal-Catalyzed/Promoted Reactions."

Nucleophilic Additions

Nucleophilic additions are one of the versatile methods for functionalizing fullerenes and generally give monoaddition products in fairly good yields under mild conditions [18]. Although 1,2-addition products are obtained in most cases, the 1,4-addition products are generated under certain circumstance when steric hindrance between addends becomes notable.

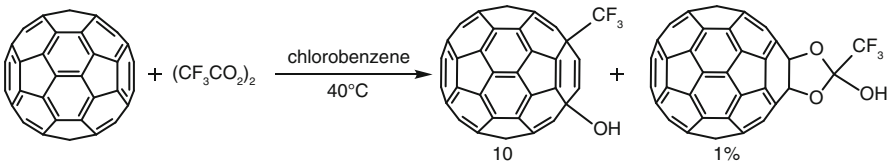

Scheme 3 Reaction of C_{60} with bis(trifluoroacetyl) peroxide

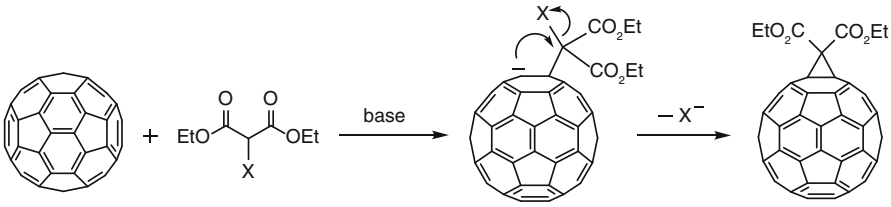

Scheme 4 Mechanism of the typical Bingel reaction

Nucleophilic additions to fullerenes can be classified into three categories based on the types of nucleophiles. For the first type of nucleophilic addition, anionic nucleophiles arising from halomalonate ester/base, phosphonium ylids, organolithiums, Grignard reagents, organocoppers, phosphinite boranes/BuLi, aldehydes/ketones/alkoxides, sodium cyanide, and potassium fluorenide/fluorene have been widely used to functionalize fullerenes. The most classical reaction for the addition of anionic nucleophile to fullerene is the so-called Bingel reaction between fullerene and halomalonate ester under the assistance of a base [8]. In the Bingel reaction, the halocarbanion, initially formed by abstracting hydrogen from the methine group of halomalonate ester, attacks the fullerene cage to afford the corresponding fullerenyl anion, followed by intramolecular nucleophilic substitution with the elimination of X^- to produce methanofullerene (Scheme 4). Another typical example of this kind of addition is the reaction of C_{60} with potassium fluorenide/fluorene in the presence of a trace amount of air to yield the first tetrakisadduct of fullerene with a fulvene-type π-system [19], which can undergo further derivatization with 1-octynyllithium or sodium cyanide to produce pentakisadducts of fullerene after the reaction was quenched with CF_3CO_2H (Scheme 5).

Besides the anionic nucleophiles, certain neutral nucleophiles such as amines including primary and secondary amines are sufficiently nucleophilic to react with fullerenes. Wudl et al. were the first to report the chemistry between fullerene and aliphatic amines such as *n*-propylamine, *n*-dodecylamine, *tert*-butylamine, and morpholine. Aliphatic amines can add readily across fullerene to generate complex reaction mixtures composed of numerous structures and isomers. Each amination reaction of fullerene adds the elements R(R′) N and H across a π-bond on fullerene (Scheme 6). As for 1,2-diamines, their addition to fullerene can give 1,2-diamino fullerene derivatives as shown in Fig. 9 [20].

The addition of zwitterionic nucleophiles is the third type of nucleophilic addition to fullerenes. Zwitterionic nucleophiles are usually derived from the reaction between dimethyl acetylenedicarboxylate and isoquinolines/quinolines or 4-dimethylaminopyridine (DMAP) [21, 22]. The reaction mechanism for C_{60}, dimethyl acetylenedicarboxylate, and DMAP is illustrated in Scheme 7 and probably involves the addition of zwitterion intermediates to the double bonds of electrophilic fullerene, followed by attack of the fullerenyl anion to the ester group to release a methoxide anion. In the final step, the DMAP moiety was replaced with a methoxy group to produce fullerene-fused cyclopent-2-en-1-one derivative.

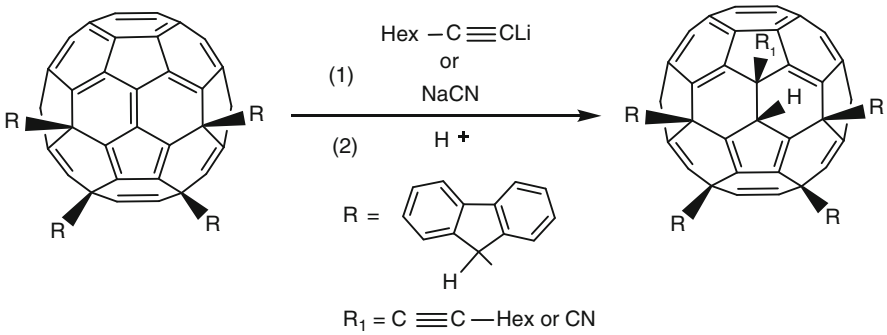

Scheme 5 Derivatization of tetrakis(9-fluorenyl)adduct of fullerene

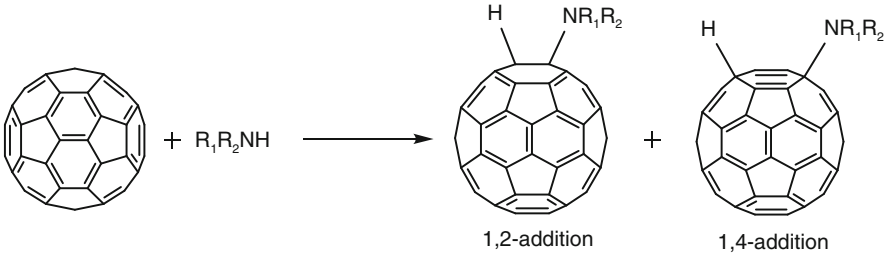

Scheme 6 Hydroamination of C_{60} with aliphatic amines

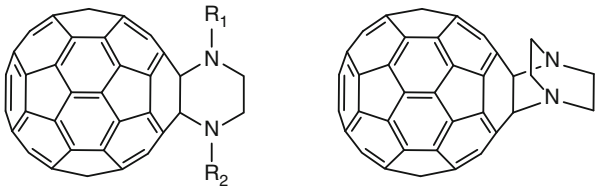

Fig. 9 1,2-Diamino derivatives from the addition of 1,2-diamines to C_{60}

Dimerization Reactions

Fullerenes can be joined together by pairs of bonds to give dimeric fullerenes [7]. Early efforts in this area were mainly directed toward the attainment of all-carbon fullerene dimers and polymers by coalescence reactions of fullerenes using physical methods such as laser irradiation. However, the coalescence products are too complex to be analyzed, the seemingly simple addition polymers have not been well characterized either. With the development of covalent fullerene chemistry, it has been possible to obtain properly all-carbon or modified fullerenes containing two fullerene cages. The main synthetic strategies for dimeric fullerenes include dimerization of either fullerene itself or a suitably functionalized fullerene and bifunctional cycloaddition reactions to fullerene.

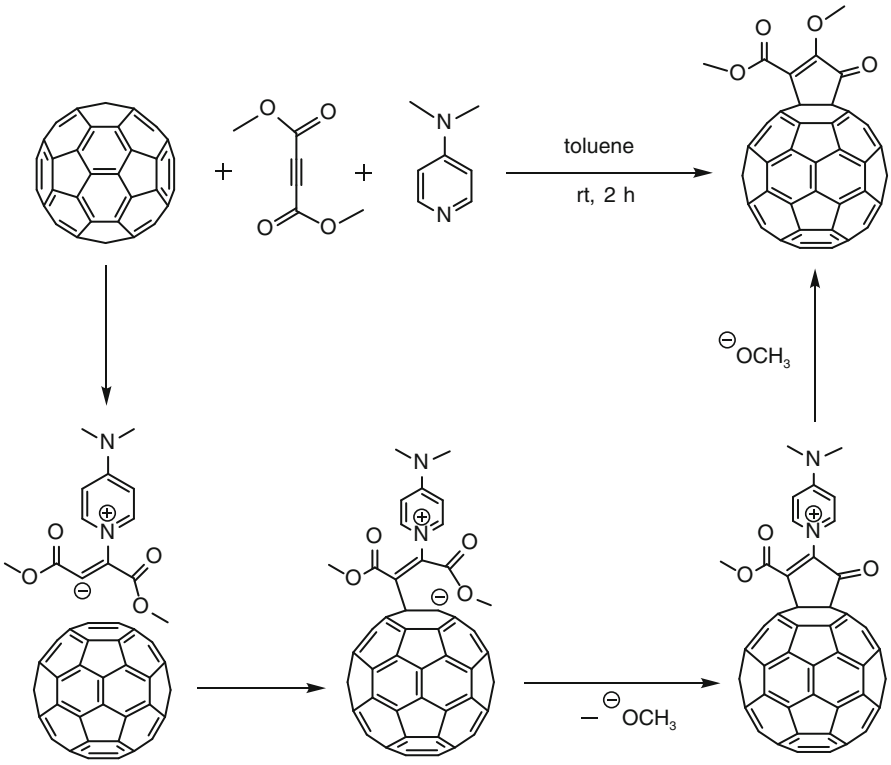

Scheme 7 Reaction pathway in the zwitterion-mediated fullerene functionalization

In general, dimeric fullerenes can be classified into three major categories based on the mode of linkage between two fullerene units (Fig. 10). The directly linked dimers by cyclic units among two fullerene cages are the first type of dimeric fullerenes, and they are usually prepared either by the thermolysis reactions of fullerene and its derivatives to afford $C_{120}O$ (Fig. 10a), $C_{121}H_2$ (Fig. 10b), $C_{120}O_2$ (Fig. 10d), $C_{120}OS$, and $C_{122}H_4$ or by the solid-state mechanochemical reactions using the technique of high-speed vibration milling (HSVM) to give C_{120} (Fig. 10c), C_{130}, $C_{120}SiPh_2$, and $C_{120}GePh_2$. The dumbbell-shaped C_{120} connected by a cyclobutane ring alone is the simplest fullerene dimer and has been first reported by Wang and co-workers in 1997 [23]. Besides the directly linked dimers via cyclic motifs, the singly-bonded dimers (Fig. 10e) with the general form of RC_n-C_nR ($n = 60, 70$) are another type of dimeric fullerenes, and are conventionally produced by the recombination of two $RC_n\cdot$ radicals, which can be generated in situ by the addition of R· to fullerene. Since the pioneering work of Krusic and co-workers, many experimental and theoretical studies on this class of dimers such as RC_{60}-$C_{60}R$ (R=H, halo, alkyl, fluoroalkyl) have been published. Furthermore, dimeric fullerenes with the acetylene spacers directly attached to the fullerene core have also been prepared either by homocoupling (Fig. 10g) of ethynylfullerenes or by reaction of

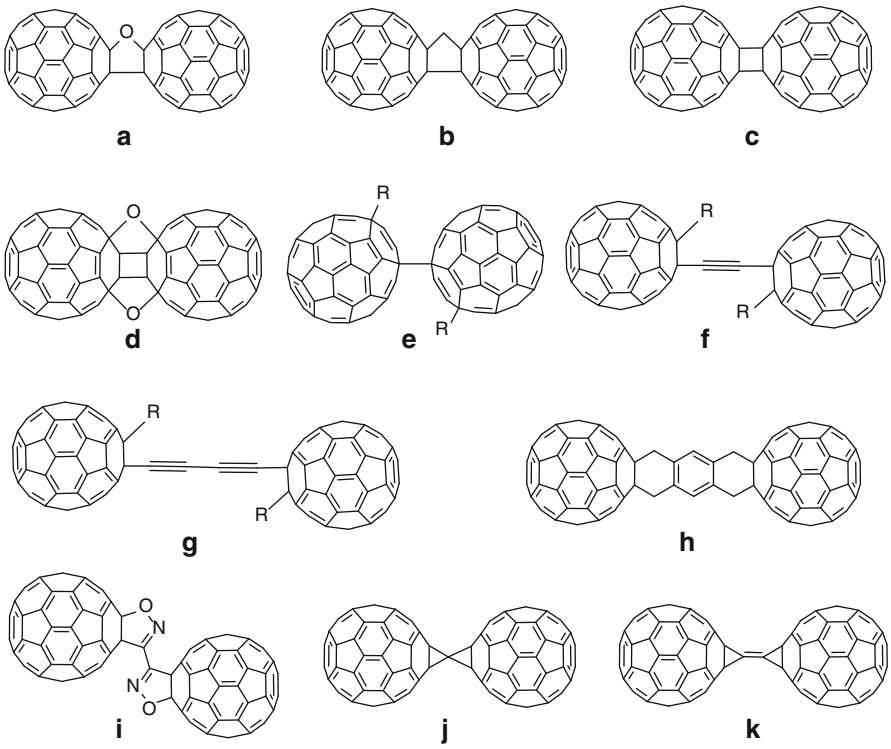

Fig. 10 Structures of different types of [60]fullerene dimers

dilithioacetylene with fullerene, followed by addition of alkyl iodide (Fig. 10f). Due to structural similarity, the singly-bonded dimers and the acetylene-linked dimers are grouped together. The bridged dimers through electroactive spacers (Fig. 10h, i) are the third type of dimeric fullerenes, and are mainly formed by the bifunctional cycloaddition reactions with two fullerene motifs. Fullerene dimers obtained in this way can find applications in many areas such as artificial photosynthesis and novel perovskite solar cells, and thus they have drawn wide attention among the scientific community. Besides the above three major fullerene dimers, other fullerene dimers such as C_{121} (Fig. 10j), C_{122} (Fig. 10k), C_{131}, and C_{141} can also be prepared either by a thermolysis reaction or by an energetic radiation-induced reaction.

Transition-Metal-Catalyzed/Promoted Reactions

Transition-metal-catalyzed/promoted reactions have been a fundamental tool in functionalizing fullerenes, and have attracted significant attention in recent years [17]. Diverse types of transition metal salts such as TBADT $[(n\text{–}Bu_4N)_4W_{10}O_{32}]$, $Mn(OAc)_3{\cdot}2H_2O$, $Fe(ClO_4)_3$, $Mg(ClO_4)_2$, $FeCl_3$, $Pd(OAc)_2$, $Pd(PPh_3)_4$, $PdCl_2(PPh_3)_2$, $PdCl_2[P(OPh)_3]_2$, $[Rh(cod)(MeCN)_2]BF_4$, $Cu(OAc)_2{\cdot}H_2O$, $Pb(OAc)_4$, $CoCl_2$dppe, and $AgCO_3$ have been employed as the promoters or catalysts

to functionalize fullerenes to produce a wide range of novel fullerene derivatives, which are difficult or impossible to obtain with traditional methods.

Orfanopoulos et al. first reported the use of TBADT as a radical initiator in fullerene chemistry [17]. In this study, the methyl C−H bond of substituted toluenes, anisoles, and thioanisole was activated by TBADT to generate *C*-centered radicals, which could be successfully trapped by fullerene to afford selectively the corresponding monofunctionalized fullerene adducts (Scheme 8). The use of TBADT in fullerenes provides a general and highly efficient strategy for C−C bond formation. In essence, different types of organic compounds such as toluenes, anisoles, thioanisole, aldehydes, ethers, thioethers, and alcohols have been used to react with fullerene to produce a series of scarce 1,2-dihydro[60]fullerene monoadducts (Scheme 8).

In 2003, Wang and co-workers first initiated the study on the radical reactions of fullerene promoted by $Mn(OAc)_3{\cdot}2H_2O$ [24]. Experimental results indicated that the in situ generated *C*-centered radicals by hydrogen-atom abstraction from various active methylene compounds with the aid of $Mn(OAc)_3{\cdot}2H_2O$ could react with C_{60}

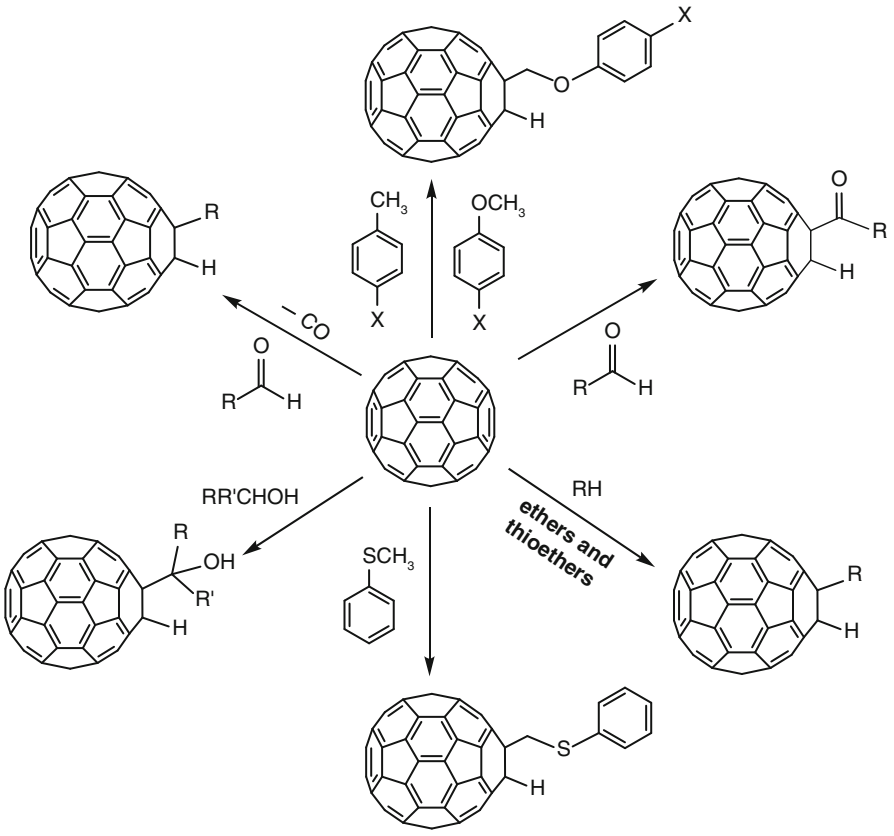

Scheme 8 Various products from the TBADT-mediated reactions of C_{60}

with short reaction times to give singly-bonded fullerene dimers or with longer reaction times to produce the corresponding 1,4-bisadducts (Scheme 9). Since then, a large variety of organic reactants including active methylene compounds, methyl ketone compounds, carboxylic acids/carboxylic anhydrides/malonic acids, aromatic aldehydes/arylmethanamines, β-enamino carbonyl compounds, diallylamines, aromatic aldehydes/diethylamine, 2-benzylmalonates, 2-arylmalonates, phosphorus compounds, and 2-arylcyanoacetates have been employed to react with C_{60} in the presence of $Mn(OAc)_3{\cdot}2H_2O$ to afford the singly-bonded fullerene dimers, 1,4- and 1,16-adducts of fullerene, methanofullerenes, fullerene-fused dihydrofurans, fullerene-fused lactones, fullerenyl esters, fullerene-fused-1-pyrrolines, fullerene-fused-2-pyrrolines, fullerene-fused pyrrolidines, fullerene-fused tetrahydronaphthalenes, fullerene-fused indanes, hydrophosphorylated fullerenes, and acetoxylated fullerenes. These products are summarized in Scheme 9.

Wang's group also reported the $Fe(ClO_4)_3$-mediated radical reaction of fullerene for the first time in 2008 [25]. In this study, the radical reaction of C_{60} with organic

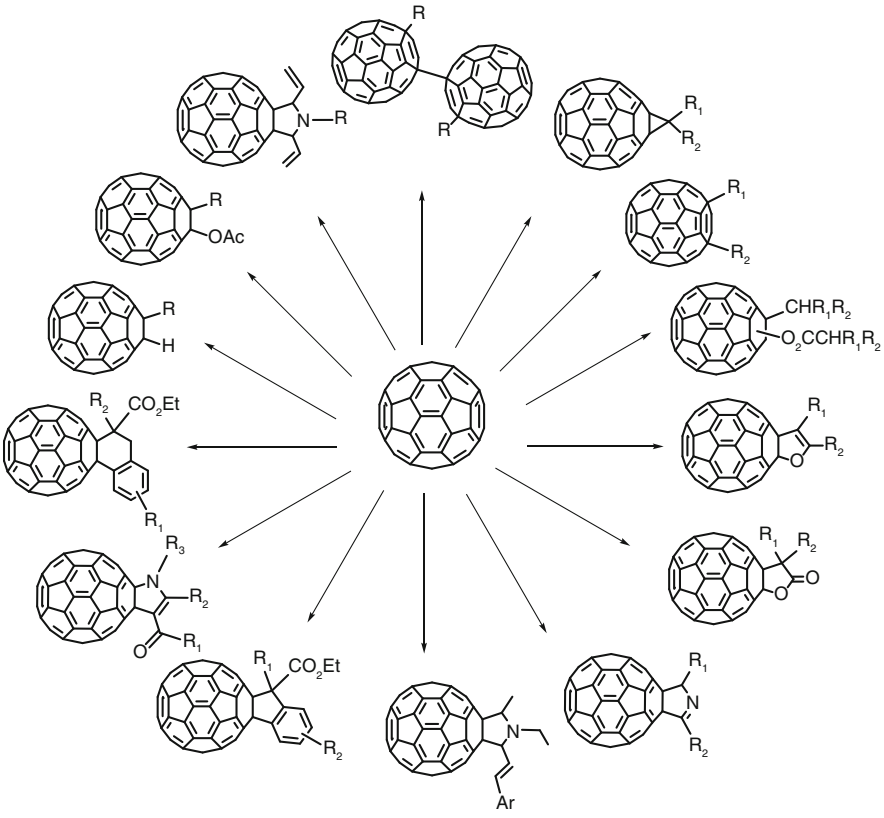

Scheme 9 Various products from the $Mn(OAc)_3{\cdot}2H_2O$-mediated reactions of C_{60}

nitriles promoted by $Fe(ClO_4)_3$ afforded a series of rare fullerooxazoles, which are very difficult to prepare by traditional methods. The direct melting of nitriles and Fe $(ClO_4)_3$ proved to be crucial for the successful realization of the reaction. After that, a large variety of novel fullerene derivatives including disubstituted fullerene-fused lactones, fullerene-fused hemiketals, fullerooxazoles, fullerene-fused 1,3-dioxolanes, fullerenyl boronic esters, oxazolidinofullerenes/thiazolidino-fullerenes, 1,2-fullerenols, fulleroxazolidines, fullerene-fused dioxanes/dioxepanes, and symmetrical 2,5-diaryl fulleropyrrolidines have been prepared via the Fe $(ClO_4)_3$-promoted reactions of C_{60} with malonate esters, β-keto esters, nitriles/primary amides, aldehydes/ketones, arylboronic acids, isocyanates/isothiocyanates, acid chlorides, *N*-sulfonyl aldimines, diols, and arylmethanamines, as shown in Scheme 10. In addition, $Mg(ClO_4)_2$ as promoter was also employed to functionalize fullerene by Li's group to afford a large number of rare fullerene derivatives such as fulleropyrrolidines and cyclopentafullerenes [26].

Palladium-catalyzed reactions of fullerene were first reported by Luh and co-workers in 1994. In this study, [3+2] cycloaddition of C_{60} with trimethylenemethane (TMM) generated in situ from $CH_2{=}C(CH_2OAc)CH_2SiMe_3$ under the assistance of $[Pd(PPh_3)_4]$ produced scarce TMM-fullerene adduct

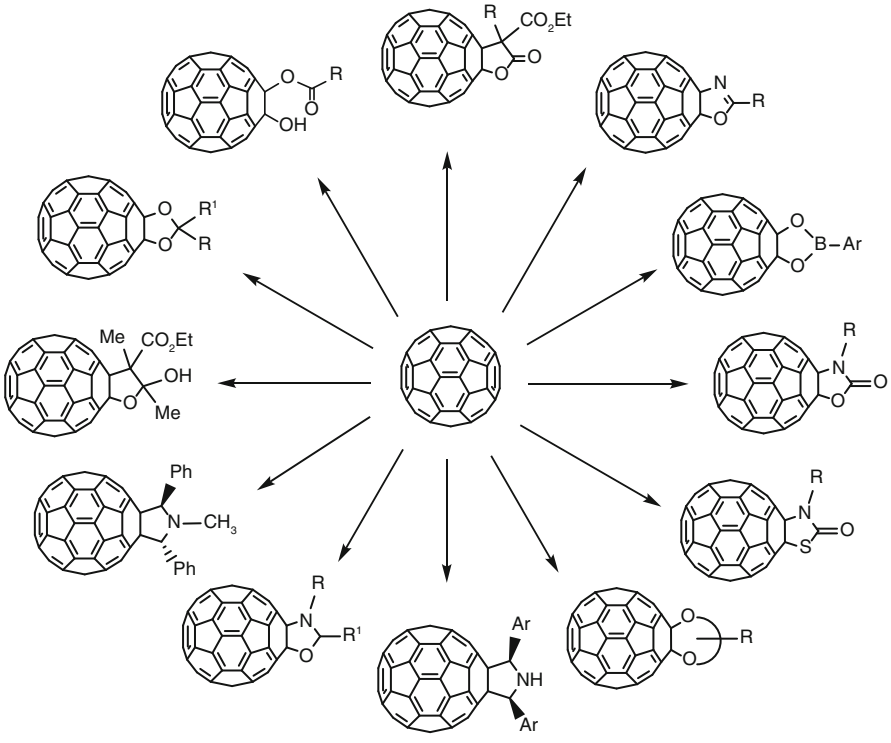

Scheme 10 $Fe(ClO_4)_3$-mediated reactions of C_{60} with various organic reagents

[27]. They also developed a novel $Pd(PPh_3)_4$-catalyzed [3+2] cycloaddition reaction of C_{60} with *cis*-$HOCH_2CH{=}CHCH_2OCO_2Et$ to afford the rare fullerotetrahydrofuran derivative [28]. Wang and Chuang achieved the synthesis of fulleroindolines, fulleroisoquinolinones, fullerosultones, fullerotetrahydroisoquinolines, fullerotetrahydrobenzooxepine, and fulleroazepines through the palladium-catalyzed heteroannulation of C_{60} with anilides, benzamides, arlysulfonic acids, *N*-benzyl sulfonamides, 2-phenylethyl alcohols/benzyl alcohols, and *N*-sulfonyl-2-aminobiaryls by the utilization of C-H activation/C-N cyclization strategy. Itami's group reported the Pd-catalyzed hydroarylation of C_{60} with arylboronic acids as well as the Pd-catalyzed tetraallylation of C_{60} with $CH{=}CHCH_2Cl$ or $CH{=}CHCH_2SnBu_3$. Moreover, they also described the Pd-catalyzed allylation and arylation of organo(hydro)fullerenes. Representative palladium-catalyzed products are summarized in Scheme 11.

Hashiguchi and Matsuo reported the polyarylation of C_{60} with aryl halides promoted by inexpensive and readily accessible $FeCl_3$ in 2011 [29]. They also described the facile one-pot syntheses of hydroxyfullerenyl esters via the reaction of C_{60} with carboxylic acids in the presence of $FeCl_3$ under mild conditions [30]. In 2013, they further disclosed the solution-phase synthesis of dumbbell-shaped C_{120} by $FeCl_3$-mediated dimerization of C_{60}, opening new possibilities for investigating

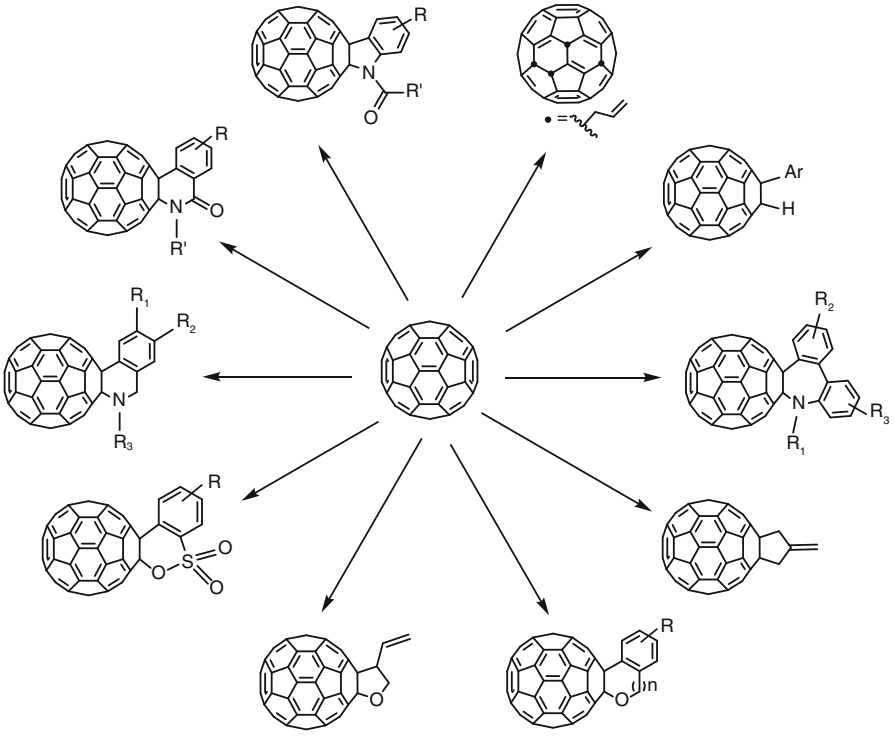

Scheme 11 Various products from Pd-catalyzed reactions of C_{60}

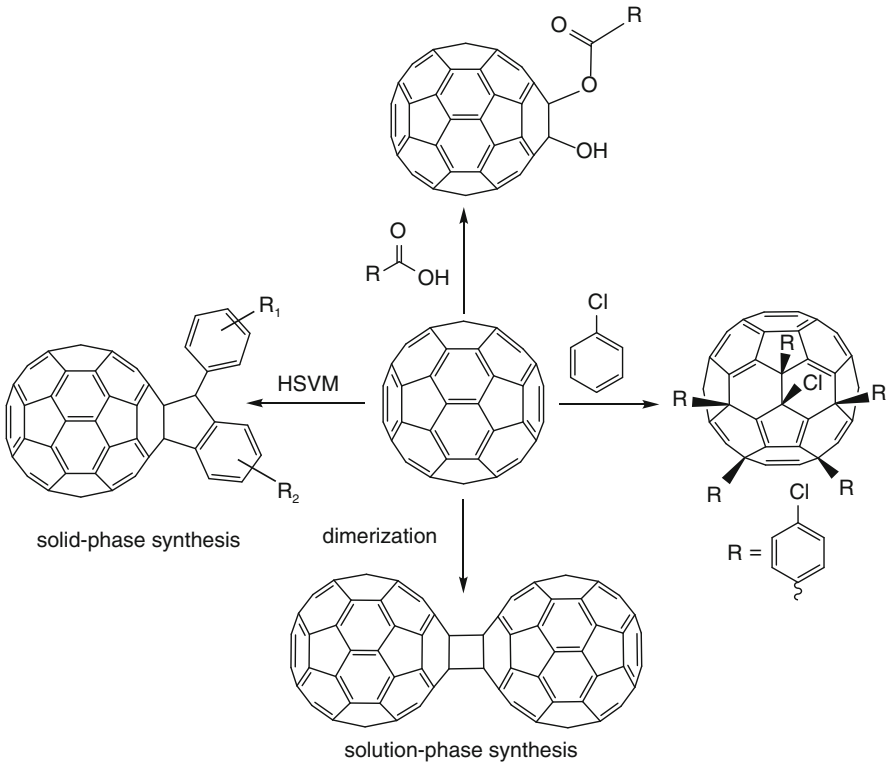

Scheme 12 Various products from $FeCl_3$-mediated reactions of C_{60}

solution-phase polymerization of fullerenes as well as for conducting applied research on C_{120} [31]. Wang's group achieved the $FeCl_3$-mediated cyclization of C_{60} with *N*-benzhydryl sulfonamides under HSVM conditions to generate fullerene-fused indane derivatives [32]. Other transition metal salts such as $[Rh(cod)(MeCN)_2]BF_4$, $Cu(OAc)_2$, $Pb(OAc)_4$, and $CoCl_2$dppe have also been employed in fullerene chemistry to give the hydroarylation/hydroalkenylation adducts of fullerene, methanofullerenes, fullerene-fused dihydrofurans, 1-fulleropyrrolines, fullerenyl esters, 1,2,3,4,5,6-hexaadduct of fullerene, ortho acid ester-type 1,3-dioxolanofullerenes, and hydroalkylation adducts of fullerene. These products from $FeCl_3$-mediated reactions of C_{60} are outlined in Scheme 12.

Aldehyde/Amine-Participated Reactions

Inexpensive and readily available aldehydes/amines can be utilized to functionalize fullerenes [16, 26, 33, 34]. Recently, the newly developed synthetic strategy based on aldehydes/amines has received increasing attention because a large variety of novel fullerene derivatives including 2,5-diaryl fulleropyrrolidines, 2-aryl-5-alkyl-fulleropyrrolidines, *N*-ethyl-2-arylvinyl-5-methyl fulleropyrrolidines, arylvinyl-substituted fulleropyrrolidines, *N*-alkyl-2,5-diaryl fulleropyrrolidines, *N*-alkyl-2,5-

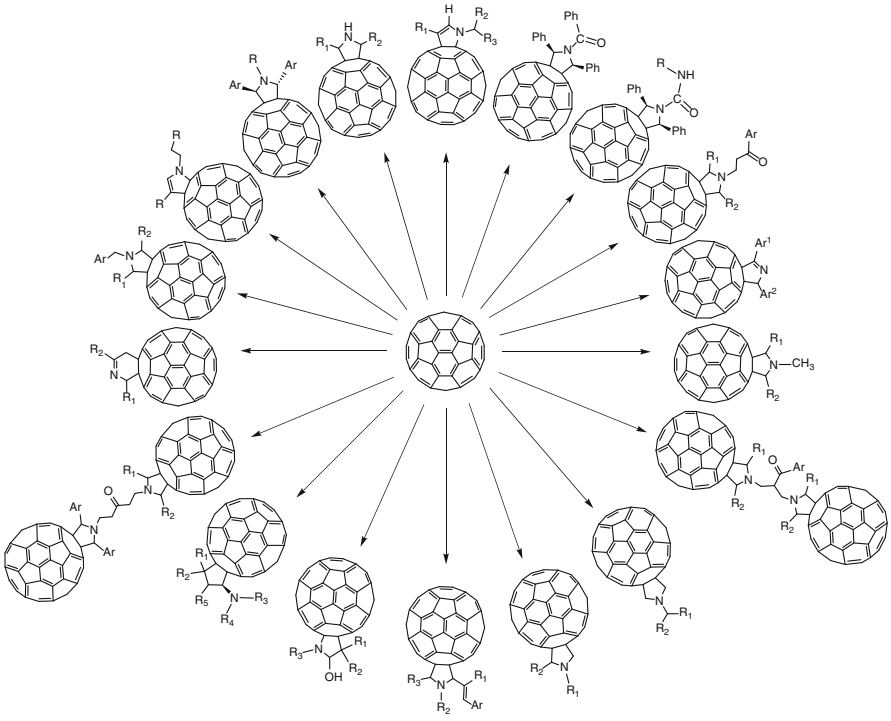

Scheme 13 Various products from the aldehyde/amine-participated reactions with C_{60}

unsubstituted/monosubstituted fulleropyrrolidines, tetrahydropyridinofullerenes, fullerotetrahydroquinolines, fulleropyrrolidin-2-ols, 1-fulleropyrrolines, 2-fulleropyrrolines, and amino-substituted cyclopentafullerenes, have been successfully prepared by using the above strategy. These products from Li's group are summarized in Scheme 13. Among these formed fullerene products, fulleropyrrolidines have been successfully applied to the study of perovskite solar cells (PSCs) as interlayer materials to improve the performance of PSCs [35].

Asymmetric Synthesis

Fullerene chirality has been recognized as an important issue in many fields such as medicinal chemistry, where the stereochemical configuration is a key factor. However, chemical modification of fullerenes often resulted in the generation of racemic organofullerenes. In the early days of synthesizing chiral fullerenes, chiral starting materials as well as racemic syntheses followed by chromatographic isolation and purification by high performance liquid chromatography (HPLC) with chiral column were usually used for the preparation of enantiomerically pure fullerene derivatives. However, the utilization of complex, expensive, and highly time-consuming HPLC or expensive chiral starting materials significantly restricts the synthesis and application of new chiral fullerene derivatives. A major breakthrough for the preparation

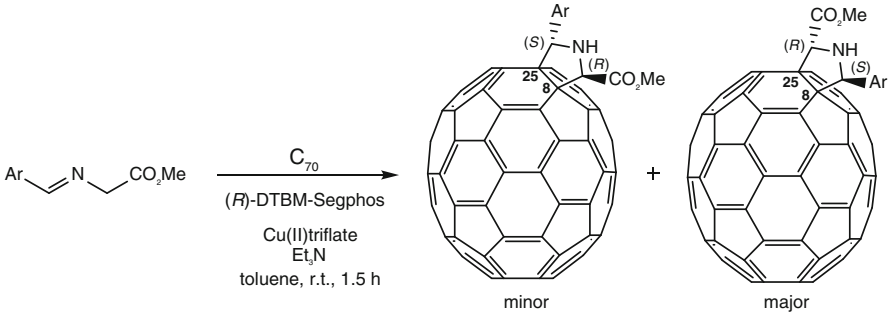

Scheme 14 *Trans*-selective cycloaddition of *N*-metalated azomethine ylides onto C_{70}

of enantiomerically pure fullerene derivatives has been achieved by Martín and co-workers through a straightforward procedure catalyzed by chiral metal catalyst from metal salts and chiral ligands to produce optically active C_{60}-fused pyrrolidine derivatives with stereochemical control [36]. This methodology by enantioselective cycloaddition of azomethine ylides to fullerene can be extended to higher fullerenes such as C_{70} (Scheme 14) and La@C_{72}($C_6H_3Cl_2$) to afford fullerene-fused pyrrolidine enantiomers with high ee values, which further demonstrates that the combination of suitable metal salts and chiral ligands is a general synthetic protocol for the preparation of chiral fullerenes. Furthermore, organocatalysis by the use of metal-free chiral catalysts is also an efficient strategy for the construction of chiral molecules. Martín et al. reported the first asymmetric organocatalytic synthesis onto fullerene to obtain novel chiral fullerene-fused cyclopentene derivatives in remarkably high enantiomeric excesses by chiral phosphine-catalyzed cycloaddition with racemic α-allenoates [37]. Single crystal X-ray crystallography plays a crucial role in unambiguous assignment of the configuration of the newly generated stereocenter.

Retro-Cycloaddition Reactions

Many kinds of organofullerenes are unstable under reductive, oxidative, or thermal conditions and tend to get rid of the functional addends from the fullerene sphere to give pristine fullerene. Such addition-retro-addition reaction has shown promising application in the protection/deprotection strategy for the purification and functionalization of fullerenes, and thus has become one of the most important reactions of fullerenes. Retro-cycloaddition reactions were commonly divided into three groups, namely, retro-Diels-Alder reaction [38], retro-cyclopropanation reaction [39], and retro-1,3-diploar cycloadditions [40]. Among these retro-cycloaddition reactions, the retro-Diels-Alder reactions were first discovered in heating the unstable products from cycloaddition of C_{60} with cyclopentadiene (Cp) (Fig. 11a) and 9,10-dimethylanthracene (Fig. 11b). The retro-cyclopropanation reactions were observed in the late 1990s by the electrochemical reduction or simply chemical reduction of methanofullerenes (Fig. 11c), which have been found to be of general applicability for different fullerenes and highly selective toward removal of cyclopropano addends in the presence of other types of addends (Fig. 11d), and thus open up the

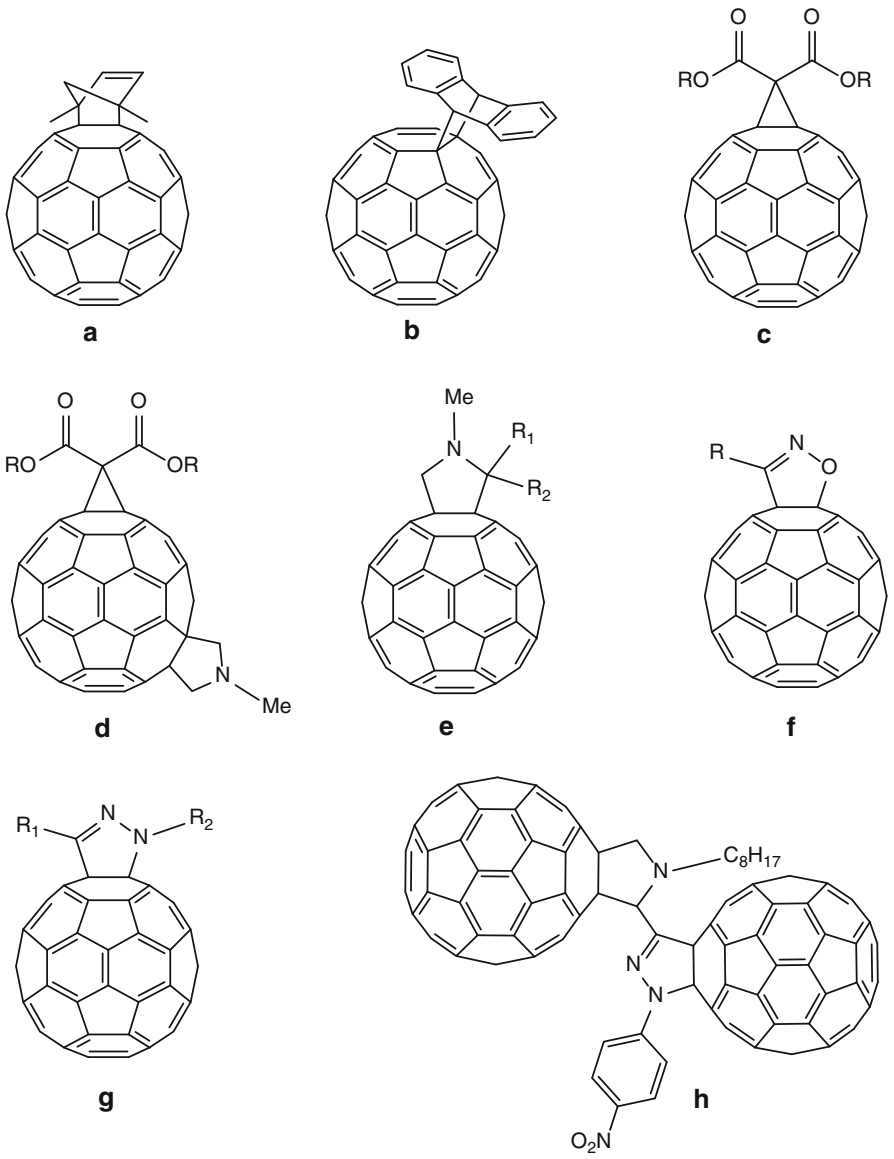

Fig. 11 Structures of different types of organofullerenes for retro-cycloaddition reactions

possibility of using bismethano addends as protecting and reversible directing groups in the regioselective multiple functionalization of fullerenes. The retro-1,3-diploar cycloadditions were realized by the decomposition of pyrrolidinofullerenes (Fig. 11e), isoxazolinofullerenes (Fig. 11f), and pyrazolinofullerenes (Fig. 11g) under a strong dipolarophile and/or a metal Lewis acid-assisted thermal conditions. Additional examples for quantitative retro-cycloaddition of pyrrolidinofullerenes

were also disclosed by electrochemical oxidation and microwave irradiation in ionic liquids. In addition, competitive retro-1,3-diploar cycloadditions in dimeric fullerenes connected through 2-pyrazolinopyrrolidino bridges (Fig. 11h) have also been studied by means of HPLC, mass spectrometry, and theoretical calculations. The results of these investigations indicate that the retro-cycloaddition reaction of pyrrolidinofullerenes is favored compared to that of 2-pyrazolinofullerenes, agreeing well with those findings predicted by theoretical calculations.

Mechanochemical Reactions

As mentioned earlier, the solubility of fullerenes in common organic solvents is usually low and thus restricts the exploration and development of their chemical reactions to some extent. This shortcoming has promoted scientists to find alternative methods for the functionalization of fullerenes. The solid-phase mechanochemical reactions of fullerenes in the absence of solvent have displayed advantages over their liquid-phase reactions because some reactions of fullerenes can only take place or undergo different reaction pathways to produce different products under solvent-free mechanochemical conditions when compared with the solution counterparts. Since the preparation of C_{60}–γ-cyclodextrin complex by classical milling in a planetary ball mill (Fritsch Pulverisette Type 701) was reported in 1994, the solvent-free mechanochemical reactions of fullerenes involving the formation of covalent bond have been extensively investigated by different groups (mainly from Wang and co-workers) under high-speed vibration milling (HSVM) conditions [41]. A large variety of fullerene derivatives such as C_{120}, He-encapsulated C_{120}, H_2/H_2O-encapsulated C_{120}, cross-dimer C_{130}, trimer C_{180}, and Si/Ge-bridged C_{60} dimers have been successfully prepared by the dimerization and trimerization reactions of C_{60} and C_{70}, Reformatsky-type reaction of C_{60}, Diels-Alder reactions of C_{60}, 1,3-dipolar cycloadditions of organic azides and diazo compounds with C_{60}, Prato reactions of C_{60} and C_{70}, arylations/alkylations of C_{60}, Bingel reactions of C_{60} and C_{70}, nucleophilic additions of C_{60}, radical reactions of C_{60}, and oxidation reactions of C_{60}. It should be noted that commercially available mixer mills such as Spex SamplePrep 5100 (2500 cycles per minute) can also be used to replace the homemade HSVM to promote mechanochemical reactions of fullerenes, making the mechanochemical protocol more practical and feasible.

Multiaddition Reactions

Compared with the easy availability of monoadducts, the synthesis of multiple adducts of fullerenes is still one of the most challenging tasks of exohedral fullerene chemistry due to the facile formation of difficult-to-isolate mixtures of regioisomers, which require the multiple and tedious chromatographic separation and purification by means of preparative HPLC. Theoretically, there are 8, 46, and 262 possible regioisomers to form when symmetrical addends are exclusively added to the [6] bonds of C_{60} to afford bisaddition, trisaddition, and tetrakisaddition, respectively. The eight patterns of bisaddition, named as *cis*-1, *cis*-2, *cis*-3, *equatorial*, *trans*-1, *trans*-2, *trans*-3, and *trans*-4, are indicated in Fig. 12, where the blue dots show the

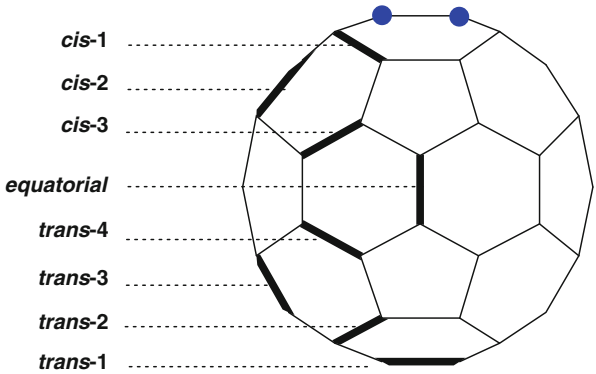

Fig. 12 Nomenclature system used to denote the sites of bisaddition to C_{60}

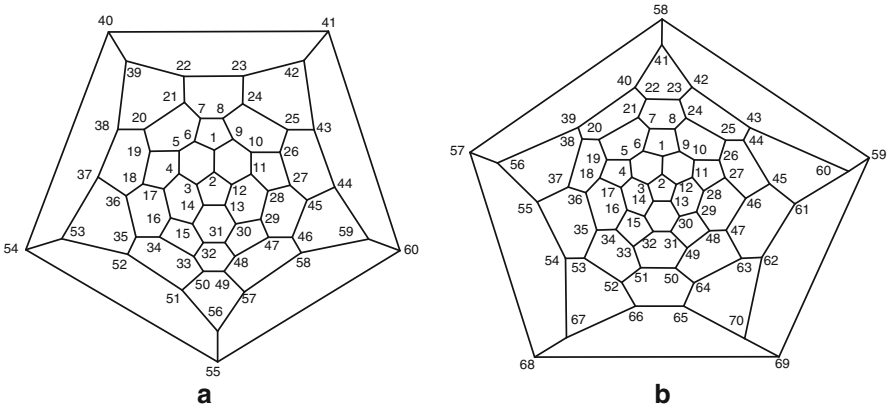

Fig. 13 Schlegel diagrams of (**a**) C_{60} and (**b**) C_{70}

first addition sites. It is impossible to clearly display where these addends are on the far side of the cage when many groups (addends) are attached to the fullerene molecule, and thus a two-dimensional diagram (Schlegel diagram) of fullerene is put forward. The Schlegel diagrams for C_{60} (a) and C_{70} (b) together with the numbering schemes that are employed to denote the positions on the cages are shown in Fig. 13.

Different types of synthetic protocols for the formation of multiple adducts of fullerenes have been developed over the past 30 years. These methods mainly include halogenation, hydrogenation, hydroxylation, radical additions (described in section titled "Radical Additions"), additions of organocopper reagents, additions of peroxides, additions of amines, and so on.

Halogenation

Halogenated fullerenes have been widely studied as versatile synthons in fullerene chemistry. Different sizes of halogens except for iodine are employed to

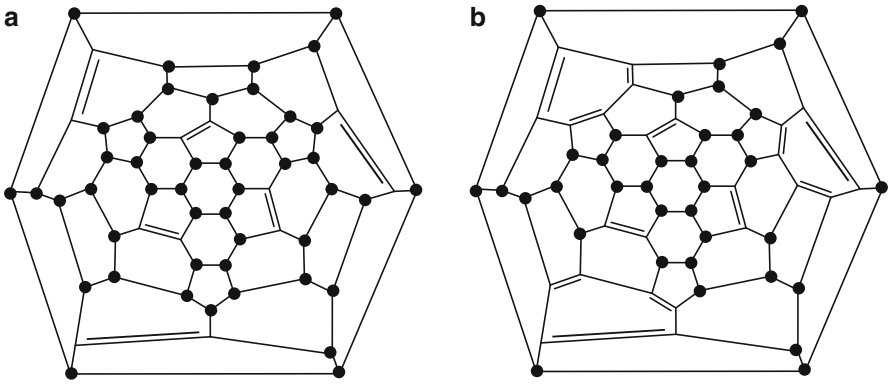

Fig. 14 Schlegel diagrams of (**a**) $C_{60}F_{48}$ and (**b**) $C_{60}F_{36}$ (● = F)

functionalize fullerenes under relatively mild conditions [42]. Fluorination of C_{60} by using different fluorinating agents such as NaF, KrF_2, MnF_3, CeF_4, $MPbF_6$ (M = Mg, Ca, Sr, Ba), Cs_2PbF_6, Cs_3PbF_7, MnF_3/KF, Cs_4CeF_8, $LiMnF_4$, $LiCoF_4$, K_2PtF_6, XeF_2, and F_2 gas produces a wide range of fluorofullerenes, from $C_{60}F_2$ to $C_{60}F_{48}$. $C_{60}F_{48}$ (Fig. 14a) can be prepared by fluorination of C_{60} with elemental fluorine in the presence of NaF. Alternatively, $C_{60}F_{48}$ (Fig. 14a) is formed in high yield via fluorination of C_{60} with a flow of F_2 gas diluted with argon. It is worth mentioning that $C_{60}F_{48}$ displays the highest fluorine content per fullerene molecule reported so far and thus has potential value as a highly concentrated source of fluorine that can be released on heating. $C_{60}F_{44}$ and $C_{60}F_{46}$ can be obtained as the most abundant species by fluorination C_{60} with KrF_2. $C_{60}F_{36}$ (Fig. 14b) can be achieved as the dominant product when binary (MnF_3 or CeF_4) or ternary fluorides ($MPbF_6$, M = Mg, Ca, Sr, Ba) are used as fluorinating agents. The less fluorinated compounds, $C_{60}F_{20}$, $C_{60}F_{18}$, $C_{60}F_{16}$, $C_{60}F_8$, and $C_{60}F_2$, can be obtained with low yields or as admixtures to the main fluorination product by using MnF_3/KF, Cs_2PbF_6, Cs_4CeF_8, $LiMnF_4$, $LiCoF_4$, K_2PtF_6, or Cs_3PbF_7. By contrast, fluorination of C_{70} by elemental fluorine methods leads to the formation of complex mixtures of $C_{70}F_n$ compounds with n ranging from 42 to 56, whereas the reaction with metal fluorides results in the generation of $C_{70}F_{34-44}$ with $C_{70}F_{36}$, $C_{70}F_{38}$, and $C_{70}F_{40}$ as the most abundant species. Two individual isomers of $C_{70}F_{38}$ have been isolated from $C_{70}F_n$ mixtures chromatographically.

Due to the larger size of Cl and Br atoms as compared with that of the F atom, addition patterns of fullerene chlorides and bromides drastically differ from those of fluorides [43]. Bromofullerenes such as $C_{60}Br_6$, $C_{60}Br_8$, $C_{60}Br_{24}$ $C_{70}Br_{10}$, and $C_{70}Br_8$ can be easily prepared either by bromination of fullerenes dissolved in organic solvents or by treatment with neat bromine. Fig. 15 shows the corresponding Schlegel diagrams of $C_{60}Br_8$ and $C_{60}Br_{24}$.

Chlorination of C_{60} with different chlorinating agents affords $C_{60}Cl_n$ products with bulk compositions ranging from $C_{60}Cl_6$ to $C_{60}Cl_{40}$. The most notable $C_{60}Cl_6$ (Fig. 16a) can be prepared by reaction of C_{60} with ICl in benzene. $C_{60}Cl_{24}$ can be

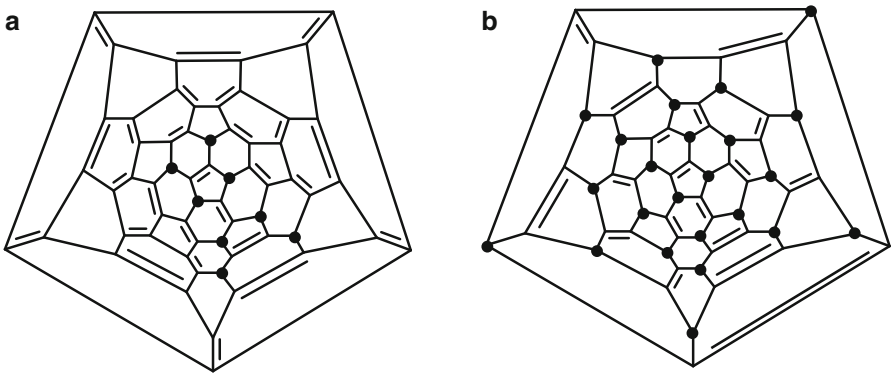

Fig. 15 Schlegel diagrams of (**a**) $C_{60}Br_8$ and (**b**) $C_{60}Br_{24}$ (● = Br)

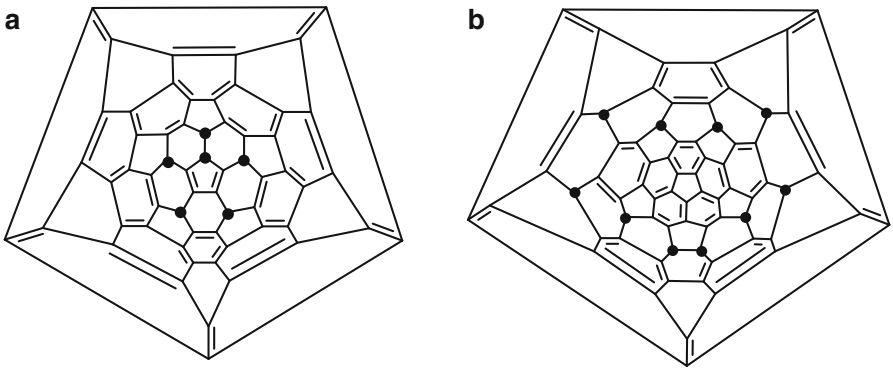

Fig. 16 Schlegel diagrams of (**a**) $C_{60}Cl_6$ and (**b**) $C_{70}Cl_{10}$ (● = Cl)

obtained by UV irradiation of a solution of C_{60} in chlorine-saturated CCl_4. Chlorofullerenes with compositions ranging from $C_{60}Cl_{12}$ to $C_{60}Cl_{32}$ can be achieved by treatment of C_{60} with liquid chlorine under UV irradiation at room temperature. As for C_{70}, chlorinating agents such as ICl, $TiCl_4$, $SnCl_4$, and $AsCl_3$ are used to produce $C_{70}Cl_{10}$ (Fig. 16b), $C_{70}Cl_{16}$, and $C_{70}Cl_{28}$

In addition to the pure fullerene halides, some halogenotrimethylfluorofullerenes [44], such as $C_{60}F_{17}(CF_3)$ (Fig. 17), $C_{60}F_n(CF_3)_m$, and $C_{60}(CF_3)_{12}Cl_{12}$, have also been prepared by the fluorination of C_{60} with K_2PtF_6, the trifluoromethylation of $C_{60}F_{18}$ with CF_3I, and the chlorination of $C_{60}(CF_3)_{12}$ with $SbCl_5$, respectively.

Halofullerenes are valuable precursors for preparation of novel fullerene derivatives by the replacement of halogen atoms by appropriate organic groups. Chlorofullerene $C_{60}Cl_6$ is one of the most studied halofullerenes due to its easy availability, molecular symmetry, and low number of halogen addends, which allows for selective substitution by various nucleophiles to give a variety of fullerene derivatives. For example, the reactions of $C_{60}Cl_6$ with *C*- and *O*-nucleophiles such

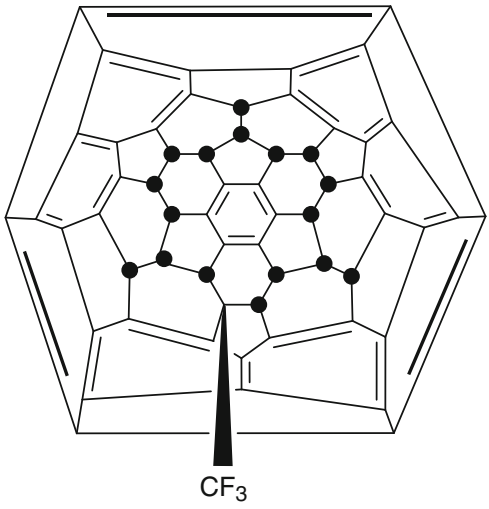

Fig. 17 Schlegel diagram of $C_{60}F_{17}(CF_3)$ (● = F)

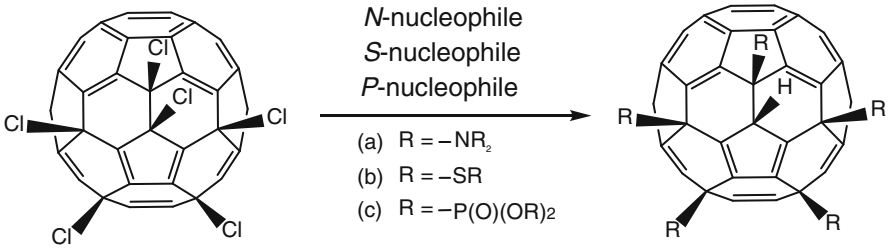

Scheme 15 Representative products from derivatization of $C_{60}Cl_6$ with various nucleophiles

as ArH/$FeCl_3$ (Friedel-Crafts reaction), $H_2C{=}CH\text{-}CH_2TMS/TiCl_4$, MeLi, ROH/NaOR, and ROH yielded $C_{60}Ar_5Cl$, $C_{60}Ar_2$, $C_{60}Ar_4$, $C_{60}(CH_2CH{=}CH_2)_6$, $C_{60}(CH_2CH{=}CH_2)_5Cl$, $C_{60}Me_6$, $C_{60}Me_5Cl$, $C_{60}Me_5O_2OH$, $C_{60}Me_5OOH$, $C_{60}(OR)_5Cl$, and 1,4-$C_{60}(OR)_2$. $C_{60}Cl_6$ can also react with organic cyanide to produce an ionic salt comprising the fullerene anion $[C_{60}(CN)_5]^-$. This anion showed unprecedented stability toward water, organic/inorganic acids, and various electrophiles in air and in solutions, which opens wide opportunities for the design of various air-stable salts that may have promising applications in the field of material science [45]. In addition, the reaction of $C_{60}Cl_6$ with *N*-substituted piperazines afforded complex mixtures of di-, tetra-, and hexaaminofullerenes as the final products by the substitution of chlorine atoms in $C_{60}Cl_6$ by amine groups together with partial elimination of addends from the fullerene cage, while the reaction of $C_{60}Cl_6$ with amine or amino acid ester salts at room temperature yielded penta-aminofullerenes $C_{60}[NHR]_5X$ (X = H, Cl) (Scheme 15a) with high selectivity probably attributed to the use of less reactive salts of amines (hydrochlorides or acetates) instead of bare amines. Polyaminofullerenes are found to be readily soluble

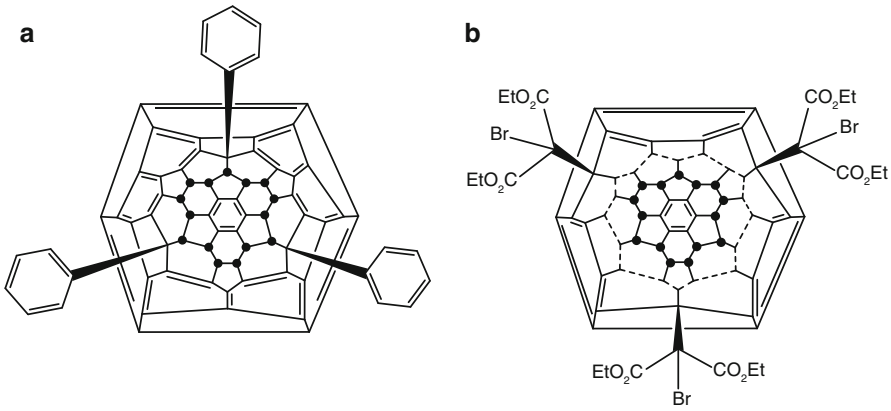

Fig. 18 Schlegel diagrams of (**a**) $C_{60}F_{15}Ph_3$ and (**b**) $C_{60}F_{15}[CBr(CO_2Et)_2]_3$ (● = F)

in aqueous acids and display strong antiviral and antibacterial activity. Furthermore, the reactions of $C_{60}Cl_6$ with thiols or trialkyl phosphates have also been shown to produce $C_{60}[SR]_5H$ (Scheme 15b) and $C_{60}[P(O)(OR)_2]_5H$ (Scheme 15c) in high yields, respectively.

Likewise, benzene can readily undergo electrophilic substitution by $C_{70}Cl_{10}$ in the presence of $FeCl_3$ to give both yellow $C_{70}Ph_{10}$ and orange-red $C_{70}Ph_8$, yet $C_{60}F_{18}$ under a similar reaction conditions is converted to $C_{60}F_{15}Ph_3$ (Fig. 18a). Intriguingly, $C_{60}F_{18}$ can be partially replaced by the $CBr(CO_2Et)_2$ moieties to produce the only known *all-trans* annulene $C_{60}F_{15}[CBr(CO_2Et)_2]_3$ [46], which contains 18π electrons in the annulene chain, giving additional (aromatic) stability (Fig. 18b). The dotted line in Fig. 18b denotes the 18 π *trans*-annulene chain.

Hydrogenation

Hydrofullerenes are the simplest covalent derivatives of fullerenes and their synthesis have been one of the earliest chemical reactions of fullerenes probably due to the potential applications of hydrofullerenes as batteries, as catalysts, or as media for storage of dihydrogen. The first reported hydrofullerene, namely, $C_{60}H_{36}$, was formed by the Birch reduction of C_{60} in 1990 [47]. Subsequent work with C_{60}, and to a lesser extent with C_{70}, has resulted in the generation of many other hydrofullerenes, including $C_{60}H_2$, $C_{70}H_2$, $C_{60}H_4$, $C_{70}H_4$, $C_{60}H_6$, $C_{70}H_8$, $C_{70}H_{10}$, and $C_{60}H_{18}$. Established routes to hydrofullerenes include Birch reduction, hydroboration, hydrozirconation, Zn(Cu) reduction, Zn/HCl reduction, catalytic hydrogenation with ruthenium on carbon, rhodium on alumina, palladium and palladium on carbon, solution-phase and solid-state hydrogenation, hydrogen radical-induced hydrogenation, transfer hydrogenation, electrochemical reduction, chemical reduction with diimide, chromous acetate, anhydrous hydrazine, and photoinduced electron transfer. It should be noted that purification of hydrofullerenes is often difficult and may require extensive use of preparative HPLC. Figure 19 shows the Schlegel diagrams for $C_{60}H_{18}$ and $C_{60}H_{36}$.

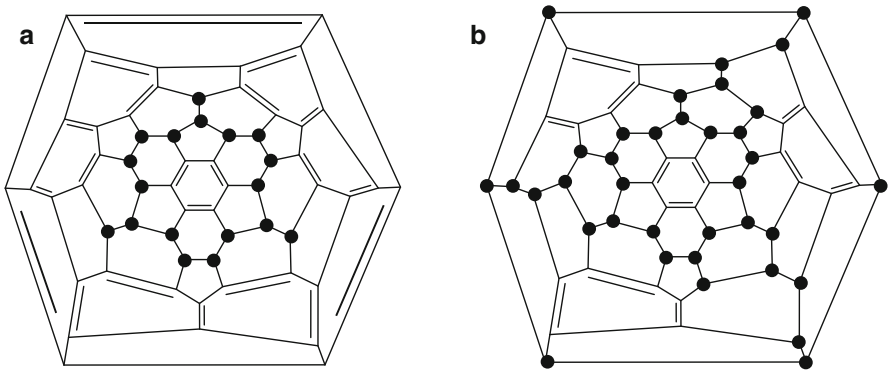

Fig. 19 Schlegel diagrams of (**a**) $C_{60}H_{18}$ and (**b**) $C_{60}H_{36}$ (● = H)

Hydroxylation

Hydroxyfullerenes, that is, fullerenols, are the fullerene derivatives with hydroxy group(s) attached to the fullerene cage, and are among the best studied fullerene derivatives. Fullerenols have shown a variety of biological functions as a neuroprotective agent, an antiproliferative agent, an antioxidant, and a glutamate receptor antagonist due to their excellent radical scavenging ability and low toxicity. Also, fullerenols are good visible-light sensitizers. For instance, degradation of pollutants catalyzed by fullerenol-modified titania can be easily achieved by photo-oxidative conversion. Furthermore, fullerenols can serve as versatile precursors for further functionalization. Polyhydroxylated fullerenes $C_{60}(OH)_n$ usually contain at least six hydroxyl groups and are prepared mainly through the use of aqueous HNO_3/H_2SO_4, nitronium tetrafluoroborate, fuming sulfuric acid, and aqueous NaOH solution. $C_{60}(OH)_n$ can also be synthesized through further hydroxylation of $C_{60}(OH)_{12}$ to introduce an estimated 36–40 hydroxy groups to fullerene skeleton. However, almost all polyhydroxylated fullerenols prepared so far are complicated mixtures of different isomers. It is impossible to isolate isomerically pure fullerenols even after exhaustive purification procedures, with a known exception where the first isomerically pure multihydroxylated fullerenol $C_{60}(OH)_8$ (Fig. 20a) was successfully prepared by Gan and co-workers through multi-step reactions involving fullerene mixed peroxides [48]. It should be noted that the synthesis of isomerically pure fullerenols with multiple different addends was also reported either by the transformation of halogenated fullerenes and fullerene mixed peroxides or by the reaction of fullerenes with organolithium reagents. For example, the fullerenol $C_{70}Ph_9OH$ was obtained as a minor product from the reaction of $C_{70}Cl_{10}$ with benzene/$FeC1_3$, which is the first fullerene with a single hydroxy group attached to the cage. Also, hydroxyepoxides $C_{60}Me_5O_2OH$ (Fig. 20b), $C_{60}Me_5OOH$, and $C_{60}Me_4PhO_2OH$ were formed by the reaction of $C_{60}Cl_6$ with methyllithium followed by hydrolysis. Moreover, the nitratofullerenol $C_{60}(OH)(ONO_2)(OO^tBu)_4$ was prepared in 58% yield by the concentrated nitric acid-mediated transformation of fullerene mixed peroxides $C_{60}(O)(OO^tBu)_4$. It is worth mentioning that the first methylated

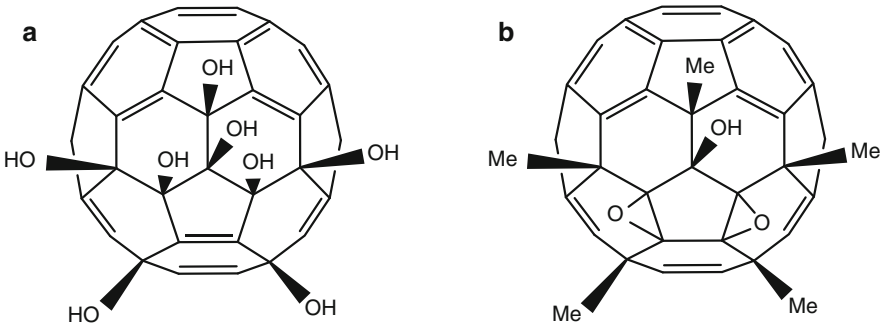

Fig. 20 Structures of (**a**) $C_{60}(OH)_8$ and (**b**) $C_{60}Me_5O_2OH$

Fig. 21 Structure of $C_{60}R_5H$

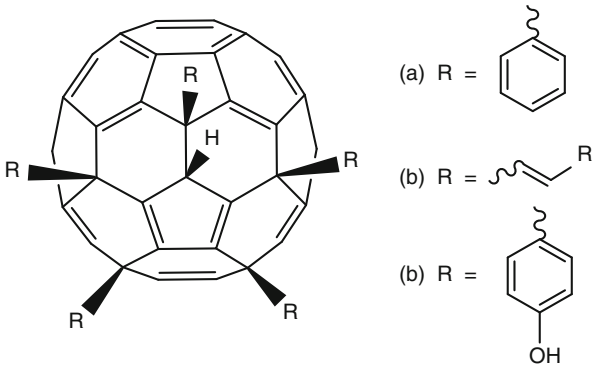

fullerenol $C_{60}Me_5O_2OH$ (Fig. 20b) can also be formed by the direct reaction between C_{60} and methyllithium.

Additions of Organocopper Reagents

Nucleophilic addition of organometallics such as alkyl, allyl, organolithium, and Grignard reagents to fullerenes usually stopped at the monoaddition stage to give the monoaddition products. To achieve the multiaddition of organometallic reagents to fullerenes, Nakamura and co-workers studied the reaction of C_{60} with a phenylcopper reagent derived from PhMgBr and $CuBr{\cdot}SMe_2$ in 1996, and found that 1,4,11,15,30-pentaaryl-2-hydro[60]fullerene $C_{60}Ph_5H$ (Fig. 21a) was unexpectedly formed in a quantitative yield with complete regioselectivity. Other organic groups such as vinyl (Fig. 21b), hydroxyphenyl (Fig. 21c), mercaptophenyl, methyl, silylmethyl, ester, 2-tetrahydrofuranyl, and carboxyl groups can also be introduced in excellent yields by the above synthetic strategy [49]. The penta-addition of organic groups can result in the generation of a cyclopentadiene by the introduction of five organic groups around one pentagon of the fullerene molecule. The cyclopentadienyl moiety can be used as a cyclopentadiene ligand for metal complexation to

produce a variety of pentahapto metal complexes such as sandwich type metal-η^5-fullerene complexes. When the above-mentioned reaction was applied to C_{70}, a tri-addition product instead of the penta-addition product was selectively produced. It should be noted that octa- and deca-additions of fullerene can also achieve by the addition of excess pyridine. For example, the organocopper reagent modified by pyridine can add to C_{60} 8 or 10 times to obtain $C_{60}Ar_8H_2$ and $C_{60}Ar_{10}H_2$. The penta-addition reactions of organocopper reagents with fullerenes as well as related multiple addition reactions have developed into a wide range of synthetic reactions with wide applications.

Additions of Peroxides

The multiple addition reaction of fullerene with *tert*-butyl peroxy radical from TBHP to afford a series of stable fullerene mixed peroxides was first reported by Gan and co-workers in 2002 [50]. For C_{60}, low concentration of *tert*-butyl peroxy radical, long reaction time and irradiation of visible light favor the formation of epoxides with the general form of $C_{60}(O)_m(OO^tBu)_n$, while high concentration of *tert*-butyl peroxy radical favors the generation of homo-peroxo adducts. For C_{70}, only the homo-peroxo adducts are formed with the general form of $C_{70}(OO^tBu)_n$ with n varies from 2 to 10. Due to its D_{5h} symmetry, C_{70} gave more isomers including four isomers for bis-adduct, two isomers for tetrakis- and hexakis-adducts, and one isomer for octakis- and decakis-adducts. Catalysis with metal salts may also be used to generate the *tert*-butyl peroxy radical. The reaction between C_{60} and TBHP in the presence of $Ru(PPh_3)_3Cl_2$ or $FeCl_3$ afforded fullerene mixed peroxide $C_{60}(O)(OO^tBu)_4$ (Fig. 22a), yet the reaction between C_{60} and TBHP in the presence of $Pb(OAc)_4$ or $(NH_4)_2Ce(NO_3)_6$ (CAN) gave hexakis-adduct $C_{60}(OO^tBu)_6$. Formation of fullerene peroxides follows the stepwise radical addition mechanism. Para-addition on the hexagon is the dominant pattern due to a strong effect of the *tert*-butyl peroxy group already attached to the fullerene cage on the next *tert*-butyl peroxy group as a

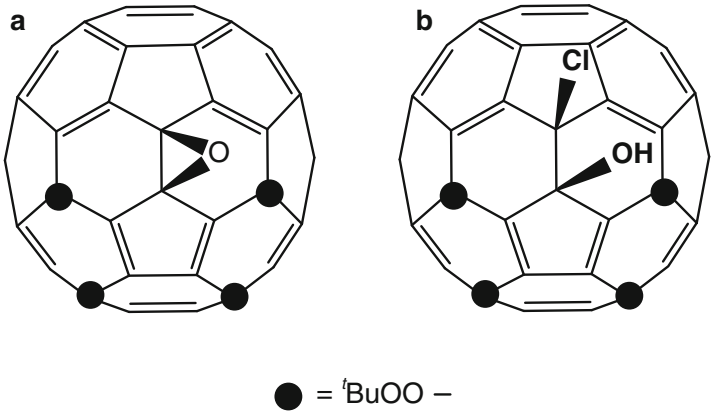

Fig. 22 Structures of (**a**) $C_{60}(O)(OO^tBu)_4$ and (**b**) $C_{60}(OH)(Cl)(OO^tBu)_4$

result of steric hindrance and/or the resulting radical stability. Both the epoxy and *tert*-butyl peroxy groups of fullerene mixed peroxides may serve as excellent oxygen sources for the formation of hydroxyl and epoxy groups. For example, $FeCl_3$-induced ring-opening of epoxy moiety in $C_{60}(O)(OO^tBu)_4$ gave the vicinal hydroxyl chloride $C_{60}(OH)(Cl)(OO^tBu)_4$ (Fig. 22b), yet the addition of sodium methoxide to 1,4-bis-adduct $C_{60}(OO^tBu)_2$ resulted in the formation of the epoxy $C_{60}(O)(OMe)(OO^tBu)$ with the loss of a *tert*-butoxide.

Additions of Amines

Additions of primary and secondary aliphatic amines to fullerene have been investigated by different research groups. In the case of primary aliphatic amines, there are very few reports on their regioselective addition to fullerene because complex product mixtures are generally produced, which have not been thoroughly characterized so far. On the other hand, secondary aliphatic amines appear to prefer a clustered 1,4-addition pattern, especially in the presence of oxygen. Hirsch and co-workers in 1995 first noted that the reaction between excess secondary amine and C_{60} could produce several well-defined adducts such as tetramorpholino[60]fullerene epoxide (Fig. 23a) when the reaction was carried out in the presence of oxygen [51]. Unfortunately, the tetramorpholino[60]fullerene epoxide was obtained in only 9% yield. Then Nakamura et al. optimized the reaction conditions for the formation of tetraamino[60]fullerene epoxide. They found that the reaction of C_{60} with secondary aliphatic amines under photochemical aerobic conditions could afford tetraaminofullerene epoxides $C_{60}(O)(NR_1R_2)_4$ in a yield of up to 98% (Fig. 23b) [52]. They also investigated the reaction in 20% v/v dimethyl sulfoxide in chlorobenzene under an atmospheric pressure of molecular oxygen and found that this new synthesis of tetraaminofullerene expoxide can be carried out by a simple procedure on a multigram scale. In addition, tetraaminofullerene epoxide $C_{60}(O)(MeNCH_2COOMe)_4$ has been reported by Gan et al. via the addition of iodine to a mixture of sarcosine methyl ester and C_{60}.

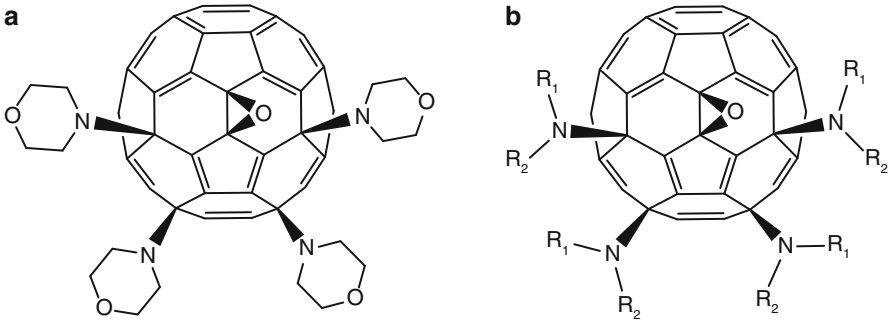

Fig. 23 Structures of (**a**) tetramorpholinofullerene epoxide (**b**) tetraaminofullerene epoxides

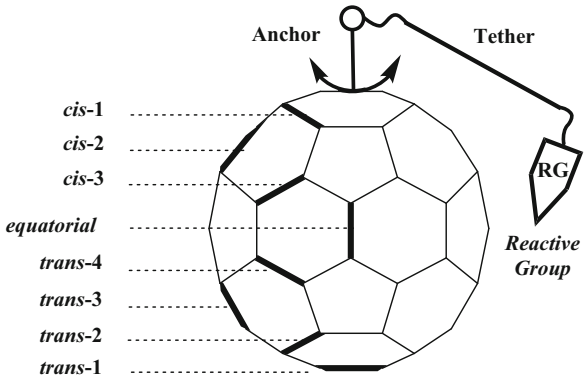

Fig. 24 Illustration of the concept of tether-directed remote functionalization of C_{60}

Tether-Directed Remote Functionalization

The defined spatial arrangement of functional addends in oligoadducts of fullerenes has proved to be very crucial for the design of compounds with interesting materials, biological, and supramolecular properties. Furthermore, the degree and pattern of multiaddition of fullerenes allow for fine tuning of the electronic and topologic properties of fullerenes. Accordingly, the region- and diastereoselective synthesis of multiadducts of fullerenes is the most important challenge in the poly-functionalization of fullerenes. In order to achieve region and stereocontrol over multiadditions to fullerenes, Diederich and co-workers first applied the tether-directed remote functionalization to the carbon cages of fullerenes in 1994, which involves the attachment of an anchor carrying a reactive group at the end of a tether to fullerenes (Fig. 24) [53]. Conformational preferences of the spacer and steric constraints ideally allow the reactive group to attack only a single and specific position within the molecular conjugate. In some cases, it is possible to remove the tether after the achievement of a selective multiaddition, and is therefore termed a template, which has been applied to provide access to a great diversity of three-dimensionally functionalized fullerene building blocks. As of today, the tether-directed remote functionalization has become the most generally applicable protocol for selective multiadditions to fullerenes.

Skeletal Modification

Skeletal modification of fullerenes primarily results in the generation of open-cage fullerene and heterofullerene derivatives.

Formation of Open-Cage Fullerenes

Open-cage fullerenes generally refer to fullerene derivatives that have suffered more than one σ-bond scission and have displayed serious π system disturbance due to the consecutive cleavage of σ- and π-carbon-carbon bonds on the fullerene cage. Open-

cage fullerenes allow small atoms or molecules to pass through their openings and be placed inside the cavity, and thus have received wide attention among the scientific community over the past decades. In 1995, a breakthrough in the controlled chemical opening of the fullerene cage was achieved by Wudl and co-workers, showing that self-photooxygenation of *N*-methoxyethoxymethyl (MEM)-substituted [5,6]-azafulleroid (Fig. 25a) produced *N*-MEM-ketolactam (Fig. 25b) as an open-cage fullerene in 65% yield [54]. Since then, self-photooxygenation reaction of fullerenes has become a very important method for the construction of open-cage fullerenes. Apart from self-photooxygenation, ring openings on the fullerene shell have also been created by Chiang and Taylor via oxidative cleavage of one or more fullerene carbon-carbon bonds. In combination with self-photooxygenative cleavage, intramolecular [4+4] cycloadditions followed by retro [2+2+2] rearrangement reactions on the fullerene shell are one of the most effective approaches to the preparation of open-cage fullerene derivatives that bear considerably large openings. Furthermore, an entirely different method for the synthesis of open-cage fullerenes by peroxide-mediated chemical transformations is also developed by Gan and co-workers. On the other hand, ring expansion reactions of holey fullerene adducts can be achieved by the addition of aromatic hydrazines, hydrazones, or 1,2-phenylenediamines to open-cage diketone fullerene derivatives as well as sulfur or selenium atom insertion into the rim of the orifice of open-cage fullerenes bearing an α,β-unsaturated carbonyl moiety. It should be noted that the examples of open-cage derivatives from C_{70} are quite limited due to its low symmetry. The first cage-opened fullerene for C_{70} was reported in 1995 via spontaneous oxidation of $C_{70}Ph_8$ to afford a bislactone derivative, namely, $C_{70}Ph_8O_4$, bearing an 11-membered-ring orifice.

The open-cage fullerenes can be used to incorporate small atoms or molecules into their cages. The first successful gas encapsulation into an open-cage fullerene derivative was reported in 2001 by Rubin et al. In this study, helium and molecular hydrogen were inserted into the fullerene bislactam derivative, although the incorporation fraction was very low. Two years later, Komatsu and co-workers reported 100% incorporation of H_2 molecule into thio-aza open-cage fullerene that bears a 13-membered-ring orifice on the fullerene framework. In 2009, Cross, Saunders, and co-workers incorporated Ar, Kr, Ne, and N_2 into open-cage fullerenes. Intriguingly, water (H_2O) molecule can also be incorporated into open-cage fullerenes. In 2004, Iwamatsu et al. reported the

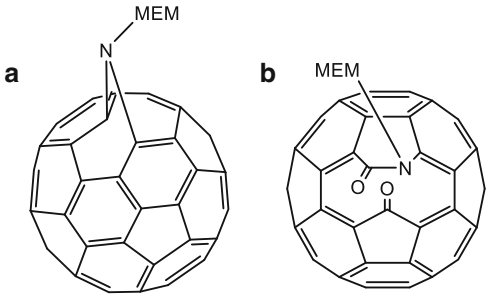

Fig. 25 Structures of (**a**) *N*-MEM-azafulleroid and (**b**) *N*-MEM-ketolactam

spontaneous encapsulation of H_2O into an open-cage bowl-shaped fullerene bearing a 20-membered ring orifice, which is the open-cage fullerene with the largest opening as of today. Apart from bowl-shaped fullerene derivatives, open-cage fullerenes with the 18-membered-ring orifice were also found to be capable of incorporating a H_2O molecule within the cage. As expected, the 19-membered-ring orifice fullerene encapsulates a H_2O molecule more efficiently. Gan and co-workers in 2009 disclosed the incorporation of H_2O molecule into three different open-cage fullerenes at about 40% ratio as determined by ^1H NMR spectroscopy. In addition, other molecules such as carbon monoxide (CO), ammonia (NH_3), and methane (CH_4) have been also successfully inserted inside the cage of open-cage fullerenes.

Formation of Heterofullerenes

Heterofullerenes are usually obtained by the substitution of one or more carbon atoms of the fullerene cage by heteroatoms such as nitrogen, boron, phosphorus, oxygen, sulfur, germanium, and platinum atoms [55]. However, in most cases, these heterofullerenes exist only in gas phase and have not been isolated for further characterization. The real preparations of heterofullerenes began in 1995 when Mattay and Hirsch individually discovered that certain exohedrally *N*-substituted epiminofullerenes and azahomofullerenes (azafulleroids) represent suitable precursors for a gas-phase rearrangement to form positively charged heterofullerenes such as $C_{59}N^+$ and $C_{69}N^+$. In the same year, Wudl's group accomplished the first synthesis of heterofullerenes in large quantities via a solution-phase reaction starting from *N*-methoxyethoxymethylketolactam (Fig. 25b) to afford aza[60]fullerene $C_{59}N$, which was generally isolated as its dimer $(C_{59}N)_2$ (Fig. 26a). It should be noted that $C_{59}N$ and $(C_{59}N)_2$ are the simplest representatives of azafullerenes. Shortly afterward, the group of Hirsch also succeeded in the bulk preparation of $(C_{59}N)_2$. Subsequently, Gan and co-workers reported a completely different method for the preparation of azafullerenes $C_{59}N(R)(OO^tBu)_4$ (R = H, Br, OH) (Fig. 26b) by addition of hydroxylamine to cage-opened oxafulleroids from fullerene-mixed peroxides $C_{60}(O)(OO^tBu)_4$ and subsequent PCl_5-induced rearrangement. They also described the synthesis of parent azafullerene $C_{59}N(H)$ via a sequential treatment of $C_{59}N(H)(OO^tBu)_4$ involving BBr_3-mediated removal of peroxo addends as the key step. Furthermore, they disclosed that the addition of hydroxylamine to $C_{59}N(Br)(OO^tBu)_4$ and a subsequent Beckman-type rearrangement afforded azahomoazafullerene $C_{59}N(NH)R$, which could be converted into the diazafullerene $C_{58}N_2$ under the conditions of MALDI-TOF mass spectroscopy.

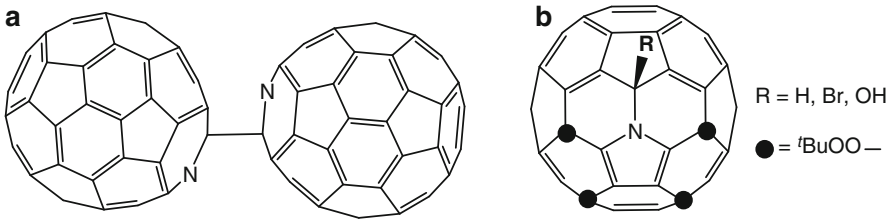

Fig. 26 Structures of azafullerenes (**a**) $(C_{59}N)_2$ and (**b**) $C_{59}N(R)(OO^tBu)_4$

It should be noted that a variety of monosubstituted azofullerenes have also been synthesized during the formation of azafullerenes and dimers by trapping the intermediate azafullerenyl radical with radicals, by reduction of the azafullerenyl with hydrogen donors, or by reaction of the corresponding azafullerenium ion with nucleophiles. For example, the first heterofullerene derivatives, namely, the monomeric alkoxy-sustituted derivatives, were formed during the synthesis of azafullerenes and dimers. In addition, the heterofullerene transformation of *N*-methoxyethoxymethyl-ketolactam (nonazafullerene precursor) (Fig. 25b) also resulted in the generation of monosubstituted azofullerene $C_{59}N(H)$ in the presence of a excess of hydroquinone. In all cases, the substituents are positioned at the 2-position next to the nitrogen atom. Further derivatizations of monosubstituted azofullerene $C_{59}NAr$, including the chlorination with ICl, hydrogenation by Zn/HCl, and fluorination by K_2PtF_6, afforded isostructural $C_{59}NCl_4Ar$, $C_{59}NH_5$, and $C_{59}NF_5$, respectively.

Concluding Remarks

In this chapter, a systematic summary of the chemical reactivity and addition pattern of C_{60} and C_{70} is provided on the basis of their chemical modification reactions, which will be of great value to scientists interested in the synthetic, material, biological, and pharmacological applications of fullerene compounds. Chemical modifications of C_{60} and C_{70} are usually divided into exohedral modification and skeletal modification. Exohedral modification affords fullerene derivatives with one or several addends covalently linked to the spherical carbon framework. The main reactions include cycloadditions, radical additions, nucleophilic additions, dimerization reactions, transition-metal-catalyzed/promoted reactions, aldehyde/amine-participated reactions, asymmetric synthesis, retro-cycloaddition reactions, mechanochemical reactions, halogenation, hydrogenation, hydroxylation, additions of organocopper reagents, additions of peroxides, and additions of amines. Skeleton modification generates open-cage fullerenes or heterofullerenes. The addition pattern of exohedral modification on fullerenes is generally classified into monoaddition and multiaddition. In the case of monoaddition, C_{60} has only two possible isomers, including 1,2- and 1,4-additions, but for C_{70}, there are eight possible isomers, including the predominant 1,2- and 5,6- additions. As for multiaddition, low regioselectivity is commonly observed and complex regioisomers are easily formed. It is expected that this chapter will bridge the gap between research communities that do not always communicate and share their knowledge to one another with enough clarity.

References

1. Kroto HW (1987) The stability of the fullerenes C_n, with n = 24, 28, 32, 36, 50, 60 and 70. Nature 329:529–531
2. Kroto HW, Heath JR, O'Brien SC, Curl RF, Smalley RE (1985) C_{60}: buckminsterfullerene. Nature 318:162–163
3. Krätschmer W, Lamb LD, Fostiropoulos K, Huffman DR (1990) Solid C_{60}: a new form of carbon. Nature 347:354–358

4. David WIF, Ibberson RM, Matthewman JC, Prassides K, Dennis TJS, Hare JP, Kroto HW, Taylor R, Walton DRM (1991) Crystal structure and bonding of ordered carbon cluster C_{60}. Nature 353:147–149
5. Ruoff RS, Tse DS, Malhotra R, Lorents DC (1993) Solubility of C_{60} in a variety of solvents. J Phys Chem 97:3379–3383
6. Semenov KN, Charykov NA, Keskinov VA, Piartman AK, Blokhin AA, Kopyrin AA (2010) Solubility of light fullerenes in organic solvents. J Chem Eng Data 55:13–36
7. Yurovskaya MA, Trushkov IV (2002) Cycloaddition to buckminsterfullerene C_{60}: advancements and future prospects. Russ Chem Bull Int Ed 51:367–443
8. Bingel C (1993) Cyclopropanation of fullerenes. Chem Ber 126:1957–1959
9. Osterodt J, Vogtle F (1996) $C_{61}Br_2$: a new synthesis of dibromomethanofullerene and mass spectrometric evidence of the carbon allotropes C_{121} and C_{122}. Chem Commun:547–548
10. Ohno T, Martin N, Knight B, Wudl F, Suzuki T, Yu H (1996) Quinone-type methanofullerene acceptors: precursors for organic metals. J Org Chem 61:1306–1309
11. Li H, Risko C, Seo JH, Campbell C, Wu G, Brédas J-L, Bazan GC (2011) Fullerene_carbene Lewis acid-base adducts. J Am Chem Soc 133:12410–12413
12. Banks MR, Cadogan JIG, Gosney I, Hodgson PKG, Langrige-Smith PRR, Millar JRA, Taylor AT (1995) Aziridino[2′,3′:1,2][60]fullerene. J Chem Soc Chem Commun:885–886
13. Heymann D, Weisman RB (2006) Fullerene oxides and ozonides. C R Chimie 9:1107–1116
14. Prato M, Li QC, Wudl F, Lucchini V (1993) Addition of azides to C_{60}: synthesis of azafulleroids. J Am Chem Soc 115:1148–1150
15. Maggini M, Scorrano G, Prato M (1993) Addition of azomethine ylides to C_{60}: synthesis, characterization, and functionalization of fullerene pyrrolidines. J Am Chem Soc 115:9798–9799
16. Shi J-L, Zhang X-F, Wang H-J, Li F-B, Zhong X-X, Liu C-X, Liu L, Liu C-Y, Qin H-M, Huang Y-S (2016) A protocol for the preparation of 2,5-diaryl fulleropyrrolidines: thermal reaction of [60]fullerene with aromatic aldehydes and arylmethanamines. J Org Chem 81:7662–7674
17. Tzirakis MD, Orfanopoulos M (2013) Radical reactions of fullerenes: from synthetic organic chemistry to materials science and biology. Chem Rev 113:5262–5321
18. Hirsch A (1995) Addition reactions of buckminsterfullerene (C_{60}). Synthesis:895–913
19. Murata Y, Shiro M, Komatsu K (1997) Synthesis, X-ray structure, and properties of the first tetrakisadduct of fullerene C_{60} having a fulvene-type π-system on the spherical surface. J Am Chem Soc 119:8117–8118
20. Kampe K, Egger N, Vogel M (1993) Diamino and tetraamino derivatives of buckminsterfullerene C_{60}. Angew Chem Intl Ed 32:1174–1176
21. Wang G-W, Li J-X (2006) Novel multicomponent reaction of [60]fullerene: the first example of 1,4-dipolar cycloaddition reaction in fullerene chemistry. Org Biomol Chem 4:4063–4064
22. Zhang W, Swager TM (2007) Functionalization of single-walled carbon nanotubes and fullerenes via a dimethyl acetylenedicarboxylate-4-dimethylaminopyridine zwitterion approach. J Am Chem Soc 129:7714–7715
23. Wang G-W, Komatsu K, Murata Y, Shiro M (1997) Synthesis and X-ray structure of dumb-bell-shaped C_{120}. Nature 387:583–586
24. Zhang T-H, Lu P, Wang F, Wang G-W (2003) Reaction of [60]fullerene with free radicals generated from active methylene compounds by manganese(III) acetate dihydrate. Org Biomol Chem 1:4403–4407
25. Li F-B, Liu T-X, Wang G-W (2008) Synthesis of fullerooxazoles: novel reactions of [60]fullerene with nitriles promoted by ferric perchlorate. J Org Chem 73:6417–6420
26. Ma W, Wang K, Huang C, Wang H-J, Li F-B, Sun R, Liu L, Liu C-Y, Asiri AM (2020) Stereoselective synthesis of amino-substituted cyclopentafullerenes promoted by magnesium perchlorate/ferric perchlorate. Org Biomol Chem 18:964–974
27. Shiu L-L, Lin T-I, Peng S-M, Her G-R, Ju DD, Lin S-K, Hwang J-H, Mou CY, Luh T-Y (1994) Palladium-catalysed [3+2] cycloaddition of trimethylenemethane (TMM) and fullerene.

Observation of the room-temperature fluorescence spectrum of the TMM-CGO adduct. J Chem Soc Chem Commun:647–648
28. Shen CKF, Chien K-M, Liu T-Y, Lin T-I, Her G-R, Luh T-Y (1995) Palladium-catalyzed [3+2] cycloaddition of 60-fullerene with *cis*-$HOCH_2CH{=}CHCH_2OCO_2Et$. Tetrahedron Lett 36: 5383–5384
29. Hashiguchi M, Watanabe K, Matsuo Y (2011) Facile fullerene modification: $FeCl_3$-mediated quantitative conversion of C_{60} to polyarylated fullerenes containing pentaaryl(chloro)[60]fullerenes. Org Biomol Chem 9:6417–6421
30. Hashiguchi M, Obata N, Maruyama M, Yeo KS, Ueno T, Ikebe T, Takahashi I, Matsuo Y (2012) $FeCl_3$-mediated synthesis of fullerenyl esters as low-LUMO acceptors for organic photovoltaic devices. Org Lett 14:3276–3279
31. Hashiguchi M, Inad H, Matsuo Y (2013) Solution-phase synthesis of dumbbell-shaped C_{120} by $FeCl_3$-mediated dimerization of C_{60}. Carbon 61:418–422
32. Su Y-T, Wang G-W (2013) $FeCl_3$-mediated cyclization of [60]fullerene with *N*-benzhydryl sulfonamides under high-speed vibration milling conditions. Org Lett 15:3408–3411
33. Li Y-F, Wang K, Wang H-J, Li F-B, Sun R, Li J-X, Liu L, Liu C-Y, Asiri AM (2020) Facile access to amino-substituted cyclopentafullerenes: novel reaction of [60]fullerene with β-substituted propionaldehydes and secondary amines in the absence/presence of magnesium perchlorate. Org Biomol Chem 18:6866–6880
34. Liu X, Wang X-Y, Sun R, Huang M-R, Liu X-S, Wang H-J, Li F-B, Liu X-F, Liu L, Liu C-Y (2021) Fullerotetrahydroquinolines: $TfOH/TsOH{\cdot}H_2O$-mediated one-pot two-step synthesis and *N*-alkylation/acylation/carboamidation reaction. Adv Synth Catal 363:4399–4421
35. Wang H, Li F, Wang P, Sun R, Ma W, Chen M, Miao W, Liu D, Wang T (2020) Chlorinated fullerene dimers for interfacial engineering toward stable perovskite solar cells with 22.3% efficiency. Adv Energy Mater 10:2000615
36. Filippone S, Maroto EE, Martín-Domenech Á, Suarez M, Martín N (2009) An efficient approach to chiral fullerene derivatives by catalytic enantioselective 1,3-dipolar cycloadditions. Nat Chem 1:578–582
37. Marco-Martínez J, Marcos V, Reboredo S, Filippone S, Martín N (2013) Asymmetric organocatalysis in fullerenes chemistry: enantioselective phosphine-catalyzed cycloaddition of allenoates onto C_{60}. Angew Chem Int Ed 52:5115–5119
38. Giovane LM, Barco JW, Yadav T, Lafleur AL, Marr JA, Howard JB, Rotello VM (1993) Kinetic stability of the fullerene C_{60}-cyclopentadiene Diels-Alder adduct. J Phys Chem 97:8560–8561
39. Moonen NNP, Thilgen C, Echegoyen L, Diederich F (2000) The chemical retro-Bingel reaction: selective removal of bis(alkoxycarbonyl)methano addends from C_{60} and C_{70} with amalgamated magnesium. Chem Commun:335–336
40. Martín N, Altable M, Filippone S, Martín-Domenech A, Martínez-Álvarez R, Suarez M, Plonska-Brzezinska ME, Lukoyanova O, Echegoyen L (2007) Highly efficient retro-cycloaddition reaction of isoxazolino[4,5:1,2][60]- and -[70]fullerenes. J Org Chem 72:3840–3846
41. Wang G-W (2021) Fullerene mechanochemistry: serendipitous discovery of dumb-bell-shaped C_{120} and beyond. Chin J Chem 39:1797–1803
42. Taylor R (2001) Fluorinated fullerenes. Chem Eur J 7:4074–4083
43. Troyanov SI, Kemnitz E (2005) Synthesis and structures of fullerene bromides and chlorides. Eur J Org Chem:4951–4962
44. Troyanov SI, Kemnitz E (2012) Synthesis and structure of halogenated fullerenes. Curr Org Chem 16:1060–1078
45. Troshin PA, Khakina EA, Peregudov AS, Konarev DV, Soulimenkov IV, Peregudova SM, Lyubovskaya RN (2010) $[C_{60}(CN)_5]^-$: a remarkably stable [60]fullerene anion. Eur J Org Chem:3265–3268
46. Wei X-W, Darwish AD, Boltalina OV, Hitchcock PB, Street JM, Taylor R (2001) The remarkable stable emerald green $C_{60}F_{15}[CBr(CO_2Et)_2]_3$: the first [60]fullerene that is also the first [18] trannulene. Angew Chem Intl Ed 40:2989–2992

47. Haufler RE, Conceicao J, Chibante LPF, Chai Y, Byrne NE, Flanagan S, Haley MM, O'Brien SC, Pan C, Xiao Z, Billups WE, Ciufolini MA, Hauge RH, Margrave JL, Wilson LJ, Curl RF, Smalley RE (1990) Efficient production of C_{60} (buckminsterfullerene), $C_{60}H_{36}$, and the solvated buckide ion. J Phys Chem 94:8634–8636
48. Zhang G, Liu Y, Liang D, Gan L, Li Y (2010) Facile synthesis of isomerically pure fullerenols and formation of spherical aggregates from $C_{60}(OH)_8$. Angew Chem Int Ed 49:5293–5295
49. Matsuo Y, Nakamura E (2008) Selective multiaddition of organocopper reagents to fullerenes. Chem Rev 108:3016–3028
50. Gan L, Huang S, Zhang X, Zhang A, Cheng B, Cheng H, Li X, Shang G (2002) Fullerenes as a *tert*-butylperoxy radical trap, metal catalyzed reaction of *tert*-butyl hydroperoxide with fullerenes, and formation of the first fullerene mixed peroxides $C_{60}(O)(OO^tBu)_4$ and $C_{70}(OO^tBu)_{10}$. J Am Chem Soc 124:13384–13385
51. Schick G, Kampeb K-D, Hirsch A (1995) Reaction of [60]fullerene with morpholine and piperidine: preferred 1,4-additions and fullerene dimer formation. J Chem Soc Chem Commun:2023–2024
52. Isobe H, Tomita N, Nakamura E (2000) One-step multiple addition of amine to [60]fullerene. Synthesis of tetra(amino)fullerene epoxide under photochemical aerobic conditions. Org Lett 2: 3663–3665
53. Isaacs L, Haldimann RF, Diederich F (1994) Tether-directed remote functionalization of buckminsterfullerene: regiospecific hexaadduct formation. Angew Chem Int Ed 33:2339–2342
54. Hummelen JC, Prato M, Wudl F (1995) There is a hole in my bucky. J Am Chem Soc 117: 7003–7004
55. Vostrowsky O, Hirsch A (2006) Heterofullerenes. Chem Rev 106:5191–5207

Functionalization of Fullerenes: Addition Reactions

10

Michio Yamada, Shigeru Nagase, and Takeshi Akasaka

Contents

Abstract

This chapter begins with the nucleophilic reactions of fullerenes, in which Grignard reagents, alkyllithium, and other carbon nucleophiles, as well as silicon and phosphorous nucleophiles, have been employed for the synthesis of a variety

M. Yamada
Tokyo Gakugei University, Koganei, Tokyo, Japan
e-mail: myamada@u-gakugei.ac.jp

S. Nagase
Kyoto University, Kyoto, Japan
e-mail: nagase@ims.ac.jp

T. Akasaka (✉)
University of Tsukuba, Tsukuba, Ibaraki, Japan
e-mail: akasaka@tara.tsukuba.ac.jp

X. Lu et al. (eds.), *Handbook of Fullerene Science and Technology*,
https://doi.org/10.1007/978-981-16-8994-9_33

of fullerene adducts. In some cases, multiple adducts have been synthesized regioselectively. The second part deals with electrophilic reactions, although reported examples of these reactions are still limited. The third part is devoted to addition–elimination reactions, which have been recognized as one of the most powerful methodologies to construct methanofullerenes. Other types of cycloadducts can also be obtained by modifying the substrates. Carbenes and silylenes are also reactive toward fullerenes; this reactivity is described in the fourth part. A variety of 1,3-dipolar cycloadditions, including the well-known Prato reactions, are summarized in the fifth part. The sixth part deals with nitrene additions, as these are relevant to 1,3-dipolar cycloadditions. The seventh part is devoted to phosphine-mediated reactions. Notably, azafulleroids and azamethanofullerenes have also been prepared via 1,3-dipolar cycloadditions followed by N_2 extrusion. Several examples of [2 + 2] cycloadditions are described in the eighth part. Finally, a variety of Diels–Alder reactions are summarized in the final part. Noteworthily, some Diels–Alder cycloadducts obtained from the reactions of fullerenes with nitrogen-containing aromatic compounds provide useful precursors for the preparation of open-cage fullerenes and endohedral fullerenes. In addition, the reversibility of the Diels–Alder reaction of C_{60} with 9,10-dimethylanthracene has been applied to achieve the regioselective synthesis of hexaadducts.

Keywords

Nucleophilic addition · Electrophilic addition · Addition–elimination reaction · Carbene addition · Silylene addition · 1,3-Dipolar cycloaddition · Nitrene addition · Phosphine-mediated reaction · [2 + 2] Cycloaddition · Diels–Alder reaction

Introduction

Research in the field of the fullerene chemistry has expanded rapidly, and many surveys have been presented in the literature. This chapter aims to provide an overview of the wide variety of addition reactions that can be used to introduce functional groups onto the surface of fullerenes, with a particular focus on the nucleophilic additions, electrophilic additions, addition–elimination reactions, carbene and silylene additions, 1,3-dipolar cycloadditions, nitrene additions, phosphine-mediated reactions, [2 + 2] cycloadditions, and Diels–Alder reactions of C_{60} that have been reported to date (see Fig. 1). Radical additions, photochemical reactions involving single-electron transfer (SET) processes, transition-metal-mediated reactions, tether-directed reactions, cage-opening reactions, and other chemical reactions of fullerene derivatives are beyond the scope of this chapter. We hope that this chapter will be useful to scientists with deep interest in the chemistry of fullerenes.

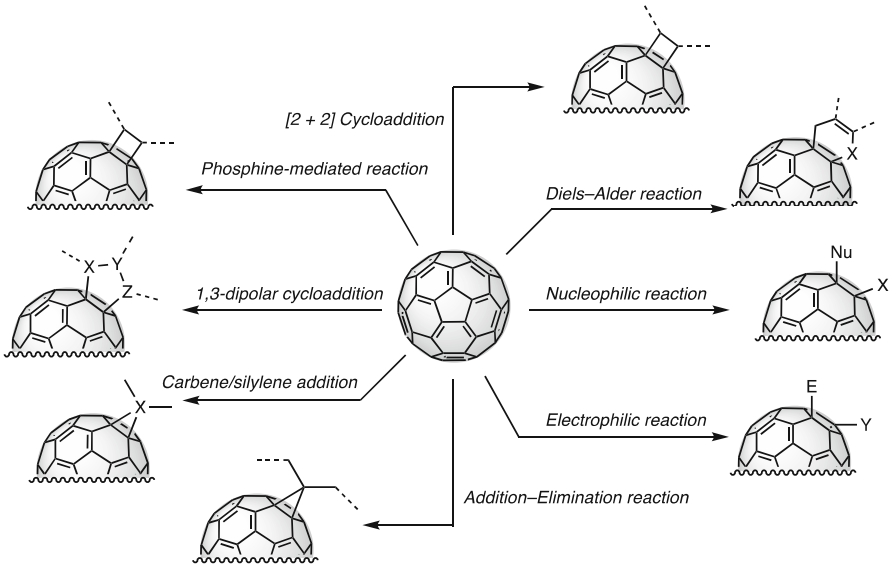

Fig. 1 Addition reactions of fullerene C_{60}

Addition Reactions

Nucleophilic Additions

Nucleophilic reactions of alkyllithium (RLi) or Grignard (RMgX) reagents with C_{60} generate R–C_{60}^- compounds, such as **1** (R = *t*Bu) in Scheme 1. Subsequent treatment of R–C_{60}^- with electrophiles such as acids or alkylhalides (R′X) results in the formation of R–C_{60}–H or R–C_{60}–R′ [1–3]. When R–C_{60}^- is reacted with O_2 or I_2, one-electron oxidation takes place to convert the intermediate into a R–C_{60}• radical compound (**3**; R = *t*Bu), which dimerizes at the C4 position to form R–C_{60}–C_{60}–R (**4**; R = *t*Bu). This dimer is in equilibrium with the radical. Hirsch et al. studied nucleophilic additions to C_{60} using titration methods and showed that the maximum yield of 1,2-*t*Bu–C_{60}–H (**2**) in the reaction of C_{60} with *t*-butyllithium followed by protonation with methanolic HCl was about 50%, as shown in Scheme 1 [4]. After the addition of approximately 1.2 equiv. of *t*-butyllithium, the concentration of 1,2-*t*Bu–C_{60}–H decreased, and the concentration of higher addition products (bis- to hexaadducts) increased markedly. A titration experiment employing the less-reactive ethylmagnesium bromide provided 1,2-Et–C_{60}–H in a maximum yield of approximately 80%. AM1 calculations for the intermediate *t*Bu–C_{60}^- demonstrated that the negative charge was not delocalized, but instead localized on the carbon across the [6,6]-bond from the butylated sp^3 carbon atom. Fagan et al. synthesized

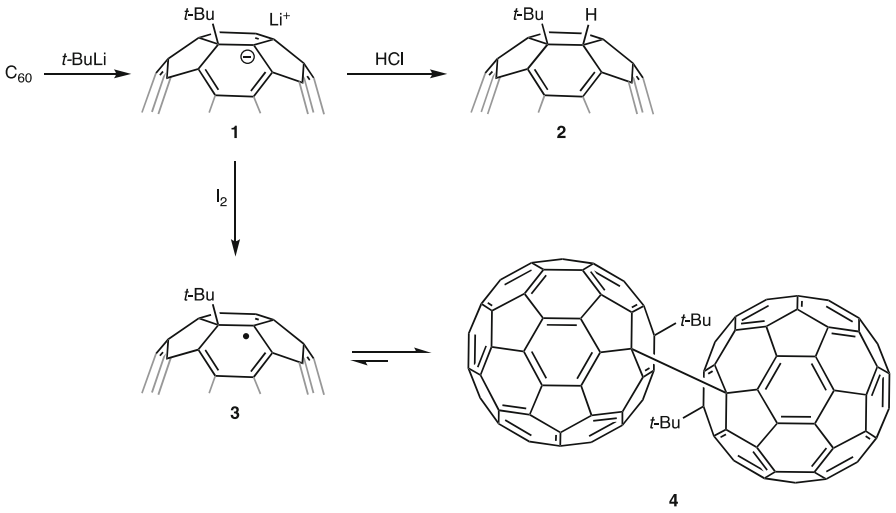

Scheme 1 Reactions of C_{60} with *t*-butyllithium

the lithium salt of the alkylated fullerenyl anion, *t*Bu–C_{60}–Li^+·$4CH_3CN$, in pure form as a green powder with a yield of 25% [2]. Protonation of the lithium salt with acetic acid in THF yielded a 10:1 mixture of 1,2- and 1,4-*t*Bu–C_{60}–H; the 1,4-adduct gradually rearranged to give the 1,2-adduct at 25 °C. In fact, the addition positions in organofullerenes prepared by nucleophilic reactions are affected by steric congestion. Protons or less bulky alkyl addends tend to favor 1,2-addition, while bulkier alkyl addends prefer 1,4-addition. In R–C_{60}–H, the proton attached to the fullerene is strongly acidic. For instance, the pKa value of **2** is 5.7. Therefore, treatment with an adequate base such as KO*t*Bu easily deprotonates R–C_{60}–H to generate R-C_{60}^-.

In related works, Fukuzumi et al. reported that the reaction of C_{60}^{2-} with *t*-butyl iodide afforded *t*BuC_{60}^- via a SET process, followed by radical coupling between the C_{60} radical anion and the *t*Bu radical [5]. Subsequent treatment of *t*Bu–C_{60}^- with benzyl bromide yielded 1,4-*t*Bu–C_{60}–CH_2Ph via an S_N2 pathway rather than an electron-transfer pathway.

The silylmethylation of C_{60} with Grignard reagents was reported by Nagashima et al., as shown in Scheme 2 [6, 7]. When the reaction was carried out in THF, the corresponding product 1,2-RMe_2SiCH_2–C_{60}–H (**5**) was obtained in 14–39% yield after quenching with aq. H_2SO_4. When toluene was used as the solvent instead of THF, 1,4-dihydrofullerenes **6** were obtained instead of **5** in 5–36% yield; the reactions in toluene were more sluggish than those in THF. The highest yield (36%) was achieved by the reaction of C_{60} with Me_2(O*i*Pr)$SiCH_2MgCl$. The formation of **6** indicated that oxidation, presumably by oxygen from the air, was involved in the reaction, leading to a radical mechanism.

The use of Grignard reagents tends to lead to lower yields of R–C_{60}–R′ compared with alkyllithium reagents. In such cases, the addition of DMF or DMSO is effective to increase the yield of R–C_{60}–R′. For instance, Matsuo and Nakamura et al. reported

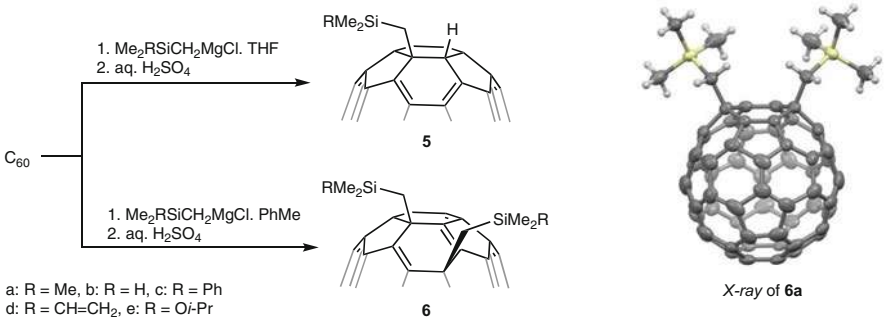

Scheme 2 Reactions of C_{60} with silylmethyl Grignard reagents

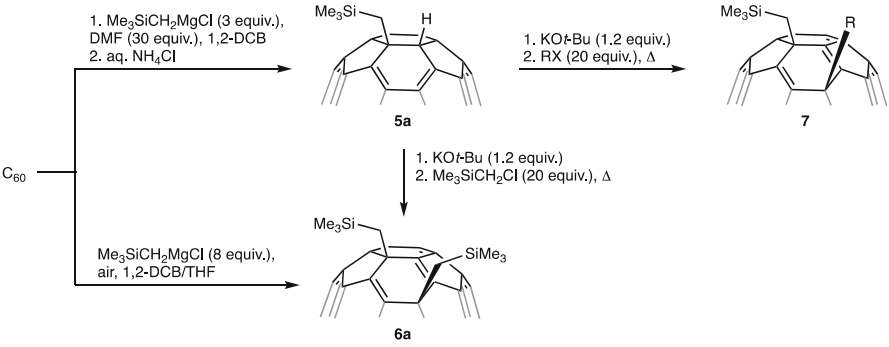

Scheme 3 Effect of DMF as an additive in the reactions of C_{60} with silylmethyl Grignard reagents

that the reaction of C_{60} with 3 equiv. of Me_3SiCH_2MgCl in 1,2-DCB in the absence of additives, followed by quenching with aqueous ammonium chloride, produced the 1,2-adduct in 10% yield with 63% unreacted C_{60}, as shown in Scheme 3 [8, 9]. When the same reaction was carried out in the presence of 30 equiv. of DMF, the yield of the 1,2-adduct reached 93%, with 7% unreacted C_{60}. The authors suggested that DMF likely improved the yield not due to its polarity, but instead by enhancing the nucleophilicity of the Grignard reagent and stabilizing the magnesium intermediate. The silylmethyl Grignard reagents Me_2RSiCH_2MgCl (R = O*i*Pr, hexyl, octyl, dodecyl, and Ph) also gave the corresponding 1,2-adducts in 83–91% yield. Using the same protocol, the reactions of C_{60} with MeMgBr and $MeOC_6H_4MgBr$ afforded the corresponding 1,2–R–C_{60}–H products in 46 and 53% yield, respectively, after quenching with aq. NH_4Cl. Treatment of **5a** with KO*t*Bu followed by heating in the presence of Me_3SiCH_2I (20 equiv.) in benzonitrile afforded **6a** in 93% yield. The silylmethyl iodide can also be replaced by a mixture of silylmethyl chloride (20 equiv.) and potassium iodide (20 equiv.). Treatment of **5a** with KO*t*Bu followed by heating in the presence an alkyl halide (20 equiv.), such as benzyl bromide, iodomethane, 1-bromohexane, diethoxyethyliodide, triethoxyethyliodide, tridecafluoro-8-iodooctane, and nonadecafluoro-11-iodoundecane, in

benzonitrile also afforded the corresponding 1,4-adducts **7** in 55–89% yield. Alternatively, the reaction of C_{60} with Me_3SiCH_2MgCl in dry air in 1,2-DCB/THF at 25 °C afforded **6a** in 54% yield. The reaction mechanism was proposed to involve oxidation of the initially formed monoalkylated C_{60} anion by oxygen to give the corresponding radical. Further treatment of **6a** with silylmethyl Grignard reagents afforded tri(organo)fullerenes such as $C_{60}(CH_2SiMe_3)_3H$.

Fullerene alkynylation can be achieved by reacting C_{60} with an alkynyllithium reagent followed by protonation with an acid or alkylation with an alkyl halide, as depicted in Scheme 4. Komatsu et al. reported the synthesis of the 1,2-adduct of $Me_3Si–C{\equiv}C–C_{60}–H$ (**9**) in 45% by the slow addition of 4 equiv. of a THF solution of [(trimethylsilyl)ethynyl]lithium to a refluxing solution of C_{60} in toluene followed by quenching the resulting black suspension containing the lithium salt of ethynylated C_{60} (**8**) with excess trifluoroacetic acid [10]. Diederich et al. also independently reported the synthesis of **9** in 58% yield via treatment of a toluene solution of C_{60} with [(trimethylsilyl)ethynyl]lithium in THF at 20 °C and subsequent quenching with acetic acid [11, 12]. The benzyl derivative $1,2–Me_3Si–C{\equiv}C–C_{60}–CH_2Ph$ (**10**) was obtained in 31% yield by refluxing **8** with benzyl bromide in THF for 2 h. Bubbling formaldehyde gas through a solution of **8** in toluene at 0 °C yielded the alcohol derivative **11** as an air-stable compound in 57% yield. However, under strongly basic conditions, the formaldehyde was rapidly eliminated. For instance, treatment of the alcohol derivative with sodium hydride in toluene in THF afforded the sodium salt **12** quantitatively, while Swern oxidation of the alcohol derivative gave the corresponding aldehyde in 53% yield.

Komatsu et al. found that the reaction of C_{60} with 1-octaethynyllithium proceeded smoothly at ambient temperature in THF to give a dark green solution of $Hex–C{\equiv}C–C_{60}^-$ [13]. After quenching with trifluoroacetic acid and subsequent medium pressure liquid chromatography (MPLC) separation, $1,2\text{-}Hex–C{\equiv}C–C_{60}–H$ (**13**) was obtained in 75% yield along with 21% unreacted C_{60}. When the reaction was carried out in refluxing toluene, **13** was obtained in 52% yield, along with the bisadduct

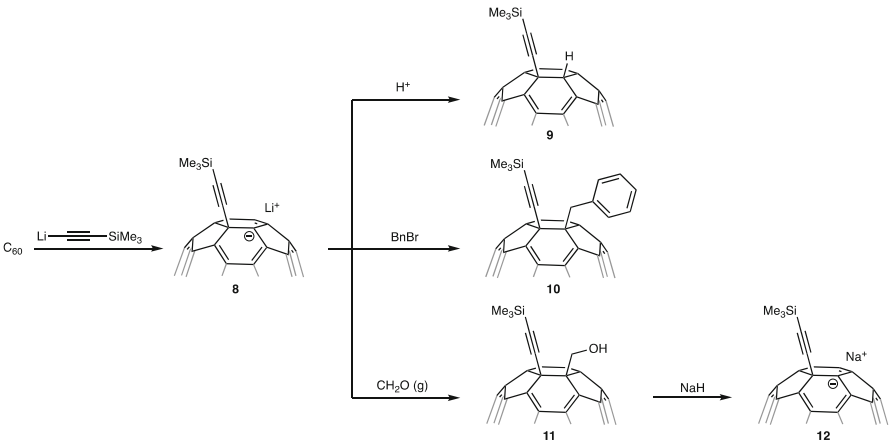

Scheme 4 Reactions of C_{60} with trimethylsilylethynyllithium

(5%) and unreacted C_{60} (16%). The 1-octaethynyl C_{60} anion **14** can be prepared by treatment of 1,2-Hex–C≡C–C_{60}–H with 1 equiv. of KO*t*Bu. The solution of **14** is sensitive to air but can be stored without decomposition under argon or nitrogen for more than half a year. Reaction of **14** with iodomethane or iodoethane afforded 1,2-Hex–C≡C–C_{60}–R (**15**; R = Me, Et) in 98% and 97% yield, respectively. When the tropylium ion was employed in place of an iodoalkane, both the 1,2- and 1,4-adducts of Hex–C≡C–C_{60}–C_7H_7 were obtained in 40% (**16**) and 32% (**17**) yield, respectively. On the other hand, the reaction of 1,2-Hex–C≡C–C_{60}^- with benzoyl chloride selectively produced the 1,4-adduct 1,4-Hex–C≡C–C_{60}–C(O)Ph (**18**) in 84% yield (Scheme 5).

The addition of a solution of sodium cyanide in DMF to a solution of C_{60} in 1,2-DCB at ambient temperature resulted in a deep green solution containing N≡C–C_{60}^- (**19**), as shown in Scheme 6 [14]. Subsequent treatment of the anion with appropriate electrophiles gave the corresponding 1,2-dehydrofullerenes (**20**). Protonation with trifluoroacetic acid at ambient temperature afforded 1,2-N≡C–C_{60}–H in 29% yield. Alkylation with methyl trifluoromethanesulfonate at ambient temperature provided 1,2-N≡C–C_{60}–CH_3 in 10% yield. Benzylation of the anion with 4-*t*-butylbenzyl bromide at 70 °C resulted in 1,2-N≡C–C_{60}–CH_2–C_6H_4–*t*Bu in 11% yield. When the anion was treated with tosyl cyanide at room temperature, 1,2-dicyanofullerene $C_{60}(CN)_2$ was obtained in 61% yield.

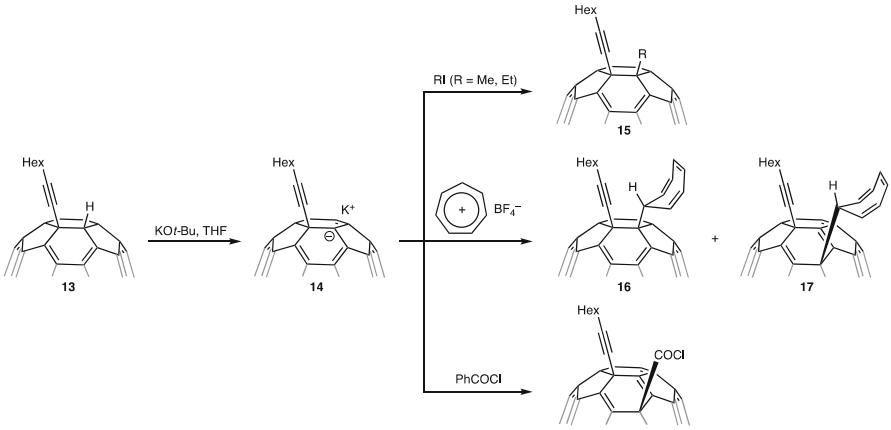

Scheme 5 Reactions of C_{60} with 1-octaethynyllithium

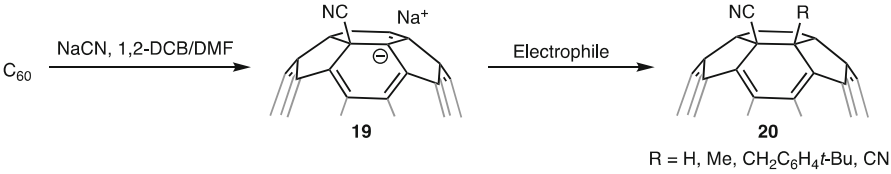

Scheme 6 Reactions of C_{60} with sodium cyanide

Komatsu et al. employed metal fluorenides in nucleophilic reactions with C_{60}, as shown in Scheme 7 [15]. Reaction of C_{60} with 2 equiv. of lithium fluorenide in THF at ambient temperature and subsequent acidification with trifluoroacetic acid afforded the corresponding 1,2-dihydrofullerene **22** in 41% yield, along with 22% unreacted C_{60}. When the dark green suspension of the fluorenyl-C_{60} anion **21** was stirred at ambient temperature for 24 h, 1,4-bisadduct **23** was formed in 22% yield, along with 21% unreacted C_{60} and a large amount of highly insoluble materials. The authors suggested that the fluorenyl-C_{60} anion was gradually oxidized by trace oxygen to form the corresponding fluorenyl-C_{60} radical. Some of the radical underwent dimerization, while the remainder reacted with the fluorenide anion to give the radical anion of **22**, which was again oxidized by trace oxygen to furnish neutral **22**. Reaction of C_{60} with the lithium salt of trimethylenebisfluorenide **24** afforded the corresponding 1,4-adduct **25** in 13% yield along with 43% unreacted C_{60}, as shown in Scheme 8.

When C_{60} was reacted with 3 equiv. of potassium fluorenide in the presence of neutral fluorene (2 equiv.) in THF for 72 h under argon, the tetrakis(9-fluorenyl) adduct **26** featuring a fulvene structure on the fullerene surface was obtained in 40% yield after high-performance liquid chromatography (HPLC) separation, as shown in Scheme 9 [16]. Detailed experiments showed that the pentaadduct anion was formed

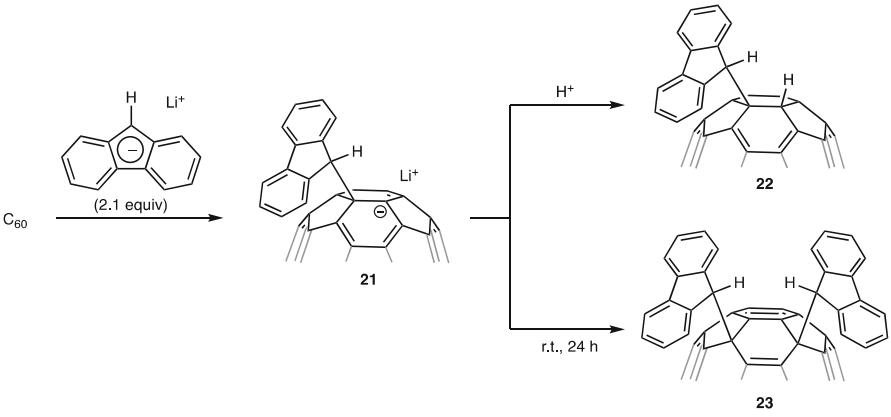

Scheme 7 Reactions of C_{60} with lithium fluorenide

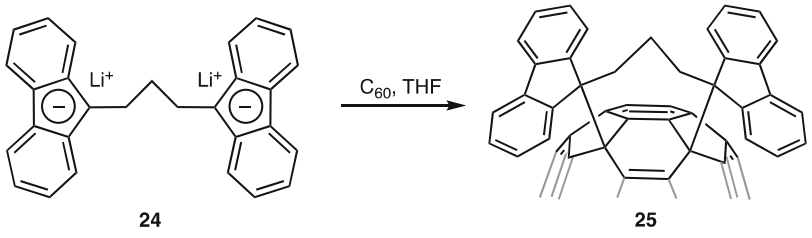

Scheme 8 Reaction of C_{60} with the lithium salt of trimethylenebisfluorenide

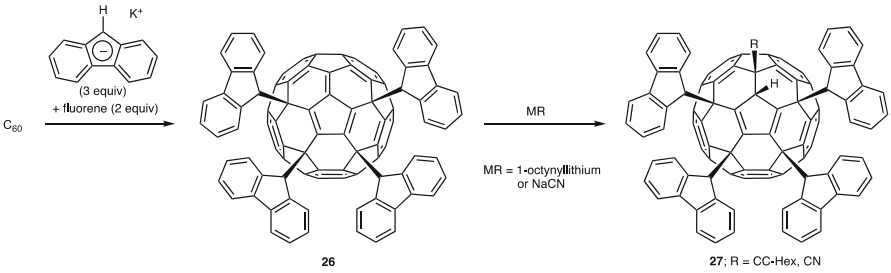

Scheme 9 Synthesis of tetrakis- and pentakisadducts

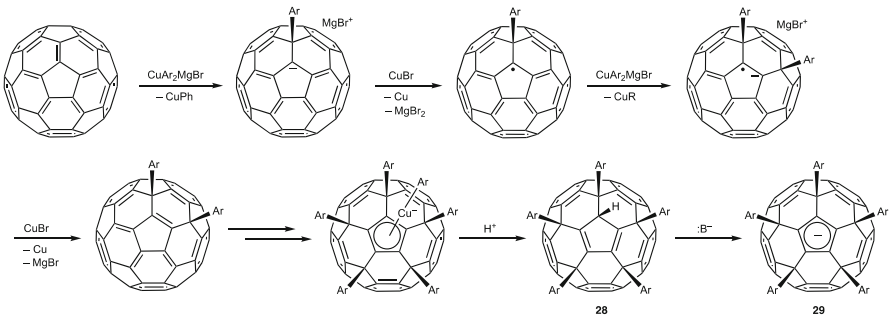

Scheme 10 Fivefold addition of organocopper reagents to C_{60}

as the major product after 24 h, and the tetraadduct was formed irreversibly from the pentaadduct anion through oxidation by trace air and subsequent detachment of a fluorenyl radical anion. In fact, protonation of the reaction mixture with a reaction time of 24 h yielded the pentaadduct with a cyclopentadiene structure in 49%. Tetrakisadduct **26** reacted with carbon nucleophiles such as 1-octynyllithium (in THF) and sodium cyanide (in DMF/1,2-DCB) to afford the corresponding pentakisadducts **27** in 63% and 68% yield, respectively.

Treatment of C_{60} with an excess of PhMgBr (16 equiv.) and CuBr·SMe_2 (16 equiv.) followed by quenching with aqueous NH_4Cl afforded the fivefold addition of phenyl groups to give $C_{60}Ph_5H$ (**28**; Ar = Ph) in 94% yield, as shown in Scheme 10 [17]. The introduction of the five phenyl groups was proposed to occur through sequential additions of the cuprate Ph_2Cu^-. The resulting pentaadducts have been applied as fullerene-based liquid crystals and vesicles. Treatment of a THF solution of **28** with alkali metal alkoxides such as Li*O*t*Bu or K*O*t*Bu at room temperature afforded the corresponding metal complexes of cyclopentadienyl anion **29**. These metal complexes are thermally stable in solution at room temperature, but air and moisture sensitive.

Eight- and tenfold additions can also be achieved by modifying the reaction conditions, as shown in Scheme 11 [18]. The addition of a large excess of a base is a viable approach to achieve such octa- and deca-additions. Loading 30 equiv. of the copper reagent and 300 equiv. of pyridine in THF/1,2-DCB (ca. 1:2:1 pyridine/

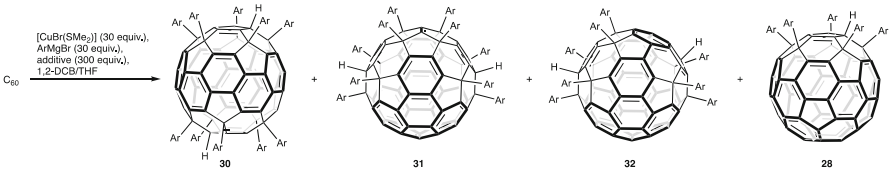

Scheme 11 Eightfold and tenfold additions to C_{60}

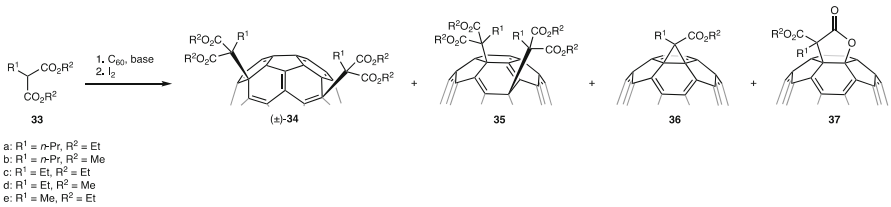

Scheme 12 Reaction of C_{60} with alkylmalonates in the presence of a base and I_2

THF/1,2-DCB) in the reaction gave decaadducts **30** and **31** in 92% yield in an approximate 1:2 ratio together with trace amounts of octaadduct **32**, which features a dibenzo-fused corannulene-type π-electron conjugated system. The decaadducts were easily separated by recrystallization and/or silica gel column chromatography. The use of a large excess of pyridine (60% v/v pyridine, 27% v/v THF, and 13% v/v 1,2-DCB) afforded **30** in 25% and **32** in 50% yield, respectively. These octa- and decaadducts were characterized as mixtures of the isomers with two hydrogen atoms at different positions. The yields of **30**, **31**, and **32** depend on the substituents of the aryl groups. For instance, an *ortho*,*para*-disubstituted phenyl copper reagent afforded predominantly octaadduct **32**.

Reacting C_{60} with alkylmalonates **33** in the presence of a base and I_2 in 1,2-DCB afforded four products: a 1,6-bisadduct (±)-**34**, 1,4-bisadduct **35**, methanofullerene **36**, and lactone-fused derivative **37**, as shown in Scheme 12 [19]. The yields of these reactions were sensitive to the reaction conditions. The yields of (±)-**34** and **35** were improved 20–28 and 22–26%, respectively, by using a 1:2:6:1 C_{60}/*t*-butylammonium hydroxide (TBAOH)·$30H_2O$/**33**/I_2 ratio and a reaction time of 2 h; a minor amount of **36** (8–9%), but no **37**, was produced. Increasing the amount of TBAOH·$30H_2O$ in the reaction of C_{60} with **33a** to 4 equiv. gave **37a** as the major product (31%) and **36a** as the minor product (7%) with no (±)-**34a** or **35a**. Treatment of **33** with a base was proposed to form the corresponding carbanion, which would then attack C_{60} to afford the fullerenyl anion intermediate $(R^1)(R^2O_2C)_2C–C_{60}^-$. This intermediate could be oxidized by I_2 to produce the fullerenyl radical intermediate $(R^1)(R^2O_2C)_2C\text{-}C_{60}$•. On the other hand, I_2 could also generate the radical intermediate $(R^1)(R^2O_2C)_2C$• from deprotonated **33**, which would undergo radical coupling reactions to afford (±)-**34** and **35**. Subjecting the fullerenyl anion intermediate to base-catalyzed hydrolysis would form the dianionic intermediate (R^1)

$(R^2O_2C)C(CO_2^-)$–C_{60}^-, the subsequent oxidative decarboxylation or oxidative radical coupling of which would result in **36** or **37**, respectively.

The addition of silicon and germanium nucleophiles to C_{60} was surveyed by Ando et al. [20, 21] They found that reactions of silyllithium reagents $R^1R^2R^3SiLi$ with C_{60} could afford the corresponding monosilylated adduct 1,2-$R^1R^2R^3Si$–C_{60}–H **39** and bissilylated adduct (±)-1,16/1,29-$R^1R^2R^3Si$–C_{60}–$SiR^1R^2R^3$ **40**, with the product selectivity depending on the silyllithium substituents, as shown in Scheme 13. For instance, slow addition of a THF solution of diisopropylphenylsilyllithium (**38a**) to a solution of C_{60} in toluene at –78 °C and subsequent quenching with EtOH afforded 1,2-*i*Pr_2PhSi–C_{60}–H (**39a**) as the sole product in 78% yield based on the unreacted C_{60}. Isopropyldiphenylsilyllithium (**38b**) also reacted with C_{60} under similar conditions to give 1,2-*i*$PrPh_2$Si–C_{60}–H (**39b**) in 80% yield based on the unreacted C_{60}. In contrast, reaction of C_{60} with tris(trimethylsilyl)silyllithium (**38d**) or di-*t*-butylphenylsilyllithium (**38e**) afforded the bissilylated adducts (±)-1,16/1,29-$(Me_3Si)_3$Si–C_{60}–$Si(SiMe_3)_3$ (**40d**) and (±)-1,16/1,29-*t*Bu_2PhSi–C_{60}–Si*t*Bu_2Ph (**40e**) as the sole products in 69% and 72% yields based on unreacted C_{60}, respectively. Similar reactivity was found for the germanium analogues; reaction of C_{60} with diisopropylphenylgermyllithium (**38h**) yielded 1,2-*i*Pr_2PhGe–C_{60}–H (**39h**), whereas reaction with di-*t*-butylphenylgermyllithium (**38i**) yielded (±)-1,16/1,29-*t*Bu_2PhGe–C_{60}–Ge–*t*Bu_2Ph (**40i**) in 76% and 87% based on unreacted C_{60}, respectively. In contrast, 4-methylphenyl group substituted silyllithium reagents such as (4-methylphenyl)di-*tert*-butylsilyllithium (**38f**) afforded not only the 1,2-monosilylated adduct **39f** and the bissilylated adduct **40f** but also the 1,4-monosilylated adduct 1,4-$R^1R^2R^3Si$–C_{60}–H (**41f**) and the monosilylated C_{60} dimer **42f** in yields of 11%, 42%, 11%, and 6% based on unreacted C_{60}, respectively, when $R^1 = R^2 = t$Bu and R^3 = 4-methylphenyl.

The reactivity of phosphorus nucleophiles toward C_{60} was investigated by Nakamura et al. [22] Lithiated secondary phosphine–boranes (**44**; R^1, R^2 = Ph or R^1 = Me, R^2 = Ph), which were prepared by deprotonation of the corresponding

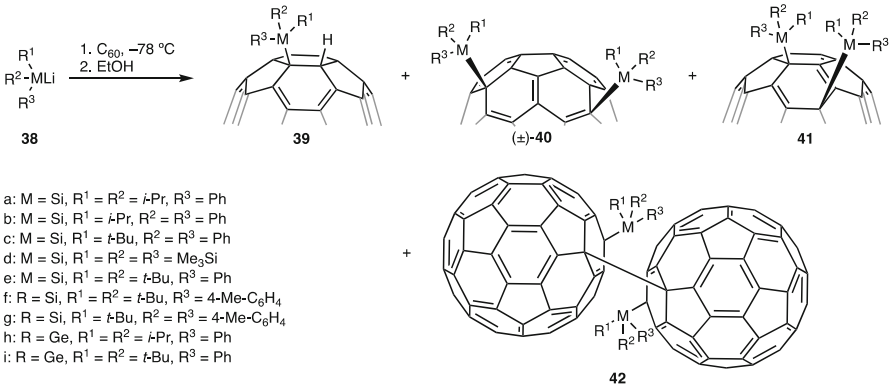

Scheme 13 Reaction of C_{60} with silyllithium or germyllithium reagents

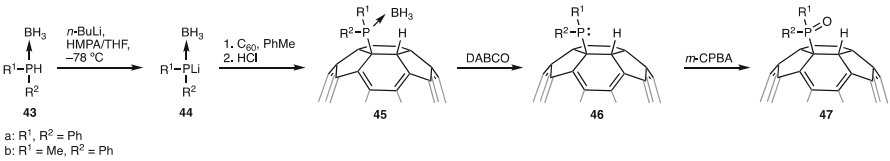

Scheme 14 Reaction of C_{60} with phosphorous nucleophiles

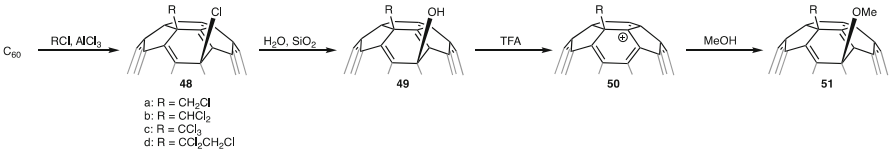

Scheme 15 Reaction of C_{60} with RCl in the presence of $AlCl_3$

phosphine–boranes **43** with *n*BuLi, were reacted with C_{60}. Subsequent protonation with hydrogen chloride yielded phosphine–borane-bearing fullerene adducts **45** in 46–82%, as shown in Scheme 14. Removal of the BH_3 group by treatment of the borane complex (R^1, R^2 = Ph) with 1,4-diazabicyclo[2.2.2]octane (DABCO) afforded phosphine derivative **46** quantitatively. The solid phosphine was moderately air-sensitive but could be handled in air without oxidation. Treatment of the phosphine derivative with 1 equiv. of *m*-CPBA afforded the phosphine oxide **47**.

Electrophilic Additions

Studies of electrophilic additions to fullerenes are still limited, as fullerenes generally behave like electron-deficient olefins. Kitagawa et al. found that treatment of C_{60} with 100 equiv. of $AlCl_3$ in RCl resulted in the formation of 1,4-R–C_{60}–Cl (**48**) in good yield (yield of **48b** (R = $CHCH_2$): 68%), as shown in Scheme 15 [23]. The derivatives readily hydrolyzed in organic solvents in the presence of silica gel to give the corresponding 1,4-R–C_{60}–OH fullerols. The hydrolysis was expected to proceed via a cationic intermediate R–C_{60}^{+}, i.e., the same structure as the intermediate of the $AlCl_3$-catalyzed addition of RCl. In this respect, the fullerenyl cation can be generated by dissolving the fullerol in trifluoroacetic acid (TFA). Subsequent quenching of the cation with methanol afforded 1,4-R–C_{60}–OMe (**51a**, **51b**). They also performed kinetic studies of S_N1 solvolysis reactions of **48** in anisole–trifluoroethanol mixed solvent and verified that the corresponding fullerenyl cations **50** had stabilities comparable to that of the *t*-butyl cation [24].

The synthesis of benzothieno[60]fullerenes **55** was accomplished through fullerenyl cation intermediates, as shown in Scheme 16 [25]. Starting from monoarylated fullerenes C_{60}ArH (**52**) with methylthio groups at the *ortho*-positions relative to the *ipso*-carbon bonded to the fullerene cage, deprotonation with KO*t*Bu followed by oxidation with excess iodine generated the fullerenyl cation

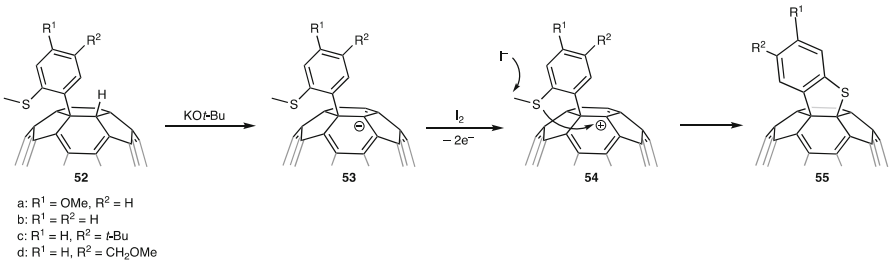

Scheme 16 Synthesis of benzothieno[60]fullerenes through fullerenyl cation intermediates

intermediate **54**. An iodide ion (I^-) formed by the reduction of I_2 facilitated demethylation and subsequent intramolecular nucleophilic addition of the sulfur atom of the substituent to the cationic carbon on the C_{60} cage. The yields of **55a–d** were 30–42%. Details of recent advances in the functionalization of C_{60} through fullerenyl cation intermediates have also been reviewed by Matsuo et al. [26]

Addition–Elimination Reactions

Deprotonation of α-halocarbanion precursors such as α-haloesters, α-haloketones, α-cyanoesters, and α-halonitromethanes generates carbon nucleophiles that can cyclopropanate fullerenes through an addition–elimination mechanism [27]. A typical example is the reaction with bromomalonate in the presence of a base such as 1,8-diazabicyclo[5.4.0]undec-7-ene (DBU) or NaH, which is known as the Bingel reaction or Bingel–Hirsch reaction [28, 29]. Nowadays, the Bingel reaction is widely used for the introduction of functional groups to fullerenes. Additionally, the Bingel reaction can also be applied for the preparation of water-soluble fullerene derivatives, as the Bingel products can be transformed into the corresponding carboxylates by subsequent hydrolysis. Dimethoxybromomethylphosphonate alkyl esters and bis-methanophosphonates were employed for the synthesis of phosphorylated methanofullerenes. Using modified Bingel conditions, α-haloanion intermediates were prepared in situ from malonates (**56**), DBU, and CBr_4 (or I_2) to provide methanofullerenes **57**, as shown in Scheme 17 [30, 31]. In a typical procedure, DBU (3 equiv.) was added to a toluene solution of C_{60}, CBr_4 (1.5 equiv.), and diethylmalonate (1.5 equiv.), followed by stirring for 6 h. Subsequent flash chromatography afforded $C_{60}C(CO_2Et)_2$ in 57% yield. Note that the reaction of diethyl bromomalonate with paramagnetic endohedral metallofullerene (EMF) La@C_{82} in the presence of DBU yielded a diamagnetic, singly bonded monoadduct La@$C_{82}CBr(CO_2Et)_2$ as the major product [32].

Diederich et al. synthesized ethynyl methanofullerenes as building blocks for molecular carbon allotropes via the Bingel-type reaction of C_{60} with 3-bromo-1,5-bis(trimethylsilyl)penta-1,4-diyne (**58**) in the presence of DBU and subsequent deprotection, as shown in Scheme 18 [33]. Oxidative coupling reactions of bis(ethynyl)methanofullerene **59** with substituted alkynes using the Hay catalyst

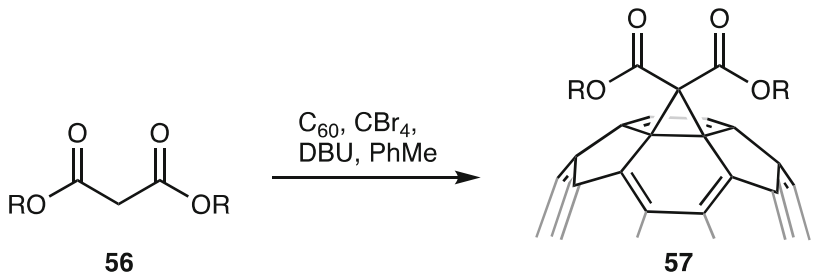

Scheme 17 Bingel–Hirsch reaction of C_{60} with malonates

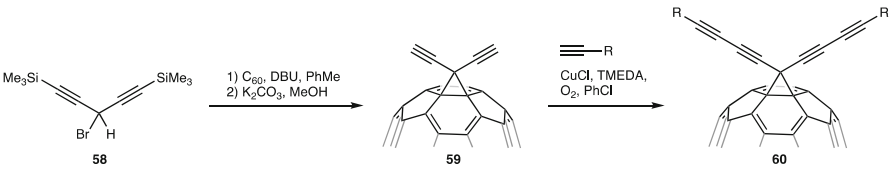

Scheme 18 Synthesis of bis(ethynyl)methanofullerene and bis(butadiynyl)methanofullerene

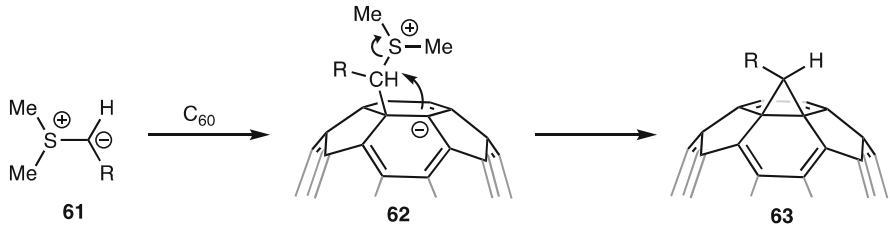

a: R = CO_2Et
b: R = CO_2t-Bu
c: R = $CH{=}CHCO_2Et$
d: R = $C(O)NEt_2$
e: R = $C(O)C_6H_5$
f: R = $C(O)C_6H_4$-*p*-OMe

Scheme 19 Reaction of C_{60} with sulfonium ylides

(CuCl, *N*,*N*,*N*′,*N*′-tetramethylethylenediamine (TMEDA), dry air) afforded bis (butadiynyl)methanofullerenes **60** in 25–43% yield.

Stabilized sulfonium ylides are also useful for the synthesis of methanofullerenes, as shown in Scheme 19 [34]. Reactions of C_{60} with stabilized sulfonium ylides **61** proceeded smoothly at ambient temperature. Such ylides can be prepared by treating the corresponding sulfonium salts with NaH or NaOH and can be isolated and stored for months at temperatures below –20 °C. The isolated yields of the methanofullerenes **63** were 32–58%.

Reaction of C_{60} with thiocyanates **64** in the presence of DBU resulted in the formation of not only the methanofullerene products **66** but also the

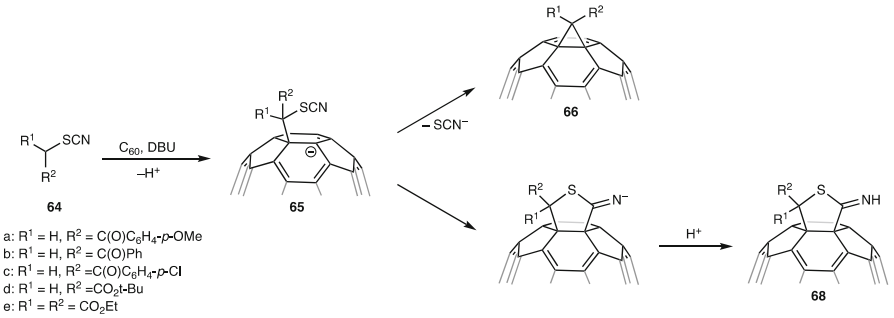

Scheme 20 Reactions of C_{60} with thiocyanates in the presence of DBU

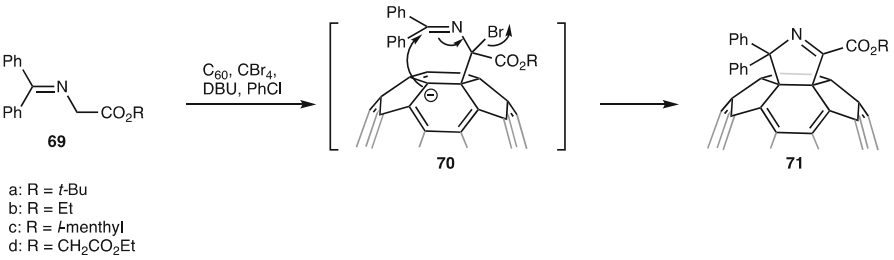

Scheme 21 Reaction of C_{60} with *N*-(diphenylmethylene)glycinates under Bingel conditions

2-iminotetrahydrothiopehene-fused products **68**, as shown in Scheme 20 [35]. The use of triethylamine, pyridine, DMAP, or DABCO in place of DBU suppressed the formation of the products. The ratio of the two products depended on the equivalents of DBU used. It was suggested that the deprotonation of the thiocyanate by DBU generates the corresponding carbanion, which attacks C_{60} to yield the fullerenyl anion intermediate **65**. Subsequent nucleophilic attack of the fullerenyl anion on the sp^3 carbon connected to the SCN group would result in the formation of **66** through an addition–elimination process. Attack of fullerenyl anion on the C≡N bond of the SCN group would form the corresponding five-membered heterocyclic anion **67**, which would subsequently be protonated to afford the final product **68**.

Reaction of C_{60} with *N*-(diphenylmethylene)glycinate (**69**) under Bingel conditions (CBr_4, DBU, PhCl) afforded the dihydroproline-fused derivatives **71** and not the corresponding methanofullerenes, as shown in Scheme 21 [36]. The products were hypothesized to arise from the nucleophilic attack of the fullerenyl anion on the carbon of the imine group in anionic intermediate **70**.

Carbene and Silylene Additions

Electrophilic carbenes react with fullerenes to form cyclopropane-annulated derivatives known as methanofullerenes. Dihalocarbenes are the simplest carbenes.

The trichloromethyl anion, CCl_3^-, is known to be a critical intermediate of dichlorocarbene, as it is unstable and equilibrates rapidly to $:CCl_2$ and Cl^-. In 1993, Nogami et al. reported that the pyrolysis of sodium trichloroacetate in the presence of C_{60} in benzene–digyme mixed solvent resulted in dichlorocarbene addition [37]. In the reaction, both mono-addition and multiple addition proceeded simultaneously. When a tenfold excess of Cl_3CCO_2Na was added to the reaction, 25% $C_{60}(CCl_2)$, 22% $C_{60}(CCl_2)_2$, and 6% $C_{60}(CCl_2)_3$ were obtained, along with 43% unreacted C_{60} after gel permeation chromatography (GPC) separation. The similar carbene adducts $C_{60}(CBr_2)$ and $C_{60}(CHCN)$ were prepared in 40% and 15% yields, respectively, by adding lithium diisopropylamide (LDA) to a toluene solution of C_{60} and $CHBr_3$ or CH_2BrCN (10 equiv.) [38]. The use of the organomercury compounds known as Seyferth reagents has also been reported. Vögtle et al. synthesized $C_{60}(CBr_2)$ in 54% yield by refluxing a mixture of C_{60} and 1 equiv. of $PhHgCBr_3$ in benzene, followed by GPC–HPLC separation [39].

Yinghuai et al. found that ultrasound irradiation of a mixture of haloform (CHX_3; C = Cl, Br, and I), NaOH, and C_{60} in the ionic liquid 1-butyl-3-methylimidazolium tetrafluoroborate ([BMIM][BF_4]) afforded the mono-adducts $C_{60}(CCX_2)$ in 63–77% yields [40]. Replacing the ionic liquid solvent with THF drastically reduced the yields (11–17%). This result suggested that the carbene mechanism was not involved in the ultrasound reaction, because it is known to be little-affected by solvent polarity. At this point, Nagase et al. studied the addition of dichlorocarbene to C_{60} computationally using density functional theory (DFT) calculations [41]. The results suggested that the addition–elimination mechanism (Bingel mechanism) was highly competitive with the carbene mechanism and that unlike the carbene mechanism, the Bingel mechanism is strongly regioselective and solvent sensitive.

Cyclopropenone acetal (CPA) is known as a source of vinylcarbene species **73**. Nakamura et al. reported that thermal reaction of C_{60} with CPA **72** derivatives produced [2 + 1] cycloadducts **74** and [2 + 3] cycloadducts **76** depending on the substituent, as shown in Scheme 22 [42, 43]. The resulting ketene acetal-bearing

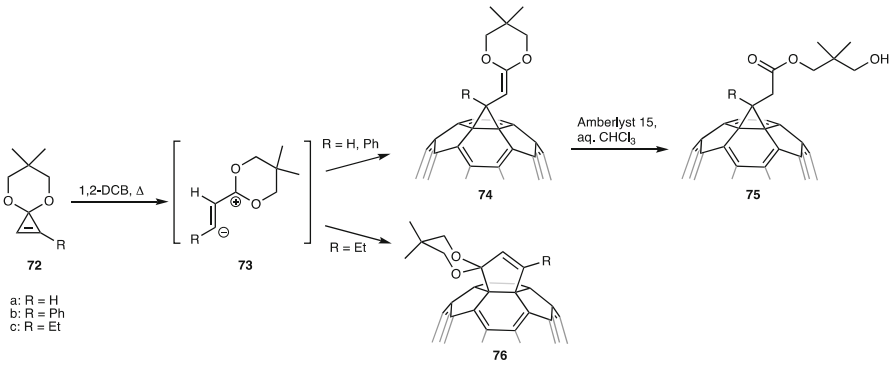

Scheme 22 Reactions of C_{60} with CPA

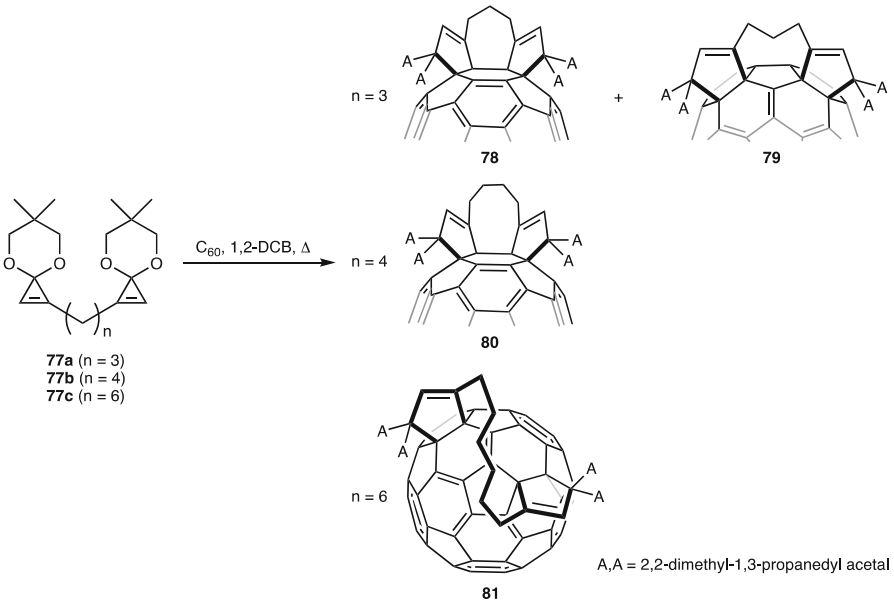

Scheme 23 Reaction of C_{60} with tethered bis-CPA

methanofullerene **74** was easily transformed into the stable methanofullerene **75** by hydrolysis.

Nakamura et al. further synthesized tris-annulating reagents in which two CPA moieties were connected with an *n*-carbon methylene tether and applied them for the tether-directed bis-functionalization of C_{60}, as shown in Scheme 23 [44]. The reaction of C_{60} with the three-carbon-tethered bis-CPA **77a** afforded the C_s-symmetric bisadducts **78** and **79** in 14 and 23% yields, respectively. When the four-carbon-tethered bis-CPA **77b** was employed for fullerene functionalization, a single isomer of the bisadduct **80** was obtained in 16% yield. In the reaction of C_{60} with the six-carbon-tethered bis-CPA **77c**, the double addition proceeded especially cleanly to afford a single isomer **81** in 41% yield.

In contrast, Suzuki et al. reported that reacting C_{60} with the unsubstituted CPA 4,9-dioxaspiro[2.5]oct-1-ene (**82**) in toluene gave the [2 + 3] cycloadduct **83** in 66% based on the reacted C_{60}, as shown in Scheme 24 [45]. Subsequent hydrolysis of **83** resulted in the formation of the cyclopentenone-fused derivative **84** in 70%.

The reactions of C_{60} with α-dicarbonyl compounds such as acenaphthenequinone (**85a**), aceanthrenequinone (**85b**), and *N*-alkylisatin (**85c**: R = $-CH_3$, $-CH_2CH{=}CH_2$, $-C(O)CH_3$) in the presence of tris(diethylamino)phosphine in 1,2-DCB resulted in the formation of methanofullerenes **86** in 20–46% yields, as shown in Scheme 25 [46]. These reactions proceeded via deoxygenation of the dicarbonyl compound by the phosphine and are likely to involve generation of the corresponding α-ketocarbenes in situ.

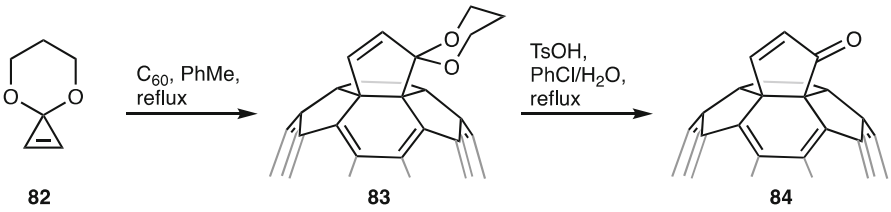

Scheme 24 Reaction of C_{60} with 4,9-dioxaspiro[2.5]oct-1-ene

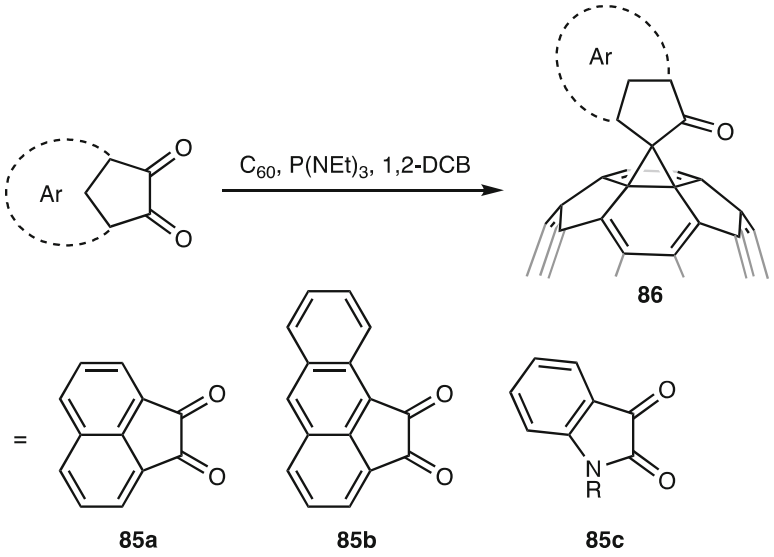

Scheme 25 Reaction of C_{60} with α-dicarbonyl compounds

Photolysis of *anti*-dodecaisopropyltricyclo[4.2.0.0^{2,5}]octasilane (**87**) in the presence of C_{60} and a trace amount of CS_2 afforded the spiro-linked methanofullerene derivative **90** in 20%, as shown in Scheme 26 [47]. This reaction might involve photochemical generation of cyclotetrasilene intermediate **88** and subsequent addition to CS_2 to yield *S*-heterocyclic carbene (SHC) **89**. Subsequent [2 + 1] cycloaddition of **89** to C_{60} would lead to the formation of **90**.

Kako et al. demonstrated that SHC addition could be achieved by the cycloaddition of disilenes and digermenes to CS_2 in the presence of C_{60}, as shown in Schemes 27 and 28 [48]. The disilenes were prepared by the photolysis of trisilane **91** in benzene using a low-pressure mercury arc lamp. The resulting solution containing the disilene Mes_2Si: (**92**) was added to a solution of C_{60} and CS_2 in benzene, giving the SHC adduct **93** in 36% yield. Compared with the photolysis of trisilanes to generate the disilenes, which requires short-wavelength UV irradiation, long-wavelength UV irradiation is sufficient to photolyze cyclotrigermenes to the

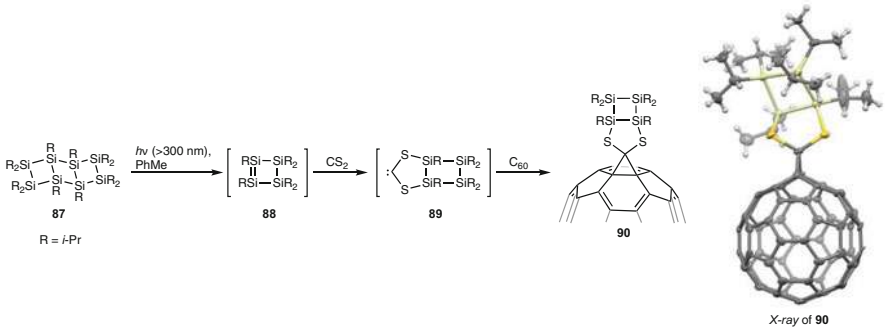

Scheme 26 Reaction of C_{60} with octasilane compounds in the presence of CS_2

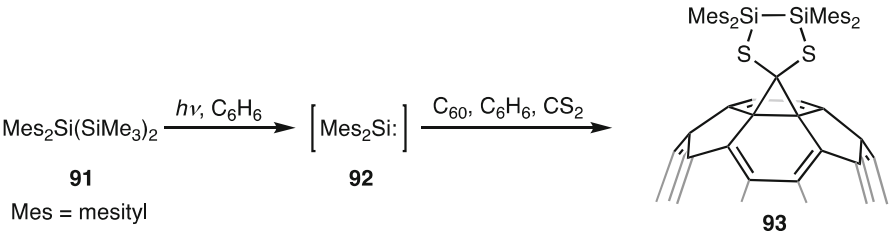

Scheme 27 Reaction of C_{60} with dimesitylsilylene in the presence of CS_2

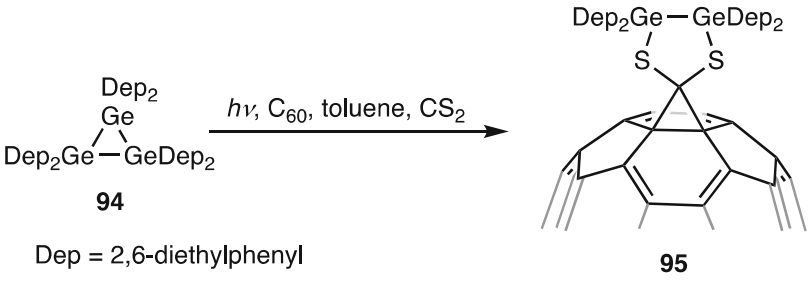

Scheme 28 Reaction of C_{60} with di(2,6-diethylphenyl)germylene in the presence of CS_2

corresponding digermenes. Therefore, one-pot synthesis of the Ge-containing SHC adduct is possible. In fact, photoirradiation of a toluene solution of C_{60} containing cyclotrigermene **94** and C_{60} using a medium-pressure mercury arc lamp afforded the corresponding SHC adduct **95** in 22% yield. The SHC addition reaction to $Sc_3N@C_{80}$ afforded the corresponding [6,6]-open fulleroid derivative $Sc_3N@C_{80}(CS_2E_2Mes_4)$ (E = Si, Ge).

Bazan reported that treatment of C_{60} or C_{70} with *N*-heterocyclic carbene (NHC) 1,3-bis(diisopropylphenyl)imisol-2-ylene (IDipp; **96**) in 1,2-DCB at ambient temperature for 24 h afforded zwitterionic Lewis acid–base adducts such as **97**, as shown in Scheme 29 [49]. X-ray crystallographic analyses suggested that the NHC was

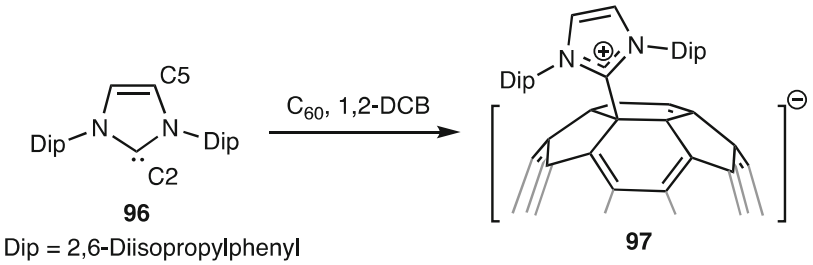

Scheme 29 Reaction of C_{60} with an *N*-heterocyclic carbene

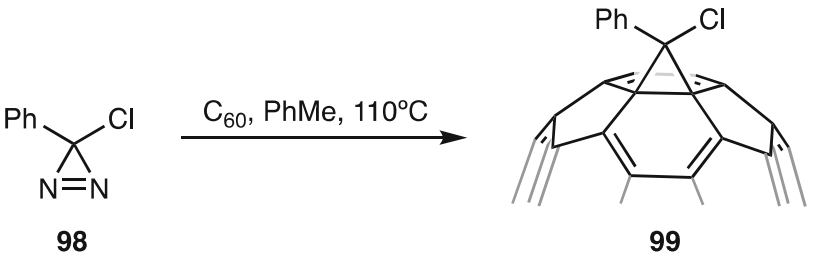

Scheme 30 Reaction of C_{60} with chlorophenyldiazirine

singly bonded to the fullerene surface. In the C_{70}–NHC adduct, the NHC group was regioselectively added to a carbon at one pole of the C_{70} cage. On the other hand, reaction of $Sc_3N@C_{80}$ with **96** afforded a singly bonded derivative, [6,6,6]-$Sc_3N@C_{80}$-IDipp, in which the addendum bonded to the cage with its "abnormal" carbene center C5 instead of the normal site C2 possibly because of the steric congestion [50].

Photolysis and thermolysis of diazirines generate diazo compounds and carbenes as reactive intermediates. These species react with fullerenes in different manners. The reactivity of diazo compounds, which are regarded as 1,3-dipoles and undergo [3 + 2] cycloadditions, is described in a later section. Reactions of carbenes with C_{60} afford [2 + 1] cycloaddition to yield the corresponding methanofullerenes. For instance, thermal reaction of C_{60} with chlorophenyldiazirine (**98**) in toluene afforded chlorophenylcarbene adduct **99** exclusively in 37% yield, as shown in Scheme 30 [51]. An overview of carbene additions to fullerenes can be found in a review by Yamada et al. [52]

Silylene addition to C_{60} was reported by Akasaka et al. Bis(2,6-diisopropylphenyl)silylene Dip_2Si: (**101**; Dip = 2,6-diisopropylphenyl) was generated in situ by photolysis of $Dip_2Si(SiMe_3)_2$ (**100**) with a low-pressure mercury lamp in a toluene solution of C_{60}, as shown in Scheme 31 [53]. $C_{60}(SiDip_2)$ (**102**) was obtained in 58% yield after flash chromatography. The addition of silylene to C_{70} afforded two isomers of $C_{70}(SiDip_2)$ in a 2:1 ratio. NMR spectroscopic studies suggested that the silylene addition took place at the a–b bond in the major kinetic

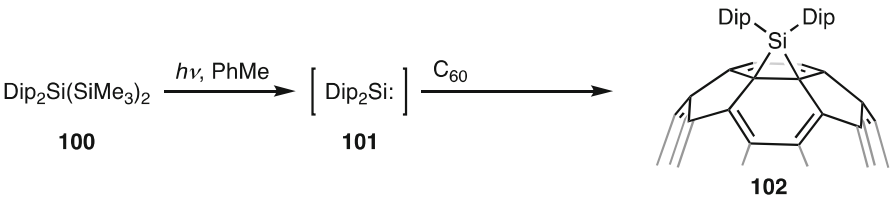

100 101 102

Scheme 31 Reaction of C_{60} with diisopropylsilylene

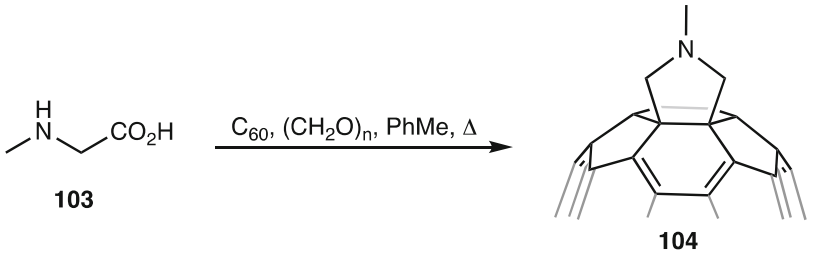

103 104

Scheme 32 Prato reaction of C_{60} with sarcosine and paraformaldehyde

product and at the c–c bond in the minor product based on symmetry criteria. Theoretical calculations suggested that the two isomers had similar energies [54].

1,3-Dipolar Cycloadditions

The 1,3-dipolar cycloaddition is one of the most utilized reactions for fullerene functionalization because of its wide applicability. The 1,3-dipoles are generally prepared in situ, as they are highly reactive under ambient conditions. Prato et al. published the first report of 1,3-dipolar cycloaddition to fullerenes in 1993, in which azomethine ylides generated in situ from paraformaldehyde and glycine were reacted with C_{60} to afford pyrrolidine ring-annulated fullerenes (referred to as pyrrolidinofullerenes or fulleropyrrolidines) [55, 56]. Accordingly, these reactions to form pyrrolidinofullerenes are also known as Prato reactions. In a general procedure, a mixture of C_{60}, *N*-methylglycine (**103**; also known as sarcosine, 2 equiv.), and paraformaldehyde (5 equiv.) was heated at reflux in toluene for 2 h to afford *N*-methylpyrroidinofullerene $C_{60}(CH_2)_2NMe$ (**104**) in 41% yield (conv. y., 82% based on C_{60} consumed) after chromatography, as shown in Scheme 32. Since this discovery, a variety of pyrrolidinofullerenes bearing functional groups have been synthesized by using substituted glycines in Prato reactions.

Appropriate substitution of azomethine ylides with hydroxyl groups results in the nucleophilic addition of hydroxyl oxygen to the C = C bond of C_{60} to afford the cyclized products. Martín et al. reported that heating a mixture of C_{60}, **103**, and 2,6-dihydroxyphenyl methyl ketone (**105**) in chlorobenzene afforded

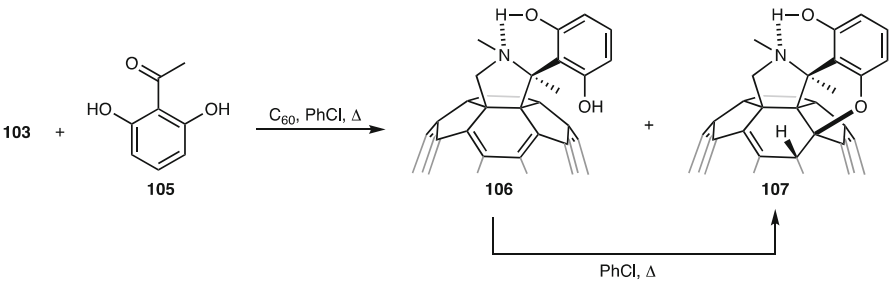

Scheme 33 Reaction of C_{60} with sarcosine and 2,6-dihydroxyphenyl methyl ketone

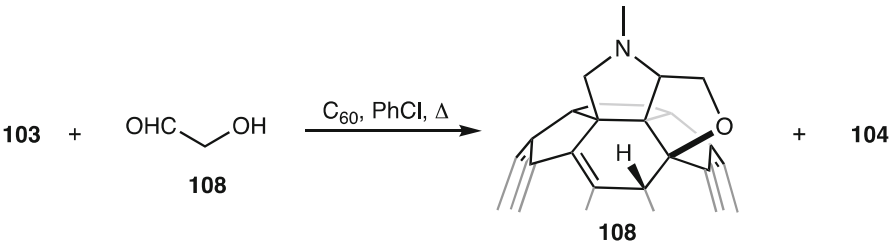

Scheme 34 Reaction of C_{60} with sarcosine and hydroxyacetaldehyde

pyrrolidinofullerene **106** and *cis*-1 bicyclic-fused fullerene derivative **107**, as shown in Scheme 33 [57]. Compound **106** is converted into **107** through intramolecular nucleophilic addition of one hydroxy group to the adjacent C = C bond of C_{60}. The methyl group on C2 of the pyrrolidine ring is required for the cyclization process. Additionally, the hydrogen bond between the second hydroxy group and the nitrogen atom of the pyrrolidine ring facilitate the formation of a favorable geometry for the nucleophilic attack.

The reaction of C_{60} with **103** and hydroxyacetaldehyde (**108**) in refluxing chlorobenzene also afforded the corresponding cyclized derivative **108** in 25% yield along with 40% **104**, as shown in Scheme 34 [58]. The corresponding hydroxymethylated pyrrolidinofullerene intermediate was not observed under the applied reaction conditions. The mechanism of the formation of **104** in this reaction is unclear.

Sulfur-containing cyclized derivative **110** was synthesized in 7% yield, accompanied by the undesired formation of 2-methylpyrrolidinofullerene **111** in 40% yield, via reaction of C_{60} with **103** and 1,4-dithiane-2,5-diol (**109**) in chlorobenzene at reflux; **109** decomposed thermally to form thioacetaldehyde in situ, as shown in Scheme 35 [59]. The formation of the corresponding pyrrolidinofullerene intermediate was not observed even at low temperatures.

The reaction of C_{60} with the propargyl-containing glycine derivatives **112** and formaldehyde in chlorobenzene afforded the corresponding pyrrolidinofullerenes **113**, which can be considered to be fuller-1,6-enynes [60]. When R^1 was H or TMS, the thermal treatment of **113** led to the formation of stable cyclobutene

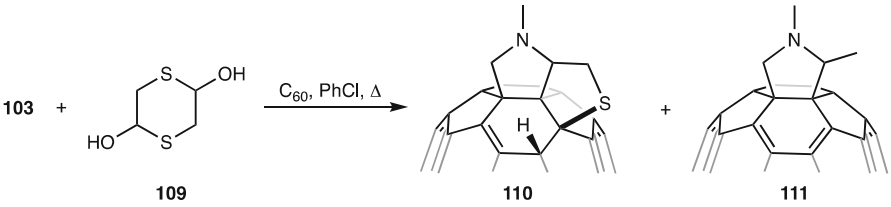

Scheme 35 Reaction of C_{60} with sarcosine and 1,4-dithiane-2,5-diol

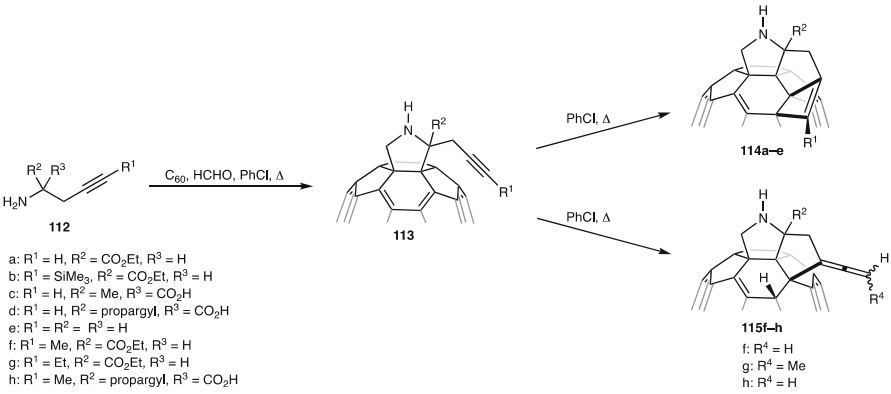

Scheme 36 Reaction of C_{60} with propargyl-containing glycine derivatives and formaldehyde

substructures on the fullerene surfaces to form **114** through a thermal intramolecular [2 + 2] cyclization mechanism, as shown in Scheme 36. In contrast, replacement of the H atom or TMS group in **113** with a methyl or ethyl group resulted in a completely different reaction outcome [61]. In fact, thermal treatment of fuller-1,6-enynes bearing an alkyl group on the terminal carbon of the alkyne moiety **113f-h** afforded the allene-containing fullerene derivatives **115** through an intramolecular ene process. Similarly, intramolecular Pauson–Khand reactions of fuller-1,6-yne and fuller-1,7-yne derivatives have also been reported by Martín et al. [62, 63]

The reaction of azomethine ylides with multiple aromatic rings with fullerenes yields fullerene derivatives with nitrogen-containing polyaromatic hydrocarbon units. Nozaki et al. reported the generation of isoquinolino[4,3,2-*de*]phenanthridine in situ by deprotonation of the corresponding precursor, iminium chloride **116**, with triethylamine under inert conditions. Reaction of the ylide with C_{60} at 40 °C afforded the corresponding adduct **117** in 65% yield, as shown in Scheme 37 [64].

Thermal ring opening of aziridines and thermal decarboxylation of oxazolidinones are also useful for the facile preparation of azomethine ylides for subsequent cycloaddition to form pyrrolidinofullerenes [55]. The reaction of C_{60} and methyl 1-benzylaziridine-2-carboxylate (**118**) in toluene under reflux led to the isolation of pyrrolidinofullerene **119** in 40% yield, as shown in Scheme 38. For aziridines, the introduction of electron-withdrawing substituents such as ester groups

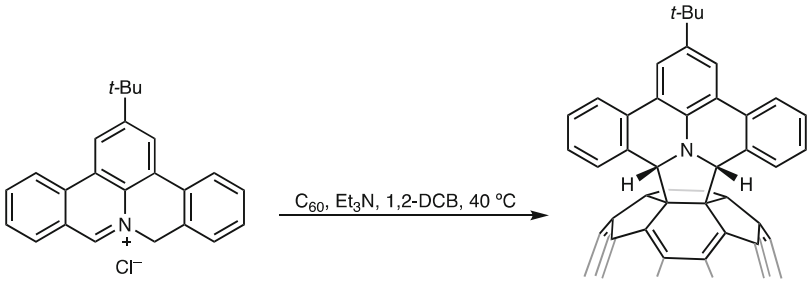

Scheme 37 Reaction of C_{60} with the isoquinolino[4,3,2-*de*]phenanthridine precursor

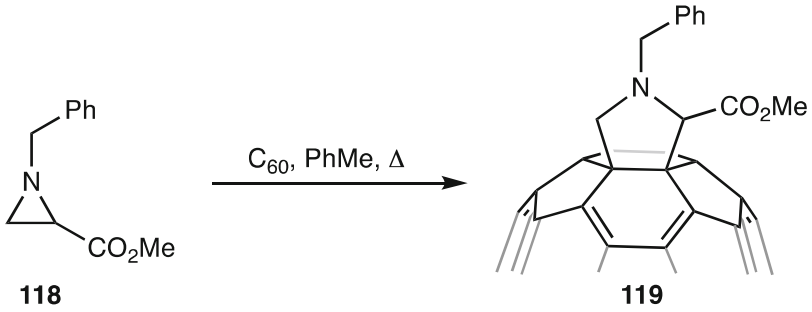

Scheme 38 Reaction of C_{60} with aziridine

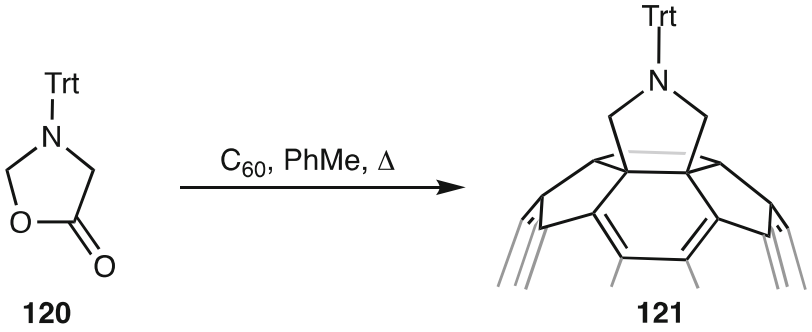

Scheme 39 Reaction of C_{60} with oxazolidinone

to the aziridine carbon stabilizes the resulting 1,3-dipoles. The reaction of C_{60} with 3-triphenylmethyl-5-oxazolidinone (**120**; Trt = triphenylmethyl) in toluene at reflux yielded pyrrolidinofullerene **121** in 39% as shown in Scheme 39.

Carbonyl ylides are also applicable as 1,3-dipoles for fullerene functionalization. Thermal treatment of tetracyanoethylene oxide (TCNEO) generates carbonyl ylides via ring opening. The intermediates react with fullerenes to afford the corresponding cycloadducts bearing tetracyanohydrofuran structures [65].

The addition of nitrile oxides to fullerenes gives fullerene-fused isoxazoline heterocycles known as isoxazolofullerenes. Nitrile oxides can be prepared via the dehydration of primary nitroalkanes. Meier reported that treatment of C_{60} with propionitrile oxide ($Et–C{\equiv}N^{+}–O^{-}$) generated in situ from nitropropane, phenylisocyanate, and triethylamine resulted in the formation of ethylisoxazoline-C_{60} in 29% yield after purification by preparative GPC [66]. Nitrile oxides can also be prepared in situ by dechlorination of hydroximoyl chlorides with a mild base such as triethyl amine or sodium bicarbonate in toluene [67, 68]. For instance, addition of 1 equiv. of triethylamine to 1 equiv. of phenylhydroximoyl chloride in toluene led to the formation of phenylisoxazoline-C_{60} in 36% yield after GPC separation. Martín et al. constructed a variety of C_{60}–electron acceptor dyads via nitrile oxide chemistry [69]. As shown in Scheme 40, nitrile oxide precursor **123** was obtained from the reaction of formylhydroquinone (**122**) with hydroxylamine hydrochloride. Further chlorination of **123** with *N*-chlorosuccinimide (NCS) and subsequent dehydrochlorination of the formed hydroximoyl chloride in the presence of pyridine yielded the corresponding nitrile oxide, which underwent [3 + 2] cycloaddition with C_{60} to afford isoxazole fullerene **124** in 19% yield. Further oxidation of **124** with dichlorodicyano-*p*-benzoquinone (DDQ) produced benzoquinone–C_{60} dyad **125** in 88% yield.

Yoshida et al. reported that reaction of C_{60} with *N*-(α-chlorobenzylidene)-*N*′-phenylhydrazine in the presence of triethylamine in benzene at reflux led to the formation of the 1,3-diphenyl-2-pyrazoline-fused derivative in 48% yield; the in situ formation of 1,3-diphenyl nitrilimine was involved in this process [70]. Langa et al. synthesized pyrazolofullerenes in two steps from the corresponding aldehydes, as shown in Scheme 41 [71]. Hydrazones **127** were prepared in 68–83% yield by the reaction of the corresponding aldehydes **126** with 4-nitrophenylhydrazine in the presence of acetic acid using ethanol as the solvent. Treatment of **127** with *N*-bromosuccinimide (NBS) in chloroform yielded the corresponding bromo-derivative as a solid after evaporation. Subsequent addition of a toluene solution of C_{60} and triethylamine to the solid and microwave irradiation afforded pyrazolinofullerenes **128** in 25–42% yield after purification by silica gel column chromatography.

Thermal reaction of C_{60} with bis(trimethylsilylmethyl) sulfoxide (**129**) afforded the tetrahydrothiophene-annulated fullerene derivative **130**, as shown in Scheme 42 [72]. The reaction involved in situ generation of the thiocarbonyl ylide intermediate through a sila-Pummerer rearrangement and subsequent 1,3-dipolar cycloaddition to

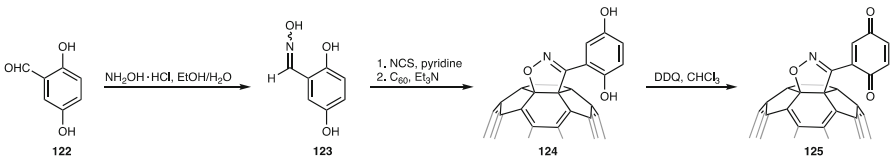

Scheme 40 Synthesis of benzoquinone–C_{60} dyad functionalized with an isoxazoline heterocycle

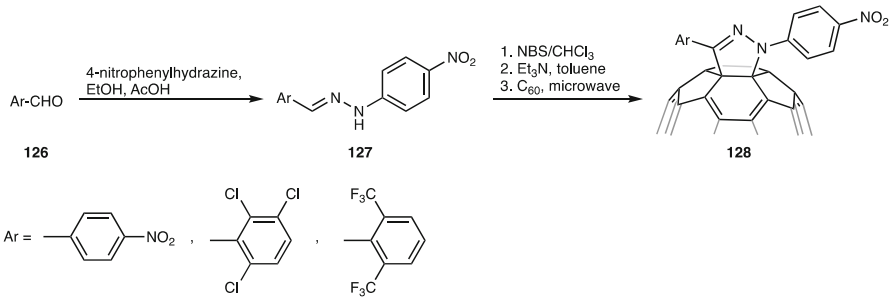

Scheme 41 Two-step synthesis of pyrazolofullerenes from aldehydes

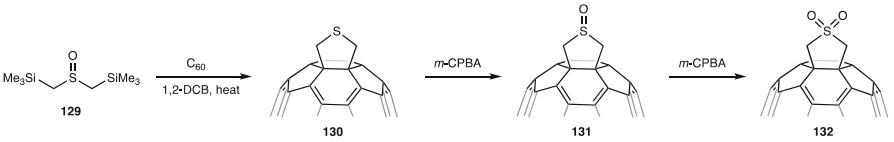

Scheme 42 Reaction of C_{60} with bis(trimethylsilylmethyl) sulfoxide and subsequent oxidation

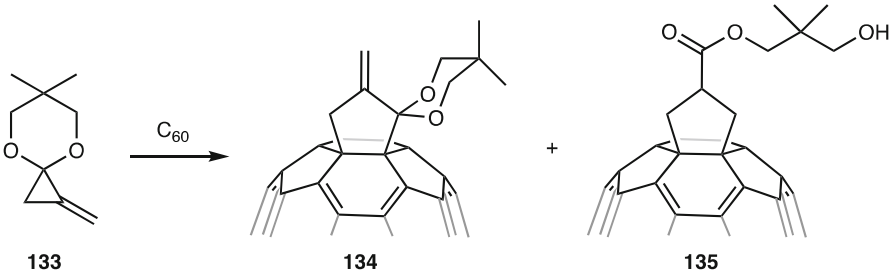

Scheme 43 Reaction of C_{60} with methylenecyclopropanone ketal

C_{60}. The tetrahydrothiophene-annulated derivative was converted into sulfoxide **131** and then to sulfone **132** by oxidation with *m*-chloroperoxybenzoic acid (*m*-CPBA).

The chemical reactivity of C_{60} toward trimethylenemethane (TMM) was investigated by Wudl and co-workers [73]. A solution of methylenecyclopropanone ketal **133** in 1,2-DCB was heated at 70 °C in the presence of C_{60} to afford alkylidenecyclopropane-fused derivative **134** and ester **135** in 34% and 27% yields, respectively, along with 35% unreacted C_{60}. The latter product was probably produced by silica gel-catalyzed hydrolysis of the ketene acetal (Scheme 43).

Thermal reactions of diazo compounds with C_{60} afford [3 + 2] cycloadditions to give the corresponding pyrazoline derivatives, which easily undergo N_2 extrusion to afford the corresponding methanofullerenes and fulleroids. To date, many kinds of diazo compounds, including diazoalkanes, diazoketones, diazoesters, diazopyruvates, diazoamides, diazophosphonates, diazothioates, and silyl diazomethanes, have been investigated to clarify their reactivities toward fullerenes [52]. When

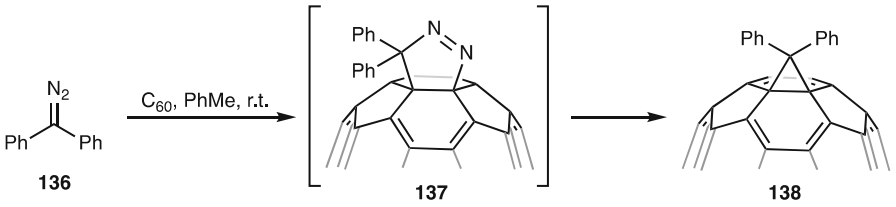

Scheme 44 Reaction of C_{60} with diphenyldiazomethane

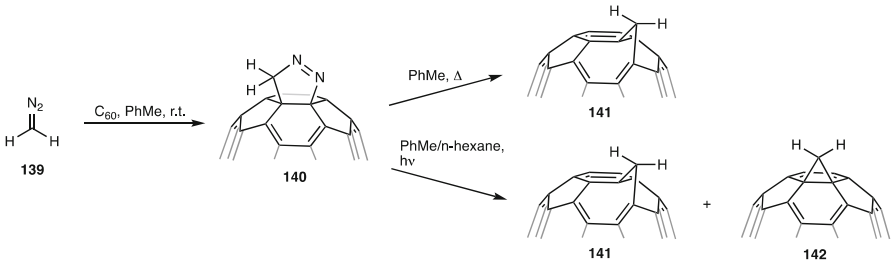

Scheme 45 Reaction of C_{60} with diazomethane

unsymmetrical diazo compounds are used, three regioisomers, one methanofullerene and two fulleroids, can be formed. The reaction conditions, stability of the pyrazoline derivatives, and formation ratio of the products depend strongly on the type of diazo compound used. For instance, the reaction of C_{60} and diphenyldiazomethane (**136**) proceeds at ambient temperature in toluene to yield the methanofullerene **138** exclusively via the formation of unisolable pyrazoline intermediate **137**, as shown in Scheme 44 [74–76].

In the reaction of C_{60} and the parent diazomethane CH_2N_2 (**139**), pyrazoline intermediate **140** can be isolated [77, 78]. Thermolysis of **140** afforded the fulleroid **141** exclusively in quantitative yield. On the other hand, photolysis yielded a 4:3 mixture of **141** and methanofullerene **142**, as shown in Scheme 45. The two regioisomers do not interconvert photochemically or thermally. Thermolysis was proposed to occur through an orbital symmetry-controlled [π2s + π2s + σ2s + σ2a] rearrangement and subsequent valence tautomerization to afford the fulleroid, while the photolysis proceeds via a diradical mechanism.

The use of tosylhydrazones instead of hazardous diazo compounds is an alternative protocol. In fact, diazo species can be prepared in situ by the thermolysis of lithium or sodium salts of tosylhydrazones. Diethynylmethanofullerenes were prepared by the reaction of C_{60} with the corresponding tosylhydrazones. 6,6-Phenyl–C_{61}–butyric acid methyl ester, known as [60]PCBM, can be prepared using this approach, as shown in Scheme 46 [79]. Tosylhydrazone **144** was prepared reacting ketone **143** with *p*-toluenesulfonylhydrazide and added to a 1,2-DCB solution of C_{60} in the presence of NaOMe and pyridine under heating to give fulleroid **145** as the kinetically favored product. Subsequent thermal rearrangement afforded [60]PCBM (**146**).

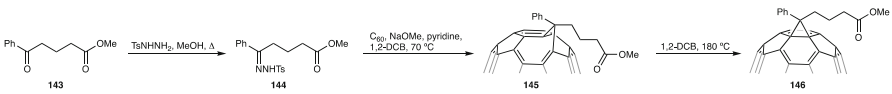

Scheme 46 Synthesis of [60]PCBM

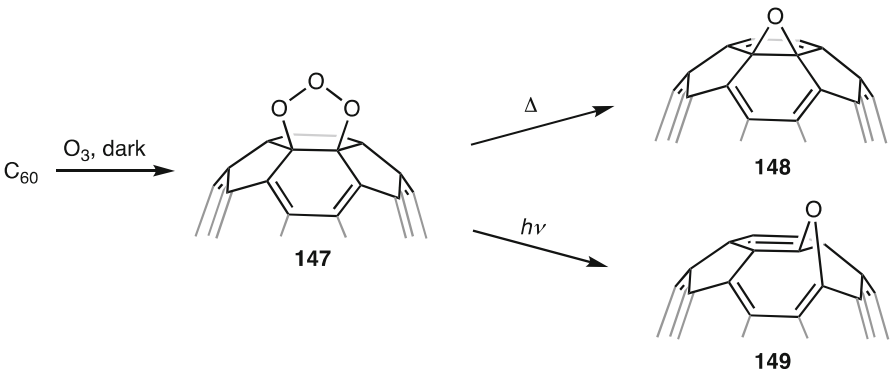

Scheme 47 Ozonation of C_{60}

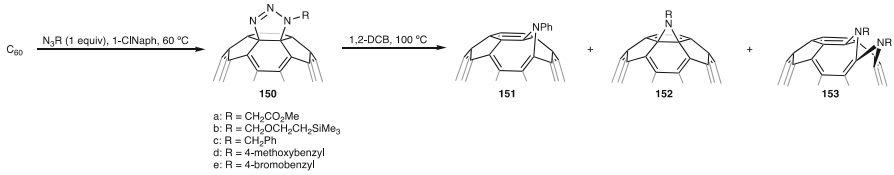

Scheme 48 Reaction of C_{60} with alkylazides

The reaction of C_{60} with ozone resulted in the formation of the [6,6]-closed epoxide $C_{60}O$ (**148**) [80]. The intermediate in the ozonation of C_{60} was characterized as 1,3-dipolar cycloadduct (i.e., ozonide) $C_{60}O_3$ (**147**) via HPLC kinetic studies. Weisman et al. succeeded in isolating **147** by ozonating a solution of C_{60} in *o*-xylene at –16 °C in the dark and subsequent HPLC separation on a PYE HPLC column cooled to 0 °C under dark conditions [81]. Thermolysis of **147** gave **148**, while photolysis afforded the [5,6]-open oxidoannulene $C_{60}O$ (**149**) (Scheme 47).

Azafulleroids and aziridinofullerenes were prepared by reaction of C_{60} with azides through 1,3-dipolar cycloaddition followed by N_2 extrusion. Treatment of a concentrated solution of C_{60} in 1-chloronapthalene with an equimolar amount of methyl azidoacetate at 60 °C afforded the corresponding triazoline intermediate **150** in 62% yield, as shown in Scheme 48 [82, 83]. Thermal treatment of **150a** in 1,2-DCB at 100 °C yielded azafulleroid **151a** (24%), methanofullerene **152a** (4%), and bisadduct **153a** (13%) together with C_{60} (22%).

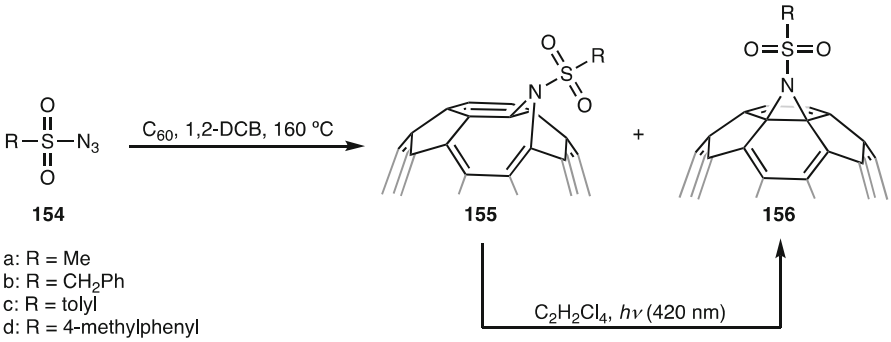

Scheme 49 Reaction of C_{60} with sulfonyl azides

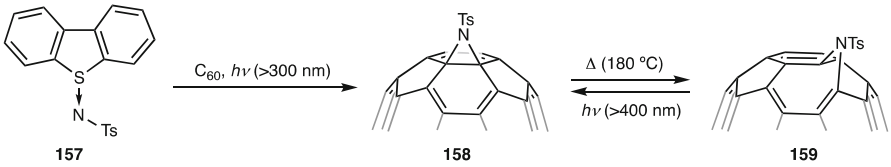

Scheme 50 Reaction of C_{60} with *N*-tosylsulfilimine

Sulfonylated azafulleroids **155** and aziridinofullerenes **156** were prepared by thermal reaction of C_{60} with sulfonyl azides **154** in 1,2-DCB at 160 °C, as shown in Scheme 49 [84]. The ratio of the two products depended on the substituents. The addition of arylated sulfonyl azides resulted in the exclusive formation of azafulleroids, whereas the addition of alkylated sulfonyl azides afforded both azafulleroids and aziridinofullerenes in similar yields. The azafulleroids were converted to aziridinofullerenes by photoirradiation ($\lambda = 420$ nm).

Nitrene Additions

Photochemical reaction of C_{60} with *N*-tosylsulfilimine **157** in toluene using a high-pressure mercury lamp (>300 nm) resulted in the formation of tosylated aziridinofullerene **158** with 80% conversion, as shown in Scheme 50 [85]. The aziridinofullerene was thermally converted to the corresponding azafulleroid **159** by heating at 180 °C for 10 h in 1,2-DCB. Reverse isomerization of the azafulleroid to the aziridinofullerene can be accomplished by photoirradiation using a halogen lamp with a filter solution (cutoff <400 nm).

Thermal reaction of C_{60} with diphenylsulfilimines **160** in 1,2-DCB at 160–170 °C afforded nitrene addition to form the corresponding monoadducts C_{60}(NR) (**161**), bisadducts $C_{60}(NR)_2$ (**162**), and trisadducts $C_{60}(NR)_3$ (**163**) featuring aziridine substructures on the fullerene surface, as shown in Scheme 51 [86]. When (*S*,*S*)-diphenyl-*N*-methylsulfilimine (**160b**) was employed for the reaction, **161b** and

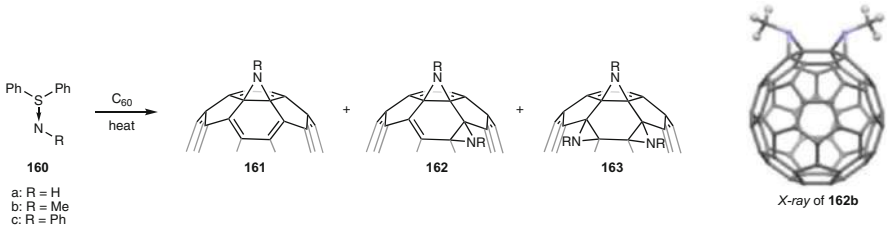

Scheme 51 Reaction of C_{60} with diphenylsulfilimines

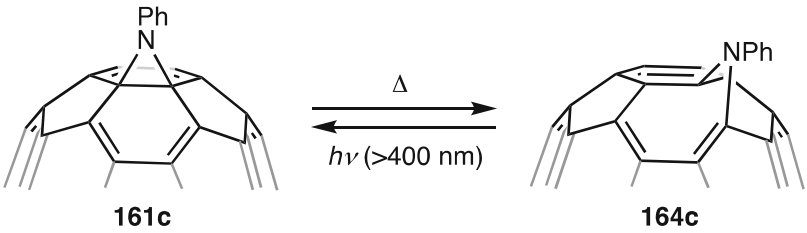

Scheme 52 Interconversion between aziridinofullerene and azafulleroid

162b were obtained in 53% and 36% yield based on the consumed C_{60}, respectively. The reaction of C_{60} with (*S*,*S*)-diphenylsulfilimine (**160a**) afforded **161a**, **162a**, and **163a** in 22%, 40%, and 12% yield, respectively, based on the consumed C_{60}. In these reactions, the sulfilimines act as nucleophiles, and the reaction involves Michael-type cycloadditions. In addition, the bisadditions and trisadditions were regioselective, and single isomers were obtained. When less reactive (*S*,*S*)-diphenyl-*N*-phenylsulfilimine (**160c**) was applied to the reaction with C_{60}, two isomers of the monoadduct, aziridinofullerene **161c** and the corresponding azafulleroid **164c**, were obtained as a mixture in 67% yield based on the consumed C_{60}; the **160c**:**161c** ratio was estimated to be 2.3:1 by HPLC analysis. Aziridinofullerene **161c** was quantitatively rearranged to **164c** by heating at 170 °C, and **164c** was converted to **161c** by photoirradiation using a halogen lamp with a filter solution (cutoff <400 nm), similarly to **158**/**159** in Scheme 52.

Phosphine-Mediated Reactions

Murata et al. reported that reaction of C_{60} with dimethyl acetylenedicarboxylate (DMAD; **165**) and triphenylphosphine in toluene at 110 °C for 120 h afforded methanofullerene **166** bearing a zwitterionic substructure in 61% yield (conv. y., 97%), as shown in Scheme 53 [87]. The reaction involves the formation of a resonance-stabilized carbene–ylide intermediate. Later, Cheng et al. found that the reaction of C_{60} with phosphorus triamides $P(NR_2)_3$ in 1,2-DCB gave more the polar fullerene derivatives **168** bearing a phosphoramidate group (<6% yield) in addition to methanofullerenes **167** (30–39% yield), as shown in Scheme 54 [88]. **168** was

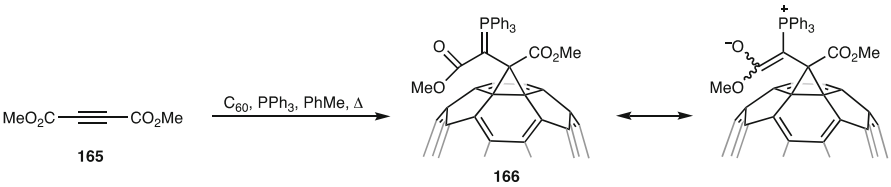

Scheme 53 Reaction of C_{60} with dimethyl acetylenedicarboxylate in the presence of triphenylphosphine

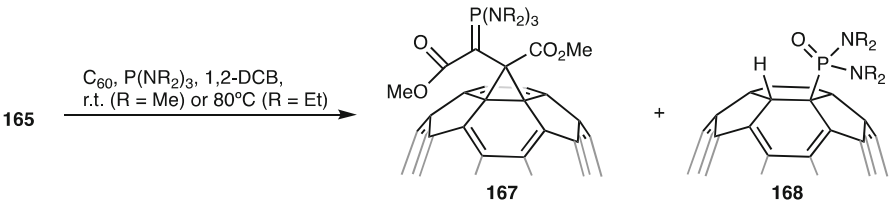

Scheme 54 Reaction of C_{60} with dimethyl acetylenedicarboxylate in the presence of phosphorus triamides

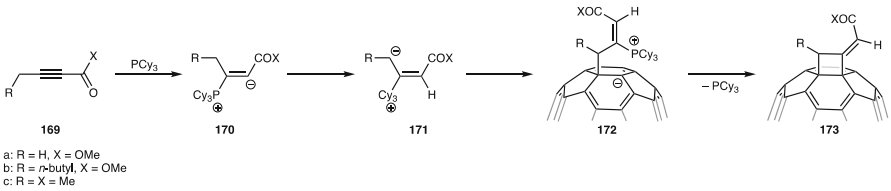

Scheme 55 Reactions of C_{60} with alk-2-ynoates and alk-2-ynones in the presence of tricyclohexylphosphine

formed by the direct addition of $P(NR_2)_3$ to C_{60}. In fact, reaction of C_{60} with $P(NR_2)_3$ in the absence of DMAD followed by hydrolysis during silica gel flash chromatography afforded **168** in 7–15%.

Reaction of C_{60} with methyl but-2-ynoate (**169a**) in the presence of PCy_3 at ambient temperature gave alkylidene cyclobutanofullerene **173a** in 23% yield, along with 76% unreacted C_{60}, as shown in Scheme 55 [89]. The ester group was determined to be *cis* to the methylene group on the cyclobutane structure based on the highly deshielded ^{1}H NMR signal of the alkenic proton at 7.82 ppm. Reaction of C_{60} with methyl oct-2-ynoate (**169b**) in the presence of PCy_3 at 70 °C also afforded the corresponding alkylidene cyclobutanofullerene **173b** in 13% yield along with unreacted C_{60} (74%). Hex-3-yn-2-one (**169c**) was reactive toward C_{60} in the presence of PCy_3 at 70 °C, giving the corresponding alkylidene cyclobutanofullerene **173c** in 17% along with 62% unreacted C_{60}, although the adduct was much less soluble than the other alkylidene cyclobutanofullerenes in common NMR solvents. These reactions involve initial nucleophilic attack of the phosphine at the β-positions of the 2-ynoates. The resulting dipolar intermediates **170** undergo a 1,3-proton shift

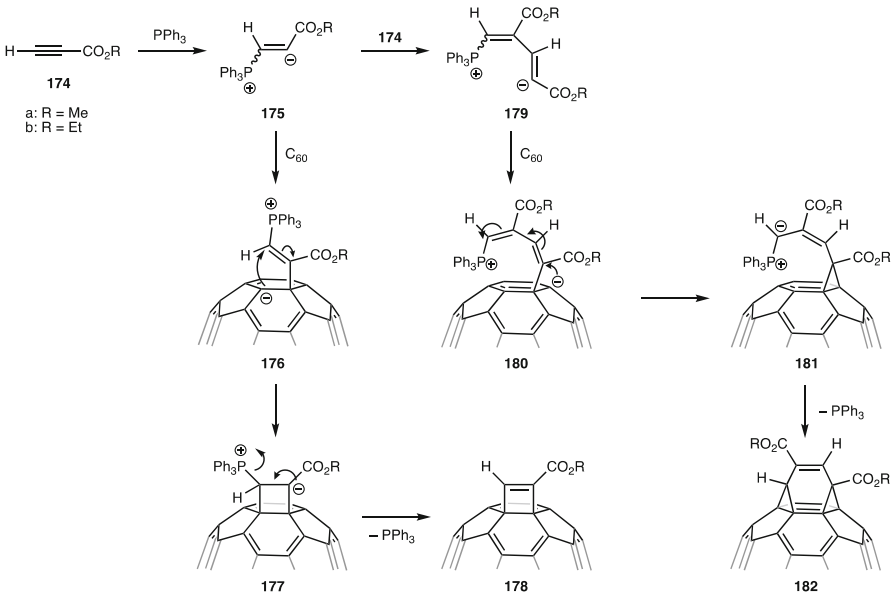

Scheme 56 Reactions of C_{60} with alkyl propiolates in the presence of triphenylphosphine

from the γ- to α-carbon to form γ-carbanions **171**. Nucleophilic addition of **171** to C_{60} and subsequent back-attack of the fullerenyl carbanion result in **173**. Intermediate **170** is expected to favor *cis* geometry between the phosphonium cation and the electron pair on the α-carbanion due to strong Coulomb attraction, consistent with the observed geometry of the alkylidene moiety in **173**.

The reaction of C_{60} with alkyl propiolates **174** in the presence of PPh_3 afforded ethenofullerenes **178** and bismethanofullerenes **182**, as shown in Scheme 56 [90]. The former derivative resulted from nucleophilic attack of zwitterionic intermediate **175** followed by elimination of the PPh_3 moiety. Alternatively, nucleophilic attack of **175** on a second alkyl propiolate molecule could take place prior to addition to the fullerene cage. Subsequent back-attack of the fullerenyl carbanion in the resulting fullerene intermediate **180** affords the first cyclopropanation to form **181**, and nucleophilic attack of the ylide moiety on the adjacent fullerene carbon results in the second cyclopropanation.

The phosphine (PR_3; R = Bu, Ph)-mediated reaction of C_{60} with buta-2,3-dienoates **183** or but-2-ynoates **184** in toluene at 80 °C afforded cyclopentene-fused fullerene derivatives **188** in 42–89% yield, as shown in Scheme 57 [91]. This reaction proceeds through [3 + 2] cycloaddition of the corresponding zwitterionic intermediate **185** to C_{60}, followed by proton transfer and subsequent elimination of the PR_3 moiety.

Reaction of C_{60} with (*E*)- or (Z)-alkyl arylpent-2-en-4-ynoates **189** in the presence of tricyclohexylphosphine ($P(cHx)_3$) yielded the corresponding cyclopentenofullerenes **196**, as shown in Scheme 58 [92]. The reaction proceeds in a chemo-,

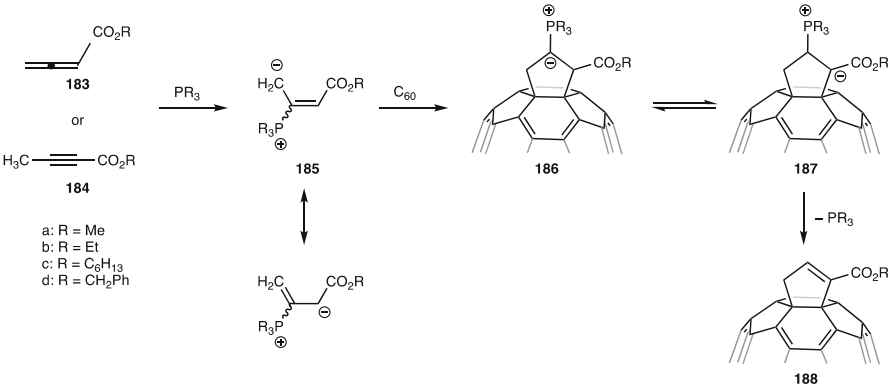

Scheme 57 Reactions of C_{60} with buta-2,3-dienoates or but-2-ynoates in the presence of phosphines

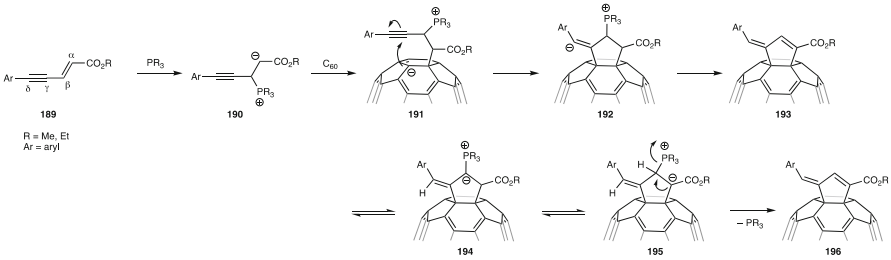

Scheme 58 Reactions of C_{60} with alkyl arylpent-2-en-4-ynoates

regio-, and stereoselective manner via the initial addition of the phosphine at the β-carbon of the enyne substrate and nucleophilic attack of the fullerenyl anion on the γ-carbon. The initial attack of PR_3 at the γ-carbon is prevented by the steric hindrance of the aryl group of the substrate. Subsequent proton transfer processes, followed by elimination of the PR_3 group, afforded the final product. The aryl ring remains *trans* to the C_{60} cage due to steric considerations.

The phosphine-mediated reactions of C_{60} with (*E*)-alkyl 5-substituted phenylpent-4-en-2-ynoates **197** afford different types of cyclopentenofullerenes **20**, as shown in Scheme 59 [93]. The reaction involves the initial addition of the PPr_3 group to the α-carbon of the substrate, followed by nucleophilic addition of the zwitterionic intermediate **198** to the C_{60} cage. Subsequent proton transfer and elimination of the PR_3 group give the final product.

[2 + 2] Cycloadditions

Compared to the numerous examples of [1 + 2], [3 + 2], and [4 + 2] cycloadducts, the syntheses of [2 + 2] cycloadducts have been limited. Several examples of

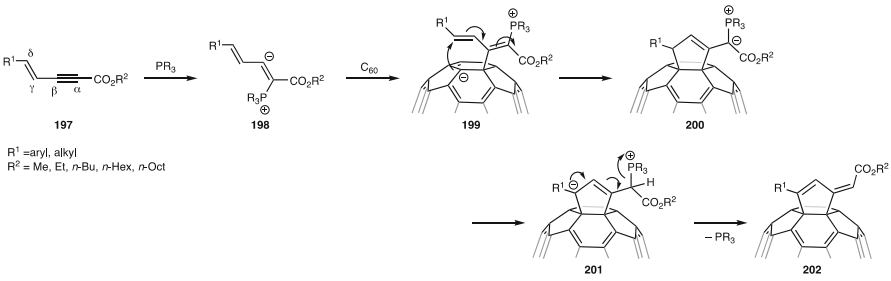

Scheme 59 Reactions of C_{60} with (*E*)-alkyl 5-substituted phenylpent-4-en-2-ynoates

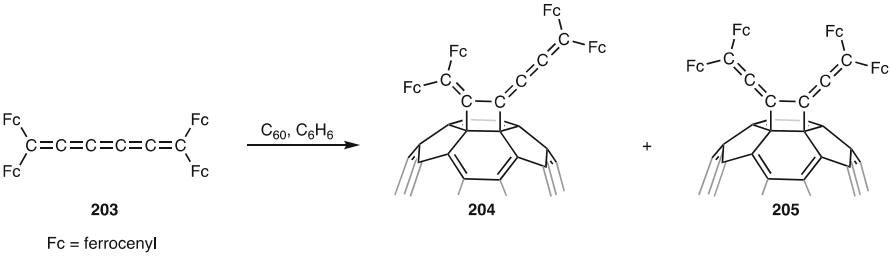

Scheme 60 Reaction of C_{60} with tetraferrocenyl[5]cumulene

photochemical [2 + 2] cylcloadditions of fullerenes are described in ▶ Chap. 11, "Radical Reaction and Photoreaction." Bildstein examined the reactivity of [5] cumulene derivatives toward C_{60} via formal [2 + 2] cycloaddition under thermal conditions. The results showed that tetraphenyl[5]cumulene did not react with C_{60}, while tetraferrocenyl[5]cumulene yielded two regioisomers of [2 + 2] cycloadducts, indicating that only very electron-rich [5]cumulenes are able to react with fullerenes [94]. The thermodynamic monoadduct **204** with [2 + 2] cycloaddition at the π-bonds of the C2–C3 carbons of the cumulene was obtained as the major product and isolated in 14% yield (conv. y., 68% based on the C_{60} consumed) by column chromatography on activated alumina with CS_2 as the eluent, as shown in Scheme 60. Purification of the minor product **205** with [2 + 2] cycloaddition at the π-bonds of the C3–C4 carbons of the cumulene failed, as it was immobilized on the column.

Thermal reaction of C_{60} with ketene acetal **206** in toluene proceeded at ambient temperature to afford the corresponding [2 + 2] cycloadduct **207** in 67% yield along with 25% recovered C_{60}, as shown in Scheme 61 [95]. The [2 + 2] cycloadduct was thermally stable, and cycloreversion was not observed upon heating at 100 °C. In contrast, hydrolysis of the cycloadduct proceeded under acidic conditions (10 equiv. of H_2SO_4 and 100 equiv. of H_2O in a 1:1 1,4-dioxane/toluene mixture at 90 °C or 10 equiv. of *p*-toluenesulfonic acid in refluxing toluene) to give the corresponding 1,2-organofullerene **208**.

Benzyne additions to fullerenes were first reported by Cooks et al. in 1992 [96]. Treatment of a benzene solution of C_{60} and isoamyl nitrite with anthranilic

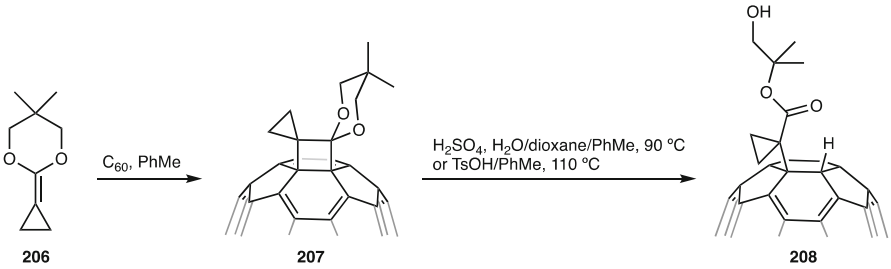

Scheme 61 Reaction of C_{60} with ketene acetal and subsequent hydrolysis

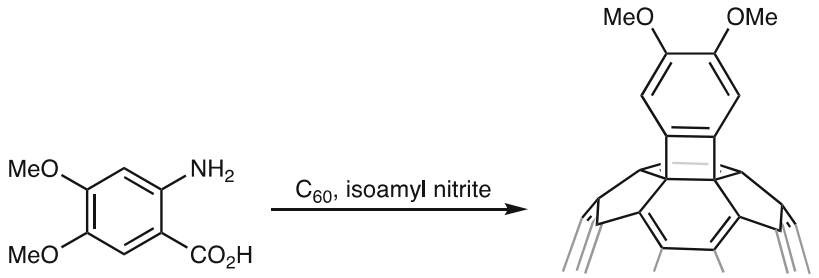

Scheme 62 Benzyne addition to C_{60}

acid at ambient temperature afforded benzyne adducts $C_{60}(C_6H_4)_n$ (n = 1–4); the monoadduct was separated from the reaction mixture by HPLC using a semi-preparative C_{18} column, although the yield was not given. Nogami et al. reported the synthesis of $C_{60}(C_6H_2OMe_2)$ (**210**) via reaction of C_{60} with 4,5-dimethoxybenzyne, which was prepared in situ from the precursors 2-amino-4,5-dimethoxyanthranilic acid (**209**) and isoamyl nitrite, in 15% yield, as shown in Scheme 62 [97]. Nishimura et al. studied benzyne bisadditions to C_{60}. When 4 equiv. of the benzyne precursors were employed for benzyne addition to C_{60} in toluene, eight regioisomers of the bisadduct $C_{60}(C_6H_2OMe_2)_2$ were obtained and characterized [98]. The regioisomeric ratio of the *trans*-1, *trans*-2, *trans*-3, *trans*-4, *e*, *cis*-3, *cis*-2, and *cis*-1 bisadducts was determined to be 1:12:15:10:25:3:14:20. Benzyne addition to C_{70} by treatment with anthranilic acid and isoamyl nitrite in benzene resulted in the formation of four isomers of the monoadduct $C_{70}(C_6H_4)$ in a 42:35:13:10 ratio [99]. Separation of these isomers was achieved by multi-step HPLC using Buckyclutcher and Buckyprep columns. The addition positions were assigned as a–b, c–c, d–d, and d–e, in descending order of yield. Benzyne additions are also applicable for functionalization of EMFs such as La@C_{82} [100] and Sc_3N@C_{80} [101]. In the former case, the unexpected addition of NO_2 radical and two benzynes led to the formation of La@$C_{82}(C_6H_4)_2NO_2$ as the diamagnetic product.

Ryu et al. reported the reaction of C_{60} with phenyl-substituted allenol ester **211** in 1,2-DCB at 80 °C to afford alkylidenecyclobutane-annulated derivative **212** in 30%

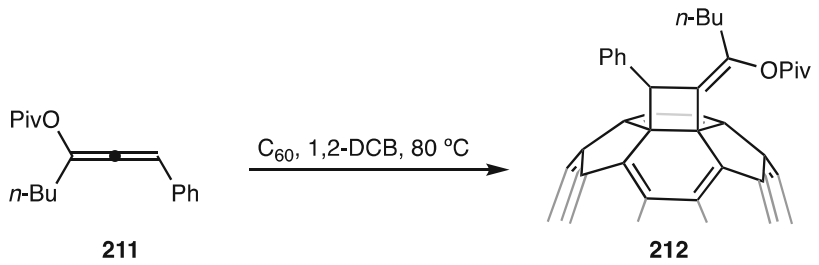

Scheme 63 Reaction of C_{60} with phenyl-substituted allenol ester

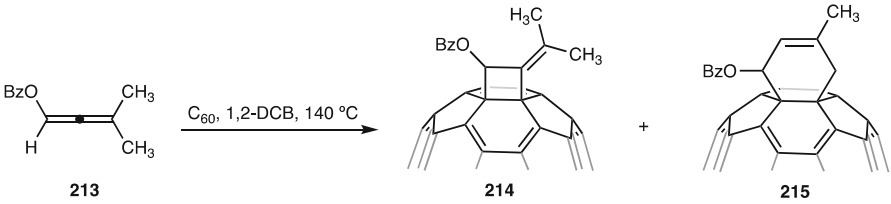

Scheme 64 Reaction of C_{60} with dimethyl-substituted allenol ester

[102]. Cycloadduct **212** was formed via [2 + 2] cycloaddition, with the alkene portion next to the acyloxyalkene portion of the allenol ester. In contrast, Yamada et al. found that reaction of C_{60} with dimethyl-substituted allenol ester **213** in 1,2-DCB at 140 °C resulted in the formation of not only the alkylidenecyclobutane-annulated derivative **214** but also the cyclohexene-annulated derivative **215** in 10% and 26% yields, respectively [103]. It is also noteworthy that cycloadduct **214** was derived via [2 + 2] cycloaddition with the acyloxyalkene portion of the allenol ester (Schemes 63 and 64).

Diels–Alder Reactions

In Diels–Alder (DA) reactions, fullerenes generally act as good dienophiles owing to their electron-deficient character. The DA reactions of C_{60} with cyclopentadiene (Cp) and anthracene are reversible [104]. For instance, heating the C_{60}-anthracene monoadduct above 60 °C in toluene gave the component molecules. Kinetic studies of the addition of Cp to C_{60} and C_{70} showed that the activation energies of these reactions were 29 and 67 kJ mol^{-1}, respectively, reflecting the increased electron density in the [6] bonds of C_{60} relative to C_{70} [105]. Hydrogenation of the C = C bond of the resulting cycloadducts was effective to prevent the retro-DA reactions. For instance, Kräutler et al. reported that the DA reaction of C_{60} with cylohexa-1,3-diene in toluene at 90 °C afforded the DA adduct in 30% after recrystallization [106]. Subsequent catalytic hydrogenation of the DA adduct with platinum (IV) oxide hydrate at 40 psi at ambient temperature resulted in the saturation of the C = C double bond of the addend to furnish the thermally stable product.

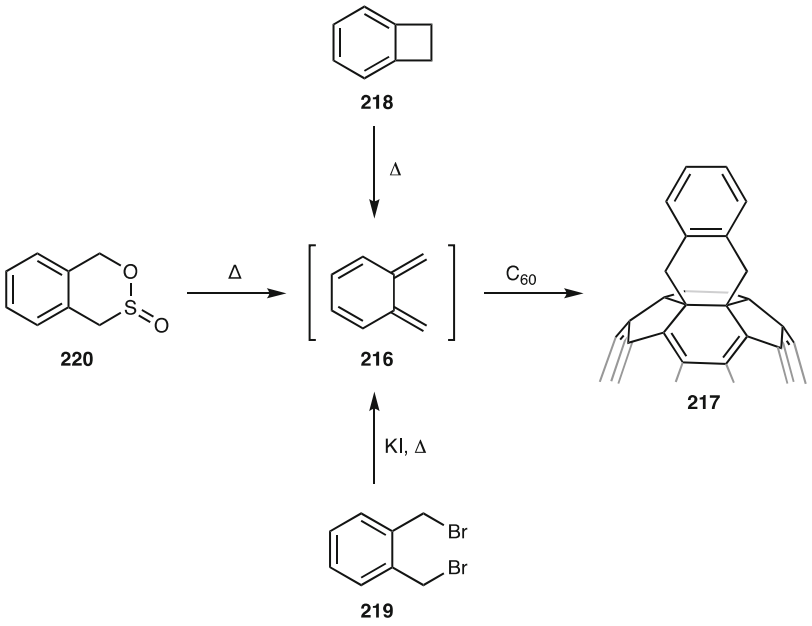

Scheme 65 Reaction of C_{60} with *o*-quinodimethane generated in situ from various precursors

Alternatively, DA reactions of C_{60} with *o*-quinodimethanes (such as **216**) afford thermally stable products (such as **217**), as they undergo aromatization. 1,2-Bis (bromomethyl)benzenes, benzocyclobutenes, benzocyclobutenones, sulfolenes, sultines, and their analogues are useful reagents to generate *o*-quinodimethane species in situ, as shown in Scheme 65 [107]. Foote et al. reacted C_{60} with benzocyclobutenol (**218**) and its methoxy ether in refluxing toluene and obtained the corresponding DA adducts in 59% and 50% yields, respectively [108]. Müllen et al. reported that heating a solution of C_{60}, 1,2-bis(bromomethyl)benzene (**219**), and KI in the presence of 18-crown-6 as a phase transfer catalyst in toluene at reflux afforded **217** in 88% based on the conversion of C_{60} [109]. Wudl et al. reported that reaction of C_{60} with sultine **220** at reflux in benzene yielded **217** in 30% (conv. y., 47% based on converted C_{60}) [107].

Rubin et al. reported that the reaction of C_{60} with 1.5 equiv. of the *o*-quinodimethane precursor **221** in toluene at reflux afforded the stable DA adduct **222** in 60% as shown in Scheme 66 [110].

Chronakis et al. applied one-pot double DA reactions for fullerene functionalization [111]. The diene–sulfone **223** was first subjected to DA reaction with C_{60} in toluene at 45–50 °C. After 12 h, dimethyl acetylenedicarboxylate (DMAD) was added without purification of the first DA adduct **224**, and the temperature was raised to 110 °C for 0.5 h to yield the expected double-DA adduct **225** in 53% (Scheme 67).

In the DA reaction of C_{60} with substituted dienes **226**, the reactivity of dienes bearing an electron-donating group, such as Danishefsky's diene (**226b**) and other

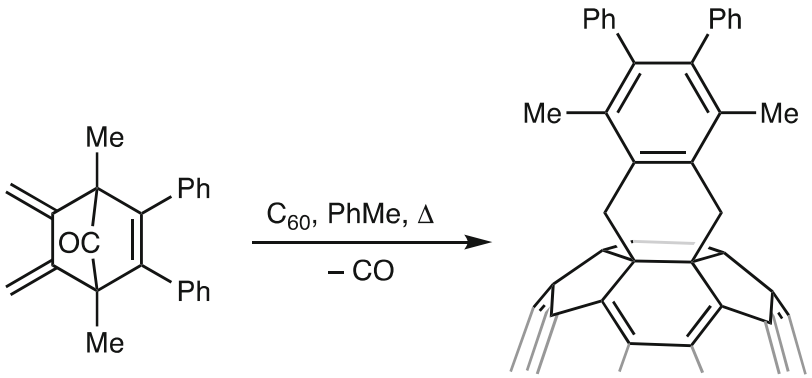

221 222

Scheme 66 Reaction of C_{60} with *o*-quinodimethane generated in-situ through CO extrusion from the precursor

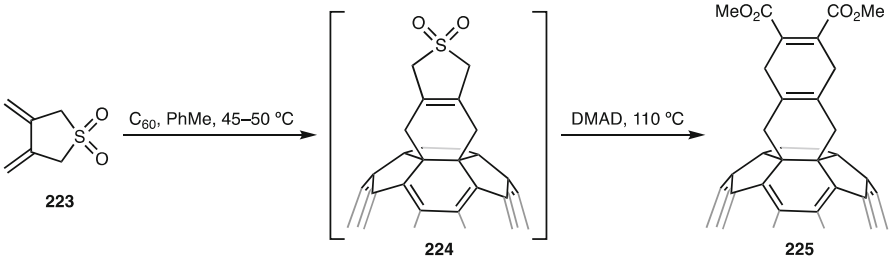

223 224 225

Scheme 67 One-pot double DA reaction for C_{60} functionalization

2-siloxy-1,3-dienes, is electronically favorable because of their high HOMO level [112]. In this case, the LUMO level of C_{60} is sufficiently low to interact with the HOMO of the electron-rich diene. In fact, the thermal reaction of C_{60} with **226** afforded the corresponding DA adducts **227** in 29–48% yield as shown in Scheme 68. C_{70} is more reactive than C_{60} in the DA reaction with electron-rich dienes because of its lower LUMO. In related works, photochemical DA reaction of C_{60} and the dimethyl analogue of Danishefsky's diene, which proceeded via a SET process, was investigated by Fukuzumi et al. [113]

Rubin et al. reported that the DA reaction of C_{60} with 1-((trimethylsilyl)oxy)-1,3-butadiene (**228**) in toluene followed by acidic aqueous workup furnished the allylic alcohol derivative **229** in 66% as shown in Scheme 69 [114]. Subsequent photolysis (sunlamp) under reflux and acidic conditions in the presence of TsOH afforded the bisfulleroid **230**. The formation of **230** involves the initial [4 + 4] photocyclization reaction and retro [2 + 2 + 2] cycloreversion.

In addition, C_{60} is capable of cycloaddition to 1,3-butadienes substituted with an electron-withdrawing group, as shown in Scheme 70 [112]. Treatment of ethyl 3-hydroxyl-2-methylenebutanoate (**231a**) with methanesulfonyl chloride/

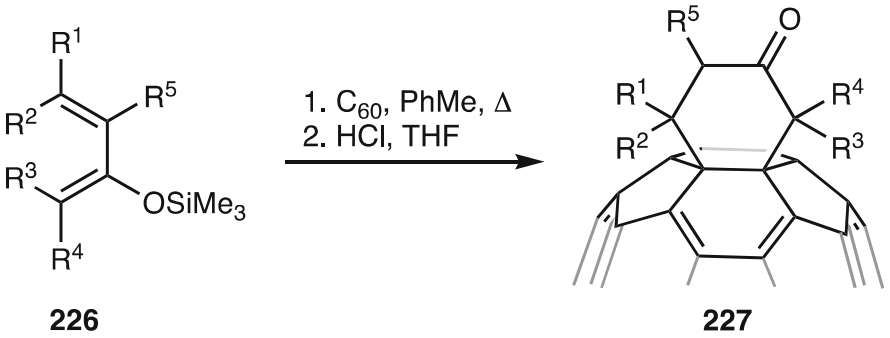

a: $R^1 = R^2 = R^3 = R^4 = R^5 = H$
b: $R^1 = OMe$, $R^2 = R^3 = R^4 = R^5 = H$
c: $R^1 = Ph$, $R^2 = R^3 = R^4 = R^5 = H$
d: $R^1 = R^2 = Me$, $R^3 = R^4 = R^5 = H$
e: $R^1 = H$, $R_2 = -CH_2CH_2-$, $R^3 = R^4 = R^5 = H$

Scheme 68 DA reaction of C_{60} with substituted dienes

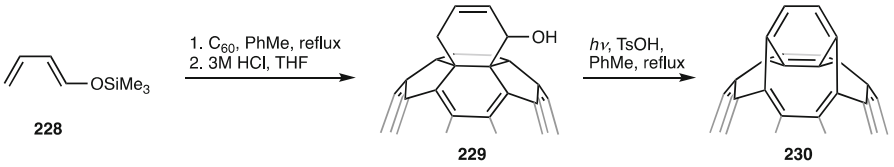

Scheme 69 DA reaction of C_{60} with 1-((trimethylsilyl)oxy)-1,3-butadiene

triethylamine gave dimers of diene **232a** in 74%. However, the dimers did not react with C_{60} in 1,2-DCB under reflux. Instead, the elimination reaction of **231a** was conducted at 150 °C in the presence of C_{60} to afford the corresponding cycloadduct **233a** in 68% yield. Acetyl- and cyano-substituted 1,3-butadienes (**232b**, **232c**) were prepared similarly by treatment of 4-hydroxy-3-methylenepentan-2-one or 3-hydroxy-2-methylenebutanenitrile with methanesulfonyl chloride/triethylamine at 150 °C in the presence of C_{60} to yield the corresponding cycloadducts in 50% and 49%, respectively. Phenylsulfonyl- and nitro-substituted 1,3-butadienes (**232d**, **232e**) were synthesized by thermal extrusion of SO_2 from the corresponding 3-substituted sulfolene **234** and applied in DA reactions with C_{60} to give the corresponding cycloadducts **233d,e** in 79% and 36% yields, respectively. The high reactivity of C_{60} toward 1,3-butadienes with electron-withdrawing substituents is due to the sufficiently low-energy LUMO of C_{60}.

Heterocyclic fullerene derivatives are also accessible through DA reactions with heteroatom-containing dienes. *o*-Aminobenzyl alcohols [115], *o*-hydroxybenzyl

alcohol [116], benzothietane [117], etc., have been applied for the synthesis of *N*, *O*, and *S*-containing heterocycles on C_{60}, as shown in Schemes 71, 72 and 73.

Nitrogen-containing aromatic compounds, such as phthalazines, 1,2,4,5-tetrazines, 1,2,3-tetrazines, and 1,2,4-triazines, have also been applied in DA reactions with C_{60}. These electron-deficient compounds are known to behave as dienes in the inverse-electron demand DA reaction. In many cases, the resulting DA adducts are subjected to further reaction steps to construct so-called open-cage fullerenes. Miller reported that thermal DA reaction between C_{60} and 3,6-diaryl-1,2,4,5-tetrazines **244** in refluxing toluene in the dark yielded cycloadducts **246** possessing a diaryldihydropyridazine function nested atop the fullerene through the formation of the initial DA product **245** followed by rapid retro-DA reaction with loss of N_2, as shown in Scheme 74 [118, 119].

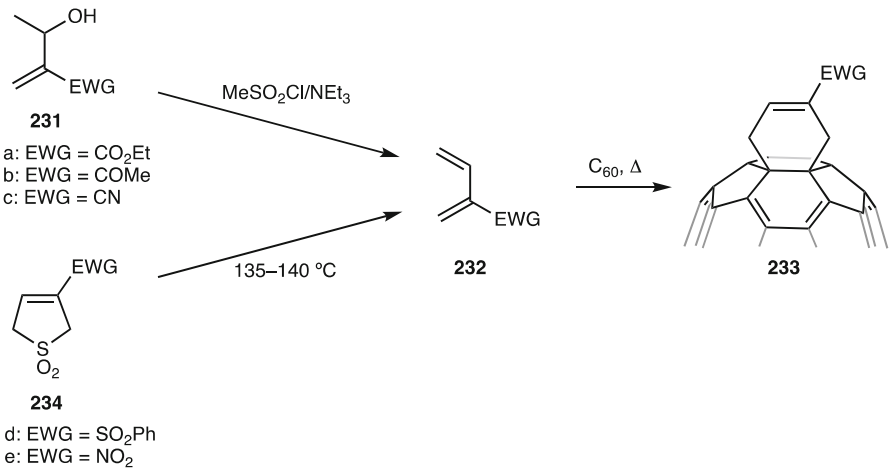

Scheme 70 DA reactions of C_{60} with 1,3-butadienes substituted with electron-withdrawing groups

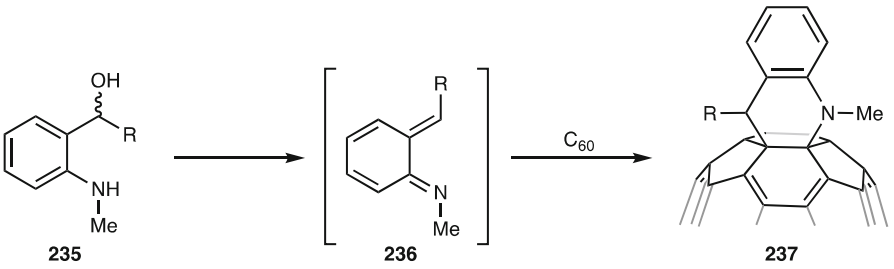

a: R = C_6H_5
b: R = *p*-$MeOC_6H_4$
c: R = 2-thienyl

Scheme 71 Reaction of C_{60} with *o*-aminobenzyl alcohols

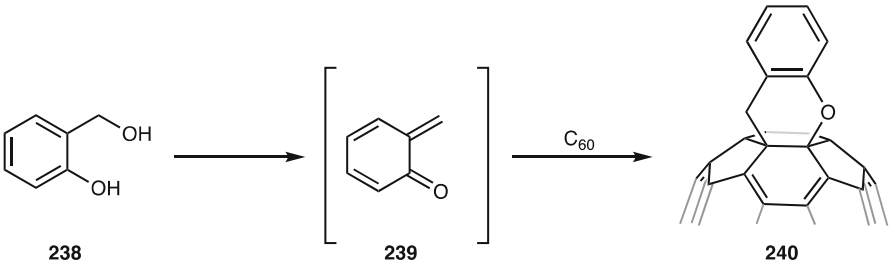

Scheme 72 Reaction of C_{60} with *o*-hydroxybenzyl alcohol

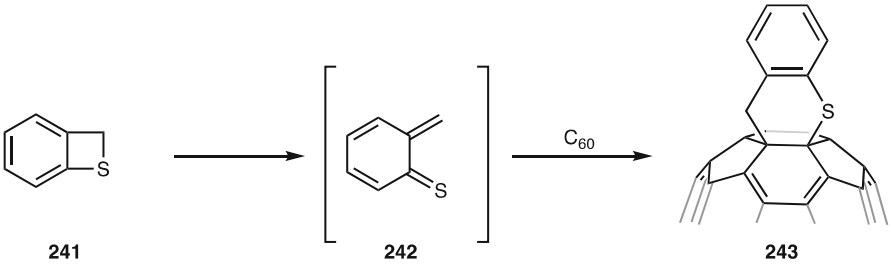

Scheme 73 Reaction of C_{60} with benzothietane

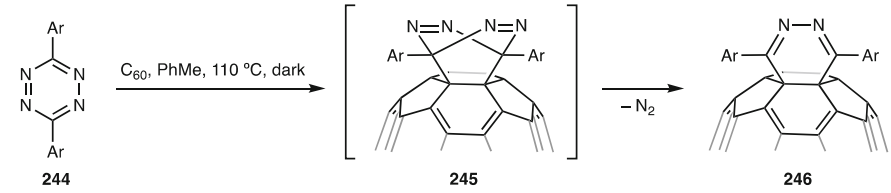

a: Ar = C_6H_5
b: Ar = 2'-pyridyl

Scheme 74 Reaction of C_{60} with 3,6-diaryl-1,2,4,5-tetrazines in the dark

Later, Rubin et al. found that fullerene derivatives incorporating a four-membered ring were obtained when reactions of C_{60} with **244** were conducted at higher temperatures (in refluxing 1,2-DCB) under photoirradiation (2 × 500 W halogen lamps) [120]. Under these conditions, the formation of the nonclassical fullerenes **250** proceeded via a photochemically promoted formal [4 + 4] cycloaddition and subsequent retro [2 + 2 + 2] cycloaddition followed by N_2 extrusion via the corresponding benzylic biradicals (**249**), as shown in Scheme 75.

When the reaction of C_{60} with 1 equiv. of phthalazine (**251**) was conducted in 1-chloronaphthalene at 255 °C for 1 h, bisfulleroid **252** was obtained in 44% yield together with 23% recovered C_{60} after flash chromatography, as shown in Scheme 76 [121].

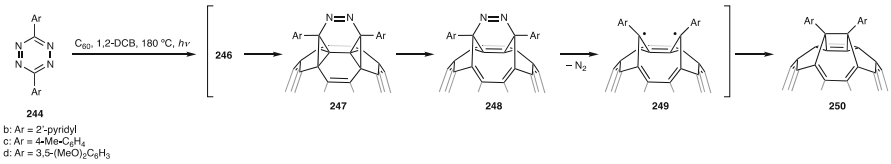

Scheme 75 Reaction of C_{60} with 3,6-diaryl-1,2,4,5-tetrazines under photoirradiation

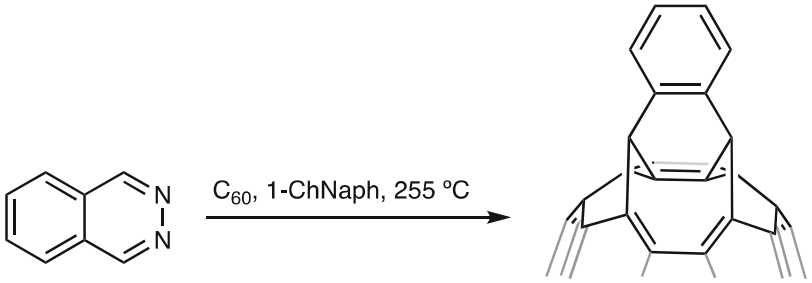

Scheme 76 Reaction of C_{60} with phthalazine

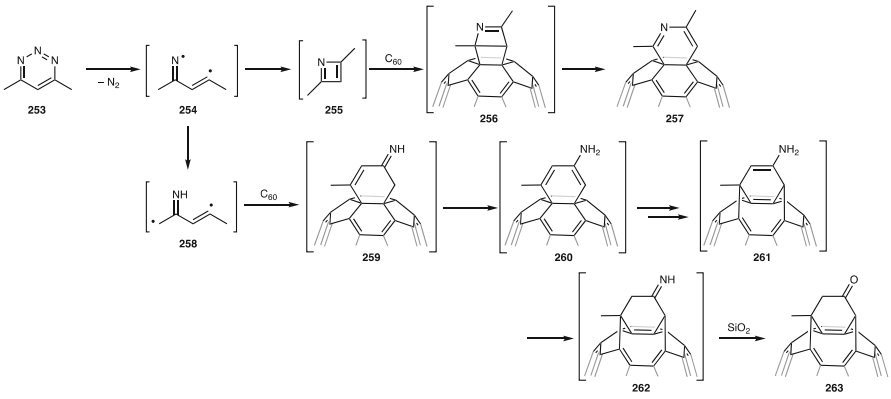

Scheme 77 Reaction of C_{60} with 4,6-dimethyl-1,2,3-triazine

Reaction of C_{60} and 3 equiv. of 4,6-dimethyl-1,2,3-triazine (**253**) in 1,2-DCB at 180 °C for 24 h followed by filtration and flash chromatography over SiO_2 afforded two products, azacyclohexadiene-fused derivative **257** in 10% yield and the unexpected bisfulleroid **263** in 7% yield, as shown in Scheme 77 [122]. Formation of **257** was proposed to proceed through the formation of the azete intermediate **255** by thermal extrusion of N_2 from **253**, subsequent [4 + 2] cycloaddition to C_{60}, and further ring enlargement. The transformation of **257** into the corresponding bisfulleroid through photochemical [4 + 4] cycloaddition followed by retro [2 + 2 + 2] cycloaddition did not proceed under photoirradiation using a high-

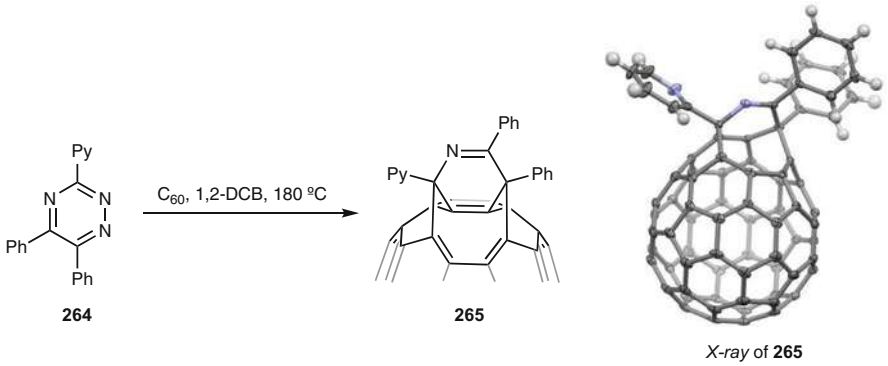

Scheme 78 Reaction of C_{60} with 3-(2-pyridyl)-5,6-diphenyl-1,2,4-triazine

pressure mercury lamp with or without heating. In the formation of **263**, diradical intermediate **254** is assumed to undergo a 1,3-hydrogen shift to **258** before the formation of **255**. Subsequent reaction of C_{60} with **258** would give imine **259**, which would isomerize to 2-aminodiene **260**. Intramolecular [4 + 4] cycloaddition followed by retro [2 + 2 + 2] cycloaddition pathways would then produce open-cage enamine **261**, which would be transformed into open-cage imine **262**. Finally, **262** would undergo hydrolysis upon contact with SiO_2 to furnish **263**.

Komatsu et al. also reported the reaction of C_{60} with 3-(2-pyridyl)-5,6-diphenyl-1,2,4-triazine (**264**) in 1,2-DCB at 180 °C to afford open-cage bisfulleroid **265** in 50% yield together with 41% unreacted C_{60}, as shown in Scheme 78 [123]. The structure of the bisfulleroid was unambiguously determined by X-ray crystallography.

The reversibility of the DA reaction of C_{60} and 9,10-dimethylanthrancene (DMA) at ambient temperature has been applied for the template-directed activation of equatorial double bonds of C_{60}. Hirsch et al. reported the regioselective synthesis of T_h-symmetric hexakisadduct $C_{66}(CO_2Et)_{12}$ using this approach [124, 125]. Reaction of C_{60} with diethyl bromomalonate in the presence of DBU and 10 equiv. of DMA followed by flash chromatography and subsequent recrystallization yielded the hexakisadduct in 23%. In fact, addition of DMA to a toluene solution of C_{60} afforded the corresponding DA adducts $C_{60}(DMA)_n$. The equilibrium of the distribution could be shifted toward the higher adducts by increasing the concentration of DMA (10 equiv.); *e*,*e*,*e*-$C_{60}(DMA)_3$ was considered to be the main component. The use of DBU as a base is advantageous, allowing the yields of the hexakisadducts to reach as high as 50%. The template-directed multiple addition strategy is also useful for 1,3-dipolar cycloadditions [126].

Cross-References

► Radical Reaction and Photoreaction

References

1. Hirsch A, Grösser T, Skiebe A, Soi A (1993) Synthesis of isomerically pure organodihydrofullerenes. Chem Ber 126(4):1061–1067
2. Fagan PJ, Krusic PJ, Evans DH, Lerke SA, Johnston E (1992) Synthesis, chemistry, and properties of a monoalkylated buckminsterfullerene derivative, *t*-BuC_{60} anion. J Am Chem Soc 114(24):9697–9699
3. Morton JR, Preston KF, Krusic PJ, Hil A, Wasserman E (1992) The dimerization of RC_{60} radicals. J Am Chem Soc 114(13):5454–5455
4. Hirsch A, Soi A, Karfunkel HR (1992) Titration of C_{60}: a method for the synthesis of organofullerenes. Angew Chem, Int Ed Engl 31(6):766–768
5. Fukuzumi S, Suenobu T, Hirasaka T, Arakawa R, Kadish KM (1998) Formation of C_{60} adducts with two different alkyl groups via combination of electron transfer and S_N2 reactions. J Am Chem Soc 120(36):9220–9227
6. Nagashima H, Terasaki H, Kimura E, Nakajima K, Itoh K (1994)
7. Nagashima H, Terasaki H, Saito Y, Jinno K, Itoh K (1995) Chlorosilanes and silyl triflates containing C_{60} as a partial structure. A versatile synthetic entry linking the C_{60} moieties with alcohols, phenols, and silica. J Org Chem 60(16):4966–4967
8. Matsuo Y, Nakamura E (2006) Synthesis of trialkyl[60]fullerene $C_{60}(CH_2SiMe_3)_3H$ and its potassium and rhodium(I) complexes. Inorg. Chim. Acta 359(6):1979–1982
9. Matsuo Y, Iwashita A, Abe Y, Li C-Z, Matsuo K, Hashiguchi M, Nakamura E (2008) Regioselective synthesis of 1,4-di(organo)[60]fullerenes through DMF-assisted monoaddition of silylmethyl Grignard reagents and subsequent alkylation reaction. J Am Chem Soc 130(46): 15429–15436
10. Komatsu K, Murata Y, Takimoto N, Mori S, Sugita N, Wan TSM (1994) Synthesis and properties of the first acetylene derivatives of C_{60}. J Org Chem 59(20):6101–6102
11. Anderson HL, Faust R, Rubin Y, Diederich F (1994) Fullerene–acetylene hybrids: on the way to synthetic molecular carbon allotropes. Angew Chem, Int Ed Engl 33(13):1366–1368
12. Timmerman P, Anderson HL, Faust R, Nierengarten J-F, Habicher T, Seiler P, Diederich F (1996) Fullerene-acetylene hybrids: towards a novel class of molecular carbon allotropes. Tetrahedron 52(14):4925–4947
13. Murata Y, Motoyama K, Komatsu K, Wan TSM (1996) Synthesis, properties, and reactions of a stable carbanion derived from alkynyldihydrofullerene: 1-Octynyl-C_{60} carbanion. Tetrahedron 52(14):5077–5090
14. Keshavarz-K M, Knight B, Srdanov G, Wudl F (1995) Cyanodihydrofullerenes and dicyanodihydrofullerene: the first polar solid based on C_{60}. J Am Chem Soc 117(45):11371–11372
15. Murata Y, Komatsu K, Wan TSM (1996) The reaction of [60]fullerene with lithium fluorenide: Formation of a novel 1,4-adduct of [60]fullerene. Tetrahedron Lett 37(39):7061–7064
16. Murata Y, Shiro M, Komatsu K (1997) Synthesis, X-ray structure, and properties of the first tetrakisadduct of fullerene C_{60} having a fulvene-type π-system on the spherical surface. J Am Chem Soc 119(34):8117–8118
17. Sawamura M, Iikura H, Nakamura E (1996) The first pentahaptofullerene metal complexes. J Am Chem Soc 118(50):12850–12851
18. Matsuo Y, Tahara K, Morita K, Matsuo K, Nakamura E (2007) Regioselective eightfold and tenfold additions of a pyridine-modified organocopper reagent to [60]fullerene. Angew Chem Int Ed 46(16):2844–2847
19. Li D, Li Z-J, He F-G, Geng C, Gao X (2019) Synthesizing 1,23-C_{60} adducts with improved efficiency: a type of stable and highly soluble C_{60} derivatives. J Org Chem 84(22):14679–14687
20. Kusukawa T, Ando W (1996) Reactions of silyllithium with C_{60}: isolation and X-ray crystallographic characterization of an unusual bissilylated-C_{60} adduct. Angew Chem, Int Ed Engl 35 (12):1315–1317

21. Kusukawa T, Ando W (1998) Substituents effects on the addition of silyllithium and germyllithium to C_{60}. J Organomet Chem 561:109–120
22. Yamago S, Yanagawa M, Nakamura E (1994) Tertiary phosphines and *P*-chiral phosphinites bearing a fullerene substituent. J Chem Soc, Chem Commun 18:2093–2094
23. Kitagawa T, Sakamoto H, Takeuchi K (1999) Electrophilic addition of polychloroalkanes to C_{60}: direct observation of aklylfullerenyl cation intermediates. J Am Chem Soc 121(17):4298–4299
24. Kitagawa T, Lee Y, Hanamura M, Sakamoto H, Konno H, Takeuchi K, Komatsu K (2002) Nucleophilic substitution of alkylchlorodihydro[60]fullerenes: thermodynamic stabilities of alkylated C_{60} cation intermediates. Chem Comm 24:3062–3063
25. Matsuo Y, Yu Y, Yang X-Y, Ueno H, Okada H, Shibuya H, Choi YS, Jin YW (2019) Synthesis of benzothieno[60]fullerenes through fullerenyl cation intermediates. J Org Chem 84(10):6270–6277
26. Lin H-S, Matsuo Y (2018) Functionalization of [60]fullerene through fullerene cation intermediates. Chem Commun 54(80):11244–11259
27. Biglova YN, Mustafin AG (2019) Nucleophilic cyclopropanation of [60]fullerene by the addition–elimination mechanism. RSC Adv 9(39):22428–22498
28. Bingel C (1993) Cyclopropanierung von fullerenen. Chem Ber 126(8):1957–1959
29. Hirsch A, Lamparth, Karfunkel HR (1994) Fullerene chemistry in three dimensions: Isolation of seven regioisomeric bisadducts and chiral trisadducts of C_{60} and di(ethoxycarbonyl)-methylene. Angew Chem, Int Ed Engl 33(4):437–438
30. Camps X, Hirsch A (1997) Efficient cyclopropanation of C_{60} starting from malonates. J Chem Soc, Perkin Trans 1(11):1595–1596
31. Nierengarten J-F, Herrmann A, Tykwinski RR, Rüttimann M, Diederich F (1997) Methanofullerene molecular scaffolding: towards C_{60}-substituted poly(triacetylenes) and expanded radialenes, preparation of C_{60}–C_{70} hybrid derivative, and a novel macrocyclization reaction. Helv Chim Acta 80(1):293–316
32. Feng L, Nakahodo T, Wakahara T, Tsuchiya T, Maeda Y, Akasaka T, Kato T, Horn E, Yoza K, Mizorogi N, Nagase S (2005) A singly bonded derivative of endohedral metallofullerene: La@C_{82}CBr($COOC_2H_5$)$_2$. J Am Chem Soc 127(49):17136–17137
33. Anderson HL, Faust R, Rubin Y, Diederich F (1994) Fullerene–acetylene hybrids: On the way to synthetic molecular carbon allotropes. Angew Chem, Int Ed Engl 33(13):1366–1368
34. Wang Y, Cao J, Schuster DI, Wilson SR (1995) A superior synthesis of [6,6]-methanofullerenes: The reaction of sulfonium ylides with C_{60}. Tetrahedron Lett 36(38):6843–6846
35. Wang G-W, Li J-X, Xu Y (2008) Synthesis of C_{60}-fused tetrahydrothiophene derivatives *via* nucleophilic cycloaddition of thiocyanates. Org Biomol Chem 6(16):2995–2999
36. Ball GE, Burley GA, Chaker L, Hawkins BC, Williams JR, Keller PA, Pyne SG (2005) Structural reassignment of the mono- and bis-addition products from the addition reactions of *N*-(diphenylmethylene)glycinate esters to [60]fullerene under Bingel conditions. J Org Chem 70(21):8572–8574
37. Tsuda M, Ishida T, Nogami T, Kurono S, Ohashi M (1993) $C_{61}Cl_2$. Synthesis and characterization of dichlorocarbene adducts of C_{60}. Tetrahedron Lett 34(43):6911–6912
38. Benito AM, Darwish AD, Kroto HW, Meidine MF, Taylor R, Walton DRM (1996) Synthesis and characterization of the methanofullerenes, C_{60}(CHCN) and C_{60}(CBr_2). Tetrahedron Lett 37(7):1085–1086
39. Osterodt J, Vögtle V (1996) $C_{61}Br_2$: a new synthesis of dibromomethanofullerene and mass spectrometric evidence of the carbon allotropes C_{121} and C_{122}. Chem Comm 4:547–548
40. Yinghuai Z, Bahnmueller S, Chibun C, Carpenter K, Hosmane NS, Maguire JA (2003) An effective system to synthesize methanofullerenes: substrate–ionic liquid–ultrasonic irradiation. Tetrahedron Lett 44(29):5473–5476
41. Gao X, Ishimura K, Nagase S, Chen Z (2009) Dichlorocarbene addition to C_{60} from the trichloromethyl anion: carbene mechanism of Bingel mechanism? J Phys Chem A 113(15):3673–3676

42. Tokuyama H, Nakamura M, Nakamura E (1993) [1 + 2] and [3 + 2] Cycloaddition reactions of vinylcarbenes with C_{60}. Tetrahedron Lett 34(46):7429–7432
43. Tokuyama H, Isobe H, Nakamura E (1995) Methano- and propanofullerenes by [1 + 2] and [3 + 2] cycloadditions of vinylcarbene species. Bull Chem Soc Jpn 68(3):935–941
44. Isobe H, Tokuyama H, Sawamura M, Nakamura E (1997) Synthetic and computational studies on symmetry-defined double cycloaddition of a new tris-annulating reagent to C_{60}. J Org Chem 62(15):5034–5041
45. Suzuki T, Maruyama Y, Akasaka T, Ando W, Kobayashi K, Nagase S (1994) Redox properties of organofullerenes. J Am Chem Soc 116(4):1359–1363
46. Romanova IP, Bogdanov AV, Mironov VF, Shaikhutdinova GR, Larionova OA, Latypov SK, Balandina AA, Yakhvarov DG, Gubaidullin AT, Saifina AF, Sinyashin OG (2011) Deoxygenation of some α-dicarbonyl compounds by tris(diethylamino)phosphine in the presence of fullerene C_{60}. J Org Chem 76(8):2548–2557
47. Nikawa H, Nakahodo T, Tsuchiya T, Wakahara T, Rahman GMA, Akasaka T, Maeda Y, Liu MTH, Meguro A, Kyushin S, Matsumoto H, Mizorogi N, Nagase S (2005) S-Heterocyclic carbene with a disilane backbone. Angew Chem Int Ed 44(46):7567–7570
48. Kako M, Arikawa Y, Kanzawa S, Yamada M, Maeda Y, Furukawa M, Akasaka T (2019) Addition of S-heterocyclic carbenes to fullerenes: Formation and characterization of dithiomethano-bridged derivatives. Helv Chim Acta 102:e1900064
49. Li H, Risko C, Seo JH, Campbell C, Wu G, Brédas J-L, Bazan GC (2011) Fullerene–carbene Lewis acid–base adducts. J Am Chem Soc 133(32):12410–12413
50. Chen M, Bao L, Ai M, Shen W, Lu X (2016) $Sc_3N@I_h$-C_{80} as a novel Lewis acid to trap abnormal *N*-heterocyclic carbenes: the unprecedented formation of a singly bonded [6,6,6]-adduct. Chem Sci 7(3):2331–2334
51. Komatsu K, Kagayama A, Murata Y, Sugita N, Kobayashi K, Nagase S, Wan TSM (1993) Reaction of C_{60} with chlorophenyldiazirine. Chem Lett 22(12):2163–2166
52. Yamada M, Akasaka T, Nagase S (2013) Carbene additions to fullerenes. Chem Rev 113(9): 7209–7264
53. Akasaka T, Ando W, Kobayashi K, Nagase S (1993) Reaction of C_{60} with silylene, the first fullerene silirane derivative. J Am Chem Soc 115(4):1605–1606
54. Akasaka T, Mitsuhida E, Ando W, Kobayashi K, Nagase S (1995) Regioselective addition of silylene on to [70]fullerene. J Chem Soc, Chem Commun 15:1529–1530
55. Maggini M, Scorrano G, Prato M (1993) Addition of azomethine ylides to C_{60}: synthesis, characterization, and functionalization of fullerene pyrrolidienes. J Am Chem Soc 115(21): 9798–9799
56. Prato M, Maggini M (1998) Fulleropyrrolidines: a family of full-fledged fullerene derivatives. Acc Chem Res 31(9):519–526
57. Izquierdo M, Osuna S, Filippone S, Martín-Domenech Á, Solá M, Martín N (2009) H-Bond-assisted regioselective (*cis*-1) intramolecular nucleophilic addition of the hydroxyl group to [60]fullerene. J Org Chem 74(4):1480–1487
58. Izquierdo M, Osuna S, Filippone S, Martín-Domenech Á, Solá M, Martín N (2009) Regioselective intramolecular nucleophilic addition of alcohols to C_{60}: one-step formation of a *cis*-1 bicyclic-fused fullerene. J Org Chem 74(16):6253–6259
59. Izquierdo M, Osuna S, Filippone S, Martín-Domenech Á, Solá M, Martín N (2009) On the regioselective intramolecular nucleophilic addition of thiols to C_{60}. Eur J Org Chem 35:6231–6238
60. Martín N, Altable M, Filippone F, Marín-Domenech Á, Güell M, Solá M (2006) Thermal [2 + 2] Intramolecular cycloadditions of fuller-1,6-enynes. Angew Chem Int Ed 45(9):1439–1442
61. Altable M, Filippone S, Martín-Domenech Á, Güell M, Solá M, Martín N (2006) Intramolecular ene reaction of 1,6-fullerenynes: a new synthesis of allenes. Org Lett 8(26):5959–5962
62. Martín N, Altable M, Filippone S, Martín-Domenech Á (2004) Highly efficient Pauson–Khand reaction with C_{60}: regioselective synthesis of unprecedented *cis*-1 biscycloadducts. Chem Commun 11:1338–1339

63. Martin N, Altable M, Filippone S, Martin-Domeneck A, Poater A, Sola M (2005) Regioselective intramolecular Pauson–Khand reactions of C_{60}: an electrochemical study and theoretical underpinning. Chem Eur J 11(9):2716–2729
64. Ito S, Tokimaru Y, Nozaki K (2015) Isoquinolino[4,3,2-*de*]phenanthridine: synthesis and its use in 1,3-dipolar cycloadditions to form nitrogen-containing polyaromatic hydrocarbons. Chem Commun 51(1):221–224
65. Jagerovic N, Elguero J, Aubagnac J-L (1996) Cycloaddition of tetracyanoethene oxide with [60]fullerene. J Chem Soc, Perkin Trans 1(6):499
66. Meier MS, Poplawska M (1993) Addition of nitrile oxides to C_{60}: formation of isooxazoline derivatives of fullerenes. J Org Chem 58(17):4524–4525
67. Meier MS, Poplawska M (1996) The addition of nitrile oxides to C_{60}. Tetrahedron 52(14): 5043–5042
68. Da Ros T, Prato M, Novello F, Maggini M, De Amici M, De Micheli C (1997) Cycloaddition of nitrile oxides to [60]fullerene. Chem Commun 1:59–60
69. Illescas BM, Martín N (2000) [60]Fullerene adducts with improved electron acceptor properties. J Org Chem 65(19):5986–5995
70. Matsubara Y, Tada H, Nagase S, Yoshida Z (1995) Intramolecular charge transfer interaction in 1,3-diphenyl-2-pyrazoline ring-fused C_{60}. J Org Chem 60(17):5372–5373
71. Delgado JL, de la Cruz P, Lopez-Arza V, Langa F, Gan Z, Araki Y, Ito O (2005) Synthesis and photoinduced intermolecular electronic acceptor ability of pyrazolo[60]fullerenes vs tetrathiafulvalene. Bull Chem Soc Jpn 78(8):1500–1507
72. Ishida H, Itoh K, Ohno M (2001) 1,3-Dipolar cycloaddition reaction of [60]fullerene with thiocarbonyl ylide and synthetic application of the cycloadduct. Tetrahedron 57(9):1737–1747
73. Prato M, Suzuki T, Foroudian H, Li Q, Khemani K, Wudl F, Leonetti J, Little RD, White T, Rickborn B, Yamago S, Nakamura E (1993) [3 + 2] and [4 + 2] Cycloadditions of C_{60}. J Am Chem Soc 115(4):1594–1595
74. Suzuki T, Li Q, Khemani KC, Wudl F, Almarsson Ö (1991) Systematic inflation of buckminsterfullerene C_{60}: synthesis of diphenyl fulleroids C_{61} to C_{66}. Science 254(5035):1186–1188
75. Suzuki T, Li Q, Khemani KC, Wudl F, Almarsson Ö (1992) Synthesis of *m*-phenylene- and *p*-phenylenebis(phenylfulleroids): two-pearl sections of pearl necklace polymers. J Am Chem Soc 114(18):7300–7301
76. Wudl F (1992) The chemical properties of buckminsterfullerene (C_{60}) and the birth and infancy of fulleroids. Acc Chem Res 25(3):157–161
77. Suzuki T, Li Q, Khemani KC, Wudl F (1992) Dihydrofulleroid H_2C_{61}: synthesis and properties of the parent fulleroid. J Am Chem Soc 114(18):7301–7302
78. Smith AB III, Strongin RM, Brard L, Furst GT, Romanow WJ, Owens KG, King RC (1993) 1,2-Methanobuckminsterfullerene ($C_{61}H_2$), the parent fullerene cyclopropane: synthesis and structure. J Am Chem Soc 115(13):5829–5830
79. Hummelen JC, Knight BW, LePeq F, Wudl F (1995) Preparation and characterization of fulleroid and methanofullerene derivatives. J Org Chem 60(3):532–538
80. Heymann D, Bachilo SM, Weisman RB, Cataldo F, Fokkens RH, Nibbering NMM, Vis RD, Chibante LPF (2000) $C_{60}O_3$, A fullerene ozonide: synthesis and dissociation to $C_{60}O$ and O_2. J Am Chem Soc 122(46):11473–11479
81. Weisman RB, Heymann D, Bachilo SM (2001) Synthesis and characterization of the "missing" oxide of C_{60}: [5,6]-Open $C_{60}O$. J Am Chem Soc 123(39):9720–9721
82. Prato M, Li QC, Wudl F, Lucchini V (1993) Addition of azides to C_{60}: synthesis of azafulleroids. J Am Chem Soc 115(3):1148–1150
83. Grösser T, Prato M, Lucchini V, Hirsch A, Wudl F (1995) Ring expansion of the fullerene core by highly regioselective formation of diazafulleroids. Angew Chem, Int Ed Engl 34(12):1343–1345
84. Ulmer L, Mattay J (2003) Preparation and characterization of sulfonyl-azafulleroid and sulfonylaziridino-fullerene derivatives. Eur J Org Chem 15:2933–2940

85. Nakahodo T, Okada M, Morita H, Yoshimura T, Ishitsuka MO, Tsuchiya T, Maeda Y, Fujiwara H, Akasaka T, Gao X, Nagase S (2008) [2+1] Cycloaddition of nitrene onto C_{60} revisited: Interconversion between an aziridinofullerene and an azafulleroid. Angew Chem Int Ed 47(7):1298–1300
86. Okada M, Nakahodo T, Ishitsuka MO, Nikawa H, Tsuchiya T, Akasaka T, Fujie T, Yoshimura T, Slanina Z, Nagase S (2011) Highly regioselective synthesis of bis-aziridino [60]fullerene with sulfilimine. Chem Asian J 6(2):416–423
87. Yamaguchi H, Murata S, Akasaka T, Suzuki T (1997) Preparation and structure of a novel methano[60]fullerene containing a stable P-ylid. Tetrahedron Lett 38(20):3529–3530
88. Chen S-Y, Cheng R-L, Tseng C-K, Venkatachalam RK, Chen Y-C, Cheng C-H, Chuang S-C (2009) Fullerene derivatives incorporating phosphoramidous ylide and phosphoramidate: synthesis and Property. J Org Chem 74(13):4866–4869
89. Liou K-F, Cheng C-H (1995) Phosphine-mediated [2 + 2] cycloaddition of internal alk-2-ynoate and alk-2-ynone to [60]fullerene. J Chem Soc, Chem Commun 24:2473–2474
90. Hsiao T-Y, Chidambareswaran SK, Cheng C-H (1998) Novel bismethanofullerenes and ethenofullerene from the reaction of propiolates with C_{60} in the presence of triphenylphosphine. J Org Chem 63(23):8617–8620
91. Shu L-H, Sun W-Q, Zhang D-W, Wu S-H, Wu H-M, Xu J-F, Lao X-F (1997) Phosphine-catalyzed [3 + 2] cycloadditions of buta-2,3-dienoates with [60]fullerene. J Chem Soc, Chem Commun 1:79–80
92. Tseng P-Y, Chuang S-C (2013) Chemo-, regio- and stereoselective tricyclohexylphosphine-catalyzed [3 + 2] cycloaddition of enynes with [60]fullerene initiated by 1,4-Michael addition: Synthesis of cyclopenteno[60]fullerenes and their electrochemical properties. Adv Synth Cat 355(11-12):2165–2171
93. Wu A-J, Tseng P-Y, Hsu W-H, Chuang S-C (2016) Tricyclohexylphosphine-catalyzed cycloaddition of enynoates with [60]fullerene and the application of cyclopentenofullerenes as n-type materials in organic photovoltaics. Org Lett 18(2):224–227
94. Bildstein B, Schweiger M, Angleitner H, Kopacka H, Wurst K, Ongania K-H, Fontani M, Zanello P (1999) Tetraferrocenyl[5]cumulene, $(Fc)_2C{=}C{=}C{=}C{=}C(Fc)_2$: Synthesis, electrochemistry, and reactivity, including nickel(0)-promoted [3]ferrocenophane formation and [2+2] cycloaddition with fullerene C_{60}. Organometallics 18(21):4286–4295
95. Yamago S, Takeichi A, Nakamura E (1994) Synthesis and [2 + 2] cycloaddition of dimethyleneketene acetals. Reaction with C_{60} and facile hydrolysis of the C–C bond connected to C_{60}. J Am Chem Soc 116(3):1123–1124
96. Hoke SH II, Molstad J, Dilettato D, Jay DJ, Carlson D, Kahr B, Cooks RG (1992) Reaction of fullerenes and benzyne. J Org Chem 57(19):5069–5071
97. Ishida T, Shinozuka K, Nogami T, Sasaki S, Iyoda M (1995) First X-ray structural determination of fullerene [2+2] cycloadduct. Chem Lett 24(4):317–318
98. Nakamura Y, Takano N, Nishimura T, Yashima E, Sato M, Kudo T, Nishimura J (2001) First isolation and characterization of eight regioisomers for [60]fullerene–benzyne bisadducts. Org Lett 3(8):1193–1196
99. Meier MS, Wang G-W, Haddon RC, Brock CP, Lloyd MA, Selegue JP (1998) Benzyne adds across a closed 5–6 ring fusion in C_{70}: evidence for bond delocalization in fullerenes. J Am Chem Soc 120(10):2337–2342
100. Lu X, Nikawa H, Tsuchiya T, Akasaka T, Toki M, Sawa H, Mizorogi N, Nagase S (2010) Nitrated benzyne derivatives of La@C_{82}: addition of NO_2 and its positional directing effect on the subsequent addition of benzynes. Angew Chem, Int Ed 49(3):594–597
101. Li FF, Pinzón JR, Mercado BQ, Olmstead MM, Balch AL, Echegoyen L (2011) [2 + 2] Cycloaddition reaction to $Sc_3N@I_h$-C_{80}. The formation of very stable [5,6]- and [6,6]-adducts. J Am Chem Soc 133(5):1563–1571
102. Ueda M, Sakaguchi T, Hayama M, Nakagawa T, Matsuo Y, Munechika A, Yoshida S, Yasuda H, Ryu I (2016) Regio- and stereo-selective intermolecular [2 + 2] cycloaddition of

allenol esters with C_{60} leading to alkylidenecyclobutane-annulated fullerenes. Chem Comm 52 (89):13175–13178
103. Yamada M, Ochi R, Yamamoto Y, Okada S, Maeda Y (2017) Tansition-metal-catalyzed divergent functionalization of [60]fullerene with propargylic esters. Org Biomol Chem 15 (40):8499–8503
104. Tsuda M, Ishida T, Nogami T, Kurono S, Ohashi M (1993) Isolation and characterization of Diels–Alder adducts of C_{60} with anthracene and cyclopentadiene. J Chem Soc, Chem Commun 16:1296–1298
105. Pang LSK, Wilson MA (1993) Reactions of C_{60} and C_{70} with cyxlopentadiene. J Phys Chem 97(26):6761–6763
106. Kräutler B, Maynollo J (1996) Diels–Alder reactions of the [60]fullerene functionalizing a carbon sphere with flexibly and with rigidly bound addends. Tetrahedron 52(14):5033–5042
107. Illescas B, Martín N, Seoane C, de la Cruz P, Langa F, Wudl F (1995) A facile formation of electroactive fullerene adducts from sultines *via* a Diels–Alder reaction. Tetrahedron Lett 36 (45):8307–8310
108. Zhang X, Foote CS (1994) Reaction of C_{60} with benzocyclobutenol: expeditious route to fullerene adducts. J Org Chem 59(18):5235–5238
109. Belik P, Gügel A, Spickerman J, Müllen K (1993) Reaction of buckminsterfullerene with *ortho*-quinodimethane: a new access to stable C_{60} derivatives. Angew Chem, Int Ed Engl 32(1):78–80
110. Rubin Y, Khan S, Freedberg DI, Yeretzian C (1993) Synthesis and X-ray structure of a Diels–Alder adduct of C_{60}. J Am Chem Soc 115(1):344–345
111. Markoulides MS, Ioannou GI, Manos MJ, Chronakis N (2013) One-pot thermally chemocontrolled double Diels–Alder strategies. A route to [4 + 2] functionalization/[4 + 2] derivatization of C_{60}. RSC Adv 3(14):4750–4756
112. Ohno M, Azuma T, Kojima S, Shirakawa Y, Eguchi S (1996) An efficient functionalization of [60]fullerene. Diels–Alder reaction using 1,3-butadienes substituted with electron-withdrawing and electron-donating (silyloxy) groups. Tetrahedron 52(14):4983–4994
113. Mikami K, Matsumoto S, Okubo Y, Fujitsuka M, Ito O, Suenobu T, Fukuzumi S (2000) Stepwise bond formation in photochemical and thermal Diels–Alder reactions of C_{60} with Danishefsky's dienes. J Am Chem Soc 122(10):2236–2243
114. Arce MJ, Viado AL, An Y-Z, Khan SI, Rubin Y (1996) Triple scission of a six-membered ring on the surface of C_{60} via consecutive pericyclic reactions and oxidative cobalt insertion. J Am Chem Soc 118(15):3775–3776
115. Martín N, Martinez-Grau A, Sanchez L, Seoane C, Torres M (1998) The first hetero-Diels–Alder reaction of C_{60} with 1-azadienes. Synthesis of tetrahydro[2',3':1,2][60]fullerene derivatives. J Org Chem 63(22):8074–8076
116. Ohno M, Azuma T, Eguchi S (1993) Buckminsterfullerene C_{60} – *o*-quinone methide cycloadduct. Chem Lett 22(11):1833–1834
117. Ohno M, Kojima S, Shirakawa Y, Eguchi S (1995) Hetero-diels-alder reaction of fullerene: Synthesis of thiochroman-fused C_{60} with *o*-thioquinone methide and oxidation to its S-oxides. Tetrahedron Lett 36(38):6899–6902
118. Miller GP, Tetreau MC (2000) Facile, completely regioselective 1,4-hydrogenations of C_{60}-diaryltetrazine monoadducts. Org Lett 2(20):3091–3094
119. Miller GP, Tetreau MC, Olmstead MM, Lord PA, Balch AL (2001) Addition of diprotic nucleophiles to a C_{60}-tetrazine monoadduct: structural reassignment and correction of a novel rearrangement. Chem Comm:1758–1759
120. Qian W, Chuang S-C, Amador RB, Jarrosson T, Sander M, Pieniazek S, Khan SI, Rubin Y (2003) Synthesis of stable derivatives of C_{62}: the first nonclassical fullerene incorporating a four-membered ring. J Am Chem Soc 125(8):2066–2067
121. Murata Y, Kato N, Komatsu K (2001) The reaction of fullerene C_{60} with phthalazine: The mechanochemical solid-state reaction yielding a new C_{60} dimer versus the liquid-phase reaction affording an open-cage fullerene. J Org Chem 66(22):7235–7239

122. Murata Y, Murata M, Komatsu K (2001) The reaction of fullerene C_{60} with 4,6-dimethyl-1,2,3-triazine: Formation of an open-cage fullerene derivative. J Org Chem 66(24):8187–8191
123. Murata Y, Murata M, Komatsu K (2003) Synthesis, structure, and properties of novel open-cage fullerenes having heteroatom(s) on the rim of the orifice. Chem Eur J 9(7):1600–1609
124. Lamparth I, Maichle-Mössmer C, Hirsch A (1994) Reversible template-directed activation of equatorial double bonds of the fullerene framework: Regioselective direct synthesis, crystal structure, and aromatic properties of Th-$C_{66}(COOEt)_{12}$. Angew Chem Int Ed Engl 34(15): 1607–1609
125. Hirsch A, Vostrowsky O (2001) C_{60} Hexakisadducts with an octahedral addition pattern – A new structure motif in organic chemistry. Eur J Org Chem:829–848
126. Castro E, Azmani K, Garcia AH, Aghabali A, Liu S, Metta-Magana AJ, Olmstead MM, Rodríguez-Fortea A, Poblet JM, Echegoyen L (2017) Unusual C_{2h}-synnteric trans-1-(bis-pyrrolidine)-tetra-malonate hexa-adducts of C_{60}: The unexpected regio- and stereocontrol mediated by malonate–pyrrolidine interaction. Chem Eur J 23(63):15937–15944

Radical Reaction and Photoreaction

11

Yutaka Maeda, Shigeru Nagase, and Takeshi Akasaka

Contents

Y. Maeda
Tokyo Gakugei University, Koganei, Tokyo, Japan
e-mail: ymaeda@u-gakugei.ac.jp

S. Nagase
Kyoto University, Kyoto, Japan
e-mail: nagase@ims.ac.jp

T. Akasaka (✉)
University of Tsukuba, Tsukuba, Ibaraki, Japan
e-mail: akasaka@tara.tsukuba.ac.jp

X. Lu et al. (eds.), *Handbook of Fullerene Science and Technology*,
https://doi.org/10.1007/978-981-16-8994-9_46

Abstract

Since the development of the bulk scale production of fullerenes, many chemists have studied the chemical reactivity and development of the chemical functionalization of these carbon allotropes. To date, numerous C_{60} reactions have been reported in the literature. Of these, radical reaction and photoreaction are major chemical reactions and many such reactions have been developed. The fullerene radical is generated by the addition of a radical to C_{60} and is stabilized by delocalized unpaired electrons. Thus, C_{60} is a very good radical scavenger and has been labeled as a "radical sponge." There are two types of photoreactions: one that activates the reaction reagent and the other that activates C_{60}. This chapter focuses on the molecular transformation of C_{60} by radical reaction and photoreaction. Radical reaction and photoreaction that are not covered in this chapter include reactions involving transition metals (see ▶ Chaps. 13, "Complexation with Transition Metals" and ▶ 14, "Transition Metal Salt-Catalyzed Reactions of [60]Fullerene" for the reactions involving transition metals and ▶ Chap. 26, "Potential of Fullerenes for Photodynamic Therapy Application" for the photochemical properties of C_{60}).

Keywords

Fullerene · Radical reaction · Photoreaction · Electron transfer · Radical ion

Introduction

The radical reaction is known as the first investigational reaction of fullerene C_{60}. Fullerene has high radical scavenging activity, owing to its high electron affinity and many conjugated double bonds. Furthermore, fullerene radicals generated by the addition of radicals are stabilized by π-conjugated systems. Owing to its high reactivity toward radical species, C_{60} has been labeled as a "radical sponge." In the early studies on the chemistry of C_{60}, the reaction of C_{60} with radical species was studied using electron spin resonance (ESR). For example, the photolysis of a toluene solution of C_{60} containing di-*t*-butyl peroxide, which is a useful reagent to produce *t*-BuO radicals, changed the purple fullerene color to light amber. The mass spectra of the resulting samples revealed the formation of multiple benzylated C_{60} adducts having up to 15 benzyl groups. ESR analysis of di-*t*-butyl peroxide in toluene solution revealed the formation of the benzyl radical upon photoirradiation [1, 2]. Thus, it was revealed that the generated benzyl radical via hydrogen abstraction by *t*-BuO radicals produces multiple radical addition products of C_{60}.

The unpaired spin population distribution of alkylated C_{60} radicals over the C_{60} surface was studied by the isotropic ^{13}C hyperfine interactions of alkylated C_{60}

radicals in ESR spectra. The results revealed that the unpaired electron is mostly located at two fused six-membered rings of the addition position [3], which is one of the reasons why a typical C_{60} radical addition reaction affords 1,2-addition products when the radical is small. In addition to alkyl radicals, radical addition reactions of alkylthio and alkoxy radicals to C_{60} have been studied by ESR and MS analyses [4]. The synthesis of C_{60} derivatives by radical reactions are described below.

This chapter also describes the C_{60} addition reaction by photoreaction. Reactions with active species, including radical species, generated by photoreactions are widely used for the derivatization of C_{60}. In addition, photoirradiation of C_{60} enhances its chemical reactivity. C_{60} has a wide-range absorption band over the visible region and the quantum yield of $^3C_{60}$* formation is 1.0; therefore, $^3C_{60}$* is readily produced by photoirradiation. C_{60} displays high electron affinity, with a reduction potential in benzonitrile of −0.42 V vs SCE, measured by cyclic voltammetry, and a triplet energy of ~36 kcal/mol. Thus, $^3C_{60}$* acts as a better electron acceptor than ground state C_{60}. Early studies have indicated a good relationship between the oxidation potentials of amines, calculated energies for electron transfer using the Rehn-Weller equation, and $^3C_{60}$* quenching rate constant [5]. The $^3C_{60}$* radical can be detected by laser flash photolysis. Typically, characteristic $^3C_{60}$* absorption bands are observed at 740 and 680 nm following excitation at 532 nm. In polar solutions such as benzonitrile, in the presence of an appropriate electron donor under Ar, quenching of $^3C_{60}$* via electron transfer from the donor is confirmed by a decrease in the characteristic absorption peaks accompanied by an increase in the characteristic transient absorption peaks of the C_{60} radical anion at 950 and 1075 nm. In addition, detection of the characteristic donor radical cation absorption can be used as a good probe for the electron transfer reaction. In fact, plots of the calculated energies for electron transfer and $^3C_{60}$* quenching rates by electron donors have revealed the powerful electron accepting ability of $^3C_{60}$*. Moreover, because $^3C_{60}$* acts as a good singlet oxygen sensitizer, a singlet oxygen may be involved in the photoreaction of C_{60} in the presence of oxygen (see Chap. 2.5 for the photophysical properties of C_{60}). Examples of the photochemical reaction of C_{60} are presented below.

Equilibrium Reaction of Alkylated C_{60} Radicals and Their Dimers

A remarkable feature of alkylated C_{60} radicals is that the intensity of their ESR signal increases with increasing temperature. For example, the ESR signal of the *t*-butylated C_{60} radical increases by one order of magnitude as the temperature is raised from 27 to 77 °C. On the other hand, the ESR signal disappears at ~3 °C. This temperature-dependent cycle can be observed for several cycles without significant radical decay. The equilibrium observation of the *t*-butylated C_{60} radicals by ESR can be explained by the thermodynamic formation and bond cleavage of the homocoupling dimer $(t\text{-BuC}_{60})_2$. The enthalpies of dimerization of various alkylated C_{60} radicals have been estimated from temperature-dependent ESR measurements, and the results have revealed the good relationship between the dimer bond strengths

and size of the alkyl groups [3, 6]. The estimated enthalpies of dissociation of the RC_{60} dimers are 35.5, 22.0, 21.6, and 17.1 kcal/mol for R = isopropyl, *t*-butyl, 1-adamantyl, and CCl_3, respectively [4]. The cyclic voltammogram of the alkylated C_{60} dimer displays reversible redox waves accompanied by the formation of two molecules of the alkylated C_{60} anion [7–9].

The reversible generation of alkylated C_{60} radicals by thermal treatment was applied to control the electron mobility of the C_{60} adduct $C_{60}\{CH_2SiMe_2[C_6H_4(2\text{-ethylhexyloxy-}2)]\}_2$ in solid state (Fig. 1) [9]. The alkylated C_{60} radical was generated reversibly up to 80 °C, whereas both the ESR signal and lifetime of the radical species increased, the latter significantly, at 130 °C. DSC analysis revealed the presence of two-phase transitions at ~73 and ~127 °C, with low exothermicity, during heating and an exothermic phase transition at ~157 °C during cooling. Therefore, it was proposed that the generated alkylated C_{60} radicals strongly interact with each other, after which the two alkylated C_{60} radicals change their molecular orientation at a certain higher temperature (Fig. 2). The temperature-dependent electron mobility of the dimer in solid state was observed. Thus, the electron mobility on heating to 197 °C was (0.1–0.3) × 10^{-3} cm^2 V^{-1} s^{-1}, while cooling to 147 °C caused an almost ten-fold increase in the mobility to 1.2 × 10^{-3} cm^2 V^{-1} s^{-1}. This electron mobility of $C_{60}\{CH_2SiMe_2[C_6H_4(2\text{-ethylhexyloxy-}2)]\}_2$ in the solid state can be rationally explained by the change in their molecular orientation described above.

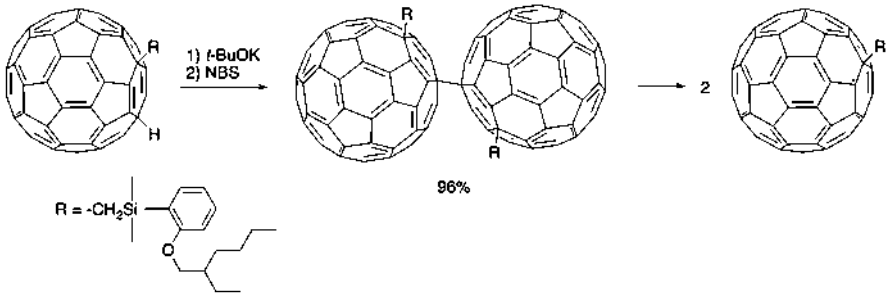

Fig. 1 Synthesis of a fullerene dimer and its thermal bond dissociation in solid state

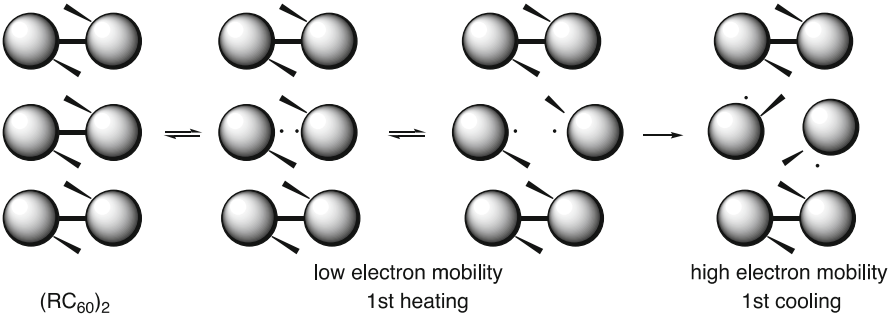

Fig. 2 Four probable states during conversion of a fullerene dimer to two radicals

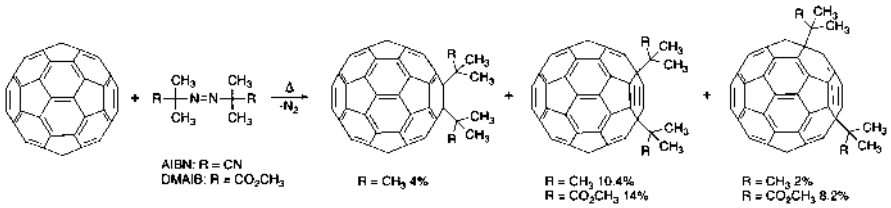

Fig. 3 Reaction of C_{60} with azo(bisisobutyronitrile) (AIBN) and dimethyl 2,2′-azo(bisisobutyrate) (DMAIB)

Radical Reaction of C_{60} with Azo(bisisobutyronitrile) (AIBN)

AIBN and its derivatives are well-known radical initiators. AIBN produces two 2-cyano-2-propyl radicals accompanied by the elimination of nitrogen [10]. The reaction of C_{60} with AIBN in a 1,2-dichlorobenzene solution at 75 °C affords three 1, x-di(2-cyano-2-propyl)-1,x-dihydrofullerene (x = 2, 4, 6) regioisomers (Fig. 3), and the 1,4-, 1,2-, and 1,6-addition products have been isolated in 10.4, 4, 2% yields, respectively. The assigned structures of these adducts were based on the characteristic absorption features attained from various analytical data including MS, ^{13}C NMR, and 2D NMR data. The formation of the 1,4-addition product as the major isomer can be explained by the steric hindrance of the 2-cyano-2-propyl groups, which decreases the formation of the 1,2-addition product. When AIBN was replaced with dimethyl 2,2′-azo(bisisobutyrate) (DMAIB), the 1,4- and 1.6-di (2-carbomethoxy-2-propyl)-dihydrofullerenes were, respectively, obtained in 14 and 8% yield by the addition of two 2-carbomethoxy-2-propyl radicals to C_{60}.

Radical Reaction of C_{60} with the Perfluoroalkyl Radical

Bis(perfluoroalkanoyl) peroxides are good precursors for perfluoroalkyl radical generation. For example, the reaction of bis(perfluoroalkanoyl) with benzene results in the formation of perfluorobenzene. The reaction of C_{60} with bis(perfluoroalkanoyl) peroxides in chlorobenzene at 40 °C under degassed conditions affords fullerene-fused 1,3-dioxolane derivatives, 1-perfluoroalkyl-4-hydroxy-1,4-dihydrofullerenes, and the perfluoroalkylated C_{60} dimer (Fig. 4) [11, 12]. The reaction mechanism for the two products is illustrated in Fig. 5. Thus, electron transfer from C_{60} to bis(perfluoroalkanoyl) peroxide affords the C_{60} radical cation and bis (perfluoroalkanoyl) peroxide radical anion, which readily decompose to the perfluoroalkyl radical, perfluoroalkanoate, and CO_2. The radical coupling of the C_{60} radical cation and perfluoroalkyl radical produces the perfluoroalkyl C_{60} cation. Subsequently, the addition of perfluoroalkanoate to the perfluoroalkyl C_{60} cation affords 1-perfluoroalkyl-4-(oxycarbonyl)perfluoroalkyl-dihydrofullerene. The product 1-perfluoroalkyl-4-hydroxy-1,4-dihydrofullerene is formed by the hydrolysis of 1,4-dihydrofullerene during work-up. On the other hand, the formation of the

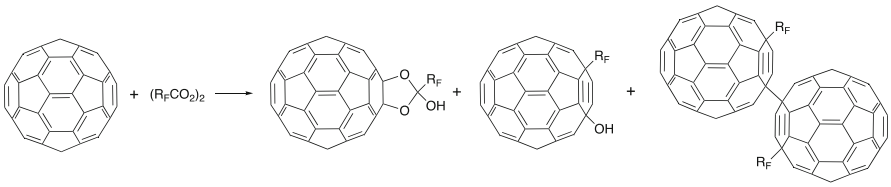

Fig. 4 Reaction of C_{60} with bis(perfluoroalkanoyl) peroxides

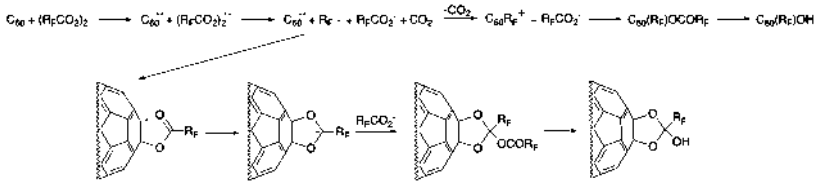

Fig. 5 Proposed reaction mechanism of the formation of 1-perfluoroalkyl-4-hydroxy-1,4-dihydrofullerenes and fullerene-fused 1,3-dioxolane derivatives from C_{60} and bis(perfluoroalkanoyl) peroxides

fullerene-fused 1,3-dioxolane derivatives is explained as follows: the reaction of C_{60} with bis(perfluoroalkanoyl) peroxide produces the C_{60} radical cation, perfluoroalkyl radical, and perfluoroalkanoate. Addition of the C_{60} radical cation and perfluoroalkanoate, subsequent intramolecular cyclization, addition of the perfluoroalkanoyl oxide anion, and hydrolysis result in the formation of the fullerene-fused 1,3-dioxolane. In this reaction, the afforded insoluble product was identified as the perfluoroalkyl C_{60} dimer by ^{13}C NMR, ^{19}F NMR, and MS spectroscopy. The alkylated C_{60} dimer is known to exist in equilibrium with the alkylated C_{60} radicals [4]. The perfluoroalkyl C_{60} dimer in benzene under reflux affords perfluoroalkyl C_{60} radicals, which are effectively trapped by tributyltin hydride to form 1-perfluoroalkyl-1,2-dihydrofullerene in 73% yield. The 1-perfluoroalkyl-1,2-dihydrofullerene is also obtained from the reaction of 1-perfluoroalkyl-4-hydroxy-1,4-dihydrofullerene with tributyltin hydride at room temperature.

The reaction of perfluoroalkyl halides with tributyltin hydride results in the formation of 1-fluoroalkyl-2-hydrofullerenes [13]. The reaction of C_{60} (1 equiv) with ethyl bromodifluoroacetate (12 equiv) in the presence of tributyltin hydride (5 equiv) was conducted in refluxing benzene solution under nitrogen atmosphere, resulting in the formation of the corresponding 1,2-dihydrofullerene in 37% yield on the basis of consumed C_{60} (Fig. 6). Formation of the 1,2-dihydrofullerenes can be explained by the presence of a radical chain reaction initiated by the tributyltin radical, whereby the tributyltin radical abstracts the bromine in bromodifluoroacetate to generate the corresponding difluoroacetate radical (Fig. 7). The addition of the difluoroacetate radical to C_{60} followed by hydrogen abstraction of the $C_{60}(CF_2COOEt)$ radical from tributyltin hydride affords the corresponding 1,2-dihydrofullerene. On the other hand, no C_{60} adducts were obtained from the

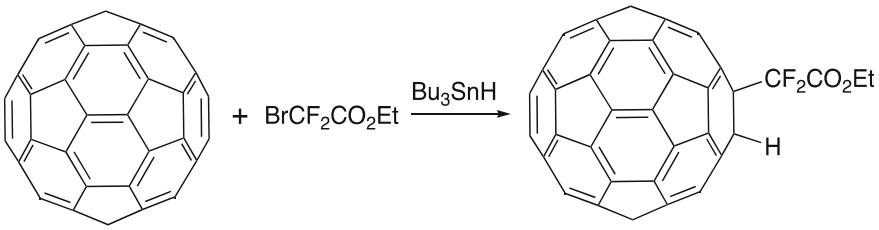

Fig. 6 Reaction of C_{60} with perfluoroalkyl halides in the presence of tributyltin hydride

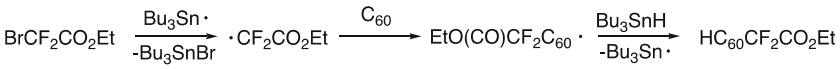

Fig. 7 Proposed reaction mechanism of the formation of 1,2-dihydrofullerenes

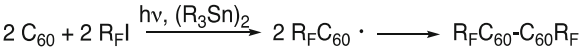

Fig. 8 Reaction of C_{60} with perfluoro iodide mediated by hexaalkylditin

reaction with *n*-$C_6F_{13}I$ under similar reaction conditions. The addition of a catalytic amount of AIBN (0.1 equiv) afforded the corresponding 1-perfluoroalkyl-1,2-dihydrofullerenes in 31% yield. AIBN probably effectively initiates the radical chain reaction. When the perfluoroalkyl bromide or perfluoroalkyl dihalide was used instead of bromodifluoroacetate, a catalytic amount of AIBN with tributyltin hydride was required in the radical chain reaction, resulting in the formation of the corresponding 1,2-dihydrofullerenes.

The efficient synthesis of fullerene dimers comprising a perfluoroalkyl group was achieved by the photochemical reaction of C_{60} with a perfluoroalkyl iodide in 1,2-dichlorobenzene, in the presence of hexaalkylditin, under nitrogen atmosphere (Fig. 8) [14]. The homolytic C–I bond cleavage in perfluoroalkyl iodides is known, but the efficiency is not good enough to form the C_{60} dimer. However, the addition of hexaalkylditin increases the efficiency of the formation of the perfluoroalkylated C_{60} dimer upon photoirradiation with a metal-halide lamp under nitrogen atmosphere. The perfluoroalkyl C_{60} dimer was isolated by a combination procedure comprising silica gel column and gel permeation chromatography. The absorption spectra of the isolated perfluoroalkyl C_{60} dimer displayed relatively similar absorption bands to those observed for the C_{60} 1,4-adduct. Therefore, based on the characteristic spectral features of the perfluoroalkyl C_{60} dimer, it is proposed that the radical recombination of the perfluoroalkyl C_{60} radical occurs at the 1,4-position of the alkyl group. Typically, the alkylated C_{60} radicals display the highest spin density at the α-position of the functionalized carbon atom in C_{60}. Therefore, the bonding of the alkylated C_{60} radical at the 1,4-position to form the C_{60} dimer was explained by the steric repulsion of the added alkylated C_{60} radicals. Photoirradiation of the dimer in benzene solution was conducted to confirm the dimer structure of the products. ESR signals corresponding to the alkylated C_{60} radicals ($g = 2.00289$, $A_1 = 2.36$,

$A_2 = 0.49$ G) were detected via photochemical C_{60}–C_{60} bond cleavage of the dimer. The $(C_3F_7C_{60})_2/(C_6F_{13}C_{60})_2$ mixture afforded $(C_3F_7C_{60})$–$(C_6F_{13}C_{60})$, while the isolated mixed dimer $(C_3F_7C_{60})$–$(C_6F_{13}C_{60})$ produced $(C_3F_7C_{60})_2$, $(C_6F_{13}C_{60})_2$, and $(C_3F_7C_{60})$–$(C_6F_{13}C_{60})$ in a 1:1:2 ratio in the photostationary state.

Charge transfer interaction of C_{60} with CF_3I and IC_4F_8I was observed in hexane solution. Photoreaction of C_{60} with 1,4-diiodooctafluorobutane in 1,2-dichlorobenzene under degassed conditions, conducted using a mercury lamp, resulted in a rapid change in the absorption spectra [15]. MS analysis of the reaction mixture revealed $C_{60}(C_4F_8I)_n$ ion peaks, while a solution of C_{60} with $C_4F_8I_2$ presented ESR signals upon photoirradiation. In addition, the same ESR spectrum was observed in the reaction mixture at higher temperatures (110–170 °C), owing to the equilibrium between the perfluoroalkylated C_{60} dimer and corresponding perfluoroalkylated C_{60} radicals. The iodooctafluorobutylated C_{60} dimer was isolated by high-performance liquid chromatography (HPLC), as a main product together with the 1,2- or 1,4-dihydrofullerene ($IC_4F_8C_{60}X$: X = H and I).

Radical Reaction of C_{60} with Arylhydrazine

The reaction of C_{60} with 4-methoxyphenylhydrazine hydrochloride was performed in refluxing chlorobenzene to produce 1-(4-methoxyphenyl)-1,2-dihydrofullerene in 37% yield together with recovered C_{60} in 61% yield (Fig. 9) [16]. A control experiment was conducted in the absence of C_{60}, under aerial conditions, to afford three chlorobiphenyl isomers. The isomer ratio (*ortho* 55%, *meta* 26%, *para* 19%) was close to that attained from the reaction of chlorobenzene with a phenyl radical, indicating the formation of the aryl radical as a reaction intermediate. On the other hand, no chlorobiphenyl isomers were obtained under nitrogen atmosphere. A reaction mechanism was proposed, based on the above control experimental results, whereby oxygen plays a key role in the oxidation of arylhydrazine to produce the corresponding aryl radical. This in turn reacts with C_{60} to afford the 1-aryl-1,2-dihydrofullerene.

The arylhydrazine hydrochloride has also been used to prepare the corresponding 1-aryl-4-hydroxy-1,4-dihydrofullerenol. The reaction of C_{60} with 4-substituted phenylhydrazine hydrochlorides and $NaNO_2$ in a toluene/H_2O mixture, at 50 °C, under air atmosphere afforded 1-aryl-4-hydroxy-1,4-dihydrofullerenol instead of 1-aryl-1,2-dihydrofullerene (Fig. 10) [17]. Both the electron-donating (4-methyl, 4-methoxy) and electron-withdrawing (4-chloro) groups on the phenyl ring could be employed in the reaction. Notably, an increase in the reaction temperature decreased the product yields. Independently, 1-aryl-2-hydroxy-1,2-dihydrofullerenol was synthesized from the nucleophilic substitution of $C_{60}O$ with an aryl group in the presence of $BF_3{\cdot}Et_2O$; however, the reaction required bulky aryl compounds.

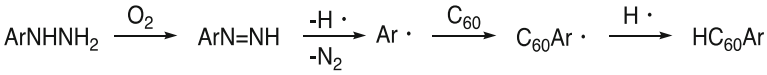

Fig. 9 Reaction of C_{60} with arylhydrazine in 4-methoxyphenylhydrazine hydrochloride

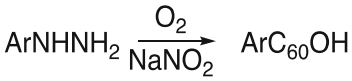

Fig. 10 Reaction of C_{60} with a phenylhydrazine hydrochloride and $NaNO_2$

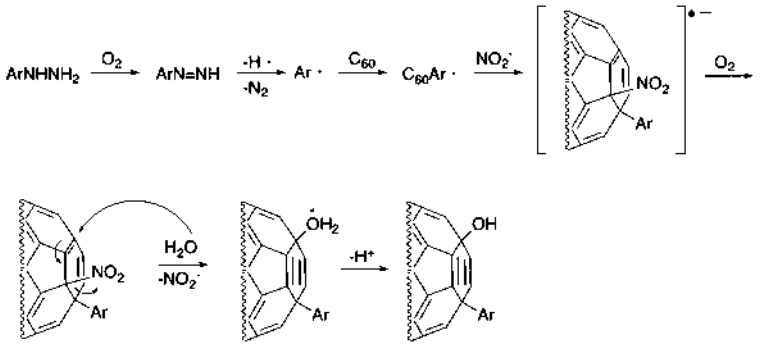

Fig. 11 Proposed reaction mechanism of 1,4-dihydrofullerene formation

In contrast, bulky aryl compounds were not required for the preparation of 1-aryl-4-hydroxy-1,4-dihydrofullerenol using arylhydrazine hydrochlorides. Control experiments revealed that when $NaNO_2$ was replaced with triethylamine, pyridine, 4-dimethylaminopyridine, aq NaOH, and aq K_2CO_3 as a base to neutralize the HCl in the phenylhydrazine hydrochlorides in the above reaction, no or trace amounts of 1-aryl-4-hydroxy-1,4-dihydrofullerenol were obtained. In addition, reaction in anhydrous toluene at 50 °C under air atmosphere afforded the 1-aryl-1,2-dihydrofullerenes ($ArC_{60}H$) in low yield. The formation of 1-aryl-2-dihydrofullerenes could be suppressed by the addition of water. In addition, 1-aryl-4-hydroxy-1,4-dihydrofullerenol did not form under nitrogen atmosphere. These control experiments indicated the importance of oxygen, $NaNO_2$, and water in the formation of 1-aryl-4-hydroxy-1,4-dihydrofullerenol. Based on the results of the control experiments, the following plausible reaction mechanism was proposed (Fig. 11): the aryl radical generated by oxidation of arylhydrazine attacks C_{60} to form the arylated C_{60} radical to which the nitrite anion is subsequently added. Oxidation of the 1-aryl-2-nitro-1,2-dihydrofullerene radical anion with oxygen and the subsequent nucleophilic substitution reaction (S_N2') of a H_2O molecule with the leaving nitrate anion produces 1-aryl-4-hydroxy-1,4-dihydrofullerenol.

Radical Addition of C_{60} with (2,2,6,6-Tetramethylpiperidinyl-1-oxy) (TEMPO)-Terminated Polystyrene

TEMPO is known as a stable radical and is used in various reactions including as a catalyst in oxidation reactions, mediator in radical polymerization, and radical scavenger in organic syntheses. TEMPO-terminated polystyrene derivatives have

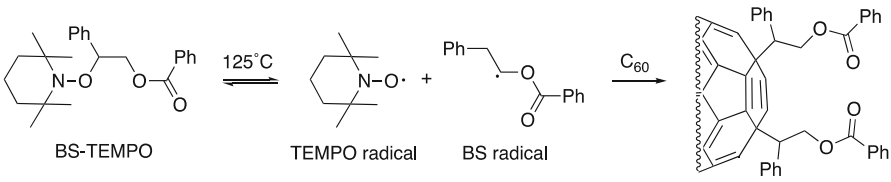

Fig. 12 Reaction of C_{60} with TEMPO-terminated polystyrene derivatives

been used in the addition reaction of C_{60}. The reaction of C_{60} with 2-benzoyloxy-1-phenylethyl (BS)-TEMPO in deaerated 1,2-dichlorobenzene at 125 °C resulted in the formation of 1,4-$C_{60}(BS)_2$ in 69% yield (Fig. 12) [18]. The addition of two BS groups at the 1,4-position was confirmed by the NMR and absorption spectra. In the proposed reaction mechanism, the BS radical and TEMPO are first generated by thermal bond dissociation with subsequent radical addition of two BS radicals to C_{60}. This radical addition reaction was also applied to the preparation of polystyrene-C_{60} (C_{60}-PS) adducts using TEMPO-terminated benzoyloxypolystyrenes under similar reaction conditions. Notably, 60–80% yields [yield = 100 x (wt of PS in C_{60}–PS)/(wt of PS–TEMPO)] of the purified product were achieved in the PS–TEMPO styrene unit range 9–100, indicating no appreciable dependence on the molecular weight of the PS moiety in this range.

Photoreaction of C_{60} with Diazirine

The photolysis and thermolysis of diazirine produce carbenes and diazo compounds. Laser flash photolysis experiments have been applied to estimate the ratio of the intermediates because the ratio of formation of the corresponding carbene and diazo compounds strongly depends on the diazirine substituents. Typically, the reaction of C_{60} with carbene affords methanofullerenes, while that of C_{60} with diazo compounds produces fulleroids. Therefore, the potential of fullerene as a chemical probe to estimate the ratio of carbene and the diazo compounds produced from diazirine, based on the methanofullerene and fulleroid yields, has been investigated. The photoreaction of 2-adamantane-2,3′-[3H]-diazirine in the presence of 10 equiv. C_{60}, using a high-mercury arc lamp, at 15 °C resulted in the formation of the corresponding adducts in 80% yield [19] (Fig. 13). A 49:51 methanofullerene-to-fulleroid isomer ratio was observed. Irradiation of 5′,5′-dimethoxyspiro[adamantane]-2,2′-[Δ31,3,4-oxadiazoline] resulted in the formation of oxadiazoline, and then oxadiazoline afforded 2-diazoadamantane (Fig. 14). After the photoreaction, C_{60} was added to the solution at −78 °C to form pyrazolinofullerene. The photoreaction of the reaction mixture at 15 °C produced the methanofullerene and fulleroid in a 12:88 ratio via the elimination of nitrogen. In addition, it was revealed that isomerization between the methanofullerene and fulleroid did not take place upon photoirradiation. Therefore, photochemically, the carbene-to-diazo formation ratio of 2-adamantane-2,3′-[3H]-diazirine was estimated

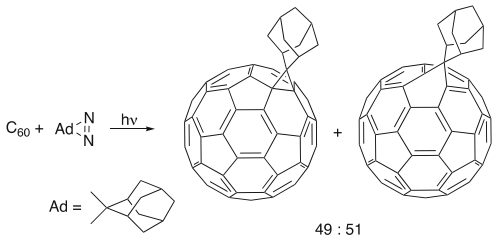

Fig. 13 Photoreaction of 2-adamantane-2,3′-[3H]-diazirine in the presence of C_{60}

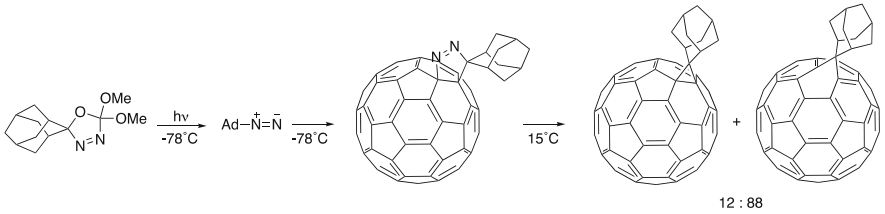

Fig. 14 Photoreaction of 5′,5′-dimethoxyspiro[adamantane]-2,2′-[Δ31,3,4-oxadiazoline] and subsequent reaction with C_{60}

at 42:58 from the results of the chemical probe experiments using C_{60}. These results are in good agreement with the results estimated by laser flash photolysis.

Nonspectroscopic methods to determine the photolytic decomposition pathways of diazirines using C_{60} have been applied to other diazirines. The photolysis of 3-chloro-3-isopropyldiazirine produces 1-chloro-2-methyl-propene. Spectroscopic analysis revealed low quantum yields of the diazo (13%) and carbene (10%) compounds. Therefore, in addition to the corresponding diazo and carbene compounds as the reactive intermediates, it has been proposed that rearrangement in the excited-state (RIES) process involves the formation of 1-chloro-2-methyl-propene [20]. The photoreaction of 3-chloro-3-isopropyldiazirine with C_{60} at −40 °C afforded the corresponding methanofullerene, pyrazolinofullerene, and 1-chloro-2-methyl-propene in 5, 13, and 82% yield, respectively (Fig. 15). Pyrazolinofullerene has been readily converted to the 5,6-open addition product at room temperature. This result, obtained from reaction with C_{60}, is in good agreement with the spectroscopic results, indicating that C_{60} can be used as a chemical probe for the photoreaction of diazirine. The proposed photoreaction pathway is presented in Fig. 16. Moreover, the substituent effects on the 3-chlorodiazirine have been well studied, as is illustrated in Figs. 17, 18 and 19 [21–23].

Photoreaction of C_{60} with Diazobenzene Oxide

The reaction of C_{60} with diazobenzene oxide presents unique reactivity depending on the structure of the cyclohexanedienone moiety. While the thermal reaction of C_{60} with diazobenzene oxides in 1,2-dichlorobenzene afforded trace amounts of products, the photoreaction of C_{60} with diazobenzene oxides using a sun lamp under nitrogen

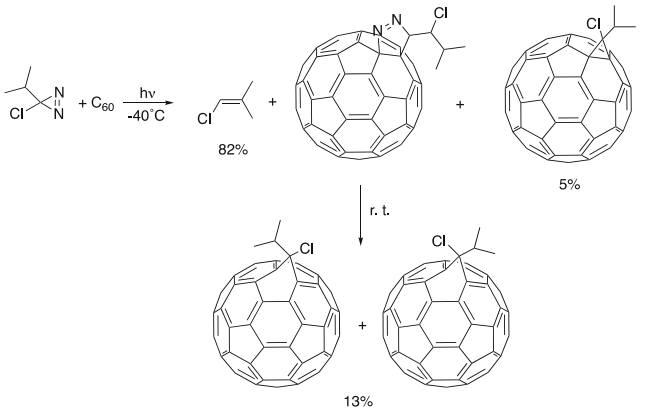

Fig. 15 Photoreaction of 3-chloro-3-isopropyldiazirine in the presence of C_{60}

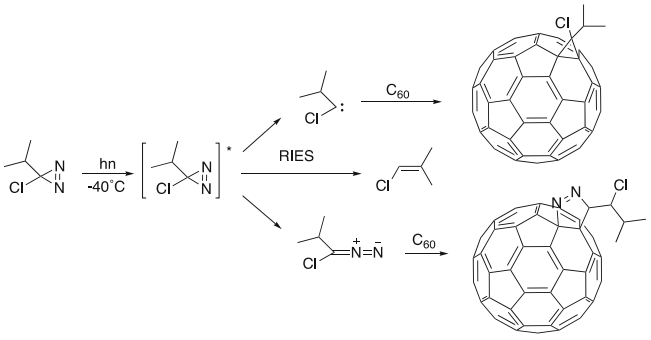

Fig. 16 Proposed reaction pathway of the photoreaction of 3-chloro-3-isopropyldiazirine in the presence of C_{60}

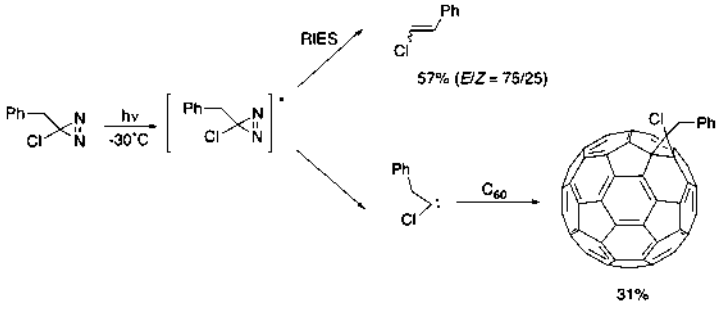

Fig. 17 Photoreaction of 3-chloro-3-chloromethyldiazirine in the presence of C_{60}

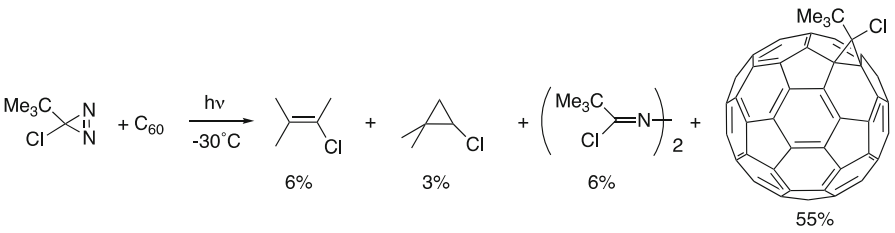

Fig. 18 Photoreaction of 3-chloro-3-*t*-butyldiazirine in the presence of C_{60}

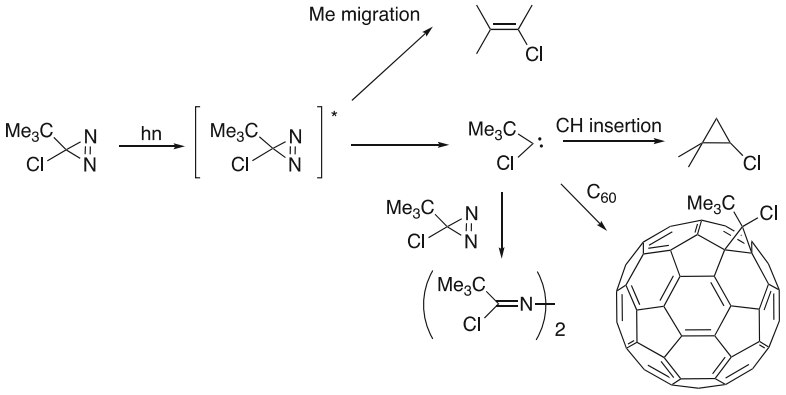

Fig. 19 Proposed reaction pathway of the photoreaction of 3-chloro-3-*t*-butyldiazirine in the presence of C_{60}

atmosphere resulted in the formation of the corresponding methanofullerenes accompanied by the elimination of nitrogen (Fig. 20) [24]. On the other hand, 10-diazoanthrone reacted with C_{60} at 60–70 °C to form the corresponding methanofullerene, with no evidence of the formation of the fulleroid isomer (Fig. 21).

Photoreaction of C_{60} with Benzocyclobutenedione

The reaction of C_{60} with benzocyclobutenone and benzocyclobutenedione produces the corresponding C_{60} addition products. Thus, the reaction of C_{60} with benzocyclobutenone afforded C_{60}-fused benzocyclohexanone in 49% yield (Fig. 22) [25]. On the other hand, the reaction of C_{60} with benzocyclobutenedione did not result in any appreciable reagent decomposition in refluxing toluene or 1,2-dichlorobenzene. The photolysis ($\lambda > 300$ nm) of a solution of C_{60} and benzocyclobutenedione afforded the corresponding methanofullerene in 35% yield with multi-adducts (Fig. 23). In this reaction, *o*-phenylene(methylene)ketone and carbene were proposed as suitable intermediates (Fig. 24).

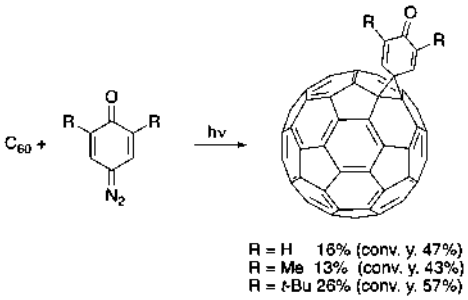

Fig. 20 Photoreaction of C_{60} with diazobenzene oxides

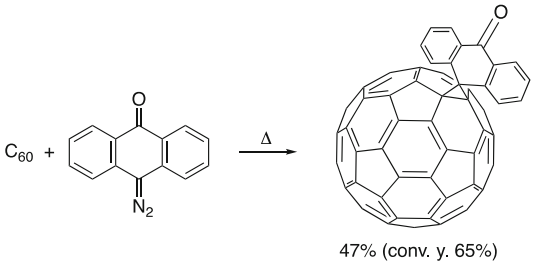

Fig. 21 Photoreaction of C_{60} with 10-diazoanthrone

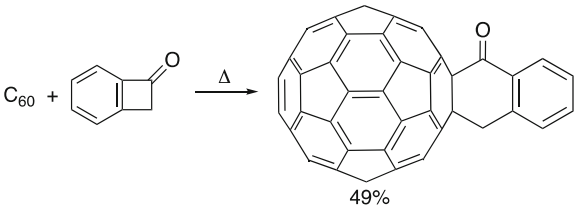

Fig. 22 Photoreaction of C_{60} with benzocyclobutenone

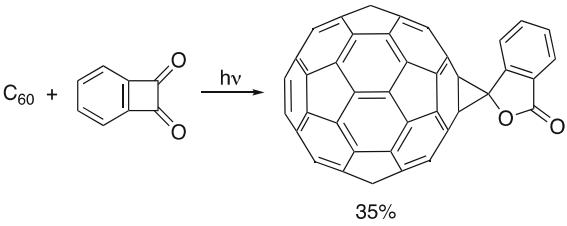

Fig. 23 Photoreaction of C_{60} with benzocyclobutenedione

Cycloaddition Reaction of C_{60} with 3,4-Fused Pyrrole-3-Sulfolenes

The [4 + 2] cycloaddition reaction of C_{60} has been studied widely as an effective approach for the derivatization of C_{60}. However, the Diels-Alder cycloadducts of fullerene undergo a cycloreversion process. Thus, to obtain stable cycloaddition

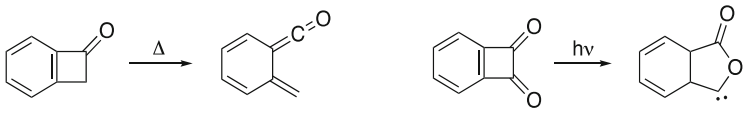

Fig. 24 Proposed reaction intermediates of the reaction of C_{60} with benzocyclobutenone and benzocyclobutenedione

Fig. 25 Reaction of C_{60} with 3,4-fused pyrrole-3-sulfolenes

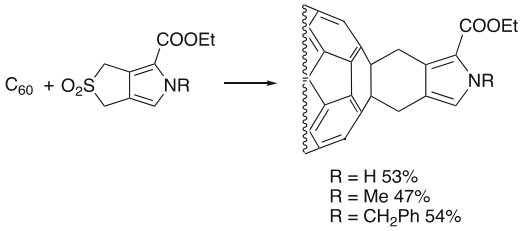

products, the formation of heteroaromatic-fused 3-sulfolenes has been conducted as follows [26]: a solution of C_{60} in 1,2-dichlorobenzene with 3,5-dihydro-4,4-dioxo-1*H*-thieno[3,4-c]pyrrole-2-carboxylates was heated at 150 °C under Ar atmosphere, resulting in the formation of the 1,2-cycloaddition products (Fig. 25). The structural determination was conducted based on their IR, NMR, and MS analytical data. As a plausible reaction mechanism, the radical addition of 3,4-dimethylidenepyrrole, generated by the thermal elimination of SO_2 from the reactant, has been proposed.

Photochemical Addition of C_{60} with an Amine

The photoreaction of C_{60} with primary and secondary amines, such as *n*-propylamine, *n*-dodexylamine, *t*-butylamine, ethylenediamine, and morpholine, under nitrogen or Ar atmosphere, readily proceeds by multiple addition on C_{60} via electron transfer. The formation of the multi-addition products $C_{60}H_n(NRR')_n$ (predominantly $n = 6$) was confirmed by elemental analysis, titration using HCl and mass and NMR spectra. Isolation and structural determination were achieved by the photoreaction of C_{60} with tertiary and secondary amines. Irradiation (350 nm light) of C_{60} and trimethylamine in toluene for 12 h afforded 1-dimethylaminomethyl-1,2-dihydrofullerene in 18% yield (Fig. 26). When the irradiation time was extended to 60 h, 1-(*N,N*-dimethylaminomethyl)-1,2-dihydrofullerene and *N*-methylpyrrolidinofullerene were obtained in 16 and 12% yield, respectively [27]. A similar photoreaction ($h\nu > 540$ nm) of C_{60} with triethylamine to obtain the corresponding pyrrolidinofullerene has also been reported [28]. In the presence of C_{60}, 1-(*N,N*-dimethylaminomethyl)-1,2-dihydrofullerene was converted to *N*-methylpyrrolidinofullerene upon irradiation (350 nm light), accompanied by the formation of $C_{60}H_2$. Thus, in the proposed formation mechanism of 1,2-dihydrofullerene and pyrrolidinofullerene, the photoinduced electron transfer affords the C_{60} and amine radical ion pair in the first step, with subsequent proton transfer and radical recombination to produce the

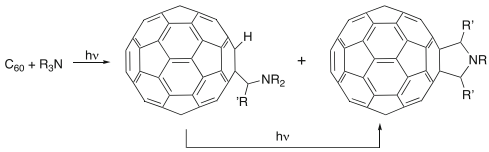

Fig. 26 Photoreaction of C_{60} with tertiary amines

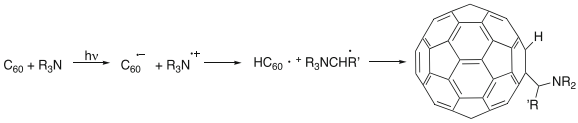

Fig. 27 Reaction mechanism of the photoreaction of C_{60} with tertiary amines

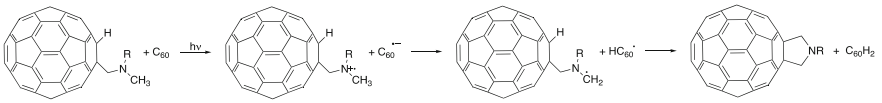

Fig. 28 Reaction mechanism of the formation of pyrrolidinofullerene from 1-aminomethyl-1,2-dihydrofullerene

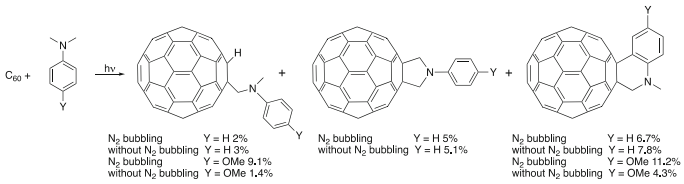

Fig. 29 Photoreaction of C_{60} with 4-substituted dimethylaniline

1,2-dihydrofullerene (Fig. 27). For the formation of the pyrrolidinofullerenes, photoinduced electron transfer from the nitrogen atom in 1,2-dihydrofullerene to C_{60} together with proton transfer affords the dihydrofullerene and HC_{60} radicals. Subsequent hydrogen atom transfer and intramolecular cyclization afford pyrrolidinofullerene and $C_{60}H_2$ (Fig. 28). When the trimethylamine was replaced with *N*,*N*-dimethylaniline, the corresponding pyrrolidinofullerene was obtained in 25% yield [27]. Detailed studies of the photoreaction of C_{60} with *N*,*N*-dimethylaniline derivatives were conducted with a high-pressure mercury lamp through a Pyrex filter [29]. In addition to the pyrrolidinofullerene, 1,2-dihydrofullerene and the cyclic addition product were obtained from *N*,*N*-dimethylaniline (Fig. 29), while pyrrolidinofullerene did not form in the reaction with 4-methoxy-*N*,*N*-dimethylaniline. The reaction efficiency increased with increasing electron-donating character of the aromatic amine, supporting the presence of a photoinduced electron transfer mechanism. Because the yields of the adducts using *N*,*N*-dimethylaniline were not affected by oxygen, it was proposed that electron transfer occurs from the aromatic tertiary amines to both $^3C_{60}$* and $^1C_{60}$*.

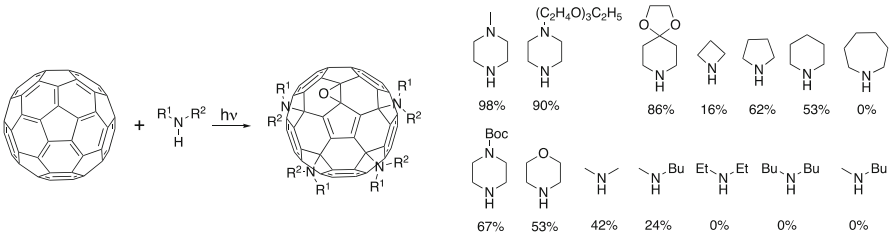

Fig. 30 Photoreaction of C_{60} with secondary amines in the presence of oxygen

Secondary amines undergo regioselective multiple addition to C_{60} upon photoirradiation in the presence of oxygen. The photoreaction of a mixture of C_{60} and 1-methylpiperazine in chlorobenzene under air with a 60 W incandescent light afforded tetraaminofullerene epoxide in 98% yield (Fig. 30). Subtle structural effects were observed in the multiple addition reaction. On the other hand, primary amines did not form an isolable adduct, although five- and six-membered cyclic amines afforded the regioselective multi-addition product in high yield [30]. A similar reaction was observed in the presence of DMSO without photoirradiation [31]. The deaerated 1:4 mixed DMSO/chlorobenzene solution of C_{60} with piperidine presented characteristic absorption peaks at 994 and 1077 nm, assigned to the C_{60} radical anion. The C_{60} radical anion persisted for at least for 2 weeks at room temperature in the absence of oxygen but reacted readily with oxygen to form tetraaminofullerene epoxide. This result revealed the strong interaction of C_{60} with amine and supported the involvement of an electron transfer mechanism. Thus, in the proposed reaction mechanism (Fig. 31), electron transfer from the amine to $^3C_{60}$* or C_{60} affords the corresponding radical ion pair. The C_{60} radical anion is oxidized by oxygen to generate C_{60} and the superoxide anion. Addition of the amine radical cation to C_{60} produces the aminated C_{60} radical, which is then oxidized by the superoxide anion radical to form the aminated C_{60} cation. Nucleophilic addition of the amine to the aminated C_{60} cation produces 1,4-diamino fullerene. Repeated addition reactions and oxygen transfers from the in-site generated H_2O_2 afford the multiple addition products, tetraaminofullerene epoxides.

Under reflux conditions in toluene, C_{60} and the glycine ester afforded a pyrrolidinofullerene comprising one ester group in <5% yield (Fig. 32). On assuming the involvement of acetone as a dimethylmethane source, however, no change was observed in the reaction rate by the addition of acetone. On the other hand, the photoreaction of C_{60} with a glycine ester under ambient conditions resulted in the formation of pyrrolidinofullerene comprising two ester groups in 60% yield (Fig. 33) [32, 33]. Interestingly, this photoreaction was thermally accelerated and the reaction rate decreased with increasing steric hindrance of the ester groups. The photoreaction of C_{60} with a sarcosine ester produced two pyrrolidinofullerenes, $C_{60}(CH_2N(CH_3)CHCOOMe)$ and $C_{60}(MeO_2CCHNHCHCOOMe)$, in 35 and 10% yield, respectively. This reaction did not proceed in the absence of oxygen under dark conditions, suggesting the involvement of oxygen. The proposed reaction (Fig. 34)

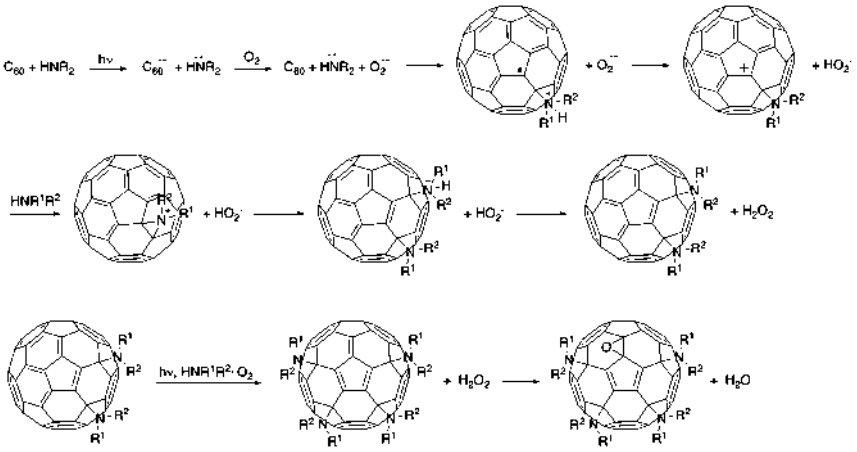

Fig. 31 Proposed reaction mechanism of the photoreaction of C_{60} with secondary amines in the presence of oxygen

Fig. 32 Reaction of C_{60} with a glycine ester

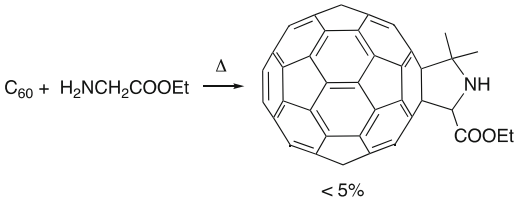

Fig. 33 Photoreaction of C_{60} with a glycine ester

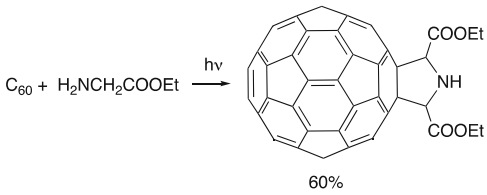

is as follows: energy transfer from $^3C_{60}$* to O_2 affords C_{60} and $^1O_2$. Hydrogen abstraction from the amino acid by $^1O_2$ produces the corresponding amino acid radical; this is followed by addition to C_{60}. Subsequently, cycloaddition of the alkylated C_{60} radical accompanied by electron transfer and elimination of the amino group afford the methanofullerene radical intermediates. The addition of another amine radical cation to the methanofullerene radical intermediate and subsequent ring expansion afford the corresponding pyrrolidinofullerene. The reaction was also extended to aminopolycarboxylates, ethylenediaminetetraacetate, and pentamethyldimethylenetriaminepentaacetate to form the corresponding pyrrolidinofullerenes comprising multicarboxylates [34].

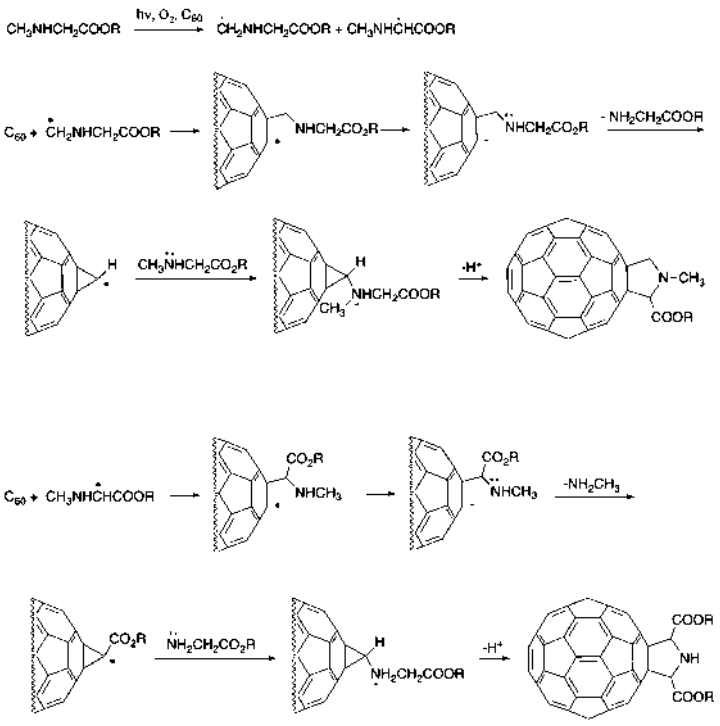

Fig. 34 Photoreaction of C_{60} with a sarcosine ester and the proposed reaction mechanism of pyrrolidinofullerene formation

Photoreaction of C_{60} with *α*-Silylamines

As mentioned above, amine acts as a good electron donor for the excited C_{60}. It is known that the introduction of an *α*-trimethylsilyl group in amine reduces its oxidation potential, thereby extending the range of electron acceptors. This property is attributed to the overlap of the high-energy $\sigma_{C\text{-}Si}$ orbital with the half-filled nitrogen p-orbital in these aminium radicals. In addition, this orbital interaction facilitates the rapid elimination of the trimethylsilyl group by nucleophiles to form carbon-centered *α*-amino radicals. This reactivity has been applied to the photoreaction of C_{60} with *α*-silylamines in a toluene-ethanol (9:1) mixed solvent to form aminomethyl-1,2-dihydrofullerenes (Fig. 35). Aminomethyl radicals have been proposed as the intermediates, generated via the photoinduced electron transfer of *α*-silylamines to $^3C_{60}$* and subsequent desilylation process by the nucleophilic addition of ethanol [35]. The addition of an aminomethyl radical to the C_{60} radical anion together with proton transfer afforded aminomethyl-1,2-dihydrofullerenes (Fig. 36). The substituent effects of *α*-silylamines have been investigated to reveal that the introduction of the electron-donating groups in *α*-silylamine increases the

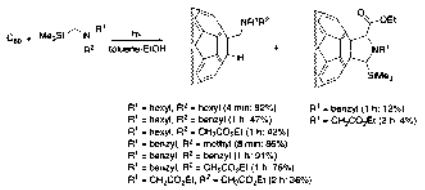

Fig. 35 Photoreaction of C_{60} with α-silyl tertiary amines

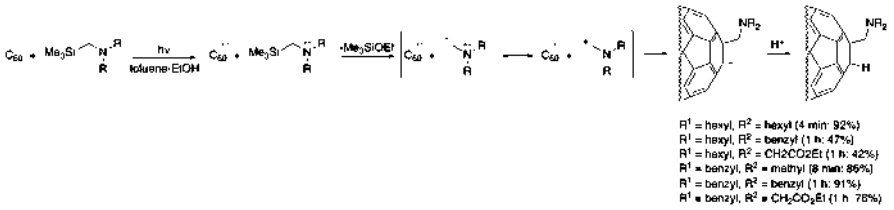

Fig. 36 Proposed reaction mechanism of the formation of 1,2-dihydrofullerene from C_{60} and α-silyl tertiary amines

yields of the formed aminomethyl-1,2-dihydrofullerenes. For example, reaction with *N,N*-dihexyl-, *N,N*-dibenzyl-, *N*-benzyl-*N*-methyl-, and *N*-benzyl-*N*-(ethyl oxycarbonylmethyl) α-silylamines afforded the corresponding 1,2-aminomethyl-1,2-dihydrofullerenes in high yield (94–76%). On the other hand, *N,N*-bis(ethyloxycarbonylmethyl)- and *N*-benzyl-*N*-hexyl-α-silylamines afforded the corresponding 1,2-dihydrofullerenes in relatively low yield (47–36%). Interestingly, pyrrilidinofullerenes were obtained as a minor product in the reaction of C_{60} with *N*-benzyl-*N*-(ethyl oxycarbonylmethyl) and *N,N*-bis(ethyl oxycarbonylmethyl)-α-silylamines in 12 and 4% yield, respectively. As mentioned above, the $^1O_2$ generated photochemically in the presence of C_{60} could be involved in the formation of pyrrolidinofullerenes in the photoreaction of C_{60} with an amine. In order to confirm the participation of $^1O_2$, the photoreaction of C_{60} with α-silylamines was conducted under oxygen atmosphere, resulting in the formation of pyrrolidinofullerenes in higher yields (Fig. 37). For example, the photoreaction of C_{60} with *N*-benzyl-*N*-(ethyl oxycarbonylmethyl) in the presence of oxygen formed the corresponding methanofullerene in 70% yield. Based on these experimental results, a plausible mechanism was proposed as follows: the reaction of $^1O_2$ with silylmethylamine affords the hydroperoxy and silylmethylamine radicals. Subsequent hydrogen abstraction affords the azomethine ylide to form the corresponding pyrrilidinofullerenes (Fig. 38).

The substituent effects of trimethylsilyl-*N*-alkyl-*N*-benzylamines on the photoreaction with C_{60} were also studied. The photoreaction of C_{60} with trimethylsilyl-*N*-alkyl-*N*-benzylamines in a toluene-ethanol (9:1) solution under nitrogen atmosphere afforded the corresponding 1,2-dihydrofullerenes. Notably, the bulkiness of the alkyl groups on the nitrogen atom affected the 1,2-dihydrofullerene yield (Fig. 39) [36]. Moreover, the electronic effects of

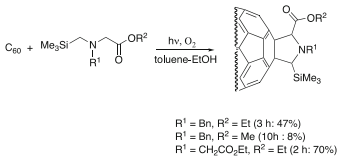

Fig. 37 Photoreaction of C_{60} with α-silyl amines: oxygen effects on pyrrolidinofullerene formation

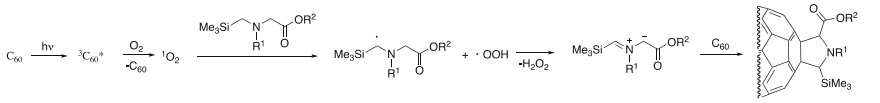

Fig. 38 Proposed reaction mechanism of the formation of pyrrolidinofullerene from C_{60} and α-silyl tertiary amines in the presence of oxygen

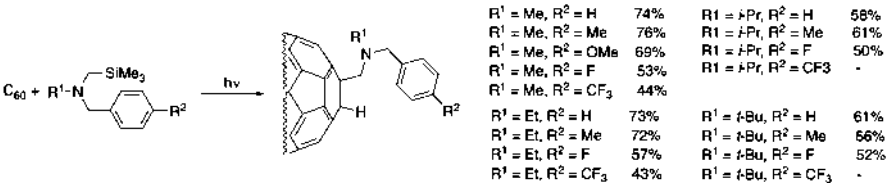

Fig. 39 Photoreaction of C_{60} with α-silyl(arylmethyl)amines

the phenyl group decreased the 1,2-dihydrofullerene yields more than they did the steric effects of alkyl group.

The substituent effects on the phenyl ring in the benzyl groups were also investigated. When *N*,*N*-bis(4-fluorophenylmethyl)-α-silylamine was used, the photoreaction efficiency and yield of 1,2-dihydrofullerene were relatively low compared to those observed with *N*,*N*-dibenzyl-α-silylamine. On the other hand, the photoreaction efficiency and yield of 1,2-dihydrofullerene increased when electro-donating groups were introduced in the phenyl ring in *N*,*N*-bis(phenylmethyl)-α-silylamine. These experimental results revealed that the electron donating groups in *N*,*N*-bis (phenylmethyl)-α-silylamine enhance the reaction efficiency [37]. When the photoreaction of *N*,*N*-bis(4-fluorophenylmethyl)α-silylamine was conducted in the presence of oxygen, the corresponding pyrollidinofullerenes were obtained selectively (Fig. 40). The generation of imine as a reaction intermediate, via hydrogen atom abstraction from aminomethyl-1,2-dihydrofullerenes by the active oxygen generated excited C_{60}, was proposed. For the formation of pyrrolidinofullerenes, involvement of $^1O_2$ was proposed.

The photochemical reaction with α-silylamines is effective for both tertiary and secondary amines. The photoreaction of C_{60} with *N*-benzyl-α-silylamines in a toluene-ethanol (9:1) mixed solvent afforded the corresponding aminomethyl-1,2-dihydrofullerenes [38, 39]. Interestingly, in the photoreaction where electron-withdrawing fluorine or trifluoromethyl groups were introduced to the *N*-benzyl-α-

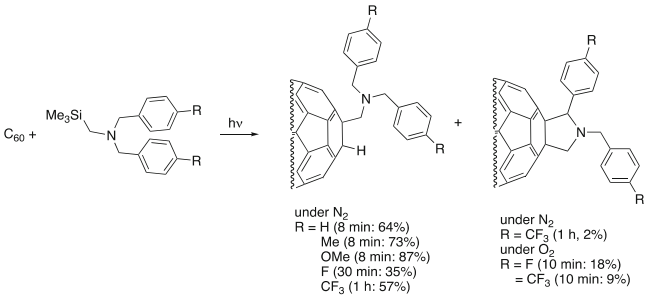

Fig. 40 Photoreaction of C_{60} with α-silyldi(arylmethyl)amines

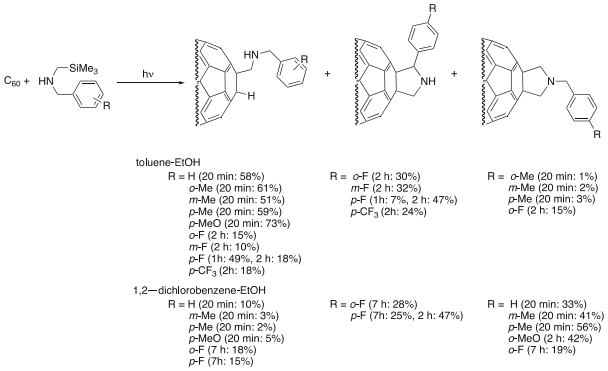

Fig. 41 Photoreaction of C_{60} with α-silyl (arylmethyl)amines

silylamine phenyl group, the corresponding pyrrolidinofullerene and 1,2-dihydrofullerene were formed competitively (Fig. 41). Typically, the introduction of electron-withdrawing groups in α-silylamines decreases the 1,2-dihydrofullerene yield and increased the pyrrolidinofullerene yield. Thus, the pyrrolidinofullerene formation yield and efficiency were significantly increased and those of the 1,2-dihydrofullerene decreased by replacing the toluene-EtOH mixed solvent with a 1,2-dichlorobenzene-EtOH mixed solvent.

The generation of azomethine ylide was proposed for the formation of pyrrolidinofullerenes from α-silylamine. Azomethine ylide is a good intermediate for pyrrolidinofullerene formation. One of the proposed reaction mechanisms is as follows (Fig. 42): photoinduced electron transfer and subsequent elimination of a trimethylsilyl group afford the corresponding aminium radicals. A second electron transfer, from the aminium radicals to C_{60}, affords iminium ions, which react with another secondary amine to form geminal diamines. Elimination of the primary amine from the geminal amine produces α-trimethylsilyl-substituted iminium ions, while subsequent solvent-promoted desilylation produces azomethine ylide. Finally, 1,3-dipole cycloaddition of azomethine ylide to C_{60} affords the *N*-benzylated pyrrolidinofullerene.

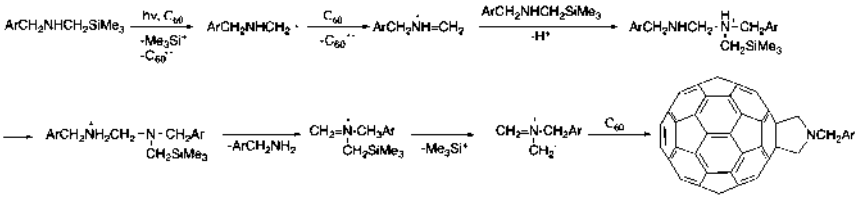

Fig. 42 Proposed reaction mechanism of the formation of pyrrolidinofullerene from C_{60} and α-silyl (arylmethyl)amines

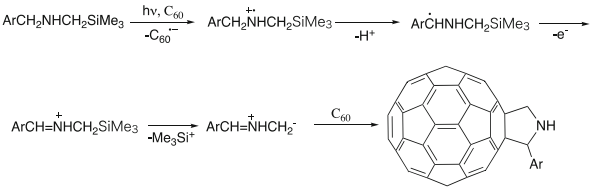

Fig. 43 Proposed reaction mechanism of the formation of pyrrolidinofullerene from C_{60} and α-silyl (arylmethyl)amines

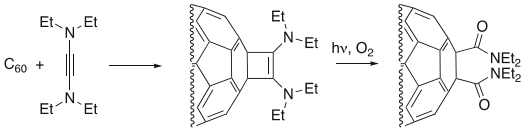

Fig. 44 Reaction of C_{60} with ethyndiamine and subsequent photooxidation reaction

In the formation of another isomer of pyrrolidinofullerene, an amine radical cation was generated via electron transfer to $^3C_{60}$*. Subsequent deprotonation and one electron oxidation of the amine radical cation formed the corresponding iminium cation. The elimination of the trimethylsilyl group from the iminium cation afforded the corresponding azomethine ylide to finally produce the pyrrolidinofullerene (Fig. 43).

The photoreaction of C_{60} and α-silyldiaryl- or α-silylarylamine in the presence of a photoredox catalyst was effective in increasing the aminomethyl-1,2-dihydrofullerene yield [40, 41].

Photoreaction of C_{60} with Alkyne and Alkene

At room temperature, C_{60} reacted with the electron-rich alkynes *N*,*N*,*N*′,*N*′-tetraethylethyndiamine and *N*,*N*-tetraethyl-2-ethylthioethyndiamine to form the [2 + 2] addition 1,2-dihydrofullerene-1,2-cyclobutene products in 52 and 47% yield, respectively (Fig. 44) [42]. The afforded cyclobutene adducts reacted with oxygen by photoirradiation via self-sensitized photooxidation to form the corresponding amide derivatives. The reaction of C_{60} and the electron-rich enynamine did not proceed in

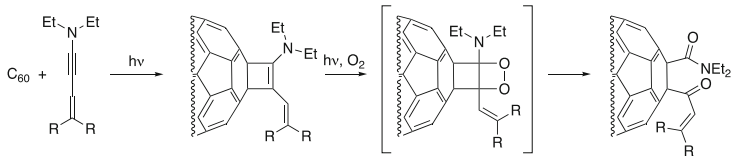

Fig. 45 Reaction of C_{60} with enynamine and subsequent photooxidation reaction

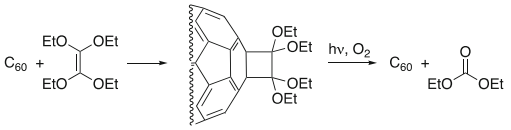

Fig. 46 Reaction of C_{60} with an electron-rich alkene and photochemical cycloreversion of the [2 + 2] cycloaddition product in the presence of oxygen

the absence of light; however, it proceeded by light irradiation (>500 nm), resulting in the formation of C_{60}-fused cyclobutenamine (Fig. 45). In the presence of oxygen, the cyclobutene adduct was photochemically converted to fullerenone amide. Similar to C_{60}, 1,2-dihydrofullerenes have also been shown to be excellent singlet oxygen sensitizers; therefore, it was proposed that a C_{60}-fused cyclobutenamine reacts with $^1O_2$ by self-sensitized photooxygenation to form a dioxetane intermediate and subsequently, the fullerenone amide [43]. The electron-rich alkenes, tetraalkoxyethylenes, react with C_{60} in reflux benzene solution. However, the attained C_{60}-fused cyclobutane was unstable in the presence of oxygen upon photoirradiation and underwent efficient photochemical cycloreversion to form C_{60} with diethyl carbonates in >95% yield (Fig. 46).

In the absence of light, C_{60} did not react with the arylalkene under deoxygenated conditions, even in the presence of a refluxing toluene solution. On the other hand, the [2 + 2] cycloaddition of C_{60} with an arylalkene proceeded upon photoirradiation with a xenon lamp (λ >500 nm). HPLC analysis revealed the formation of the [2 + 2] adduct in 30% yield after 30 min reaction, based on the recovered C_{60}. For example, *cis*-1-(*p*-methoxyphenyl)-ethylene-2-d_1 afforded both C_{60}-fused *cis*- and *trans*-cyclobutene accompanied by the formation of *trans*-1-(*p*-methoxyphenyl)-ethylene-2-d_1 (Fig. 47) [44, 45]. When 1-(*p*-methoxyphenyl)-ethylene was replaced with (*E*)-1-(*p*-methoxyphenyl)-prop-1-ene or (*Z*)-1-(*p*-methoxyphenyl)-prop-1-ene, C_{60} fused *trans*-cyclobutane was obtained. Based on the results of this stereochemistry and the secondary isotope effects of the reaction with *p*-methoxystyrene derivatives, a stepwise reaction mechanism through an open intermediate (dipole of biradical) between $^3C_{60}$* and the ground state of the arylalkene was proposed (Fig. 48). This stepwise mechanism was also supported by the formation of the thermodynamically more stable *trans* cycloadduct over the corresponding *cis* cycloadduct from *cis*/*trans*-4-propenylanisole.

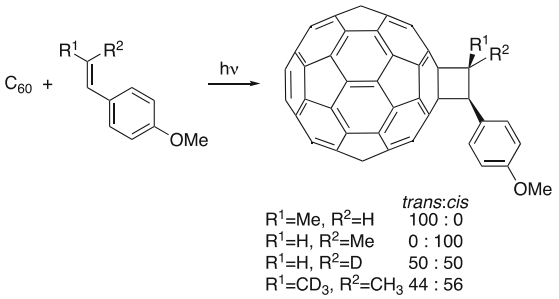

Fig. 47 Photoreaction of C_{60} with an arylalkene

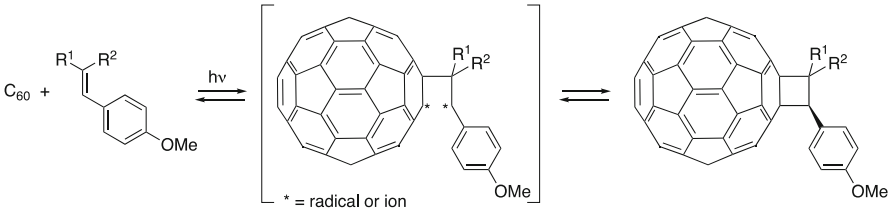

Fig. 48 Proposed reaction mechanism of the photoreaction of C_{60} with an arylalkene

Dienes

The reversible photochemical [2 + 2] addition of a diene to C_{60} was achieved by the reaction of C_{60} with 1,3-butadiene derivatives (Fig. 49). For example, the photoreaction of C_{60} with 20-fold excess 2,5-dimethyl-2,4-hexadiene afforded 6,6-(61,61-dimethyl-62-(2′-methyl)propenylcyclobutane) dihydrofullerene in 60% yield [46]. The yield was dependent on the concentration of the reactant but did not increase with prolonged reaction time. The isolated cyclobutene adduct afforded C_{60} and the diene by cycloreversion in 3 min at room temperature, which is consistent with an equilibrium between C_{60} and the diene.

The photoreaction of C_{60} with *trans*, *trans*-2,4-hexadiene resulted in the formation of the *trans*-cyclobutene, *cis*-cyclobutene, and Diels-Alder adducts in 69.4, 8.8, and 21.8% yield, respectively. The control experiment revealed that the Diels-Alder adduct was produced from a thermal reaction without photoirradiation. On the other hand, the photocycloaddition of *cis*, *cis*-2,4-hexadiene to C_{60} produced the *trans*-cyclobutene adduct as the major product. A reaction mechanism involving the electron transfer and subsequent stepwise radical coupling of the resulting radical ion pair was confirmed by the above described stereochemical studies and secondary isotope effects on the photoreaction of the diene and C_{60}. The experimental results indicated that the lifetime of the biradical intermediate was long enough to afford the thermodynamically more stable *trans*-cyclobutane products.

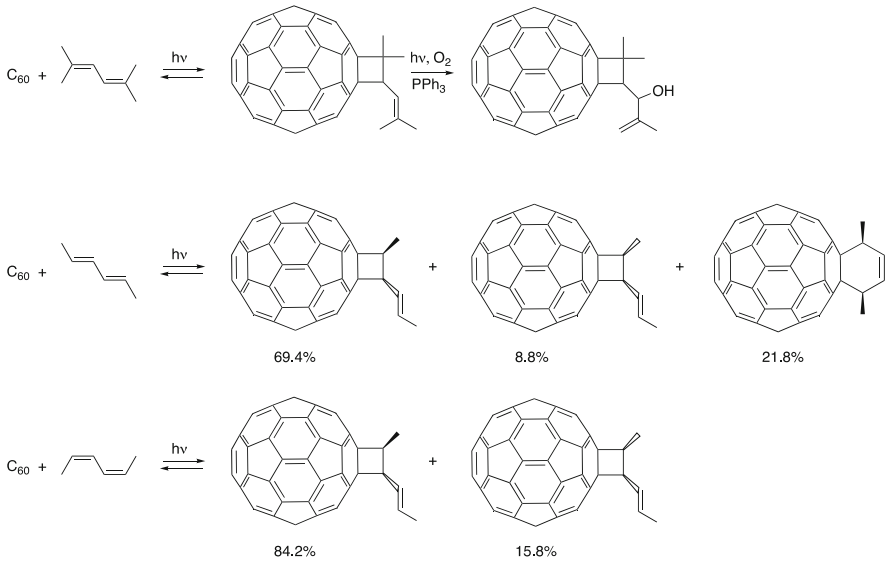

Fig. 49 Photoreaction of C_{60} with a diene

Fig. 50 Photoreaction of C_{60} with Danishefsky's diene

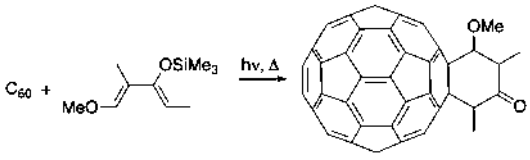

The photochemical Diels-Alder reaction of C_{60} was conducted using Danishefsky's diene to confirm the stepwise reaction mechanism based on the product stereochemistry, kinetics, and detection of the radical intermediates (Fig. 50) [47, 48]. The formation of the 1,4-*trans*-adduct as the major Diels-Alder product and the observed rate constants of $^3C_{60}$* quenching and C_{60} radical anion generation by laser flash experiments agree well with the proposed photoinduced electron transfer and stepwise addition of the radical ion pair (Fig. 51.).

Enone and Dienone

The [2 + 2] photocycloaddition of the cyclic enone of C_{60} under Ar atmosphere was also performed (Fig. 52). The cycloaddition only occurred upon light absorption by the enones, suggesting that the excited cyclic enones were key intermediates in the reaction [49]. The stepwise [2 + 2] photocycloaddition via a triplet 1,4-biradical of

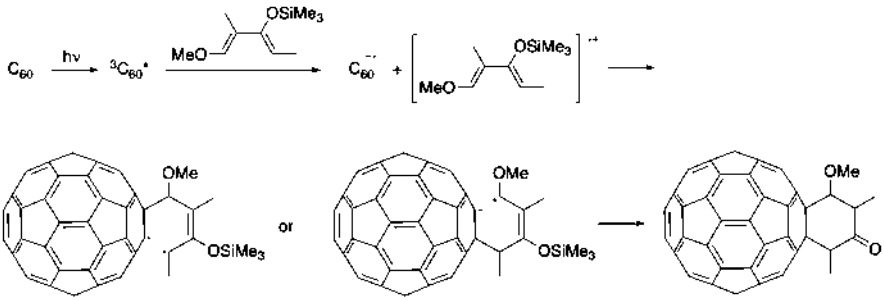

Fig. 51 Reaction mechanism of the photoreaction of C_{60} with Danishefsky's diene

Fig. 52 Photoreaction of C_{60} with cyclohexenone

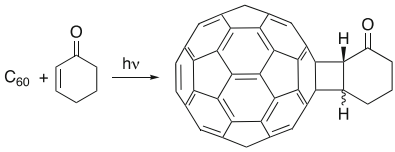

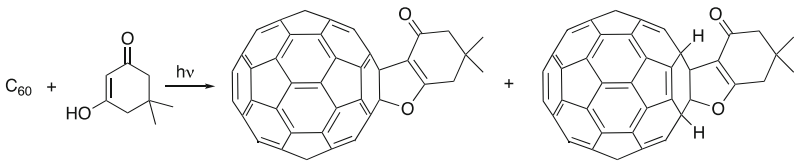

freeze-pump thaw	2.6%	7.1%
argon bubbling	4.6%	4.9%
O_2 bubbling	0%	0%

Fig. 53 Photoreaction of C_{60} with 3-hydroxycyclohex-2-en-1-one

the enone was proposed based on the formation of both the *cis*- and *trans*-fused cycloadducts. The photocycloaddition of acyclic enones and dienones to C_{60} was also conducted to obtain the [2 + 2] addition products with high regio- and stereoselectivity, attributed to the relative stability of the afforded biradical intermediates and isomers.

The photoreaction of C_{60} with cyclic 1,3-diones in benzene solution produced two fused furanylfullerenes (Fig. 53) [50]. The ratio of the adducts was dependent on the deaerating method of the solvent prior to irradiation. In addition, the photoreaction did not proceed following O_2 bubbling. The proposed reaction mechanism is illustrated in Fig. 54.

The regio- and stereoselective [2 + 2] photocycloaddition of C_{60} was conducted using acyclic enones [51]. The [2 + 2] cycloaddition was reversible and reached equilibrium upon photoirradiation. The photoreaction of C_{60} with *trans*-6-methyl-

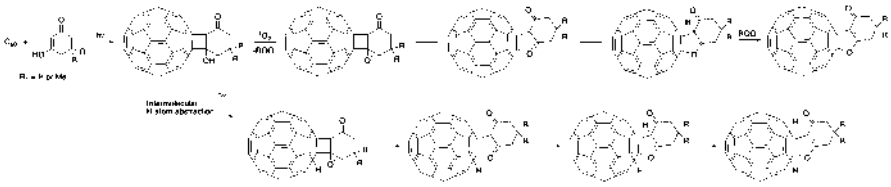

Fig. 54 Proposed reaction mechanism of the formation of fused furanylfullerenes from C_{60} with 3-hydroxycyclohex-2-en-1-one

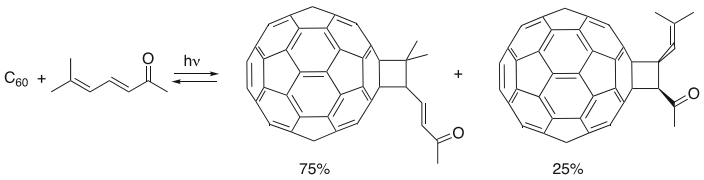

Fig. 55 Photoreaction of C_{60} with 6-methyl-3,5-heptadien-2-one

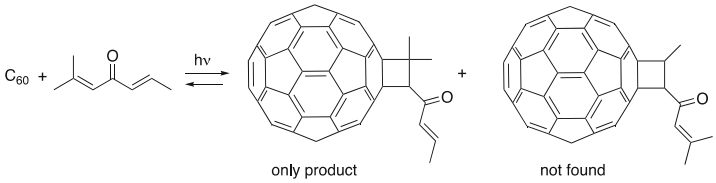

Fig. 56 Photoreaction of C_{60} with 2-methyl-2,5-heptadien-4-one

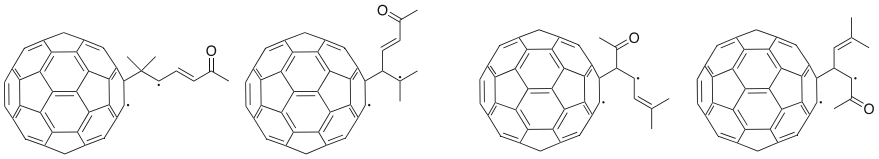

Fig. 57 Possible intermediates in the reaction of C_{60} with 3-hydroxycyclohex-2-en-1-one

3,5-heptadien-2-one and *trans*-2-methyl-2,5-heptadien-4-one in deoxygenated toluene with a xenon lamp afforded the corresponding [2 + 2] addition products regio- and stereoselectively (Figs. 55 and 56). The high selectivity was attributed to the stability of the possible radical intermediates. Since the radical intermediates that formed the main products were more stable than the other radical intermediates (Figs. 57 and 58, respectively), the [2 + 2] cycloaddition proceeded regio- and stereoselectively under thermodynamic control.

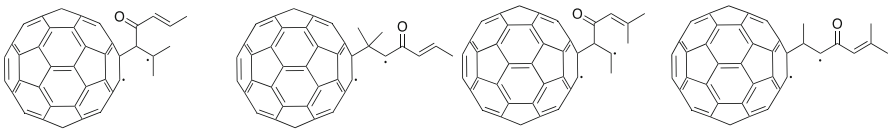

Fig. 58 Possible intermediates in the reaction of C_{60} with 3-hydroxycyclohex-2-en-1-one

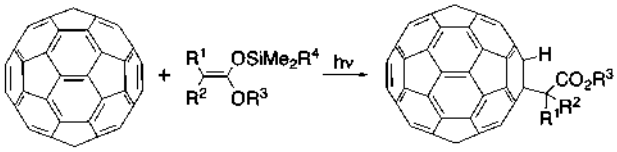

a R^1, R^2, R^3, R^4 = Me, Me, Me, Me	80%
b R^1, R^2, R^3, R^4 = H, Me, Et, Me	59%
c R^1, R^2, R^3, R^4 = H, Me, Et, *t*-Bu	51%
d R^1, R^2, R^3, R^4 = H, H, Et, Me	62%
e R^1, R^2, R^3, R^4 = H, H, Et, *t*-Bu	7%
f R^1, R^2, R^3, R^4 = H, Ph, Et, Me	54%
g R^1, R^2, R^3, R^4 = OCH_2Ph, Ph, CH_2Ph, Me	0%

Fig. 59 Photoreaction of C_{60} with ketene silyl acetals

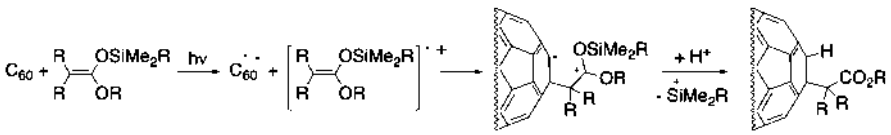

Fig. 60 Photoreaction mechanism of C_{60} with ketene silyl acetals

Photoreaction of C_{60} with Ketene Silyl Acetals

The photochemical reaction of C_{60} with ketene silyl acetals proceeded via the 1,2-dihydrofullereneacetates as illustrated in Fig. 59 [52, 53]. The reaction mechanism was confirmed by a control experiment using spin trap reagents, with the results suggesting that the reaction involved photoinduced electron transfer from the ketene silyl acetates to $^3C_{60}$*. In addition, the formation of the corresponding radical ion pair generated by the photoinduced electron transfer was detected by a laser flash photolysis experiment in benzonitrile. The determined rate constant of the electron transfer by laser flash photolysis strongly evidenced the electron transfer mechanism (Fig. 60).

Photoreaction of C_{60} with Epoxide and Cyclopropenylidene

The photoreaction of C_{60} with *trans*-aroyl-3-aryl oxiranes in toluene with a high-voltage mercury lamp predominantly afforded the *cis* isomer of the C_{60}-fused tetrahydrofuran derivatives (Fig. 61) [54]. The introduction of electron-withdrawing groups in the aryl group accelerated the reaction rate. Conversely, the reaction did not proceed when a nitro group was introduced in the aryl group. The introduction of a methoxy group or chlorine atom in the benzoyl group decreased the product yields.

The preparation of five-, seven-, and nine-membered cyclic C_{60} adducts was achieved by the photoreaction of C_{60} with dienyl cyclopropanes [55]. A toluene solution of C_{60} and a 30-fold excess of 2-(*trans*-2′-phenylcyclopropyl)-5-methyl-2,4-hexadiene afforded the corresponding cycloaddition products (Fig. 62). Consumption of dienyl cyclopropane was suppressed by the addition of 10 equiv. rubrene, a well-known triplet quencher. In addition, 1,2-diphenyl- and 1-methyl-2-phenyl cyclopentane did not produce the addition product of C_{60} upon photoirradiation. Based on these experimental results, an electron transfer mechanism from the dienyl cyclopropane to $^3C_{60}$* was proposed as follows: the incipient radical cation undergoes ring opening and addition of the C_{60} radical anion affords the biradical intermediate. The allylic radical delocalized in the dienyl group afforded the five-, seven-, and nine-membered cyclic C_{60} adducts in 60, 16, and 24% yield, respectively.

On expanding this photoreaction, the tandem (3 + 2) cycloaddition of the vinyl biscyclopropane derivatives with C_{60} was developed [56]. This reaction afforded

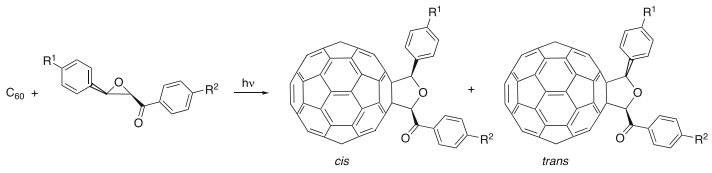

	cis	*trans*
R^1 = OMe, R^2 = H	29%	20%
R^1 = Me, R^2 = H	42%	25%
R^1 = H, R^2 = H	34%	19%
R^1 = Cl, R^2 = H	20%	13%
R^1 = NO_2, R^2 = H	-	-
R^1 = H, R^2 = OMe	21%	14%
R^1 = H, R^2 = Cl	32%	24%
R^1 = H, R^2 = NO_2	-	-

Fig. 61 Photoreaction of C_{60} with *trans*-aroyl-3-aryl oxiranes

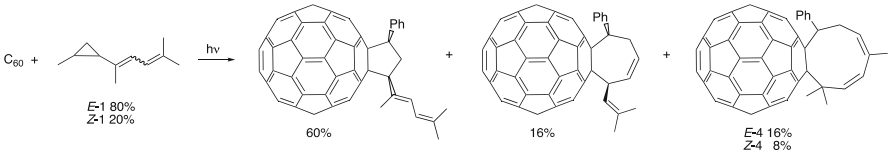

Fig. 62 Photoreaction of C_{60} with dienyl cyclopropanes

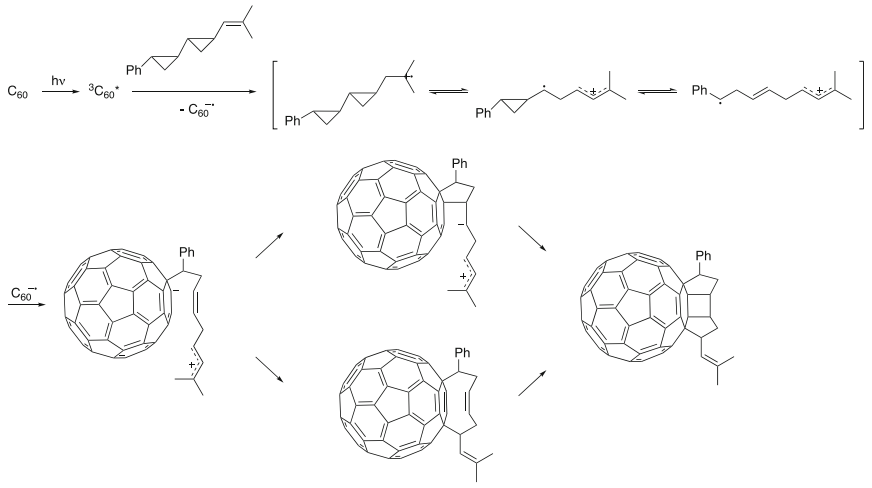

Fig. 63 Tandem (3 + 2) cycloaddition of C_{60} with vinyl biscyclopropane derivatives and its proposed reaction mechanism

cis-1 tricyclic-fused organofullerenes bearing a 5-4-5 fused tricyclic ring system. The proposed reaction mechanism via electron transfer from the vinyl biscyclopropane derivatives to $^3C_{60}$* and stepwise ring opening is presented in Fig. 63.

Photoreaction of C_{60} with NADH and NAD Dimer Analogues

Nicotinamide adenine dinucleotide (NAD^+/NADH) is well-known for its role in electron transport. The photoreaction of C_{60} with NADH and NAD dimer $(BNA)_2$ analogues were also studied in detail [57]. Thus, in a deaerated PhCN solution, $(BNA)_2$ acted as a two-electron donor to $^3C_{60}$* to produce 2 equiv. C_{60} radical anion and 2 equiv. BNA^+ via bond cleavage of the dimer (Fig. 64). C_{60} radical anion formation was observed by monitoring the characteristic absorption peaks at 600 and 1080 nm. When BNAH was replaced with *t*-BuBNAH, the *t*-butylated C_{60} anion was formed via photoinduced electron transfer from *t*-BuBNAH to $^3C_{60}$*. Subsequently, the *t*-Bu radical was eliminated from the *t*-BuBNAH radical cation and readily attacked the C_{60} radical anion to form the *t*-butylated C_{60} anion. The addition of trifluoroacetic acid and benzyl bromide to the *t*-butylated C_{60} anion produced 1,2-*t*-BuC_{60}H and 1,4-*t*-Bu(benzyl)C_{60}, respectively (Fig. 65).

The photoreaction of C_{60} with 10-methyl-9,10-dihydroacridine ($AcrH_2$) in deaerated PhCN in the presence of trifluoroacetic acid afforded 1,2-$C_{60}H_2$ in 70% yield (Fig. 66) [58]. The reaction mechanism was confirmed by the control and laser flash photolysis experiments. As the first step, electron transfer from $AcrH_2$ to $^3C_{60}$*, followed by proton transfer, produced the AcrH and HC_{60} radicals. The second electron transfer from the AcrH radical to the HC_{60} radical and subsequent protonation of the HC_{60} anion by trifluoroacetic acid yielded $AcrH^+$ and 1,2-$C_{60}H_2$.

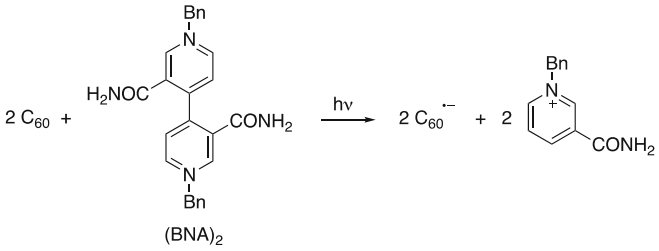

Fig. 64 Photoreaction of C_{60} with $(BNA)_2$

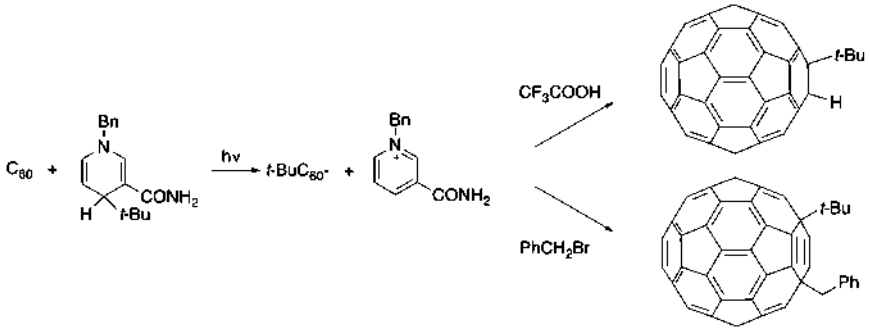

Fig. 65 Photoreaction of C_{60} with *t*-BuBNAH

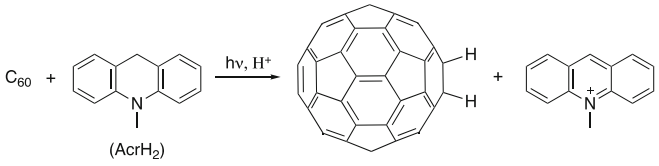

Fig. 66 Photoreaction of C_{60} with $AcrH_2$

The photocatalytic oligomerization of C_{60} proceeded in the presence of a 9-mesityl-10-methylacridinium ion (Acr^+-Mes). Acr^+-Mes has a long lifetime and high oxidation and reduction abilities (Fig. 67) [59]. The photoreaction of C_{60} with Acr^+-Mes was conducted in a deaerated acetonitrile-toluene solution under visible light irradiation ($\lambda = 430$ nm). Matrix-assisted laser desorption/ionization time of flight (MALDI-TOF) MS analysis of the photoproducts revealed the formation of fullerene oligomers such as C_{120}, C_{180}, and C_{240}. The respective IR peaks observed at 1493, 1454, and 1430 cm^{-1} were in good agreement with the reported values for C_{120} (1431, 1428, 1261 cm^{-1}) and the fullerene oligomer (1493, 1458, 1423 cm^{-1}), respectively. In the laser flash photolysis experiment of C_{60} and Acr^+-Mes in

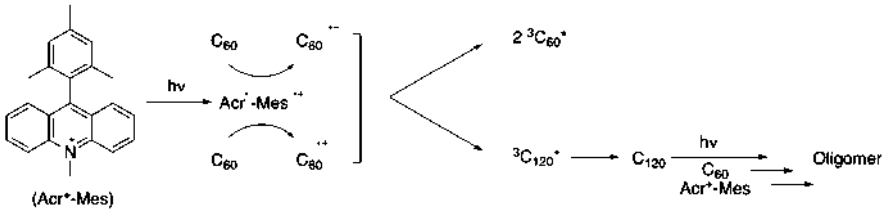

Fig. 67 Photocatalytic oligomerization of C_{60} in the presence of Acr^{+}-Mes

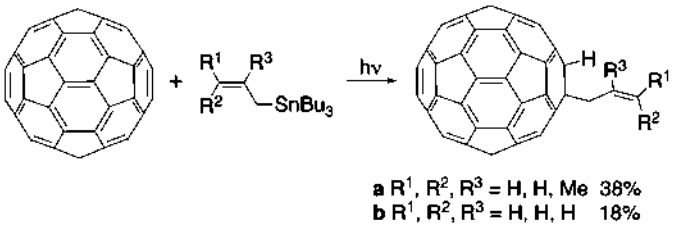

Fig. 68 Photoreaction of C_{60} with allyltributyltin

deaerated PhCN, a transient absorption band assigned to $^{3}C_{60}$* was observed at 740 nm. The observed characteristic bands assigned to the C_{60} radical cation (960 nm) and C_{60} radical anion (1080 nm) were accompanied by a decrease in the $^{3}C_{60}$* band. The ESR signals of the C_{60} radical anion and C_{60} radical cation were observed under irradiation of a deaerated acetonitrile-toluene solution containing C_{60} at −130 °C. The free energy changes of the photoinduced electron transfer from both C_{60} to the Mes radical cation moiety and the Acr radical moiety to C_{60} were negative, indicating that the electron transfer proceeded exothermically.

Photoreaction of C_{60} with Allyltributyltin

The formation of 1-allyl-1,2-dihydrofullerenes was conducted by the photoreaction of C_{60} with allyltributyltin in benzene solution with a high-pressure mercury lamp (Fig. 68) [60]. In this reaction, the α-addition products were obtained selectively. The selective formation of the α-addition product occurred because the α-addition product was preferred kinetically and thermodynamically over the γ-addition product. The electron transfer mechanism from allyltributyltin to $^{3}C_{60}$* was confirmed by a laser flash photolysis experiment in benzonitrile solution and the observed rate constants of the quenching of $^{3}C_{60}$* showed good agreement with the oxidation potentials of allyltributyltin.

Photoreaction of C_{60} with Organosilicon Compounds

The photolysis of 1,1,1,3,3,3-hexamethyl-2,2-bis(2,5-diisopropylphenyl)trisilane with a low-pressure mercury lamp has been used to generate silylene, which was subsequently reacted with C_{60} (Fig. 69) [61]. The photoreaction of C_{60} with 1,1,1,3,3,3-hexamethyl-2,2-bis(2,6-diisopropylphenyl)trisilane afforded the methanofullerene-type silylated C_{60} in 58% yield. The high selectivity was confirmed by theoretical calculation of the diphenyl silylene adducts of C_{60}, revealing that the methanofullerene-type addition product was thermodynamically more stable than the fulleroid-type addition product.

It is well-known that the Si–Si bond is cleaved by 254 nm photoirradiation to form silyl radicals. The photoirradiation of disilane in the presence of C_{60} afforded the corresponding bis-silylated fullerenes (Fig. 70) [62, 63]. The 1,6-addition (1,16- or 1,29- addition) products were selectively formed as thermodynamically stable isomers. The AM1 molecular orbital calculation of several bis(trimethylsilyl)-fullerene suggested that the 1,2-adduct was the most stable and the relative stabilities of the isomers decreased with increasing number of double bonds at the 5,6-junction (Table 1). On the other hand, the 1,6-adduct of $(t\text{-BuPh}_2\text{Si})_2C_{60}$ was 35.6 kcal/mol more stable than that of the corresponding 1,2-adduct. This was rationally explained by steric repulsion between the bulkiness of addenda [63]. The photoreaction of C_{60} with 1,1,2,2-tetraphenyl-1,2-bis(trimethylsilyl)disilane produced 1,6-bissilylated fullerene and cyclic 1,2-addition products. The reaction mechanism was confirmed by laser flash photolysis, in which radical ions were not observed upon

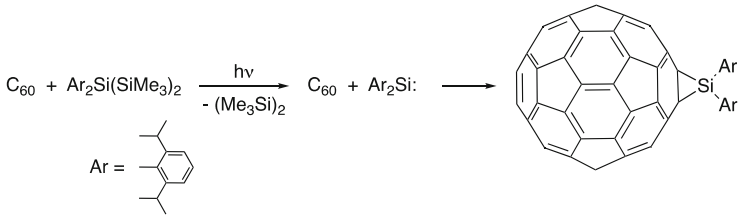

Fig. 69 Photoreaction of C_{60} with disilane, tetrasilane, or hexasilane

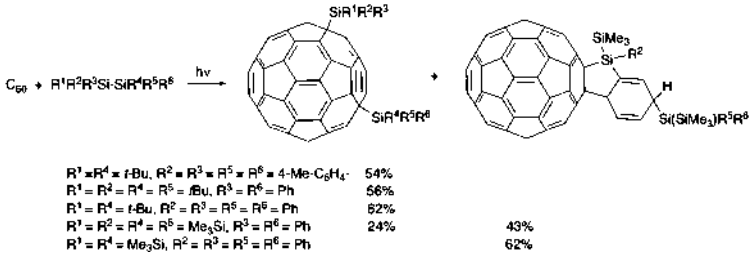

Fig. 70 Photoreaction of C_{60} with 1,1,1,3,3,3-hexamethyl-2,2-bis(2,6-diisopropylphenyl)trisilane

Table 1 Relative energies (kcal/mol) and number of double bonds at the 5,6-junction of the $(Me_3Si)_2C_{60}$ isomers

Addition position	Relative energy	Number of double bonds at 5,6-junction
1, 1	0	0
2, 2	19.9	4
3, 3	38.6	6
3′, 3′	4.6	2
4, 4	36.4	6
4′, 4′	39.3	8
5, 5	23.8	4
6, 6	47.8	8
7, 7	36.4	10

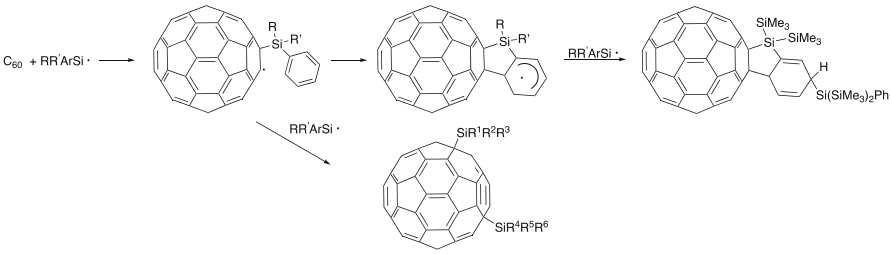

Fig. 71 Reaction mechanism of the formation of bis-silylated fullerene and the cyclic 1,2-addition products

photoirradiation at >300 nm, supporting the radical addition mechanism (Fig. 71). In addition, a control experiment using the radical scavengers tetrachloromethane and cumene suppressed the formation of bis-silylated C_{60} and produced chlorosilane and 1-silyl-1,2-dihydrofullerene. For the generation of the cyclic 1,2-addition products bonded at the silyl and phenyl groups, the intramolecular cyclization of the silylated C_{60} radical and subsequent addition of another silyl radical to the resulting phenyl radical in the silyl fullerene was proposed. When these disilanes were replaced with tetrasilane, the cyclic 1,2-addition products were selectively obtained; however, no silylene and 1,6-addition products were observed.

The photoreaction of C_{60} with 1,2-bis(diethylamino)-1,1,2,2-tetraphenyldisilane afforded diethylaminodiphenylsilyl-1,2-dihydrofullerene, in 68% yield, as the major product accompanied by the formation of bis-silylated C_{60} as the minor product (Fig. 72) [64]. Proton transfer from the amine radical cation to the C_{60} radical anion accompanied by silyl radical formation upon photoirradiation was proposed as a plausible reaction mechanism.

The photoreaction of C_{60} with cyclic disilane and digermane was also performed. The photoreaction of 3,4-benzo-1,1,2,2-tetraisopropyl-1,2-disilacyclobutane in toluene with a low-pressure mercury lamp resulted in an unidentified mixture [65]. However, irradiation in a toluene-*t*-BuOH mixed

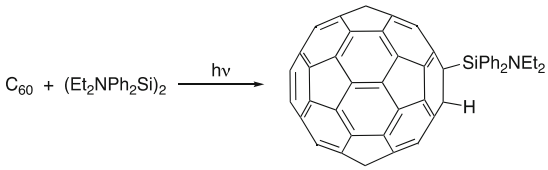

Fig. 72 Photoreaction of C_{60} with 1,2-bis(diethylamino)-1,1,2,2-tetraphenyldisilane

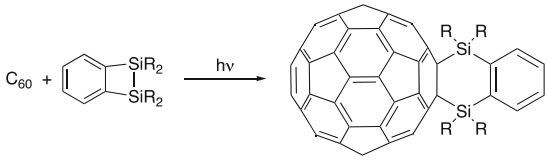

Fig. 73 Photoreaction of C_{60} with 3,4-benzo-1,1,2,2-tetraisopropyl-1,2-disilacyclobutane

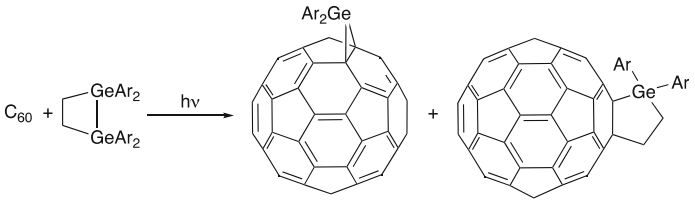

Fig. 74 Photoreaction of C_{60} with 1,1,2,2-tetraaryl-1,2-digermacyclobutane

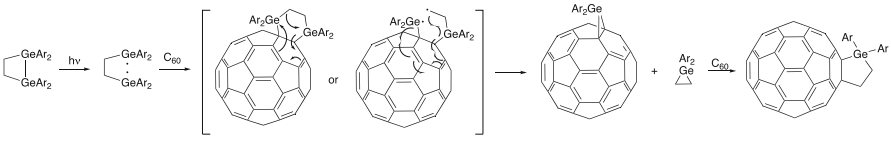

Fig. 75 Proposed reaction mechanism of the reaction of C_{60} with 1,2-digermacyclobutane

solvent afforded 6,6-(1,2-disilacyclohexane)dihydrofullerene in 14% yield (Fig. 73). Although the effect of *t*-BuOH is unclear, a radical addition mechanism was proposed because the photoreaction does not proceed under the irradiation of a high-pressure mercury lamp (>300 nm). On the other hand, the photoreaction of C_{60} with 1,1,2,2-tetraaryl-1,2-digermacyclobutane in toluene with a high-pressure mercury lamp (>300 nm) produced 6,5-closed-(diarylgermacyclopropane)-dihydrofullerene and 1,2-(germacyclopentane)dihydrofullerene in 57 and 43% conversion yield, respectively (Fig. 74) [66]. The structure of the 6,5-closed adduct was confirmed by NMR, MS, and computational studies. As a plausible reaction mechanism, bis-germylation and subsequent fragmentation in a concerted stepwise manner were proposed for the formation of these germyl fullerenes (Fig. 75).

Polysilanes have been attracting significant interest, owing to their electronic properties as a result of the extensive delocalization of σ-electrons along the silicon

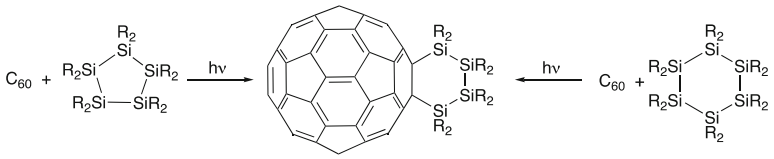

Fig. 76 Photoreaction of C_{60} with cyclooligosilanes

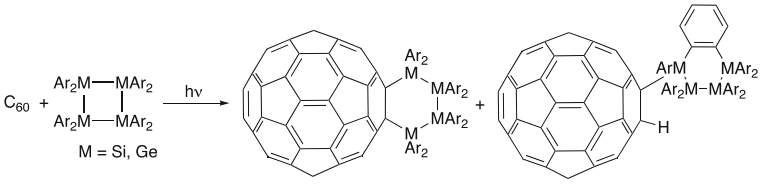

Fig. 77 Photoreaction of C_{60} with cyclotetrasilane and cyclotetrogermane

chain. In fact, fullerene-doped polysilane has been reported to display good photoconductivity [67]. In this context, the incorporation of C_{60} in polysilane was conducted photochemically. The photoreaction of C_{60} with dodecamethylcyclohexasilane and decamethylcyclopentasilane produced the 1,2-cyclic bis-silylated fullerene $C_{60}(SiMe_2)_4$ (Fig. 76) [68]. The cyclohexasilane was reported to afford the cyclotetrasilane with the elimination of two silylene units. Therefore, a reaction mechanism involving the stepwise elimination of silylene from cyclohexasilane to afford the 1,4-diradical, followed by radical addition to C_{60}, was proposed. On the other hand, the photoreaction of octaphenylcyclotetrasilane with C_{60} produced the rearranged 1,2-dihydrofullerene [65]. When the cyclotetrasilane was replaced with cyclotetragermane, (tetragermacyclohexane)dihydrofullerene and rearranged 1,2-dihydrofullerene were obtained (Fig. 77).

A C_{60} and polysilane mixture in deaerated benzene photoirradiated with a low-pressure mercury lamp resulted in the formation of C_{60}-polysilane adducts [68]. The percentage weight of C_{60} in the polysilane was estimated by elemental analysis. For example, the percentage weight of C_{60} in phenylmethylpolysilane after photoreaction was estimated at 14 wt%. Notably, photoreaction with C_{60} did not occur upon irradiation at >300 nm. In addition, the photoreaction was suppressed in the presence of tetrachloromethane, which is a good silyl radical scavenger. These control experiments indicated the generation of silyl radicals as intermediates of the photoreaction.

The photochemical generation of S-heterocyclic carbene with a disilane backbone was verified using C_{60}. The photolysis of *anti*-docecaisopropyltricyclo[4.2.0.0^{2,5}] octasilane with CS_2 in the presence of C_{60} afforded methanofullerene in 20% yield (Fig. 78) [69]. The disilane backbone S-heterocyclic carbene has been prepared by the reaction of disilene with carbon disulfide [70]. In the photoreaction, [2 + 3] cycloaddition of carbon disulfide and cyclotetrasilene, generated by photolysis of the octasilane, afforded S-heterocyclic carbene, which readily reacted with C_{60} to form the methanofullerene.

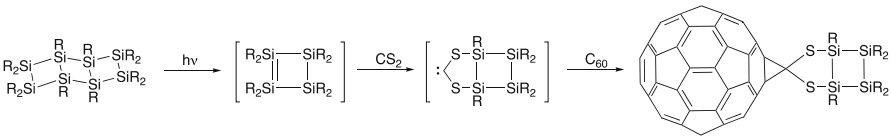

Fig. 78 Photoreaction of *anti*-docecaisopropyltricyclo[4.2.0.0^{2,5}]octasilane with CS_2 in the presence of C_{60}

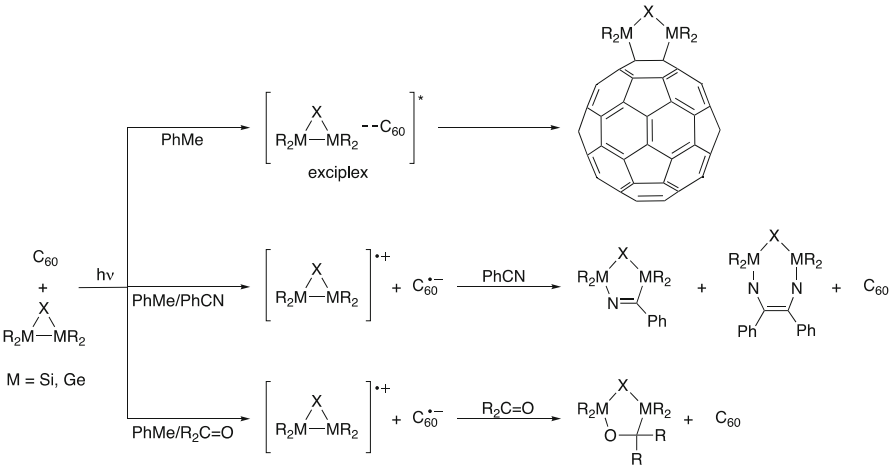

Fig. 79 Photoreaction of C_{60} with disilirane

It is well-known that the strained Si–Si σ-bond is a good electron donor. On the other hand, excited C_{60} acts as a good electron acceptor. Therefore, the bis-silylation of fullerene using the disilacyclopropane disilirane has been developed photochemically (Fig. 79). The photoreaction of C_{60} with 1,1,2,2-tetramesityl-1,2-disilirane in toluene led to the ready formation of 1,2-bis-silylated C_{60} in 82% yield [71]. This reaction proceeded upon irradiation at >300 nm and was suppressed in the presence of diazabicyclo[2.2.2]octane or tetramethoxybenzene. In a laser flash photolysis experiment, $^3C_{60}$* quenching by disilirane was observed, while the formation of the C_{60} radical anion was not observed. Based on these results, the formation of an exciplex of $^3C_{60}$* and disilirane as plausible intermediates was proposed. For the detection of the C_{60} radical anion, photolysis of C_{60} with disilirane was conducted in benzonitrile solution as the polar solvent. An increase in C_{60} radical anions accompanied by a decrease in $^3C_{60}$* was observed in benzonitrile by laser flash photolysis experiments; however, disilirane and benzonitrile addition products were formed instead of the C_{60} adducts [72]. This indicated that the exciplex of C_{60} and disilirane formed in non-polar solvents to readily afford the C_{60} adduct. On the other hand, solvated radical ions were formed in polar solvents, thereby leading to the ready formation of the solvated product due to the high reactivity of the disilirane radical cation. Similar to the photochemical bis-silylation reaction, photochemical

bis-germylation to C_{60} in toluene solution was conducted to form bisgermylated fullerene [73, 74]. On the other hand, solvated products were formed in the photoreaction of C_{60} with digermirane in benzonitrile. Systematic studies have been conducted on the photoinduced electron transfer reaction between C_{60} and cyclic organosilicon compounds [75]. To confirm the reactivity of the disilirane radical cation, disilirane was generated electrochemically, resulting in the formation of the bis-silylated adducts of the nitrile and carbonyl compounds.

The photochemical addition of the silacyclopropane sililane to C_{60} was also performed. The selectivity was less than that observed for disilirane and photoirradiation (>400 nm) of sililane with C_{60} afforded various silylated C_{60} products depending on the substituents, as illustrated in Fig. 80 [76]. Along with the 1,2- and 1,4-cycloaddition adducts and hydrosilyl fullerenes, a 1,2-adduct at the 5,6-ring junction of C_{60} was isolated in moderate yield. The first X-ray crystal structure analysis of the 1,2-closed-addition product at the 5,6-ring junction was conducted using the silacyclopentane adduct. The results revealed an absorption band extending to a longer wavelength (1300 nm) as a characteristic spectral feature of the 1,2-closed-addition product at the 5,6-ring junction.

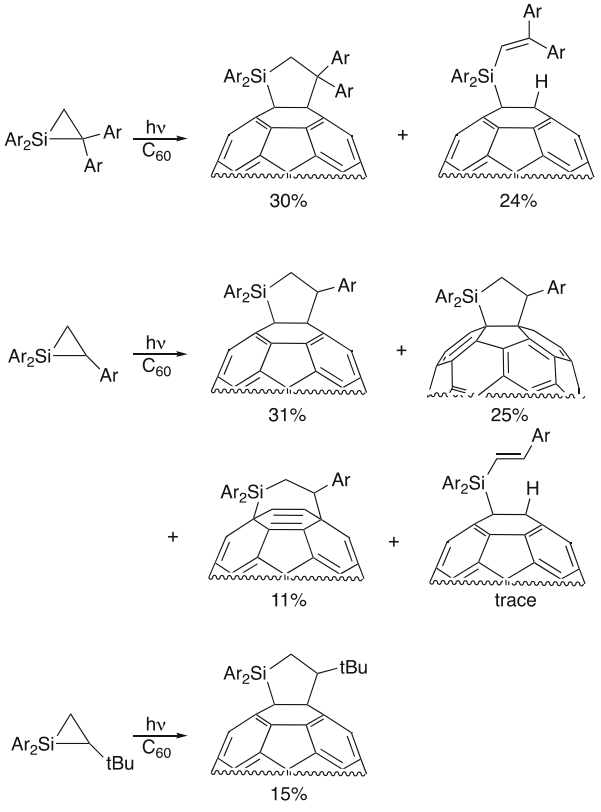

Fig. 80 Photoreaction of C_{60} with disilirane

Photoreaction of C_{60} with Disulfide

As mentioned above, the homolytic photocleavage reaction of the sulfur-sulfur bond proceeds easily to form the thiyl radical. Addition of the thiyl and seleno radicals to the double bonds proceeded efficiently when the disulfides and diselenides coexisted, because of the high reactivity of the thiyl radical to olefin and that of the seleno radical to the free radical. Under these conditions, the photoreaction of C_{60} with dendrimer disulfide and diphenyl diselenide in 1,2-dichlorobenzene was conducted to form dithiolated C_{60} in 16% yield (Fig. 81) [77]. In this reaction, no selenyl fullerene was obtained. In contrast, the dithiolated C_{60} did not form in the absence of diphenyl diselenide.

The formation of selenylfullerenes was achieved photochemically using selenium-containing dibenzo[*b*,*g*]cyclooctane derivatives [78]. The photoreaction (hν >300 nm) of a benzene solution of an equivalent amount of C_{60} and dibenzo[*b*,*g*][1,5]diselenocin afforded C_{60}-fused benzocyclobutane in 30% yield (Fig. 82). When dibenzo[*b*,*g*][1,5] diselenocin was replaced with dibenzo[*b*,*g*][1,5]oxaselenacin, C_{60}-fused benzocyclobutane was formed in 53% yield (Fig. 83). The proposed reaction mechanisms are respectively illustrated in Figs. 84 and 85.

Photoreaction of C_{60} with Sulfilimine

Sulfilimines are known to generate the *N*-substituted nitrene both thermally and photochemically. *N*-sulfenylsulfilimine is known as a precursor of sulfenylnitrene, which reacts with an alkene to form the corresponding aziridine under mild

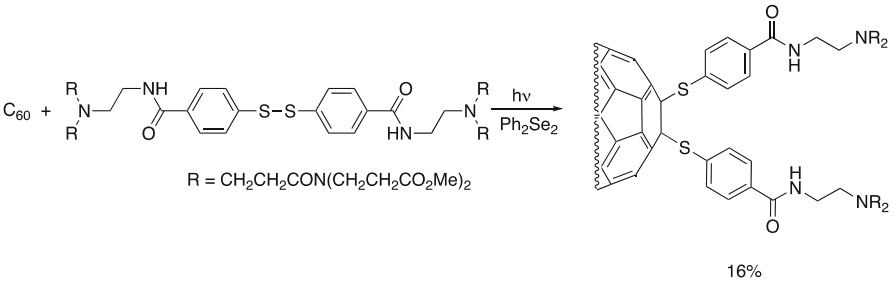

Fig. 81 Photoreaction of C_{60} with dendron disulfide

Fig. 82 Photoreaction of C_{60} with dibenzo[*b*,*g*][1,5] diselenocin

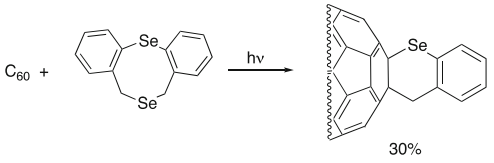

Fig. 83 Photoreaction of C_{60} with dibenzo[*b*,*g*][1,5] oxaselenacin

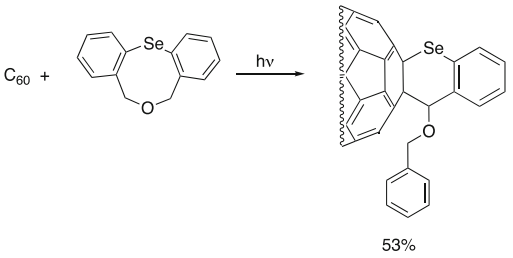

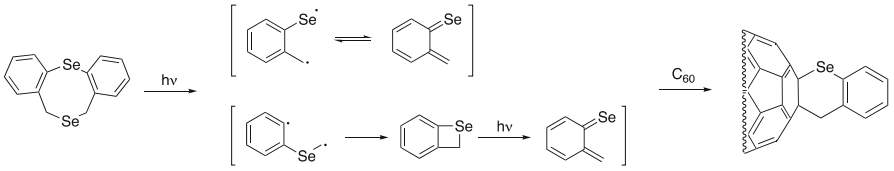

Fig. 84 Proposed reaction mechanism of C_{60} with dibenzo[*b*,*g*][1,5]diselenocin

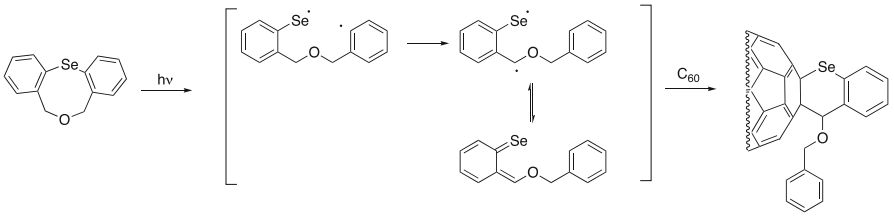

Fig. 85 Proposed reaction mechanism of C_{60} with dibenzo[*b*,*g*][1,5]oxaselenacin

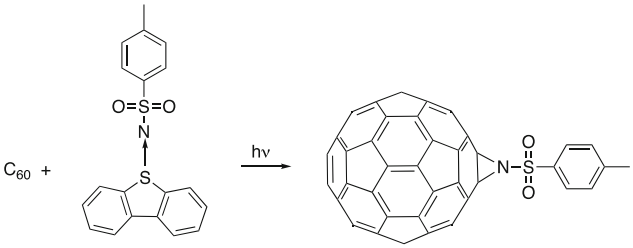

Fig. 86 Photoreaction of C_{60} with *N*-sulfenylsulfilimine

conditions. The photochemical (>300 nm) reaction of C_{60} with sulfilimine in toluene under degassed conditions afforded azirizinofullerene in 80% yield (Fig. 86) [79]. The monoadduct in 1,2-dichlorobenzene was converted to the (5,6)-open azafulleroid at 180 °C, while the [5,6]-open azafulleroid was photochemically (>400 nm) converted to aziridinofullerene (Fig. 87). The single crystal X-ray

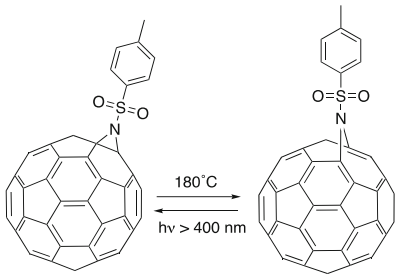

Fig. 87 Photo and thermal isomerization between azirizinofullerene and the [5,6]-open azafulleroid

analysis of the azirizinofullerene and the [5,6]-open azafulleroid was conducted to reveal their molecular structures.

Cross-References

- ▶ Chemical Reactivity and Addition Pattern on C_{60} and C_{70}
- ▶ Functionalization of Fullerenes: Addition Reactions
- ▶ Theoretical Prediction of Fullerene Reactivity

References

1. Krusic P J, Wasserman E, Parkinson B A, Malone B, Holler Jr E R (1991) Electron spin resonance study of radical reactivity of C_{60}. J Am Chem Soc 113(16):6274–6275
2. Krusic P J, Wasserman E, Keizer P N, Morton J R, Preston K F (1991) Radical reaction of C_{60}. Science 254(5035):1183–1185
3. Cremonini M A, Lunazzi L, Placucci G (1993) Addition of alkylthio and alkoxy radicals to C_{60} studied by ESR. J Org Chem 58(17):4735–4738
4. Morton J R, Preston K F, Krusic P J, Wasserman E (1992) Electron paramagnetic resonance spectra of R-C_{60} radicals. Evidence for RC60C60R dimers. J Chem Soc Perkin Trans 2 1425–1429
5. Arbogast J W, Foote C S. Kao M. (1992) Electron transfer to triplet C_{60}. J Am Chem Soc114 (6):2277–2279
6. Morton J R, Preston K F, Krusic P J, Hill S A, Wasserman E (1992) The dimerization of RC_{60} radicals. J Am Chem Soc 114(13):5454–5455
7. Cheng F, Murata Y, Komatsu K (2002) Synthesis, X-ray structure, and properties of the singly bonded C_{60} dimer having diethoxyphosphorylmethyl groups utilizing the chemistry of C_{60}^{2-}. Org Lett 4(15):2541–2544
8. Wang G-W, Wang C-Z, Zhu S-E, Murata Y (2011) Manganese(III) acetate-mediated radical reaction of [60]fullerene with phosphonate esters affording unprecedented separable singly-bonded [60]fullerene dimers. Chem Commun 47(21):6111–6113
9. Abe Y, Tanaka H, Guo Y, Matsuo Y, Nakamura E (2014) Mobility of long-lived fullerene radical in solid state and nonlinear temperature dependence. J Am Chem Soc 136(9):3366–3369
10. Ford W T, Nishioka T, Qiu F (2000) Dimethyl azo(bisisobutyrate) and C_{60} produce 1,4- and 1,16-di(2-carbomethoxy-2-propyl)-1,x-dihydro[60]fullerenes. J Org Chem 65(18):5780–5784

11. Yoshida M, Morinaga Y, Iyoda M, Kikuchi K, Ikemoto I, Achiba Y (1993) Reaction of C_{60} with diacyl peroxide containing perfluoroalkyl groups. The first example of electron transfer reaction via $C_{60}^{+\cdot}$ in solution. Tetrahedron Lett 34(47):7629–7632
12. Yoshida M, Morishima A, Morinaga Y, Iyoda M (1994) Reactions of fullerols and fullerene dimer containing perfluoroalkyl groups with tributyltin hydride. Tetrahedron Lett 35(48):9045–9046
13. Yoshida M, Suzuki D, Iyoda M (1996) Convenient synthesis of 1-fluoroalkyl-2-hydro[60] fullerene using fluoroalkyl halide with tributyltin hydride under radical conditions. Chem Lett 25(12):1097–1098
14. Yoshida M, Sultana F, Uchiyama N, Yamada T, Iyoda M (1999) Efficient synthesis of fullerene dimers containing a fluoroalkyl group. Tetrahedron Lett 40(22):735–736
15. Vorobiev A K, Gazizov R R, Borschevskii, Y, Markov V Y, Ioutsi V A, Brotsman V A, Sidorov L N (2017) Fullerene as photocatalyst: Visible-light induced reaction of perfluorinated a,w-diiodoalkanes with C_{60}. J Phys Chem A 121(1):113–121
16. Chen Z- X, Wang G- W (2005) One-pot sequential synthesis of acetoxylated [60]fullerene derivatives. J Org Chem 70(6):2380–2383
17. Wang G -W, Lu Y -M, Chen Z-X (2009) 1,4-Fullerenols C_{60}ArOH: Synthesis and Functionalization. Org Lett 11(7):1507–1510
18. Okamura H, Terauchi T, Minoda M, Fukuda T, Komatsu K (1997) Synthesis of 1,4-dipolystyryldihydro[60]fullerenes by using 2,2,6,6-tetramethyl-1-polystyroxyroxypiperidine as a radical source. Macromolecules 30(18):5279–5284
19. Akasaka T, Liu M T H, Niino Y, Maeda Y, Wakahara T, Okamura M, Kobayashi K, Nagase S (2000) Photolysis of diazirines in the presence of C_{60}: A chemical probe for carbene/diazomethane partitioning. J Am Chem Soc 122(29):7134–7135
20. Wakahara T, Niino Y, Kato T, Maeda Y, Akasaka T, Liu M T H, Kobayashi K, Nagase S (2002) A nonspectroscopic method to determine the photolytic decomposition pathways of 3-chloro-3-alkyldiazirine: Carbene, diazo and rearrangement in excited state. J Am Chem Soc 124 (32):9465–9468
21. Ishitsuka M O, Niino Y, Wakahara T, Akasaka T, Liu M T H, Kobayashi K, Nagase S (2004) A verification of the photolytic decomposition pathways of 3-tert-butyl-3-chlorodiazirine based on the application of the C_{60} probe technique. Tetrahedron Lett 45(33):6321–6322
22. Ishitsuka M O, Enoki H, Nikawa H, Wakahara T, Tsuchiya T, Akasaka T, Liu M T H (2007) Determination of the photolytic decomposition pathways of benzylchlorodiazirine by C_{60} probe technique. Tetrahedron Lett 48(5):859–681
23. Sato S, Yamada M, Wakahara T, Tsuchiya T, Ishitsuka M O, Akasaka T, Liu M T H (2007) Photo-labeling of C_{60} with 3-trifluoromethyl-3-phenyldiazirine. Tetrahedron Lett 48(36):6290–6293
24. Ohno T, Martin N, Knight B, Wudl F, Suzuki T, Yu H (1996) Quinone-type methanofullerene acceptors: Precursors for organic metals. J Org Chem 61(4):1306–1309
25. Tomioka H, Yamamoto K (1995) Reaction of [60]fullerene with benzocyclobutenone and benzocyclobutenedione. J Chem Soc Chem Commun (19):1961–1962
26. Ishida H, Itoh K, Ito S, Ono N, Ohno M (2001) Cycloaddition reaction of [60]fullerene with 3,4-fused pyrrolo-3-sulfolenes. Synlett (2):296–298
27. Liou K-F, Cheng C-H (1996) Photoinduced reactions of tertiary amines with [60]fullerenes; addition of an a-C-H bond of amines to [60]fullerene. J Chem Soc Chem Commun (12):1423–1424
28. Lawson G E, Kitaygorodskiy A, Ma B, Bunker C E, Sun Y-P (1995) Photoinduced inter- and intra-molecular electron transfer reaction of [60]fullerene and a tertiary amine. Formation of the cycloadduct *N*-ethyl-trans-2'-5'-dimethylpyrrolidino[3',4':1,2][60]fullerene. J Chem Soc Chem Commun (21):2225–2226
29. Nakamura Y, Suzuki M, O-kawa K, Konno T, Nishimura J (2005) Photoreactions between [60] fullerene and various aromatic tertiary amines. J Org Chem70(21):8472–8477
30. Isobe H, Tomita N, Nakamura E (2000) One-step multiple addition of amine to [60]fullerene. Synthesis of tetra(amino)fullerene epoxide under photochemical aerobic conditions. Org Lett 2 (23):3663–3665

31. Isobe H, Tanaka T, Nakanishi W, Leimiegre L, Nakamura E (2005) Resioselective oxygenative tetraamination of [60]fullerene-mediated reduction of molecular oxygen by amine via ground state single electron transfer in dimethyl sulfoxide. J Org Chem 70(12):4826–4832
32. Gan L B, Zhou D J, Luo C P, Tan H S Huang C H, Lu M J, Pan J Q, Wu Y (1996) Synthesis of Fullerene amino acid derivatives by direct interaction of amino acid ester with C_{60}. J Org Chem 61(6):1954–1961
33. Skanji R, Messaouda M B, Zhang Y, Abderrabba M, Szwarc H, Moussa F (2012) Sequential photo-addition of glycine methyl-ester to [60]fullerene Tetrahedron 68(12):2713–2718
34. Gan L, Jiang J, Zhang W, Su Y, Shi Y, Huang C, Pan J, Lü M, Wu Y (1998) Synthesis of pyrrolidine ring-fused fullerene multivarboxylates by photoreaction. J Org Chem 63(13):4240–4247
35. Lim S H, Yi J, Moon G M, Ra C S, Nahm K, Cho D W, Kim K, Hyung T G, Yoon U C, Lee G Y, Kim S, Kim J, Mariano P S (2014) Method for the synthesis of amine-functionalized fullerenes involving SET-promoted photoreactions of α-silylamines. J Org Chem 79(15):6946–6958
36. Jeong H C, Lim S H, Sohn Y, Kim Y -I, Jang H, Cho D W, Mariano P S (2017) Electronic and steric effects controlling efficiencies of photoaddition reactions of fullerene C_{60} with *N*-α-trimethylsilyl-*N*-alkyl-*N*-benzylamines. Tetrahedron Lett 58(10):949–954
37. Lim S H, Yi J, Ra C S, Nahm K, Cho D W, Lee G Y, Kim J, Yoon U C, Mariano P S (2015) SET-promoted photoaddition reactions of *N*-α-trimethylsilylmethyl-*N*,*N*-dibenzylamines with fullerene C_{60}. Electronic factors that govern photoaddition efficiencies. Tetrahedron Lett 56 (23):3014–3018
38. Jeoog H C, Lim S H, Cho D W, Kim S H, Mariano P S (2016) Single electron transfer promoted photoaddition reactions of α-trimethylsilyl substituted secondary N-alkylamine with fullerene C_{60}. Org Biomol Chem (14):10502–10510
39. Lim S H, Jeong H C, Sohn Y, Kim Y-I, Cho D W, Woo H-J, Shin I-S, Yoon U C, Mariano P S (2016) Single electron transfer-promoted photochemical reactions of secondary *N*-trimethylsilylmethyl-*N*-benzylamines leading to aminomethylation of fullerene C_{60}. J Org Chem 81(6):2460–2473
40. Lim S H, Cho D W, Mariano P S (2018) Catalyst free, visible-light promoted photoaddition reactions between C_{60} and *N*-trimethylsilylmethyl-substituted tertiary amines for synthesis of aminomethyl-1,2-dihydrofullerenes. Tetrahedron 74(3):383–391
41. Miyake Y, Ahida Y, Nakajima K, Nishibayashi Y (2014) Visible-light-mediated addition of α-aminoalkyl radicals to [60]fullerene by using photoredox catalysts. Chem Eur J 20 (20):6120–6125
42. Zhang X, Foote C S (1995) [2+2] Cycloadditions of fullerenes: Synthesis and characterization of $C_{62}O_3$ and $C_{72}O_3$, the first fullerene anhydrides. J Am Chem Soc 117(15):4271–4275
43. Zhang X, Fan A, Foote C S (1996) [2+2] Cycloaddition of fullerenes with electron-rich alkenes and alkynes. J Org Chem 61(16):5456–5461
44. Vassilikogiannakis G, Orfanopoulos M (1997) Stereochemistry and isotope effects of the [2+2] photocycloadditions of arylalkenes to C_{60}. A stepwise mechanism. J Am Chem Soc 119 (31):7394–7395
45. Vassilikogiannakis G, Hatzimarinali M, Orfanopoulos M (2000) Mechanism of the [2+2] photocycloaddition of fullerene C_{60} with styrenes. J Org Chem65(24):8180–8187
46. Vassilikogiannakis G, Chronakis N, Orfanopoulos M (1998) A new [2+2] functionalization of C_{60} with alkyl-substituted 1,3-butadienes: A mechanistic approach. Stereochemistry and isotope effects. J Am Chem Soc 120(38):9911–9920
47. Mikami K, Matsumoto S, Okubo Y, Suenobu T, Fukuzumi S (1997) Single electron transfer Diels-Alder reaction of fullerene with Danishefsky's diene. Synlett 7:1130–1132
48. Mikami K, Matsumoto S, Okubo Y, Fujitsuka M, Ito O, Suenobu T, Fukuzumi S (2000) Stepwise bond formation in photochemical and thermal Diels-Alder reactions of C_{60} with Danishefsky's dienes. J Am Chem Soc 122(10):2236–2243
49. Schuster D I, Cao J, Kaprinidis N, Wu Y, Jensen A W, Lu Q, Wang H, Wilson S R (1996) [2+2] Photocycloaddition of cyclic enones to C_{60}. J Am Chem Soc 118(24):5639–5647

50. Jensen A W, Khong A, Saunders M, Wilson S R, Schuster D I (1997) Photocycloaddition of cyclic 1,3-diones to C_{60}. J Am Chem Soc 119(31):7303–7307
51. Vassilikogiannakis G, Orfanopoulos M (1999) Regio- and stereoselectivity of the [2+2] photocycloaddition of acyclic enones to C_{60}. J Org Chem 64(10):3392–3393
52. Tokuyama H, Isobe H, Nakamura E (1994) Photoaddition of silyl ketene acetal to [60]fullerene. Synthesis of a-fullerene-substituted carboxylic esters. J Chem Soc Chem Commun (24):2753–2754
53. Mikami K, Matsumoto S, Ishida A, Takamuku S, Suenobu T, Fukuzumi S (1997) Addition of ketene silyl acetals to the triplet excited state of C_{60} via photoinduced electron transfer leading to the fullereneacetates. J Am Chem Soc 117(45):11134–11141
54. Miao C-B, Tian Z-Y, Ruan X-J, Sun X-Q, Yang H-T (2011) Reaction of [60]fullerene with epoxides under photo-irradiation: Synthesis of C_{60}-fused tetrahydrofuran derivatives. Heterocycles 83(7):1615–1620
55. Hatzimarinaki M, Orfanopoulos M (2006) Novel methodology for the preparation of five-, seven, and nine-membered fused rings on C_{60}. Org Lett 8(9):1775–1778
56. Tzirakis M D, Alberti M N, Orfanopoulos M (2011) Photocycloaddition of biscyclopropyl alkenes to C_{60}: An unprecedented approach toward *cis*-1 tricyclic-fused fullerenes. Org Lett 13 (13):3364–3367
57. Fukuzumi S, Suenobu T, Oatz M, Hirasaka T, Itoh S, Fujitsuka M, Ito O (1998) Selective one-electron and two-electron reduction of C_{60} with NADH and NAD dimer analogues via photoinduced electron transfer. J Am Chem Soc 120(32):8060–8068
58. Fukuzumi S, Suenobu T, Kawamura S, Ishida A, Mikami K (1997) Selective two-electron reduction of C_{60} by 10-methyl-9,10-dihydroacridine via photoinduced electron transfer. Chem Commun (3):291–292
59. Okubo K, Iwata R, Yanagimoto T, Fukuzumi S (2007) Enhanced photoinduced oligomerization of fullerene via radical coupling between fullerene radical cation and radical anion using 9-mesityl-10-methylacridinium ion. Chem Commun (30):3139–3141
60. Fukuzumi S, Suenobu T, Fujitsuka M, Ito O, Tonoi T, Matsumoto S, Mikami K (1999) Addition of group 14 organometallic compounds to C_{60} via photoinduced electron transfer. Direct detection of radical ion pair intermediates. J Organomet Chem 574(1):32–29
61. Akasaka T, Kobayashi K, Nagase S, Ando W (1993) Reaction of C_{60} with silylene, the first fullerene silirane derivative. J Am Chem Soc 115(4):1605–1606
62. Kusukawa T, Ando W (1997) Photochemical reactions of oligosilanes with C_{60}. Organometallics 16(19):4027–4029
63. Akasaka T, Suzuki T, Maeda Y, Ara M, Wakahara T, Kobayashi K, Nagase S, Kako M, Nakadaira Y, Fujitsuka M, Ito O (1999) Photochemical bissilylation of C_{60} with disilane. J Org Chem 64(2):566–569
64. Wakahara T, Rahman G M A, Maeda Y, Kako M, Sato S, Okamura M, Akasaka T, Kobayashi K, Nagase S (2003) Redox properties of carbosilylated and hydrosilylated fullerene derivatives. ITE Lett 4:67–73
65. Kusukawa T, Shike A, Ando W (1996) Photochemical functionalization of C_{60} with cyclosilanes and cyclogermane. Tetrahedron 52(14):4995–5005
66. Kabe Y, Ohgaki H, Yamagaki T, Nakanishi H, Ando W (2001) The photochemical reaction of 1,2-digermacyclobutane with C_{60}: possible example of a closed [6,5]-bridged fullerene derivative of germacyclopropane. J Organomet Chem 636(1–2):82–90
67. Wang Y, West R, Yuan C-H (1993) Fullerene-doped polysilane photoconductor. J Am Chem Soc 115(9):3844–3845
68. Wakahara T, Kondo T, Okamura M, Akasaka T, Hamada Y, Suzuki T, Kako M, Nakadaira Y (2000) Photochemical bis-silylation of C_{60}: synthesis of a novel C_{60} main chain polysilane. J Organomet Chem 611(1–2):78–84
69. Nikawa H, Nakahodo T, Tsuchiya T, Wakahara T, Rahman G M A, Akasaka T, Maeda Y, Liu M T H, Meguro A, Kyushin S, Matsumoto H, Mizorogi N, Nagase S (2005) S-heterocyclic carbene with a disilane backborn. Angew Chem Int Ed 44(46):7567–7570

70. Fabian J, Krebs A, Schonemann D, Schaefer W (2000) 1,3-Heterocumulene-to-alkyne [3+2] cycloaddition reactions: A theoretical and experimental study. J Org Chem 65(26):8940–8947
71. Akasaka T, Ando W, Kobayashi K, Nagase S (1993) Photochemical [2+3] cycloaddition of C_{60} with disiranes. J Am Chem Soc 115(22):10366–10367
72. Akasaka T, Maeda Y, Wakahara T, Okamura M, Fujitsuka M, Ito O, Kobayashi K, Nagase S, Kako M, Nakadaira Y, Horn E (1999) Novel metal-free bis-silylation: C_{60}-sensitized reaction of disilirane with benzonitorile. Org Lett 1(10):1509–1512
73. Akasaka T, Maeda Y, Wakahara T, Mizushima T, Ando W, Waelchli M, Suzuki T, Kobayashi K, Nagase S, Kako M, Nakadaira Y, Fujitsuka M, Ito O, Sasaki Y, Yamamoto K, Erata T (2000) A first photochemical bis-germylation of C_{60} with digermirane. Org Lett 2(17):2671–2674
74. Maeda Y, Takahashi S, Wakahara T, Akasaka T, Sasaki Y, Fujitsuka M, Ito O, Kobayashi K, Nagase S, Kako M, Nakadaira Y (2000) Metal-free bis-germylation: C_{60}-sensitized reaction of digermiran with benzonitrile. ITE Lett 1:408
75. Sasaki Y, Konishi T, Fujitsuka M, Ito O, Maeda Y, Wakahara T, Akasaka T, Kako M, Nakadaira Y (2000) Photoinduced electron-transfer reaction between C_{60} and cyclic silicon compounds. J Organomet Chem 599(2):216–220
76. Nagatsuka J, Sugitani S, Kako M, Nakahodo T, Mizorogi N, Ishitsuka M O, Maeda Y, Tsuchiya T, Akasaka T, Gao X, Nagase S (2010) Photochemical addition of C_{60} with siliranes: Synethsis and characterization of carbosilylated and hydrosilylated C_{60} derivatives. J Am Chem Soc 132(34):12106–12120
77. Takaguchi Y, Katayose Y, Yanagimoto Y, Moriyoshiya J, Aoyama H, Wakahara T, Maeda Y, Akasaka T (2003) Photoinduced dithiolation of fullerene[60] with dendrimer disulfide. Chem Lett 32(12):1124–1125
78. Nakahodo T, Takahashi K, Ishitsuka M O, Tsuchiya T, Maeda Y, Fujihara H, Nagase S, Akasaka T (2008) Synthesis of selenylfullerene with selenium-containing dibenzo[b,g]cyclooctane moiety. Tetrahedron Lett 49(14):2302–2305
79. Nakahodo T, Okada M, Morita H, Yoshimura T, Ishitsuka O M, Tsuchiya T, Maeda Y, Fujihara H, Akasaka T, Gao X, Nagase S (2008) [2+1] Cycloaddition of nitrene onto C_{60} revisited: Interconversion between an aziridinofullerene and an azofulleroid. Angew Chem Int Ed 47(7):1298–1300

Electrochemistry and Organic Electrochemistry of Fullerenes

12

Xiang Gao

Contents

Abstract

This chapter is divided into two parts, the electrochemistry of fullerenes and their derivatives and electrosynthesis of fullerene derivatives. For the electrochemistry of fullerenes, attention is paid to the application of cyclic voltammetry in revealing the redox processes of fullerenes. The electrochemistry of different fullerenes is also discussed. As for the fullerene derivatives, the effects of the nature of addends, the number of addends, and the addition pattern are discussed. In addition, the stability difference between different isomers is discussed, and the electrochemistry of the singly bonded C_{60} anionic species is shown. For the electrosynthesis of fullerene derivatives, the review starts from the typical reactions of fullerene dianions with alkyl bromides or iodides. Then it is extended to the dianions of fullerene derivatives, where a unique regioselectivity is shown. The reactions of fullerene dianions with O_2 and PhCN is also discussed, which afford a new type of fullerene oxazoline compounds. In addition, the application

X. Gao (✉)
Adare Pharma Solutions, Philadelphia, PA, USA
e-mail: gx8802@yahoo.com

X. Lu et al. (eds.), *Handbook of Fullerene Science and Technology*,
https://doi.org/10.1007/978-981-16-8994-9_34

of electrochemistry for reaction mechanism study and heterocyclic rearrangement are discussed.

Keywords

Fullerenes · Electrochemistry · Isomer effect · Organic electrochemistry · Fullerene heterocyclic derivatives · Anions · Reaction mechanism · Rearrangement

Introduction

Fullerenes are a class of three-dimensional closed cage molecules made exclusively of carbon atoms, which represented a new form of the carbon element besides the well-known amorphous carbon, diamond, and graphite at the time when it was discovered in 1985 [1]. Soon after the macroscopic preparation of fullerenes was reported [2], the electrochemical property of C_{60} was studied and was among one of the first properties studied for fullerenes [3]. Nowadays, the electrochemical data are important parameters considered for fullerene derivatives, as they are closely related to the LUMO levels of the compounds and are important for the applications of the compounds to organic solar cells [4].

In addition to revealing the electrochemical property, the electrochemistry method has also been shown to be a unique approach for preparing fullerene derivatives. The first electrochemical synthesis of fullerene derivatives was carried out by reacting of CH_3I with C_{60}^{2-}, which was generated with the controlled-potential bulk electrolysis under inert atmosphere [5]. Different from the electron-deficient neutral fullerenes, anionic fullerene species are electron-rich species and may result in fullerene derivatives that are otherwise difficult to be obtained via the reaction of neutral fullerenes. In addition, the heterocyclic C_{60} derivatives undergo reductive rearrangement, and the mechanism is revealed by the electrochemical method [6], which has been further applied to preparing novel heterocyclic fullerene derivatives.

Electrochemistry of Fullerenes and Their Derivatives

Fullerenes

Electrochemical Reductions

Theoretical calculations on the highly symmetrical C_{60} molecule predicted that the molecule has threefold degenerate LUMOs [7], indicating that neutral C_{60} is capable of accepting up to six electrons by reduction. Soon after the discovery of the macroscopic preparation of fullerenes [2], the cyclic voltammetry of C_{60}, the most abundant fullerene, was reported [3]. Two one-electron transfer quasi-reversible reduction waves were shown for C_{60} at a glassy carbon button electrode in

CH_2Cl_2 containing 0.05 M $[(n\text{-}Bu)_4N]BF_4$ ($TBABF_6$, tetrabutylammonium tetrafluoroborate), demonstrating for the first time that C_{60} is electron deficient with the acceptance of two electrons. However, no further electrochemical reductions of C_{60} were examined in this work even though the electrochemical potential window of the $CH_2Cl_2/(n\text{-}Bu)_4NBF_4$ system could be extended to a more negative potential readily. An intense interest was then stirred in exploring more reduction processes of C_{60}. The third reduction wave of C_{60} was observed in the same $CH_2Cl_2/(n\text{-}Bu)_4NBF_4$ system as that used in Ref. 6 by further extending the reduction potential [8]; however, the reduction potential was still not extended to the limit of the electrochemical reduction window of the solvent system. The fourth reduction wave of C_{60} was soon reported, still in the $CH_2Cl_2/(n\text{-}Bu)_4NBF_4$ system by simply scanning into the more negative potential region, and this time, the reduction potential finally was extended to the limit of the electrochemical reduction potential window of the $CH_2Cl_2/(n\text{-}Bu)_4NBF_4$ system [9]. Pentaanion of C_{60} (C_{60}^{5-}) was observed when C_6H_6 containing $[(n\text{-}C_6H_{13})_4N]ClO_4$ (tetra-*n*-butylammonium perchlorate, TBAP) as the supporting electrolyte was used, which exhibited a wider reduction potential with respect to the $CH_2Cl_2/(n\text{-}Bu)_4NBF_4$ solvent system [10]. The reduction potential window of the solvent was finally extended negative enough by using either CH_3CN/toluene (between 15% and 20% by volume of acetonitrile in toluene) containing 0.1 M $TBAPF_6$ (tetra-*n*-butylammonium hexafluorophosphate) at −10 °C [11] or in a mixture of DMF-toluene (volume ratio = 2:3) with 0.1 M $TEAPF_6$ (tetraethylammonium hexafluorophosphate) at −88 °C [12], where Echegoyen et al. and Ohsawa et al. independently demonstrated that C_{60} is capable of accepting up to six electrons via stepwise one-electron transfer processes, consistent with the theoretical prediction [7]. The $E_{1/2}$ reduction potentials in CH_3CN/toluene were determined to be −0.98, −1.37, −1.87, −2.35, −2.85, and −3.26 V relative to Fc/Fc^+ (ferrocene/ferrocenium), respectively, and −0.81, −1.24, −1.77, −2.22, −2.71, and −3.12 V relative to Fc/Fc^+, respectively, in DMF-toluene (2:3). The potential difference in the two solvent systems is likely caused by the solvent effect, where the anionic C_{60} species are likely more stabilized by the more polar DMF solvent, resulting in a lower reduction potential for C_{60} in DMF-toluene solvent. Figure 1 shows the cyclic voltammogram and the differential pulse voltammogram of C_{60} in CH_3CN/toluene at −10 °C.

Meanwhile, the electrochemical property of C_{70}, the second most abundant fullerene member next to C_{60}, had also attracted significant attention. Echegoyen at al. showed that C_{70} was also capable of accepting up to six electrons, similar to C_{60} [11]. Figure 2 shows the cyclic voltammogram and the differential pulse voltammogram of C_{70} in CH_3CN/toluene at −10 °C, with six one-electron transfer quasi-reversible reduction processes. The $E_{1/2}$ potentials for the reductions of C_{70} are −0.97, −1.34, −1.78, −2.21, −2.70, and −3.07 V relative to Fc/Fc^+, respectively, which are in general slightly anodically shifted with respect to those of C_{60}.

The electrochemistry of C_{76} was also studied in order obtain a more comprehensive understanding of the electrochemical property of fullerenes. Figure 3 shows the cyclic voltammogram of C_{76} measured in 50:50 v/v benzonitrile/toluene (PhCN/toluene) containing 0.1 M TBAP [13]. Within the reduction potential window, four

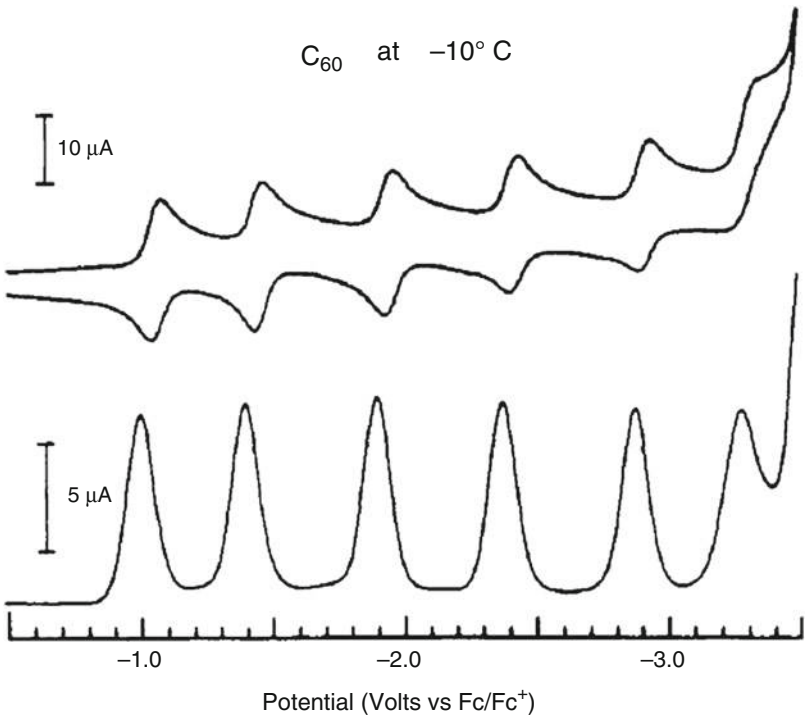

Fig. 1 Cyclic voltammogram and the differential pulse voltammogram of C_{60} in CH_3CN/toluene containing 0.1 M $TBAPF_6$ at −10 °C. 100 mV/s scan rate for cyclic voltammetry. 50 mV pulse, 50 ms pulse width, 300 ms period, 25 mV/s scan rate for differential pulse voltammetry. (Taken from Ref. [11])

one-electron transfer reduction processes were shown with $E_{1/2}$ at −0.26, −0.60, −1.11, and −1.53 V relative to SCE (saturated calomel electrode), which corresponded −0.76, −1.10, −1.61, and −2.03 V vs Fc/Fc^+ under the experimental condition ($E[Fc/Fc^+] = +0.50$ V vs SCE). Compared with C_{60} and C_{70}, a significant anodic shift is shown for the reduction of C_{76}, demonstrating that C_{76} is more electron deficient than C_{60} and C_{70}, consistent with the larger π-electron conjugation presented in C_{76} with respect to C_{60} and C_{70}.

In addition to C_{60}, C_{70}, and C_{76}, C_{84} is the next most available fullerene for study. Different from C_{60}, C_{70}, and C_{76}, where there is only one constitutional isomer for each fullerene (two enantiomers for C_{76}), C_{84} exists in several isomeric forms, complicating the electrochemical study of C_{84}. The cyclic voltammetry of six isomers of C_{84} [D_2(IV), D_{2d}(II), C_2(IV), D_{2d}(I), C_s(b), and D_2(II)] was performed [14], which showed $E_{1/2}$ potentials of −0.60, −0.96, −1.37, −1.60, and −1.77 V vs Fc/Fc^+ in benzonitrile (PhCN) containing 0.05 M PPNCl (PPN = $[(C_6H_5)_3P]_2N^+$) for the reduction of D_2(IV) isomer; −0.61, −0.96, −1.33, and −1.63 V for the D_{2d}(II) isomer; −0.28, −0.63, and −1.46 V for the C_2(IV) isomer; −0.64, −0.98, and −1.37 V for the D_{2d}(I) isomer; −0.43 and −0.79 V for the C_s(b) isomer; and

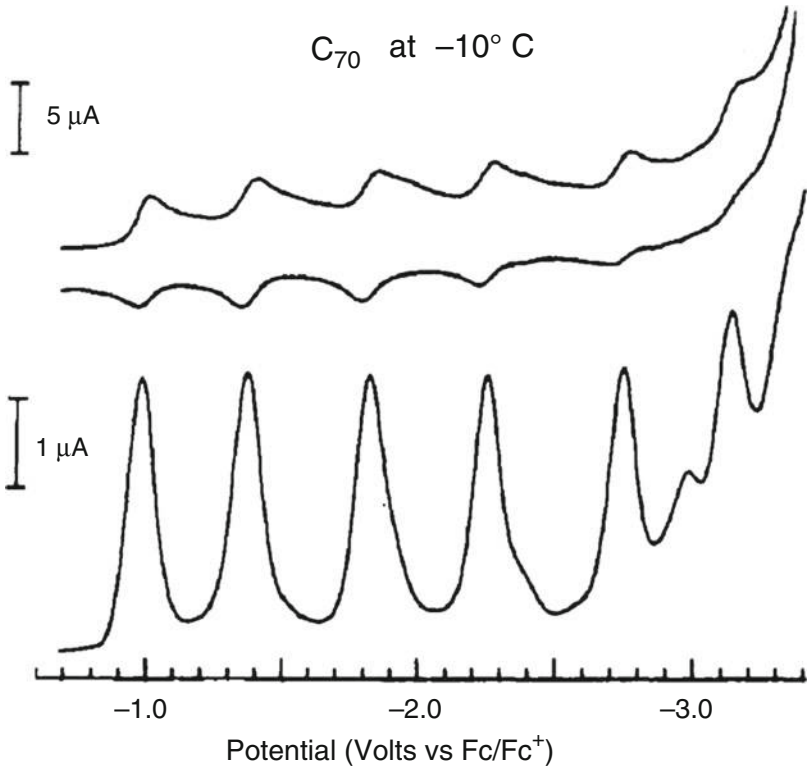

Fig. 2 Cyclic voltammogram and the differential pulse voltammogram of C_{70} in CH_3CN/toluene containing 0.1 M $TBAPF_6$ at −10 °C. 100 mV/s scan rate for cyclic voltammetry. 50 mV pulse, 50 ms pulse width, 300 ms period, 25 mV/s scan rate for differential pulse voltammetry. (Taken from Ref. [11])

−0.46, −0.80, −1.15, and −1.51 V for the D_2(II) isomer. The result shows that C_{84} is easier to be reduced compared to C_{60}, C_{70}, and C_{76} and once again consistent with the greater π-conjugation presented in the larger fullerene carbon cages.

Electrochemical Oxidations

In contrast to the reversible multistep one-electron transfer electrochemical reductions of fullerenes, the electrooxidation of fullerenes typically occurred via the irreversible multi-electron transfer process, as in the cases of C_{60} and C_{70}, where a four-electron transfer oxidation was reported with $E^{ox} = +1.30$ V vs Fc/Fc^+ in PhCN containing 0.1 M $TBAPF_6$ [10]. After the revelation of C_{60}^{6-} and C_{70}^{6-}, more attention is paid to the reversible oxidation of fullerenes. Echegoyen et al. reported the reversible one-electron oxidation of both C_{60} and C_{70} in TCE (trichloroethylene) containing 0.1 M $TBAPF_6$ [15]. Figure 4 shows the cyclic voltammograms and OSWV (Osteryoung square wave voltammetry) scans for C_{60} and C_{70} in 0.1 M $(TBA)PF_6$/TCE at room temperature.

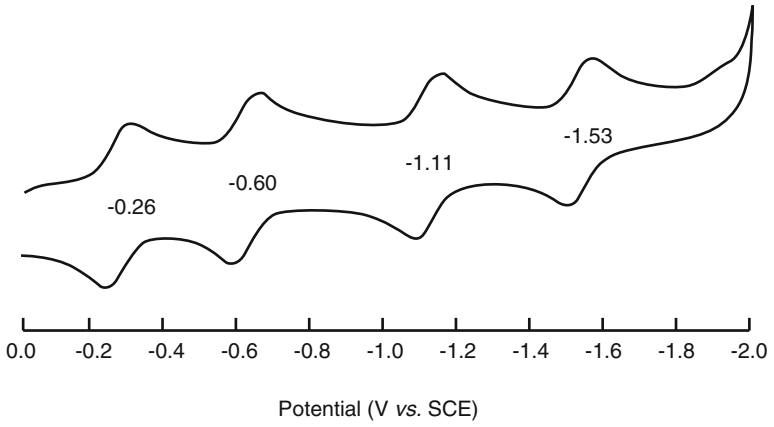

Fig. 3 Cyclic voltammogram of C_{76} in 50:50 v/v PhCN/toluene, 0.1 M TBAP. Scan rate 0.1 V/s. (Taken from Ref. [13])

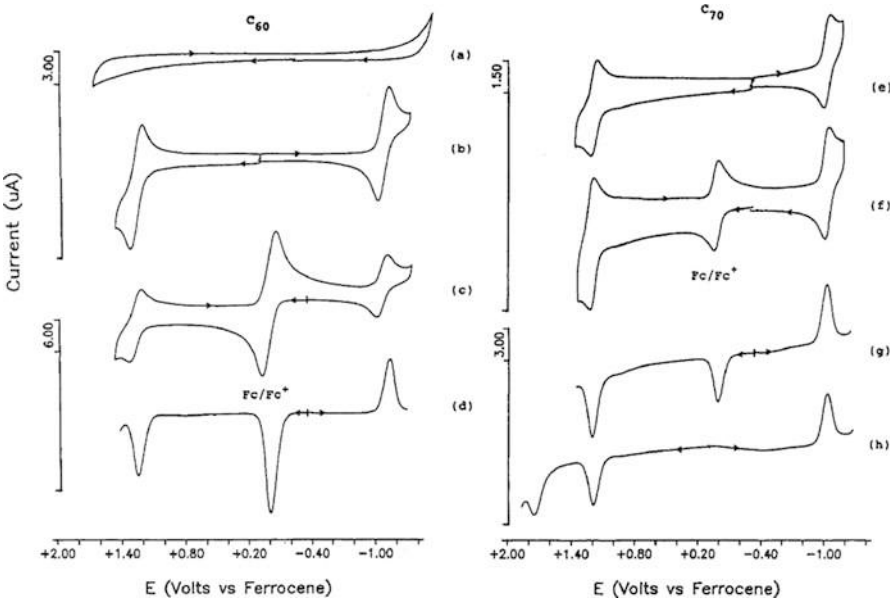

Fig. 4 Cyclic voltammograms and OSVW scans for C_{60} and C_{70} in 0.1 M (TBA)PF_6/TCE at room temperature. Cyclic voltammograms were run at a scan rate of 100 mV/s, while OSWVs were run at 60 mV/s. (**a**) background solvent-electrolyte system. (**b**) C_{60}, no ferrocene added. The cathodic and anodic cyclic scans were performed separately. (**c**) Same as **b** after addition of ferrocene. (**d**) OSWV of the solution in **c**. Cathodic and anodic scans were performed separately. (**e**) C_{70} without added ferrocene. Cathodic and anodic cyclic scans were performed separately. (**f**) Same as **e** after addition of ferrocene. (**g**) OSWV of the solution in **f**. Cathodic and anodic scans were performed separately. (**h**) OSWV of the solution as in **e**, without ferrocene added, scanned to more positive potential to show the second oxidation wave for C_{70}. (Taken from Ref. [15])

As is shown in Fig. 4, a quasi-reversible oxidation wave appears at +1.26 V and +1.20 V vs Fc/Fc^+ at room temperature for C_{60} and C_{70}, respectively. Notably, the quasi-reversible anodic waves for C_{60} and C_{70} have the same current intensity as the respective reversible first cathodic wave, indicating that they all correspond to the transfer of the same number of electrons, which is confirmed to be one electron by the electrochemical reduction study [11]. The potential difference between the first anodic and the first cathodic waves for C_{60} and C_{70} are 2.32 and 2.22 V, respectively, which can be interpreted as the energy difference between the HOMO and the LUMO in solution. The result showed for the first time that the monocationic C_{60} and C_{70} species are stable under certain conditions, consistent with some recently reported reactions of C_{60} that undergo via the cationic C_{60} intermediates [16, 17].

Derivatives of Fullerenes

The electron-deficient π-electron conjugation of fullerenes is disrupted when addition occurs, which would typically result in less electron affinity of the molecules with an increased LUMO level. However, the addition of strong electron-withdrawing addends may compensate for the loss of electron affinity caused by the disruption of the π-electron conjugation. In general, the electrochemical property of fullerene derivatives is affected by the nature, the number, and the addition pattern of the addends.

Nature of the Addends

In general, the electroreduction potentials of C_{60} derivatives are negatively shifted with respect to C_{60} due to the cleavage of the π-electron conjugation of the fullerene cage. Saturation of a double bond may cause a cathodic shift of about 50~150 mV for the reduction potentials [18]. The electroreduction potentials of the derivatives may also be affected by the inductive effect of the addends, where the potentials may be shifted positively by strong electron-withdrawing addend.

$PC_{61}BM$ ([6,6]-Phenyl C_{61} butyric acid methyl ester, Fig. 5) [19] is an important fullerene acceptor molecule used for both polymer [4] and perovskite [20] solar cells

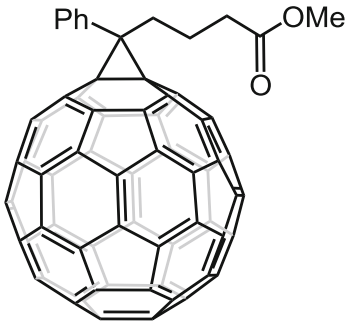

Fig. 5 Illustrated structure of $PC_{61}BM$

and for efficient electrochemical reduction of CO_2 to formate [21]. The study showed that the $E_{1/2}$ reduction potentials of the compound were −1169, −1549, and −2050 mV vs Fc/Fc^+, respectively, in 0.1 M $TBAPF_6$ o-DCB (o-dichlorobenzene) solution, which were negatively shifted by about 100~150 mV compared to the $E_{1/2}$ reduction potentials of C_{60} at −1056, −1451, and −1906 mV measured under the same condition [19]. Such a negative shift of the reduction potentials of $PC_{61}BM$ is due to the cleavage of one double bond in C_{60} and is an indication that the LUMO level of $PC_{61}BM$ is increased compared with that of C_{60}. Such a LUMO energy increase can help to improve the V_{OC} (open-circuit voltage) of the polymer solar cells, which is important in enhancing the performance of the devices [4].

1,2-$(CN)_2C_{60}$ (dicyano C_{60}) was subjected to the electrochemical measurement [22]. The compound is a C_{60} derivative that has two strong electron-withdrawing cyano addends as shown in Fig. 6. The result showed $E_{1/2}$ reduction potentials of −935, −1330, −1800, and −2225 mV vs Fc/Fc^+ for 1,2-$(CN)_2C_{60}$ in DMF/toluene (v/v = 2:3), which was positively shifted with respect to the reduction potentials of −1056, −1451, −1906, and −2384 mV vs Fc/Fc^+ measured under the same condition, demonstrating that 1,2-$(CN)_2C_{60}$ is more electron deficient with a decreased LUMO level compared with C_{60}. Since $PC_{61}BM$ and 1,2-$(CN)_2C_{60}$ have the same addition pattern (1,2-addition) [23], and both have only one double bond cleaved, the electrochemical difference between the two compounds should be due to the inductive effect of the addends.

Another example for the addend effect is the electrochemical difference between [60]fulleropyrrolidine (**1**) and [60]fulleropyrrolidinium cation (**2**) [24]. Figure 7 shows the structures of **1** and **2**. The electrochemical measurements were performed for **1**, **2**, and C_{60} in THF containing 0.05 M $TABPF_6$. Compound **1** exhibits $E_{1/2}$ reduction potentials at −0.44, −0.99, −1.60, −2.10, and −2.83 V vs SCE, while compound **2** exhibits $E_{1/2}$ reduction potentials at −0.29, −0.79, −1.34, −1.84, and −2.66 vs SCE. Under identical condition, C_{60} shows $E_{1/2}$ reduction potentials at −0.35, −0.94, −1.50, −1.99, and −2.50 V vs SCE. The result shows a significant

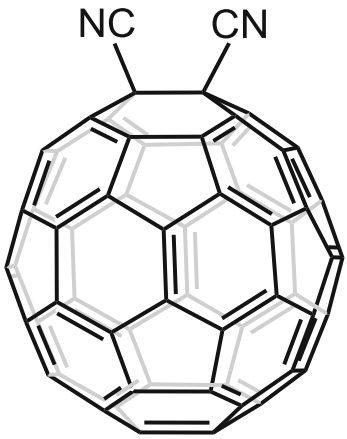

Fig. 6 Illustrated structure of 1,2-$(CN)_2C_{60}$

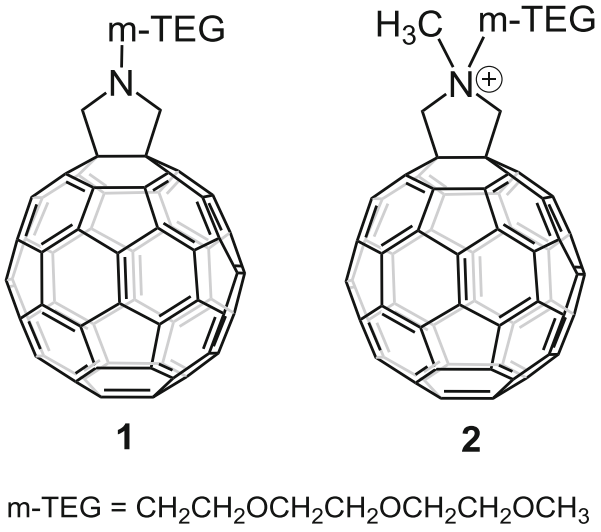

Fig. 7 Illustrated structures of [60]fulleropyrrolidine **1** and [60] fulleropyrrolidinium cation **2**

effect of the addend toward the electrochemical property of fullerene derivatives, where **2** with the strong electron-deficient pyrrolidium cation addend not only exhibits more electron affinity compared to the neutral pyrrolidine analogue **1** but is also more electron deficient than C_{60}.

Number of Addends

In addition to the nature of the addends, the number of addends also affects the electrochemical property of fullerene derivatives as it is closely related to the number of π bonds cleaved in the fullerenes. Compared to the monoadducts, bisadducts typically exhibit less electron affinity with increased LUMO energy level, which are more difficult to be reduced and exhibit better photovoltaic performance due to the improved V_{OC} of the solar cells [4]. In general, there are eight types of C_{60} bisadducts as shown in Fig. 8 [25]. The bisadducts of [60]fulleropyrrolidines (**3**, Fig. 9) were prepared, and all eight isomers were obtained. Table 1 lists the reduction $E_{1/2}$ potentials along with C_{60} and the monoadduct (**1** in Fig. 7).

As shown in Table 1, the monoadduct (**1**) is more difficult to be reduced than C_{60}, while all the bisadducts (**3**) are even more difficult to be reduced compared to **1**. The result shows explicitly that the cleavage of π bond in C_{60} would decrease the electronegativity of the fullerene π-conjugation. Consequently, the more addends, the less electronegativity of the fullerene derivatives.

Addition Pattern: Isomer Effect

C_{60} Derivatives

Due to the presence of many reaction sites, it is conventional to form isomers for fullerene derivatives with different addition pattern, which may also affect the

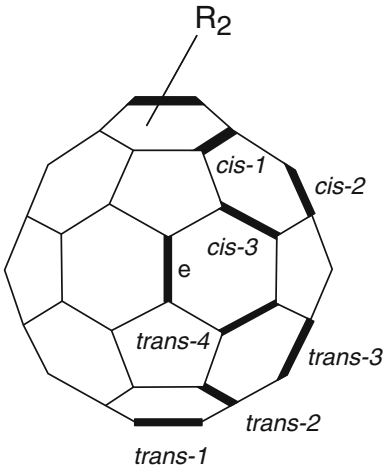

Fig. 8 Relative positional relationship of the eight different double bonds with respect to the existing R_2. (Taken from Ref. [25])

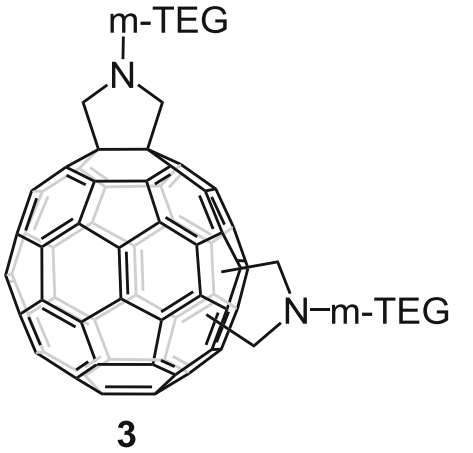

3

m-TEG = $CH_2CH_2OCH_2CH_2OCH_2CH_2OCH_3$

Fig. 9 Illustrated structures of bisadducts of [60] fulleropyrrolidine **3**

electrochemical property of fullerene derivatives. Figure 10 shows the 1,2-, 1,4-, and 1,16-addition patterns to C_{60}. The 1,2-addition retains the electronic structure of C_{60} by keeping all the double bonds between two hexagons, where the addends are added with the ortho-addition pattern between the two six-membered rings. Such an addition pattern is preferential for cycloadditions and additions of noncyclic groups that are less steric demanding. The 1,4-addition introduces one [5,6]-double bond between a five- and a six-membered rings via the para-addition across a six-membered ring, which is predicted to increase the system energy by 8.5 kcal/mol [26]. Such an addition pattern is preferential for the bulky addends, where the

Table 1 $E_{1/2}$ values (V vs SCE, 25 °C) of eight regioisomers of N-m-TEG-fulleropyrrolidine bisadducts **3**, monoadduct **1** compounds, and C_{60}

Species	$E_{1/2}$ (V)				
C_{60}	−0.35	−0.94	−1.50	−1.99	−2.50
1	−0.44	−0.99	−1.60	−2.10	−2.83
3-trans-1	−0.51	−1.05	−1.76	−2.18	
3-trans-2	−0.53	−1.06	−1.85	−2.30	
3-trans-3	−0.60	−1.14	−1.84	−2.26	
3-trans-4	−0.61	−1.16	−1.74	−2.18	
3-equatorial	−0.62	−1.15	−1.85	−2.30	
3-cis-3	−0.64	−1.20	−1.76	−2.24	
3-cis-2	−0.65	−1.18	−1.85	−2.31	
3-cis-1	−0.56	−1.10	−1.84	−2.31	

Measured in THF containing 0.05 M $TABPF_6$
Taken from Ref. [24]

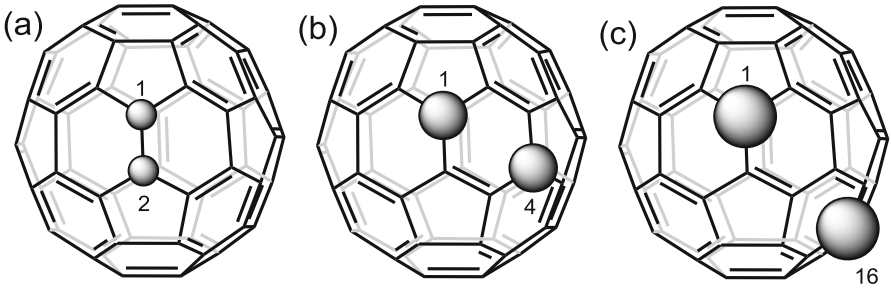

Fig. 10 Illustrated structures of (a) 1,2-, (b) 1,4-, and (c) 1,16-adducts of C_{60}

unfavorable energy increase could be compensated for by a decrease in steric hindrance. As the addends become even larger, the reaction might undergo the 1,16-addition with the addends being further apart, where two unfavorable [5,6]-double bonds are introduced.

The electrochemistry of 1,2-Bn_2C_{60} and 1,4-Bn_2C_{60} (Bn = benzyl) represents a good example of the isomer effect [27]. The measurements were performed in PhCN containing 0.1 M TBAP. 1,2-Bn_2C_{60} exhibited three quasi-reversible one-electron transfer reductions within the cathodic potential limit of the solvent with $E_{1/2}$ at −0.62, −1.04, and −1.57 V vs SCE, while the 1,4-Bn_2C_{60} showed three quasi-reversible one-electron transfer reductions at −0.52, −1.01, and −1.52 V vs SCE, demonstrating that the 1,4-C_{60} adducts are more electron deficient than the 1,2-C_{60} adducts.

The electrochemistry of two isomeric tetraadducts of C_{60}, 1,4,10,24-Bn_4C_{60}, and 1,2,4,15-Bn_4C_{60} was also studied to probe into the addition effect [28]. Figure 11 shows the illustrated structures of the 1,4,10,24-Bn_4C_{60} and 1,2,4,15-Bn_4C_{60}.

Figure 12 shows the cyclic voltammograms of 1,4,10,24-Bn_4C_{60} and 1,2,4,15-Bn_4C_{60} recorded in PhCN containing 0.2 M TBAP. It shows three one-electron transfer reductions with $E_{1/2}$ at −0.69, −1.12, and −1.88 V vs SCE for 1,4,10,24-Bn_4C_{60}. The 1,2,4,15-Bn_4C_{60} also exhibits three one-electron transfer reductions,

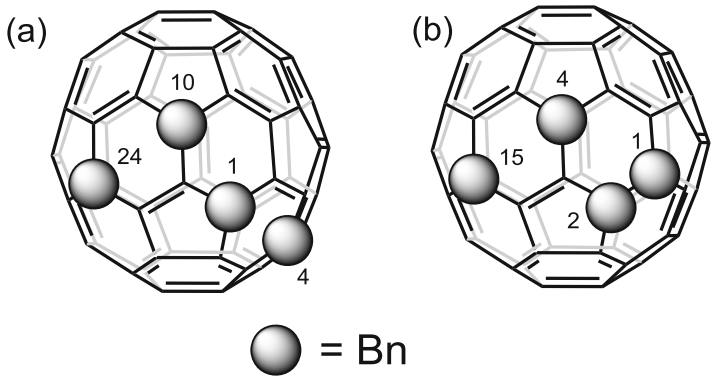

Fig. 11 Illustrated structures of (**a**) 1,4,10,24-Bn_4C_{60} and (**b**) 1,2,4,15-Bn_4C_{60}

with $E_{1/2}$ at −0.74, −1.15, and −1.85 V vs SCE. The result shows that 1,4,10,24-Bn_4C_{60} is more electron deficient than 1,2,4,15-Bn_4C_{60} with the reduction potentials positively shifted. Notably, the 1,4,10,24-Bn_4C_{60} contains two 1,4-additions, while 1,2,4,15-Bn_4C_{60} contains one 1,4-addition and one 1,2-addition, consistent with the conclusion drawn from the 1,2-Bn_2C_{60} and 1,4-Bn_2C_{60} that the 1,4-C_{60} adducts are more electron deficient than the 1,2-C_{60} adducts.

The 1,4- and 1,6-addition effect toward the electrochemical property of C_{60} derivatives were studied using two sets of compounds, 1,4-$(CN(CH_3)_2C)_2C_{60}$, 1,16-$(CN(CH_3)_2C)_2C_{60}$, and 1,4-$(CH_3CO_2(CH_3)_2C)_2C_{60}$, 1,16-$(CH_3CO_2(CH_3)_2C)_2C_{60}$ [29]. The electrochemical measurements were carried out in o-DCB containing 0.1 M TBAP. The result showed $E_{1/2}$ of −0.41, −0.81, and −1.32 V vs Ag/AgCl for 1,4-$(CN(CH_3)_2C)_2C_{60}$; −0.21, −0.61, and −1.29 V vs Ag/AgCl for 1,16-$(CN(CH_3)_2C)_2C_{60}$; −0.55, −0.94, and −1.41 V vs Ag/AgCl for 1,4-$(CH_3CO_2(CH_3)_2C)_2C_{60}$; and −0.37, −0.76, and −1.43 V vs Ag/AgCl for 1,16-$(CH_3CO_2(CH_3)_2C)_2C_{60}$, where the 1,16-$C_{60}$ adducts were all more electron deficient than the respective 1,4-C_{60} adducts.

Overall, the result shows for C_{60} derivatives, the electron deficiency decreases from the 1,16-adducts to 1,4-adducts and 1,2-adducts. Such a difference is well related to the number of double bonds in the pentagons in C_{60} [30], where the 1,16-C_{60} adducts bear two double bonds in pentagons, 1,4-C_{60} adducts bear one double bond in a pentagon, and 1,2-C_{60} adducts has no double bond in pentagon.

C_{70} Derivatives

Due to the lower symmetry of C_{70} molecule (D_{5h}), the single addition is more complicated compared to the case of C_{60} and would typically result in several isomers. Figure 13 shows the illustrated structures of these isomers, where there are three ortho-adducts and two para-adducts. The ortho-adducts are classified as α-isomer (1,2-adduct), β-isomer (5,6-adduct), and δ-isomer (7,8-isomer), while the para-adducts are classified as the 2,5- and 7,23-adducts.

The α-, β-, and δ-C_{70}QM (C_{70} o-quinodimethane monoadducts) were prepared by reaction of C_{70}^{2-} with α,α′-dibromo-o-xylene under argon at room temperature

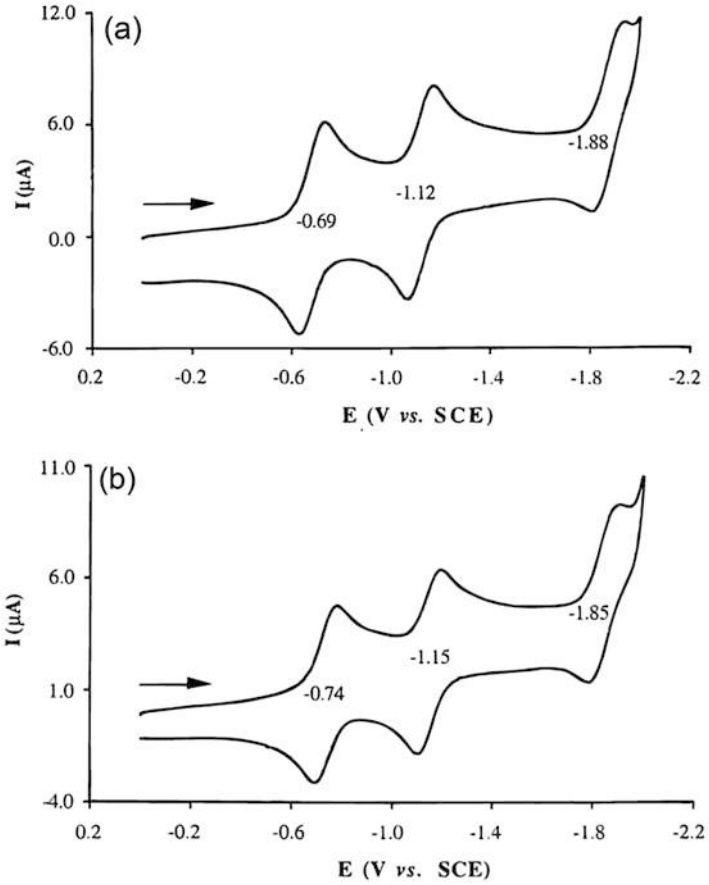

Fig. 12 Cyclic voltammograms of (**a**) 1,4,10,24-Bn_4C_{60} and (**b**) 1,2,4,15-Bn_4C_{60} recorded in PhCN containing 0.2 M TBAP. Scan rate = 100 mV/s. (Taken from Ref. 28])

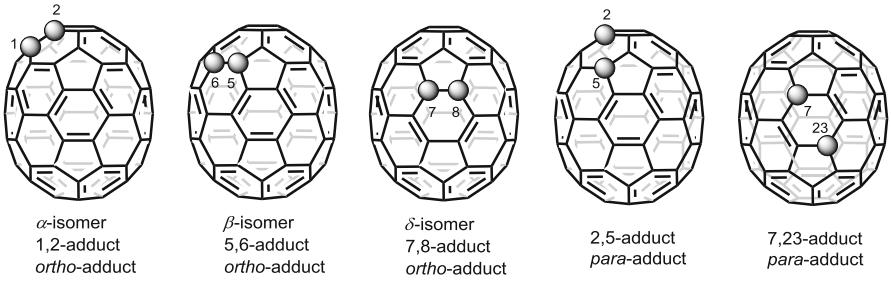

Fig. 13 Illustrated structures of isomeric C_{70} derivatives resulted from single addition

[31]. Among them, the δ-isomer was rarely obtained from the reactions of neutral C_{70} but could be obtained in significant amount using C_{70}^{2-}. Figure 14 shows the

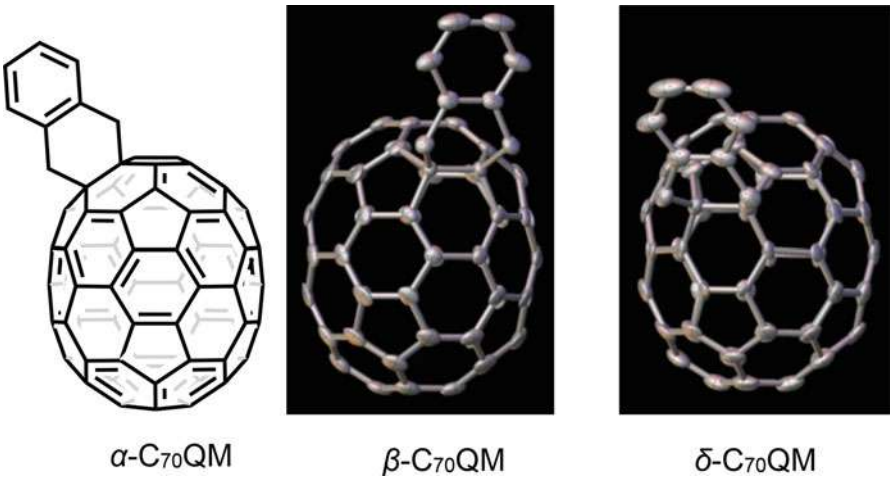

Fig. 14 Illustrated structure of α-C_{70}QM and the single-crystal structures of β-C_{70}QM and δ-C_{70}QM. (The single-crystal structures of β-C_{70}QM and δ-C_{70}QM are taken from Ref. [31])

illustrated structure of α-C_{70}QM and the single-crystal structures of β-C_{70}QM and δ-C_{70}QM.

The three isomers were subjected to the cyclic voltammetry measurement in o-DCB containing 0.1 M TBAP. Figure 15 shows the cyclic voltammograms of the three isomers, with the $E_{1/2}$ reduction potentials of −1.22, −1.60, and −2.00 V vs Fc/Fc^+ for α-C_{70}QM; −1.19, −1.59, and −2.05 V vs Fc/Fc^+ for β-C_{70}QM; and −0.97, −1.46, and −2.01 V vs Fc/Fc^+ for δ-C_{70}QM. Under the same conditions, $E_{1/2}$ reduction potentials for C_{70} are −1.08, −1.46, and −1.88 and −2.31 V Fc/Fc^+ [31]. The result shows that the first reduction potentials for both α-C_{70}QM and β-C_{70}QM are negatively shifted with respect to C_{70}, likely due to the cleavage of the one double bond in C_{70}, similar to the case of C_{60} derivatives. Surprisingly, the first reduction potential for the δ-C_{70}QM is positively shifted compared to C_{70} by about 110 mV even though one double bond in the C_{70} π-electron conjugation is cleaved, suggesting that the π-electron conjugation in the equatorial region of C_{70} is likely electron-donating rather than electron-withdrawing as that in C_{60} and in the polar region of C_{70}.

The electrochemical difference between the ortho- and para-adducts is shown by the compounds of 1-Bn-2MeOC_{70} and 2-MeO-5-BnC_{70} [32]. Figure 16 shows the cyclic voltammograms of 1-Bn-2MeOC_{70} and 2-MeO-5-BnC_{70} measured in PhCN containing 0.1 M TBAP. Three quasi-reversible one-electron transfer reduction waves with $E_{1/2}$ at −1.05, −1.43, and −1.84 V vs Fc/Fc^+ for the ortho-adduct of 1-Bn-2MeOC_{70}. In contrast, the para-adduct of 2-MeO-5-BnC_{70} shows two quasi-reversible one-electron transfer reduction waves with $E_{1/2}$ at −0.83 V and −1.24 V vs Fc/Fc^+. Further reductions show two more reduction waves with $E_{1/2}$ at −1.42 V and −1.83 V vs Fc/Fc^+. However, the difference between the second and third reduction waves is too small (0.18 V) for C_{70} and C_{70} derivatives, indicating that the

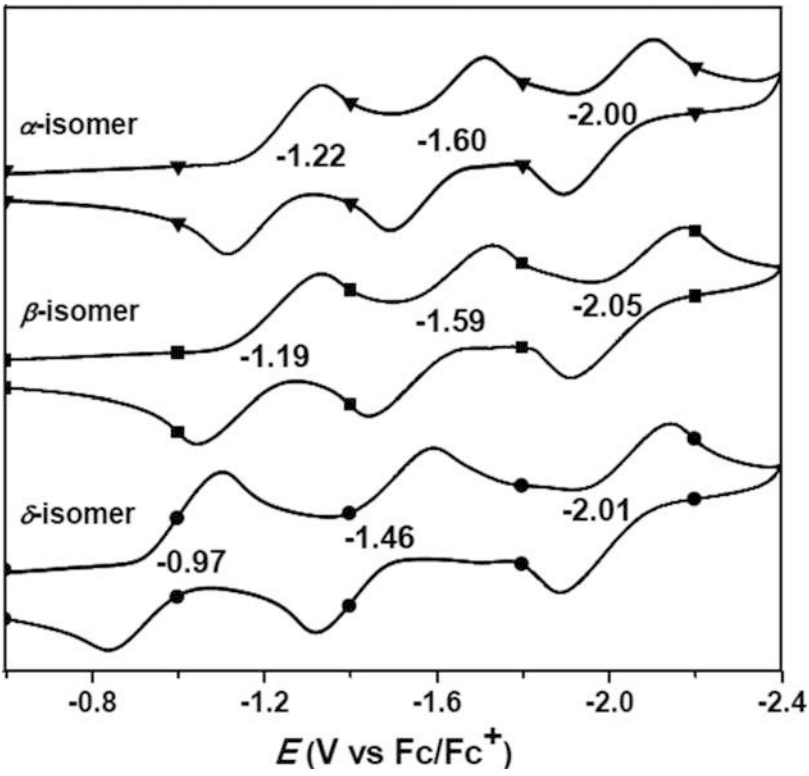

Fig. 15 Cyclic voltammograms of α-C_{70}QM, β-C_{70}QM, and δ-C_{70}QM measured in o-DCB containing 0.1 M TBAP. Scan rate = 100 mV/s. (Taken from Ref. [31])

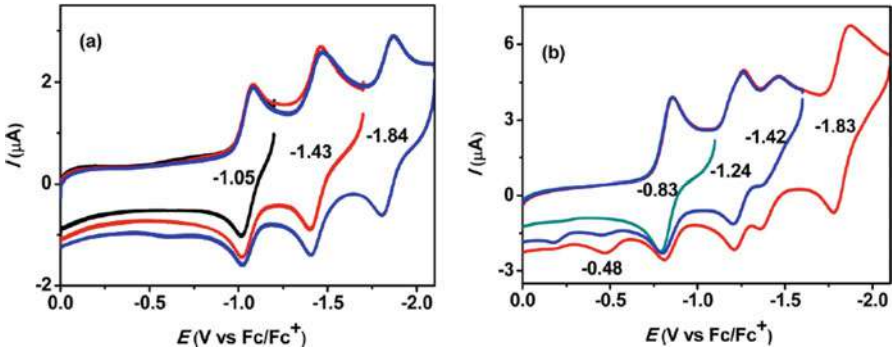

Fig. 16 Cyclic voltammograms of (**a**) 1-Bn-2MeOC_{70} and (**b**) 2-MeO-5-BnC_{70} in PhCN containing 0.1 M TBAP. Scan rate = 100 mV/s. (Taken from Ref. [32])

third and fourth reductions are unlikely related to anionic species of 2-MeO-5-BnC_{70} but rather the anionic species of 5-BnC_{70}, where the methoxy group is lost from the

molecule upon receiving two electrons. Overall, the result confirms that the para-adduct is more electron deficient than the analogous ortho-adduct, while the para-adduct is less stable with respect to the ortho-adduct upon reduction.

The electrochemical difference between the isomeric C_{70} derivatives was studied with 1-H-2-BnC_{70} and 7,23-HBnC_{70} [33]. Figure 17 shows the cyclic voltammograms of 1-H-2-BnC_{70} and 7,23-HBnC_{70} measured in PhCN containing 0.1 M TBAP.

Four reduction waves with $E_{1/2}$ at −0.57, −0.96, −1.34, and −1.79 V vs SCE are shown for 1-H-2-BnC_{70}. A negative potential shift is observed for the reduction of 1-H-2-BnC_{70} compared to the reduction of C_{70} ($E_{1/2}$: −0.45, −0.85, −1.30, and −1.72 V vs SCE under the same conditions), which is likely due to the cleavage of the electronegative π-electron conjugation of fullerenes as observed for conventional C_{60} derivatives.

The cyclic voltammogram of 7,23-HBnC_{70} indicates that the anionic species of the compound is unstable. It starts to decompose after it acquires one electron. The compound exhibits an irreversible first redox process with the E_{pc} at −0.41 V and three subsequent quasi-reversible redox processes with $E_{1/2}$ at −0.94, −1.40, and −1.89 V vs SCE, which is likely related to the anionic intermediate of 7-BnC_{70}^{-} species due to the reductive loss of H [33]. Notably, the reduction potential of 7,23-HBnC_{70} is not only positively shifted with respect to that of 1-H-2-BnC_{70} but also more positive than that of C_{70} ($E_{pc}{}^{1st} = -0.49$ V). Such a strong electron deficiency is also observed for another equatorial product, 7,8-C_{70}QM, as discussed above (Fig. 15), suggesting that the π-electron conjugation in the equatorial region of C_{70} is electropositive rather than electronegative, where the cleavage of the conjugation at the equatorial region would likely increase the overall electronegativity of the molecule. In addition, the result once again shows that the anions of the para-adducts are unstable compared to those of the ortho-adducts.

In summary, the result shows that for C_{70} derivatives, the equatorial adducts are in general more electron deficient than the polar adducts, the para-adducts are more

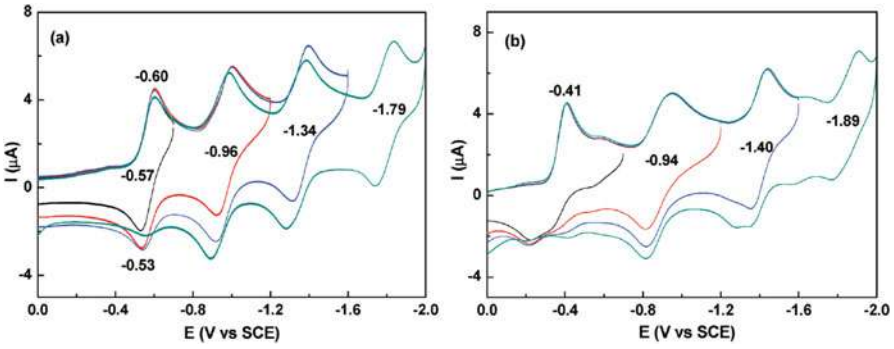

Fig. 17 Cyclic voltammograms of (**a**) 1-H-2-BnC_{70} and (**b**) 7,23-HBnC_{70} in PhCN containing 0.1 M TBAP. Scan rate = 100 mV/s. (Taken from Ref. [33])

electron-deficient than the ortho-adducts, and the anions of the para-adducts are less stable than the anions of the ortho-adducts.

Stability Difference Between Anions of Isomeric Fullerene Derivatives

The electrochemical study of two pairs of isomeric C_{70} derivatives 1-Bn-2-MeOC_{70} and 2-MeO-5-BnC_{70} and 1-H-2-BnC_{70} and 7,23-HBnC_{70} has shown that the anions of the ortho-adducts are more stable, while the anions of the para-adducts are less stable [32, 33]. Further study reveals more information on stability difference between the anions of isomeric fullerene derivatives. Figure 18 shows the cyclic voltammograms of 1,2-OMeBnC_{60} and 1,4-OMeBnC_{60} [32]. The result shows three quasi-reversible one-electron reduction waves with $E_{1/2}$ at −0.94, −1.40, and −1.89 V vs Fc/Fc^+ for 1,2-OMeBnC_{60} in PhCN containing 0.1 M TBAP, which is typical for the fullerene derivatives in view of both the reversibility and redox potentials, where the potentials are cathodically shifted with respect to those of C_{60} due to the cleavage of the π-conjugation. As for 1,4-OMeBnC_{60}, the first redox wave shows an irreversibility nature with the E_{pc} at −0.98 V vs Fc/Fc^+ and a broad oxidation wave ranging from about −0.90 to −0.48 V vs Fc/Fc^+, indicating that a chemical process likely occurs as the compound acquires one electron. Further reduction of the compound results in two quasi-reversible redox waves with $E_{1/2}$ at −1.51 and −1.91 V and an irreversible oxidation wave around −0.50 V, which are comparable to the redox processes involving the singly bonded C_{60} and dimeric species [34], suggesting that the compound undergoes a reductive cleavage of the methoxy group. The monoanions of 1,4-OMeBnC_{60} were generated with controlled-potential bulk electrolyses (CPE) by applying a potential at −1.30 V vs Fc/Fc^+, and a transfer of only one electron per mole molecule was strictly controlled. The singly reduced 1,4-OMeBnC_{60} was oxidized back to neutral by CPE with a potential set at

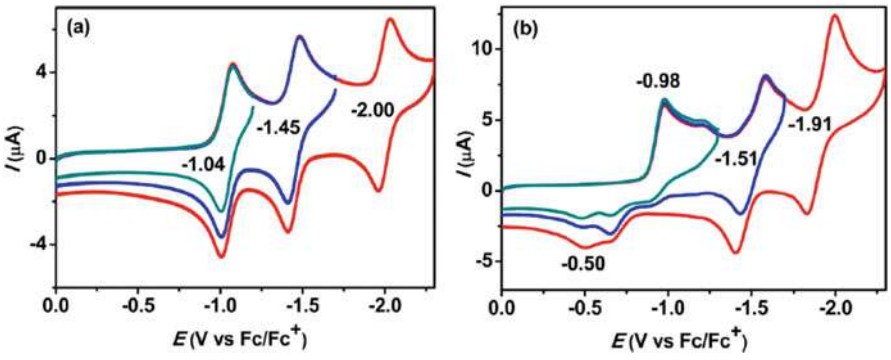

Fig. 18 Cyclic voltammograms of (**a**) 1,2-OMeBnC_{60} and (**b**) 1,4-OMeBnC_{60} in PhCN containing 0.1 M TBAP. Scan rate = 100 mV/s. (Taken from Ref. [30])

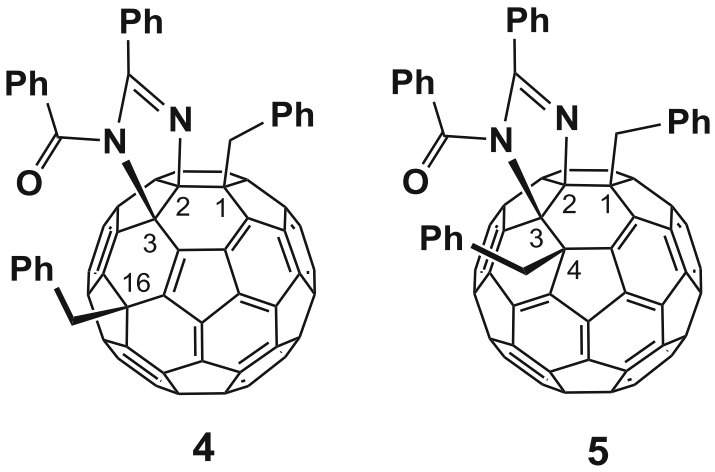

Fig. 19 Illustrated structures of **4** (1,2,3,16-adduct) and **5** (1,2,3,4-adduct) with partial labeling of the carbon atoms in C_{60}. (Taken from Ref. [35])

0 V vs Fc/Fc^+, and the obtained products were subjected to the HPLC analysis [32]. The result showed that $BnC_{60}-C_{60}Bn$ was formed in addition to the recovered 1,4-$OMeBnC_{60}$, demonstrating that the methoxy group was removed from 1,4-$OMeBnC_{60}$ upon reduction. Similar to the result of C_{70} derivatives, the anions of the ortho-adducts are more stable than the anions of para-adduct.

Two more isomers of C_{60} multi-adducts were examined to reveal more information regarding the stability difference between the isomers [35]. Figure 19 shows the structures of two benzyl C_{60} imidazoline derivatives (**4** and **5**) with the 1,2,3,16- and 1,2,3,4-configuration. Figure 20 shows the cyclic voltammograms of the two compounds.

Two important features are shown in the cyclic voltammograms of **4** and **5**. First, **4** exhibits a stronger electron deficiency than **5** by showing a more positive $E_{1/2}$ potential for the first redox wave (−0.52 vs −0.58 V vs SCE). Such a strong electron affinity is associated with the [5,6]-double bond in **4** as previous work indicates [30] and is consistent with the general trend for the reduction potential difference between the ortho- and para-adducts of C_{60} and C_{70} [27, 28, 32, 33]. Second, the anions of **5** are surprisingly more stable than the anions of **4** even though an opposite stability order is observed for the neutral compounds with **4** being more stable than **5**. Both the mono- and dianions of **5** are stable on the time frame of cyclic voltammetry, while only the monoanion of **4** is stable under the same condition. Further reductions result in more complicated anionic species for **4** compared with **5**, confirming the less stability of the anions of **4** with respect to those of **5**.

The less stability of the anions of **4** with respect to the anions of **5** is consistent with the result that the anions of the para-adducts of C_{60} and C_{70} are in general less stable than the respective anions of the ortho-adducts [32, 33], suggesting that the stability of anionic fullerene derivatives is more likely related to the

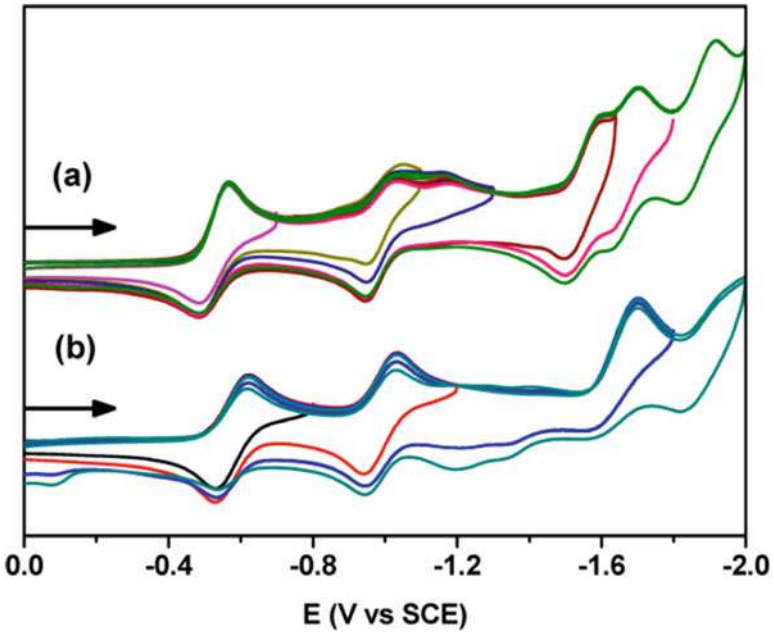

Fig. 20 Cyclic voltammograms of (**a**) **4** and (**b**) **5** in PhCN containing 0.1 M TBAP. Scan rate = 100 mV/s. (Taken from Ref. [35])

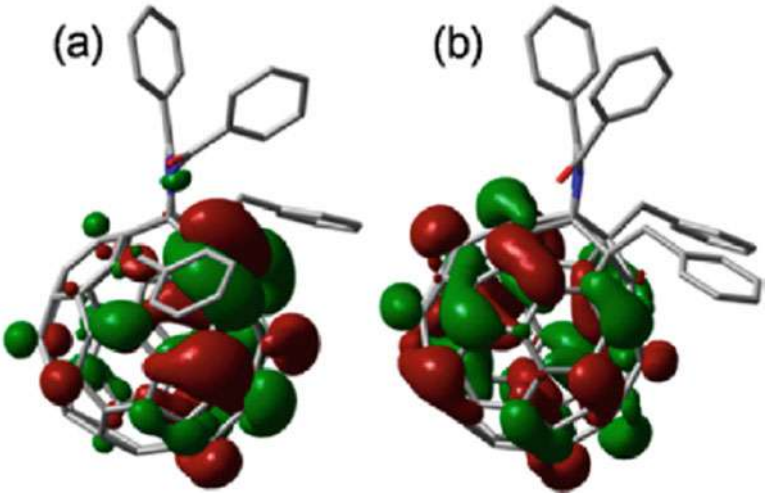

Fig. 21 Calculated HOMOs at an isosurface value of 0.02 for (**a**) **4** and (**b**) **5**. (Taken from Ref. [35])

electronic structure of the compounds rather than the stability the neural compounds because **4** is in fact more stable than **5**. Figure 21 displays the calculated HOMO

plots of $\mathbf{4}^{2-}$ and $\mathbf{5}^{2-}$, which consisted of the two extra electrons by reduction. For $\mathbf{4}^{2-}$ (1,2,3,16-adduct), the HOMO is mainly localized at the C_{60} hemisphere having the [5,6]-double bond, while the HOMO is delocalized over the entire C_{60} surface for $\mathbf{5}^{2-}$ (1,2,3,4-adduct). It shows that the presence of the [5,6]-double bond significantly affects the HOMO distributions of C_{60} derivatives. It would result in a congestion of the negative charges within a region in close proximity to the imidazoline heterocycle in $\mathbf{4}^{2-}$, which would likely destabilize the species as the heterocycle is subjected to reductive cleavage.

In summary, the result shows that the anions of fullerene derivatives containing the para-addition are less stable than the anions of adducts containing the ortho-addition, which is likely related to the presence of the [5,6]-double bond in fullerenes due to the congestion of negative charges at this type of bond as predicted by theoretical calculations, where reductive cleavage may be more likely to occur.

Unsaturated Anionic Intermediates

In addition to fullerene derivatives, the unsaturated anionic fullerene intermediates also have exhibited electrochemical activities. $BnC_{60}-C_{60}Bn$ is a singly bonded C_{60} dimer, which has meso and racemic isomers as shown in Fig. 22. Upon reduction, $BnC_{60}-C_{60}Bn$ would decompose into BnC_{60}^{-}, which would also show reversible one-electron transfer reduction processes. Figure 23 shows the cyclic voltammograms of $BnC_{60}-C_{60}Bn$ [34].

The compound exhibits an irreversible first reduction wave with E_{pc} at −0.50 V and E_{pa} at −0.06 V vs SCE. The large peak-to-peak separation for the first irreversible redox couple (∼440 mV) indicates that a chemical reaction is involved in the redox process, where BnC_{60}^{-} is generated when $BnC_{60}-C_{60}Bn$ accepts two electrons during the first reduction process, while $BnC_{60}^{\bullet}$ is generated when BnC_{60}^{-} is oxidized, which would subsequently result in $BnC_{60}-C_{60}Bn$ via radical combination reactions. The two quasi-reversible one-electron transfer reductions with $E_{1/2}$ at −0.94 and −1.36 V vs SCE upon further reduction correspond to the reduction of BnC_{60}^{-} to $BnC_{60}^{2-\bullet}$ and $BnC_{60}^{2-\bullet}$ to BnC_{60}^{3-}, respectively. Notably, the reduction

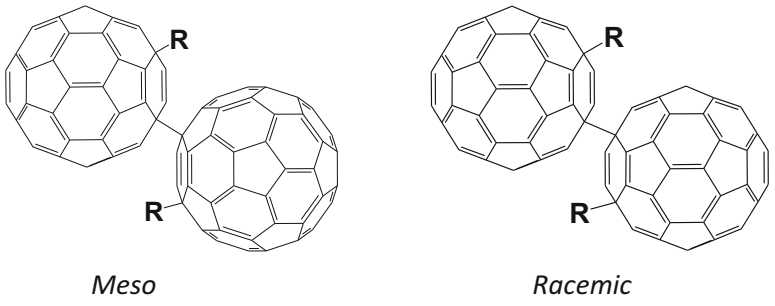

Fig. 22 Illustrated structures of the meso and racemic isomers of $BnC_{60}-C_{60}Bn$

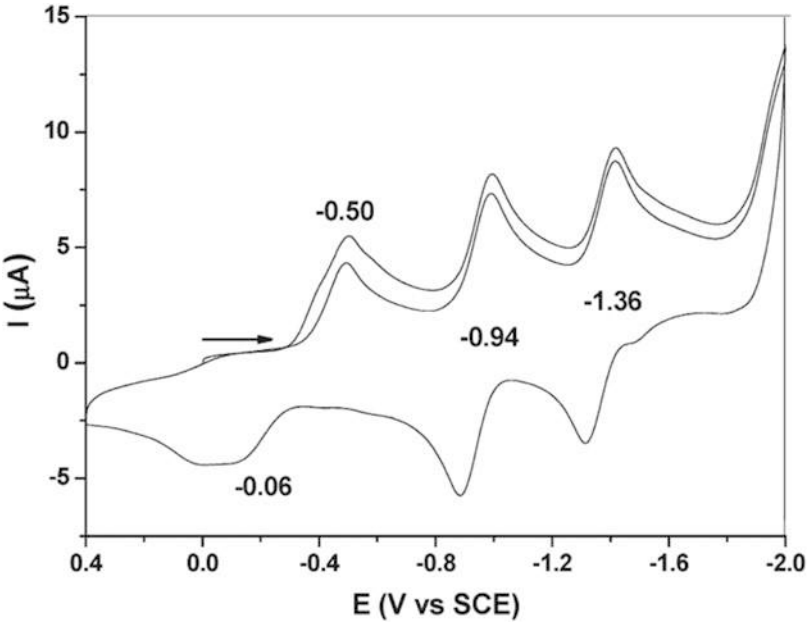

Fig. 23 Cyclic voltammograms of BnC_{60}−$C_{60}Bn$ in PhCN containing 0.1 M TBAP. Scan rate = 100 mV/s. (Taken from Ref. [34])

potentials for $BnC_{60}^{-}/BnC_{60}^{2-\bullet}$ and $BnC_{60}^{2-\bullet}/BnC_{60}^{3-}$ are positively shifted with respect to the $E_{1/2}$ potentials for 1,4-$Bn_2C_{60}^{-\bullet}$/1,4-$Bn_2C_{60}^{2-}$ (−1.01 V vs SCE) and 1,4-$Bn_2C_{60}^{2-}$/1,4-$Bn_2C_{60}^{3-\bullet}$ (−1.52 V vs SCE), and 1,2-$Bn_2C_{60}^{-\bullet}$/1,2-$Bn_2C_{60}^{2-}$ (−1.04 V vs SCE) and 1,2-$Bn_2C_{60}^{2-}$/1,2-$Bn_2C_{60}^{3-\bullet}$ (−1.57 V vs SCE) [27], consistent with the general effect of the number of addends on the reduction potentials of fullerene derivatives, where the derivatives with less addends are more electron deficient.

Electrosynthesis of Fullerene Derivatives

C_{60} and C_{60} Derivatives

Reactions of C_{60}^{2-}

Neutral fullerenes are typically reactive toward nucleophiles due to strong electron deficiency. Meanwhile, such strong electron deficiency makes it readily for fullerenes to be reduced to dianions, which are reactive toward electrophiles and may result in fullerene derivatives that are otherwise difficult to be obtained from the reactions of neutral fullerenes. Due to the precise control of the potential, the dianion of C_{60} (C_{60}^{2-}) can be facilely generated with the controlled-potential bulk electrolysis.

Kadish et al. reported the first electrosynthesis of fullerene derivatives using C_{60}^{2-}, which was generated with controlled-potential bulk electrolysis at −1.1 V vs SCE in 0.1 M TBAP PhCN solution in a drybox [5]. The purple color of neutral C_{60} solution gradually turned into a dark-red color of C_{60}^{2-} solution as the electrolysis proceeded. The potentiostat was turned off after the generation of C_{60}^{2-} was complete. A 100-fold excess of neat methyl iodide was added all at once to the solution and reacted for ca. 40 min. The solution was then subjected to the exhaustive electrooxidation with a potential of −0.2 V vs SCE, which was sufficiently positive to electrooxidize the unreacted C_{60}^{2-} but not the liberated iodide. The reaction afforded a mixture of two separable products in a 44% yield. The products were assigned as the 1,2-$(CH_3)_2C_{60}$ and 1,4-$(CH_3)_2C_{60}$ on the basis of the electrochemical, chromatographic, spectroscopic, and computational results. Due to the small size of the methyl group, the 1,2-$(CH_3)_2C_{60}$ was considered as the major product.

Fukuzumi and Kadish et al. further studied the reaction of chemically generated C_{60}^{2-} with benzyl bromide to investigate the reaction mechanism of C_{60}^{2-} with alkyl halides [36]. Scheme 1 shows the proposed mechanism for the reaction of C_{60}^{2-} with benzyl bromide. As is shown in the scheme, the reaction of $C_{60}^{2-}$with $PhCH_2Br$ proceeds via stepwise procedures, where the first step is the electron transfer from C_{60}^{2-} to $PhCH_2Br$ with the generation of $C_{60}^{-\bullet}$ and $PhCH_2^{\bullet}$, which

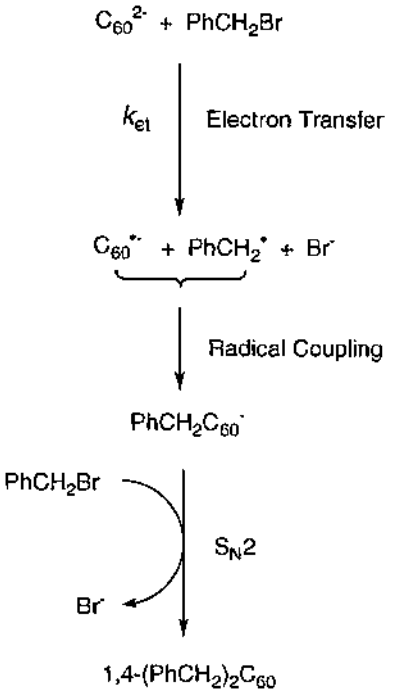

Scheme 1 Proposed mechanism for the reaction of C_{60}^{2-} with benzyl bromide. (Taken from Ref. [36])

would then form the singly bonded anionic intermediate of $PhCH_2C_{60}^-$ via radical coupling reaction. The $PhCH_2C_{60}^-$ intermediate would then react with another molecule of $PhCH_2Br$ via S_N2 reaction to afford the 1,4-$(PhCH_2)_2C_{60}$, where the para-addition pattern is preferential due to bulky size of the benzyls. It is interesting to note under certain circumstances, the stepwise added benzyls can be differentiated, which is important in exploring reaction mechanism involved in anionic intermediates of fullerene species.

The reaction of C_{60}^{2-} with benzyl bromide was revisited, which showed the formation of new products in addition to the conventional product of 1,4-$(PhCH_2)_2C_{60}$ [27]. C_{60}^{2-} was generated electrochemically with the bulk electrolysis at −1.10 V vs SCE in 0.1 M TBAP PhCN solution under an atmosphere of either N_2 or Ar. The potentiostat was switched off after electrogeneration of C_{60}^{2-} was complete. A 10–50-fold excess of $PhCH_2Br$ was then added to the solution all at once, and the reaction was allowed to proceed for 40 min with stirring. The reaction afforded methanofullerene $C_{61}HPh$, 1,2-$HPhCH_2C_{60}$, 1,4-$(PhCH_2)_2C_{60}$, and 1,2-$(PhCH_2)_2C_{60}$ (Fig. 24) with an isolation yield of ca. 3%, 2%, 55%, and 3%, respectively.

The methanofullerene $C_{61}HPh$ was likely formed from the reaction intermediate of $PhCH_2C_{60}^-$, where one of the benzylic protons was removed to achieve the cyclopropanation. As for 1,2-$HPhCH_2C_{60}$, it was likely formed from the protonation reaction of $PhCH_2C_{60}^-$. The formation of 1,2-$(PhCH_2)_2C_{60}$ indicated that the compound itself is a stable compound; however, it is likely less stable compared with 1,4-$(PhCH_2)_2C_{60}$ due to the steric hindrance brought by the two closely positioned bulky benzyls; therefore, the yield for 1,2-$(PhCH_2)_2C_{60}$ is much lower compared to that of 1,4-$(PhCH_2)_2C_{60}$.

Interestingly, the yield of 1,2-$HPhCH_2C_{60}$ could be improved dramatically when the reaction of C_{60}^{2-} with benzyl bromide was carried out in DMF [37], different from the case when the reaction was performed in PhCN, demonstrating a significance of solvent effect on the reaction. Scheme 2 shows the reactions of electrochemically generated C_{60}^{2-} with benzyl bromide carried out in DMF and PhCN.

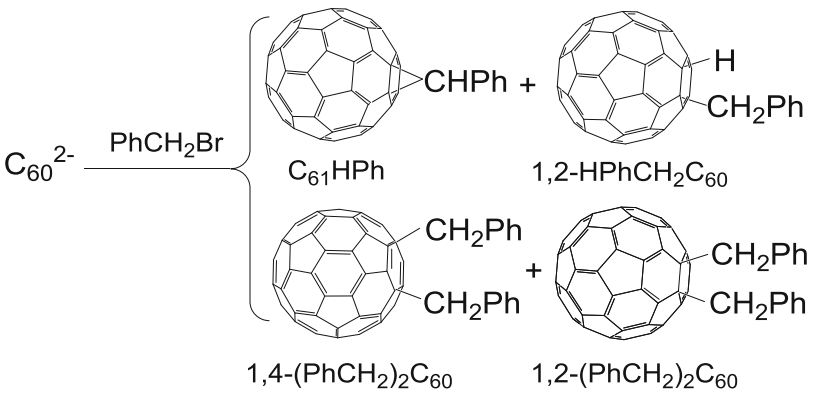

Fig. 24 Revisited reaction of C_{60}^{2-} with $PhCH_2Br$. (Taken from Ref. [27])

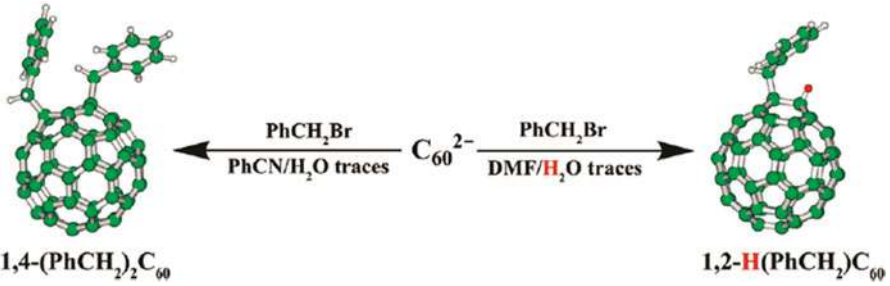

Scheme 2 Reaction of C_{60}^{2-} with $PhCH_2Br$ in 0.1 M TBAP PhCN and in DMF. (Taken from Ref. [37])

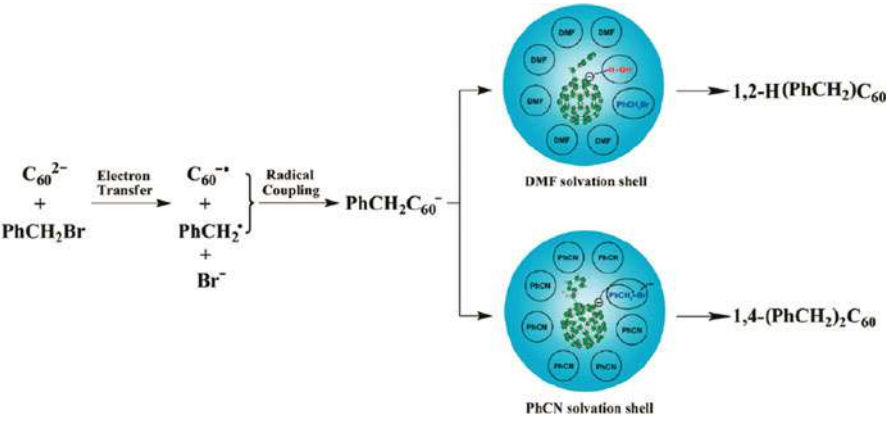

Scheme 3 Proposed reaction mechanism of C_{60}^{2-} with $PhCH_2Br$ involving water residue in DMF and PhCN. (Taken from Ref. [37])

The result difference between the two solvents is likely from the reactivity difference of water residue toward RC_{60}^- in DMF and PhCN. Both DMF and PhCN have large solubility for anionic C_{60} species, including the reaction intermediates of RC_{60}^-, suggesting that the formed RC_{60}^- can be well solvated by the solvent molecules. The RC_{60}^- intermediates can undergo either protonation by water to form 1,2-HRC_{60} or an S_N2 reaction with benzyl bromide to form di(organo)[60]fullerenes. In the case of DMF, since water residue is miscible with the solvent, it can be present in the DMF solvation shell in a significant amount; therefore, the water residue is more readily available for the reaction with $PhCH_2C_{60}^-$ with the formation of 1,2-$H(PhCH_2)C_{60}$ as the major product. In contrast, the water molecules are very ineffective in entering into the PhCN solvation shell since they are immiscible with PhCN, making it difficult for H_2O to approach $PhCH_2C_{60}^-$, which would preferentially react with $PhCH_2Br$ with the formation of 1,4-$(PhCH_2)_2C_{60}$ as the major product. The increase of the amount of water in PhCN can help more water molecules to enter into the PhCN solvation shell, leading to the formation of more 1,2-HRC_{60}. However, it is still not as effective as using the DMF

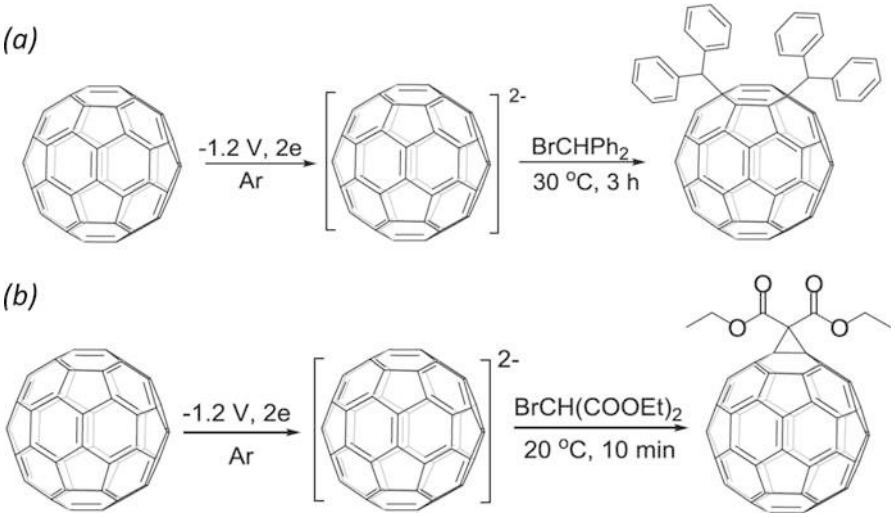

Scheme 4 Reaction of C_{60}^{2-} with (**a**) $BrCHPh_2$ and (**b**) $BrCH(CO_2Et)_2$ in 0.1 M TBAP o-DCB. (Taken from Ref. [38])

solvent in forming the 1,2-$H(PhCH_2)C_{60}$ due to the immiscibility of water with PhCN. The proposed reaction mechanism showing the different reactivity of C_{60}^{2-} in DMF and PhCN is illustrated in Scheme 3.

The reactions of electrochemically generated C_{60}^{2-} with bulky addends were investigated recently in order to pursue for the 1,16-C_{60} adducts [38]. C_{60}^{2-} was generated via controlled-potential bulk electrolysis at −1.20 V vs SCE in 0.1 M TBAP o-DCB solution and reacted with diphenylbromomethane ($BrCHPh_2$) and diethyl 2-bromomalonate ($BrCH(CO_2Et)_2$), respectively. Scheme 4 shows the reaction of C_{60}^{2-} with $BrCHPh_2$ and $BrCH(CO_2Et)_2$. Interestingly, no 1,16-adducts were formed in both cases, and the 1,4-adduct was formed for the reaction with $BrCHPh_2$, while methanofullerene was formed for the reaction with $BrCH(CO_2Et)_2$. It was intriguing to note the use of $BrCH(CO_2Et)_2$ is more effective than the use of dibromomalonate ester $Br_2C(CO_2Et)_2$. Scheme 4 shows the reactions of C_{60}^{2-} with $BrCHPh_2$ and $BrCH(CO_2Et)_2$.

The mechanism for the formation of the methanofullerene via the reaction of C_{60}^{2-} with $BrCH(CO_2Et)_2$ is proposed as shown in Scheme 5, where a single-electron transfer from the anionic intermediate to $BrCH(CO_2Et)_2$ is involved, followed by the radical coupling reactions between C_{60} and the malonate accompanied by the cleavage of $H^{\bullet}$ radical.

Reactions of the Dianions of Fullerene Derivatives

1,4-$(PhCH_2)_2C_{60}^{2-}$

In addition to C_{60}^{2-}, the dianions of C_{60} derivatives have also been used for fullerene derivatization. Two $(PhCH_2)_4C_{60}$ isomers were obtained from the reaction of electrochemically generated 1,4-$(PhCH_2)_2C_{60}^{2-}$. The two tetrabenzyl C_{60} isomers were

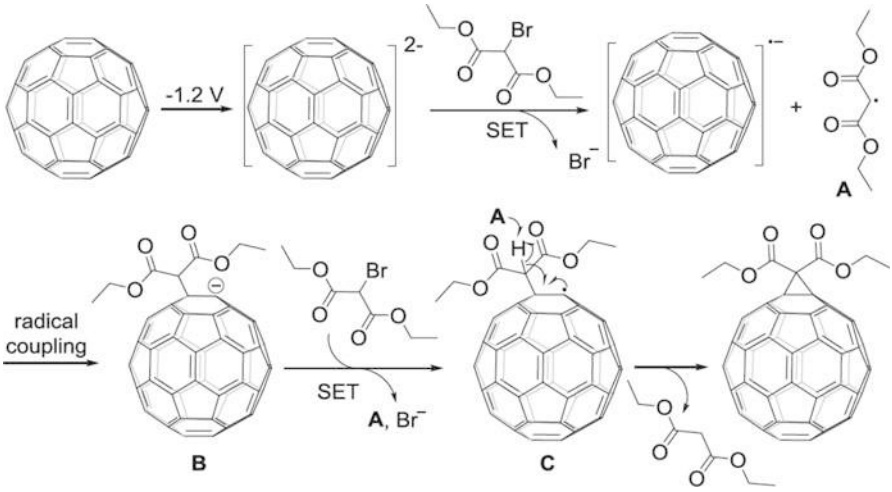

Scheme 5 Proposed reaction mechanism of C_{60}^{2-} with diethyl 2-bromomalonate. (Taken from Ref. [38])

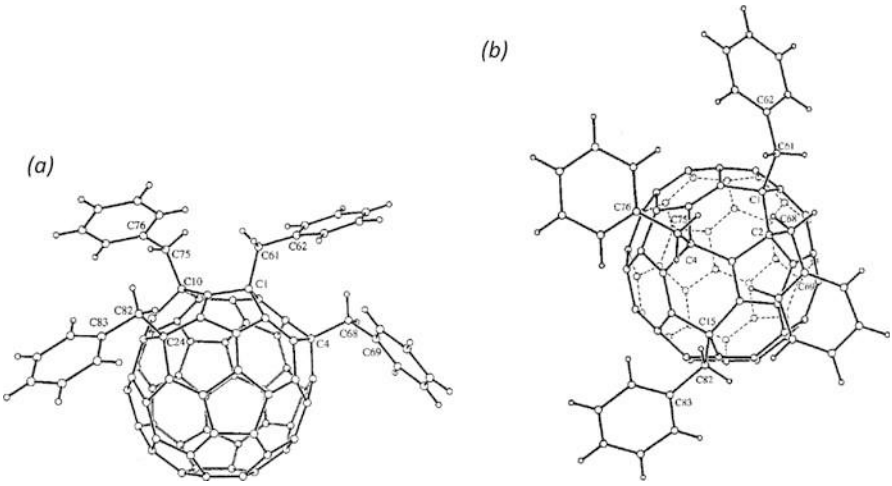

Fig. 25 Single-crystal structures of (**a**) 1,4,10,24-$(PhCH_2)_4C_{60}$ and (**b**) 1,2,4,15-$(PhCH_2)_4C_{60}$. (Taken form Ref. [28])

labeled as the 1,4,10,24-$(PhCH_2)_4C_{60}$ and 1,2,4,15-$(PhCH_2)_4C_{60}$, respectively, where 1,4,10,24-$(PhCH_2)_4C_{60}$ is a 1,4;1,4-adduct and 1,2,4,15-$(PhCH_2)_4C_{60}$ is a 1,2;1,4-adduct [28]. Figure 25 shows the single-crystal structures of the two compounds, and Fig. 26 shows the illustrated structures of the two isomers.

The result shows that the two isomers are structurally related with the difference of the position of only one benzyl group, suggesting that the two compounds are likely formed from the same intermediate of $(PhCH_2)_3C_{60}^-$ with the benzyls at A, B,

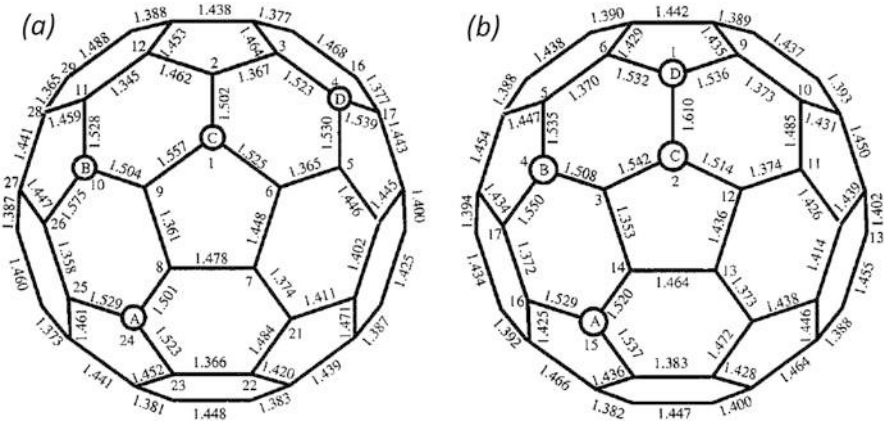

Fig. 26 Illustrated structures of (**a**) 1,4,10,24-$(PhCH_2)_4C_{60}$ and (**b**) 1,2,4,15-$(PhCH_2)_4C_{60}$ with partial labeling of the C_{60} atoms. The positions of benzyls on the C_{60} molecule are indicated with circles A, B, C, and D. The number next to each C–C bond represents the bond length in angstroms. (Taken form Ref. [28])

and C carbon atoms. Notably, the 1,2,4,15-configuration has been shown to be a preferential configuration for multiple nucleophilic additions to neutral C_{60} involving both the 1,2- and 1,4-addition patterns, where the reactions undergo via the cyclopentadienyl addition manner through a stable 10π indenyl anionic intermediates with the 1,4,15-configuration [39]. However, no report on synthesis of the 1,4,10,24-adducts from neutral C_{60} has appeared. The result demonstrated the unique regioselectivity for the reactions of the dianion of 1,4-$(PhCH_2)_2C_{60}$.

1,2-$(PhCH_2)HC_{60}^{2-}$

The electrochemical reaction of 1,2-$(PhCH_2)HC_{60}^{2-}$ was studied, which resulted in $PhCH_2C_{60}$-$C_{60}CH_2Ph$ dimer after oxidation [34]. Figure 27 shows the cyclic voltammograms of neutral 1,2-$(PhCH_2)HC_{60}$, the in situ cyclic voltammograms recorded after transferring one and two electrons to 1,2-$(PhCH_2)HC_{60}$ via controlled-potential bulk electrolysis (CPE), and the in situ cyclic voltammogram after oxidation of the dianionic solution back to neutral with a potential at 0 V vs SCE.

As is shown in Fig. 27a, the neutral 1,2-$(PhCH_2)HC_{60}$ undergoes three quasi-reversible one-electron transfer redox processes with the $E_{1/2}$ at −0.54, −0.94, and −1.50 V vs SCE, which are positively shifted with respect to the $E_{1/2}$ of 1,2-$(PhCH_2)_2C_{60}$ (−0.62, −1.04, and −1.57 V vs SCE) [27], reflecting the difference of electron donation ability between the H atom and the benzyl group. Notably, the three anionic species of the reduction are stable on the cyclic voltammetric time scale.

As for the in situ cyclic voltammogram of the reduced 1,2-$(PhCH_2)HC_{60}$ species after bulk electrolytic reduction at −0.70 V (Fig. 27b), which is suitable for transferring one electron to the molecule, the voltammetry scan was started at the

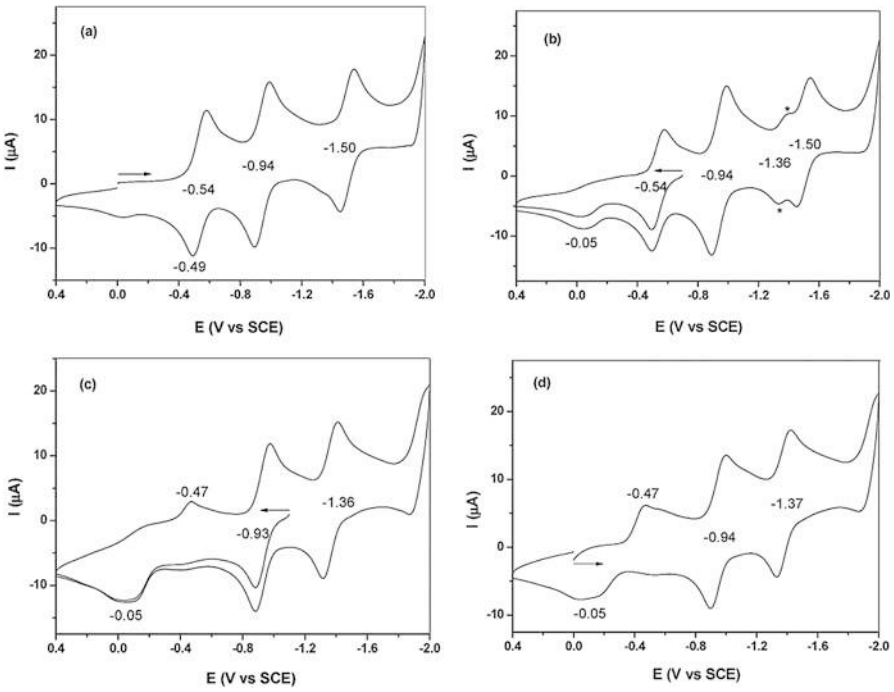

Fig. 27 Cyclic voltammograms of 1,2-($PhCH_2$)HC_{60} (**a**) in neutral state, (**b**) after transferring one electron to 1,2-($PhCH_2$)HC_{60} with controlled-potential bulk electrolysis (CPE) at −0.70 V vs SCE, (**c**) after transferring two electrons to 1,2-($PhCH_2$)HC_{60} with CPE at −1.10 V, and (**d**) after oxidizing the anionic solution shown in panel c back to neutral with a potential at 0 V. The arrows indicate the initial potential and the scan direction for the cyclic voltammetry measurement. The measurements were carried out in benzonitrile containing 0.1 M TBAP at a scan rate of 0.1 V/s. (Taken form Ref. [34])

bulk electrolysis potential of −0.70 V, because this is supposed to be the equilibrium potential ($I = 0$ μA) for the produced monoanionic species. In fact, it shows that the initial current is very close to zero, indicating that the bulk anionic species in solution have one formal negative charge as expected. It is noteworthy that the current heights for both the first redox couple at −0.54 V and the third one at −1.50 V are decreased; meanwhile, the redox couple at −0.94 V remains almost unchanged. An extra reversible redox couple labeled with asterisks appears at $E_{1/2}$ of −1.36 V, along with a new irreversible oxidation wave at −0.05 V, which are likely to correspond to the reduction of $PhCH_2C_{60}^{2-\bullet}$ and oxidation of $PhCH_2C_{60}^{-}$ as compared to the cyclic voltammogram of $PhCH_2C_{60}$-$C_{60}CH_2Ph$ (Fig. 23), indicating that a small amount of monoanionic 1,2-($PhCH_2$)HC_{60} decomposes into $PhCH_2C_{60}^{-}$ species. Such a decomposition of the monoanionic 1,2-($PhCH_2$)HC_{60} on the bulk electrolysis time scale is verified by the HPLC of the crude product, which was obtained by oxidizing the monoanionic 1,2-($PhCH_2$)HC_{60} back to neutral with a potential at 0 V, where a small amount of $PhCH_2C_{60}$-$C_{60}CH_2Ph$ dimer was obtained.

Figure 27c shows the in situ cyclic voltammogram of the anionic product obtained after 1,2-($PhCH_2$)HC_{60} was electrolyzed at −1.10 V vs SCE, which is suitable for transferring two electrons to 1,2-($PhCH_2$)HC_{60}. As is shown in the cyclic voltammogram, the redox couples corresponding to 1,2-($PhCH_2$)HC_{60} species (−0.54, −0.94, −1.50 V) are completely missing, while well-resolved reversible redox couples appear at −0.93 and −1.36 V, which correspond to the redox processes of anionic singly bonded $PhCH_2C_{60}$ species. The small reduction peak at −0.47 V is due to the first reduction of the $PhCH_2C_{60}$-$C_{60}CH_2Ph$ dimer formed via the oxidation of $PhCH_2C_{60}^-$ at about −0.05 V. Notably, the initial current of the in situ cyclic voltammogram is very close to zero when the voltammetry is started at −1.10 V, indicating that the anionic species in the solution bear two formal negative charges, in equilibrium with the electrolysis potential. The result therefore indicates that the fullerenyl H atom is lost from 1,2-($PhCH_2$)HC_{60} after the molecule receives two electrons with the formation of $PhCH_2C_{60}^{2-\bullet}$.

The doubly reduced 1,2-($PhCH_2$)HC_{60} species was oxidized back to neutral with CPE at the potential of 0 V vs SCE. Figure 27d displays the in situ cyclic voltammogram of the crude reaction mixture after the oxidation is completed, which shows an intense irreversible reduction wave with E_{pc} at −0.47 V and E_{pa} at −0.05 V. Two quasi-reversible redox couples are shown at −0.94 and −1.37 V vs SCE. The cyclic voltammogram is essentially identical to that of $PhCH_2C_{60}$-$C_{60}CH_2Ph$ (Fig. 23), suggesting that 1,2-($PhCH_2$)HC_{60} is converted to $PhCH_2C_{60}$-$C_{60}CH_2Ph$ after transferring two electrons. The formation of $PhCH_2C_{60}$-$C_{60}CH_2Ph$ is confirmed by the HPLC analysis of the reaction mixture.

A reaction mechanism is proposed as shown in Scheme 6. It shows that the fullerenyl hydrogen atom is cleaved from 1,2-($PhCH_2$)HC_{60}^{2-}, which leads to the formation of $PhCH_2C_{60}^{2-\bullet}$. With the subsequent removal of two electrons from $PhCH_2C_{60}^{2-\bullet}$, chiral $PhCH_2C_{60}^{\bullet}$ are then produced as a result of the presence of two possible hexagons containing the mono addend, leading to the formation of both the meso and racemic dimers by the radical couplings of different $PhCH_2C_{60}^{\bullet}$.

$C_{60}QM^{2-}$

C_{60} o-quinodimethane bisadducts ($C_{60}(QM)_2$, also known as $NC_{60}BA$, dihydronaphthyl-based C_{60} bisadducts) are promising electron acceptors for bulk heterojuction (BHJ) organic solar cells (OSCs) [4]. Traditional Diels-Alder approach typically resulted in regioisomers of trans-1, trans-2, trans-3, trans-4, e, cis-3, and cis-2 [40], which were difficult to purify and might consequently obscure the structure-performance study of the organofullerene acceptors. Interestingly, a strong regiocontrol with generation of fewer regioisomers was developed via the electrosynthesis of $C_{60}(QM)_2$ starting with the dianion of $C_{60}QM$ (C_{60} o-quinodimethane monoadduct), where pure regioisomers of cis-2, trans-3, and e $C_{60}(QM)_2$ were obtained, and the structures were solved with single-crystal X-ray diffraction [41].

Scheme 7 shows the electrosynthesis of $C_{60}(QM)_2$ starting with the dianion of $C_{60}QM$. $C_{60}QM^{2-}$ was generated electrochemically by bulk electrolysis of $C_{60}QM$ at a potential of −1.2 V vs SCE in 0.1 M TBAP DMF solution under argon atmosphere at room temperature. The reaction afforded three major products of the

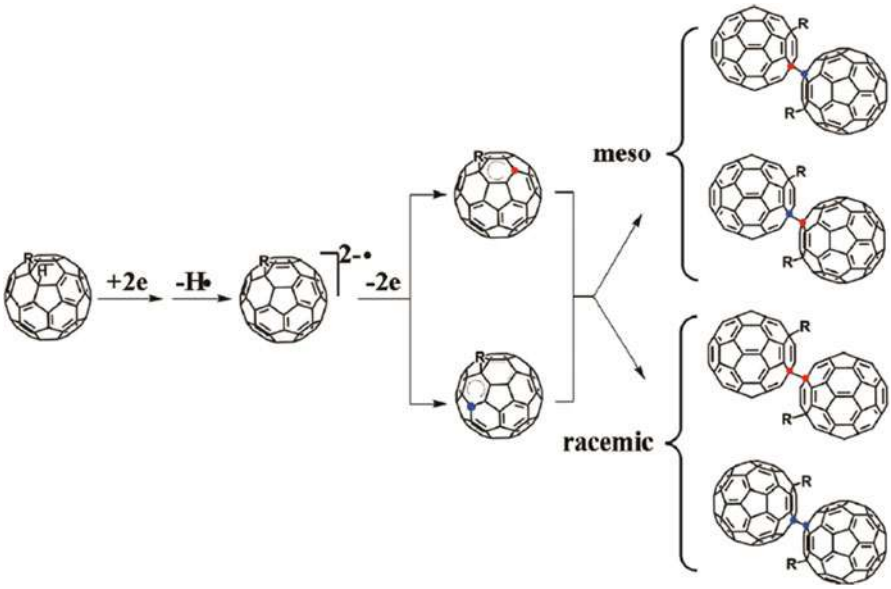

Scheme 6 Proposed reaction mechanism for the formation of meso and racemic $PhCH_2C_{60}$-$C_{60}CH_2Ph$ dimers from doubly reduced1,2-$(PhCH_2)HC_{60}$. (Taken from Ref. [34])

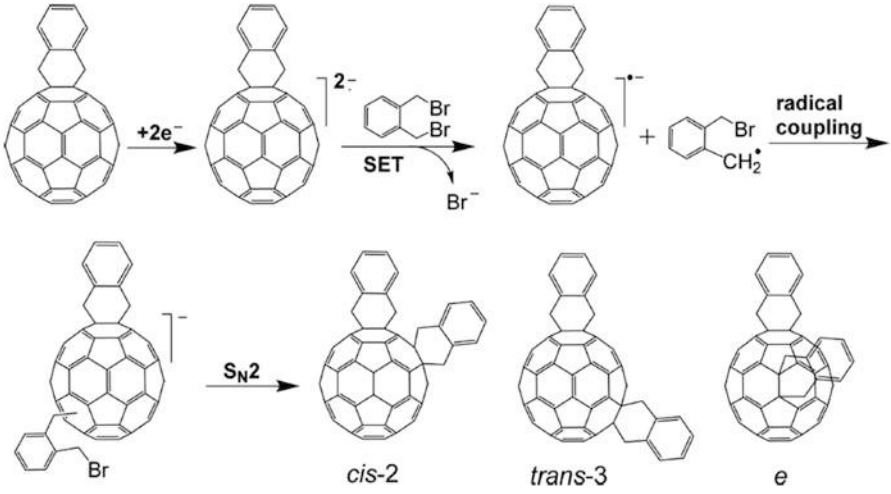

Scheme 7 Formation of $C_{60}(QM)_2$ from the reaction of $C_{60}QM^{2-}$ with α,α′-dibromo-o-xylene. (Taken from Ref. [41])

cis-2, trans-3, and e regioisomers with an isolated yield of 13.8%, 32.4%, and 20.1%, respectively. Compared to the traditional Diels-Alder approach, the electrosynthetic method produces fewer regioisomers and more cis-2 isomer.

Previous work has shown that the reaction of C_{60}^{2-} with alkyl bromide (RBr) undergoes via single-electron transfer (SET) from C_{60}^{2-} to RBr, affording $C_{60}^{\bullet-}$ and alkyl radical ($R^{\bullet}$), which subsequently reacts with each other by radical coupling to form RC_{60}^{-} and eventually produces organo[60]fullerene by S_N2 reaction with another RBr [36]. A similar mechanism is expected for the formation of $C_{60}(QM)_2$ through the reaction of $C_{60}QM^{2-}$ with α,α′-dibromo-o-xylene. The electron spin density distribution in $C_{60}QM^{\bullet-}$ is therefore crucial in understanding the regiocontrol exhibited by the reaction because the reaction with o-$BrCH_2(C_6H_4)CH_2^{\bullet}$ would preferentially occur at the C_{60} carbon atom with a large electron spin density in $C_{60}QM^{\bullet-}$.

Figure 28 illustrates the eight types of [6,6]-double bonds in $C_{60}QM$ and labels the carbon atoms with the larger electron spin density value in the eight types of double bonds in $C_{60}QM^{\bullet-}$ calculated with the Gaussian 09 software package at the B3LYP/6-31G level. The calculation predicts that the carbon atoms at e, cis-2, and trans-3 double bonds bear the largest three electron spin densities of 0.078, 0.070, and 0.052, consistent with the preferential formation of the e, cis-2, and trans-3 $C_{60}(QM)_2$ bisadducts. A relatively large electron spin density of 0.030 is predicted to localize at the cis-1 double bond. However, the formation of the cis-1 $C_{60}(QM)_2$ is unlikely due to the large steric hindrance between the two closely positioned bulky o-quinodimethane addends. The result indicates that the distribution of the electron spin density plays a key role in achieving the regiocontrol of the reaction, demonstrating a promising potential for the electrosynthesis in the regiocontrolled synthesis of fullerene bisadducts.

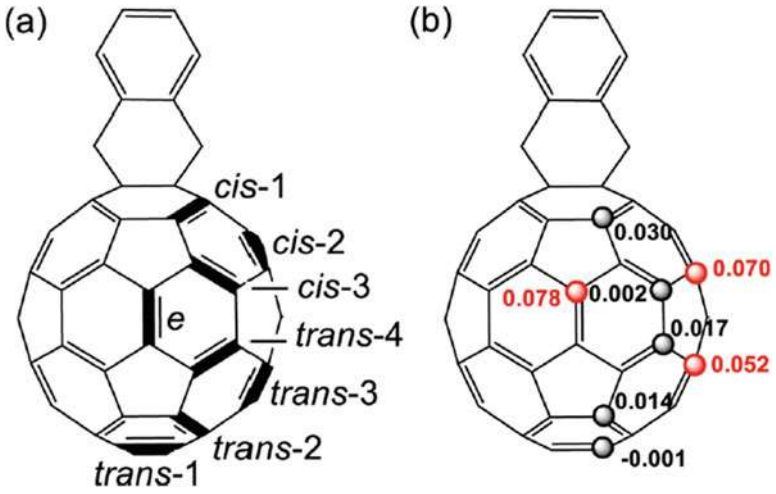

Fig. 28 (**a**) Relative positional relationship of the eight types of [6,6]-double bonds with respect to the existing hydronaphthalene addend in $C_{60}QM$. (**b**) Labeling of the carbon atoms with larger electron spin density in the eight types of double bonds in $C_{60}QM^{\bullet-}$. The largest three values are marked in red. (Taken from Ref. [41])

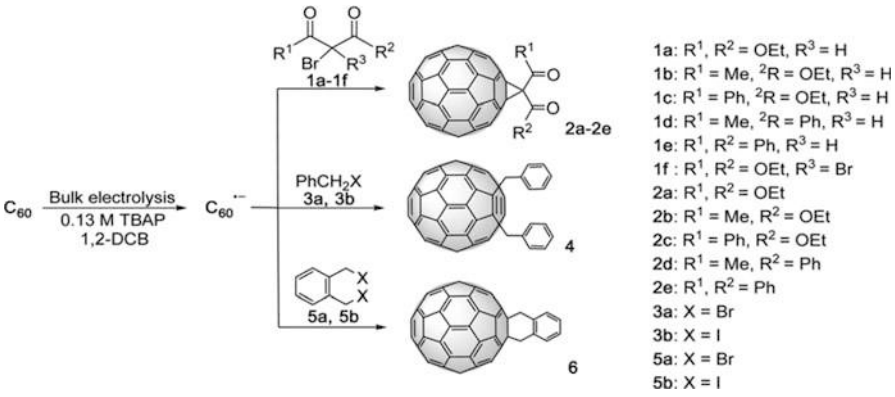

Scheme 8 Reaction of $C_{60}^{\bullet-}$ with alkyl halides. (Taken from Ref. [42])

Reactions of $C_{60}^{\bullet-}$

Interestingly, in addition to C_{60}^{2-}, C_{60} radical monoanion can also react alkyl halides to form C_{60} derivatives. Maeda and co-workers have recently shown the reactions electrochemically generated C_{60} radical monoanion with alkyl halides [43]. Scheme 8 shows the reaction scope of the work.

In a typical reaction, $C_{60}^{\bullet-}$ (1.67×10^{-3} M) was generated by bulk electrolysis in 1,2-dichlorobenzene containing 0.13 M TBAP. Then 10 equiv. of the alkyl halide was added to the solution. The formation of $C_{60}^{\bullet-}$ was confirmed by monitoring the characteristic peaks of $C_{60}^{\bullet-}$ at 1089 nm using the in situ vis-near-infrared (vis-NIR) absorption spectroscopy [43]. The reactions afforded methanofullerene, 1,4-dialkylated C_{60}, and cycloaddition products from the active methylene compounds, benzyl halides, and alkyl dibromides, respectively.

The authors proposed that the reaction proceeds via electron transfer from $C_{60}^{\bullet-}$ to the alkyl halide, and the generated alkyl radical then attacks C_{60}. The key point for the proposed mechanism is that two $C_{60}^{\bullet-}$ molecules are consumed in the formation of the monoadducts, consistent with a high recovery of C_{60} from the reaction, which is different from the reactions of C_{60}^{2-}.

Electrochemically Formation of C_{60} Oxazoline Derivatives: Reactions Involving PhCN

Reactions of C_{60}^{3-}

It is well accepted that the reaction of C_{60}^{2-} can be effectively produced with controlled-potential bulk electrolysis at −1.10 V vs SCE in 0.1 M TBAP PhCN, which would react with benzyl bromide to form 1,4-$(PhCH_2)_2C_{60}$, trace amount of 1,2-$(PhCH_2)_2C_{60}$, 1,2-$HPhCH_2C_{60}$, and [6,6]methanofullerene $C_{61}HPh$ [27]. During the reaction, PhCN is the solvent, and it would not be involved in the reaction. However, during our reaction of electrochemically over-reduced C_{60}^{2-} with $PhCH_2Br$, an unexpected reaction involving PhCN was discovered, where a small

amount of the more reactive C_{60}^{3-} was likely generated and led to the formation of a new type of C_{60} oxazoline derivatives [44].

The procedures for the electrolysis were similar to previous work, with an applied potential of −1.10 V vs SCE in 0.1 M TBAP PhCN solution under an atmosphere of Ar or N_2 [27], except that the reducing potential was continuously applied even after the theoretical number of coulombs required for a full conversion of C_{60} to C_{60}^{2-} had been reached. Notably, an extra irreversible anodic wave at −0.50 V vs SCE appeared in addition to the redox waves of C_{60} in the in situ cyclic voltammogram of the generated anionic C_{60} solution, where the reducing potential was continuously applied after the electrogeneration of C_{60}^{2-} was complete, indicating a reaction involving anionic C_{60} had occurred. The extra irreversible anodic wave became stronger as the reducing potential was applied for a longer time. However, the cyclic voltammogram of the anionic C_{60} solution was completely distorted and featureless of the C_{60} moiety if the solution was kept under the external potential for too long, leading to the formation of more toluene or CS_2 insoluble product. The potentiostat was switched off when the irreversible anodic wave at −0.50 V vs SCE became prominent, and at the same time, the features of C_{60} moiety were retained as shown in Fig. 29, then 10 equiv of $PhCH_2Br$ was added to the solution all at once, and the reaction was allowed to proceed for 40 min with stirring.

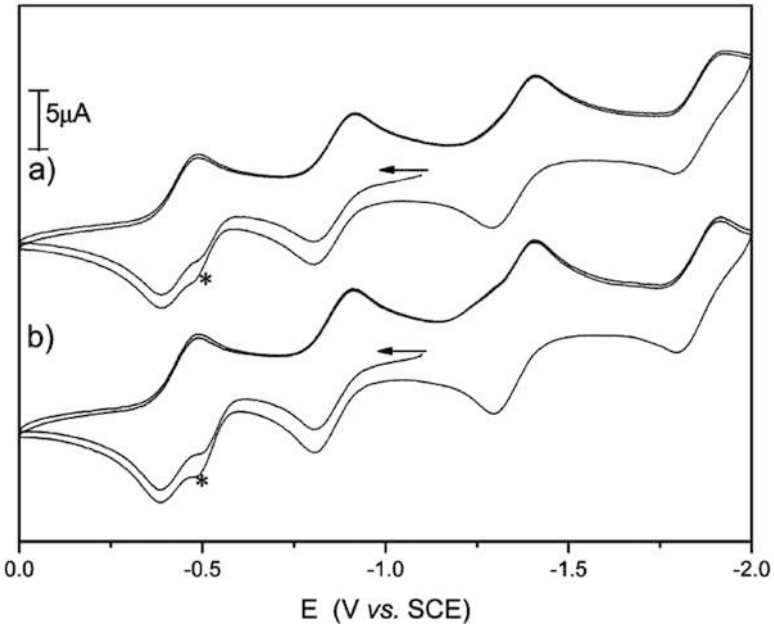

Fig. 29 Cyclic voltammograms of the resulting anionic C_{60} with a coulometric value of slightly more than two electrons per molecule in benzonitrile solution containing 0.1 M TBAP under (**a**) Ar and (**b**) N_2. The asterisks denote the extra irreversible anodic wave at −0.50 V vs SCE. (Taken from Ref. [44])

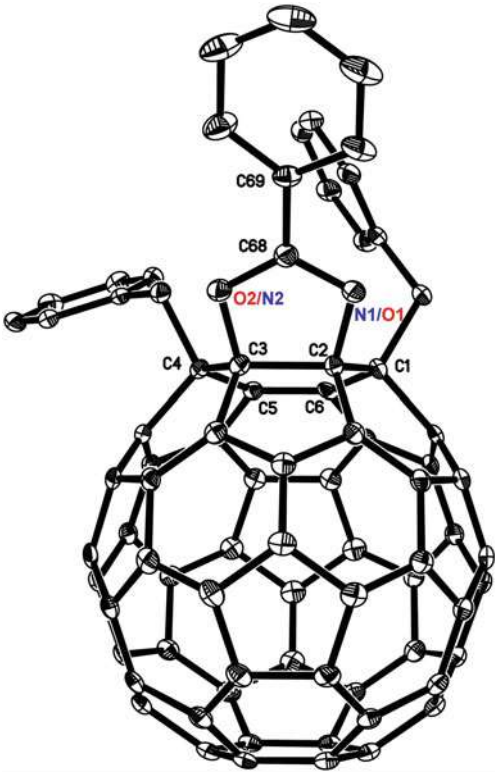

Fig. 30 ORTEP diagram for one 1,4-dibenzyl-2,3-cyclic phenylimidate C_{60} (**6**) molecule with 20% thermal ellipsoids. Hydrogen atoms and CS_2 molecule were omitted for clarity. (Taken from Ref. [44])

Unlike previously reported result of reactions between C_{60}^{2-} and benzyl bromide, where the only major product is 1,4-$(PhCH_2)_2C_{60}$ [27], 1,4-dibenzyl-2,3-cyclic phenylimidate C_{60} (**6**), a C_{60} oxazoline benzyl derivative, is found to be produced along with 1,4-$(PhCH_2)_2C_{60}$ as the major product. The structure of **6** was resolved with the X-ray single-crystal diffraction analysis. Figure 30 shows the X-ray single-crystal structure of **6**. It shows that two benzyl groups are bonded to C_{60} at C1 and C4, respectively, while an oxazoline heterocycle is bonded to C_{60} via two heteroatoms at C2 and C3 positions. It is interesting to note the molecule of the product actually consists of a substructure of benzonitrile, indicating that the solvent, benzonitrile, takes part in the reaction.

In order to have a better understanding of the reaction, experiments were performed where the procedures were exactly the same as those for the generation of compound **6**, except no benzyl bromide was added to the anionic C_{60} benzonitrile solution. The solution was then oxidized back to neutral electrochemically. A new product characterized as [6,6] cyclic phenylimidate C_{60} (**7**) was obtained and fully characterized with HRMS, ^1H and ^{13}C NMR, and UV-vis spectroscopies. Figure 31 shows the illustrated structure of **7**.

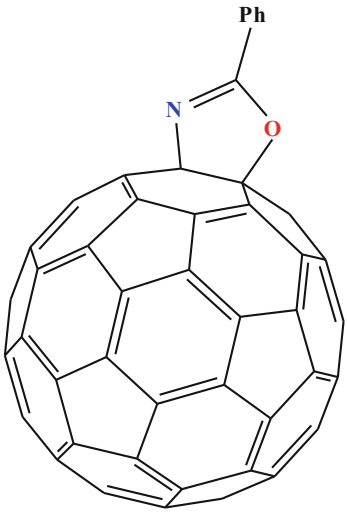

Fig. 31 Illustrated structure of [6,6] cyclic phenylimidate C_{60} (7). (Taken from Ref. [44]

Control experiments with neutral, monoanionic, dianionic, and trianionic C_{60} were carried out to probe further into the reaction. As for the reaction of monoanionic C_{60}, it was generated with a reducing potential of -0.70 V vs SCE, and the reducing potential was continuously applied after C_{60}^{-} was fully generated, and the total reaction time was also 3 h. For the reaction of the dianionic C_{60}, the reduction was stopped once the number of electrons reached 90% of the theoretical number required for the conversion to C_{60}^{2-}. As for trianionic C_{60}, it was generated electrochemically with a reducing potential of −1.60 V vs SCE in benzonitrile, and the electrolysis was terminated once the theoretical number of coulombs required for the conversion of C_{60} to C_{60}^{3-} was reached. Notably, there was no reaction product for the neutral, monoanionic, and dianionic C_{60} benzonitrile solution. While the cyclic voltammogram of the resulting C_{60}^{3-} is very similar to that of the anionic C_{60} benzonitrile solution shown in Fig. 29, with the appearance of the irreversible anodic peak at around −0.50 V vs SCE, a significant amount of compound **7** was obtained from the C_{60}^{3-} benzonitrile solution with an isolation yield much higher than that obtained from the over-reduced dianionic C_{60} solution, indicating that the more reactive C_{60}^{3-} is likely the real reactive species for the observed reaction in the anionic C_{60} benzonitrile solution.

Notably, previous work on the ESR studies of the C_{60} monoanion suggests the possibility that a significant amount of higher C_{60} anions can be generated at a less negative reducing potential [45]. It has been shown that there is often a narrow spike in addition to the broad line width signal present in the ESR spectrum of the C_{60} monoanion. The narrow spike is assigned to a trace amount of anionic C_{60} derivatives formed by the reaction of higher C_{60} anions, indicating that higher C_{60} anions can be generated at a much less negative potential suitable for generating C_{60} monoanion [45]. It is therefore possible that a significant amount of C_{60}^{3-} can be

generated when more than a theoretical number of reducing charges are transferred, even though the reducing potential is less negative than the half-wave potential of C_{60}^{2-}/C_{60}^{3-} (−1.32 V vs SCE), especially when C_{60}^{3-} could be consumed in the reaction.

There are two questions remaining for the reaction. First, a careful examination shows that the oxazoline heterocycle is located at the [6,6]-bond (between two six-membered rings) of C_{60} in **7**, while it is located at the [5,6]-bond (between a six-membered ring and a five-membered ring) of C_{60} in **6** upon reductive benzylation, demonstrating a rearrangement of the oxazoline heterocycle upon reduction. The question is which heteroatom, N or O, is rearranged? Second, what is the source of O in the oxazolino heterocycle?

Reactions of C_{60} Oxazoline Dianion with $PhCH_2Br$ and $PhCD_2Br$: Electrochemical and H/D-Labeling Study of Oxazolino[60]Fullerene Rearrangement

The question regarding the reductive rearrangement of the oxazoline heterocycle was studied by cyclic voltammetry and H/D labeling reaction [6]. Figure 32 shows the cyclic voltammogram of neutral and dianionic **7** in 0.1 M TBAP PhCN solution.

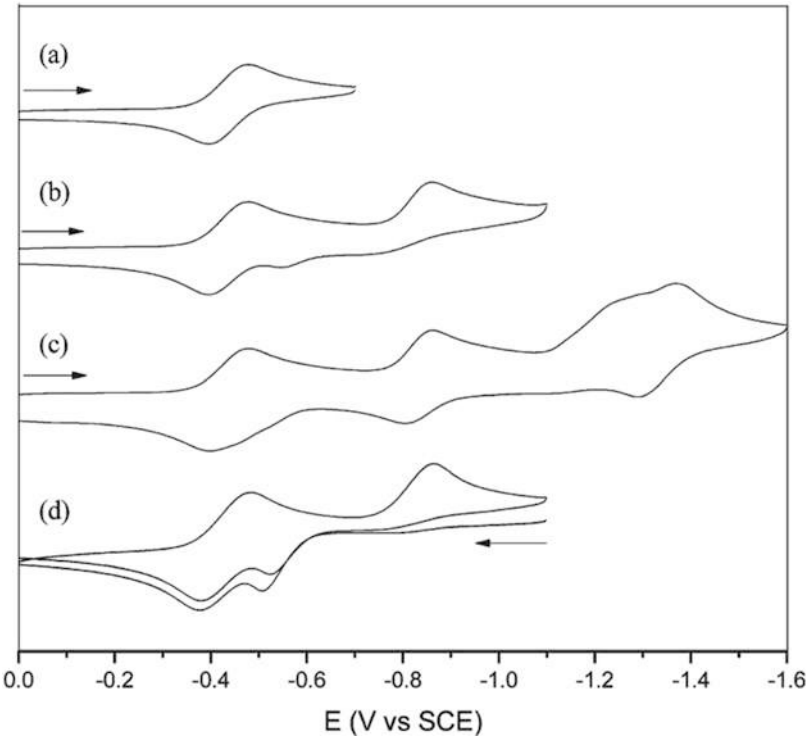

Fig. 32 Cyclic voltammograms of **7** in benzonitrile containing 0.1 M TBAP at a scan rate of 0.1 V/s. (**a**–**c**) are for neutral **7**, while (**d**) is for the in situ generated dianionic **7**. (Taken from Ref. [6])

As for the neutral compound, the first redox is a quasi-reversible one-electron transfer process with $E_{1/2}$ of −0.44 V vs SCE, indicating that the monoanion is stable with the electron being transferred between the fullerene cage and the electrode. As for the second reduction, the compound is cleanly reduced with an E_p^{red} at −0.86 V. However, the anodic peak corresponding to the oxidation of this dianionic species is completely missing in the expected potential region, which is usually about 60–100 mV more positive with respect to the E_p^{red}. Instead, a small anodic peak appears around −0.54 V, followed by a reversible anodic peak corresponding to the oxidation of monoanionic **7** at −0.39 V. It indicates that the heterocycle is still on the C_{60} cage of dianionic **7**, but a heterolytic cleavage of one C_{60}-X (X = O or N) bond likely occurs, with one electron at the C_{60} cage and the other electron at the heteroatom. Consequently, dianionic **7** will not be oxidized at a potential suitable for removing one electron from the C_{60} core having two electrons, and the oxidation peak around −0.54 V should correspond to the electron removal from the addend. As the potential is further scanned to the third reduction, multiple reduction waves appear in the region, indicating that the remaining C_{60}-Y (Y = O or N) bond in dianionic **7** is further cleaved, and the heterocycle is removed completely to afford C_{60}.

Figure 32d shows the cyclic voltammogram of the in situ generated dianionic **7**, which confirms that the dianionic **7** is stable without decomposition to C_{60} under the experimental conditions. Compared with Fig. 32b, the anodic peak around −0.53 V is much more prominent, and the height of current is almost identical to that of the second reduction, indicating that it is indeed the oxidation process corresponding to the one reduced at −0.86 V. Notably, this peak was used previously as an indicator to monitor the formation of C_{60} oxazolines even though the origin of it was not fully understood at that time [44]. Due to the unusual positive shift of this wave potential, it indicates that the oxidation likely originates from a process where the electron is taken away from the hetero addend directly rather than from the C_{60} cage. In addition, judging by the reversibility of the subsequent oxidation wave ($\mathbf{7}^-/\mathbf{7}$), it indicates that compound **7** is fully recovered at the stage of $\mathbf{7}^-$, i.e., the C_{60}-X bond is formed upon giving up an electron from $\mathbf{7}^{2-}$.

Previous work has shown that the reaction of C_{60}^{2-} with benzyl bromide proceeds via a stepwise manner [36]; a stepwise addition of $PhCH_2Br$ and $PhCD_2Br$ to dianionic **7** was designed as shown in Scheme 9 in order to differentiate the benzyl groups added in the first and second steps, where X and Y denote the heteroatoms. Two different routes in which $PhCH_2Br$ and $PhCD_2Br$ were added in opposite order were employed to obtain a complete picture of the reaction. Equivalent amounts of $PhCH_2Br$ and $PhCD_2Br$ (molar ratio of $PhCH_2Br$ or $PhCD_2Br$: **7** = 5:1) were used to eliminate the concentration effect, and the chemicals were added separately with a time interval of 3 min. The products obtained from route A and route B are designated as **6A** and **6B**, respectively.

Figure 33 shows the HMBC NMR spectra of **6A** and **6B**. Two AB quartets centered at 4.10 ppm (AB_q, $\Delta\nu_{AB}$ = 324 Hz, J_{AB} = 13.2 Hz) and 4.06 ppm (AB_q, $\Delta\nu_{AB}$ = 258 Hz, J_{AB} = 13.2 Hz) are shown in the ^{1}H NMR. As expected, the intensity of one of the two AB quartets is decreased due to the presence of excessive $PhCD_2$, which facilitates the assignment of the correlated doublets within each

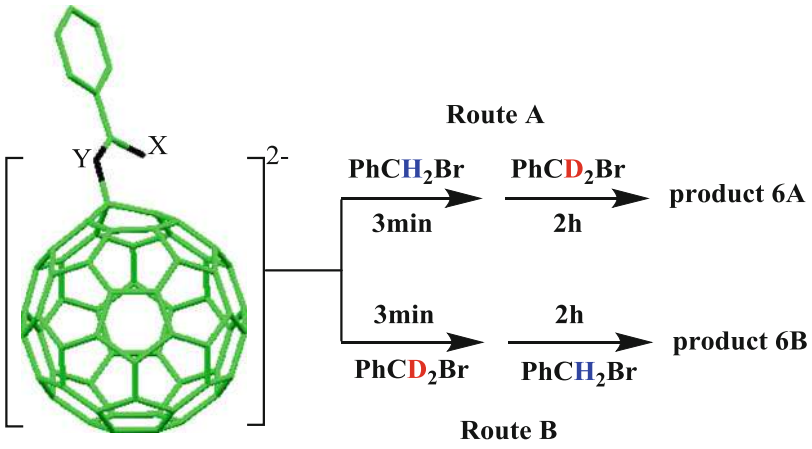

Scheme 9 Stepwise reaction of $PhCH_2Br$ and $PhCD_2Br$ with dianionic **7**. (Taken from Ref. [6])

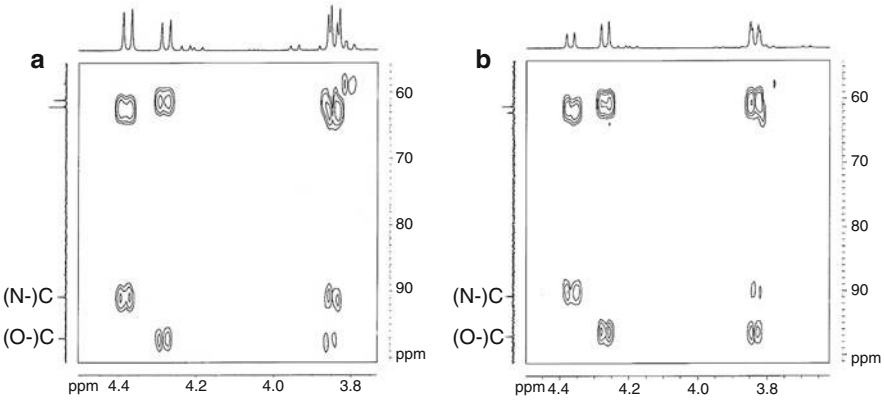

Fig. 33 Expanded HMBC NMR spectrum of product (**a**) **6A** and (**b**) **6B** in CS_2 with DMSO-d_6 as the external lock. (Taken from Ref. [6])

quartet. For **6A**, the AB quartet in the lower field has shown a higher intensity, implying that the corresponding benzyls should bear more methylene hydrogen atoms, indicating that this quartet is likely to originate from the benzyls added in the first step, since $PhCH_2Br$ was used in the first step. While the AB quartet in the upper field shows a reduced intensity, and it is therefore likely to originate from the benzyls that were added to dianionic **7** during the second step. On the contrary, the intensity of the two AB quartets is reversed, which is in good agreement with the reversed order of the addition. The results verify that the AB quartet in the lower field is due to the methylene protons of benzyls added during the first step, while the AB quartet in the upper field corresponds to the methylene protons of benzyls added during the second step.

Another important information from the NMR characterization is that the AB quartet corresponding to the methylene protons of the first-step addition benzyls (higher intensity in **6A**, lower intensity in **6B**) is correlated via the $^3J_{CH}$ couplings with the C_{60} sp^3 carbon atoms at 90.8 ppm, which is the carbon atom bonded to the nitrogen atom. In contrast, the AB quartet corresponding to the methylene protons of the benzyls involved in the second-step addition (lower intensity in **6A**, higher intensity in **6B**) is correlated via the $^3J_{CH}$ couplings with the C_{60} sp^3 carbon atoms at 97.1 ppm, which is the carbon atom bonded to the oxygen atom. The result shows explicitly that the benzyl added during the first step is positioned next to the C_{60}-N bond, while the benzyl added during the second step is positioned next to the C_{60}-O bond.

Previous work has shown that for an RC_{60}^- intermediate, the subsequent addition would typically take either 1,2- or 1,4-addition relative to the existing addend depending on the steric hindrance between the addends. For the case of dianionic **7**, a 1,4-addition of the benzyl relative to the C_{60}-Y bond is unlikely judging from the structure of **6**, as no benzyl group is positioned at the para-carbon relative to the C_{60}-N or C_{60}-O bond. Consequently, the first added benzyl group could only be added at the ortho-carbon atom with respect to the C_{60}-Y bond, which is in fact the C_{60}-N bond according to the HMBC NMR result. The result therefore shows unambiguously that the C_{60}-O bond is cleaved in the dianion of **7** (C_{60} oxazoline), while the C_{60}-N remains bonding.

The Origin of the O Atom in C_{60} Oxazoline: Reactions of C_{60}^{2-} with O_2 and PhCN

The reaction of C_{60}^{2-} with O_2 in PhCN solution was examined in order to have a better understanding of the reaction for the formation of C_{60} oxazoline [46]. Figure 34 shows the cyclic voltammograms of the in situ generated C_{60} dianion in 0.1 M TBAP PhCN solution under argon and with the addition of different amount of air along with the flow of argon. The most notable feature is the deformation of the cyclic voltammograms (CVs) of C_{60}^{2-} after addition of air (oxygen), indicating a reaction involving C_{60}^{2-} and O_2 occurred. An irreversible anodic wave appeared at −0.53 V vs SCE, which was observed during the formation of C_{60} oxazoline [44] and was assigned to the singly bonded dianionic oxazolino C_{60} intermediate [6]. The irreversible anodic wave kept increasing as more air was introduced. However, the overall yield of the heterocyclic product might decrease due to the formation of more polymerized materials.

Notably, the potentiostat was switched off once the theoretical number of electrons required for reducing C_{60} to C_{60}^{2-} was achieved to avoid the production of C_{60}^{3-}. The generated C_{60}^{2-} was exposed to oxygen by injecting 100 mL of air along with the flow of Ar. The color of the solution changed immediately from red to green. C_{60} oxazoline **7** was produced if the reaction mixture was oxidized electrochemically back to neutral with a potential of 0 V vs SCE, while dibenzyl C_{60} oxazoline **6** was produced if the reaction mixture was quenched with benzyl bromide. A reaction mechanism for the formation of C_{60} oxazoline derivatives is proposed and is shown in Scheme 10, where the formation of C_{60}^--O^- intermediate

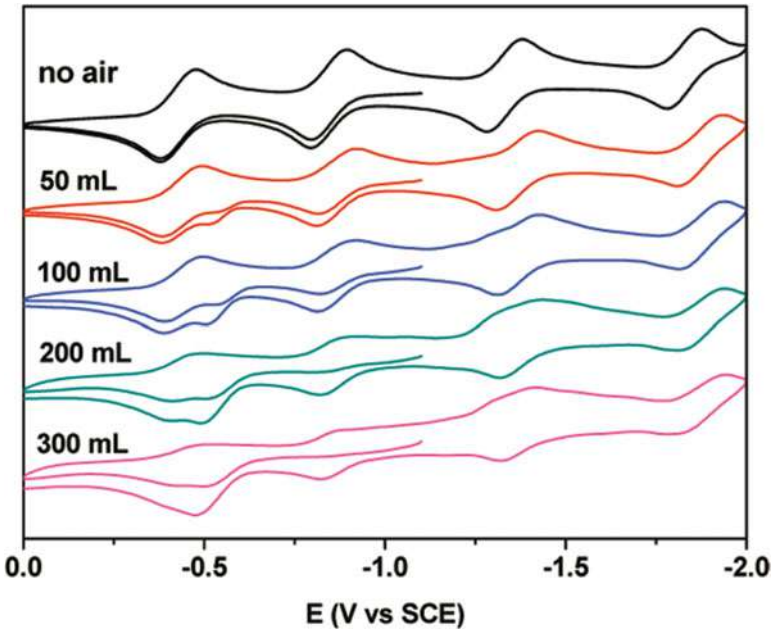

Fig. 34 In situ CVs of 200 mg of dianionic C_{60} in 150 mL of PhCN solution containing 0.1 M TBAP with the addition of 0, 50, 100, 200, and 300 mL of air along with the flow of argon. (Taken from Ref. [46])

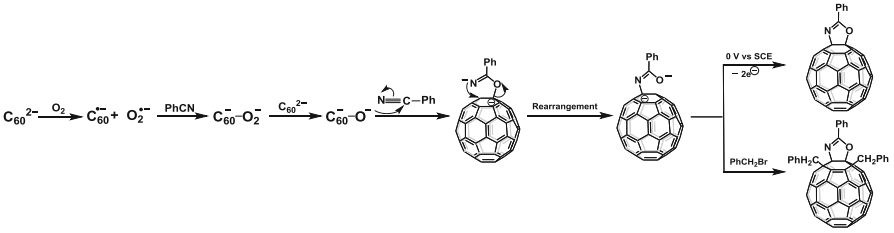

Scheme 10 Proposed mechanism for the aerobic oxidations of C_{60}^{2-} in the presence of PhCN. (Taken from Ref. [46] with slight modification)

is the key for the reaction. Notably, a rearrangement of the oxazolino heterocycle occurs in the dianionic intermediate, where the two electrons are distributed in C_{60} and oxygen atom, respectively, as previous work reveals [6].

The result therefore shows that C_{60}^{2-} can react with O_2 to form C_{60}^{-}-O^{-} intermediate, which may further react with PhCN and for the C_{60} oxazoline compound, demonstrating that the origin of the oxygen atom in C_{60} oxazoline compounds is from O_2. Notably, previous work has shown that the more reactive C_{60}^{3-} is required for the formation of C_{60} oxazoline under inert atmosphere [44], and this is

because there is only trace amount of O_2 available in the system, and it demonstrates that a complete removal of O_2 is difficult even under strict degassing conditions.

Electrochemical Synthesis of C_{70} Derivatives

Reactions of C_{70}^{2-} with Benzyl Bromides

The initial study of C_{70}^{2-} and benzyl bromide showed that two isomers of $(PhCH_2)_2C_{70}$ were obtained [47]. However, the structural assignment of the two isomers was ambiguous at that time due to the difficulty in separating the isomers. The reactions of C_{70}^{2-} with a series of $ArCH_2Br$ (Ar = Ph, o-, m-, p-BrC_6H_4) were revisited [48], where C_{70}^{2-} was generated with CPE at −1.10 V vs SCE in freshly distilled PhCN solution containing 0.1 M TBAP under an argon atmosphere. The potentiostat was switched off after the electrolytic formation of C_{70}^{2-} was complete, and a 50-fold excess of $ArCH_2Br$ was added into the solution under inert atmosphere. The reaction was allowed to proceed for about 3 h with stirring at 50 °C. Two types of regioisomers were obtained as the major products. Single-crystal structures of the two types of isomers were obtained, which showed that the two types of isomers were the 2,5-$(ArCH_2)_2C_{70}$ and 7,23-$(ArCH_2)_2C_{70}$ [48]. Figure 35 shows the illustrated structures of 2,5-$(ArCH_2)_2C_{70}$ and 7,23-$(ArCH_2)_2C_{70}$.

The reaction of C_{70}^{2-} with $PhCH_2Br$ was also carried out in 0.1 M TBAP DMF solution [33], where protonation is more readily to occur [37]. C_{70}^{2-} was effectively generated with CPE at −1.10 V vs SCE in 0.1 M TBAP DMF solution under an argon atmosphere at about 15 °C. The potentiostat was switched off after the electrolytic formation of C_{70}^{2-} was complete, and a 30-fold excess of $PhCH_2Br$ was added to the solution under inert atmosphere. The reaction was allowed to proceed for about 4 h with stirring. Products of 7,23-$(PhCH_2)_2C_{70}$, 7,23-$(PhCH_2)HC_{70}$, 1-$PhCH_2$-2-HC_{70}, 5,6-$(PhCH_2)HC_{70}$, and 1-H-2-$PhCH_2C_{70}$ were obtained, where the 1-H-2-$PhCH_2C_{70}$ and 7,23-$(PhCH_2)HC_{70}$ are the major products.

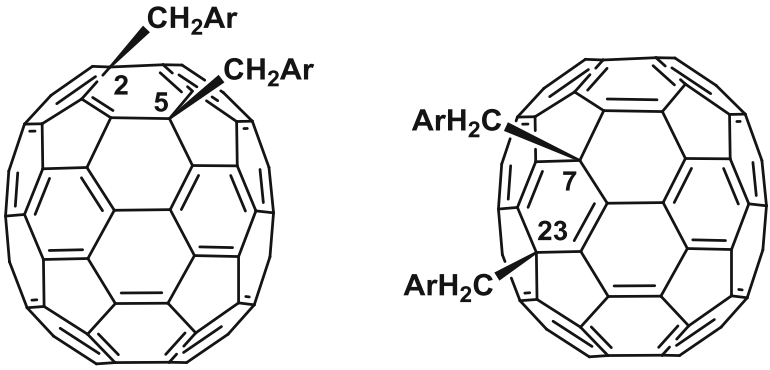

Fig. 35 Illustrated structures of 2,5-$(ArCH_2)_2C_{70}$ and 7,23-$(ArCH_2)_2C_{70}$

Figure 36 shows the illustrated structures of 7,23-$(PhCH_2)_2C_{70}$, 7,23-$(PhCH_2)HC_{70}$, 1-$PhCH_2$-2-HC_{70}, 5,6-$(PhCH_2)HC_{70}$, and 1-H-2-$PhCH_2C_{70}$.

The reaction of C_{70}^{2-} with α,α′-dibromo-o-xylene was also examined [31]. C_{70} was electrolyzed at −1.00 V vs SCE in PhCN solution containing 0.1 M TBAP under an argon atmosphere. The potentiostat was switched off after the electrolytic formation of C_{70}^{2-} was completed, and a 10-fold excess of α,α′-dibromo-o-xylene was added to the solution under argon. The reaction was allowed to proceed for approximately 1 h with stirring. For comparison, a control experiment of neutral C_{70} with α,α′-dibromo-o-xylene was performed at 160 °C in refluxing o-DCB solution, following reported procedures [49].

Figure 37 shows the HPLC chromatograms of the reaction products obtained from the reaction of C_{70}^{2-} and neutral C_{70}. Impressively, the reaction of C_{70}^{2-} produced a large amount of the δ-C_{70}QM, which was comparable to the amount of both α- and β-C_{70}QM. In contrast, very tiny amount of the δ-C_{70}QM was obtained from the reaction of neutral C_{70}, while the major products are the α- and β-C_{70}QM (refer to Fig. 14 for the structures of the α-, β- and δ-C_{70}QM).

Typically, the polar region of C_{70} is more reactive compared to the equatorial region due to the more strain experienced by the carbon atoms in the polar region.

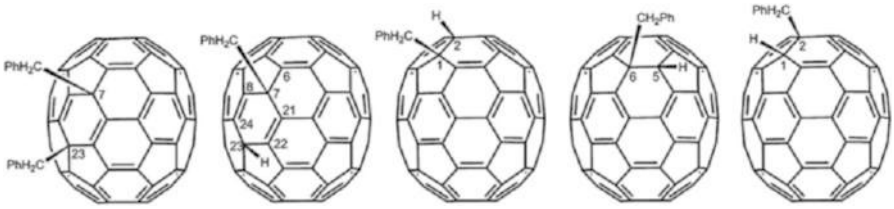

Fig. 36 Illustrated structures of 7,23-$(PhCH_2)_2C_{70}$, 7,23-$(PhCH_2)HC_{70}$, 1-$PhCH_2$-2-HC_{70}, 5,6-$(PhCH_2)HC_{70}$, and 1-H-2-$PhCH_2C_{70}$

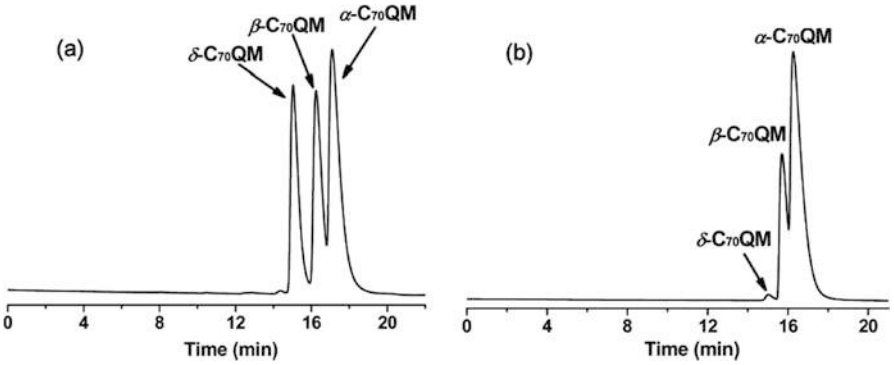

Fig. 37 HPLC traces of the C_{70}QM mixture obtained from the reaction of α,α′-dibromo-o-xylene with (**a**) C_{70}^{2-} and (**b**) neutral C_{70}. Flow rate = 2.0 mL/min; wavelength = 380 nm. (Taken from Ref. [31])

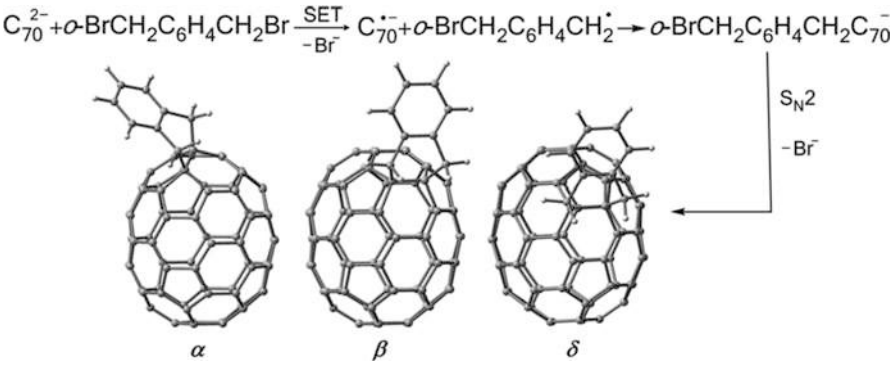

Scheme 11 Proposed mechanism for the reaction of C_{70}^{2-} with α,α′-dibromo-o-xylene. (Taken from Ref. [31])

Consequently, the α- and β-C_{70} adducts are conventional products, while the δ-C_{70} adducts are rarely produced from the reaction of neutral C_{70} [50]. However, it is noteworthy that for all the electrosynthesis involving C_{70}^{2-}, the reactions afford significant amount of equatorial products such as the 7,23-adducts and δ-adduct formed, indicating that the carbon atoms in the equatorial region of C_{70} are activated upon reduction.

The reactions of C_{60} and C_{70} dianions with alkyl halides (RX) are initiated by single-electron transfer (SET) from C_{2n}^{2-} (n = 30 or 35) to RX, generating fullerene monoanion and alkyl radicals ($C_{2n}^{\bullet-}$ and $R^{\bullet}$), which would couple with each other to produce the RC_{2n}^- intermediate, followed by S_N2 reaction with another RX to afford the final product [36, 47]. Scheme 11 illustrates the possible mechanism for the reaction of C_{70}^{2-} with α,α′-dibromo-o-xylene. Consequently, the electron spin density distribution in $C_{70}^{\bullet-}$ would be critical in determining the regioselectivity of the reaction as it would couple with the o-$BrCH_2C_6H_4CH_2^{\bullet}$ to form the reaction intermediate.

Computational calculations were performed to rationalize the exhibited regioselectivity for the reactions of C_{70}^{2-}. The Mulliken spin density distribution in $C_{70}^{\bullet-}$ was calculated with Gaussian09 at the B3LYP/6-311G(d) level, where the highest spin densities are 0.078, 0.007, 0.071, 0.104, and −0.045 for the a, b, c, d, and e-carbons (see Fig. 38 for the a, b, c, d, and e carbons and α, β, γ, and δ bonds of C_{70}), respectively, suggesting that large spin densities are located at the types of d-, a-, and c-carbons. Computational calculations (B3LYP/6-31G) on o-$BrCH_2C_6H_4CH_2C_{70}^-$ predicted energy levels of 0.0, 6.6, 4.1, 3.2, and 19.2 kcal/mol for the a-, b-, c-, d-, and e-bound intermediates. The result predicates that the typically inert d-carbons are activated in $C_{70}^{\bullet-}$ due to the location of large spin density and stability of the d-bound intermediate. Consequently, the d-, a-, and c-bound o-$BrCH_2C_6H_4CH_2C_{70}^-$ are formed preferentially, which would result in the δ-, α-, and β-isomers by subsequent intramolecular S_N2 reaction via the ortho-addition manner. In contrast, the b- and e-bound intermediates are unlikely to form due to either the unfavorable spin density distribution at b-carbons or the instability of the e-bound intermediate. It is noteworthy

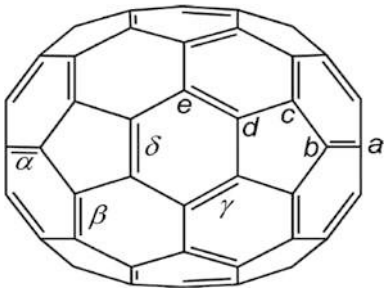

Fig. 38 Schematic illustration of C_{70}. Carbon atoms of the five different types in C_{70} are assigned conventionally as a, b, c, d, and e. Double bonds of four different types are assigned conventionally as α, β, γ, and δ. (Taken from Ref. [31])

that the d-bound o-$BrCH_2C_6H_4CH_2C_{70}^-$ could in principle result in both δ- and γ-isomers. However, calculations at the B3LYP/6-31G level predicted energy levels of 0.0, 2.9, 9.0, and 19.5 kcal/mol for the α-, β-, δ-, and γ-isomers, respectively, implying that the γ-isomer is unlikely to be stable, rationalizing the unavailability of this isomer.

C_{70} Oxazolines

On the basis of C_{60}^{2-}, oxazolination of C_{70}^{2-} was achieved via the aerobic oxidation in the presence of PhCN [51]. Typically, C_{70}^{2-} was generated by controlled-potential bulk electrolysis (−1.00 V vs SCE) in PhCN containing 0.1 M TBAP. C_{70} oxazoline (**8**) was then obtained via introduction of air into the system, followed by I_2 oxidation of anionic solution. Compound **9**, a cis-1 C_{70} derivative with respect to the apical pentagon, is obtained from the benzylation of dianionic **8**, which can be generated either in situ via the aerobic oxidation of C_{70}^{2-} in PhCN or via the controlled-potential bulk electrolysis of **8** at −1.00 V vs SCE. Figure 39 shows the structure illustration of **8** and the single-crystal structure of **9**.

A reaction mechanism is proposed for the formation **8** and **9** and is shown in Scheme 12. Notably, since the apical carbon is the most reactive carbon in C_{70} [50], during the formation of **8**, the O atom would be preferentially at C2 (apical carbon) and consequently form the C2-bound intermediate. However, due to retaining of the C_{2n}-N ($n = 30$ or 35) bond in the dianionic intermediate [6, 51], a rearrangement of N and O atoms would occur for the dianionic intermediate, where the N atom would be selectively positioned at the apical carbon atom of C_{70}. As for the formation of **9**, it is noteworthy that the O atom is still the one that rearranged during the reductive benzylation reaction.

Figure 40 shows the cyclic voltammograms of **9** recorded in PhCN containing 0.1 M TBAP with a scan rate of 0.1 V/s. The compound exhibits three quasi-reversible redox processes with $E_{1/2}$ at −0.56, −0.98, and −1.38 V vs SCE, which are negatively shifted by about 80−140 mV with respect to those of C_{70} (−0.45, −0.85, and −1.30 V vs SCE) measured under the same conditions, probably due to the cleavage of the conjugated π-electrons in the polar region of C_{70}.

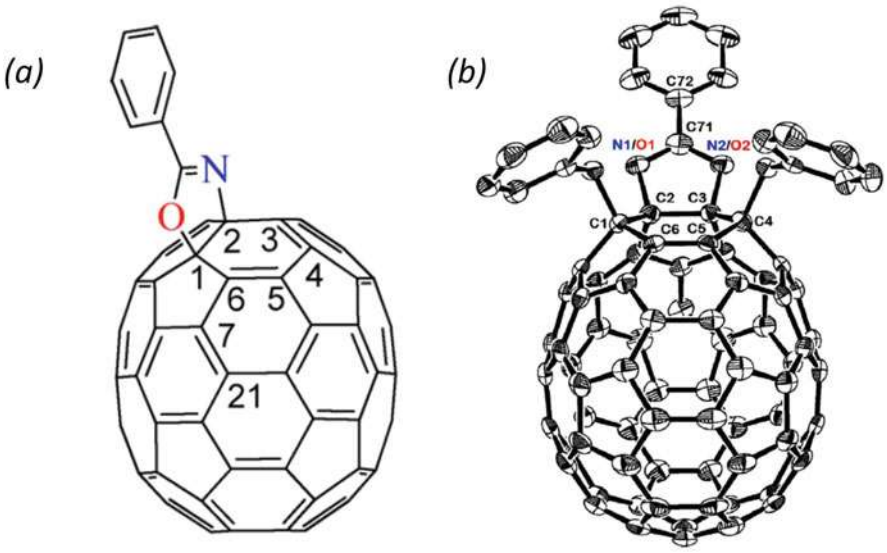

Fig. 39 Structure illustration of (**a**) C_{70} oxazoline compound **8** and (**b**) single-crystal structure of the cis-1 dibenzyl C_{70} oxazoline compound **9**. (Taken from Ref. [51])

Heterocyclic Compounds

The reductive rearrangement of heterocycles on fullerene cages is not only observed for the oxazolines but also observed for a variety of heterocycles. Two more examples of imidazolines and indolines are shown below.

Imidazolines

Scheme 13 shows the reductive benzylation of C_{60} imidazoline. After accepting two electrons, the C_{60} imidazoline undergoes rearrangement with the cleavage of amino N-C_{70} bond [35]. Due to the bulky size of the imidazoline heterocycle, the major product has the 1,2,3,16-configuration with the first addend having the ortho-addition and the second addend having the para-addition (**11**), while the product with the cis-1 configuration (**12**) similar to 1,4-dibenzyl-2,3-cyclic phenylimidate C_{60} (**6**) is a minor product. In addition, another 1,2,3,16-compound (**13**) with the first addend having the para-addition and the second addend having the ortho-addition is obtained as a minor product.

Indolines

Upon accepting two electrons, C_{60} indolines also undergo rearrangement with the cleavage of the C_{60}-N bond and react with benzyl bromide [52]. Scheme 14 shows the reactions of electrochemically generated dianion of C_{60} indoline with benzyl bromide. Due to bulky size of the indoline, the first addend takes the 1,4-addition, while the second addend takes the 1,2-addition, and results in adducts with the 1,2,3,16-configuration.

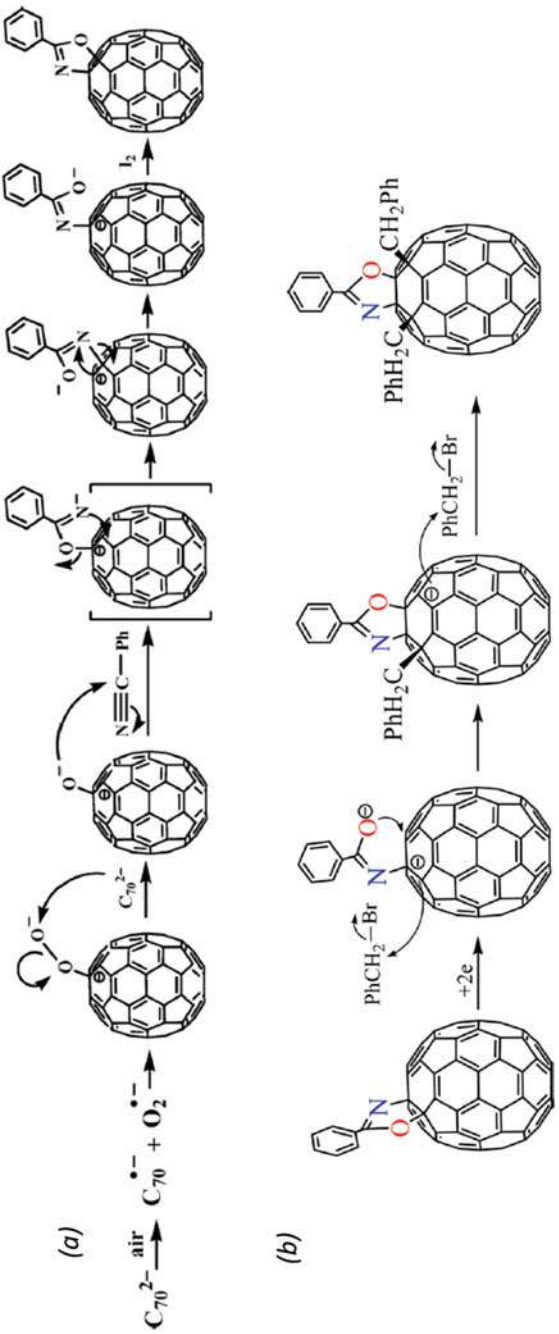

Scheme 12 Proposed reaction mechanisms for (**a**) formation of **8** and (**b**) formation of **9**. (Taken from Ref. [51])

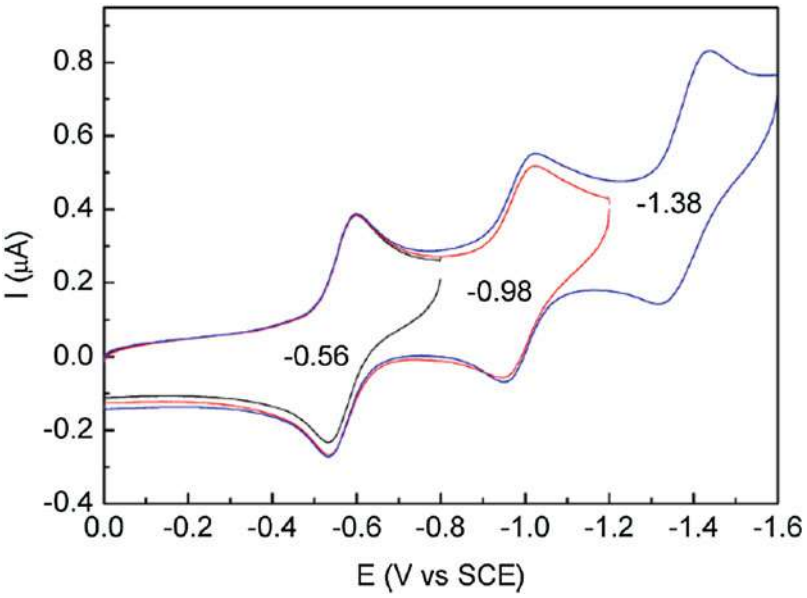

Fig. 40 Cyclic voltammograms of compound **9** in PhCN containing 0.1 M TBAP with a scan rate of 0.1 V/s. (Taken from Ref. [51])

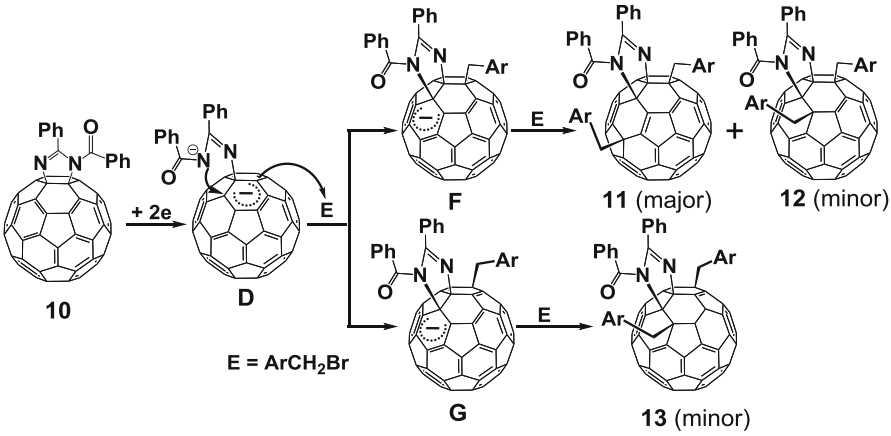

Scheme 13 Proposed mechanism for the reactions of C_{60} imidazoline dianion with $ArCH_2Br$ (Ar = Ph and o-BrPh). (Taken from Ref. [35] with slight modification)

1,4,9-$R_3C_{60}^-$ Stable Intermediate

Previous work on multiple nucleophilic additions to C_{60} has proposed a stable 10π indenyl $R_3C_{60}^-$ intermediate with the 1,4,15-configuration [39], which is important in rationalizing the regioselectivity for C_{60} multiple additions.

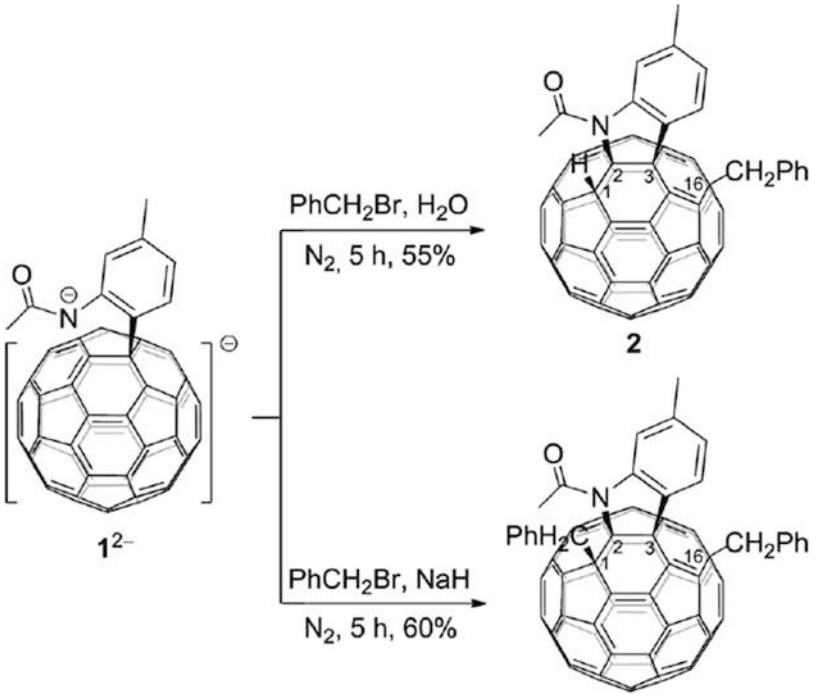

Scheme 14 Reaction of the dianion of C_{60} indoline with benzyl bromide under different reaction conditions. (Taken from Ref. [52])

We have found that upon reduction, singly bonded 1,2,4,15-C_{60} dimers with an oxazoline or imidazoline heterocycle dissociate into monoanionic 1,2,4-C_{60} intermediates, which surprisingly leads to the formation of 1,2,3,16-C_{60} rather than 1,2,4,15-C_{60} adducts of the original configuration by further benzylation, even though the analogue of dibenzylated C_{60} oxazoline with a 1,2,4,15-configuration is stable and has been obtained [53]. Scheme 15 illustrates the reductive benzylation reactions of the 1,2,4,15-C_{60} dimers with an oxazoline or imidazoline heterocycle.

The result indicates that the 1,2,4-$R_3C_{60}^-$ intermediate is unlikely stable. It may undergo rearrangement to form the 1,4,9-$R_3C_{60}^-$, where the oxygen or the amino nitrogen atom migrates, similar to the oxazoline and imidazoline heterocycles. Figure 41 shows the structure illustration of the 1,4,9-$R_3C_{60}^-$ intermediate having the oxazoline or imidazoline heterocycle.

Theoretical calculations were performed for the conversion of 1,2,4-$R_3C_{60}^-$ (**A**) to 1,4,9-$R_3C_{60}^-$ (**B**) with the Gaussian09 package to provide further insight into the reaction. Geometry optimization, transition state identification, and vibrational frequency analyses were carried out at the B3LYP/6-31G level, whereas the energy was calculated at the B3LYP/6-311G(d) level. Figure 42 shows the energy profiles for the conversion of **A** to **B**, along with the calculated bond lengths of the O−C_{60} and amino N−C_{60} in each species. In addition, the calculations have located two

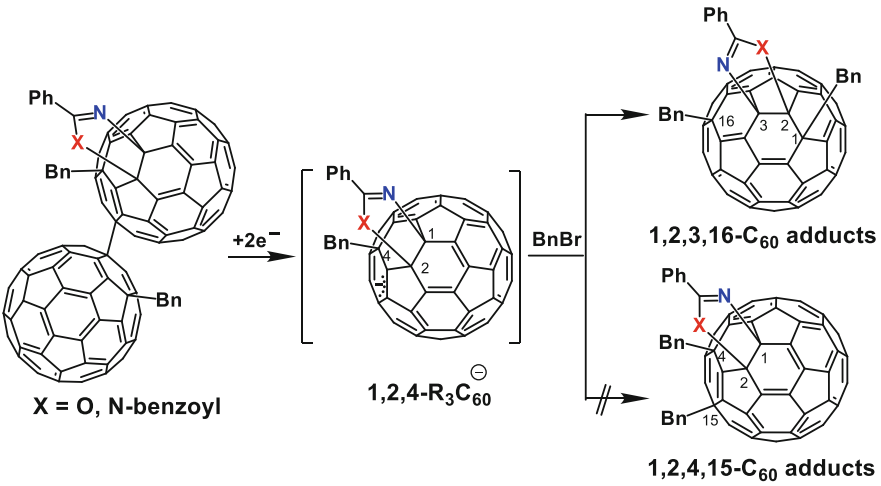

Scheme 15 Reductive benzylation of singly bonded 1,2,4,15-C_{60} dimers with an oxazoline or imidazoline heterocycle. (Taken from Ref. [53])

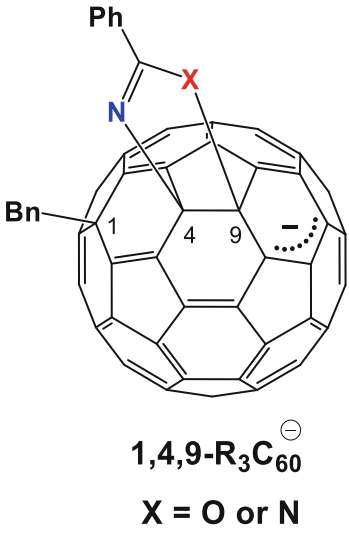

Fig. 41 Structure illustration of the 1,4,9-$R_3C_{60}^-$ intermediate. (Taken from Ref. [53] with slight modification)

transition states **TS1** and **TS2** and an intermediate state **INT1**. Small activation barriers of 7.5 and 9.9 kcal/mol are predicted for the migration of the O−C_{60} and amino N−C_{60} bonds from the [6,6]-bond to the [5,6]-bond, respectively. The calculations also predict **B** is more energetically favorable over **A** by 6.3 and 6.7 kcal/mol for oxazoline and imidazoline, respectively, consistent with the experimentally observed conversion of 1,2,4-$R_3C_{60}^-$ to 1,4,9-$R_3C_{60}^-$. The variations of the O−C_{60} and amino N−C_{60} bond lengths in 1,2,4-$R_3C_{60}^-$, **TS1**, **INT1**, **TS2**, and

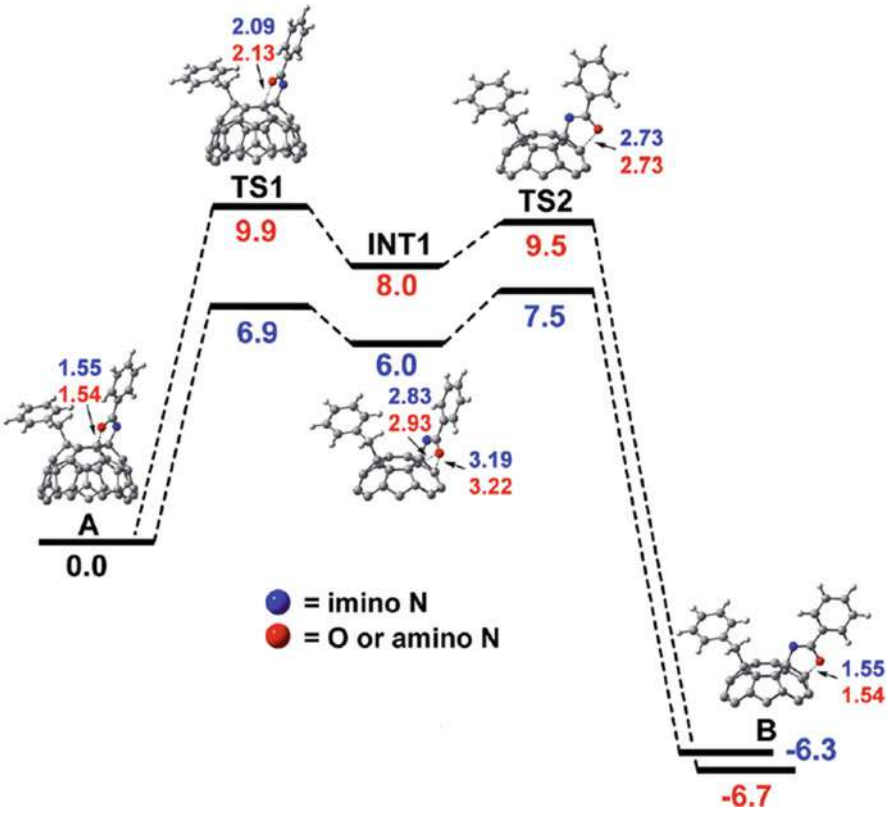

Fig. 42 Computed energy profiles for the conversion of A to B. Energies are given in kcal/mol, and bond lengths are given in angstroms (Å). The blue and red numbers represent the results of C_{60} oxazoline and C_{60} imidazoline, respectively. (Taken from Ref. [53])

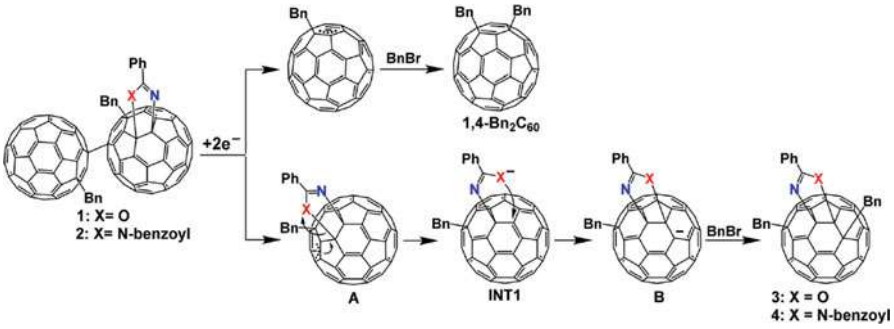

Scheme 16 Reaction mechanism for the reductive benzylation of singly bonded 1,2,4,15-C_{60} dimers with an oxazoline or imidazoline heterocycle. (Taken from Ref. [54])

1,4,9-$R_3C_{60}^-$ are in good agreement with cleavage and formation of the X−C_{60} bond during the relocation of the heteroatom, where the X−C2 bond is broken in **TS1**, and the X−C9 bond is formed in **TS2** by migrating the O or amino N atom from C2 to C9 via I**NT1**.

Scheme 16 shows the reaction mechanism for the reductive benzylation of singly bonded 1,2,4,15-C_{60} dimers with an oxazoline or imidazoline heterocycle, where the conversion of the 1,2,4-$R_3C_{60}^-$ to 1,4,9-$R_3C_{60}^-$ is crucial in achieving the products.

The result shows explicitly that the 1,4,9-$R_3C_{60}^-$ is a stable anionic intermediate, which is important in rationalizing the product structure of the base-promoted consecutive enolate addition reaction of [60]fullerene with ketones reaction, where C_{60} derivatives with the 1,4,9,25- and 1,4,9,12-configurations were obtained [54].

References

1. Kroto HW, Heath JR, O'Brien SC, Curl RF, Smalley RE (1985) C_{60}: buckminsterfullerene. Nature 318:162–163
2. Krätschmer W, Lamb LD, Fostiropoulos K, Huffman DR (1990) Solid C_{60}: a new form of carbon. Nature 347:354–358
3. Haufler RE, Conceicao J, Chibante LPF, Chai Y, Byrne NE, Flanagan S, Haley MM, O'Brien SC, Pan C, Xiao Z, Billups WE, Ciufolini MA, Hauge RH, Margrave JL, Wilson LJ, Curl RF, Smalley RE (1990) Efficient production of C_{60} (buckminsterfullerene), $C_{60}H_{38}$, and the solvated buckide ion. J Phys Chem 94:8634–8636
4. Li Y (2013) Fullerene-bisadduct acceptors for polymer solar cells. Chem Asian J 8:2316–2328
5. Caron C, Subramanian R, D'Souza F, Kim J, Kutner W, Jones MT, Kadish KM (1993) Selective electrosynthesis of $(CH_3)_2C_{60}$: a novel method for the controlled functionalization of fullerenes. J Am Chem Soc 115:8505–8506
6. Yang W-W, Li Z-J, Li F-F, Gao X (2011) Electrochemical and H/D-labeling study of oxazolino [60]fullerene rearrangement. J Org Chem 76:1384–1389
7. Haddon RC, Brus LE, Raghavachari K (1986) Electronic structure and bonding in icosahedral C_{60}. Chem Phys Lett 125:459–464
8. Allemand P-M, Koch A, Wudl F, Rubin Y, Diederich F, Alvarez MM, Anz SJ, Whetten RL (1991) Two different fullerenes have the same cyclic voltammetry. J Am Chem Soc 113:1050–1051
9. Dubois D, Kadish KM, Flanagan S, Haufler RE, Chibante LPF, Wilson LJ (1991) Spectroelectrochemical study of the C_{60} and C_{70} fullerenes and their mono-, di-, tri-, and tetraanions. J Am Chem Soc 113:4364–4366
10. Dubois D, Kadish KM, Flanagan S, Wilson LJ (1991) Electrochemical detection of fulleronium and highly reduced fulleride (C_{60}^{5-}) ions in solution. J Am Chem Soc 113:7773–7774
11. Xie Q, Pérez-Cordero E, Echegoyen L (1992) Electrochemical detection of C_{60}^{6-} and C_{70}^{6-}: enhanced stability of fullerides in solution. J Am Chem Soc 114:3978–3980
12. Ohsawa Y, Saji T (1992) Electrochemical detection of C_{60}^{6-} at low temperature. J Chem Soc Chem Commun:781–782
13. Gao X, Van Caemelbecke E, Kadish KM (1998) Visible and near-infrared absorption spectra of singly and doubly reduced C_{76} fullerene anions. Electrochem Solid-State Lett 1:222–223
14. Azamar-Barrios JA, Dennis TJS, Sadhukan S, Shinohara H, Scuseria GE, Pénicaud A (2001) Characterization of six isomers of [84]fullerene C_{84} by electrochemistry, electron spin resonance spectroscopy, and molecular energy levels calculations. J Phys Chem A 105:4627–4632
15. Xie Q, Arias F, Echegoyen L (1993) Electrochemically-reversible, single-electron oxidation of C_{60} and C_{70}. J Am Chem Soc 115:9818–9819

16. Yang X-Y, Lin H-S, Jeon I, Matsuo Y (2018) Fullerene-cation-mediated noble-metal-free direct introduction of functionalized aryl groups onto [60]fullerene. Org Lett 20:3372–3376
17. Yang X-Y, Lin H-S, Matsuo Y (2019) Highly selective synthesis of tetrahydronaphthaleno[60] fullerenes via fullerene-cation-mediated intramolecular cyclization. J Org Chem 84:16314–16322
18. Echegoyen L, Echegoyen LE (1998) Electrochemistry of fullerenes and their derivatives. Acc Chem Res 31:593–601
19. Hummelen JC, Knight BW, LePeq F, Wudl F, Yao J, Wilkins CL (1995) Preparation and characterization of fulleroid and methanofullerene derivatives. J Org Chem 60:532–538
20. Deng L-L, Xie S-Y, Gao F (2018) Fullerene-based materials for photovoltaic applications: toward efficient, hysteresis-free, and stable perovskite solar cells. Adv Electron Mater 4: 1700435
21. Chen Z, Mou K, Yao S, Liu L (2018) Highly selective electrochemical reduction of CO_2 to formate on metal-free nitrogen-doped $PC_{61}BM$. J Mater Chem A 6:11236–11243
22. Keshavarz-K M, Knight B, Srdanov G, Wudl F (1995) Cyanodihydrofullerenes and dicyanodihydrofullerene: the first polar solid based on C_{60}. J Am Chem Soc 117:11371–11372
23. Powell WH, Cozzi F, Moss GP, Thilgen C, Hwu RJ-R, Yerin A (2002) Nomenclature for the C_{60}-I_h and C_{70}-$D_{5h(6)}$ fullerenes. Pure Appl Chem 74:629–695
24. Carano M, Da Ros T, Fanti M, Kordatos K, Marcaccio M, Paolucci F, Prato M, Roffia S, Zerbetto F (2003) Modulation of the reduction potentials of fullerene derivatives. J Am Chem Soc 125:7139–7144
25. Hirsch A, Lamparth I, Grösser T, Karfunkel HR (1994) Regiochemistry of multiple additions to the fullerene core: synthesis of a T_h-symmetric hexakisadduct of C_{60} with bis(ethoxycarbony1) methylene. J Am Chem Soc 116:9385–9386
26. Matsuzawa N, Dixon DA, Fukunaga T (1992) Semiempirical calculations of dihydrogenated buckminsterfullerenes, $C_{60}H_2$. J Phys Chem 96:7594–7604
27. Zheng M, Li F-F, Shi Z, Gao X, Kadish KM (2007) Electrosynthesis and characterization of 1,2-dibenzyl C_{60}: a revisit. J Org Chem 72:2538–2542
28. Kadish KM, Gao X, Van Caemelbecke E, Suenobu T, Fukuzumi S (2000) Electrosynthesis and structural characterization of two $(C_6H_5CH_2)_4C_{60}$ isomers. J Am Chem Soc 122:563–570
29. Ford WT, Nishioka T, Qiu F, D'Souza F, Choi J-p (2000) Dimethyl azo(bisisobutyrate) and C_{60} produce 1,4- and 1,16-di(2-carbomethoxy-2-propyl)-1,x-dihydro[60]fullerenes. J Org Chem 65:5780–5784
30. Popov AA, Kareev IE, Shustova NB, Stukalin EB, Lebedkin SF, Seppelt K, Strauss SH, Boltalina OV, Dunsch L (2007) Electrochemical, spectroscopic, and DFT study of $C_{60}(CF_3)_n$ frontier orbitals (n = 2−18): the link between double bonds in pentagons and reduction potentials. J Am Chem Soc 129:11551–11568
31. Yang W-W, Li Z-J, Li S-H, Wu S-L, Shi Z, Gao X (2017) Reductive activation of C_{70} equatorial carbons and structurally characterized C_{70} δ-adduct with closed [5,6]-ring fusion. J Org Chem 82:9253–9257
32. Chang W-W, Li Z-J, He F-G, Sun T, Gao X (2015) Electronic vs steric effects on the stability of anionic species: a case study on the ortho and para regioisomers of organofullerenes. J Org Chem 80:1557–1563
33. Ni L, Chang W-W, Hou H-L, Li Z-J, Gao X (2011) Preparation and characterisation of an equatorial para-adduct of $(PhCH_2)HC_{70}$ from the reaction of C_{70}^{2-} with benzyl bromide and H_2O: addition effects in the polar and equatorial regions of C_{70}. Org Biomol Chem 9:6646–6653
34. Yang W-W, Li Z-J, Gao X (2011) Formation of singly bonded $PhCH_2C_{60}-C_{60}CH_2Ph$ dimers from 1,2-$(PhCH_2)HC_{60}$ via electroreductive $C_{60}-H$ activation. J Org Chem 76:6067–6074
35. Hou H-L, Li Z-J, Gao X (2014) Reductive benzylation of C_{60} imidazoline with a bulky addend. Org Lett 16:712–715
36. Subramanian R, Kadish KM, Vijayashree MN, Gao X, Jones MT, Miller MD, Krause KL, Suenobu T, Fukuzumi S (1996) Chemical generation of C_{60}^{2-} and electron transfer mechanism for the reactions with alkyl bromides. J Phys Chem 100:16327–16335

37. Yang W-W, Li Z-J, Gao X (2010) Reaction of C_{60}^{2-} with organic halides revisited in DMF: proton transfer from water to RC_{60}^{-} and unexpected formation of 1,2-dihydro[60]fullerenes. J Org Chem 75:4086–4094
38. Liu K-Q, Wang G-W (2019) Reactions of the electrochemically generated dianion of [60] fullerene with bulky secondary alky bromides. Tetrahedron Lett 60:1049–1052
39. Sawamura M, Toganoh M, Suzuki K, Hirai A, Iikura H, Nakamura E (2000) Stepwise synthesis of fullerene cyclopentadienide $R_5C_{60}^{-}$ and indenide $R_3C_{60}^{-}$. An approach to fully unsymmetrically substituted derivatives. Org Lett 2:1919–1921
40. Kitaura S, Kurotobi K, Sato M, Takano Y, Umeyama T, Imahori H (2012) Effects of dihydronaphthyl-based [60]fullerene bisadduct regioisomers on polymer solar cell performance. Chem Commun 48:8550–8552
41. Li Z-J, Wang S, Li S-H, Sun T, Yang W-W, Shoyama K, Nakagawa T, Jeon I, Yang X, Matsuo Y, Gao X (2017) Regiocontrolled electrosynthesis of [60]fullerene bisadducts: photovoltaic performance and crystal structures of C_{60} o-quinodimethane bisadducts. J Org Chem 82: 8676–8685
42. Maeda Y, Sanno M, Morishita T, Sakamoto K, Sugiyama E, Akita S, Yamada M, Suzuki M (2019) Reaction of the C_{60} radical anion with alkyl halides. New J Chem 43:6457–6460
43. Khaled MM, Carlin RT, Trulove PC, Eaton CR, Eaton SS (1994) Electrochemical generation and electron paramagnetic resonance studies of C_{60}^{-}, C_{60}^{2-}, and C_{60}^{3-}. J Am Chem Soc 116: 3465–3474
44. Zheng M, Li F-F, Ni L, Yang W-W, Gao X (2008) Synthesis and identification of heterocyclic derivatives of fullerene C_{60}: unexpected reaction of anionic C_{60} with benzonitrile. J Org Chem 73:3159–3168
45. Rapta P, Bartl A, Gromov A, Staško A, Dunsch L (2002) In situ ESR/Vis/NIR spectroelectrochemistry of [60]fullerene: the origin of ESR "Spikes" and the reactivity of pristine fullerene anions. Chem Phys Chem 3:351–356
46. Hou H-L, Gao X (2012) Aerobic oxidations of C_{60}^{2-} in the presence of PhCN and $PhCH_2CN$: oxygenation versus dehydrogenation reactions. J Org Chem 77:2553–2558
47. Kadish KM, Gao X, Gorelik O, Van Caemelbecke E, Suenobu T, Fukuzumi S (2000) Electrogeneration and characterization of $(C_6H_5CH_2)_2C_{70}$. J Phys Chem A 104:2902–2907
48. Li S-H, Li Z-J, Yang W-W, Gao X (2013) Reactions of C_{70}^{2-} with organic halides revisited: unusual magnetic equivalence for the diastereotopic methylene protons in 2,5-$(PhCH_2)_2C_{70}$. J Org Chem 78:7208–7215
49. Meng X, Zhang W, Tan Z, Du C, Li C, Bo Z, Li Y, Yang X, Zhen M, Jiang F, Zheng J, Wang T, Jiang L, Shu C, Wang C (2012) Dihydronaphthyl-based [60]fullerene bisadducts for efficient and stable polymer solar cells. Chem Commun 48:425–427
50. Thilgen C, Diederich F (1999) The higher fullerenes: covalent chemistry and chirality. Top Curr Chem 199:135–171
51. Ni L, Yang W-W, Li Z-J, Wu D, Gao X (2012) Regioselective oxazolination of C_{70}^{2-} and formation of cis-1 C_{70} adduct with respect to the apical pentagon. J Org Chem 77:7299–7306
52. Xiao Y, Zhu S-E, Liu D-J, Suzuki M, Lu X, Wang G-W (2014) Regioselective electrosynthesis of rare 1,2,3,16-functionalized [60]fullerene derivatives. Angew Chem Int Ed 53:3006–3010
53. Li Z-J, Li S-H, Sun T, Hou H-L, Gao X (2015) Reductive benzylation of singly bonded 1,2,4,15-C_{60} dimers with an oxazoline or imidazoline heterocycle: unexpected formation of 1,2,3,16-C_{60} adducts and insights into the reactivity of singly bonded C_{60} dimers. J Org Chem 80:3566–3571
54. Chen S, Li Z-J, Li S-H, Gao X (2015) Base-promoted consecutive enolate addition reaction of [60]fullerene with ketones. Org Lett 17:5192–5195

Complexation with Transition Metals

13

Changwang Pan

Contents

Abstract

The electron-deficiency fullerenes that resemble olefins are facile to react with nucleophilic transition metals to form related complexes with novel structures and unique properties. So far, mononuclear, multinuclear metal complexes and ionic salts of fullerenes have been prepared by the reaction with metal clusters. The coordination reactions of C_{60}, higher fullerenes and metallofullerenes have usually shown very high regioselectivity to afford mono-, bis-, and even tetra- and hexa-adducts. Various crystallographic structures and spectroscopic results demonstrate that the mononuclear cluster binds to a C–C bond or a single carbon atom on the fullerene, forming η^2 or η^1 coordination, respectively, leading to the distortion of fullerene cage. In the multinuclear metal complexes of fullerenes, the metal clusters except for $Ir_4(CO)_8(PMe_3)_4$ will uniformly coordinate with the

C. Pan (✉)
College of Chemistry and Chemical Engineering, Jinggangshan University, Ji'an, Jiangxi, China
e-mail: panchangwang@jgsu.edu.cn

X. Lu et al. (eds.), *Handbook of Fullerene Science and Technology*,
https://doi.org/10.1007/978-981-16-8994-9_12

fullerenes in η^2 fashion, such as the typical μ_3-η^2:η^2:η^2-C_{60} coordination seen in trinuclear complexes, and the binding mode could undergo a transformation to a mixed coordination of η^2 and η^1 through the insertion of ligands into the multinuclear clusters. Remarkably, some metal clusters act like bridges to link fullerenes, forming dimers and even organometallic fullerene polymers. In addition, the electrochemical studies of η^2-C_{60} complexes indicate that the redox process is related to the reduction of fullerenes and the oxidation of metal clusters.

Keywords

Fullerene · Transition metal · Coordination · Exohedral functionalization · Dimerization · Polymer

Introduction

The rapid development of the functionalization of fullerenes has been facilitated by the ability to prepare mass quantities of fullerenes, and the exohedral reaction of fullerenes with transition metal atoms or clusters has drawn a lot of attention. The electron-deficiency fullerenes prefer to react with nucleophilic transition metals to form related products. Four types of reaction between fullerenes and transition metals can be summarized as follows. The first reaction is the direct coordination of the transition metal with the carbon atoms and C–C bonds on the fullerene cage to form various coordination complexes as shown in Fig. 1. The second is the reduction of fullerenes with metal clusters, forming ions of fullerene. The third and fourth types are the co-crystallization of fullerenes with metal and the coordination of fullerene derivatives. In the latter two types of reaction, the formation of related products is mostly dependent on the supramolecular interaction and the coordination of substituent groups, respectively; as such, it cannot reflect the complexation nature of fullerenes with metal and so is not mentioned here. Consequently, the coordination and reduction of fullerenes with transition metal clusters will be the focus of this chapter; specifically, the transition-metal complexes of fullerenes will be discussed in detail from the aspect of their preparations and structures.

Mononuclear Metal Complexes of Fullerenes

η^1-Fashion Metal Complexes of Fullerenes

η^1 coordination is a rare fashion of organometallic complexes of fullerenes, and it is usually found in cases where metal clusters are attached to fullerenes through the multiple coordination fashion. The first pure η^1-fashion complex of fullerene was prepared by treating C_{60} with a $[Ru(CO)_2]_2(\eta^5\text{-}C_5H_5)_2$ dimer in solvent [1]. The metal dimer does not co-crystallize, but directly reacts with the fullerene through the cleavage of the Ru–Ru bond and the addition of the resulting radicals to C_{60}. Black

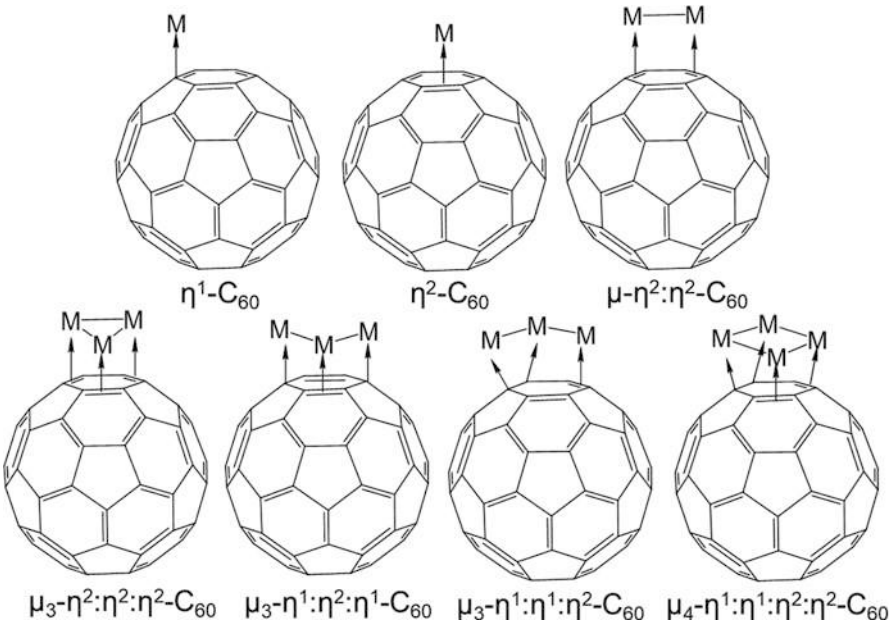

Fig. 1 The coordination fashions in complexation of fullerene with metals

crystals of the product $[Ru(CO)_2(\eta^5\text{-}C_5H_5)]_2(\eta^1\text{-}C_{60})$ (**1**) that are suitable for single-crystal X-ray diffraction (XRD) were obtained through the diffusion of hexane into the saturated solution of **1** in dichloromethane. The crystallographic results reveal that two $Ru(CO)_2(\eta^5\text{-}C_5H_5)_2$ units are added to the opposite ends of a hexagon on the fullerene cage and are oriented with C_1 symmetry and that each Ru atom is bonded to one carbon atom with the distances 2.206 Å (Ru1-C1) and 2.201 Å (Ru2-C7). These are longer than the distances seen in Ru complex $Ru(\eta^5\text{-}C_{60}Me_5)CH_3(CO)_2$, representing the typical η^1 coordination (Fig. 2a). The elongation of the Ru–C distance is most likely caused by the steric hindrance of the addition group. Theoretical calculations show that the η^1-coordinated bond is formed by a large overlap between the Ru d_σ orbital and the C p_σ involved in the lowest unoccupied molecular orbital (LUMO) (π^*) of C_{60}, which is different from the η^2-coordinated bond [2].

Photolysis has been proven to be more effective at breaking the Ru–Ru bond to yield radicals with metal centers and thereby accelerating the complexation of fullerenes with a Ru complex [1]. A similar photoirradiation reaction has been conducted through the reaction of $Re_2(CO)_{10}$ with fullerenes, following which the bis-adduct $C_{60}[Re(CO)_5]_2$ was detected through spectroscopic characterization [3]. However, this adduct is very unstable and reversible, and therefore tends to revert into its starting materials. When the metallofullerene $Y@C_{2v}(9)\text{-}C_{82}$ is applied to react with $Re_2(CO)_{10}$, a stable product $Re(CO)_5[\eta^1\text{-}Y@C_{2v}(9)\text{-}C_{82}]$ (**2**) suitable for characterizations is obtained [4]. The results of the reaction mixture monitored through high-performance liquid chromatography (HPLC), demonstrate that this

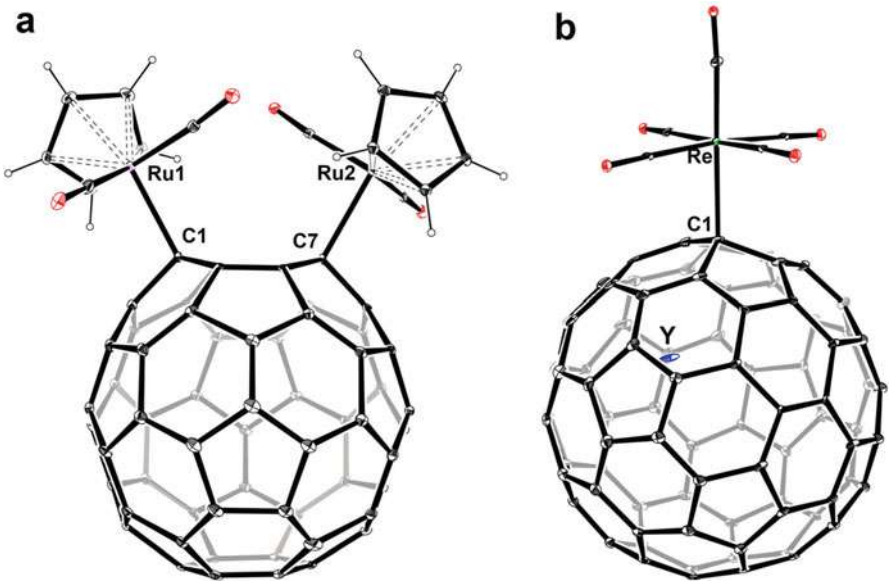

Fig. 2 Crystallographic structures of (**a**) $[Ru(CO)_2(\eta^5\text{-}C_5H_5)]_2(\eta^1\text{-}C_{60})$ and (**b**) $Re(CO)_5[\eta^1\text{-}Y@C_{2v}(9)\text{-}C_{82}]$. (From data in Refs. [1, 4])

reaction possesses high regioselectivity and a high conversion yield (>95%) although 24 nonequivalent addition sites exist on the $C_{2v}(9)$-C_{82}. The structure of **2**, firmly determined by XRD, shows that the rhenium atom coordinates in an η^1 fashion with a [5,6,6]-carbon atom (C1) on the top hexagon of the cage (Fig. 2b). The coordination of the rhenium moiety can influence the fullerene cage and the internal metal ion. The bonds of fullerene near the coordination site are elongated to 1.58 Å, indicative of a C−C single-bond character. Accordingly, this causes a slight distortion of the fullerene cage by changing the hybridization type from sp^2 to sp^3. The internal Y position is changed compared to that of the parent metallofullerene, moving from that under the hexagonal ring along the C_2 axis of the cage to that departing from the C_2 axis and the addition site. This off-axis position of the Y atom found in **2** is probably due to the charge redistribution on the cage caused by the one-electron transfer from the Re cluster confirmed by the Vis−NIR and electron paramagnetic resonance (EPR) results.

η^2-Fashion Metal Complexes of Fullerenes

Since the discovery of fullerene, it has taken a long time to confirm whether it behaves like an aromatic or an electron-deficient alkene. Fagan elegantly answers this question through the reaction of fullerenes with the complex $[Cp^*Ru(CH_3CN)_3]^+O_3SCF_3^-$ ($Cp^* = C_5(CH_3)_5$). The Ru complex possesses remarkable selectivity, exclusively losing three acetonitrile ligands and coordinating with

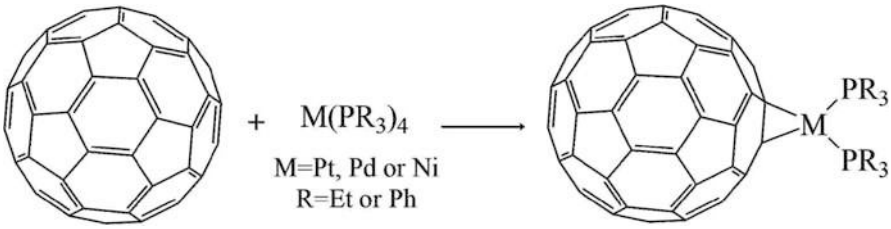

Scheme 1 Reactions of fullerene with $M(PR_3)_4$ (M = Pt, Pd or Ni; R = Et or Ph)

electron-rich planar arenes, resulting in an η^6-arene complex during reaction with the mixture of alkenes and aromatic ligands [5]. However, the reaction of fullerenes with a tenfold excess of $[Cp^*Ru(CH_3CN)_3]^+O_3SCF_3^-$ results in a different product $[Cp^*Ru(CH_3CN)_2C_{60}]^{3+}(O_3SCF_3^-)_3$. The experimental results demonstrate that C_{60} is more chemically similar to electron-deficient alkenes than to arenes. Calculations provide a quantitative description of the relative ability of C_{60} to bond as an η^6 ligand, confirming that η^6 bonding is unfavorable due to the decreased overlap of the splayed-out orbitals of a C_{60} and C_{70} hexagon with the frontier orbitals of transition-metal fragments [6].

Inspired by this work, Fagan then tried to research the reactions of fullerenes with organometallic compounds that bond strongly to alkenes, such as the zero-valent complex $M(PR_3)_4$ (M = Ni, Pd or Pt; R = Et or Ph) (Scheme 1), and all the reaction solution color changed instantly to dark emerald green [7]. The overall structures and properties of relative complexes are similar; however, the orientations of some ligands may show slight differences when they stack up into crystals. Figure 3 shows the structure of the palladium complex $(Ph_3P)_2Pd(\eta^2\text{-}C_{60})$ (**3**) [8]. The phenyl ligands are located near the C_{60} fragment for better π–π contact in $(Ph_3P)_2Pt(\eta^2\text{-}C_{60})$, whereas the platinum complex does not have such contact [9].

Interestingly, the complexation of C_{60} with an excess of $M(PEt_3)_4$ (M = Ni, Pd or Pt) can lead to hexa-adducts [10]. Only one structural isomer was found for Ni, Pd, and Pt complexes with high yield and these complexes have been shown by spectroscopic analysis to be isostructural. The single-crystal X-ray results of $[(Et_3P)_2Pt]_6(\eta^2\text{-}C_{60})$ (**4**) reveal that six platinum atoms coordinate with fullerenes in η^2 fashion, forming an octahedral shape that surrounds the fullerene (Fig. 4). At the same time, the related carbon atoms are pulled out from the C_{60} framework and are close to sp^3 hybridized carbon, resulting in the elongation of the C–C bond. The core of the complex, which excludes all the outer ethyl groups, possesses a nearly perfect T_h-point-group symmetry. The octahedral array of six coordinated sites means that the platinum atoms lie far away from each other, decreasing the steric hindrance of the ligands and protecting all of the remaining 24 [6,6]-bonds from further attack by platinum atoms. The hexa-adduct **4** can react with diphenylacetylene and lose one platinum fragment, forming the penta-adducts $[(Et_3P)_2Pt]_5(\eta^2\text{-}C_{60})$.

The electrochemical properties of $(Ph_3P)_2Pt(\eta^2\text{-}C_{60})$, $(Et_3P)_2M(\eta^2\text{-}C_{60})$ (M = Ni, Pd and Pt), and $[(Et_3P)_2Pt]_nC_{60}$ (n = 2–4) were also investigated [11, 12]. The results

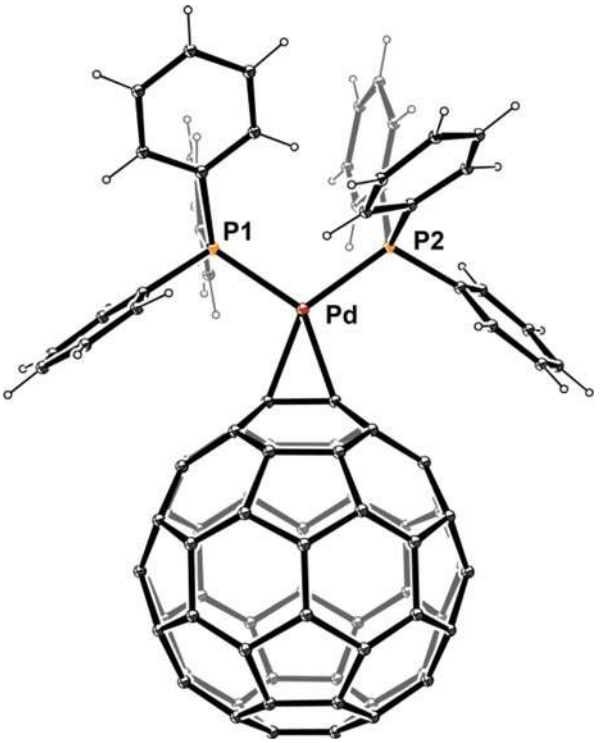

Fig. 3 Crystallographic structure of $(Ph_3P)_2Pd(\eta^2\text{-}C_{60})$. (From data in Ref. [8])

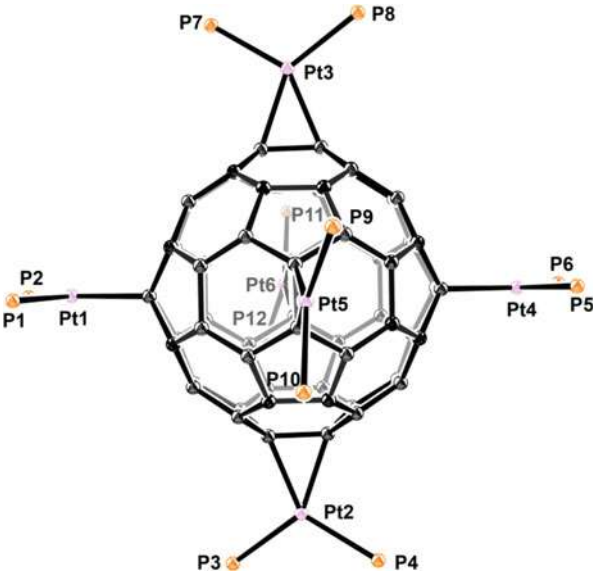

Fig. 4 Crystallographic structure of $[(Et_3P)_2Pt]_6(\eta^2\text{-}C_{60})$. (From data in Ref. [9]). The 12 ethyl groups are deleted for clarity

show three or four reduction peaks and indicate that the reduction potentials negatively shift for all the mono-adducts. The reduction of the metal complex of fullerene is harder because the coordination of the metal could lower the electron affinity by removing one C–C bond from the conjugate system. This behavior of the negative shift of reduction potential is typical for all the η^2 complexes of fullerenes. The first irreversible oxidation potentials are strongly influenced by metal fragments, compared to $(Et_3P)_2M(\eta^2\text{-}C_{60})$ (M = Ni, Pd and Pt), where the reduction is independent of the metal. The above results demonstrate that the reduction and oxidation processes are C_{60}-based and metal-based, respectively. The addition of more metals will further reduce the electron affinity of C_{60}. The electrochemical study of $[(Et_3P)_2Pt]_n(\eta^2\text{-}C_{60})$ (n = 1–4) shows that a remarkable linear relationship exists between the reversible potentials and the addition number, with 0.36 V of negative shift per the addition of one metal [11]. In addition, the dissociation of $(Et_3P)_2M(\eta^2\text{-}C_{60})$ (M = Ni, Pd and Pt) was observed under the reduction, while the rate of dissociation increases with the degree of reduction.

A similar Fagan complex of the higher fullerene C_{70} was prepared through the addition of four molar equivalents of $(Ph_3P)_2Pt(\eta^2\text{-}C_2H_4)$ to a solution of C_{70} in benzene. The successive formation of $[(Ph_3P)_2]_nPtC_{60}$ (n = 1–4) was observed, and the tetra-adduct **(5)** was isolated as the final product [13]. Single crystals of **5** that are suitable for characterization were obtained through the slow diffusion of diethyl ether/methanol. The crystallographic structure given in Fig. 5 shows that four platinum atoms coordinate with the C–C bonds of C_{70}, residing in a single plane. Two positions of the Pt (Pt1 and Pt2) fragments coordinated to the C–C bonds are consistent with those in Vaska's compound, but the pattern of the remaining two positions is different. The other two (Pt3 and Pt4) fragments are attached to less-pyramidalized C–C bonds, resulting in the maximum separation from the first two

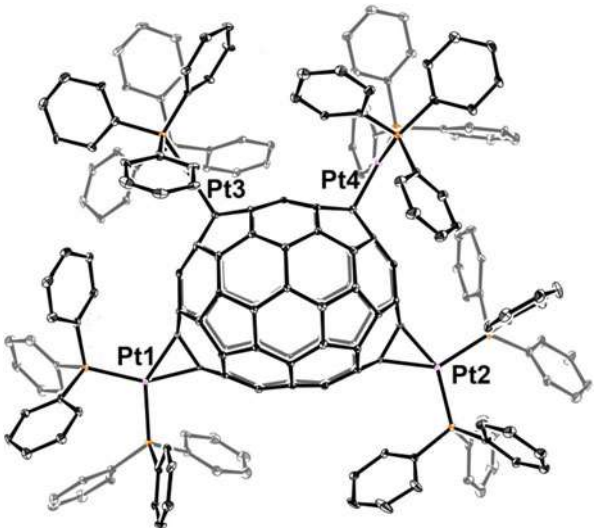

Fig. 5 Crystallographic structure of $[(Ph_3P)_2]_4Pt(\eta^2\text{-}C_{70})$. (From data in Ref. [13]). Hydrogen atoms are removed for clarity

fragments. This array means that the whole molecular structure excluding the phenyl groups possesses a C_{2v} symmetry. Accordingly, steric factors, symmetry, and solubility all play major roles in determining the pattern of addition.

Vaska's complex, $Ir(CO)Cl(PPh_3)_2$, is known to react with electron-deficient olefins such as tetracyanoethylene (TCNE) and tetrafluoroethylene (TFE) to form stable η^2 adducts. Compared with Fagan complexes, $Ir(CO)Cl(PPh_3)_2$ and related complexes are coordinated to fullerenes with no displacement of any ligands in the reaction process. In a typical reaction, the equimolar mixture of C_{60} and $Ir(CO)Cl(PPh_3)_2$ under an N_2 atmosphere immediately leads to a deep-brown solution, while the $Ir(CO)Cl(PPh_3)_2C_{60}$ (**6**) precipitates with a 45% yield after a few minutes [14]. Crystals suitable for X-ray were obtained through direct diffusion of a benzene solution of one reagent into the other, and the crystallographic structure shown in Fig. 6 reveals the iridium is attached to C_{60} in a η^2 fashion and the coordination makes coordinated carbon atoms (C1 and C2) away from the fullerene framework. This is similar to the results shown in Fagan complexes, further proving that C_{60} behaves like an electron-deficit olefin.

The infrared (IR) spectrum of **6** shows that the monoxide-stretching frequency ν(CO) increases to 2014 cm^{-1}. Such an increase is consistent with those of other complexes of fullerenes that have CO ligands. The signal peak of CO in IR is usually utilized to determine the degree of electron withdrawal from the metal and the

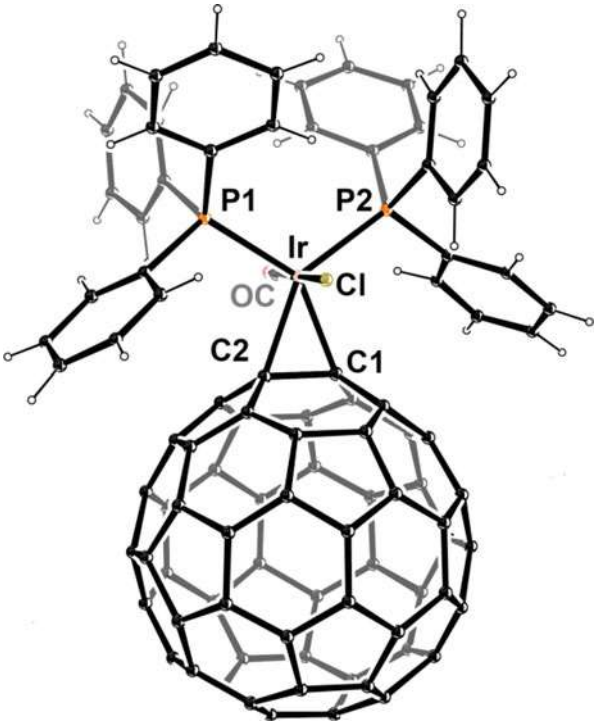

Fig. 6 Crystallographic structure of $Ir(CO)Cl(PPh_3)_2(\eta^2\text{-}C_{60})$. (From data in Ref. [14])

reversibility of the complexation. However, the increased amplitude is less than those for the TFE (2052 cm^{-1}) and TCNE (2057 cm^{-1}) adducts, indicating that C_{60} is less reactive to remove electron density from iridium than electron-rich olefins through d-to-π back-bonding. Accordingly, the product is unstable and a reversible decomposition of **6** is observed in the IR spectrum during the crystalline complex re-dissolution in dichloromethane. In actuality, similar processes also exist for other Vaska's complexes of fullerenes. Such reversible processes facilitate the single-crystal growth because the dissociation and reassociation involved allow the selection of a single molecular species from a mixture during the dynamic process of crystal growth [15].

Alkyl groups have been used to displace phenyl groups and thereby achieve higher reactivity of Vaska's complex, and relative complexation always results in the multi-addition of fullerenes. C_{60} reactions with the excesses of $Ir(CO)Cl(PMe_2Ph)_2$, $Ir(CO)Cl(PMe_3)_2$, or $Ir(CO)Cl(PEt_3)_2$ were conducted and bis-adducts were selectively crystallized [16, 17]. The reaction of C_{60} with a tenfold excess of either $Ir(CO)Cl(PMe_3)_2$ or $Ir(CO)Cl(PEt_3)_2$ in benzene also results in two complexes, $[Ir(CO)Cl(PMe_3)_2]_2(\eta^2\text{-}C_{60})$ (**7**) and $[Ir(CO)Cl(PEt_3)_2]_2(\eta^2\text{-}C_{60})$ (**8**). The two Ir atoms in **7** and **8** bind [6, 6]-bonds at the trans-1 positions at opposite ends of the fullerene (Fig. 7) [16]. The selective isolation of the double-addition products probably occurs as a result of the low solubility of these isomers, which possess the lowest polarity and highest symmetry of all of the possible regioisomers of these double-addition products. Remarkably, $[Ir(CO)Cl(PEt_3)_2]_2C_{60}$ does dissolve in o-dichlorobenzene and has enough solubility in a 6:4 o-dichlorobenzene/toluene mixture to ensure its effective

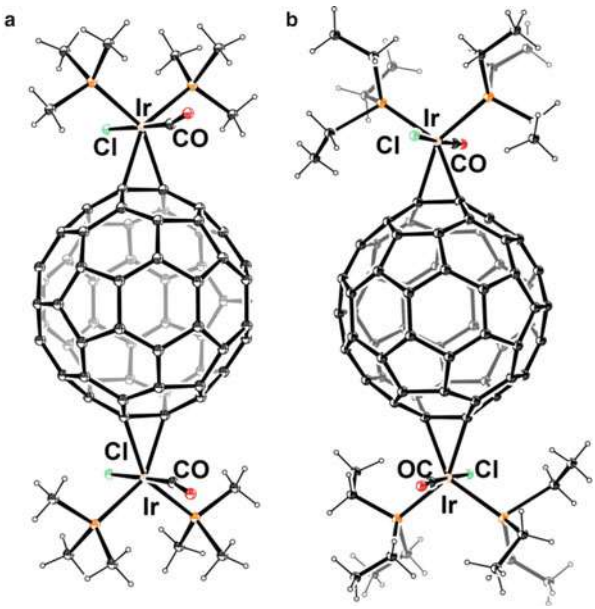

Fig. 7 Crystallographic structures of (**a**) $[Ir(CO)Cl(PMe_3)_2]_2(\eta^2\text{-}C_{60})$ and (**b**) $[Ir(CO)Cl(PEt_3)_2]_2(\eta^2\text{-}C_{60})$. (From data in Ref. [16])

examination by a pulsed nuclear magnetic resonance (NMR) study [16]. The results measured at different temperatures ranging from 20 to −80 °C show that the reversible degree of complexation is dependent on the temperature.

The reaction between C_{60} and $Ir(CO)Cl(PMe_2Ph)_2$ in the inert atmosphere leads to the rapid precipitation of deep-violet material consisting of well-formed purple-black obelisks, small purple plates, clumps of needles, and apparently amorphous materials [17]. Crystallographic results of obelisks and plates show that both the complexes are conformational isomers of the bis-adduct $[Ir(CO)Cl(PMe_2Ph)_2]_2(\eta^2\text{-}C_{60})$ (**9a** and **9b**)and that the two iridium atoms are likewise coordinated to a C–C bond with η^2 fashion at the trans-1 position in favor of the electronic and steric interaction (Fig. 8). However, the orientation of phenyl is different in these two isomers. Figure 7 shows the phenyl rings in **9a** lie near the C_{60} moiety for a π–π stack while the phenyl groups in **9b** do not interact with the surface of C_{60}. For the sake of a better π–π contact between fullerene and other ligands, a modified phosphine ligand $PCH_2C_6H_4OCH_2C_6H_5$ (Ph_2Pbob) was introduced into the iridium complex $Ir(CO)Cl(Ph_2Pbob)_2$, and the structure of the corresponding complex of fullerene $Ir(CO)Cl(Ph_2Pbob)_2(\eta^2\text{-}C_{60})$ (**10**) shows an overall geometry that closely resembles that of **6**. The two benzyloxybenzyl groups

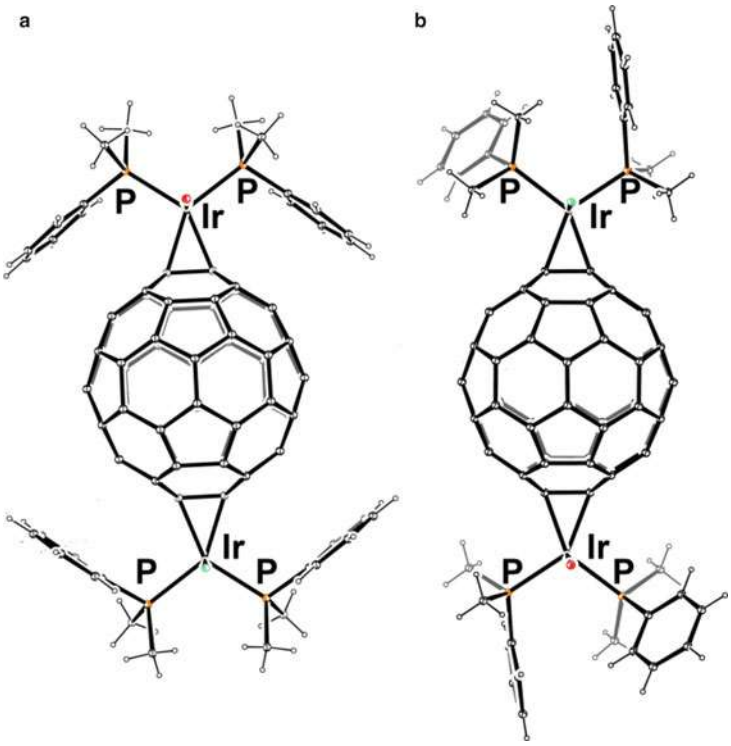

Fig. 8 Crystallographic structures of $[Ir(CO)Cl(PMe_2Ph)_2]_2(\eta^2\text{-}C_{60})$ isomers (**a**) **9a** and (**b**)**9b**. (From data in Ref. [17])

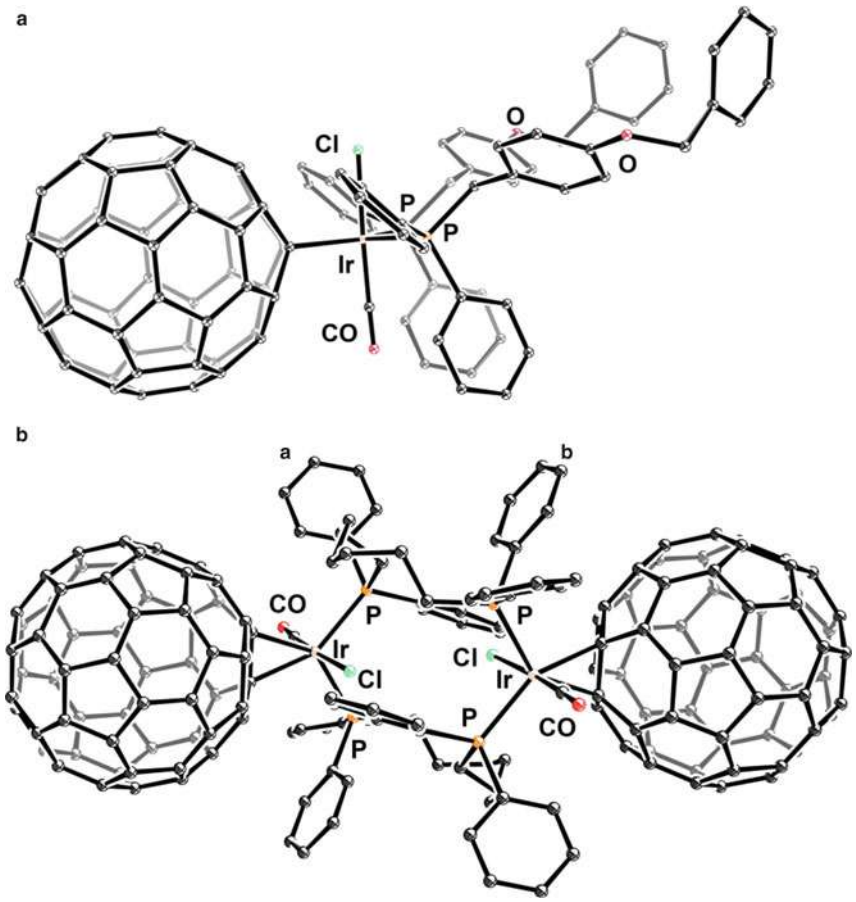

Fig. 9 Crystallographic structures of (**a**) $Ir(CO)Cl(Ph_2Pbob)_2(\eta^2\text{-}C_{60})$ and (**b**) $Ir_2(CO)_2Cl_2(Ph_2P(CH_2)_7PPh_2)_2(\eta^2\text{-}C_{60})_2$. (From data in Refs. [18, 20]). Hydrogen atoms are omitted for clarity

of **10** jointly form a cradle to fix the C_{60} portion of the adjacent complex (Fig. 9a), while the remaining two phenyl groups lie over 5:6 ring fusions for face-to-face contact with fullerene [18].

Similar complexes of C_{70} cannot be synthesized, and this is probably due to the disadvantageous space matching between the two benzyloxybenzyl groups and the fullerene [18]. Other modified phosphine ligands, PPh2(G-1) and PPh2(G-2) (G-1 = 3,5-bis(benzyloxy)benzyl; G-2 = 3,5-bis((3,5-bis(benzyloxy)oxy)benzyl), were also used to prepare and study the reversibility of the complex of C_{60} through a line-width ^{31}P NMR analysis. The addition of the dendrimer-containing arms to Vaska's compound only mildly alters the electronic properties of the complex, however, the solubility is greatly altered. The complex still maintains the metal–fullerene interaction, even in such solvents as ethers, alkanes and alcohols that normally cause fullerene precipitation [19].

The coordination of the binuclear complexes $Ir_2(CO)_2Cl_2(Ph_2P(CH_2)_nPPh_2)_2$ (n = 5 or 7) that possess macrocycles to C_{60} were conducted, and the related product $Ir_2(CO)_2Cl_2(Ph_2P(CH_2)_7PPh_2)_2(\eta^2\text{-}C_{60})_2$ (**11**) was characterized by single-crystal XRD [20]. The results show that the iridium centers are bound to 6:6 ring fusions of C_{60}. It is noted that, rather than attach to a single fullerene, two iridium atoms coordinate with two fullerenes to form dumbbell-shaped fullerene dimers. This is caused by the geometric constraints of the diphosphine ligands, which preclude the possibility of the addition of both iridium atoms to a single fullerene. Compared to the dimer $Ir_2(CO)_2Cl_2(Ph_2P(CH_2)_7PPh_2)_2(\eta^2\text{-TCNE})_2$, **11** is different in terms of the arrangement of the bridging alkyl chains. In $Ir_2(CO)_2Cl_2(Ph_2P(CH_2)_7PPh_2)_2(\eta^2\text{-TCNE})_2$, the alkyl chains are arranged in the fully extended form. However, the alkyl chains in **11** have twisted arrangements as shown in Fig. 9b.

Higher fullerenes such as C_{70} and C_{84} also possess similar Vaska reactions. Their reactivity and selectivity should be considerable, as C_{70} has eight types of C–C bonds and four types of [6] bonds, thus there are four potential positions at which metal can be coordinated. However, an equimolar mixture of C_{70} with Ir(CO)Cl $(PPh_3)_2$ in benzene results in a single adduct $Ir(CO)Cl(PPh_3)_2(\eta^2\text{-}C_{70})$ (**12**) [21]. Figure 10a shows the crystallographic structure of **12**. The geometry of iridium is similar to that in $Ir(CO)Cl(PPh_3)_2C_{60}$; the metal is bound in an η^2 fashion, with the [6] bond at one pole of C_{70}. This bond has the highest pyramidalization and is facile

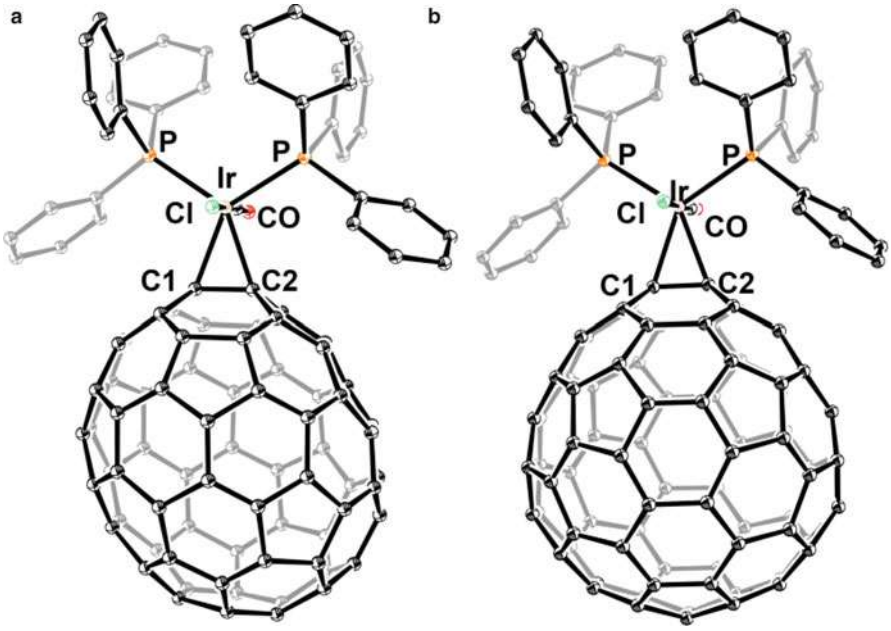

Fig. 10 Crystallographic structures of (**a**) $Ir(CO)Cl(PPh_3)_2(\eta^2\text{-}C_{70})$ and (**b**) Ir(CO)Cl $(PPh_3)_2(\eta^2\text{-}C_{84})$. (From data in Refs. [21, 22]). Hydrogen atoms are omitted for clarity

to coordinate with metal to release the steric strain, and the two coordinated carbon atoms (C1 and C2) are obviously pulled out away from the C_{70} fullerene. Accordingly, the strain of the bond on the carbon cage plays a key role in the selective formation of **12**. In addition, the bis-adduct of C_{70} to the Vaska-type complex has also been obtained by treating C_{70} with a 6- to 12-fold excess of $Ir(CO)Cl(PMe_2Ph)_2$ and the structure is similar to that of the bis-adduct $[Ir(CO)Cl(PMe_2Ph)_2]_2(\eta^2\text{-}C_{60})$.

Remarkably, the coordination of fullerenes with Vaska's complexes is not only regioselective, forming a single adduct, it also has the selectivity to react with a specific isomer. A mixture of C_{84} isomers synthesized through the arc-discharge method is applied to react with $Ir(CO)Cl(PPh_3)_2$ and the structure of the product, $Ir(CO)Cl(PPh_3)_2C_{84}$, is then determined by X-ray study (Fig. 10b). The results show that the coordinated fullerene is a less abundant C_{84} isomer with $D_{2d}(23)$ symmetry [22]. This is the first time that the C_{84} isomer has been separated through addition reaction and crystallization. The preferential reaction of the metal complex with such $D_{2d}(23)\text{-}C_{84}$ isomer is a consequence of the higher reactivity of this isomer compared to others. The π-density calculations show that C_{84} isomers have more localized π bonds than C_{60}, C_{70} and the most abundant isomer of C_{84} ($D_2\text{-}C_{84}$), and the coordinated bond in $D_{2d}(23)\text{-}C_{84}$ has the highest π-bond order. Accordingly, the reaction of $Ir(CO)Cl(PPh_3)_2$ with a mixture of C_{84} isomers regioselectively forms $Ir(CO)Cl(PPh_3)_2(\eta^2\text{-}C_{84})$ with specific isomers and addition sites.

Reagents containing hydrogen, $MH(CO)(PPh_3)_3$ (M = Ir and Rh), are commonly used as typical catalysts for the homogeneous hydrogenation of olefins. Remarkably, the mixture of $RhH(CO)(PPh_3)$ with a fullerene (C_{60} or C_{70}) directly forms the complex $IrH(CO)(PPh_3)(\eta^2\text{-}C_{60}/C_{70})$ by displacing the PPh_3 ligand instead of hydrogenating the fullerene [23, 24]. Consequently, the hydrogenation of fullerene has been better achieved with the heterogeneous rhodium complex as a catalyst. In addition, metallic hydride complexes $IrRh[H(CO)(PPh_3)_2]_2(\eta^2\text{-}C_{60})$ could also be produced with similar reaction methods [25]. The electrochemical properties of these η^2-fullerene complexes involving the metal rhodium and iridium were studied. Compared with the pristine C_{60}/C_{70}, these exohedral metallic hydride complexes have more negative reduction potentials and the degree of this negative shift depends only slightly on the metal nature including the metal type and the number of the metal while the oxidation step is related to the oxidation of the metal center, which is typical behavior in metal-coordinated C_{60} complexes [26, 27].

A series of η^2-fashion complexes of fullerenes have been synthesized through the photolysis of $M(CO)_4(dppe)$ (M = Mo, W; dppe = $Ph_2CH_2CH_2Ph_2$) followed by their chromatographic separation (Scheme 2). The related fullerene complexes, $W(CO)_3(dppe)(\eta^2\text{-}C_{60})$, $Mo(CO)_3(dppe)(\eta^2\text{-}C_{60})$, and $Mo(CO)_3(dppe)(\eta^2\text{-}C_{70})$, are quite stable under the effects of air, moisture, and heat [28]. The IR spectra show that the $\nu(CO)$ increases by 2–4 cm^{-1} by changing the metal center from Mo to W, and that the $\nu(CO)$ of the C_{70} complex has a slight blue shift of 1–3 cm^{-1} in comparison with C_{60} complexes, indicating that C_{70} is more electronegative than C_{60}. Their structures are determined by X-ray diffraction, and the results show that metal atoms bind to the [6, 6]-bonds, forming distorted octahedral geometries with the dppe and fullerenes in a *mer* configuration. Similar reactions were achieved by

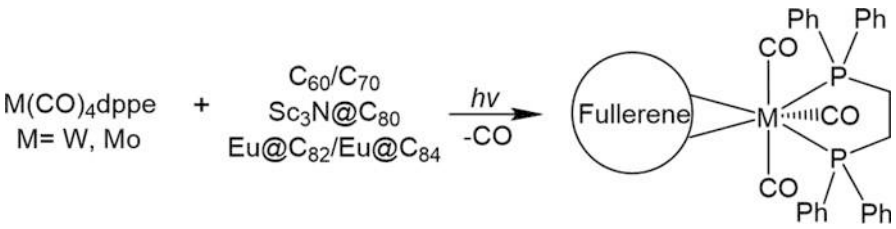

Scheme 2 Reactions of fullerenes with $M(CO)_4$(dppe) (M = Mo and W)

replacing the acetonitrile ligand of *fac*-$Mo(CO)_3$(MeCN)(dppe) with C_{60}, resulting in a single isomer *fac*-$Mo(CO)_3$(dppe)(η^2-C_{60}) in high yield (> 84%) whereas a mixture of *fac* and *mer* isomers was obtained during reaction with $Mo(CO)_4$(dppe) or *fac*-$W(CO)_3$(dppe)(MeCN) [29, 30].

Although the organometallic chemistry of metallofullerenes lags far behind that of fullerenes, the photoirradiated reactions of the tungsten complex $W(CO)_4$(dppe) with metallofullerenes have been systematically researched. The reactions of the cluster metallofullerenes $Sc_3N@I_h(7)$-C_{80} and $Sc_3N@D_{5h}(6)$-C_{80} lead to the regioselective formation of the stable complexes $W(CO)_3(Ph_2PC_2H_4PPh_2)[\eta^2$-$Sc_3N@I_h(7)$-$C_{80}$/$Sc_3N@D_{5h}(6)$-$C_{80}]$ (**14** and **15**), representing the first example of an air-stable mononuclear complex of metallofullerene. The crystallographic results show that the internal three scandium atoms lie away the coordinated [6] bond, maintaining the planar configuration with the center of the N atom (Fig. 11) [31]. The IR spectra of **14** and **15** show the ν(CO) has undergone a 6–18 cm^{-1} red shift compared with $W(CO)_3$(dppe)(η^2-C_{60}). Similar reactions are reported in the monometallofullerenes $Eu@C_2(5)$-C_{82} and $Eu@C_2(13)$-C_{84}, which afford only one complex, $W(CO)_3$(dppe)$[\eta^2$-$Eu@C_2(5)$-C_{82}/$Eu@C_2(13)$-$C_{84}]$ (**16** and **17**) even though 62/63 different types of nonequivalent C–C bonds exist in the $C_2(5)$-C_{82}/$C_2(13)$-C_{84} cages, respectively [32]. Theoretical results have demonstrated that the LUMO distributions that are influenced by charge transfer from the Eu and steric strain on the cages play a key role in the high regioselectivity. Their crystallographic results demonstrate that the motional behavior of the Eu atom inside the cage is significantly restricted upon coordination as a result of electrostatic potential redistribution, which resembles those in their co-crystals with Ni (OEP) (OEP is the dianion of octaethylporphyrin).

Heating the solution of fullerenes (C_{60} or C_{70}) with $M(CO)_4$(phen) (M = W and Mo; phen = 1, 10-phenanthroline) and dibutyl maleate (dbm) in toluene results in new types of tungsten and molybdenum complexes, $M(CO)_2$(phen)(dbm)(η^2-C_{60}) (M = Mo and W) (**18** and **19**) and Mo(phen)(dbm)(η^2-C_{70}) (**20**) [33, 34]. In contrast to phosphine ligands, the nitrogen ligand could enable the strong interaction between fullerene and metal fragment, which would be conductive to the stabilization of the final complexes of fullerenes. At the same time, the introduction of the dbm group to a long alkyl chain leads to good solubility of complexes in many solvents, even better than that of fullerenes. The structures of **18** and **19** show that all the geometries of coordination are octahedrally distorted and that the metal atom binding to the

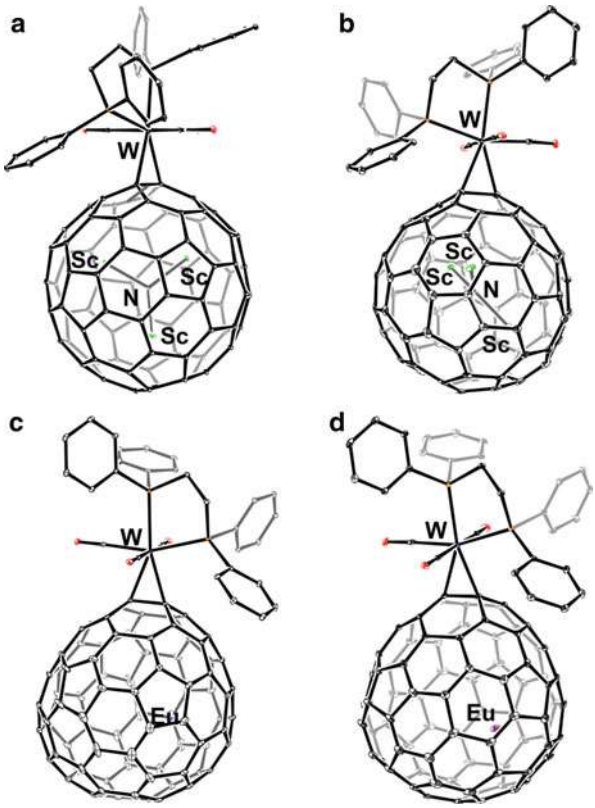

Fig. 11 Crystallographic structures of (**a**) $W(CO)_3(dppe)[\eta^2\text{-}Sc_3N@I_h(7)\text{-}C_{80}]$, (**b**) $W(CO)_3(dppe)[\eta^2\text{-}Sc_3N@D_{5h}(6)\text{-}C_{80}]$, (**c**) $W(CO)_3(dppe)[\eta^2\text{-}Eu@C_2(5)\text{-}C_{82}]$ and (**d**) $W(CO)_3(dppe)[\eta^2\text{-}Eu@C_2(13)\text{-}C_{84}]$. (From data in Refs. [31, 32]). Only the major positions for encapsulated species are shown and the hydrogen atoms are omitted for clarity

[6, 6]-bond on the fullerene is almost coplanar with the two CO groups and phen (Fig. 12).

The formation of a metal complex of fullerenes can usually be achieved using zero-valent metal. Metal ionic (such as Mn(-I), Ni(II) and Co(II)) clusters are able to directly coordinate with fullerenes. The reaction of $[Mn(\text{-I})(CO)_5]^-$ with C_{60} yields the first fullerene complex in the negative oxidation state $[Mn(Co)_4(\eta^2\text{-}C_{60})]^-$ [35]. The reduction of the Ni(II)(dppp)Cl_2 (dppp = 1,3-bis(diphenyphosphino) propan) and C_{60} with sodium fluorenone in o-dichlorobenzene results in Ni(II) (dppp)$(\eta^2\text{-}C_{60})$ (**20**). The IR results show a slight shift to lower frequencies at 1416 cm^{-1} compared to C_{60}, which is probably due to a π back-donation. The results indicate that both the C_{60} and metal in the complex have neutral states consistent with the EPR-silent signal. Figure 13 shows the crystallographic structure of **20** and it reveals that the Ni atom coordinates through η^2-coordination to the [6, 6]-bond of C_{60}, forming Ni–C bonds with the lengths of 1.951 Å (Ni-C1) and 1.948 Å (Ni-C2), which are the shortest M–C bonds among the known η^2 complexes of fullerenes. A similar elongation of the coordinated C–C bond is observed as a

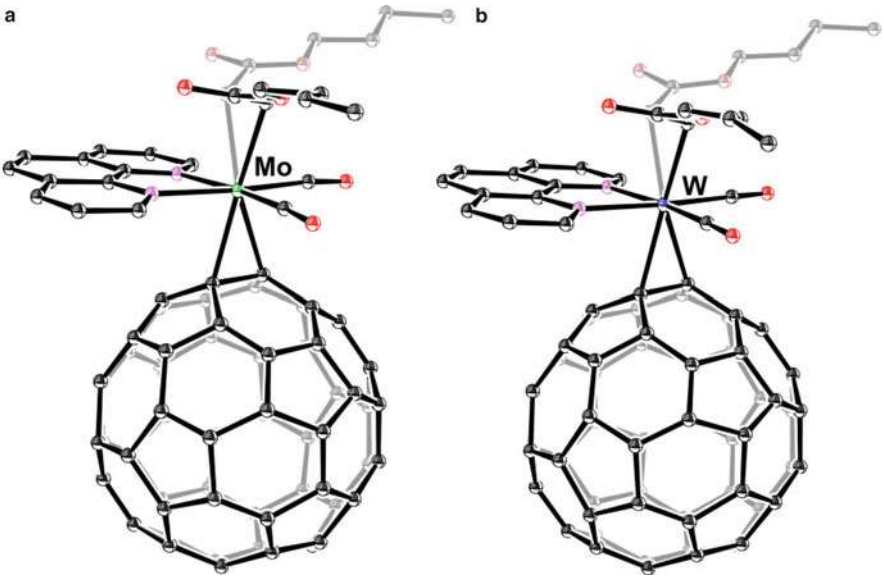

Fig. 12 Crystallographic structures of (**a**) $Mo(CO)_2(phen)(dbm)(\eta^2\text{-}C_{60})$ and (**b**) $W(CO)_2(phen)(dbm)(\eta^2\text{-}C_{60})$. (From data in Ref. [34]). The hydrogen atoms in complexes are omitted for clarity

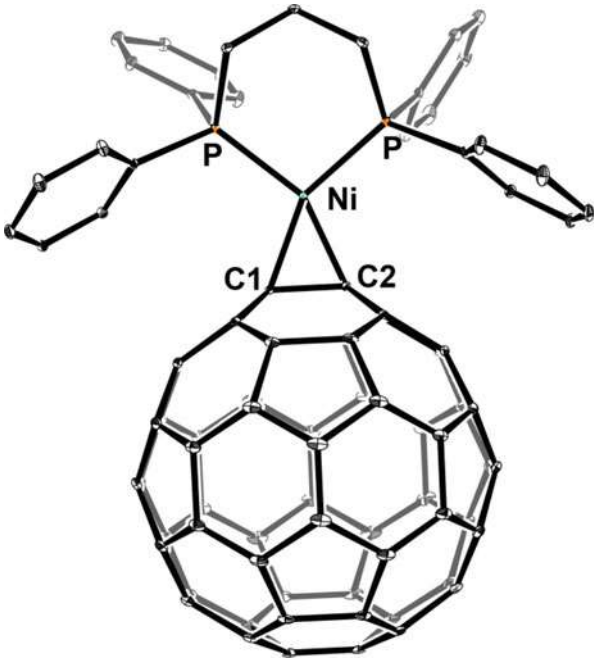

Fig. 13 Crystallographic structure of Ni(II)(dppp)$(\eta^2\text{-}C_{60})$. Hydrogen atoms in the complex are omitted for clarity. (From data in Ref. [35])

result of the metal-to-C_{60} π back-donation [36]. The mixture of Co(II)(dppe)Cl_2 or Co(II)(dppf)Br_2 (dppf = 1,1′-bis-(diphenylphosphino)ferrocene) with C_{60} that contains a few drops of benzonitrile under a similar reduction leads to two complexes with paramagnetic metal centers: Co(dppe)(C_6H_5CN)(η^2-C_{60}) (**21**) and Co(dppf)(C_6H_5CN)(η^2-C_{60}) (**22**) [37]. The cobalt atoms are coordinated by [6,6]-bonds of C_{60} with two phosphorus atoms and one nitrogen atom, leading to the geometries of distorted square pyramid for C_2CoP_2 units (Fig. 14). The IR and visible−NIR spectra of **21** and **22** indicate the neutral state of fullerenes and zerovalent cobalt atoms Co^0 with a low-spin (S = 1/2) state.

In addition to the above metal complexes, there are other metals that could react with fullerenes to form η^2-fashion complexes. Although the first determination of the crystallographic structure of C_{60} is performed on its derivative with the osmium complex OsO_4(pyridine)$_2$, its structure shows two carbon atoms on the fullerene surface that are each linked to one oxygen atom, rather than to the osmium atom [38]. A similar situation is also found in the complex $C_{60}S_2Fe_2(CO)_6$, in which two sulfur atoms act as bridges linking the metal complex and the fullerene [39]. The first mononuclear η^2-C_{60} complex of osmium has been obtained by refluxing the mixture of C_{60}, $OsH_2(CO)(PPh_3)_3$ and ^{t}BuNC in toluene; the X-ray results show the molecule Os(CO)(^{t}BuNC)$(PPh_3)_2$(η^2-C_{60}) (**23**) has an ordered C_{60} moiety with a normal olefin-type π-coordination to the osmium atom (Fig. 15) [40].

The fullerene complex with the Group IVB metals, $Cp_2Ti(\eta^2$-$C_{60})$ (Cp = cyclopentadienyl), is prepared through the reaction of the bis(trimethylsilyl)

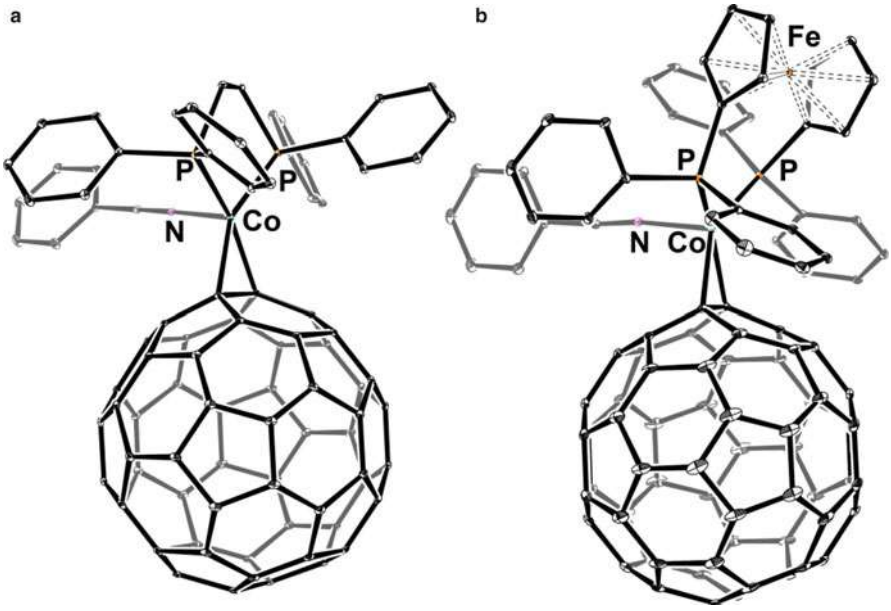

Fig. 14 Crystallographic structures of (**a**) Co(dppe)(C_6H_5CN)(η^2-C_{60}) and (**b**) Co(dppf)(C_6H_5CN)(η^2-C_{60}). (From data in Ref. [37]). Hydrogen atoms in the complex are omitted for clarity

acetylene complex $Cp_2Ti(\eta^2\text{-}Me_3SiC_2SiMe_3)$ with an equimolar amount of C_{60}. The molecular structure demonstrates that the influence of coordination on the geometry of the fullerene is similar to that seen in other complexes. However, treatment of C_{60} with the Group IVB cluster Cp_2ZrHCl yields intermediates $[Cp_2ZrCl]_nC_{60}H_n$ and finally results in the hydrometalation of the fullerene after the hydrolysis of the intermediates (Scheme 3) [41] (Fig. 15).

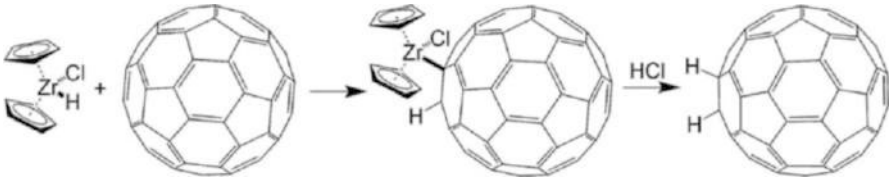

Scheme 3 The reaction of C_{60} with Cp_2ZrHCl

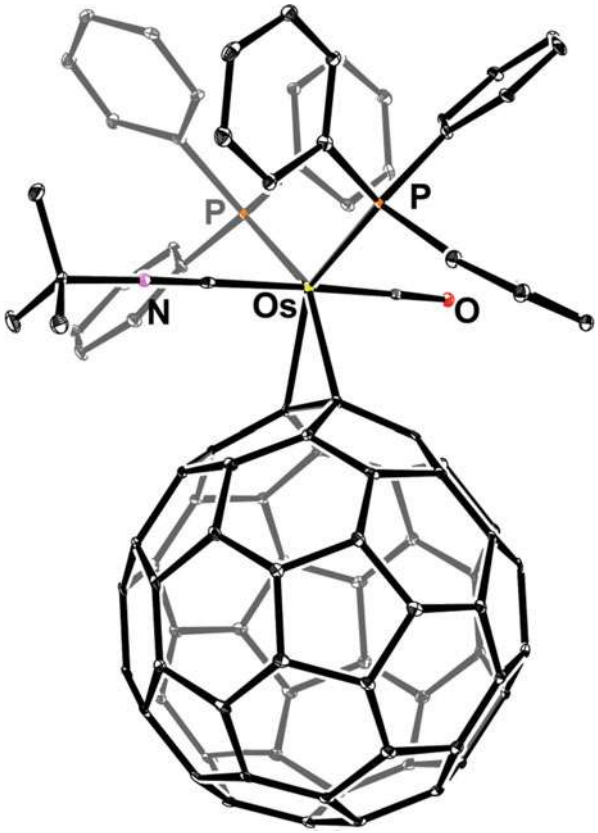

Fig. 15 Crystallographic structure of $Os(CO)(^tBuNC)(PPh_3)_2(\eta^2\text{-}C_{60})$. Hydrogen atoms in the complex are omitted for clarity. (From data in Ref. [40])

η^5-Fashion Metal Complexes of Fullerenes

The η^5-fashion coordination of pristine fullerenes has not yet been observed. However, the functionalization of fullerenes with five methyl/phenyl groups makes the pentagon ring isolated by addition groups on the cage possess similar reactivity with cyclopentadiene and shows the reactivity with metal elements in Groups 6–11 as well as Group 13. For example, the first pentahaptofullerene metal complex characterized by crystallography is (η^5-$C_{60}Ph_5$)Tl (**24**) [42]. Its structure shows that the thallium atom lies in the cavity created by the five phenyl groups and that it is equally attached to the five carbons highlighted with red color in Fig. 16 (η^5-coordination) with an average bond length of 2.87 Å.

Binuclear Metal Complexes of Fullerenes

The first multinuclear complex of fullerenes has been prepared through the reaction of C_{60} with an equimolar amount of the binuclear iridium cluster Ir_2Cl_2(l,5-COD)$_2$ (COD = cyclooctadiene) in benzene at room temperature [43]. The crystalline product **25** suitable for X-ray characterization was obtained by diffusing a benzene solution of C_{60} into an Ir_2Cl_2(l,5-COD)$_2$ benzene solution. Figure 17 shows two Ir_2Cl_2(l,5-COD)$_2$ clusters binding to the opposite sites of the C_{60} framework, while two iridium atoms in the metal cluster, which are linked by two Cl atoms, coordinate to two [6,6]-bonds on one hexagon. In the Ir_2Cl_2(l,5-COD)$_2$ fragment in **25**, the $IrCl_2Ir$ unit has a butterfly configuration, the Ir–Cl distances range from 2.398 Å to

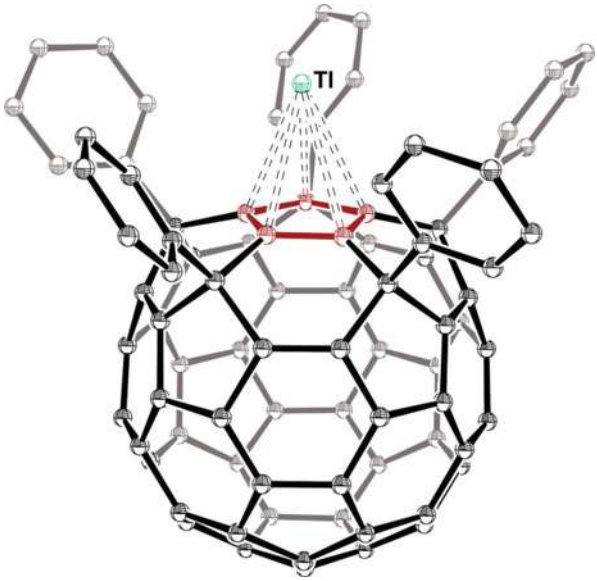

Fig. 16 Crystallographic structure of (η^5-$C_{60}Ph_5$)Tl. (From data in Ref. [42]). The coordinated pentagon ring is highlighted with red color and hydrogen atoms in the complex are omitted for clarity

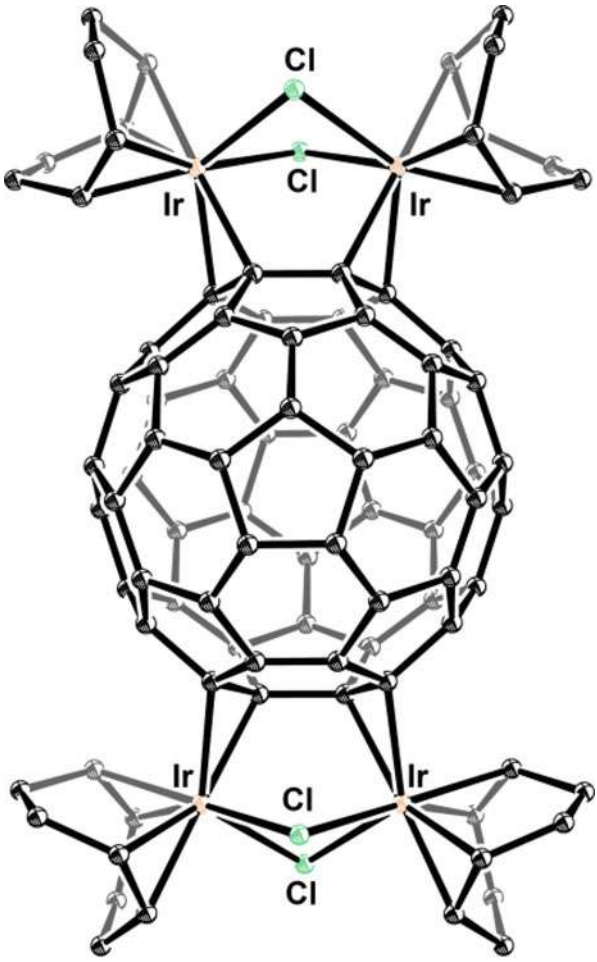

Fig. 17 Crystallographic structure of $[Ir_2Cl_2(l,5\text{-}COD)_2]_2(\eta^2{:}\eta^2\text{-}C_{60})$. (From data in Ref. [43]). Hydrogen atoms in the complex are omitted for clarity

2.552 Å, and the Ir–Ir and the Cl–Cl distances are 3.465 and 3.170 Å, respectively. The angles of Ir–Cl–Ir are 85.56° and 92.13°. The whole complex of $[Ir_2Cl_2(l,5\text{-}COD)_2]_2(\eta^2{:}\eta^2\text{-}C_{60})$ has a C_{2h}-point-group symmetry.

Treatment of C_{60} with stoichiometric amounts of $[Cp^*Ru(\mu\text{-}H)_2]_2$ and $[Cp^*Ru(\mu\text{-}Cl)_2]_2$ leads to a complex $Ru_2Cp^*_2(\mu\text{-}H)(\mu\text{-}Cl)(\eta^2{:}\eta^2\text{-}C_{60})$ (**26**). When the amount of $[Cp^*Ru(\mu\text{-}Cl)_2]_2$ is increased twice, a complex $Ru_2Cp^*_2(\mu\text{-}Cl)_2(\eta^2{:}\eta^2\text{-}C_{60})$ (**27**) was obtained along with **26**, the structures of which are determined through crystallography [44]. Figure 18 shows the structures of **26** and **27**. The complex **26** has two Ru atoms bound to two adjacent [6] junctions of the C_{60} molecule. A hydrogen and a chlorine act as bridges, separately linking two Ru atoms. The Ru–Ru distance is as short as 2.955 Å, forming the Ru–Ru single bond. In contrast to **26**, the presence of two chlorine atoms in **27** results in the metal atoms being further away from each other.

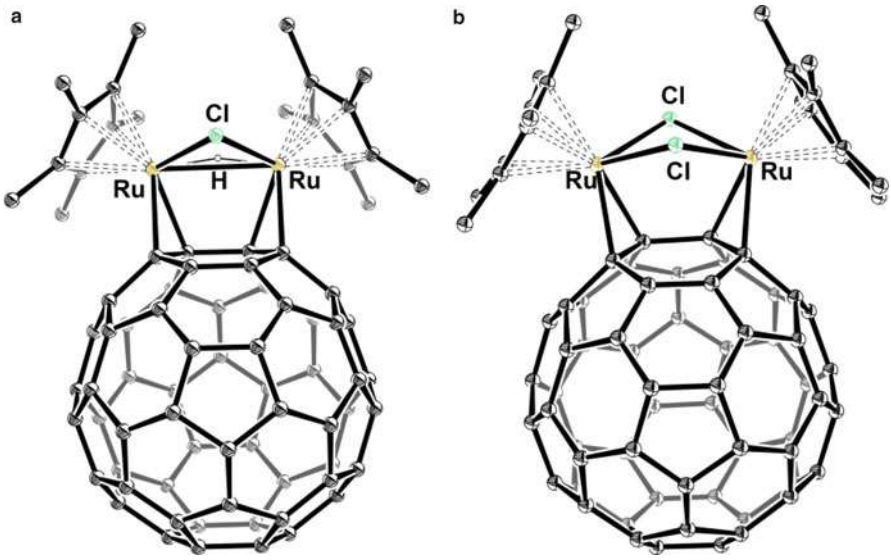

Fig. 18 Crystallographic structures of $Ru_2Cp^*_2(\mu\text{-H})(\mu\text{-Cl})(\eta^2{:}\eta^2\text{-}C_{60})$ and $Ru_2Cp^*_2(\mu\text{-Cl})_2(\eta^2{:}\eta^2\text{-}C_{60})$. (From data in Ref. [44]). Hydrogen atoms in the complex are omitted for clarity

A similar M–M single bond is also observed in complex $Re_2H_8(PMe_3)_4(\eta^2{:}\eta^2\text{-}C_{60})$, which is prepared through the addition of an equimolar polyhedroid-containing $Re_2H_8(PMe_3)_4$ to a solution of C_{60} in benzene [26]. The Re–Re distance is unambiguously determined to be 2.89 Å, which is comparable with a single-bond distance, while the positions of the metal hydride atoms cannot be ascertained. The IR, fast atom bombardment mass spectrometry (FAB MS) and NMR results indicate that the final product is the polyhedroid-containing complex of fullerene $Re_2H_8(PMe_3)_4(\eta^2{:}\eta^2\text{-}C_{60})$.

Trinuclear Metal Complexes of Fullerenes

Heating the mixture of the trinuclear cluster $Os_3(CO)_{11}(Men)$ and the equimolar amount of C_{60} at 80 °C for 5 min leads to the first trinuclear metal complex of fullerene. The product $Os_3(CO)_{11}(\eta^2\text{-}C_{60})$ (**28**) was purified by preparative thin-layer chromatography at −15 °C. $Os_3(CO)_{10}(MeCN)(\eta^2\text{-}C_{60})$ (**29**), $Os_3(CO)_{10}(PPh_3)(\eta^2\text{-}C_{60})$ (**30**), and $Os_3(CO)_9(PPh_3)(\eta^2\text{-}C_{60})_2$ (**31**) are obtained under similar reaction conditions, and their structures have been confirmed by spectroscopic data (^1H and ^{13}C NMR, IR). Interestingly, there is a relationship to convert under certain conditions among the complexes **28**–**31** (Scheme 4). The CO ligand in the complexes can be readily removed by Me_3NO and then replaced with either MeCN or PPh_3 to convert a related complex. Complexes **28** and **29** can be converted to each other through decarbonylation with a Me_3NO and MeCN reagent at −50 °C or by

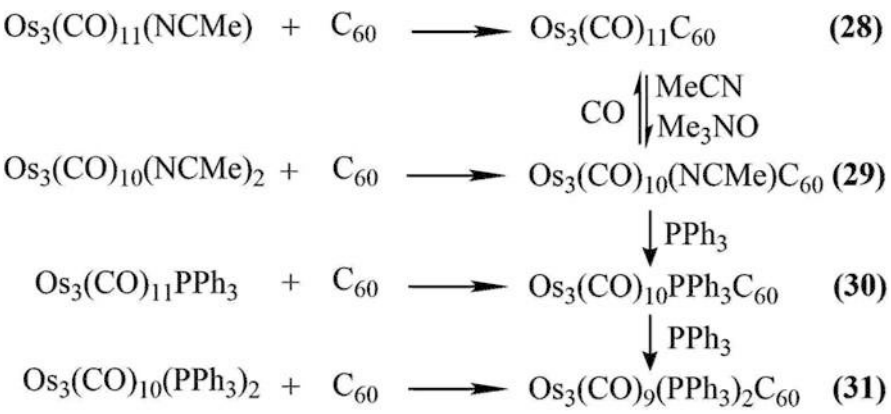

Scheme 4 Reactions of trinuclear osmium clusters with C_{60}

exposing **29** to CO gas. Complex **29** could react with PPh_3 to afford **30** and then continue further reaction with PPh_3 to give **31** [45].

Although the theoretical calculations prove the possibility of forming a η^6-coordination to one hexagon of fullerene, the experimental results of studies on the η^6–C_{60} complex have not been observed to date. The failure to form a stable η^6–C_{60} complex should be attributed to the weak orbital overlap that occurs during coordination. In actuality, the fullerene reacts more like cyclohexatriene than benzene, with trinuclear metallic clusters and a tendency to coordinate with fullerenes in a μ_3-η^2:η^2:η^2-C_{60} fashion [46]. The thermolysis of $Os_3(CO)_{10}(MeCN)(\eta^2\text{-}C_{60})$ affords the trinuclear complex $Os_3(CO)_9(\mu^3\text{-}\eta^2\text{:}\eta^2\text{:}\eta^2\text{-}C_{60})$, which has a yield of 23%. This has also been obtained from the reaction of $Os_3(CO)_{10}(MeCN)_2$ with C_{60} with a higher yield (32%) [47]. The first structural elucidation of the μ_3-η^2:η^2:η^2-C_{60} coordination is conducted on $Ru_3(CO)_9C_{60}$ (**32**), which is prepared by the reaction of $Ru_3(CO)_{12}$ and C_{60} in the mixed solvent of n-hexane and chlorobenzene [48]. Single-crystal XRD analysis of this compound shows that the triangular plane of the Ru_3 unit is parallel to a six-membered ring on the C_{60} carbon cage, and each Ru is coordinated with the C–C double bond one the six-membered ring (Fig. 19). $Re_3(\mu\text{-}H)_3(CO)_{11}(NCMe)$ can react with C_{60} to produce $Re_3(\mu\text{-}H)_3(CO)_9(\mu_3\text{-}\eta^2\text{:}\eta^2\text{:}\eta^2\text{-}C_{60})$, and the CO ligands in the complex could be replaced by other groups to form $Re_3(\mu\text{-}H)_3(CO)_8(L)(\mu_3\text{-}\eta^2\text{:}\eta^2\text{-}C_{60})$ (L = PPh_3 or $CNCH_2Ph$) complexes [49]. Similarly, the CO groups in trinuclear complexes, $Ru_3(CO)_9C_{60}$ and $Os_3(CO)_9C_{60}$, can also be substituted by phosphonic ligands, forming $M_3(CO)_{9\text{-}n}(PPh_3)_n$ (M = Ru and Os; n = 1 and 2) or $Os_3(CO)_{9\text{-}n}(PMe_3)_n$ (n = 1–3) [50–52].

The above examples show that the ligands in trinuclear complexes can be replaced or partially removed. It is more interesting that some unique ligands can also be inserted into M_3 units, breaking the M–M bond. Accordingly, this would induce the change in the coordination bond between metal and fullerene from a π bond to a σ bond. Heating the $Os_3(CO)_8(CNR)(\mu_3\text{-}\eta^2\text{:}\eta^2\text{:}\eta^2\text{-}C_{60})$ (R = $CH_2C_6H_5$) or its photolysis in the presence of an excess of benzyl isocyanide give $Os_3(CO)_8(CNR)$

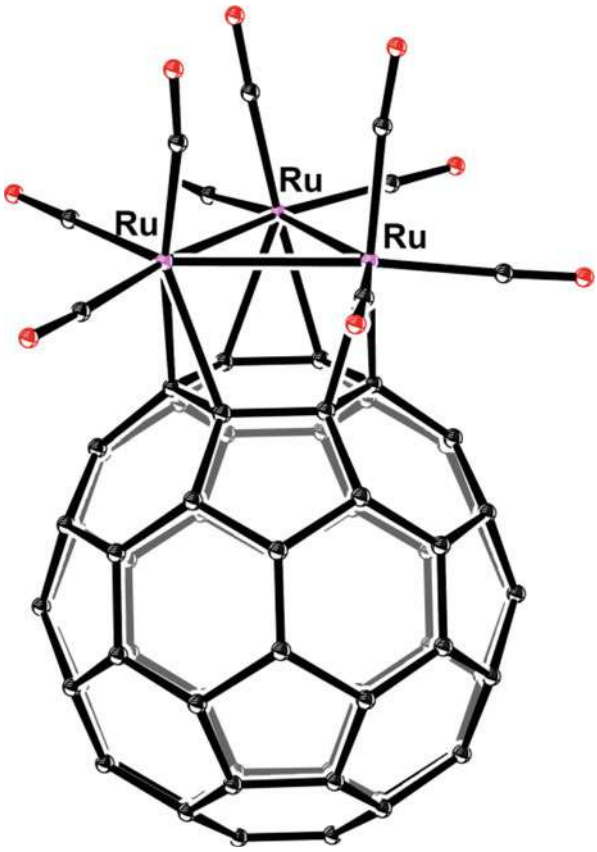

Fig. 19 Crystallographic structure of $Ru_3(CO)_9(\mu^3\text{-}\eta^2\text{:}\eta^2\text{:}\eta^2\text{-}C_{60})$. (From data in Ref. [48])

(μ_3-η^2:η^2:η^2-C_{60}) (R = $CH_2C_6H_5$) (**33**) and the isocyanide-inserted product $Os_3(CO)_9(\mu_3\text{-}CNR)(\mu_3\text{-}\eta^1\text{:}\eta^2\text{:}\eta^1\text{-}C_{60})$ (**34**), respectively. Their structures are given in Fig. 20a, b. The continued reaction of **33** with CNR in chlorobenzene at 80 °C leads to two isomeric complexes with a mixed coordination fashion of η^1 and η^2 [53]. The CNR group inserts into an Os–Os bond, forming a four-electron donor μ_3–η^2 bond mode with three osmium atoms and thereby inducing the deformation of the Os_3 plane. The two isomers of $Os_3(CO)_8(CNR)(\mu_3\text{-}CNR)(\mu_3\text{-}\eta^1\text{:}\eta^2\text{:}\eta^1\text{-}C_{60})$ (**35a** and **35b**) formed by the reaction are distinguished by the position of the CNR group outside the Os_3 unit. The CNR group coordinates to the central Os metal at the equatorial position in the first isomer (**35a**) (Fig. 20c), and one terminal Os metal in the second isomer (**35b**) (Fig. 20d). The crystallographic analysis of **35a** shows that each of the two terminal Os atoms is connected to one carbon atom on a C_6-ring of C_{60} with bond lengths of 2.25 and 2.26 Å. At the same time, the central Os atom at the equator binds to the [6, 6]-bond on the same C_6-ring with an average π-bond length of 2.42 Å, indicating that the complex has a μ_3-η^1:η^2:η^1 mixed coordination mode. It is obvious that the orbital reorganization of coordination is influenced by

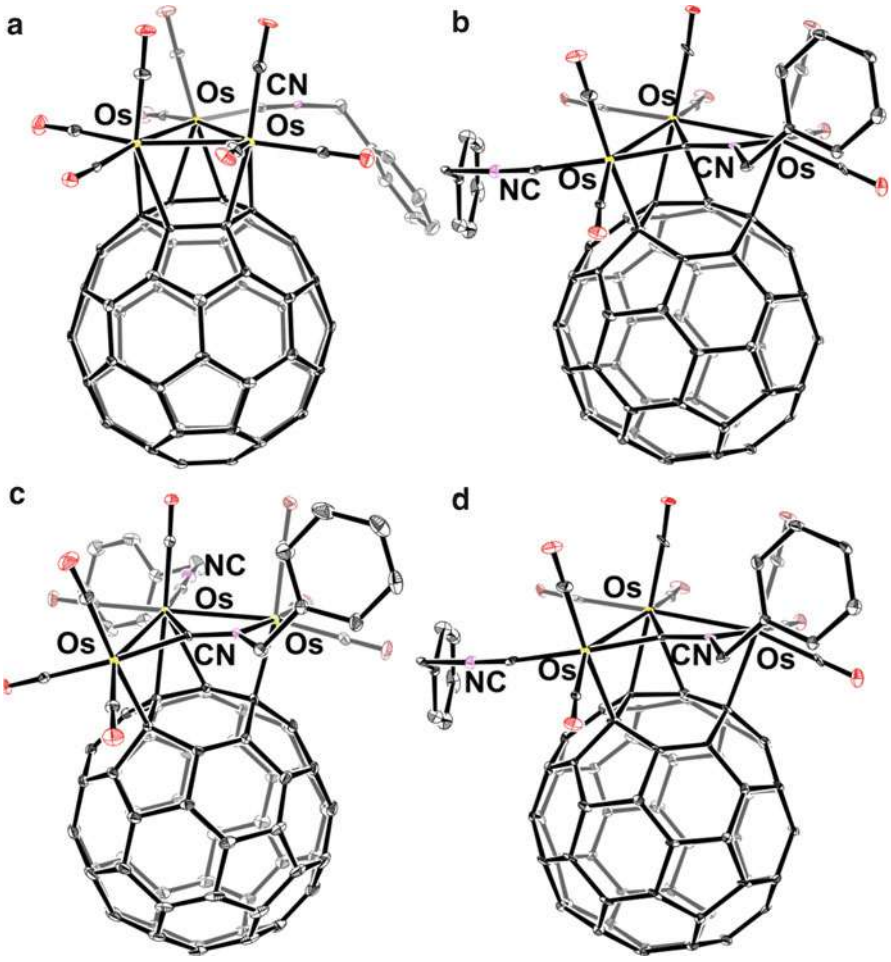

Fig. 20 Crystallographic structures of (**a**) $Os_3(CO)_8(CNR)(\mu_3\text{-}\eta^2\text{:}\eta^2\text{:}\eta^2\text{-}C_{60})$, (**b**) $Os_3(CO)_9(\mu_3\text{-}CNR)(\mu_3\text{-}\eta^1\text{:}\eta^2\text{:}\eta^1\text{-}C_{60})$ and two isomers of $Os_3(CO)_8(CNR)(\mu_3\text{-}CNR)(\mu_3\text{-}\eta^1\text{:}\eta^2\text{:}\eta^1\text{-}C_{60})$ (**c**) **35a** and (**d**) **35b**. (From data in Refs. [52, 53])

the inserted CNR group, which is rationalized through the electron effect. The inserted four-donor CNR group breaks one Os–Os bond with two electrons and destroys the d–π interaction of the Os–C_2 bond with the remaining two electrons, thus forming two Os–C σ bonds.

The CO group in two isomers can be replaced with ligands similar to those in the trinuclear Os and Ru complexes. For example, **35b** can undergo decarbonylation reaction with Me_3NO/MeCN and then combine with one PPh_3 ligand to a terminal osmium atom. Interestingly, this will lead to the further reorganization of coordination of three osmium atoms for $Os_3(CO)_8(CNR)(\mu_3\text{-}\eta^2\text{:}\eta^2\text{:}\eta^2\text{-}C_{60})$. This shows that the bonding mode changes from $\mu_3\text{-}\eta^1\text{:}\eta^2\text{:}\eta^1\text{-}C_{60}$ in the original **35b** to $\mu_3\text{-}\eta^1\text{:}\eta^1\text{:}\eta^2\text{-}C_{60}$. Meanwhile,

PPh_3 ligands are also easily replaced by CO ligands, so this substitution can achieve the reversible conversion of two bonding modes. When a PMe_3 ligand with lower steric hindrance is selected to replace CO in **35b**, it can replace the CO group near the central Os atom at the equatorial position, which indicates that the metal atoms coordinated with the phosphine ligand tend to form a π-interaction with the carbon atoms of the carbon cage. As the reaction temperature increases, $Os_3(CO)_8(CNR)(\mu_3\text{-}\eta^2\text{:}\eta^2\text{:}\eta^2\text{-}C_{60})$ ($CNR = CH_2C_6H_5$) continually reacts with PPh_3 and the coordinated CO group decreases, forming $Os_3(CO)_6(CNR)(\mu_3\text{-}CNCH_2C_6H_4)(PPh_3)(\mu\text{-}PPh_2)(\mu\text{-}\eta^2\text{:}\eta^2\text{-}C_{60})$ compounds. Its structure shows that one Os–Os bond is broken in the Os_3 unit. One osmium atom is released to form a five-membered ring with the inserted CNR group, while the other two osmium atoms are connected with C_{60} in the form of $\mu\text{-}\eta^2\text{:}\eta^2\text{-}C_{60}$ [54].

Treatment of $(\mu\text{-}H)_3Re_3(CO)_{11}(NCMe)$ with a carbide cluster metallofullerene $Sc_2C_2@C_{3v}(8)\text{-}C_{82}$ in chlorobenzene at reflux for 3.5 h results in $(\mu\text{-}H)_3Re_3(CO)_9(\eta^2\text{:}\eta^2\text{-}Sc_2C_2@C_{3v}(8)\text{-}C_{82})$ (**36**) [55]. The overall structure of the metal fragment is similar to that in $(\mu\text{-}H)_3Re_3(CO)_9(\mu_3\text{-}\eta^2\text{:}\eta^2\text{:}\eta^2\text{-}C_{60})$ [49], and the metal carbide Sc_2C_2 is slightly compressed compared to the parent metallofullerene caused by the elongation of the C_{82} cage and the charge-density redistribution that occurs after the complexation (Fig. 21).

It has been thought to be full of challenges to let three and even more six-member rings involved together in the coordination for a long time. Recently, a set of complexes of C_{60} containing multiple trinuclear clusters have been prepared under a more drastic solvothermal method. The reactions of C_{60} with Cu_2O and fluorocarboxylic/dicarboxylic acid under solvothermal conditions in aromatic solvents have been examined, and crystals for four copper complexes of C_{60} (**37**–**40**) found in the final reaction mixtures, which are suitable for single-crystal XRD, were obtained. The results show that every three copper atoms together form a triangular Cu_3 unit, and then the unit coordinates to a hexagon on the fullerene with a $Cu_3\text{-}[(\mu_3\text{-}\eta^2\text{:}\eta^2\text{:}\eta^2)\text{-}C_{60}]$ structure. Noteworthily, the copper atoms don't bond to each other but are linked together through bridging of ligands. The resulting four complexes are $[Cu_3(C_3F_7COO)_3(H_2O)_3]_2C_{60}$ (**37**), $[Cu_3(C_3F_7COO)_3(H_2O)](\mu_2\text{-}H_2O)[Cu_3(\text{-}C_3F_7COO)_3(H_2O)\text{-}\ (C_3F_7COOH)]_2[Cu_3(C_3F_7COO)_2(H_2O)_4]C_{60}$ (**38**), $[Cu_{24}(\text{-}C_5F_6O_4)_{12}(\mu_2\text{-}H_2O)_{12}]C_{60}$ (**39**), and $[Cu_{24}(C_5H_6O_4)_{12}(HOOCC_3H_6COOH)_6]C_{60}$ (**40**) [56]. Complex **37** is a bis-adduct of fullerene in which two Cu_3 units coordinate to two six-membered rings at the opposite (Fig. 22a). Doubling the concentration of heptafluorobutyric acid leads to a complex **38** containing four Cu_3 units (Fig. 22b). In complexes **39** and **40**, the eight Cu_3 units coordinate to eight alternate (but not adjacent) hexagons on the fullerene, and they wonderfully form a large Archimedean rhombicuboctahedron coated on the C_{60} surface to construct a $C_{60}@Cu_{24}$ core−shell structure (Fig. 20c, d). The twenty-four Cu atoms bind to twenty-four [6] bonds, while the remaining six [6] bonds which form an octahedral vertex are vacant. The carboxylate ligands synergistically bridging the metal atoms play a key role in the formation of complexes. In comparison with the non-fluorinated carboxylate, the poorly coordinated fluorocarboxylic acid is more favorable to the association of C_{60} and Cu^+.

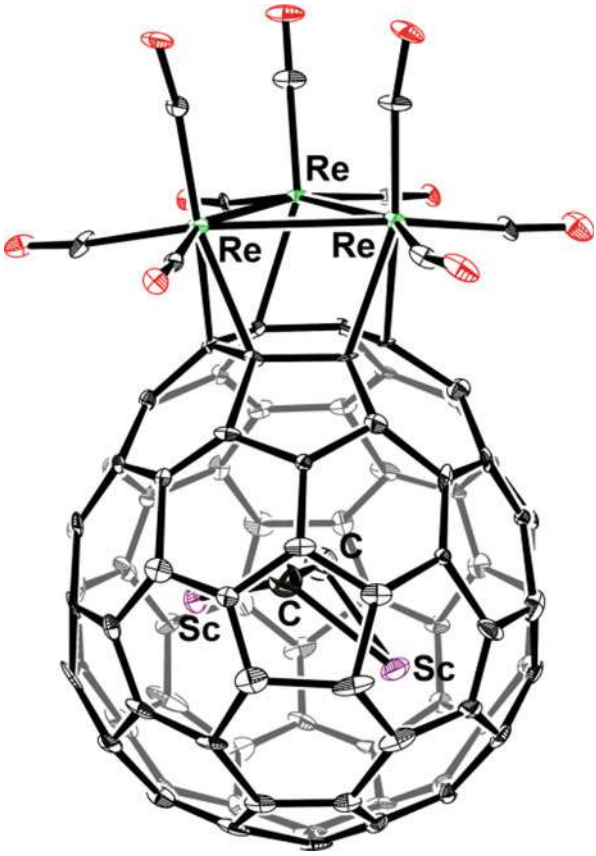

Fig. 21 Crystallographic structure of $Re_3(CO)_9(\eta^2{:}\eta^2{:}\eta^2\text{-}Sc_2C_2@C_{3v}(8)\text{-}C_{82})$. (From data in Ref. [55])

Tetra-, Penta-, and Hexanuclear Metal Complexes of Fullerenes

As for the tetranuclear metal complex of fullerene, only one case has been reported to date which is found in the dimer of fullerene bridged with a metal cluster. The structure will be discussed in detail in the next section. The coordination of higher nuclear metal clusters with C_{60} is limited to the penta- and hexanuclear metal complexes of fullerenes. The pentanuclear metal complexes $Ru_5C(CO)_xL(\mu_3\text{-}\eta^2{:}\eta^2{:}\eta^2\text{-}C_{60})$ (L = PPh_3, dppe and dppf) are obtained through the reaction of $Ru_5C(CO)_{15}$ with $C_{60,}$ followed by the addition of PPh_3, dppe or dppf [57, 58]. Similarly, the hexanuclear metal clusters Ru_6C, $PtRu_5C$, and Rh_6 can react with C_{60} to produce related complexes [59]. Their structures show the coordinate fashions to C_{60} for these clusters are the same as those in trinuclear clusters which has the $\mu_3\text{-}\eta^2{:}\eta^2{:}\eta^2\text{-}C_{60}$ coordination mode (Fig. 23). $Ru_6C(CO)_{17}$ and C_{60} were refluxed in chlorobenzene, followed by the addition of 1,2-bis(dipheylphosphino)methane

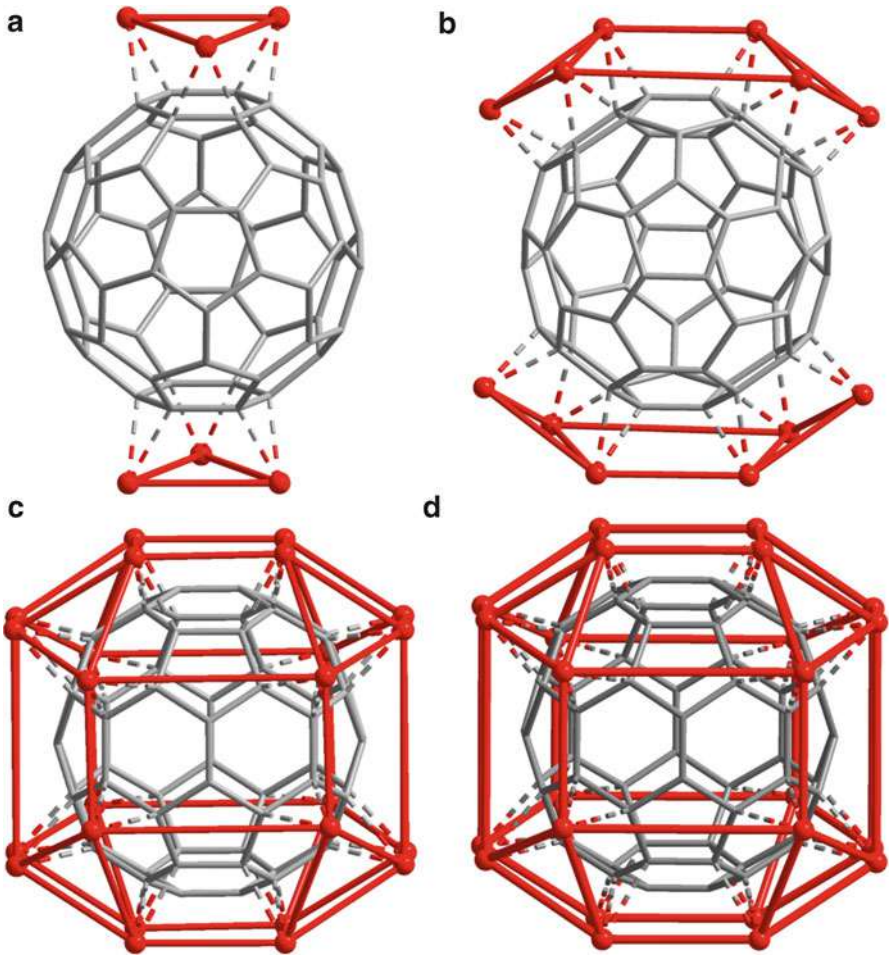

Fig. 22 Structures of copper complexes of C_{60}: (**a**) **37**, (b) **38**, (**c**) **39** and (**d**) **40**. Only the fullerene (gray) and Cu atoms (red) are shown for clarity. (From data in Ref. [56])

(dppm), affording $Ru_6C(CO)_{12}(dppm)(\mu_3\text{-}\eta^2\text{:}\eta^2\text{:}\eta^2\text{-}C_{60})$ [57]. In these multi-nuclear complexes, the transformation of coordination fashion between metal clusters and C_{60} mostly occurs in $\mu\text{-}\eta^2\text{:}\eta^2\text{-}C_{60}$ and $\mu_3\text{-}\eta^2\text{:}\eta^2\text{:}\eta^2\text{-}C_{60}$ through the introduction of the ligands CO and CNR group, as mentioned above [60].

Metal Cluster-Bridged Dimerizations of Fullerenes

The interest in the complexation of metal clusters with multiple fullerenes has been increasing, however, many of these have been observed in the gas phase [61]. The first neutral bis-fullerene complexes were synthesized through the reaction

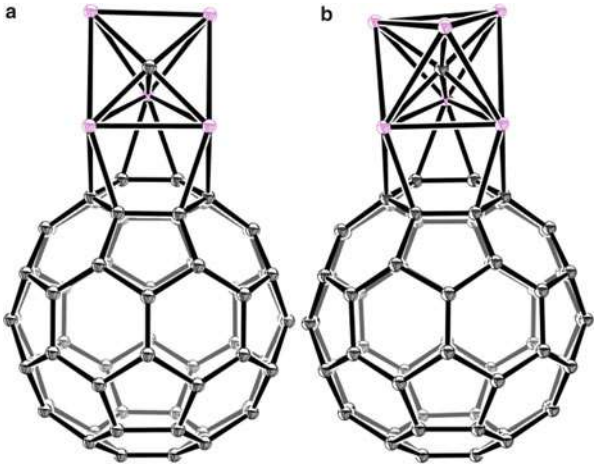

Fig. 23 Crystallographic structures of (**a**) $Ru_5C(CO)_{11}(PPh_3)(\mu_3\text{-}\eta^2\text{:}\eta^2\text{:}\eta^2\text{-}C_{60})$ and (**b**) $Ru_6C(CO)_{12}(dppm)(\mu_3\text{-}\eta^2\text{:}\eta^2\text{:}\eta^2\text{-}C_{60})$. The ligands are removed for clarity. (From data in Ref. [57])

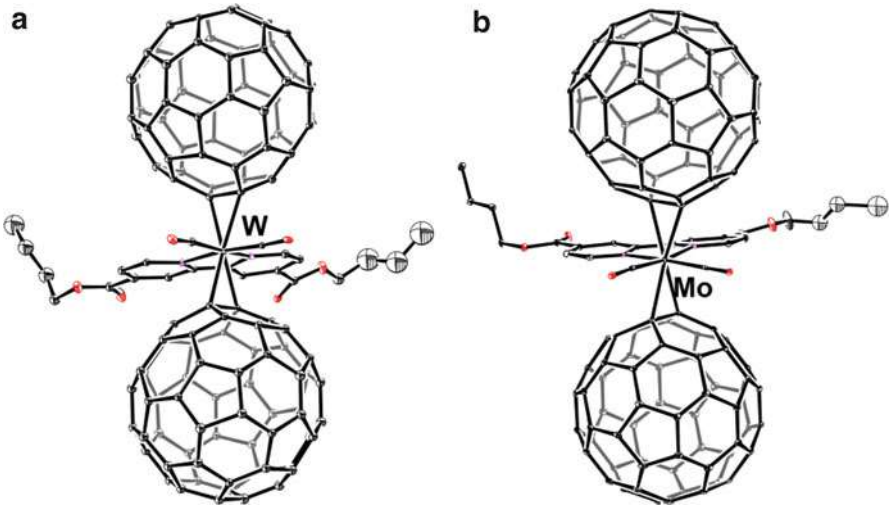

Fig. 24 Crystallographic structures of (**a**) $W(CO)_2(dbcbipy)(\eta^2\text{-}C_{60})_2$ and (**b**) $Mo(CO)_2(dbcbipy)(\eta^2\text{-}C_{60})_2$. (From data in Ref. [62]). Hydrogen atoms are removed for clarity

of $M(CO)_4(dbcbipy)$ (M = W or Mo; dbcbipy = 4,4-di(butyl carboxyl)-2,2-bipyridine) with two equivalents of C_{60} in xylene or toluene [62]. $W(CO)_2(dbcbipy)(\eta^2\text{-}C_{60})_2$ (**41**) and $Mo(CO)_2(dbcbipy)(\eta^2\text{-}C_{60})_2$ (**42**) were separated by chromatography with the yields of 24% and 26%, respectively. In these molecules, the metal atom affords an equatorial plane with two pyridine and two CO ligands, and binds to the [6] bonds on the two fullerenes, leading to a dumbbell-shaped complex (Fig. 24).

Nickel or cobalt complexes can also act like bridges linking two fullerene molecules with η^2 coordination. Unlike the reduction of fullerene to form an ionic complex with $Co(Ph_3P)_2Br_2$ [63], the addition of a few drops of benzonitrile into a solution of C_{60} and $Co(Ph_3P)_2Br_2$ that has been reduced by sodium fluorenone produces a deep-green solution. Black crystals then precipitate through the diffusion of hexane into the solution [64]. The reaction and crystal-growth process need to remain in a strictly anaerobic condition. Note that benzonitrile plays a very important role in the formation of the product. The coordination of cobalt with benzonitrile provides a twisted pentagonal pyramid environment, which is conducive to the formation of coordination bonds between the cobalt atom and the fullerenes. The structure of $[Co(Ph_3P)(C_6H_5CN)]_2(\mu_2\text{-}\eta^2\text{:}\eta^2\text{-}C_{60})_2$ (**43**) sensitive to oxygen is determined by synchrotron radiation X-ray diffraction. Figure 25a shows two neutral fullerene cages that are bridged by two asymmetric η^2-fashion Co − C bonds of 2.048–2.058 and 2.110–2.128 Å lengths, respectively; each cobalt atom also coordinates a triphenylphosphine ligand and a benzonitrile molecule, forming the geometry of a distorted pentagonal pyramid. The two fullerene cages in **43** are unusually close to each other. The center-to-center distance between the fullerene spheres is 9.696 Å, the shortest C–C contact between the two cages is 2.815 Å, and the distance between the cobalt atoms in the product is 5.308(3) Å. The magnetic properties of **43** were studied using superconducting quantum interference devices (SQUID) and EPR techniques. The EPR spectra show a strong isotropic signal with a g-factor of 2.3053 and a line width of 10.7 mT (ΔH), indicating that the zero-valent Co atoms possess a d^9-electron configuration in the S = 1/2 spin state at 298 K. The two close paramagnetic Co atoms in **43** have a strong magnetic interaction. The SQUID and EPR results also reveal that the dimer has a thermally excited triplet (S = 1) state in

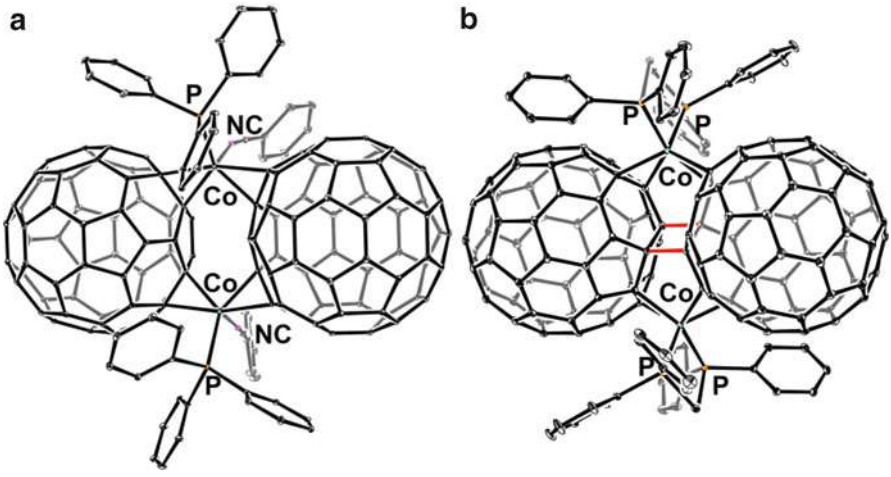

Fig. 25 Crystallographic structures of (**a**) $[Co(Ph_3P)(C_6H_5CN)]_2(\mu_2\text{-}\eta^2\text{:}\eta^2\text{-}C_{60})_2$ and (**b**) $[Co(dppe)]_2(\mu_2\text{-}\eta^2\text{:}\eta^2\text{-}C_{60})_2$. (From data in Refs. [64, 65]). Hydrogen atoms are removed for clarity

the 300–50 K range, which could transfer to a diamagnetic state due to the antiferromagnetic ordering of spins within the dimer that occur below 50 K. When a mixture of $Ni(Ph_3P)_2Br_2$ and C_{60} is reduced with zinc dust in o-dichlorobenzene at 160 °C, a dimer of the fullerene $[Ni(Ph_3P)]_2(\mu_2\text{-}\eta^2\text{:}\eta^2\text{-}C_{60})_2$ (**44**) is obtained. The EPR results reveal that the Ni atoms in **44** are diamagnetic due to a d^{10} electron configuration, which is in agreement with the results of the density functional calculations.

Remarkably, a directly bonded dimer $[Co(dppe)]_2(\mu_2\text{-}\eta^2\text{:}\eta^2\text{-}C_{60})_2$ (**45**) was synthesized by the reaction of fullerene with $Co(dppe)Cl_2$ under the reduction of zinc dust. The X-ray results show that each cobalt atom coordinates with two C–C bonds on two fullerenes and one dppe ligand, forming a distorted tetrahedral geometry. Additionally, they show two interfullerene C–C single bonds highlighted with red color in Fig. 25b with a length of 1.571 Å sandwiched between two tetrahedral units [65]. Consequently, the center-to-center distance between the fullerene spheroids in **45** is only 9.07 Å, which is shorter than the distances in dimers **43** and **44**. The dimerization is probably induced by the fact that the coordination of Co forces the two cages close enough to each other to form a bond. The IR spectrum of **45** shows a similar $F_{1u}(4)$ band at 1435 cm^{-1} to that of the neutral dimer $(C_{60})_2$, and the UV-Vis-NIR spectrum shows a band of C_{60} at 329 nm and a broad absorption at about 700 nm, which is attributable to a charge transfer from metal to fullerene. The fullerene ion signal is not observed. Accordingly, the fullerene in **45** is neutral and the coordinated cobalt atoms should have zero oxidation state, similar to those in **44**. The calculations demonstrate that the paramagnetic cobalt atoms in the dimers of C_{60} bridged by Co clusters have moderate magnetic coupling that is mediated by fullerenes through the spin-polarized π-electronic system.

Multiple-nuclear metal clusters are also able to bridge fullerenes to form the dimer. The reaction of the cluster $Ir_4(CO)_8(PMe_3)_4$ with four equivalents of C_{60} in refluxing o-dichlorobenzene (o-DCB) for 2 h, followed by treatment with 0.15 equivalents of CNR ($R = CH_2C_6H_5$) at 70 °C for 2 h, results in a dimer containing tetranuclear iridium complex, $Ir_4(CO)_3(\mu_4\text{-}CH)(PMe_3)_2(\mu\text{-}PMe_2)(CNR)(\mu\text{-}\eta^2\text{:}\eta^2\text{-}C_{60})(\mu_4\text{-}\eta^1\text{:}\eta^1\text{:}\eta^2\text{:}\eta^2\text{-}C_{60})$ (**46**) [66]. The molecular structure of **46** shows that the Ir_4 unit transforms from a tetrahedral geometry in an original cluster to a square planar geometry, and it binds to one fullerene via $\mu\text{-}\eta^2\text{:}\eta^2\text{-}C_{60}$ coordination fashion, and to the other fullerene via $\mu_4\text{–}\eta^1\text{:}\eta^1\text{:}\eta^2\text{:}\eta^2\text{-}C_{60}$ mixed fashion (Fig. 26a). The face of the unit is nearly parallel to one hexagon on the fullerene framework and is coordinated to Ir_4 in mixed fashion. Interestingly, a methyne unit participates in the coordination with four iridium atoms. The reaction of C_{60} with the deuterium complex $Ir_4(CO)_8(P(CD)_3)_4$ was conducted to determine the origin of the μ_4-CH unit. The absence of the μ_4-CH signal at δ 15.52 in the ^1H NMR spectrum of the related product implies that methyne moiety should be derived from the methyl groups in the PMe_3 ligand. The reaction of hexanuclear complex $Rh_6(CO)_9(dppm)_2(\mu_3\text{-}\eta^2\text{:}\eta^2\text{:}\eta^2\text{-}C_{60})$ with excess C_{60} in refluxing chlorobenzene results in a fullerene–metal sandwich complex $Rh_6(CO)_5(dppm)_2(CNR)(\mu_3\text{-}\eta^2\text{:}\eta^2\text{:}\eta^2\text{-}C_{60})_2$ (Fig. 26b) [59].

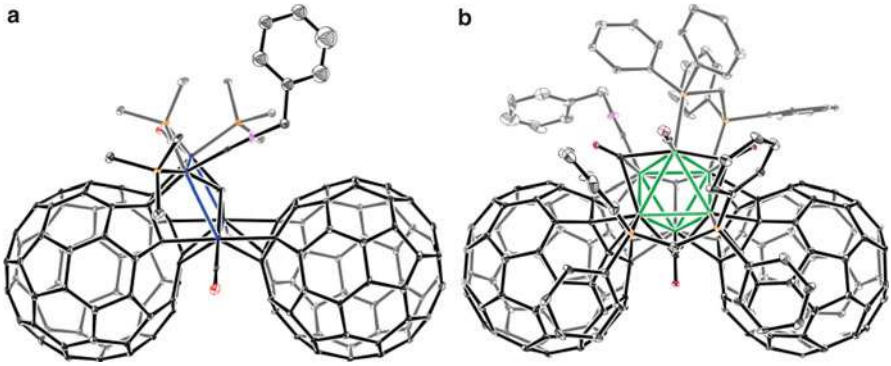

Fig. 26 Crystallographic structures of (**a**) $Ir_4(CO)_3(\mu_4\text{-}CH)(PMe_3)_2(\mu\text{-}PMe_2)(CNR)(\mu\text{-}\eta^2\text{:}\eta^2\text{-}C_{60})(\mu_4\text{-}\eta^1\text{:}\eta^1\text{:}\eta^2\text{:}\eta^2\text{-}C_{60})$ and (**b**) $Rh_6(CO)_5(dppm)_2(CNR)(\mu_3\text{-}\eta^2\text{:}\eta^2\text{:}\eta^2\text{-}C_{60})_2$. (From data in Refs. [59, 66]). The Ir_4 and Ru_6 clusters are highlighted with blue and green colors, respectively, and hydrogen atoms are removed for clarity

Organometallic Polymers of Fullerenes

Addition of the complex $Pd_2(DBA)_3{\cdot}CHCl_3$ (DBA = dibenzylacetone) into a benzene solution of C_{60} yields a black, amorphous, air-stabilized solid. In contrast to the Fagan complexes of fullerene, the solid is insoluble in common solvents and is considered to be a polymer consisting of carbon and palladium: $C_{60}Pd_n$ [67]. The composition and structure of the polymer strongly depend on the reaction conditions: $C_{60}Pd_1$ forms a one-dimensional linear polymer with alternating palladium atoms and C_{60} units in the chain, while the Pd:C_{60} ratio in the polymer increases significantly, from 1:1 to 1:3, in line with the regeneration of free C_{60} by heating the suspension of the palladium polymer $C_{60}Pd_1$ under reflux. A formation mechanism of the polymer is proposed and it shows that the one-dimensional polymer $C_{60}Pd_1$ is formed at the first stage, following which $C_{60}Pd_n$ is formed through the insertion of further palladium atoms between the polymer chains. The structure of $C_{60}Pd_3$ shows that each C_{60} atom is coordinated to six metal atoms, analogous to the structure in the hexa-adduct of fullerene $[(Et_3P)_2Pt]_6(\eta^2\text{-}C_{60})$, and each metal links two cages as seen in the dimer. The extra Pd atoms in $C_{60}Pd_n$ ($n > 3$) should be deposited on the surface of $C_{60}Pd_3$. The polymers could afford the palladium complex of fullerene $(R_3P)_2Pd(\eta^2\text{-}C_{60})$ through their reactions with organic phosphonic reagents.

A similar platinum polymer, $C_{60}Pt_n$, has also been prepared through the reaction of C_{60} with $Pt(dba)_2$ or $Pt(cod)_2$ (cod = cycloocta-1,5-diene) [68, 69]. The cleavage of carbon–platinum bonds and their change into the complexes $(\eta^2\text{-}C_{60})PtL_2$ or $C_{60}Pt$ were also conducted through their reactions with phosphines or phosphites. Other reactions of the polymers $C_{60}Pd_n$ and $C_{60}Pt_n$ with isocyanide ligands afford the organometallic complexes $(\eta^2\text{-}C_{60})M(CNR)_2$ (M = Pt and Pd; R = ^{t}Bu, 2,6-$Me_2C_6H_3$, 2,4,6-$Me_3C_6H_2$, and cyclohexyl). The further reaction of $(\eta^2\text{-}C_{60})Pt(CNR)_2$ with isocyanide

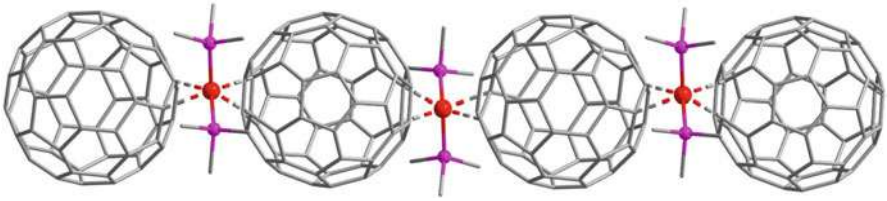

Fig. 27 Structure of linear fullerene polymer $[Ni(PMe_3)_2(\mu\text{-}\eta^2, \eta^2\text{-}C_{60})]_\infty$. (From data in Ref. [72])

ligands results in a novel complex, $(\eta^2\text{-}C_{60})(CNR)_2Pt(CNR)_2$, in which two isocyanide ligands act as bridges to link the Pt atom and the fullerene [70].

Black solid $C_{60}M_n$ (M = Pt, Pd, Ir, and Rh) has also been observed during the electroreduction of C_{60} and a transition-metal compound in a 4:1 toluene/acetonitrile (4,1 v/v) solution with tetra(n-butyl)ammonium perchlorate as the supporting electrolyte [71]. These films are insoluble in common organic solvents and deposit on the surface of the electrode. This electrochemical synthesis of redox-active films represents a significant approach to the organometallic polymer of carbon nanomaterials.

The structural determination of organometallic polymers of fullerenes has been considered to be overly challenging for a long time. A fullerene polymer $[Ni(PMe_3)_2(\mu\text{-}\eta^2, \eta^2\text{-}C_{60})]_\infty$ (**47**), which was characterized by single-crystal XRD for the first time, was obtained by the reduction of a stoichiometric mixture of $Ni(PMe_3)_2Cl_2$ and C_{60} under reduction with zinc dust in o-dichlorobenzene for 10 min at 160 °C [72]. Crystals suitable for characterization were obtained through the slow diffusion of n-hexane into a solution of **47**. The results show two nickel atoms coordinated to two [6, 6]-bonds at the opposite sides of a C_{60} framework, and each of them is bound to two fullerene units, forming a one-dimensional linear arrangement (Fig. 27). The results from optical and EPR spectra reveal that the fullerenes and nickel atoms in **47** are neutral and that the polymer has a diamagnetic state. Recently, a solvothermal method was used to prepare a fullerene polymer. Heating the mixture of C_{60}, imidazole, and CuO in a mixture of chlorobenzene and ammonia under 180 °C affords $[(CuIm)_2C_{60}]_n$ (Im = imidazolate) (**48**) with a yield of 79.8% [73]. The crystallographic structure of **48** shows two copper atoms bound to the [6,6]-bonds at opposite sides, forming a linear chain similar to that in **47**, while the fullerenes in two $(CuIm)_n$ chains are cross-linked by Cu_2Im units. Consequently, the overall polymer possesses a 2D sheet-like configuration (Fig. 28). This material shows extraordinary chemical stability and high photo-detective performance in visible region. The calculations demonstrate that its excellent photo-detective properties mostly come from the C_{60} molecule itself, while the coordination of copper significantly enhances the molecule's ability to absorb visible light.

Reduction of Fullerenes with Metal Clusters

It is well known that fullerenes exhibit electron-withdrawing properties and are facile to accept electrons from metal clusters. However, most fullerenes in complexes have a neutral state, as indicated by spectral analysis. Similar to the reduction

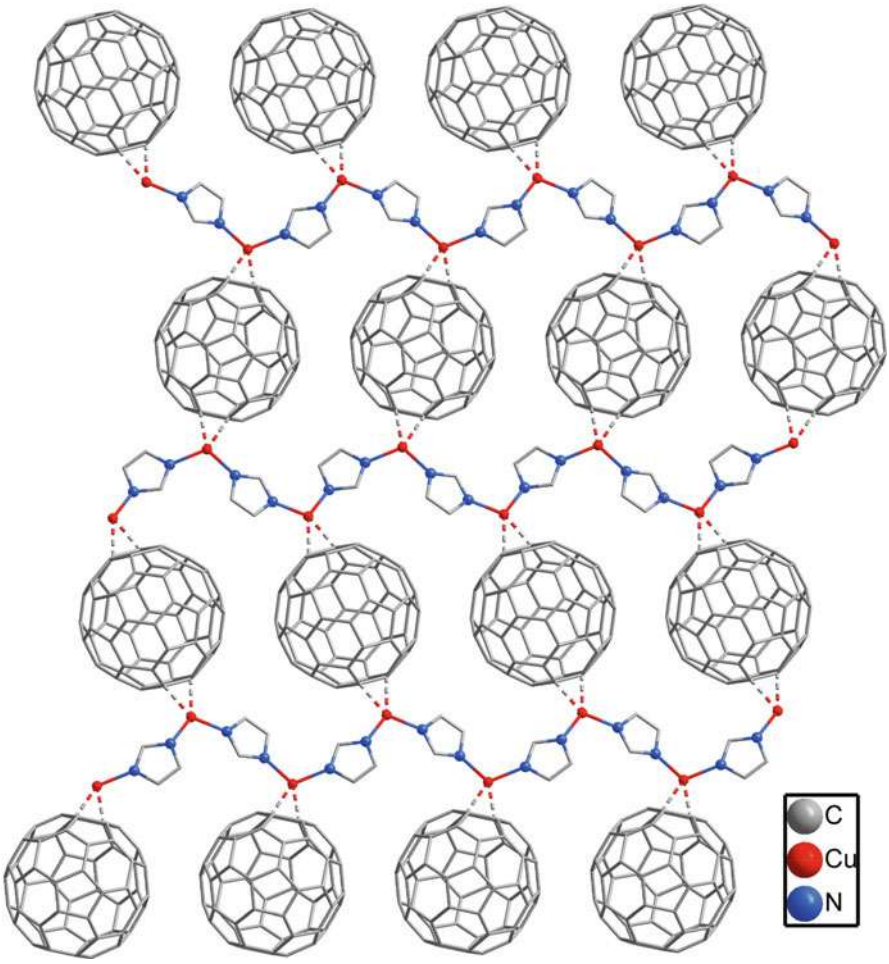

Fig. 28 Structure of fullerene polymer $[(CuIm)_2C_{60}]_n$ (Im = imidazolate). (From data in Ref. [73])

of fullerene with metals, a few metal clusters could transfer electrons to a fullerene, leading to the formation of fullerene ions instead of complexation. The typical metal-cluster reducing agents are metallocenes. $K[(Cp^*)_2Mn]$ has been regarded as one of the most potent compounds used to reduce fullerenes, and its reaction produces a trivalent ion of fullerene, rather than a complex of fullerene [74]. The obtained crystalline formation $K_3C_{60}\cdot 7(THF)$ is not superconducting; however, it will achieve the superconductive property after the solvent is removed and annealing performed at 300 °C for 12 h.

A set of ionic complexes of fullerenes has been obtained by the similar reduction with the metallocenes (Scheme 5). The spectral results demonstrate that C_{60} was reduced to $C_{60}^{\bullet-}$, C_{60}^{2-} and C_{70}^{-} by metal complexes. These salts show a typical semiconductive behavior, similar to the salts of fullerene radical ions, with a conductivity of 10^{-5}–10^{-2} $S\cdot cm^{-1}$ [75]. For example, the addition of $NiCp^*_2$ into

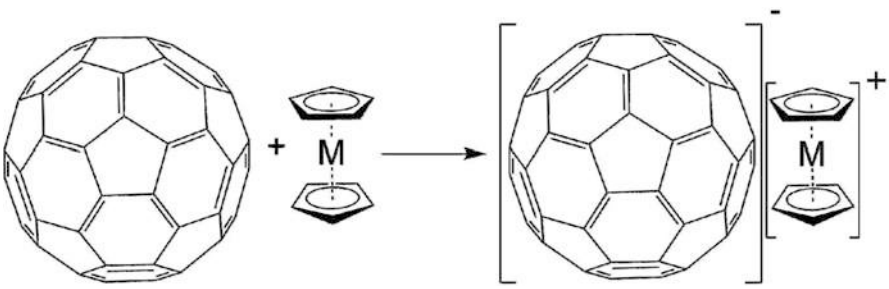

Scheme 5 Reduction reaction of fullerene with metallocenes

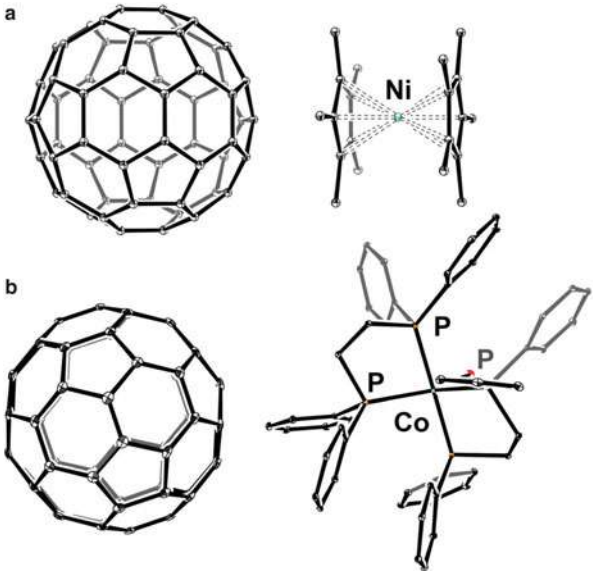

Fig. 29 Crystallographic structures of (**a**) $[NiCp^*_2]^+$ ($C_{60}^{\bullet-}$) and (**b**) $[Co(dppe)_2]^+(C_{60}^{\bullet-})$. (From data in Refs. [76, 78])

the carbon disulfide solution of C_{60} under anaerobic conditions affords product **42**. The X-ray results show that the $NiCp^*_2{}^+$ cation lies near a pentagonal ring of the C_{60} anion and that the two faces of the Cp* ring and the five-membered rings on the fullerene are nearly parallel, with an average interplanar distance of 3.17 Å (Fig. 29a), and the fullerene has a strong Jahn–Teller distortion by ionization [76]. Remarkably, the reduction of fullerene could lead to a single-bond dimerization in some complexes at low temperatures and the dimer recovers to fullerene ion by heating [77].

Co(I) and Co(II) complexes, $Co(dppe)_2Cl$ and $Co(dppe)Br_2$, could react with C_{60} under a reduction with sodium cyclopentadienylcobalt dicarbonyl ($NaCpCo(CO)_2$) and tetrakis(dimethylamino)ethylene (TDAE), respectively [78, 79]. The reaction conditions are similar to the coordination reaction between the fullerenes and Ni^{2+}/

Co^{2+} complexes. However, the reactions afford the ionic complexes $Co(dppe)_2^{+}(C_{60}^{\bullet-})$ and $[Co(dppe)_2CO]^{+}C_{60}^{\bullet-}$, instead of a coordinated compound (Fig. 29b). The reduction of C_{60} with different amounts of $Ru(bpy)_3$ (bpy = 2,2-bipyridine) in an inert atmosphere results in three salts of fullerene, which are determined to be $[Ru(bpy)_3]^{+}C_{60}^{-}$, $[Ru(bpy)_3]^{+}{}_2(C_{60}^{2-})$, and $[Ru(bpy)_3]^{2+}(C_{60}^{-})_2$ through the UV-vis-NIR spectra and element analysis [80]. The salts $[Ru(bpy)_3]^{+}C_{60}^{-}$ and $[Ru(bpy)_3]^{2+}(C_{60}^{-})_2$ have higher electric conductivities (0.020 and 0.095 $S{\cdot}cm^{-1}$, respectively) than other fullerene salts at room temperature, while the conductive mechanism is rationalized from an electron-hopping model in this immobilized redox system.

Conclusion

In summary, numerous experiments have shown that electron-deficient fullerenes resemble conjugated polyenes rather than aromatic compounds and that they are facile to accept electrons transferred from transition-metal clusters, forming complexes or ionic salts. The coordination reactions of transition metals with fullerenes and even lower-symmetry metallofullerenes exhibit very high regioselectivity and usually yield only one adduct, which is highly conducive to obtaining products in sufficient quantities allowing the study of their structures and properties. Thanks to the rapid development of crystallography, the structures of many mono- and multinuclear metal complexes, metal-bridged dimers and organometallic polymers of fullerenes have been unambiguously determined. The structures indicate that there are two major coordination modes in pristine fullerenes, namely, η^1 and η^2. The addition of metal clusters could pull the coordinated carbon atoms away from the cages, leading to the distortion and decrease of the symmetry of fullerene cages. At the same time, the optical, electrochemical, and magnetic properties of fullerenes and complexes can also be modified through coordination. In addition, the introduction of new synthetic approaches, such as the solvothermal method, provides more possibilities and a practical route to identifying novel metal complexes of fullerenes.

Cross-References

- ▶ Functionalization of Fullerenes: Addition Reactions
- ▶ Radical Reaction and Photoreaction
- ▶ Theoretical Prediction of Fullerene Reactivity

References

1. Bowles FL, Olmstead MM, Balch AL (2014) Preparation and crystallographic characterization of $C_{60}\{\eta^1\text{-}Ru(CO)_2(\eta^5\text{-}C_5H_5)\}_2$: a locally crowded organometallic fullerene without the usual η^2-bonding. J Am Chem Soc 136:3338–3341. https://doi.org/10.1021/ja4120677

2. Zheng H, Zhao X, Sakaki S (2017) [2 + 2]-type reaction of metal–metal σ-bond with fullerene forming an η^1-C_{60} metal complex: mechanistic details of formation reaction and prediction of a new η^1-C_{60} metal complex. Inorg Chem 56:6746–6754. https://doi.org/10.1021/acs.inorgchem.7b00902
3. Zhang S, Brown TL, Du Y, Shapley JR (1993) Metalation of fullerene (C_{60}) with penta-carbonylrhenium radicals. Reversible formation of $C_{60}\{Re(CO)_5\}_2$. J Am Chem Soc 115:6705–6709. https://doi.org/10.1021/ja00068a030
4. Xie Y-P, Pan C, Bao L et al (2019) Regioselective coordination of $Re_2(CO)_{10}$ to $Y@C_{2v}(9)$-C_{82}: an unprecedented η^1 complex stabilized by intramolecular electron transfer. Organometallics 38:2259–2263. https://doi.org/10.1021/acs.organomet.9b00209
5. Fagan PJ, Ward MD, Calabrese JC (1989) Molecular engineering of solid-state materials: organometallic building blocks. J Am Chem Soc 111:1698–1719. https://doi.org/10.1021/ja00187a024
6. Goh S-K, Marynick DS (2001) Ability of fullerenes to act as η^6 ligands in transition metal complexes. A comparative PM_3(tm)–density functional theory study. J Comput Chem 22:1881–1886. https://doi.org/10.1002/jcc.1138
7. Fagan PJ, Calabrese JC, Malone B (1992) Metal complexes of buckminsterfullerene (C_{60}). Acc Chem Res 25:134–142. https://doi.org/10.1021/ar00015a006
8. Bashilov VV, Petrovskii PV, Sokolov VI et al (1993) Synthesis, crystal, and molecular structure of the palladium(0)-fullerene derivative (.eta.2-C_{60})$Pd(PPh_3)_2$. Organometallics 12:991–992. https://doi.org/10.1021/om00028a003
9. Fagan PJ, Calabrese JC, Malone B (1991) The chemical nature of buckminsterfullerene (C_{60}) and the characterization of a platinum derivative. Science 252:1160–1161. https://doi.org/10.1126/science.252.5009.1160
10. Fagan PJ, Calabrese JC, Malone B (1991) A multiply-substituted buckminsterfullerene (C_{60}) with an octahedral array of platinum atoms. J Am Chem Soc 113:9408–9409. https://doi.org/10.1021/ja00024a079
11. Lerke SA, Parkinson BA, Evans DH, Fagan PJ (1992) Electrochemical studies on metal derivatives of buckminsterfullerene (C_{60}). J Am Chem Soc 114:7807–7813. https://doi.org/10.1021/ja00046a029
12. Lerke SA, Evans DH, Fagan PJ (1995) Voltammetric study of the oxidation of metal derivatives of buckminsterfullerence (C_{60}). Electroanal Chem 383:127–132. https://doi.org/10.1016/0022-0728(94)03630-L
13. Balch AL, Hao L, Olmstead MM (1996) Patterns of multiple additions to fullerene C_{70}: isolation and structural characterization of $[C_{70}\{Pt(PPh_3)_2\}_4]$. Angew Chem Int Ed 35:188–190. https://doi.org/10.1002/anie.199601881
14. Balch AL, Catalano VJ, Lee JW (1991) Accumulating evidence for the selective reactivity of the 6-6 ring fusion of fullerene, C_{60}. Preparation and structure of (.eta.2-C_{60})$Ir(CO)Cl(PPh_3)_2 \cdot 5C_6H_6$. Inorg Chem 30:3980–3981. https://doi.org/10.1021/ic00021a003
15. Balch AL, Olmstead MM (1998) Reactions of transition metal complexes with fullerenes (C_{60}, C_{70}, etc.) and related materials. Chem Rev 98:2123–2166. https://doi.org/10.1021/cr960040e
16. Balch AL, Lee JW, Noll BC, Olmstead MM (1994) Multiple additions of vaska-type iridium complexes to C_{60}. Preferential crystallization of the "Para" double addition products: $C_{60}\{Ir(CO)Cl(PMe_3)_2\}_2 \cdot 2C_6H_6$ and $C_{60}\{Ir(CO)Cl(PEt_3)_2\}_2 \cdot C_6H_6$. Inorg Chem 33:5238–5243. https://doi.org/10.1021/ic00101a015
17. Balch AL, Lee JW, Noll BC, Olmstead MM (1992) A double addition product of C_{60}: $C_{60}\{Ir(CO)Cl(PMe_2Ph)_2\}_2$. Individual crystallization of two conformational isomers. J Am Chem Soc 114:10984–10985. https://doi.org/10.1021/ja00053a058
18. Balch AL, Catalano VJ, Lee JW, Olmstead MM (1992) Supramolecular aggregation of an (.eta.2-C_{60}) iridium complex involving phenyl chelation of the fullerene. J Am Chem Soc 114:5455–5457. https://doi.org/10.1021/ja00039a084
19. Catalano VJ, Parodi N (1997) Reversible C60 binding to dendrimer-containing Ir(CO)Cl$(PPh_2R)_2$ complexes. Inorg Chem 36:537–541. https://doi.org/10.1021/ic9612764

20. Lee JW, Olmstead MM, Vickery JS, Balch AL (2000) A dumbbell shaped fullerene dimer with an inorganic linker. Addition of C_{60} and tetracyanoethylene to $Ir_2(CO)_2Cl_2(Ph_2P(CH_2)nPPh_2)_2$ (n=5 or 7). J Clust Sci 11:67–77. https://doi.org/10.1021/ja00053a058
21. Balch AL, Catalano VJ, Lee JW et al (1991) (.eta.2-C_{70})Ir(CO)Cl(PPh_3)$_2$: the synthesis and structure of an iridium organometallic derivative of a higher fullerene. J Am Chem Soc 113: 8953–8955. https://doi.org/10.1021/ja00023a057
22. Balch AL, Ginwalla AS, Lee JW et al (1994) Partial separation and structural characterization of C_{84} isomers by crystallization of (.eta.2-C_{84})Ir(CO)Cl($P(C_6H_5)_3$)$_2$. J Am Chem Soc 116:2227–2228. https://doi.org/10.1021/ja00084a106
23. Balch AL, Lee JW, Noll BC, Olmstead MM (1993) Structural characterization of {(.eta.2-C_{60}) RhH(CO)(PPh_3)$_2$}: product of the reaction of fullerene C_{60} with the hydrogenation catalyst carbonylhydridotris(triphenylphosphine)rhodium. Inorg Chem 32:3577–3578. https://doi.org/10.1021/ic00069a001
24. Schreiner S, Gallaher TN, Parsons HK (1994) Synthesis of metal fullerene derivatives from chloro hydrido transition metal complexes. Inorg Chem 33:3021–3022. https://doi.org/10.1021/ic00091a051
25. Usatov AV, Peregudova SM, Denisovich LI et al (2000) Exohedral mono- and bimetallic hydride complexes of rhodium and iridium with C_{60} and C_{70}: syntheses and electrochemical properties. J Organomet Chem 599:87–96. https://doi.org/10.1016/S0022-328X(99)00757-3
26. Chernega AN, Green MLH, Haggitt J, Stephens AHH (1998) New transition-metal derivatives of the fullerene C_{60}. J Chem Soc Dalton Trans 755–768. https://doi.org/10.1039/A707618E
27. Peregudova SM, Denisovich LI, Martynova EV et al (2008) Electrochemical oxidation and reduction of osmium and iridium complexes with fullerene C_{60}. Russ J Electrochem 44:249–253. https://doi.org/10.1134/s102319350802016x
28. Hsu H-F, Du Y, Albrecht-Schmitt TE et al (1998) Structural comparison of $M(CO)_3(dppe)(\eta^2$-$C_{60})$ (M = Mo, W), $Mo(CO)_3(dppe)(\eta^2$-$C_{70})$, and $W(CO)_3(dppe)(\eta^2$-trans-$C_2H_2(CO_2Me)_2)$. Organometallics 17:1756–1761. https://doi.org/10.1021/om971013x
29. Song L-C, Zhu Y-H, Hu Q-M (1997) The first fullerene tungsten complex containing a dppb ligand fac/mer-$W(CO)_3(dppb)(\eta^2$-$C_{60})$via displacement reaction of fac-$W(CO)_3$(MeCN)(dppb). Polyhedron 16:2141–2143. https://doi.org/10.1016/S0277-5387(96)00603-1
30. Song L-C, Zhu Y-H, Hu Q-M (1998) The chemical reactivity of fullerene C_{60} towards fac-$Mo(CO)_3$ (MeCN)(dppe) and $Mo(CO)_4$(dppe). Synthesis, characterization and reactions of the novel fullerene molybdenum derivative fac-$Mo(CO)_3(dppe)(\eta^2$-$C_{60})$. Polyhedron 17:469–473. https://doi.org/10.1016/S0277-5387(97)00370-7
31. Bao L, Liu B, Li X et al (2016) $W(CO)_3(Ph_2PC_2H_4PPh_2)(\eta^2$-$Sc_3N@I_h$-$C_{80}$/$Sc_3N@D_{5h}$-$C_{80})$: regioselective synthesis and crystallographic characterization of air-stable mononuclear complexes of endohedral fullerenes. Dalton Trans 45:11606–11610. https://doi.org/10.1039/C6DT00790B
32. Bao L, Yu P, Li Y et al (2019) Highly regioselective complexation of tungsten with Eu@C_{82}/Eu@C_{84}: interplay between endohedral and exohedral metallic units induced by electron transfer. Chem Sci 10:4945–4950. https://doi.org/10.1039/C9SC01479A
33. Cui P, Li L, Tang K, Jin X (2001) The crystal structure of the molybdenum complex of [70] fullerene $Mo(\tilde{\eta}_2$-$C_{70})(CO)_2$(Phen)(Dbm) · $2C_3H_8O$ · $2.5H_2O$ (Phen = 1,10-Phenanthroline, Dbm = Dibutyl maleate). J Chem Res 2001:240–242. https://doi.org/10.3184/030823401103169621
34. Tang K, Zheng S, Jin X et al (1997) Syntheses and structural characterizations of novel tungsten and molybdenum complexes of fullerene $[M(\eta^2$-$C_{60})(CO)_2$(phen)(dbm)]· $2C_6H_6$·C_5H_{12} (M = W or Mo, phen = 1,10-phenanthroline, dbm = dibutyl maleate). J Chem Soc Dalton Trans 3585–3587. https://doi.org/10.1039/A704145D
35. Bengough MN, Thompson DM, Baird MC, Enright GD (1999) Synthesis and structures of the novel manganese(−I) fullerene-[60] complexes $M[Mn(CO)_4(\eta^2$-$C_{60})]$ (M = Na, PPN). Organometallics 18:2950–2952. https://doi.org/10.1021/om990361r

36. Konarev DV, Khasanov SS, Yudanova EI, Lyubovskaya RN (2011) The η^2 complex of nickel Bis(diphenylphosphanyl)propane with fullerene: Ni(dppp)(η^2-C_{60})·(solvent) obtained by reduction. Eur J Inorg Chem 2011:816–820. https://doi.org/10.1002/ejic.201001059
37. Konarev DV, Khasanov SS, Troyanov SI et al (2013) Mononuclear coordination complexes of fullerene C_{60} with zerovalent cobalt having S = 1/2 spin state: Co(η^2-C_{60})(L)(C_6H_5CN)·(o-$C_6H_4Cl_2$) (L = 1,2-bis(diphenylphosphino)ethane and 1,1′-bis(diphenylphosphino)ferrocene). Inorg Chem 52:13934–13940. https://doi.org/10.1021/ic401577m
38. Hawkins JM, Meyer A, Lewis TA et al (1991) Crystal structure of osmylated C_{60}: confirmation of the soccer ball framework. Science 252:312–313. https://doi.org/10.1126/science.252.5003.312
39. Westmeyer MD, Rauchfuss TB, Verma AK (1996) Iron sulfido derivatives of the fullerenes C_{60} and C_{70}. Inorg Chem 35:7140–7147. https://doi.org/10.1021/ic960728+
40. Usatov AV, Martynova EV, Neretin IS et al (2003) The first mononuclear η^2-C_{60} complex of osmium: synthesis and X-ray crystal structure of [(η^2-C_{60})Os(CO)(t-BuNC)(PPh_3)$_2$]. Eur J Inorg Chem 2003:2041–2044. https://doi.org/10.1002/ejic.200300078
41. Ballenweg S, Gleiter R, Krätschmer W (1993) Hydrogenation of buckminsterfullerene C_{60} via Hydrozirconation: a new way to organofullerenes. Tetrahedron Lett 34:3737–3740. https://doi.org/10.1016/S0040-4039(00)79214-8
42. Sawamura M, Iikura H, Nakamura E (1996) The first pentahaptofullerene metal complexes. J Am Chem Soc 118:12850–12851. https://doi.org/10.1021/ja962681x
43. Rasinkangas M, Pakkanen TT, Pakkanen TA et al (1993) Multimetallic binding to fullerenes: C_{60}{Ir_2C_{12}(1,5-COD)$_2$}$_2$. A novel coordination mode to fullerenes. J Am Chem Soc 115:4901–4901. https://doi.org/10.1021/ja00064a065
44. Mavunkal IJ, Chi Y, Peng S-M, Lee G-H (1995) Preparation and structure of Cp*2Ru_2(μ-Cl)(μ-X)(C_{60}), X = H and Cl. Novel dinuclear fullerene complexes with and without direct ruthenium-ruthenium bonding. Organometallics 14:4454–4456. https://doi.org/10.1021/om00010a005
45. Park JT, Cho J-J, Song H (1995) Triosmium cluster derivatives of [60]fullerene. J Chem Soc Chem Commun:15–16. https://doi.org/10.1039/C39950000015
46. Lee K, Song H, Park JT (2003) [60]fullerene−metal cluster complexes: novel bonding modes and electronic communication. Acc Chem Res 36:78–86. https://doi.org/10.1021/ar020149a
47. Park JT, Song H, Cho J-J et al (1998) Synthesis and characterization of η^2-C_{60} and μ_3-η^2,η^2,η^2-C_{60} triosmium cluster complexes. Organometallics 17:227–236. https://doi.org/10.1021/om970689p
48. Hsu H-F, Shapley JR (1996) $Ru_3(CO)^9$(μ_3-η^2,η^2,η^2-C_{60}): a cluster face-capping, arene-like complex of C_{60}. J Am Chem Soc 118:9192–9193. https://doi.org/10.1021/ja962077m
49. Song H, Lee Y, Choi Z-H et al (2001) Synthesis and characterization of μ_3-η^2,η^2,η^2-C_{60} trirhenium hydrido cluster complexes. Organometallics 20:3139–3144. https://doi.org/10.1021/om0101341
50. Hsu H-F, Shapley JR (2000) Triruthenium cluster complexes of C_{60} and C_{70}: carbonyl site exchange probed via triphenylphosphine ligand derivatives. J Organomet Chem 599:97–105. https://doi.org/10.1016/S0022-328X(00)00016-4
51. Song H, Lee K, Park JT, Choi M-G (1998) Synthesis, structure, and electrochemical studies of μ_3-η^2,η^2,η^2-C_{60} triosmium complexes. Organometallics 17:4477–4483. https://doi.org/10.1021/om980361b
52. Song H, Lee K, Park JT et al (2000) Fluxional processes and structural characterization of μ_3-η^2,η^2,η^2-C_{60} triosmium cluster complexes, $Os_3(CO)_{9-n}(PMe_3)_n$(μ_3-η^2,η^2,η^2-C_{60}) (n=1, 2, 3). J Organomet Chem 599:49–56. https://doi.org/10.1016/S0022-328X(99)00715-9
53. Song H, Lee CH, Lee K, Park JT (2002) Ligand-induced conversion of π to σ C_{60}−metal cluster complexes: full characterization of the μ_3-η^1:η^2:η^1-C60 bonding mode. Organometallics 21:2514–2520. https://doi.org/10.1021/om020109a
54. Song H, Lee K, Choi M-G, Park JT (2002) [60]Fullerene as a versatile four-electron donor ligand. Organometallics 21:1756–1758. https://doi.org/10.1021/om020038f

55. Chen C-H, Yeh W-Y, Liu Y-H, Lee G-H (2012) [(μ-H)$_3$Re$_3$(CO)$_9$(η^2,η^2,η^2-Sc$_2$C$_2$@C$_{3v}$(8)-C$_{82}$)]: face-capping cluster complex of an endohedral fullerene. Angew Chem Int Ed 51: 13046–13049. https://doi.org/10.1002/anie.201207261
56. Zhan S-Z, Zhang G-H, Li J-H et al (2020) Exohedral cuprofullerene: sequentially expanding metal olefin up to a C$_{60}$@Cu$_{24}$ rhombicuboctahedron. J Am Chem Soc 142:5943–5947. https://doi.org/10.1021/jacs.0c00090
57. Lee K, Hsu H-F, Shapley JR (1997) Coordination of C$_{60}$ to penta- and hexaruthenium cluster frames. Organometallics 16:3876–3877. https://doi.org/10.1021/om970265v
58. Lee K, Shapley JR (1998) Face-coordinated C$_{60}$ complexes with carbido pentaruthenium cluster cores including a bimetallic platinum−pentaruthenium complex. Organometallics 17: 3020–3026. https://doi.org/10.1021/om971091k
59. Lee K, Song H, Kim B et al (2002) The first fullerene−metal sandwich complex: an unusually strong electronic communication between two C$_{60}$ cages. J Am Chem Soc 124:2872–2873. https://doi.org/10.1021/ja017496k
60. Lee K, Lee CH, Song H et al (2000) Interconversion between μ-η^2,η^2-C$_{60}$ and μ$_3$-η^2,η^2,η^2-C$_{60}$ on a carbido pentaosmium cluster framework. Angew Chem Int Ed 112:1871–1874. https://doi.org/10.1002/(SICI)1521-3757(20000515)112:10<1871::AID-ANGE1871>3.0.CO;2-9
61. Zimmerman PA, Hercules DM (1993) Formation and detection of fullerene metal complexes using time-of-flight secondary ion mass spectrometry. Appl Spectrosc AS 47:1545–1547
62. Jin X, Xie X, Tang K (2002) Syntheses and X-ray crystal structures of dumbbell-shaped bis-fullerene tungsten and molybdenum complexes. Chem Commun 750–751. https://doi.org/10.1039/B200793B
63. Konarev DV, Kuźmin AV, Simonov SV et al (2011) Structure and properties of ionic fullerene complex Co+(dppe)$_2$·(C$_{60}^{\cdot-}$)·(C$_6$H$_4$C$_{12}$)$_2$: distortion of the ordered fullerene cage of C60$^{\cdot-}$ radical anions. Dalton Trans 40:4453–4458. https://doi.org/10.1039/C1DT10039D
64. Konarev DV, Troyanov SI, Nakano Y et al (2013) Magnetic coupling in the fullerene dimer {Co(Ph$_3$P)(C$_6$H$_5$CN)}$_2$(μ$_2$-η^2:η^2-C$_{60}$)$_2$ with two zerovalent cobalt atoms as bridges. Organometallics 32:4038–4041. https://doi.org/10.1021/om400392c
65. Konarev DV, Troyanov SI, Ustimenko KA et al (2015) Formation of {Co(dppe)}$_2${μ$_2$-η^2:η^2-η^2:η^2-[(C$_{60}$)$_2$]} dimers bonded by single C–C bonds and bridging η^2-coordinated cobalt atoms. Inorg Chem 54:4597–4599. https://doi.org/10.1021/acs.inorgchem.5b00637
66. Lee G, Cho Y-J, Park BK et al (2003) Two metal centers bridging two C$_{60}$ cages as a wide passage for efficient interfullerene electronic interaction. J Am Chem Soc 125:13920–13921. https://doi.org/10.1021/ja037106p
67. Nagashima H, Nakaoka A, Saito Y et al (1992) C$_{60}$Pd$_n$: the first organometallic polymer of buckminsterfullerene. J Chem Soc Chem Commun:377–379. https://doi.org/10.1039/C39920000377
68. van Wijnkoop MF, Meidine MG, Avent A et al (1997) Platinum(0)–[60]fullerene complexes with chelating diphosphine ligands. Syntheses and characterisation of [Pt(η^2-C$_{60}$)(L–L)] [L–L = Ph$_2$P(CH$_2$)$_n$PPh$_2$, n = 2 or 3]. J Chem Soc Dalton Trans:675–678. https://doi.org/10.1039/A605357B
69. Nagashima H, Kato Y, Yamaguchi H et al (1994) Synthesis and reactions of organoplatinum compounds of C$_{60}$, C$_{60}$Pt$_n$. Chem Lett 23:1207–1210. https://doi.org/10.1246/cl.1994.1207
70. Nagashima H, Nakazawa M, Furukawa T, Itoh K (1996) Organopalladium and platinum complexes of C$_{60}$ bearing isonitrile ligands. Chem Lett 25:405–406. https://doi.org/10.1246/cl.1996.405
71. Balch AL, Costa DA, Winkler K (1998) Formation of redox-active, two-component films by electrochemical reduction of C$_{60}$ and transition metal complexes. J Am Chem Soc 120:9614–9620. https://doi.org/10.1021/ja9805526
72. Konarev DV, Khasanov SS, Nakano Y et al (2014) Linear coordination fullerene C$_{60}$ polymer [{Ni(Me$_3$P)$_2$}(μ-η^2,η^2-C$_{60}$)]$_\infty$ bridged by zerovalent nickel atoms. Inorg Chem 53:11960–11965. https://doi.org/10.1021/ic501551y

73. Zhan S-Z, Li J-H, Li Y et al (2021) Ultra-stable 2D cuprofullerene imidazolate polymer as a high-performance visible-light photodetector. Sci China Mater 64:1563–1569. https://doi.org/10.1007/s40843-020-1589-7
74. Liu X, Wan WC, Owens SM, Broderick WE (1994) Superconducting alkali metal fullerides: development of a versatile solution-phase route from soluble M_3C_{60} precursors. J Am Chem Soc 116:5489–5490. https://doi.org/10.1021/ja00091a071
75. Konarev DV, Lyubovskaya RN (2012) Molecular design, study of the structures and properties of ionic fullerene compounds. Russ Chem Rev 81:336. https://doi.org/10.1070/RC2012v081n04ABEH004273
76. Wan WC, Liu X, Sweeney GM, Broderick WE (1995) Structural evidence for the expected Jahn-Teller distortion in monoanionic C_{60}: synthesis and X-ray crystal structure of decamethylnickelocenium buckminsterfulleride. J Am Chem Soc 117:9580–9581. https://doi.org/10.1021/ja00142a033
77. Konarev DV, Khasanov SS, Saito G et al (2003) Formation of single-bonded $(C_{60}^-)_2$ and $(C_{70}^-)_2$ dimers in crystalline ionic complexes of fullerenes. J Am Chem Soc 125:10074–10083. https://doi.org/10.1021/ja035546a
78. Konarev DV, Kuzmin AV, Andronov MG et al (2018) Distortion and electronic structure of ordered $C_{60}^{\bullet-}$ radical anions in the salt with $\{CoI(dppe)_2CO\}^+$ cations (dppe: 1,2-bis (diphenylphosphino)ethane). Inorg Chim Acta 483:504–509. https://doi.org/10.1016/j.ica.2018.08.046
79. Konarev DV, Kuźmin AV, Simonov SV et al (2011) Structure and properties of ionic fullerene complex $Co^+(dppe)_2 \cdot (C_{60}^{\cdot-}) \cdot (C_6H_4C_{l2})_2$: distortion of the ordered fullerene cage of $C60^{\bullet-}$ radical anions. Dalton Trans 40:4453–4458. https://doi.org/10.1039/C1DT10039D
80. Hong J, Shores MP, Elliott CM (2010) Establishment of structure-conductivity relationship for Tris(2,2′-bipyridine) ruthenium ionic C60 salts. Inorg Chem 49:11378–11385. https://doi.org/10.1021/ic1013126

Transition Metal Salt-Catalyzed Reactions of [60]Fullerene

14

Qing-Song Liu, Wen-Qiang Lu, and Guan-Wu Wang

Contents

Abstract

Transition metal salt-catalyzed reactions of [60]fullerene have been one of the most powerful methods for the chemical modifications of [60]fullerene and have attracted extensive attention due to their high selectivities and excellent

Q.-S. Liu · W.-Q. Lu · G.-W. Wang (✉)
Hefei National Laboratory for Physical Sciences at Microscale and Department of Chemistry, University of Science and Technology of China, Hefei, China
e-mail: gwang@ustc.edu.cn

X. Lu et al. (eds.), *Handbook of Fullerene Science and Technology*,
https://doi.org/10.1007/978-981-16-8994-9_35

reaction efficiencies. Transition metal salts such as those of palladium, rhodium, copper, and others have been widely employed as catalysts for the synthesis of diversified [60]fullerene derivatives.

Keywords

[60]Fullerene · Transition metal salts · Palladium catalysis · Rhodium catalysis · Copper catalysis

Introduction

As the third allotrope of carbon, fullerenes have unique cage-like molecular structures. In 1985, Kroto, Smalley, and Curl discovered the first fullerene: [60] fullerene (C_{60}). Inspired by the geodesic dome designed by Buckminster Fuller for the World Exposition in 1967, C_{60} was initially named as Buckminsterfullerene. In 1990, Krätschmer and coworkers achieved the gram-scale preparation of C_{60} for the first time. The discovery of fullerenes has expanded the scope of molecular research from the two-dimensional planar molecule of benzene to a large number of three-dimensional cage molecules, which have a wide range of application prospects. Due to the huge potential applications in materials, nanoscience, and biology [1–4], various fullerene derivatives with novel structures have been synthesized over the past decades. Many efforts have been put forth to establish different approaches and strategies. Up to now, numerous reactions have been exploited to functionalize C_{60}, such as nucleophilic additions, cycloadditions, and radical additions. Among the numerous protocols, the transition metal salt-mediated reactions have been one of the most efficient methods for the construction of various fullerene derivatives [5–12]. But the excessive use of transition metal salts in the reactions would result in a large amount of wastes. Therefore, the use of a small amount of transition metal salts to catalyze the reactions has aroused wide concern. In this chapter, the synthesis of diversified fullerene derivatives catalyzed by different transition metal salts is reviewed, mainly including palladium-, rhodium-, and copper-catalyzed fullerene reactions. The substrate scopes of these protocols and the plausible reaction mechanisms of selected reactions are also discussed.

Palladium-Catalyzed Reactions of C_{60}

The Pd-catalyzed reactions are important means for the derivatization of fullerenes. In this section, we will describe the Pd-catalyzed reactions of C_{60} with different substrates.

Pd-Catalyzed Allylations and Arylations of C_{60}

Luh and coworkers first reported the [3 + 2] cycloaddition of C_{60} with $CH_2 = C(CH_2OAc)CH_2SiMe_3$ with the aid of a stoichiometric amount of $[Pd(PPh_3)_4]$ and 1 equiv. of $Ph_2PCH_2CH_2PPh_2$ to afford the TMM-C_{60} adduct **1** (Fig. 1) [13]. The same group soon developed the Pd-catalyzed [3 + 2] cycloaddition of C_{60} with *cis*-$HOCH_2CH{=}CHCH_2OCO_2Et$ with a catalytic amount of the same palladium species and 1 equiv. of the same ligand to generate the C_{60}-fused tetrahydrofuran derivative **2** in 59% yield (Scheme 1) [14]. Although the mechanism of this reaction was not established, nucleophilic addition of the π-allylpalladium alkoxide intermediate to C_{60} may occur leading to the fullerenyl anion, which may undergo another nucleophilic addition to the π-allylpalladium system to give **2** (Scheme 2).

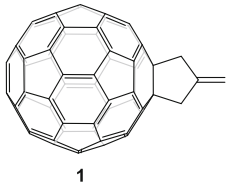

Fig. 1 The structure of TMM-C_{60} adduct **1**

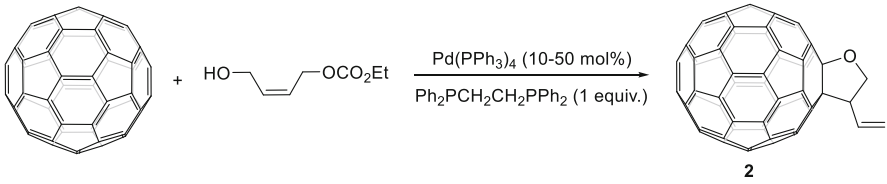

Scheme 1 Pd-catalyzed [3 + 2] cycloaddition of C_{60} with *cis*-$HOCH_2CH{=}CHCH_2OCO_2Et$

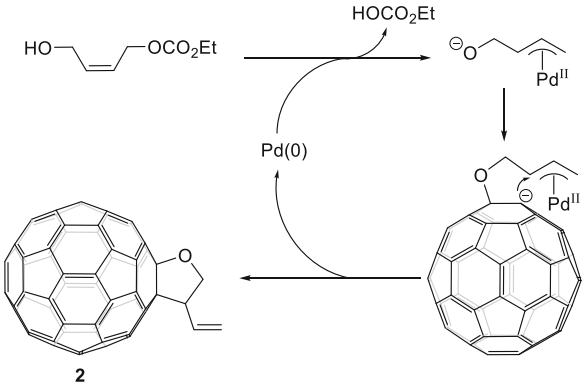

Scheme 2 Proposed reaction mechanism for the formation of **2**

In 2008, the Itami group developed the Pd-catalyzed hydroarylation of C_{60} with boronic acids [15]. The hydroarylated products **3** were obtained in 29–60% yields through the reactions of C_{60} with arylboronic acids in the presence of a catalytic amount of Pd(2-PyCH=NPh)$(OCOC_6F_5)_2$ in *o*-dichlorobenzene (1,2-$C_6H_4Cl_2$)/H_2O at 60 °C (Scheme 3). Since the corresponding palladium diacetate complex easily decomposed under air/moisture, the pentafluorobenzoate moiety clearly enhanced the activity and stability of the palladium catalyst.

They later examined the Pd-catalyzed allylation reaction using the above-synthesized $ArC_{60}H$ [16]. For example, treatment of aryl(hydro)fullerene **3-1** (1 equiv.) with methallyl methyl carbonate (2 equiv.) in 1,2-$C_6H_4Cl_2$ at 80 °C in the presence of [Pd$(dba)_3$]·$CHCl_3$ (10 mol%; dba = *trans,trans*-dibenzylideneacetone) and $P(OPh)_3$ (80 mol%) furnished the C–H bond allylation product **4** in 85% yield (Scheme 4).

On the basis of the previous work [15, 16], Itami and coworkers unveiled the Pd-catalyzed regioselective unsymmetrical tetraallylation of C_{60} in 2009 [17]. First, they investigated the reaction of C_{60} with CH_2 = $CHCH_2Cl$ and CH_2 = $CHCH_2SnBu_3$ with $PdCl_2[P(OPh)_3]_2$ as the catalyst and 1,2-$C_6H_4Cl_2$ as the solvent at 50 °C. Tetraallylated product **5** and diallylated 1,2-adduct (**6b**, vide infra) were obtained with yields of 74% and 8%, respectively (Scheme 5).

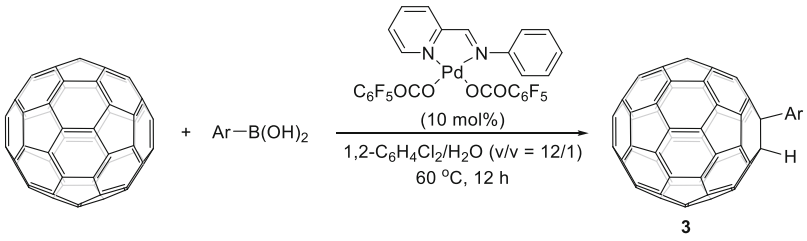

Scheme 3 Pd-catalyzed reactions of C_{60} with boronic acids

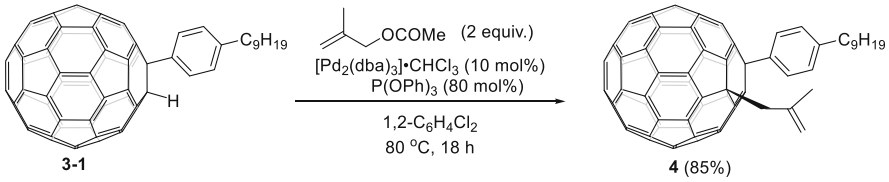

Scheme 4 Pd-catalyzed allylation of $ArC_{60}H$

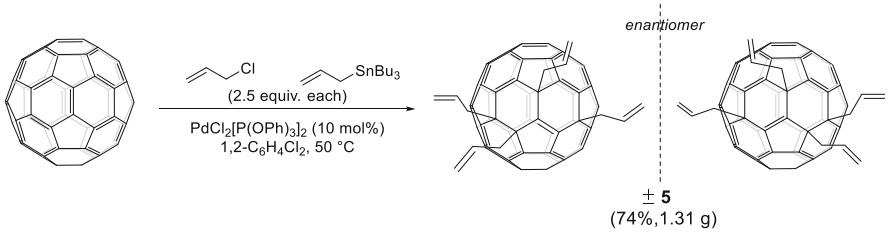

Scheme 5 Pd-catalyzed tetraallylation of C_{60}

The achievement of regioselective unsymmetrical tetraallylation was notable from both synthetic and mechanistic viewpoints. To gain mechanistic insight into this unprecedented multi-addition, they began by investigating the stepwise reactions. When the amounts of allylating agents were decreased to 1.2 equiv., 1,4-diallyl-C_{60} (**6a**, 28%) and 1,2-diallyl-C_{60} (**6b**, 10%) were obtained along with **5** (28%) and C_{60} (29%). Subsequently, it was found that the diallylation conditions could convert **6a** to **5** smoothly (74%), while the diallylation of **6b** was sluggish (20%) (Scheme 6) [17]. Mechanistic analysis revealed that both steric (for the first diallylation) and electronic (for the second diallylation) factors were responsible for the high regioselectivity.

Based on the experimental results and previous literature report [16], the proposed mechanism of regioselective tetraallylation of C_{60} is shown in Scheme 7. Bis(π-allyl)palladium, which was synthesized from allylating agents, reacted with C_{60} to give the delocalized fullerenyl anion **A** with (π-allyl)Pd^{+} as the counter cation. Then, a second C_{60}–allyl bond was formed, possibly through

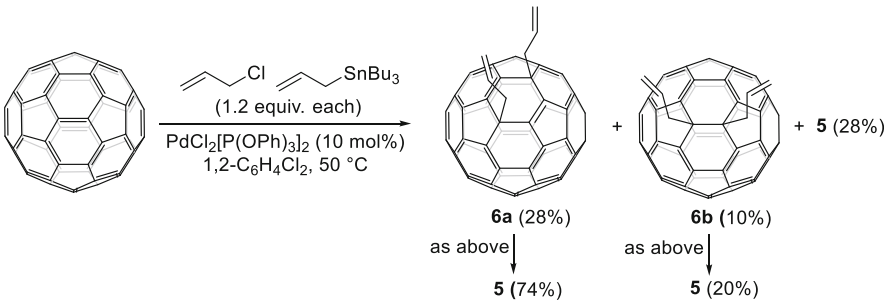

Scheme 6 The stepwise process of Pd-catalyzed tetraallylation of C_{60}

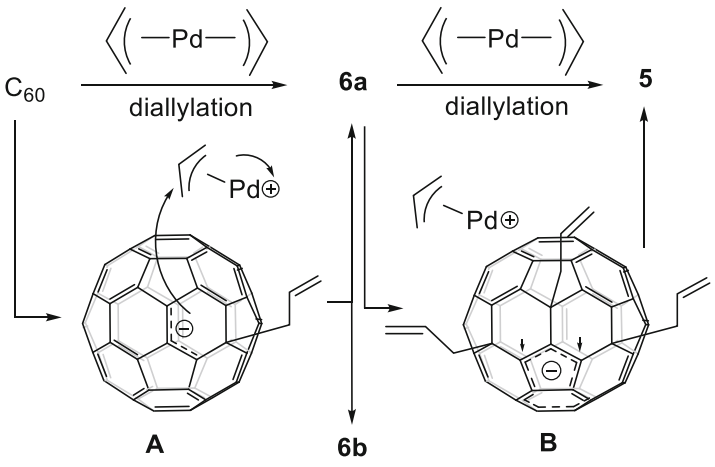

Scheme 7 Possible mechanism for tetraallylation of C_{60}

the nucleophilic attack of the fullerenyl anion on the electrophilic allyl group on Pd, resulting in the diallylated products **6a** and **6b**. The preferential attack of the fullerenyl anion at position 4 (leading to **6a**) may be responsible for the spatial position. The second nucleophilic attack of diallyl palladium on **6a** occurred in the form of stable 10π indenyl anion **B** with (π-allyl)Pd^{+} as counter cation. The final C_{60}–allyl bond formation on the specified fullerenyl carbon yielded enantiomers of **5** [17].

The ring-closing metathesis reaction and hydrogenation of the tetraallylated product took place in the presence of Ru- and Rh-catalysts, respectively. Moreover, it was found that chiral phosphoramidites were effective chiral ligands for the enantioselective tetraallylation of C_{60}. Pronounced enantioselectivity up to 88% ee was realized in the production of tetraallylated C_{60} [18].

Jin, Yamamoto, and coworkers reported the Pd-catalyzed bisfunctionalization of active alkenes by *β*-acetonitrile-*α*-allyl addition in 2012 [19]. This methodology was successfully applied to the synthesis of unsymmetrical 1,4-disubstituted C_{60}. The experimental results showed that the reaction of C_{60} with cyanoacetic acid allyl ester proceeded smoothly in the presence of $Pd(PPh_3)_4$ (1 mol%), the ratio of 1,4-disubstituted product **7a** and 1,2-disubstituted product **7b** was 87:13, the total yield was 31%, and the recovery of C_{60} was 40% (Scheme 8).

In 2019, Liu, Zhang, and coworkers disclosed the Pd-catalyzed decarboxylative heterocyclization of C_{60} [20]. The use of 10 mol% of $Pd(PPh_3)_4$ as the catalyst and 1,2-$C_6H_4Cl_2$ as the solvent for the reactions of C_{60} with vinylethylene carbonates at 60–100 °C for 4–6 h provided products **8** in 36–73% yields (Scheme 9). In comparison, the reactions of C_{60} with 2-alkylidenetrimethylene carbonates at 80–130 °C for 1.5–5 h formed products **9** in 46–61% yields (Scheme 10).

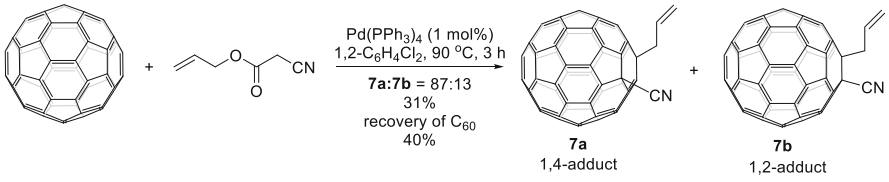

Scheme 8 Pd-catalyzed reaction of C_{60} with cyanoacetic acid allyl ester

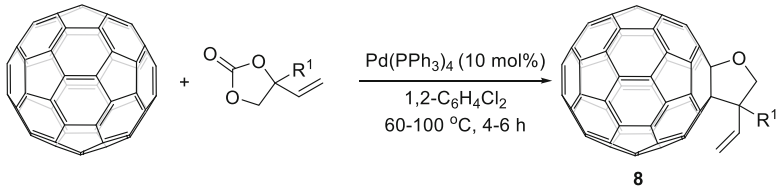

Scheme 9 Pd-catalyzed synthesis of C_{60}-fused tetrahydrofurans

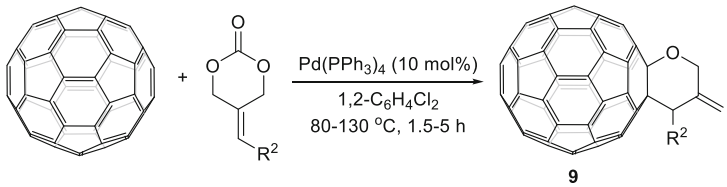

Scheme 10 Pd-catalyzed synthesis of C_{60}-fused tetrahydropyrans

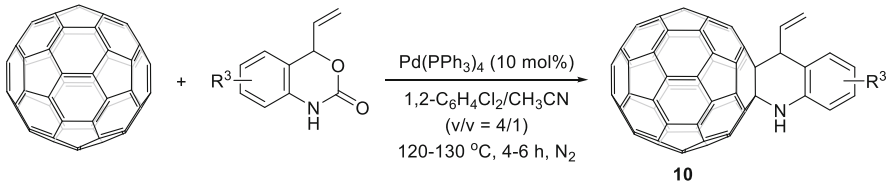

Scheme 11 Pd-catalyzed synthesis of C_{60}-fused tetrahydroquinolines

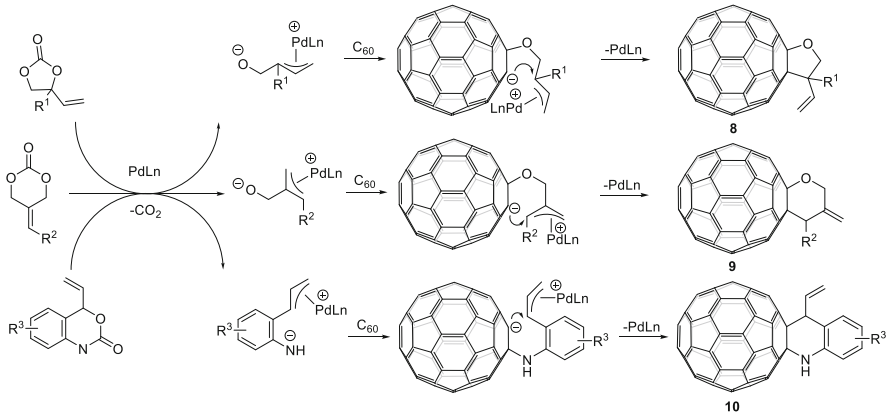

Scheme 12 Proposed reaction mechanisms for the formations of **8**, **9**, and **10**

The reactions of C_{60} with vinyl benzoxazinanones in 1,2-$C_6H_4Cl_2$/CH_3CN (v/v = 4/1) at 120–130 °C for 4–6 h produced the desired products **10** in 21–28% yields (Scheme 11). Significantly, the reactions of C_{60} with vinyl benzoxazinanones required the protection of an inert atmosphere. Using the established method, vinyl-substituted C_{60}-fused tetrahydrofuran/pyran/quinoline compounds could be efficiently prepared under simple reaction conditions through formal [2 + 3] and [2 + 4] heterocyclization reactions. Based on the experimental results and previous literature [21–23], the proposed reaction mechanisms for the decarboxylative transformations are illustrated in Scheme 12. Oxidative addition of a Pd(0) species to vinylethylene carbonates, 2-alkylidenetrimethylene carbonates and vinyl benzoxazinanones afforded *O*- and *N*-containing zwitterionic π-allylpalladium

intermediates accompanied by the release of carbon dioxide. Then, the nucleophilic addition of zwitterionic intermediates formed in situ to electron-deficient C_{60} furnished the fullerenyl anion species. Finally, intramolecular cyclization gave formal [2 + 3] and [2 + 4] cycloaddition products **8**, **9**, and **10**.

Liu, Zhang, and coworkers described the synthesis of polysubstituted C_{60}-fused cyclopentanes **11** in 20–62% yields through the Pd-catalyzed three-component tandem coupling–carboannulation reactions (Scheme 13) [24]. The Pd(0)-catalyzed coupling reactions of C_{60} with 2-(2,3-allyl) malonates and (heteroaryl) iodides had a wide range of substrates and good functional group compatibility. The optimized conditions for three-component cyclization were determined as follows: $Pd(PPh_3)_4$ (10 mol%) as the catalyst, Rb_2CO_3 (1 equiv.) as the base in 1,2–$C_6H_4Cl_2/CH_3CN$ (v/v = 4/1) at 100–110 °C for 3–5 h under an air atmosphere. The proposed reaction mechanism is shown in Scheme 14. The oxidative addition of $Pd(PPh_3)_4$ to the aryl/hetaryl iodides generated the aryl/hetarylpalladium iodides. Subsequently, the regioselective insertion of allenes to aryl/hetarylpalladium iodides at the central sp carbon gave the zwitterionic π-allylpalladium species in the presence of Rb_2CO_3. Coordination with C_{60} and subsequent nucleophilic attack by the carboanion produced the fullerenyl palladium complexes. Finally, intramolecular cyclization provided formal [2 + 3] cycloaddition products **11**.

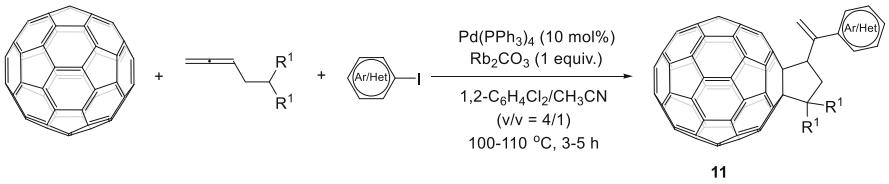

Scheme 13 Pd-catalyzed synthesis of C_{60}-fused cyclopentanes

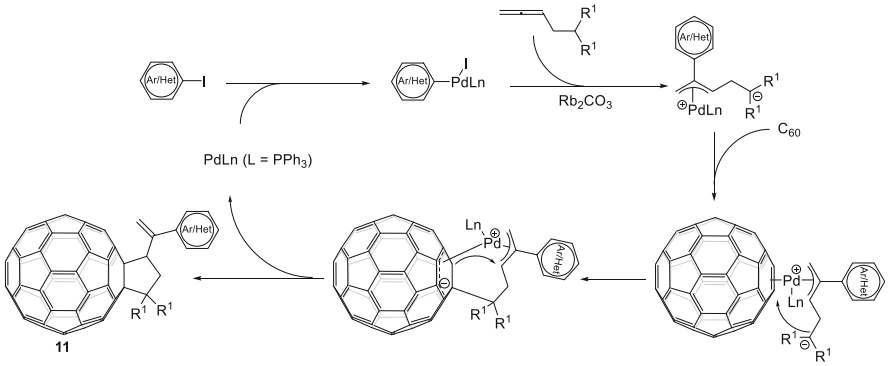

Scheme 14 Proposed reaction mechanism for the formation of **11**

Pd-Catalyzed C–H Activation Reactions of C_{60}

Synthesis of C_{60}-fused Heterocycles via Pd-Catalyzed C–H Activation Reactions

Pd-Catalyzed Amide-Directed C–H Activations

In 2009, the Wang group reported the Pd-catalyzed heteroannulations of C_{60} with various *o*-iodoaniline derivatives to give C_{60}-fused indoline derivatives **12** in 30–42% yields (Scheme 15) [25]. The optimized reaction conditions were selected as follows: $Pd(OAc)_2$ (20 mol%) as the catalyst, 1,2-bis(diphenylphosphino)ethane (DPPE) (10 mol%) as the ligand, 1,4-diazabicyclo[2,2,2]octane·$6H_2O$ (DABCO·$6H_2O$) (2 equiv.) as the base, and chlorobenzene (PhCl) as the solvent at 130 °C for 24 h.

Based on the above reaction results and previous literature [26, 27], a plausible mechanism is shown in Scheme 16. The reaction started with oxidative addition of the in situ generated Pd(0) species by aryl iodides, leading to the formation of aryl-palladium intermediates, subsequent coordination and insertion processes resulted in

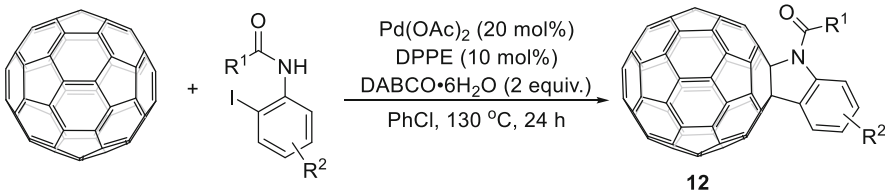

Scheme 15 Pd-catalyzed reactions of C_{60} with *o*-iodoanilines

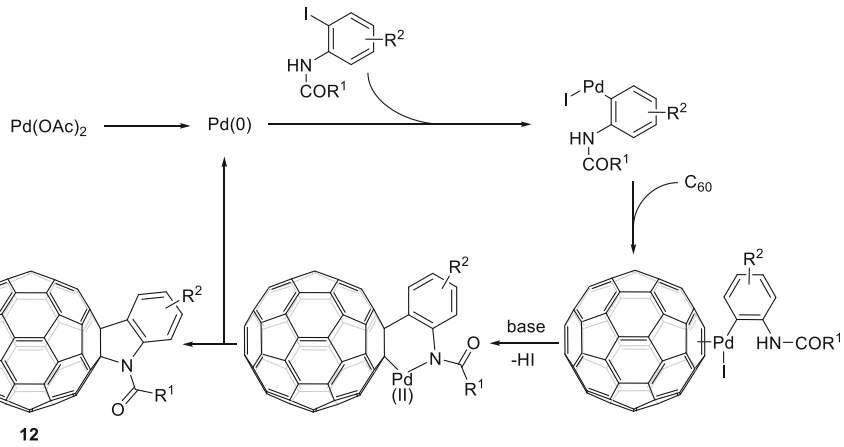

Scheme 16 Proposed reaction mechanism for the formation of **12**

the six-membered palladacycles of C_{60}. The final reductive elimination provided the indoline-fused C_{60} derivatives **12** and regenerated a Pd(0) species. However, the halide byproduct was produced, and a large number of *o*-iodoanilines were expensive or difficult to prepare, thus limiting further application of this reaction.

The Wang group first applied the Pd-catalyzed C–H activation strategy to functionalize C_{60} soon afterwards [28]. It is obvious that it would be highly desirable to utilize anilides instead of *o*-iodoanilines as starting materials. The optimized reaction conditions were selected as follows: $Pd(OAc)_2$ (10–50 mol%) as the catalyst, *p*-toluenesulfonic acid (PTSA) (1 equiv.) as the acid, $K_2S_2O_8$ (5 equiv.) as the oxidant, and 1,2-$C_6H_4Cl_2$/MeCN (v/v = 8/1) or PhCl as the solvent at 130 °C for 0.5–24 h. As shown in Scheme 17, acetanilide and other acetanilides bearing electron-donating groups and electron-withdrawing groups on the phenyl ring afforded products **12** in 20–53% yields (69–91% yields based on consumed C_{60}).

Based on the above reaction results and earlier research reports [27, 29, 30], a plausible mechanism is shown in Scheme 18. The reaction may involve the insertion of the amide-oriented Pd(II) complexes into the aryl *ortho* C–H bond, and then the insertion of C_{60} into the aryl-palladium bond to produce the six-membered palladacycles of C_{60}, which underwent reductive elimination to produce **12** and Pd (0). The latter was oxidized to a Pd(II) species by an oxidizing agent to complete the catalytic cycle.

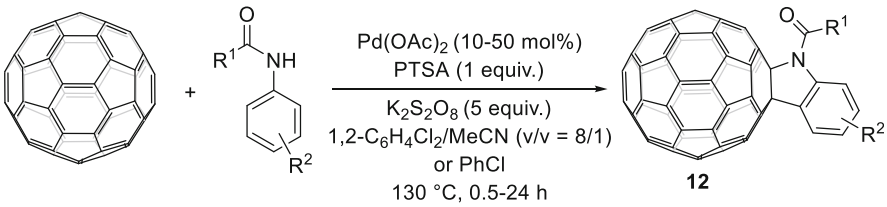

Scheme 17 Pd-catalyzed reactions of C_{60} with anilides

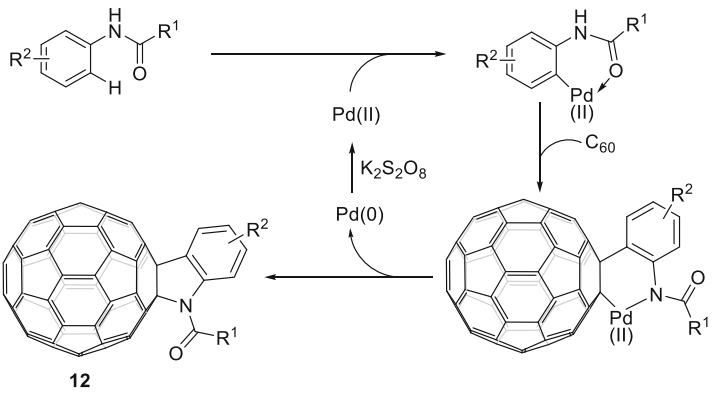

Scheme 18 Proposed reaction mechanism for the formation of **12**

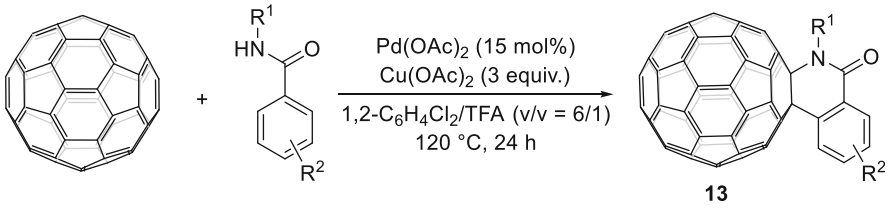

Scheme 19 Pd-catalyzed reactions of C_{60} with benzamides

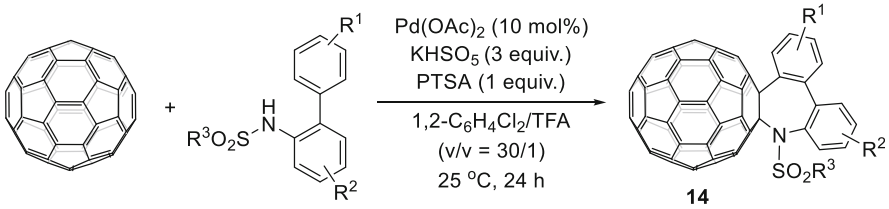

Scheme 20 Pd-catalyzed reactions of C_{60} with *N*-sulfonyl-2-aminobiaryls

Subsequently, Chuang, Wang, and coworkers described the Pd-catalyzed reactions of C_{60} with benzamides via C–H bond activation [31]. The optimized reaction conditions were determined as follows: $Pd(OAc)_2$ (15 mol%) as the catalyst, $Cu(OAc)_2$ (3 equiv.) as the oxidant, and 1,2-$C_6H_4Cl_2$/trifluoroacetic acid (TFA) (v/v = 6/1) as the solvent at 120 °C for 24 h. A variety of substrates with either electron-donating or electron-withdrawing groups on the phenyl rings of benzamides were examined, and fulleroisoquinolinones **13** were isolated in 6–53% yields (8–64% yields based on converted C_{60}) (Scheme 19).

2-Aminobiaryls have been utilized to construct different sizable heterocycles. The Chuang group reported the Pd-catalyzed synthesis of [60]fulleroazepines **14** in 19–58% yields from the reactions of C_{60} with *N*-sulfonyl-2-aminobiaryls through C–H bond activation and sequential C–C and C–N bond formation (Scheme 20) [32]. The optimized reaction conditions were selected as follows: $Pd(OAc)_2$ (10 mol %) as the catalyst, $KHSO_5$ (3 equiv.) as the oxidant, PTSA as the acid, and 1,2-$C_6H_4Cl_2$/TFA (v/v = 30/1) as the solvent at 25 °C for 24 h.

The Wang group demonstrated the Pd-catalyzed reactions of C_{60} with *N*-benzyl sulfonamides to produce the C_{60}-fused tetrahydroisoquinolines **15** with yields of 17–33% (Scheme 21) [33]. Different from the reactions of C_{60} with *N*-sulfonyl-2-aminobiaryls, they had different site selectivity, that is, the *ortho* C–H activation. The optimized reaction conditions were chosen as follows: $Pd(OAc)_2$ (10–20 mol%) as the catalyst, mesitylenesulfonic acid dehydrate (MesSA) (1–2 equiv.) as the acid, $K_2S_2O_8$ (5 equiv.) as the oxidant, and 1,2-$C_6H_4Cl_2$ as the solvent at 80–100 °C for 1.5–6 h. Intriguingly, **15** rearranged to provide fulleroindanes **16** in 48–74% yields in the presence of 3 equiv. of MesSA (Scheme 22). In addition, the sulfonamide group in **16** could be removed or replaced by an aryl group through the $FeCl_3$-promoted

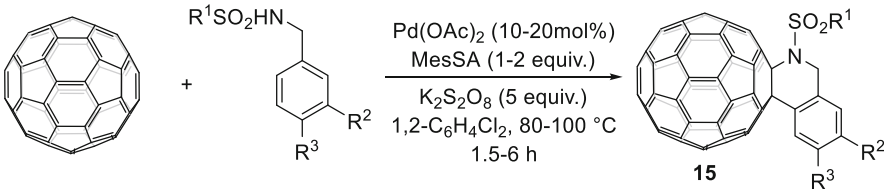

Scheme 21 Pd-catalyzed reactions of C_{60} with *N*-benzyl sulfonamides

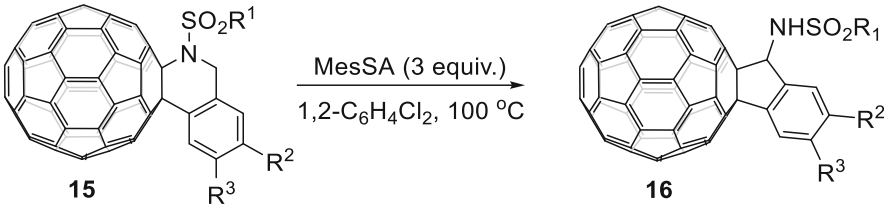

Scheme 22 Conversion of fullerotetrahydroisoquinolines **15** to fulleroindanes **16**

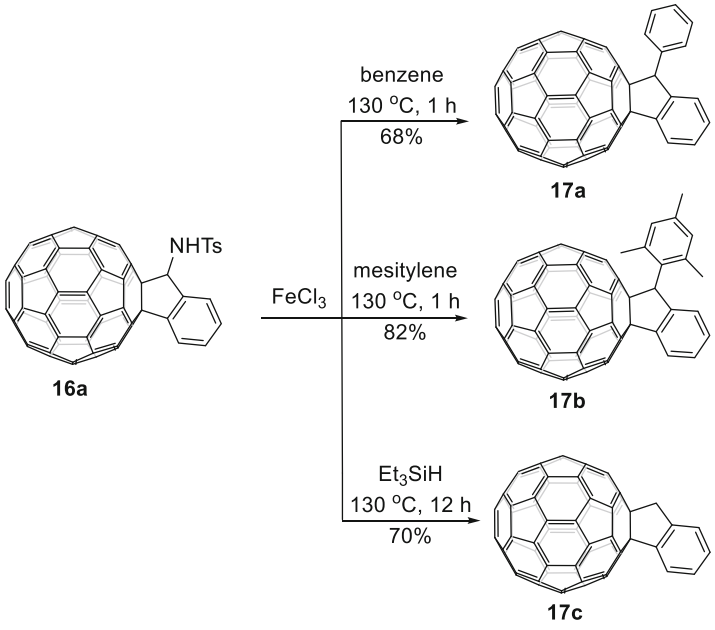

Scheme 23 Transformations of fulleroindane **16a**

reduction and Friedel-Crafts reaction to afford fulleroindanes **17a**–**c** in 68–82% yields (Scheme 23).

The Wang group later extended the above Pd-catalyzed reactions to *N*-(2-arylethyl) sulfonamides to afford the C_{60}-fused tetrahydrobenzazines **18** in

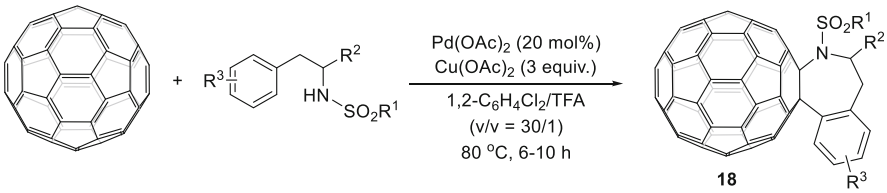

Scheme 24 Pd-catalyzed reactions of C_{60} with *N*-(2-arylethyl)sulfonamides

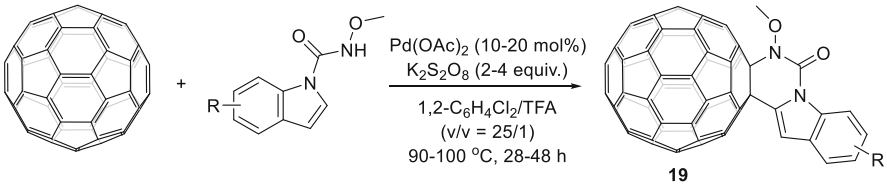

Scheme 25 Pa-catalyzed heteroannulations of C_{60} with indole-1-carboxamides

12–47% yields (Scheme 24) [34]. The optimized reaction conditions were selected as follows: $Pd(OAc)_2$ (20 mol%) as the catalyst, $Cu(OAc)_2$ (3 equiv.) as the oxidant, and 1,2-$C_6H_4Cl_2$/TFA (v/v = 30/1) as the solvent at 80 °C for 6–10 h. The chemical structures of the products were similar to the above results, changing from a six-membered ring to a seven-membered ring. In addition, **18** were found to undergo trifluoromethanesulfonic acid (TfOH)-facilitated rearrangement.

Chen, Wang, and coworkers recently reported a highly efficient heteroannulations between C_{60} and indole-1-carboxamides to generate the C_{60}-fused 3,4-dihydropyrimido[1,6-α]indol-1(2*H*)-ones **19** in 20–35% yields (Scheme 25) [35]. The optimized conditions were determined as follows: $Pd(OAc)_2$ (10–20 mol %) as the catalyst, $K_2S_2O_8$ (2–4 equiv.) as the oxidant in 1,2-$C_6H_4Cl_2$/TFA (v/v = 25/1) at 90–100 °C for 28–48 h. The process was characterized by good functional group compatibility and mild reaction conditions. In addition, the formed **19** could be derivatized via an electrochemical method to access the 1,2,3,4-, 1,2,3,16-, and 1,4,9,25-adducts.

Pd-Catalyzed Sulfonic Acid/Hydroxy-Directed C–H Activations

The electron-deficient aromatic ring of arylsulfonic acid is not readily available for the C–H activation step. However, the Wang group successfully synthesized C_{60}-fused sultones **20** in 18–30% yields by the Pd-catalyzed reactions of aryl sulfonic acids with C_{60} through an unprecedented sulfonic group-directed C–H bond activation (Scheme 26) [36]. The optimized reaction conditions were selected as follows: $Pd(OAc)_2$ (10–20 mol%) as the catalyst, $K_2S_2O_8$ (3 equiv.) as the oxidant, and 1,2-$C_6H_4Cl_2$/CH_3CN (v/v = 8/1) as the solvent at 140 °C for 24 h.

In 2014, the Wang group realized the hydroxyl-directed C–H activation/C–O cyclization reactions of phenethyl alcohols and benzyl alcohols with C_{60} to afford the C_{60}-fused tetrahydrobenzooxepine and isochroman derivatives **21** in 20–43%

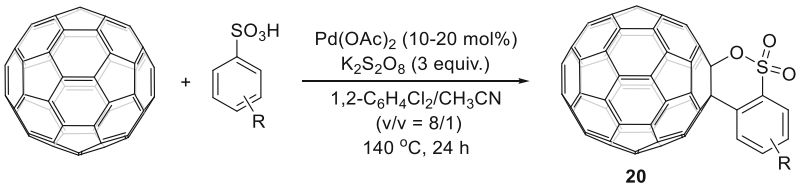

Scheme 26 Pd-catalyzed reactions of C_{60} with arylsulfonic acids

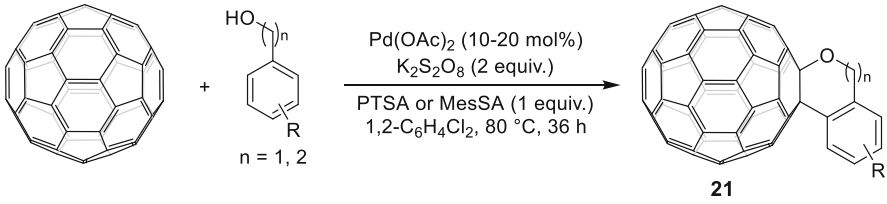

Scheme 27 Pd-catalyzed reactions of C_{60} with phenethyl alcohols and benzyl alcohols

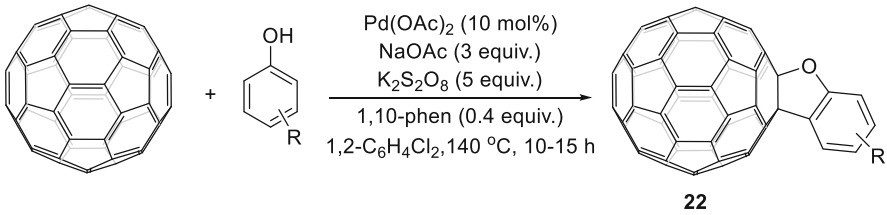

Scheme 28 Pd-catalyzed reactions of C_{60} with phenols

yields [37]. It should be noted that the Pd-catalyzed C–H activation of benzyl alcohols had no precedent. The screening results of Pd-catalyzed reactions of 2-phenylethanols showed that $K_2S_2O_8$ was the best oxidant, and the sulfonic acids such as PTSA and MesSA played a key role in the reaction. Unlike the previous Pd-catalyzed hydroxyl-directed C–H activations, this protocol did not require extra base additives as well as amino acid ligands, and both C_{60}-fused tetrahydrobenzooxepine and isochroman derivatives **21** were obtained for the first time (Scheme 27).

Then, the Wang group reported the Pd-catalyzed heteroannulation reactions between C_{60} with phenols to synthesize C_{60}-fused benzofurans **22** in 32–63% yields (Scheme 28) [38]. The optimized reaction conditions were selected as follows: Pd $(OAc)_2$ (10 mol%) as the catalyst, 1,10-phenanthroline (1,10-phen, 0.4 equiv.) as the ligand, NaOAc (3 equiv.) as the base, $K_2S_2O_8$ (5 equiv.) as the oxidant, and 1,2-$C_6H_4Cl_2$ as the solvent at 140 °C for 10–15 h.

The Wang group recently disclosed the Pd-catalyzed reactions of C_{60} with 4-hydroxycoumarins to provide C_{60}-fused furochromenones **23** in 31–52% yields (Scheme 29) [39]. The optimized reaction conditions were selected as follows:

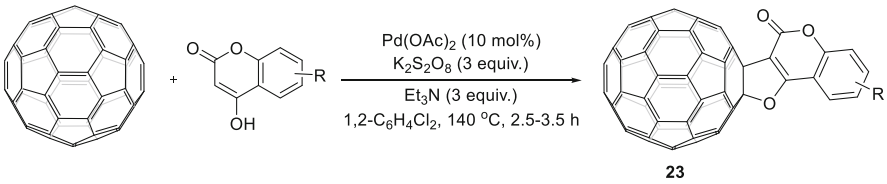

Scheme 29 Pd-catalyzed reactions of C_{60} with 4-hydroxycoumarins

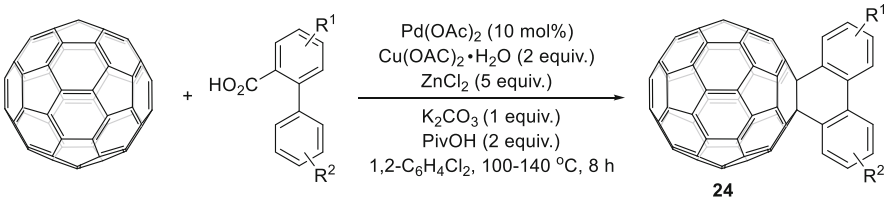

Scheme 30 Pd-catalyzed synthesis of C_{60}-fused dihydrophenanthrenes

$Pd(OAc)_2$ (10 mol%) as the catalyst, $K_2S_2O_8$ (3 equiv.) as the oxidant, triethylamine (Et_3N, 3 equiv.) as the base, and 1,2-$C_6H_4Cl_2$ as the solvent at 140 °C for 2.5–3.5 h. It should be noted that unlike the addition of acid mentioned above, this reaction required the addition of Et_3N, which greatly improved the reactivity.

Synthesis of C_{60}-fused Carbocycles via the Pd-Catalyzed C–H Activation Reactions

In 2015, the Wang group described the synthesis of the C_{60}-fused dihydrophenanthrenes **24** in 19–46% yields through the Pd-catalyzed decarboxylative annulations of C_{60} with 2-arylbenzoic acids (Scheme 30) [40]. The optimized reaction conditions were selected as follows: $Pd(OAc)_2$ (10 mol%) as the catalyst; $Cu(OAc)_2{\cdot}H_2O$ (2 equiv.) as the oxidant; $ZnCl_2$ (5 equiv.), K_2CO_3 (1 equiv.), and PivOH (2 equiv.) as the additives; and 1,2-$C_6H_4Cl_2$ as the solvent at 100–140 °C for 8 h. K_2CO_3 and PivOH were shown to be beneficial additives in Pd-catalyzed directed arylations.

In 2016, the Wang group achieved the synthesis of C_{60}-fused spiroindanes **25** in 20–50% yields through the Pd-catalyzed C–H activation annulations of C_{60} with 2-aryl cyclic 1,3-dicarbonyl compounds (Scheme 31) [41]. The optimized reaction conditions were selected as follows: $Pd(PhCN)_2Cl_2$ (10–50 mol%) as the catalyst, 1,4-benzoquinone (BQ) (2 equiv.) as the oxidant, PTSA (1 equiv.) as the additive, and 1,2-$C_6H_4Cl_2$ as the solvent at 100–120 °C for 5–24 h.

In 2021, Liu, Zhang, and coworkers reported the Pd-catalyzed domino spiral cyclization of C_{60} [42]. Products **26** were obtained from the reactions of C_{60} with 1-iodo-2-((2-arylallyl)oxy)benzenes. The use of 5–10 mol% of $Pd(PPh_3)_4$ as the catalyst and 2 equiv. of cesium carbonate (Cs_2CO_3) as the base in PhCl at 130–140 °C for 24–48 h provided the desired products **26** in 27–50% yields (Scheme 32). Under the Pd-catalyzed conditions, the conversion underwent domino

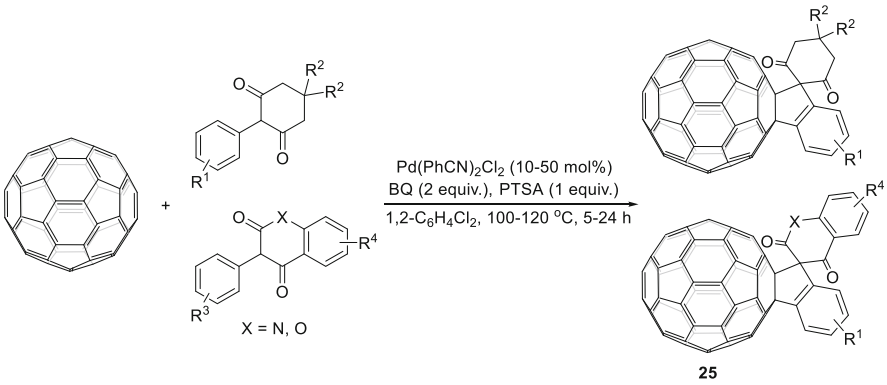

Scheme 31 Pd-catalyzed reactions of C_{60} with 2-aryl cyclic 1,3-dicarbonyl compounds

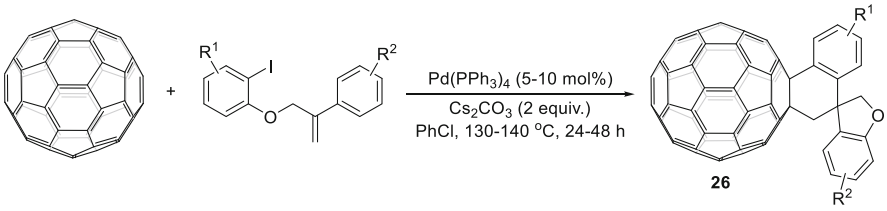

Scheme 32 Pd-catalyzed reactions of C_{60} with 1-iodo-2-((2-arylallyl)oxy)benzenes

Heck/C–H activation and provided a series of fullerene-fused spiral ring derivatives in a general and flexible manner.

Miscellaneous Pd-Catalyzed Reactions of C_{60}

Jin, Peng, and coworkers developed a convenient and efficient Pd-catalyzed C–H activation and hydroxylation of C_{60} with aryl compounds for the synthesis of C_{60}-fused dihydrofurans **27** in 13–39% yields and 1,4-fullerenols **28** in 16–34% yields [43]. The optimized reaction conditions of synthesis of C_{60}-fused dihydrofurans were selected as follows: $Pd(OAc)_2$ (20 mol%) as the catalyst, $Cu(OAc)_2$ (5 equiv.) as the oxidant, and PhCl/TFA (v/v = 8/1) as the solvent at 100–120 °C for 18–24 h (Scheme 33). In comparison, the optimized reaction conditions of synthesis of 1,4-fullerenols were selected as follows: $Pd(OAc)_2$ (20–40 mol%) as the catalyst, $K_2S_2O_8$ (5 equiv.) as the oxidant, and PhCl/TFA (v/v = 4/1) as the solvent at 120 °C for 10–12 h (Scheme 34).

Jin, Peng, and coworkers reported the synthesis of *N*-unsubstituted 2-fulleropyrrolines in 21–43% yields through the Pd-catalyzed *N*-heteroannulation reactions of C_{60} with benzoyl hydrazone esters (Scheme 35) [44]. The optimized conditions were determined as follows: $Pd(OAc)_2$ (20 mol%) as the catalyst,

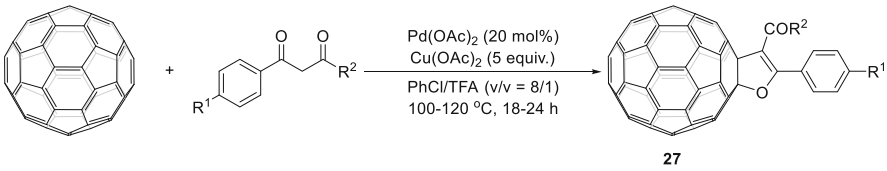

Scheme 33 Pd-catalyzed synthesis of C_{60}-fused dihydrofurans

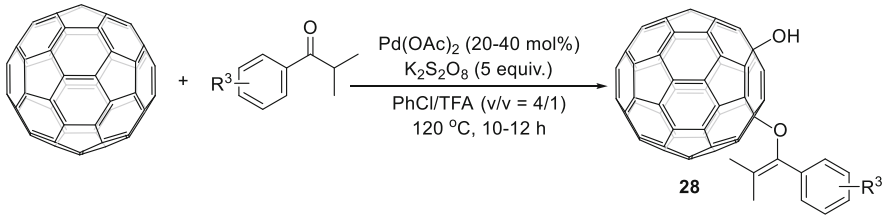

Scheme 34 Pd-catalyzed synthesis of 1,4-fullerenols

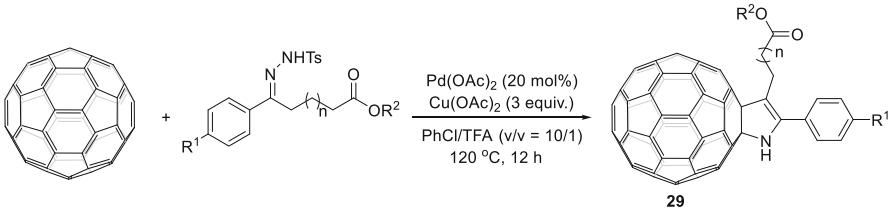

Scheme 35 Pd-catalyzed heteroannulations of C_{60} with benzoyl hydrazone esters

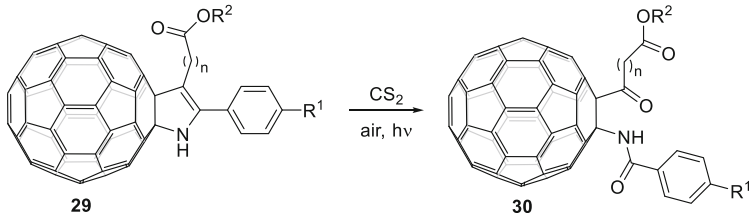

Scheme 36 Photochemical reactions of **29** with O_2

$Cu(OAc)_2$ (3 equiv.) as the oxidant in PhCl/TFA (v/v = 10/1) at 120 °C for 12 h. In addition, the self-sensitive photooxidations of electron-rich 2-fulleropyrrolines **29** in air-saturated carbon disulfide (CS_2) at room temperature were studied. The scarce ketoamide fullerene derivatives **30** were formed in 54–78% yields under very mild conditions (Scheme 36).

Scheme 37 Rhodium-catalyzed hydrogenation of C_{60}

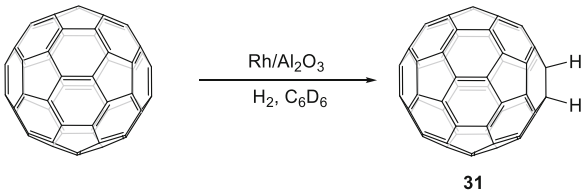

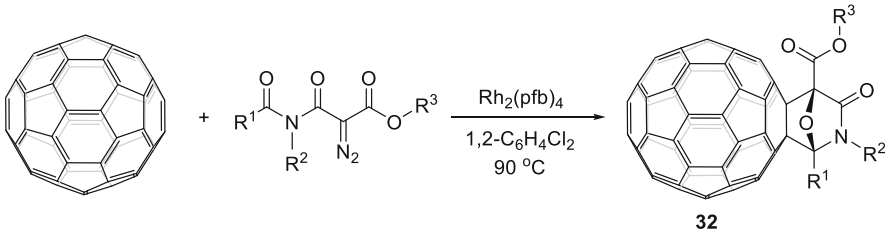

Scheme 38 Rh-catalyzed reactions of C_{60} with diazo imides

Rhodium-Catalyzed Reactions of C_{60}

Rh-Catalyzed Hydrogenations of C_{60}

In 1993, the Becker group disclosed that the Rh-catalyzed reduction of C_{60} produced a mixture of hydrogenated products with $C_{60}H_2$ as the main product for the first time [45]. The hydrogenated compounds were obtained by reducing C_{60} with Rh(0) on aluminum oxide and molecular hydrogen in deuterated benzene (C_6D_6) at ambient temperature and pressure. Compound **31** was identified as the main product by ^{1}H NMR and the yield was 14% (Scheme 37).

Rh-Catalyzed Cycloaddition Reactions of C_{60}

Among the many functionalized reactions of C_{60}, the cycloaddition reaction is the cleanest and most useful. In 1994, Wudl, Padwa, and coworkers reported the Rh-catalyzed reactions of diazo imides with C_{60} [46]. As shown in Scheme 38, the reactions of four diazo imide isomunchnone precursors with C_{60} were carried out in the presence of a rhodium catalyst (pfb = perfluorobutyrate). The cycloadducts **32** were obtained in 24–52% yields.

The Nair group showed the Rh-catalyzed cycloaddition reactions of the in situ generated carbonyl ylides with C_{60} [47, 48]. The reactions of C_{60} with diazo ketones in the presence of a catalytic amount of dirhodium tetraacetate ($Rh_2(OAc)_4$) in toluene at room temperature gave the expected products **33** in 31–53% yields (Scheme 39).

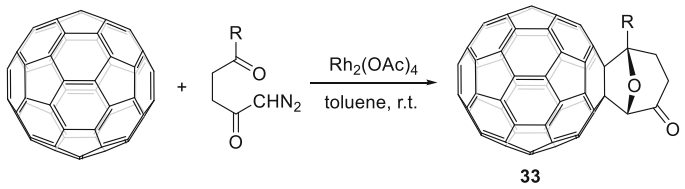

Scheme 39 Rh-catalyzed reactions of C_{60} with diazo ketones

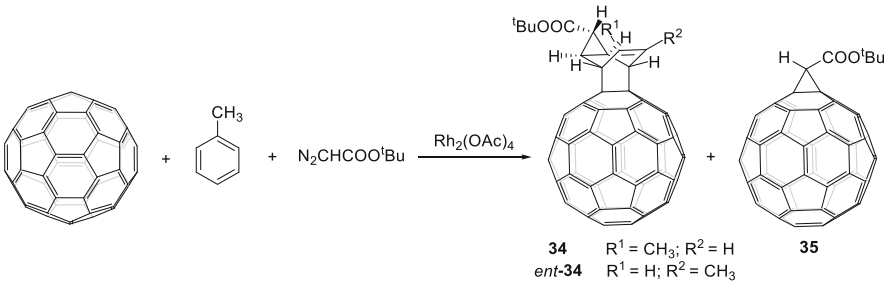

Scheme 40 Rh-catalyzed reaction of C_{60} with *tert*-butyl diazoacetate and toluene

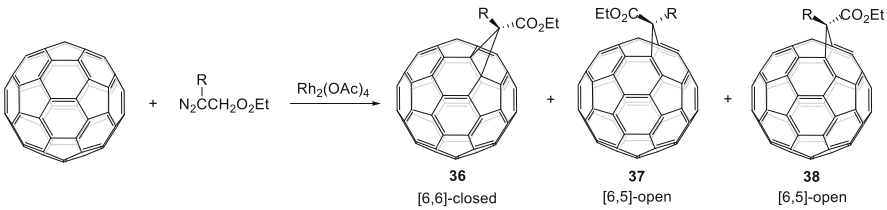

Scheme 41 Rh-catalyzed reactions of C_{60} with α-diazoesters

The Duczek group reported the Rh-catalyzed reaction of C_{60} with *tert*-butyl diazoacetate and toluene [49]. The Rh-catalyzed cyclopropanation of toluene by *tert*-butyl diazoacetate produced the norcaradiene intermediate, which underwent Diels-Alder reaction with C_{60} afforded norcaradiene-type adducts such as the tricycloadduct **34**/*ent*-**34** in 43% yield along with methanofullerene **35** in 4% yield based on converted C_{60} (Scheme 40).

The Pellicciari group described the Rh-mediated reactions of C_{60} with α-diazoesters [50]. The best results were obtained when the reactions between C_{60} and α-diazoesters were carried out in α-methylnaphthalene in the presence of an equimolar amount of $Rh_2(OAc)_4$, and the methanofullerenes **36** were obtained exclusively in 33–42% yields along with trace or none of fulleroids **37** and **38** (Scheme 41).

The Itoh group developed the Rh-catalyzed three-component domino coupling reactions of C_{60} with 1,6-dialkynes and hydrosilane to afford C_{60}-fused carbocycles **39** in 28–58% isolated yields (Scheme 42) [51]. In the Diels-Alder cycloaddition

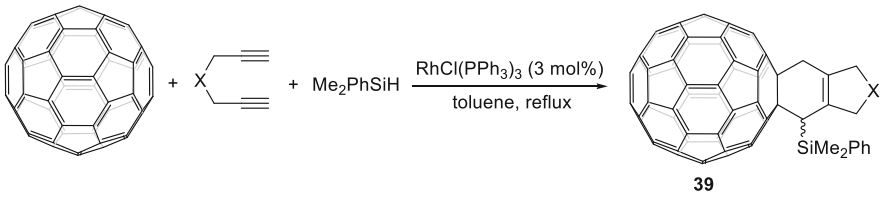

Scheme 42 Rh-catalyzed synthesis of C_{60}-linked carbo- and heterocycles

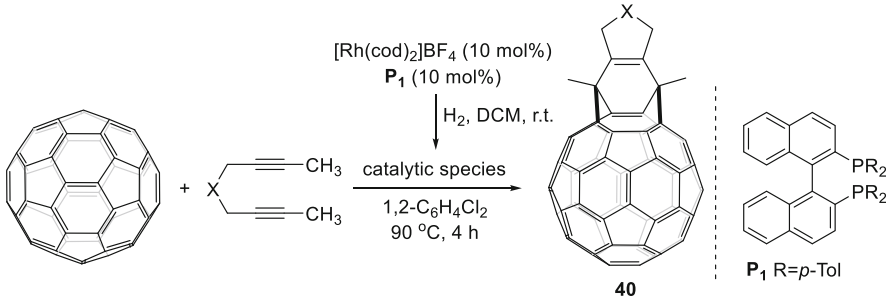

Scheme 43 Rh-catalyzed [2 + 2 + 2] cycloaddition of C_{60} with diynes

reactions of C_{60}, dienylsilanes were undoubtedly effective diene components and were generated from 1,6-dialkynes and hydrosilane through rhodium catalysis.

Transition metal-catalyzed [2 + 2 + 2] cycloaddition reaction is the preferred method for the synthesis of six-membered rings. C_{60} is a valuable candidate for [2 + 2 + 2] cycloaddition reactions with alkynes because of its typical reactivity of electron-deficient olefin. Artigas et al. reported the open-cage fullerenes **40** in 10–61% isolated yields through the Rh-catalyzed [2 + 2 + 2] cycloadditions of C_{60} with diynes, and subsequent formal [4 + 4]/retro-[2 + 2 + 2] rearrangements (Scheme 43) [52]. The optimized conditions were determined as follows: $[Rh(cod)_2]BF_4$ (10 mol%) as the catalyst, Tol-BINAP (**P_1**) as the diphosphine in 1,2-$C_6H_4Cl_2$ at 90 °C for 4 h. Significantly, a mixture of $[Rh(cod)_2]BF_4$ and **P_1** was activated with molecular hydrogen in dichloromethane solution prior to the addition of the substrate.

Rh-Catalyzed Arylations and Alkenylations of C_{60}

The Itami group developed the Rh-catalyzed arylations and alkenylations of C_{60} with boronic acids to provide hydrofullerenes **3** in 12–69% yields (Scheme 44) [53, 54]. The optimized conditions were determined as follows: $[Rh(cod)(MeCN)_2]BF_4$ (10 mol%) or $[RhOH(cod)]_2$ (10 mol%) as the catalyst in 1,2-$C_6H_4Cl_2/H_2O$ (v/v = 4/1) at 60–100 °C for 12 h. The experimental results showed that water was a necessary additive to promote the reaction. The reaction generally had high

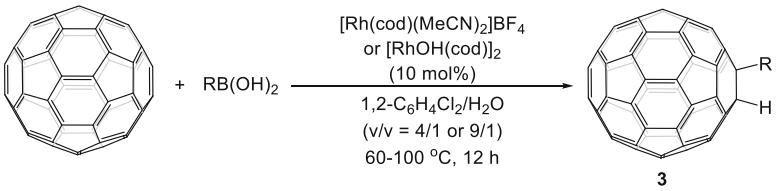

Scheme 44 Rh-catalyzed arylations and alkenylations of C_{60}

regioselectivity and additive selectivity. Encouraged by the good results for the reactions of C_{60}, the optimized reaction conditions were applied to C_{70} [54]. The results showed that C_{70} could also produce the desired product $PhC_{70}H$ successfully. By X-ray crystal structure analysis, the reaction site of C_{70} for the organometallic hydroarylation reaction was determined for the first time. The arylation of C_{60} was also used to synthesize a product with the 2,6-dimethoxyphenyl group directly attached to the fullerene cage, a novel organic photovoltaics receptor material [55]. The methoxy groups placed at closest proximity to the fullerene core offered a distinct advantage over conventional methanofullerenes in the stabilization of LUMO energies, due to the through-space interaction between the methoxy and fullerene moieties.

Copper-Catalyzed Reactions of C_{60}

Cu-Catalyzed Heteroannulations of C_{60}

Due to the influence of two electronegative atoms directly linked to the C_{60} cage, fulleroimidazoles and fullerooxazoles have proved to possess better electron-acceptor character than pristine C_{60}, and are beneficial for the preparation of organic photovoltaic devices. However, there exist only a few methods for the preparation of them and these reactions have some limitations, such as poor selectivity, high toxicity, and high cost [56–58]. In 2013, the Yang group disclosed a simple and efficient method for the preparation of fulleroimidazoles **41** in 24–48% yields and fullerooxazoles **42** in 18–36% yields via the copper-catalyzed oxidative intermolecular reactions of amidines or amides with C_{60} using air as the oxidant (Scheme 45) [59]. The optimized reaction conditions were selected as follows: CuI (0.4 equiv.) as the catalyst, 1,10-phen (0.4 equiv.) as the ligand, and PhCl as the solvent at 130 °C for 6–12 h under air atmosphere.

Based on the previous literature [60, 61], a proposed mechanism is shown in Scheme 46. This transformation was initiated via one-electron oxidation of amidine or amide by a Cu(II) species, which resulted in the formation of a nitrogen radical species, and subsequent capture by C_{60} to afford a fullerenyl radical. Complexation of the amidine or amide moiety to a Cu(II) species generated a C_{60}–Cu(II) radical complex accompanied by proton elimination. In path A, intramolecular coupling of

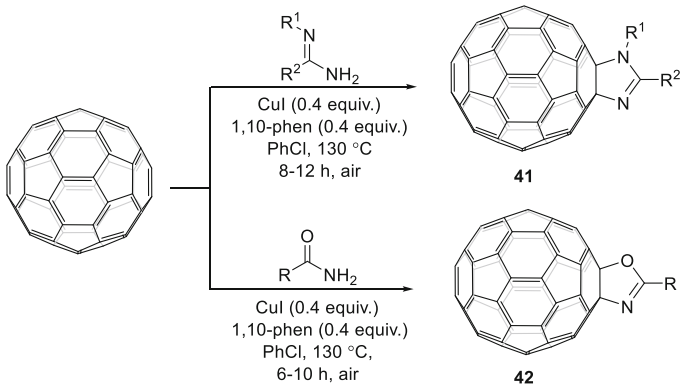

Scheme 45 Cu-catalyzed synthesis of fulleroimidazoles and fullerooxazoles

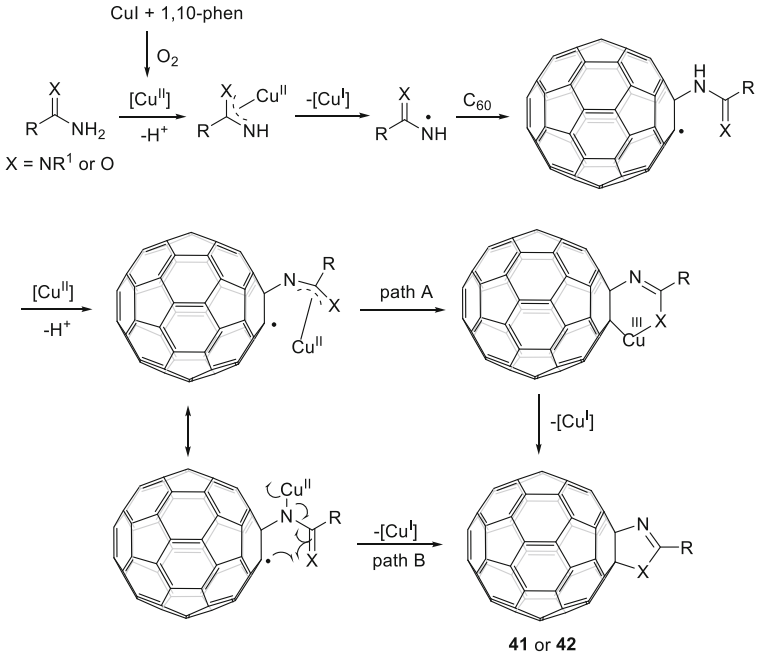

Scheme 46 Proposed reaction mechanism for the formation of **41** and **42**

the carbon radical with the Cu(II) in the C_{60}–Cu(II) species gave the metallocycle C_{60}–Cu(III), which underwent reductive elimination to generate **41** or **42**. In path B, homolytic cleavage of the N–Cu bond and subsequent intramolecular cyclization could also generate **41** or **42**.

Although both 1- and 2-fulleropyrrolines possess a nitrogen atom bonding to the fullerene cage, 1-fulleropyrrolines have a C=N bond, whereas 2-fulleropyrrolines

contain a C=C bond. The synthesis of 2-fulleropyrrolines with a nitrogen atom attached to the fullerene cage has been studied by the Wang and Yang groups [62, 63]. However, the formation of 1-fulleropyrrolines had not been achieved until 2015. The Wang group constructed 1-fulleropyrrolines **43** in 17–35% yields by the Cu(I)-catalyzed heteroannulations of C_{60} with ketoxime acetates (Scheme 47) [64]. The optimal reaction conditions for the molar ratio of the reagents C_{60}, ketoxime acetate, CuBr, and $NaHSO_3$ was 1: 1.5: 0.2: 10, and a temperature of 150 °C.

Oxime esters, which are readily available and highly reactive, have been widely used as internal oxidants for the formation of nitrogen-containing scaffolds in the presence of transition metal catalysts [65, 66]. However, oxime acetate derivatives substituted by N, O, and S at the *α*-position had not been explored for the synthesis of C_{60}-fused *N*-containing heterocycles derivatives. In 2018, Liu, Zhang, and coworkers reported the copper-catalyzed redox-neutral *N*-heteroannulation reactions of *α*-functionalized oxime acetates containing *N*-, *O*-, and *α*-substituents at the *α*-position with C_{60} [67]. Surprisingly, the unexpected 2-substituted fulleropyrrolidines and various mono- and disubstituted 1-fulleropyrrolines **44**–**46** were synthesized in 16–55% yields (Schemes 48, 49, and 50).

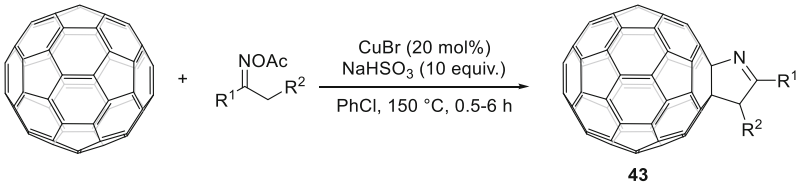

43

Scheme 47 Cu-catalyzed reactions of C_{60} with ketoxime acetates

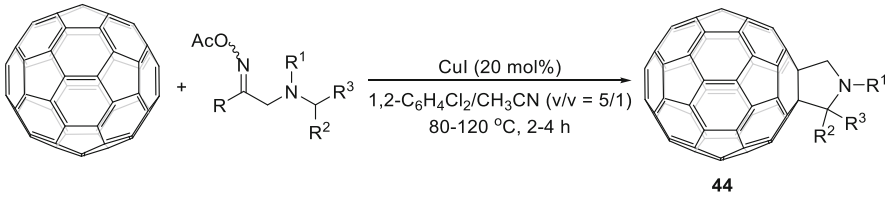

44

Scheme 48 Cu-catalyzed reactions of C_{60} with *α*-*N*-substituted oxime acetates

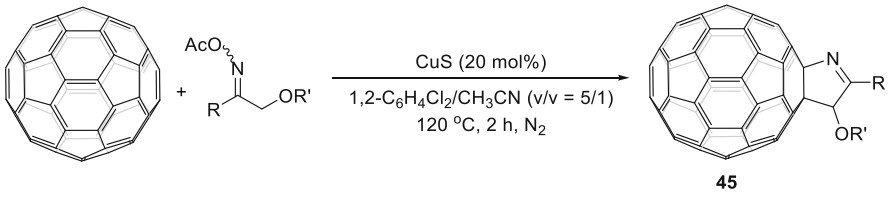

45

Scheme 49 Cu-catalyzed reactions of C_{60} with *α*-*O*-substituted oxime acetates

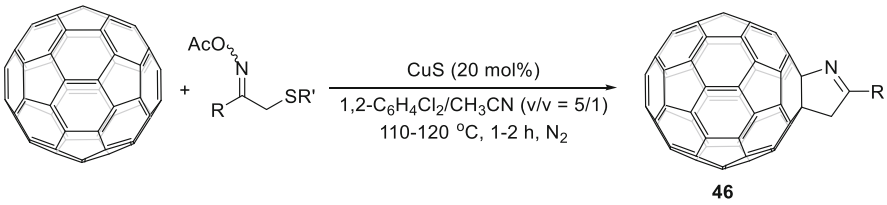

Scheme 50 Cu-catalyzed reactions of C_{60} with *α*-*S*-substituted oxime acetates

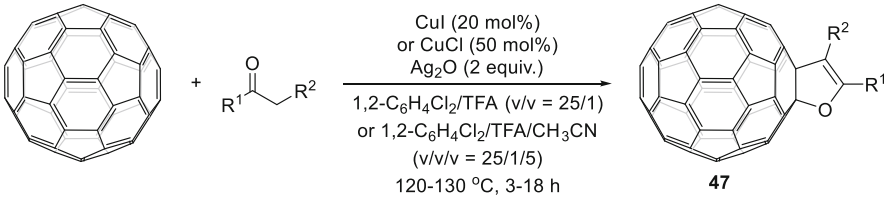

Scheme 51 Cu-catalyzed reactions of C_{60} with carbonyl compounds

As a useful basic unit, furan has attracted growing attention in the organic optoelectronic area, especially for the fusion of furan rings to an all-carbon aromatic system [68]. However, probably because of the lack of the available fullerene derivatives, the organic electronic research on the furan-fused fullerene derivatives was rarely seen. Nowadays, the reported methods to synthesize these compounds still have some limitations, such as low yields and a narrow substrates scope, which restrict their applications in related fields. Therefore, development of the efficient methods with broad substrates scope for the formation of furan-fused fullerene derivatives is highly demanding. Recently, Liu, Zhang, and coworkers developed the Cu(I)/Ag(I)-mediated synergistic annulation reactions of C_{60} with diarylethanones, benzoyl-acetonitriles or *β*-dicarbonyl compounds for the formation of diverse disubstituted dihydrofuran-fused C_{60} derivatives **47** in 18–48% yields (Scheme 51) [69]. The optimized reaction conditions were selected as follows: CuI (20 mol%) or CuCl (50 mol%) as the catalyst, Ag_2O (2 equiv.) as the oxidant, and 1,2-$C_6H_4Cl_2$/TFA (v/v = 25/1) or 1,2-$C_6H_4Cl_2$/TFA/CH_3CN (v/v/v = 25/1/5) as the solvent at 120–130 °C for 3–18 h.

As well known, [4 + 2] cycloaddition is one of the most used methods to form C_{60}-fused six-membered derivatives [70, 71]. In 2018, the Wang group reported the synthesis of fullerotetrahydroquinolines **48** via hetero–Diels–Alder reactions of C_{60} with the in situ generated aza-*o*-quinone methides (aoQMs) from *N*-(*o*-chloromethyl)aryl sulfonamides with the catalysis of Cu_2O (Scheme 52) [72]. The optimized reaction conditions were selected as follows: Cu_2O (20–50 mol%) as the catalyst, 1,10-phen (30–75 mol%) as the ligand, and PhCl as the solvent at 120–140 °C for 3–6 h. The reactions showed good tolerance for diverse electron-donating or electron-withdrawing groups at different positions on the aromatic ring of substrates, giving the corresponding products **48** in 20–36% yields.

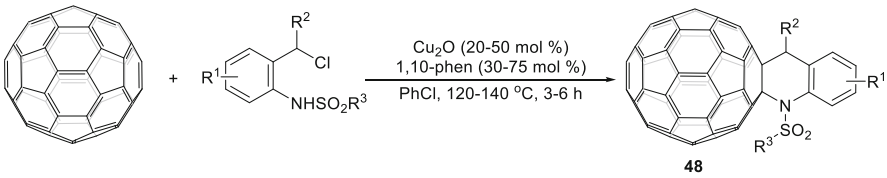

Scheme 52 Cu-catalyzed [4 + 2] cycloaddition reaction of C_{60}

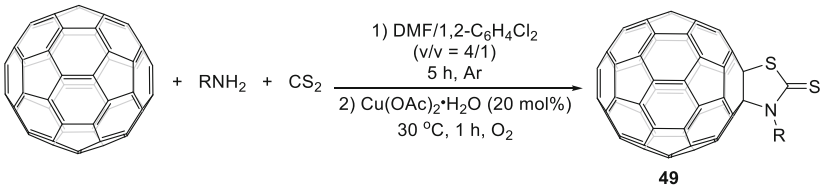

Scheme 53 Cu-catalyzed reactions of C_{60} with CS_2 and aliphatic primary amines

CS_2 is an excellent solvent for fullerenes, and the Wang group's previous work on the thiolation of C_{60} with CS_2 and amino acid esters has provided the synthesis of C_{60}- fused thiolactams via the isothiocyanate intermediate formed by losing the H_2S molecule from dithiocarbamic acid [73, 74]. Nevertheless, the sulfur atom is linked to the C_{60}-fused heterocycle instead of the fullerene cage. Recently, the Gao group reported the copper-catalyzed aerobic oxidative reactions of C_{60} with aliphatic primary amines and CS_2 at 30 °C for 1 h to produce [60]fullerothiazolidinethiones **49**, of which the sulfur atom directly bound to the C_{60} skeleton, in 22–43% yields (Scheme 53) [75].

On the basis of the experimental results and the literature reports, a plausible reaction mechanism was proposed (Scheme 54). Carbon disulfide reacted with primary amine to afford the dithiocarbamic acid. The single electron transfer (SET) from the dithiocarbamic acid to C_{60} under the argon atmosphere led to the formation of $C_{60}^{\bullet -}$ and aminium cation radical, followed by the aerobic oxidative amination and the loss of a proton to form the C_{60}–N bond. Finally, intramolecular C_{60}–S bond formation occurred to afford product **49** via the Cu-catalyzed aerobic oxidation.

Since 2005, the Wang group has reported several methods to synthesize various fullerene derivatives with the aid of copper salts [76]. However, further exploration and development of fullerene reactions catalyzed/mediated by the copper salts still remained as a challenge. The Yang group explored the CuI-catalyzed reactions of C_{60} with amino alcohols with aerobic oxygen as the sole oxidant [77]. For 2-/3-amino alcohols, aminooxygenation reactions occurred to provide fulleromorpholine and fullerooxazepane derivatives **50** in 7–35% yields. When a tethered furan ring existed, a further intramolecular [4 + 2] reaction with the neighboring double bond took place to give the *cis*-1 products **51** in 16–21% yields. In the case of 4-/5-amino alcohols, methanofullerenes linking with cyclic amides were obtained in 15–50% yields for **52** through cyclic enamine intermediates (Scheme 55).

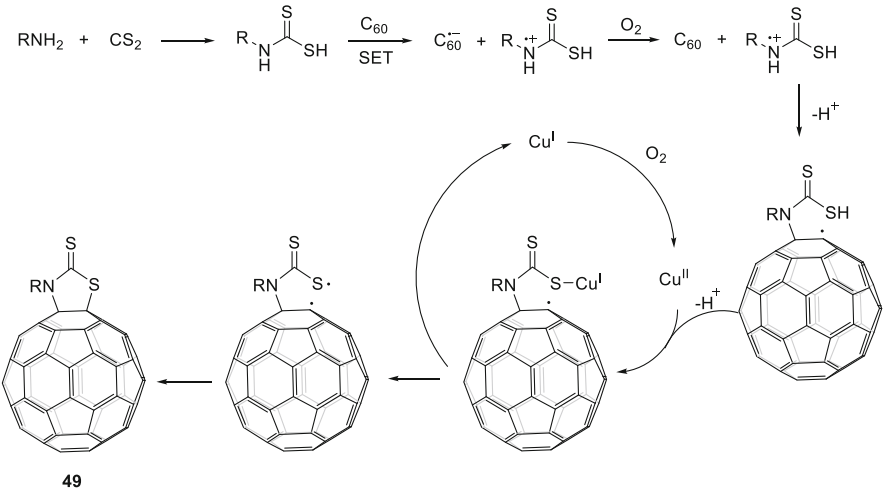

Scheme 54 Proposed reaction mechanism for the formation of **49**

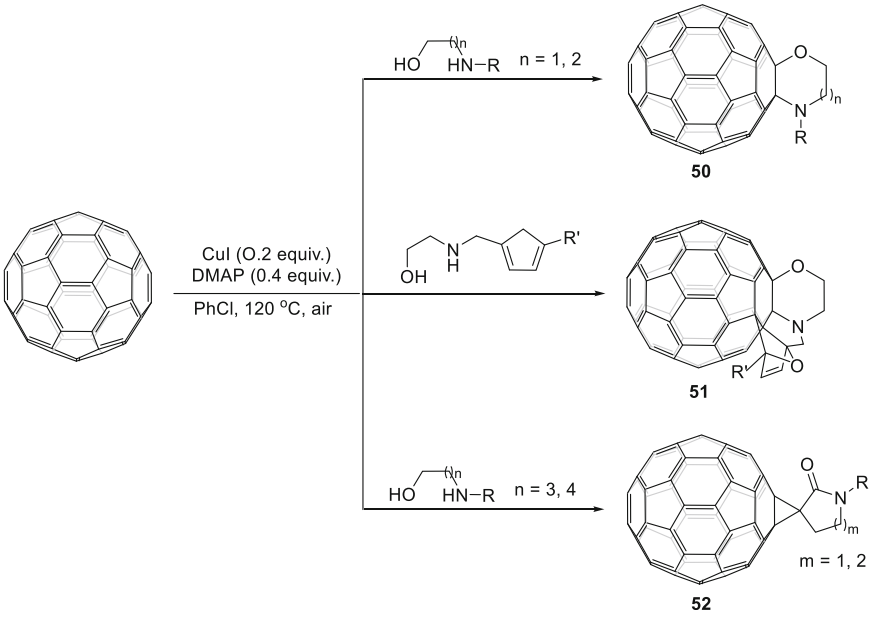

Scheme 55 Cu-catalyzed reactions of C_{60} with amino alcohols

Recently, the Wang group unveiled the synthesis of fullerotetrahydropyridazines by the copper-catalyzed reactions of C_{60} with hydrazides to afford products **53** in 8–40% yields (Scheme 56) [78]. The optimized reaction conditions were selected as follows: $Cu(OAc)_2 \cdot H_2O$ (20–50 mol%) as the catalyst, 1,10-phen (0.4–1 equiv.) as

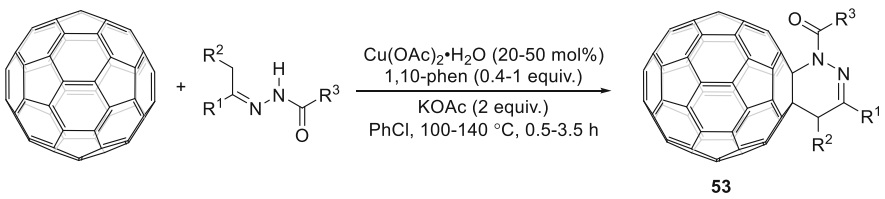

Scheme 56 Cu-catalyzed reactions of C_{60} with hydrazides

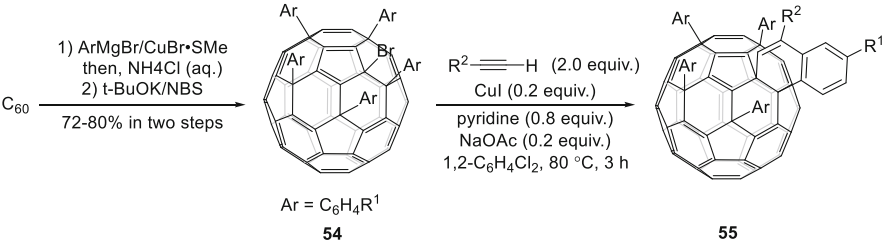

Scheme 57 Cu-catalyzed reactions of fullerene bromides with alkynes

the ligand, KOAc (2 equiv.) as the base, and PhCl as the solvent at 100–140 °C for 0.5–3.5 h.

Cu-Catalyzed Functionalizations of Fullerene Derivatives

In 2010, Matsuo, Nakamura, and coworkers described an unusual and effective Cu-catalyzed C–C bond-forming reactions of arylacetylenes or enynes with $C_{60}Ar_5Br$ to form products **55** with a dihydronaphthalene ring fused to the fullerene sphere in 13–94% yields (Scheme 57) [79]. The optimized reaction conditions were selected as follows: CuI (20 mol%) as the catalyst, pyridine (0.8 equiv.) or NaOAc (2.0 equiv.) as the base, and 1,2-$C_6H_4Cl_2$ as the solvent at 80 °C for 3 h. This was a rare catalytic reaction of fullerenes and involved a formal C–H bond activation process.

On the basis of the literature report [80] and the experimental results, a proposed mechanism was described (Scheme 58). The copper-mediated radical mechanism started with a SET [81, 82] from Cu(I) to $C_{60}Ph_5Br$ **54A** to produce a cyclopentadienyl radical **54B**, which then reacted with an alkyne to generate the vinyl radical intermediate **54C**. The intermediate **54C** was added to the nearby aryl group to form the radical **54D**. Subsequently, the radical **54D** could be oxidized by Cu(II) in the presence of a base to form the annulation product **55** and the Cu(I) was regenerated at the same time.

Due to the interaction of two adjacent fullerene cages, the single-bonded fullerene dimer $RC_{60}–C_{60}R$ is expected to display interesting optical and electronic properties [83, 84]. However, some reported methods to synthesize the elaborated fullerene

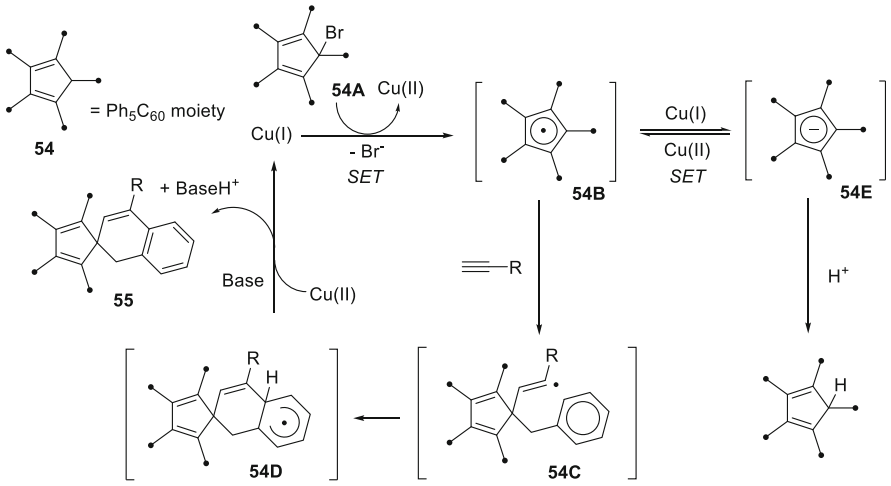

Scheme 58 Proposed reaction mechanism for the formation of **55**

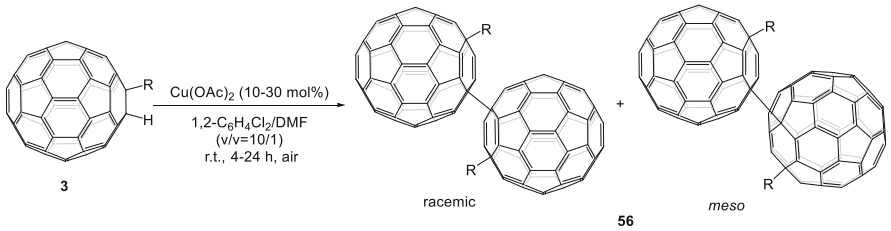

Scheme 59 Cu-catalyzed homo-dimerizations of monosubstituted hydrofullerenes

dimers were limited by the poor functional group tolerance, low yield, and the use of excess amounts of reagents [85, 86]. Nowadays, functionalization of fullerenes by transition-metal catalysis has been widely used, but there was no report on the catalytic dimerization for the synthesis of single-bonded fullerene dimers before 2012. Delightedly, Jin, Yamamoto, and coworkers reported the copper-catalyzed homodimerization products **56** from monofunctionalized hydrofullerenes in 70–96% yields (Scheme 59) [87]. The optimized reaction conditions were selected as follows: $Cu(OAc)_2$ (10–30 mol%) as the catalyst and 1,2-$C_6H_4Cl_2$/DMF (v/v = 10/1) as the solvent under air at room temperature. In contrast to the previously reported methods, this method featured broad substrate scope, good functional group tolerance, higher yield, and mild conditions.

Matsuo, Nakamura, and coworkers have disclosed that a fullerene monoradical could be oxidized to a fullerene cation in the presence of $CuCl_2$, which then reacted with nucleophiles to afford the corresponding 1,4- or 1,2-fullerenes, respectively [85, 88]. 1,4-Fullerene derivatives have been applied to n-type semiconductors for high performance organic photovoltaics and thin film transistors [89]. In 2013, Jin, Yamamoto, and coworkers reported the copper-catalyzed C–H aminations of the

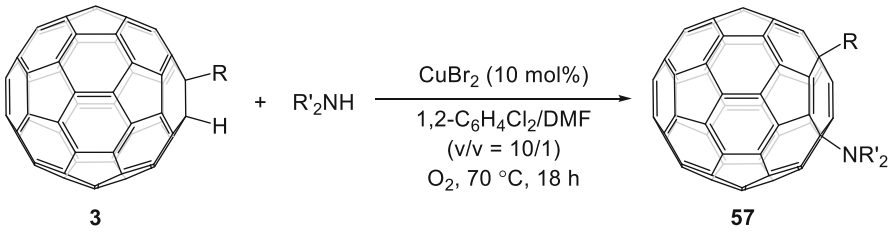

3 57

Scheme 60 Cu-catalyzed C–H aminations of hydrofullerenes

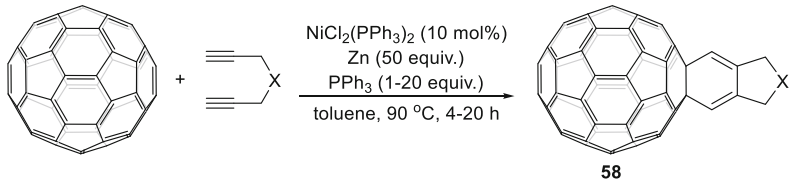

58

Scheme 61 Ni-catalyzed [2 + 2 + 2] cycloadditions of C_{60} with diynes

monosubstituted hydrofullerenes with various amines to give aminated 1,4-fullerene derivatives **57** in 41–96% yields (Scheme 60) [90]. The optimized reaction conditions were selected as follows: $CuBr_2$ (10 mol%) as the catalyst and 1,2-$C_6H_4Cl_2$/DMF (v/v = 10/1) as the solvent under an oxygen atmosphere at 70 °C for 18 h.

Other Transition Metal-Catalyzed Reactions of C_{60}

Nickel-Catalyzed Reactions of C_{60}

Due to the limitation of specific substrates and complicated steps, only a few cyclohexadiene derivatives of C_{60} have been reported. In 1998, the Cheng group reported the synthesis of C_{60}-fused cyclohexadiene derivatives **58** via the Ni-mediated cycloadditions of bisalkynes to C_{60} [91]. Due to gradual decomposition of the nickel complex under the reaction conditions, more than a stoichiometric amount of the nickel complex was required to achieve a high yield of the cycloaddition product. In the presence of $NiCl_2(PPh_3)_2$ (1.2 equiv.), PPh_3 (16 equiv.), and zinc powder (52 equiv.) in toluene at 90 °C, 1,6-diynes underwent a [2 + 2 + 2] cycloaddition reactions with C_{60} to provide the desired six-membered ring products **58** in 47–75% yields (Scheme 61). The reaction could proceed with a catalytic amount of $NiCl_2(PPh_3)_2$ (10 mol%), and product **58a** from 4,4-bis (methoxycarbonyl)hepta-1,6-diyne was isolated in 50% yield. Furthermore, products **58** could undergo interesting photoinduced intramolecular [4 + 4] cycloadditions, leading to the formation of bisfulleroids in 84–92% yields.

In 2015, the Jin group described the Ni-catalyzed 1,4-difunctionalizations of C_{60} with benzyl bromides to give **59** in 55–85% yields (Scheme 62) [92]. Various

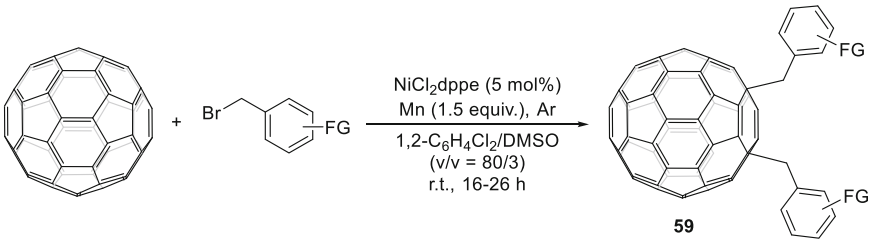

Scheme 62 Ni-catalyzed reactions of C_{60} with benzyl bromides

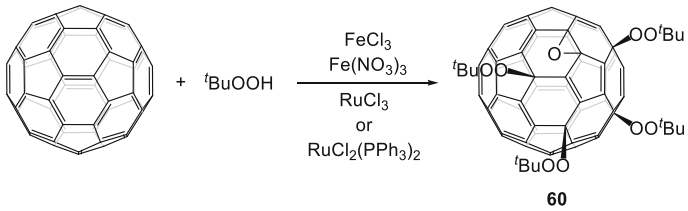

Scheme 63 Fe- or Ru-catalyzed reaction of C_{60} with *tert*-butyl hydroperoxide

functional groups were tolerated for the 1,4-dibenzylation reactions. The optimized conditions were determined as follows: $NiCl_2$dppe (5 mol%) as the catalyst, Mn (1.5 equiv.) as the reductant in 1,2-$C_6H_4Cl_2$/DMSO at room temperature. It was noted that the use of anhydrous DMSO was a key to improve the selectivity of **59**.

Iron-Catalyzed Reactions of C_{60}

In 2002, the Gan group published iron- or ruthenium-catalyzed reaction of *tert*-butyl hydroperoxide with C_{60} and obtained the first fullerene mixed peroxides $C_{60}(O)(OO^tBu)_4$ [93]. In this reaction, C_{60} played the role as a *tert*-butylperoxy radical trap to afford product **60** (Scheme 63).

Silver(I)-Catalyzed Reactions of C_{60}

In 2009, Martín and coworkers disclosed the enantioselective catalytic synthesis of chiral pyrrolidinofullerenes **61** under very mild conditions at low temperatures and with high yields [94]. The use of catalytic amounts of chiral Ag(I) or Cu(II)-complexes determined the stereochemical outcome of chiral pyrrolidinofullerenes. Chiral ligand (10 mol%) and Ag(I) (10 mol%) or Cu(II) (10 mol%) were dissolved in toluene and the reactions were stirred at −15 °C or room temperature for 0.5–25 h giving the chiral *cis*- and *trans-products* **61** in 25–88% yields (Scheme 64).

In 2016, Liu, Zhang, and coworkers developed the Ag(I)-catalyzed three-component annulation reactions of C_{60} with sulfonylhydrazones and nitriles to provide C_{60}-fused dihydropyrroles **62** (Scheme 65) [95]. A variety of sulfonylhydrazones

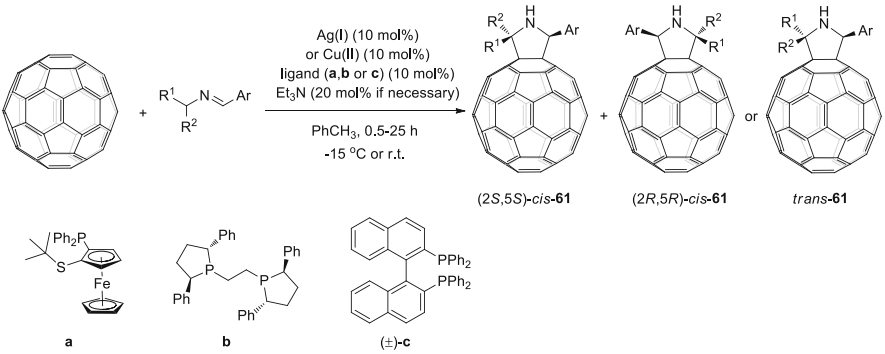

Scheme 64 Ag- or Cu-catalyzed reactions of C_{60} with azomethines

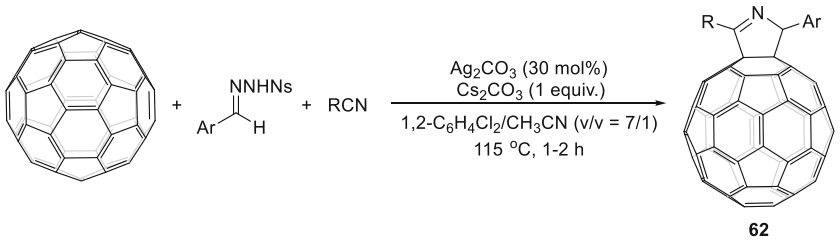

Scheme 65 Ag-catalyzed three-component annulation reactions of C_{60}

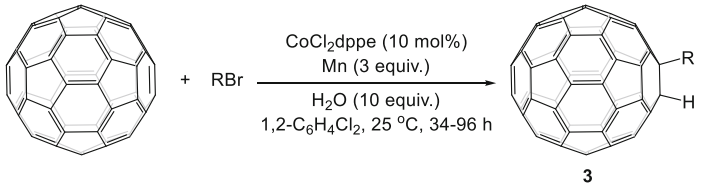

Scheme 66 Co-catalyzed reactions of C_{60} with alkyl bromides

with different substituent groups on the phenyl ring could react with C_{60} and nitriles to give C_{60}-fused dihydropyrroles **62** in 14–53% yields. The reaction exhibited a broad substrate scope and excellent functional-group tolerance, and also allowed the synthesis of fullerene-based macromolecules.

Cobalt-Catalyzed Reactions of C_{60}

Yamamoto, Jin, and coworkers reported the Co-catalyzed hydroalkylations of C_{60} with active alkyl bromides, and monoalkylated fullerenes **3** could be obtained in 36–78% yields under mild reaction conditions (Scheme 66) [96]. The optimized conditions were determined as follows: $CoCl_2$dppe (10 mol%) as the catalyst, manganese (Mn) (3 equiv.) as the reductant, and H_2O (10 equiv.) as the additive in

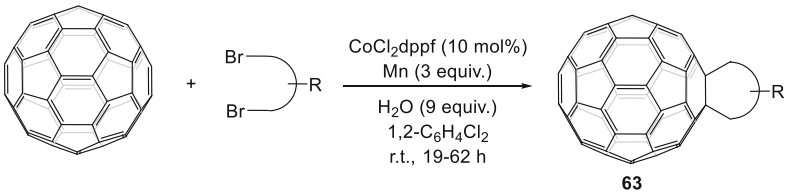

Scheme 67 Co-catalyzed reactions of C_{60} with active dibromides

1,2-$C_6H_4Cl_2$ at 25 °C for 34–96 h under argon atmosphere. The use of $CoCl_2$dppe/Mn/H_2O under an argon atmosphere was the key to the success of this conversion. The reaction most likely occurred through the free radical (R·) formation by the Co (0 or I) complex, followed by the addition to C_{60}. A variety of functional groups such as ester, cyano, methoxy, and α-methyl groups on the benzyl moiety were tolerated, affording the monoalkylated products **3** in good yields. Allyl bromide, cinnamyl bromide, propargyl bromide, and 1-bromo-2-butyne were also active alkyl sources. This hydroalkylation method was utilized to synthesize a zinc porphyrin attached C_{60}, a dendrimer attached C_{60}, and a fullerene dimer.

Jin and coworkers later extended the above co-catalyzed free radical cycloaddition to active dibromides to synthesize three-, five-, six-, and seven-membered carbocycle-fused monoadducts of C_{60} **63** in 19–73% yields (Scheme 67) [97].

Conclusion

Fullerene derivatives have broad application prospects in the fields of life sciences and materials science, and the synthesis of novel fullerene derivatives is an important research direction. As efficient methods, transition metal-catalyzed reactions have been widely used in the synthesis of novel fullerene derivatives. This book chapter overviews the palladium-, rhodium-, copper-, and other transition metal-catalyzed reactions of C_{60} to provide different kinds of functionalized fullerene derivatives. Over the past 30 years, fullerene chemistry has developed rapidly, and many chemists have made great contribution to the chemical modification of fullerenes. However, to increase the diversity of new chemical structures, the transition metal-catalyzed reactions are required to be developed further. The ambiguous mechanisms still need to be explored and clarified. It is expected that the transition metal-catalyzed reactions of fullerenes will continue to be a hot research topic and will result in discovery of many new reactions.

References

1. Nakamura E, Isobe H (2003) Functionalized fullerenes in water. The first 10 years of their chemistry, biology, and nanoscience. Acc Chem Res 36:807–815
2. Guldi DM, Illescas BM, Atienza CM, Wielopolski M, Martín N (2009) Fullerene for organic electronics. Chem Soc Rev 38:1587–1597

3. Li C-Z, Yip H-L, Jen AK-Y (2012) Functional fullerenes for organic photovoltaics. J Mater Chem 22:4161–4177
4. Zhu S-E, Li F, Wang G-W (2013) Mechanochemistry of fullerenes and related materials. Chem Soc Rev 42:7535–7570
5. Peng J, Xiang J-J, Wang H-J, Li F-B, Huang Y-S, Liu L, Liu C-Y, Asiri AM, Alamry KA (2017) DMAP-mediated synthesis of fulleropyrrolines: reaction of [60]fullerene with aromatic aldehydes and arylmethanamines in the absence or presence of manganese(III) acetate. J Org Chem 82:9751–9764
6. Zhang M, Wang H-J, Li F-B, Zhong X-X, Huang Y-S, Liu L, Liu C-Y, Asiri AM, Alamry KA (2018) Stereoselective synthesis of *N*-ethyl-2-arylvinyl-5-methyl fulleropyrrolidines: reaction of [60]fullerene with aromatic aldehydes and triethylamine/diethylamine in the absence or presence of manganese(III) acetate. Org Biomol Chem 16:2975–2985
7. Liu Q, Liu T-X, Ma N, Tu C, Wang R, Zhang G (2019) Cu(II)/Mn(III)-promoted synergistic radical A-heteroannulation reaction: synthesis of [60]fullerene-fused tetrahydroquinoline derivatives. J Org Chem 84:7255–7264
8. Liu T-X, Liu Y, Chao D, Zhang P, Liu Q, Shi L, Zhang Z, Zhang G (2014) Iron-mediated internal-oxidant relay cascade reaction: strategy to synthesize fullerenooxazoles and hydroxyfullerenyl amides. J Org Chem 79:11084–11090
9. Zhang X-F, Li F-B, Wu J, Shi J-L, Liu Z, Liu L (2015) Synthesis of fullerene-fused dioxanes/dioxepanes: ferric perchlorate-mediated one-step reaction of [60]fullerene with diols. J Org Chem 80:6037–6043
10. Liu T-X, Zhang Z, Liu Q, Zhang P, Jia P, Zhang Z, Zhang G (2014) Synthesis of [60]fullerene-fused tetrahydroazepinones and azepinonimines via $Cu(OAc)_2$-promoted *N*-heteroannulation reaction. Org Lett 16:1020–1023
11. Wu J, Liu C-X, Wang H-J, Li F-B, Shi J-L, Liu L, Li J-X, Liu C-Y, Huang Y-S (2016) Cu$(OAc)_2$-mediated reaction of [60]fullerene with aldehydes and primary amines for the synthesis of fulleropyrrolines. J Org Chem 81:9296–9307
12. Yang H-T, Tan Y-C, Yang Y, Sun X-Q, Miao C-B (2016) $Cu(OAc)_2$-mediated reaction of C_{60} with ureas for the preparation of fulleroimidazolidinones. J Org Chem 81:1157–1163
13. Shiu L-L, Lin T-I, Peng S-M, Her G-R, Ju DD, Lin S-K, Hwang J-H, Mou CY, Luh T-Y (1994) Palladium-catalysed [3 + 2] cycloaddition of trimethylenemethane (TMM) and fullerene. Observation of the room-temperature fluorescence spectrum of the TMM–C_{60} adduct. J Chem Soc Chem Commun:647–648
14. Shen CKF, Chien K-M, Liu T-Y, Lin T-I, Her G-R, Luh T-Y (1995) Palladium-catalyzed [3 + 2] cycloaddition of 60-fullerene with *cis*-$HOCH_2CH{=}CHCH_2OCO_2Et$. Tetrahedron Lett 36:5383–5384
15. Mori S, Nambo M, Chi L-C, Bouffard J, Itami K (2008) A bench-stable Pd catalyst for the hydroarylation of fullerene with boronic acids. Org Lett 10:4609–4612
16. Nambo M, Itami K (2009) Palladium-catalyzed carbon–carbon bond formation and cleavage of organo(hydro)fullerenes. Chem Eur J 15:4760–4764
17. Nambo M, Wakamiya A, Yamaguchi S, Itami K (2009) Regioselective unsymmetrical tetraallylation of C_{60} through palladium catalysis. J Am Chem Soc 131:15112–15113
18. Nambo M, Wakamiya A, Itami K (2012) Palladium-catalyzed tetraallylation of C_{60} with allyl chloride and allylstannane: mechanism, regioselectivity, and enantioselectivity. Chem Sci 3:3474–3481
19. Lu S, Jin T, Bao M, Asiri AM, Yamamoto Y (2012) Palladium-catalyzed bisfunctionalization of active alkenes by β-acetonitrile-α-allyl addition: application to the synthesis of unsymmetric 1,4-di(organo)fullerene derivatives. Tetrahedron Lett 52:1210–1213
20. Liu Q, Liu T-X, Ru Y, Zhu X, Zhang G (2019) Palladium-catalyzed decarboxylative heterocyclizations of [60]fullerene: preparation of novel vinyl-substituted [60]fullerene-fused tetrahydrofurans/pyrans/quinolines. Chem Commun 55:14498–14501
21. Weaver JD, Recio A, Grenning AJ, Tunge JA (2011) Transition metal-catalyzed decarboxylative allylation and benzylation reactions. Chem Rev 111:1846–1913
22. Khan A, Zhang YJ (2015) Palladium-catalyzed asymmetric decarboxylative cycloaddition of vinylethylene carbonates with electrophiles: construction of quaternary stereocenters. Synlett 26:853–860

23. Guo W, Gómez JE, Cristòfol À, Xie J, Kleij AW (2018) Catalytic transformations of functionalized cyclic organic carbonates. Angew Chem Int Ed 57:13735–13747
24. Liu Q, Liu T-X, Ma J, Zhang G (2020) Palladium-catalyzed three-component tandem coupling-carboannulation reaction leading to polysubstituted [60]fullerene-fused cyclopentanes. Org Lett 22:284–289
25. Zhu B, Wang G-W (2009) Synthesis of [60]fulleroindolines: palladium-catalyzed hetero-annulations of [60]fullerene with *o*-iodoanilines. J Org Chem 74:4426–4428
26. Emrich DE, Larock RC (2004) Palladium-catalyzed heteroannulation of cyclic alkenes by functionally substituted aryl iodides. J Org Chem 689:3756–3766
27. Wan X, Ma Z, Li B, Zhang K, Cao S, Zhang S, Shi Z (2006) Highly selective C–H functionalization/halogenation of acetanilide. J Am Chem Soc 128:7416–7417
28. Zhu B, Wang G-W (2009) Palladium-catalyzed heteroannulation of [60]fullerene with anilides via C–H bond activation. Org Lett 11:4335–4337
29. Yang S, Li B, Wan X, Shi Z (2007) Ortho arylation of acetanilides via Pd(II)-catalyzed C–H functionalization. J Am Chem Soc 129:6066–6067
30. Li B-J, Tian S-L, Fang Z, Shi Z-J (2008) Multiple C–H activations to construct biologically active molecules in a process completely free of organohalogen and organometallic components. Angew Chem Int Ed 47:1115–1118
31. Chuang S-C, Rajeshkumar V, Cheng C-A, Deng J-C, Wang G-W (2011) Annulation of benzamides with [60]fullerene through palladium(II)-catalyzed C–H bond activation. J Org Chem 76:1599–1604
32. Rajeshkumar V, Chan F-W, Chuang S-C (2012) Palladium-catalyzed and hybrid acids-assisted synthesis of [60]fulleroazepines in one pot under mild conditions: annulation of *N*-sulfonyl-2-aminobiaryls with [60]fullerene through sequential C–H bond activation, C–C and C–N bond formation. Adv Synth Catal 354:2473–2483
33. Su Y-T, Wang Y-L, Wang G-W (2012) Palladium-catalysed heteroannulation of [60]fullerene with *N*-benzyl sulfonamides and subsequent functionalization. Chem Commun 48:8132–8134
34. Su Y-T, Wang Y-L, Wang G-W (2014) Palladium-catalyzed heteroannulation of [60]fullerene with *N*-(2-arylethyl)sulfonamides via C–H bond activation. Org Chem Front 1:689–693
35. Hussain M, Chen M, Yang S, Wang G-W (2019) Palladium-catalyzed heteroannulation of indole-1-carboxamides with [60]fullerene and subsequent electrochemical transformations. Org Lett 21:8568–8571
36. Li F, Liu T-X, Wang G-W (2012) Synthesis of [60]fullerene-fused sultones via sulfonic acid group-directed C–H bond activation. Org Lett 14:2176–2179
37. Zhai W-Q, Peng R-F, Jin B, Wang G-W (2014) Synthesis of [60]fullerene-fused tetrahydrobenzooxepine and isochroman derivatives via hydroxyl-directed C–H activation/C–O cyclization. Org Lett 16:1638–1641
38. Li F, Wang J-J, Wang G-W (2017) Palladium-catalyzed synthesis of [60]fullerene-fused benzofurans via heteroannulation of phenols. Chem Commun 53:1852–1855
39. Hussain M, Niu C, Wang G-W (2020) Palladium-catalyzed synthesis of [60]fullerene-fused furochromenones and further electrochemical functionalization. Org Chem Front 7:1249–1254
40. Zhou D-B, Wang G-W (2015) Palladium-catalyzed decarboxylative annulation of 2-arylbenzoic acids with [60]fullerene via C–H bond activation. Org Lett 17:1260–1263
41. Zhou D-B, Wang G-W (2016) Synthesis of [60]fullerene-fused spiroindanes by palladium-catalyzed oxidative annulation of [60]fullerene with 2-aryl cyclic 1,3-dicarbonyl compounds. Org Lett 18:2616–2619
42. Ma J, Liu T-X, Zhang P, Zhang C, Zhang G (2021) Palladium-catalyzed domino spirocyclization of [60]fullerene: synthesis of diverse [60]fullerene-fused spiro[4,5]/[5,5] derivatives. Chem Commun 57:49–52
43. Yan Y-T, Gao W, Jin B, Shan D-S, Peng R-F, Chu S-J (2018) Palladium-catalyzed reaction of [60]fullerene with aroyl compounds via enolate-mediated sp^2 C–H bond activation and hydroxylation. J Org Chem 83:672–683

44. Zheng T, Shan D-S, Jin B, Peng R-F (2018) Synthesis and self-sensitized photooxidation of 2-fulleropyrrolines by palladium(II)-catalyzed heteroannulation of [60]fullerene with benzoyl hydrazone esters. Org Biomol Chem 16:8845–8853
45. Becker L, Evans TP, Bada JL (1993) Synthesis of $C_{60}H_2$ by rhodium-catalyzed hydrogenation of C_{60}. J Org Chem 58:7630–7631
46. Gonzalez R, Knight BW, Wudl F, Semones MA, Padwa A (1994) The reversible cycloaddition of isomiunchnones to C_{60}. J Org Chem 59:7949–7951
47. Nair V, Sethumadhavan D, Sheela KC, Eigendorf GK (1999) Cycloaddition reactions of carbonyl ylides to [60]fullerene: synthesis of novel C_{60} derivatives. Tetrahedron Lett 40:5087–5090
48. Nair V, Sethumadhavan D, Sheela KC, Nair SM, Eigendorf GK (2002) Dipolar cycloaddition of carbonyl ylides with [60]fullerene: formation of novel heterocycle fused fullerene derivatives. Tetrahedron 58:3009–3013
49. Duczek W, Radeck W, Niclas H-J, Ramm M, Costisella B (1997) Diels-alder cycloaddition of substituted norcaradienes with [60]fullerene. Tetrahedron Lett 38:6651–6654
50. Pellicciari R, Annibali D, Costantino G, Marinozzi M, Natalini B (1997) Dirhodium tetraacetate-mediated decomposition of ethydiazoacetate and ethyldiazo-malonate in the presence of fullerene. A new procedure for the selective synthesis of [6-6]-closed methanofullerenes. Synlett 10:1196–1198
51. Muraoka T, Asaji H, Yamamoto Y, Matsuda I, Itoh K (2000) Rhodium-catalyzed silylative carbocyclization on C_{60}. Chem Commun:199–200
52. Artigas A, Pla-Quintana A, Lledó A, Roglans A, Solà M (2018) Expeditious preparation of open-cage fullerenes by rhodium(I)-catalyzed [2 + 2 + 2] cycloaddition of diynes and C_{60}: an experimental and theoretical study. Chem Eur J 24:10653–10661
53. Nambo M, Noyori R, Itami K (2007) Rh-catalyzed arylation and alkenylation of C_{60} using organoboron compounds. J Am Chem Soc 129:8080–8081
54. Nambo M, Segawa Y, Wakamiya A, Itami K (2011) Selective introduction of organic groups to C_{60} and C_{70} using organoboron compounds and rhodium catalyst: a new synthetic approach to organo(hydro)fullerenes. Chem Asian J 6:590–598
55. Matsumoto F, Iwai T, Moriwaki K, Takao Y, Ito T, Mizuno T, Ohno T (2012) Design of fullerene derivatives for stabilizing LUMO energy using donor groups placed in spatial proximity to the C_{60} cage. J Org Chem 77:9038–9043
56. Li F-B, Liu T-X, Wang G-W (2008) Synthesis of fullerooxazoles: novel reactions of [60] fullerene with nitriles promoted by ferric perchlorate. J Org Chem 73:6417–6420
57. He C-L, Liu R, Li D-D, Zhu S-E, Wang G-W (2013) Synthesis and functionalization of [60] fullerene-fused imidazolines. Org Lett 15:1532–1535
58. Hou H-L, Gao X (2012) Aerobic oxidations of C_{60}^{2-} in the presence of PhCN and $PhCH_2CN$: oxygenation versus dehydrogenation reactions. J Org Chem 77:2553–2558
59. Yang H-T, Liang X-C, Wang Y-H, Yang Y, Sun X-Q, Miao C-B (2013) CuI-catalyzed oxidative [3 + 2] reaction of fullerene with amidines or amides using air as the oxidant: preparation of fulleroimidazole or fullerooxazole derivatives. Org Lett 15:4650–4653
60. Cheung CW, Buchwald SL (2012) Room temperature copper(II)-catalyzed oxidative cyclization of enamides to 2,5-disubstituted oxazoles via vinylic C–H functionalization. J Org Chem 77:7526–7537
61. Li J, Neuville L (2013) Copper-catalyzed oxidative diamination of terminal alkynes by amidines: synthesis of 1,2,4-trisubstituted imidazoles. Org Lett 15:1752–1755
62. Wang G-W, Yang H-T, Miao C-B, Xu Y, Liu F (2006) Radical reactions of [60]fullerene with β-enamino carbonyl compounds mediated by manganese(III) acetate. Org Biomol Chem 4:2595–2599
63. Yang H-T, Liang X-C, Wang Y-H, Yang Y, Sun X-Q, Miao C-B (2013) $CuCl_2$-mediated reaction of [60]fullerene with amines in the presence or absence of dimethyl acetylenedicarboxylate: preparation of fulleropyrroline or aziridinofullerene derivatives. J Org Chem 78:11992–11998

64. Jiang S-P, Su Y-T, Liu K-Q, Wu Q-H, Wang G-W (2015) Copper(I)-catalyzed heteroannulation of [60]fullerene with ketoxime acetates: preparation of novel 1-fulleropyrrolines. Chem Commun 51:6548–6551
65. Huang H, Ji X, Wu W, Jiang H (2015) Transition metal-catalyzed C–H functionalization of *N*-oxyenamine internal oxidants. Chem Soc Rev 44:1155–1171
66. Li J, Hu Y, Zhang D, Liu Q, Dong Y, Liu H (2017) Transition metal-catalyzed reactions involving oximes. Adv Synth Catal 359:710–771
67. Liu T-X, Hua S, Ma N, Zhang P, Bi J, Zhang Z, Zhang G (2018) Reactivity and synthetic applications of α-functionalized oxime acetates: divergent access to fulleropyrrolidines and mono- and disubstituted 1-fulleropyrrolines via copper-catalyzed redox-neutral *N*-hetero-annulation with [60]fullerene. Adv Synth Catal 360:142–152
68. Anderson S, Taylor PN, Verschoor GLB (2004) Benzofuran trimers for organic electroluminescence. Chem Eur J 10:518–527
69. Xia S, Liu T-X, Zhang P, Ma J, Liu Q, Ma N, Zhang Z, Zhang G (2018) Broad synthesis of disubstituted dihydrofuran-fused [60]fullerene derivatives via Cu(I)/Ag(I)-mediated synergistic annulation reaction. J Org Chem 83:862–870
70. Murata Y, Kato N, Fujiwara K, Komatsu K (1999) Solid-state [4 + 2] cycloaddition of fullerene C_{60} with condensed aromatics using a high-speed vibration milling technique. J Org Chem 64:3483–3488
71. Yang H-T, Ren L-W, Miao C-B, Dong C-P, Yang Y, Xi H-T, Meng Q, Jiang Y, Sun X-Q (2013) DMAP-catalyzed [3 + 2] and [4 + 2] cycloaddition reactions between [60]fullerene and unmodified Morita-Baylis-Hillman adducts in the presence of Ac_2O. J Org Chem 78:1163–1170
72. Jiang S-P, Lu W-Q, Liu Z, Wang G-W (2018) Synthesis of fullerotetrahydroquinolines via [4 + 2] cycloaddition reaction of [60]fullerene with in situ generated aza-*o*-quinone methides. J Org Chem 83:1959–1968
73. Wang G-W, Li J-X, Li Y-J, Liu Y-C (2006) Novel reactions of [60]fullerene with amino acid esters and carbon disulfide. J Org Chem 71:680–684
74. Li J-X, Wang G-W (2012) Synthesis of [60]fullerene-fused thiolactams and thiaimidates. Tetrahedron Lett 53:1610–1612
75. Wu S-L, Gao X (2018) Copper-catalyzed aerobic oxidative reaction of C_{60} with aliphatic primary amines and CS_2. J Org Chem 83:2125–2130
76. Jiang S-P, Wu Q-H, Wang G-W (2017) Copper-promoted synthesis of 2-fulleropyrrolines via heteroannulation of [60]fullerene with α-amino ketones. J Org Chem 82:10823–10829
77. Yang H-T, Ge J, Lu X-W, Sun X-Q Miao C-B (2017) Copper-catalyzed functionalizations of C_{60} with amino alcohols. J Org Chem 82:5873–5880
78. Jiang S-P, Liu Z, Lu W-Q, Wang G-W (2018) Synthesis of fullerotetrahydropyridazines via the copper-catalyzed heteroannulation of [60]fullerene with hydrazides. Org Chem Front 5:1188–1193
79. Xiao Z, Matsuo Y, Nakamura E (2010) Copper-catalyzed formal [4 + 2] annulation between alkyne and fullerene bromide. J Am Chem Soc 132:12234–12236
80. Birkett PR, Taylor R, Wachter NK, Carano M, Paolucci F, Roffia S, Zerbetto F (2000) The electrochemistry of $C_{60}Ph_5Cl$: a very special fullerene derivative. J Am Chem Soc 122:4209–4212
81. Clavaguera S, Khan SI, Rubin Y (2009) Unexpected de-arylation of a pentaaryl fullerene. Org Lett 11:1389–1391
82. Isobe H, Tanaka T, Nakanishi W, Lemiègre L, Nakamura E (2005) Regioselective oxygenative tetraamination of [60]fullerene. Fullerene-mediated reduction of molecular oxygen by amine via ground state single electron transfer in dimethyl sulfoxide. J Org Chem 70:4826–4832
83. Segura JL, Martín N (2000) [60]Fullerene dimers. Chem Soc Rev 29:13–25
84. Luo H, Araki Y, Fujitsuka M, Ito O, Cheng F, Murata Y, Komatsu K (2004) Dissociative electron attachment of singly bonded [60]fullerene dimer studied by laser flash photolysis. J Phys Chem B 108:11915–11920

85. Zhang Y, Matsuo Y, Li C-Z, Tanaka H, Nakamura E (2011) A scalable synthesis of methano[60]fullerene and congeners by the oxidative cyclopropanation reaction of silylmethylfullerene. J Am Chem Soc 133:8086–8089
86. Cheng F, Murata Y, Komatsu K (2002) Synthesis, X-ray structure, and properties of the singly bonded C_{60} dimer having diethoxyphosphorylmethyl groups utilizing the chemistry of C_{60}^{2-}. Org Lett 4:2541–2544
87. Lu S, Jin T, Kwon E, Bao M, Yamamoto Y (2012) Highly efficient $Cu(OAc)_2$-catalyzed dimerization of monofunctionalized hydrofullerenes leading to singlebonded [60]fullerene dimers. Angew Chem Int Ed 51:802–806
88. Zhang Y, Matsuo Y, Nakamura E (2011) Regiocontrolled synthesis of 1,2-di(organo)fullerenes via copper-assisted 1,4-aryl migration from silicon to carbon. Org Lett 13:6058–6061
89. Li C-Z, Matsuo Y, Niinomi T, Sato Y, Nakamura E (2010) Face-to-face C_6F_5–[60]fullerene interaction for ordering fullerene molecules and application to thin-film organic photovoltaics. Chem Commun 46:8582–8584
90. Si W, Lu S, Bao M, Asao N, Yamamoto Y, Jin T (2014) Cu-catalyzed C–H amination of hydrofullerenes leading to 1,4-difunctionalized fullerenes. Org Lett 16:620–623
91. Hsiao T-Y, Santhosh KC, Liou K-F, Cheng C-H (1998) Nickel-promoted first enediyne cycloaddition reaction on C_{60}: synthesis and photochemistry of the fullerene derivatives. J Am Chem Soc 120:12232–12236
92. Si W, Zhang X, Asao N, Yamamoto Y, Jin T (2015) Ni-catalyzed direct 1,4-difunctionalization of [60]fullerene with benzyl bromides. Chem Commun 51:6392–6394
93. Gan L, Huang S, Zhang X, Zhang A, Cheng B, Cheng H, Li X, Shang G (2002) Fullerenes as a tert-butylperoxy radical trap, metal catalyzed reaction of *tert*-butyl hydroperoxide with fullerenes, and formation of the first fullerene mixed peroxides $C_{60}(O)(OO^tBu)_4$and $C_{70}(OO^tBu)_{10}$. J Am Chem Soc 124:13384–13385
94. Filippone S, Maroto EE, Martín-Domenech Á, Suarez M, Martín N (2009) An efficient approach to chiral fullerene derivatives by catalytic enantioselective 1,3-dipolar cycloadditions. Nat Chem 1:578–582
95. Chao D, Liu T-X, Ma N, Zhang P, Fu Z, Ma J, Liu Q, Zhang F, Zhang Z, Zhang G (2016) Silver (I)-mediated three-component annulation reaction of [60]fullerene, sulfonylhydrazones, and nitriles: leading to diverse disubstituted [60]fullerene-fused dihydropyrroles. Chem Commun 52:982–985
96. Lu S, Jin T, Bao M, Yamamoto Y (2011) Cobalt-catalyzed hydroalkylation of [60]fullerene with active alkyl bromides: selective synthesis of monoalkylated fullerenes. J Am Chem Soc 133:12842–12848
97. Lu S, Si W, Bao M, Yamamoto Y, Jin T (2013) Co-catalyzed radical cycloaddition of [60]fullerene with active dibromides: selective synthesis of carbocycle-fused fullerene monoadducts. Org Lett 15:4030–4033

Theoretical Prediction of Fullerene Reactivity

15

Pei Zhao, Mengyang Li, and Tao Yang

Contents

Abstract

Over the last a few decades, a great diversity of reactions have been developed to functionalize empty and endohedral fullerenes, the most common being Diels-Alder cycloaddition, 1,3-dipolar cycloaddition, Bingel-Hirsch cycloaddition, [2 + 2] cycloaddition, free-radical reactions, and carbene reactions. Various

Pei Zhao and Mengyang Li contributed equally with all other contributors.

P. Zhao · M. Li · T. Yang (✉)
Ministry of Education Key Laboratory for Non-Equilibrium Synthesis and Modulation of Condensed Matter, School of Physics, Xi'an Jiaotong University, Xi'an, Shaanxi, China
e-mail: pei@ims.ac.jp; lmy0916@stu.xjtu.edu.cn; taoyang1@xjtu.edu.cn

X. Lu et al. (eds.), *Handbook of Fullerene Science and Technology*,
https://doi.org/10.1007/978-981-16-8994-9_45

fullerenes have been found to exhibit the different chemical reactivity and regioselectivity in these reactions, especially for the endohedral fullerenes with diverse encapsulated species. This chapter emphasizes the importance of theoretical prediction for the fullerene reactivity. The most favorable addition site among numerous nonequivalent carbon atoms can be unambiguously determined; meanwhile, essential physical factors including charge density, spin density, and pyramidalization angle have been demonstrated to be quite useful for predicting the potential addition sites on the fullerene surface.

Keywords

Theoretical prediction · Chemical functionalization · Quantum chemical calculations · Cycloaddition · Radical reaction

Introduction

With an even number of sp^2-hybridized carbon atoms, fullerenes are spherical carbon cages that generally consist of exactly 12 pentagonal rings and a certain number of hexagonal rings. Exohedral functionalization of fullerenes via chemical reactions is one of the most important synthesis methods for complex fullerene derivatives with important applications in various fields. The encapsulation of endohedral fullerenes (EFs), which possess different reactivity because of the significant interaction between the encapsulated species and the outer carbon cages. More importantly, since the free fullerene cages always satisfy the isolated pentagon rule (IPR), the presence of inner atoms or clusters in endohedral fullerenes could stabilize non-IPR fullerenes with a different number of the pentagon adjacencies (PAs), resulting in the presence of more C-C bond types. As shown in Fig. 1, six different C-C bond types A to F exist in fullerene cages, in which types E and F are only present in non-IPR cages.

Various cycloaddition reactions have been developed to functionalize the fullerene cages, such as [4 + 2] Diels-Alder cycloaddition, [3 + 2] 1,3-dipolar cycloaddition, [2 + 1] Bingel-Hirsch cycloaddition, and [2 + 2] cycloaddition; the resulted regioselectivity varies for distinct fullerenes due to the difference in the cage topology and the inner species. Meanwhile, free-radical reactions also play an important role in the exohedral functionalization of fullerenes, and the reactions of various chemical radicals including C-, Si-, O-, S-, P-, and metal-centered radicals as well as different carbenes with fullerenes have been experimentally realized.

Due to numerous nonequivalent carbon atoms in fullerenes, and the diversity of addition sites on fullerene cages has made studies involving their chemical reactivity not so straightforward. Theoretical studies, which usually employ the quantum chemical methods, not only provide a better understanding of the reactivity of empty fullerenes and endohedral fullerenes in terms of figuring regioselectivity (possible addition sites) and reaction mechanism, but also are the powerful tool to predict the reactivity. In this chapter, we mainly emphasize the important theoretical works in predicting as well as explaining the fullerene reactivity.

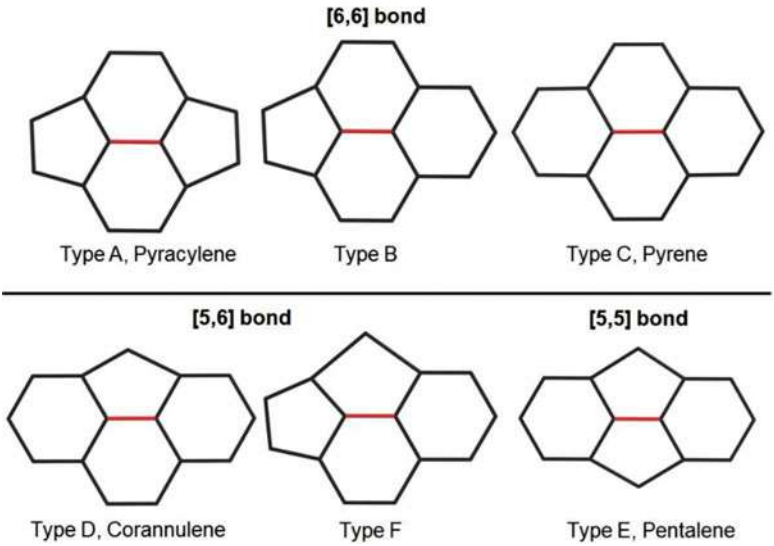

Fig. 1 Representation of the different [6,6], [5,6], and [5,5] bond types in fullerene cages

Cycloaddition Reactions

Diels-Alder Cycloaddition

Diels-Alder (DA) cycloaddition, which results in six-membered exohedral rings on fullerene surfaces, is one of the most straightforward procedures for fullerene functionalization. To disclose the reactivity of $Sc_3N@I_h$-C_{80} for the DA reaction and obtain the origin of regioselectivity, Campanera et al. have performed LDA/TZP calculations [1] and concluded that the most reactive sites possess high Mayer bond orders and high pyramidalization angles. Because DA reactions are facilitated by electron-withdrawing dienophiles, the endohedral fullerenes are less reactive than the free fullerene cages due to their lower electron affinities after the charge transfer from the Sc_3N unit to the outer carbon cage, which was corroborated by the much larger reaction energies on the free C_{80} cage [1]. Besides the electronic effect caused by the encapsulated nitride, a geometric effect on the double bond character and pyramidalization angle of the C-C bonds appears. Those C-C bonds near the scandium atoms become completely deactivated as the result of an extremely low double bond character while other C-C bonds retain their main characteristics [1]. To this point, the theoretical study on DA reaction of $Sc_2C_2@C_{3v}(8)$-C_{82} revealed that the pyracylene [6,6] bond (type-A) in the sumanene-type hexagon is the most reactive site according to both kinetic and thermodynamic considerations, because the reactive [6,6] bond is far

away from the Sc_2C_2 cluster and avoids the deactivation from the metallic cluster [2]. Noteworthy, the [6,6] bond is not the most thermodynamically or kinetically favorable for the free $C_{3v}(8)$-C_{82}.

In order to disclose the effect of encapsulated metallic species on exohedral reactivity of fullerene cages, Solà and coworkers studied the DA reaction of 1,3-butadiene with all nonequivalent bonds of D_{3h}-C_{78}, $Sc_3N@D_{3h}$-C_{78} [3], $Y_3N@D_{3h}$-C_{78} [4], and $Ti_2C_2@D_{3h}$-C_{78} [5] by BP86/TZP//BP86/DZP calculations. The DA reaction over the free fullerene and the endohedral derivatives was predicted to lead to totally different cycloadducts, based on the thermodynamic and kinetic results. As shown in Fig. 2, the thermodynamic and kinetic products for the free fullerene were obtained for the cycloaddition to the [5,6] bond **b** and the pyracylenic [6,6] bond **1**, respectively. In the case of $Sc_3N@D_{3h}$-C_{78}, both the kinetic and thermodynamic products correspond to the addition to the type-B [6,6] bond **6** which is situated far away from the Sc atoms. The preferred addition site for the $Y_3N@D_{3h}$-C_{78} compound is the corannulene-type [5,6]-bond **d** situated close to one

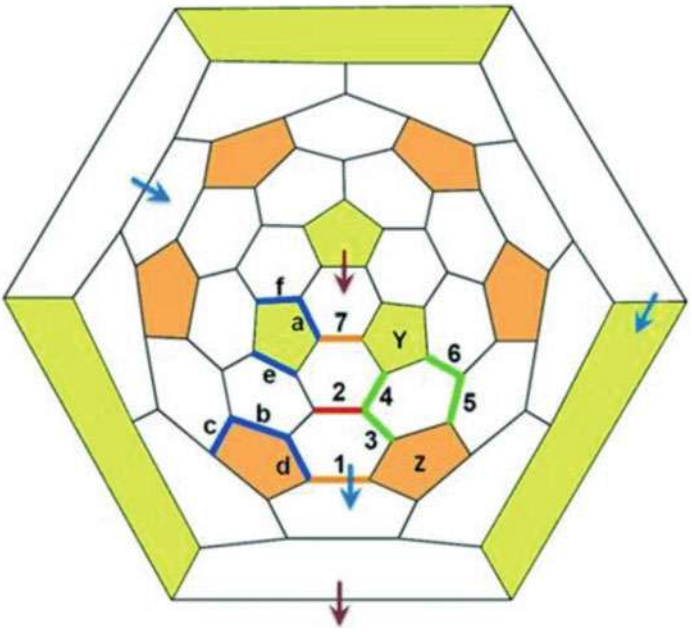

Fig. 2 Schlegel diagram of D_{3h}-C_{78}. For $M_3N@C_{78}$ (M = Sc, Y), the positions of the Sc/Y atoms facing the different bonds are symbolized by blue arrows. Note that the pyramidal structure of Y_3N inside C_{78} results in more nonequivalent bonds, but the positions of the Y atoms are similar to those in $Sc_3N@C_{78}$. For $Ti_2C_2@C_{78}$, red arrows are used to indicate the position of Ti atoms in the Schlegel diagram. Different [6,6] and [5,6] bonds are labeled by numbers and alphabets, respectively. The two types of nonequivalent five-membered rings are marked in yellow for type **Y** (formed by **f**, **a**, **f**, **e**, and **e** bonds, which are far away from the metal atoms) and orange for type **Z** (formed by **b**, **c**, **b**, **d**, and **d** bonds, which are close to the metal atoms). (Reproduced with permission from Ref. [5]. Copyright 2012 Wiley-VCH Verlag GmbH & Co. KGaA, Weinheim)

which possesses one of the longest C–C bond distances. Two main reasons were deduced for the preference for this unusual long C-C bond:[4] (1) The high strain of the fullerene cage caused by Y_3N can be partially released after reaction with the C-C bond close to the Y atom; (2) the pyramidal structure of the Y_3N cluster inside D_{3h}-C_{78} can adopt a more planar structure due to the additional space gained. When it comes to $Ti_2C_2@D_{3h}$-C_{78}, the corannulene-type [5,6] bonds **c** and **f**, and the type-B [6,6] bond **3,** are thermodynamically and kinetically preferred.

The Ti_2C_2 and Sc_3N clusters have similar encapsulation energies and similar effect on reactivity were concluded to be responsible for the different regioselectivities: (1) charge transfer from the metallic cluster to the cage that changes certain C-C bond lengths; (2) fullerene deformation caused by the presence of a metallic cluster inside, which influences the C-C bond lengths and their reactivity; and (3) changes in LUMOs of the fullerene cage induced by the metallic cluster that determine the final predisposition of different bonds to interact with the HOMO of the diene. By using the activation strain model in combination with the energy decomposition analysis, a recent theoretical study explored the physical factors behind the reduced DA reactivity of the metallofullerene $Sc_3N@C_{78}$ as compared with free C_{78} [6]. The main reason was found to be the less stabilizing interaction between the deformed reactants along the reaction coordinate induced by the Sc_3N moiety.

Solà group also theoretically investigated the DA reactivity of the non-IPR C_2(22010)-C_{78} isomer with two PA units, which is the most favorable isomer for trapping the Y_3N cluster and can make the trimetallic nitride adopt a planar structure [4]. Among the considered bonds, the type-E [5,5]-bond (Fig. 1) which does not exist in IPR fullerene cages is theoretically predicted to be the most reactive site. The preferred addition at the [5,5] bond was also found for $Sc_3N@C_2$(22010)-C_{78}. Apparently, these [5,5] bonds exhibit the high surface curvature, revealing the significant role of the local strain in the chemical reactivity.

Zhao et al. performed a systematic theoretical study on all nonequivalent bonds of D_{3h}-C_{68} and $Sc_3N@D_{3h}$-C_{68} with three PA units to disclose the DA reactivity in non-IPR fullerenes [7]. Based on BP86/6-31G(d)~Lanl2dz calculations, for the free C_{68}, the [5,5] bond is the thermodynamically favored, whereas the type-F [5,6] bond adjacent to the [5,5] bond is the best addition site kinetically. In the case of $Sc_3N@C_{68}$, the [5,5] bond becomes the most reactive site, revealing the importance of the metallic cluster. Thus, the reactive C-C bonds are localized in the highly strained PA unit in the free and endohedral fullerenes. The authors also found that the pyramidalization angles of the C-C bonds correlate better with the reactivity trend in C_{68} and $Sc_3N@C_{68}$ compared to bond lengths and molecular orbitals. Therefore, the PA motif in non-IPR isomers has a dominant role in the exohedral reactivity.

Interestingly, a theoretical study on DA reaction of non-IPR YNC$@C_{2v}$(19138)-C_{76} with cyclopentadiene (Cp) shows the preferred additions at a corannulene-type [5,6]-bond and a pyracylene-type [6,6]-bond, both of which are remote from the highly strained PA motif [8]. For free C_{76}, the [5,5] bond is the most favorable addition site. To disclose the origin of this interesting regioselectivity, the authors performed further analyses and found that the short bond length, large π-orbital axis

vector (POAV) value, and the suitable unoccupied molecular orbital lobes with large distributions of those [5,6]- and [6,6]-bonds could be responsible for their high reactivity toward Cp, demonstrating that the regioselectivity is controlled by a series of physical factors.

Solà and coworkers systematically studied the DA and retro-DA reactions of Cp and Cp* to La@C_{2v}-C_{82} by means of BLYP-D_2/TZP//BLYP-D_2/DZP calculations [9], which has been successfully realized in experiments [10–12]. The results demonstrated that the Cp and Cp* have the same regioselectivity with preferred attack on the C21–C23 [5,6] bond. Meanwhile, the much higher stability of the La@C_{82}Cp* adduct comes from the much higher long-range dispersion interactions in the Cp* case, which enhance the stabilization of the reactant complex, transition state, and products with respect to the separated reactants. This stabilization for the La@C_{82}Cp* case decreases the Gibbs reaction energy, thus allowing competition between the direct and retro reactions and making dissociation more difficult (Fig. 3).

The exohedral reactivity of noble gas (Ng) endohedral fullerenes for DA reaction was also theoretically discussed, in which no charge transfer occurs between the trapped noble gas and the fullerene cage. Solà et al. studied the thermodynamics and the kinetics of the DA cycloaddition of 1,3-*cis*-butadiene on all nonequivalent bonds of free C_{60}, Ng@C_{60}, and Ng_2@C_{60} (Ng = He-Xe) by means of BP86(ZORA)/TZP calculations [13]. Their results demonstrated that the presence of single noble gases in Ng@C_{60} almost does not affect the exohedral reactivity of C_{60}, that is, the pyracylenic [6,6] C-C bond was determined to be more reactive than [5,6] C-C bonds.

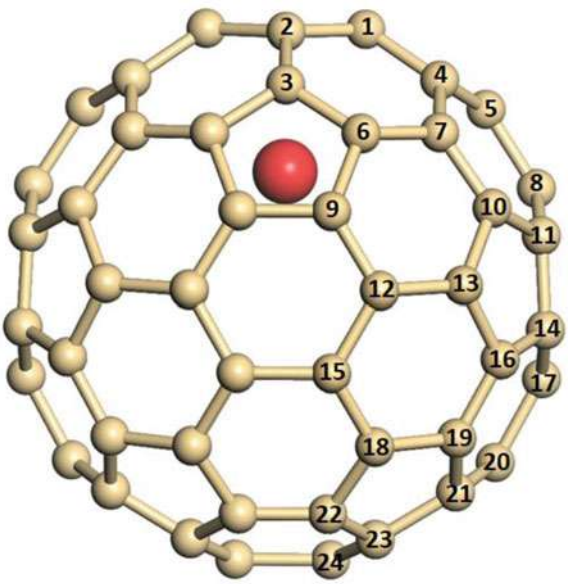

Fig. 3 Schematic drawing of La@C_{2v}-C_{82} with atom labels

For the $Ng_2@C_{60}$ complexes, the similar exohedral reactivity of $He_2@C_{60}$ and $Ne_2@C_{60}$ with C_{60} is found, whereas the presence of Ar_2 or Kr_2 inside C_{60} gives rise to the highly exothermic reactions. In particular, the reactivity of $Xe_2@C_{60}$ is getting extremely exothermic and highly unselective, where the DA reaction is equally favored over [6,6] or [5,6] bonds situated close to the initial C_5 axis. The following three factors were found to contribute significantly to the high reactivity of C_{60} with the heavy noble gas atoms inside: (1) Trapping the larger noble gas atoms such as Kr or Xe inside the cage reduces the LUMO energy; (2) the fullerene cages are highly deformed with the heavy noble gas dimers inside, while the breakage of the C-C bonds resulted from the DA reaction can effectively release the carbon cage strain; and (3) the compression of the Ng_2 dimer can be released after the exohedral functionalization.

1, 3-Dipolar Cycloaddition

1,3-dipolar cycloaddition is another straightforward procedure for fullerene functionalization, providing pyrrolidinofullerene derivatives (Prato reaction), as shown in Scheme 1. In order to disclose the different cycloaddition adducts for $Sc_3N@C_{80}$ and $Y_3N@C_{80}$, especially the [6,6] to [5,6] isomerization mechanism of the $Y_3N@C_{80}$ adducts, Poblet et al. performed density functional theory (DFT) calculations at BP86/TZP level [14]. The calculations on the $Y_3N@$(N-ethylpyrrolidino-C_{80}) indicated that the isomerization process takes place through a pirouette-kind of mechanism instead of involving the retro-cycloaddition reaction from the [6,6] adduct [14]. As for the 1,3-dipolar cycloaddition on $M_3N@I_h$-C_{80} (M = Sc, Y), the [5,6] regioisomers were found to be more stable than the [6,6] ones, whereas the relative stability of the [5,6] one with respect to the [6,6] one decreases when substituting Sc by Y [14]. Consequently, the larger charge transfer and larger cluster size of $Y_3N@I_h$-C_{80} prefer the [6,6] regioisomer over the [5,6] regioisomer. The activation barrier corresponding to the [6,6] addition (0.4 kcal·mol^{-1}) on $Y_3N@C_{80}$ is smaller than that of the [5,6] one (3.9 kcal·mol^{-1}). However, in the case of $Sc_3N@C_{80}$, the activation barrier for the [5,6] addition (1.7 kcal·mol^{-1}) is

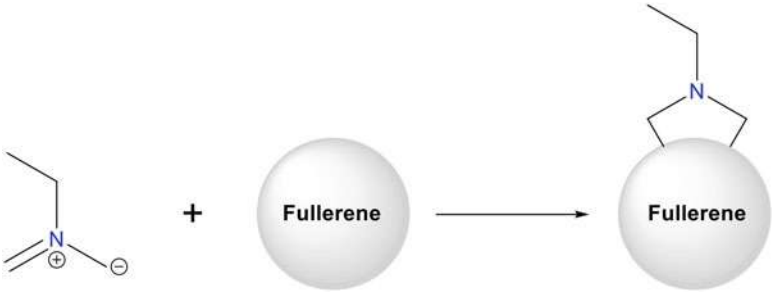

Scheme 1 1,3-Dipolar cycloaddition (Prato) reaction using N-ethylazomethine ylide as a dipole

slightly lower than for the [6,6] one (2.3 kcal·mol^{-1}). Therefore, the kinetically favored [6,6] product isomerizes to the thermodynamically stable [5,6] product in the case of $Y_3N@C_{80}$; however, no isomerization is observed once the most stable regioisomer is formed.

The isomerization of [6,6]- and [5,6]-fulleropyrrolidines of $M_3N@I_h$-C_{80} (M = Sc, Lu, Y, Gd) was systematically investigated by using three types of fulleropyrrolidine [15]. The regio-ratios of the thermodynamic Prato products are solely determined by the size of M_3N inside C_{80}, in a good agreement with theoretical results that the energy difference between [5,6]- and [6,6]-adducts is only slightly affected by the substituent of azomethine ylide. In contrast, the reaction rate of the isomerization from [5,6]-adducts to [6,6]-adducts is dependent on both the substituent of exohedral functional groups and the endohedral metal-cluster size.

As for the [6,6]-to-[5,6] isomerization process, BP86-D2/TZP//BP86-D2/DZP calculations revealed that the energy of [6,6]-intermediate (denoted as $I_{[6,6]}$) after breaking one of the C-C bonds of the pyrrolidine ring was higher than the corresponding [6,6]-adduct with energies of 22.1 and 29.4 kcal·mol^{-1} for $M_3N@I_h$-C_{80} (M = Sc, Y) products with the ester group, respectively, as shown in Fig. 4a [15]. Thus, the faster isomerization rate in the case of $Sc_3N@I_h$-C_{80} was rationalized. For the subsequent rotation of the C-C bond of the fullerene-dipole, the resulting [5,6]-intermediate (denoted as $I_{[5,6]}$) of $Sc_3N@I_h$-C_{80} presents an activation barrier of 3.5 kcal·mol^{-1} with respect to $I_{[6,6]}$, smaller than that of $Y_3N@I_h$-C_{80} (5.5 kcal·mol^{-1}). The observed $I_{[6,6]}$ and $I_{[5,6]}$ intermediates possess similar

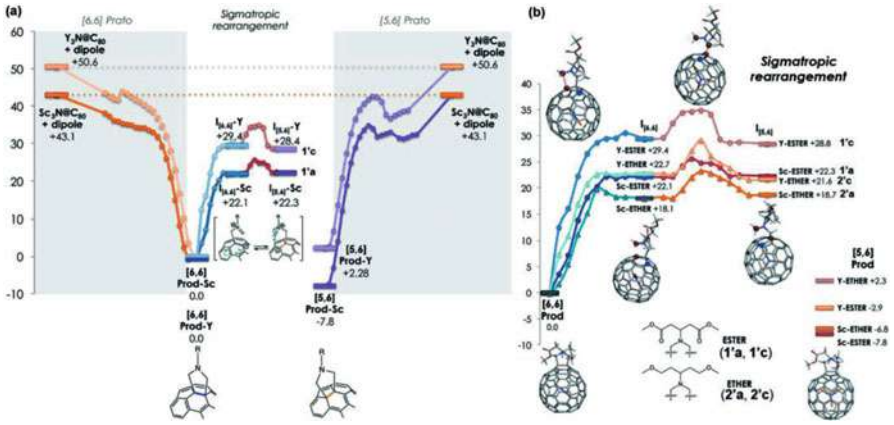

Fig. 4 (**a**) The [6,6]-to-[5,6] isomerization process of bis-ester 1′ (methyl ester) of $Sc_3N@C_{80}$ (1'a, dark colors) and $Y_3N@C_{80}$ (1'c, light colors) calculated at the BP86-D2/TZP//BP86-D2/DZP level of theory. b) Diagram of the sigmatropic [6,6]-to-[5,6] rearrangement in Prato adducts of $Sc_3N@C_{80}$ and $Y_3N@C_{80}$ for 1′ (bismethyl ester, in circles) and 2′ (bis-methyl ether, in triangles) calculated at the BP86-D2/TZP//BP86-D2/DZP level of theory. Optimized stationary points are represented by horizontal lines, and restrained optimizations were performed along the reaction coordinate (i.e., linear-transit optimizations) in triangles and circles. All energies are expressed in kcal·mol^{-1}. (Reproduced with permission from Ref. [15]. Copyright 2014 Wiley-VCH Verlag GmbH & Co. KGaA, Weinheim)

stabilities for both cases (i.e., M = Sc, Y). These rotational barriers with respect to $I_{[6,6]}$ are approximately 5.0 and 6.5 kcal·mol^{-1} for bis-ether adducts 2'a and 2'c (M = Sc and Y), respectively (Fig. 4b). Both $I_{[6,6]}$ and $I_{[5,6]}$ are destabilized with respect to the bis-ether dipole by approximately 3–4 and 6–7 kcal·mol^{-1} for 1'a and 1'c, respectively (Fig. 4b). This result is in line with the slower isomerization rates observed experimentally for the bis-ester dipole. Analysis of the EF and dipole charges for $I_{[6,6]}$ indicated that the slower isomerization rates observed for the bis-ester compounds come from the lower negative and positive charges accumulated on the EF and dipole, respectively. The isomerization for the electron-withdrawing carbonyl-based derivative is hampered because of disruption of the charge distribution on both the dipole and fullerene directly required for the sigmatropic rearrangement.

Later, the regioselective bis-addition on $M_3N@I_h$-C_{80} (M = Y, Gd) with a large metal cluster inside was observed for the first time with N-ethylglycine and formaldehyde, whereas no bis-adducts was detected for $M_3N@I_h$-C_{80} (M = Sc, Lu) under the same conditions [16]. The main kinetic bis-adduct of $Y_3N@C_{80}$ was determined to be an asymmetric [6,6] [6,6] adduct and will convert to a mixture of regioisomers upon heating via a sigmatropic rearrangement. However, the main kinetic bis-adduct of $Gd_3N@C_{80}$ (the [6,6] [6,6] adduct) exists stably under thermal conditions without isomerization. DFT calculations disclosed three thermodynamically preferred bis-adducts of $Gd_3N@C_{80}$: two [6,6] [6,6] bis-adducts (marked in blue in Fig. 5a) with second addition sites of 57 − 58 (lowest energy) and 20 − 22 (0.8 kcal·mol^{-1} higher than 57 − 58) and one [6,6] [5,6] bis-adduct with a second addition site of 16 − 20 (0.6 kcal·mol^{-1} higher than 57 − 58) [16]. Combined with the experimental observations, the most favorable addition site of 57 − 58 is determined as the only addition site that could lead to stable bis-adducts (Fig. 5a). The other thermodynamically stable [6,6] [6,6] bis-adduct at 20 − 22 is approximately as stable as the adjacent [5,6] bond 16 − 20, and therefore [6,6]-to-[5,6] isomerization would be expected. Meanwhile, the orientations of Gd_3N in the three most favorable bis-adducts are identical, with endohedral Gd atoms directly facing the substituted C − C bonds. This indicates that the large inner metal cluster is completely fixed inside the cage after the first Prato reaction, which directs the second Prato addition toward those bonds situated in close contact.

The most favorable thermodynamic sites for the second addition on $Y_3N@C_{80}$ were one [5,6] bond (16 − 20 with the lowest energy) and two [6,6] bonds (22 − 23 and 57 − 58 with stabilities of 0.5 and 0.6 kcal·mol^{-1} relative to 16 − 20, respectively) (Fig. 5b) [16]. The bonds 57 − 58 and 22 − 23, which are completely surrounded by less stable [5,6] positions, could not be possible as second addition sites since no isomerization should be observed in these isomers. The obtained thermodynamic stabilities suggest that the second Prato addition to $Y_3N@C_{80}$ might be kinetically favored at the 20 − 22 [6,6] bond, which could subsequently isomerize to the most stable 16 − 20 [5,6] and 22 − 23 [6,6] positions. Linear transit calculations indicated a slightly lower activation barrier for bond 20 − 22 (the relative energy of the bis-adduct is 1.4 kcal·mol^{-1}) with respect to 22 − 23. From these observations, bond 20 − 22 is estimated to be the kinetic bis-adduct site and

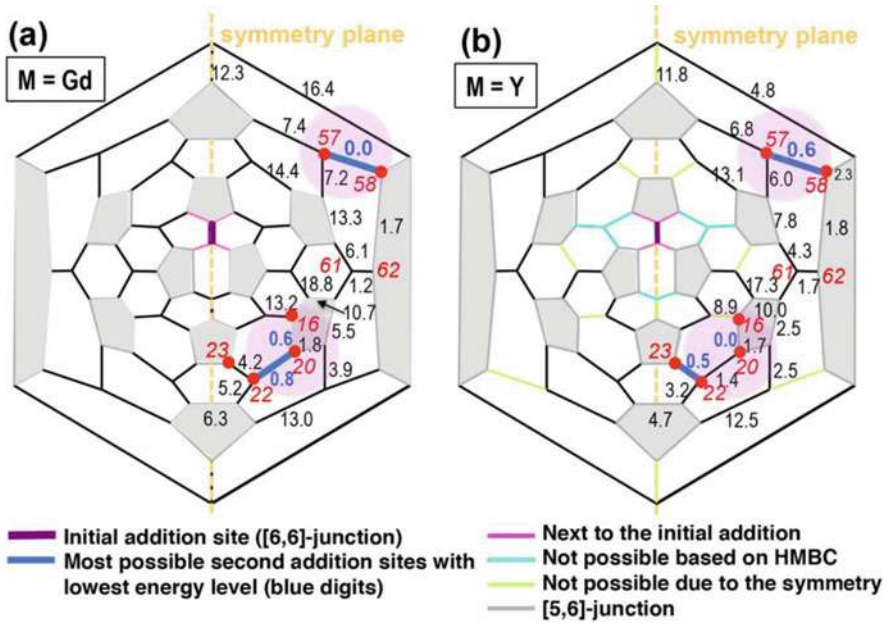

Fig. 5 (**a**, **b**) Schlegel structures of (**a**) $Gd_3N@C_{80}$ and (**b**) $Y_3N@C_{80}$ with relative stabilities for 23 different bis-adducts calculated at the BP86-D2/TZP//BP86-D2/DZP level of theory. Blue thick bonds represent the second addition sites of bis-adducts with the lowest energies (nonitalic numbers are energies in kcal·mol^{-1}, and red italic numbers correspond to the positions), and bonds situated close to the metal cluster are highlighted in pink. (Reproduced with permission from Ref. [16]. Copyright 2015 American Chemical Society)

bonds 16 − 20 and 22 − 23 as the thermodynamic bis-adduct sites for $Y_3N@C_{80}$. The smaller Y_3N cluster is able to rotate slightly to face the attacked C − C bond, making the second Prato addition less selective than that with the Gd_3N cluster. For monoadducts with larger metal clusters such as Y_3N and Gd_3N, one of the metal atoms directly faces the attacked bond, which leads to an enhanced reactivity of those more pyramidalized areas situated close to the other two metal atoms. In contrast, for the cases of $Sc_3N@C_{80}$ and $Lu_3N@C_{80}$ with smaller clusters, the lowest-energy monoadducts do not present any of the metal atoms facing the attacked C − C bond. This different orientation of the M_3N unit directs the bis-addition to other regions of the fullerene cage.

Bingel-Hirsch Reaction

Bingel-Hirsch (BH) reaction refers to the nucleophilic [2 + 1] cycloaddition of bromodiethylmalonate in the presence of a base such as 1,8-diazabicyclo[5.4.0]-undec-7-ene (DBU) and yields extremely stable cycloadducts (see Scheme 2). To advance the understanding of the reactivity properties of IPR and non-IPR

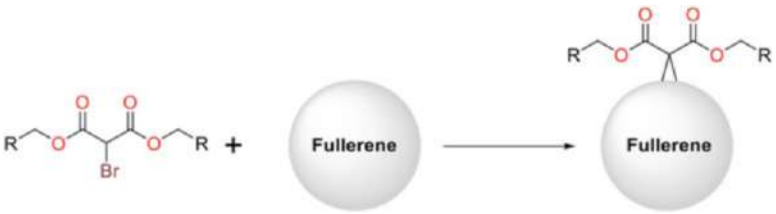

Scheme 2 [2 + 1] Bingel-Hirsch cycloaddition reaction between bromomalonate and fullerenes

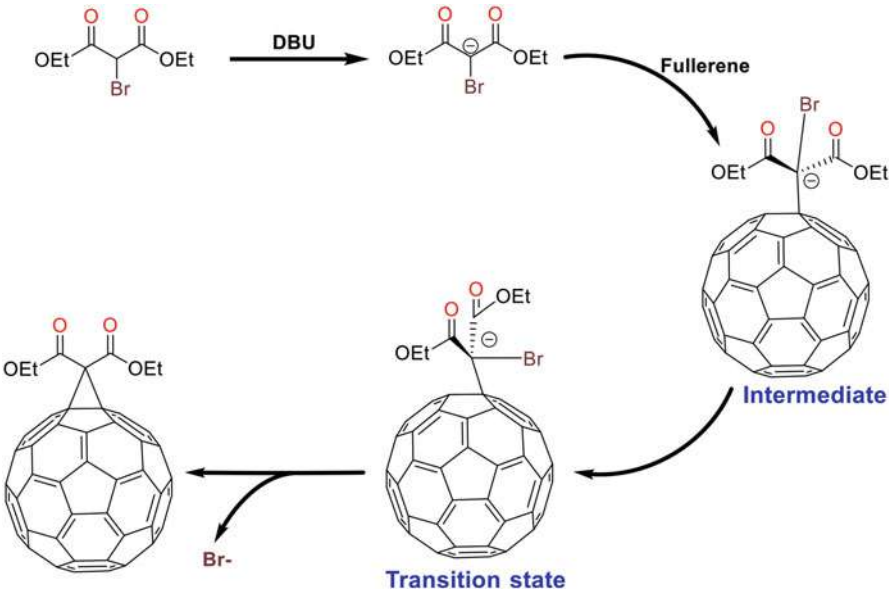

Scheme 3 General mechanism of the BH reaction on the fullerene cage

fullerenes, Poblet et al. performed an extensive theoretical study of the BH addition of bromomalonate on $Sc_3N@I_h$-C_{80} and $Sc_3N@D_{3h}$-C_{68} by considering all non-equivalent C-C bonds [17]. The additions at the [5,6] and [6,6] bonds on $Sc_3N@I_h$-C_{80} led to isoenergetic products (the [6,6] adduct is only 0.6 kcal·mol^{-1} lower in energy), in which one Sc atom is pointing out to the functionalized bond that has been broken yielding an open-fulleroid cage, as observed previously for $Y_3N@I_h$-C_{80} [18]. A mixture of the [6,6] and [5,6] adducts would be observed if the reaction is under thermodynamic control, which cannot explain the high regioselectivity at the [6,6] bond observed in experiments [19].

After considering the kinetic aspects of the reaction process (Scheme 3), the intermediate (INT) and the transition state (TS) that yield the [6,6] regioisomer show lower energies than those corresponding to the [5,6] one (the INT and the TS for the [6,6] regioisomer are 1.7 and 7.2 kcal·mol^{-1} lower than those for the [5,6] regioisomer). Based on these results, it has been concluded that the BH reaction

on $Sc_3N@I_h$-C_{80} must take place under kinetic control. Furthermore, the rate-determining step of the BH reaction is the conversion of INTs to products, because the formation of the INTs is a barrierless process. For the non-IPR $Sc_3N@D_{3h}$-C_{68}, the addition to a type-B [6,6] bond exhibited the most stable INT followed by the lowest-energy TS, which coincides with the adduct proposed from NMR experiments. All the $Sc_3N@D_{3h}$-C_{68} products also show an open-fulleroid structure in which the functionalized C-C bond is broken. In contrast to $Sc_3N@I_h$-C_{80}, the Sc_3N cluster is not able to rotate inside the D_{3h}-C_{68} cage due to the smaller cage size as well as the strong interactions between the three Sc^{3+} ions and the three pentalene units. Overall, the BH reaction has shown analogous reaction paths for IPR and non-IPR EFs, and a [6,6] mono-addition under kinetic control has been identified in both cases.

In order to predict the preferred addition site of EFs in BH reaction, Solà and coworkers theoretically studied the BH addition of diethylbromomalonate to the 13 nonequivalent bonds of $Sc_3N@D_{3h}$-C_{78} by using DFT calculations [20]. The INT at the 666 carbon atom with three pentagonal rings on neighboring positions is the lowest intermediate in energy, leading to the kinetic BH adduct at the type-B [6,6] bond next to a less aromatic five-membered ring (MR) for $Sc_3N@D_{3h}$-C_{78}, which coincides with the addition site observed in experiments [21]. Based on the analysis of the BH derivatization of $Sc_3N@D_{3h}$-C_{78} in terms of aromaticity and nucleophilicity, the predicted aromaticity criterion (PAC) was proposed, which is a set of aromaticity-based criteria for the BH addition on IPR EFs, as shown in Fig. 6. The most aromatic (and therefore lowest in energy) INTs lead to the lowest activation barriers for the BH addition. The PAC criteria state that (1) the lowest-energy INT should be located in a 666 region (C-666) because of smaller disruption of the aromaticity than those in a 566 region, and (2) among all possible C-666 s, those possessing more pentagonal rings adjacent to the 666 region (denoted as α-positions in Fig. 6) will likely be more favored. According to PAC, the lowest-energy TSs for the cyclopropane ring closure will occur on: (1) 5-MRs and (2) among all 5-MRs,

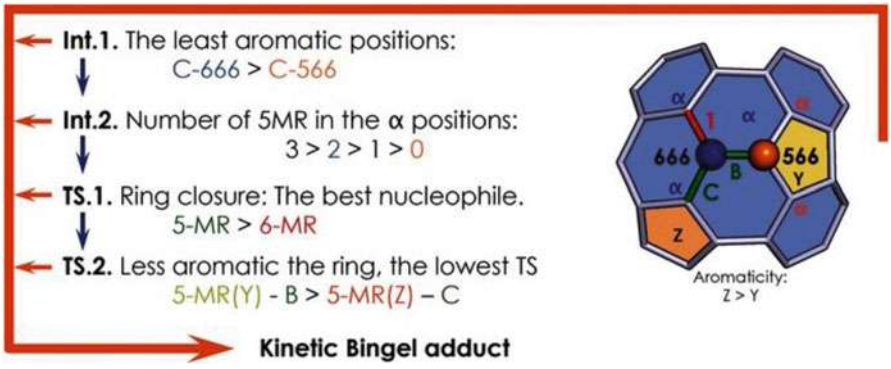

Fig. 6 Predictive aromaticity criteria (PAC) for the BH addition to IPR EMFs. (Reproduced with permission from Ref. [20]. Copyright 2016 Wiley-VCH Verlag GmbH & Co. KGaA, Weinheim)

those located far from the metal cluster (denoted as Y rings, Y-5-MRs). These 5-MRs rings exhibit a lower aromaticity and less-negative charge compared to those situated close to the metal atoms (denoted as Z rings, Z-5-MRs), that is, Y-5-MRs are preferred over Z-5-MRs. Meanwhile, the validity of PAC for $Sc_3N@D_{5h}$-C_{80} was verified by an extensive computational study of the BH reaction and by experimental functionalization [20].

By using BP86-D3(BJ)/TZP//BP86-D3(BJ)/DZP calculations, the BH reaction of $La@C_{2v}$-C_{82} was explored by Osuna, Solà, and coworkers to determine the possible addition sites [22]. The results show that $La@C_{2v}$-C_{82} is not particularly regioselective under BH conditions, which is consistent with the experimental results [23–25]. Type-B [6,6] bond of C2-C3 (see Fig. 3 for atom labels) is the kinetically and thermodynamically most favorable BH adduct, and the resulting fulleroid is corresponding to the conventional BH product observed in experiments. However, the addition at C15-C18 site cannot be totally disregarded. The more stable fulleroids with respect to the corresponding methanofullerenes can be attributed to (1) the breaking of the attacked C-C bond in the fullerene cage stabilizes the LUMO and destabilizes the HOMO of the carbon cage, making frontier orbital interactions more favorable; (2) all carbon atoms keep their sp^2 hybridization forming homoaromatic rings, maintaining their π-delocalization. Moreover, activation strain analysis reveals that the open-cage adduct tends to be more stabilized than the closed-cage one because of the higher interaction between the reactants. Two of the four singly bonded derivatives with the highest yields were assigned to the thermodynamically most stable INTs at C2 and C23 atoms. Computations suggested that these INTs are traps on the BH reaction pathways. Formation of the final BH adduct is kinetically hampered, leading to accumulation of these INTs. Likewise, the remaining two experimentally reported singly bonded derivatives with a reduced product distribution are probably attacks at C19 and C21 [23]. However, the formations of singly bonded derivatives at C7, C11, C13, and C18 are also feasible considering the stability of their corresponding INTs.

No identifiable adduct was detected for $Sc_3N@I_h$-C_{80} under the standard BH reaction conditions [26]. However, the same cycloaddition reaction gave two unconventional singly bonded monoadducts for $TiSc_2N@I_h$-C_{80} with a relative yield of 6:1, indicating the enhanced reactivity compared to $Sc_3N@I_h$-C_{80} and obvious change in the addition pattern [27]. Similarly to singly bonded monoadducts of $La@C_{2v}$-C_{82} [24], experimental results revealed that the paramagnetic properties of the pristine $TiSc_2N@I_h$-C_{80} disappear in the monoadducts. To clarify the possible addition site, DFT calculations were performed and found that the observed major and minor monoadducts should be respective additions at the 666 and 566 C atoms [28]. After considering different orientations of the inner $TiSc_2N$ cluster, the functionalized sites locate above the Ti–Sc edge of the inner cluster in these two singly bonded monoadducts. The singly bonded product from the 666 atom is 4.0 kcal·mol^{-1} lower in energy than that from the 566 atom. As for the formation of single bond adducts, a nucleophilic reaction occurs at the first step, followed by the oxidation of an INT with oxidants (fullerenes or trace oxygen in solvent) to afford the final adduct. Because the formation of INTs occurs without an energy barrier, that is,

any carbon atom on the cage could be attacked by the carbanion, the more stable INT would be more favorable. Calculations revealed that the negatively charged INT at the 666 atom is more stable than that at the 566 one; thus, addition on the 666 atom is kinetically preferred, which can be attributed to the more positive charge of the 666 C atom. Meanwhile, the investigations on the formation process of two conventional cycloadducts show that the [6,6] product would be experimentally favorable.

[2+2] Cycloaddition Reaction

[2+2] cycloaddition of benzyne on fullerenes has been successfully realized in experiment [29, 30]. A theoretical study based on DFT calculations for [2 + 2] cycloadditions of benzyne to $M_3N@C_{80}$ (M = Sc, Y) suggested a diradical mechanism rather than a carbene mechanism, in which the formation of the diradical intermediate is the rate-determining step [31]. As shown in Fig. 7, through rotation of benzyne moiety on the fullerene surface, the diradical intermediate on the 566 site

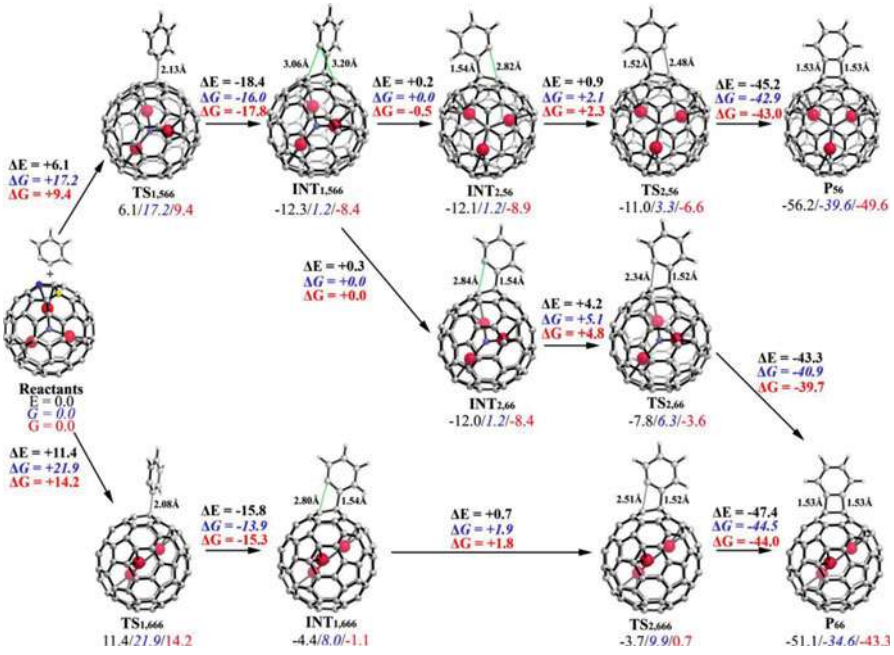

Fig. 7 Energy profiles (in kcal·mol^{-1}) of [2 + 2] cycloaddition of benzyne with $Sc_3N@C_{80}$. The different colors of energies are used to denote different levels of theory: electronic energies E at the B3LYP/Lanl2dz ~ 6-311G(d,p) level, in black; Gibbs free energies G at the B3LYP/Lanl2dz ~ 6-311G(d,p) level, in blue; and Gibbs free energies G at the B3LYP-D3/Lanl2dz ~ 6-311G(d,p) level, in red. The 566 and 666 sites are colored by blue and yellow in the reactants, respectively. (Reproduced with permission from Ref. [31]. Copyright 2015 American Chemical Society)

could isomerize to two new diradical intermediates which give rise to the [5,6] and [6,6] benzoadducts, respectively. However, the diradical INT on the 666 site only produces the [6,6] benzoadduct. In the case of $Sc_3N@C_{80}$, $\mathbf{P_{56}}$ is preferred kinetically and thermodynamically, accounting well the experimental observation that the yields of $\mathbf{P_{56}}$ and $\mathbf{P_{66}}$ are 70% and 15%, respectively [29]. Moreover, the reaction mechanism of benzyne with $Y_3N@C_{80}$ was theoretically predicted, and the significant effect of the endohedral cluster on the chemical reactivity was found. For $Y_3N@C_{80}$, $\mathbf{P_{66}}$ becomes more preferred thermodynamically with respect to $\mathbf{P_{56}}$, while $\mathbf{P_{66}}$ could also kinetically complete with $\mathbf{P_{56}}$ as a consequence of the similar energy barriers of the involved transition states. Noteworthy, the much lower energy barrier of $\mathbf{TS_{1,66}}$ in $Y_3N@C_{80}$ with respect to that in $Sc_3N@C_{80}$ indicates the high chemical reactivity of $Y_3N@C_{80}$. Therefore, it has been concluded that both [5,6] and [6,6] $Y_3N@C_{80}$ benzoadducts can be obtained. More interestingly, $Sc_3N@C_{80}$ and $Y_3N@C_{80}$ afford closed-cage and open-cage benzoadducts, respectively, indicating that the endohedral cluster could alter cycloadducts from the closed cage to the open cage.

Further analyses were carried out to explain the origin of regioselectivity in this [2 + 2] cycloaddition of $M_3N@C_{80}$ (M = Sc, Y). In both cases, the 566 C atom is more strained than the 666 one according to the POAV values, resulting in the higher reactivity of 566 site. With the larger Y_3N cluster encapsulated, POAV values of carbon atoms are further increased, suggesting the higher reactivity of $Y_3N@C_{80}$. The selectivity of $\mathbf{TS_{1,566}}$ and $\mathbf{TS_{1,666}}$ was analyzed by the distortion/interaction model. The results demonstrated that the two $\mathbf{TS_1}$ structures of $Sc_3N@C_{80}$ have larger distortion energies than those of $Y_3N@C_{80}$, while the corresponding interaction energies are comparable in both EMFs, indicating that the distortion energy rather than interaction energy determines the energy barriers of the key reaction step. The distortion energy and the destabilized interaction energy are both larger in $\mathbf{TS_{1,666}}$ compared to $\mathbf{TS_{1,566}}$ for $Sc_3N@C_{80}$; thus, these two terms bring about the higher energy barrier of $\mathbf{TS_{1,666}}$ with respect to $\mathbf{TS_{1,566}}$. In contrast, only the larger interaction energy in $\mathbf{TS_{1,666}}$ with respect to $\mathbf{TS_{1,566}}$ contributes to the higher energy barrier of $\mathbf{TS_{1,666}}$ for $Y_3N@C_{80}$, while their distortion energies are the same. Furthermore, those distortion energies in $Y_3N@C_{80}$ are smaller than those in $Sc_3N@C_{80}$, which is ascribed to the strain release of the larger Y_3N cluster in $\mathbf{TS_1}$. Therefore, the local strain energy of the fullerene cage plays a significant role in controlling the regioselectivity.

The reaction mechanism study of the [2 + 2] cycloaddition with benzyne on C_{60} was later studied by BP86-D2/TZP//BP86-D2/DZP calculations, which also follows the diradical mechanism [32]. Once the biradical singly bonded intermediate structure is formed, the rotation of benzyne in such an intermediate leads to the formation of closed-cage [2 + 2] cycloadducts in a practically barrierless process. The attack on a [6,6] bond of the cage produces the most kinetically and thermodynamically preferred reaction pathway, while the attack on a [5,6] bond can kinetically compete with the attack on a [6,6] bond. Thus, the reaction mainly occurs at the [6,6] site accompanied by the possible formation of the [5,6] product as observed in experiments [33].

Radical Reactions

Initially, the unpaired electron in the $RC_{60}^{\bullet}$ is mostly confined to the three carbon atoms *ortho* and to the two carbon atoms *para* to the point of attachment of R [34]. It is now clear that the unpaired electron in the adduct is largely restricted to two fused six-membered rings having the substituent R on one of the carbons of the shared edge (the [6,6[bond) [35]. On the other hand, C_{60} has only one equivalent carbon atom, but there are numerous fullerene molecules that possess low symmetry with a few nonequivalent carbon atoms. As a result, theoretical investigation would be a powerful option to determine the selective reaction sites and reaction mechanisms of radical reaction of fullerenes.

C-Centered Radicals

Reactions of C_{60} with photolytically and thermally generated alkyl radicals $R^{\bullet}$ are one of the first radical reactions which were studied upon fullerenes. Furthermore, the reaction mechanism of alkyl radicals, including methyl, ethyl, propyl, and butyl radicals, with C_{60} was investigated in theory. The binding energies of alkyl radicals to C_{60} were distributed in the range of 31.8–35.1 kcal·mol^{-1} at the CAM-B3LYP/6-311G(d,p) level. As shown in Fig. 8, it was found that the activation barriers before alkyl addition were calculated to be 2.1–2.8 kcal·mol^{-1} [36]. However, the addition of radicals to ellipsoidal C_{70} has not been investigated until 1994. Unlike C_{60} with equivalent carbon atoms, C_{70} can generate five isomeric CH_3C_{70} radicals (Fig. 9). Theoretical results indicate that fourth isomer must be identified with the energetically less-favored structure E controlled by kinetics [35].

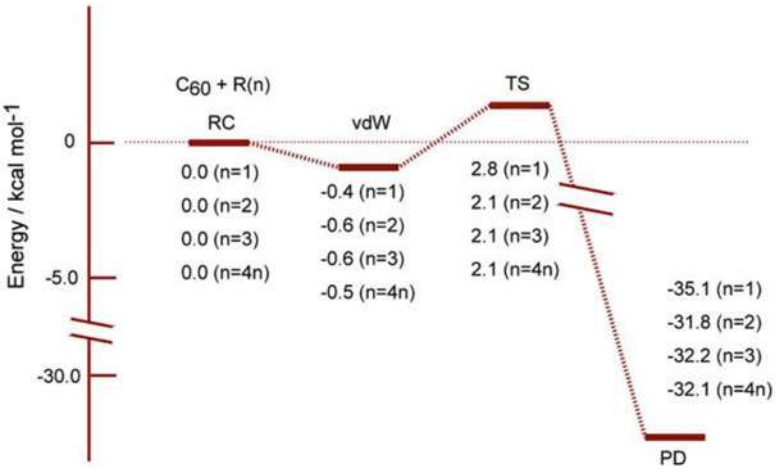

Fig. 8 Potential energy diagrams of alkyl radical addition reaction to C_{60} surface. The values indicate relative energies (in kcal·mol^{-1}) along the reaction coordinate. (Reproduced with permission from Ref. [36]. Copyright 2016 The Japan Society of Applied Physics)

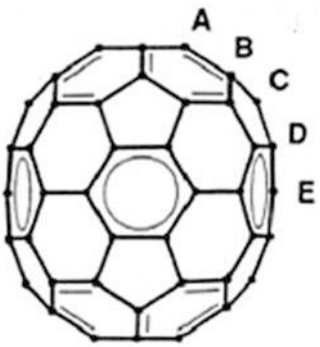

Fig. 9 Five possible reaction sites of C_{70} to radicals. (Reproduced with permission from Ref. [35]. Copyright 1994 American Chemical Society)

Semiempirical molecular orbital (MO) and the DFT calculations were carried out for $HC_{60}^{\bullet}$ and the five $HC_{70}^{\bullet}$ isomers as models for the corresponding alkyl and aryl analogs in order to describe their unpaired electron distribution and as an aid in the assignment of the observed spectra for $RC_{70}^{\bullet}$ isomers. The results of the subsequent addition of radicals to C_{60} prove the possibility of the formation of one-, two-, three-, and four-addition products based on reaction energies. It should be noted that the products of odd additions of vinyl radicals are fullerenyl radicals, which are comparable in stability with stable radicals such as triphenylmethyl. These results should only be used in combination with the kinetic analysis, that is, consideration of the probability of the course of possible reactions in the polymerization system during the complete monomer conversion [37]. Additionally, structural peculiarities of C_{20}, C_{24}, C_{30}, C_{36}, C_{40}, C_{60}, C_{70}, and C_{76}, and respective fullerenyl radicals formed by additions of $Me^{\bullet}$ radicals to fullerenes, have been studied by the PBE method. The heat effects (ΔH_r°) are calculated based on the elementary reactions $C_n + R^{\bullet} \rightarrow {}^{\bullet}RC_n$. Curvature indices (local curvature) of reaction sites in the fullerenes have been calculated as $k = 2\sin\theta_P/a$, where a is the average distance between the reaction sites and the neighboring atoms and θ_P is pyramidality angles of reaction sites. Linear correlations (Fig. 10) between heat effects of the reactions of radical addition to fullerenes and the local curvature of the fullerenes surface have been found first. It is important that these correlations cover fullerenes with both isolated (C_{60}, C_{70}, C_{76}) and shared pentagons (C_{20}, C_{24}, C_{30}, C_{36}, C_{40}). These linear correlations can be described as a common property for fullerene family. This correlation has been verified for the prediction of reactivity of experimentally obtained D_3-C_{78} and D_{2d}-C_{84} and also hypothetic C_{540} to $Me^{\bullet}$ radicals [38].

O-Centered Radicals

Typically, alkoxy radicals ($RO^{\bullet}$) photolytically generated will react with fullerenes; however, its reaction process is indistinct. The stepwise additions of four growing methyl methacrylate (MMA) radicals to C_{60} have been theoretically investigated. This reaction set is a reliable approximation for understanding the MMA

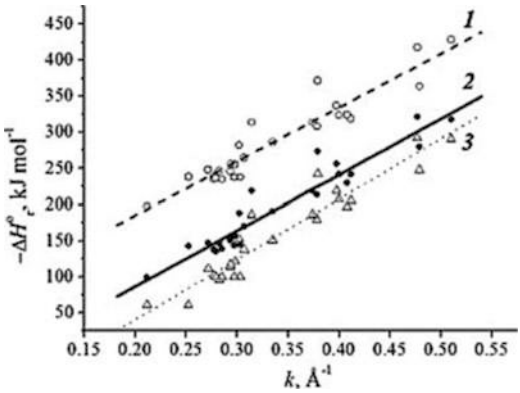

Fig. 10 Correlations between the heats (ΔH°_{r}) of F$^{\bullet}$ radical, H$^{\bullet}$ radical, and Me$^{\bullet}$ radical addition to fullerenes and the curvature indices of reaction sites. (Reproduced with permission from Ref. [38]. Copyright 2011 Elsevier B.V)

polymerization process within the presence of C_{60}. The authors have analyzed the geometries of the fullerene-MMA adducts and energy parameters of their formation, including heat effects and activation enthalpies. The results showed that three MMA growing radicals are favorably attached to C_{60}, and the fullerene-MMA trisadduct is a stable radical of the allyl type. It is inactive for further radical addition, and the elimination of the hydrogen from the growing MMA radical is preferable. The effects of steric factors and structures of the products of multiple growing MMA radical additions to C_{60} on the radical polymerization of MMA within the presence of C_{60} fullerene are considered. The spin density distribution of the model MMA radical has the highest values on the tertiary carbon atom (0.52 a.u.) and the oxygen atom of the carbonyl group (0.14 a.u.). Consequently, the interaction of this macroradical with the fullerene C_{60} is possible through the mentioned atoms, that is, with the formation of the C-C or O-C bonds, as shown in Fig. 11 [39].

The interaction of OH radical with C_{60} has been studied by the DFT in order to elucidate the radical scavenge mechanism of fullerene. The OH radical was examined as an organic radical with high reactivity. The calculational results show that while the OH radical binds to the C_{60}, a strong C-O bond will be formed. The binding energies were calculated to be 36.4 and 35.2 kcal·mol^{-1} at the B3LYP/6-31G(d) and B3LYP/6-311G(d,p), respectively. The potential energy curve plotted as a function of C-O distance shows that the OH radical approaches to the carbon atom of C_{60} without activation barrier. Also, it was found that the hybridization of carbon atom attached by OH radical easily changes from sp^2 to sp^3-hybridization states. The unpaired electron is widely distributed over the C_{60} surface in the C_{60}(OH) radical complex [40].

S-Centered Radicals

The addition of S-centered radicals to fullerenes has also been well documented in the literature. Similarly, alkyl disulfides (RSSR) and bis(alkylthio)mercury

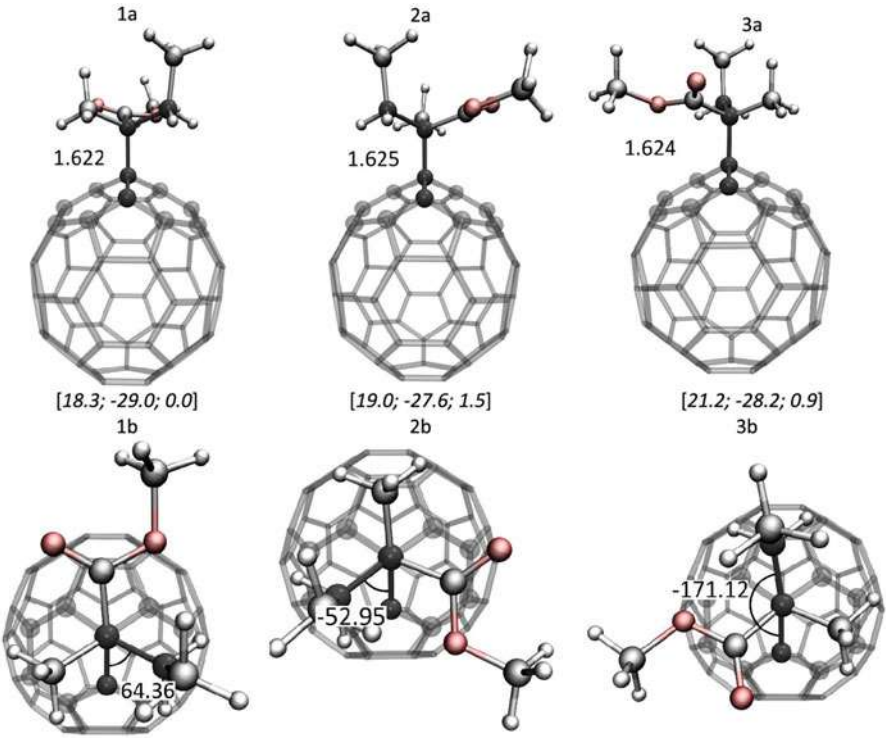

Fig. 11 Different conformations of the adduct $RC_{60}^{\bullet}$ and energetic parameters [$\Delta H^{\neq}$; ΔH°; H°_{rel}] of the addition of the first growing methyl methacrylate (MMA) radical to the C_{60} fullerene. The lengths of the C-C bonds between the MMA moiety and fullerene (in Å; 1a, 2a, 3a) and torsion angles between the CH_2-C group of MMA and the 2–1 carbon atoms of the fullerene parts of the monoadducts (1b, 2b, 3b) are also shown. (Reproduced with permission from Ref. [39]. Copyright 2020 Wiley Periodicals LLC)

compounds (RSHgSR) can be generally used as the source of the alkylthio radicals ($RS^{\bullet}$). The addition of S-centered radicals to C_{50}, C_{60}, C_{70}, and C_{100} has been investigated based on the PBE functional with double-zeta basis set and polarization functions [41]. The radical species which have been studied on the additions of them to fullerenes included $^{\bullet}S$, $^{\bullet}SH$, $^{\bullet}SCH_3$, $^{\bullet}SCH_2CH_3$, $^{\bullet}SC_6H_5$, $^{\bullet}SCH_2C_6H_5$, and the open-disulfide $^{\bullet}SCH_2CH_2CH_2CH_2S^{\bullet}$ radicals. Sulfur was found to be the most reactive S-centered radical with a preference of attachment to a [6,6] bond of C_{60} rather than to a [5,6] bond of C_{60}, because the [6,6] bond shows much more π-bond characters. Moreover, the stabilizing effect of the phenyl substituent group on the S-centered radical makes $^{\bullet}SC_6H_5$ very unreactive, which is not the case for $^{\bullet}SCH_2C_6H_5$. The results also show that the addition of a single S-centered radical to C_{60} leads to a weak C-S bond. However, the binding energy of $^{\bullet}SR$ radicals with C_{60} fullerene will increase while adding two or more radicals to C_{60}.

Addition of Metal-Centered Radicals

In the past decades, the transition-metal fullerene complexes with distinguished coordinated bonds have been widely studied. Specially, $C_{60}[CpRu(CO)_2]_2$ is the only one transition-metal fullerene complex with pure η^1-coordinated bond, which was synthesized via the reaction of dinuclear Ru complex $[CpRu(CO)_2]_2$ with C_{60}. However, the bonding nature and the formation mechanism of η^1-coordinated metal-fullerene complexes are still unclear. In 2017, Zhao, Sakaki, and coworkers carried out a theoretical study on η^1-coordinated $C_{60}[CpRu(CO)_2]_2$ with M06 and wB97XD functionals, and the results disclose that the η^1-coordinated bond is formed by a large overlap between the d_σ orbital of Ru and p_σ orbital of C which is involved in the lowest unoccupied molecular orbital (LUMO) (π^*) of C_{60} [42], as shown in Fig. 12, unlike the well-known η^2-coordinated metal-fullerene complex which has a π-type coordinate bond with the d_π orbital of metal atoms. The binding energy per one Ru-C bond is much smaller than those of η^2-coordinated $Pt(PMe_3)_2(C_{60})$ and $IrH(CO)(PH_3)_2(C_{60})$ because of the d orbital of Ru with much lower energy. The formation reaction occurs via Ru-Ru bond cleavage on the C_{60} surface followed by a direction change of $CpRu(CO)_2$ to afford $C_{60}[CpRu(CO)_2]_2$ in a stepwise manner via two asymmetrical transition states to avoid a symmetry-forbidden character. The calculated Gibbs activation energy ($\Delta G^{\circ\ddagger}$) is very high, and the Gibbs reaction energy

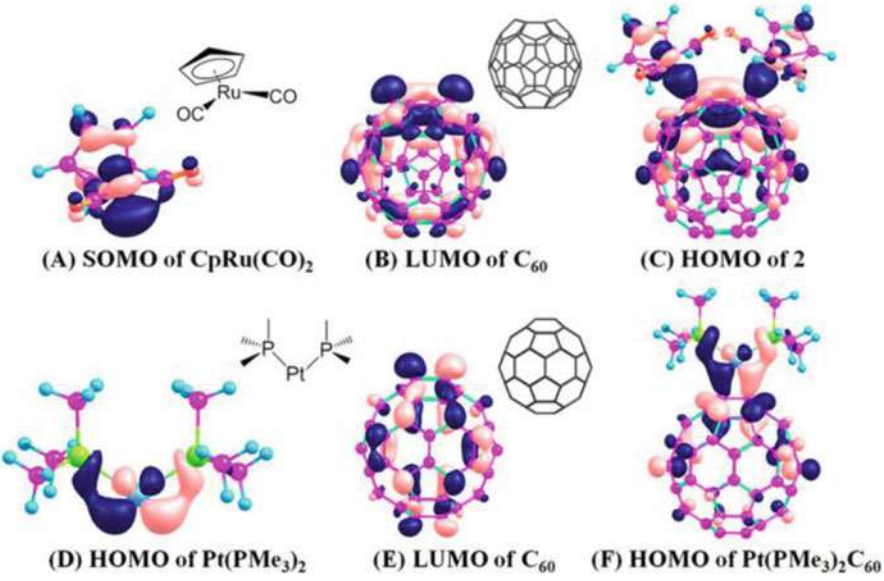

Fig. 12 (**a**) SOMO of $CpRu(CO)_2$; (**b**) LUMO of C_{60}; (**c**) HOMO of **2**; (**d**) HOMO of $Pt(PMe_3)_2$; (**e**) LUMO of C_{60}; and (**f**) HOMO of $Pt(PMe_3)_2(C_{60})$. Geometries of $CpRu(CO)_2$, $Pt(PMe_3)_2$, and C_{60} were taken to be the same as those in corresponding complexes. The complex of $CpRu(CO)_2C_{60}$ is marked as **2**. (Reproduced with permission from Ref. [42]. Copyright 2017 American Chemical Society)

(ΔG°) is moderately negative, which is consistent with the experimental observations of a very slow reaction rate and very small yield. The charge transfer from $CpRu(CO)_2$ to fullerene (Ru → C_{60}) is significant in the reaction, but the value is small due to the presence of the Ru d orbital at low energy, resulting in the high $\Delta G^{\circ\ddagger}$ and moderately negative ΔG°.

The utilization of $Li^+@C_{60}$ is theoretically predicted to accelerate the reaction and increase the yield of $Li^+@C_{60}[CpRu(CO)_2]_2$, because the charge transfer (Ru → C_{60}) is enhanced by the low energy of LUMO for $Li^+@C_{60}$. It was also predicted that $Li^+@C_{60}[Re(CO)_4(PMe_3)]_2$ is a next promising target for the synthesis of the η^1-coordinated metal-fullerene complex, but the syntheses of $C_{60}[Co(CO)_4]_2$, $C_{60}[Re(CO)_5]_2$, $Li^+@C_{60}[Co(CO)_4]_2$, and $Li^+@C_{60}[Re(CO)_5]_2$ are difficult. The use of nonpolar solvent is another important factor for the synthesis of the η^1-coordinated metal complex with $Li^+@C_{60}$. This theoretical investigation will give significant guidance to the addition of metal-centered radicals to fullerenes in further experimental and theoretical studies.

Addition of Hydrogen and Halogens

Hydrogenated fullerenes, also known as fullerene hydrides, are the simplest derivatives of the fullerenes. Due to their unique properties and their synthetic utility, several direct or indirect protocols have been developed for their preparation. Halogenation reactions were among the first reactions to be studied in fullerene chemistry. In general, halogenation and hydrides of fullerenes are considered as the radical process which can be achieved for fluorination, chlorination, and bromination but not iodination. Due to the large number of possible isomeric forms for the exohedral fullerenes (such as more than 50 billion for $C_{60}X_8$), Wang et al. proposed the exohedral fullerene stabilization index (XSI) model, exclusively based on topological arguments, that allows one to predict the relative stability of exohedral fullerenes without the need for electronic structure calculations or geometry optimizations [43, 44]. The model incorporates the effects of π delocalization, cage strain, and steric hindrance and works pretty well in predicting the cage topology and addends' distribution of the experimentally observed exohedral fullerenes. However, it is noteworthy that although a radical mechanism has been suggested in several cases, the exact mechanism of halogenation and hydrides in some other cases is still unclear, and so, it is not unlikely that some of the previously studied reactions do not proceed via a pure radical mechanism. This will be the ultimate target for further theoretical research.

Carbene Additions to Fullerenes

Carbenes, divalent carbon species, are well-known reactive intermediates to form new carbon-carbon bond. Importantly, carbenes exhibit diverse reactivity because they could exhibit two spin states including singlet and triplet. Singlet carbenes show

electrophilic and nucleophilic characters, whereas triplet carbenes possess diradical reactivity. Consequently, various chemical reactions will occur when fullerenes meet carbenes. In this regard, carbene additions to fullerenes are of great importance and attract both experimental and computational scientists. Here, some significant theoretical studies on the carbene reactions of fullerenes will be highlighted.

Dihalocarbenes

Dihalocarbene, which is among the simplest and most representative carbene species, is widely used in synthetic chemistry. Addition of dichlorocarbene to C_{60} was reported in experiments about two decades ago. Bettinger calculated the energy profiles for addition of dichlorocarbene to C_{60} by using DFT [45]. In addition of dichlorocarbene to a [6,6] or [5,6] bond of C_{60}, one transition state for each addition site ($TS_{[6,6]}$ or $TS_{[5,6]}$), which is 1.8 or 4.1 kcal·mol^{-1} higher in energy than the reactant, was found in both cases (Fig. 13). Relative energies of the two transition states are in agreement with the Bell-Evans-Polyani principle. In fact, the [6,6] closed methanofullerene is thermally more stable than the [5,6] open fulleroid. Addition of the singlet carbene to C_{60} proceeds similarly to reaction of the carbene with typical alkenes. The reaction is generally regarded as occurring in two phases. In the first phase, the carbene approaches suprafacial to the π system to maximize interaction between the highest occupied molecular orbital (HOMO) and the LUMO of carbene. In the second phase, the nonbonding electron pair of the carbene participates in nucleophilic interaction with the LUMO of the olefin.

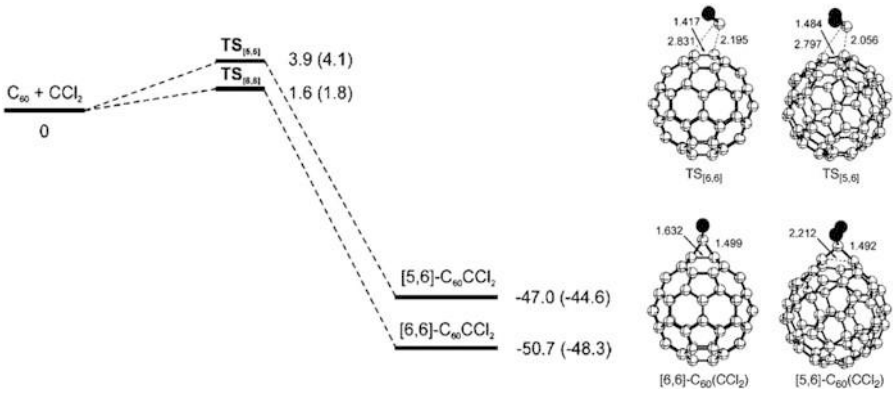

Fig. 13 Schematic energy profile (in kcal·mol^{-1}) for reaction of C_{60} with singlet dichlorocarbene as computed at the B3LYP/6-311G(d,p)//B3LYP6-31G(d) level of theory. Zero-point-corrected data are given in parentheses. Transition structures and products computed for addition of singlet dichlorocarbene (chlorine, black spheres) to the [6,6] and [5,6] bonds of C_{60} at the B3LYP/6-31G (d) level of theory. (Reproduced with permission from Ref. [45]. Copyright 2006 Wiley-VCH Verlag GmbH & Co. KGaA, Weinheim)

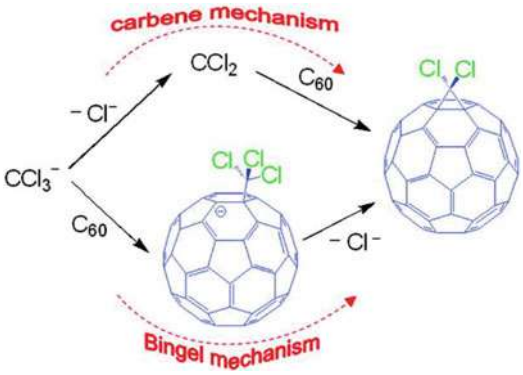

Scheme 4 Two possible reaction mechamisms for the addition of CCl_3^- to C_{60}, including carbene mechanism and Bingel mechanism. (Reproduced with permission from Ref. [46]. Copyright 2009 American Chemical Society)

Nagase, Chen, and coworkers conducted comparative studies of the carbene mechanism and the addition-elimination mechanism in the dichlorocarbene addition to C_{60} from trichloromethyl anion (Scheme 4) [46]. Their calculations show that the addition of CCl_3^- to C_{60} is an exothermic, barrierless process, affording $C_{60}(CCl_3)^-$ as the exclusive intermediate, and the addition-elimination mechanism is highly regioselective, which is in conformity with the results of the reactions of C_{70} with two different carbene reagents previously reported. The energy profiles via the carbene mechanism to compare the addition-elimination mechanism were obtained at the same level of theory, as shown in Fig. 14. Two reaction paths involving one-step concerted formation of the [6,6] adduct or the [5,6] adduct were found. The theoretical results suggest that the carbene mechanism slightly prefers the [6,6] adduct to the [5,6] adduct, whereas the addition-elimination mechanism affords the [6,6] adduct as the exclusive product. The energy of CCl_3^- is lower than the sum of energies of CCl_2 and Cl^- by 8.0 kcal·mol^{-1}, revealing that the concentration of CCl_3^- is higher than that of CCl_2 at equilibrium. The authors also studied the dependence of solvent dielectric constants on the activation energies of the rate-determining steps, of which results show that highly polar solvents effectively enhance the rate via the addition-elimination mechanism. Those results would help the further understanding of the carbene reaction of fullerenes in experiment.

Decomposition of Diazo Compounds

Diazo compounds are useful carbene reagents to functionalize fullerenes. In general, thermal reactions of diazo compounds to C_{60} afford a mixture of three regioisomers, marked as the [6,6] closed methanofullerene and the two [5,6] open fulleroids. Compounds **41** and **11** do not interconvert photochemically or thermally. Diederich and coworkers demonstrated stepwise addition of diazomethane to C_{2v}-symmetry C_{60} pentakis adducts. They proposed a mechanism for thermal and photochemical N_2 extrusion from pyrazoline intermediates to rationalize formation of the products, as shown in Fig. 15, in which fullerene cages are shown in part for clarity

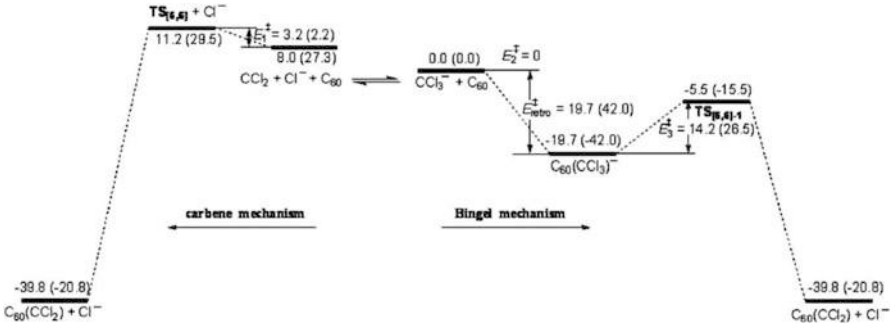

Fig. 14 Energy profiles (in kcal·mol^{-1}) reflecting the competition between the carbene and Bingel mechanisms for the reaction of CCl_3^- and C_{60}. Geometry optimization was performed in the gas phase at the B3LYP/6-31 + G(d) level, and single-point energies were computed in THF at the same level. The gas phase energies are given in parentheses. Zero-point energies (unscaled) were included. (Reproduced with permission from Ref. [46]. Copyright 2009 American Chemical Society)

[47]. Starting from pyrazoline **40**, its thermolysis provides an orbital symmetry controlled [π_2s + π_2s + σ_2s + σ_2a] rearrangement with high regioselectivity norcaradiene **42** with subsequent valence tautomerization to yield cycloheptatriene-like fulleroid **41**. The thermally allowed Woodward-Hoffmann mechanism was also supported by ab initio and density functional calculations of the model systems. In contrast, photolysis of **40** adopts a diradical mechanism (**43** and **44**), giving a mixture of **41** and **11**.

Decomposition of Diazirines

Photodecomposition of diazirines will generate carbenes and diazo intermediates, both of which are reactive toward fullerenes. Of particular interest is that addition of carbenes and diazo intermediates to C_{60} proceeds via different reaction pathways, resulting in a mixture of diastereomers with different formation ratios. In general, addition of carbenes to C_{60} can be regarded as concerted [2 + 1] addition, leading to the formation of [6,6] closed methanofullerenes exclusively. Addition of diazo compounds follows [3 + 2] cycloaddition to form pyrazoline intermediates. Subsequently, N_2 extrusion from the pyrazoline intermediates takes place by a thermally allowed Woodward-Hoffmann or a biradical mechanism. The former mechanism leads to [5,6] open fulleroids exclusively, whereas the latter mechanism engenders a mixture of [5,6] open fulleroids and [6,6] closed methanofullerenes.

In 2013, Zhao, Nagase, and Akasaka firstly investigated the cycloadditions of diazoadamantane (AdN_2) and adamantylidene carbene (Ad:) to tetragon-incorporating C_{2v}-symmetric C_{62} fullerene and the isomerizations of the cycloadducts by the M06-2X/6-31G(d). The calculation results show that the 1,3-dipolar reaction of AdN_2 occurs in the [4,6] junction to generate a

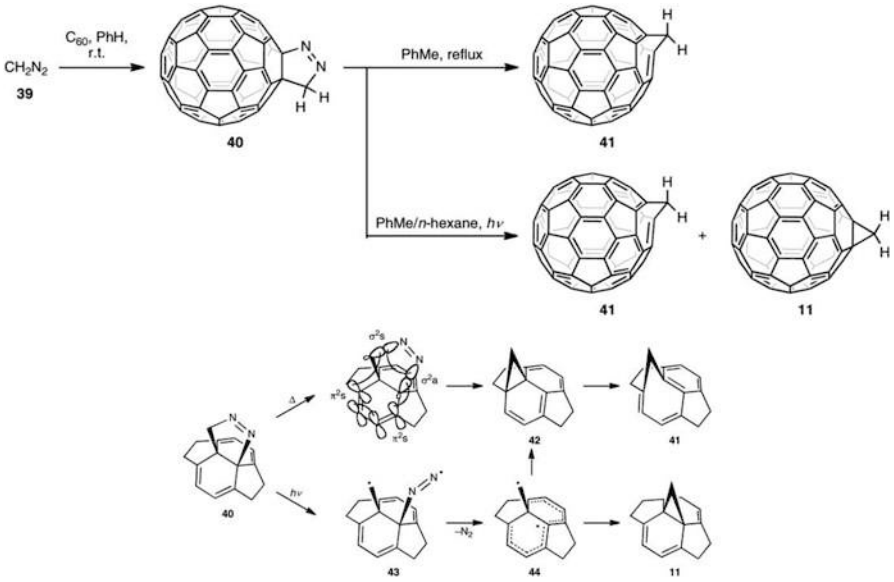

Fig. 15 Reaction of diazomethane toward C_{60} (top) and a proposed mechanism for thermal and photochemical N_2 extrusion from pyrazoline intermediates to rationalize formation of the products, in which fullerene cages are shown in part for clarity (bottom). (Reproduced with permission from Ref. [48]. Copyright 2013 American Chemical Society)

heteropentagonal pyrazoline in the squared region, and the subsequent dinitrogen elimination was found to be a stereoselective concerted mechanism leading to an exclusive [6,6]-bridged C_{62}Ad structure. The thermal and photochemical rearrangements of the formed [6,6]-C_{62}Ad were discussed, and the results imply that the [4,6]-fulleroids are the major rearrangement products according to both kinetic and thermodynamic considerations. In the case of [2 + 1] cycloadditions to C_{62}, an individual open [4,6]-bridged adamantanofullerene was predicted as the major adduct of singlet Ad: carbene by a direct concerted mechanism. On the other hand, a mixture of three interconvertible regioisomers was found to be the main products of triplet carbene addition through a stepwise radical reaction pathway. All of above-mentioned three reaction mechanisms are possible for the reaction of 2-adamantane-2,3-[3*H*]-diazirine with nonclassical C_{62} [49].

The DFT calculations with M06-2X-GD3 functional also provide the plausible reaction mechanism of Ad addition on C_{84}, showing that the initial [3 + 2] cycloaddition at the (a–a) bond (Fig. 16) with in situ generated diazoadamantane takes place, followed by N_2 extrusion, to form a pyrazoline intermediate. Subsequent decomposition of the pyrazoline via a concerted [π^2s + π^2s + σ^2a + σ^2s] pathway can afford the [5,6]-(a–b)-open fulleroid, C_{84}(Ad)-A, as the kinetic product. In addition, DFT calculations suggest that interconversion from C_{84}(Ad)-A to C_{84}(Ad)-B (Fig. 17), which is thermodynamically favorable, occurs via a [1,5]-sigmatropic shift. In the case of Sc_2C_2@C_{84}, four Ad monoadducts were obtained in the photolysis of **1**,

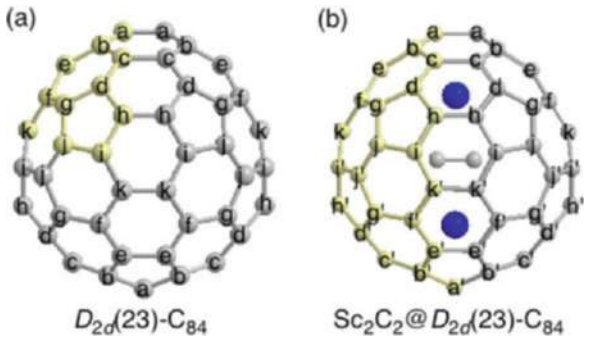

Fig. 16 (**a**) Structure of $D_{2d}(23)$-C_{84}, where the 11 nonequivalent carbon atoms on the cage are labeled as a–k. (**b**) Structure of $Sc_2C_2@D_{2d}(23)$-C_{84}, where the 22 nonequivalent carbon atoms on the cage are labeled as a–k and a′–k′. Lowering of the molecular symmetry results from the Sc_2C_2 cluster placement because the C_2 unit is not parallel to the main C_2 axis. (Reproduced with permission from Ref. [50]. Copyright 2016 American Chemical Society)

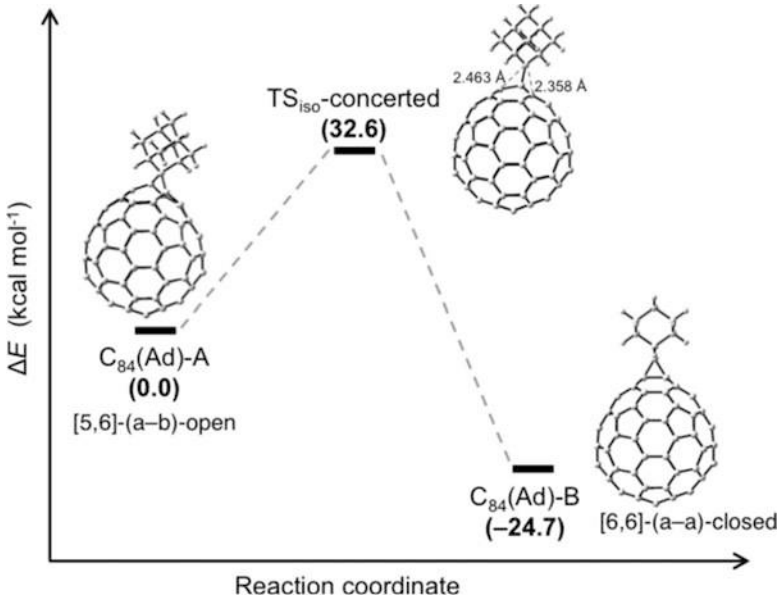

Fig. 17 Energy profiles (in kcal·mol^{-1}) for the concerted interconversion mechanism from C_{84}(Ad)-A to C_{84}(Ad)-B. (Reproduced with permission from Ref. [50]. Copyright 2013, American Chemical Society)

including $Sc_2C_2@C_{84}$(Ad)-A, $Sc_2C_2@C_{84}$(Ad)-B, $Sc_2C_2@C_{84}$(Ad)-C, and $Sc_2C_2@C_{84}$(Ad)-D. As for the thermal interconversion of $Sc_2C_2@C_{84}$(Ad)-A and $Sc_2C_2@C_{84}$(Ad)-B to $Sc_2C_2@C_{84}$(Ad)-C, the addend moves to bind with an adjacent bond, as proposed for the interconversion of empty C_{84}(Ad)-A to C_{84}(Ad)-B. Based on this hypothesis, the possible addition sites in $Sc_2C_2@C_{84}$(Ad)-A and

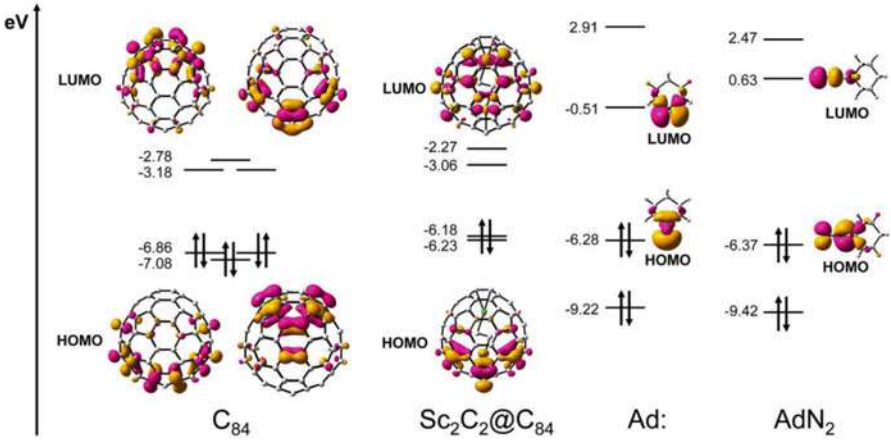

Fig. 18 MO diagrams of C_{84}, $Sc_2C_2@C_{84}$, Ad carbene, and diazoadamantane. (Reproduced with permission from Ref. [50]. Copyright 2013 American Chemical Society)

$Sc_2C_2@C_{84}$(Ad)-B can be limited to (k–k), (k–f), (h′–i′), and (i′–j′). DFT calculations show that $Sc_2C_2@C_{84}$(Ad)-C is the most thermodynamically stable among the candidates. However, the final structural identification for $Sc_2C_2@C_{84}$(Ad)-A and $Sc_2C_2@C_{84}$(Ad)-B as well as that for $Sc_2C_2@C_{84}$(Ad)-D was unable to be achieved because one cannot deny the possibility of carbene transfer or a "walk on the sphere" rearrangement. Based on the fact that $Sc_2C_2@C_{84}$ is not reactive toward in situ generated diazoadamantane, it was concluded that the Ad addition to $Sc_2C_2@C_{84}$ proceeded via a carbene mechanism. Their different chemical reactivities derive from the encapsulation of Sc_2C_2 cluster, which raises the HOMO and LUMO levels of the D_{2d}(23)-C_{84} carbon cage (Fig. 18). However, raising the HOMO level might become favorable for the addition of electrophilic Ad carbene to the carbon cage [50].

Conclusions

Theoretical prediction in various chemical reactions on empty and endohedral fullerenes has achieved great progress up to now. Several physical factors including charge density, spin density, POAV value, etc. have been found to be of high importance in controlling the addition site and the reaction rate. However, due to (1) many feasible reaction sites in fullerene cages; (2) various morphologies and sizes of fullerene cages; (3) the diversity of the encapsulation clusters; and (4) the dynamic motion of the encapsulation clusters, it is still a great challenge to excellently predict the chemical reactivity of fullerenes by using theoretical methods, especially for the endohedral fullerenes. The recent developments of machine learning and quantum computations lead to the dawn of solving such complex problems. In the near future, by employing the large-scale quantum-chemical

calculations with quantum computer and machine learning, the fullerene reactivity database and the "structure-activity relationship" model between structure and reactivity could be established, which will become one of the most powerful theoretical tools for realizing the exact prediction of fullerene reactivity.

Cross-References

- ▶ Chemical Reactions of Endohedral Metallofullerenes
- ▶ Functionalization of Fullerenes: Addition Reactions
- ▶ Radical Reaction and Photoreaction

Acknowledgments The authors gratefully acknowledge financial support from the National Natural Science Foundation of China (22003048, U1866203, 92066207) and Natural Science Foundation of Shaanxi Province (2021JLM-27, 2020JZ-03).

References

1. Campanera JM, Bo C, Poblet JM (2006) Exohedral reactivity of trimetallic nitride template (TNT) endohedral metallofullerenes. J Org Chem 71(1):46–54. https://doi.org/10.1021/jo051665s
2. Zhao P, Zhao X, Ehara M (2016) Regioselectivity of $Sc_2C_2@C_{3v}(8)$-C_{82}: role of the Sumanene-type hexagon in Diels–Alder reaction. J Org Chem 81(18):8169–8174. https://doi.org/10.1021/acs.joc.6b00947
3. Osuna S, Swart M, Campanera JM, Poblet JM, Solà M (2008) Chemical reactivity of D_{3h}-C_{78} (Metallo)fullerene: regioselectivity changes induced by Sc_3N encapsulation. J Am Chem Soc 130(19):6206–6214. https://doi.org/10.1021/ja711167v
4. Osuna S, Swart M, Solà M (2009) The Diels−Alder reaction on endohedral $Y_3N@C_{78}$: the importance of the fullerene strain energy. J Am Chem Soc 131(1):129–139. https://doi.org/10.1021/ja8048783
5. Garcia-Borràs M, Osuna S, Luis JM, Swart M, Solà M (2012) The Exohedral Diels–Alder reactivity of the titanium carbide endohedral metallofullerene $Ti_2C_2@D_{3h}$-C_{78}: comparison with D_{3h}-C_{78} and $M_3N@D_{3h}$-C_{78} (M=Sc and Y) reactivity. Chem Eur J 18(23):7141–7154. https://doi.org/10.1002/chem.201103701
6. Bickelhaupt FM, Solà M, Fernández I (2015) Understanding the reactivity of endohedral metallofullerenes: C_{78} versus $Sc_3N@C_{78}$. Chem Eur J 21(15):5760–5768. https://doi.org/10.1002/chem.201500067
7. Yang T, Zhao X, Nagase S, Akasaka T (2014) Diels–Alder reaction on free C_{68} fullerene and endohedral $Sc_3N@C_{68}$ fullerene violating the isolated pentagon rule: importance of pentagon adjacency. Chem Asian J 9(9):2604–2611. https://doi.org/10.1002/asia.201402435
8. Zhao P, Hu S, Lu X, Zhao X (2019) Diels–Alder cycloaddition on nonisolated-pentagon-rule C_{2v}(19 138)–C_{76} and $YNC@C_{2v}$(19 138)–C_{76}: the difference in regioselectivity caused by the inner metallic cluster. J Org Chem 84(22):14571–14578. https://doi.org/10.1021/acs.joc.9b02103
9. Garcia-Borràs M, Luis JM, Swart M, Solà M (2013) Diels–Alder and Retro-Diels–Alder cycloadditions of (1,2,3,4,5-Pentamethyl)cyclopentadiene to $La@C_{2v}$-C_{82}: regioselectivity and product stability. Chem Eur J 19(14):4468–4479. https://doi.org/10.1002/chem.201203517
10. Maeda Y, Miyashita J, Hasegawa T, Wakahara T, Tsuchiya T, Nakahodo T, Akasaka T, Mizorogi N, Kobayashi K, Nagase S, Kato T, Ban N, Nakajima H, Watanabe Y (2005)

Reversible and regioselective reaction of La@C_{82} with cyclopentadiene. J Am Chem Soc 127(35):12190–12191. https://doi.org/10.1021/ja053983e
11. Maeda Y, Sato S, Inada K, Nikawa H, Yamada M, Mizorogi N, Hasegawa T, Tsuchiya T, Akasaka T, Kato T, Slanina Z, Nagase S (2010) Regioselective exohedral functionalization of La@C_{82} and its 1,2,3,4,5-Pentamethylcyclopentadiene and Adamantylidene Adducts. Chem Eur J 16(7):2193–2197. https://doi.org/10.1002/chem.200902512
12. Sato S, Maeda Y, Guo J-D, Yamada M, Mizorogi N, Nagase S, Akasaka T (2013) Mechanistic study of the Diels–Alder reaction of paramagnetic endohedral metallofullerene: reaction of La@C_{82} with 1,2,3,4,5-Pentamethylcyclopentadiene. J Am Chem Soc 135(15):5582–5587. https://doi.org/10.1021/ja309763f
13. Osuna S, Swart M, Solà M (2009) Reactivity and Regioselectivity of Noble gas endohedral fullerenes Ng@C_{60} and Ng_2@C_{60} (Ng=He–Xe). Chem Eur J 15(47):13111–13123. https://doi.org/10.1002/chem.200901224
14. Rodríguez-Fortea A, Campanera JM, Cardona CM, Echegoyen L, Poblet JM (2006) Dancing on a fullerene surface: isomerization of Y_3N@(N-Ethylpyrrolidino-C_{80}) from the 6,6 to the 5,6 Regioisomer. Angew Chem Int Ed 45(48):8176–8180. https://doi.org/10.1002/anie.200604052
15. Aroua S, Garcia-Borràs M, Osuna S, Yamakoshi Y (2014) Essential factors for control of the equilibrium in the reversible rearrangement of M_3N@I_h-C_{80} fulleropyrrolidines: exohedral functional groups versus endohedral metal clusters. Chem Eur J 20(43):14032–14039. https://doi.org/10.1002/chem.201403743
16. Aroua S, Garcia-Borràs M, Bölter MF, Osuna S, Yamakoshi Y (2015) Endohedral metal-induced Regioselective formation of Bis-Prato adduct of Y_3N@I_h-C_{80} and Gd_3N@I_h-C_{80}. J Am Chem Soc 137(1):58–61. https://doi.org/10.1021/ja511008z
17. Alegret N, Rodríguez-Fortea A, Poblet JM (2013) Bingel–Hirsch addition on endohedral metallofullerenes: kinetic versus thermodynamic control. Chem Eur J 19(16):5061–5069. https://doi.org/10.1002/chem.201203522
18. Lukoyanova O, Cardona CM, Rivera J, Lugo-Morales LZ, Chancellor CJ, Olmstead MM, Rodríguez-Fortea A, Poblet JM, Balch AL, Echegoyen L (2007) "Open rather than closed" malonate Methano-fullerene derivatives. The formation of methanofulleroid adducts of Y_3N@C_{80}. J Am Chem Soc 129(34):10423–10430. https://doi.org/10.1021/ja071733n
19. Pinzón JR, Zuo T, Echegoyen L (2010) Synthesis and electrochemical studies of Bingel–Hirsch derivatives of M_3N@I_h-C_{80} (M=Sc, Lu). Chem Eur J 16(16):4864–4869. https://doi.org/10.1002/chem.200903155
20. Garcia-Borràs M, Cerón MR, Osuna S, Izquierdo M, Luis JM, Echegoyen L, Solà M (2016) The regioselectivity of Bingel–Hirsch cycloadditions on isolated pentagon rule endohedral metallofullerenes. Angew Chem 128(7):2420–2423
21. Cai T, Xu L, Shu C, Champion HA, Reid JE, Anklin C, Anderson MR, Gibson HW, Dorn HC (2008) Selective formation of a symmetric Sc_3N@C_{78} Bisadduct: adduct docking controlled by an internal trimetallic nitride cluster. J Am Chem Soc 130(7):2136–2137. https://doi.org/10.1021/ja077630m
22. Martínez JP, Garcia-Borràs M, Osuna S, Poater J, Bickelhaupt FM, Solà M (2016) Reaction mechanism and regioselectivity of the Bingel–Hirsch addition of dimethyl Bromomalonate to La@C_{2v}-C_{82}. Chem Eur J 22(17):5953–5962. https://doi.org/10.1002/chem.201504668
23. Feng L, Wakahara T, Nakahodo T, Tsuchiya T, Piao Q, Maeda Y, Lian Y, Akasaka T, Horn E, Yoza K, Kato T, Mizorogi N, Nagase S (2006) The Bingel Monoadducts of La@C_{82}: synthesis, characterization, and electrochemistry. Chemistry 12(21):5578–5586. https://doi.org/10.1002/chem.200501545
24. Feng L, Nakahodo T, Wakahara T, Tsuchiya T, Maeda Y, Akasaka T, Kato T, Horn E, Yoza K, Mizorogi N, Nagase S (2005) A singly bonded derivative of endohedral metallofullerene: La@C_{82}CBr($COOC_2H_5$)$_2$. J Am Chem Soc 127(49):17136–17137. https://doi.org/10.1021/ja055484j
25. Feng L, Tsuchiya T, Wakahara T, Nakahodo T, Piao Q, Maeda Y, Akasaka T, Kato T, Yoza K, Horn E, Mizorogi N, Nagase S (2006) Synthesis and characterization of a Bisadduct of La@C_{82}. J Am Chem Soc 128(18):5990–5991. https://doi.org/10.1021/ja058390i

26. Cardona CM, Kitaygorodskiy A, Echegoyen L (2005) Trimetallic nitride endohedral metallofullerenes: reactivity dictated by the encapsulated metal cluster. J Am Chem Soc 127(29): 10448–10453. https://doi.org/10.1021/ja052153y
27. Yang S, Chen C, Li X, Wei T, Liu F, Wang S (2013) Bingel–Hirsch monoadducts of $TiSc_2N@I_h$-C_{80} versus $Sc_3N@I_h$-C_{80}: reactivity improvement via internal metal atom substitution. Chem Commun 49(92):10844–10846. https://doi.org/10.1039/C3CC46277C
28. Zhao P, Dang J-S, Zhao X (2016) Bingel–Hirsch reaction mechanisms on $TiSc_2N@I_h$-C_{80}: the role of endohedral titanium nitride. Phys Chem Chem Phys 18(14):9709–9714. https://doi.org/10.1039/C6CP00389C
29. Li F-F, Pinzón JR, Mercado BQ, Olmstead MM, Balch AL, Echegoyen L (2011) [2 + 2] cycloaddition reaction to $Sc_3N@I_h$-C_{80}. The formation of very stable [5,6]- and [6,6]-adducts. J Am Chem Soc 133(5):1563–1571. https://doi.org/10.1021/ja1097176
30. Lu X, Nikawa H, Tsuchiya T, Akasaka T, Toki M, Sawa H, Mizorogi N, Nagase S (2010) Nitrated Benzyne derivatives of $La@C_{82}$: addition of NO_2 and its positional directing effect on the subsequent addition of Benzynes. Angew Chem Int Ed 49(3):594–597. https://doi.org/10.1002/anie.200905024
31. Yang T, Nagase S, Akasaka T, Poblet JM, Houk KN, Ehara M, Zhao X (2015) (2 + 2) cycloaddition of Benzyne to endohedral metallofullerenes $M_3N@C_{80}$ (M = Sc, Y): a rotating-intermediate mechanism. J Am Chem Soc 137(21):6820–6828. https://doi.org/10.1021/jacs.5b01444
32. Martínez JP, Langa F, Bickelhaupt FM, Osuna S, Solà M (2016) (4 + 2) and (2 + 2) cycloadditions of Benzyne to C_{60} and Zig-Zag single-walled carbon nanotubes: the effect of the curvature. J Phys Chem C 120(3):1716–1726. https://doi.org/10.1021/acs.jpcc.5b11499
33. Hoke SH, Molstad J, Dilettato D, Jay MJ, Carlson D, Kahr B, Cooks RG (1992) Reaction of fullerenes and benzyne. J Org Chem 57(19):5069–5071. https://doi.org/10.1021/jo00045a012
34. Morton JR, Preston KF, Krusic PJ, Hill SA, Wasserman E (1992) The dimerization of fullerene RC_{60} radicals [R = alkyl]. J Am Chem Soc 114(13):5454–5455. https://doi.org/10.1021/ja00039a083
35. Borghi R, Lunazzi L, Placucci G, Krusic PJ, Dixon DA, Knight LB (1994) Regiochemistry of radical addition to C_{70}. J Phys Chem 98(21):5395–5398. https://doi.org/10.1021/j100072a001
36. Tachikawa H, Kawabata H (2015) Addition reaction of alkyl radical to C_{60} fullerene: density functional theory study. Jpn J Appl Phys 55(2S):02BB01
37. Diniakhmetova DR, Friesen AK, Kolesov SV (2016) Quantum chemical modeling of the addition reactions of 1-n-phenylpropyl radicals to C_{60} fullerene. Int J Quantum Chem 116(7): 489–496. https://doi.org/10.1002/qua.25071
38. Sabirov DS, Bulgakov RG (2011) Reactivity of fullerenes family towards radicals in terms of local curvature. Comput Theor Chem 963(1):185–190. https://doi.org/10.1016/j.comptc.2010.10.016
39. Diniakhmetova DR, Friesen AK, Kolesov SV (2020) Reactions of fullerene C_{60} with methyl methacrylate radicals: a density functional theory study. Int J Quantum Chem 120(18):e26335. https://doi.org/10.1002/qua.26335
40. Tachikawa H, Iyama T, Abe S (2011) DFT study on the interaction of fullerene (C_{60}) with hydroxyl radical (OH). Phys Procedia 14:139–142. https://doi.org/10.1016/j.phpro.2011.05.027
41. Denis PA, Iribarne F (2011) Addition of sulfur radicals to fullerenes. Int J Quantum Chem 111(15):4266–4275. https://doi.org/10.1002/qua.22940
42. Zheng H, Zhao X, Sakaki S (2017) [2 + 2]-type reaction of metal–metal σ-bond with fullerene forming an η^1-C_{60} metal complex: mechanistic details of formation reaction and prediction of a new η^1-C_{60} metal complex. Inorg Chem 56(11):6746–6754. https://doi.org/10.1021/acs.inorgchem.7b00902
43. Wang Y, Díaz-Tendero S, Alcamí M, Martín F (2017) Relative stability of empty exohedral fullerenes: π delocalization versus strain and steric hindrance. J Am Chem Soc 139(4): 1609–1617. https://doi.org/10.1021/jacs.6b11669

44. Wang Y, Díaz-Tendero S, Alcamí M, Martín F (2018) Topology-based approach to predict relative stabilities of charged and functionalized fullerenes. J Chem Theory Comput 14(3): 1791–1810. https://doi.org/10.1021/acs.jctc.7b01048
45. Bettinger HF (2006) Addition of carbenes to the sidewalls of single-walled carbon nanotubes. Chem Eur J 12(16):4372–4379. https://doi.org/10.1002/chem.200501217
46. Gao X, Ishimura K, Nagase S, Chen Z (2009) Dichlorocarbene addition to C_{60} from the trichloromethyl anion: carbene mechanism or Bingel mechanism? Chem A Eur J 113(15): 3673–3676. https://doi.org/10.1021/jp900265g
47. Haldimann RF, Klärner F-G, Diederich F (1997) Reactions of C_{2v}-symmetrical C_{60} pentakis-adducts with diazomethane: regioselective formation of hexakis- to octakis-adducts and mechanism of methanofullerene formation by addition of diazomethane followed by dinitrogen extrusion. Chem Commun 2:237–238. https://doi.org/10.1039/A607483I
48. Yamada M, Akasaka T, Nagase S (2013) Carbene additions to fullerenes. Chem Rev 113(9): 7209–7264. https://doi.org/10.1021/cr3004955
49. Dang J-S, Wang W-W, Nagase S, Zhao X (2013) Regiochemistry of nonclassical C_{62} fullerene: role of tetragonal carbocyclic ring in cycloadditions and thermal/photoinduced interconversions of Fulleroid derivatives. J Phys Chem C 117(24):12882–12889. https://doi.org/10.1021/jp402621e
50. Yamada M, Tanabe Y, Dang J-S, Sato S, Mizorogi N, Hachiya M, Suzuki M, Abe T, Kurihara H, Maeda Y, Zhao X, Lian Y, Nagase S, Akasaka T (2016) D_{2d}(23)-C_{84} versus Sc_2C_2@D_{2d}(23)-C_{84}: impact of endohedral Sc_2C_2 doping on chemical reactivity in the photolysis of diazirine. J Am Chem Soc 138(50):16523–16532. https://doi.org/10.1021/jacs.6b10751

Part IV

Endofullerenes

Introduction and Classification of Endohedral Metallofullerenes

16

Wangqiang Shen, Pengwei Yu, Xinyue Tian, and Xing Lu

Contents

Abstract

The cavities of the fullerene can provide nanometer-scale space to host a variety of metal(s) or otherwise unstable metal clusters to produce a new class of metallo-organic compounds, known as endohedral metallofullerenes (EMFs). These unique hybrid molecules are stabilized by charge transfer and subsequent coordination between the inner metallic units and the outer fullerene cages, which endow EMFs with characteristic physio-chemical properties and structures that differ from empty fullerenes. Compared with traditional empty fullerenes, the charge transfer and subsequent coordination between the inner metallic units and the outer fullerene cage make the formed molecules possess new structures and different physio-chemical properties. Accordingly, we believe that currently described and not yet discovered EMFs will demonstrate enormous potential related to the practical applications in the materials, biology, catalysis,

W. Shen · P. Yu · X. Tian
School of Materials Science and Engineering, Huazhong University of Science and Technology, Wuhan, Hubei, China

X. Lu (✉)
Huazhong University of Science and Technology, Wuhan, Hubei, China
e-mail: lux@hust.edu.cn

X. Lu et al. (eds.), *Handbook of Fullerene Science and Technology*,
https://doi.org/10.1007/978-981-16-8994-9_25

photoelectric conversion, etc. Herein, a systematic and comprehensive summary of the new structures and unprecedented properties of EMFs are presented according to the categories of monometallofullerenes, dimetallofullerenes, trimetallofullerenes, and clusterfullerenes. Finally, perspectives regarding the novel structures and potential applications of EMFs are proposed.

Keywords

Endohedral metallofullerenes · Molecular structures · Metallic clusters · Cluster-cage interaction · X-ray crystallography · Density functional calculations

Introduction

The discovery of C_{60}, the most representative fullerene, opened the door for scientists to explore carbon nanomaterials [1]. However, early studies of fullerenes were limited to the theoretical calculations because fullerene synthesis attempts resulted in extremely low yields. The invention of the Krätschmer-Huffman DC arc discharge synthesis method in 1990 made large-scale fullerene preparation, structural characterization, and property research possible [2]. Unlike other carbon nanomaterials (carbon nanotubes, graphene, etc.), fullerenes can be dissolved in most organic solvents because of the specificity of their molecular structures. Thus, very pure fullerene-based substances can be synthesized and thoroughly characterized [3, 4]. One of the most typical features of fullerenes is the hollow carbon cages, which can entrap atoms, molecules, and metallic clusters, opening a possibility of creating a variety of new classes of hybrid molecules (also known endofullerenes) with specific targeted properties [5–8].

Various approaches of incorporation of different species into the fullerene cages were reported. For instance, isolated molecules (H_2, H_2O, and H_2O_2) can be entrapped by a so-called fullerene-surgery method to create unique systems to investigate the properties of these isolated molecules [9–11]. However, no apparent interactions between the entrapped molecules and the fullerene shell were observed. Metal atoms or clusters were also successfully placed inside fullerene cages. The resulting composite molecules, called endohedral metallofullerenes (EMFs), possessed a unique charge transfer mechanism from the trapped metals to the surrounding cage. In fact, only 1 week after the discovery of C_{60}, Smalley et al. hypothesized that La atoms can be entrapped into fullerene cages on the basis of mass spectrometric detection of a LaC_{60} complex [12]. Subsequently, they experimentally verified this hypothesis for the first time by extracting several EMFs, that is, La@C_{60}, La@C_{70}, and La@C_{82}, from the raw ash [13]. Thereafter, with the invention and adoption of the Krätschmer-Huffman DC arc discharge method, more and more metals, such as alkali metals, alkaline earth metals, group 3, 4, 5 elements, and lanthanides, were encapsulated into the fullerene cages to form the corresponding EMFs.

Compared with traditional empty fullerenes, the strong interaction and electron transfer between the internal metals and the outer cage make the formed molecules possess many new properties. For example, the intercalation of alkali metals makes the corresponding EMFs exhibit low-temperature superconducting properties [14], and the encapsulation of magnetic metals, such as Dy and Tb, allows the formed compounds to have excellent magnetic properties [6]. Therefore, we strongly believe that both currently described and not yet discovered EMFs will demonstrate enormous potential related to the practical applications in the materials, biology, catalysis, photoelectric conversion, etc. The unique properties of the EMFs depend on the types of the entrapped clusters. In view of this, this chapter will discuss the EMF classification based on this criterion.

Classification

Elements capable of forming endofullerenes are shown with color in Fig. 1. Incorporation of the CO, NH_3, H_2O, and H_2O_2 molecules occurs through their trapping by the open-caged fullerenes. Nonmetals (e.g., N, P) and inert gases can be inserted into the fullerene cages in their atomic forms. Incorporation of the rare-earth elements (La, Sc, Gd, Lu, etc.) into fullerenes increases the variety of EMF species dramatically, especially in comparison to the EMFs containing alkali-earth (Ca, Ba, etc.) and group 4 (Ti, Zr, etc.) metals [5–7]. Based on the encapsulated unit type, EMFs can be classified into monometallofullerenes (mono-EMFs), dimetallofullerenes (di-EMFs), trimetallofullerenes (tri-EMFs), and clusterfullerenes (cluster-EMFs).

	1	2	3	4	5	6	7	8	9	10	11	12	13	14	15	16	17	18
	IA																	VIII A
1	H $1s^1$	IIA											IIIA	IVA	VA	VIA	VII7	He $1s^2$
2	Li $2s^1$	Be $2s^2$											B $2s^22p^1$	C $2s^22p^2$	N $2s^22p^3$	O $2s^22p^4$	F $2s^22p^5$	Ne $2s^22p^6$
3	Na $3s^1$	Mg $3s^2$	IIIB	IVB	VB	VIB	VIIB	VIII			IB	IIB	Al $3s^23p^1$	Si $3s^23p^2$	P $3s^23p^3$	S $3s^23p^4$	Cl $3s^23p^5$	Ar $3s^23p^6$
4	K $4s^1$	Ca $4s^2$	Sc $3d^14s^2$	Ti $3d^24s^2$	V $3d^34s^2$	Cr $3d^54s^1$	Mn $3d^54s^2$	Fe $3d^64s^2$	Co $3d^74s^2$	Ni $3d^84s^2$	Cu $3d^{10}4s^1$	Zn $3d^{10}4s^2$	Ga $4s^24p^1$	Ge $4s^24p^2$	As $4s^24p^3$	Se $4s^24p^4$	Br $4s^24p^5$	Kr $4s^24p^6$
5	Rb $5s^1$	Sr $5s^2$	Y $4d^15s^2$	Zr $4d^25s^2$	Nb $4d^45s^1$	Mo $4d^55s^1$	Tc $4d^55s^2$	Ru $4d^75s^1$	Rh $4d^85s^1$	Pd $4d^{10}$	Ag $4d^{10}5s^1$	Cd $4d^{10}5s^2$	In $5s^25p^1$	Sn $5s^25p^2$	Sb $5s^25p^3$	Te $5s^25p^4$	I $5s^25p^5$	Xe $5s^25p^6$
6	Cs $6s^1$	Ba $6s^2$	*	Hf $5d^26s^2$	Ta $5d^36s^2$	W $5d^46s^2$	Re $5d^56s^2$	Os $5d^66s^2$	Ir $5d^76s^2$	Pt $5d^96s^1$	Au $5d^{10}6s^1$	Hg $5d^{10}6s^2$	Tl $6s^26p^1$	Pb $6s^26p^2$	Bi $6s^26p^3$	Po $6s^26p^4$	At $6s^26p^5$	Rn $6s^26p^6$
7	Fr $7s^1$	Ra $7s^2$	**	.....														

*	La $5d^16s^2$	Ce $4f^15d^16s^2$	Pr $4f^36s^2$	Nd $4f^46s^2$	Pm $4f^56s^2$	Sm $4f^66s^2$	Eu $4f^76s^2$	Gd $4f^75d^16s^2$	Tb $4f^96s^2$	Dy $4f^{10}6s^2$	Ho $4f^{11}6s^2$	Er $4f^{12}6s^2$	Tm $4f^{13}6s^2$	Yb $4f^{14}6s^2$	Lu $4f^{14}5d^16s^2$
**	Ac $6d^27s^2$	Th $6d^27s^2$	Pa $5f^26d^17s^2$	U $5f^36d^17s^2$	Np $5f^46d^17s^2$	Pu $5f^67s^2$	Am $5f^77s^2$	Cm $5f^76d^17s^2$	Bk $5f^97s^2$	Cf $5f^{10}7s^2$	Es $5f^{11}7s^2$	Fm $5f^{12}7s^2$	Md $5f^{13}7s^2$	No $5f^{14}7s^2$	Lr $5f^{14}6d^17s^2$

Fig. 1 Elements in the periodic table that can be encapsulated inside fullerene cages to form the corresponding endofullerenes (marked in color)

The latter ones are further categorized into sub-branches depending on the types of metallic and nonmetallic elements of the clusters.

Mono-EMFs

Mono-EMFs (often abbreviated as $M@C_{2n}$) contain only one metal atom inside the fullerene cage. The most famous and well-studied mono-EMF is $La@C_{82}$ [13]. Mono-EMFs are ideal prototypes to study M-C_{2n} interactions at the sub-nanometer scale [13]. Since the $La@C_{82}$ was reported in 1991, an enormous variety of air-stable $M@C_{2n}$ were discovered with M from alkali and alkaline-earth metals to actinide metals [15]. When the metal atom is trapped inside the fullerene cage, the electrons from the metal transfer to the empty π-type orbitals of the cage, forming a structure that can be described as $M^{x+}@(C_{2n})^{x-}$ [5, 7]. Mono-EMFs are typically divided into divalent, trivalent, and tetravalent mono-EMFs depending on how many electrons were transferred from the entrapped metal to the carbon cage.

Typically, the synthesis yield for the divalent mono-EMFs is significantly lower than for the trivalent ones. Thus, often scientists do not have sufficient quantities of pure divalent mono EMFs for thorough characterization and study. However, it was confirmed that alkaline-earth (Ca, Ba, Sr) and some rare earth (Sm, Eu, Tm, Yb) metals transfer two electrons to the C_{2n} cage forming divalent mono-EMFs [5, 7]. Other rare earth metals (Y, Ce, Sc, Pr, Nd, La, Gd, Tb, Ho, Er, Dy, and Lu) transfer three electrons to the carbon cage after they are encapsulated into cage, thus forming the corresponding trivalent mono-EMFs with the $M^{3+}@(C_{2n})^{3-}$-type electronic structure [5, 7]. Among the reported trivalent mono-EMFs, the $M@C_{82}$ species attracted the exceptionally high interest of researchers worldwide. Their molecular structures and physiochemical properties are well-characterized and studied because these EMFs can be obtained with a relatively high yield. Additionally, their excellent solubility in common organic solvents assists in obtaining high quantities of very pure $M@C_{82}$. In fact, it was discussions around the $Y@C_{82}$ structure that clarified the long scientific debate whether the metal is inside the cage [16]. Currently, a great variety of $M@C_{82}$ mono-EMFs have been isolated and characterized, including $Sc@C_{82}$, $Ce@C_{82}$, $Pr@C_{82}$, $Dy@C_{82}$, $Tb@C_{82}$, $Gd@C_{82}$, $Ho@C_{82}$, $Sm@C_{82}$, $Lu@C_{82}$, $Nd@C_{82}$, and $Er@C_{82}$ [5, 7, 15, 17]. Fig. 2 shows the single-crystal structures of the two prototypes of $M@C_{82}$ class members: $Y@C_{2v}(9)$-C_{82} and $Er@C_{2v}(9)$-C_{82}. It is noteworthy that EMFs all have undifferentiated spherical carbon cage structures, thus leading to the common crystal disorder. At present, co-crystallization of EMFs with M^{II}(OEP) (M = Co, Ni, Cu, and Zn, OEP = octaethylporphrin) has been developed one of the most useful methods to obtain high-quality crystals of crystallizing EMFs for single-crystal XRD study [18–20].

The first actinide containing mono-EMFs ($U@T_d$-C_{28}) was reported in 1992 [23]. Since then, these mono-EMFs remained an exciting research area but still underexplored. The molecular structure of $Th@C_{3v}(8)$-C_{82} (shown in Fig. 3a) was first confirmed experimentally (by X-ray crystallography) in 2017 [24]. Since then, the molecular structures of other mono-actinide EMFs ($Th@C_1(28324)$-C_{80},

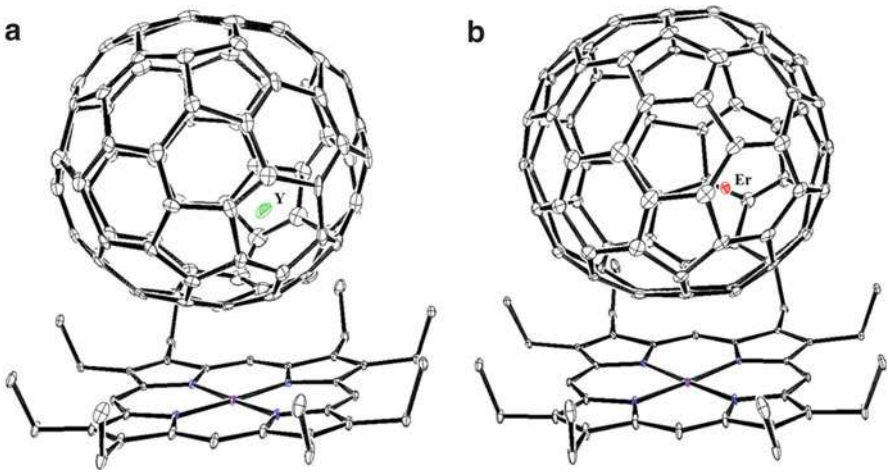

Fig. 2 The ORTEP drawings of (a) Y@C_{2v}(9)-C_{82}·Ni(OEP) [21] and (b) Er@C_{2v}(9)-C_{82}·Ni(OEP) [22] with 20% thermal ellipsoids. Only the major sites of the metal atoms and one cage orientation are shown. Solvent molecules and hydrogen atoms are omitted for clarity. Y, Er, Ni, and N atoms are highlighted in green, red, purple, and blue, respectively

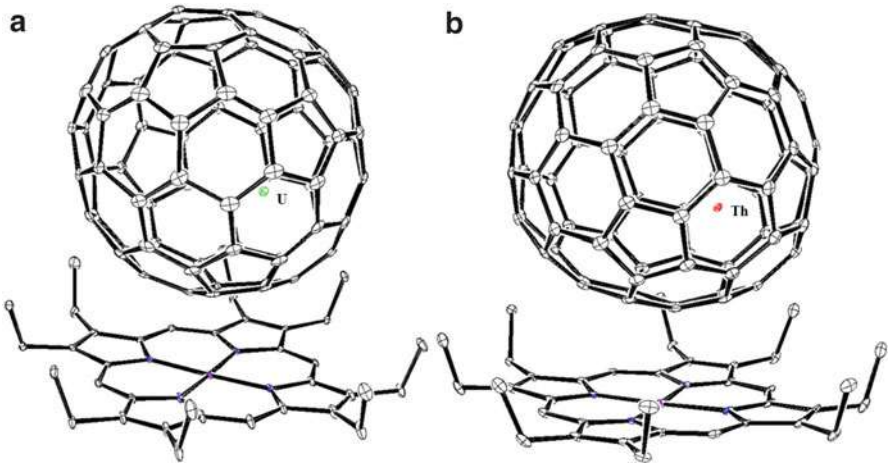

Fig. 3 The ORTEP drawings of (a) Th@C_{3v}(8)-C_{82}·Ni(OEP) [24] and (b) U@C_{2v}(9)-C_{82}·Ni(OEP) [25] with 20% thermal ellipsoids. Only the major sites of the metal atoms and one cage orientation are shown. Solvent molecules and hydrogen atoms are omitted for clarity. Th, U, Ni, and N atoms are highlighted in green, red, purple, and blue, respectively

Th@C_1(11)-C_{86}, U@D_{3h}(1)-C_{74}, U@C_1(17418)-C_{76}, U@C_1(28324)-C_{80}, U@C_2(5)-C_{82}, U@D_2(21)-C_{84}, U@C_s(15)-C_{86}, and U@C_1(11)-C_{86}) were verified by the single-crystal X-ray diffraction (XRD) by Echegoyen et al. [25–28] It is worth noting that the isomeric U@C_{2v}(9)-C_{82} (see Fig. 3b) exhibits a trivalent electronic configuration U^{3+}@C_{2v}(9)-$C_{82}{}^{3-}$, which represents a rare example for cage-isomer

dependent charge-transfer state of the entrapped metals. In other mono-actinide EMFs, the entrapped metal transfers four electrons to the outer cage.

Undoubtedly, there are still many unknown mono-EMFs yet to be synthesized and explored. M@C_{3v}(134)-C_{94} (M = Ca, Tm, Sm) are the mono-EMFs possessing the largest cages reported so far [29, 30]. In 2010, a mono-EMF, namely, $Li^+@C_{60}$, was successfully isolated by Aoyagi et al., and its molecular structure was unambiguously characterized by single crystal XRD crystallography [14]. It is the mono-EMFs possessing the smallest cages that can be successfully separated and structural characterized.

Di-EMFs

Dimetallofullerenes (di-EMFs) were discovered almost simultaneously with mono-EMFs. However, their low yields made it difficult to structural identify them. Thus, reports on their characterization and properties were lacking [5]. $La_2@C_{80}$ was the first di-EMFs synthesized by Alvarez et al. by arc discharge in 1991 [31]. Subsequently, Akasaka et al. used [13]C nuclear magnetic resonance (NMR) and single-crystal XRD to explore $La_2@C_{80}$ molecular structure and La location inside the C_{80} cage [32]. The results demonstrated that the chemical environment of both La atoms is the same since they freely rotate inside the cage. EMFs with a composition of M_2C_{2n} can sometimes correspond to carbide cluster metallofullerenes (CCMFs), $M_2C_2@C_{2n-2}$. Therefore, single-crystal XRD stands as one of the most reliable solutions for their structural identification. Among the reported di-EMFs, the production of di-EMFs with C_{80} and C_{82} cages are relatively more abundant. Therefore, in the past few decades, a series of C_{80}- and C_{82}-based di-EMFs were isolated and characterized, that is, $Ce_2@C_{80}$, $La_2@C_{80}$, $Y_2@C_{82}$, $Sc_2@C_{82}$, $Er_2@C_{82}$, $Dy_2@C_{80}$ and $Tm_2@C_{82}$ [5, 7]. At the same time, di-EMFs with other carbon cages, such as $Sc_2@C_{66}$, $Pr_2@C_{72}$, $Ce_2@C_{2n}$ (2n = 72, 78), $La_2@C_{2n}$ (2n = 72, 76, 78, 100), $Sm_2@C_{2n}$ (2n = 88, 90, 92, 104) have also been successively separated and characterized [33–39].

Most of the fullerene cages are ideal hosts to contain clusters of multiple metals. Therefore, research of the metal-metal bonds of the di-EMFs attracts tremendous interest [41, 42]. In 2012, Popov et al. [43] confirmed theoretically (by DFT calculations and quantum theory of atoms in molecules (QTAIM) topological analysis) the existence of the covalent bonds between the metals inside $M_2@C_{76}$, $M_2@C_{82}$ (M = Sc, Y, Lu), and $Y_3@C_{80}$ EMF cages. In 2015, Yamada et al. demonstrated the formation of the single-electron La-La bond for the first time [44]. When $La_2@I_h(7)$-C_{80} reacts with a triazinyl radical, the unpaired electron is transferred to the molecular orbital of the internal La_2 cluster. As a result, a stable monoadduct with a single-electron La-La bond forms inside the cage. Subsequently, Shinohara et al. proposed that $M_2@I_h(7)$-C_{80} EMFs (with M = Y, Gd, Dy, etc.) are unstable radicals because only one unpaired electron occupies the M-M bond orbital, while the other electron is delocalized over the fullerene cage [45].

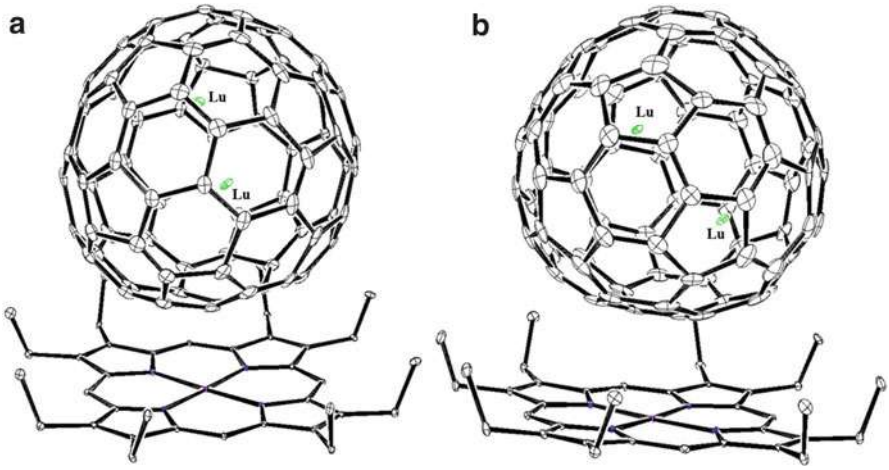

Fig. 4 The ORTEP drawings of (**a**) $Lu_2@C_s(6)$-C_{82}·Ni(OEP) [40] and (**b**) $Lu_2@C_{3v}(8)$-C_{82}·Ni(OEP) [40] with 20% thermal ellipsoids. Only the major sites of the metal atoms and one cage orientation are shown. Solvent molecules and hydrogen atoms are omitted for clarity. Lu, Ni, and N atoms are highlighted in green, purple, and blue, respectively

In 2019, Popov and colleagues successfully stabilized these molecules by utilizing the benzyl radical addition, and a covalent lanthanide-lanthanide bond was finally ascertained inside the corresponding carbon cage [48]. Meanwhile, experimental evidence of the metal-metal bond in pristine $Lu_2@C_{76–88}$ isomers were also reported recently [40]. Crystallographically obtained Lu-Lu distances corresponded to the Lu-Lu single bond length. Thus, a direct Lu^{2+}-Lu^{2+} bond was experimentally confirmed. Figure 4a and b show the molecular structures of $Lu_2@C_{82}$ isomers. Similarly, direct metal-metal bonds were also identified for $Y_2@C_{82}$ and $Er_2@C_{82–86}$ isomers [46, 49]. The one-electron Er-Er bond was theoretically shown to exist in $Er_2@C_1(12)$-C_{84} isomer (see Fig. 5a). Recently, a metal-metal bond has also been found in an actinide-containing di-EMF, $U_2@I_h(7)$-C_{80}, representing the first prototype of an unsupported actinide-actinide bonds in EMFs (see Fig. 5b) [47].

It is worth noting that the di-EMF, $Sc_2@C_{66}$ was one of the first reported EMFs that violated the isolated pentagon rule (IPR) [33]. Fig. 6a shows the single crystal structures of $Sc_2@C_{2v}(4059)$-C_{66}. After that, more and more EMFs that violated IPR were separated and characterized, which greatly enriched the large family of EMFs. Additionally, since the two encapsulated metal atoms both transfer electrons to the outer cage, the interaction between the metal atom and the carbon cage is strengthened, resulting in the formation of di-EMFs with various cage sizes. In 2006, the first di-EMFs with large carbon cage (C_{100}), $Dy_2@C_{100}$ were successfully synthesized and isolated, making this kind of di-EMFs with large carbon cages begin to attract extensive attention from many scientists [50]. $La_2@C_{100}$ is the first higher di-EMFs whose structure is accurately characterized by single crystal XRD method. Subsequently, a series of higher Sm-based di-EMFs, $Sm_2@C_{2n}$ ($2n = 88, 90, 92, 104$) have

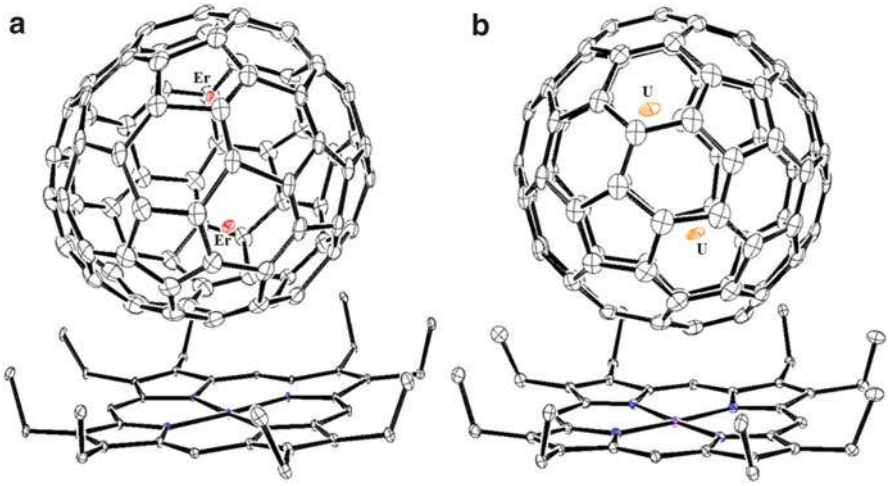

Fig. 5 The ORTEP drawings of (**a**) $Er_2@C_1(12)$-C_{84}·Ni(OEP) [46] and (**b**) $U_2@I_h(7)$-C_{80}·Ni(OEP) [47] with 20% thermal ellipsoids. Only the major sites of the metal atoms and one cage orientation are shown. Solvent molecules and hydrogen atoms are omitted for clarity. Er, U, Ni, and N atoms are highlighted in red, orange, purple, and blue, respectively

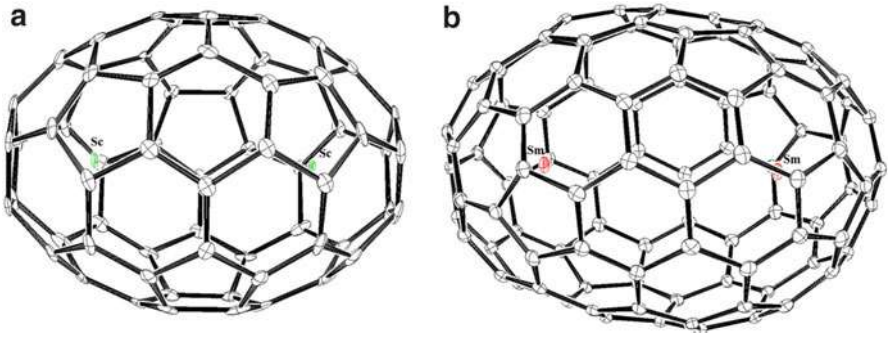

Fig. 6 The ORTEP drawings of (**a**) $Sc_2@C_{2v}(4059)$-C_{66} [33] and (**b**) $Sm_2@D_{3d}(822)$-C_{104} [38] with 20% thermal ellipsoids. Only the major sites of the metal atoms and one cage orientation are shown. Solvent molecules and hydrogen atoms are omitted for clarity. Sc and Sm atoms are highlighted in green and red, respectively

been successfully separated and characterized [38, 39]. Among them, $Sm_2@D_{3d}(822)$-C_{104} is the di-EMFs with the largest carbon cage reported so far, and its molecular structure is shown in Fig. 6b.

Tri-EMFs

Whether three metal atoms can be encapsulated in a fullerene cage as a trimetallic (M_3) cluster has puzzled researchers for many years. Early studies analyzed EMFs

containing identical metal atoms (Er_3C_{74}, Y_3C_{80}, and Dy_3C_{98}) using mass-spectrometry or Fourier transform infrared spectroscopy but without crystallographic confirmation. Thus, whether these compounds were conventional tri-EMFs or CCMFs could not be concluded with confidence [51–53]. DFT studies indicated that Y_3C_{80} is likely a conventional tri-EMF described as $Y_3@I_h(7)$-C_{80} since it is more stable than its $Y_3C_2@C_{78}$ isomer. However, there are no experimental structural data to confirm this hypothesis [52]. In 2013, Zerbetto et al. performed a full XRD-based structural characterization of $Sm_3@I_h(7)$-C_{80} and verified that all three Sm atoms coexist stably inside a cage without the support of any stand-alone nonmetallic atoms needed to offset their positive charges [54].

Cluster-EMFs

Cluster-EMFs are a new type of EMFs, which differ from traditional fullerenes in that its internal metallic units are composed of metal atoms and nonmetal atoms (C, N, O, S, etc.). This feature attracted scientists worldwide because of unique interactions and charge transfer mechanisms occurring among the atoms of the entrapped metal, the nonmetal atoms and the carbon cage. To date, a wide variety of cluster-EMFs with various entrapped cluster chemistry was discovered, described, synthesized, and characterized, which is discussed in the following sections.

Nitride Clusterfullerenes (NCFs)

The first nitride clusterfullerene (NCF) and the first pristine EMF to be characterized by single crystal diffraction, $Sc_3N@C_{80}$, was reported in 1999 by Stevenson, Dorn, Balch, et al. [55] Its structural analysis (XRD) revealed that its inner Sc_3N component morphology was triangular, with the N atom surrounded by three Sc atoms. Thus, these clusters can be described as M_3N and are classified as trimetallic nitride template (TNT) family. Studies have shown that Sc, Y, and most of the lanthanide elements, such as La, Nd, Gd, Tb, Dy, Ho, Er, Lu, can form the corresponding M_3N clusters encased in the fullerene cages [5–7]. Interestingly, the M_3N clusters prefer a planar geometry inside the cages, hence a correlation between the cluster size and cage size is revealed. For instance, Sc^{3+} has the smallest ion radius among all the metals that can form NCFs, thus the carbon cages of NCFs formed by it are relatively small. So far, a series of Sc-based NCFs with small carbon cages, that is, $Sc_3N@C_{68}$, $Sc_3N@C_{70}$, $Sc_3N@C_{78}$, $Sc_3N@C_{80}$, and $Sc_3N@C_{82}$ have been successfully isolated and structurally characterized [56–60].

Additionally, the size and shape of the entrapped M_3N cluster could also determine the corresponding cage symmetry. As the ion radius increases, when the larger metal ions, such as Lu^{3+}, Y^{3+}, or Gd^{3+}, encapsulated into fullerene cage to form the corresponding NCFs, the sizes of their carbon cages are expanded to C_{2n} ($2n = 78–88$). Moreover, when the ion radius of the internal metal is further increased, $M_3N@C_{88}$ ($M = Nd^{3+}$, Pr^{3+}, or Ce^{3+}) becomes the formed NCFs with the highest yield [62, 63]. As for the La^{3+} with the largest ion radius, the formed La_3N cluster is more inclined to be enclosed in the larger C_{96} [64]. Besides, the size and shape of the internal cluster also have significant effect in determining the cage symmetry of

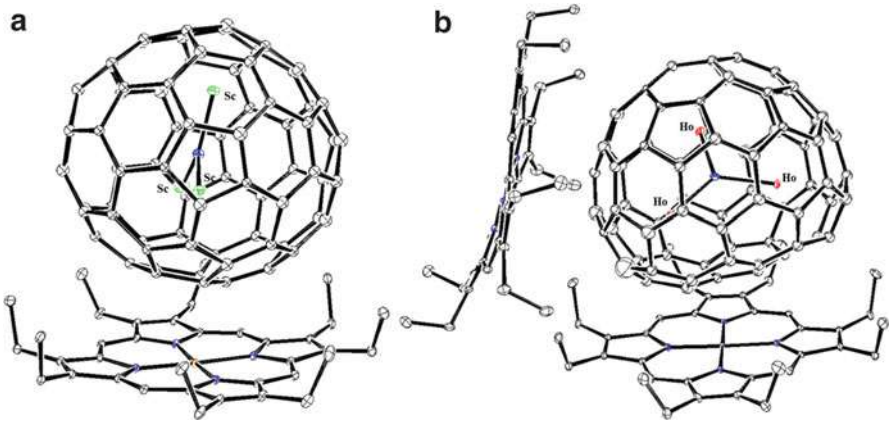

Fig. 7 The ORTEP drawings of (**a**) $Sc_3N@D_{3h}(5)$-C_{78}·Co(OEP) [59] and (**b**) $Ho_3N@C_2(22010)$-C_{78}·2Ni(OEP) [61] with 20% thermal ellipsoids. Only the major sites of the metal atoms and one cage orientation are shown. Solvent molecules and hydrogen atoms are omitted for clarity. Sc, Ho, Co, Ni, and N atoms are highlighted in green, red, orange, purple, and blue, respectively

the cages. For example, the small Sc_3N cluster presents a planar geometry inside the $D_{3h}(5)$-C_{78} cage (see Fig. 7a) [59], whereas the large M_3N (M = Gd, Ho, Tb) prefers a non-IPR $C_2(22010)$-C_{78} cage to keep its planar geometry (Fig. 7b shows the molecular structure of $Ho_3N@C_2(22010)$-C_{78}) [61, 65]. It is worth noting that for the M_3N (M = Gd, Tb, Dy, Ho, Er, Tm, Lu, and Sc) units inside the $I_h(7)$-C_{80} cage, a previous study showed that when the sum of the Shannon-Prewitt crystal radii of the three metal ions involved exceeds 3.05 Å, the configuration of the internal M_3N unit will change from a planar geometry to a pyramidalized structure. This result is applicable to endohedrals in which all three metal ions are identical or totally different [66]. For example, the X-ray structure of $Gd_3N@I_h(7)$-C_{80} shows that the Gd_3N unit within the $I_h(7)$-C_{80} cage is pyramidal [67].

Mixed-metal-NCFs, containing two or three different metals clustered together inside the carbon cage, represent an important sub-branch of NCFs. Simultaneous incorporation (into a carbon cage) of two or three rare earth metals to form a mixed metal NCF is relatively easy because of the excellent coordination ability of these metals. Thus, an array of mixed metal NCFs, such as $LaSc_2N@C_{80}$, $CeSc_2N@C_{80}$, $ErSc_2N@C_{80}$, $HoSc_2N@C_{80}$, $CeLu_2N@C_{80}$, $GdSc_2N@C_{80}$, $Gd_2ScN@C_{80}$, $TbSc_2N@C_{80}$, $DyEr_2N@C_{80}$, $DyGd_2N@C_{80}$, and $DyErScN@C_{80}$, have been successfully isolated and characterized in the last few years [68–73]. Noteworthily, $LaSc_2N@C_s$(hept)-C_{80} is the first NCFs with a seven-membered ring on the cage that violates IPR (see Fig. 8a). In 2009, Yang et al. proved that the transition metal Ti and rare earth elements can both be entrapped into fullerene cage with forming mixed nitride clusters under N_2 atmosphere. By utilizing this strategy, they have successfully synthesized $TiSc_2N@C_{80}$ and $TiY_2N@C_{80}$ [74]. Subsequently, with the assistance of rare earth elements, another transition metal element V was also successfully encapsulated into fullerene cages. In 2016, Yang and coworkers

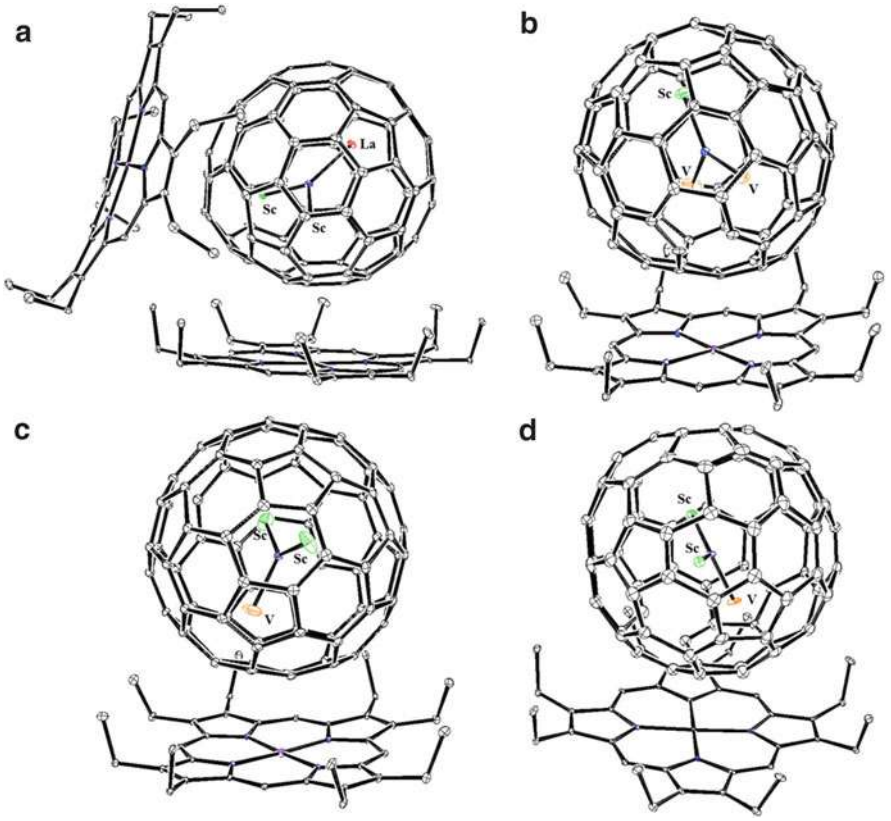

Fig. 8 The ORTEP drawings of (**a**) $LaSc_2N@C_s$(hept)-C_{80}·2Ni(OEP) [69], (**b**) $V_2ScN@I_h(7)$-C_{80}·Ni(OEP) [75], (**c**) $VSc_2N@I_h(7)$-C_{80}·Ni(OEP) [75], and (**d**) $V_2ScN@D_{5h}(6)$-C_{80}·Ni(OEP) [76] with 20% thermal ellipsoids. Only the major sites of the metal atoms and one cage orientation are shown. Solvent molecules and hydrogen atoms are omitted for clarity. Sc, La, V, Ni, and N atoms are highlighted in green, red, orange, purple, and blue, respectively

successfully synthesized two V_xSc_{3-x} based mixed metal NCFs, namely $V_2ScN@I_h(7)$-C_{80} and $VSc_2N@I_h(7)$-C_{80} [75]. Fig. 8b and c show their molecular structures. After that, the other two mixed metal NCFs, that is, $V_2ScN@D_{5h}(6)$-C_{80} (see Fig. 8d) and $VSc_2N@D_{5h}(6)$-C_{80} have also been successfully obtained and structural characterized [76]. The comprehensive characterizations of these mixed transition metal NCFs experimentally confirmed that the Ti and V roles were crucial in determining the structure and properties of the corresponding NCFs. More importantly, the introduction of transition metal elements extended the research field of NCFs to group IV and V elements, which opens a new path for the further development of EMFs.

Very recently, a U-based NCF, $U_2N@I_h(7)$-C_{80}, the first NCF that violates the well-established trimetallic nitride template, was synthesized and fully characterized [77]. In this molecule, the novel U=N=U cluster features two U=N bonds with

uneven bond distances, which leads to a rare unsymmetrical structure, showing the unique bonding variety for actinide clusters stabilized by fullerene cages.

Carbide Clusterfullerenes (CCMFs)

Carbide cluster fullerenes (CCMFs) containing M_2C_2 units inside the fullerenes were first classified as-EMFs due to the lack of accurate experimental data [78]. In 2001, the analysis of a long-known $Sc_2@C_{86}$, which combined maximum entropy method coupled with Rietveld analysis of the synchrotron powder diffraction data, revealed its CCMF nature described as $Sc_2C_2@D_{2d}(23)$-C_{84} (see Fig. 9a). Later, NMR and single-crystal XRD confirmed these findings [79]. Combination of all these methods later allowed to reassign $Sc_3@C_{82}$, $Sc_2@C_{70}$, $Sc_2@C_{76}$, $Sc_2@C_{82}$, and $Sc_2@C_{84}$ from the di-EMF group to CCMFs and describe them as $Sc_3C_2@I_h(7)$-C_{80}, $Sc_2C_2@C_{2v}(6073)$-C_{68}, $Sc_2C_2@D_{3h}(1)$-C_{74}, $Sc_2C_2@C_{2v}(5)$-C_{80}, $Sc_2C_2@C_s(6)$-C_{82}, $Sc_2C_2@C_{2v}(9)$-C_{82}, and $Sc_2C_2@C_{3v}(8)$-C_8, respectively [80–83]. It is also found that the small Sc_2C_2-unit tend to be encapsulated into a cage smaller than C_{88}, and the Sc···Sc distance increases along with the cage size to maintain strong metal-cage interactions. In 2015, Echegoyen et al. reported the synthesis, separation, and structural characterization of a Sc-based CCMF, namely, $Sc_2C_2@C_{2v}(9)$-C_{86} [84]. XRD results show that the internal Sc_2C_2 cluster adopts a planar configuration in the cage, which is completely different from the typical butterfly-shaped structure in the other reported CCMFs. A subsequent study reported the synthesis and characterization of a CCMF, namely $Sc_2C_2@C_s$(hept)-C_{88}, in which a zigzag Sc_2C_2 unit was entrapped inside and a heptagon ring was located on the cage (see Fig. 9b). This is the largest CCMFs with encapsulating a Sc_2C_2 cluster reported so far [85].

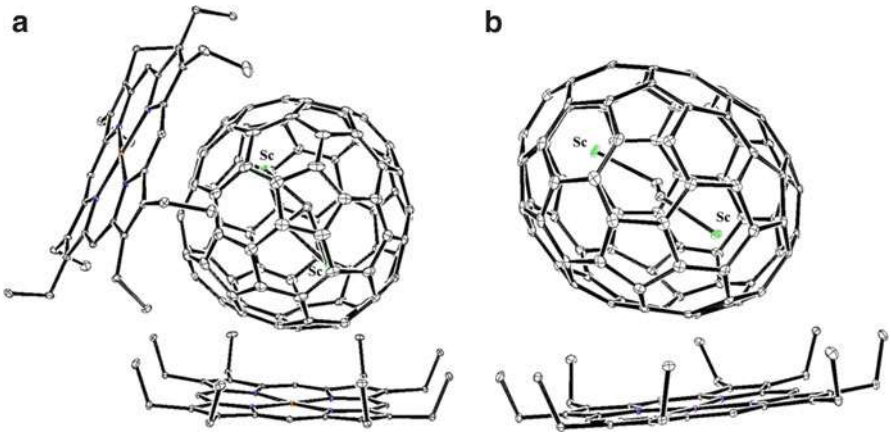

Fig. 9 The ORTEP drawings of (**a**) $Sc_2C_2@D_{2d}(23)$-C_{84}·Co(OEP) [79] and (**b**) $Sc_2C_2@C_s$(hept)-C_{88}·Ni(OEP) [85] with 20% thermal ellipsoids. Only the major sites of the metal atoms and one cage orientation are shown. Solvent molecules and hydrogen atoms are omitted for clarity. Sc, Co, Ni, and N atoms are highlighted in green, orange, purple, and blue, respectively

Despite all efforts and progress on understanding the structures of $M_2C_{2@}C_{2n}$ (M = Lu, Er, Y, La, etc.), data on the CCMFs with the inner clusters larger than Sc_2C_2 but smaller than La_2C_2 were scarce before 2018. After 2018, a series of collaborations reported several CCMFs, including $Y_2C_2@C_{86–92}$, $Lu_2C_2@C_{86–92}$, $Er_2C_2@C_{80–90}$, $La_2C_2@C_{90–104}$, which are all fully characterized by single-crystal XRD [49, 86–89]. Similar to the other EMFs, the ionic radius of the metal ions that can be enclosed inside a CCMF cage directly correlates with a cage size and increases as the number of carbon cage atoms increases. Thus, Sc_2C_2, Er_2C_2, and La_2C_2 clusters are typically observed for the $C_{72–88}$, $C_{80–92}$, and $C_{90–104}$ fullerene cages, respectively [49, 86–89]. Moreover, the CCMF cage-dependency could be understood by comparing $Lu_2C_2@C_{76–86}$ [90] and $Y_2C_2@C_{86–92}$ [49] structures with their corresponding di-EMF isomers. Namely, the inner M_2C_{2n} clusters are more inclined to change from M_2 to M_2C_2 as the carbon cage becomes larger. Even more cluster expansion accompanied by the cage elongation was reported for $Er_2C_2@C_{80–88}$ [87] and $Lu_2C_2@C_{88–92}$ [86]. In this configuration, the shapes of these M_2C_2 clusters were similar to a compressed butterfly shape. If these large cages expanded even more, then the M_2C_2 units stretch into zigzags. Thus, M_2C_2 cluster geometry can be tuned by changing the outer cage size. Another confirmation of this tendency was demonstrated by Lu et al. [91], who successfully characterized $Y_2C_2@C_1(1660)$-C_{108} CCMF by single-crystal XRD. The Y_2C_2 cluster adopts a previously predicted linear configuration, which indicates its almost negligible compression by the large cage. To date, $Y_2C_2@C_1(1660)$-C_{108} is the largest EMF thoroughly characterized crystallographically (see Fig. 10a).

A relatively new CCMF family member is $U_2C@I_h(7)$-C_{80} [92], which was identified by single-crystal XRD (see Fig. 10b). The U atoms possess a +5 valence state, unlike similar mono-EMFs containing U. Additionally, $U_2C@I_h(7)$-C_{80} contains two short U=C bonds, which together form a nonlinear U=C=U bond angle. Very recently, two other novel uranium-containing CCMFs were recently fully characterized and described: $U_2C_2@I_h(7)$-C_{80} and $U_2C_2@D_{3h}(5)$-C_{78} [93]. The uranium atoms in these U_2C_2 clusters exhibit oxidation states (U^{4+}) different from the uranium in $U_2C@I_h(7)$-C_{80} (which is U^{5+}) [92]. Thus, even U oxidation states depend on the cluster configuration, which, in turn, affects the outer cage morphology.

Crystallographic analysis of $TiLu_2C@I_h(7)$-C_{80} [94] (see Fig. 11a) and $Sc_2TiC@I_h(7)$-C_{80} [95] revealed a rare example of multiple bonds between a metal and the central nonmetallic atom of the endohedral cluster [94, 95]. Another similar example includes an unprecedented Ti_3C_3 entrapped in $I_h(7)$-C_{80} cage of a very stable $Ti_3C_3@I_h(7)$-C_{80} compounds (see Fig. 11b) [96]. X-ray data strongly supported the hypothesis that the C_3-unit possessed a cyclopropane-like structure with its plane almost perpendicular to the plane of Ti atoms. Such an arrangement indicates unique coordination between C and Ti. Subsequently, Lu et al. thoroughly described freshly synthesized $Ti_2C_2@D_{3h}(5)$-C_{78}, $Ti_2C_2@C_{3v}(8)$-C_{82}, and $Ti_2C_2@C_s(6)$-C_{82} EMFs, all of which contain unsupported Ti_2C_2 clusters inside their carbon cages [97]. Their crystallographic data, corroborated by their computations, revealed two different configurations of the Ti_2C_2 clusters placed inside all

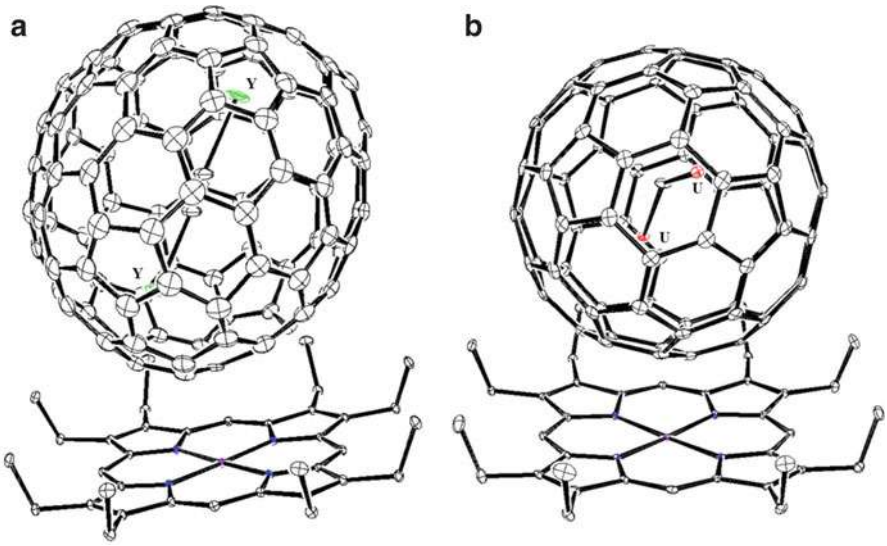

Fig. 10 The ORTEP drawings of (**a**) $Y_2C_2@C_1(1660)$-C_{108}·Ni(OEP) [91] and (**b**) $U_2C@I_h(7)$-C_{80}·Ni(OEP) [92] with 20% thermal ellipsoids. Only the major sites of the metal atoms and one cage orientation are shown. Solvent molecules and hydrogen atoms are omitted for clarity. Y, U, Ni, and N atoms are highlighted in green, red, purple, and blue, respectively

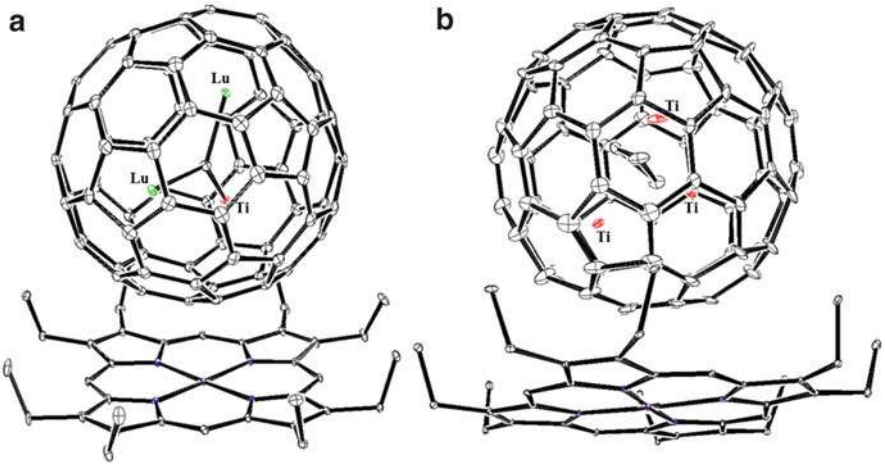

Fig. 11 The ORTEP drawings of (a) $TiLu_2C@I_h(7)$-C_{80}·Ni(OEP) [94] and (b) $Ti_3C_3@I_h(7)$-C_{80}·Ni(OEP) [96] with 20% thermal ellipsoids. Only the major sites of the metal atoms and one cage orientation are shown. Solvent molecules and hydrogen atoms are omitted for clarity. Lu, Ti, Ni, and N atoms are highlighted in green, red, purple, and blue, respectively

these fullerenes. Such unique discovery can only be explained by the different outer cage shapes and different oxidation states of the Ti atoms in the clusters.

Oxide Clusterfullerenes (OCFs)

Studies have demonstrated that the presence of oxygen will reduce the yield of EMFs during arc synthesis, thus the partial pressure of oxygen is generally kept as low as possible [5, 7]. However, in 2009, Stevenson et al. found that introducing a small amount of oxygen in the preparation process can produce a series of oxide clusterfullerenes (OCFs) with different kinds of oxide clusters, namely, $Sc_4(\mu_{3-})O_2@I_h(7)\text{-}C_{80}$, $Sc_2(\mu_{2-})O@C_s(6)\text{-}C_{82}$, and $Sc_4(\mu_{3-})O_3@I_h(7)\text{-}C_{80}$ [98–100]. It is worth noting that different oxide clusters exhibit different configurations in the same fullerene cage. For example, the first OCF with a single-crystal structure is $Sc_4(\mu_{3-})O_2@I_h(7)\text{-}C_{80}$, in which the four Sc atoms form a twisted tetrahedron with two bridged O atoms asymmetrically on two sides of the tetrahedron (see Fig. 12a). In contrast, $Sc_4(\mu_{3-})O_3@I_h(7)\text{-}C_{80}$ cluster configuration could be described as an addition of an oxygen atom to the empty Sc_4 tetrahedron face (see Fig. 12b).

Later, Chen et al. synthesized and characterized several Sc-based OCFs: $Sc_2O@T_d(2)\text{-}C_{76}$, $Sc_2O@C_{2v}(3)\text{-}C_{78}$, $Sc_2O@D_{3h}(5)\text{-}C_7$, $Sc_2O@C_{2v}(5)\text{-}C_{80}$, and $Sc_2O@C_{3v}(8)\text{-}C_{82}$. Their approach involved the usage of the CO_2 environment [101–104]. Feng et al. reported the synthesis and structural characterization of a series of Ho-containing OCFs, that is, $Ho_2O@C_{2n}$ ($2n = 74, 84, 92$) [105–107]. The configuration of the internal Ho_2O clusters was specific to the outer cage shape: elliptic non-IPR $C_2(13333)\text{-}C_{74}$ and $D_{2d}(51591)\text{-}C_{84}$ cages contained linear Ho_2O clusters to match up the cage shapes (see Fig. 13a and b). Very recently, Chen et al. synthesized and separated Dy-based OCFs ($Dy_2O@C_s(6)\text{-}C_{82}$, $Dy_2O@C_{2v}(9)\text{-}C_{82}$, and $Dy_2O@C_{3v}(8)\text{-}C_{82}$) and fully characterized their single-molecule magnet (SMM) properties [108]. Although all these $Dy_2O@C_{82}$ isomers exhibited SMM behavior with broad hysteresis, their temperature and magnetization relaxation

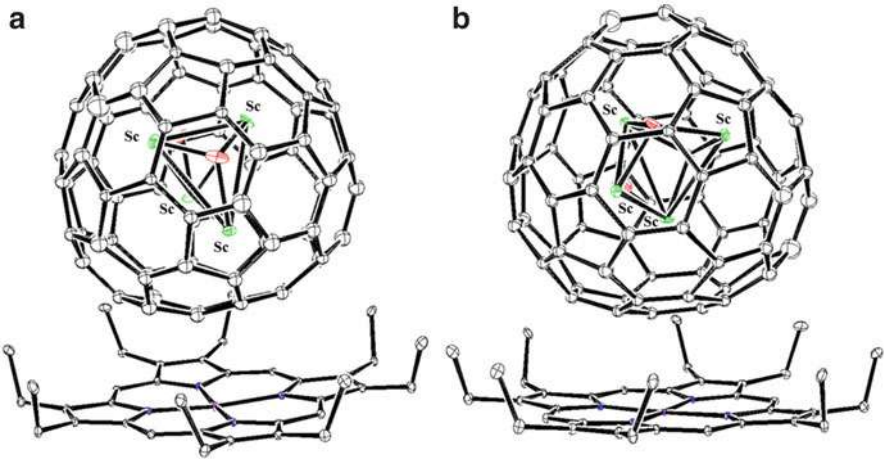

Fig. 12 The ORTEP drawings of (**a**) $Sc_4(\mu_{3-})O_2@I_h(7)\text{-}C_{80}$·Ni(OEP) [98] and (**b**) $Sc_4(\mu_{3-})O_3@I_h(7)\text{-}C_{80}$·Ni(OEP) [100] with 20% thermal ellipsoids. Only the major sites of the metal atoms and one cage orientation are shown. Solvent molecules and hydrogen atoms are omitted for clarity. Sc, O, Ni, and N atoms are highlighted in green, red, purple, and blue, respectively

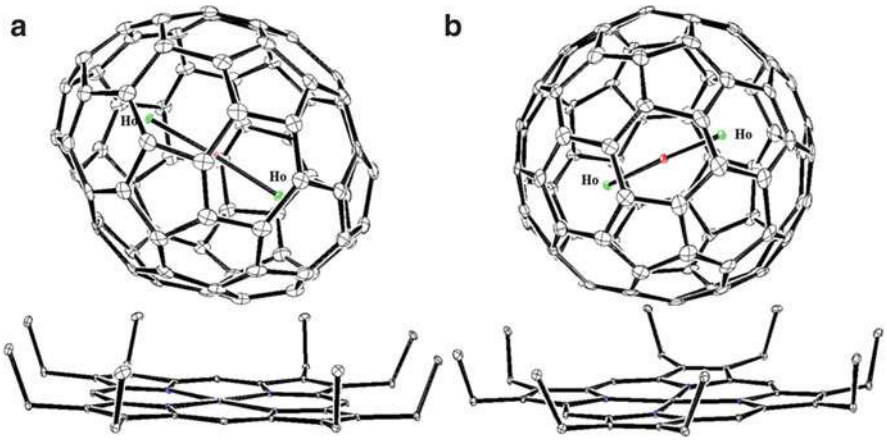

Fig. 13 The ORTEP drawings of (a) $Ho_2O@C_2$(13333)-C_{74}·Ni(OEP) [105] and (b) $Ho_2O@D_{2d}$(51591)-C_{84}·Ni(OEP) [106] with 20% thermal ellipsoids. Only the major sites of the metal atoms and one cage orientation are shown. Solvent molecules and hydrogen atoms are omitted for clarity. Ho, O, Ni and N atoms are highlighted in green, red, purple, and blue, respectively

strongly depended on the morphology of the outer cage. These findings opened yet another branch involving EMFs: magnetism as a function of the atom interactions as well as size and shape of the outer carbon cage.

Sulfide Clusterfullerenes (SCFs)

Similarly, sulfide cluster fullerenes (SCFs) can be synthesized by introducing sulfur (in a solid or gaseous form) into the arc discharge reactor. For example, Dunsch et al. used solid CH_5N_3·HSCN as a sulfur source to obtained EMFs with M_2S clusters (with M = Sc, Y, Dy, and Lu) [109]. Echegoyen et al. introduced SO_2 gas into the reactor and obtained two $Sc_2S@C_{82}$ isomers: $Sc_2S@C_s$(6)-C_{82} and $Sc_2S@C_{3v}$(8)-C_{82}, which were then characterized in great detail by single-crystal XRD [102]. Shortly after that, they repeated their successes and isolated two more new members of the SCFs family: $Sc_2S@C_{70}$ and $Sc_2S@C_{72}$, containing a pair of adjacent five-membered rings on the corresponding cages [103]. The most recent progress included complete characterization of Dy-containing mixed-metallic SCFs: $DyScS@C_s$(6)-C_{82} and $DyScS@C_{3v}$(8)-C_{82} (see Figs. 14a and 9b) [112]. Single-crystal XRD showed that the conformation of the DyScS clusters inside the carbon cages was different from the Dy_2S clusters in their $Dy_2S@C_s$(6)-C_{82} and $Dy_2S@C_{3v}$(8)-C_{82} analogs. Both isomers exhibited SMM behavior judging by their magnetic hysteresis loops below 7 K.

Hydrocarbide Clusterfullerenes (HCCFs), Carbonitride Clusterfullerenes (CNCFs), and Cyanide Clusterfullerenes (CYCFs)

In 2007, Dunsch and coworkers modified the DC arc-discharge method by adding a small quantity of CH_4 and successfully synthesized a novel hydrocarbide

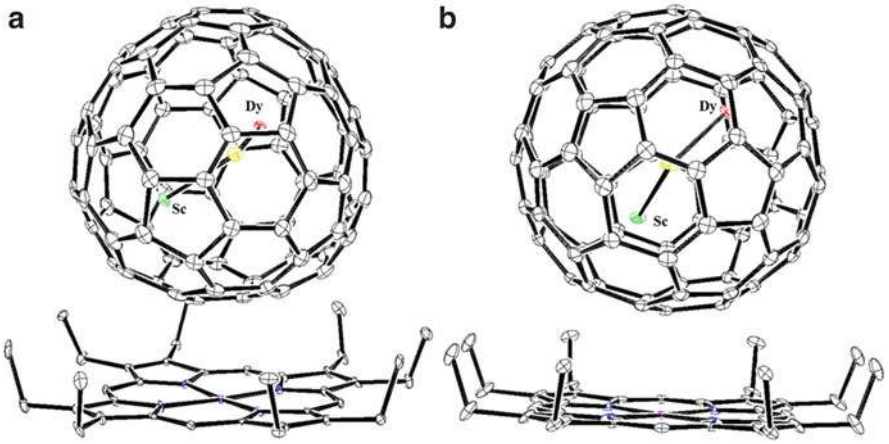

Fig. 14 The ORTEP drawings of (**a**) DyScS@C_s(6)-C_{82}·Ni(OEP) [112] and (**b**) DyScS@C_{3v}(8)-C_{82}·Ni(OEP) [112] with 20% thermal ellipsoids. Only the major sites of the metal atoms and one cage orientation are shown. Solvent molecules and hydrogen atoms are omitted for clarity. Sc, Dy, S, Ni, and N atoms are highlighted in green, red, orange, purple, and blue, respectively

clusterfullerene (HCCF), $Sc_3CH@C_{80}$, containing a five-atom Sc_3CH cluster in the cage [113]. Recently, Wang and coworkers [114] were first to obtain and fully characterize a new metallofullerene $Sc_4CNH@I_h(7)$-C_{80}, containing an encapsulated Sc tetrahedron supported by penta-CN and H anions. In this molecule, the internal polyhedral Sc_4CNH is the most complex endohedral cluster discovered to date. Thus, the fullerene cages can actually host otherwise unstable metallic units.

In 2010, Wang et al. discovered a carbonitride clusterfullerene (CNCF) $Sc_3NC@I_h(7)$-C_{80} with a planar Sc_3NC cluster, in which N atom is in the center, and C atom is located on one side of the triangle formed by three Sc atoms (see Fig. 15a) [115]. Soon afterward, they isolated another Sc-based CNCF and characterized it spectroscopically. With the help of the simulations, they were able to describe its structure as $Sc_3NC@C_2(22010)$-C_{78}. Notably, the cage structure of this CNCF was completely different from that of $Sc_3N@D_{3h}(5)$-C_{78}. Thus, the introduction of just one additional C atom changes the fullerene molecular structure and stability [116].

In 2013, Yang et al. achieved a breakthrough by being the first to synthesize a cyanide-containing EMF with just one metal atom in the cluster [117]. Their thorough research provided the research community with the following formula: YNC@C_s(6)-C_{82} (see Fig. 15b). With this discovery, their work unlocked another branch for the endohedral clusterfullerene research: cyanide clusterfullerenes (CYCFs). The CYCF discovery was revolutionary because it demonstrated that monometallofullerenes could exist not only in their simple form $M@C_{2n}$. Additionally, their work also broke the stigma that clusterfullerenes require 2–4 metal atoms to form a stable cluster. Since then, Y- and Tb-CYCFs were obtained as well: TbNC@C_{2v}(19138)-C_{76}, YNC@C_{2v}(19138)-C_{76}, YNC@C_s(6)-C_{82}, TbNC@C_s(6)-

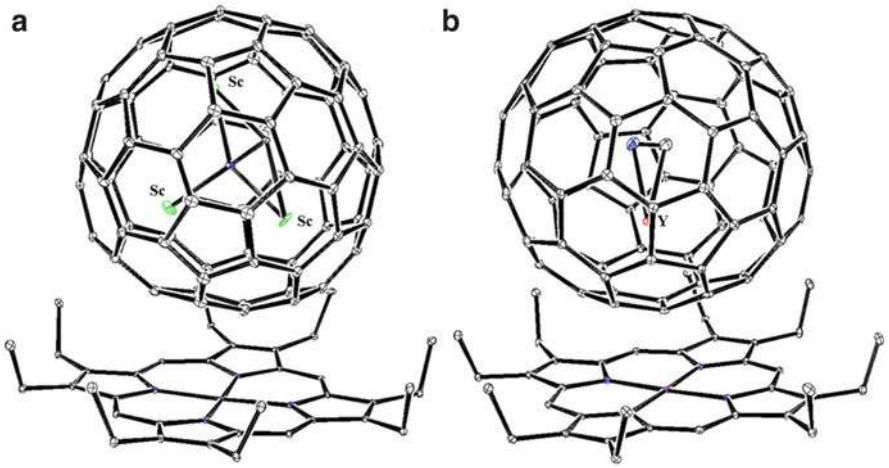

Fig. 15 The ORTEP drawings of (**a**) $Sc_3NC@I_h(7)$-C_{80}·Ni(OEP) [115] and (**b**) $YNC@C_s(6)$-C_{82}·Ni(OEP) [117] with 20% thermal ellipsoids. Only the major sites of the metal atoms and one cage orientation are shown. Solvent molecules and hydrogen atoms are omitted for clarity. Sc, Y, Ni and N atoms are highlighted in green, red, purple, and blue, respectively

C_{82}, $TbNC@C_{2v}(9)$-C_{82}, $YCN@C_2(13)$-C_{84}, $TbNC@C_2(5)$-C_{82}, and $YCN@D_{2d}(23)$-C_{84} [118, 119]. The TbNC clusters in the $TbNC@C_{82}$ isomers are triangles [119], while the CYCFs with the C_{76} cages, $MNC@C_{2v}(19138)$-C_{76} (M = Tb, Y) contained almost linear MNC clusters [118]. The most recent breakthrough was the incorporation of Lu-containing clusters into CYCFs. After thorough characterization by XRD, these novel compounds were described as $LuNC@C_{2v}(19138)$-C_{76}, $LuNC@C_2(5)$-C_{82}, $LuNC@C_s(6)$-C_{82}, and $LuNC@C_{2v}(9)$-C_{82}. The geometry of the entrapped LuNC cluster in the $LuNC@C_{2v}(19138)$-C_{76} CYCF is linear. However, when the cage changed from C_{76} to C_{82} (as in the $LuNC@C_2(5)$-C_{82}), the LuNC cluster became triangular. These findings provide yet another confirmation that the cage structure plays a key role in the cluster configuration regulation [120].

Hetero EMFs (aza-EMFs)

Theoretical analysis suggested that fullerene cage C atoms can be substituted by B or N atoms. Currently, only N-containing hetero-fullerene cages (also called aza-fullerenes) were demonstrated experimentally. The first species of aza-fullerenes is $C_{59}N$, which exists as a dimer because of its paramagnetic nature [121, 122]. In 1997, Akasaka et al. [123] detected the signals of $[La_2@C_{79}N]^+$ and $[La@C_{81}N]^+$ ions for the first time using fast atom bombardment mass spectrometry. The subsequent theoretical calculations further confirmed the possibility that the neutral $La_2@C_{79}N$ and $La@C_{81}N$ molecules can also exist and even be stable. In 2008, Dorn et al. successfully prepared and separated $M_2@I_h(7)$-$C_{79}N$ (M = Y, Tb) and then Balch and Olmstead characterized their molecular structures by single-

crystal XRD (Fig. 16a shows the structure of $Tb_2@I_h(7)$-$C_{79}N$) [124]. However, the exact N position in the fullerene cage was hard to specify using just the experimental data because of a severe disorder of the cage and similar X-ray scattering from C and N. Only simulations provided some insights: N atoms very likely replace C atoms in the [5, 6] position because the resulting structure is the most thermodynamically stable. ESR coupled with simulations confirmed the localization of the electron from the N on the two equivalent metal centers. Thus, a metal-metal bond forms inside the fullerene cage. Subsequently, $Gd_2@I_h(7)$-$C_{79}N$ was also obtained by a similar method [125]. The EPR and theoretical calculation results show that the unpaired electron has also been transferred between the two equivalent Gd^{3+} in the carbon cage, forming a single-electron double-centered metal-metal bond.

The most unique compound in the aza-EMFs family, experimentally obtained, is $La_3N@C_{79}N$, which contains a nitride cluster trapped inside a relatively small C_{80} cage [126]. The uniqueness was not only in the nitrogen presence in the cage structure and inside the cage. It modified the view, first suggested by Echegoyen et al., that large clusters like La_3N could only be trapped by large cages like C_{96}. Their simulations also confirmed that the most stable configuration is obtained when the N atom substitutes the C atom in the [5, 6] position. Very recently, Shi et al. reported the crystallographic data, quantum coherence, diverse Rabi cycles, and magnetic susceptibility of $Gd_2@I_h(7)$-$C_{79}N$ (see Fig. 16b) [127]. This compound exhibits the largest ground state with multiple Rabi cycles. Such a configuration can tolerate manipulations of the arbitrary superposition states between the adjacent levels. The resulting quantum phase memory time of the high-spin states of $Gd_2@I_h(7)$-$C_{79}N$ can reach 5 μs at 5 K.

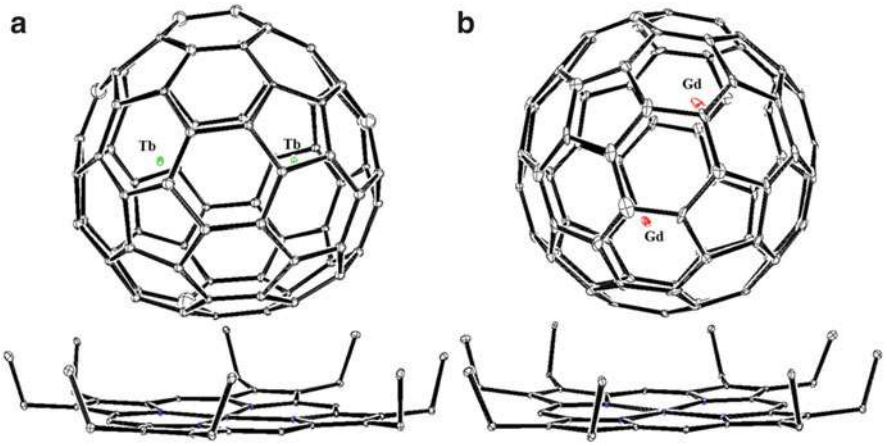

Fig. 16 The ORTEP drawings of (a) $Tb_2@I_h(7)$-$C_{79}N$·Ni(OEP) [124] and (b) $Gd_2@I_h(7)$-$C_{79}N$·Ni(OEP) [125] with 20% thermal ellipsoids. Only the major sites of the metal atoms and one cage orientation are shown. Solvent molecules and hydrogen atoms are omitted for clarity. Tb, Gd, Ni, and N atoms are highlighted in green, red, purple, and blue, respectively

Conclusion

EMFs, namely fullerenes with metallic species encapsulated inside, represent as an ideal platform to investigate the metal-metal or metal-carbon interactions at the sub-nanometer scale. Thanks to the discovery of La@C_{82} in 1990, a new era in fullerene research was opened. The research on EMFs has become the fastest growing and most active branch of fullerene research during the past three decades. This chapter presents a systematic overview of EMFs reported to date according to the categories of monometallofullerenes, dimetallofullerenes, trimetallofullerenes, and clusterfullerenes, spanning from their syntheses, molecular structures to their physio-chemical properties and potential applications. As one of the important members of new carbon materials, the importance of EMF is growing rapidly, although there are severe challenges in the current early stage. For example, most of the EMFs are unable to obtain sufficient yields for characterizing their structures and properties due to their low yield and numerous possible isomers. Accordingly, more effective synthesis and extraction methods to obtain pure samples of EMFs are helpful to promote the future development of EMFs research. Additionally, although more than 30 years have passed since the finding of EMFs, many mysteries, such as the formation mechanism, the nature of metal-metal/mental-carbon bonding, and the electronic/geometric matching between the internal moieties and the external cages, are still unclear. Therefore, searching for new EMFs is one of the best solutions to the above questions. Finally, practical applications of EMFs are also awaiting detailed exploration. Because of the presence of the charge transfer and subsequent coordination between the inner metallic units and the outer fullerene cage, we are sure that currently described and not yet discovered EMFs will demonstrate enormous potential related to the practical applications in the material science, optoelectronic, and photoelectric conversion.

References

1. Kroto HW, Heath JR, O'Brien SC, Curl RF, Smalley RE (1985) C_{60}: Buckminsterfullerene. Nature 318(6042):162–163
2. Krätschmer W, Lamb LD, Fostiropoulos K, Huffman DR (1990) Solid C_{60}: a new form of carbon. Nature 347(6291):354–358
3. Giacalone F, Martín N (2006) Fullerene polymers: synthesis and properties. Chem Rev 106(12):5136–5190
4. Guldi M, Fullerenes D (2000) Three dimensional electron acceptor materials. Chem Commun 5:321–327
5. Popov AA, Yang S, Dunsch L (2013) Endohedral Fullerenes. Chem Rev 113(8):5989–6113
6. Yang S, Wei T, Jin F (2017) When metal clusters meet carbon cages: endohedral Clusterfullerenes. Chem Soc Rev 46(16):5005–5058
7. Lu X, Feng L, Akasaka T, Nagase S (2012) Current status and future developments of endohedral Metallofullerenes. Chem Soc Rev 41(23):7723–7760
8. Rodríguez-Fortea A, Balch L, Poblet AM (2011) Endohedral metallofullerenes: a unique host–guest association. Chem Soc Rev 40(7):3551–3563

9. Komatsu K, Murata M, Murata Y (2005) Encapsulation of molecular hydrogen in fullerene C_{60} by organic synthesis. Science 307(5707):238–240
10. Murata M, Murata Y, Komatsu K (2006) Synthesis and properties of endohedral C_{60} encapsulating molecular hydrogen. J Am Chem Soc 128(24):8024–8033
11. Li Y, Lou N, Xu D, Pan C, Lu X, Gan L (2018) Oxygen-delivery materials: synthesis of an open-cage fullerene derivative suitable for encapsulation of H_2O_2 and O_2. Angew Chem Int Ed 57(43):14144–14148
12. Heath JR, O'Brien SC, Zhang Q, Liu Y, Curl RF, Tittel FK, Smalley RE (1985) Lanthanum complexes of spheroidal carbon shells. J Am Chem Soc 107(25):7779–7780
13. Chai Y, Guo T, Jin C, Haufler RE, Chibante LPF, Fure J, Wang L, Alford JM, Smalley RE (1991) Fullerenes with metals inside. J Phys Chem 95(20):7564–7568
14. Aoyagi S, Nishibori E, Sawa H, Sugimoto K, Takata M, Miyata Y, Kitaura R, Shinohara H, Okada H, Sakai T, Ono Y, Kawachi K, Yokoo K, Ono S, Omote K, Kasama Y, Ishikawa S, Komuro T, Tobita H (2010) A layered ionic crystal of polar Li@C-60 Superatoms. Nat Chem 2(8):678–683
15. Shen W, Hu S, Lu X (2020) Endohedral metallofullerenes: new structures and unseen phenomena. Chem Eur J 26(26):5748–5757
16. Lu X, Nikawa H, Feng L, Tsuchiya T, Maeda Y, Akasaka T, Mizorogi N, Slanina Z, Nagase S (2009) Location of the yttrium atom in $Y@C_{82}$ and its influence on the reactivity of cage carbons. J Am Chem Soc 131(34):12066–12067
17. Yang H, Jin H, Wang X, Liu Z, Yu M, Zhao F, Mercado BQ, Olmstead MM, Balch AL (2012) X-Ray crystallographic characterization of new soluble endohedral Fullerenes utilizing the popular C_{82} Bucky cage. Isolation and structural characterization of $Sm@C_{3v}(7)$-C_{82}, $Sm@C_s(6)$-C_{82}, and $Sm@C_2(5)$-C_{82}. J Am Chem Soc 134(34):14127–14136
18. Roy M, Olmstead MM, Balch AL (2019) Metal ion effects on fullerene/porphyrin cocrystallization. Cryst Growth Des 19(11):6743–6751
19. Olmstead MM, Costa DA, Maitra K, Noll BC, Phillips SL, Van Calcar PM, Balch AL (1999) Interaction of curved and flat molecular surfaces. The structures of crystalline compounds composed of fullerene (C_{60}, $C_{60}O$, C_{70}, and $C_{120}O$) and metal octaethylporphyrin units. J Am Chem Soc 121(30):7090–7097
20. Baldauf LM, Ghiassi KB, Olmstead MM, Balch AL (2020) Fullerene nanostructures: how the oblong shape of C_{70} forms a cocrystal with an enormous asymmetric unit and related cocrystals. Nanoscale 12(39):20356–20363
21. Bao L, Pan C, Slanina Z, Uhlik F, Akasaka T, Lu X (2016) Isolation and crystallographic characterization of the labile isomer of $Y@C_{82}$ cocrystallized with Ni(OEP): unprecedented dimerization of pristine metallofullerenes. Angew Chem Int Ed 55(32):9234–9238
22. Hu S, Liu T, Shen W, Slanina Z, Akasaka T, Xie Y, Uhlik F, Huang W, Lu X (2019) Isolation and structural characterization of $Er@C_{2v}(9)$-C_{82} and $Er@C_s(6)$-C_{82}: regioselective dimerization of a pristine endohedral metallofullerene induced by cage symmetry. Inorg Chem 58(3): 2177–2182
23. Guo T, Diener MD, Chai Y, Alford MJ, Haufler RE, McClure SM, Ohno T, Weaver JH, Scuseria GE, Smalley RE (1992) Uranium stabilization of C_{28}: a tetravalent fullerene. Science 257(5077):1661–1664
24. Wang Y, Morales-Martínez R, Zhang X, Yang W, Wang Y, Rodríguez-Fortea A, Poblet JM, Feng L, Wang S, Chen N (2017) Unique four-electron metal-to-cage charge transfer of Th to a C_{82} fullerene cage: complete structural characterization of $Th@C_{3v}(8)$-C_{82}. J Am Chem Soc 139(14):5110–5116
25. Cai W, Morales-Martínez R, Zhang X, Najera D, Romero L, Metta-Magaña A, Rodríguez-Fortea A, Fortier S, Chen N, Poblet M, Echegoyen L (2017) Single crystal structures and theoretical calculations of uranium endohedral Metallofullerenes ($U@C_{2n}$, $2n = 74, 82$) show cage isomer dependent oxidation states for U. Chem Sci 8(8):5282–5290
26. Cai W, Abella L, Zhuang J, Zhang X, Feng L, Wang Y, Morales-Martínez R, Esper R, Boero M, Metta-Magaña A, Rodríguez-Fortea A, Poblet JM, Echegoyen L, Chen N (2018)

Synthesis and characterization of non-isolated-pentagon-rule actinide endohedral metallofullerenes U@C_1(17418)-C_{76}, U@C_1(28324)-C_{80}, and Th@C_1(28324)-C_{80}: low-symmetry cage selection directed by a tetravalent ion. J Am Chem Soc 140(51): 18039–18050
27. Cai W, Alvarado J, Metta-Magaña A, Chen N, Echegoyen L (2020) Interconversions between uranium mono-Metallofullerenes: mechanistic implications and role of asymmetric cages. J Am Chem Soc 142(30):13112–13119
28. Wang Y, Morales-Martínez R, Cai W, Zhuang J, Yang W, Echegoyen L, Poblet M, Rodríguez-Fortea A, Chen N (2019) Th@C_1(11)-C_{86} : an actinide encapsulated in an unexpected C_{86} fullerene cage. Chem Commun 55(63):9271–9274
29. Che Y, Yang H, Wang Z, Jin H, Liu Z, Lu C, Zuo T, Dorn HC, Beavers CM, Olmstead MM, Balch AL (2009) Isolation and structural characterization of two very large, and largely empty, endohedral fullerenes: tm@C_{3v}-C_{94} and ca@C_{3v}-C_{94}. Inorg Chem 48(13):6004–6010
30. Jin H, Yang H, Yu M, Liu Z, Beavers CM, Olmstead MM, Balch AL (2012) Single samarium atoms in large fullerene cages. Characterization of two isomers of Sm@C_{92} and four isomers of Sm@C_{94} with the X-Ray crystallographic identification of Sm@C_1(42)-C_{92}, Sm@C_s(24)-C_{92}, and Sm@C_{3v}(134)-C_{94}. J Am Chem Soc 134(26):10933–10941
31. Alvarez MM, Gillan EG, Holczer K, Kaner RB, Min KS, Whetten RL (1991) Lanthanum carbide (La_2C_{80}): a soluble dimetallofullerene. J Phys Chem 95(26):10561–10563
32. Akasaka T, Nagase S, Kobayashi K, Walchli M, Yamamoto K, Funasaka H, Kako M, Hoshino T, Erata T (1997) 13C and ^{139}La NMR studies of La_2@C_{80}: first evidence for circular motion of metal atoms in endohedral dimetallofullerenes. Angew Chem Int Ed 36(15): 1643–1645
33. Yamada M, Kurihara H, Suzuki M, Guo JD, Waelchli M, Olmstead MM, Balch AL, Nagase S, Maeda Y, Hasegawa T, Lu X, Akasaka T (2014) Sc_2@C_{66} revisited: an endohedral fullerene with scandium ions nestled within two unsaturated linear Triquinanes. J Am Chem Soc 136(21):7611–7614
34. Zhao Y, Yu H, Lian Y (2016) Experimental and theoretical evaluation of structures of Pr_2@C_{72} and its functionalized adduct with adamantylidene carbene. RSC Adv 6(116):115113–115119
35. Lu X, Nikawa H, Nakahodo T, Tsuchiya T, Ishitsuka MO, Maeda Y, Akasaka T, Toki M, Sawa H, Slanina Z, Mizorogi N, Nagase S (2008) Chemical understanding of a non-IPR metallofullerene: stabilization of encaged metals on fused-pentagon bonds in La_2@C_{72}. J Am Chem Soc 130(28):9129–9136
36. Suzuki M, Mizorogi N, Yang T, Uhlik F, Slanina Z, Zhao X, Yamada M, Maeda Y, Hasegawa T, Nagase S, Lu X, Akasaka T (2013) La_2@C_s(17 490)-C_{76}: a new non-IPR dimetallic metallofullerene featuring unexpectedly weak metal–pentalene interactions. Chem Eur J 19(50):17125–17130
37. Beavers CM, Jin H, Yang H, Wang ZM, Wang X, Ge H, Liu Z, Mercado BQ, Olmstead MH, Balch AL (2011) Very large, soluble endohedral fullerenes in the series La_2C_{90} to La_2C_{138}: isolation and crystallographic characterization of La_2@D_5(450)-C_{100}. J Am Chem Soc 133(39):15338–15341
38. Mercado BQ, Jiang A, Yang H, Wang Z, Jin H, Liu Z, Olmstead MM, Balch AL (2009) Isolation and structural characterization of the molecular nanocapsule Sm_2@D_{3d}(822)-C_{104}. Angew Chem Int Ed 121(48):9278–9280
39. Yang H, Jin H, Hong B, Liu Z, Beavers CM, Zhen H, Wang Z, Mercado BQ, Olmstead MM, Balch AL (2011) Large endohedral fullerenes containing two metal ions, Sm_2@D_2(35)-C_{88}, Sm_2@C_1(21)-C_{90}, and Sm_2@D_3(85)-C_{92}, and their relationship to endohedral fullerenes containing two gadolinium ions. J Am Chem Soc 133(42):16911–16919
40. Shen W, Bao L, Wu Y, Pan C, Zhao S, Fang H, Xie Y, Jin P, Peng P, Li F-F, Lu X (2017) Lu_2@C_{2n} (2n = 82, 84, 86): crystallographic evidence of direct Lu–Lu bonding between two divalent lutetium ions inside fullerene cages. J Am Chem Soc 139(29):9979–9984
41. Bao L, Peng P, Lu X (2018) Bonding inside and outside fullerene cages. Acc Chem Res 51(3): 810–815

42. Liu F, Spree L, Krylov DS, Velkos G, Avdoshenko SM, Popov AA (2019) Single-electron lanthanide-lanthanide bonds inside Fullerenes toward robust redox-active molecular magnets. Acc Chem Res 52(10):2981–2993
43. Popov A, Avdoshenko S, Martín Pendás A, Dunsch L (2012) Bonding between strongly repulsive metal atoms: an oxymoron made real in a confined space of endohedral metallofullerenes. Chem Commun 48(65):8031–8050
44. Yamada M, Kurihara H, Suzuki M, Saito M, Slanina Z, Uhlik F, Aizawa T, Kato T, Olmstead MM, Balch AL, Maeda Y, Nagase S, Lu X, Akasaka T (2015) Hiding and recovering electrons in a dimetallic endohedral fullerene: air-stable products from radical additions. J Am Chem Soc 137(1):232–238
45. Wang Z, Kitaura R, Shinohara H (2014) Metal-dependent stability of pristine and functionalized unconventional dimetallofullerene $M_2@I_h$-C_{80}. J Phys Chem C 118(25): 13953–13958
46. Hu S, Shen W, Yang L, Duan G, Jin P, Xie Y, Akasaka T, Lu X (2019) Crystallographic and theoretical investigations of $Er_2@C_{2n}$ (2n = 82, 84, 86): indication of distance-dependent metal–metal bonding nature. Chem Eur J 25(49):11538–11544
47. Zhang X, Wang Y, Morales-Martínez R, Zhong J, de Graaf C, Rodríguez-Fortea A, Poblet JM, Echegoyen L, Feng L, Chen N (2018) $U_2@I_h(7)$-C_{80}: crystallographic characterization of a long-sought dimetallic actinide endohedral fullerene. J Am Chem Soc 140(11): 3907–3915
48. Liu F, Velkos G, Krylov DS, Spree L, Zalibera M, Ray R, Samoylova NA, Chen C-H, Rosenkranz M, Schiemenz S, Ziegs F, Nenkov K, Kostanyan A, Greber T, Wolter AUB, Richter M, Büchner B, Avdoshenko SM, Popov AA (2019) Air-stable redox-active nanomagnets with lanthanide spins radical-bridged by a metal–metal bond. Nat Commun 10(1):571
49. Pan C, Shen W, Yang L, Bao L, Wei Z, Jin P, Fang H, Xie Y, Akasaka T, Lu X (2019) Crystallographic characterization of Y_2C_{2n} (2n = 82, 88–94): direct Y–Y bonding and cage-dependent cluster evolution. Chem Sci 10(17):4707–4713
50. Yang S, Dunsch L (2006) Di- and tridysprosium endohedral metallofullerenes with cages from C_{94} to C_{100}. Angew Chem Int Ed 45(8):1299–1302
51. Tagmatarchis N, Aslanis E, Prassides K, Shinohara H (2001) Mono-, Di- and Trierbium endohedral Metallofullerenes: production, separation, isolation, and spectroscopic study. Chem Mater 13(7):2374–2379
52. Popov AA, Zhang L, Dunsch L (2010) A Pseudoatom in a cage: Trimetallofullerene $Y_3@C_{80}$ mimics $Y_3N@C_{80}$ with nitrogen substituted by a Pseudoatom. ACS Nano 4(2):795–802
53. Iiduka Y, Wakahara T, Nakahodo T, Tsuchiya T, Sakuraba A, Maeda Y, Akasaka T, Yoza K, Horn E, Kato T, Liu MTH, Mizorogi N, Kobayashi K, Nagase S (2005) Structural determination of Metallofullerene Sc_3C_{82} revisited: a surprising finding. J Am Chem Soc 127(36): 12500–12501
54. Xu W, Feng L, Calvaresi M, Liu J, Liu Y, Niu B, Shi Z, Lian Y, Zerbetto F (2013) An experimentally observed Trimetallofullerene $Sm_3@I_h$-C_{80}: encapsulation of three metal atoms in a cage without a nonmetallic mediator. J Am Chem Soc 135(11):4187–4190
55. Stevenson S, Rice G, Glass T, Harich K, Cromer F, Jordan MR, Craft J, Hadju E, Bible R, Olmstead MM, Maitra K, Fisher AJ, Balch AL, Dorn HC (1999) Small-bandgap endohedral Metallofullerenes in high yield and purity. Nature 401(6748):55–57
56. Wei T, Wang S, Liu F, Tan Y, Zhu X, Xie S, Yang S (2015) Capturing the long-sought small-bandgap endohedral fullerene $Sc_3N@C_{82}$ with low kinetic stability. J Am Chem Soc 137(8): 3119–3123
57. Olmstead MM, Lee HM, Duchamp JC, Stevenson S, Marciu D, Dorn HC, Balch AL (2003) Sc3N@C68: folded Pentalene coordination in an endohedral fullerene that does not obey the isolated pentagon rule. Angew Chem Int Ed 115(8):928–931
58. Yang S, Popov AA, Dunsch L (2007) Violating the isolated pentagon rule (IPR): the endohedral non-IPR C_{70} cage of $Sc_3N@C_{70}$. Angew Chem Int Ed 46(8):1256–1259

59. Olmstead MM, de Bettencourt-Dias A, Duchamp JC, Stevenson S, Marciu D, Dorn HC, Balch AL (2001) Isolation and structural characterization of the endohedral fullerene $Sc_3N@C_{78}$. Angew Chem Int Ed 40(7):1223–1225
60. Krause M, Dunsch L (2004) Isolation and characterisation of two $Sc_3N@C_{80}$ isomers. ChemPhysChem 5(9):1445–1449
61. Stevenson S, Rothgeb AJ, Tepper KR, Duchamp J, Dorn HC, Powers XB, Roy M, Olmstead MM, Balch AL (2019) Isolation and crystallographic characterization of two, nonisolated pentagon endohedral Fullerenes: $Ho_3N@C_2(22010)$-C_{78} and $Tb_3N@C_2(22010)$-C_{78}. Chem. – Eur. J. 25(54):12545–12551
62. Melin F, Chaur MN, Engmann S, Elliott B, Kumbhar A, Athans AJ, Echegoyen L (2007) The large $Nd_3N@C_{2n}$ ($40 \leq n \leq 49$) cluster fullerene family: preferential templating of a C_{88} cage by a Trimetallic nitride cluster. Angew Chem Int Ed 46(47):9032–9035
63. Chaur MN, Athans AJ, Echegoyen L (2008) Metallic nitride endohedral Fullerenes: synthesis and electrochemical properties. Tetrahedron 64(50):11387–11393
64. Chaur MN, Melin F, Ashby J, Elliott B, Kumbhar A, Rao AM, Echegoyen L (2008) Lanthanum nitride endohedral Fullerenes $La_3N@C_{2n}$ ($43 \leq n \leq 55$): preferential formation of $La_3N@C_{96}$. Chem Eur J 14(27):8213–8219
65. Beavers CM, Chaur MN, Olmstead MM, Echegoyen L, Balch AL (2009) Large metal ions in a relatively small fullerene cage: the structure of $Gd_3N@C_2(22010)$-C_{78} departs from the isolated pentagon rule. J Am Chem Soc 131(32):11519–11524
66. Olmstead MM, Zuo T, Dorn HC, Li T, Balch AL (2017) Metal ion size and the Pyramidalization of Trimetallic nitride units inside a fullerene cage: comparisons of the crystal structures of $M_3N@I_h$-C_{80} (M=Gd, Tb, Dy, Ho, Er, tm, Lu, and Sc) and some mixed metal counterparts. Inorganica Chim Acta 468:321–326
67. Stevenson S, Paige Phillips J, Reid J, Olmstead M, Prasad Rath SL, Balch A (2004) Pyramidalization of Gd_3N inside a C_{80} cage. The synthesis and structure of $Gd_3N@C_{80}$. Chem Commun 24:2814–2815
68. Schlesier C, Liu F, Dubrovin V, Spree L, Büchner B, Avdoshenko SM, Popov AA (2019) Mixed dysprosium-lanthanide nitride clusterfullerenes $DyM_2N@C_{80}$-I_h and $Dy_2MN@C_{80}$-I_h (M = Gd, Er, Tm, and Lu): synthesis, molecular structure, and quantum motion of the endohedral nitrogen atom. Nanoscale 11(27):13139–13153
69. Stevenson S, Rose CB, Maslenikova JS, Villarreal JR, Mackey MA, Mercado BQ, Chen K, Olmstead MM, Balch AL (2012) Selective synthesis, isolation, and crystallographic characterization of $LaSc_2N@I_h$-C_{80}. Inorg Chem 51(24):13096–13102
70. Dreiser J, Westerström R, Zhang Y, Popov AA, Dunsch L, Krämer K, Liu S-X, Decurtins S, Greber T (2014) The Metallofullerene field-induced single-ion magnet $HoSc_2N@C_{80}$. Chem Eur J 20(42):13536–13540
71. Stevenson S, Thompson HR, Arvola KD, Ghiassi KB, Olmstead MM, Balch AL (2015) Isolation of $CeLu_2N@I_h$-C_{80} through a non-chromatographic, two-step chemical process and crystallographic characterization of the Pyramidalized $CeLu_2N$ within the icosahedral cage. Chem Eur J 21(29):10362–10368
72. Stevenson S, Chancellor CJ, Lee HM, Olmstead MM, Balch AL (2008) Internal and external factors in the structural organization in cocrystals of the mixed-metal endohedrals ($GdSc_2N@I_h$-C_{80}, $Gd_2ScN@I_h$-C_{80}, and $TbSc_2N@I_h$-C_{80}) and nickel(II) octaethylporphyrin. Inorg Chem 47(5):1420–1427
73. Nie M, Xiong J, Zhao C, Meng H, Zhang K, Han Y, Li J, Wang B, Feng L, Wang C, Wang T (2019) Luminescent single-molecule magnet of Metallofullerene $DyErScN@I_h$-C_{80}. Nano Res 12(7):1727–1731
74. Yang S, Chen C, Li X, Wei T, Liu F, Wang S (2013) Bingel–Hirsch Monoadducts of $TiSc_2N@I_h$-C_{80} versus $Sc_3N@I_h$-C_{80}: reactivity improvement via internal metal atom substitution. Chem Commun 49(92):10844

75. Wei T, Wang S, Lu X, Tan Y, Huang J, Liu F, Li Q, Xie S, Yang S (2016) Entrapping a group-VB transition metal, vanadium, within an endohedral Metallofullerene: $V_xSc_{3-x}N@I_h$-C_{80} (x = 1, 2). J Am Chem Soc 138(1):207–214
76. Wei T, Jin F, Guan R, Huang J, Chen M, Li Q, Yang S (2018) Blending non-Group-3 transition metal and rare-earth metal into a C_{80} fullerene cage with D_{5h} symmetry. Angew Chem Int Ed 57(32):10273–10277
77. Li X, Roselló Y, Yao Y-R, Zhuang J, Zhang X, Rodríguez-Fortea A, de Graaf C, Echegoyen L, Poblet JM, Chen N (2021) $U_2N@I_h(7)$-C_{80}: fullerene cage encapsulating an unsymmetrical U (IV)=N=U(V) cluster. Chem Sci 12(1):282–292
78. Lu X, Akasaka T, Nagase S (2013) Carbide cluster Metallofullerenes: structure, properties, and possible origin. Acc Chem Res 46(7):1627–1635
79. Wang C-R, Kai T, Tomiyama T, Yoshida T, Kobayashi Y, Nishibori E, Takata M, Sakata M, Shinohara H (2001) A scandium carbide endohedral Metallofullerene: (Sc2C2)@C84. Angew Chem Int Ed 40(2):397–399
80. Lu X, Nakajima K, Iiduka Y, Nikawa H, Tsuchiya T, Mizorogi N, Slanina Z, Nagase S, Akasaka T (2012) The Long-Believed $Sc_2@C_{2v}(17)$-C_{84} Is Actually $Sc_2C_2@C_{2v}(9)$-C_{82} : Unambiguous Structure Assignment and Chemical Functionalization. Angew Chem Int Ed 51(24):5889–5892
81. Lu X, Nakajima K, Iiduka Y, Nikawa H, Mizorogi N, Slanina Z, Tsuchiya T, Nagase S, Akasaka T (2011) Structural elucidation and regioselective functionalization of an unexplored carbide cluster metallofullerene $Sc_2C_2@C_s(6)$-C_{82}. J Am Chem Soc 133(48): 19553–19558
82. Wang Y, Tang Q, Feng L, Chen N (2017) $Sc_2C_2@D_{3h}(14246)$-C_{74}: a missing piece of the clusterfullerene puzzle. Inorg Chem 56(4):1974–1980
83. Fang H, Cong H, Suzuki M, Bao L, Yu B, Xie Y, Mizorogi N, Olmstead MM, Balch AL, Nagase S, Akasaka T, Lu X (2014) Regioselective benzyl radical addition to an open-shell cluster metallofullerene. Crystallographic studies of cocrystallized $Sc_3C_2@I_h$-C_{80} and its singly bonded derivative. J Am Chem Soc 136(29):10534–10540
84. Chen C-H, Ghiassi KB, Cerón MR, Guerrero-Ayala MA, Echegoyen L, Olmstead MM, Balch AL (2015) Beyond the butterfly: $Sc_2C_2@C_{2v}$ (9)-C_{86}, an endohedral fullerene containing a planar, twisted Sc_2C_2 unit with remarkable crystalline order in an unprecedented carbon cage. J Am Chem Soc 137(32):10116–10119
85. Chen C-H, Abella L, Cerón MR, Guerrero-Ayala MA, Rodríguez-Fortea A, Olmstead MM, Powers XB, Balch AL, Poblet JM, Echegoyen L (2016) Zigzag Sc_2C_2 carbide cluster inside a [88]fullerene cage with one heptagon, $Sc_2C_2@C_s$(Hept)-C_{88}: a kinetically trapped fullerene formed by C_2 insertion? J Am Chem Soc 138(39):13030–13037
86. Shen W, Bao L, Yu P, Yang L, Li B, Yu P, Jin P, Lu X (2020) Isolation and crystallographic characterization of $Lu_2C_2@C_{2n}$ (2n = 88–92): internal cluster stretching upon outer cage expansion. Carbon 164:157–163
87. Hu S, Zhao P, Shen W, Ehara M, Xie Y, Akasaka T, Lu X (2020) Crystallographic characterization of $Er_2C_2@C_{80-88}$: cluster stretching with cage elongation. Inorg Chem 59(3): 1940–1946
88. Zhao S, Zhao P, Cai W, Bao L, Chen M, Xie Y, Zhao X, Lu X (2017) Stabilization of Giant Fullerenes $C_2(41)$-C_{90}, $D_3(85)$-C_{92}, $C_1(132)$-C_{94}, $C_2(157)$-C_{96}, and $C_1(175)$-C_{98} by encapsulation of a large La_2C_2 cluster: the importance of cluster–cage matching. J Am Chem Soc 139(13):4724–4728
89. Cai W, Bao L, Zhao S, Xie Y, Akasaka T, Lu X (2015) Anomalous compression of $D_5(450)$-C_{100} by encapsulating La_2C_2 cluster instead of La2. J Am Chem Soc 137(32):10292–10296
90. Shen W, Bao L, Hu S, Yang L, Jin P, Xie Y, Akasaka T, Lu X (2019) Crystallographic characterization of Lu_2C_{2n} (2n = 76–90): cluster selection by cage size. Chem Sci 10(3): 829–836

91. Pan C, Bao L, Yu X, Fang H, Xie Y, Akasaka T, Lu X (2018) Facile access to Y_2C_{2n} (2n = 92–130) and crystallographic characterization of $Y_2C_2@C_1(1660)$-C_{108}: a giant nanocapsule with a linear carbide cluster. ACS Nano 12(2):2065–2069
92. Zhang X, Li W, Feng L, Chen X, Hansen A, Grimme S, Fortier S, Sergentu D-C, Duignan TJ, Autschbach J, Wang S, Wang Y, Velkos G, Popov AA, Aghdassi N, Duhm S, Li X, Li J, Echegoyen L, Schwarz WHE, Chen N (2018) A diuranium carbide cluster stabilized inside a C_{80} fullerene cage. Nat Commun 9(1):2753
93. Zhuang J, Abella L, Sergentu D-C, Yao Y-R, Jin M, Yang W, Zhang X, Li X, Zhang D, Zhao Y, Li X, Wang S, Echegoyen L, Autschbach J, Chen N (2019) Diuranium (IV) carbide cluster U_2C_2 stabilized inside fullerene cages. J Am Chem Soc 141(51):20249–20260
94. Svitova AL, Ghiassi KB, Schlesier C, Junghans K, Zhang Y, Olmstead MM, Balch AL, Dunsch L, Popov AA (2014) Endohedral fullerene with μ_3-carbido ligand and titanium-carbon double bond stabilized inside a carbon cage. Nat Commun 5:3568
95. Junghans K, Ghiassi KB, Samoylova NA, Deng Q, Rosenkranz M, Olmstead MM, Balch AL, Popov AA (2016) Synthesis and isolation of the titanium–scandium endohedral Fullerenes—$Sc_2TiC@I_h$-C_{80}, $Sc_2TiC@D_{5h}$-C_{80} and $Sc_2TiC_2@I_h$-C_{80}: metal size tuning of the TiIV/TiIII redox potentials. Chem Eur J 22(37):13098–13107
96. Yu P, Shen W, Bao L, Pan C, Slanina Z, Lu X (2019) Trapping an unprecedented Ti_3C_3 unit inside the icosahedral C_{80} fullerene: a crystallographic survey. Chem Sci 10(47): 10925–10930
97. Yu P, Bao L, Yang L, Hao D, Jin P, Shen W, Fang H, Akasaka T, Lu X (2020) Crystallographic characterization of $Ti_2C_2@D_{3h}(5)$-C_{78}, $Ti_2C_2@C_{3v}(8)$-C_{82}, and $Ti_2C_2@C_s(6)$-C_{82}: identification of unsupported Ti_2C_2 cluster with cage-dependent configurations. Inorg Chem 59(13): 9416–9423
98. Stevenson S, Mackey MA, Stuart MA, Phillips JP, Easterling ML, Chancellor CJ, Olmstead MM, Balch AL (2008) A distorted tetrahedral metal oxide cluster inside an icosahedral carbon cage. Synthesis, isolation, and structural characterization of $Sc_4(M_3\text{-}O)_2@I_h$-C_{80}. J Am Chem Soc 130(36):11844–11845
99. Mercado BQ, Stuart MA, Mackey MA, Pickens JE, Confait BS, Stevenson S, Easterling ML, Valencia R, Rodríguez-Fortea A, Poblet JM, Olmstead MM, Balch AL (2010) $Sc_2(M_2\text{-}O)$ trapped in a fullerene cage: the isolation and structural characterization of $Sc_2(M_2\text{-}O)@C_s(6)$-$C_{82}$ and the relevance of the thermal and entropic effects in fullerene isomer selection. J Am Chem Soc 132(34):12098–12105
100. Q. Mercado; M. Olmstead; M. Beavers, ; L. Easterling.; Stevenson, S.; A. Mackey; E. Coumbe; D. Phillips.; Paige Phillips, J.; M. Poblet; L. Balch. A seven atom cluster in a carbon cage, the crystallographically determined structure of $Sc_4(\mu_3\text{-}O)_3@I_h$-$C_{80}$. Chem Commun 2010, 46 (2), 279–281
101. Yang T, Hao Y, Abella L, Tang Q, Li X, Wan Y, Rodríguez-Fortea A, Poblet JM, Feng L, Chen N (2015) $Sc_2O@T_d(19151)$-C_{76}: hindered cluster motion inside a tetrahedral carbon cage probed by crystallographic and computational studies. Chem Eur J. 21(31): 11110–11117
102. Hao Y, Tang Q, Li X, Zhang M, Wan Y, Feng L, Chen N, Slanina Z, Adamowicz L, Uhlík F (2016) Isomeric $Sc_2O@C_{78}$ related by a single-step stone–Wales transformation: key links in an unprecedented fullerene formation pathway. Inorg Chem 55(21):11354–11361
103. Tang Q, Abella L, Hao Y, Li X, Wan Y, Rodríguez-Fortea A, Poblet JM, Feng L, Chen N (2015) $Sc_2O@C_{2v}(5)$-C_{80}: Dimetallic oxide cluster inside a C_{80} fullerene cage. Inorg Chem 54(20):9845–9852
104. Tang Q, Abella L, Hao Y, Li X, Wan Y, Rodríguez-Fortea A, Poblet JM, Feng L, Chen N (2016) $Sc_2O@C_{3v}(8)$-C_{82}: a missing isomer of $Sc_2O@C_{82}$. Inorg Chem 55(4):1926–1933
105. Liu A, Nie M, Hao Y, Yang Y, Wang T, Slanina Z, Cong H, Feng L, Wang C, Uhlik F (2019) $Ho_2O@C_{74}$: Ho_2O cluster expands within a small non-IPR fullerene cage of $C_2(13333)$-C_{74}. Inorg Chem 58(8):4774–4781

106. Cong H, Liu A, Hao Y, Feng L, Slanina Z, Uhlik F (2019) $Ho_2O@C_{84}$: crystallographic evidence showing linear metallic oxide cluster encapsulated in IPR fullerene cage of $D_{2d}(51591)$-C_{84}. Inorg Chem 58(16):10905–10911
107. Yu Y, Slanina Z, Wang F, Yang Y, Lian Y, Uhlik F, Xin B, Feng L (2020) $Ho_2O@D_3(85)$-C_{92}: highly stretched cluster dictated by a giant cage and unexplored isomerization. Inorg Chem 59(15): 11020–11027
108. Yang W, Velkos G, Liu F, Sudarkova SM, Wang Y, Zhuang J, Zhang H, Li X, Zhang X, Büchner B, Avdoshenko SM, Popov AA, Chen N (2019) Single molecule magnetism with strong magnetic anisotropy and enhanced Dy···Dy coupling in three isomers of Dy-oxide clusterfullerene $Dy_2O@C_{82}$. Adv Sci 6(20):1901352
109. Dunsch L, Yang S, Zhang L, Svitova A, Oswald S, Popov AA (2010) Metal sulfide in a C_{82} fullerene cage: a new form of endohedral clusterfullerenes. J Am Chem Soc 132(15):5413–5421
110. Chen N, Beavers CM, Mulet-Gas M, Rodríguez-Fortea A, Munoz EJ, Li Y-Y, Olmstead MM, Balch AL, Poblet JM, Echegoyen L (2012) $Sc_2S@C_s(10528)$-C_{72}: a dimetallic sulfide endohedral fullerene with a non isolated pentagon rule cage. J Am Chem Soc 134(18):7851–7860
111. Chen N, Mulet-Gas M, Li Y-Y, Stene R, Atherton C, Rodríguez-Fortea A, Poblet M, Echegoyen L (2013) $Sc_2S@C_2(7892)$–C_{70} : a metallic sulfide cluster inside a non-IPR C_{70} cage. Chem Sci 4(1):180–186
112. Cai W, Bocarsly JD, Gomez A, Lee RJL, Metta-Magaña A, Seshadri R, Echegoyen L (2020) High blocking temperatures for DyScS endohedral fullerene single-molecule magnets. Chem Sci 11(48):13129–13136
113. Krause M, Ziegs F, Popov AA, Dunsch L (2007) Entrapped bonded hydrogen in a fullerene: the five-atom cluster Sc_3CH in C_{80}. ChemPhysChem 8(4):537–540
114. Zhao C, Tan K, Nie M, Lu Y, Zhang J, Wang C, Lu X, Wang T (2020) Scandium tetrahedron supported by H anion and CN Pentaanion inside fullerene C_{80}. Inorg Chem 59(12): 8284–8290. https://doi.org/10.1021/acs.inorgchem.0c00681
115. Wang T-S, Feng L, Wu J-Y, Xu W, Xiang J-F, Tan K, Ma Y-H, Zheng J-P, Jiang L, Lu X, Shu C-Y, Wang C-R (2010) Planar quinary cluster inside a fullerene cage: synthesis and structural characterizations of $Sc_3NC@C_{80}$-I_h. J Am Chem Soc 132(46):16362–16364
116. Wu J, Wang T, Ma Y, Jiang L, Shu C, Wang C (2011) Synthesis, isolation, characterization, and theoretical studies of $Sc_3NC@C_{78}$-C_2. J Phys Chem C 115(48):23755–23759
117. Yang S, Chen C, Liu F, Xie Y, Li F, Jiao M, Suzuki M, Wei T, Wang S, Chen Z, Lu X, Akasaka T (2013) An improbable monometallic cluster entrapped in a popular fullerene cage: $YCN@C_s(6)$-C_{82}. Sci Rep 3(1):1–5
118. Liu F, Wang S, Gao C-L, Deng Q, Zhu X, Kostanyan A, Westerström R, Jin F, Xie S-Y, Popov AA, Greber T, Yang S (2017) Mononuclear clusterfullerene single-molecule magnet containing strained fused-pentagons stabilized by a nearly linear metal cyanide cluster. Angew Chem Int Ed 56(7):1830–1834
119. Liu F, Gao C-L, Deng Q, Zhu X, Kostanyan A, Westerström R, Wang S, Tan Y-Z, Tao J, Xie S-Y, Popov AA, Greber T, Yang S (2016) Triangular monometallic cyanide cluster entrapped in carbon cage with geometry-dependent molecular magnetism. J Am Chem Soc 138(44):14764–14771
120. Shen W, Hu Z, Yu P, Wei Z, Jin P, Shi Z, Lu X (2020) An experimental and theoretical study of $LuNC@C_{76,82}$ revealing a cage-cluster selection rule. Inorg Chem Front 7(23):4563–4571
121. Hummelen JC, Knight B, Pavlovich J, González R, Wudl F (1995) Isolation of the heterofullerene $C_{59}N$ as its dimer $(C_{59}N)_2$. Science 269(5230):1554–1556
122. Brown CM, Cristofolini L, Kordatos K, Prassides K, Bellavia C, González R, Keshavarz-K, Wudl F, Cheetham AK, Zhang JP, Andreoni W, Curioni A, Fitch AN, Pattison P (1996) On the crystal structure of Azafullerene $(C_{59}N)_2$. Chem Mater 8(11):2548–2550
123. Akasaka T, Okubo S, Wakahara T, Yamamoto K, Kobayashi K, Nagase S, Kato T, Kako M, Nakadaira Y, Kitayama Y, Matsuura K (1999) Endohedrally metal-doped heterofullerenes: $La@C_{81}N$ and $La_2@C_{79}N$. Chem Lett 28(9):945–946

124. Zuo T, Xu L, Beavers CM, Olmstead MM, Fu W, Crawford TD, Balch AL, Dorn HC (2008) $M_2@C_{79}N$ (M = Y, Tb): isolation and characterization of stable endohedral metallofullerenes exhibiting M−M bonding interactions inside Aza[80]fullerene cages. J Am Chem Soc 130(39):12992–12997
125. Fu W, Zhang J, Fuhrer T, Champion H, Furukawa K, Kato T, Mahaney JE, Burke BG, Williams KA, Walker K, Dixon C, Ge J, Shu C, Harich K, Dorn HC (2011) $Gd_2@C_{79}N$: isolation, characterization, and monoadduct formation of a very stable heterofullerene with a magnetic spin state of S = 15/2. J Am Chem Soc 133(25):9741–9750
126. Chaur MN, Melin F, Ashby J, Elliott B, Kumbhar A, Rao AM, Echegoyen L (2008) Lanthanum nitride endohedral fullerenes $La_3N@C_{2n}$ (43 <= n <= 55): preferential formation of $La_3N@C_{96}$. Chem Eur J 14(27):8213–8219
127. Hu Z, Dong B-W, Liu Z, Liu J-J, Su J, Yu C, Xiong J, Shi D-E, Wang Y, Wang B-W, Ardavan A, Shi Z, Jiang S-D, Gao S (2018) Endohedral metallofullerene as molecular high spin qubit: diverse Rabi cycles in $Gd_2@C_{79}N$. J Am Chem Soc 140(3):1123–1130

Preparation of Endohedral Metallofullerenes

17

Ning Chen, Jiaxin Zhuang, Xiaomeng Li, and Meihe Jin

Contents

Abstract

Endohedral metallofullerenes (EMFs) have been extensively studied due to their unique structural characteristics and physiochemical properties. Over the past three decades, researchers have developed different methods for the synthesis of endohedral metallofullerenes, including the Krätschmer-Huffman DC arc-discharge, laser ablation, radio frequency furnace, ion bombardment, and hot-atom chemistry method et al. Among them, DC arc-discharge method is the most popular technique used to date, since it enables the macroscopic synthesis of fullerenes species in a relatively simple and cost-effective way. With the application and modification of this method, metallofullerenes and endohedral clusterfullerenes with variable clusters encapsulated inside different cages have been synthesized and isolated. Besides, the laser ablation method still plays an important role on the investigation of endohedral fullerene formation mechanism. Separation methods also play key role in the preparation of novel endohedral fullerenes, as the soot extract obtained from DC arc-discharge method often contains a large variety of different fullerene species. High-performance liquid chromatography (HPLC) is widely used for the separation and purification of

N. Chen (✉) · J. Zhuang · X. Li · M. Jin
College of Chemistry, Chemical Engineering and Materials Science, Soochow University, Suzhou, Jiangsu, P. R. China
e-mail: chenning@suda.edu.cn

X. Lu et al. (eds.), *Handbook of Fullerene Science and Technology*,
https://doi.org/10.1007/978-981-16-8994-9_26

EMFs as it can yield highly purified EMFs with variable HPLC columns and recycling techniques applied. However, it is also known for its time-consuming procedures and is only suitable for samples on milligram scale. Thus, various nonchromatographic strategies have been developed for simpler and more efficient separation procedure, such as chemical and electrochemical methods. This chapter provides a detailed and comprehensive overview of the synthetic methods of EMFs and highlights the recent development in this field, followed by a summarization of different separation and purification methods.

Keywords

Endohedral fullerenes · Synthesis · DC arc-discharge method · Separation · High-performance liquid chromatography

Introduction

In 1985, soon after the discovery of empty fullerenes C_{60}, C_{70} etc., Smalley, Kroto, and coworkers carried their exploration by laser ablation of graphite discs impregnated with lanthanum chloride, anticipating the entrapment of lanthanum into the cavity of fullerenes. Such hypothesis was experimentally confirmed by the observation of the mass signal indicative of the formation of a metal fullerene complex, LaC_{60} [1], which was the first evidence of endohedral metallofullerenes (EMFs). Although in the first few years laser ablation was the most popular method in EMF synthesis, the product yield of EMFs by this method was extremely low. The other new techniques, such as resistive heating [2], radio frequency furnace [3], et al., were also reported in the following studies, but the product yield of EMFs remained at a similar extremely low level. A major breakthrough happened in 1990 when Krätschmer and Huffman reported the direct current arc-discharge method, which, for the first time, resulted in the macroscopic synthesis of fullerenes [4]. This method enabled isolation and characterization of variable fullerenes for the first time, which essentially boosted the EMF research. Other synthetic methods, however, have not been abandoned and continued to be useful for some specific applications. For example, the laser ablation method still plays a key role in the investigation of fullerene-forming mechanism [5, 6]. Nevertheless, in the past three decades, most of the studies on the synthesis of novel EMFs were based on the modified Krätschmer-Huffman method. A symbolic discovery was the first metal-nonmetal cluster endohedral fullerene, $Sc_3N@C_{80}$, which was synthesized with an accidental leak of ambient air, once considered as harmful factor for the synthesis of EMFs, into the arcing chamber. This milestone discovery gave inspiration to the following synthesis of novel EMF molecules, which includes the introduction of a wide range of gas atmospheres into the arcing chamber, doping the graphite rods with different reagents and optimizing the design of the apparatus, etc. Benefiting from the development of synthetic methods of EMFs, to date, a large variety of metal ions and metallic clusters have been successfully encapsulated into variable fullerene

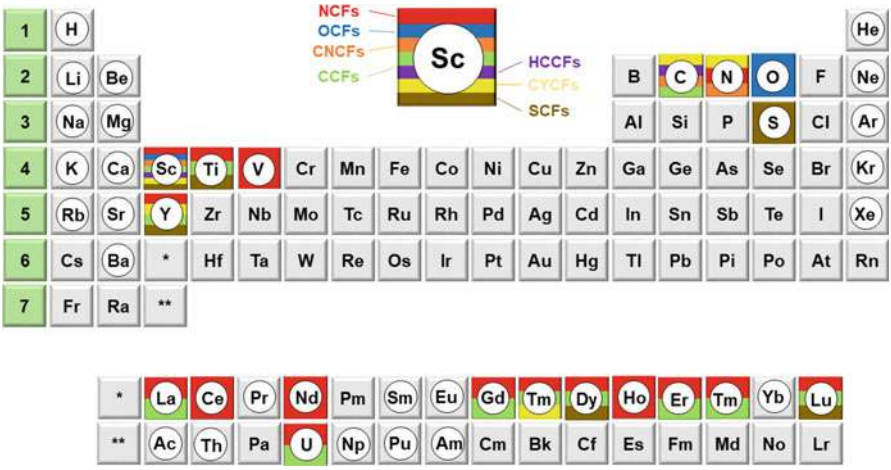

Fig. 1 A periodic table highlighting the elements that have been encapsulated into fullerene cage. Different clusterfullerenes are marked with different colors. The circles indicate that the elements can form conventional metallofullerenes

cages. Figure 1 summarized the elements that have been encapsulated into fullerene cage in a periodic table. It can be clearly seen that most of rare earth metals can be encapsulated and form both conventional metallofullerenes and clusterfullerenes. Among them, Sc demonstrates the largest flexibility as encapsulated element by the formation of multiple types of endohedral clusterfullerenes such as NCFs, OCFs, SCFs, CCFs, CCNFs, etc. Non-rare-earth metal Ti can be embedded in the form of NCFs, SCFs, and CCFs. Recent researches also reveal that actinide elements, such as Th and U, can also form stable conventional metallofullerenes and cluster fullerenes. On the other hand, nonmetal element (N, C, O, and S) is crucial for the stabilization of the encaged metallic clusters when metal ions are encapsulated into fullerene cages. In this chapter, we summarize the methods which have been used for the synthesis and separation of these EMFs and highlight the recent development in this research field.

Synthesis and Separation of Endohedral Metallofullerenes

Synthesis of Endohedral Metallofullerenes

Direct Current Arc-Discharge Method

The Krätschmer-Huffman direct current arc-discharge method is the most popular method for the synthesis of EMFs. Figure 2 shows a typical Krätschmer-Huffman generator. Before the arcing process, generally, metal oxide (or metal alloy)/graphite composite rods are subject to a high-temperature (above ca. 1000 °C) pretreatment. At such high temperature, the metal oxides are reduced and various metal carbides

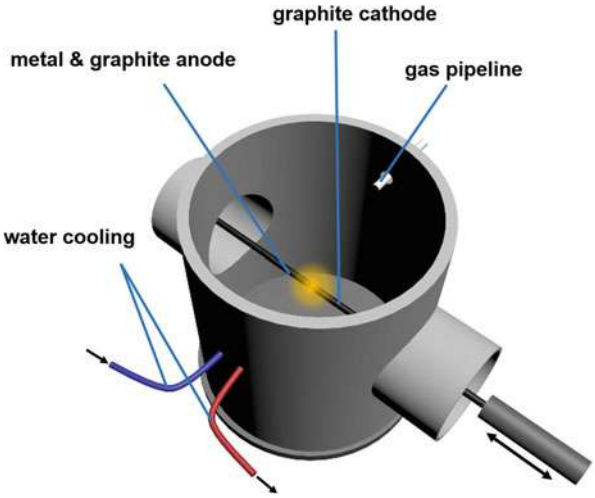

Fig. 2 Schematic diagram of a Krätschmer-Huffman generator

can be formed in the composite rods. This process was proved to be crucial for the following synthesis of EMFs since uniformly dispersed metal atoms or ions in a composite rod likely boost the yield EMFs during the arcing process. In addition to preliminary annealing, some other techniques like "in situ activation" were also used under specific circumstances for higher productivity. This method was carried out by contacting the filled rod and the cathode graphite rod under a low dc current for a while in order to remove the hydrated/adsorbed water [7].

In a typical procedure of the arcing process, preheated graphite rods filled with metal oxide (or metal) and graphite powder are used as the positive electrodes to conduct arc-discharging direct current under the protection of low-pressure helium, and the high temperature generated by the arc vaporizes the graphite and metal to yield the soot containing empty fullerenes as well as endohedral metallofullerenes (EMFs). The soot is then collected for further handling. For example, under He flow at 50 torr in the direct current arcing chamber, Shinohara and coworkers prepared macroscopic amount of $Y@C_{82}$ and confirmed the endohedral nature of the EMF by X-ray powder diffraction analysis for the first time [8]. Up to now, almost all isolated conventional mono- and dimetallofullerenes, as well as the sole example of structurally characterized trimetallofullerene $Sm_3@I_h$-C_{80}, have been prepared following this method [9]. In particular, recent progress on actinide monometallic/dimetallic fullerenes have been made based on the successful macroscopic synthesis of these species by the DC arc-discharge method, which attracted great attention from researchers of both fullerene and actinide chemistry. More details about the synthesis of conventional EMFs have been summarized in several previous reviews and book chapters [10, 11]. For the direct current arc-discharge method, the yield of EMFs is sensitive to multiple factors such as current density, He gas pressure, the type of the metal or nonmetal source selected, the ratio of metal and carbon, the capacity of the chamber, the distance

between two electrodes (the width of the arc zone), and the size of a composite rod. Though the mechanism has not been fully understood yet, these complex factors had been proved to have substantial impact on the thermodynamic and kinetic characteristics of the fullerene formation. Thus, researchers have tried to modify and optimize the synthetic methods for each specific targeted product, respectively.

Nitride Cluster Fullerenes (NCFs)

Nitride cluster fullerenes were first reported by Dorn et al. [12] In 1994, an unidentified scandium endohedral fullerene species (with a mass-to-charge ratio, m/z of 1109) was observed by them from the extraction of scandium metallofullerene soot [12]. Later, they found that intentional introduction of N_2 into the reactor dramatically enhanced the yield of this product to about 3−5% of the soot extract. The identity of this species was then confirmed as an endohedral fullerene with an unprecedented trimetallic nitride cluster trapped inside, i.e., $Sc_3N@C_{80}$ [13]. In this report, graphite rods filled with M_xO_y/graphite (M = metal) were vaporized in a Krätschmer-Huffman generator in a dynamic helium atmosphere (300 torr) containing a small amount of nitrogen (1–3 torr). Up to now, almost all nitride cluster fullerenes reported followed the structural template of $M_3N@C_{2n}$. This method was thereby named as the "trimetallic nitride template" (TNT) technique by Dorn et al. and known as the most widely used synthetic method for nitride cluster fullerenes (NCFs) [13]. Following these methods, a wide variety of NCFs, such as $Sc_3N@C_{2n}$ ($2n$ = 68, 70, 78-82) [13–20], $Y_3N@C_{2n}$ ($2n$ = 78-88) [21–23], $Gd_3N@C_{2n}$ ($2n$ = 78-88) [24–28], $Tb_3N@C_{2n}$ ($2n$ = 80, 84-88) [29, 30], and $Tm_3N@C_{2n}$ ($2n$ = 78-86) [31, 32] et al. were successfully synthesized. Though dynamic gas flow was first introduced in the synthesis and continued used by Dorn and Stevenson group, however, most of abovementioned NCFs synthesized by other groups were obtained by the usage of static gas atmosphere. For example, very recently, a new isomer of $Sc_3N@C_{82}$, $Sc_3N@C_s$(39663)-C_{82}, was successfully synthesized [14]. In this work, a static 266 mbar He and 5 mbar N_2 was introduced into the arcing chamber as the reactive gas atmosphere. Currently, there is no report analyzing the effect of dynamic and static gas atmosphere on the product yield or selectivity of the NCFs. Either to choose dynamic gas flow or static gas atmosphere largely depends on the synthetic apparatus available in different labs. In some of following researches, the nitrogen gas was replaced by reactive gaseous or solid reagents like NH_3, metal nitrate, metal cyanide, etc. to improve the selectivity of the NCFs.

Despite the different synthetic methods or metal oxides, all the obtained lanthanide-based NCFs strictly obey the "trimetallic nitride template" (TNT) rule. However, in 2020, $U_2N@I_h(7)$-C_{80} was synthesized and characterized by Chen and coworkers with small portion of NH_3 as the nitrogen source, which broke the long-standing TNT structural template, suggesting actinide cluster fullerenes may not obey general rules adapted from the lanthanide-based cluster fullerenes. Figure 3 shows the molecular structures of some typical NCFs.

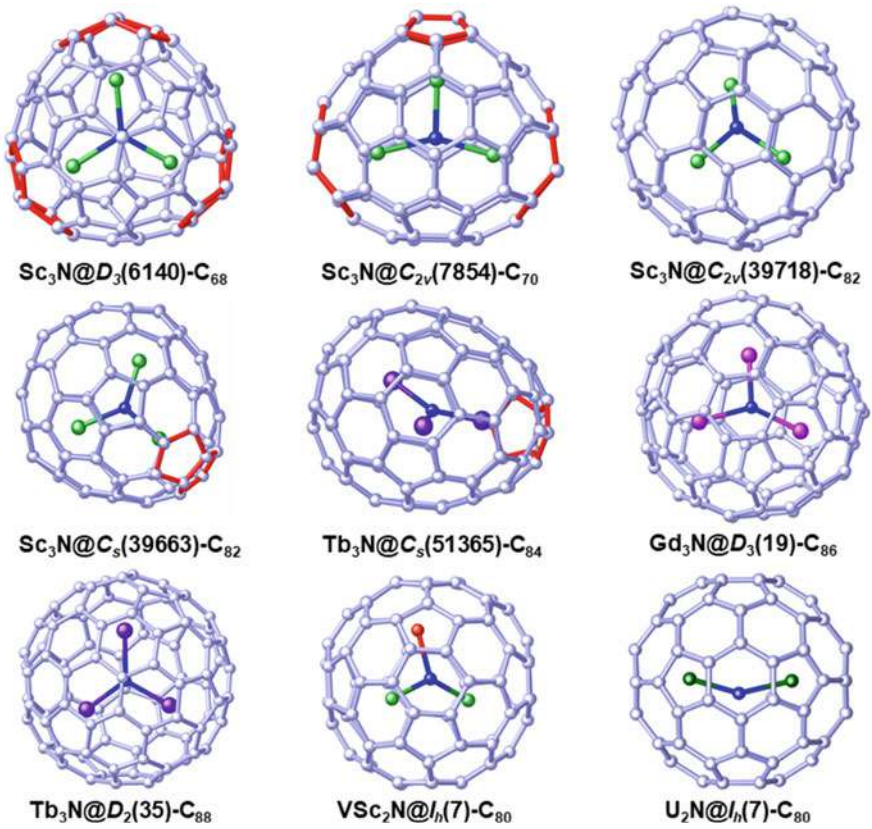

Fig. 3 Molecular structures of representative nitride clusterfullerenes. The adjacent pentagons of the cages are highlighted in red

Gaseous Nitrogen Source

The majority of the NCFs reported to date were synthesized using N_2 as the nitrogen source. The most representative member of this family is $Sc_3N@C_{80}$, which was first reported and has the highest yield among all the EMFs synthesized to date. In the initial report of the synthesis of $Sc_3N@C_{80}$ by Dorn and Stevenson et al, graphite rods filled with Sc_2O_3/graphite (3 wt%/97 wt%) were vaporized in a Kratschmer-Huffman generator in a dynamic helium atmosphere (300 torr) containing a small amount of nitrogen (1 ± 3 torr). A single rod typically yields 60 mg soluble fullerenes and endohedral metallofullerenes, which were extracted from the carbon soot using carbon disulphide [13]. In 2000, the first non-IPR (nonisolated pentagon rule) endohedral fullerene $Sc_3N@C_{68}$ was synthesized by this method and successfully separated by the same group [15]. For this synthetic process, a dynamic mixed atmosphere of N_2 and helium was also utilized in the arcing chamber. Besides, heterogeneous metallic NCFs, such as $CeSc_2N@C_{80}$ [33], $Gd_xSc_{3-x}N@C_{2n}$ ($x = 0$-3, $2n = 78$-86) [34–37], $V_xSc_{3-x}N@C_{80}$ ($x = 1, 2$) [38], et al., were also synthesized

with N_2 as the gas source when the graphite rods doped with mixed metal oxides were vaporized under direct current. In 2006, the heterogeneous NCF with three different metals, $ScYErN@C_{80}$, was successfully synthesized and isolated by Chen et al., under a 98% He/2% N_2 atmosphere at 300 torr. A composite Sc/Ni, Y/Ni, and Er/Ni alloy powder was employed in the synthetic progress, in which Ni functioned as catalyst [39].

However, the relative yield of EMFs obtained by the N_2 gas source method is rather low, generally less than 2% of the total raw fullerene extract. Consequently, the overwhelming amounts of empty fullerenes has to be removed by the multistage HPLC separation procedures, which became the bottleneck of the EMF preparation process. In 2003, a breakthrough was made by the introduction of the reactive gaseous nitrogen source, NH_3, as proposed by the Dunsch and coworkers [40]. In their report, carbon rods filled with lanthanide metal oxide powder were arc-burned in the arcing chamber with the introduction of 10–20 mbar of NH_3 and 200 mbar of helium [40]. The substitution of N_2 by NH_3 considerably increased the selectivity of the NCFs. For $Sc_3N@C_{2n}$, the selectivity reached as high as 90% (see Fig. 4 for the one-step HPLC separation of the raw soot extract as prepared by the abovementioned method). Utilizing this method, $Dy_3N@C_{2n}$ ($39 \leq n \leq 44$), was even synthesized with the selectivity as high as 98% [41]. This synthetic method simplified the separation and isolation procedures for EMFs, but the introduction of NH_3 also exerts a considerable negative impact on the net yield of fullerene products as well as the total yield of EMFs. In addition, with the presence of NH_3, large amount of hydrocarbon complexes were also by-produced, which require extra purification treatment.

Nevertheless, gaseous nitrogen source has been the most commonly used in the synthesis of NCFs. The choice of either N_2 or NH_3 depends on the different requirements of the synthetic targets. Generally, the introduction of N_2 can result in a higher net yield of NCFs while NH_3 is preferable when simplified HPLC separation procedures are needed.

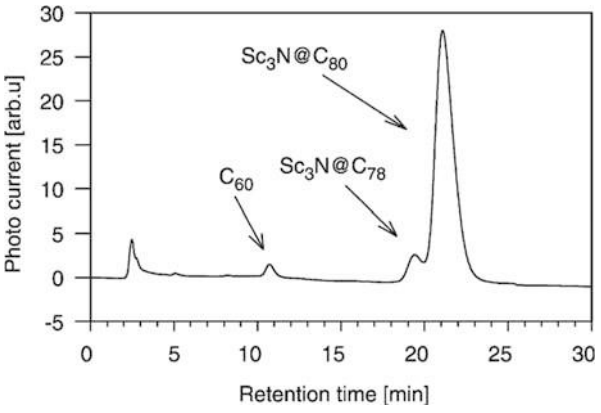

Fig. 4 HPLC of a $Sc_3N@C_{2n}$ soot extract as prepared by the reactive gas method at a Buckyprep column with toluene as an eluent. Copyright 2003 Elsevier Ltd

Moreover, to increase the product yield of NCFs, some metallic catalysts like Ni, Cu, and Fe_xN were doped into the graphite rods together with metal oxide, to improve the stability of the resulting arc and thus the yield of EMFs [29, 39, 42]. Stevenson et al. did a systematic research on the effect of Cu as catalyst on the product yield of empty fullerenes and $Sc_3N@C_{80}$, which showed that, with the dope of Cu at the optimal amount, the net yield of $Sc_3N@C_{80}$ can be increased by ca. three times (Fig. 5) [42].

Solid Nitrogen Source

In a standard arc-discharge process, the carbon rods filled with metallic oxide powder are supposed to be pretreated under high temperature to facilitate the formation of metal carbide. Dorn and coworkers modified the synthesis of NCFs by adding nitrogen-containing solid compound, calcium cyanamide (CaNCN), along with the metal oxide into the drilled carbon rods [40]. A proposed reaction scheme suggested the formation of the gaseous dinitrogen accompanied by the formation of solid-phase metal nitride during the arcing process. Similar to the NH_3 gas method, the relative yield of $Sc_3N@C_{80}$ was significantly increased up to 42%. However, the application of inorganic solid nitrogen source did not become a preferable choice for the synthesis of NCF, due to its low productivity and the relatively low yield, which is possibly ascribed to the high sensitivity of the abovementioned reactions to the traces of water and hydrocarbons [40].

In another effort to selectively synthesize NCFs, Stevenson and coworkers reported the "Chemically Adjusting Plasma Temperature, Energy, and Reactivity" (CAPTEAR) method by utilizing copper nitrate hydrate ($Cu(NO_3)_2{\cdot}2H_2O$) as an additive in the metallic mixture in 2007 [43]. In this report, experimental results suggested that copper nitrate hydrate decomposed when heated during the arcing process, which could tune the temperature and energy of the plasma environment, and plays a key role in the formation of variable fullerene species. In particular, the in situ release of gaseous nitrogen source (NO_x) and catalyst interaction of copper are supposed to exert a synergistic effect on the formation of NCFs as well as the empty fullerenes. In variable synthetic conditions, the percentage composition of C_{60} and $Sc_3N@C_{80}$ in the soot extract were inversely related, whereas those of C_{70} and higher empty-cage C_{2n} fullerenes remained almost unaffected. $Sc_3N@C_{80}$ with 96% purity was obtained in soot extracts (see Fig. 6. for detailed effect of the CAPTEAR). Additionally, in a following research, the mixed-metal NCF, $LaSc_2N@I_h\text{-}C_{80}$, was prepared using CAPTEAR method. A 10 wt% addition of $Cu(NO_3)_2{\cdot}2.5H_2O$ to a mixture of La_2O_3 and Sc_2O_3 decreases the amount of C_{60} and C_{70} found in soot extracts by an order of magnitude. By combining a stoichiometric twofold excess of La to Sc atoms in the arc reactor, fullerene extract containing a greater abundance of $LaSc_2N@I_h\text{-}C_{80}$ relative to $Sc_3N@I_h\text{-}C_{80}$ was obtained [44].

Dunsch and coworkers also investigated the effect of a series of solid organic compounds as the nitrogen source during the arcing processes. In the synthesis of EMFs based on a variety of metals (Dy, Sc, Y, Gd, and Lu, as well as mixed metals Sc/Dy, Sc/Gd, Sc/Lu, and Lu/Ce), guanidinium thiocyanate ($CH_5N_3{\cdot}HSCN$) and guanidinium hydrochloride ($CH_5N_3{\cdot}HCl$) were adopted respectively as the solid

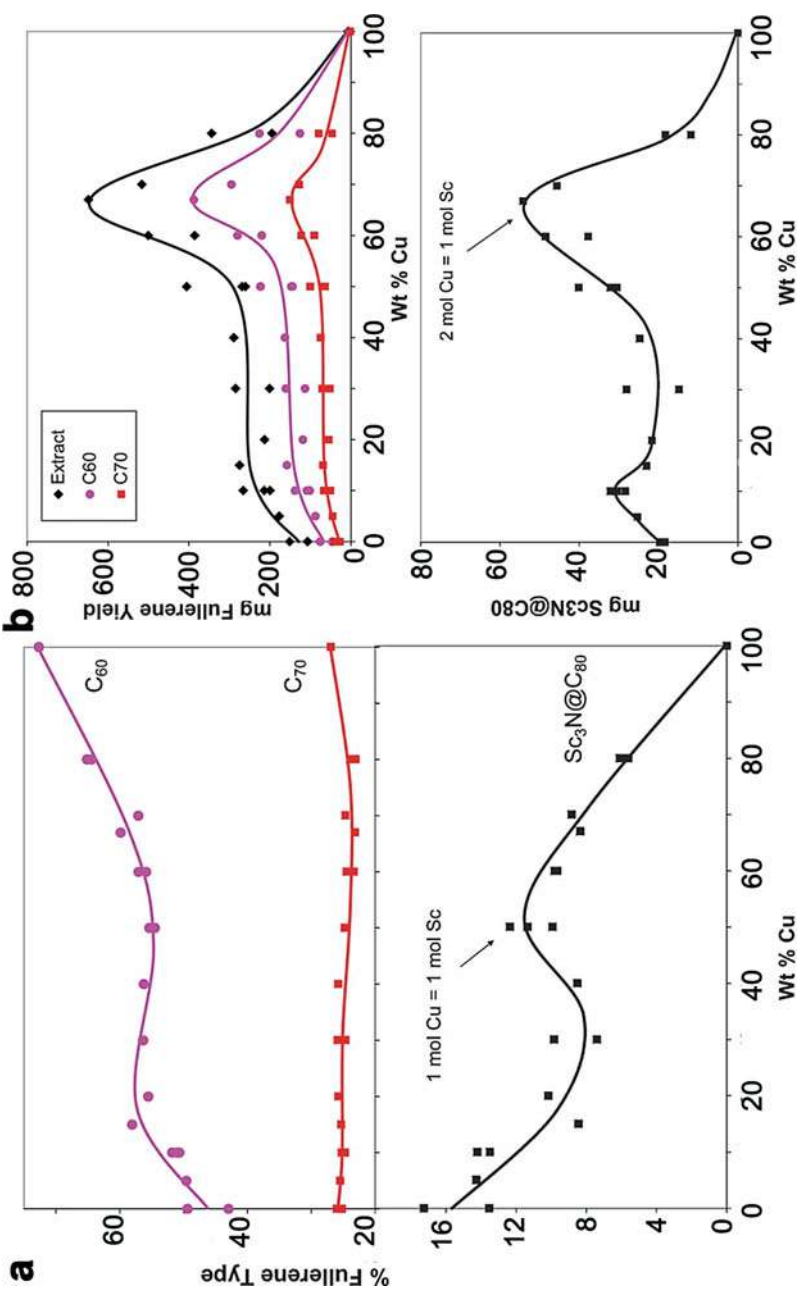

Fig. 5 The diagrams showing the effect of Cu as catalyst on (**a**) the relative yield of different types of fullerenes; (**b**) net mg quantity produced of extract, empty-cage fullerenes (up), and $Sc_3N@C_{80}$ (down). (Copyright 2007 The Royal Society of Chemistry)

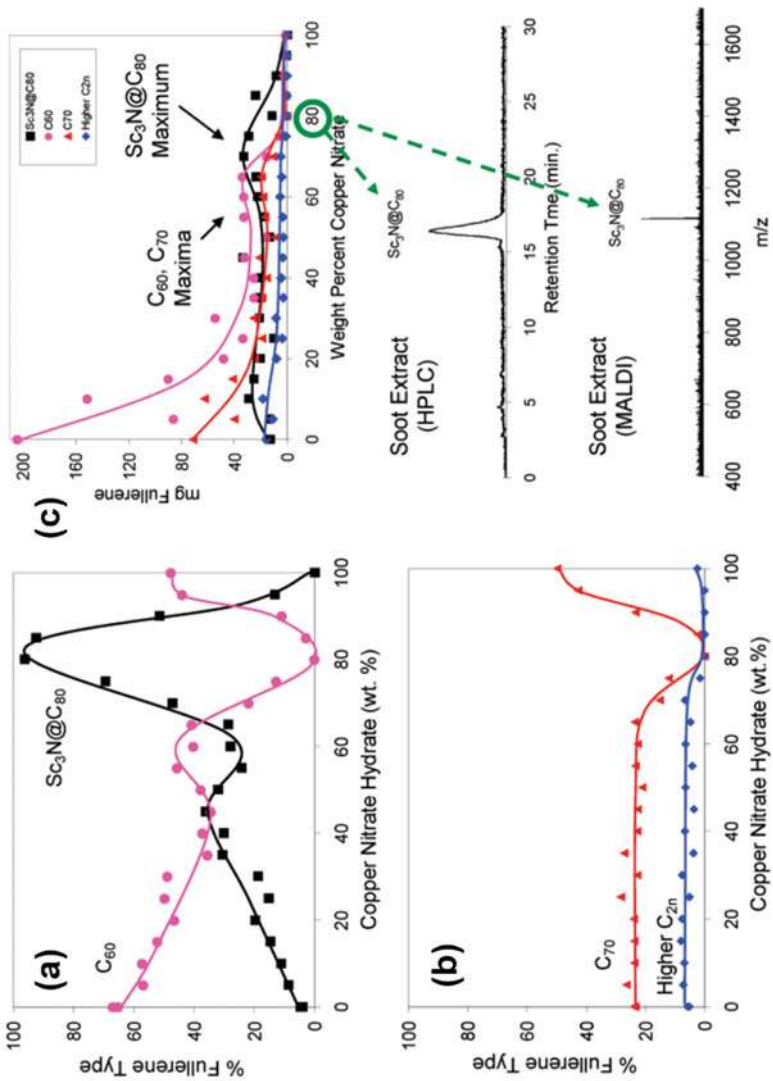

Fig. 6 Comparison of relative yield of (**a**) $Sc_3N@C_{80}$ and C_{60} versus the weight percentage of added $Cu(NO_3)_2{\cdot}2.5H_2O$ and (**b**) C_{70} and higher fullerenes; (**c**) Comparison of the mg yield of $Sc_3N@C_{80}$ and empty fullerenes, when the weight percentage of $Cu(NO_3)_2{\cdot}2.5H_2O$ reaches 80%, the relative yield of $Sc_3N@C_{80}$ surpasses 96%. (Copyright 2007 American Chemical Society

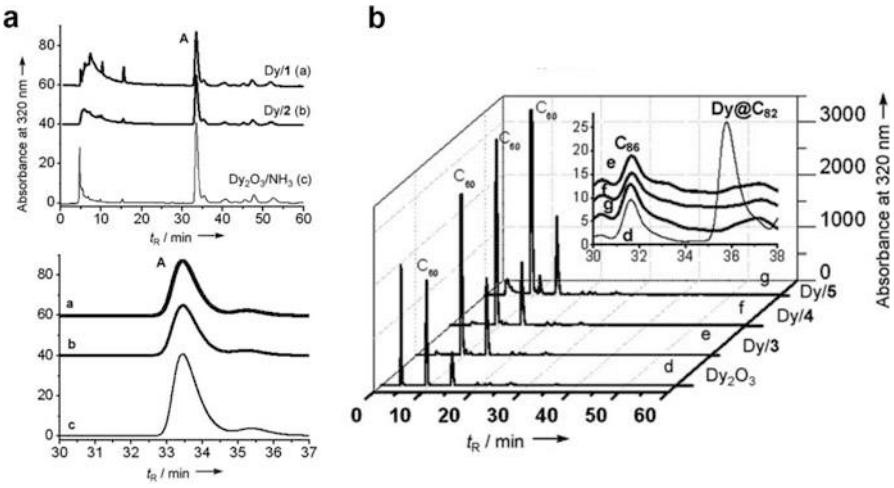

Fig. 7 The HPLC profiles comparing the effect of different solid nitrogen sources (**1**: guanidinium thiocyanate; **2**: guanidinium hydrochloride; **3**: 3,5-diamino-1,2,4-triazole; **4**: thiosemicarbazide; and **5**: ammonium thiocyanate;). (Copyright 2010 Wiley-VCH Verlag GmbH & Co. KGaA, Weinheim)

nitrogen sources, namely the "Selective Organic Solid " (SOS) method [45]. These solid nitrogen sources were mixed with the graphite powder and the metal oxide powder and were packed into the hollow graphite rods. Specifically for Dy-based EMFs, experimental results suggested that the introduction of the organic compound and Dy and C at a ratio of 2.5:1:10 exerts comparable effects as that of NH_3 with respect to the yield and selectivity for NCFs. In this work, Dunsch and coworkers also tried five different solid nitrogen sources for the synthesis of Dy-based EMFs following similar synthetic protocols. Figure 7 shows the different effects of these five nitrogen sources on the yield of Dy-based EMFs. It shows that when 3,5-diamino-1,2,4-triazole, thiosemicarbazide, and ammonium thiocyanate were utilized as nitrogen sources, no NCFs were found in the resulting fullerene extract, suggesting the high sensitivity of NCF formation to the plasma environment. However, with guanidinium thiocyanate and Dy/guanidinium hydrochloride as nitrogen sources, $Dy_3N@I_h$-C_{80} (marked as Fraction A) can be obtained with relatively high yield, which was only slightly lower than that obtained in the Dy_2O_3/NH_3 extract. Other nitrogen-rich organic compounds, melamine and urea, were also applied as effective organic solid nitrogen sources toward the synthesis of NCFs [46, 47].

Metal Carbide Clusterfullerenes (CCFs)

Metal carbide clusterfullerenes (CCFs) is a classical type of EMFs family in which the metallic carbide unit is embedded in the cage cavity. Up to now, the synthetic process of CCFs is mainly based on conventional direct current arc-discharge method, in which metallic oxide and graphite composite rods were vaporized in

the Krätschmer-Huffman generator under helium atmosphere [48–50]. The first CCF, $Sc_2C_2@C_{84}$, was reported by Shinohara and coworkers in 2001. In this report, Sc_2O_3/graphite composite rods were annealed at 1600 °C and vaporized in the direct current arcing reactor under a 17 L/min flow of helium at 50–100 torr [51]. In fact, as the metallic carbide can be directly generated from graphite and the metal oxide/alloy, the general synthetic conditions of CCFs are very similar to those of the conventional metallofullerenes, such as a static and optimum atmosphere. By using the abovementioned method, an abundance of CCFs have been successfully synthesized so far, including $Sc_2C_2@C_{68}$ [52], $Sc_2C_2@C_{2n}$ ($2n$ = 80-88) [53–60], $Sc_3C_2@C_{80}$ [61, 62], $Y_2C_2@C_{2n}$ ($2n$ = 82, 88-94) [63–66], $La_2C_2@C_{2n}$ ($2n$ = 90-104) [67–69], $Gd_2C_2@C_{2n}$ ($2n$ = 88-92) [70], $Tm_2C_2@C_{82}$ [71], $Ti_2C_2@C_{78}$ [72–75], $Dy_2C_2@C_{82}$ [76], $Er_2C_2@C_{2n}$ ($2n$ = 82, 92) [77, 78], $Lu_3C_2@C_{88}$ [79], and $ErYC_2@C_{82}$ [80]. The selected molecular structures of CCFs are presented in Fig. 13.

Metal alloys such as Sc/Ni, Y/Ni, and Er/Ni were also employed as the metal source in the preparation of metal carbide clusterfullerenes. Wang and coworkers vaporized the rods packed with a mixture of Sc/Ni_2 alloy and graphite powder in a weight ratio of 2:1 in a Krätschmer-Huffman generator at 200 torr He atmosphere. $Sc_4C_2@C_{80}$ and $Sc_2C_2@C_s$-C_{72} were successfully obtained by this method [81, 82]. $Sc_4C_2@C_{80}$ represents the first metallofullerene which exhibits a unique Russian-doll nesting structure [81]. In some cases, ^{13}C-labeled graphite powder was utilized in the synthesis of ^{13}C-enriched fullerenes for the ^{13}C NMR study. For instance, Dorn and coworkers utilized ^{13}C labeled graphite powder as the packed material and obtained a series of ^{13}C-labeled yttrium/gadolinium carbide EMFs [83, 84]. In the case of $Y_2C_2@C_1(51383)$-C_{84}, 99% ^{13}C-labelled amorphous carbon was packed inside the rod, which accounts for 25% of the mass of the total reacting carbon content (overall ^{13}C content is 26 wt% or 24 mol%) from the packed rod. As a result, ~10% ^{13}C enrichment was found in the fullerene product. The ^{13}C-enriched $Y_2C_2@C_1(51383)$-C_{84} represents the first pentalene-containing CCF determined by unambiguous X-ray structural characterization by then and the unique non-IPR $C_1(51383)$-C_{84} cage shed light on the top-down EMF formation mechanism [83].

Very recently, Lu's group synthesized an unprecedented titanium carbide clusterfullerene, $Ti_3C_3@I_h$-C_{80}, by evaporating graphite rods packed with mixed TiC and graphite powder under a 400 mbar He atmosphere and 100 A current [85]. In this work, instead of TiO_2, TiC was chosen as a precursor during the arc-discharge process, and the molar ratio of Ti/C was 1:10. $Ti_3C_3@I_h$-C_{80} represents the first structurally disclosed clusterfullerene with only transition metal Ti encaged inside a carbon cage. Inside the icosahedral C_{80} fullerene cage, the unexpected Ti_3C_3 cluster was found to adopt a novel coordination fashion by which the cyclopropane-like C_3 unit perpendicularly coordinates to the Ti_3 moiety.

Similar to the preparation of NCFs, reactive gas was also introduced into the arcing process to increase the product yield of specific CCFs. Popov and coworkers reported the modified arc-discharging synthesis of a mixed titanium-lutetium CCF, $TiLu_2C@I_h(7)$-C_{80}, by introducing various nitrogen sources such as ammonia(NH_3), melamine($C_3N_6H_6$), nitrogen(N_2), and methane(CH_4) in 2014 [86]. $TiLu_2C@I_h(7)$-C_{80}

was initially detected in the presence of NH_3 and was a minor product under $C_3N_6H_6$/N_2 conditions. Synthetic experiments were then performed in the absence of nitrogen source with only He atmosphere but no $TiLu_2C@I_h(7)$-C_{80} was detected. However, they surprisingly found out that $TiLu_2C@I_h(7)$-C_{80} appeared to be one of the main EMF products when 12 mbar methane (CH_4) was added into 238 mbar He atmosphere. Accordingly, a reactive atmosphere technique with methane (CH_4) was considered as the optimum method for synthesizing $TiLu_2C@I_h(7)$-C_{80}. Subsequently, the same group reported the arc-discharge synthesis of a series of M-Ti CCFs $M_2TiC@C_{80}$ (M = Y, Nd, Gd, Dy, Er, Lu) as well as $Dy_2TiC_2@C_{80}$ and showed that the application of CH_4 dramatically increased the selectivity of lanthanide-Ti CCFs [87]. Under the optimized conditions, pure $M_2TiC@C_{80}$ (Lu, Dy, and Gd) could be obtained by a single HPLC separation step. A systematic investigation was then performed by the same group on the influence of both metal oxide and the CH_4 atmosphere on the resulting clusterfullerene products. It revealed that the Sc-Ti/CH_4 system helped the formation of $Sc_2TiC@C_{2n}$ ($2n$ = 68, 78, 80) and $Sc_2TiC_2@C_{80}$ clusterfullerenes, the Sc/CH_4 system contributed to Sc-based CCFs as well as $Sc_3CH@C_{80}$, and the Ti/CH_4 system produced only empty fullerenes (see Fig. 8 for an overview of the favored species under different synthetic conditions) [88].

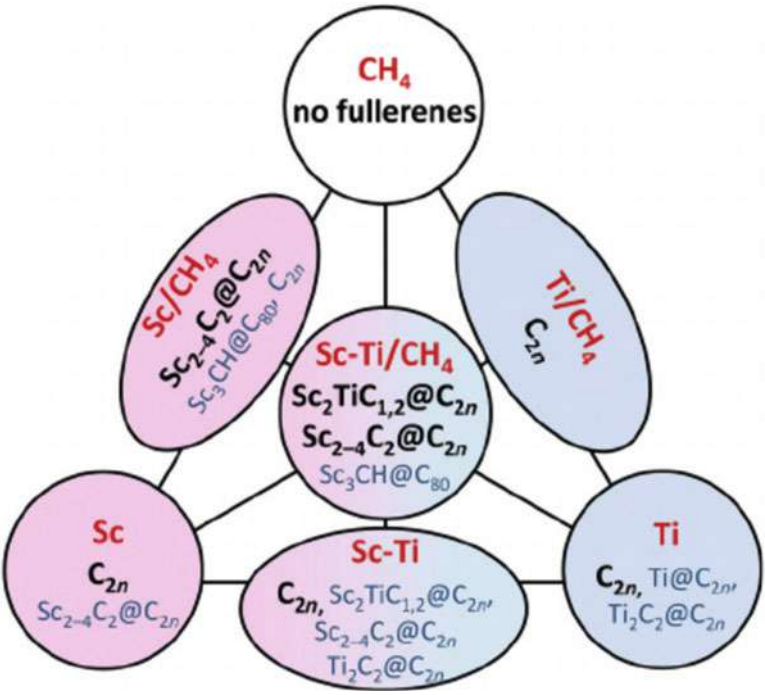

Fig. 8 Overview of the EMF syntheses conditions and resulting fullerenes (the amount of graphite and helium gas is constant for all syntheses). Initial conditions (metals and reactive gas) are printed in red, the main fullerene products in black, and the minor fullerene products in blue. (Copyright 2016 Wiley-VCH Verlag GmbH & Co. KGaA)

Metal Oxide/Sulfide Clusterfullerenes (OCFs and SCFs)

In the past decade, great advances have been made in the study of metal oxide/sulfide clusterfullerenes (OCFs and SCFs). In the early study of EMFs, air was thought to have a negative effect on the production of fullerenes. However, Stevenson and coworkers innovatively introduced flowing air as reactive gas during the arc-discharge process and found out that various types of OCFs, such as $Sc_4O_2@C_{80}$, $Sc_4O_3@C_{80}$, and $Sc_2O@C_{82}$, could be successfully synthesized during this process [89–91]. In these studies, the air flow was set to 6 torr/min and experiments were conducted under a dynamic flow of He/air at 300–400 torr. In particular, they found that the production of $Sc_4O_2@C_{80}$ was improved with the increase of the air flow rate and determined that a flow of 12 torr/min is optimal. Furthermore, the CAPTEAR method was introduced to determine the effect of copper nitrate ($Cu(NO_3)_2$) on the formation of $Sc_4O_2@C_{80}$. Though detailed mechanism was not clarified, the results indicated that increasing content of copper nitrate dramatically improved the yield of $Sc_4O_2@C_{80}$, likely due to the impact of NO_x from the decomposed copper nitrate, while the addition of pure metallic copper did not show any improvement [89]. In 2014, Feng and Chen et al. expanded the OCF family by developing a new synthetic method to produce OCFs, and instead of O_2 or air, CO_2 was introduced into the Krätschmer-Huffman generator as the oxygen source. The DC arc discharging was carried out under 3×10^4 pa He/CO_2 atmosphere (the ratio of He/CO_2 is 9/1 in volume) and current of 100 A [92]. Different from the OCFs obtained in Stevenson's work, which are mostly based on C_{80} cage, an extensive family of $Sc_2O@C_{2n}$ ($2n$ = 35-47) was produced successfully by this method [92]. Controlled experiments were also performed in which only a He/air atmosphere was used but the products were mainly empty cages and NCFs. The results revealed that the introduction of CO_2 has significant contribution to the formation of OCFs. Utilizing this method, a variety of OCFs such as $Sc_2O@C_{2n}$ ($2n$ = 70, 76, 80 and 82) [93–96], $Sc_3O@C_{80}$ [97], $Ho_2O@C_{2n}$ ($2n$ = 74, 84) [98, 99], $Dy_2O@C_{82}$ [100], and $ScGdO@C_{3v}(8)$-C_{82} [101] were synthesized and characterized.

As mentioned above, guanidinium thiocyanate (CH_5N_3·HSCN) was adopted as a solid nitrogen source for the synthesis of NCFs. Dunsch and coworkers also utilized this compound as the solid sulfur source for the synthesis of sulfide clusterfullerenes (SCFs). In 2010, Dunsch, Yang, and coworkers reported the first detection of SCFs, i.e., $M_2S@C_{82}$ (M = Sc, Y, Dy, Lu) by modified Krätschmer-Huffman method using the CH_5N_3·HSCN (GT)/metal/graphite powder mixture [102]. Herein, an optimized molar ratio of GT/metal/graphite powder mixture of 2.5:1:10 was utilized. Soon afterwards, Echegoyen et al. reported a novel method for the synthesis of SCFs by the introduction of SO_2 into the arcing reactor, despite that it was proposed by the former report that the presence of oxygen as in many gaseous compounds of sulfur would interfere with the formation of sulfide structure. Interestingly, different from the results from the solid sulfur source method, in which only the C_{82} cage–based SCFs were detected, it was found that the introduction of SO_2 resulted in the successful synthesis of an extensive family of $Sc_2S@C_{2n}$ ($2n$ = 80-100). In particular, two isomers of the most abundant $Sc_2S@C_{82}$ were isolated and characterized

[103]. In the synthesis of these compounds, a mixed atmosphere of He (200 torr)/SO_2 (20 torr) was used. Following the SO_2 gas source method, the same group succeeded in the synthesis and characterization of two non-isolated pentagon rule SCFs $Sc_2S@C_s(10528)$-C_{72} and $Sc_2S@C_2(7892)$-C_{70} [104, 105]. Moreover, $Ti_2S@C_{78}$, featuring the first sulfide clusterfullerene with non-rare-earth metals inside the cage, was also successfully synthesized in a conventional Krätschmer-Huffman reactor using a TiO_2–graphite powder mixture in a weight ratio of 1:4 in a mixture of helium (200 torr) and SO_2 (20 torr) atmosphere [106]. Figure 13 shows the molecular structures of typical OCF and SCF.

Metal Cyanide Clusterfullerenes (CYCFs)

It is used to be considered improbable for a single metal atom to form an encapsulated metal cluster in the fullerene cage. Yang et al., however, broke this doctrine by the successful synthesis of the first CYCF, $YCN@C_s(6)$-C_{82}, using a modified Krätschmer-Huffman DC arc-discharge method [107]. In this method, TiO_2, though not involved in the resulting EMF structure, was added into the graphite rods along with Y_2O_3 and graphite powder with a molar ratio of 1:1:15 (Y:Ti:C). The corresponding graphite rods were vaporized under the 10 mbar N_2 and 400 mbar He atmosphere [107]. Reference synthetic experiments were also carried out by removing TiO_2 but keeping the other conditions unchanged. It is rather apparent that, as shown in Fig. 9, the resulting mass peak of 1099 corresponding to a molecular form of YNC_{83} appeared only in the $Y_2O_3/TiO_2/N_2$ extract and was absent from the Y_2O_3/N_2 crude extract. These results highlighted the key role of TiO_2 in the formation of Y-based CYCFs, though the mechanism behind it remained unclear. Similarly, several investigations of the effect of TiO_2 on the formation of Tb-based of CYCFs were also conducted. Interestingly, the mass peak at m/z = 1169, which

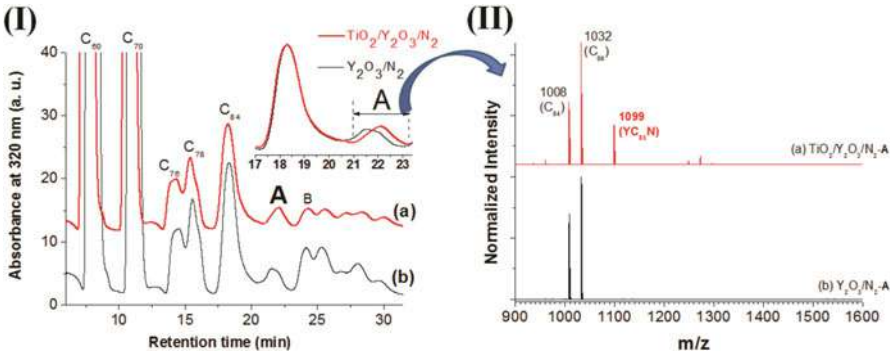

Fig. 9 (I) Chromatograms of the fullerene extract mixtures synthesized from Y_2O_3/TiO_2 with N_2 addition ($Y_2O_3/TiO_2/N_2$, a), Y_2O_3 with N_2 addition (Y_2O_3/N_2, b). 20 × 250 mm 5PYE column; flow rate 15.0 mL/min; injection volume 15 mL; toluene as eluent (mobile phase); 25 °C. (II) Negative-ion laser desorption time-of-flight (LD-TOF) mass spectra of the fraction **A** collected from $Y_2O_3/TiO_2/N_2$ (**a**) and Y_2O_3/N_2 (**b**). (Copyright 2013 Springer Nature)

represents the signal of $TbNC_{83}$, appeared in both Tb_4O_7/N_2 and $Tb_4O_7/TiO_2/N_2$ conditions, though the addition of TiO_2 seems to increase the relative yield of $TbCN@C_{82}$ as shown in Fig. 10. This indicates that TiO_2 was not essential for the formation of Tb-based CYCFs, suggesting that the formation of CYCFs might depend sensitively on the nature of the encapsulated metal materials [48, 108–110]. Subsequently, Yang and coworkers obtained many other examples of CYCFs with the same synthetic method, such as $TbCN@C_s(6)$-C_{82} [109], $TbCN@C_{2v}(9)$-C_{82} [109], $TbCN@C_{2v}(19138)$-C_{76} [110], $YCN@C_{2v}(19138)$-C_{76} [110] as well as a series of trifluoromethyl derivatives of CYCFs, $YCN@C_2(13)$-$C_{84}(CF_3)_{16/18}$ [111], $YCN@D_{2d}(23)$-$C_{84}(CF_3)_{16/18}$ [111], and $YCN@C_s(6)$-$C_{82}(CF_3)_{16/18}$ [112]. As for the derivatives, the starting pristine fullerene compound were firstly accessed by the conventional DC arc-discharge method and the resulting $YCN@C_{2n}$-containing subfractions from HPLC (2–3 mg) were treated with gaseous CF_3I in quartz ampoules around 450 °C for 2 h. Figure 11 displays the single-crystal X-ray structure of $YCN@C_s(6)$-$C_{82}(CF_3)_{16}$ and $YCN@C_s(6)$-$C_{82}(CF_3)_{18}$. Very recently, the same group reported the synthesis of three isomers of $DyCN@C_{82}$ [113]. In this work, they utilized a low-cost and ancient pigment, Prussian blue ($Fe_4[Fe(CN)_6]_3$), as an efficient dual-functional solid cyanide/nitrogen source, providing the simplified but high-yield syntheses of novel Dy-based CYCFs. They also designed the control experiments in which two analogous ferrocyanide and ferricyanide complexes $K_4[Fe(CN)_6]_3$ and $K_3[Fe(CN)_6]$ were applied to elucidate the roles of the Fe(II) and Fe(III) cations within $Fe_4[Fe(CN)_6]_3$ on the formation of CYCFs, and proposed the plausible thermal decomposition mechanism of $Fe_4[Fe(CN)_6]_3$ during DC arc-discharge process. During the experiments, the graphite rods filled with a mixture of Dy_2O_3, $Fe_4[Fe_3(CN)_6]$, $K_3[Fe(CN)_6]$, or $K_4[Fe(CN)_6]$ and graphite powder with a certain molar ratio were subjected to DC arc-discharging reactor under 400 mbar He atmosphere and an input current of 120 A and the reference discharging experiment by using 10 mbar N_2 as the nitrogen source was also carried out. It turned out that the application of $Fe_4[Fe(CN)_6]_3$ with the Dy:[CN]:C molar ratio of 1:1:15 is the optimal synthetic condition for these Dy-based CYCFs as the sum yield of $DyCN@C_{2n}$ ($2n = 76, 82$) was about 2.8 times higher than that obtained by using gaseous N_2 as compared in Table 1 and Fig. 12. These investigations, undoubtedly, will shed light on the low-cost and high-yield syntheses of rarely accessible endohedral fullerenes to their wide applications.

Metal Hydrocarbon Clusterfullerenes (HCCFs)

As discussed above, CH_4 not only can effectively boost the selectivity of arc-discharge synthesis of Ti-containing CCFs but also plays a key role in the synthesis of metal hydrocarbide clusterfullerenes (HCCFs). The first HCCF, $Sc_3CH@C_{80}$ was synthesized and isolated by Dunsch and coworkers in 2007 using a modified Krätschmer-Huffman DC arc-discharge strategy with a mixture of 200 mbar He and 20 mbar reactive CH_4 gas atmosphere [114]. In 2014, Wang et al. reported the synthesis and characterization of another HCCF, $Sc_4C_2H@I_h$-C_{80}, by arc discharging the metal-doped rods under the atmosphere of 6 torr H_2 and 194 torr He [115]. In particular, they discovered that, as the hydrogen ratio increased,

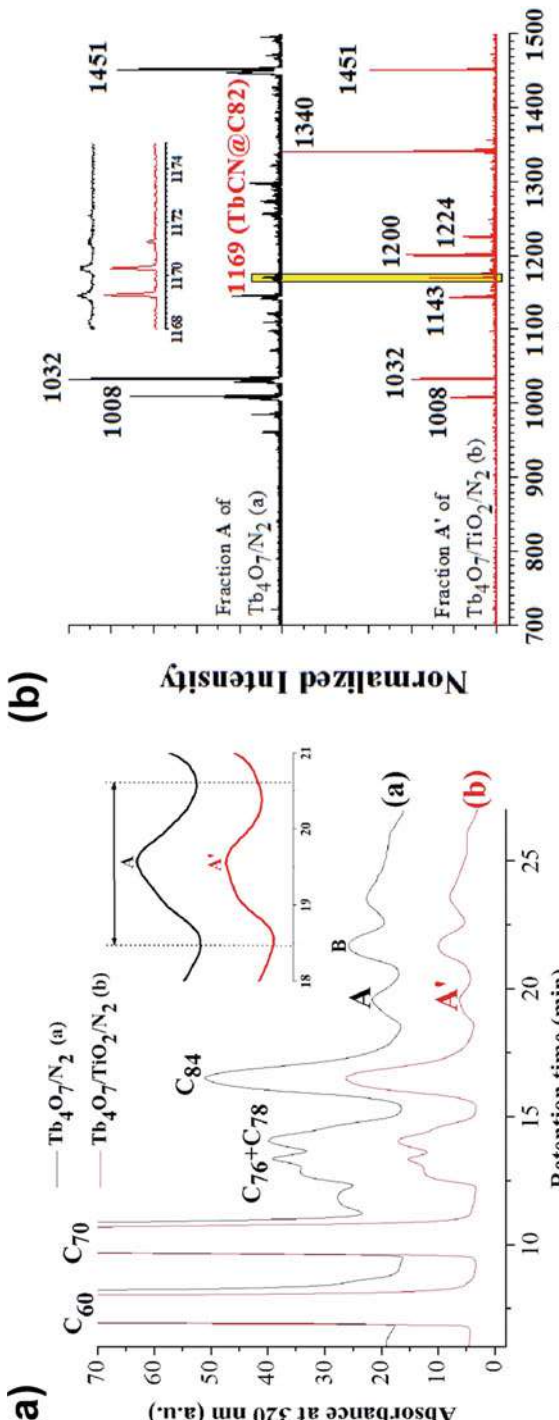

Fig. 10 (**a**) Chromatograms of the fullerene extract mixtures synthesized from Tb_4O_7 with addition of N_2 (Tb_4O_7/N_2) and Tb_4O_7/TiO_2 with addition of N_2 ($Tb_4O_7/TiO_2/N_2$). HPLC conditions: 20 × 250 mm 5PYE column; flow rate: 15 mL·min^{-1}; injection volume: 15 mL; toluene as eluent; 40 °C. Fraction B mainly contains Tb@C_{82} and Tb_2C_2@C_{82}. Inset: Enlarged chromatographic region of 18–21 min containing fraction A (A'). (**b**) Positive-ion laser desorption time-of-flight (LD-TOF) mass spectra of fractions A and A' collected from Tb_4O_7/N_2 (curve a) and $Tb_4O_7/TiO_2/N_2$ (curve b), respectively. Inset: Enlarged spectra in the region of m/z = 1168–1175. The mass peaks at 1143, 1340, and 1451 in curve (b) correspond to endohedral fullerenes Tb@C_{82}, $TiTb_2N$@C_{80}, and Tb_3N@C_{80}, respectively, other mass peaks (1008, 1032, 1200, and 1224) are assigned to empty fullerenes. (Copyright 2014 American Chemical Society)

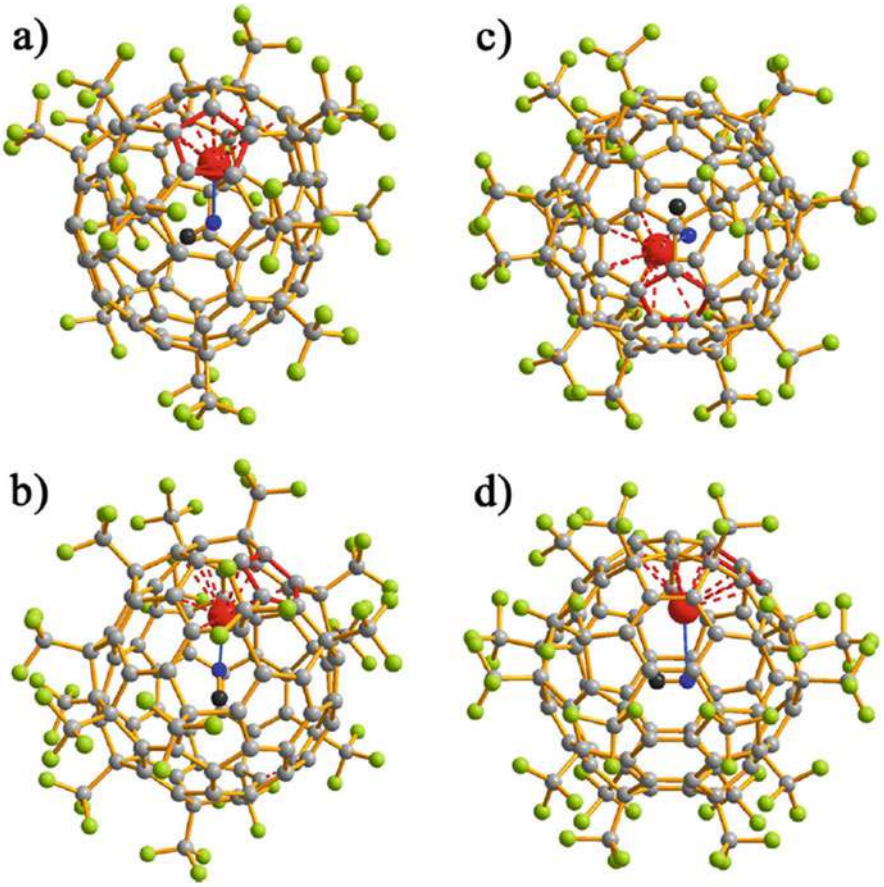

Fig. 11 Two views of the YCN@C_s(6)-$C_{82}(CF_3)_{16}$ (**a** and **b**) and YCN@C_s(6)-$C_{82}(CF_3)_{18}$ (**c** and **d**) molecules. The fragments involved in Y coordination are highlighted with red; N and C atoms of the CN groups are shown in blue and black, respectively. (Copyright 2016 American Chemical Society)

the yield of $Sc_4C_2H@I_h$-C_{80} increased simultaneously, highlighting the key role of H_2 in this synthesis process. $Sc_4C_2H@I_h$-C_{80} was found to be a stable paramagnetic metallofullerene molecule whereas its structurally closely related CCF $Sc_4C_2@I_h$-C_{80} is diamagnetic. Thus, it was proposed that implanting the H-atom into the encapsulated clusters would be feasible for preparing stable paramagnetic metallofullerenes.

Metal Carbonitride Clusterfullerenes (CNCFs)

In 2010, Wang et al. reported the successful synthesis of a series of metallic carbonitride clusterfullerenes (CNCFs) [116]. They adopted Sc/Ni_2 alloy as the metal source, the weight ratio of Sc/Ni_2 alloy and graphite powder in 2:1, and

Table 1 The relative yields and retention times of three isomers of DyCN@C_{82}

Extract (Fraction)		DyCN@C_2(5)-C_{82} (**A-3**)	DyCN@C_s(6)-C_{82} (**A-4**)	DyCN@C_{2v}(9)-C_{82} (**A-5**)
Isomer label		I	II	III
Retention time (*tret*/min)		22.63–26.86	25.46–29.56	26.37–30.82
Relative yield	Dy_2O_3/N_2	21.7%	10.6%	9.9%
	$Dy_2O_3/Fe_4[Fe(CN)_6]_3$	29.2%	15.1%	16.8%
	$Dy_2O_3/K_3[Fe(CN)_6]$	30.1%	15.7%	14.7%
	$Dy_2O_3/K_4[Fe(CN)_6]$	34.1%	17.0%	19.15%

used mixed atmosphere of 6 torr N_2 and 194 torr He. Though the synthetic method is conventional, three novel clusterfullerenes $Sc_3NC@I_h(7)$-C_{80}, $Sc_3NC@C_2(22010)$-C_{78}, and $Sc_3(C_2)(CN)@I_h(7)$-C_{80} were isolated and characterized in this work for the first time [116–118]. $Sc_3NC@I_h(7)$-C_{80} features an unprecedented planar quinary cluster inside the C_{80} cage, as presented in Fig. 13 and $Sc_3(C_2)(CN)@I_h(7)$-C_{80} represents the sole example in EMF family which could encapsulate the carbide/cyanide alloyed moiety. Figure 13 shows the typical molecular structure of representative cluster fullerenes including the CCF $Gd_2C_2@C_1(51383)$-C_{84}, the OCFs $Dy_2O@C_{3v}(8)$-C_{82} and $Sc_4O_3@I_h(7)$-C_{80}, the SCF $Sc_2S@C_s(10528)$-C_{72}, the CYCF $YCN@C_{2v}(19138)$-C_{76} as well as the CNCF $Sc_3CN@I_h(7)$-C_{80}.

Actinide Endohedral Metallofullerenes

Actinide endohedral metallofullerenes represent a unique branch in EMF family. The original exploration of actinide EMFs could be dated back to 1992 when Smalley et al. traced a series of uranium-based EMFs with the laser vaporization method [119]. Although efforts were devoted to the encapsulation of other actinides inside fullerene cages [120–122], it was not until 2017 that the first actinide EMF, $Th@C_{3v}(8)$-C_{82}, was macroscopically synthesized and structurally identified by Chen et al. [123, 124] Actinide EMFs were prepared by the DC arc-discharge method in which the core-drilled graphite rods, packed with ThO_2/graphite powder or U_3O_8/graphite powder mixture, were vaporized in the Krätschmer-Huffman arcing chamber under the helium atmosphere. The collected soot was refluxed in carbon disulfide (CS_2) or chlorobenzene under noble gas atmosphere protection. Conventional multistage HPLC separation procedures were employed to isolate and purify these actinide EMFs. Although there is no major modification on the synthetic strategy, the molecular structures and the bonding motifs of the actinide fullerenes obtained from the conventional arc-discharging method turned out to be very different from those of the known lanthanide-based EMFs, due to the various charge states and complicated electronic structures of actinide elements. Chen, Echegoyen, and coworkers synthesized and characterized various types of actinide EMFs based on thorium and uranium, i.e., $Th@C_{3v}(8)$-C_{82}, $U@D_{3h}$-C_{74} [125], $U@C_2(5)$-C_{82} [125], $U@C_{2v}(9)$-C_{82} [125], $U@C_1(17418)$-C_{76} [126], $U@C_1(28324)$-C_{80} [126],

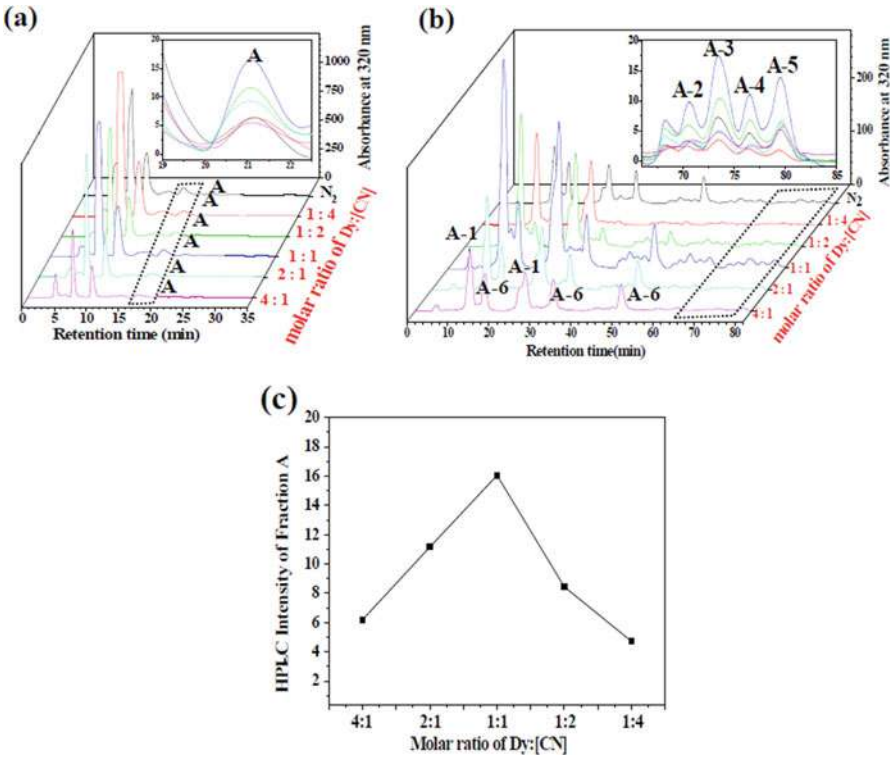

Fig. 12 HPLC chromatograms of $Dy_2O_3/Fe_4[Fe(CN)_6]_3$ extracts with different Dy:[CN] molar ratios and HPLC intensity of fraction A. (**a**) HPLC chromatograms of $Dy_2O_3/Fe_4[Fe(CN)_6]_3$ fullerene extracts with different Dy:[CN] molar ratios (20 mm × 250 mm 5PYE column; flow rate 15.0 mL min^{-1}; injection volume 15 mL; toluene as the eluent (mobile phase); 40 °C). The dotted rhombus marks the enlarged region containing fraction **A**. Inset: the enlarged region of retention time ranging from 19–23 min. (**b**) Recycling HPLC chromatograms of fraction **A** obtained with different Dy:[CN] molar ratios (10 mm × 250 mm Buckyprep-M column; flow rate 5.0 mL min^{-1}; injection volume 5 mL; toluene as the eluent (mobile phase); 40 °C). The dotted rhombus marks the enlarged region containing subfractions **A-2** to **A-6**. Inset: the enlarged region of retention time ranging from 66–85 min. (**c**) Dependence of HPLC peak intensity of fraction **A** on the Dy:[CN] molar ratio. (Copyright the Partner Organisations 2021)

Th@C_1(28324)-C_{80} [126], Th@C_1(11)-C_{86} [127], Th@T_d(19151)-C_{76} [128], U_2@I_h(7)-C_{80} [129], Th_2@I_h(7)-C_{80} [130], U_2C@I_h(7)-C_{80} [131], U_2C_2@I_h(7)-C_{80} [132], U_2C_2@D_{3h}(5)-C_{78} [132], Sc_2CU@I_h(7)-C_{80} [133], and U_2N@I_h(7)-C_{80} [134]. The molecular structures of these actinide EMFs have been shown in Fig. 14. Among them, Th@C_{3v}(8)-C_{82} was found to be the first isolated metallofullerene with four electrons transferred from the metal to the cage, differing dramatically from the lanthanide-based metallofullerenes. A novel U_2C@I_h(7)-C_{80} encapsulating an unprecedented U=C=U cluster was also obtained [131]. In U_2C_2@I_h(7)-C_{80} and U_2C_2@D_{3h}(5)-C_{78}, both U_2C_2 clusters transfer six electrons to the cage, different

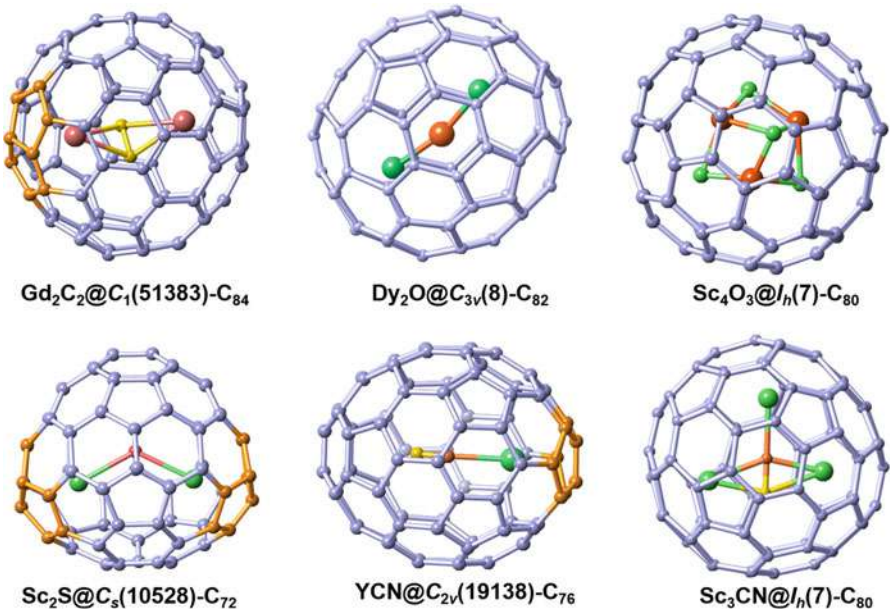

Fig. 13 Single crystal structure of the selected representative cluster EMFs

from the four electron transfer of lanthanide-based M_2C_2, mainly due to the IV oxidation state of U [132]. Moreover, for U@C_1(17418)-C_{76}, U@C_1(28324)-C_{80}, Th@C_1(28324)-C_{80}, and Th@C_1(11)-C_{86}, the encapsulated tetravalent metal ions and the resulting strong host-guest interactions were found to be responsible for the stabilization of these novel chiral fullerene cages. As discussed in the "Nitride Cluster Fullerene" section, the reactive gaseous nitrogen source NH_3 can play an effective role for the synthesis of NCFs. An attempt to achieve the actinide NCFs was also successful where an unexpected actinide fullerene $U_2N@I_h(7)$-C_{80} was synthesized under a 200 torr helium atmosphere with the addition of 1 torr NH_3 by Chen and coworkers in 2020 [134]. Interestingly, $U_2N@I_h(7)$-C_{80} is by far the first endohedral fullerene that violates the well-established TNT stoichiometry for nitride clusterfullerenes and features two U=N bonds with uneven bond distances of 2.058(3) Å and 1.943(3) Å, respectively. It is noteworthy that the dimetallic EMF featured a strong covalent actinide-actinide bond inside the fullerene cage, $Th_2@I_h(7)$-C_{80}, which was also successfully obtained using the typical direct current arc-discharge method very recently [130]. The intriguing structural features and physicochemical properties of actinide endohedral metallofullerenes display remarkable differences from the known lanthanide-based analogues. Thus, continuous synthetic endeavor to explore these intriguing actinide fullerene compounds will not only deepen the understanding of fundamental fullerene chemistry, but also provide new insights into the fullerene formation mechanism and actinide bonding motifs.

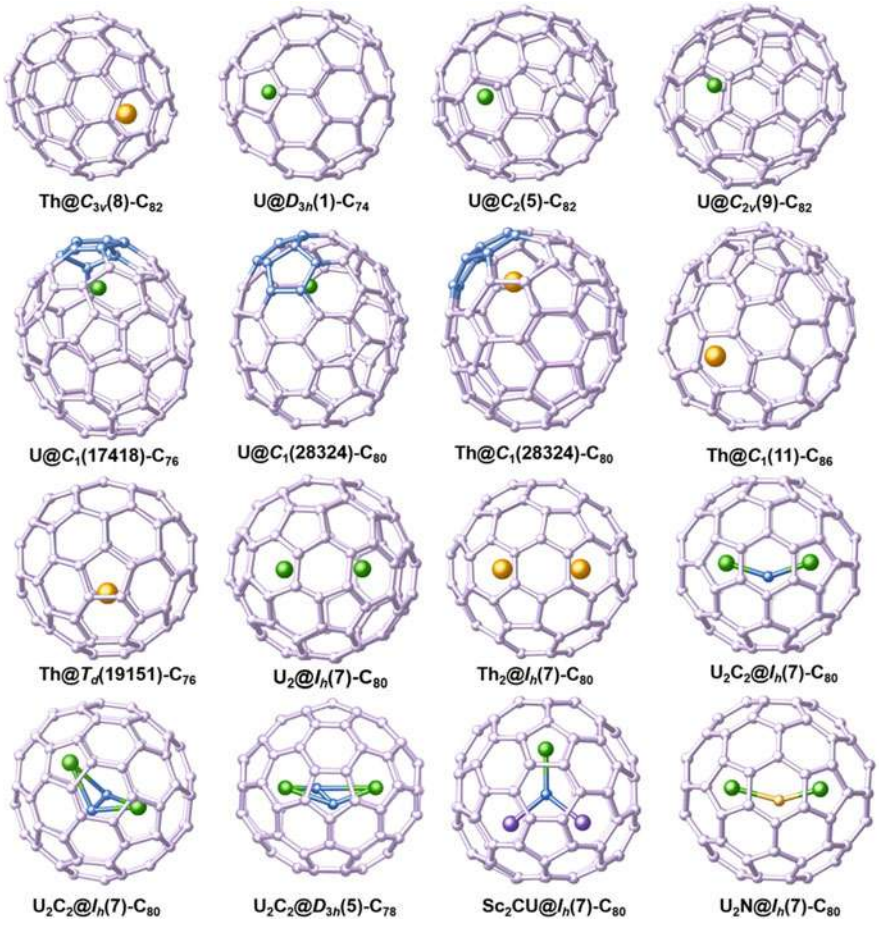

Fig. 14 Single crystal X-ray structures of the actinide EMFs. The U atoms are highlighted in green; the Th atoms are highlighted in orange, and the adjacent pentagons of the cages are highlighted in blue

Stabilization by Chemical Functionalization

Some EMF species, although essentially formable in the arcing process and can be detected by mass spectroscopy, are thermodynamically instable under ambient conditions. These "missing" species, highly reactive and insoluble in their pristine form, could hardly obtained from the carbon soot as isolated compound by conventional extraction and HPLC methods. Hence, exohedral derivatization were adopted as desirable method to capture and stabilize these unique structures from raw soot. The first successful synthesis of exohedral adducts of EMFs, i.e., La@C_{82}, were reported by Akasaka and coworkers in 1995 [135]. To date, two derivative strategies have been proved to be effective in stabilizing these missing EMF species [136]. The

first introduced method is in situ derivation of unstable EMFs during extraction process. Nagase, Akasaka, and coworkers reported the formation of La@D_{3h}(1)-$C_{74}(C_6H_3Cl_2)$ by a radical coupling reaction between La@C_{74} and dichlorophenyl radicals, generated from 1,2,4-trichlorobenzene (TCB) when refluxing the extract of soot containing lanthanum EMFs [137]. Thereafter a series of unstable EMFs, such as La@C_2(10612)-C_{72} [138], La@C_{2v}(3)-C_{80} [139], and La@C_{3v}(7)-C_{82} [140], have also been obtained as their dichlorophenyl derivatives by the TCB extraction method. Recently, Y_2@C_{80} and Dy_2@C_{80} were obtained in the form of air-stable benzyl monoadducts by Popov and coworkers. These two products were formed by DMF reflux reduction of the EMFs and subsequent reaction of the as-reduced EMF anions with benzyl bromide [141]. Both of the EMF monoadducts, i.e., Y_2@$C_{80}(CH_2Ph)$ and Dy_2@$C_{80}(CH_2Ph)$, feature an unpaired electron trapped between metal ions. Figure 15 shows the synthetic route of M_2@$C_{80}(CH_2Ph)$ (M = Dy/Y) and the molecular structure of Dy_2@$C_{80}(CH_2Ph)$.

In situ trifluoromethylation of reactive EMFs during the arcing process is another feasible way for the capturing of some of the long-sought-after "missing" EMFs. Shinohara et al. demonstrated that carbon arc production in the presence of polytetrafluoroethene (PTFE) could lead to direct generation of trifluoromethyl derivatives of the corresponding EMFs. During this process, the temperature is high enough to evaporate PTFE as well as metal and carbon. Thus, by placing PTFE (10 g) near the arc zone, some intrinsically unstable EMF species were stabilized in the form of their trifluoromethylation derivatives, including Y@$C_{70}(CF_3)_3$, Y@$C_{72}(CF_3)$, two isomers of Y@$C_{74}(CF_3)$, and Y@$C_{74}(CF_3)_3$. The pristine forms of these EMFs typically have open-shell electronic structures. The addition of the CF_3 groups results in the corresponding stable derivative compound with closed-shell structures [142]. Very recently, Gd@C_{60} and La@C_{60} were stabilized and separated for the first time by the in situ trifluoromethylation during the arc-discharge synthesis of the metallofullerenes [143]. In this work, the arc-discharge reactor is modified for polytetrafluoroethene (PTFE) rods (40 g) to be placed near the discharge area. The high-temperature arc discharge efficiently evaporates polytetrafluoroethylene (PTFE) placed near the arc zone to produce CF_3 radicals to facilitate the in situ CF_3-functionalization, capturing and stabilizing the transiently formed Gd@C_{60} and La@C_{60}. Figure 16 shows the schematic diagram of the exclusively designed arc reactor and the molecular structure of one isomer of Gd@$C_{60}(CF_3)_5$.

Laser Ablation (or Laser Vaporization) Method

Soon after the discovery of C_{60}, laser ablation (or laser vaporization) method was adopted for the first detection of EMFs [1]. Pioneered by Smalley and coworkers, mass signals of a series of endohedral metallofullerenes, including La@C_{60}, La@C_{74}, and La@C_{82}, were observed with the laser ablation technique [144]. In a typical laser ablation experiment, metal oxide/graphite composite rods were placed in a furnace at 1200 °C under a flow of argon or helium gas. A Nd:YAG laser at 532 nm was focused on the target rods. Fullerene compounds were thus produced upon the laser vaporization and then carried away by the flowing gas carrier. In the

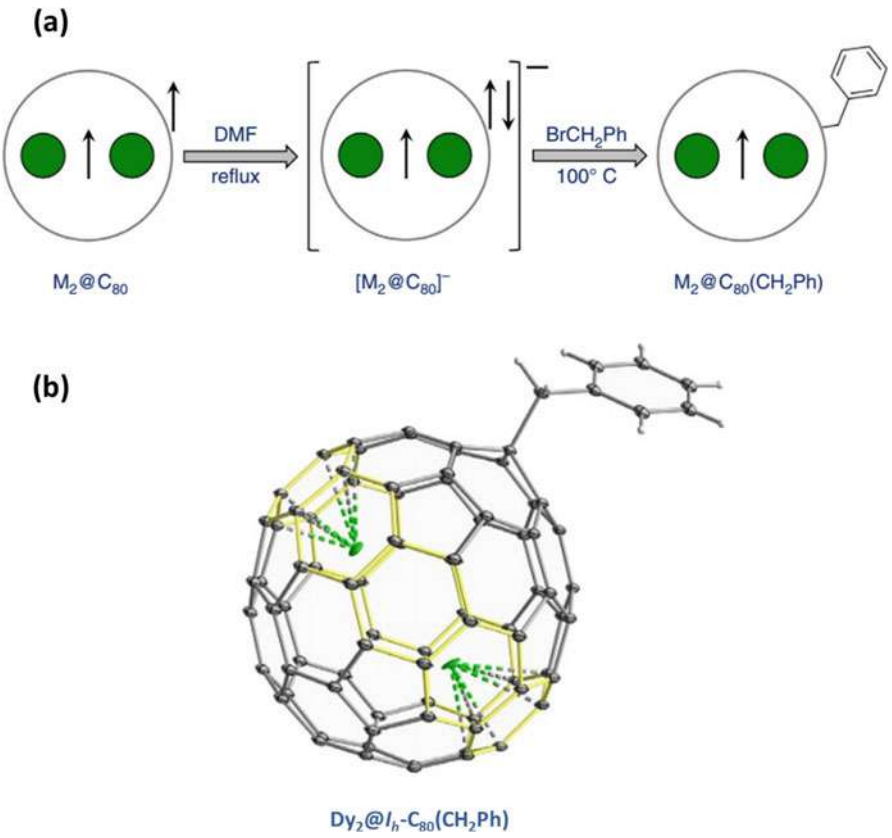

Fig. 15 (**a**) Description of the synthetic route for $M_2@C_{80}$ derivative with single electron M–M bond (M = Y, Dy): $M_2@C_{80}$ molecules synthesized by arc-discharge method are present in triplet state in the soot; upon reduction with DMF, soluble monoanions are formed, the surplus electron goes to the cage, and the M–M SOMO is preserved. At the next stage, anions are reacted with benzyl bromide, which leads to stable noncharged monoadducts. (**b**) Molecular structure of $Dy_2@C_{80}(CH_2Ph)$. (Copyright 2017 Springer Nature)

early stage of EMF studies, a few of EMFs, such as $Y@C_{82}$ and uranium-containing EMF species, were synthesized by this method [119, 145].

Although the laser vaporization strategy has been largely abandoned by researchers today due to the expensive laser source and low productivity, it is still a useful method for the study of the fullerene formation mechanism. In recent years, the Kroto and Dunk group developed the laser vaporiztion technique for in situ analyses of fullerene and EMF formation mechanism [5, 6, 122, 146]. During these experiments, cluster source block involving three channels was configured and simultaneously rotated with the target rods as shown in Fig. 17. One of the channels was utilized to introduce helium in the rods region and another one was aligned with the helium channel to cluster the resulting vapor species. At the same time, the third channel was directed into the target area to admit the laser beam. Vaporization of the target rod was achieved

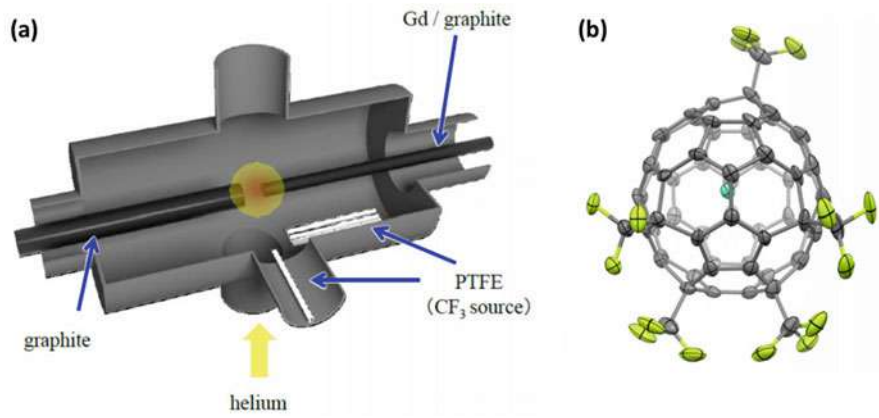

Fig. 16 (**a**) Schematic diagram of the modified Krätschmer-Huffman generator exclusively designed for in situ trifluoromethylation of EMFs. (**b**) The Molecular structure of an isomer of $Gd@C_{60}(CF_3)_5$. (Copyright 2018 Springer Nature)

by a single laser shot fired from a 532 nm Nd:YAG laser. After the accumulation of ions produced by ten individual vaporization events, the positive ions were transferred to the ICR cell for further Fourier-transform ion cyclotron resonance (FT-ICR) mass spectrometer analyses [5]. Based on this strategy, by vaporizing the rods composed of graphite powder and the metal oxides (UO_2, TiO_2, ZrO_2, or Hf_2O_2), Dunk and coworkers investigated the smallest stable fullerene $M@C_{28}$ (M = Ti, Zr, U) and proposed that $M@C_{28}$ was formed by a bottom-up growth mechanism [122]. Furthermore, such a laser vaporization and FT-ICR method was applied by the same group for the synthesis of $Na@C_{2n}$, in which a Na-doped carbon rod was subjected to laser ablation [146]. The results showed that the Na atoms and ions appeared to catalyze the nucleation of fullerenes in oxygen- and hydrogen-rich environments. Interestingly, the successful capture of Na by the carbon cage actually helped to understand the Na trapping mechanism taking place during carbon condensation in supernova ejecta, since carbonaceous presolar grains of supernovae were determined to be the carrier of anomalous ^{22}Ne, which is the decay isotope of ^{22}Na. Based on the results, it was proposed that metallofullerene formation was the basic process that traps radioactive ^{22}Na in condensing carbon of stellar environments before decaying into ^{22}Ne. It is conceivable that further exploration of fullerene synthesis under laser vaporization strategy will provide more insights into the fundamental fullerene growth mechanism as well as fullerene astrochemistry.

Radio Frequency Furnace Method

Radio frequency furnace method for the synthesis of fullerenes was originally designed by Jansen et al. in 1992 [147]. Generally, the carbon and metal source were evaporated simultaneously under dynamic flow of helium at different temperatures in the radio frequency furnace and the evaporated carbon and metal ion mixture were cooled in the fullerene formation area. Since the first preparation of $La@C_{82}$ in a

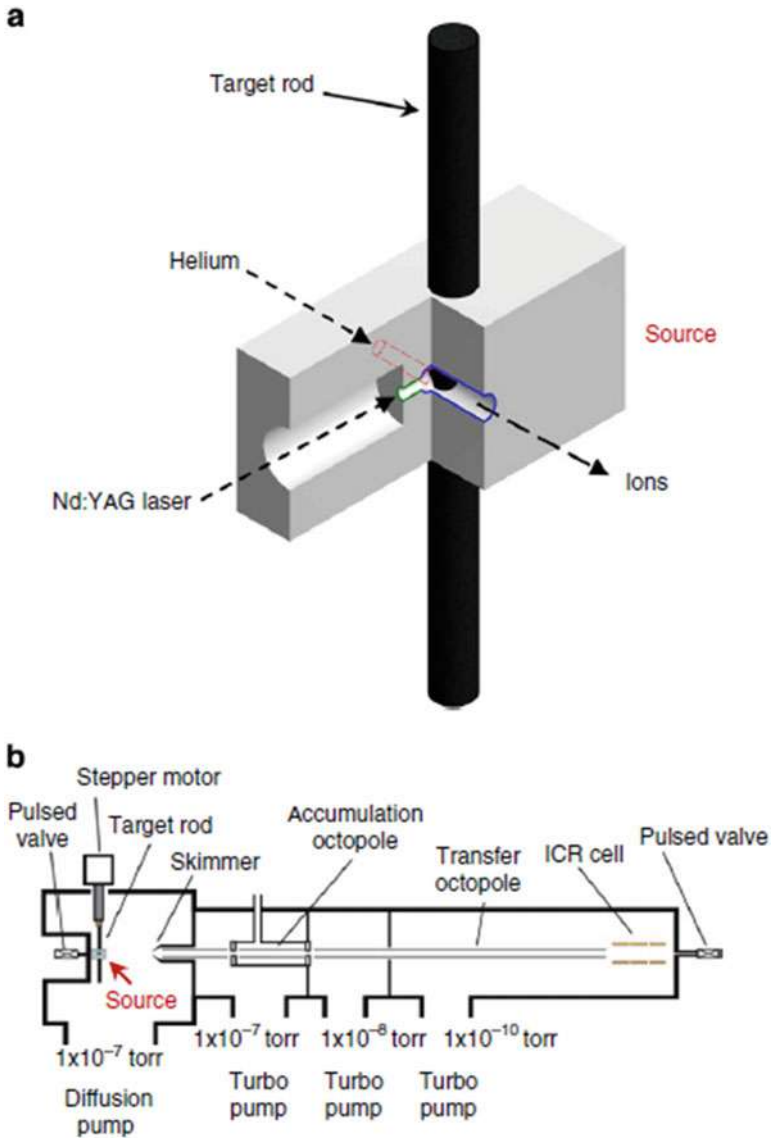

Fig. 17 Cluster source block and instrument schematic. Cutaway view of cluster source block (**a**) and instrument schematic (**b**) A channel (red outline) runs from a pulsed valve into the region containing the target rod to introduce a flow of helium. A second channel (green) runs orthogonally into the target area to admit the laser beam. A single laser pulse strikes a fullerene-graphite target rod, which desorbs the fullerenes and converts graphite to atomic carbon and C_2. Another channel (blue) is located downstream from the target, aligned with the helium introduction channel to allow confinement and interaction of the desorbed fullerenes with carbon vapor produced from graphite. After the gas exits this channel, it enters high vacuum and undergoes a free jet expansion. The clusters are then skimmed into octopoles, where ions are accumulated and then transported to the ICR cell for detection. The target rod is simultaneously rotated and translated by a stepper motor. Note: the instrument schematic is not to scale. (Copyright 2012 Springer Nature)

radio frequency furnace [3], this approach was found to easily enable the formation of $M@C_{2n}$ EMFs with smaller cages ($2n < 80$) [148–150]. Furthermore, Krokos developed a new radio frequency furnace with cold plasma introduced to the fullerene formation region, thus leading to the successful synthesis of $Sc_4C_2@C_{80}$ and $Sc_3N@C_{2n}$. The formation mechanism of these NCFs were analyzed by this method, which suggests that the nucleation of the endohedral element in the carbon cage takes place in the last stage of the fullerene evolution process [151].

Ion Bombardment and Hot-Atom Chemistry Method

Endohedral alkali-metal fullerenes, hardly accessible by the DC arc-discharge method, can be obtained by the ion bombardment method. In this method, fullerene materials are exposed to an intense beam of alkali ions at suitable energy. Ions are implanted into the fullerene cage but would not destroy it. By this means, Campbell et al. discovered $M@C_{60}$ (M = Li, Na, K, Rb) and pointed that the values for the energetic thresholds for capture of alkali ions were approximately 6 eV for Li^+ and increased to approximately 40 eV for K^+ [152, 153]. Nevertheless, the insolubility of C_{60}-based endohedral alkali-metal fullerenes inevitably limited the characterization of their definite structures and physiochemical properties. In this context, Tobita and coworkers successfully isolated and characterized $Li@C_{60}$ in the form of cationic salt, $[Li^+@C_{60}](SbCl_6^-)$ [154]. In order to achieve pristine $Li@C_{60}$, they adopted an irradiation method by which energetic Li^+ ions were irradiated onto a target plate while the vapor of C_{60} was deposited on the same plate. After that, the oxidation process of $Li@C_{60}$ occurred in the reaction of the resulting deposit with tris(4-bromophenyl)ammoniumyl hexachloroantimonate in a mixture of *o*-DCB and acetonitrile. Finally, a monomeric $[Li^+@C_{60}]$ was isolated as the $SbCl_6$ salt, $[Li^+@C_{60}](SbCl_6^-)$. However, the same group later found that $[Li^+@C_{60}](SbCl_6^-)$ was slightly unstable, especially when exposed to moisture. They therefore adopted HPLC to examine the purification of $[Li^+@C_{60}](SbCl_6^-)$ and added tetra-*n*-butylammonium hexafluorophosphate ($TBAPF_6$) into the mobile phase. Surprisingly, another form of $Li^+@C_{60}$ salt, $[Li^+@C_{60}][PF_6^-]$, was isolated during elution. This method opens a new way for the isolation and the crystallization of C_{60}-based metallofullerenes [155].

The hot-atom chemistry process can be described as neutron activation of metallofullerenes where the existing EMF products was irradiated in a neutron flux reactor and the resulting neutron-activated metal isotopes can penetrate into the fullerene cage by a recoil process of the nuclear reactions. This technique is usually applied for the synthesis of radioactive EMFs. Kikuchi and coworkers successfully encapsulated radioactive [159]Gd and [161]Tb atoms into fullerene cages [156]. This technique was also developed for the neutron activation of [165] $Ho_x@C_{2n}$ [157] and the generation of $^7Be@C_{60}$ [158] and $^{212}Pb@C_{60}$ [159].

Extraction of Endohedral Metallofullerenes

Fullerenes and endohedral fullerenes are soluble in a variety of organic solvents such as CS_2, toluene, *o*-xylene, *o*-DCB, et al. Therefore, solvent extraction is by now the most commonly used method for the separation of fullerenes from the raw carbon

soot. The charge transfer from the encapsulated species renders the exterior cages of EMFs anisotropic charge distribution, which leads to large dipole moments [160]. The difference of polarity existing between empty fullerenes and EMFs can be used in the rough separation of EMFs from empty fullerenes by solvent extraction. For example, in 1998, Yagubskii et al. used a two-step xylene-N,N-dimethylformamide (DMF) extraction method and efficiently separated La- and Y-containing EMFs from empty fullerenes. *O*-xylene was first utilized to elute empty fullerenes from the soot. Then, the same soot was again extracted by polar solvent DMF [161]. The resulting DMF extracts contained mainly EMFs. Similarly, a variety of other extraction methods have also been explored for solvent extraction separation of EMFs, including polar solvent extraction [162–164], high-temperature high-pressure extraction [165, 166], and solid-phase extraction [167].

Separation of Endohedral Metallofullerenes

The arc-discharge method enabled macroscopic synthesis of fullerenes and EMFs. However, the soot extract obtained from the arcing process is often the complex mixture of various kinds of fullerenes and EMFs, making the separation of specific products extremely difficult. The first macroscopic preparation of relatively pure C_{60} was accomplished by Krätschmer et al. with the sublimation method [4]. Since then, taking advantage of the different properties of different EMFs, several separation protocols have been developed. Up to now, high-performance liquid chromatography (HPLC), capable of isolating highly purified fullerene samples, is still the primary method applied for the separation and purification of EMFs. However, this method is known for its time-consuming and tedious procedures. Thus, some alternative methods have also been developed based on the varying physicochemical properties of the fullerene products, to avoid or largely reduce the tedious HPLC processes. For example, the significant differences between empty fullerenes and EMFs facilitates the macroscopic separation of these two species by the pretreatment of the soot extract with specific Lewis acids like $AlCl_3$ and $TiCl_4$, which selectively form complexes with the EMFs [168, 169]. A variety of different separation methods for EMFs are summarized below.

Separation by Sublimation

EMFs with various cages or different encaged species generally have different sublimation point, which facilitates their large-scale separation from the soot extract. For example, Smalley and coworkers heated the raw soot containing EMFs in He gas up to 650 °C. At this temperature, EMFs such as La@C_{2n} ($2n = 60, 74, 82$) began to sublimate and were then condensed in a cold trap and were thus roughly separated [144]. However, this method is only suitable for the preliminary enrichment of some specific EMFs. As the sublimation point of some EMFs, especially the cage isomers, are in fact very close, this method cannot be applied for a complete isolation process and is seldom used in the current EMF studies.

High-Performance Liquid Chromatography (HPLC)

Up to date, high-performance liquid chromatography, though costly and time consuming, is still the most widely used method for the separation of EMF mixtures, due to its high stability and reliability. This method is based on the different distribution of fullerenes between a stationary and a mobile phase in a chromatographic column, which is intrinsically determined by the electronic structures of various fullerene species. HPLC columns are packed with different stationary phase made up of silica gel substrate bonded with specific function groups. These functionalized silica gel substrates have strong and divergent interactions with the different fullerenes passing by, which results in different retention time of the different fullerene species on the corresponding HPLC columns. For example, Buckyprep column by Nacalai Tesque, Inc. is packed with pyrenylpropyl-group-functioned silica gel as the stationary phase, which has good separating efficiency on EMF structural isomers. The Cosmosil Buckyprep-M column by Nacalai Tesque, Inc. is packed with phenothiazinyl-group-functioned silica gel as the stationary phase. This columm demonstrates ultrahigh retaining effect on EMFs and is an efficient column for the separation of EMFs from empty fullerenes. 5PBB column by Nacalai Tesque, Inc. is packed with pentabromobenzy-group-functioned silica gel as the stationary phase, which has excellent ability to separate fullerenes by the size of the carbon cage.

Figure 18 demonstrates the HPLC separations of actinide EMFs using Buckyprep, Buckyprep-M, and 5PBB column. As shown in Fig. 18a, a facile isolation of $U_2@C_{80}$ from empty fullerenes C_{2n} ($2n$ = 70-112) have been achieved by Buckyprep column. After this step of separation, the purity of $U_2@C_{80}$ and $U_2C@C_{80}$ can reach more than 95% and 80% respectively. Figure 18b shows that Buckyprep column also can be used for efficient separation of pristine Th@C_{3v}(8)-C_{82} and three carbene derivatives Th@C_{3v}(8)-C_{82}Ad (Ad = adamantylidene) isomers. Figure 18c shows that Buckyprep-M column could be used for crude separation of EMFs from hollow fullerenes owing to the ultrahigh retaining effect on EMFs, as the empty fullerenes mostly flow out before 25 min and endohedral fullerenes flow out after 30 min. Figure 18d shows that Th@C_{76}, $Sc_3N@C_{78}$, and $Sc_3N@C_{80}$ flow out from the 5PBB column in sequence according to the size of the carbon cage.

Besides these most commonly used HPLC columns, other commercially available columns include Buckyprep-D, 5PYE, etc. Table 2 lists these HPLC columns, their stationary phase and their usages. With continual modification and optimization of the HPLC instruments in the recent years, HPLC instruments can now operate in the recycling mode, capable of isolating of most of the known fullerene samples, including cage isomers or EMFs with the same cage. This technique is especially useful for the separation of mixed metallic NCFs. For example, the variation of a single atom in the $A_xB_{3-x}N$ (A, B = metal) cluster generally leads to very subtle change in the electronic property of the entire molecule as well as the retention time of the different species on a single column. Thus, recycling HPLC and the combination of different columns are needed to obtain these samples with high purity. For example, Yang and coworkers successfully separated a series of mixed metallic

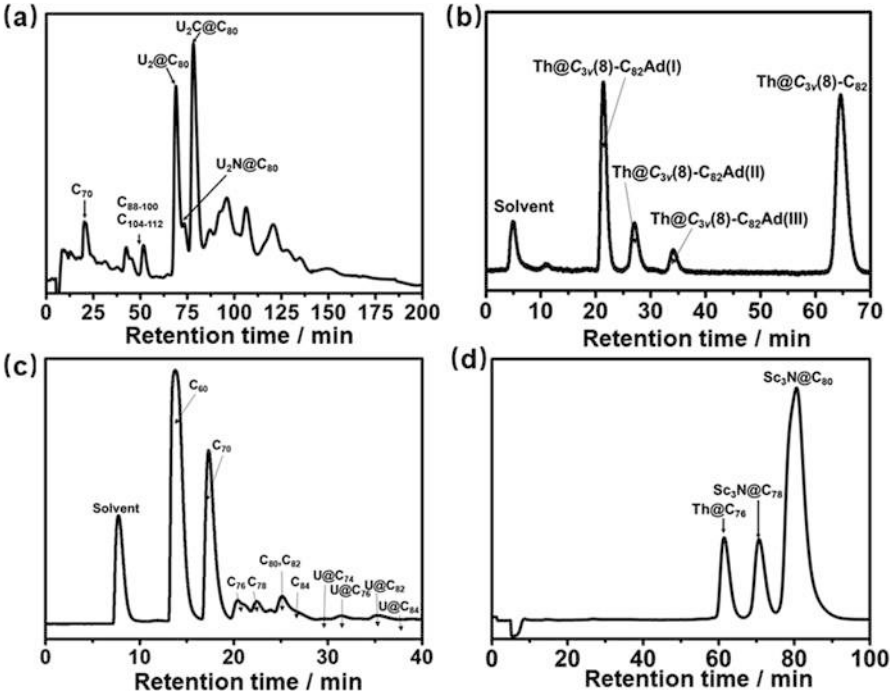

Fig. 18 (**a**) Use Buckyprep column for the separation of U-based EMFs from empty fullerenes C_{2n}. HPLC conditions: Buckyprep column (10 mm × 250 mm): flow rate, 4 mL min^{-1}; toluene as the mobile phase; wavelength 310 nm. (**b**) Separate three Th@C_{3v}(8)-C_{82}Ad isomers using Buckyprep column. HPLC conditions: Buckyprep column (10 mm × 250 mm): flow rate, 4 mL min^{-1}; toluene as the mobile phase; wavelength 310 nm. (**c**) Use Buckyprep-M column for the separation of U-based EMFs U@C_{2n} from empty fullerenes C_{2n}. HPLC conditions: Buckyprep-M column (25 mm × 250 mm): flow rate, 10 mL min^{-1}; toluene as the mobile phase; wavelength 310 nm. (**d**) Use 5PBB column for the separation of EMFs in different cage sizes. HPLC conditions: 5PBB column (10 mm × 250 mm): flow rate, 4 mL min^{-1}; toluene as the mobile phase; wavelength 310 nm

NCFs, $Gd_xSc_{3-x}N@C_{80}$ ($x = 1,2$) using the HPLC recycling mode [36]. In the first step, by a linear combination of two Buckyprep columns, four HPLC fractions were obtained, among which fraction A contains two products, $GdSc_2N@C_{80}$ and $Gd_2ScN@C_{80}$. Figure 19 displays the recycling HPLC chromatograms of fractions A and B. The recycling HPLC was then applied for the separation of these two products due to their nearly identical cage structures. Finally, as confirmed by LDI-TOF, $Gd_2ScN@I_h$-C_{80} and $GdSc_2N@I_h$-C_{80} were completely separated and isolated with high purity after 13 cycles [36]. Similarly, $Sc_xY_{3-x}N@I_h$-C_{80} ($x = 1,2$), $ScYErN@I_h$-C_{80} were isolated via recycling HPLC processes on the Buckyprep column by Wang and coworkers [39].

However, the HPLC method has its inevitable disadvantages. Since the capacity of the column is very limited, HPLC is not suitable for large-scale separation of

Table 2 Parameters of typical HPLC columns for fullerene separation

Manufacturer	Product name	Stationary phase	Separation feature
Nakalai Tesque Co. Ltd.	Buckyprep	Pyrenylpropyl group	Standard column for fullerene separation. Separation for metallofullerenes, higher and derivatized fullerenes
	Buckyprep-M	Phenothiazinyl group	Separation for metallofullerenes
	Buckyprep-D	Nitro-carbazoyl group	For preparative separation of metallofullerenes and derivatized fullerenes For separation of derivatized fullerenes such as C_{60}
	PBB	Pentabromobenzyl group	Designed for preparative separation of fullerenes and higher fullerenes
	PYE	Pyrenylethyl group	Separation with high molecular shape selectivity or π-π interactions Excellent separation for structural isomers
	NPE	Nitrophenylethyl group	Separation with dipole-dipole and π-π interactions Excellent separation for structural isomers

EMFs. In addition, the arc-discharge synthetic method often results in overwhelmingly large amounts of empty fullerenes, which also severely complicated HPLC processes. For example, in 1999, a four-stage HPLC procedure with different commercially available columns (PBB and Buckyclutcher) and different eluents were used to separate $Sc_3N@C_{80}$ in milligram [13]. Besides, most of the EMFs with higher cages have very long retention time on the columns, which makes the separation process extremely time consuming and tedious. For example, Balch and coworkers reported that the dimetallic EMF, $Gd_2@C_{98}$, could be retained in the 5PBB column for over 260 min before it was ultimately eluted [70]. In order to circumvent these drawbacks, researchers have been devoted to finding more efficient nonchromatographic methods for the isolation of EMFs.

Chemical and Electrochemical Separation of EMFs

Electrochemical studies revealed notable differences between the redox potentials of EMFs and those of empty fullerenes, which inspired the non-HPLC separation methods of EMFs. Akasaka and coworkers investigated the macroscopic separation of EMFs based on the facile electrochemical reduction of these EMFs [170]. In this work, the mixed C_{60} and EMFs in o-DCB was held at a constant potential of 0.00 V relative to a saturated calomel electrode (SCE). The reduced EMFs, soluble in polar solvent, were conveniently extracted and thus separated from the anion of empty fullerenes, which are insoluble in polar solvent. Moreover, electrochemical studies

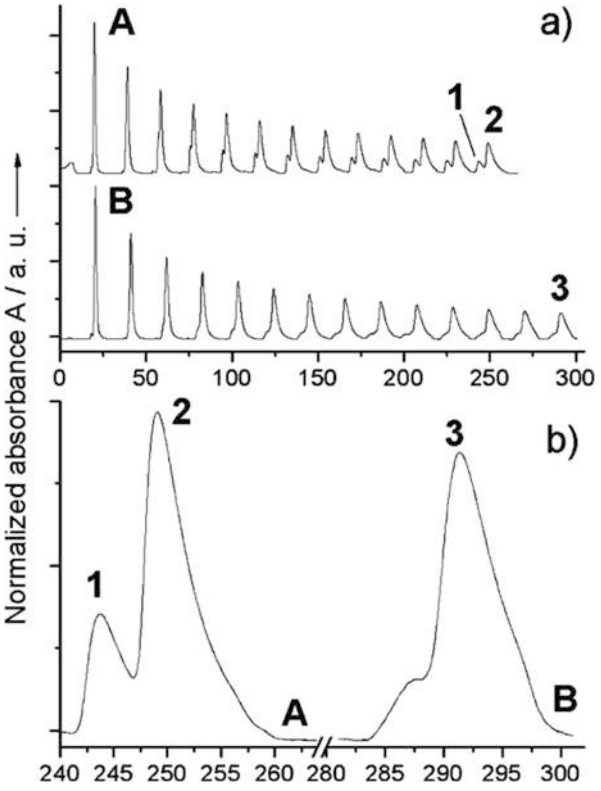

Fig. 19 (**a**) Chromatograms of the isolated fractions A and B by recycling HPLC (10 × 250 mm Buckyprep-M column; flow rate 5.0 mL min^{-1}, injection volume 5 mL; toluene as eluent; 25 °C). (**b**) Chromatograms of fractions A and B in the final cycle by recycling HPLC based on (**a**). (Copyright 2006 Wiley-VCH Verlag GmbH & Co. KGaA, Weinheim)

also discovered that EMF isomers with the same cage size could exhibit different oxidation potentials. Thus, the electrochemical method was also utilized to isolate EMF isomers which otherwise would require a complicated recycling HPLC process to be purified. In 2005, Echegoyen and coworkers designed a facile protocol for the separation of the D_{5h} and I_h cage isomers of $Sc_3N@C_{80}$ by a selective chemical oxidation process [171]. In this method, tris(p-bromophenyl)-aminium hexachloroantimonate (TPBAH), which has an oxidation potential between the first oxidations of the I_h and D_{5h} isomers, was used as the oxidant to preferentially oxidize the D_{5h} isomer with a lower oxidation potential and enabled the separation of these two isomers (the Osteryoung square wave voltammetry of the two EMF isomers and TPBAH are shown in Fig. 20).

Nitride cluster fullerenes often shows higher kinetic chemical stability than those of the other fullerenes in Diels-Alder reactions [172]. Taking this advantage, Dorn et al. designed a facile single-step reaction to selectively separate the $M_3N@C_{80}$ species (M = lanthanide atom, e.g., Sc, Gd, Y, Lu, etc.) from the fullerene extract. In this work, a reactive resin (cyclopentadiene-functionalized styrene-divinylbenzene resin) was prepared and packed in the column. Then, the solution of fullerene extract containing NCFs, conventional EMFs, and empty fullerenes were applied to this

column. The results showed that empty fullerenes and conventional metallofullerenes reacted with the resin while the less reactive NCFs passed through the column. Thus, the collected fullerene solution contained only the highly purified NCFs. Following this work, a modified method using cyclo-pentadienyl (CPD) and amino functionalized silica to selectively bind and eliminate the more reactive contaminant fullerenes was reported by Stevenson et al., namely the "SAFA" (stir and filter approach). The schematic of the "SAFA" to purify MNF samples is shown in Fig. 21 [173]. In their work, the fullerene extract was added to a slurry of reactive CPD or amino-functionalized silica gel, stirred and filtered. The fullerene contaminant was trapped by the solid support and stayed on the filter, leaving the unreactive NCFs in the filtrate. The results show that purified NCFs (+98%) were obtained by this method with variable amino-functionalized silica gel applied at room temperature. On the other hand, the application of CPD silica gel was unsuccessful in room temperature. But when the reaction temperature was elevated, NCFs with 98% purity were obtained with this method. Compared with the previously reported route based on cyclopentadiene-functionalized resin, this method utilizes a much cheaper silica-based solid support, and does not require flowing solvent. With the application of amino-functionalized silica, NCFs can be isolated with high purity conveniently under ambient conditions. Later, the "SAFA" was also applied to isolate $Sc_3N@I_h$-C_{80} and $Sc_3N@D_{5h}$-C_{80} isomers [174] as well as $LaSc_2N@I_h$-C_{80} [43, 44].

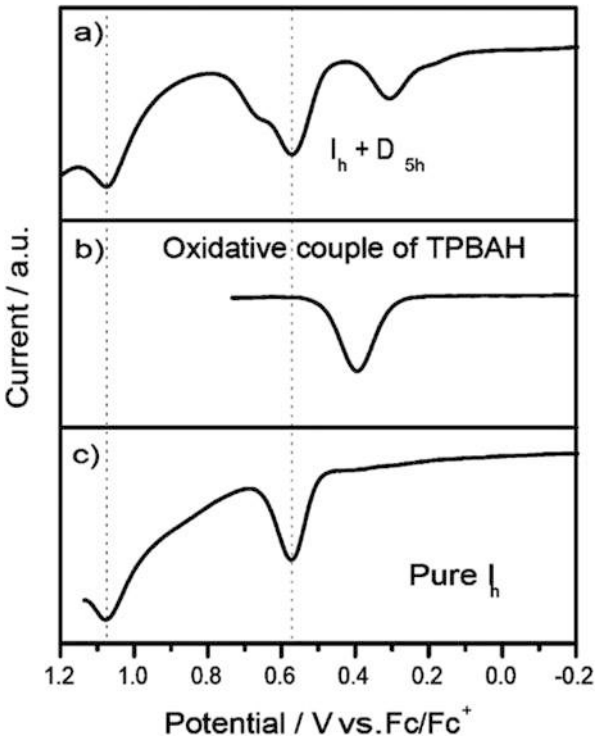

Fig. 20 The Osteryoung square wave voltammetry of (**a**) the I_h and D_{5h} $Sc_3N@C_{80}$ isomer mixture, (**b**) the oxidation wave of the neutral amine oxidant precursor, and (**c**) pure $Sc_3N@I_h$-C_{80}. (Copyright 2005 American Chemical Society)

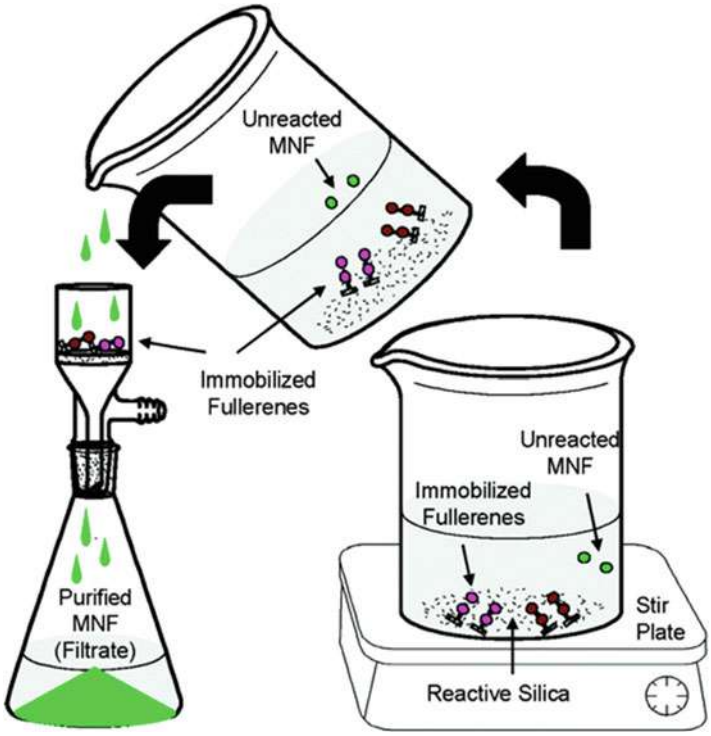

Fig. 21 Schematic of the "Stir and Filter Approach" (SAFA) to purifying MNF samples. (Copyright 2006 American Chemical Society)

Solid reaction was also performed for the isolation of NCFs from the soot extract. In Dorn and coworker's report, 9-methylanthracene was utilized to react directly with the Sc- or Lu-based NCFs raw soot extract. They found out that by applying this method, almost complete conversion of empty-cage fullerenes to 9-methylanthracene adduct can be achieved. After the reaction, the solid mixture was washed by ether and the remaining insoluble extract containing over 60% NCFs was then facilely purified with one-step HPLC process [175].

Lewis acids was first used for the separation of C_{60} from other empty-cage fullerenes (e.g., C_{70}) in 1997, based on the fact that C_{60} shows inert nature compared to the higher reactivity of other fullerene species with Lewis acids [176]. In 2009, Stevenson et al. reported that some metallic NCFs and oxometallic fullerenes showed high reactivity with an array of Lewis acids such $AlCl_3$, $AlBr_3$, and $FeCl_3$, whereas empty-cage fullerenes are largely unreactive, detailed isolation processes are shown in Fig. 22 [168]. Experimentally determined reaction rate constants exhibited linear correlation to the electrochemical band gaps of corresponding EMFs, which is in good alignment with the following reactivity order: $Sc_4O_2@I_h$-C_{80} > $Sc_3N@C_{78}$ > $Sc_3N@C_{68}$ > $Sc_3N@D_{5h}$-C_{80} > $Sc_3N@I_h$-C_{80}. Thus, by optimizing the Lewis acids, molar ratios, and kinetic differences, they accomplished

the purification of $Sc_3N@I_h$-C_{80} without HPLC and a considerable enrichment of $Sc_4O_2@I_h$-C_{80}, $Sc_3N@C_{78}$, $Sc_3N@C_{68}$, and $Sc_3N@D_{5h}$-C_{80}, which largely simplify the subsequent facile HPLC separation.

Similar method was taken by the Shinohara group to separate EMFs from the crude fullerene extract with higher efficiency in 2012. In their report, the strong electrophilic Lewis acid, $TiCl_4$, was utilized for the selective complexation with mono- and dimetallofullerenes [169]. Immediately after the addition of $TiCl_4$ into the crude fullerene extract solution, complex formed between EMFs and $TiCl_4$, which could easily decompose and be recovered to pure metallofullerenes by a simple water treatment. The spectroscopic studies suggest that the electron transfer from the entrapped metals to the

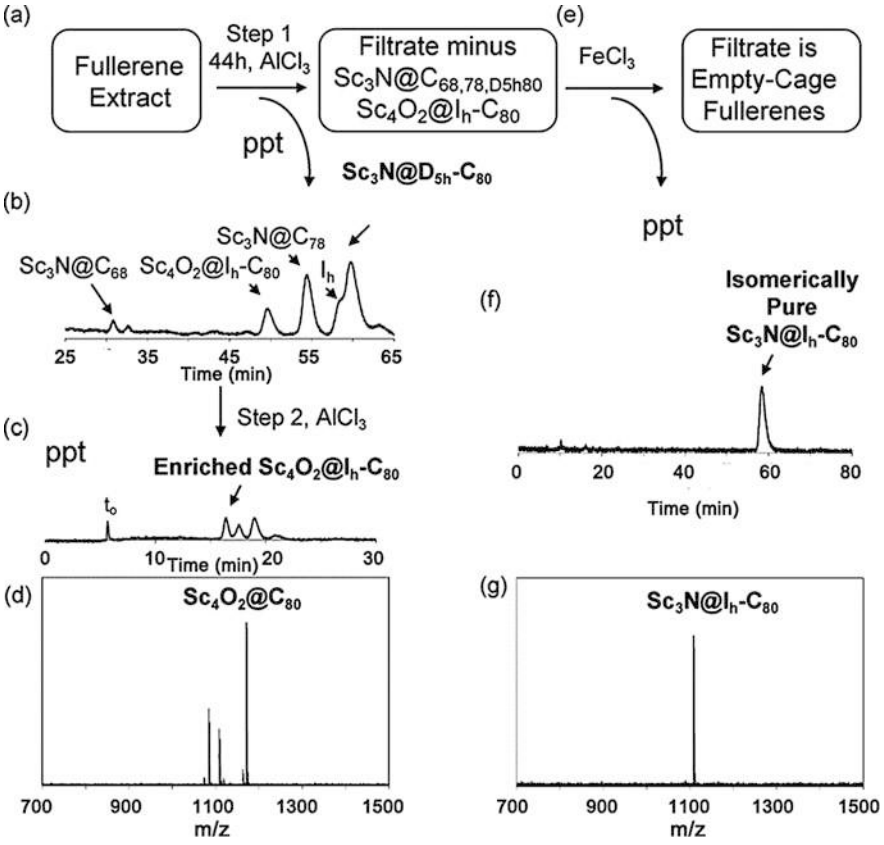

Fig. 22 (**a**–**d**) Scheme, HPLC, and MALDI data demonstrating the isolation of enriched samples of $Sc_4O_2@I_h$-C_{80}, $Sc_3N@C_{68}$, $Sc_3N@C_{78}$, and $Sc_3N@D_{5h}$-C_{80} using complexation with $AlCl_3$ and subsequent decomplexation via the addition of water. (**e**–**g**) Isolation scheme, HPLC chromatogram, and MALDI mass spectrum of isomerically purified $Sc_3N@I_h$-C_{80} using the complexation/decomplexation approach. HPLC flow rates are (b,f) 0.3 mL/min toluene and (c) 0.5 mL/min xylenes with 360 nm detection, a 4.6 × 250 mm PYE column, and injection volumes of 50μL. (Copyright 2009 American Chemical Society)

Lewis acid plays a key role in the exclusive complexation between the two species. Shinohara and coworkers conducted a systematic research on a variety of EMFs and found that efficient separation can be achieved for the EMFs whose oxidation potential are lower than 0.62 − 0.72 V versus $Fe(Cp)_2^{+/0}$ couple. Very recently, this method was applied and modified by Chen's group to efficiently isolate a series of cage isomers of dysprosium OCFs [100]. The separation protocol was modified with EDTA water solution to facilitate a more efficient decomposition of the EMF-$TiCl_4$ complexes. Figure 23 displays the separation effect of Gd-containing EMFs by the $TiCl_4$ method.

Recently, supramolecular chemistry was applied for the separation of clusterfullerenes. In 2018, Ribas and Echegoyen reported that a novel Cu(II)-based tetragonal prismatic nanocapsule could sequentially and selectively entrap $U_2@I_h$-C_{80} and $Sc_2CU@I_h$-C_{80} from the soot extract [133]. To be specific, mixed U/Sc-based arc soot extract, which contains empty fullerenes, $Sc_3N@C_{80}$, $Sc_2CU@C_{80}$, and $U_2@C_{80}$, was soaked with the Cu(II)-based tetragonal prismatic nanocapsule in toluene. The experimental results indicated that the nanocapsule selectively captured the $U_2@C_{80}$ and $Sc_2CU@C_{80}$ sequentially and formed the corresponding precipitation. Afterwards, these U-containing EMFs were easily released and $U_2@C_{80}$ and $Sc_2CU@C_{80}$ with high purity were obtained in one step. (The separation scheme by this method is shown in Fig. 24). DFT calculations show that the linear double-conical symmetry of the electron density induced by the presence of the two encaged U ions of $U_2@C_{80}$ facilitates a stronger host-guest interaction between it and the nanocapsule, which enables its prior capture by the nanocapsule.

Summary and Outlook

Over the past three decades, as summarized in this chapter, various synthetic methods of endohedral metallofullerenes, including the Krätschmer-Huffman DC arc-discharge, laser ablation, radio frequency furnace, ion bombardment, and hot-atom chemistry method, et al., have been developed by researchers. High-performance liquid chromatography (HPLC) is widely used for the separation and purification of EMFs as it can yield highly purified EMFs with variable HPLC columns and recycling techniques applied. Various nonchromatographic strategies have also been developed for simpler and more efficient separation procedure, such as chemical and electrochemical methods. Combined together, these methods enable the synthesis and isolation of a large variety of novel endohedral fullerene compounds with high purity. The successful preparation of these novel endohedral fullerenes with high purity, together with the significantly advanced characterization technology in the recent years, enable the precise determination of the molecular structures of a large variety of the novel endohedral fullerenes and revealed exciting chemical and physical properties of these unique nanocarbon compounds, which shed light on its prospective applications on the fields of biomedicine, photovoltaic devices, and molecular electronics.

However, synthetic and separation methods of endohedral fullerenes, though steadily improved over the years, are still based on the methodologies which were

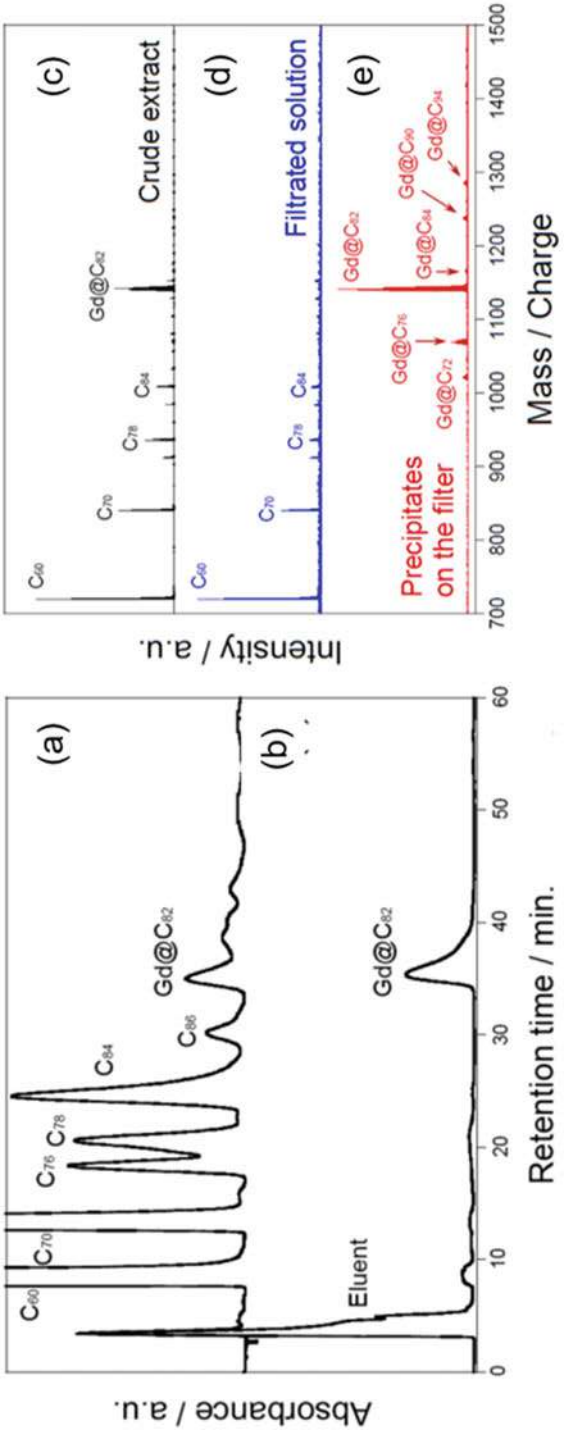

Fig. 23 HPLC chromatograms of (**a**) Gd@C_{82}-containing crude extract and (**b**) Gd@C_{82} metallofullerenes separated by a 10 min reaction with $TiCl_4$ and negative ion LD-MS of (**c**) crude extract, (**d**) filtered solution, and (**e**) precipitates on the filter for Gd metallofullerenes. (Copyright 2012 American Chemical Society)

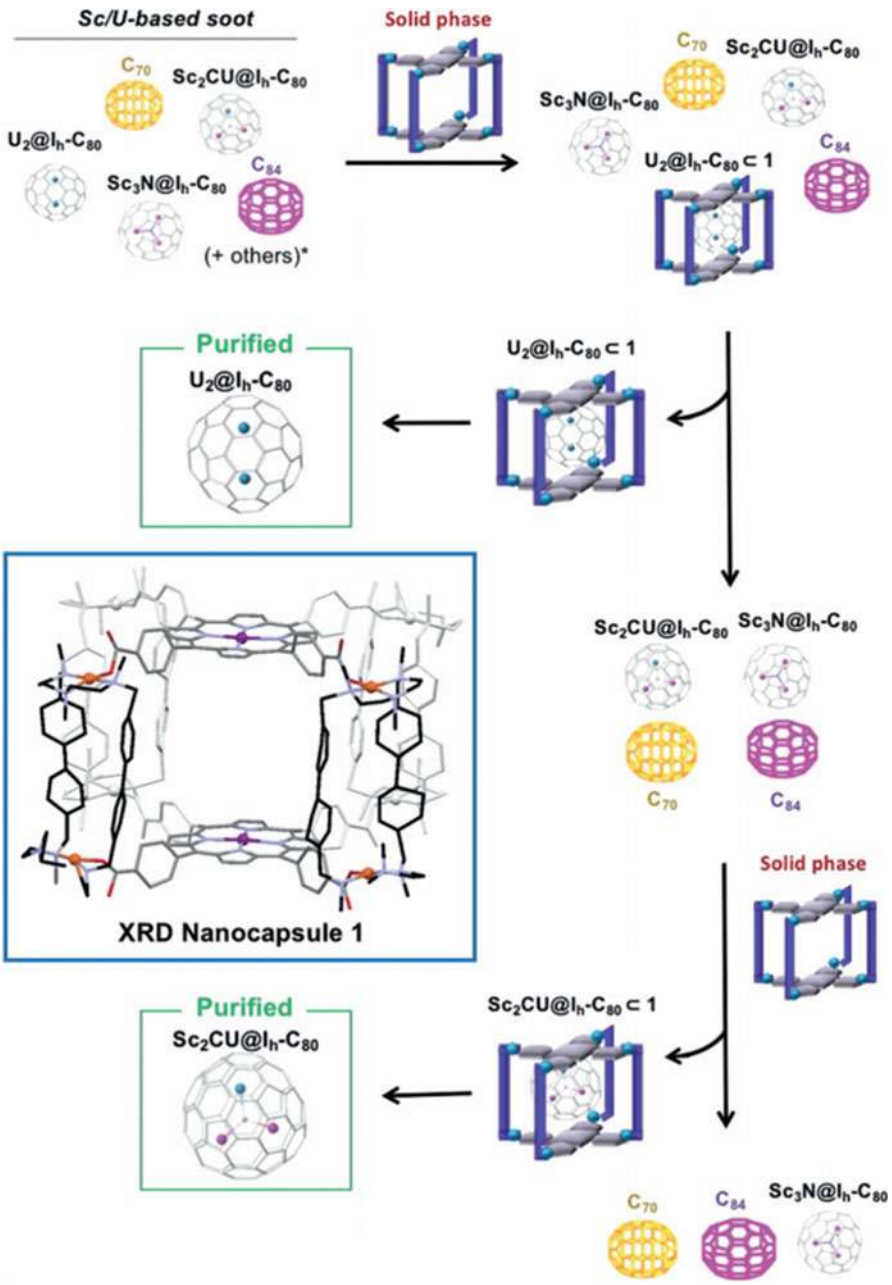

Fig. 24 Straightforward purification method for selective and sequential encapsulation of $U_2@C_{80}$ and $Sc_2CU@C_{80}$ from raw soot using nanocapsule. The inset shows the structure of the nanocapsule (Cu orange, Zn purple). (Copyright 2018 Wiley-VCH Verlag GmbH & Co. KGaA, Weinheim)

found in the earlier years of the endohedral fullerene study. In fact, to date, the synthesis and separation have become a major bottleneck for the study and in particular, application of the endohedral fullerenes. Among all the abovementioned synthetic techniques, Krätschmer-Huffman DC arc-discharging method is still the predominant method used in synthesis of endohedral fullerenes, as it can afford a relatively stable production and relatively high yields. But even with this method, the drawback is clear: product yield of the most endohedral fullerenes is still extremely low compared to conventional chemical synthesis and the selectivity of a certain endohedral fullerene, in most of cases, cannot be controlled. Except for the most abundant $Sc_3N@C_{80}$, in most of operations, burning of hundreds of graphite rods only yield in pure product in mg scale or even lower. In addition, though chemical separation technique has made major progress in the recent years, the costly and time-consuming HPLC procedures are still required in the final steps of the purification of the endohedral fullerene samples. This extremely low product yield and time-consuming purification processes are the main reasons that endohedral fullerenes are still inaccessible to most of the foreseeable industrial application. Therefore, major breakthrough is urgently needed and the quest for efficient synthetic routes to make larger quantities of these novel structures available for different studies for both fundamental and applied research should be the major topic in this field in the future. Besides, to improve the selectivity of endohedral fullerenes during the synthetic process is also essential for the future application of endohedral fullerenes. Researchers have demonstrated the possibility of improving the selectivity of target clusterfullerenes during the arcing process by the usage of reactive gas and solid compounds. Modification of synthetic conditions to further improve the selectivity of the endohedral fullerenes during the production will also be an efficient way and research focus for the improvement of product yield of endohedral fullerenes in the future study.

On the other hand, the exploring of novel endohedral fullerenes is still needed and may unveil previously unknown bonding motifs and physiochemical properties of these fascinating molecules. The study of actinide endohedral fullerenes, though still in its early stage, has clearly shown that different electronic structures of actinide metal ion results in amazing endohedral structures which breaks the doctrines previously set up by the study of lanthanide-based endohedral fullerenes. The incorporation of V and Ti into the endohedral metallic clusters also results in unique oxidation states and bonding motifs. Thus, further effort of synthesizing endohedral fullerenes which incorporates metals beyond 4f elements may not only enrich the endohedral fullerene family, but possibly open the door to a new world of novel nanocarbon materials.

References

1. Heath JR et al (1985) Lanthanum complexes of spheroidal carbon shells. J Am Chem Soc 107: 7779–7780
2. Funasaka H et al (1993) Preparation of fullerene derivatives by resistive heating with graphite crucible. Fuller Sci Technol 1:437–448

3. Jansen M, Peters G, Wagner N (1995) Zur Bildung von Fullerenen und endohedralen metallofullerenen: Darstellung im Hochfrequenzofen. Z Anorg Allg Chem 621:689–693
4. Kratschmer W, Lamb LD, Fostiropoulos K, Huffman DR (1990) Solid C_{60}: a new form of carbon. Nature 347:354–358
5. Dunk PW et al (2012) Closed network growth of fullerenes. Nat Commun 3:855
6. Mulet-Gas M et al (2017) Transformation of doped graphite into cluster-encapsulated fullerene cages. Nat Commun 8:1222
7. Liu F et al (2013) A series of inorganic solid nitrogen sources for the synthesis of metal nitride clusterfullerenes: the dependence of production yield on the oxidation state of nitrogen and counter ion. Inorg Chem 52:3814–3822
8. Takata M et al (1995) Confirmation by X-ray diffraction of the endohedral nature of the metallofullerene Y@C_{82}. Nature 377:46–49
9. Xu W et al (2013) An experimentally observed Trimetallofullerene $Sm_3@I_h$-C_{80}: encapsulation of three metal atoms in a cage without a nonmetallic mediator. J Am Chem Soc 135:4187–4190
10. Popov AA, Yang S, Dunsch L (2013) Endohedral fullerenes. Chem Rev 113:5989–6113
11. Lu X, Feng L, Akasaka T, Nagase S (2012) Current status and future developments of endohedral metallofullerenes. Chem Soc Rev 41:7723–7760
12. Stevenson S et al (1994) Automated HPLC separation of endohedral metallofullerene Sc@C_{2n} and Y@C_{2n} fractions. Anal Chem 66:2675–2679
13. Stevenson S et al (1999) Small-bandgap endohedral metallofullerenes in high yield and purity. Nature 401:55–57
14. Guo M et al (2021) A non-isolated pentagon rule C_{82} cage stabilized by a stretched Sc_3N cluster. Chem Commun 57:4150–4153
15. Olmstead MM et al (2003) $Sc_3N@C_{68}$: folded pentalene coordination in an endohedral fullerene that does not obey the isolated pentagon rule. Angew Chem Int Ed 42:900–903
16. Yang S, Kalbac M, Popov A, Dunsch L (2006) A facile route to the non-IPR fullerene $Sc_3N@C_{68}$: synthesis, spectroscopic characterization, and density functional theory computations (IPR = isolated pentagon rule). Chem Eur J 12:7856–7863
17. Yang S, Popov AA, Dunsch L (2007) Violating the isolated pentagon rule (IPR): the endohedral non-IPR C_{70} cage of $Sc_3N@C_{70}$. Angew Chem Int Ed 46:1256–1259
18. Olmstead MM et al (2001) Isolation and structural characterization of the endohedral fullerene $Sc_3N@C_{78}$. Angew Chem Int Ed 40:1223–1225
19. Duchamp JC et al (2003) An isomer of the endohedral metallofullerene $Sc_3N@C_{80}$ with D_{5h} symmetry. Chem Phys Lett 375:655–659
20. Wei T et al (2015) Capturing the long-sought small-bandgap endohedral fullerene $Sc_3N@C_{82}$ with low kinetic stability. J Am Chem Soc 137:3119–3123
21. Ma Y et al (2011) Size effect of endohedral cluster on fullerene cage: preparation and structural studies of $Y_3N@C_{78}$-C_2. Nanoscale 3:4955–4957
22. Fu W et al (2009) ^{89}Y and ^{13}C NMR cluster and carbon cage studies of an yttrium metallofullerene family, $Y_3N@C_{2n}$ (n = 40−43). J Am Chem Soc 131:11762–11769
23. Burke BG et al (2010) Investigation of $Gd_3N@C_{2n}$ ($40 \leq n \leq 44$) family by Raman and inelastic electron tunneling spectroscopy. Phys Rev B 81:115423
24. Beavers CM, Chaur MN, Olmstead MM, Echegoyen L, Balch AL (2009) Large metal ions in a relatively small fullerene cage: the structure of $Gd_3N@C_2$(22010)-C_{78} departs from the isolated pentagon rule. J Am Chem Soc 131:11519–11524
25. Stevenson S et al (2004) Pyramidalization of Gd_3N inside a C_{80} cage. The synthesis and structure of $Gd_3N@C_{80}$. Chem Commun 2004:2814–2815
26. Mercado BQ et al (2008) Is the isolated pentagon rule merely a suggestion for endohedral fullerenes? The structure of a second egg-shaped endohedral fullerene—$Gd_3N@C_s$(39663)-C_{82}. J Am Chem Soc 130:7854–7855
27. Zuo T et al (2008) New egg-shaped fullerenes: non-isolated pentagon structures of $Tm_3N@C_s$(51365)-C_{84} and $Gd_3N@C_s$(51365)-C_{84}. Chem Commun 2008:1067–1069

28. Chaur MN et al (2010) Structural and electrochemical property correlations of metallic nitride endohedral metallofullerenes. J Phys Chem C 114:13003–13009
29. Zuo T et al (2007) Isolation and structural characterization of a family of endohedral fullerenes including the large, chiral cage fullerenes $Tb_3N@C_{88}$ and $Tb_3N@C_{86}$ as well as the I_h and D_{5h} isomers of $Tb_3N@C_{80}$. J Am Chem Soc 129:2035–2043
30. Beavers CM et al (2006) $Tb_3N@C_{84}$: an improbable, egg-shaped endohedral fullerene that violates the isolated pentagon rule. J Am Chem Soc 128:11352–11353
31. Krause M, Wong J, Dunsch L (2005) Expanding the world of endohedral fullerenes – the $Tm_3N@C_{2n}$ ($39 \leq n \leq 43$) Clusterfullerene family. Chem Eur J 11:706–711
32. Zuo T et al (2008) Preparation and structural characterization of the Ih and the D_{5h} isomers of the endohedral fullerenes $Tm_3N@C_{80}$: icosahedral C_{80} cage encapsulation of a Trimetallic nitride magnetic cluster with three uncoupled Tm^{3+} ions. Inorg Chem 47:5234–5244
33. Wang X et al (2006) Preparation and structure of $CeSc_2N@C_{80}$: an icosahedral carbon cage enclosing an acentric $CeSc_2N$ unit with buried f Electron spin. J Am Chem Soc 128:8884–8889
34. Svitova AL, Popov AA, Dunsch L (2013) Gd–Sc-based mixed-metal nitride cluster fullerenes: mutual influence of the cage and cluster size and the role of scandium in the electronic structure. Inorg Chem 52:3368–3380
35. Stevenson S, Chancellor CJ, Lee HM, Olmstead MM, Balch AL (2008) Internal and external factors in the structural organization in cocrystals of the mixed-metal endohedrals ($GdSc_2N@I_h$-C_{80}, $Gd_2ScN@I_h$-C_{80}, and $TbSc_2N@I_h$-C_{80}) and nickel(II) octaethylporphyrin. Inorg Chem 47:1420–1427
36. Yang S, Kalbac M, Popov A, Dunsch L (2006) Gadolinium-based mixed-metal nitride clusterfullerenes $Gd_xSc_{3-x}N@C_{80}$ ($x = 1, 2$). Chem Phys Chem 7:1990–1995
37. Yang S, Popov A, Kalbac M, Dunsch L (2008) The isomers of gadolinium scandium nitride clusterfullerenes $Gd_xSc_{3-x}N@C_{80}$ ($x = 1, 2$) and their influence on cluster structure. Chem Eur J 14:2084–2092
38. Wei T et al (2016) Entrapping a group-VB transition metal, vanadium, within an endohedral Metallofullerene: $V_xSc_{3-x}N@I_h$-C_{80} ($x = 1, 2$). J Am Chem Soc 138:207–214
39. Chen N, Zhang E-Y, Wang C-R (2006) C_{80} encaging four different atoms: the synthesis, isolation, and characterizations of $ScYErN@C_{80}$. J Phys Chem B 110:13322–13325
40. Dunsch L, Krause M, Noack J, Georgi P (2004) Endohedral nitride cluster fullerenes: formation and spectroscopic analysis of $L_{3-x}M_xN@C_{2n}$ ($0 \leq x \leq 3$; N = 39,40). J Phys Chem Solids 65:309–315
41. Yang S, Dunsch L (2005) A large family of dysprosium-based trimetallic nitride endohedral fullerenes: $Dy_3N@C_{2n}$ ($39 \leq n \leq 44$). J Phys Chem B 109:12320–12328
42. Stevenson S et al (2007) Effect of copper metal on the yield of $Sc_3N@C_{80}$ metallofullerenes. Chem Commun 2007:4263–4265
43. Stevenson S et al (2007) Chemically adjusting plasma temperature, energy, and reactivity (CAPTEAR) method using NO_x and combustion for selective synthesis of $Sc_3N@C_{80}$ metallic nitride fullerenes. J Am Chem Soc 129:16257–16262
44. Stevenson S et al (2012) Selective synthesis, isolation, and crystallographic characterization of $LaSc_2N@I_h$-C_{80}. Inorg Chem 51:13096–13102
45. Yang S, Zhang L, Zhang W, Dunsch L (2010) A facile route to metal nitride clusterfullerenes by using Guanidinium salts: a selective organic solid as the nitrogen source. Chem Eur J 16: 12398–12405
46. Jiao M et al (2012) Urea as a new and cheap nitrogen source for the synthesis of metal nitride clusterfullerenes: the role of decomposed products on the selectivity of fullerenes. Chem Eur J 18:2666–2673
47. Svitova A, Braun K, Popov AA, Dunsch L (2012) A platform for specific delivery of lanthanide–scandium mixed-metal cluster fullerenes into target cells. ChemistryOpen 1:207–210
48. Yang S, Wei T, Jin F (2017) When metal clusters meet carbon cages: endohedral clusterfullerenes. Chem Soc Rev 46:5005–5058

49. Shinohara H (2000) Endohedral metallofullerenes. Rep Prog Phys 63:843–892
50. Liu F, Guan J, Wei T, Wang S, Yang S (2013) Synthesis and isolation of endohedral fullerenes-a general review. In Endohedral fullerenes. WORID SCIENTIFIC, pp19–60
51. Wang C-R et al (2001) A scandium carbide endohedral metallofullerene: $(Sc_2C_2)@C_{84}$. Angew Chem Int Ed 40:397–399
52. Shi Z-Q, Wu X, Wang C-R, Lu X, Shinohara H (2006) Isolation and characterization of $Sc_2C_2@C_{68}$: a metal-carbide endofullerene with a non-IPR carbon cage. Angew Chem Int Ed 45:2107–2111
53. Lu X et al (2011) Structural elucidation and regioselective functionalization of an unexplored carbide cluster metallofullerene $Sc_2C_2@C_s(6)$-C_{82}. J Am Chem Soc 133:19553–19558
54. Kurihara H et al (2012) X-ray structures of $Sc_2C_2@C_{2n}$ (n = 40-42): in-depth understanding of the core-shell interplay in carbide cluster metallofullerenes. Inorg Chem 51:746–750
55. Kurihara H et al (2011) $Sc_2C_2@C_{80}$ rather than $Sc_2@C_{82}$: templated formation of unexpected $C_{2v}(5)$-C_{80} and temperature-dependent dynamic motion of internal Sc_2C_2 cluster. J Am Chem Soc 133:2382–2385
56. Kurihara H et al (2012) Chemical understanding of carbide cluster metallofullerenes: a case study on $Sc_2C_2@C_{2v}(5)$-C_{80} with complete X-ray crystallographic characterizations. J Am Chem Soc 134:3139–3144
57. Iiduka Y et al (2007) Experimental and theoretical studies of the scandium carbide endohedral Metallofullerene $Sc_2C_2@C_{82}$ and its Carbene derivative. Angew Chem Int Ed 46:5562–5564
58. Yamazaki Y et al (2008) Observation of ^{13}C NMR chemical shifts of metal carbides encapsulated in fullerenes: $Sc_2C_2@C_{82}$, $Sc_2C_2@C_{84}$, and $Sc_3C_2@C_{80}$. Angew Chem Int Ed 47: 7905–7908
59. Chen CH et al (2015) Beyond the butterfly: $Sc_2C_2@C_{2v}(9)$-C_{86}, an endohedral fullerene containing a planar, twisted Sc_2C_2 unit with remarkable crystalline order in an unprecedented carbon cage. J Am Chem Soc 137:10116–10119
60. Chen CH et al (2016) Zigzag Sc_2C_2 carbide cluster inside a [88]fullerene cage with one heptagon, $Sc_2C_2@C_s$(hept)-C_{88}: a kinetically trapped fullerene formed by C_2 insertion? J Am Chem Soc 138:13030–13037
61. Iiduka Y et al (2005) Structural determination of metallofullerene Sc_3C_{82} revisited: a surprising finding. J Am Chem Soc 127:12500–12501
62. Nishibori E et al (2006) High-resolution analysis of $(Sc_3C_2)@C_{80}$ metallofullerene by third generation synchrotron radiation X-ray powder diffraction. J Phys Chem B 110:19215–19219
63. Pan C et al (2019) Crystallographic characterization of Y_2C_{2n} (2n = 82, 88–94): direct Y–Y bonding and cage-dependent cluster evolution. Chem Sci 10:4707–4713
64. Inoue T, Tomiyama T, Sugai T, Shinohara H (2003) Spectroscopic and structural study of Y_2C_2 carbide encapsulating endohedral metallofullerene: $(Y_2C_2)@C_{82}$. Chem Phys Lett 382:226–231
65. Inoue T et al (2004) Trapping a C_2 radical in endohedral metallofullerenes: synthesis and structures of $(Y_2C_2)@C_{82}$ (Isomers I, II, and III). J Phys Chem B 108:7573–7579
66. Nishibori E et al (2006) A C_2 molecule entrapped in the pentagonal-dodecahedral Y_2 cage in $Y_2C_2@C_{82}$(III). ChemPhysChem 7:345–348
67. Cai W et al (2015) Anomalous compression of $D_5(450)$-C_{100} by encapsulating La_2C_2 cluster instead of La_2. J Am Chem Soc 137:10292–10296
68. Cai W, Li FF, Bao L, Xie Y, Lu X (2016) Isolation and crystallographic characterization of $La_2C_2@C_s(574)$-C_{102} and $La_2C_2@C_2(816)$-C_{104}: evidence for the top-down formation mechanism of fullerenes. J Am Chem Soc 138:6670–6675
69. Zhao S et al (2017) Stabilization of Giant fullerenes $C_2(41)$-C_{90}, $D_3(85)$-C_{92}, $C_1(132)$-C_{94}, $C_2(157)$-C_{96}, and $C_1(175)$-C_{98} by encapsulation of a large La_2C_2 cluster: the importance of cluster-cage matching. J Am Chem Soc 139:4724–4728
70. Yang H et al (2008) Detection of a family of gadolinium-containing endohedral fullerenes and the isolation and crystallographic characterization of one member as a metal−carbide encapsulated inside a large fullerene cage. J Am Chem Soc 130:17296–17300

71. Sado Y et al (2014) Structure of Tm_2 and Tm_2C_2 encapsulated in low-symmetry $C_{82}(C_s(6))$ fullerene cage by single crystal X-ray diffraction. Chem Phys Lett 600:38–42
72. Cao B et al (2001) EELS and ^{13}C NMR characterization of pure $Ti_2@C_{80}$ metallofullerene. J Am Chem Soc 123:9679–9680
73. Tan K, Lu X (2005) Ti_2C_{80} is more likely a titanium carbide endohedral metallofullerene $(Ti_2C_2)@C_{78}$. Chem Commun 2005:4444–4446
74. Yumura T, Sato Y, Suenaga K, Iijima S (2005) Which do endohedral Ti_2C_{80} Metallofullerenes prefer energetically: $Ti_2@C_{80}$ or $Ti_2C_2@C_{78}$? A theoretical study. J Phys Chem B 109:20251–20255
75. Sato Y et al (2006) Direct imaging of intracage structure in titanium-carbide endohedral metallofullerene. Phys Rev B 73:193401
76. Tagmatarchis N, Shinohara H (2000) Production, separation, isolation, and spectroscopic study of dysprosium endohedral Metallofullerenes. Chem Mater 12:3222–3226
77. Ito Y et al (2007) Enhanced 1520 nm photoluminescence from Er^{3+} ions in Di-erbium-carbide Metallofullerenes $(Er_2C_2)@C_{82}$ (Isomers I, II, and III). ACS Nano 1:456–462
78. Stevenson S et al (2018) Identifying a needle in a haystack: isolation and structural characterization of Er_2C_{94} as the carbide $Er_2C_2@D_3(85)$-C_{92}. Chem Eur J 24:13479–13484
79. Xu W et al (2011) Entrapped planar Trimetallic carbide in a fullerene cage: synthesis, isolation, and spectroscopic studies of $Lu_3C_2@C_{88}$. J Phys Chem C 115:402–405
80. Okimoto H et al (2008) Element-specific magnetic properties of Di-erbium $Er_2@C_{82}$ and $Er_2C_2@C_{82}$ metallofullerenes: a synchrotron soft X-ray magnetic circular dichroism study. J Phys Chem C 112:6103–6109
81. Wang T-S et al (2009) Russian-doll-type metal carbide endofullerene: synthesis, isolation, and characterization of $Sc_4C_2@C_{80}$. J Am Chem Soc 131:16646–16647
82. Feng Y et al (2013) Structural and electronic studies of metal carbide clusterfullerene $Sc_2C_2@C_s$-C_{72}. Nanoscale 5:6704–6707
83. Zhang J et al (2013) A missing link in the transformation from asymmetric to symmetric metallofullerene cages implies a top-down fullerene formation mechanism. Nat Chem 5:880
84. Zhang J et al (2012) Nanoscale fullerene compression of an yttrium carbide cluster. J Am Chem Soc 134:8487–8493
85. Yu P et al (2019) Trapping an unprecedented Ti_3C_3 unit inside the icosahedral C_{80} fullerene: a crystallographic survey. Chem Sci 10:10925–10930
86. Svitova AL et al (2014) Endohedral fullerene with μ_3-carbido ligand and titanium-carbon double bond stabilized inside a carbon cage. Nat Commun 5:3568
87. Junghans K et al (2015) Methane as a selectivity booster in the arc-discharge synthesis of endohedral fullerenes: selective synthesis of the single-molecule magnet $Dy_2TiC@C_{80}$ and its congener $Dy_2TiC_2@C_{80}$. Angew Chem Int Ed Engl 54:13411–13415
88. Junghans K et al (2016) Synthesis and isolation of the Titanium-Scandium endohedral fullerenes-$Sc_2tic@I_h$-C_{80}, Sc_2 $TiC@D_{5h}$-C_{80} and $Sc_2TiC_2@I_h$-C_{80}: metal size tuning of the Ti(IV) /Ti(III) redox potentials. Chem Eur J 22:13098–13107
89. Stevenson S et al (2008) A distorted tetrahedral metal oxide cluster inside an icosahedral carbon cage. Synthesis, isolation, and structural characterization of $Sc_4(\mu_3\text{-}O)_2@I_h$-$C_{80}$. J Am Chem Soc 130:11844–11845
90. Mercado BQ et al (2010) A seven atom cluster in a carbon cage, the crystallographically determined structure of $Sc_4(\mu_3\text{-}O)_3@I_h$-$C_{80}$. Chem Commun 46:279–281
91. Mercado BQ et al (2010) $Sc_2(\mu_2\text{-}O)$ trapped in a fullerene cage: the isolation and structural characterization of $Sc_2(\mu_2\text{-}O)@C_s(6)$-$C_{82}$ and the relevance of the thermal and entropic effects in fullerene isomer selection. J Am Chem Soc 132:12098–12105
92. Zhang M et al (2014) Facile synthesis of an extensive family of $Sc_2O@C_{2n}$ (n = 35–47) and chemical insight into the smallest member of $Sc_2O@C_2(7892)$–C_{70}. J Phys Chem C 118:28883–28889
93. Feng L et al (2016) Endohedrally stabilized C_{70} isomer with fused pentagons characterized by crystallography. Dalton Trans 45:8142–8148

94. Yang T et al (2015) $Sc_2O@T_d(19151)$-C_{76}: hindered cluster motion inside a tetrahedral carbon cage probed by crystallographic and computational studies. Chem Eur J 21:11110–11117
95. Tang Q et al (2016) $Sc_2O@C_{3v}(8)$-C_{82}: a missing isomer of $Sc_2O@C_{82}$. Inorg Chem 55:1926–1933
96. Tang Q et al (2015) $Sc_2O@C_{2v}(5)$-C_{80}: dimetallic oxide cluster inside a C_{80} fullerene cage. Inorg Chem 54:9845–9852
97. Abella L et al (2016) $Sc_3O@I_h(7)$-C_{80}: a trimetallic oxide clusterfullerene abundant in the raw soot. J Phys Chem C 120:26159–26167
98. Liu A et al (2019) $Ho_2O@C_{74}$: Ho_2O cluster expands within a small non-IPR fullerene cage of $C_2(13333)$-C_{74}. Inorg Chem 58:4774–4781
99. Cong H et al (2019) $Ho_2O@C_{84}$: crystallographic evidence showing linear metallic oxide cluster encapsulated in IPR fullerene cage of $D_{2d}(51591)$-C_{84}. Inorg Chem 58:10905–10911
100. Yang W et al (2019) Single molecule magnetism with strong magnetic anisotropy and enhanced Dy···Dy coupling in three isomers of Dy-oxide Clusterfullerene $Dy_2O@C_{82}$. Adv Sci 6:1901352
101. Yang W et al (2018) Mixed dimetallic cluster fullerenes: $ScGdO@C_{3v}(8)$-C_{82} and $ScGdC_2@C_{2v}(9)$-C_{82}. Inorg Chem 57:11597–11605
102. Dunsch L et al (2010) Metal sulfide in a C_{82} fullerene cage: a new form of endohedral clusterfullerenes. J Am Chem Soc 132:5413–5421
103. Chen N et al (2010) Synthesis of a new endohedral fullerene family, $Sc_2S@C_{2n}$ (n = 40–50) by the introduction of SO_2. Chem Commun 46:4818–4820
104. Chen N et al (2013) $Sc_2S@C_2(7892)$–C_{70}: a metallic sulfide cluster inside a non-IPR C_{70} cage. Chem Sci 4:180–186
105. Chen N et al (2012) $Sc_2S@C_s(10528)$-C_{72}: a dimetallic sulfide endohedral fullerene with a non isolated pentagon rule cage. J Am Chem Soc 134:7851–7860
106. Li F-F et al (2013) $Ti_2S@D_{3h}(24109)$-C_{78}: a sulfide cluster metallofullerene containing only transition metals inside the cage. Chem Sci 4:3404
107. Yang S et al (2013) An improbable monometallic cluster entrapped in a popular fullerene cage: $YCN@C_s(6)$-C_{82}. Sci Rep 3:1487
108. Liu F et al (2014) Putting a terbium-monometallic cyanide cluster into the C_{82} fullerene cage: $TbCN@C_2(5)$-C_{82}. Inorg Chem 53:5201–5205
109. Liu F et al (2016) Triangular monometallic cyanide cluster entrapped in carbon cage with geometry-dependent molecular magnetism. J Am Chem Soc 138:14764–14771
110. Liu F et al (2017) Mononuclear clusterfullerene single-molecule magnet containing strained fused-pentagons stabilized by a nearly linear metal cyanide cluster. Angew Chem 129:1856–1860
111. Jin F, Wang S, Tamm NB, Yang S, Troyanov SI (2017) Synthesis, isolation, and trifluoromethylation of two isomers of C_{84} -based monometallic cyanide clusterfullerenes: interplay between the endohedral cluster and the exohedral addends. Angew Chem Int Ed Engl 56:11990–11994
112. Jin F et al (2016) Trifluoromethyl derivatives of a monometallic cyanide cluster fullerene, $YCN@C_{82}(6)(CF_3)_{16/18}$. Inorg Chem 55:12523–12526
113. Xin J et al (2021) Ancient pigment to treasure: Prussian blue as a cheap solid cyanide/nitrogen dual-source affording the high-yield syntheses of pricey endohedral clusterfullerenes. Inorg Chem Front 8:1719–1726
114. Krause M, Ziegs F, Popov AA, Dunsch L (2007) Entrapped bonded hydrogen in a fullerene: the five-atom cluster Sc_3CH in C_{80}. ChemPhysChem 8:537–540
115. Feng Y et al (2014) Electron-spin excitation by implanting hydrogen into metallofullerene: the synthesis and spectroscopic characterization of $Sc_4C_2H@I_h$-C_{80}. Chem Commun 50:12166–12168
116. Wang T-S et al (2010) Planar quinary cluster inside a fullerene cage: synthesis and structural characterizations of $Sc_3NC@C_{80}$-I_h. J Am Chem Soc 132:16362–16364

117. Wu J et al (2011) Synthesis, isolation, characterization, and theoretical studies of $Sc_3NC@C_{78}$-C_2. J Phys Chem C 115:23755–23759
118. Wang T, Wu J, Feng Y (2014) Scandium carbide/cyanide alloyed cluster inside fullerene cage: synthesis and structural studies of $Sc_3(\mu_3\text{-}C_2)(\mu_3\text{-}CN)@I_h\text{-}C_{80}$. Dalton Trans 43:16270–16274
119. Guo T et al (1992) Uranium stabilization of C_{28}: a tetravalent fullerene. Science 257:1661
120. Akiyama K et al (2001) Isolation and characterization of light actinide metallofullerenes. J Am Chem Soc 123:181–182
121. Akiyama K et al (2003) Production and characterization of actinide metallofullerenes. J Radioanal Nucl Chem 255:155–158
122. Dunk PW et al (2012) The smallest stable fullerene, $M@C_{28}$ (m = Ti, Zr, U): stabilization and growth from carbon vapor. J Am Chem Soc 134:9380–9389
123. Wang Y et al (2017) Unique four-Electron metal-to-cage charge transfer of Th to a C_{82} fullerene cage: complete structural characterization of $Th@C_{3v}(8)\text{-}C_{82}$. J Am Chem Soc 139:5110–5116
124. Cai W, Chen CH, Chen N, Echegoyen L (2019) Fullerenes as Nanocontainers that stabilize unique actinide species inside: structures, formation, and reactivity. Acc Chem Res 52:1824–1833
125. Cai W et al (2017) Single crystal structures and theoretical calculations of uranium endohedral metallofullerenes ($U@C_{2n}$, 2n = 74, 82) show cage isomer dependent oxidation states for U. Chem Sci 8:5282–5290
126. Cai W et al (2018) Synthesis and characterization of non-isolated-pentagon-rule actinide endohedral metallofullerenes $U@C_1(17418)\text{-}C_{76}$, $U@C_1(28324)\text{-}C_{80}$, and $Th@C_1(28324)\text{-}C_{80}$: low-symmetry cage selection directed by a tetravalent ion. J Am Chem Soc 140:18039–18050
127. Wang Y et al (2019) $Th@C_1(11)\text{-}C_{86}$: an actinide encapsulated in an unexpected C_{86} fullerene cage. Chem Commun 55:9271–9274
128. Jin M et al (2019) $Th@T_d(19151)\text{-}C_{76}$: a highly symmetric fullerene cage stabilized by a tetravalent actinide metal ion. Inorg Chem 58:16722–16726
129. Zhang X et al (2018) $U_2@I_h(7)\text{-}C_{80}$: crystallographic characterization of a long-sought dimetallic actinide endohedral fullerene. J Am Chem Soc 140:3907–3915
130. Zhuang J et al (2021) Characterization of a strong covalent Th^{3+}-Th^{3+} bond inside an $I_h(7)\text{-}C_{80}$ fullerene cage. Nat Commun 12:2372
131. Zhang X et al (2018) A diuranium carbide cluster stabilized inside a C_{80} fullerene cage. Nat Commun 9:2753
132. Zhuang J et al (2019) Diuranium(IV) Carbide Cluster U_2C_2 stabilized inside fullerene cages. J Am Chem Soc 141:20249–20260
133. Fuertes-Espinosa C et al (2018) Purification of uranium-based endohedral metallofullerenes (EMFs) by selective supramolecular encapsulation and release. Angew Chem Int Ed 57:11294–11299
134. Li X et al (2021) $U_2N@I_h(7)\text{-}C_{80}$: fullerene cage encapsulating an unsymmetrical U(iv)=N=U(v) cluster. Chem Sci 12:282–292
135. Akasaka T et al (1995) Exohedral adducts of $La@C_{82}$. Nature 374:600–601
136. Yamada M, Akasaka T, Nagase S (2018) Salvaging reactive fullerenes from Soot by exohedral derivatization. Angew Chem Int Ed 57:13394–13405
137. Nikawa H et al (2005) Missing metallofullerene $La@C_{74}$. J Am Chem Soc 127:9684–9685
138. Wakahara T et al (2006) $La@C_{72}$ having a non-IPR carbon cage. J Am Chem Soc 128:14228–14229
139. Nikawa H et al (2009) Missing metallofullerene with C_{80} cage. J Am Chem Soc 131:10950–10954
140. Akasaka T et al (2010) Dichlorophenyl derivatives of $La@C_{3v}(7)\text{-}C_{82}$: endohedral metal induced localization of pyramidalization and spin on a triple-hexagon junction. Angew Chem Int Ed Engl 49:9715–9719

141. Liu F et al (2017) Single molecule magnet with an unpaired electron trapped between two lanthanide ions inside a fullerene. Nat Commun 8:16098
142. Wang Z et al (2013) Missing small-bandgap metallofullerenes: their isolation and electronic properties. Angew Chem Int Ed Engl 52:11770–11774
143. Nakagawa A et al (2018) Crystalline functionalized endohedral C_{60} metallofullerides. Nat Commun 9:3073
144. Chai Y et al (1991) Fullerenes with metals inside. J Phys Chem 95:7564–7568
145. Weaver JH et al (1992) XPS probes of carbon-caged metals. Chem Phys Lett 190:460–464
146. Dunk PW et al (2013) Metallofullerene and fullerene formation from condensing carbon gas under conditions of stellar outflows and implication to stardust. Proc Natl Acad Sci 110:18081
147. Peters G, Jansen M (1992) A new fullerene synthesis. Angew Chem Int Ed Engl 31:223–224
148. Reich A, Panthöfer M, Modrow H, Wedig U, Jansen M (2004) The structure of $Ba@C_{74}$. J Am Chem Soc 126:14428–14434
149. Haufe O, Hecht M, Grupp A, Mehring M, Jansen M (2005) Isolation and spectroscopic characterization of new endohedral fullerenes in the size gap of C_{74} to C_{76}. Z Anorg Allg Chem 631:126–130
150. Bucher K, Epple L, Mende J, Mehring M, Jansen M (2006) Synthesis, isolation and characterization of new endohedral fullerenes $M@C_{72}$ (M = Eu, Sr, Yb). Phys Status Solidi B 243:3025–3027
151. Krokos E (2010) Plasma coupled radio frequency furnace: the synthesis, separation, and elucidation of the elusive Sc_4C_{82} fullerene. J Phys Chem C 114:7626–7630
152. Tellgmann R, Krawez N, Lin SH, Hertel IV, Campbell EEB (1996) Endohedral fullerene production. Nature 382:407–408
153. Campbell EEB, Tellgmann R, Krawez N, Hertel IV (1997) Production and LDMS characterisation of endohedral alkalifullerene films. J Phys Chem Solids 58:1763–1769
154. Aoyagi S et al (2010) A layered ionic crystal of polar $Li@C_{60}$ superatoms. Nat Chem 2:678–683
155. Okada H et al (2012) Preparation of endohedral fullerene containing lithium ($Li@C_{60}$) and isolation as pure hexafluorophosphate salt ($[Li^+@C_{60}][PF_6^-]$). RSC Adv 2:10624
156. Kikuchi K et al (1994) Encapsulation of radioactive ^{159}Gd and ^{161}Tb atoms in fullerene cages. J Am Chem Soc 116:9775–9776
157. Cagle DW et al (1996) Synthesis, characterization, and neutron activation of holmium metallofullerenes. J Am Chem Soc 118:8043–8047
158. Ohtsuki T et al (1996) Insertion of be atoms in C_{60} fullerene cages: $be@C_{60}$. Phys Rev Lett 77: 3522–3524
159. Diener MD, Alford JM, Kennel SJ, Mirzadeh S (2007) $^{212}Pb@C_{60}$ and its water-soluble derivatives: synthesis, stability, and suitability for radioimmunotherapy. J Am Chem Soc 129: 5131–5138
160. Fuchs D et al (1996) Extraction and chromatographic elution behavior of endohedral metallofullerenes:? Inferences regarding effective dipole moments. J Phys Chem 100:725–729
161. Laukhina E et al (1998) Novel proficient method for isolation of endometallofullerenes from fullerene-containing soots by two-stepo-xylene–N, N-dimethylformamide extraction. J Mater Chem 8:893
162. Xiao J, Savina MR, Martin GB, Francis AH, Meyerhoff ME (1994) Efficient HPLC purification of endohedral Metallofullerenes on a porphyrin-silica stationary phase. J Am Chem Soc 116:9341–9342
163. Ding J, Yang S (1996) Efficient N,N-Dimethylformamide extraction of endohedral metallofullerenes for HPLC purification. Chem Mater 8:2824–2827
164. Lian Y, Shi Z, Zhou X, Gu Z (2004) Different extraction behaviors between divalent and trivalent endohedral metallofullerenes. Chem Mater 16:1704–1714
165. Liu BB et al (1996) High yield synthesis and extraction of $La@C_{2n}$. Solid State Commun 97: 407–410

166. Capp C, Wood TD, Marshall AG, Coe JV (1994) High-pressure toluene extraction of La@C_n for even n from 74 to 90. J Am Chem Soc 116:4987–4988
167. Tso TSC et al (1996) Solid phase extraction as a simple method for the enrichment of endohedral metallofullerenes. Tetrahedron Lett 37:9294–9252
168. Stevenson S et al (2009) Selective complexation and reactivity of metallic nitride and oxometallic fullerenes with Lewis acids and use as an effective purification method. Inorg Chem 48:11685–11690
169. Akiyama K et al (2012) Non-HPLC rapid separation of metallofullerenes and empty cages with $TiCl_4$ Lewis acid. J Am Chem Soc 134:9762–9767
170. Tsuchiya T et al (2004) Reduction of endohedral metallofullerenes: a convenient method for isolation. Chem Mater 16:4343–4346
171. Elliott B, Yu L, Echegoyen L (2005) A simple isomeric separation of D_{5h} and Ih $Sc_3N@C_{80}$ by selective chemical oxidation. J Am Chem Soc 127:10885–10888
172. Ge Z, Duchamp JC, Cai T, Gibson HW, Dorn HC (2005) Purification of endohedral trimetallic nitride fullerenes in a single, facile step. J Am Chem Soc 127:16292–16298
173. Stevenson S et al (2006) Nonchromatographic "Stir and Filter Approach" (SAFA) for isolating $Sc_3N@C_{80}$ metallofullerenes. J Am Chem Soc 128:8829–8835
174. Stevenson S et al (2007) Rapid removal of D_{5h} isomer using the "Stir and Filter Approach" and isolation of large quantities of Isomerically pure $Sc_3N@C_{80}$ metallic nitride fullerenes. J Am Chem Soc 129:6072–6073
175. Angeli CD et al (2008) Purification of Trimetallic nitride templated endohedral metallofullerenes by a chemical reaction of congeners with eutectic 9-Methylanthracene. Chem Mater 20:4993–4997
176. Olah GA et al (1997) Friedel-crafts reactions of buckminsterfullerene. Fuller Sci Technol 5: 389–405

Structures and Properties of Endohedral Metallofullerenes

18

Xiaole Jiang, Muqing Chen, and Shangfeng Yang

Contents

Abstract

Endohedral metallofullerenes (EMFs) are a unique class of fullerenes, featuring encapsulation of metal ions or clusters within hollow fullerene cages. Owing to electron transfer from the inner species to the outer fullerene cage, EMFs exhibit unique electronic, physical, and chemical properties. In this chapter, we focus on the structures and properties of EMFs. Determining molecular structures of EMFs has been fulfilled by single-crystal X-ray diffraction crystallography, which can unambiguously tell both the isomeric structures of the outer carbon cages and the geometrical position of the inner species. The electronic properties of EMFs have been extensively investigated by UV-vis-NIR absorption spectroscopy and electrochemistry, revealing the important role of intramolecular electron transfer on the entire EMF molecule. Moreover, magnetic properties especially single

X. Jiang · M. Chen (✉) · S. Yang (✉)
Hefei National Laboratory for Physical Science at Microscale, CAS Key Laboratory of Materials for Energy Conversion, Department of Materials Science and Engineering, University of Science and Technology of China, Hefei, China
e-mail: jiangle@mail.ustc.edu.cn; mqchen@ustc.edu.cn; sfyang@ustc.edu.cn

X. Lu et al. (eds.), *Handbook of Fullerene Science and Technology*,
https://doi.org/10.1007/978-981-16-8994-9_27

molecular magnetisms resulted from the unique coordination interactions within the encapsulated metal clusters are among the most intriguing physical properties of EMFs, which are inaccessible by empty fullerenes, rendering potential applications of EMFs in quantum computing and high-density storage devices.

Keywords

Endohedral metallofullerene · Luminescence · Single-molecule magnet

Introduction

Endohedral metallofullerenes (EMFs) are a unique class of fullerenes, featuring encapsulation of metal ions or clusters within hollow fullerene cages. Electron transfer from the inner encapsulated species to the fullerene cage, rendering fascinating electronic, physical, and chemical properties different from the empty fullerenes. Early studies focused on those EMFs with species encapsulating purely metal ions ($M_x@C_{2n}$), until Dorn et al. discovered an unprecedented EMF, $Sc_3N@C_{80}$ as the first member of metal nitride clusterfullerenes (NCFs), by accidentally introducing nitrogen gas into the Krätschmer–Huffman DC-arc discharging generator in 1999 [1]. Significantly different from the previously reported EMFs based on encapsulation of metal atom(s) only, for NCF represented by $Sc_3N@C_{80}$, a metal nitride cluster consisting of both metal and nonmetal atoms is encapsulated. This structural feature significantly enlarges the family member of EMFs since different metal and nonmetal atoms can be combined to form a large variety of metal clusters, with which endohedral clusterfullerenes become nowadays the largest branch of EMFs [2].

EMFs are classifiable into two types according to the encased species: conventional EMFs and cluster EMFs. Conventional EMFs including mono-EMFs, di-EMFs, and tri-EMFs. For cluster EMFs, following the advance in NCFs, several other types of endohedral clusterfullerenes have been isolated and structurally characterized, including metal carbide clusterfullerenes (CCFs) [3], metal oxide clusterfullerenes (OCFs) [4], metal sulfide clusterfullerenes (SCFs) [5], metal cyanide clusterfullerenes (CYCFs) [6], and metal hydrocarbide clusterfullerenes (HCCFs) [7] and metal carbonitride clusterfullerenes (CNCFs) [8]. The involvement of nonmetal atom(s) enables specific geometric configuration of the encapsulated metal cluster, consequently the coordination interaction between the encapsulated metal cluster and the outer carbon cage becomes tunable, thus bringing about some new physical and chemical properties of endohedral clusterfullerenes such as single molecule magnetism [2, 9, 10].

Several exhaustive reviews on all aspects of EMFs have been published by different groups [2, 11–14]. In this chapter, we focus on the structures and properties of EMFs. We first discuss their molecular structures, demonstrating the large variety of EMFs identified during the past decade. Moreover, the intrinsic properties of EMFs, including especially their electronic, optical, and magnetic properties, are discussed in details.

Molecular Structures of EMFs

Structure Characterization

Elucidating the molecular structures of EMFs is crucial to understand their properties. Structure elucidation of EMFs is not easy since the inner species (metal ions or clusters) are shielded by the outer carbon cages. After more than two decades, several effective characterization methods have been developed in determining the molecular structures of EMFs, including single-crystal X-ray diffraction crystallography, ^{13}C NMR spectroscopy, and vibrational spectroscopy combined with quantum chemical calculations [11]. Among them, after the first synchrotron X-ray diffraction study on $Y@C_{82}$ powder in 1995 which provided the evidence of its endohedral nature [15], single-crystal X-ray diffraction (XRD) crystallography has been extensively used to determine unambiguously both the isomeric structures of the outer carbon cages and the geometrical position of the inner species, and turns out to be the most credible method [2, 12–14]. However, one drawback for using single-crystal XRD to determine the molecular structures of EMFs and empty fullerenes such as C_{60} is the rotational disorder of the fullerene molecules in their crystals, resulting in difficulties in not only obtaining high-quality single crystals but also structural refinement [13]. To solve this problem, co-crystallizing EMF molecule with a host molecule so as to hamper the rotation of EMF molecule has been developed since the late 1990s [1]. The dominant host molecules employed during the last two decades are metalloporphyrines developed by Balch and Olmstead, including Ni(II)- or Co(II)-OEP (OEP = 2,3,7,8,12,13,17,18-octaethylporphyrin dianion, see Fig. 1a) [16]. Very recently, Xie, Yang et al. designed and synthesized a new host molecule, decapyrrylcorannulene (abbreviated as DPC, see Fig. 1b), which is capable of holding almost all commonly known types of fullerene including EMFs toward effective co-crystallization [17]. Single crystal growth of both types of EMF-containing co-crystallized supramolecules has been accomplished, followed by unambiguous structure determinations by single-crystal XRD (Fig. 1). Besides the co-crystallization strategy, exohedral chemical derivatization appears to be

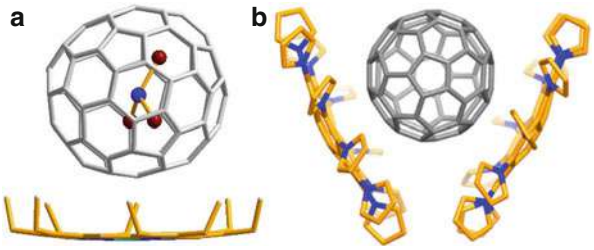

Fig. 1 Single-crystal X-ray diffraction studies of $Sc_3N@$-C_{2v}(39718)-C_{82}·Ni^{II}(OEP)·$2C_6H_6$ with 30% thermal ellipsoids; only one orientation of fullerene cage (0.50 occupancy) and the major site of Sc_3N are shown; the solvent molecule (benzene), another orientation of the fullerene cage, the minor site of Sc_3N, and hydrogen atoms of the porphyrin are all omitted for clarity (**a**); crystallographic structure of co-crystals between DPC and C_{60} (**b**)

another approach to effectively hinder the rotation of EMF molecules via attaching functional groups onto the carbon cage [18, 19].

Conventional Endohedral Metallofullerenes

Contrary to endohedral clusterfullerenes discovered in 1999, conventional endohedral metallofullerenes including mono-metallofullerenes (mono-EMFs), dimetallofullerenes (di-EMFs), and trimetallofullerenes (tri-EMFs), for which only metal atom(s) are encapsulated within fullerene cages, were extensively studied before 1999 [13]. As the earliest members of EMF family, mono-EMFs represent a simple model for elucidating intramolecular metal-cage interactions. So far, the encapsulated metals of mono-EMFs are mainly rare earth metals including Group-IIIB (Sc, Y) and lanthanide metals (La-Lu), while actinide metals (Th and U) and a few main-group metals including group-IIA (Ca, Sr, Ba), group-IA (Li, Na, K), and group-IVB transition metals (Ti, Zr, Hf) were also reported to form mono-EMFs. Despite of the diversity of the types of encapsulated metals, a common feature of mono-EMFs is that the encapsulated metal atom is always located off-center, imposing a two to four electrons transfer from the encapsulated metal to the outer carbon cage [13, 20].

Ba@D_{3h}-C_{74} is the first mono-EMFs, whose structure was determined by single-crystal X-ray diffraction co-crystallized with Co^{II}(OEP). For mono-EMFs, the most popular fullerene cage reported up to now is C_{82}. Interestingly, $C_2(5)$-C_{82}, $C_s(6)$-C_{82}, $C_{2v}(9)$-C_{82}, and $C_{3v}(7)$-C_{82} are found to be the most commonly isolated isomeric cages for mono-EMFs based on divalent rare earth metals, while mono-EMFs based on trivalent rare earth metals tend to have $C_{2v}(9)$-C_{82}, and $C_s(6)$-C_{82} isomeric cages. Noteworthy, single-crystal XRD structures of the pristine M@C_{82} mono-EMFs were not reported until the structure characterizations of La@$C_{2v}(9)$-C_{82} [21] (Fig. 2a) and Gd@$C_{2v}(9)$-C_{82} [22] co-crystallized with Ni^{II}(OEP) by Akasaka et al. in 2012. XRD results showed that the metal was located along the C_2 axis and under a hexagonal ring for both of La and Gd. Since then, many mono-EMFs were characterized by single-crystal XRD, such as Yb@C_{82} with $C_2(5)$, $C_s(6)$, and $C_{2v}(9)$ isomers [23], and Sm@C_{2n} with $2n = 82$ ($C_{2v}(5)$, $C_{2v}(6)$, $C_{3v}(7)$, and $C_{2v}(9)$ isomers) [24], $2n = 84$ ($C_2(11)$,

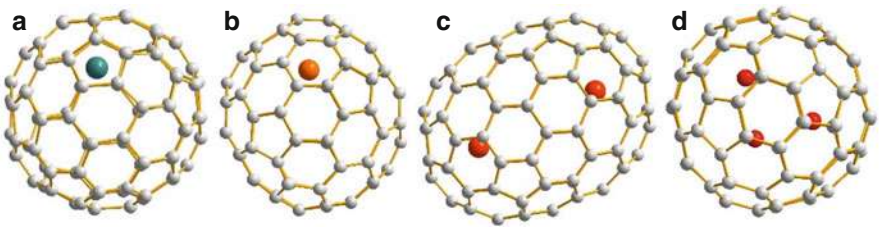

Fig. 2 Molecular structures of selected conventional metallofullerenes: La@$C_{2v}(9)$-C_{82} (**a**), Th@$C_{3v}(8)$-C_{82} (**b**), Sm_2@$D_{3d}(822)$-C_{104} (**c**), and Sm_3@$I_h(7)$-C_{80} (**d**)

$C_2(13)$, and $C_{3d}(19)$ isomers) [25], $2n = 90$ ($C_2(40)$, $C_2(42)$, $C_2(45)$, and $C_{2v}(46)$ isomers) [26], $2n = 92$ ($C_s(24)$, $C_1(42)$ isomers) [27], and $2n = 94$ ($C_{3v}(134)$) [27]. Among the reported mono-EMFs with chemical structures determined experimentally by single-crystal XRD, the smallest cage is based on La@$C_2(10612)$-C_{72} determined from its monoadduct of La@C_{72}-$C_6H_3Cl_2$, which has a non-IPR (IPR = isolated pentagon rule) cage containing a pair of fused pentagons [28], whereas the largest cage is based on M@-$C_{3v}(134)$-C_{94} (M = Ca, Tm, Sm). For Ca@C_{94}-$C_{3v}(134)$, single-crystal XRD results reveal that Ca^{2+} cation is located near C_3 axis and close to a [6,6] junction [29].

Recently a series of actinide metal-based mono-EMFs were reported by Chen, Echegoyen, and coworkers. Th@$C_{3v}(8)$-C_{82} discovered in 2017 represents the first member of this branch, for which single-crystal XRD results revealed that Th located over a cage carbon at the intersection of three hexagons with a short Th-C distance of 2.340(14) Å (Fig. 2b) [20]. Intriguingly, a unique four-electron-transfer found from the encapsulated Th to the outer C_{82} cage was proposed for Th@$C_{3v}(8)$-C_{82}, which is distinctly different from the cases of all previously reported mono-EMFs. Soon later, a series of Th-based mono-EMFs were isolated by the same group, including Th@$T_d(19151)$-C_{76} [30], Th@$C_1(28324)$-C_{80} [31], Th@$C_1(11)$-C_{86} [32], all of which were found to have the four-electron-transfer from Th to the outer carbon cages. Likewise, another actinide metal U was also encapsulated into carbon cages successfully, exemplified by several mono-EMFs such as U@D_{3h}-C_{74}, U@$C_2(5)$-C_{82}, and U@$C_{2v}(9)$-C_{82} with molecular structures determined unambiguously by single-crystal XRD [33]. DFT calculations reveal that U@D_{3h}-C_{74} and U@$C_2(5)$-C_{82} have fourfold electron transfer process whereas a threefold electron transfer is preferred for U@$C_{2v}(9)$-C_{82} [33]. In particular, two U-based mono-EMFs bearing non-IPR cages, U@$C_1(17418)$-C_{76}, U@$C_1(28324)$-C_{80}, have also been isolated very recently and demonstrated to exhibit a fourfold electron transfer process [31]. According to these results, clearly the electronic properties of the actinide metal-based mono-EMFs are dramatically different from those of lanthanide metal-based mono-EMFs [20, 30–33].

Di-EMFs based on encapsulation of two metal atoms can also form along with mono-EMFs, but usually exhibit lower yields. Therefore, the number of structurally determined di-EMFs is far less than that of mono-EMFs [13]. The most popular fullerene cage for di-EMFs is $I_h(7)$-C_{80}, which is stabilized due to a six-electron-transfer from the encapsulated two metal atoms [34]. Later on, in addition to $M_2@I_h(7)$-C_{80}, the family members of di-EMFs based on light lanthanide metals (La, Ce, Pr) were extended to other cages such as $D_2(10611)$-C_{72}, $C_s(17490)$-C_{76}, $D_{3h}(5)$-C_{78}, $D_{5h}(6)$-C_{80}, $I_h(7)$-C_{80}, $C_s(6)$-C_{82}, $C_{2v}(9)$-C_{82}, and $D_{5h}(450)$-C_{100} [34–41]. Among them, $La_2@D_5(450)$-C_{100} is the largest structurally characterized di-EMF based on trivalent metals, for which the encapsulated La^{3+} ions are located under a [5,6]-junction and a La-La distance is 5.7744 Å [41]. On the other hand, similar to the case of mono-EMFs, divalent lanthanide metals have been also reported to form di-EMFs, and $Sm_2@D_{3d}(822)$-C_{104} di-EMF represents the largest structurally characterized di-EMF based on divalent metals, for which each Sm^{3+} ion is located under a triple hexagon

junction and a Sm-Sm distance is 5.7744 Å according to single-crystal XRD results (Fig. 2c) [42]. Interestingly, Sc, Y, and "late" lanthanides (Er, Lu) prefer a trivalent state in mono-EMFs, while in di-EMFs, they adopt a formal 2+ charge state with the metal-metal bond in the M_2 cluster [43]. The most abundant di-EMFs of this type are $M_2@C_{82}$-$C_{3v}(8)$ and $M_2@C_{82}$-$C_s(6)$ [44–47]. Also known are $Er_2@C_{82}$-$C_{2v}(9)$ [48] and $Lu_2@C_{76}$-$T_d(1)$ [49].

More recently, Chen, Echegoyen, and coworkers successfully synthesized and isolated a di-EMF based on actinide metal, $U_2@C_{80}$ [50]. The molecular structure of $U_2@I_h(7)$-C_{80} was definitely determined by single-crystal XRD, indicating that the U ions are located under hexagons, close to or slightly off a C_2 axis and the U-U bond distance ranges from 3.46 to 3.79 Å [50]. In addition, the closest U-C distances are distributed in the range of 2.24–2.82 Å, which is shorter than that reported for the U-C methanide bond (such as 2.779 Å), indicating strong bonding interactions between the encapsulated U metal and the outer $I_h(7)$-C_{80} cage [50]. Moreover, X-ray absorption spectroscopy (XAS) results reveal that the two U ions are in +3 oxidation state resulted from a U-U single bond [50].

As a special case of di-EMFs, dimetallo-azafullerenes $M_2@C_{79}N$ (M = Y, Tb, Gd) were isolated and structurally characterized by Dorn et al. [51]. For $Tb_2@C_{79}N$, single-crystal XRD results reveal that the two Tb atoms are encapsulated inside the pseudo-$I_h(7)$ cage similar to $I_h(7)$-C_{80} cage, for which one carbon atom is replaced by nitrogen atom on the carbon cage. However, deficiency exists in distinguishing between carbon and nitrogen atom by XRD study, so the structure of $M_2@C_{79}N$ was further predicted by DFT theoretical calculations, proposing that the nitrogen atom is likely to be located on the pentagon-hexagon-hexagon junction [51].

As the rare case, tri-EMFs with three metal atoms encapsulated are more difficult to form than mono- and di-EMFs. Up to now, only few tri-EMFs such as $Er_3@C_{74}$ [52], $Tb_3@C_{80}$ [53], $Y_3@C_{80}$ [54], $Sm_3@C_{80}$ [54], and $Dy_3@C_{98}$ [55] have been reported. Except $Sm_3@C_{80}$, the other tri-EMFs were mainly proposed by mass spectrometry without definite structure determination, whether they are in the form of tri-EMFs or carbide clusterfullerenes remains unclear yet. The reason why tri-EMFs have generally quite low yield is likely due to the strong Coulomb repulsion among the encapsulated three metal cations inside carbon cage. As a result, to reduce the repulsion, nonmetal atoms are generally necessary and consequently endohedral clusterfullerenes form preferably. Nevertheless, in 2013, Feng, Shi, and coworkers managed to isolate $Sm_3@I_h(7)$-C_{80} as the only tri-EMF with structure determined experimentally by single-crystal XRD. Interestingly, among the encapsulated three Sm atoms, two Sm atoms reside under hexagonal rings with metal-to-ring-centroid distances of 2.108 and 2.136 Å, respectively, whereas the third Sm atom is close to a 6,6-bond with a metal-to-carbon bond distance of 2.247 Å (Fig. 2d) [56]. The unambiguous identification of $Sm_3@I_h(7)$-C_{80} as the tri-EMF instead of a carbide clusterfullerene is quite important, since it indicates that three metal atoms can be stabilized within a fullerene cage without involvement of any nonmetal mediator [56].

Endohedral Clusterfullerenes

Metal Nitride Clusterfullerenes (NCFs)

As the first endohedral clusterfullerene, $Sc_3N@I_h(7)$-C_{80} NCF has the highest yield among all endohedral fullerenes reported up to now, which even exceeds that of the well-known abundant empty fullerene C_{84} [1]. Such a high production yield of NCF triggers tremendous interests on endohedral clusterfullerenes. The molecular structure of $Sc_3N@I_h(7)$-C_{80} was unambiguously determined by single-crystal XRD and ^{13}C NMR spectroscopy by Dorn et al. [1], indicating that the encapsulated Sc_3N cluster exhibits a planar geometry with three Sc atoms forming an equilateral triangle and nitrogen atom locating in the center, and the Sc-N distances are 1.966–2.011 Å (Fig. 3a) [11]. Soon later, the less abundant isomer of $Sc_3N@I_h(7)$-C_{80}, $Sc_3N@D_{5h}(6)$-C_{80} (Fig. 3b), and several other analogous Sc-NCFs with smaller cages such as $Sc_3N@C_{68}$ [57, 58], $Sc_3N@C_{70}$ [59], $Sc_3N@C_{78}$ [60] were also isolated and determined by single-crystal XRD [61]. In 2015, Yang et al. successfully isolated the long-sought Sc-NCF with cage larger than C_{80}, $Sc_3N@C_{82}$, which is predicted to have low kinetic stability due to small bandgap (Fig. 3c). The isomeric cage of $C_{2v}(39718)$-C_{82} for $Sc_3N@C_{82}$ determined by single-crystal XRD is consistent with the most stable isomer predicted by DFT calculations but dramatically different to those of the reported analogs lanthanide-based $M_3N@C_s(39663)$-C_{82} (M = Gd, Y) bearing a non-IPR C_{82} isomeric cage [62]. This reveals strong

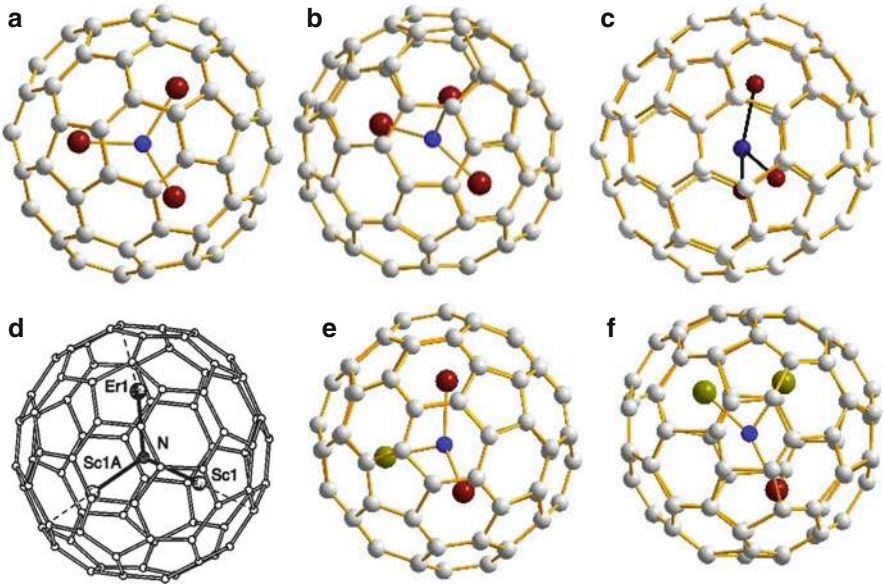

Fig. 3 Molecular structures of selected NCFs: $Sc_3N@I_h(7)$-C_{80} (**a**), $Sc_3N@D_{5h}(6)$-C_{80} (**b**), $Sc_3N@C_{2v}(39718)$-C_{82} (**c**), $ErSc_2N@I_h(7)$-C_{80} (**d**), $VSc_2N@I_h$-C_{80} (**e**), and $V_2ScN@I_h$-C_{80} (**f**)

dependence of the cage isomeric structure on the size of the encaged metal for C_{82}-based NCFs.

The geometric structure of the encapsulated metal nitride cluster has been found to sensitively depend on the size of the metal ion as exemplified by NCFs based on I_h-C_{80} which represents the most common cage of known NCFs. For rare earth metals with relatively small ionic radii like Sc, Lu, and Dy [1, 63, 64], the metal nitride clusters within NCFs always exhibit the planar configuration, whereas those rare earth metals with larger ionic radii such as Y, Tb, and Gd [65–67] tend to form pyramidal nitride clusters within NCFs. A direct observational evidence is that the central N atom within Y_3N cluster is displaced 0.13 Å out of the Y_3 plane within $Y_3N@C_{80}$, while the displacement of N atom increases to 0.5 Å for $Gd_3N@C_{80}$ [65, 67]. This phenomenon can be explained as the change of suffered suppression of the inner metal nitride clusters within a limited space of the carbon cage [2]. For the similar reason, the cage size distribution of $M_3N@C_{2n}$ NCFs is also dependent sensitively on the size of the encapsulated metal, i.e., larger metals prefer to be encapsulated within larger fullerene cages. For instance, while C_{80} is the most abundant cage for NCFs based on Sc, Y, and lanthanide metals Gd-Lu, C_{88} becomes the preferred cage for encapsulating larger metal nitride clusters like Nd_3N, Pr_3N, and Ce_3N [68], and a further increase of the cluster size to La_3N results in the change of the preferential cage to C_{96} [69].

In addition to the homogeneous M_3N cluster, mixed metal NCFs (MMNCFs) encapsulating metal nitride clusters consisting of two or three different metals have also been synthesized, isolated, and structurally characterized. In 2000, $ErSc_2N@I_h(7)$-C_{80} as the first MMNCF was isolated and unambiguously determined by single-crystal XRD, revealing the asymmetric nature of the encapsulated $ErSc_2N$ cluster (Fig. 3d) [70]. Since then, a series of MMNCFs have been isolated and their molecular structures have been extensively investigated, leading to the observation of an interesting phenomenon that, by substituting the large lanthanide metal within M_3N cluster with another rare earth metal (L) with smaller size to form $M_xL_{3-x}N$ mixed metal nitride cluster, the original pyramidal geometry of the encapsulated M_3N clusters tends to adopt a planar structure [66, 71, 72]. For example, when Sc^{3+} (ionic radius of 0.75 Å) substitutes Gd^{3+} (ionic radius of 0.94 Å), both $GdSc_2N$ and Gd_2ScN clusters within $GdSc_2N@I_h(7)$-C_{80} and $Gd_2ScN@I_h(7)$-C_{80} exhibit planar geometry, which is quite different from the pyramidal Gd_3N cluster within $Gd_3N@I_h(7)$-C_{80} [67]. According to the single-crystal XRD results of $GdSc_2N@I_h(7)$-C_{80} and $Gd_2ScN@I_h(7)$-C_{80}, the Gd atoms are located under a hexagon while Sc atoms prefer to stay close to [5,6]-junctions. With the change of the composition of the $Gd_xSc_{3-x}N$ cluster, the metal-metal and metal-carbon distances show difference: for $GdSc_2N@I_h(7)$-C_{80}, the Gd-C distances from the nearest hexagon are 2.459–2.509 Å and the Sc-C distances are 2.268–2.381 Å, which change to a 2.394–2.641 Å and 2.246–2.269 Å, respectively, for $Gd_2ScN@I_h(7)$-C_{80} [71]. Furthermore, MMNCFs encapsulating three different metals such as $ScYErN@C_{80}$ [73] and $DyErScN@I_h$-C_{80} [74] have been also reported, which, however, have lower yields than the homogeneous NCF counterparts and thus require tedious separation.

Noteworthy, MMNCF can also provide an ideal template to encapsulate non-group-3 metals. Since Sc is capable of promoting the production yield of Sc-based MMNCFs due to the high yield of $Sc_3N@C_{80}$, group-4 transition metal Ti and group-5 transition metal vanadium (V) have been successful encapsulated in the form of MMNCFs [75, 76]. In 2009, Yang et al. successfully synthesized and isolated $TiSc_2N@I_h$-C_{80} as the first Ti-containing NCF by mixing TiO_2 and Sc_2O_3 in the raw material, demonstrating the feasibility of encapsulating non-group-3 metal in the form of NCF. With the lack of single-crystal XRD proof, the molecular structure of $TiSc_2N@I_h$-C_{80} was elucidated from vibrational spectroscopic study combined with quantum chemical calculations [75]. Later on, Yang et al. succeeded in encapsulating V into fullerene cage for the first time and isolated two V-containing MMNCFs $V_xSc_{3-x}N@C_{80}$ (x = 1–2), for which the cage is unambiguously determined to be $I_h(7)$-C_{80} by single-crystal XRD and the encapsulated VSc_2N/V_2ScN clusters are planar (Fig. 3e, f) [76].

Metal Carbide Clusterfullerenes (CCFs)

The discovery of NCF brings about an idea whether other types of metal clusters can be encapsulated into fullerene cage as well. This came true in 2001 when Wang and coworkers identified that $Sc_2C_2@C_{84}$ is the actual structure of assumed di-EMF Sc_2C_{86} by ^{13}C MMR spectrum and synchrotron X-ray structural analyses, which encapsulates a metal carbide [3]. This finding opens a new branch of endohedral clusterfullerenes, metal carbide clusterfullerene (CCF), for which a metal carbide comprised of a carbide moiety C_2 and metal atoms are encapsulated within a fullerene cage [3]. Since then, a number of CCFs have been isolated and determined by single-crystal XRD, which is necessary to distinguish $M_2C_2@C_{2n}$ CCF with the counterpart $M_2@C_{2n+2}$ di-EMFs [3]. Among them, the most common CCFs have the formula of $M_2C_2@C_{2n}$ (M = Sc, Y, La, Gd, Tb, Dy, Er, Tm, Lu), and the encapsulated M_2C_2 clusters are always in bent shape described as a butterfly. Generally, the locations of metal ions within fullerene cages are disordered, and the inner metal carbide units are found in disorder within CCFs as well, resulting in changeable butterfly shapes. In particular, based on ^{13}C NMR spectroscopic characterization and DFT calculations of a series of $Y_2C_2@C_{2n}$ ($2n$ = 40–59), Dorn and co-workers proposed that the butterfly geometry is dependent on the cage size of CCFs, i.e., the geometries of M_2C_2 unit change from the folded butterfly geometry to a planar configuration and eventual form a linear structure when fullerene cage size expands from C_{92} to C_{100} [77]. Indeed, the butterfly geometry of M_2C_2 unit has been confirmed by single-crystal XRD for a number of CCFs, including $Sc_2C_2@C_{2n}$ ($2n$ = 72, 74, 80–84) [3, 78–80]; $Tb_2C_2@C_s(6)$-C_{82} [81]; $Lu_2C_2@C_{2v}(9)$-C_{86}, $Lu_2C_2@C_s(32)$-C_{88}, and $Lu_2C_2@D_2(35)$-C_{88} [82]; and $Gd_2C_2@D_3(85)$-C_{92} [83]. Among them, the largest CCF with unambiguous structure characterization isolated up to now is $Y_2C_2@C_1(1660)$-C_{108} (Fig. 4a), which was reported by Lu and coworkers in 2018. The Y_2C_2 unit takes a linear structure with a Y-C-C-Y dihedral angle of 173.1° [84].

In particular, an unusual geometry of the encapsulated metal carbide unit is found for $Sc_2C_2@C_{2v}(9)$-C_{86} CCF, which was successfully synthesized and isolated by

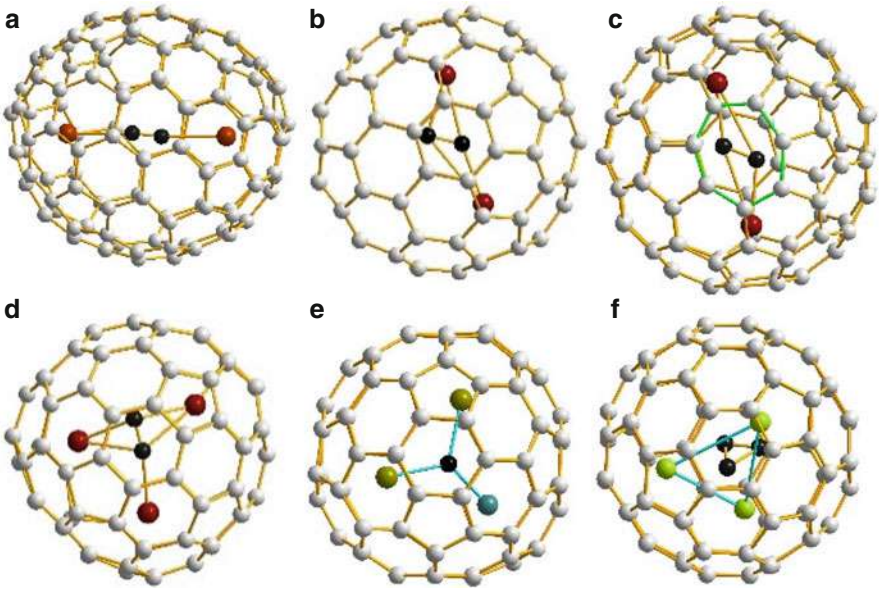

Fig. 4 Molecular structures of $Y_2C_2@C_1(1660)$-C_{108} (**a**), $Sc_2C_2@C_{2v}(9)$-C_{86} (**b**), $Sc_2C_2@C_s(hept)$-C_{88} (**c**), $Sc_3C_2@I_h$-C_{80} (**d**), $TiLu_2C@I_h$-C_{80} (**e**), and $Ti_3C_3@I_h$-C_{80} (**f**)

Echegoyen and coworkers [85]. As shown in Fig. 4b, the inner Sc_2C_2 unit within $Sc_2C_2@C_{2v}(9)$-C_{86} takes a planar and twisted geometry instead of butterfly shape, where the two Sc atoms take different distance from the C_2 unit. The Sc atoms are symmetrically positioned over hexagonal faces, and the Sc-C distances are in the range from 2.267(2) to 2.495(2) Å for Sc1 and from 2.272(2) to 2.470(2) Å for Sc2 [85], respectively, and the C-C bond length is 1.212(4) Å, which is typical for M_2C_2 carbides [85]. One year later, the same group synthesized and isolated anther unprecedented CCF, $Sc_2C_2@C_s(hept)$-C_{88}, which is the first CCF bearing a heptagon ring on the carbon cage (Fig. 4c). The single-crystal XRD results reveal a planar and zigzag structure of the encapsulated Sc_2C_2 cluster, which is quite different from that within $Sc_2C_2@C_{2v}(9)$-C_{86}, suggesting a progressive stretching process. Intriguingly, on the outer C_{88} cage there is one heptagon adjacent to a pair of fused pentagons, and the involvement of one heptagon results in the increase of the number of pentagons to 13 [86].

Besides dimetallic carbide M_2C_2, trimetallic carbide M_3C_2 has been also encapsulated in the form of CCF successfully. As a special representative, $Sc_3C_2@I_h$-C_{80} was previously assigned erroneously as a tri-EMF "$Sc_3@C_{82}$" and correctly confirmed by single-crystal XRD and ^{13}C NMR spectroscopy. According to the single-crystal XRD results, the encapsulated Sc_3C_2 cluster adopts a "bat ray" configuration with the C_2-line deviating from the Sc_3 plane by 7.2° (Fig. 4d) [87, 88]. In another trimetallic CCF with a larger cage, $Lu_3C_2@C_{88}$, the encapsulated Lu_3C_2 cluster changes to a planar structure as revealed by Wang et al. [89]. With a further increase

of the number of encapsulated metal atom to four, the yield of tetrametallic CCF dramatically decreases. So far only one tetrametallic CCF, $Sc_4C_2@C_{80}$, is reported by Wang et al. in 2009. On the basis of the FTIR and Raman spectroscopic study in combination with DFT calculations, $Sc_4C_2@C_{80}$ was proposed to exhibit an unprecedented Russian-doll nesting structure, in which the Sc atoms form a tetrahedron with the C_2 unit nested inside [90]. Nevertheless, the actual molecular structure of $Sc_4C_2@C_{80}$ is yet to be experimentally confirmed by single-crystal XRD.

In addition to the conventional form of M_xC_2 ($x = 2$–4), metal carbides with odd numbers of carbon atom have been also reported to form CCFs. As a special case of trimetallic CCF, $TiLu_2C@C_{80}$ discovered in 2014 by Popov and coworkers is unique in terms of the encapsulation of only a single carbon atom within the carbide. Dramatically different from the previously found CCFs bearing a C_2 moiety, for the $TiLu_2C$ carbide within $TiLu_2C@C_{80}$, an unprecedented Ti=C double bond was proposed (Fig. 4e) [91]. Later on, the same group isolated a series of analogues compounds, including $TiM_2C@C_{80}$ (M = Lu, Er, Dy, Y, Gd). Besides, by adding melamine as an additive into Krätschmer-Huffman generator during vaporization of graphite rods packed with mixture of Sc/Ti oxides, a series of mixed-metal CCFs $Sc_2TiC@C_{2n}$ ($2n = 68$, 78, 80) and $Sc_2TiC_2@C_{80}$ were also synthesized [92]. More recently, Lu et al. reported an unprecedented Ti_3C_3 cluster encapsulated within the I_h-C_{80} cage. The single-crystal XRD results reveal a novel coordination fashion that the cyclopropane-like C_3 unit is nearly perpendicular to the plane consisted of three titanium atoms. Each Ti atom within $Ti_3C_3@I_h$-C_{80} is centered above a [5,6]-ring junction with the average Ti-C (cage) distances of 2.12, 2.12, and 2.13 Å, respectively, featuring Ti-C single bonds (Fig. 4f) [93].

Metal Oxide Clusterfullerenes (OCFs)

In 2008, Stevenson et al. synthesized and isolated the first metal oxide cluster-containing clusterfullerene (OCF) $Sc_4(\mu_3\text{-}O)_2@I_h$-$C_{80}$ by using the DC arc-discharge method with the presence of O_2 and $Cu(NO_3)_2$. According to single-crystal XRD results, the encapsulated Sc_4O_2 cluster within $Sc_4(\mu_3\text{-}O)_2@I_h$-$C_{80}$ exhibits a distorted tetrahedral set of Sc atoms, and the bridging oxygen atoms are asymmetrically positioned on two of the triangular faces of the Sc4 tetrahedron, with the Sc-O distances falling into the range of Sc-O bond lengths (1.87–2.29 Å) observed for other scandium complexes containing a bridging oxide group (Fig. 5a) [94]. Later on, $Sc_4O_3@C_{80}$ and $Sc_2O@C_{82}$ were also reported by the same group and characterized by single-crystal XRD [95]. The geometry structure of Sc_4O_3 unit is similar to that of Sc_4O_2, comprises Sc4 tetrahedrons with three oxygen atoms bridging three Sc-triangular faces (Fig. 5b). On the other hand, the Sc_2O cluster within $Sc_2O@C_s(6)$-C_{82} has a V-shape with a Sc–O–Sc angle of 156.6°, and the Sc-O bond lengths are 1.867 and 1.934 Å [95]. A more close-up study revealed that the $C_s(6)$-C_{82} cage possessed a unique band of ten contiguous hexagons and the Sc ions were located along that set of ten contiguous hexagons (Fig. 5d) [95].

By applying CO_2 as reactive gas atmosphere in the DC arc-discharge synthesis, Feng, Chen et al. isolated and characterized a series of $Sc_2O@C_{2n}$ ($2n = 70$, 76, 80,

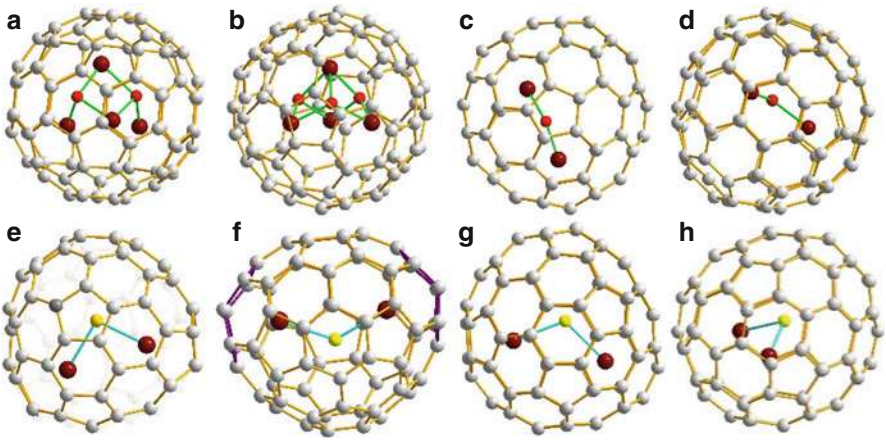

Fig. 5 Molecular structures of $Sc_4O_2@I_h(7)$-C_{80} (**a**), $Sc_4O_3@I_h(7)$-C_{80} (**b**), $Sc_2O@C_{2v}(5)$-C_{80} (**c**), $Sc_2O@C_{s(6)}$-C_{82} (**d**), $Sc_2S@C_2(7892)$-C_{70} (**e**), $Sc_2S@C_s(10528)$-C_{72} (**f**), $Sc_2S@C_{3v}(8)$-C_{82} (**g**), and Sc2S@Cs(6)-C_{82} (**h**)

82) OCFs, giving a chance to directly compare the geometric structures of the encapsulated Sc_2O cluster within such OCFs [96]. For the $C_{2v}(5)$-C_{80} cage (Fig. 5d), the Sc–O–Sc angle is 160.79°, which is larger than that within $Sc_2O@C_s(6)$-C_{82} and $Sc_2O@C_{3v}(8)$-C_{82}. When the cage size decreases to C_{76}, the Sc–O–Sc angle decreases to 133.9° within $Sc_2O@T_d(19151)$-C_{76} and further to 131.24° within $Sc_2O@C_2(7892)$-C_{70}. This phenomenon indicates a compressing effect of the smaller fullerene cage to the encapsulated metal oxide cluster [96]. Surprisingly, when the encapsulated metal changes to Ho, the encapsulated Ho_2O clusters within $Ho_2O@C_2(13333)$-C_{74} [97] and $Ho_2O@D_{2d}(51591)$-C_{84} [98] exhibit an almost linear configuration, with a Ho–O–Ho cluster angle of $>170°$. This case is distinct from the Sc_2O cluster within the small fullerene cages [96].

Very recently, Chen and coworkers successfully synthesized and isolated the first mixed-metal OCF, $ScGdO@C_{82}$ [99], whose molecular structure were determined by UV–vis–NIR spectroscopies and electrochemical studies combined with DFT calculations. The optimized Sc–O–Gd angle for $ScGdO@C_{3v}(8)$-C_{82} is 146°, which is somewhat smaller than those found in the already characterized $Sc_2O@C_s(6)$-C_{82} (162°) and $Sc_2O@C_{3v}(8)$-C_{82}(156°).

Metal Sulfide Clusterfullerenes (SCFs)

Similar to the case of $M_2O@C_{2n}$ OCF, metal sulfide clusterfullerenes (SCFs) in the form of $M_2S@C_{2n}$ have been also reported. As the first member of SCF, $M_2S@C_{82}$ (M = Sc, Y, Dy, and Lu) were discovered by Dunsch and coworkers in 2010, which was synthesized by a modified DC arc-discharge method with guanidium thiocyanate (CH_5N_3·HSCN) introduced as the sulfur source. The cage isomeric structures of $M_2S@C_{82}$ (M = Sc, Y, Dy, and Lu) were proposed to be $C_{3v}(8)$ by FTIR spectroscopy combined with DFT theoretical calculations [5]. Soon later on, Echegoyen et al.

used an alternative DC arc-discharge method with SO_2 incorporated as the sulfur source and succeeded in isolating two isomers of $Sc_2S@C_{82}$, namely $Sc_2S@C_s(6)$-C_{82} and $Sc_2S@C_{3v}(8)$-C_{82}, whose molecular structures were unambiguously characterized by single-crystal XRD. According to their crystallographic data, both of the encapsulated Sc_2S cluster have V-shape geometry, while the Sc–S–Sc angles of Sc_2S cluster are different, which are respectively 113.84(3)° and 97.34(13)° in $Sc_2S@C_s(6)$-C_{82} and $Sc_2S@C_{3v}(8)$-C_{82} (Fig. 5g, h) [100]. In 2012, the same group isolated an analogous SCF based on a smaller fullerene cage of C_{72}–$Sc_2S@C_s(10528)$-C_{72}. Single-crystal XRD results reveal that the $C_s(10528)$-C_{72} isomer is a non-IPR cage and the Sc_2S cluster is in V-shape with a Sc–S–Sc angle of 125.36(14)° (Fig. 5f) [101]. Likewise, another non-IPR SCF, $Sc_2S@C_2(7892)$-C_{70}, was also isolated by the same group (Fig. 5e) [102]. With the absence of crystallographic data, the Sc–S–Sc angle was predicted by DFT calculations to be 97.8°, much smaller than those for $Sc_2S@C_s(6)$-C_{82}(113.84°) and $Sc_2S@C_s(10528)$-C_{72} (125.36°) but close to that for $Sc_2S@C_{3v}(8)$-C_{82} (97.34°). These systematic studies reveal that, upon varying the size and isomeric structure of the fullerene cage, the encapsulated Sc_2O cluster within OCFs changes its geometry accordingly.

Non-Sc SCFs have been scarcely reported. In 2017, Popov et al. synthesized $Dy_2S@C_{82}$ by using DC arc-discharge synthesis with Dy_2S_3 used as a source of metal and sulfur, and isolated two isomers of $C_s(6)$ and $C_{3v}(8)$ [103]. As an another example, $Ti_2S@C_{78}$ was also isolated, representing the only SCF with non-group-3 metal encapsulated. Despite of the lack of single-crystal XRD, the molecular structure of $Ti_2S@C_{78}$ was proposed by DFT calculations, predicting that the Ti_2S cluster within the $D_{3h}(24109)$-C_{78} cage is almost linear with a Ti–S–Ti angle of 172°, which is significantly larger than that of the Sc_2S cluster within Sc-based SCFs as discussed above. More intriguingly, since the Ti is predicted to has a valence state of four, the Ti_2S cluster may transfer six electrons to the outer C_{78} cage. This is dramatically different to the four-electron-transfer occurring in SCFs based on rare earth metals [104].

Metal Cyanide Clusterfullerenes (CYCFs)

For the abovementioned metal clusters, multiple (two to four) metal atoms are always required and the nonmetal atom is limited to either a single atom (N, O, S) or homogeneously multiple atoms (C_2). These dogmas were broken by the discovery of metal cyanide clusterfullerene (CYCF) by Yang et al. in 2013. $YNC@C_s(6)$-C_{82} as the first member of CYCF features encapsulation of a triangular YNC cluster within a common $C_s(6)$-C_{82} cage according to single-crystal XRD results. Interestingly, both N and C atoms are located near the cage center, while the Y metal is located between the $[CN]^-$ unit (Fig. 6a). The determined N–C bond length (0.935 Å) is smaller than that of the C–N triplet bonds in cyano coordination complexes and nitrile compounds, indicating an extraordinary bonding nature in the YNC cluster within the fullerene cage [6]. The unprecedented triangular configuration of the YNC cluster is quite different from the linear structures commonly found in traditional metal cyanide complexes.

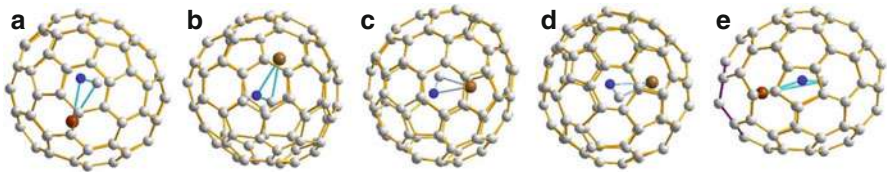

Fig. 6 Molecular structures of YCN@C_s(6)-C_{82} (**a**), TbCN@C_2(5)-C_{82} (**b**), TbCN@C_s(6)-C_{82} (**c**), TbCN@C_{2v}(9)-C_{82} (**d**), and YNC@C_{2v}(19138)-C_{76} (**e**)

Later on, a series of CYCFs have been successively isolated by the same group, including three isomers of TbNC@C_{82} (C_2(5), C_s(6), C_{2v}(9)), and MCN@C_{2v}(19138)-C_{76} (M = Tb, Y) with a non-IPR C_{76} cage [105, 106]. For TbNC@C_{82} (C_2(5), C_s(6), C_{2v}(9) (Fig. 6b–d), single-crystal XRD results reveal that the encapsulated TbNC cluster takes the triangular configuration similar to the case of YNC within YNC@C_s(6)-C_{82}. Upon changing the cage isomeric structure from C_2(5), C_s(6) to C_{2v}(9), the distance of the shorter Tb-C(N)/Tb-N(C) bond decreases significantly from 2.32(3), 2.10(2) to 1.98(4) Å, and the longer Tb-N(C)/Tb-C(N) bond changes from 2.36(5), 2.217(16) to 2.37(3) Å. More intriguingly, the C-N bond length increases from 0.94(5), 1.02(3) to 1.05(4) Å. Eventually, all these changes in bond length make the triangular TbNC cluster distorted with the Tb-C(N)-N(C) angle varying by up to 20° [105]. Therefore, the geometric structure of the encapsulated MNC cluster is closely dependent on the cage isomeric structure, and this is similar to cases of OCFs and SCFs discussed above [100].

The strong dependence of the geometric structure of the entrapped MNC cluster on the outer fullerene cage is confirmed further by crystallographic study of MNC@C_{2v}(19138)-C_{76} (M = Tb, Y). Astonishingly, the MNC cluster within non-IPR C_{2v}(19138)-C_{76} cage takes a nearly linear configuration with the M–N–C bond angle being 154.9(13)° for Tb and 160.4(7)° for Y (Fig. 6e), which is quite different from the triangular geometries of the MNC (M = Tb, Y) clusters within the IPR-obeying C_{82} cages. This phenomenon is interpreted by the stronger metal-cage interaction demanded for stabilizing the fused pentagons on the non-IPR C_{72} cage, which results in weakening of the coordination bonding between the metal atom and [NC] ligand [2].

Metal Hydrocarbide Clusterfullerenes (HCCFs)

In 2007, Dunsch and coworkers synthesized and isolated an unprecedented hydrogen-containing endohedral clusterfullerene containing a metal hydrocarbide cluster, namely $Sc_3CH@C_{80}$. Unfortunately, the unambiguous structural determination of $Sc_3CH@C_{80}$ HCCF has not been available yet. According to DFT calculations, the encapsulated Sc_3CH cluster within I_h-C_{80} cage is slightly pyramidal (with pyramid height 0.25 Å, see Fig. 7a) and Sc-C bonds are somewhat longer than Sc-N bonds within $Sc_3N@C_{80}$ [7].

Later on, another HCCF, $Sc_4C_2H@C_{80}$, was synthesized and isolated by Wang et al. in 2014, which is, however, not characterized by single-crystal XRD yet [107].

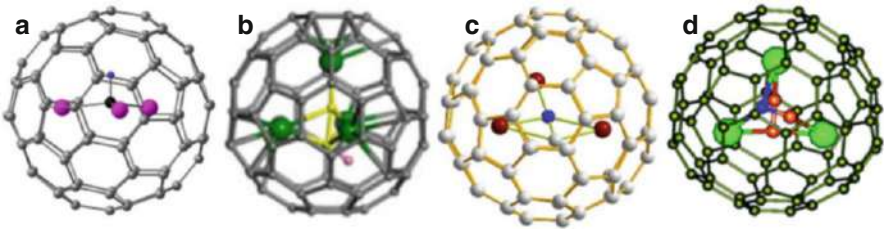

Fig. 7 Molecular structures of $Sc_3CH@C_{80}$ (**a**), $Sc_3C_2H@C_{80}$ (**b**), $Sc_3CN@I_h(7)$-C_{80} (**c**), and $Sc_3C_2CN@I_h$-C_{80} (**d**)

DFT calculations predicted that the four Sc atoms within the encapsulated Sc_4C_2H cluster form a tetrahedron embracing the C_2 unit (Fig. 7b) [107].

Metal Carbonitride Clusterfullerenes (CNCFs)

As the first example of metal carbonitride clusterfullerene (CNCF), $Sc_3NC@I_h$-C_{80} was synthesized and structurally characterized by single-crystal XRD by Wang et al. [8]. The encapsulated Sc_3NC shows a planar geometry, with the C atom situated on one side of the triangle formed by three Sc atoms and the N atom located in the center of the Sc3 triangle (Fig. 7c). The N-C bond length is 1.193(11) Å, which is much larger than that within $YNC@C_s(6)$-C_{82} CYCF (0.935 Å) as discussed above, revealing the difference on the bonding nature of the [NC] moiety between CYCF and CNCF [8]. This is interpreted by their difference on the formal charge the [NC] moiety, which is −3 for $Sc_3NC@I_h$-C_{80} and − 1 for $YNC@C_s(6)$-C_{82}, respectively [6, 105]. Likewise, $Sc_3NC@C_{78}$ was also isolated by the same group, and even within the smaller C_{78} cage, the encapsulated Sc_3NC cluster is expected to be still planar [108].

Later on, Wang and coworkers isolated a new clusterfullerene based on combination of metal carbide and carbonitride, $Sc_3C_2CN@C_{80}$. According to DFT calculations, within such a complicated carbide/carbonitride alloyed cluster, the C_2 and [CN] moieties are located on both sides of the Sc_3 triangle and coordinated to three Sc atoms (Fig. 7d). Noteworthy, the calculated Sc-C (carbonitride) distance (2.27 Å) is longer than those of Sc-N (carbonitride) (2.21 and 2.23 Å) and those within $Sc_3CN@I_h$-C_{80}, whereas the Sc-C (carbide) distances (2.20 and 2.35 Å) are much longer than Sc-C (carbide) distances in $Sc_3C_2@I_h$-C_{80} CCF (2.07 Å) [109].

Properties of EMFs

Electronic Properties

UV-Vis-NIR Absorption Property

UV-vis-NIR spectroscopy as an important optical spectroscopic technique has been widely used in studying the optical absorption and electronic properties of EMFs due to its facility and low demand for sample amount. In specific, UV-vis-NIR results

provide valuable information of the carbon cage symmetry and the optical HOMO-LUMO gap, since the electronic absorption of EMFs mainly results from $\pi \rightarrow \pi^*$ transition of the carbon cage, which is determined by not only the isomeric structure but also the charge state of the carbon cage [13, 110]. As an important parameter of UV-vis-NIR results of EMFs, the optical HOMO-LUMO bandgap is the energy of the lowest energy excitation and usually reflects the electronic stability of EMF [13]. Because the absorption bands of EMFs are often broad with some bands even overlapped, it is often difficult to assign the lowest energy excitation of EMF. Hence, the optical bandgap ($E_{g,\ optical}$, in eV) of EMF is generally estimated from the absorption onset (λ_{onset}, in nm) of the UV-vis-NIR spectroscopy according to an approximate equation $E_{g,\ optical} = 1240/\lambda_{onset}$, and a borderline of 1.0 eV for $E_{g,\ optical}$ is often used to distinguish large and small band-gap EMFs, which corresponds to the stability of EMFs in most cases [2, 11, 13, 19].

For conventional EMFs, it has been found that the UV-vis-NIR spectral patterns of EMFs based on different metal atoms but with the same cage isomer and charge state are usually similar, indicating that their electronic absorption properties are determined by the carbon cage and almost independent on the encapsulated metal [13, 110]. For example, UV-vis-NIR absorption spectra are quite similar in a series of mono-EMFs Ln@C_{2v}(9)-C_{82} (Ln = Y, La, Ce, Pr, Nd, Gd, Tb, Dy, Ho, Er, Lu) with the same charge state of $Ln^{3+}@C_{82}^{3-}$, but dramatically different from those of C_{82}^{2-}-based Ln@C_{2v}(9)-C_{82} (Ln = Sm, Eu, Tm, and Yb) mono-EMFs encapsulating divalent rare earth metals [110]. Furthermore, based on this rule, the cage structure of an unknown EMF may be determined roughly if its UV-vis-NIR absorption spectrum is similar to the absorption spectrum of a known EMF with the cage structure definitely by single-crystal XRD, although the definite structure still needs to be eventually determined by other structure characterization methods discussed in section "Structure Characterization" [13]. As a convincing example, UV-vis-NIR spectroscopy was applied successfully in determining the molecular structures of three isomers of $Tm_2@C_{82}$ by Shinohara and coworkers [111]. Figure 8a–c compares UV-vis-NIR spectra of three isomers of $Tm_2@C_{82}$ in CS_2 solution, indicating that their absorption spectra are different from each other. Moreover, the absorption spectra of $Tm_2@C_{82}$ (I, II, III) are similar to those of $Y_2@C_{82}$ (I, II, III) reported previously, whose cage isomers are determined by ^{13}C NMR spectra to be respectively C_s(6), C_{2v}(9), and C_{3v}(8) [45], suggesting that $Tm_2@C_{82}$ (I, II, III) also have C_s(6), C_{2v}(9), and C_{3v}(8) cage isomers, respectively. Indeed, the C_s(6) cage isomer of $Tm_2@C_{82}$ (I) was later confirmed by single-crystal XRD [112], confirming the correctness of the estimated structure by UV-vis-NIR spectroscopic characterization. Likewise, since the UV-vis-NIR spectra of $Tm_2C_2@C_{82}$ (I, II, III) CCFs are similar to those of the corresponding isomers of $Tm_2@C_{82}$ isomers (Fig. 8d–f), the C_s(6), C_{2v}(9), and C_{3v}(8) cage isomers can be assigned to $Tm_2C_2@C_{82}$ (I, II, III) as well according to the empirical rule [111].

Since clusterfullerenes exhibit different numbers of electron transfer to conventional EMFs which are dependent on the type of the encapsulated metal cluster, clusterfullerenes often have different UV-vis-NIR spectroscopic features to those of conventional EMFs with the same carbon cages due to the diversity on the charge

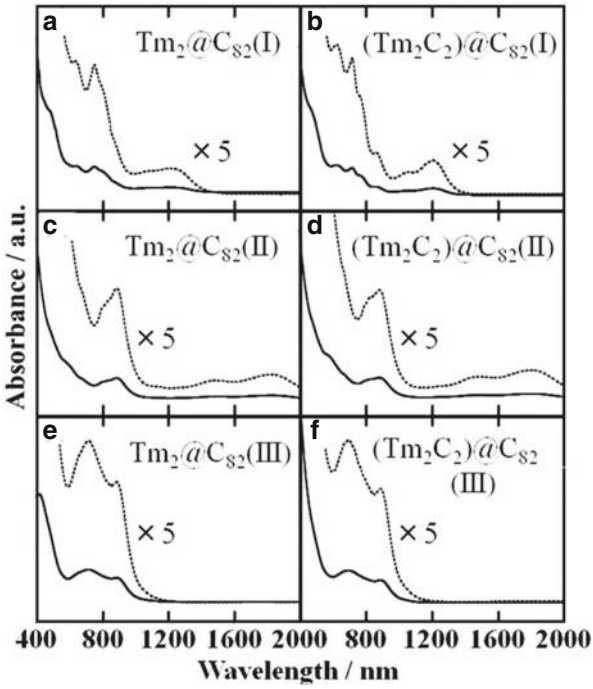

Fig. 8 (**a**–**f**) UV-vis-NIR absorption spectra of $Tm_2@C_{82}$ (I, II, III) and $(Tm_2C_2)@C_{82}$ (I, II, III) in CS_2. The dotted lines are vertical expansions of the spectra

state of carbon cage [2, 13]. For NCFs, the formal charge state of the carbon cage is −6, which is quite different to the −3 charge state of C_{82} cage of mono-EMFs $Ln@C_{2v}(9)$-C_{82} (Ln = Y, La, Ce, Pr, Nd, Gd, Tb, Dy, Ho, Er, Lu). For instance, $M_3N@I_h$-C_{80} (M = Sc, Y, Tb, Dy, Tm, Lu) NCFs exhibit almost same UV-vis-NIR absorption spectra [13], whereas the UV-vis-NIR spectra of $Sc_3N@I_h(7)$-C_{80} and $Sc_3N@D_{5h}(6)$-C_{80} are obviously different, with the absorption onsets being 820 and 920 nm, respectively [113]. In addition, the isomeric cage structure, the electronic absorption properties of NCFs are sensitively dependent on the size of fullerene cage even with the same charge state [2]. For example, Yang et al. systematically studied the electronic absorption properties of a series of $Dy_xSc_{3-x}N@C_{2n}$ ($x = 1$–2, $2n = 68$, 70, 76–86) MMNCFs and compared them with those of the previously reported Dy- and Sc-based NCFs, and concluded that $Dy_xSc_{3-x}N@C_{2n}$ ($x = 1$–2, $2n = 68$, 70, 76–86) MMNCFs are all large bandgap NCFs (except $DySc_2N@C_{76}$ and $Dy_2ScN@C_{84}$ with optical bandgaps being very close to 1.0 eV). On the contrary, for $Dy_3N@C_{2n}$ ($2n = 78$–88) NCFs, the small cages ($2n = 78$, 80, 82) have large optical bandgap (1.38–1.51 eV) whereas the optical bandgap of those based on larger cages ($2n = 84$, 86, 88) are significantly smaller (0.80–0.84 eV) [114, 115]. These results indicate significant perturbation of the encapsulated mixed metal nitride on the electronic absorption properties of MMNCFs [114].

It should be noted that, when the encapsulated metals have significant contributions to the frontier orbitals, the above rule for preliminary structure characterization

of an unknown EMF by comparing its UV-vis-NIR absorption spectrum with a known carbon cage structure should be no longer used [116, 117]. For instance, Yang et al. compared the UV-vis-NIR spectra of $Lu_xSc_{3-x}N@I_h(7)$-C_{80} ($x = 0$–3) and $Lu_xSc_{3-x}N@D_{5h}(6)$-C_{80} ($x = 0$–2) [117]. As shown in Fig. 9, for $Lu_xSc_{3-x}N@I_h(7)$-C_{80} ($x = 0$–3), significant differences in the range of 600–700 nm have been found from their UV-vis-NIR absorption spectra. In particular, a doublet peak with absorption maxima at 686/659 nm is observed in the spectrum of $Lu_3N@I_h(7)$-C_{80}, and the absorption spectrum of $Sc_3N@I_h(7)$-C_{80} exhibits a broad single band with an absorption maximum at 735 nm. For $Lu_xSc_{3-x}N@I_h(7)$-C_{80} MMNCFs, the absorption maxima of $Lu_2ScN@I_h(7)$-C_{80} and $LuSc_2N@I_h(7)$-C_{80} slightly red-shifted to 691/666 and 706/685 nm, respectively [117]. Besides, in the higher energy absorption range, $Lu_3N@I_h(7)$-C_{80} and $Lu_2ScN@I_h(7)$-C_{80} display the strongest visible absorption peak at 403 nm, which is red-shifted relative to those of $LuSc_2N@I_h(7)$-C_{80} and $Sc_3N@I_h(7)$-C_{80} [117]. Likewise, the differences in absorption spectra of $Lu_xSc_{3-x}N@D_{5h}(6)$-C_{80} ($x = 0$–2) is also observed. The absorption spectrum of $Lu_2ScN@D_{5h}(6)$-C_{80} exhibits an absorption peak at 714 nm,

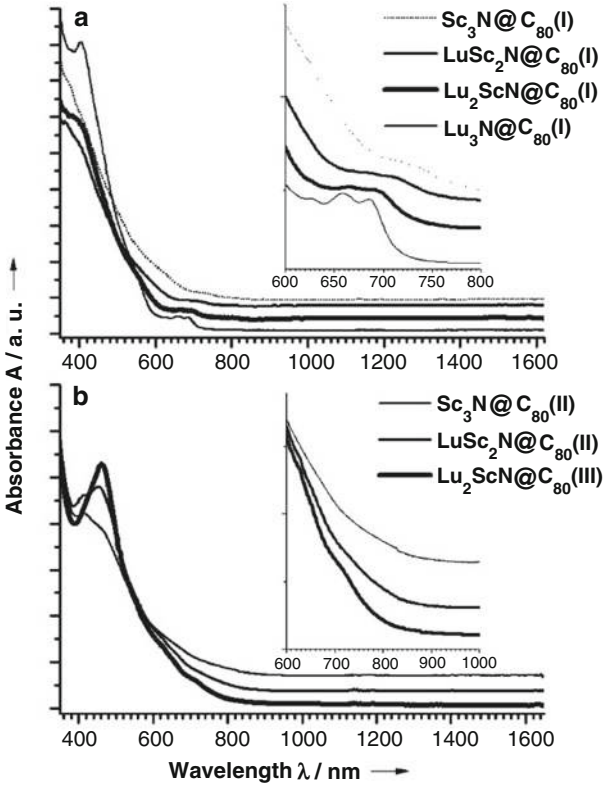

Fig. 9 UV − vis−NIR spectra of $Lu_xSc_{3-x}N@_{Ih}(7)$-C_{80} ($x = 0$–3) (**a**) and $Lu_xSc_{3-x}N@D_{5h}(6)$-C_{80} ($x = 0$–2) (**b**) dissolved in toluene. The insets show the enlarged spectral region

which is, however, red-shifted to ca. 727 nm for $LuSc_2N@D_{5h}(6)$-C_{80} and disappears for $Sc_3N@D_{5h}(6)$-C_{80} [117]. Another typical example is the obvious difference in UV-vis-NIR absorption spectra among three EMFs, including $Sc_3N@D_{3h}(5)$-C_{78}, $La_2@D_{3h}(5)$-C_{78}, and $Ti_2C_2@D_{3h}(5)$-C_{78} [39, 60, 118], who have the exactly same fullerene cage $D_{3h}(5)$-C_{78} bearing the same charge state (−6). This phenomenon is interpreted by their difference on metal-cage interactions among them, resulting in differential contributions of the encapsulated metal to the frontier orbitals of EMFs and hence the distinct energy excitation [13].

Electrochemical Properties

Conventional Metallofullerenes

Electrochemistry can afford a direct access to the molecular energy levels and intramolecular electron transfer mechanism, thus has been extensively applied to investigate the electronic properties of EMFs. For mono-EMFs, the frontier molecular orbitals are mainly located at the carbon cage, hence the electrochemical behavior is primarily determined by the outer fullerene cage like empty fullerenes. As a result, similar to the UV-vis-NIR absorption properties, the redox behavior of mono-EMFs with the same cage isomer and charge state are usually same and independent on the encapsulated metal atom [2, 11–13]. Mono-EMFs typically exhibit multiple reversible reduction steps and one to two oxidation steps which can be detected in ambient conditions. For example, Suzuki et al. reported that trivalent metal-based mono-EMFs such as $M@C_{82}$ (M = Y, La, Ce, Gd, Er) exhibit almost same redox potentials with small variations [119]. In this case, since three electrons transferred from the encapsulated metal ions to the outer carbon cage, an open-shell electronic structure was formed. As a result, $M@C_{2v}(9)$-C_{82} (M = Y, La, Ce, Gd, Er) mono-EMFs exhibit relatively small electrochemical gaps (≤0.5 eV) with the first oxidation potential at ~0.07 V. When the cage isomer of $M@C_{82}$ changes to $C_s(6)$-C_{82}, their electrochemical gaps of $M@C_s(6)$-C_{82} (M = La, Pr) become smaller (0.40 V), and the first oxidation potentials are more negative (−0.07 V), suggesting that $M@C_s(6)$-C_{82} are easier to oxidize than $M@C_{2v}(9)$-C_{82} counterparts.

For divalent metal-based $M^{II}@C_{2n}$ (M = Ca, Sm, Eu, Tm, Yb) mono-EMFs, since the electronic structures turn into close-shell, their first oxidation potentials are generally more positive than those of $M^{III}@C_{2n}$ [120–123], while their reduction potentials negatively shift relative to those of $M^{III}@C_{2n}$. Therefore, the electrochemical gaps of close-shell $M^{II}@C_{2n}$ are larger than those of open-shell $M^{III}@C_{2n}$ mono-EMFs. Similar results are found for the recently reported tetravalent metal-based $M^{IV}@C_{2n}$ (M = Th, U), and specifically $Th@C_{80}$ has the record lowest first reduction potential of −1.22 V [31, 32].

Unlike mono-EMFs, electrochemical studies of di-EMFs are much less mainly due to the challenge of structure discrimination of $M_2@C_{2n}$ di-EMFs and $M_2C_2@C_{2n-2}$ CCFs. Early electrochemical studies of di-EMFs were focused on $M_2@C_{2n}$ (M = Ce, La, n = 36, 39, 40) [37–39]. The first report on electrochemical study of di-EMF is $La_2@I_h(7)$-C_{80} in 1995, showing two reversible reduction steps and two reversible oxidation steps at ambient condition. Particularly, its first

oxidation and reduction potentials are +0.56 and −0.31 V, respectively, indicating that $La_2@I_h(7)$-C_{80} possesses strong electron withdrawing ability as well as a relatively small electrochemical gap compared to empty fullerenes. Furthermore, theoretical calculations predicted that the accepted electrons in $La_2@I_h(7)$-C_{80} would be stabilized between the two lanthanum atoms instead of the outer carbon cage. This speculation was later confirmed by experimental study of the radical addition reaction of $La_2@I_h(7)$-C_{80} [124].

Later on, electrochemical studies of La-based di-EMFs with other cages were also reported, and it is found that the LUMO level located on encapsulated di-metals is affected by the size of carbon cage, leading to altered reduction potentials and electron withdrawing abilities. When the isomeric structure of C_{80} cage changes to $D_{5h}(6)$, the first oxidation potential of $La_2@D_{5h}(6)$-C_{80} shifts negatively by approximately 330 mV, while the reduction potential was close to that of the $La_2@I_h(7)$-C_{80} isomer. When the cage size decreases to C_{78} and C_{72}, $La_2@D_{3h}(5)$-C_{78} and $La_2@D_2(10611)$-C_{72} have the first oxidation potentials of 0.26 V, 0.24 V, and first reduction potentials of −0.68 V, −0.40 V, respectively. Noteworthy, their first oxidation potentials are negatively shifted relative to that of $La_2@I_h(7)$-C_{80}, indicating that the first oxidation potentials of $La_2@C_{2n}$ di-EMFs are sensitively dependent on the cage size. On the other hand, when the encapsulated La atom is substituted by Ce atom to form $Ce_2@C_{2n}$ di-EMFs, the first reduction potential shifts negatively by about 0.1 V while the oxidation potential keeps almost constant [35–37, 40].

Recently, systematic electrochemical studies of a series of di-EMFs including $Er_2@C_{2n}$, $Y_2@C_{2n}$, and $Lu_2@C_{2n}$ were reported by Lu et al. Among them, $Lu_2@C_{2n}$ ($Lu_2@T_d(2)$-C_{76}, $Lu_2@D_{3h}(5)$-C_{78}, $Lu_2@C_{2v}(5)$-C_{80}, $Lu_2@C_{2v}(7)$-C_{84}, $Lu_2@C_s(8)$-C_{86}, $Lu_2@C_s(15)$-C_{86}, $Lu_2@C_1(26)$-C_{88},) have the first oxidation potentials in the range of 0.13–0.34 V and the first reduction potentials in the range of −1.25 to −1.46 V [82]. In specific, $Y_2@C_{82}$-$C_s(6)$ and $Y_2@C_{82}$-$C_{3v}(8)$ have ultralow first oxidation potentials of −0.16 V [125].

For tri-EMF, so far only electrochemical study of $Sm_3@I_h(7)$-C_{80} was reported, indicating two reversible oxidation steps and two reduction steps, for which the first reduction is reversible while the second one is irreversible. The first oxidation potential of $Sm_3@I_h(7)$-C_{80} (0.30 V) is much lower than those of $La_2@I_h(7)$-C_{80} (0.56 V), indicating a stronger electron-donating ability. The first reduction potential of $Sm_3@I_h(7)$-C_{80} (−0.83 V) is much more negative than that of $La_2@I_h(7)$-C_{80} (−0.31 V). As a result, the electrochemical potential gap of $Sm_3@C_{80}$-$I_h(7)$ is 1.13 V, larger than that of $La_2@I_h(7)$-C_{80} (0.87 V) [6].

Clusterfullerenes

Electrochemical studies of clusterfullerenes especially NCFs have been extensively reported in recent years, thanks to the great efforts on their syntheses affording large amount of samples. In 2004 Dunsch et al. reported the first electrochemical study of $Sc_3N@I_h(7)$-C_{80} NCF, revealing two reduction potentials of −1.24 and −1.62 V as well as one oxidation potential of 0.62 V. Thus, the electrochemical gap of $Sc_3N@I_h(7)$-C_{80} is calculated to be 1.86 V, which is significantly larger than that of $La_2@I_h(7)$-C_{80} (0.87 V) with the same cage [113]. Later on, Echegoyen and

coworkers investigated the electrochemical behavior of $Sc_3N@I_h(7)$-C_{80} in acetonitrile/toluene, and pointed out that the reduction steps are irreversible in the same way as they are in o-dichlorobenzene [126]. Moreover, further studies on the redox property of $Sc_3N@I_h(7)$-C_{80} by ESR spectroscopic characterization and theoretical calculations revealed that the accepted electron in the process of electrochemical reduction was located on the LUMO of Sc_3N cluster [127, 128].

In addition to $Sc_3N@C_{80}$, other non-Sc $M_3N@I_h(7)$-C_{80} (M = Y, Nd, Pr, Gd, Tb, Dy, Ho, Er, Tm, and Lu) NCFs have commonly irreversible redox behavior with the first oxidation potential being in the range of 0.65–0.70 V, which is more positive than that of $Sc_3N@C_{80}$ (0.6 V) [129]. In addition, the HOMO of non-Sc $M_3N@C_{80}$ was unveiled to localize on the carbon cage, resulting in inhibited electronic state of M_3N cluster toward external oxidation according to theoretical calculations [130]. Besides the $I_h(7)$-C_{80} isomer, another commonly studied isomer of $M_3N@C_{80}$ is $M_3N@D_{5h}(6)$-C_{80}, for which the first oxidation potentials shift cathodically by 0.25–0.30 V relative to those of $I_h(7)$ counterparts [131]. On the other hand, the first reduction potential of $Sc_3N@D_{5h}(6)$-C_{80} is 0.07 V more negative than that of $Sc_3N@I_h(7)$-C_{80}. This phenomenon is also observed for other $M_3N@C_{80}$ (M = Dy, Tm, Lu, Gd) NCFs [132–134].

In 2013, the redox properties of two Ce-based MMNCFs $CeM_2N@I_h(7)$-C_{80} (M = Sc, Y, Lu) were studied, showing similar reduction behavior to those of $M_3N@C_{80}$ featuring two irreversible reduction steps which are typical carbon cage-determined reduction processes [135]. Furthermore, theoretical results revealed that the electrochemical oxidation of Ce-based MMNCFs was dependent on the cluster/cage size. When the inherent strain of the encapsulated CeM2N cluster is high enough, the oxidation takes place preferably on the internal Ce atom, otherwise the oxidation tends to occur on the fullerene cage [135].

As special cases of MMNCFs, non-group-3 metal-based MMNCFs such as $TiM_2N@I_h(7)$-C_{80} (M = Sc, Y) are found by Yang and coworkers to exhibit remarkably different redox behavior compared to the corresponding $M_3N@I_h(7)$-C_{80} (M = Sc, Y) [75, 136]. For instance, $TiSc_2N@I_h(7)$-C_{80} exhibits one reversible oxidation at +0.16 V and three reversible reduction steps at −0.94, −1.58, and −2.21 V. Compared to $Sc_3N@I_h(7)$-C_{80}, the first oxidation potential of $TiSc_2N@I_h(7)$-C_{80} shifts cathodically by 0.46 V and the first reduction potential shifts anodically 0.3 V. As a result, the electrochemical gap of $TiSc_2N@I_h(7)$-C_{80} is 1.10 V, which is much smaller than that of $Sc_3N@I_h(7)$-C_{80} (1.86 V). Intriguingly, the most remarkable change for the redox property of $TiSc_2N@I_h(7)$-C_{80} compared to $Sc_3N@I_h(7)$-C_{80} is that the three reduction steps of $TiSc_2N@I_h(7)$-C_{80} all become electrochemically reversible under the same conditions. This phenomenon is interpreted that for $TiSc_2N@I_h(7)$-C_{80}, both oxidation and reduction occur at the endohedral cluster, changing the valence state of Ti from Ti^{III} to Ti^{II} in $TiSc_2N@C_{80}^-$ (reduction) and Ti^{IV} in $TiSc_2N@C_{80}^+$ (oxidation), whereas for $Sc_3N@I_h(7)$-C_{80}, these processes take place on the carbon cage instead [136]. A similar phenomenon is later observed for another non-group-3 metal-based MMNCF $V_xSc_{3-x}N@C_{80}$ (I_h, $x = 1$–2), which show even more intriguing features. $VSc_2N@I_h(7)$-C_{80} exhibits a complex reduction pattern with up to five reduction steps, including four reversible reduction

steps at −0.42, −0.66, −1.33, and −1.71 V, and one irreversible reduction step at −2.32 V. Besides, the oxidation step becomes irreversible, and this is scarcely reported for rare earth metal-based NCFs [76]. Along with the different redox behavior of $TiM_2N@I_h(7)$-C_{80} (M = Sc, Y), these results indicate the peculiarity of electrochemical properties of MMNCFs based on the transition metals.

For CCFs, few electrochemical studies have been also reported. As the first report, $Sc_2C_2@C_{3v}(8)$-C_{82} CCF shows an irreversible reduction potential at −0.94 V and two reversible reduction steps as well as a reversible first reversible oxidation at 0.47 V [137]. For another isomer $Sc_2C_2@C_{2v}(9)$-C_{82}, two reversible reduction and two reversible oxidation steps are detected, resulting in a electrochemical gap of 0.99 V, which is the smallest value among $Sc_2C_2@C_{2n}$ CCFs [138]. On the contrary, the redox property of $Er_2C_2@C_{90}$ CCF appears insensitive to the cage isomer, since the redox potentials of $Er_2C_2@C_2(43)$-C_{90}, $Er_2C_2@C_2(44)$-C_{90}, $Er_2C_2@C_2(40)$-C_{90}, $Er_2C_2@C_1(21)$-C_{90} are quite similar, and the corresponding electrochemical gaps are all around 1.0 V [139]. More recently, Lu reported a dedicated electrochemical study of a series of $Lu_2C_2@C_{2v}(9)$-C_{86}, $Lu_2C_2@C_s(32)$-C_{88}, and $Lu_2C_2@D_2(35)$-C_{88}CCFs, which exhibit one or two oxidation steps as well as four reduction steps with relatively large electrochemical gap in the range of 1.19–1.39 eV, indicating their high stability and better reversibility of the redox processes than the corresponding Lu-based di-EMFs [82].

As the first SCF, $Sc_2S@C_{3v}(8)$-C_{82} shows one reversible oxidation step at 0.48 V and one irreversible reduction at −1.03 V, followed by two reversible steps at −1.16 and −1.61 V. Interestingly, such a redox behavior is quite similar to that of a $Sc_2C_2@C_{3v}(8)$-C_{82} CCF, and this can be understood by their identity on the cage isomer and similarity on the electronic configuration featuring in four-electron-transfer [5, 13]. For another isomer $Sc_2S@C_{82}$-$C_s(6)$, the first oxidation potential shifts cathodically to 0.39 V and the reduction steps became fairly reversible. Noteworthy, derived from the similarity on the electronic configuration, the first reduction (−0.98 V) and oxidation (0.39 V) potentials of $Sc_2S@C_s(6)$-C_{82} SCF are very close to those of $Sc_2O@C_s(6)$-C_{82} OCF (−0.96 and 0.35 V, respectively) and $Sc_2C_2@C_s(6)$-C_{82} CCF (−0.93 and 0.42 V, respectively) [43]. However, there is obvious difference on the second reduction step among these three different types of clusterfullerenes with the same cage. The second reduction step of $Sc_2S@C_s(6)$-C_{82} SCF was very close to the first one (−0.98 and −1.12 V, respectively), while the gap between the first and the second reduction steps exceeded 0.3 V for $Sc_2O@C_s(6)$-C_{82} OCF and $Sc_2C_2@C_s(6)$-C_{82} CCF [100]. This phenomenon was interpreted by their geometrical differences that the Sc_2S cluster is much more constrained by the cage than the Sc_2O cluster, which affects the cluster-cage interactions and consequently the electrochemical property [140].

In 2013, Yang et al. reported the first electrochemical study of $YNC@C_s(6)$-C_{82} CYCF, which exhibits one reversible oxidation step at 0.56 V and four reversible reduction steps at −0.59, −0.84, −1.76, and −1.92 V, respectively. A striking feature is that the first two reduction steps as well as the last two reduction steps are mutually close whereas the separation between the second and third reduction steps are much larger (0.92 V). Interestingly, the reduction behavior of

YNC@C_s(6)-C_{82} highly resemble to that of t Yb@C_s(6)-C_{82} mono-EMF with comparably large separation (0.89 V) between the second and third reduction steps. This is due to their identity on the cage isomer and similarity on the two-electron-transfer electronic configuration [123].

More recently, Yang et al. studied systematically the electrochemical properties of a series of Tb-based CYCFs, including three isomers of TbNC@C_{82} and non-IPR CYCF TbNC@C_{76} (Fig. 10a), so as to unveil the influences of cage size and isomeric structure on the redox property of TbNC@C_{2n} CYCF [105, 141, 142]. TbNC@C_2(5)-C_{82} possesses one reversible oxidation step and four reversible reduction steps with the reduction potentials of −0.88, −0.97, −1.55, and −1.91 V, respectively, which also have the similarity of the reported Yb@C_2(5)-C_{82} with the difference being less than 0.05 V [105, 142]. The first oxidation potential of TbNC@C_2(5)-C_{82} at 0.50 V is slightly shifted negatively relative to that of YNC@C_s(6)-C_{82} (0.56 V) but positively shifted relative to that of Yb@C_2(5)-C_{82} (0.38 V). These results reveal that both the fullerene cage and the encapsulated cluster have a dramatic influence on the oxidation properties correlating with the HOMO level of TbNC@C_{2n} CYCF [6, 105, 123]. For TbNC@C_s(6)-C_{82}, although its encapsulated cluster is different to that within YNC@C_s(6)-C_{82}, their redox properties are almost identical, which is due to their similarity on the frontier molecular orbitals predominately localized on the carbon cage [105]. Moreover, TbNC@C_{2v}(9)-C_{82} shows four reversible reduction potentials at −0.46, −0.81, −1.78, and −1.96 V, respectively, and one reversible oxidation potential at 0.55 V [105]. Furthermore, when the cage size decreases from C_{82} to C_{76}, the over redox pattern of TbNC@C_{2v}(19138)-C_{76} looks similar with those of TbNC@C_{82} despite of the appreciable shifts of the redox potentials. TbNC@C_{2v}(19138)-C_{76} exhibits four reversible reduction potentials at −0.91, −1.26, −1.78, and −2.19 V, respectively, as well as one reversible oxidation potential at 0.45 V, which are almost identical to those of YNC@C_{2v}(19138)-C_{76} (Fig. 10b).

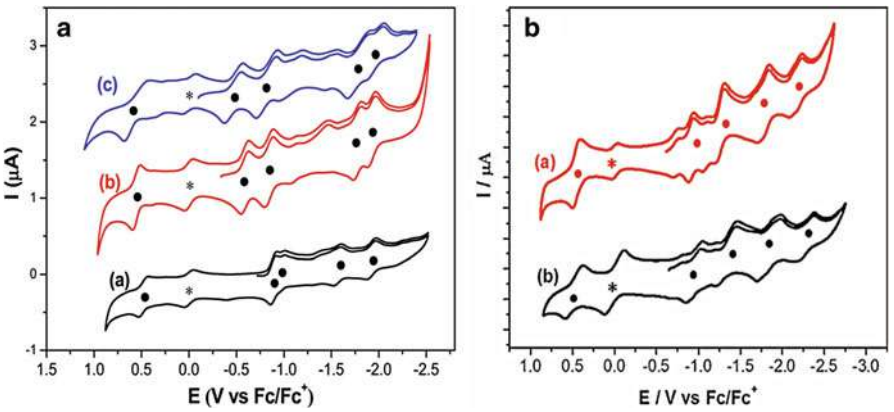

Fig. 10 Cyclic voltammograms of A: TbNC@C_2(5)-C_{82} (**a**), TbNC@C_s(6)-C_{82} (**b**), and TbNC@C_{2v}(9)-C_{82} (c); B: TbNC@C_{2v}(19138)-C_{76} (**a**), YNC@C_{2v}(19138)-C_{76} (**b**) measured in o-DCB solution

Besides, the separation between the second and third separation for TbNC@C_{2v}(19138)-C_{76} (0.52 V) is obviously smaller than that of TbNC@C_{2v}(9)-C_{82} (0.97 V). All these results reveal that the carbon cage plays a decisive role on the electronic structure of CYCF [6, 105, 106, 142].

Optical Properties

Luminescence Property

Although the luminescence properties of lanthanide metal-containing inorganic compounds have been widely reported, for lanthanide metal-based EMFs, the luminescence of endohedral lanthanide ions can hardly be detected because the majority of lanthanide ions emit in the visible range which overlaps the intensive absorption region of fullerene cages [13]. So far only few luminescence studies of EMFs were reported, mostly based on a near-infrared (NIR) $^4I_{13/2} \rightarrow {}^4I_{15/2}$ luminescence of Er^{3+}-based EMFs. In 1997, Ding et al. studied the luminescence property of purified $Er_2@C_{82}$ in the frozen CS_2 solution at 30 K, and concluded that the fluorescence aroused from the $^4I_{13/2} \rightarrow {}^4I_{15/2}$ transition of Er^{3+} within $Er_2@C_{82}$, which was weak and the lifetime was less than 10 μs due to quenching by the overlapping electric state of the fullerene cage [143].

A follow-up photoluminescence (PL) studies of $Er_2@C_{82}$ (I, II, III, corresponding to C_s(6), C_{2v}(9), and C_{3v}(8), respectively) in comparison with those of $Er_2C_2@C_{82}$ (I, II, III) CCFs were reported by Shinohara and coworkers in 2007. The PL spectra of $Er_2C_2@C_{82}$ (I, II, III) in CS_2 solution at room temperature exhibited similar emission patterns correspond well with $^4I_{13/2} \rightarrow {}^4I_{15/2}$ transition of Er^{3+}, but differ in the PL intensities, revealing the dependence of the PL intensity on the cage isomeric structure [144]. Among them, the PL intensity of $Er_2C_2@C_{82}$ (III) was nearly 150 times stronger than $Er_2C_2@C_{82}$ (I, II), caused by the differences in absorbance of their carbon cages at about 1500 nm where absorption of Er^{3+} occurs. Besides, $Er_2C_2@C_{82}$ (II) exhibited a broad absorption band at around 1500 nm, and the absorption onset of $Er_2C_2@C_{82}$ (I) was at ca.1550 nm with a slight absorption at ca.1520 nm, whereas the onset of $Er_2C_2@C_{82}$ (III) absorption was at about 1250 nm and no absorption bands were observed at 1520 nm [144]. Furthermore, the PL spectra of $Er_2@C_{82}$ (I, II, III) showed a pattern similar to $Er_2C_2@C_{82}$ (I, II, III), as shown in Fig. 11. Their overall spectra are almost the same but the spectra intensities were different from each other, also due to the diversity of the absorbance of these carbon cages at ca. 1500 nm [144]. It was found that the PL intensities of $E_2C_2@C_{82}$ (I, II, III) CCFs originated from the encapsulated Er^{3+} at 1520 nm were significantly higher than those of $Er_2@C_{82}$ (I, II, III) di-EMFs with same cage symmetry, and the $E_2C_2@C_{82}$ (III) exhibited the strongest PL intensity. The authors suggested that the encapsulated C_2 unit between the two Er ions played an important role in widening the HOMO–LUMO energy gap of the C_{82} cage and further decreased the absorbance at ca. 1520 nm [144].

In 2001, Dorn et al. reported the fluorescence lifetimes and emission studies of $Er_xSc_{3-x}N@C_{80}$ (x = 1–3) MMNCFs based on their CS_2 solutions at a

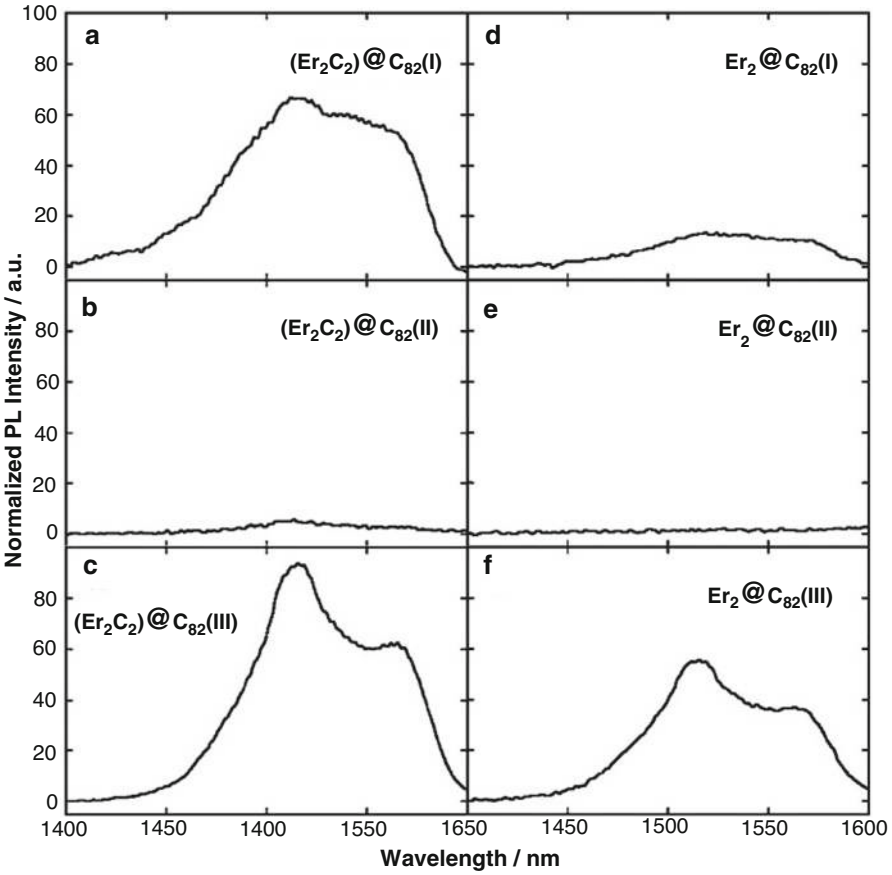

Fig. 11 PL spectra of $Er_2C_2@C_{82}$ (I, II, III) and $Er_2@C_{82}$ (I, II, III) in CS_2 solvent at room temperature. The irradiation times are 120, 120, 1, 120, 120, and 120 s, respectively. These spectra are normalized with the absorbance at 400 nm

concentration of 10^{-3} M [145]. The fluorescence spectra of $Er_3N@C_{80}$, $Er_2Sc@C_{80}$, and $ErSc_2@C_{80}$ measured at 1.6 K by using liquid helium exhibited eight principal lines in the range of 1510 and 1610 nm, corresponding to $^4I_{13/2} \rightarrow {}^4I_{15/2}$ transition of Er^{3+} ion [145]. Interestingly, two sharp lines (4–6 cm^{-1}) around 1520 cm^{-1} were observed in fluorescence spectra of $ErSc_2N@C_{80}$ and $Er_2ScN@C_{80}$, indicating a doublet structure of $^4I_{13/2} \rightarrow {}^4I_{15/2}$ transition, while only a single line at 1517.2 cm^{-1} was observed for $Er_3N@C_{80}$. They tentatively interpreted this phenomenon by the different positions of encapsulated Er atoms within the fullerene cage, as both $ErSc_2N@C_{80}$ and $Er_2Sc@C_{80}$ molecules have two configurations compared to $Er_3N@C_{80}$ with only one configuration detected by single-crystal XRD [13, 145]. In addition, the fluorescence lifetimes of $Er_xSc_{3-x}N@C_{80}$ from 1.6 K to room temperature were measured to be 1.51, 1.57, and 1.15 μs for $ErSc_2N@C_{80}$, $Er_2ScN@C_{80}$, and $Er_3N@C_{80}$ at 1.6 K, respectively, and the values were reduced by

10–20% when the temperature increased from 2 to 300 K. All the $Er_xSc_{3-x}N@C_{80}$ MMNCFs exhibited low quantum efficiency of about 10^{-4}, because of the quenching via interactions with the high-frequency vibrations of the carbon cage [145].

In addition to Er-based EMFs, few luminescence studies of EMFs based on other metals were also reported. In 2016, Shinohara et al. reported NIR photoluminescence studies of a series of Tm-based EMFs, including $Tm@C_{82}$ (I, II, III, IV) and $Tm@C_{88}$ (I, II, III, IV) mono-EMFs, $Tm_2@C_{82}$ (I, II, III) di-EMFs, and $Tm_2C_2@C_{82}$ (I, II, III) CCFs, so as to unravel the dependence of luminescence properties of on the type of EMF and the fullerene cage size [111]. Among them, only a few EMFs emitted PL, including $Tm@C_{88}$ (III, IV) and $Tm_2C_2@C_{82}$ (I, III), whereas no PL signals were detected for the others isomers of $Tm@C_{88}$ and $Tm_2C_2@C_{82}$, especially all $Tm@C_{82}$ and $Tm_2@C_{82}$. This suggests that PL of Tm^{2+} ion depends sensitively on the type of EMF and fullerene cage size [111]. The PL signals are assigned respectively to the $^2F_{5/2} \rightarrow {}^2F_{7/2}$ transition of trivalent Tm^{2+} ion (1200 nm, for $Tm@C_{88}$ (III, IV)) and from $^3H_4 \rightarrow {}^3F_4$ (excited at 800 nm) or $^3F_4 \rightarrow {}^3H_6$ (excited at 405 nm) transitions of Tm^{3+} ion (1300–2000 nm, for $Tm_2C_2@C_{82}$ (I, III)). This means that the PL properties of $Tm_2C_2@C_{82}$ is also dependent on the excitation energy. In addition, the PL properties of these Tm-based EMFs correlate strongly with their HOMO−LUMO band gaps:$Tm_2C_2@C_{82}$ (III) with a relatively large HOMO–LUMO gap of 0.99 eV exhibited the strongest PL intensity among $Tm_2@C_{82}$ (I, II, III) and $Tm_2C_2@C_{82}$ (I, II, III), whereas no PL was observed for $Tm_2@C_{82}$ (II) and $Tm_2C_2@C_{82}$ (II) whose HOMO−LUMO band gaps were 0.50 and 0.53 eV, respectively. This indicates an quenching effect of those fullerene cage [111]. Noteworthy, $Tm_2@C_{82}$ (III) has a relatively large HOMO−LUMO gap but no PL has been observed yet. This is quite different from the case of Er-based EMFs discussed above, in which both $Er_2@C_{82}$ (III) and $Er_2C_2@C_{82}$ (III) emit PL at around 1.5 μm [111].

Very recently, Wang et al. designed and isolated $DyErScN@I_h\text{-}C_{80}$ MMNCF and investigated its NIR emission [74]. Several emission peaks were observed from the photoluminescence spectra of $DyErScN@C_{80}$ which were stemmed from $^4I_{13/2} \rightarrow {}^4I_{15/2}$ transition of Er^{3+} ion, because the PL peaks in the same region were not fund in either $Sc_3N@C_{80}$ or $DySc_2N@C_{80}$ PL spectra. The authors proposed that the special ternary metal cluster and the corresponding crystal field lead to the typical photoluminescence spectrum of $DyErScN@C_{80}$, such as the new splitting peaks from Er^{3+} ion, which were attributed to the different orientations of DyErScN cluster within C_{80} fullerene cage as well as the dipole field from Dy^{3+} ion [74].

Nonlinear Optic Properties

In 1998, Du et al. studied the third-order nonlinear optical property of $Dy@C_{82}$ in CS_2 solution, and its second hyperpolarizability was determined to be $(3.0 \pm 0.5) \times 10^{-30}$ esu at 532 nm performed by 70 ps laser pulses. The theoretical results showed that $Dy@C_{82}$ has a higher delocalized p electron density over the carbon cage surface than the empty fullerene C_{82}, corresponding to the electron

transfer from the encapsulated Dy atom to the carbon cage, and resulting in the enhanced nonlinear optical response [146]. In 2004, Shinohara et al. systematically investigated the nonlinear optical properties of several fullerenes, including two empty fullerenes C_2-C_{82}, C_2-C_{92}, and Dy-containing EMFs Dy@C_{82} (I), Dy_2@C_{82} (I), and Er-containing EMFs Er_2@C_{92} (IV), and found their optical Kerr effect spectra. The results showed that the second hyperpolarizability was enhanced by encapsulating one atom inside the fullerene cage, but was decreased when the number of the encapsulated atom increased to two. As a result, Dy@C_{82} (I) exhibited the largest second polarizability, whereas that of Dy_2@C_{82} (I) was the weakest among C_2-C_{82}, Dy@C_{82} (I) and Dy_2@C_{82} (I) [147]. More recently, Wang et al. reported theoretical studies on the nonlinear optical properties of EMF heterodimers, including Li@C_{60}-Y@C_{82}, Li@C_{60}-Y_2@C_{80}, and Y@C_{82}-Y_2@C_{80}. They proposed that the first hyperpolarizabilities of these EMF heterodimers increase remarkably relative to the corresponding pristine EMFs, due to the charge transfer transitions between two EMF moieties with different electron accepting abilities [148].

Magnetic Properties

Resulted from the encapsulation of lanthanide ions bearing unpaired 4f electrons, EMFs exhibit fascinating magnetic properties, enabling promising applications of EMFs in spintronics, quantum information processing, high-density information storage, single-molecule magnet (SMM), and medical imaging [9, 10, 106, 149]. Due to the diversity of the encapsulated species and consequently the coordination interactions between the encapsulated species and outer fullerene cages, magnetic properties of EMFs are very complex and affected by several factors. The conventional paramagnetic EMFs are trivalent metal-based mono-EMFs with the electronic configuration of M^{3+}@$C_{2n}{}^{3-}$, for which the paramagnetic nature is originated from the fullerene cage with a −3 charge state. The second case is that the encapsulated metal ions have unpaired 4f electrons and thus are intrinsically paramagnetic, rendering paramagnetic properties of the entire EMF molecules. The third case is that several paramagnetic metal ions are encapsulated within fullerene cage, imposing exchange interactions between these paramagnetic metal ions [13]. In addition, the solvent and crystal field induced anisotropy and hybridization with the π-electrons of the fullerene cage also play an important role on the magnetic moments of EMFs [13]. Electron spin resonance (ESR) spectroscopy, superconducting quantum interference device (SQUID), and X-ray magnetic dichroism (XMCD) are the most widely used approaches to probe the effective magnetic properties of EMFs.

La@C_{82} is the first paramagnetic EMF studied by ESR spectroscopy, showing an octet feature with a hyperfine coupling (hfc) constant of 1.25 G and g-factor of 2.0010. Since the hfc value is smaller than that of La^{2+} cation (~50 G), the oxidation state of the encapsulated La atom within La@C_{82} is proposed to be 3+ could be assigned to the metal atom in [150]. Later on, the paramagnetic properties of Sc@C_{82} and Y@C_{82} mono-EMFs were investigated by ESR spectroscopy.

Furthermore, the electron spin manipulation based on these paramagnetic species has been realized by changing temperatures and exohedral modification.

The first study on the magnetic properties of conventional mono-EMFs by SQUID is reported by Funasaka et al. in 1995, showing that $Gd@C_{82}$ and $La@C_{82}$ have inverse susceptibility with effective magnetic moments (μ_{eff}) of −0.65 K/6.90 μB and 0.89 K/0.38 μB, respectively. Noteworthy, the Gd^{3+} ion encapsulated within C_{82} cage exhibits slightly smaller effective magnetic moment than that of the free Gd^{3+} ion in its $^8S_{7/2}$ state ($J = S = 7/2$, $g = 2.0$, $\mu_{eff} = 7.94\ \mu_B$) by Curie−Weiss law and from the Brillouin function, and this is due to collective effect of the metal ion ($S = 7/2$) and carbon cage ($S_{cage} = 1/2$) spins.

Different to the simple case of $Gd@C_{82}$ with the orbital angular momentum (L) in the half-filled 4f-shell being equal to zero, for other lanthanide metal-based mono-EMFs, the residual orbital moment and the spin moment simultaneously contribute to the more complex situation. For example, $Ho@C_{82}$, $Tb@C_{82}$, $Dy@C_{82}$, and $Er@C_{82}$ exhibit a reciprocal magnetic susceptibility plot versus temperature at low applied field ($H = 0.1$–0.5 T) below 20 K [151].

While conventional mono-EMFs exhibit relatively simple paramagnetic behavior, for clusterfullerenes, the encapsulation of multiple metal and nonmetal atoms results in new phenomenon in their magnetic properties. Among them, NCFs are particularly interesting since up to three magnetic metal ions can be encapsulated. In 2005, Dunsch et al. firstly investigated the magnetic properties of $M_3N@C_{80}$ (M = Ho, Tb) by SQUID, determining the effective magnetic moments of 17 and 21 μ_B for $Tb_3N@C_{80}$ and $Ho_3N@C_{80}$, respectively, by fitting the magnetization by the Langevin function [152]. Since the magnetic moments of $M_3N@C_{80}$ (M = Ho, Tb) are much smaller than the values expected for collinear alignment of the moments of three independent M^{3+} ions (27 and 30 μ_B for Tb and Ho, respectively), they proposed that the ligand field of the central nitrogen atom leads to preferred alignment of the magnetic moments along the metal-nitrogen bonds [152]. Following this method, the magnetic properties of other homogeneous NCFs such as $Er_3N@C_{80}$, $Tm_3N@C_{80}$, and $Gd_3N@C_{80}$ were studied later [153–155].

A new finding on the fascinating magnetic properties of NCFs was reported by Greber and coworkers in 2012. Both XMCD and SQUID studies of $DySc_2N@I_h(7)$-C_{80} MMNCF show a characteristic butterfly-shape hysteresis of magnetization curves at temperatures below 6 K (Fig. 12). Besides, the magnetization curves show long relaxation time of magnetization, thus $DySc_2N@I_h(7)$-C_{80} is identified to be a mononuclear single-molecular magnet (SMM) [10]. Furthermore, upon decreasing the temperature to 3.5 K, relaxation of magnetization presents a double-exponential decay with slower thermally activated process, leading to an estimated thermally driven relaxation of 24 ± 0.5 K at the field of 0.3 T [156]. A follow-up systematic study of $Dy_xSc_{3-x}N@C_{80}$ ($x = 1$–3) by the same group revealed that all three NCFs behave as SMMs with distinct hysteresis. Besides, their magnetic ground states are found to be tunable by modulating the composition of encapsulated cluster ($Dy_xSc_{3-x}N$). In zero field, the magnetization of $DySc_2N@C_{80}$ decayed via quantum tunneling, while ferromagnetic coupling of

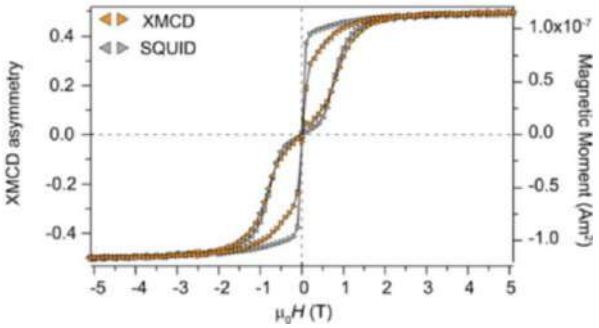

Fig. 12 Magnetization curves of $DySc_2N@C_{80}$ measured at T = 2 K by XMCD and SQUID showing a characteristic butterfly shape hysteresis pattern

the individual dysprosium moments resulted in remanence for $Dy_2ScN@C_{80}$ and in a frustrated ground state for $Dy_3N@C_{80}$ [149].

Without changing the composition of encapsulated magnetic metal cluster, SMM properties of clusterfullerenes can be also tuned by changing the isomeric structure or size of the outer fullerene cage as revealed for $TbCN@C_{2n}$ CYCFs by Yang et al. According to a systematic SQUID study on the SMM properties of three isomers of $TbCN@C_{82}$ (C_2, C_s, C_{2v}), their magnetic moments are determined to be 9.0, 9.1, and 10.2 μ_B, respectively. Their magnetic relaxation times saturated at the lowest temperatures of 1.8 K except for $TbNC@C_{2v}(9)$-C_{82}, hence their lifetimes for the quantum tunneling of the magnetization were in the order of 10–50 ms. Since the magnetic relaxation times measured at 1.8 K increased sensitively with shortening the Tb-C(N) distance, magnetic relaxation time of $TbNC@C_{82}$ is revealed to depend sensitively on atomic distance within TbNC unit was illustrated [105]. Furthermore, by decreasing the cage size from C_{82} to C_{76}, the magnetic relaxation time can be further tuned as revealed by the follow-up SQUID study of $TbCN@C_{2v}(19138)$-C_{76} [106].

Chemical functionalization is recently demonstrated to be a novel approach to modulate the SMM properties of EMFs. In 2017, Popov et al. synthesized a benzyl monoadduct of $Dy_2@C_{80}$ di-EMF, $Dy_2@C_{80}(CH_2Ph)$, by radical addition reaction, and found that it acted as a SMM with large magnetic moment of 21 μ_B and a record-high blocking temperature as well as a high thermal barrier of magnetization reversal at 613 K. Moreover, the magnetic properties of $Dy_2@C_{80}(CH_2Ph)$ can be facilely tuned by forming stable cations and anions via redox chemistry [157]. More recently, the same group reported that a series of air-stable $Ln_2@C_{80}(CH_2Ph)$ ($Ln_2 = Y_2$, Gd_2, Tb_2, Dy_2, Ho_2, Er_2, TbY, TbGd) SMMs, featuring a metal-metal bond between two lanthanide atoms. The 4f moments and a single electron between metal atoms contribute to the strong exchange interaction, which is beneficial for the glued lanthanide spins. In particular, $Tb_2@C_{80}(CH_2Ph)$ exhibits a superior gigantic coercivity of 8.2 T at 5 K and a 100 s blocking temperature of magnetization of 25.2 K, verifying that the Ln-Ln bonding orbital in $Ln_2@C_{80}(CH_2Ph)$ is redox active and thus enabling electrochemical tuning of the magnetism [157].

Concluding Remarks

During the past two decades, the research field of EMF has dramatically blossomed especially due to the discovery of endohedral clusterfullerenes, as witnessed by isolations of many exotic compounds and unveiling the extraordinary properties such as single molecular magnetism (SMM). Based on the modified DC-arc discharging method, versatile EMFs with different encapsulated species (mainly metal clusters) and fullerene cages have been successfully synthesized and isolated. As the prerequisite for understanding the properties of EMFs, determining their molecular structures of EMFs is of high important and thus has been extensively studied, mostly fulfilled by single-crystal X-ray diffraction crystallography, which can unambiguously tell both the isomeric structures of the outer carbon cages and the geometrical position of the inner species. Owing to electron transfer from the encapsulated species (metal ions or clusters) to the outer fullerene cage, EMFs exhibit unique electronic, optical, and magnetic properties as reviewed in details here. UV-vis-NIR absorption spectroscopy has been commonly applied to characterize the electronic properties of EMFs, providing valuable structural information and even affording preliminary structural determination of new EMFs in some cases. The electrochemical properties of EMFs appear quite intriguing especially the endohedral electrochemistry, and electrochemical study offers a direct access to the molecular energy levels and intramolecular electron transfer mechanism. Limited studies on the luminescence properties of Er-based EMFs enable a better understanding to their luminescence mechanisms. The magnetic properties of EMFs are originated from the unpaired electrons on the fullerene cages as well as the endohedral lanthanides with unpaired 4f electrons, and particularly single molecular magnetisms resulted from the unique coordination interactions within the encapsulated metal clusters render potential applications of EMFs in quantum computing and high-density storage devices.

The comprehensive studies on the structures and properties of EMFs significantly deepen our insights into the stability and structure-property correlation of EMFs, yet there are still some open questions to be addressed. For instance, given that clusterfullerenes provide a powerful platform to encapsulate a large variety of metal and nonmetal atoms, whether can other types of atoms especially d-block transition metals be encapsulated in the form of clusterfullerenes? In terms of the magnetic properties of EMFs, deeper mechanistic understandings of the SMM behavior of clusterfullerenes are still needed, with which more accurate manipulation of paramagnetic properties of EMFs can be desirably anticipated. Utilizing such intriguing SMM properties, promising applications of EMFs in information processing on the basis of construction of ordered arrays of EMFs would become feasible.

Acknowledgments This work was partially supported by the National Basic Research Program of China (2017YFA0402802) and National Natural Science Foundation of China (51925206, U1932214).

References

1. Stevenson S, Rice G, Glass T, Harich K, Cromer F, Jordan MR, Craft J, Hadju E, Bible R, Olmstead MM, Maitra K, Fisher AJ, Balch AL, Dorn HC (1999) Small-bandgap endohedral metallofullerenes in high yield and purity. Nature 401(6748):55–57
2. Yang S, Wei T, Jin F (2017) When metal clusters meet carbon cages: endohedral clusterfullerenes. Chem Soc Rev 46(16):5005–5058. https://doi.org/10.1039/c6cs00498a
3. Wang CR, Kai T, Tomiyama T, Yoshida T, Kobayashi Y, Nishibori E, Takata M, Sakata M, Shinohara H (2001) A scandium carbide endohedral metallofullerene: $(Sc_2C_2)@C_{84}$. Angew Chem Int Ed 40(2):397–399. https://doi.org/10.1002/1521-3773(20010119)40:2<397::Aid-anie397>3.3.Co;2-3
4. Stevenson S, Mackey MA, Stuart MA, Phillips JP, Easterling ML, Chancellor CJ, Olmstead MM, Balch AL (2008) A distorted tetrahedral metal oxide cluster inside an Icosahedral carbon cage. Synthesis, isolation, and structural characterization of $Sc_4(\mu_3\text{-}O)_2@I_h\text{-}C_{80}$. J Am Chem Soc 130(36):11844–11845. https://doi.org/10.1021/ja803679u
5. Dunsch L, Yang S, Zhang L, Svitova A, Oswald S, Popov AA (2010) Metal sulfide in a C_{82} fullerene cage: a new form of endohedral clusterfullerenes. J Am Chem Soc 132(15):5413–5421. https://doi.org/10.1021/ja909580j
6. Yang S, Chen C, Liu F, Xie Y, Li F, Jiao M, Suzuki M, Wei T, Wang S, Chen Z, Lu X, Akasaka T (2013) An improbable monometallic cluster entrapped in a popular fullerene cage: $YCN@C_s(6)\text{-}C_{82}$. Sci Rep 3. https://doi.org/10.1038/srep01487
7. Krause M, Ziegs F, Popov AA, Dunsch L (2007) Entrapped bonded hydrogen in a fullerene: the five-atom cluster Sc_3CH in C_{80}. ChemPhysChem 8(4):537–540. https://doi.org/10.1002/cphc.200600363
8. Wang T-S, Feng L, Wu J-Y, Xu W, Xiang J-F, Tan K, Ma Y-H, Zheng J-P, Jiang L, Lu X, Shu C-Y, Wang C-R (2010) Planar quinary cluster inside a fullerene cage: synthesis and structural characterizations of $Sc_3NC@I_h\text{-}C_{80}$. J Am Chem Soc 132(46):16362–16364. https://doi.org/10.1021/ja107843b
9. Yang W, Velkos G, Liu F, Sudarkova SM, Wang Y, Zhuang J, Zhang H, Li X, Zhang X, Buechner B, Avdoshenko SM, Popov AA, Chen N (2019) Single molecule magnetism with strong magnetic anisotropy and enhanced Dy...Dy coupling in three isomers of Dy-Oxide clusterfullerene $Dy_2O@C_{82}$. Adv Sci 6(20). https://doi.org/10.1002/advs.201901352
10. Westerstroem R, Dreiser J, Piamonteze C, Muntwiler M, Weyeneth S, Brune H, Rusponi S, Nolting F, Popov A, Yang S, Dunsch L, Greber T (2012) An endohedral single-molecule magnet with long relaxation times: $DySc_2N@C_{80}$. J Am Chem Soc 134(24):9840–9843. https://doi.org/10.1021/ja301044p
11. Dunsch L, Yang S (2007) Metal nitride cluster fullerenes: their current state and future prospects. Small 3(8):1298–1320. https://doi.org/10.1002/smll.200700036
12. Yang S, Liu F, Chen C, Jiao M, Wei T (2011) Fullerenes encaging metal clusters-clusterfullerenes. Chem Commun 47(43):11822–11839. https://doi.org/10.1039/c1cc12318a
13. Popov AA, Yang S, Dunsch L (2013) Endohedral fullerenes. Chem Rev 113(8):5989–6113. https://doi.org/10.1021/cr300297r
14. Lu X, Feng L, Akasaka T, Nagase S (2012) Current status and future developments of endohedral metallofullerenes. Chem Soc Rev 41(23):7723–7760. https://doi.org/10.1039/c2cs35214a
15. Takata M, Umeda B, Nishibori E, Sakata M, Saito Y, Ohno M, Shinohara H (1995) Confirmation by X-ray-diffraction of the endohedral aature of the metallofullerene $Y@C_{82}$. Nature 377(6544):46–49. https://doi.org/10.1038/377046a0
16. Rodriguez-Fortea A, Balch AL, Poblet JM (2011) Endohedral metallofullerenes: a unique host–guest association. Chem Soc Rev 40(7):3551–3563. https://doi.org/10.1039/c0cs00225a

17. Xu Y-Y, Tian H-R, Li S-H, Chen Z-C, Yao Y-R, Wang S-S, Zhang X, Zhu Z-Z, Deng S-L, Zhang Q, Yang S, Xie S-Y, Huang R-B, Zheng L-S (2019) Flexible decapyrrylcorannulene hosts. Nat Commun 10. https://doi.org/10.1038/s41467-019-08343-6
18. Yamada M, Akasaka T, Nagase S (2010) Endohedral metal atoms in pristine and functionalized fullerene cages. Acc Chem Res 43(1):92–102. https://doi.org/10.1021/ar900140n
19. Lu X, Akasaka T, Nagase S (2011) Chemistry of endohedral metallofullerenes: the role of metals. Chem Commun 47(21):5942–5957. https://doi.org/10.1039/c1cc10123d
20. Wang Y, Morales-Martinez R, Zhan X, Yang W, Wang Y, Rodriguez-Fortea A, Poblet JM, Feng L, Wang S, Chen N (2017) Unique four-electron metal-to-cage charge transfer of Th to a C_{82} fullerene cage: complete structural characterization of Th@C_{3v}(8)-C_{82}. J Am Chem Soc 139(14):5110–5116. https://doi.org/10.1021/jacs.6b13383
21. Sato S, Nikawa H, Seki S, Wang L, Luo G, Lu J, Haranaka M, Tsuchiya T, Nagase S, Akasaka T (2012) A co-crystal composed of the paramagnetic endohedral metallofullerene La@C_{82} and a nickel porphyrin with high electron mobility. Angew Chem Int Ed 51(7):1589–1591. https://doi.org/10.1002/anie.201106912
22. Suzuki M, Lu X, Sato S, Nikawa H, Mizorogi N, Slanina Z, Tsuchiya T, Nagase S, Akasaka T (2012) Where does the metal cation stay in Gd@C_{2v}(9)-C_{82}? A single-crystal X-ray diffraction study. Inorg Chem 51(9):5270–5273. https://doi.org/10.1021/ic300186y
23. Suzuki M, Slanina Z, Mizorogi N, Lu X, Nagase S, Olmstead MM, Balch AL, Akasaka T (2012) Single-crystal X-ray diffraction study of three Yb@C_{82} isomers cocrystallized with Ni-II(octaethylporphyrin). J Am Chem Soc 134(45):18772–18778. https://doi.org/10.1021/ja308706d
24. Yang H, Jin H, Wang X, Liu Z, Yu M, Zhao F, Mercado BQ, Olmstead MM, Balch AL (2012) X-ray crystallographic characterization of new soluble endohedral fullerenes utilizing the popular C_{82} bucky cage. Isolation and structural characterization of Sm@C_{3v}(7)-C_{82}, Sm@C_s(6)-C_{82}, and Sm@C_2(5)-C_{82}. J Am Chem Soc 134(34):14127–14136. https://doi.org/10.1021/ja304867j
25. Yang H, Yu M, Jin H, Liu Z, Yao M, Liu B, Olmstead MM, Balch AL (2012) Isolation of three isomers of Sm@C_{84} and X-ray crystallographic characterization of Sm@D_{3d}(19)-C_{84} and Sm@C_2(13)-C_{84}. J Am Chem Soc 134(11):5331–5338. https://doi.org/10.1021/ja211785u
26. Yang H, Jin H, Zhen H, Wang Z, Liu Z, Beavers CM, Mercado BQ, Olmstead MM, Balch AL (2011) Isolation and crystallographic identification of four isomers of Sm@C_{90}. J Am Chem Soc 133(16):6299–6306. https://doi.org/10.1021/ja111465n
27. Jin H, Yang H, Yu M, Liu Z, Beavers CM, Olmstead MM, Balch AL (2012) Single samarium atoms in large fullerene cages. Characterization of two isomers of Sm@C_{92} and four isomers of Sm@C_{94} with the X-ray crystallographic identification of Sm@C_1(42)-C_{92}, Sm@C_s(24)-C_{92}, and Sm@C_{3v}(134)-C_{94}. J Am Chem Soc 134(26):10933–10941. https://doi.org/10.1021/ja302859r
28. Wakahara T, Nikawa H, Kikuchi T, Nakahodo T, Rahman GMA, Tsuchiya T, Maeda Y, Akasaka T, Yoza K, Horn E, Yamamoto K, Mizorogi N, Slanina Z, Nagase S (2006) La@C_{72} having a non-IPR carbon cage. J Am Chem Soc 128(44):14228–14229. https://doi.org/10.1021/ja064751y
29. Che Y, Yang H, Wang Z, Jin H, Liu Z, Lu C, Zuo T, Dorn HC, Beavers CM, Olmstead MM, Balch AL (2009) Isolation and structural characterization of two very large, and largely empty, endohedral fullerenes: Tm@C_{3v}-C_{94} and Ca@C_{3v}-C_{94}. Inorg Chem 48(13):6004–6010. https://doi.org/10.1021/ic900322d
30. Jin M, Zhuang J, Wang Y, Yang W, Liu X, Chen N (2019) Th@Td(19151)-C_{76}: a highly symmetric fullerene cage stabilized by a tetravalent actinide metal ion. Inorg Chem 58(24):16722–16726. https://doi.org/10.1021/acs.inorgchem.9b02863
31. Cai W, Abella L, Zhuang J, Zhang X, Feng L, Wang Y, Morales-Martinez R, Esper R, Boero M, Metta-Magana A, Rodriguez-Fortea A, Poblet JM, Echegoyen L, Chen N (2018) Synthesis and characterization of non-isolated-pentagon-rule actinide endohedral

metallofullerenes U@C_1(17418)-C_{76}, U@C_1(28324)-C_{80}, and Th@C_1(28324)-C_{80}: low-symmetry cage selection directed by a tetravalent ion. J Am Chem Soc 140(51):18039–18050. https://doi.org/10.1021/jacs.8b10435

32. Wang Y, Morales-Martinez R, Cai W, Zhuang J, Yang W, Echegoyen L, Poblet JM, Rodriguez-Fortea A, Chen N (2019) Th@C_1(11)-C_{86}: an actinide encapsulated in an unexpected C_{86} fullerene cage. Chem Commun 55(63):9271–9274. https://doi.org/10.1039/c9cc04613e
33. Cai W, Morales-Martinez R, Zhang X, Najera D, Romero EL, Metta-Magana A, Rodriguez-Fortea A, Fortier S, Chen N, Poblet JM, Echegoyen L (2017) Single crystal structures and theoretical calculations of uranium endohedral metallofullerenes (U@C_{2n}, 2n = 74, 82) show cage isomer dependent oxidation states for U. Chem Sci 8(8):5282–5290. https://doi.org/10.1039/c7sc01711a
34. Akasaka T, Nagase S, Kobayashi K, Walchli M, Yamamoto K, Funasaka H, Kako M, Hoshino T, Erata T (1997) ^{13}C and ^{139}La NMR studies of La_2@C_{80}: first evidence for circular motion of metal atoms in endohedral dimetallofullerenes. Angew Chem Int Ed Engl 36(15):1643–1645. https://doi.org/10.1002/anie.199716431
35. Yamada M, Wakahara T, Tsuchiya T, Maeda Y, Kako M, Akasaka T, Yoza K, Horn E, Mizorogi N, Nagase S (2008) Location of the metal atoms in Ce_2@C_{78} and its bis-silylated derivative. Chem Commun 5:558–560. https://doi.org/10.1039/b712568b
36. Yamada M, Wakahara T, Tsuchiya T, Maeda Y, Akasaka T, Mizorogi N, Nagase S (2008) Spectroscopic and theoretical study of endohedral dimetallofullerene having a non-IPR fullerene cage: Ce_2@C_{72}. J Phys Chem A 112(33):7627–7631. https://doi.org/10.1021/jp804260d
37. Yamada M, Mizorogi N, Tsuchiya T, Akasaka T, Nagase S (2009) Synthesis and characterization of the D_{5h} isomer of the endohedral dimetallofullerene Ce_2@C_{80}: two-dimensional circulation of encapsulated metal atoms inside a fullerene cage. Chem Eur J 15(37):9486–9493. https://doi.org/10.1002/chem.200900713
38. Kato H, Taninaka A, Sugai T, Shinohara H (2003) Structure of a missing-caged metallofullerene: La_2@C_{72}. J Am Chem Soc 125(26):7782–7783. https://doi.org/10.1021/ja0353255
39. Cao BP, Wakahara T, Tsuchiya T, Kondo M, Maeda Y, Rahman GMA, Akasaka T, Kobayashi K, Nagase S, Yamamoto K (2004) Isolation, characterization, and theoretical study of La_2@C_{78}. J Am Chem Soc 126(30):9164–9165. https://doi.org/10.1021/ja048599g
40. Yamada M, Nakahodo T, Wakahara T, Tsuchiya T, Maeda Y, Akasaka T, Kako M, Yoza K, Horn E, Mizorogi N, Kobayashi K, Nagase S (2005) Positional control of encapsulated atoms inside a fullerene cage by exohedral addition. J Am Chem Soc 127(42):14570–14571. https://doi.org/10.1021/ja054346r
41. Beavers CM, Jin H, Yang H, Wang Z, Wang X, Ge H, Liu Z, Mercado BQ, Olmstead MM, Balch AL (2011) Very large, soluble endohedral fullerenes in the series La_2C_{90} to La_2C_{138}: isolation and crystallographic characterization of La_2@D_5(450)-C_{100}. J Am Chem Soc 133(39):15338–15341. https://doi.org/10.1021/ja207090e
42. Mercado BQ, Jiang A, Yang H, Wang Z, Jin H, Liu Z, Olmstead MM, Balch AL (2009) Isolation and structural characterization of the molecular nanocapsule Sm_2@D_{3d}(822)-C_{104}. Angew Chem Int Ed 48(48):9114–9116. https://doi.org/10.1002/anie.200904662
43. Mercado BQ, Chen N, Rodriguez-Fortea A, Mackey MA, Stevenson S, Echegoyen L, Poblet JM, Olmstead MM, Balch AL (2011) The shape of the Sc_2(μ_2-S) unit trapped in C_{82}: crystallographic, computational, and electrochemical studies of the isomers, Sc_2(μ_2-S)@C_s(6)-C_{82} and Sc_2(μ_2-S)@C_{3v}(8)-C_{82}. J Am Chem Soc 133(17):6752–6760. https://doi.org/10.1021/ja200289w
44. Kurihara H, Lu X, Iiduka Y, Mizorogi N, Slanina Z, Tsuchiya T, Nagase S, Akasaka T (2012) Sc_2@C_{3v}(8)-C_{82} vs. Sc_2C_2@C_{3v}(8)-C_{82}: drastic effect of C_2 capture on the redox properties of scandium metallofullerenes. Chem Commun 48(9):1290–1292. https://doi.org/10.1039/c2cc16422a

45. Inoue T, Tomiyama T, Sugai T, Okazaki T, Suematsu T, Fujii N, Utsumi H, Nojima K, Shinohara H (2004) Trapping a C_2 radical in endohedral metallofullerenes: synthesis and structures of $(Y_2C_2)@C_{82}$ (isomers I, II, and III). J Phys Chem B 108(23):7573–7579. https://doi.org/10.1021/jp049865f
46. Olmstead MM, de Bettencourt-Dias A, Stevenson S, Dorn HC, Balch AL (2002) Crystallographic characterization of the structure of the endohedral fullerene $\{Er_2@C_{82}$ isomer I$\}$ with C_s cage symmetry and multiple sites for erbium along a band of ten contiguous hexagons. J Am Chem Soc 124(16):4172–4173. https://doi.org/10.1021/ja0116019
47. Olmstead MM, Lee HM, Stevenson S, Dorn HC, Balch AL (2002) Crystallographic characterization of isomer 2 of $Er_2@C_{82}$ and comparison with isomer 1 of $Er_2@C_{82}$. Chem Commun 22:2688–2689. https://doi.org/10.1039/b209270k
48. Plant SR, Dantelle G, Ito Y, Ng TC, Ardavan A, Shinohara H, Taylor RA, Briggs GAD, Porfyrakis K (2009) Acuminated fluorescence of Er^{3+} centres in endohedral fullerenes through the incarceration of a carbide cluster. Chem Phys Lett 476(1–3):41–45. https://doi.org/10.1016/j.cplett.2009.05.042
49. Umemoto H, Ohashi K, Inoue T, Fukui N, Sugai T, Shinohara H (2010) Synthesis and UHV-STM observation of the T-d-symmetric Lu metallofullerene: $Lu_2@T_d$-C_{76}. Chem Commun 46(31):5653–5655. https://doi.org/10.1039/c0cc00824a
50. Zhang X, Wang Y, Morales-Martinez R, Zhong J, de Graaf C, Rodriguez-Fortea A, Poblet JM, Echegoyen L, Feng L, Chen N (2018) $U_2@I_h(7)$-C_{80}: crystallographic characterization of a long-sought dimetallic actinide endohedral fullerene. J Am Chem Soc 140(11):3907–3915. https://doi.org/10.1021/jacs.7b10865
51. Zuo T, Xu L, Beavers CM, Olmstead MM, Fu W, Crawford D, Balch AL, Dorn HC (2008) $M_2@C_{79}N$ (M = Y, Tb): isolation and characterization of stable endohedral metallofullerenes exhibiting M-M bonding interactions inside a C_{80} fullerene cages. J Am Chem Soc 130(39):12992–12997. https://doi.org/10.1021/ja802417d
52. Tagmatarchis N, Aslanis E, Prassides K, Shinohara H (2001) Mono-, di- and trierbium endohedral metallofullerenes: production, separation, isolation, and spectroscopic study. Chem Mater 13(7):2374–2379. https://doi.org/10.1021/cm000955g
53. Lian YF, Shi ZJ, Zhou XH, Gu ZN (2004) Different extraction behaviors between divalent and trivalent endohedral metallofullerenes. Chem Mater 16(9):1704–1714. https://doi.org/10.1021/cm0344156
54. Popov AA, Zhang L, Dunsch L (2010) A pseudoatom in a cage: trimetallofullerene $Y_3@C_{80}$ mimics $Y_3N@C_{80}$ with nitrogen substituted by a pseudoatom. ACS Nano 4(2):795–802. https://doi.org/10.1021/nn901422z
55. Yang SF, Dunsch L (2006) Di- and tridysprosium endohedral metallofullerenes with cages from C_{94} to C_{100}. Angew Chem Int Ed 45(8):1299–1302. https://doi.org/10.1002/anie.200502417
56. Xu W, Feng L, Calvaresi M, Liu J, Liu Y, Niu B, Shi Z, Lian Y, Zerbetto F (2013) An experimentally observed trimetallofullerene $Sm_3@I_h$-C_{80}: encapsulation of three metal atoms in a cage without a nonmetallic mediator. J Am Chem Soc 135(11):4187–4190. https://doi.org/10.1021/ja400490u
57. Stevenson S, Fowler PW, Heine T, Duchamp JC, Rice G, Glass T, Harich K, Hajdu E, Bible R, Dorn HC (2000) Materials science – a stable non-classical metallofullerene family. Nature 408(6811):427–428. https://doi.org/10.1038/35044199
58. Olmstead MM, Lee HM, Duchamp JC, Stevenson S, Marciu D, Dorn HC, Balch AL (2003) $Sc_3N@C_{68}$: folded pentalene coordination in an endohedral fullerene that does not obey the isolated pentagon rule. Angew Chem Int Ed 42(8):900. https://doi.org/10.1002/anie.200390237
59. Yang S, Popov AA, Dunsch L (2007) Violating the isolated pentagon rule (IPR): the endohedral non-IPR C_{70} cage of $Sc_3N@C_{70}$. Angew Chem Int Ed Engl 46(8):1256–1259. https://doi.org/10.1002/anie.200603281

60. Olmstead MM, de Bettencourt-Dias A, Duchamp JC, Stevenson S, Marciu D, Dorn HC, Balch AL (2001) Isolation and structural characterization of the endohedral fullerene $Sc_3N@C_{78}$. Angew Chem Int Ed 40(7):1223. https://doi.org/10.1002/1521-3773(20010401)40:7<1223::Aid-anie1223>3.3.Co;2-2
61. Cai T, Xu L, Anderson MR, Ge Z, Zuo T, Wang X, Olmstead MM, Balch AL, Gibson HW, Dorn HC (2006) Structure and enhanced reactivity rates of the D_{5h} $Sc_3N@C_{80}$ and $Lu_3N@C_{80}$ metallofullerene isomers: the importance of the pyracylene motif. J Am Chem Soc 128(26): 8581–8589. https://doi.org/10.1021/ja0615573
62. Wei T, Wang S, Liu F, Tan Y, Zhu X, Xie S, Yang S (2015) Capturing the long-sought small-bandgap endohedral fullerene $Sc_3N@C_{82}$ with low kinetic stability. J Am Chem Soc 137(8): 3119–3123. https://doi.org/10.1021/jacs.5b00199
63. Stevenson S, Lee HM, Olmstead MM, Kozikowski C, Stevenson P, Balch AL (2002) Preparation and crystallographic characterization of a new endohedral, $Lu_3N@C_{80}$·5 (o-xylene), and comparison with $Sc_3N@C_{80}$·5 (o-xylene). Chem Eur J 8(19):4528–4535. https://doi.org/10.1002/1521-3765(20021004)8:19<4528::Aid-chem4528>3.0.Co;2-8
64. Yang S, Troyanov SI, Popov AA, Krause M, Dunsch L (2006) Deviation from the planarity – a large Dy_3N cluster encapsulated in an I_h-C_{80} cage: an X-ray crystallographic and vibrational spectroscopic study. J Am Chem Soc 128(51):16733–16739. https://doi.org/10.1021/ja066814i
65. Fu W, Xu L, Azurmendi H, Ge J, Fuhrer T, Zuo T, Reid J, Shu C, Harich K, Dorn HC (2009) Y_{89} and ^{13}C NMR cluster and carbon cage studies of an yttrium metallofullerene family, $Y_3N@C_{2n}$ (n = 40–43). J Am Chem Soc 131(33):11762–11769. https://doi.org/10.1021/ja902286v
66. Zuo T, Beavers CM, Duchamp JC, Campbell A, Dorn HC, Olmstead MM, Balch AL (2007) Isolation and structural characterization of a family of endohedral fullerenes including the large, chiral cage fullerenes $Tb_3N@C_{88}$ and $Tb_3N@C_{86}$ as well as the I_h and D_{5h} isomers of $Tb_3N@C_{80}$. J Am Chem Soc 129(7):2035–2043. https://doi.org/10.1021/ja066437+
67. Chaur MN, Melin F, Elliott B, Athans AJ, Walker K, Holloway BC, Echegoyen L (2007) $Gd_3N@C_{2n}$ (n = 40, 42, and 44): remarkably low HOMO-LUMO gap and unusual electrochemical reversibility of $Gd_3N@C_{88}$. J Am Chem Soc 129(47):14826–14829. https://doi.org/10.1021/ja075930y
68. Chaur MN, Melin F, Elliott B, Kumbhar A, Athans AJ, Echegoyen L (2008) New $M_3N@C_{2n}$ endohedral metallofullerene families (M = Nd, Pr, Ce; n = 40–53): expanding the preferential templating of the C_{88} cage and approaching the C_{96} cage. Chemistry 14(15):4594–4599. https://doi.org/10.1002/chem.200800044
69. Chaur MN, Melin F, Ashby J, Elliott B, Kumbhar A, Rao AM, Echegoyen L (2008) Lanthanum nitride endohedral fullerenes $La_3N@C_{2n}$ ($43 < \text{or} = n < \text{or} = 55$): preferential formation of $La_3N@C_{96}$. Chemistry 14(27):8213–8219. https://doi.org/10.1002/chem.200800881
70. Olmstead MM, de Bettencourt-Dias A, Duchamp JC, Stevenson S, Dorn HC, Balch AL (2000) Isolation and crystallographic characterization of $ErSc_2N@C_{80}$: an endohedral fullerene which crystallizes with remarkable internal order. J Am Chem Soc 122(49):12220–12226. https://doi.org/10.1021/ja001984v
71. Stevenson S, Chancellor CJ, Lee HM, Olmstead MM, Balch AL (2008) Internal and external factors in the structural organization in cocrystals of the mixed-metal endohedrals ($GdSc_2N@I_h$-C_{80}, $Gd_2ScN@I_h$-C_{80}, and $TbSc_2N@I_h$-C_{80}) and nickel(II) octaethylporphyrin. Inorg Chem 47(5):1420–1427. https://doi.org/10.1021/ic701824q
72. Wang X, Zuo T, Olmstead MM, Duchamp JC, Glass TE, Cromer F, Balch AL, Dorn HC (2006) Preparation and structure of $CeSc_2N@C80$: an icosahedral carbon cage enclosing an acentric $CeSc_2N$ unit with buried f electron spin. J Am Chem Soc 128(27):8884–8889. https://doi.org/10.1021/ja061434i

73. Chen N, Zhang E-Y, Wang C-R (2006) C_{80} encaging four different atoms: the synthesis, isolation, and characterizations of ScYErN@C_{80}. J Phys Chem B 110(27):13322–13325. https://doi.org/10.1021/jp0629821
74. Nie M, Xiong J, Zhao C, Meng H, Zhang K, Han Y, Li J, Wang B, Feng L, Wang C, Wang T (2019) Luminescent single-molecule magnet of metallofullerene DyErScN@I_h-C_{80}. Nano Res 12(7):1727–1731. https://doi.org/10.1007/s12274-019-2429-1
75. Yang S, Chen C, Popov AA, Zhang W, Liu F, Dunsch L (2009) An endohedral titanium(III) in a clusterfullerene: putting a non-group-III metal nitride into the C_{80}-I_h fullerene cage. Chem Commun 42:6391–6393. https://doi.org/10.1039/b911267g
76. Wei T, Wang S, Lu X, Tan Y, Huang J, Liu F, Li Q, Xie S, Yang S (2016) Entrapping a group-VB transition metal, vanadium, within an endohedral metallofullerene: $V_xSc_{3-x}N@I_h$-C_{80} (x = 1, 2). J Am Chem Soc 138(1):207–214. https://doi.org/10.1021/jacs.5b10115
77. Zhang J, Fuhrer T, Fu W, Ge J, Bearden DW, Dallas J, Duchamp J, Walker K, Champion H, Azurmendi H, Harich K, Dorn HC (2012) Nanoscale fullerene compression of an yttrium carbide cluster. J Am Chem Soc 134(20):8487–8493. https://doi.org/10.1021/ja300134x
78. Feng Y, Wang T, Wu J, Feng L, Xiang J, Ma Y, Zhang Z, Jiang L, Shu C, Wang C (2013) Structural and electronic studies of metal carbide clusterfullerene Sc_2C_2@C_s-C_{72}. Nanoscale 5(15):6704–6707. https://doi.org/10.1039/c3nr01739g
79. Wang Y, Tang Q, Feng L, Chen N (2017) Sc_2C_2@D_{3h}(14246)-C_{74}: a missing piece of the clusterfullerene puzzle. Inorg Chem 56(4):1974–1980. https://doi.org/10.1021/acs.inorgchem.6b02512
80. Kurihara H, Lu X, Iiduka Y, Mizorogi N, Slanina Z, Tsuchiya T, Akasaka T, Nagase S (2011) Sc_2C_2@C_{80} rather than Sc_2@C_{82}: templated formation of unexpected C_{2v}(5)-C_{80} and temperature-dependent dynamic motion of internal Sc_2C_2 cluster. J Am Chem Soc 133(8):2382–2385. https://doi.org/10.1021/ja1107723
81. Liu F, Wei T, Wang S, Guan J, Lu X, Yang S (2014) A bent Tb_2C_2 cluster encaged in a C_s(6)-C_{82} cage: synthesis, isolation and X-ray crystallographic study. Fullerenes Nanotubes Carbon Nanostruct 22(1–3):215–226. https://doi.org/10.1080/1536383x.2013.801839
82. Shen W, Bao L, Hu S, Yang L, Jin P, Xie Y, Akasaka T, Lu X (2019) Crystallographic characterization of Lu_2C_{2n} (2n = 76–90): cluster selection by cage size. Chem Sci 10(3):829–836. https://doi.org/10.1039/c8sc03886d
83. Yang H, Lu C, Liu Z, Jin H, Che Y, Olmstead MM, Balch AL (2008) Detection of a family of gadolinium-containing endohedral fullerenes and the isolation and crystallographic characterization of one member as a metal-carbide encapsulated inside a large fullerene cage. J Am Chem Soc 130(51):17296–17300. https://doi.org/10.1021/ja8078303
84. Slanina Z, Uhlik F, Pan C, Akasaka T, Lu X, Adamowicz L (2018) Computed stabilization for a giant fullerene endohedral: Y_2C_2@C_1(1660)-C_{108}. Chem Phys Lett 710:147–149. https://doi.org/10.1016/j.cplett.2018.08.051
85. Chen C-H, Ghiassi KB, Ceron MR, Guerrero-Ayala MA, Echegoyen L, Olmstead MM, Balch AL (2015) Beyond the butterfly: Sc_2C_2@C_{2v}(9)-C_{86}, an endohedral fullerene containing a planar, twisted Sc_2C_2 unit with remarkable crystalline order in an unprecedented carbon cage. J Am Chem Soc 137(32):10116–10119. https://doi.org/10.1021/jacs.5b06425
86. Chen CH, Abella L, Ceron MR, Guerrero-Ayala MA, Rodriguez-Fortea A, Olmstead MM, Powers XB, Balch AL, Poblet JM, Echegoyen L (2016) Zigzag Sc_2C_2 carbide cluster inside a [88] fullerene cage with one heptagon, Sc_2C_2@Cs(hept)-C_{88}: a kinetically trapped fullerene formed by C_2 insertion? J Am Chem Soc 138(39):13030–13037. https://doi.org/10.1021/jacs.6b07912
87. Iiduka Y, Wakahara T, Nakahodo T, Tsuchiya T, Sakuraba A, Maeda Y, Akasaka T, Yoza K, Horn E, Kato T, Liu MTH, Mizorogi N, Kobayashi K, Nagase S (2005) Structural determination of metallofullerene Sc_3C_{82} revisited: a surprising finding. J Am Chem Soc 127(36):12500–12501. https://doi.org/10.1021/ja054209u
88. Nishibori E, Terauchi I, Sakata M, Takata M, Ito Y, Sugai T, Shinohara H (2006) High-resolution analysis of (Sc_3C_2)@C_{80} metallofullerene by third generation synchrotron radiation

X-ray powder diffraction. J Phys Chem B 110(39):19215–19219. https://doi.org/10.1021/jp061740i
89. Xu W, Wang T-S, Wu J-Y, Ma Y-H, Zheng J-P, Li H, Wang B, Jiang L, Shu C-Y, Wang C-R (2011) Entrapped planar trimetallic carbide in a fullerene cage: synthesis, isolation and spectroscopic studies of $Lu_3C_2@C_{88}$. J Phys Chem C 115(2):402–405. https://doi.org/10.1021/jp1087459
90. Wang T-S, Chen N, Xiang J-F, Li B, Wu J-Y, Xu W, Jiang L, Tan K, Shu C-Y, Lu X, Wang C-R (2009) Russian-doll-type metal carbide endofullerene: synthesis, isolation, and characterization of $Sc_4C_2@C_{80}$. J Am Chem Soc 131(46):16646. https://doi.org/10.1021/ja9077842
91. Svitova AL, Ghiassi KB, Schlesier C, Junghans K, Zhang Y, Olmstead MM, Balch AL, Dunsch L, Popov AA (2014) Endohedral fullerene with μ_3-carbido ligand and titanium-carbon double bond stabilized inside a carbon cage. Nat Commun 5. https://doi.org/10.1038/ncomms4568
92. Junghans K, Ghiassi KB, Samoylova NA, Deng Q, Rosenkranz M, Olmstead MM, Balch AL, Popov AA (2016) Synthesis and isolation of the titanium-scandium endohedral fullerenes-$Sc_2TiC@I_h$-C_{80}, $Sc_2TiC@D_{5h}$-C_{80} and $Sc_2TiC_2@I_h$-C_{80}: metal size tuning of the Ti-IV/Ti-III redox potentials. Chem Eur J 22(37):13098–13107. https://doi.org/10.1002/chem.201601655
93. Yu P, Shen W, Bao L, Pan C, Slanina Z, Lu X (2019) Trapping an unprecedented Ti_3C_3 unit inside the icosahedral C_{80} fullerene: a crystallographic survey. Chem Sci 10(47):10925–10930. https://doi.org/10.1039/c9sc04315b
94. Mercado BQ, Olmstead MM, Beavers CM, Easterling ML, Stevenson S, Mackey MA, Coumbe CE, Phillips JD, Phillips JP, Poblet JM, Balch AL (2010) A seven atom cluster in a carbon cage, the crystallographically determined structure of $Sc_4(\mu_3\text{-}O)_3@I_h$-$C_{80}$. Chem Commun 46(2):279–281. https://doi.org/10.1039/b918731f
95. Valencia R, Rodriguez-Fortea A, Stevenson S, Balch AL, Poblet JM (2009) Electronic structures of scandium oxide endohedral metallofullerenes, $Sc_4(\mu_3\text{-}O)_n@I_h$-$C_{80}$ (n = 2, 3). Inorg Chem 48(13):5957–5961. https://doi.org/10.1021/ic900686a
96. Zhang M, Hao Y, Li X, Feng L, Yang T, Wan Y, Chen N, Slanina Z, Uhlík F, Cong H (2014) Facile synthesis of an extensive family of $Sc_2O@C_{2n}$ (n = 35–47) and chemical insight into the smallest member of $Sc_2O@C_2(7892)$–C_{70}. J Phys Chem C 118(49):28883–28889. https://doi.org/10.1021/jp509975w
97. Liu A, Nie M, Hao Y, Yang Y, Wang T, Slanina Z, Cong H, Feng L, Wang C, Uhlik F (2019) $Ho_2O@C_{74}$: Ho_2O cluster expands within a small non-IPR fullerene cage of $C_2(13333)$-C_{74}. Inorg Chem 58(8):4774–4781. https://doi.org/10.1021/acs.inorgchem.8b03145
98. Cong H, Liu A, Hao Y, Feng L, Slanina Z, Uhlik F (2019) $Ho_2O@C_{84}$: crystallographic evidence showing linear metallic oxide cluster encapsulated in IPR fullerene cage of $D2_d(51591)$-C_{84}. Inorg Chem 58(16):10905–10911. https://doi.org/10.1021/acs.inorgchem.9b01318
99. Yang W, Abella L, Wang Y, Li X, Gu J, Poblet JM, Rodriguez-Fortea A, Chen N (2018) Mixed dimetallic cluster fullerenes: $ScGdO@C3_v(8)$-C_{82} and $ScGdC_2@C_{2v}(9)$-C_{82}. Inorg Chem 57(18):11597–11605. https://doi.org/10.1021/acs.inorgchem.8b01646
100. Chen N, Chaur MN, Moore C, Pinzon JR, Valencia R, Rodriguez-Fortea A, Poblet JM, Echegoyen L (2010) Synthesis of a new endohedral fullerene family, $Sc_2S@C_{2n}$ (n = 40–50) by the introduction of SO_2. Chem Commun 46(26):4818–4820. https://doi.org/10.1039/c0cc00835d
101. Chen N, Beavers CM, Mulet-Gas M, Rodriguez-Fortea A, Munoz EJ, Li Y-Y, Olmstead MM, Balch AL, Poblet JM, Echegoyen L (2012) $Sc_2S@C_s(10528)$-C_{72}: a dimetallic sulfide endohedral fullerene with a non isolated pentagon rule cage. J Am Chem Soc 134(18):7851–7860. https://doi.org/10.1021/ja300765z
102. Yang T, Zhao X, Nagase S (2013) Quantum chemical insight of the dimetallic sulfide endohedral fullerene $Sc_2S@C_{70}$: does it possess the conventional D_{5h} cage? Chem Eur J 19(8):2649–2654. https://doi.org/10.1002/chem.201203388

103. Chen C-H, Krylov DS, Avdoshenko SM, Liu F, Spree L, Yadav R, Alvertis A, Hozoi L, Nenkov K, Kostanyan A, Greber T, Wolter AUB, Popov AA (2017) Selective arc-discharge synthesis of Dy_2S-clusterfullerenes and their isomer-dependent single molecule magnetism. Chem Sci 8(9):6451–6465. https://doi.org/10.1039/c7sc02395b
104. Li F-F, Chen N, Mulet-Gas M, Triana V, Murillo J, Rodriguez-Fortea A, Poblet JM, Echegoyen L (2013) $Ti_2S@D_{3h}(24109)$-C_{78}: a sulfide cluster metallofullerene containing only transition metals inside the cage. Chem Sci 4(9):3404–3410. https://doi.org/10.1039/c3sc51124c
105. Liu F, Gao CL, Deng Q, Zhu X, Kostanyan A, Westerstrom R, Wang S, Tan YZ, Tao J, Xie SY, Popov AA, Greber T, Yang S (2016) Triangular monometallic cyanide cluster entrapped in carbon cage with geometry-dependent molecular magnetism. J Am Chem Soc 138(44):14764–14771. https://doi.org/10.1021/jacs.6b09329
106. Liu F, Wang S, Gao C-L, Deng Q, Zhu X, Kostanyan A, Westerstrom R, Jin F, Xie S-Y, Popov AA, Greber T, Yang S (2017) Mononuclear clusterfullerene single-molecule magnet containing strained fused-pentagons stabilized by a nearly linear metal cyanide cluster. Angew Chem Int Ed 56(7):1830–1834. https://doi.org/10.1002/anie.201611345
107. Feng Y, Wang T, Wu J, Zhang Z, Jiang L, Han H, Wang C (2014) Electron-spin excitation by implanting hydrogen into metallofullerene: the synthesis and spectroscopic characterization of $Sc_4C_2H@I_h$-C_{80}. Chem Commun 50(81):12166–12168. https://doi.org/10.1039/c4cc05783j
108. Wu J, Wang T, Ma Y, Jiang L, Shu C, Wang C (2011) Synthesis, isolation, characterization, and theoretical studies of $Sc_3NC@C_{78}$-C_2. J Phys Chem C 115(48):23755–23759. https://doi.org/10.1021/jp2081929
109. Wang T, Wu J, Feng Y (2014) Scandium carbide/cyanide alloyed cluster inside fullerene cage: synthesis and structural studies of $Sc_3(\mu_3\text{-}C_2)(\mu_3\text{-}CN)@I_h$-$C_{80}$. Dalton Trans 43(43):16270–16274. https://doi.org/10.1039/c4dt01781a
110. Shinohara H (2000) Endohedral metallofullerenes. Rep Prog Phys 63(6):843–892. https://doi.org/10.1088/0034-4885/63/6/201
111. Wang Z, Izumi N, Nakanishi Y, Koyama T, Sugai T, Tange M, Okazaki T, Shinohara H (2016) Near-infrared photoluminescence properties of endohedral mono- and dithulium metallofullerenes. ACS Nano 10(4):4282–4287. https://doi.org/10.1021/acsnano.5b07780
112. Sado Y, Aoyagi S, Izumi N, Kitaura R, Kowalczyk T, Wang J, Irle S, Nishibori E, Sugimoto K, Shinohara H (2014) Structure of Tm_2 and Tm_2C_2 encapsulated in low-symmetry $C_{82}(C_s(6))$ fullerene cage by single crystal X-ray diffraction. Chem Phys Lett 600:38–42. https://doi.org/10.1016/j.cplett.2014.03.047
113. Krause M, Dunsch L (2004) Isolation and characterisation of two $Sc_3N@C_{80}$ isomers. ChemPhysChem 5(9):1445–1449. https://doi.org/10.1002/cphc.200400085
114. Wei T, Liu F, Wang S, Zhu X, Popov AA, Yang S (2015) An expanded family of dysprosium-scandium mixed-metal nitride clusterfullerenes: the role of the lanthanide metal on the carbon cage size distribution. Chemistry 21(15):5750–5759. https://doi.org/10.1002/chem.201406265
115. Yang SF, Dunsch L (2005) A large family of dysprosium-based trimetallic nitride endohedral fullerenes: $Dy_3N@C_{2n}$ ($39 <= n <= 44$). J Phys Chem B 109(25):12320–12328. https://doi.org/10.1021/jp051597d
116. Yang S, Popov AA, Dunsch L (2008) Large mixed metal nitride clusters encapsulated in a small cage: the confinement of the C_{68}-based clusterfullerenes. Chem Commun 25:2885–2887. https://doi.org/10.1039/b803200a
117. Yang S, Popov AA, Chen C, Dunsch L (2009) Mixed metal nitride clusterfullerenes in cage isomers: $Lu_xSc_{3-x}N@C_{80}$ ($x = 1, 2$) as compared with $M_xSc_{3-x}N@C_{80}$ (M = Er, Dy, Gd, Nd). J Phys Chem C 113(18):7616–7623. https://doi.org/10.1021/jp9005263
118. Cao BP, Hasegawa M, Okada K, Tomiyama T, Okazaki T, Suenaga K, Shinohara H (2001) EELS and C^{13} NMR characterization of pure $Ti_2@C_{80}$ metallofullerene. J Am Chem Soc 123(39):9679–9680. https://doi.org/10.1021/ja016484w

119. Hu S, Liu T, Shen W, Slanina Z, Akasaka T, Xie Y, Uhlik F, Huang W, Lu X (2019) Isolation and structural characterization of Er@C_{2v}(9)-C_{82} and Er@C_s(6)-C_{82}: regioselective dimerization of a pristine endohedral metallofullerene induced by cage symmetry. Inorg Chem 58(3): 2177–2182. https://doi.org/10.1021/acs.inorgchem.8b03313
120. Zhang Y, Xu J, Hao C, Shi Z, Gu Z (2006) Synthesis, isolation, spectroscopic and electrochemical characterization of some calcium-containing metallofullerenes. Carbon 44(3):475–479. https://doi.org/10.1016/j.carbon.2005.08.018
121. Liu J, Shi Z, Gu Z (2009) The cage and metal effect: spectroscopy and electrochemical survey of a series of Sm-containing high metallofullerenes. Chemistry 4(11):1703–1711. https://doi.org/10.1002/asia.200900234
122. Xu J, Li M, Shi Z, Gu Z (2005) Electrochemical survey: the effect of the cage size and structure on the electronic structures of a series of ytterbium metallofullerenes. Chemistry 12(2):562–567. https://doi.org/10.1002/chem.200500210
123. Lu X, Slanina Z, Akasaka T, Tsuchiya T, Mizorogi N, Nagase S (2010) Yb@C_{2n} (n = 40, 41, 42): new fullerene allotropes with unexplored electrochemical properties. J Am Chem Soc 132(16):5896–5905. https://doi.org/10.1021/ja101131e
124. Bao L, Chen M, Pan C, Yamaguchi T, Kato T, Olmstead MM, Balch AL, Akasaka T, Lu X (2016) Crystallographic evidence for direct metal-metal bonding in a stable open-shell La2@Ih-C80 derivative. Angew Chem Int Ed Engl 55(13):4242–4246. https://doi.org/10.1002/anie.201511930
125. Pan C, Shen W, Yang L, Bao L, Wei Z, Jin P, Fang H, Xie Y, Akasaka T, Lu X (2019) Crystallographic characterization of Y_2C_{2n} (2n = 82, 88–94): direct Y–Y bonding and cage-dependent cluster evolution. Chem Sci 10(17):4707–4713. https://doi.org/10.1039/c9sc00941h
126. Plonska-Brzezinska ME, Athans AJ, Paige Phillips J, Stevenson S, Echegoyen L (2008) A reinvestigation of the electrochemical behavior of $Sc_3N@C_{80}$. J Electroanal Chem 614(1–2):171–174. https://doi.org/10.1016/j.jelechem.2007.11.013
127. Popov AA, Dunsch L (2008) Hindered cluster rotation and ^{45}Sc hyperfine splitting constant in distonoid anion radical $SC_3N@C_{80}^{(-)}$, and spatial spin-charge separation as a general principle for anions of endohedral fullerenes with metal-localized lowest unoccupied molecular orbitals. J Am Chem Soc 130(52):17726–17742. https://doi.org/10.1021/ja804226a
128. Jakes P, Dinse KP (2001) Chemically induced spin transfer to an encased molecular cluster: an EPR study of $Sc_3N@C_{80}$ radical anions. J Am Chem Soc 123(36):8854–8855. https://doi.org/10.1021/ja016047h
129. Yang S, Zalibera M, Rapta P, Dunsch L (2006) Charge-induced reversible rearrangement of endohedral fullerenes: electrochemistry of tridysprosium nitride clusterfullerenes $Dy_3N@C_{2n}$ (2n = 78, 80). Chemistry 12(30):7848–7855. https://doi.org/10.1002/chem.200501578
130. Valencia R, Rodriguez-Fortea A, Clotet A, de Graaf C, Chaur MN, Echegoyen L, Poblet JM (2009) Electronic structure and redox properties of metal nitride endohedral fullerenes $M_3N@C_{2n}$ (M = Sc, Y, La, and Gd; 2n = 80, 84, 88, 92, 96). Chemistry 15(41):10997–11009. https://doi.org/10.1002/chem.200900728
131. Duchamp JC, Demortier A, Fletcher KR, Dorn D, Iezzi EB, Glass T, Dorn HC (2003) An isomer of the endohedral metallofullerene $Sc_3N@C_{80}$ with D_{5h} symmetry. Chem Phys Lett 375(5–6):655–659. https://doi.org/10.1016/s0009-2614(03)00844-3
132. Elliott B, Yu L, Echegoyen L (2005) A simple isomeric separation of D_{5h} and I_h $Sc_3N@C_{80}$ by selective chemical oxidation. J Am Chem Soc 127(31):10885–10888. https://doi.org/10.1021/ja052446r
133. Hu S, Zhao P, Shen W, Yu P, Huang W, Ehara M, Xie Y, Akasaka T, Lu X (2019) Crystallographic characterization of $Er_3N@C_{2n}$ (2n = 80, 82, 84, 88): the importance of a planar Er_3N cluster. Nanoscale 11(28):13415–13422. https://doi.org/10.1039/c9nr04330f
134. Shen WQ, Bao LP, Hu SF, Gao XJ, Xie YP, Gao XF, Huang WH, Lu X (2018) Isolation and crystallographic characterization of $Lu_3N@C_{2n}$ (2n = 80–88): cage selection by cluster size. Chemistry 24(62):16692–16698. https://doi.org/10.1002/chem.201804651

135. Zhang Y, Schiemenz S, Popov AA, Dunsch L (2013) Strain-driven endohedral redox couple Ce-IV/Ce-III in nitride clusterfullerenes $CeM_2N@C_{80}$ (M = Sc, Y, Lu). J Phys Chem Lett 4(15):2404–2409. https://doi.org/10.1021/jz4009773
136. Chen C, Liu F, Li S, Wang N, Popov AA, Jiao M, Wei T, Li Q, Dunsch L, Yang S (2012) Titanium/yttrium mixed metal nitride clusterfullerene $TiY_2N@C_{80}$: synthesis, isolation, and effect of the group-III metal. Inorg Chem 51(5):3039–3045. https://doi.org/10.1021/ic202354u
137. Iiduka Y, Wakahara T, Nakajima K, Nakahodo T, Tsuchiya T, Maeda Y, Akasaka T, Yoza K, Liu MT, Mizorogi N, Nagase S (2007) Experimental and theoretical studies of the scandium carbide endohedral metallofullerene $Sc_2C_2@C_{82}$ and its carbene derivative. Angew Chem Int Ed Engl 46(29):5562–5564. https://doi.org/10.1002/anie.200701049
138. Lu X, Nakajima K, Iiduka Y, Nikawa H, Tsuchiya T, Mizorogi N, Slanina Z, Nagase S, Akasaka T (2012) The long-believed $Sc_2@C_{2v}(17)$-C_{84} is actually $Sc_2C_2@C_{2v}(9)$-C_{82}: unambiguous structure assignment and chemical functionalization. Angew Chem Int Ed Engl 51(24):5889–5892. https://doi.org/10.1002/anie.201201325
139. Hu S, Shen W, Zhao P, Xu T, Slanina Z, Ehara M, Zhao X, Xie Y, Akasaka T, Lu X (2019) Crystallographic characterization of $Er_2C_2@C_2(43)$-C_{90}, $Er_2C_2@C_2(40)$-C_{90}, $Er_2C_2@C_2(44)$-C_{90}, and $Er_2C_2@C_1(21)$-C_{90}: the role of cage-shape on cluster configuration. Nanoscale 11(37):17319–17326. https://doi.org/10.1039/c9nr06466d
140. Tang Q, Abella L, Hao Y, Li X, Wang Y, Rodriguez-Fortea A, Poblet JM, Feng L, Chen N (2016) $Sc_2O@C_{3v}(8)$-C_{82}: a missing isomer of $Sc_2O@C_{82}$. Inorg Chem 55(4):1926–1933. https://doi.org/10.1021/acs.inorgchem.5b02901
141. Liu F, Wang S, Gao CL, Deng Q, Zhu X, Kostanyan A, Westerstrom R, Jin F, Xie SY, Popov AA, Greber T, Yang S (2017) Mononuclear clusterfullerene single-molecule magnet containing strained fused-pentagons stabilized by a nearly linear metal cyanide cluster. Angew Chem Int Ed Engl 56(7):1830–1834. https://doi.org/10.1002/anie.201611345
142. Liu F, Wang S, Guan J, Wei T, Zeng M, Yang S (2014) Putting a terbium-monometallic cyanide cluster into the C_{82} fullerene cage: $TbCN@C_2(5)$-C_{82}. Inorg Chem 53(10):5201–5205. https://doi.org/10.1021/ic500353k
143. Ding XY, Alford JM, Wright JC (1997) Lanthanide fluorescence from Er^{3+} in $Er_2@C_{82}$. Chem Phys Lett 269(1–2):72–78. https://doi.org/10.1016/s0009-2614(97)00261-3
144. Ito Y, Okazaki T, Okubo S, Akachi M, Ohno Y, Mizutani T, Nakamura T, Kitaura R, Sugai T, Shinohara H (2007) Enhanced 1520 nm photoluminescence from Er^{3+} ions in di-erbium-carbide metallofullerenes $(Er_2C_2)@C_{82}$ (isomers I, II, and III). ACS Nano 1(5):456–462
145. Macfarlane RM, Bethune DS, Stevenson S, Dorn HC (2001) Fluorescence spectroscopy and emission lifetimes of Er^{3+} in $Er_xSc_{3-x}N@C_{80}$ (x = 1–3). Chem Phys Lett 343(3–4):229–234. https://doi.org/10.1016/s0009-2614(01)00701-1
146. Gu G, Huang HJ, Yang SH, Yu P, Fu JS, Wong GK, Wan XG, Dong JM, Du YW (1998) The third-order non-linear optical response of the endohedral metallofullerene $Dy@C_{82}$. Chem Phys Lett 289(1–2):167–173. https://doi.org/10.1016/s0009-2614(98)00381-9
147. Xenogiannopoulou E, Couris S, Koudoumas E, Tagmatarchis N, Inoue T, Shinohara H (2004) Nonlinear optical response of some isomerically pure higher fullerenes and their corresponding endohedral metallofullerene derivatives: C_{82}–C_{2v}, $Dy@C_{82}$ (I), $Dy_2@C_{82}$ (I), C_{92}–C_2 and $Er_2@C_{92}$ (IV). Chem Phys Lett 394(1–3):14–18. https://doi.org/10.1016/j.cplett.2004.06.093
148. Jiang Y, Wang D, Xu D, Zhang J, Wang Z (2018) Dimerization of metallofullerenes to obtain materials with enhanced nonlinear optical properties. ChemPhysChem 19(22):2995–3000. https://doi.org/10.1002/cphc.201800797
149. Westerstroem R, Dreiser J, Piamonteze C, Muntwiler M, Weyeneth S, Kraemer K, Liu S-X, Decurtins S, Popov A, Yang S, Dunsch L, Greber T (2014) Tunneling, remanence, and frustration in dysprosium-based endohedral single-molecule magnets. Phys Rev B 89(6). https://doi.org/10.1103/PhysRevB.89.060406

150. Kato T, Suzuki S, Kikuchi K, Achiba Y (1993) ESR study of the electronic-structures of metallofullerenes – a comparison between La@C_{82} and Sc@C_{82}. J Phys Chem 97(51):13425–13428. https://doi.org/10.1021/j100153a001
151. Huang HJ, Yang SH, Zhang XX (2000) Magnetic properties of heavy rare-earth metallofullerenes M@C_{82} (M = Gd, Tb, Dy, Ho, and Er). J Phys Chem B 104(7):1473–1482. https://doi.org/10.1021/jp9933166
152. Wolf M, Muller KH, Skourski Y, Eckert D, Georgi P, Krause M, Dunsch L (2005) Magnetic moments of the endohedral cluster fullerenes Ho_3N@C_{80} and Tb_3N@C_{80}: the role of ligand fields. Angew Chem Int Ed 44(21):3306–3309. https://doi.org/10.1002/anie.200461500
153. Smirnova TI, Smirnov AI, Chadwick TG, Walker KL (2008) Characterization of magnetic and electronic properties of trimetallic nitride endohedral fullerenes by SQUID magnetometry and electron paramagnetic resonance. Chem Phys Lett 453(4–6):233–237. https://doi.org/10.1016/j.cplett.2008.01.036
154. Zuo T, Olmstead MM, Beavers CM, Balch AL, Wang G, Yee GT, Shu C, Xu L, Elliott B, Echegoyen L, Duchamp JC, Dorn HC (2008) Preparation and structural characterization of the I_h and the D_{5h} isomers of the endohedral fullerenes Tm_3N@C_{80}: icosahedral C_{80} cage encapsulation of a trimetallic nitride magnetic cluster with three uncoupled Tm^{3+} ions. Inorg Chem 47(12):5234–5244. https://doi.org/10.1021/ic800227x
155. Chen L, Carpenter EE, Hellberg CS, Dorn HC, Shultz M, Wernsdorfer W, Chiorescu I (2011) Spin transition in Gd_3N@C_{80}, detected by low-temperature on-chip SQUID technique. J Appl Phys 109(7). https://doi.org/10.1063/1.3536514
156. Ishikawa N, Sugita M, Ishikawa T, Koshihara S, Kaizu Y (2004) Mononuclear lanthanide complexes with a long magnetization relaxation time at high temperatures: a new category of magnets at the single-molecular level. J Phys Chem B 108(31):11265–11271. https://doi.org/10.1021/jp0376065
157. Liu F, Krylov DS, Spree L, Avdoshenko SM, Samoylova NA, Rosenkranz M, Kostanyan A, Greber T, Wolter AUB, Buechner B, Popov AA (2017) Single molecule magnet with an unpaired electron trapped between two lanthanide ions inside a fullerene. Nat Commun 8. https://doi.org/10.1038/ncomms16098

Chemical Reactions of Endohedral Metallofullerenes

19

Yajing Hu and Fang-Fang Li

Contents

Abstract

Fullerene encapsulating a metal, La@C_{82}, was discovered in 1985, which introduced a new era in the field of endohedral metallofullerenes (EMFs). Thereafter, EMFs have attracted significant research attention. EMFs exhibit different physical and chemical properties compared to the empty fullerenes owing to their unique properties, including transferring electrons from the encapsulated metal or metal cluster to the fullerene cages. EMF derivatives have shown promising applications in solar cells, energy storage and conversion, materials science, biomedicine, and biochemistry. Therefore, the exohedral chemical functionalization of EMFs is crucial for the development of novel metallofullerene materials. The Bingel–Hirsch reaction, [2 + 2] cycloaddition reaction, [2 + 3] cycloaddition reaction, Diels–Alder reaction, carbene reaction, radical recombination reaction, metal complexation reaction, and the electrochemical reaction

Y. Hu · F.-F. Li (✉)
State Key Laboratory of Materials Processing and Die and Mould Technology, School of Materials Science and Engineering, Huazhong University of Science and Technology, Wuhan, People's Republic of China
e-mail: ffli@hust.edu.cn

X. Lu et al. (eds.), *Handbook of Fullerene Science and Technology*,
https://doi.org/10.1007/978-981-16-8994-9_28

have been successfully applied for the functionalization of EMFs, thereby affording many new structures with enhanced properties and promising applications. In this chapter, chemical reactions of EMFs, including classical EMFs and clusterfullerenes, are summarized.

Keywords

Endohedral metallofullerenes · Chemical functionalization · Bingel-Hirsch reactions · [2+2] cycloaddition reactions · [2+3] cycloaddition reactions · Diels-Alder reactions · Carbene reactions · Radical recombination reactions · Metal complexation reactions · Electrochemical reactions

Introduction

The chemical functionalization of pristine endohedral metallofullerenes (EMFs) has provided many materials with enhanced physicochemical properties such as solubility, electron transport ability, thermal and photostability, redox characteristics, and electronic configurations [1–12]. New electrochemical interactions can be accomplished by coupling the electronic properties of the EMF and addend (in single and multiple additions). The change in redox chemistry can be attributed to the overall variation in the electronic configuration of the cage, resulting from changes in the sp^2 to sp^3 hybridization of the bonded carbons and the loss of symmetry caused by derivatization.

Similarly, functionalizing the EMF cage adds a new dimension to the control of electronic and other properties that facilitate several potential applications, such as biomedicine and organic photovoltaics. The water-soluble hydroxylated Gd@C_{82} derivatives, such as Gd@$C_{82}(OH)_{40}$ [13], Gd@$C_{82}(OH)_{22}$ [14], Gd@$C_{82}O_6(OH)_{16}(NHC_2H_4CO_2H)_8$ [15], Gd@$C_{82}O_6(OH)_{16}(NHCH_2CH_2COOH)_8$ [16], and Gd@$C_{82}O_2(OH)_{16}(C(PO_3Et_2)_2)_{10}$ [17], could serve as magnetic resonance imaging contrast agents. Ho_x@$C_{82}(OH)_y$ was found to be a good radiotracer and therapeutic radiopharmaceutical, which could be a useful component in drug design [18]. The radiolabeled Lu-chelated ^{177}Lu-DOTA-f-Gd_3N@C_{80} was used for effective brachytherapy [19, 20]. For applications in organic photovoltaics, Lu_3N@C_{80}-PCBH was used as an acceptor material in polymeric solar cells [21]. Similarly, the donor–acceptor dyads based on EMFs, such as the Sc_3N@I_h-C_{80}-ferrocene dyad [22], Sc_3N@I_h-C_{80}-TPA dyads [23], Sc_3N@I_h-C_{80}-ZnP dyads [24], La_2@I_h-C_{80}-exTTF [25], and Ce_2@I_h-C_{80}-ZnP [26], are promising materials in organic photovoltaic cells. Therefore, synthesizing a variety of EMF derivatives for future applications is crucial. Ever since the first functionalized EMF, i.e., La@$C_{82}(Mes_2Si)_2CH_2$ [27], was reported, myriad types of reactions have been developed for EMFs, such as the Bingel–Hirsch reaction, [2 + 2] cycloaddition reaction, [2 + 3] cycloaddition reaction, Diels–Alder reaction, carbene reaction, radical recombination reaction, metal complexation reaction, and electrochemical reaction (Scheme 1).

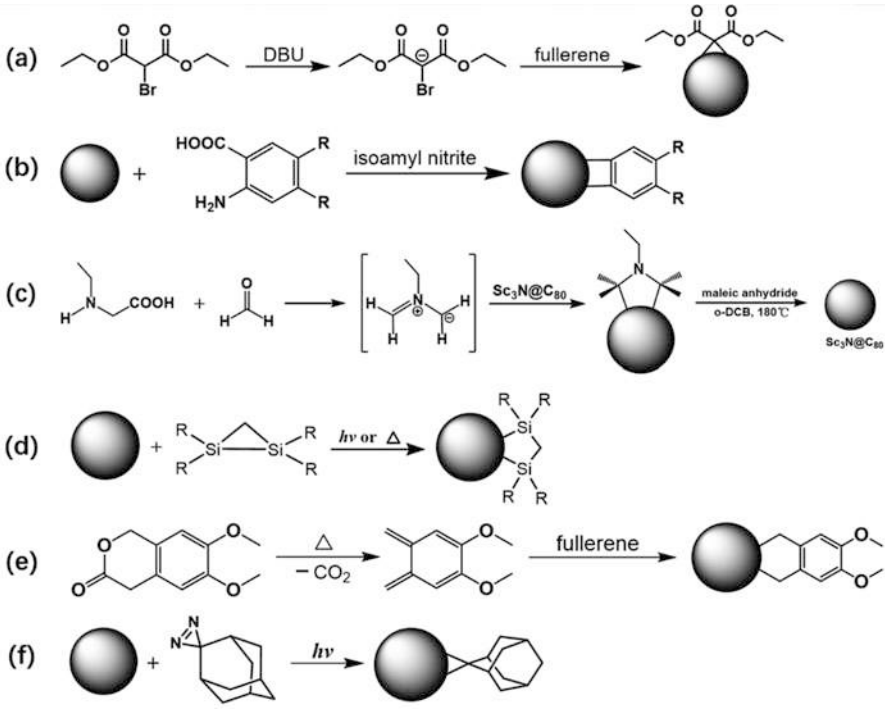

Scheme 1 Several reaction types of EMFs: (**a**) Bingel–Hirsch reaction; (**b**) [2 + 2] cycloaddition reaction; (**c**) Prato reaction of $Sc_3N@I_h$-C_{80} and the corresponding retro-cycloaddition of N-ethylpyrrolidino-$Sc_3N@I_h$-C_{80}; (**d**) Disilirane addition reaction; (**e**) Diels–Alder reaction; and (**f**) carbene reaction

Bingel–Hirsch Reaction

In 2005, the first Bingel monoadduct of $Y_3N@I_h$-C_{80} was synthesized by Echegoyen et al. under conventional Bingel–Hirsch reaction conditions (Scheme 1a), i.e., reacting the fullerene with excess diethyl bromomalonate in the presence of trace 1,8-diazobicyclo-[5.4.0]under-7-ene (DBU) at room temperature. The NMR results of the product suggested a [6,6]-symmetric addition pattern [28]. Thereafter, the same group synthesized another methanofulleroid adduct of $Y_3N@C_{80}$, namely $Y_3N@C_{80}$-$C(CO_2CH_2Ph)_2$, under the same conditions and successfully obtained its crystal structure (Fig. 1a), which showed [6,6]-open-cage structure with one of the inner metal ions located adjacent to the site of addition [29]. However, $Sc_3N@I_h$-C_{80}, the most abundant species of the EMFs, showed no reactivity toward Bingel–Hirsch reaction under the same conditions, similar to $Lu_3N@I_h$-C_{80} [28, 30]. In 2010, Echegoyen et al. found that when dimethylformamide (DMF) was mixed with *o*-dichlorobenzene (*o*-DCB), the Bingel–Hirsch reaction of $M_3N@I_h$-C_{80} (M = Sc, Lu) occurred, and the methano-bridged monoadducts were successfully synthesized.

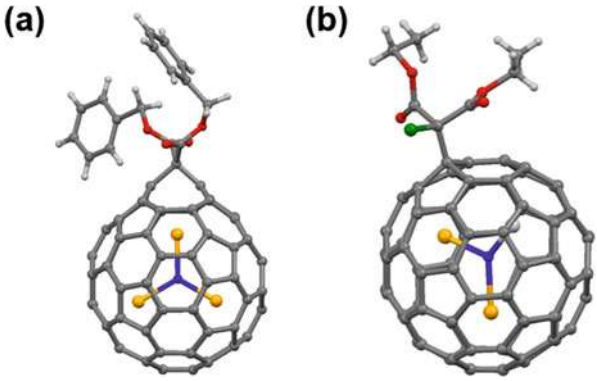

Fig. 1 Single-crystal structures of (**a**) $Y_3N@C_{80}$-C$(CO_2CH_2Ph)_2$ and (**b**) $TiY_2N@I_h$-$C_{80}C(CO_2C_2H_5)_2Br$

According to the theoretical calculations, the presence of polar solvent DMF can lower the transition state energy of the Bingel–Hirsch reaction route [31].

Unlike diamagnetic $Sc_3N@I_h$-C_{80}, when paramagnetic $TiSc_2N@I_h$-C_{80} underwent the Bingel–Hirsch reaction, two isomeric monoadducts were obtained, and the bromomalonate group was considered to attach onto the cage via a C–C single bond according to the NMR and ESR results. The paramagnetic property of the pristine $TiSc_2N@I_h$-C_{80} disappeared upon the addition of the bromomalonate group [32]. This singly bonded addition pattern was confirmed by another Bingel–Hirsch reaction of $TiY_2N@I_h$-C_{80}; the product was successfully crystallized and examined by single-crystal X-ray crystallography, which verified a singly bonded monoadduct (Fig. 1b) with an addition pattern dramatically different from the cyclopropane adducts of $Y_3N@I_h$-C_{80}, demonstrating the influences of endohedral metal species on reactivity and addition pattern of trimetallic nitride clusterfullerenes (NCFs) [33]. The isomeric $Sc_3N@D_{5h}$-C_{80} had more nonequivalent bonds than the I_h isomer, and the Bingel–Hirsch reaction of $Sc_3N@D_{5h}$-C_{80} led to three different monoadduct isomers, with the major product as an unsymmetric [6,6]-open adduct [34].

Monometallic fullerenes generally have open-shell structures, which exhibit high reactivities toward the Bingel–Hirsch reaction. Akasaka et al. conducted the Bingel–Hirsch reaction on the open-shell $La@C_{82}$ [35], and four ESR-inactive regioisomers of singly bonded monoadduct and one ESR-active cycloadduct were obtained. Fig. 2a shows the crystal structure of one Bingel adduct of $La@C_{82}$, the malonate group of which was singly bonded to the cage at the [5,6,6]-ring junction. Notably, the singly bonded monoadducts of EMFs showed higher thermal stability and effective electrochemical reversibility compared to the corresponding cycloadducts, which may undergo the retro-Bingel reaction during electron transfer on the cyclic voltammetric timescale [36]. In addition, when the Bingel–Hirsch reaction of $La@C_{82}$ was conducted at 60 °C, one bisadduct $La@C_{82}[CH(COOC_2H_5)_2]_2$ was formed, which tended to crystallize to a dimer at 90 K, see Fig. 2b [37].

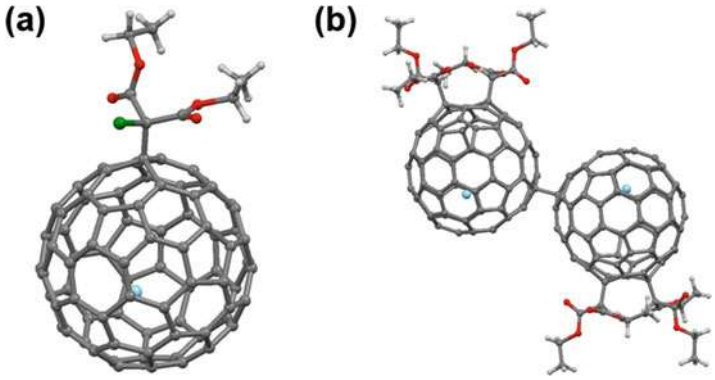

Fig. 2 Single-crystal structures of (**a**) $La@C_{82}C(CO_2C_2H_5)_2Br$ and (**b**) $La@C_{82}[CH(COOC_2H_5)_2]_2$ dimer

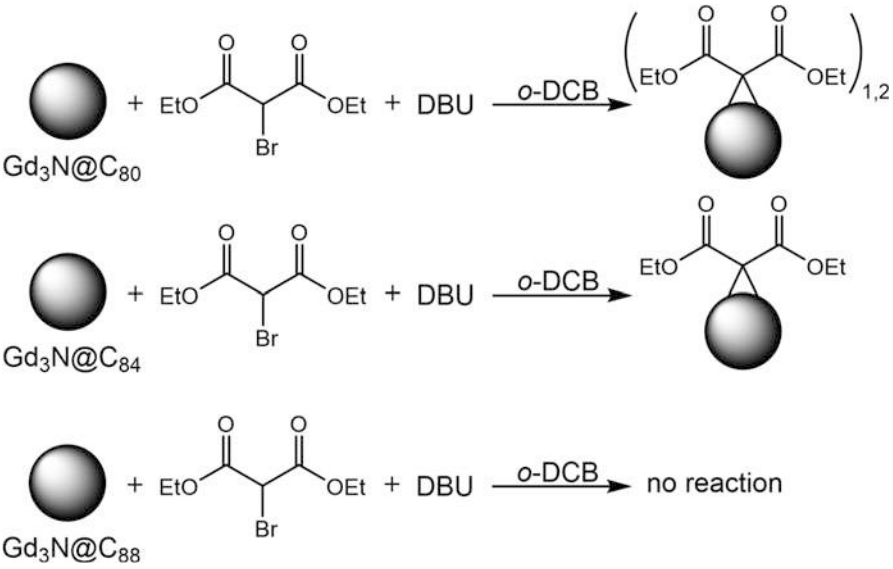

Scheme 2 Bingel–Hirsch reaction of $Gd_3N@C_{2n}$ ($n = 40$, 42, and 44)

The impact of cage size on the Bingel–Hirsch reaction of EMFs was studied by performing the reaction on three $Gd_3N@C_{2n}$ species ($2n = 80$, 84, and 88) (Scheme 2). The results demonstrated that the reactivity decreased when the size of fullerene cages increased, since the larger cage resulted in a lower degree of pyramidalization [38]. In contrast, fullerenes with a smaller cage, such as $Sc_3N@C_{68}$, exhibited higher reactivity toward the Bingel reaction and yielded one [6,6]-open monoadduct and a mixture of multiadducts [39]. The Bingel–Hirsch reaction of $Sc_3N@C_{78}$ was investigated as well, and one monoadduct and one symmetric bis(ethyl malonate) adduct were separated; the

malonate groups were considered to add onto the cage in the [6,6]-closed addition pattern (Fig. 3) [40].

Previous studies have shown that the low reactivity of $Sc_3N@I_h$-C_{80} toward the Bingel–Hirsch reaction was because of the weak electrophilicity of its cage. The introduction of a positive charge on $M_3N@I_h$-C_{80} (M = Sc or Lu) is expected to increase the electron affinity of the cages, and the resulting cations should be more reactive toward nucleophiles than the neutral species. As a proof of concept, Li et al. synthesized the $Sc_3N@I_h$-C_{80} monocation through both chemical and electrochemical methods. Subsequently, the Bingel–Hirsch reaction of cationic $Sc_3N@I_h$-C_{80} was performed under conventional conditions. As anticipated, the $Sc_3N@I_h$-C_{80} cation demonstrated high reactivity toward the bromomalonate anion. Unexpectedly, a [5,6]-open Bingel adduct of $Sc_3N@I_h$-C_{80} was obtained for the first time, along with the normal [6,6]-adduct (Fig. 4) [41]. The cations of EMFs are much easier to be obtained than those of empty fullerenes, as can be seen from their cyclic voltammograms. This advantage provides further opportunity for the development of EMF cation reactions.

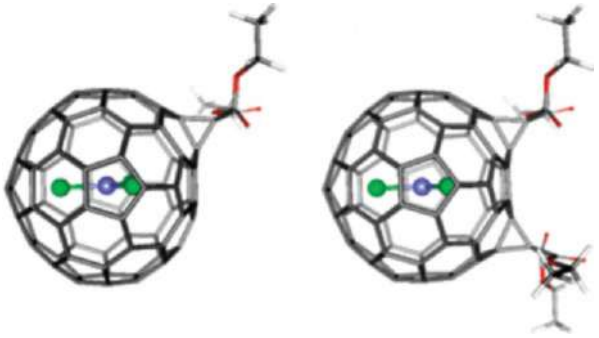

Fig. 3 Optimized structures of Bingel products of $Sc_3N@C_{78}$. (Reproduced with permission from Ref. [40]. Copyright 2008 American Chemical Society)

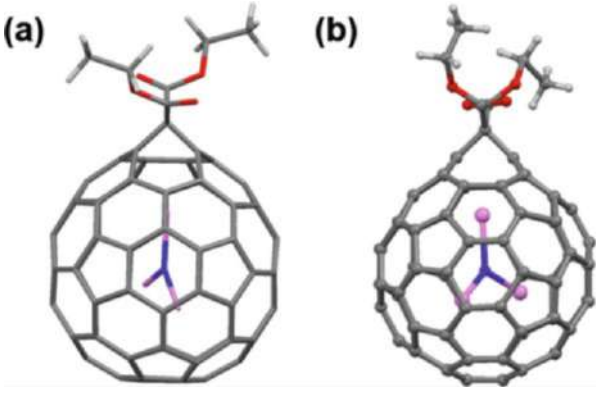

Fig. 4 (**a**) Optimized structure of the [5,6]-open Bingel monoadduct of $Sc_3N@I_h$-C_{80} and (**b**) single-crystal structure of [6,6]-open Bingel monoadduct of $Sc_3N@I_h$-C_{80}

The Bingel–Hirsch reaction mechanism for neutral fullerenes has been well established (Scheme 3). The reaction was initiated by the nucleophilic addition of deprotonated bromomalonate anion to the fullerene cage [34, 42]. However, the Bingel–Hirsch reaction mechanism of $[Sc_3N@I_h\text{-}C_{80}]^+$ was different, as proposed by Li et al. [41] As shown in Scheme 4, the neutral $Sc_3N@I_h\text{-}C_{80}$ was first oxidized to the radical monocation, which can be readily attacked by a diethyl bromomalonate anion to form a radical intermediate. Notably, an additional diethyl bromomalonate

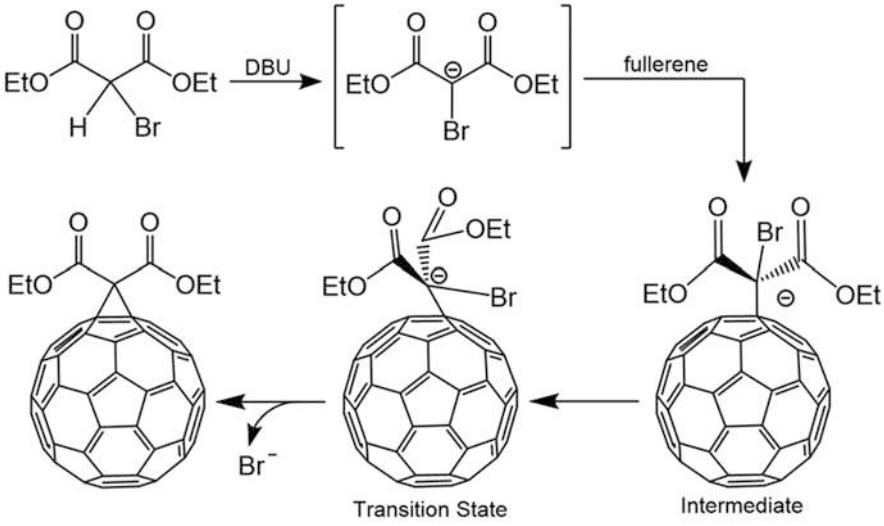

Scheme 3 General mechanism of the Bingel–Hirsch reaction of neutral fullerenes

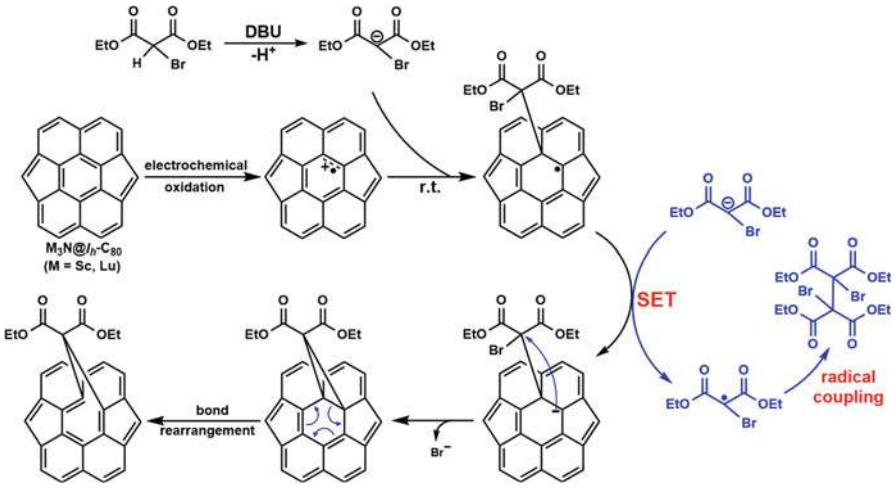

Scheme 4 Bingel–Hirsch reaction Mechanism of cationic $Sc_3N@I_h\text{-}C_{80}$

anion then acted as an organic electron donor to the cage of radical intermediate, i.e., a SET process. Once the radical was reduced to the anion intermediate by electron transfer, the reaction proceeded as a conventional Bingel–Hirsch reaction.

Benzyne Addition Reaction ([2 + 2] Cycloaddition Reaction)

The most representative [2 + 2] cycloaddition reaction of fullerenes is the benzyne addition (Scheme 1b). The first example of the benzyne addition of EMFs was reported in 2004 by Lu et al. An open-shell Gd@C_{82} was reacted with benzyne in situ generated by the reaction of isoamyl nitrite with anthranilic acid, and two isomeric monoadducts Gd@C_{82}(C_6H_4) were formed [43]. Similarly, the open-shell La@C_{82} was adopted to undergo the same reaction. Unexpectedly, a series of La@C_{82}(C_6H_4)$_n$$NO_2$ (n = 1–10) was synthesized, the –NO_2 group of which was singly bonded to the cage, whereas the –C_6H_4 groups were attached in a cycloaddition way. The tris-adduct La@C_{82}(C_6H_4)$_2$$NO_2$ was successfully crystallized (Fig. 5a), showing that the –NO_2 group was singly bonded to the [5,6,6]-ring junction, and the two –C_6H_4 groups were cyclically added to [5,6]-ring fusions of the cage. The paramagnetic character of pristine La@C_{82} was quenched due to the single addition of the –NO_2 group [44].

In 2011, the benzyne addition reaction was applied to the trimetallic nitride template endohedral metallofullerene (TNT–EMF), $Sc_3N@I_h$-C_{80}, and two thermally stable [5,6]- and [6,6]-monoadducts were successfully obtained (Fig. 5b, c). Interestingly, both [5,6]- and [6,6]-monoadducts exhibited electrochemically reversible cathodic behavior. To the best of our knowledge, this was the first report on the electrochemically reversible behavior of a [6,6]-derivative of $Sc_3N@I_h$-C_{80} [45]. In the same year, Wang et al. reported the [2 + 2] cycloaddition reaction of $Sc_3N@I_h$-C_{80} under inert gas and open-air conditions. Both [5,6]- and [6,6]-benzyne monoadducts were synthesized under inert gas protection. An unusual open-cage adduct, $Sc_3N@I_h$-C_{80}(C_6H_2)(OC_3H_6)$_2$O, was formed along with the benzyne monoadducts in air under otherwise identical conditions (Fig. 5d). This open-cage adduct was generated from further oxygenation of the [5,6]-adduct [46].

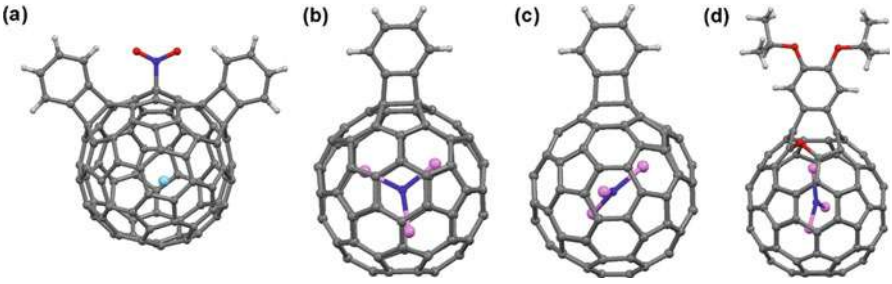

Fig. 5 Single-crystal structures of (**a**) La@C_{82}(C_6H_4)$_2$$NO_2$, (**b**, **c**) [5,6]- and [6,6]-benzyne monoadducts of $Sc_3N@I_h$-C_{80} and (**d**) $Sc_3N@I_h$-C_{80}(C_6H_2)(OC_3H_6)$_2$O

[2 + 3] Cycloaddition Reaction

The most representative [2 + 3] cycloaddition reaction of fullerenes is the Prato reaction, which gives rise to the corresponding pyrrolidino-ring-fused derivatives (Scheme 1c). The first Prato reaction of $Sc_3N@I_h$-C_{80} with azomethine ylides was reported in 2005 [47, 48], yielding a [5,6]-pyrrolidino monoadduct. However, N-ethylpyrrplidino-$Sc_3N@C_{80}$ underwent the retro-cycloaddition reaction to form the parent NCF under high-temperature reflux in the presence of maleic anhydride (Scheme 1c) [49]. Unexpectedly, when the same reaction was applied to $Y_3N@I_h$-C_{80} and $Er_3N@I_h$-C_{80} with larger inner trimetallic nitride clusters than $Sc_3N@I_h$-C_{80}, the [6,6]-N-triphenylmethyl pyrrolidine monoadducts, instead of [5,6]-isomers, were produced. However, the kinetically preferred [6,6]-product underwent an isomerization progress under thermal conditions to form the more thermodynamically stable [5,6]-isomer (Scheme 5) [28, 50].

A larger charge transfer to the cage and larger size of the TNT cluster (Y>Sc) appeared to stabilize the [6,6]-regioisomer. The Prato reaction of $Sc_xGd_{3-x}N@I_h$-C_{80} (x = 0–3) was investigated by reacting with N-ethylglycine and formaldehyde [51]. It was found that the [5,6]-adduct was favored for the smallest cluster, (Sc_3N)-based NCF, the [6,6]-adduct was dominant for the largest cluster, (Gd_3N)-based NCF,

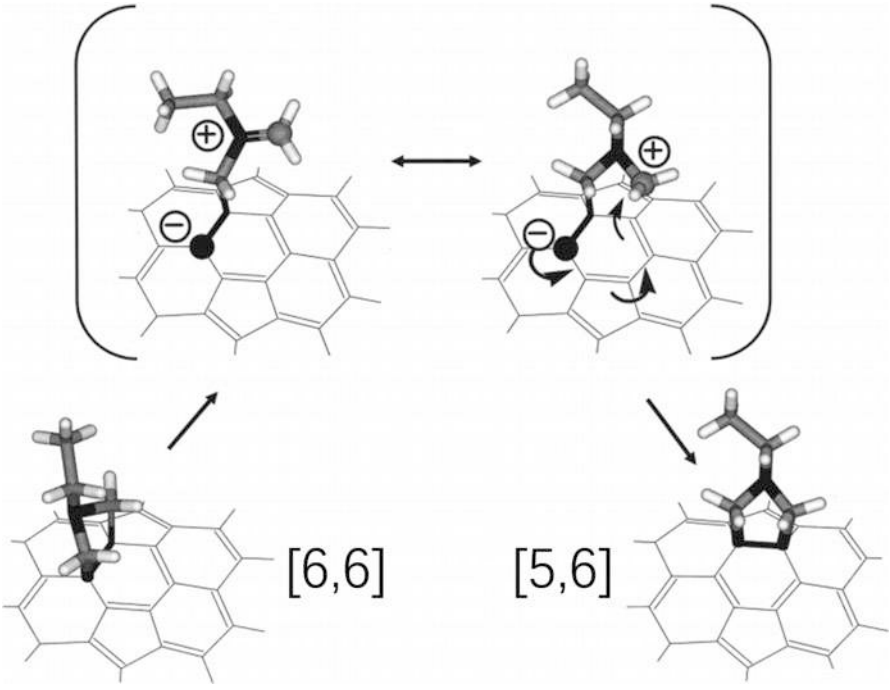

Scheme 5 Proposed isomerization process mechanism of the Prato reaction product of $Y_3N@I_h$-C_{80}. (Reproduced with permission from Ref. [50]. Copyright 2006 American Chemical Society)

and both [5,6]- and [6,6]-adducts were formed for the middle-sized cluster, (Sc_2GdN and $ScGd_2N$)-based NCFs. Similar results were observed from $Sc_{3-x}Y_xN@C_{80}$ ($x = 0$–3) [52]. Poblet et al. carried out theoretical calculations and concluded that the NCFs with entrapped, small-sized clusters preferred to form the [5,6]-addition derivatives, whereas for NCFs with large-sized clusters, the active reaction site changed to the [6,6]-addition site, which is in accordance with the abovementioned experimental results [53].

Later, Yamakoshi et al. adopted a new glycine derivative and formaldehyde as the reagents to react with four types of NCFs, $M_3N@I_h\text{-}C_{80}$ (M = Gd, Y, Lu, and Sc; ion radius: $Gd^{3+} > Y^{3+} > Lu^{3+} > Sc^{3+}$), and found that all the reactions produced both the [5,6]- and [6,6]-adducts (Scheme 6); in contrast, the four [6,6]-adducts converted to the corresponding [5,6]-adducts under the thermal conditions. Unexpectedly, the thermal conversion of $Gd_3N@C_{80}$ adducts was much slower than $Sc_3N@C_{80}$, which can be attributed to the influence of endohedral metal clusters. Larger cluster sizes resulted in a lower degree of thermal isomerization [54]. By tuning the reaction conditions, the bis-, tris-, and tetra-Prato adducts of $Y_3N@I_h\text{-}C_{80}$ and $Gd_3N@I_h\text{-}C_{80}$, along with the monoadducts, were successfully synthesized, separated, and characterized (Scheme 7) [55, 56].

The addition pattern of the Prato reaction of EMFs partly depends on the ylide reagent. When the $Sc_3N@I_h\text{-}C_{80}$ was adopted to react with N-triphenylmethyl-5-oxazolidinone via corresponding azomethine ylide, both the thermodynamic [5,6]-adduct and kinetic [6,6]-adduct were obtained (Fig. 6a, b). The kinetic product would convert to the thermodynamically more stable [5,6]-isomer by forming a

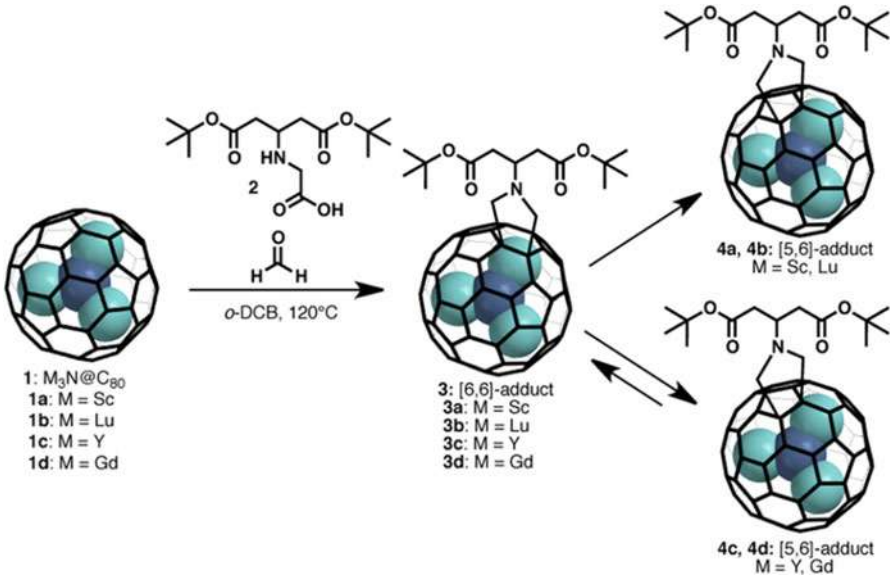

Scheme 6 Prato reaction of $M_3N@I_h\text{-}C_{80}$ (M = Sc, Lu, Y, and Gd). (Reproduced with permission from Ref. [54]. Copyright 2012 American Chemical Society)

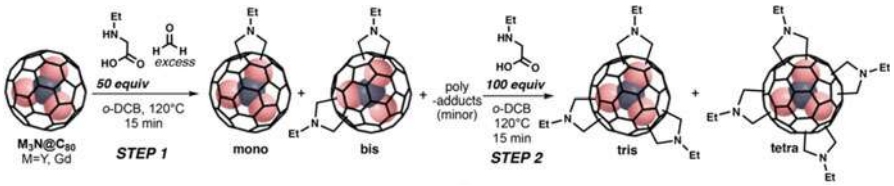

Scheme 7 Prato reactions of $M_3N@C_{80}$ (M = Y and Gd) with the generation of mono-, bis-, tris-, and tetra-adducts. (Reproduced with permission from Ref. [56]. Copyright 2020 American Chemical Society)

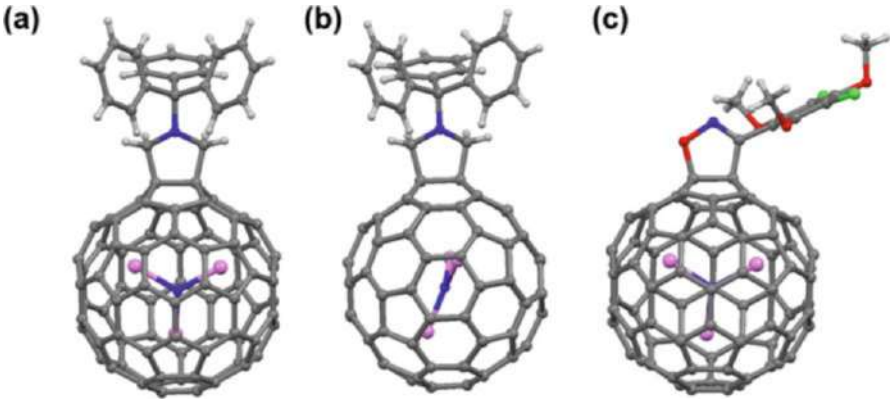

Fig. 6 Single-crystal structures of (**a**, **b**) [5,6]- and [6,6]-N-tritylpyrrolidino $Sc_3N@I_h$-C_{80} and (**c**) the first isoxazoline ring containing [5,6]-addition derivative of $Sc_3N@I_h$-C_{80}

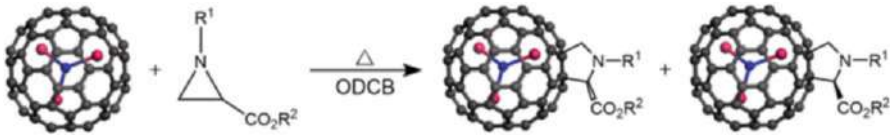

Scheme 8 Formation of the two [5,6]-pyrrolidino $Sc_3N@I_h$-C_{80} diastereomers

zwitterionic species resulting from the initial attack of the azomethine ylide, which has a negative charge on the C_{80} cage and a positive charge on the azomethine ylide moiety [57]. However, when $Sc_3N@I_h$-C_{80} reacted directly with aziridine, a pair of [5,6]-pyrrolidino $Sc_3N@I_h$-C_{80} diastereomers was isolated (Scheme 8) [58]. The 1,3-dipolar cycloaddition of $Sc_3N@I_h$-C_{80} with 3,5-dichloro-2,4,6-trimethoxybenzonitrile oxide provides the first isoxazoline ring containing [5,6]-addition derivative (Fig. 6c) [59]. As for the more reactive $Sc_3N@D_{5h}$-C_{80}, the presence of pyracylene motif in the D_{5h} isomer undoubtedly led to enhanced reactivity toward the 1,3-dipolar tritylazomethine ylide, and both the N-tritylpyrrolidino mono- and bis-adducts were synthesized [60].

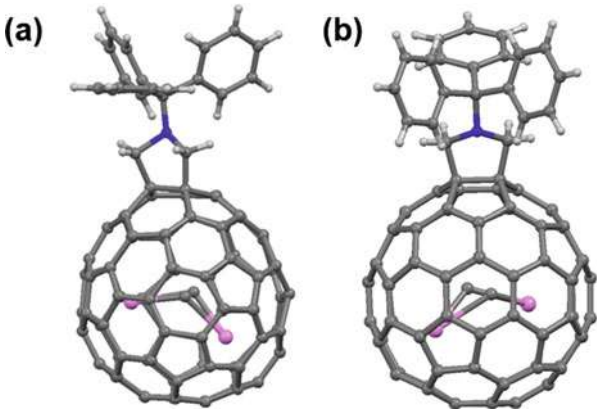

Fig. 7 Single-crystal structures of (**a**) [6,6]-N-tritylpyrrolidino $Sc_2C_2@C_s(6)$-C_{82} and (**b**) [5,6]-N-tritylpyrrolidino $Sc_2C_2@C_{2v}(9)$-C_{82}

For the carbide cluster metallofullerenes (CCFs), the 1, 3-dipolar reaction of $Sc_2C_2@C_s(6)$-C_{82} was investigated by performing the reaction with 3-triphenylmethyl-5-oxazolidinone at elevated temperatures. There are 44 different kinds of nonequivalent cage carbons, but only one [6,6]-monoadduct was formed (Fig. 7a), demonstrating the high regioselectivity of the reaction. The inner two Sc atoms were located far from the addition site as a consequence of the cage symmetry and the rigid shape of the cluster [61]. However, when the same reaction was conducted on $Sc_2C_2@C_{2v}(9)$-C_{82}, low regioselectivity was observed and three monoadduct isomers were obtained. One of the major products was assigned as a [5,6]-closed structure (Fig. 7b) by X-ray data. The other two minor products were seemingly [6,6]-isomers [62]. The Prato reaction of $Sc_3C_2@C_{80}$ produced only one [5,6]-fulleropyrrolidine monoadduct, and the spin divergence of endohedral Sc_3C_2 cluster was induced by exohedral modification, resulting in distinct differences in the ESR patterns of adduct and pristine fullerene. Chemical modification has been proven to be a powerful technique to change the configuration of the inner cluster, as well as to tune the electronic and paramagnetic properties of an endofullerene [63]. The Prato reaction was also applied to monometallofullerenes ($La@C_{82}$, $Gd@C_{82}$, and $Y@C_{82}$), dimetallofullerenes ($La_2@C_{80}$, $Ce_2@C_{80}$, and $Y_2@C_{79}N$), and afforded the corresponding metallofulleropyrrolidines [64–72].

Interestingly, the Prato reaction has been successfully applied to prepare graphene/nanotube-fullerene hybrids (Fig. 8). The $Sc_3N@C_{80}$ molecules were connected to graphene or carbon nanotubes through the N-five-membered heterocycle ring. Such an efficient synthesis of hybrids solves the long-lasting puzzle about the construction of carbon-allotrope-only architectures not limited to graphene-like graphene oxide, and particularly pioneers the utilization of EMFs. This represents a breakthrough and will pave the way for multi-functional architectures and their applications in various fields, such as solar cells and electronic devices [73, 74].

Another typical [2 + 3] cycloaddition reaction of EMFs is the disilirane addition reaction (Scheme 1d) [6]. In 1995, the first example of an exohedral adduct of EMF

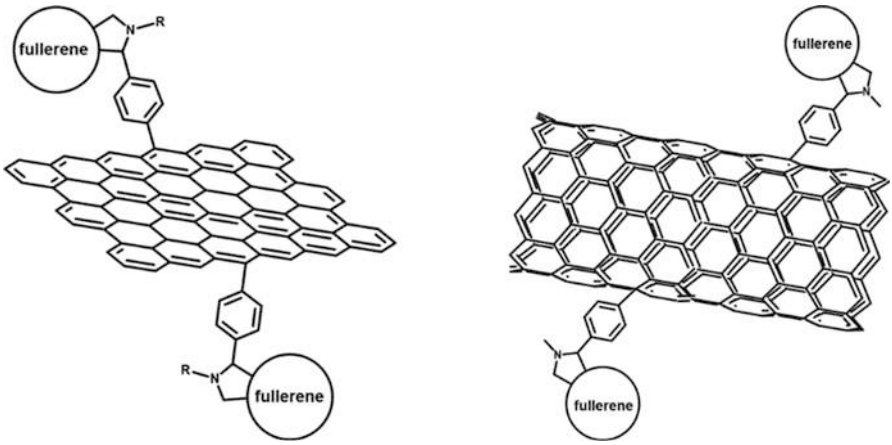

Fig. 8 Graphene/nanotube-fullerene hybrids

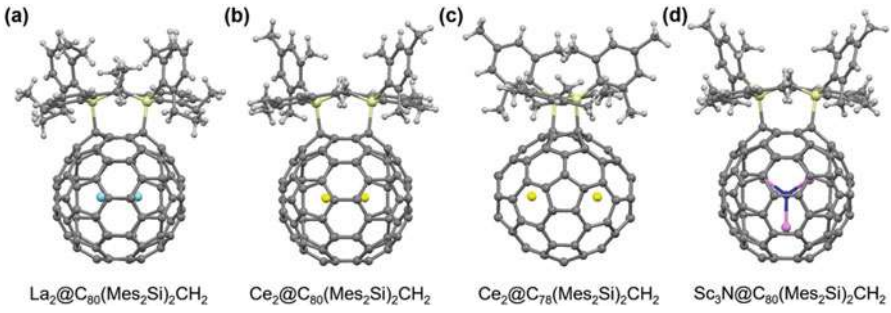

Fig. 9 Single-crystal structures of (**a**) $La_2@C_{80}(Mes_2Si)_2CH_2$, (**b**) $Ce_2@C_{80}(Mes_2Si)_2CH_2$, (**c**) $Ce_2@C_{78}(Mes_2Si)_2CH_2$ and (**d**) $Sc_3N@C_{80}(Mes_2Si)_2CH_2$

was reported by reacting $La@C_{2v}$-C_{82} with disilirane under thermal or photo-irradiation conditions to yield $La@C_{82}(Mes_2Si)_2CH_2$ [27]. Later on, the same reaction was applied to other monometallofullerenes, such as $Gd@C_{82}$ [75], $La@C_{82}$ isomers [76], $Pr@C_{82}$ [77], and $Y@C_{82}$ [78]. However, when the pristine $M@C_{82}$ (M = Y, La, and Ce) were reduced to their anions, they showed no reactivity toward the disilirane, but their cations could react with disilirane and produce the corresponding 1:1 adducts. The reactivity of $M@C_{82}$ toward disilirane was tuned by ionization, increased by oxidation, and decreased by reduction [79]. The disilirane addition reaction was also extended to the dimetallofullerenes, such as $La_2@C_{80}$ [80, 81], $Sc_2@C_{84}$ [80], $Ce_2@C_{80}$ [82, 83], and $Ce_2@C_{78}$ [84]. Fig. 9 shows the single-crystal structures of bis-silylated derivatives of $La_2@C_{80}$, $Ce_2@C_{80}$, and $Ce_2@C_{78}$. Moreover, trimetallofullerene $Sc_3@C_{82}$ showed high reactivity toward disilirane, as it possesses both high electron-accepting and electron-donating ability [85].

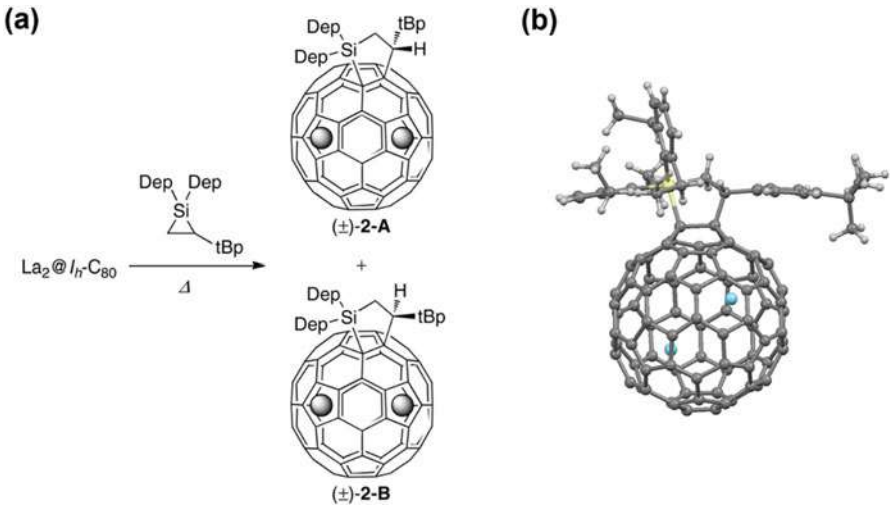

Fig. 10 (**a**) Reaction of $La_2@I_h$-C_{80} with silirane. (**b**) Single-crystal structure of one of the carbosilylated adducts. (Reproduced with permission from Ref. [89]. Copyright 2010 American Chemical Society)

For NCF, $Sc_3N@I_h$-C_{80}, which has the same carbon cage (I_h) and electronic state (C_{80}^{6-}) as $La_2@C_{80}$, can only react with disilirane under photochemical conditions [86, 87]; this is in contrast with the fact that $La_2@I_h$-C_{80} reacts both photochemically and thermally [80], demonstrating the effect of encapsulated species on the reactivity. Fig. 9d shows the single-crystal structure of bis-silylated derivative of $Sc_3N@I_h$-C_{80}. The same reaction was also applied to $Lu_3N@I_h$-C_{80}, and several isomeric products were obtained [88].

Carbosilylation of $La_2@I_h$-C_{80} with silirane (silacyclopropane) can proceed only under thermal heating conditions, generating two diastereomers of the carbosilylated adducts (Fig. 10a). Fig. 10b shows the single-crystal structure of one diastereomer [89]. However, when $Sc_3N@I_h$-C_{80} reacted with silirane, the reaction occurred under photoirradiation conditions, and two [5,6]-adducts and one [6,6]-adduct were formed. Thermal isomerization reactions of the adducts were observed, which may be ascribed to the notion that the photochemical functionalization of EMFs may be advantageous to obtain thermally labile regioisomeric adducts [90].

Diels–Alder Reaction

The first Diels–Alder reaction of EMF was reported in 2002. $Sc_3N@I_h$-C_{80} reacted with ^{13}C-labeled 6,7-dimethoxyisochroman-3-one (Scheme 1e), and one symmetric [5,6]-monoadduct formed as characterized by NMR and X-ray crystallography (Fig. 11a) [91, 92]. Then, the Diels–Alder reactions of both the I_h and D_{5h} isomers of $M_3N@C_{80}$ (M = Lu and Sc) were investigated by reacting with cyclopentadiene-

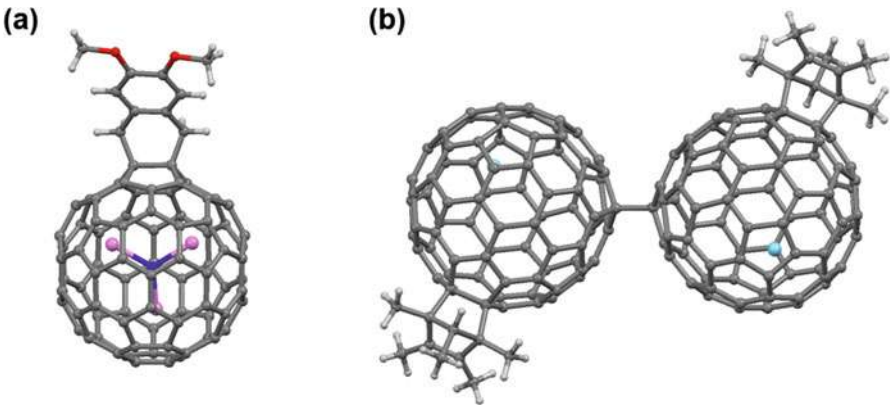

Fig. 11 (**a**) Single-crystal structures of Diels–Alder cycloadduct of $Sc_3N@C_{80}$ and (**b**) $La@C_{82}Cp^*$ dimer

functionalized resin. D_{5h} isomers showed higher reactivity than the I_h isomers. Owing to the different reactivities of the two isomers, such reaction can serve as a method for the separation of I_h and D_{5h} TNT–EMF mixtures [60]. Moreover, when $Gd_3N@C_{80}$ underwent the Diels–Alder reaction with a molar excess of 6,7-dimethoxy-3-isochromanone in trichlorobenzene (TCB) solution, both the mono- and bis-adducts were formed as confirmed by MALDI–TOF MS [93].

The Diels–Alder reaction of the open-shell $La@C_{82}$ with 1,2,3,4,5-pentamethylcyclopentadiene (Cp*) produced both mono- and bis-adducts. Unfortunately, the monoadduct decomposed to $La@C_{82}$ and Cp* after sitting at 298 K for 12 h, and 60% of the monoadduct formed a dimer during the crystallization process (Fig. 11b), as described in the Bingel bisadduct of $La@C_{82}$ [94]. As for the endohedral heterofullerenes, a slightly enhanced chemical reactivity of the $Y_2@C_{79}N$ toward the supported cyclopentadiene moiety was observed in comparison with that of $Gd_2@C_{79}N$ [95]. To gain more insight into the reactivity of fullerenes when the metal cluster was encapsulated into the cage, a detailed theoretical study was carried out for the Diels–Alder reactivity of all the nonequivalent bonds in $Sc_3N@C_{78}$. The results showed that the Diels–Alder reaction over the free fullerene and the EMF results in totally different cycloadducts [96].

Carbene Reaction

Carbenes, as a kind of divalent carbon species, are well-known reactive intermediates that facilitate the formation of a new carbon–carbon bond. The carbenes can exhibit both electrophilic and nucleophilic characters and demonstrate a diverse reactivity toward fullerenes (Scheme 1f). The first carbene addition toward EMFs was reported in 2004 by the irradiation of $La@C_{82}$ solution and an excess molar amount of 2-adamantane-2-3-[3H]-diazirine (AdN_2) at room temperature. There are

24 nonequivalent carbons and 19 nonequivalent [6,6]-bonds in La@C_{82}, but the reaction showed high regioselectivity and only one monoadduct La@C_{82}(Ad) was generated, which was assigned to be in a [6,6]-open addition pattern (Fig. 12a) [97]. Thereafter, the same reaction process was applied to Gd@C_{82}, Ce@C_{82}, and Y@C_{82}, respectively, and all the products showed the [6,6]-addition pattern (Fig. 12b–d) [98–100]. However, when Sc@C_{82} underwent the same reaction, since the numbers of reactive nonequivalent cage carbons increased, the regioselectivity was reduced and four monoadduct isomers were formed. The most abundant product was proved to be a [6,6]-open adduct [101].

Carbene reactions of dimetallofullerenes can be conducted under thermal or photochemical conditions. The reaction of $La_2@D_{3h}$-C_{78} with AdN_2 produced four isomeric monoadducts $La_2@C_{78}$(Ad), and the results showed that the addition occurred at both [5,6]- and [6,6]-positions around the pole and equator of the cage. The major isomer was identified as a [5,6]-open structure (Fig. 13a) [102]. Photochemical reaction of the non-IPR $La_2@D_2$-C_{72} and Ad group yielded six monoadduct isomers, and three isomers were successfully crystallized, which were proved to be [5,6]-open structures (Fig. 13b). There were two pairs of fused pentagons in

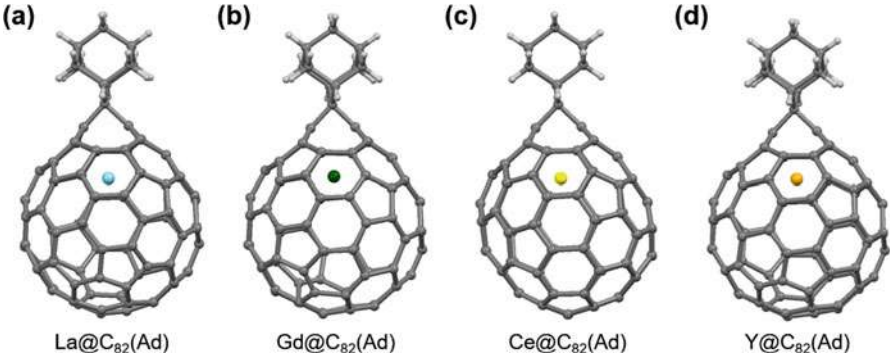

Fig. 12 Single-crystal structures of (**a**) La@C_{82}(Ad), (**b**) Gd@C_{82}(Ad), (**c**) Ce@C_{82}(Ad) and (**d**) Y@C_{82}(Ad)

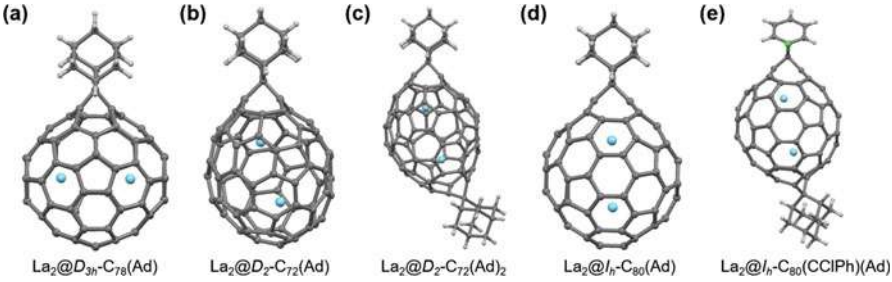

Fig. 13 Single-crystal structures of (**a**) $La_2@D_{3h}$-C_{78}(Ad), (**b**) $La_2@D_2$-C_{72}(Ad), (**c**) $La_2@D_2$-$C_{72}(Ad)_2$, (**d**) $La_2@I_h$-C_{80}(Ad) and (**e**) $La_2@I_h$-C_{80}(CClPh)(Ad)

non-IPR $La_2@D_2$-C_{72}, one at each end of the cage. The [5,5]-bond junctions were very reactive due to the high surface curvature, but the adducts turned out to be either [5,6]- or [6,6]-adducts because the [5,5]-bond junctions in $La_2@C_{72}$ were stabilized by the encaged metals. Electronic spectra and electrochemical studies revealed that the essential electronic structures of $La_2@C_{72}$ were retained in six isomers, and the Ad group acted as a weak electron-donating group toward $La_2@C_{72}$ [103]. Moreover, by extending the reaction time, another Ad group could add on the cage to form the bis-adducts $La_2@C_{72}(Ad)_2$. One of the most abundant bis-adducts was identified as the one with a [5,6][5,6]-open structure (Fig. 13c), where the two Ad groups were attached to two fused-pentagon regions on each side of the C_{72} cage [104]. The photochemical reaction of $M_2@I_h$-C_{80} (M = La and Ce) with AdN_2 afforded the corresponding adducts, $M_2@C_{80}(Ad)$. The single-crystal structure of $La_2@C_{80}(Ad)$ displayed a [6,6]-open addition pattern, and the inner La–La distance was elongated due to the expansion of the inner space of the cage by the bond cleavage (Fig. 13d) [105]. Another example of carbene addition of $La_2@I_h$-C_{80} was a two-step double addition of carbene groups. Chlorophenylcarbene reacted with $La_2@I_h$-C_{80} first to form the [6,6]-open $La_2@C_{80}(CClPh)$, and then, a second Ad carbene group added to the cage to form $La_2@C_{80}(CClPh)(Ad)$. Three isomeric bis-adducts were separated and a single-crystal structure of one product was obtained (Fig. 13e). The results showed that the two carbene groups were attached at the two poles of the cage, in line with the positions of inner metal atoms [106].

The CCFs also showed good reactivities toward the carbene reaction. The correct structure of $Sc_3C_2@C_{80}$, which was previously identified as $Sc_3@C_{82}$ structure, was determined via the carbene reaction between $Sc_3C_2@C_{80}$ and Ad. The [6,6]-adduct was successfully crystallized (Fig. 14a) [107]. However, when the same reaction was applied to $Sc_2C_2@C_{82}$ and $Sc_2C_2@C_{80}$, the Ad group preferred to locate at the [5,6]-open site (Fig. 14b, c) [108, 109]. It was found that the addition mostly took place at a cage region on top of the cluster arch. After functionalization, the two Sc atoms likely to move through the C2-unit were almost fixed relative to the cage [110]. To investigate the impact of endohedral cluster doping on the chemical reactivity, the carbene reaction was applied to both D_{2d}-C_{84} and $Sc_2C_2@D_{2d}$-C_{84}. The results showed that only two Ad adducts formed for D_{2d}-C_{84}, but the photoirradiation of $Sc_2C_2@D_{2d}$-C_{84}

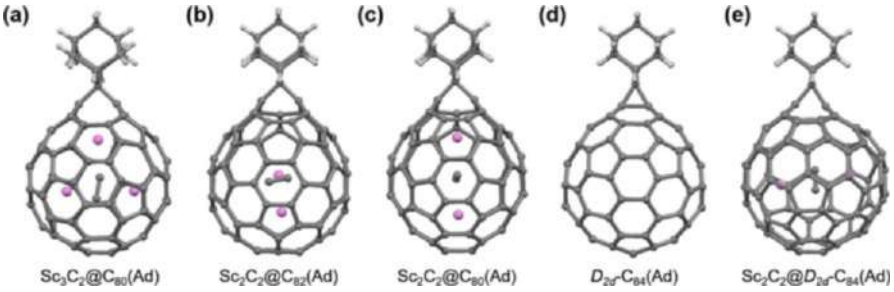

Fig. 14 Single-crystal structures of (**a**) $Sc_3C_2@C_{80}(Ad)$, (**b**) $Sc_2C_2@C_{82}(Ad)$, (**c**) $Sc_2C_2@C_{80}(Ad)$, (**d**) D_{2d}-$C_{84}(Ad)$ and (**e**) $Sc_2C_2@D_{2d}$-$C_{84}(Ad)$

and diazirine afforded four Ad monoadducts. More importantly, the minor isomer C_{84}(Ad)-B was a [6,6]-closed methanofullerene (Fig. 14d), the reaction mechanism of which should be a [3 + 2] cycloaddition followed by N_2 extrusion. However, in the case of $Sc_2C_2@D_{2d}$-C_{84}, the [6,6]-open fulleroid was formed (Fig. 14e). Thus, the Ad addition to $Sc_2C_2@C_{84}$ should proceed via a carbene mechanism [111].

The carbene reaction of $Lu_3N@I_h$-C_{80} with bis(2,6-diethylphenyl)silylene afforded a novel silylene-bridged derivative under thermal conditions. The as-formed [6,6]-silacyclopropane transformed slowly to [5,6]-silafulleroid under ambient light (Fig. 15a) [112]. The first example of stable [6,6]-open and [5,6]-open methanofullerene derivatives from the carbene reaction of $Sc_3N@I_h$-C_{80} was reported in 2013. $Sc_3N@I_h$-C_{80} reacted with diaryldiazo compounds, yielding both [5,6]- and [6,6]-open monoadducts [113]. Later on, adamantylidene addition to $M_3N@I_h$-C_{80} (M = Sc and Lu) and $Sc_3N@D_{5h}$-C_{80} was investigated. For the I_h isomers, both [5,6]- and [6,6]-monoadducts were formed (Fig. 15b). For $Sc_3N@D_{5h}$-C_{80}, which has nine types of C–C bonds in the D_{5h}-C_{80} cage, the reaction exhibited high regioselectivity and only three major isomeric Ad monoadducts were formed. For $Lu_3N@I_h$-C_{80}, several bis-adducts were synthesized and one of the products was successfully crystallized (Fig. 15c). The crystal structure showed that both Ad groups located close to the inner Lu atoms, demonstrating that the sites for multiple additions can be governed by the orientation of the endohedral trimetallic nitride cluster [114].

The reaction of N-heterocyclic carbene (NHC) with $Sc_3N@I_h$-C_{80} was successfully performed by Lu et al., and a Lewis acid–base pair product was afforded (Scheme 9), which was different from that of empty fullerene; the abnormal carbene center of NHC was connected to a triple-hexagon-junction (THJ) carbon atom of $Sc_3N@I_h$-C_{80} via a single bond (Fig. 16a). By analyzing the charge density distribution, it was found that the electron-rich NHC was prone to attack one of the THJ carbons with low electron densities to form the single-bonded adduct. Owing to the steric hindrance between the normal NHC moiety and $Sc_3N@I_h$-C_{80}, the cage tended to selectively trap the rare, abnormal NHC [115]. However, when the reaction was conducted in the presence of oxygen, the normal carbene center of the NHC singly bonded to a THJ cage carbon together with an oxygen atom bridging the same THJ carbon atom and a neighboring carbon atom, forming an epoxy structure (Fig. 16b).

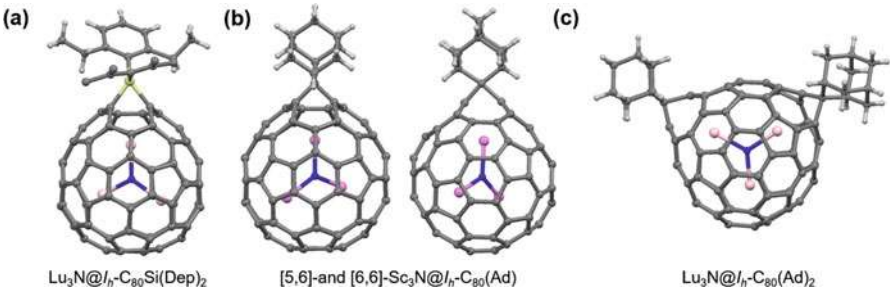

Fig. 15 Single-crystal structures of (**a**) $Lu_3N@I_h$-$C_{80}Si(Dep)_2$, (**b**) [5,6]- and [6,6]-$Sc_3N@I_h$-C_{80}(Ad) and (**c**) $Lu_3N@I_h$-$C_{80}(Ad)_2$

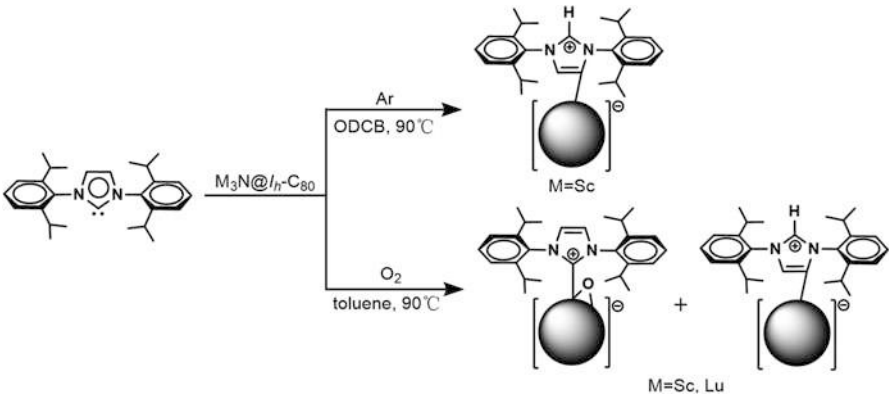

Scheme 9 Reactions between $M_3N@I_h$-C_{80} (M = Sc and Lu) and NHC

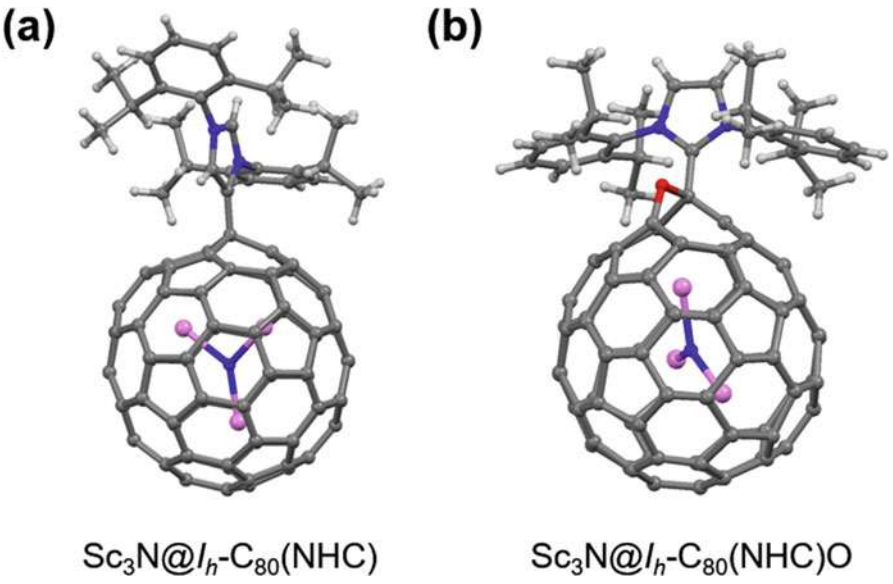

Fig. 16 Single-crystal structures of (**a**) $Sc_3N@I_h$-C_{80}(NHC) and (**b**) $Sc_3N@I_h$-C_{80}(NHC)O

The addition of this oxygen atom was considered to release the steric hindrance between the bulky NHC moiety and the fullerene cage mentioned above [116].

Radical Recombination Reaction

The lanthanum monometallofullerenes are known to have open-shell electronic structures and some of them, such as La@C_{60} and La@C_{74}, are insoluble in organic solvents used in the conventional extraction process of soot. Until 2005, Nagase et al.

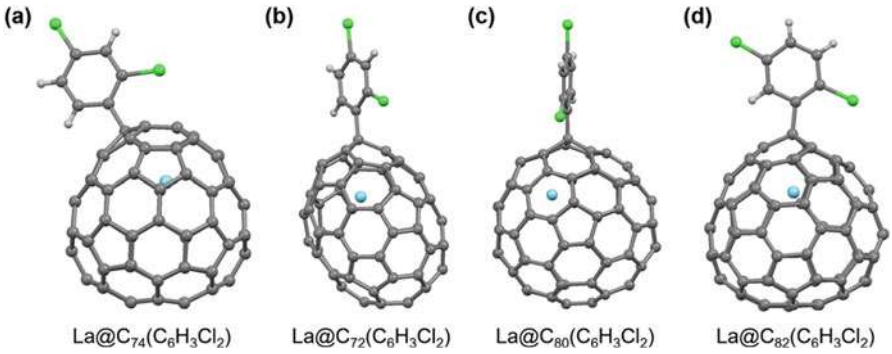

Fig. 17 Single-crystal structures of (**a**) La@C_{74}($C_6H_3Cl_2$), (**b**) La@C_{72}($C_6H_3Cl_2$), (**c**) La@C_{80}($C_6H_3Cl_2$) and (**d**) La@C_{82}($C_6H_3Cl_2$)

found that the insoluble La@C_{74} could react with 1,2,4-trichlorobenzene (TCB) under reflux during the extraction [117, 118]. One Cl^- of the TCB molecule was removed to produce the dichlorophenyl radical, which then recombined with the C_{74} cage possessing a high radical character to yield the soluble derivative La@C_{74}($C_6H_3Cl_2$). Thus, the structure of La@C_{74} was verified by the successful crystallization of La@C_{74}($C_6H_3Cl_2$), see Fig. 17a of the single-crystal structure. Ever since this derivatization method was discovered, some unconventional EMFs were detected, and their structures were determined through this radical recombination reaction. Derivatives such as the La@C_{72}($C_6H_3Cl_2$) [119], La@C_{80}($C_6H_3Cl_2$) [120], and La@C_{82}($C_6H_3Cl_2$) [121] were produced (Fig. 17b–d). Hence, some of the missing-cage species and new cages of higher EMFs were obtained.

In addition, it was found that a series of substituted benzenes can be used as a radical precursor to react with La@C_{82} for selectively forming stable and novel derivatives (Fig. 18a) [122]. The thermal reaction of La@C_{82} with 3-triphenylmethyl-5-oxazolidinone in toluene afforded benzyl monoadduct La@C_{82}($CH_2C_6H_5$), which can also be obtained by the photoirradiation of La@C_{82} in toluene without the existence of 3-triphenylmethyl-5-oxazolidinone. However, when the reaction was conducted in benzene, metallofulleropyrrolidine La@C_{82}($C_2H_4NCPh_3$) was formed. Photoirradiation of La@C_{82} in 1,2-dichlorobenzene, in the presence of α,α,2,4-tetrachlorotoluene, afforded the monoadducts La@C_{82}($CHClC_6H_3Cl_2$). The single-crystal structure of one of the products is shown in Fig. 18b.

In general, the benzyl radical addition of EMFs tends to form closed-shell adducts by attaching an odd number of addends to open-shell EMFs, whereas even number of groups are added to closed-shell EMFs. Regioselective benzyl radical addition to the open-shell Sc_3C_2@I_h-C_{80} only formed one monoadduct, Sc_3C_2@I_h-C_{80}($CH_2C_6H_5$) (Fig. 19a), where the benzyl moiety was singly bonded to the [5,6,6]-juncture cage carbon [123]. In contrast, for the closed-shell NCF, the photochemical activation of benzyl bromide in the presence of Sc_3N@I_h-C_{80} formed the bisadduct Sc_3N@I_h-C_{80}($CH_2C_6H_5$)$_2$ (Fig. 19b), which showed a selective 1,4-addition pattern [124]. Unexpectedly, benzyl radical addition to the closed-

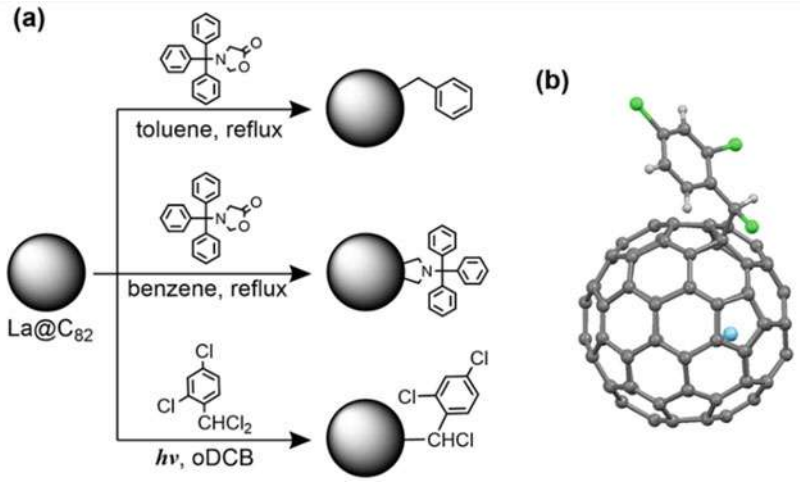

Fig. 18 (**a**) Radical addition reactions and Prato reaction of La@C_{82}. (**b**) Single-crystal structure of La@C_{82}($CHClC_6H_3Cl_2$)

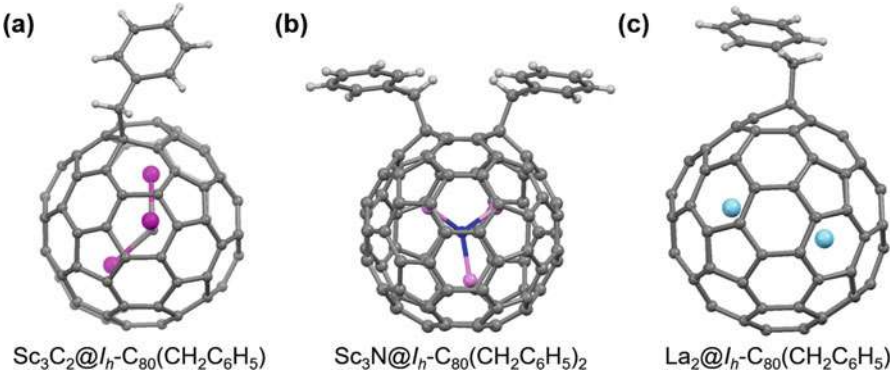

Fig. 19 Single-crystal structures of (**a**) $Sc_3C_2@I_h$-$C_{80}(CH_2C_6H_5)$, (**b**) $Sc_3N@I_h$-$C_{80}(CH_2C_6H_5)_2$ and (**c**) $La_2@I_h$-$C_{80}(CH_2C_6H_5)$

shell $La_2@I_h$-C_{80} formed a stable, open-shell fullerene radical $La_2@I_h$-$C_{80}(C_7H_7)$ instead of the anticipated closed-shell bisadduct [125]. It was found that the inner La_2 cluster can accept the unpaired electron into their σ-bonding orbital to stabilize the open-shell fullerene radical. Fig. 19c shows the single-crystal structure of $La_2@I_h$-$C_{80}(C_7H_7)$, the benzyl group of which was singly bonded to the [5,6,6]-ring junction.

The trifluoromethylation of EMFs is also a typical radical addition reaction. The CF_3 derivatives of EMFs are usually stable and more soluble in common organic solvents; therefore, trifluoromethylation reaction is often used for the extraction of EMFs. For example, the trifluoromethylation of Y@C_{82}- or Gd@C_{82}-enriched EMF extract with

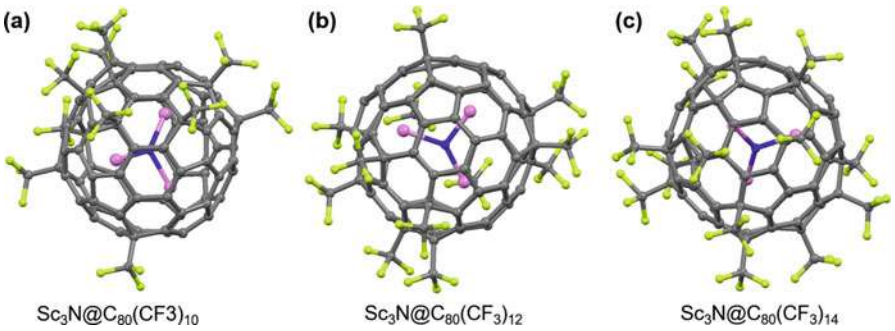

Fig. 20 Single-crystal structures of (**a**) $Sc_3N@C_{80}(CF_3)_{10}$, (**b**) $Sc_3N@C_{80}(CF_3)_{12}$ and (**c**) $Sc_3N@C_{80}(CF_3)_{14}$

silver(I) trifluoroacetate (CF_3CO_2Ag) formed two isomers of $Y@C_{82}(CF_3)_5$ [126] and a pentakis-adduct $Gd@C_{82}(CF_3)_5$, respectively [127]. The trifluoromethylation of $Sc_3N@C_{80}$ (I_h and D_{5h}) with gaseous CF_3I generated the bis-adducts $Sc_3N@(C_{80}\text{-}I_h)(CF_3)_2$ and $Sc_3N@(C_{80}\text{-}D_{5h})(CF_3)_2$ as main products, confirmed to be a 1,4-addition pattern [128]. In addition, the poly(perfluoroalkylation) of $Sc_3N@C_{80}$ produced a series of multiadducts $Sc_3N@C_{80}(CF_3)_n$ ($n = 2$–18) at high temperature. Fig. 20 shows the single-crystal structures of some multiadducts [129–131].

Metal Complexation Reactions

There are many examples of metal complexation reactions of empty fullerenes, but exohedral transition metal adducts of EMFs are rarely studied owing to the low yield and unique reactivity of EMFs. The investigation of EMF organometallic chemistry started from the coordination of $Sc_2C_2@C_{3v}(8)\text{-}C_{82}$ with $(\mu\text{-}H)_3Re_3(CO)_{11}(NCMe)$, which produced the air-stable $(\mu\text{-}H)_3Re_3(CO)_9(\eta^2,\eta^2,\eta^2\text{-}Sc_2C_2@C_{3v}(8)\text{-}C_{82})$ [132]. Fig. 21a shows the single-crystal structure of the complex, in which the Re_3 cluster was added to one hexagon of the cage. Although the interaction between the encaged Sc_2C_2 cluster and exohedral Re_3 cluster was not observed, the geometry and electronic properties of $Sc_2C_2@C_{3v}(8)\text{-}C_{82}$ were altered after the coordination. Treatment of $Li^+@C_{60}$ with $Ir(CO)Cl(PPh_3)_2$ and platinum complexes produced the η^2-adduct, $Ir(CO)Cl(PPh_3)_2(\eta^2\text{-}Li^+@C_{60})$ (Fig. 21b) and Pt[1,1′-bis(diphenylphosphino)-ferrocene](η^2-$Li^+@C_{60}$), respectively (Fig. 21c). Both adducts showed the [6,6]-addition pattern, and the Li^+ was localized in a single position near the site of bonding to the external metal [133]. Two isomeric $Sc_3N@C_{80}$ (I_h and D_{5h}) were used to react with $W(CO)_4(Ph_2PC_2H_4PPh_2)$, and only one mononuclear complex for each isomer was formed [134]. The tungsten center coordinates with the cages in an η^2 fashion on the [6,6]-bond in both adducts. Fig. 21d shows the single-crystal structure of the adduct of I_h isomer. The complexation reaction of open-shell EMF was reported as well. Photoreaction of $Y@C_{2v}(9)\text{-}C_{82}$ with $Re_2(CO)_{10}$ produced the organometallic complex with an η^1 fashion (Fig. 21e), where the Re atom attaches to the [5,6,6]-ring junction via a single

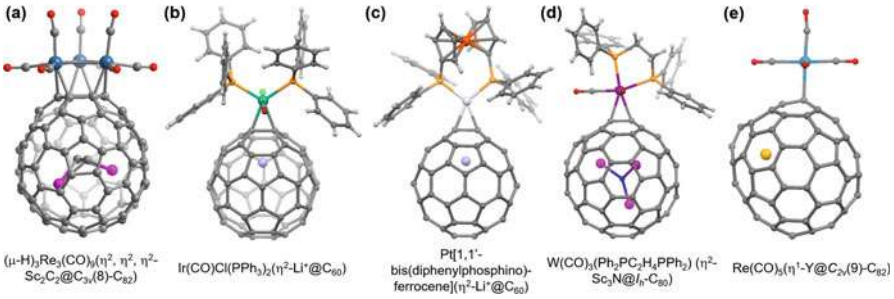

Fig. 21 Single-crystal structures of (**a**) $(\mu\text{-H})_3Re_3(CO)_9(\eta^2,\eta^2,\eta^2\text{-}Sc_2C_2@C_{3v}(8)\text{-}C_{82})$, (**b**) $Ir(CO)Cl(PPh_3)_2(\eta^2\text{-}Li^+@C_{60})$, (**c**) Pt[1,1′-bis(diphenylphosphino)-ferrocene]$(\eta^2\text{-}Li^+@C_{60})$, (**d**) $W(CO)_3(Ph_2PC_2H_4PPh_2)$ $(\eta^2\text{-}Sc_3N@I_h\text{-}C_{80})$ and (**e**) $Re(CO)_5(\eta^1\text{-}Y@C_{2v}(9)\text{-}C_{82})$

Re−C σ bond [135]. The exohedral Re moiety could transfer one electron to the EMF, resulting in an air-stable closed-shell structure.

Electrochemical Reactions of EMFs

The electrochemically synthetic method was successfully applied to EMFs in 2011. EMFs were subjected to electrochemical reduction or electrochemical oxidation to prepare the EMF anions or cations, respectively, which showed different reactivities compared with the corresponding neutral species and provided more possibilities for functionalizations that are otherwise difficult to achieve. The first example of the electrochemical functionalization of EMFs was reported in 2011. $Sc_3N@I_h\text{-}C_{80}$ and $Lu_3N@I_h\text{-}C_{80}$ were reduced by controlled potential electrolysis (CPE) to generate the $[Sc_3N@I_h\text{-}C_{80}]^{2-}$ and $[Lu_3N@I_h\text{-}C_{80}]^{2-}$ ions, respectively, which then underwent nucleophilic reaction with benzal bromide. Unexpectedly, the $[Sc_3N@I_h\text{-}C_{80}]^{2-}$ showed extremely low reactivity toward benzal bromide, whereas $[Lu_3N@I_h\text{-}C_{80}]^{2-}$ exhibited higher activity and afforded one [6,6]-open $Lu_3N@I_h\text{-}C_{80}\text{-}(CHC_6H_5)$ product (Scheme 10a) [136]. Different fullerene anionic states exhibited different reactivities as a result of their different nucleophilicities. When the non-nucleophilic $[Sc_3N@I_h\text{-}C_{80}]^{2-}$ was further reduced to its trianion, it showed high nucleophilicity to the benzal bromide, and one [6,6]-open $Sc_3N@I_h\text{-}C_{80}\text{-}(CHC_6H_5)$ was synthesized (Scheme 10a) [137]. Anionic fullerenes could act as nucleophilic reagents to react with electrophilic reagents. By the same token, the fullerene cations can act as electron-defect reagents to react with nucleophilic reagents, which was proved recently by the Bingel–Hirsch reaction of $[M_3N@I_h\text{-}C_{80}]^+$ (M = Sc, Lu) generated by either CPE or the chemical oxidation method. The $[Sc_3N@I_h\text{-}C_{80}]^+$ demonstrated higher reactivity toward the nucleophile than the neutral species, and both [5,6]- and [6,6]-monoadducts were prepared (Scheme 10b, Fig. 4) [41]. The electrochemical method provides a new strategy to activate and functionalize EMFs, and as a complement to the neutral fullerene chemistry.

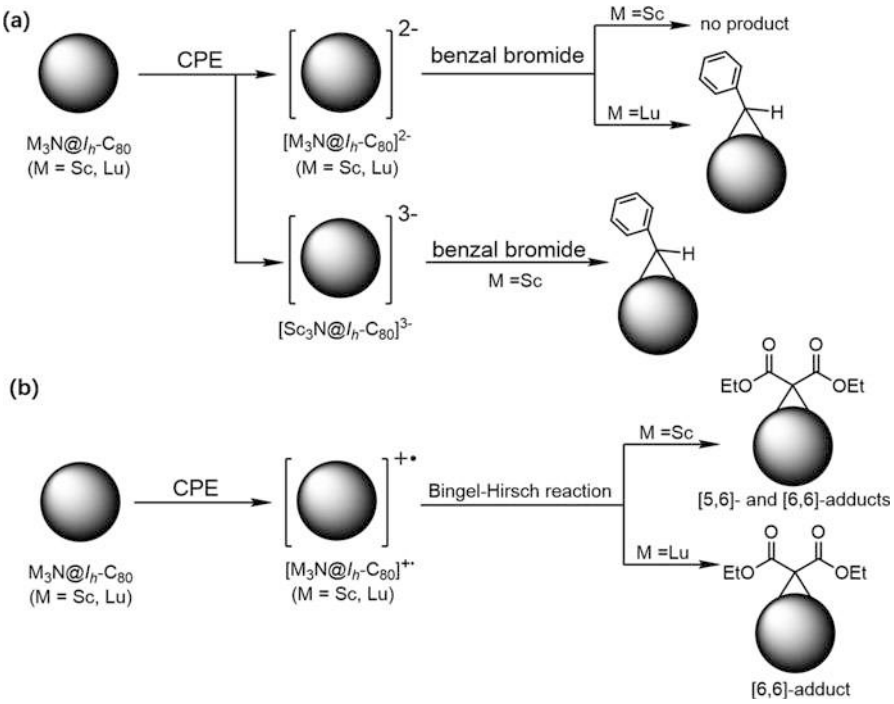

Scheme 10 (**a**) The reaction of EMF anions with benzal bromide. (**b**) Bingel–Hirsch reaction of EMF cations

Conclusion

In this chapter, we have discussed the chemical reactions of endohedral metallofullerenes, including the Bingel–Hirsch reaction, [2 + 2] cycloaddition reaction, [2 + 3] cycloaddition reaction, Diels–Alder reaction, carbene reaction, radical recombination reaction, metal complexation reaction, and electrochemical reaction. Among them, electrosynthesis holds promise to prepare EMFs derivatives that are otherwise difficult to access. Classical EMFs and clusterfullerenes of various sizes, endohedral species, and their functionalized derivatives were discussed as well. The functionalization of endohedral metallofullerenes is crucial for the development of new materials with tunable structures and properties for potential applications. Therefore, the exploration of new synthetic strategies for EMFs derivatives is still an important task.

References

1. Dunsch L, Yang S (2007) Metal nitride cluster fullerenes: their current state and future prospects. Small 3:1298
2. Popov AA, Yang S, Dunsch L (2013) Endohedral fullerenes. Chem Rev 113:5989

3. Tzirakis MD, Orfanopoulos M (2013) Radical reactions of fullerenes: from synthetic organic chemistry to materials science and biology. Chem Rev 113:5262
4. Cai W, Chen C-H, Chen N, Echegoyen L (2019) Fullerenes as nanocontainers that stabilize unique actinide species inside: structures, formation, and reactivity. Acc Chem Res 52:1824
5. Zhang J, Stevenson S, Dorn HC (2013) Trimetallic nitride template endohedral metallofullerenes: discovery, structural characterization, reactivity, and applications. Acc Chem Res 46:1548
6. Kako M, Nagase S, Akasaka T (2017) Functionalization of endohedral metallofullerenes with reactive silicon and germanium compounds. Molecules 22:1179
7. Akasaka T, Osuka A, Fukuzumi S, Kandori H, Aso Y (2015) Chemical science of π-electron systems. Springer I-IV
8. Yamada M, Akasaka T (2014) Emergence of highly elaborated π-space and extending its functionality based on nanocarbons: new vistas in the fullerene world. Bull Chem Soc Jpn 87:1289
9. Lu X, Bao L, Akasaka T, Nagase S (2014) Recent progress in the chemistry of endohedral metallofullerenes. Chem Commun 50:14701
10. Lu X, Feng L, Akasaka T, Nagase S (2012) Current status and future developments of endohedral metallofullerenes. Chem Soc Rev 41:7723
11. Akasaka T, Wudl F, Nagase S (2010) Chemistry of nanocarbons. John Wiley & Sons, Ltd 261–286
12. Yamada M, Akasaka T, Nagase S (2010) Endohedral metal atoms in pristine and functionalized fullerene cages. Acc Chem Res 43:92
13. Mikawa M, Kato H, Okumura M, Narazaki M, Kanazawa Y, Miwa N, Shinohara H (2001) Paramagnetic water-soluble metallofullerenes having the highest relaxivity for MRI contrast agents. Bioconjug Chem 12:510
14. Qu L, Cao W, Xing G, Zhang J, Yuan H, Tang J, Cheng Y, Zhang B, Zhao Y, Lei H (2006) Study of rare earth encapsulated carbon nanomolecules for biomedical uses. J Alloys Compd 400:408–412
15. Shu C-Y, Ma X-Y, Zhang J-F, Corwin FD, Sim JH, Zhang E-Y, Dorn HC, Gibson HW, Fatouros PP, Wang C-R, Fang X-H (2008) Conjugation of a water-soluble gadolinium endohedral fulleride with an antibody as a magnetic resonance imaging contrast agent. Bioconjug Chem 19:651
16. Shu C-Y, Gan L-H, Wang C-R, Pei XL, Han HB (2006) Synthesis and characterization of a new water-soluble endohedral metallofullerene for MRI contrast agents. Carbon 44:496
17. Shu C-Y, Wang C-R, Zhang J-F, Gibson HW, Dorn HC, Corwin FD, Fatouros PP, Dennis TJS (2008) Organophosphonate functionalized Gd@C_{82} as a magnetic resonance imaging contrast agent. Chem Mater 20:2106
18. Cagle DW, Kennel SJ, Mirzadeh S, Alford JM, Wilson L (1999) *In vivo* studies of fullerene-based materials using endohedral metallofullerene radiotracers. J Proc Natl Acad Sci 96:5182
19. Shultz MD, Wilson JD, Fuller CE, Zhang J, Dorn HC, Fatouros PP (2011) Metallofullerene-based nanoplatform for brain tumor brachytherapy and longitudinal imaging in a murine orthotopic xenograft model. Radiology 261:136
20. Wilson JD, Broaddus WC, Dorn HC, Fatouros PP, Chalfant CE, Shultz MD (2012) Metallofullerene-nanoplatform-delivered interstitial brachytherapy improved survival in a murine model of glioblastoma multiforme. Bioconjug Chem 23:1873
21. Ross RB, Cardona CM, Guldi DM, Sankaranarayanan SG, Reese MO, Kopidakis N, Peet J, Walker B, Bazan GC, Van Keuren E, Holloway BC, Drees M (2009) Endohedral fullerenes for organic photovoltaic devices. Nat Mater 8:208
22. Pinzón JR, Plonska-Brzezinska ME, Cardona CM, Athans AJ, Gayathri SS, Guldi DM, Herranz MÁ, Martín N, Torres T, Echegoyen L (2008) Sc_3N@C_{80}-ferrocene electron-donor/acceptor conjugates as promising materials for photovoltaic applications. Angew Chem Int Ed 47:4173
23. Pinzón JR, Gasca DC, Sankaranarayanan SG, Bottari G, Torres T, Guldi DM, Echegoyen L (2009) Photoinduced charge transfer and electrochemical properties of triphenylamine I_h-Sc_3N@C_{80} donor−acceptor conjugates. J Am Chem Soc 131:7727

24. Wolfrum S, Pinzón JR, Molina-Ontoria A, Gouloumis A, Martín N, Echegoyen L, Guldi DM (2011) Utilization of $Sc_3N@C_{80}$ in long-range charge transfer reactions. Chem Commun 47:2270
25. Takano Y, Herranz MÁ, Martín N, Radhakrishnan SG, Guldi DM, Tsuchiya T, Nagase S, Akasaka T (2010) Donor−acceptor conjugates of lanthanum endohedral metallofullerene and π-extended tetrathiafulvalene. J Am Chem Soc 132:8048
26. Guldi DM, Feng L, Radhakrishnan SG, Nikawa H, Yamada M, Mizorogi N, Tsuchiya T, Akasaka T, Nagase S, Ángeles Herranz M, Martín N (2010) A molecular $Ce_2@I_h$-C_{80} switch—unprecedented oxidative pathway in photoinduced charge transfer reactivity. J Am Chem Soc 132:9078
27. Akasaka T, Kato T, Kobayashi K, Nagase S, Yamamoto K, Funasaka H, Takahashi T (1995) Exohedral adducts of $La@C_{82}$. Nature 374:600
28. Cardona CM, Kitaygorodskiy A, Echegoyen L (2005) Trimetallic nitride endohedral metallofullerenes: reactivity dictated by the encapsulated metal cluster. J Am Chem Soc 127:10448
29. Lukoyanova O, Cardona CM, Rivera J, Lugo-Morales LZ, Chancellor CJ, Olmstead M M, Rodríguez-Fortea A, Poblet JM, Balch AL, Echegoyen L (2007) "Open rather than closed" malonate methano-fullerene derivatives. The formation of methanofulleroid adducts of $Y_3N@C_{80}$. J Am Chem Soc 129:10423
30. Zhiguo Z, Jing Z, Sadler R, Jianzhong Y, Coleman A (2007) Synthesis of trimetasphere pyrrolidino derivatives: reaction of $Lu_3N@C_{80}$ with N-ethylglycine in the presence and absence of aldehyde. ECS Trans 2:103
31. Pinzón JR, Zuo T, Echegoyen L (2010) Synthesis and electrochemical studies of Bingel-Hirsch derivatives of $M_3N@I_h$-C_{80} (M=Sc, Lu). Chem Eur J 16:4864
32. Yang S, Chen C, Li X, Wei T, Liu F, Wang S (2013) Bingel–Hirsch monoadducts of $TiSc_2N@I_h$-C_{80} versus $Sc_3N@I_h$-C_{80}: reactivity improvement via internal metal atom substitution. Chem Commun 49:10844
33. Wang S, Huang J, Gao C, Jin F, Li Q, Xie S, Yang S (2016) Singly bonded monoadduct rather than methanofullerene: manipulating the addition pattern of trimetallic nitride clusterfullerene through one endohedral metal atom substitution. Chem Eur J 22:8309
34. Garcia-Borràs M, Cerón MR, Osuna S, Izquierdo M, Luis JM, Echegoyen L, Solà M (2016) The regioselectivity of Bingel–Hirsch cycloadditions on isolated pentagon rule endohedral metallofullerenes. Angew Chem Int Ed 55:2374
35. Feng L, Nakahodo T, Wakahara T, Tsuchiya T, Maeda Y, Akasaka T, Kato T, Horn E, Yoza K, Mizorogi N, Nagase S (2005) A singly bonded derivative of endohedral metallofullerene: $La@C_{82}CBr(COOC_2H_5)_2$. J Am Chem Soc 127:17136
36. Feng L, Wakahara T, Nakahodo T, Tsuchiya T, Piao Q, Maeda Y, Lian Y, Akasaka T, Horn E, Yoza K, Kato T, Mizorogi N, Nagase S (2006) The Bingel monoadducts of $La@C_{82}$: synthesis, characterization, and electrochemistry. Chem Eur J 12:5578
37. Feng L, Tsuchiya T, Wakahara T, Nakahodo T, Piao Q, Maeda Y, Akasaka T, Kato T, Yoza K, Horn E, Mizorogi N, Nagase S (2006) Synthesis and characterization of a bisadduct of $La@C_{82}$. J Am Chem Soc 128:5990
38. Chaur MN, Melin F, Athans AJ, Elliott B, Walker K, Holloway BC, Echegoyen L (2008) The influence of cage size on the reactivity of trimetallic nitride metallofullerenes: a mono- and bis-methanoadduct of $Gd_3N@C_{80}$ and a monoadduct of $Gd_3N@C_{84}$. Chem Commun 2665
39. Cai T, Xu L, Shu C, Reid JE, Gibson HW, Dorn HC (2008) Synthesis and characterization of a non-IPR fullerene derivative: $Sc_3N@C_{68}[C(COOC_2H_5)_2]$. J Phys Chem C 112:19203
40. Cai T, Xu L, Shu C, Champion HA, Reid JE, Anklin C, Anderson MR, Gibson HW, Dorn HC (2008) Selective formation of a symmetric $Sc_3N@C_{78}$ bisadduct: adduct docking controlled by an internal trimetallic nitride cluster. J Am Chem Soc 130:2136
41. Hu Y, Solé-Daura A, Yao Y-R, Liu X, Liu S, Yu A, Peng P, Poblet JM, Rodríguez-Fortea A, Echegoyen L, Li F-F (2020) Chemical reactions of cationic metallofullerenes: an alternative route for exohedral functionalization. Chem Eur J 26:1748

42. Alegret N, RodrÍguez-Fortea A, Poblet JM (2013) Bingel-Hirsch addition on endohedral metallofullerenes: kinetic versus thermodynamic control. Chem Eur J 19:5061
43. Lu X, Xu J, He X, Shi Z, Gu Z (2004) Addition of benzyne to Gd@C_{82}. Chem Mater 16:953
44. Lu X, Nikawa H, Tsuchiya T, Akasaka T, Toki M, Sawa H, Mizorogi N, Nagase S (2010) Nitrated benzyne derivatives of La@C_{82}: addition of NO_2 and its positional directing effect on the subsequent addition of benzynes. Angew Chem Int Ed 49:594
45. Li F-F, Pinzón JR, Mercado BQ, Olmstead MM, Balch AL, Echegoyen L (2011) [2 + 2] cycloaddition reaction to $Sc_3N@I_h$-C_{80}. The formation of very stable [5,6]- and [6,6]-adducts. J Am Chem Soc 133:1563
46. Wang G-W, Liu T-X, Jiao M, Wang N, Zhu S-E, Chen C, Yang S, Bowles FL, Beavers CM, Olmstead MM, Mercado BQ, Balch AL (2011) The cycloaddition reaction of I_h-$Sc_3N@C_{80}$ with 2-Amino-4,5-diisopropoxybenzoic acid and isoamyl nitrite to produce an open-cage metallofullerene. Angew Chem Int Ed 50:4658
47. Cai T, Ge Z, Iezzi EB, Glass TE, Harich K, Gibson HW, Dorn HC (2005) Synthesis and characterization of the first trimetallic nitride templated pyrrolidino endohedral metallofullerenes. Chem Commun 3594
48. Cardona CM, Kitaygorodskiy A, Ortiz A, Herranz MÁ, Echegoyen L (2005) The first fulleropyrrolidine derivative of $Sc_3N@C_{80}$: pronounced chemical shift differences of the geminal protons on the pyrrolidine ring. J Org Chem 70:5092
49. Martín N, Altable M, Filippone S, Martín-Domenech A, Echegoyen L, Cardona CM (2006) Retro-cycloaddition reaction of pyrrolidinofullerenes. Angew Chem Int Ed 45:110
50. Cardona CM, Elliott B, Echegoyen L (2006) Unexpected chemical and electrochemical properties of $M_3N@C_{80}$ (M = Sc, Y, Er). J Am Chem Soc 128:6480
51. Chen N, Zhang E-Y, Tan K, Wang C-R, Lu X (2007) Size effect of encaged clusters on the exohedral chemistry of endohedral fullerenes: a case study on the pyrrolidino reaction of $Sc_xGd_{3-x}N@C_{80}$ ($x = 0-3$). Org Lett 9:2011
52. Chen N, Fan L-Z, Tan K, Wu Y-Q, Shu C-Y, Lu X, Wang C-R (2007) Comparative spectroscopic and reactivity studies of $Sc_{3-x}Y_xN@C_{80}$ ($x = 0-3$). J Phys Chem C 111:11823
53. Rodríguez-Fortea A, Campanera JM, Cardona CM, Echegoyen L, Poblet JM (2006) Dancing on a fullerene surface: isomerization of $Y_3N@$(N-ethylpyrrolidino-C_{80}) from the 6,6 to the 5,6 regioisomer. Angew Chem Int Ed 45:8176
54. Aroua S, Yamakoshi Y (2012) Prato reaction of $M_3N@I_h$-C_{80} (M = Sc, Lu, Y, Gd) with reversible isomerization. J Am Chem Soc 134:20242
55. Aroua S, Garcia-Borràs M, Bölter MF, Osuna S, Yamakoshi Y (2015) Endohedral metal-induced regioselective formation of bis-Prato adduct of $Y_3N@I_h$-C_{80} and $Gd_3N@I_h$-C_{80}. J Am Chem Soc 137:58
56. Semivrazhskaya O, Aroua S, Yulikov M, Romero-Rivera A, Stevenson S, Garcia-Borràs M, Osuna S, Yamakoshi Y (2020) Endohedral metal-induced regioselective formation of bis-Prato adduct of $Y_3N@I_h$-C_{80} and $Gd_3N@I_h$-C_{80}. J Am Chem Soc 142:12954
57. Cai T, Slebodnick C, Xu L, Harich K, Glass TE, Chancellor C, Fettinger JC, Olmstead MM, Balch AL, Gibson HW, Dorn HC (2006) A pirouette on a metallofullerene sphere: interconversion of isomers of N-tritylpyrrolidino I_h $Sc_3N@C_{80}$. J Am Chem Soc 128:6486
58. Maeda Y, Kimura M, Ueda C, Yamada M, Kikuchi T, Suzuki M, Wang W-W, Mizorogi N, Karousis N, Tagmatarchis N, Hasegawa T, Olmstead MM, Balch AL, Nagase S, Akasaka T (2014) Isolation and characterization of [5,6]-pyrrolidino-$Sc_3N@I_h$-C_{80} diastereomers. Chem Commun 50:12552
59. Bao L, Chen M, Shen W, Pan C, Ghiassi KB, Olmstead MM, Balch AL, Akasaka T, Lu X (2016) Regioselective synthesis and crystallographic characterization of isoxazoline-ring-fused derivatives of $Sc_3N@I_h$-C_{80} and C_{60}. Inorg Chem 55:4075
60. Cai T, Xu L, Anderson MR, Ge Z, Zuo T, Wang X, Olmstead MM, Balch AL, Gibson HW, Dorn HC (2006) Structure and enhanced reactivity rates of the D_{5h} $Sc_3N@C_{80}$ and $Lu_3N@C_{80}$ metallofullerene isomers: the importance of the pyracylene motif. J Am Chem Soc 128:8581

61. Lu X, Nakajima K, Iiduka Y, Nikawa H, Mizorogi N, Slanina Z, Tsuchiya T, Nagase S, Akasaka T (2011) Structural elucidation and regioselective functionalization of an unexplored carbide cluster metallofullerene $Sc_2C_2@C_s(6)$-C_{82}. J Am Chem Soc 133:19553
62. Lu X, Nakajima K, Iiduka Y, Nikawa H, Tsuchiya T, Mizorogi N, Slanina Z, Nagase S, Akasaka T (2012) The long-believed $Sc_2@C_{2v}(17)$-C_{84} is actually $Sc_2C_2@C_{2v}(9)$-C_{82}: unambiguous structure assignment and chemical functionalization. Angew Chem Int Ed 51:5889
63. Wang T, Wu J, Xu W, Xiang J, Lu X, Li B, Jiang L, Shu C, Wang C (2010) Spin divergence induced by exohedral modification: ESR study of $Sc_3C_2@C_{80}$ fulleropyrrolidine. Angew Chem Int Ed 49:1786
64. Cao B, Wakahara T, Maeda Y, Han A, Akasaka T, Kato T, Kobayashi K, Nagase S (2004) Lanthanum endohedral metallofulleropyrrolidines: synthesis, isolation, and EPR characterization. Chem Eur J 10:716
65. Takano Y, Obuchi S, Mizorogi N, García R, Herranz MÁ, Rudolf M, Wolfrum S, Guldi DM, Martín N, Nagase S, Akasaka T (2012) Stabilizing ion and radical ion pair states in a paramagnetic endohedral metallofullerene/π-extended tetrathiafulvalene conjugate. J Am Chem Soc 134:16103
66. Tsuchiya T, Rudolf M, Wolfrum S, Radhakrishnan SG, Aoyama R, Yokosawa Y, Oshima A, Akasaka T, Nagase S, Guldi DM (2013) Coordinative interactions between porphyrins and C_{60}, $La@C_{82}$, and $La_2@C_{80}$. Chem Eur J 19:558
67. Feng L, Lu X, He X, Shi Z, Gu Z (2004) Reactions of endohedral metallofullerenes with azomethine ylides: an efficient route toward metallofullerene-pyrrolidines. Inorg Chem Commun 7:1010
68. Lu X, He X, Feng L, Shi Z, Gu Z (2004) Synthesis of pyrrolidine ring-fused metallofullerene derivatives. Tetrahedron 60:3713
69. Sawai K, Takano Y, Izquierdo M, Filippone S, Martín N, Slanina Z, Mizorogi N, Waelchli M, Tsuchiya T, Akasaka T, Nagase S (2011) Enantioselective synthesis of endohedral metallofullerenes. J Am Chem Soc 133:17746
70. Yamada M, Wakahara T, Nakahodo T, Tsuchiya T, Maeda Y, Akasaka T, Yoza K, Horn E, Mizorogi N, Nagase S (2006) Synthesis and structural characterization of endohedral pyrrolidinodimetallofullerene: $La_2@C_{80}(CH_2)_2NTrt$. J Am Chem Soc 128:1402
71. Yamada M, Okamura M, Sato S, Someya CI, Mizorogi N, Tsuchiya T, Akasaka T, Kato T, Nagase S (2009) Two regioisomers of endohedral pyrrolidinodimetallofullerenes $M_2@I_h$-$C_{80}(CH_2)_2NTrt$ (M=La, Ce; Trt=trityl): control of metal atom positions by addition positions. Chem Eur J 15:10533
72. Ma Y, Wang T, Wu J, Feng Y, Jiang L, Shu C, Wang C (2012) Susceptible electron spin adhering to an yttrium cluster inside an azafullerene $C_{79}N$. Chem Commun 48:11570
73. Wei T, Martin O, Yang S, Hauke F, Hirsch A (2019) Modular covalent graphene functionalization with C_{60} and the endohedral fullerene $Sc_3N@C_{80}$: a facile entry to synthetic-carbon-allotrope hybrids. Angew Chem Int Ed 58:816
74. Wei T, Martin O, Chen M, Yang S, Hauke F, Hirsch A (2019) Covalent inter-carbon-allotrope architectures consisting of the endohedral fullerene $Sc_3N@C_{80}$ and single-walled carbon nanotubes. Angew Chem Int Ed 58:8058
75. Akasaka T, Nagase S, Kobayashi K, Suzuki T, Kato T, Yamamoto K, Funasaka H, Takahashi T (1995) Exohedral derivatization of an endohedral metallofullerene $Gd@C_{82}$. Chem Commun 1343
76. Kato T, Akasaka T, Kobayashi K, Nagase S, Yamamoto K, Funasaka H, Takahashi T (1996) ESR study on the reactivity of two isomers of LaC_{82} with disilirane. Appl Magn Reson 11:293
77. Akasaka T, Okubo S, Kondo M, Maeda Y, Wakahara T, Kato T, Suzuki T, Yamamoto K, Kobayashi K, Nagase S (2000) Isolation and characterization of two $Pr@C_{82}$ isomers. Chem Phys Lett 319:153

78. Yamada M, Feng L, Wakahara T, Tsuchiya T, Maeda Y, Lian Y, Kako M, Akasaka T, Kato T, Kobayashi K, Nagase S (2005) Synthesis and characterization of exohedrally silylated M@C_{82} (M = Y and La). J Phys Chem B 109:6049
79. Maeda Y, Miyashita J, Hasegawa T, Wakahara T, Tsuchiya T, Feng L, Lian Y, Akasaka T, Kobayashi K, Nagase S, Kako M, Yamamoto K, Kadish KM (2005) Chemical reactivities of the cation and anion of M@C_{82} (M = Y, La, and Ce). J Am Chem Soc 127:2143
80. Akasaka T, Nagase S, Kobayashi K, Suzuki T, Kato T, Kikuchi K, Achiba Y, Yamamoto K, Funasaka H, Takahashi T (1995) Synthesis of the first adducts of the dimetallofullerenes La_2@C_{80} and Sc_2@C_{84} by addition of a disilirane. Angew Chem Int Ed 34:2139
81. Wakahara T, Yamada M, Takahashi S, Nakahodo T, Tsuchiya T, Maeda Y, Akasaka T, Kako M, Yoza K, Horn E, Mizorogi N, Nagase S (2007) Two-dimensional hopping motion of encapsulated La atoms in silylated La_2@C_{80}. Chem Commun 2680
82. Yamada M, Nakahodo T, Wakahara T, Tsuchiya T, Maeda Y, Akasaka T, Kako M, Yoza K, Horn E, Mizorogi N, Kobayashi K, Nagase S (2005) Positional control of encapsulated atoms inside a fullerene cage by exohedral addition. J Am Chem Soc 127:14570
83. Yamada M, Mizorogi N, Tsuchiya T, Akasaka T, Nagase S (2009) Synthesis and characterization of the D_{5h} isomer of the endohedral dimetallofullerene Ce_2@C_{80}: two-dimensional circulation of encapsulated metal atoms inside a fullerene cage. Chem Eur J 15:9486
84. Yamada M, Wakahara T, Tsuchiya T, Maeda Y, Kako M, Akasaka T, Yoza K, Horn E, Mizorogi N, Nagase S (2008) Location of the metal atoms in Ce_2@C_{78} and its bis-silylated derivative. Chem Commun 558
85. Wakahara T, Sakuraba A, Iiduka Y, Okamura M, Tsuchiya T, Maeda Y, Akasaka T, Okubo S, Kato T, Kobayashi K, Nagase S, Kadish KM (2004) Chemical reactivity and redox property of Sc_3@C_{82}. Chem Phys Lett 398:553
86. Iiduka Y, Ikenaga O, Sakuraba A, Wakahara T, Tsuchiya T, Maeda Y, Nakahodo T, Akasaka T, Kako M, Mizorogi N, Nagase S (2005) Chemical reactivity of Sc_3N@C_{80} and La_2@C_{80}. J Am Chem Soc 127:9956
87. Wakahara T, Iiduka Y, Ikenaga O, Nakahodo T, Sakuraba A, Tsuchiya T, Maeda Y, Kako M, Akasaka T, Yoza K, Horn E, Mizorogi N, Nagase S (2006) Characterization of the bis-silylated endofullerene Sc_3N@C_{80}. J Am Chem Soc 128:9919
88. Sato K, Kako M, Mizorogi N, Tsuchiya T, Akasaka T, Nagase S (2012) Bis-silylation of Lu_3N@I_h-C_{80}: considerable variation in the electronic structures. Org Lett 14:5908
89. Yamada M, Minowa M, Sato S, Kako M, Slanina Z, Mizorogi N, Tsuchiya T, Maeda Y, Nagase S, Akasaka T (2010) Thermal carbosilylation of endohedral dimetallofullerene La_2@I_h-C_{80} with silirane. J Am Chem Soc 132:17953
90. Kako M, Sugiura T, Miyabe K, Yasui M, Yamada M, Maeda Y, Guo J-D, Nagase S, Akasaka T (2017) Preparation, structural determination, and characterization of electronic properties of [5,6]- and [6,6]-carbosilylated Sc_3N@I_h-C_{80}. Chem Asian J 12:1391
91. Iezzi EB, Duchamp JC, Harich K, Glass TE, Lee HM, Olmstead MM, Balch AL, Dorn HC (2002) A symmetric derivative of the trimetallic nitride endohedral metallofullerene, Sc_3N@C_{80}. J Am Chem Soc 124:524
92. Lee HM, Olmstead MM, Iezzi E, Duchamp JC, Dorn HC, Balch AL (2002) Crystallographic characterization and structural analysis of the first organic functionalization product of the endohedral fullerene Sc_3N@C_{80}. J Am Chem Soc 124:3494
93. Stevenson S, Stephen RR, Amos TM, Cadorette VR, Reid JE, Phillips JP (2005) Synthesis and purification of a metallic nitride fullerene bisadduct: exploring the reactivity of Gd_3N@C_{80}. J Am Chem Soc 127:12776
94. Maeda Y, Sato S, Inada K, Nikawa H, Yamada M, Mizorogi N, Hasegawa T, Tsuchiya T, Akasaka T, Kato T, Slanina Z, Nagase S (2010) Regioselective exohedral functionalization of La@C_{82} and its 1,2,3,4,5-pentamethylcyclopentadiene and adamantylidene adducts. Chem Eur J 16:2193

95. Fu W, Zhang J, Fuhrer T, Champion H, Furukawa K, Kato T, Mahaney JE, Burke BG, Williams KA, Walker K, Dixon C, Ge J, Shu C, Harich K, Dorn HC (2011) $Gd_2@C_{79}N$: isolation, characterization, and monoadduct formation of a very stable heterofullerene with a magnetic spin state of S = 15/2. J Am Chem Soc 133:9741
96. Osuna S, Swart M, Campanera JM, Poblet JM, Solà M (2008) Chemical reactivity of D_{3h} C_{78} (metallo)fullerene: regioselectivity changes induced by Sc_3N encapsulation. J Am Chem Soc 130:6206
97. Maeda Y, Matsunaga Y, Wakahara T, Takahashi S, Tsuchiya T, Ishitsuka MO, Hasegawa T, Akasaka T, Liu MTH, Kokura K, Horn E, Yoza K, Kato T, Okubo S, Kobayashi K, Nagase S, Yamamoto K (2004) Isolation and characterization of a carbene derivative of $La@C_{82}$. J Am Chem Soc 126:6858
98. Akasaka T, Kono T, Takematsu Y, Nikawa H, Nakahodo T, Wakahara T, Ishitsuka MO, Tsuchiya T, Maeda Y, Liu MTH, Yoza K, Kato T, Yamamoto K, Mizorogi N, Slanina Z, Nagase S (2008) Does $Gd@C_{82}$ have an anomalous endohedral structure? Synthesis and single crystal X-ray structure of the carbene adduct. J Am Chem Soc 130:12840
99. Takano Y, Aoyagi M, Yamada M, Nikawa H, Slanina Z, Mizorogi N, Ishitsuka MO, Tsuchiya T, Maeda Y, Akasaka T, Kato T, Nagase S (2009) Anisotropic magnetic behavior of anionic $Ce@C_{82}$ carbene adducts. J Am Chem Soc 131:9340
100. Lu X, Nikawa H, Feng L, Tsuchiya T, Maeda Y, Akasaka T, Mizorogi N, Slanina Z, Nagase S (2009) Location of the yttrium atom in $Y@C_{82}$ and its influence on the reactivity of cage carbons. J Am Chem Soc 131:12066
101. Hachiya M, Nikawa H, Mizorogi N, Tsuchiya T, Lu X, Akasaka T (2012) Exceptional chemical properties of $Sc@C_{2v}(9)$–C_{82} probed with adamantylidene carbene. J Am Chem Soc 134:15550
102. Cao B, Nikawa H, Nakahodo T, Tsuchiya T, Maeda Y, Akasaka T, Sawa H, Slanina Z, Mizorogi N, Nagase S (2008) Addition of adamantylidene to $La_2@C_{78}$: isolation and single-crystal X-ray structural determination of the monoadducts. J Am Chem Soc 130:983
103. Lu X, Nikawa H, Nakahodo T, Tsuchiya T, Ishitsuka MO, Maeda Y, Akasaka T, Toki M, Sawa H, Slanina Z, Mizorogi N, Nagase S (2008) Chemical understanding of a non-IPR metallofullerene: stabilization of encaged metals on fused-pentagon bonds in $La_2@C_{72}$. J Am Chem Soc 130:9129
104. Lu X, Nikawa H, Tsuchiya T, Maeda Y, Ishitsuka MO, Akasaka T, Toki M, Sawa H, Slanina Z, Mizorogi N, Nagase S (2008) Bis-carbene adducts of non-IPR $La_2@C_{72}$: localization of high reactivity around fused pentagons and electrochemical properties. Angew Chem Int Ed 47:8642
105. Yamada M, Someya C, Wakahara T, Tsuchiya T, Maeda Y, Akasaka T, Yoza K, Horn E, Liu MTH, Mizorogi N, Nagase S (2008) Metal atoms collinear with the spiro carbon of 6,6-open adducts, $M_2@C_{80}$(Ad) (M = La and Ce, Ad = adamantylidene). J Am Chem Soc 130:1171
106. Ishitsuka MO, Sano S, Enoki H, Sato S, Nikawa H, Tsuchiya T, Slanina Z, Mizorogi N, Liu MTH, Akasaka T, Nagase S (2011) Regioselective bis-functionalization of endohedral dimetallofullerene, $La_2@C_{80}$: extremal La–La distance. J Am Chem Soc 133:7128
107. Iiduka Y, Wakahara T, Nakahodo T, Tsuchiya T, Sakuraba A, Maeda Y, Akasaka T, Yoza K, Horn E, Kato T, Liu MTH, Mizorogi N, Kobayashi K, Nagase S (2005) Structural determination of metallofullerene Sc_3C_{82} revisited: a surprising finding. J Am Chem Soc 127:12500
108. Iiduka Y, Wakahara T, Nakajima K, Nakahodo T, Tsuchiya T, Maeda Y, Akasaka T, Yoza K, Liu MTH, Mizorogi N, Nagase S (2007) Experimental and theoretical studies of the scandium carbide endohedral metallofullerene $Sc_2C_2@C_{82}$ and its carbene derivative. Angew Chem Int Ed 46:5562
109. Kurihara H, Lu X, Iiduka Y, Mizorogi N, Slanina Z, Tsuchiya T, Akasaka T, Nagase S (2011) $Sc_2C_2@C_{80}$ rather than $Sc_2@C_{82}$: templated formation of unexpected $C_{2v}(5)$-C_{80} and temperature-dependent dynamic motion of internal Sc_2C_2 cluster. J Am Chem Soc 133:2382
110. Kurihara H, Lu X, Iiduka Y, Nikawa H, Mizorogi N, Slanina Z, Tsuchiya T, Nagase S, Akasaka T (2012) Chemical understanding of carbide cluster metallofullerenes: a case study on

$Sc_2C_2@C_{2v}(5)$–C_{80} with complete X-ray crystallographic characterizations. J Am Chem Soc 134:3139
111. Yamada M, Tanabe Y, Dang J-S, Sato S, Mizorogi N, Hachiya M, Suzuki M, Abe T, Kurihara H, Maeda Y, Zhao X, Lian Y, Nagase S, Akasaka T (2016) $D_{2d}(23)$-C_{84} versus $Sc_2C_2@D_{2d}(23)$-C_{84}: impact of endohedral Sc_2C_2 doping on chemical reactivity in the photolysis of diazirine. J Am Chem Soc 138:16523
112. Sato K, Kako M, Suzuki M, Mizorogi N, Tsuchiya T, Olmstead MM, Balch AL, Akasaka T, Nagase S (2012) Synthesis of silylene-bridged endohedral metallofullerene $Lu_3N@I_h$-C_{80}. J Am Chem Soc 134:16033
113. Izquierdo M, Cerón MR, Olmstead MM, Balch AL, Echegoyen L (2013) [5,6]-open methanofullerene derivatives of I_h-C_{80}. Angew Chem Int Ed 52:11826
114. Yamada M, Abe T, Saito C, Yamazaki T, Sato S, Mizorogi N, Slanina Z, Uhlík F, Suzuki M, Maeda Y, Lian Y, Lu X, Olmstead MM, Balch AL, Nagase S, Akasaka T (2017) Adamantylidene addition to $M_3N@I_h$-C_{80} (M=Sc, Lu) and $Sc_3N@D_{5h}$-C_{80}: synthesis and crystallographic characterization of the [5,6]-open and [6,6]-open adducts. Chem Eur J 23:6552
115. Chen M, Bao L, Ai M, Shen W, Lu X (2016) $Sc_3N@I_h$-C_{80} as a novel Lewis acid to trap abnormal N-heterocyclic carbenes: the unprecedented formation of a singly bonded [6,6,6]-adduct. Chem Sci 7:2331
116. Chen M, Shen W, Peng P, Bao L, Zhao S, Xie Y, Jin P, Fang H, Li F-F, Lu X (2017) Evidence of oxygen activation in the reaction between an N-heterocyclic carbene and $M_3N@I_h(7)$–C_{80}: an unexpected method of steric hindrance release. J Org Chem 82:3500
117. Nikawa H, Kikuchi T, Wakahara T, Nakahodo T, Tsuchiya T, Rahman GMA, Akasaka T, Maeda Y, Yoza K, Horn E, Yamamoto K, Mizorogi N, Nagase S (2005) Missing metallofullerene $La@C_{74}$. J Am Chem Soc 127:9684
118. Lu X, Nikawa H, Kikuchi T, Mizorogi N, Slanina Z, Tsuchiya T, Nagase S, Akasaka T (2011) Radical derivatives of insoluble $La@C_{74}$: X-ray structures, metal positions, and isomerization. Angew Chem Int Ed 50:6356
119. Wakahara T, Nikawa H, Kikuchi T, Nakahodo T, Rahman GMA, Tsuchiya T, Maeda Y, Akasaka T, Yoza K, Horn E, Yamamoto K, Mizorogi N, Slanina Z, Nagase S (2006) $La@C_{72}$ having a non-IPR carbon cage. J Am Chem Soc 128:14228
120. Nikawa H, Yamada T, Cao B, Mizorogi N, Slanina Z, Tsuchiya T, Akasaka T, Yoza K, Nagase S (2009) Missing metallofullerene with C_{80} cage. J Am Chem Soc 131:10950
121. Akasaka T, Lu X, Kuga H, Nikawa H, Mizorogi N, Slanina Z, Tsuchiya T, Yoza K, Nagase S (2010) Dichlorophenyl derivatives of $La@C_{3v}(7)$-C_{82}: endohedral metal induced localization of pyramidalization and spin on a triple-hexagon junction. Angew Chem Int Ed 49:9715
122. Takano Y, Yomogida A, Nikawa H, Yamada M, Wakahara T, Tsuchiya T, Ishitsuka MO, Maeda Y, Akasaka T, Kato T, Slanina Z, Mizorogi N, Nagase S (2008) Radical coupling reaction of paramagnetic endohedral metallofullerene $La@C_{82}$. J Am Chem Soc 130:16224
123. Fang H, Cong H, Suzuki M, Bao L, Yu B, Xie Y, Mizorogi N, Olmstead MM, Balch AL, Nagase S, Akasaka T, Lu X (2014) Regioselective benzyl radical addition to an open-shell cluster metallofullerene. Crystallographic studies of cocrystallized $Sc_3C_2@I_h$-C_{80} and its singly bonded derivative. J Am Chem Soc 136:10534
124. Shu C, Slebodnick C, Xu L, Champion H, Fuhrer T, Cai T, Reid JE, Fu W, Harich K, Dorn HC, Gibson HW (2008) Highly regioselective derivatization of trimetallic nitride templated endohedral metallofullerenes via a facile photochemical reaction. J Am Chem Soc 130:17755
125. Bao L, Chen M, Pan C, Yamaguchi T, Kato T, Olmstead M, Balch A, Akasaka T, Xing L (2016) Crystallographic evidence for direct metal-metal bonding in a stable open-shell $La_2@I_h$-C_{80} derivative. Angew Chem Int Ed 55:4242
126. Kareev IE, Lebedkin SF, Bubnov VP, Yagubskii EB, Ioffe IN, Khavrel PA, Kuvychko IV, Strauss SH, Boltalina OV (2005) Trifluoromethylated endohedral metallofullerenes: synthesis and characterization of $Y@C_{82}(CF_3)_5$. Angew Chem Int Ed 44:1846

127. Kareev IE, Bubnov VP, Yagubskii EB (2008) Endohedral gadolinium-containing metallofullerenes in the trifluoromethylation reaction. Russ Chem Bull 57:1486
128. Shustova NB, Popov AA, Mackey MA, Coumbe CE, Phillips JP, Stevenson S, Strauss SH, Boltalina OV (2007) Radical trifluoromethylation of $Sc_3N@C_{80}$. J Am Chem Soc 129:11676
129. Shustova NB, Peryshkov DV, Kuvychko IV, Chen Y-S, Mackey MA, Coumbe CE, Heaps DT, Confait BS, Heine T, Phillips JP, Stevenson S, Dunsch L, Popov AA, Strauss SH, Boltalina OV (2011) Poly(perfluoroalkylation) of metallic nitride fullerenes reveals addition-pattern guidelines: synthesis and characterization of a family of $Sc_3N@C_{80}(CF_3)_n$ ($_n$ = 2−16) and their radical anions. J Am Chem Soc 133:2672
130. Yang S, Chen C, Jiao M, Tamm NB, Lanskikh MA, Kemnitz E, Troyanov SI (2011) Synthesis, isolation, and addition patterns of trifluoromethylated D_{5h} and I_h isomers of $Sc_3N@C_{80}$: $Sc_3N@D_{5h}$-$C_{80}(CF_3)_{18}$ and$Sc_3N@I_h$-$C_{80}(CF_3)_{14}$. Inorg Chem 50:3766
131. Wei T, Tamm NB, Yang S, Troyanov SI (2014) New trifluoromethylated derivatives of metal nitride clusterfullerenes: $Sc_3N@I_h$-$C_{80}(CF_3)_{14}$ and $Sc_3N@D_{5h}$-$C_{80}(CF_3)_{16}$. Chem Asian J 9:2449
132. Chen C-H, Yeh W-Y, Liu Y-H, Lee G-H (2012) [$(\mu\text{-H})_3Re_3(CO)_9(\eta^2,\eta^2,\eta^2\text{-}Sc_2C_2@C_{3v}(8)\text{-}C_{82})$]: face-capping cluster complex of an endohedral fullerene. Angew Chem Int Ed 51:13046
133. Watanabe T, Itoh MF, Komuro T, Okada H, Sakai T, Ono Y, Kawachi K, Kasama Y, Tobita H (2014) Iridium and platinum complexes of $Li^+@C_{60}$. Organometallics 33:608
134. Bao L, Liu B, Li X, Pan C, Xie Y, Lu X (2016) $W(CO)_3(Ph_2PC_2H_4PPh_2)(\eta^2\text{-}Sc_3N@I_h\text{-}C_{80}/Sc_3N@D_{5h}\text{-}C_{80})$: regioselective synthesis and crystallographic characterization of air-stable mononuclear complexes of endohedral fullerenes. Dalton Trans 45:11606
135. Xie Y-P, Pan C, Bao L, Slanina Z, Akasaka T, Lu X (2019) Regioselective coordination of $Re_2(CO)_{10}$ to $Y@C_{2v}(9)$-C_{82}: an unprecedented η^1 complex stabilized by intramolecular electron transfer. Organometallics 38:2259
136. Li F-F, RodrÍguez-Fortea A, Poblet JM, Echegoyen L (2011) Reactivity of metallic nitride endohedral metallofullerene anions: electrochemical synthesis of a $Lu_3N@I_h$-C_{80} derivative. J Am Chem Soc 133:2760
137. Li F-F, RodrÍguez-Fortea A, Peng P, Campos Chavez GA, Poblet JM, Echegoyen L (2012) Electrosynthesis of a $Sc_3N@I_h$-C_{80} methano derivative from trianionic $Sc_3N@I_h$-C_{80}. J Am Chem Soc 134:7480

Endohedral Nitrogen Fullerenes

20

Shen Zhou and Kyriakos Porfyrakis

Contents

Abstract

There is a remarkable molecule that can be said to be nature's atomic trap. This molecule is called an endohedral nitrogen fullerene. Endohedral nitrogen fullerenes (ENFs) and related molecules are the subject of this chapter. Endohedral

S. Zhou
School of Chemistry and Chemical Engineering, South China University of Technology, Guangzhou, China

College of Aerospace Science and Engineering, National University of Defence Technology, Changsha, China
e-mail: zhoushen@nudt.edu.cn

K. Porfyrakis (✉)
School of Engineering, University of Greenwich, Kent, UK
e-mail: k.porfyrakis@greenwich.ac.uk

X. Lu et al. (eds.), *Handbook of Fullerene Science and Technology*,
https://doi.org/10.1007/978-981-16-8994-9_30

fullerenes were discovered almost as soon as their empty-cage equivalents. However, ENFs were only available for studies more than a decade after the discovery of fullerenes. A number of endohedral metallofullerenes have been made in significant amounts. However, there are only a handful of ENFs studied to date. ENFs are remarkable for another reason too. Nitrogen is one of the most reactive elements known to science. This is somewhat concealed by the relative inertness of the nitrogen molecule. The nitrogen-nitrogen triple bond is after all one of the strongest bonds in the universe. However atomic nitrogen retains its high reactivity. So how come atomic nitrogen is stable inside a fullerene molecule? Well, it turns out the nitrogen wave function just about "fits snugly" inside the fullerene cage. This chapter describes the different methods of production of ENFs. The properties and chemical functionalization of ENFs are also explored with the aim to summarize progress made towards applications. There is still some way to go before ENFs can be used in real-life applications. This chapter describes what progress has been made and what challenges lay ahead before nature's atomic traps find their way in commercially available products.

Keywords

Fullerenes · Endohedral fullerenes · ENF · Functionalization · Electron spin · Relaxation times · Quantum computing · Atomic clocks

Introduction

Endohedral nitrogen fullerene (ENF) is normally denoted as $N@C_{60}$ or $N@C_{70}$ ($P@C_{60}$ is also added in this group as phosphorous is in the same group as nitrogen) depending on the size of the fullerene cage and the nitrogen element encapsulated. Originated from Greek ἔνδον ("endon" – within) and ἕδρα ("hedra" – face of a geometrical figure), the word "endohedral" vividly describes the core-shell configuration of this type of fullerene molecules. Considering the sub-nano-sized hollow structure of a pristine fullerene, scientists have been trying to make use of the inner space by putting atomic species inside the cage. Metal ions and metal containing clusters turned out to be the most widely studied encapsulated species. Due to the electronegativity difference between metal and carbon elements, electron transfer commonly takes place from the endohedral metallocluster to the carbon cage. Hence, the properties of fullerene cage and endohedral cluster are significantly correlated, and researchers can utilize the metal cluster as a path to tune the electrical and optical behavior of fullerene for applications such as electronics and photovoltaics.

Having the similar geomatic configuration to endohedral metallofullerenes, ENFs, on the other hand, are quite unique. There is negligible chemical interaction between the carbon cage and the encapsulated nitrogen atom. It is not preferred in the perspective of tuning the properties of fullerene; but in terms of obtaining undisturbed atomic properties of the encapsulated species, it would be particularly valuable. As far as chemical approaches are concerned, ENF turned out to be the

only way to obtain atomic nitrogen (and phosphorous) in a solid-state form at room temperature.

While the proper chemical inertness successfully isolates and protects the reactive nitrogen and phosphorous atom in its atomistic ground state of $^4S_{3/2}$, the all-carbon structure of the fullerene cage further provides a magnetically clean environment because the zero-nuclear spin of carbon-12, the predominantly abundant isotope of carbon in nature. Hence, the electron spin ($S = 3/2$) of the atomic nitrogen is also magnetically isolated and protected and further leads to ultra-long spin relaxation times and significant quantum behaviors. In order to obtain similarly long spin relaxation times, inorganic chemists have synthesized coordination compounds with zero-nuclear spin ligand atoms, such as oxygen and sulfur, to magnetically isolate the electron spin located in the central metal ion. As an electron spin container, the high symmetry of fullerene is another useful property. Compared with coordination compounds and defects in crystals, the electron spin in ENF has little anisotropy. Hence, the spin quantum behavior in a powder ensemble can be more homogeneous. Spin relaxation related to zero-field splitting and spin orbital coupling, which demands the symmetry breaking, are less likely to take place.

Based on the aforementioned unique properties, applications such as a molecular qubit for quantum computing and solid-state atomic clocks for portable navigation devices have been proposed. It is worthwhile to systematically study ENF and to develop its synthesis techniques and chemical modification approaches, as well as to understand its electronic and magnetic structures and its spin properties in both time and frequency domains. In this chapter, we will review the discovery and synthesis of ENF and then elucidate the unique spin property of it. Lastly, a variety of chemical functionalization methods of ENF will be summarized.

Discovery of Endohedral Nitrogen Fullerene

The sub-nano-sized hollow structure of fullerene intrigued researchers to put atomistic species inside. Inspired by the successful implantation of noble gas atoms and even a positive muon into fullerenes, a nitrogen ion implantation experiment of fullerene was conducted in 1996, which lead to the discovery of $N@C_{60}$. The low-yielding product was evidenced by X-band EPR (electron paramagnetic resonance) and ENDOR (electron nuclear double resonance) spectra [1]. Later on, a more systematic study on atomic nitrogen encapsulated in fullerenes was reported by altering the exohedral chemical functionalization groups, as well as the enlarged fullerene size [2]. $N@C_{70}$ was readily prepared utilizing the same approach of $N@C_{60}$, and using gas-phase precursors to replace N_2, phosphorous was also tried [3]. Up to now, the successfully synthesized ENFs include $N@C_{60}$, $N@C_{70}$ (and $P@C_{60}$) (Fig. 1a, b), and their chemical derivatives. While the most sensitive and informative characterization technique for ENF is EPR spectroscopy, there has also been mass spectrum evidence of the formation of $N@C_{60}$ [4, 5]. Unfortunately, limited by the extremely low availability of ENF (and to some extent by the poor crystallinity of fullerene), there has no single-crystal XRD experiment that has been

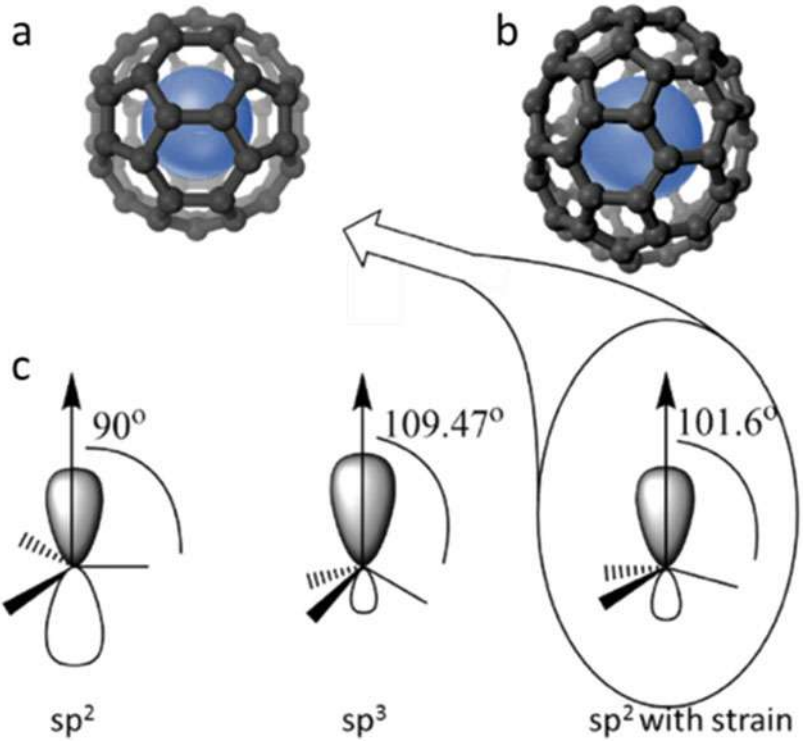

Fig. 1 (**a**, **b**) Molecular models of ENF depending on the size of the fullerene cage. (**c**) Comparison of bond angles in an ideally planar sp^2-hybridized carbon, an ideally tetrahedral sp^3-hybridized carbon, and the distorted sp^2-hybridized carbon in a C_{60} cage.

successfully performed to conclusively define the molecular structure of this new type of fullerene.

Both experimental [6, 7] and theoretical [8, 9] studies point out that ENF, as a new type of endohedral fullerene, has no ionic bond nor covalent bond between the cage and the nitrogen atom, which means the molecule forms a delicate van der Waals core-shelled configuration. The absence of the ionic interaction is due to the electron deficiency of both the fullerene and the nitrogen atom, which prohibits charge transfer between the core and shell. The reason for no covalent interactions lies in the extreme kinetic inertness of the inner surface of the carbon cage. Although all carbons on the cage are near sp^2-hybridized, their bond angles are closer to those of an sp^3 carbon due to the non-planar geometry of the spherical cage surface (Fig. 1c) [10]. Therefore, the formation of an endohedral covalent bond is sterically hindered.

The reason why a reactive nitrogen atom can be stabilized lies in the uncommon van der Waals core-shelled configuration, which prohibits the nitrogen atom kinetically to be released or to react with its surroundings. When the kinetic barrier is overcome by heating or illuminating the sample, decomposition of the endohedral structure of ENF will commence, which has been evidenced by the decay of the

characteristic EPR signal of atomic nitrogen spin. When the size of the fullerene cage is gradually increased, the curvature diminishes, and the tendency of forming an endohedral covalent bond is less sterically hindered. As a result, $N@C_{70}$ has been reported to be less stable than $N@C_{60}$, whereas high fullerenes such as C_{84} have not been reported with the equivalent atomistic endohedral products [3].

Preparation of ENF

Synthesis

Due to the limited thermostability of ENF, it is synthesized ex situ of conventional fullerene formation procedures, in which high temperatures created by laser ablation or electrical arc are generally involved. Namely, all ENFs are obtained by using pre-synthesized fullerene as the starting material and encapsulating a nitrogen or a phosphorous atom afterwards. This section will focus on reviewing the method of nitrogen implantation, since there are more reports about it and phosphorous implantation did not exceed those methods.

There are several techniques applied in the literature to put a nitrogen atom inside a fullerene, which can be categorized into four methods depending on the source of the nitrogen ion (Table 1). The collected fullerene soot after the synthesis procedure is not entirely soluble. The soluble fraction of the fullerene soot contains the desired

Table 1 Features of different methods to perform nitrogen implantation into fullerenes

Method		Starting material per batch	Yield of the crude product	Spin concentration	For phosphorous implantation
Separated ion source and fullerene source	Kaufman ion source implantation [11]	500 mg	200 mg	Up to 60 ppm	Yes, by replacing N_2 with PH_3
	Hall ion source implantation [12]	500 mg	100 ~ 150 mg	200 ppm	No reports
Coupled ion source and fullerene source	Glow discharge plasma implantation [13, 14]	Lack of reports	10 ~ 50 mg	5 ~ 15 ppm	No reports
	Radio frequency coupled plasma implantation [15]	200 mg	1–8 mg	20 ~ 8300 ppm	No reports

ENF, and the spin concentration represents the amount of ENF contained in the crude product. To date, the overall yield is still very low and requires intensive purification procedure afterwards.

All reported methods require an effective sublimation of fullerene so that the implantation can be more effective. Depending on the source of the nitrogen ions, the sublimation system can be either relatively isolated or considerably coupled to the ion generation system. Kaufman ion source implantation [1] and Hall ion source implantation are of the first type (Fig. 2). The synthesis takes place in a vacuum chamber evacuated by pumping system with high speed to sustain the dynamic vacuum of the system (a low pressure is preferred so that the fullerene can sublime more effectively), and the free mean path of the nitrogen ion is sufficient to reach a fullerene molecule from the ion generating spot. An effusion cell is used to sublime fullerene, which is gradually deposited on a water-cooled copper target to form a thin film. A thickness monitor can be used to record and feedback control the fullerene deposition rate. Nitrogen ions generated by a Kaufman ion source or Hall ion source bombard the sublimed fullerene simultaneously. A Kaufman ion source can delicately control the dispersion of ion energy, but the total ion beam current is limited, and thereby it is preferred to align the deposition target with an angle so that both the fullerenes and nitrogen ions can efficiently reach the same deposition target and maximize the utility of the ions. On the other hand, a Hall ion source is more effective in creating large ion beam current but with less energy precision. As a result, it is preferred to avoid a direct ion bombardment on the copper target, on which all products deposits, and only let the ion implantation to take place in the vapor phase, because the large beam current with undesired energy was found to cause the as-prepared ENF to decompose.

Glow discharge plasma implantation and radio frequency coupled plasma implantation synthesize the nitrogen plasma within the fullerene sublimation region. As Fig. 3 (a) shows, the setup for glow discharge plasma implantation is similar to a

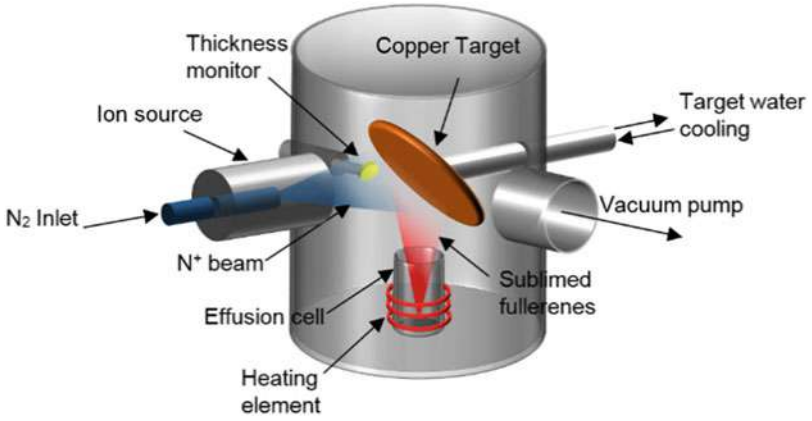

Fig. 2 Experiment setup of nitrogen implantation apparatus using an isolated ion source system such as Kaufman ion source or Hall ion source

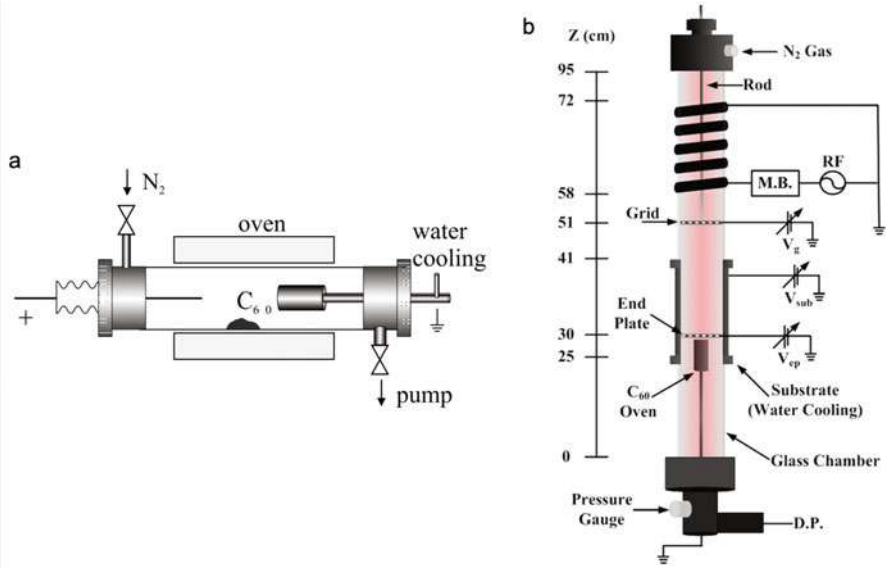

Fig. 3 (**a**) Schematic view of a glow discharge reactor. Figure reproduced from Pietzak, B. et al. [13] (**b**) Schematic view of nitrogen implantation apparatus with RF plasma. (Figure reproduced from Cho. S. C. et al. [15])

luminescence tube. Simultaneous gas inlet and pumping are used to maintain the N_2 atmosphere at a pressure of 0.1 mbar, while C_{60} is vaporized by a tube furnace. The nitrogen plasma is formed by high-voltage ionization of N_2, which subsequently collides with C_{60} to form $N@C_{60}$. The dissociation process of N_2 under a relatively high gas pressure is less efficient; hence, not only $N@C_{60}$ but also $N_2@C_{60}$ is found in the product. To overcome this problem, radio frequency (RF) plasma implantation demonstrated in Fig. 3 (b) was implemented [16, 17]. The nitrogen ions are created from nitrogen gas by a radio frequency plasma generator and are then mixed with sublimated C_{60} within the electric field region. The introduction of RF, which triggers a Lorentz force on the charged particles and changes their trajectories to a coil shape, significantly improves the probability of collision between nitrogen ions and fullerene cages. Thus, the spin yield was reported to be better than an ordinary plasma method, after some fine-tuning of the chamber pressure, grid voltage, and oven temperature.

Comparing these methods, using an isolated ion source is easy to implement and scale-up, so it is the method of choice to synthesize $N@C_{60}$. Moreover, fullerene in the synthetic system is less likely to decompose. Unfortunately, the spin content in the crude product is difficult to improve further. Coupling the ion generating and fullerene sublimating region is beneficial in design and overhaul the implantation condition, but the harsh ion generating reaction conditions, such as high temperature and high voltage, could decompose the starting material as well as the product much more significantly.

Overall, the synthesis of ENF is a rather specialized topic; currently the low yield caused by insufficient implantation and unavoidable decomposition during the ion bombardment is the main challenge. Research is being undertaken to tackle these two contradictory limiting factors.

Spin Enrichment

Since the synthesized crude product of ENF always contains significant amounts of empty-cage fullerenes, enriching the spin-active species from the crude product is another important topic. Due to their almost identical chemical and physical properties (except for paramagnetism), no effective separation methods were reported other than high-performance liquid chromatography (HPLC). In contrast to ordinary chromatography practices utilizing polarity-induced affinity between the mobile and stationary phases, the current HPLC method for ENF purification is primarily based on the π-π interaction between the analyte and the stationary phase, where polarizability is the most relevant intermolecular force [18–20]. Either pure toluene [6, 7, 21, 22] or a mixture of hexane/toluene [4, 23, 24] has typically been used as the main eluting solvents to effectively dissolve fullerenes. Different types of HPLC columns have been applied to the enrichment of spin, such as PBB [7, 21], BuckyPrep [4, 6, 23, 24], and PYE [4, 7, 22].

The retention time (t_R) ratio between ENF and pristine fullerene is also extremely low ($\alpha = 1.027$ for $N@C_{60}$:C_{60}). These characteristics make HPLC incapable of separating them completely with a single process, so the purification is normally performed in a repetitive manner, which means each preparative HPLC procedure only slightly enriches the spin content. During the initial stages of the preparative HPLC procedure, it is necessary to process large quantities of the mixture and separate some of the empty fullerene cages out of the mixture. As the enrichment proceeds, the sample volume shrinks exponentially, so the later stages of the HPLC procedure work on small quantities of samples. At the low purity stage, external cw-EPR measurements are used to reconstruct the $N@C_{60}$ peak which is not detectable using the HPLC detector [21]. At the high purity stage, researchers have managed to use the HPLC detector signal to directly visualize the $N@C_{60}$ peak within the preparative HPLC spectrum (Fig. 4).

Spin Properties

Spin Hamiltonian

The absence of endohedral chemical bonding and the spherical structure of the cage make the paramagnetic ENF systems similar to an atomic nitrogen or atomic phosphorous, which has three unpaired electrons in the degenerate 2p orbitals in the ground state of $^4S_{3/2}$. The effective spin Hamiltonian of ENF can be written as:

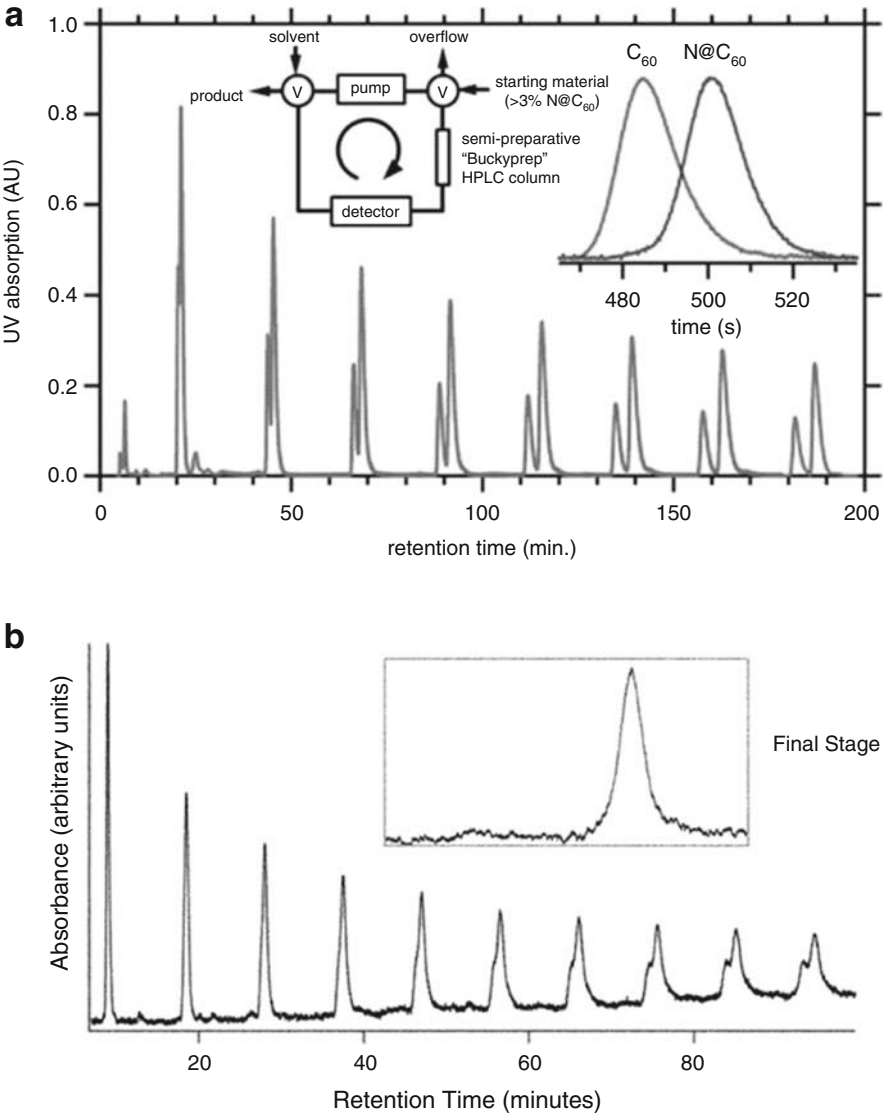

Fig. 4 (**a**) Recycling HPLC chart (eighth cycle) for $N@C_{60}/C_{60}$, using BuckyPrep with 4:1 toluene/hexane. (Inset) HPLC setup in recycling mode and analytical HPLC trace of the pure substances using BuckyPrep with toluene. Figure reproduced from Harneit, W. et al. [23] (**b**) Recycling HPLC chart resolving of C60 from $N@C_{60}$ on a PBB column using toluene as the elute. (Figure reproduced from Kanai, M. et al. [7])

$$\hat{\mathcal{H}} = \frac{\mu_B}{\hbar} \boldsymbol{B}_0^T \boldsymbol{g} \hat{\boldsymbol{S}} + \hat{\boldsymbol{S}}^T \boldsymbol{A} \hat{\boldsymbol{I}}^{(N)} + \hat{\boldsymbol{S}}^T \boldsymbol{D} \hat{\boldsymbol{S}}$$

where μ_B is the Bohr magneton, $\boldsymbol{B}_0$ is the external field, $\bar{\bar{\boldsymbol{g}}}$ is the g-tensor of the electron spin, $\bar{\bar{\boldsymbol{A}}}$ is the hyperfine coupling (HFC) tensor between the electron spin and nitrogen or phosphor nucleus, and $\bar{\bar{\boldsymbol{D}}}$ represents the zero-field splitting (ZFS) tensor. The Zeeman energy of the nucleus and HFC between the electron spin and ^{13}C nuclei on the fullerene cage have been omitted here because of their negligible impact. Due to the near spherical symmetry fullerene, the g-tensor and the HFC tensor are isotropic, and the ZFS tensor equals to or very close to zero depending on C_{60} or C_{70} cage. All these spin features result in a relatively simple EPR spectrum, e.g., the spectrum of $^{14}N@C_{60}$ in Fig. 5 (a) and (b) showing the triplet pattern and energy diagram caused by the HFC of the ^{14}N nuclear spin ($I = 1$), respectively [23]. The different nuclear spins of the endohedral atom will lead to different strengths of HPC. For ^{14}N, the HPC is as small as 15 MHz, whereas for ^{31}P, the HPC is 138 MHz. The main reason lies in the different gyromagnetic ratios of the nuclear spin. Overall, the HPC of ENF is relatively weak; this is due to the unpaired electrons located on the p-orbital, which has zero-density distribution on the center of the atom and thus prohibits the Fermi contact interaction, which is the main HPC contribution component.

The uniqueness of the spectrum not only lies in the simple pattern but is also represented by the ultra-sharp resonance peaks. To resolve the linewidth of the peak, a high-resolution EPR measurement has been reported for $^{14}N@C_{60}$ (Fig. 5 (c) and (d)), which zoomed in the small range of each of the triplet signals [26]. The linewidth was measured to be less than 0.3μT, and more detailed spin features down to the 10^5 Hz scale, such as the pattern caused by the second-order hyperfine splitting of the nitrogen nuclear spin and the HFC of the ^{13}C nuclear spin, were also detected. [25–27]

Spin Dynamic Properties

The fundamental reason of the sharp spin signal of ENF is the long election spin relaxation time [28, 29]. The relaxation time consists of the spin-lattice relaxation time (T_1) and the spin-spin relaxation time (T_2), which respectively parameterize the decay of longitudinal and transverse magnetization when the electron spin is polarized along the X direction of the Bloch sphere (Fig. 6a). Spin-lattice relaxation involves interaction of the spin system with lattice vibrations (phonons), such as direct process, Raman process, and Orbach process [30]. Spin-spin relaxation can be caused by a field inhomogeneity and/or a direct interaction between the spins without energy transfer to the lattice [31]. T_2 is always shorter than T_1 for a given spin system; hence, it is often the decoherence time relevant for quantum technologies [32].For $^{14}N@C_{60}$ as an example, $T_2 = 80\mu s$ via carefully optimized spin echo detection was measured (Fig. 6b), which is one of the longest spin-spin relaxation times for molecular radicals at room temperature [33].

The high structural symmetry of the whole molecule and a strong protection effect from the cage have been proposed as the main reasons for this behavior

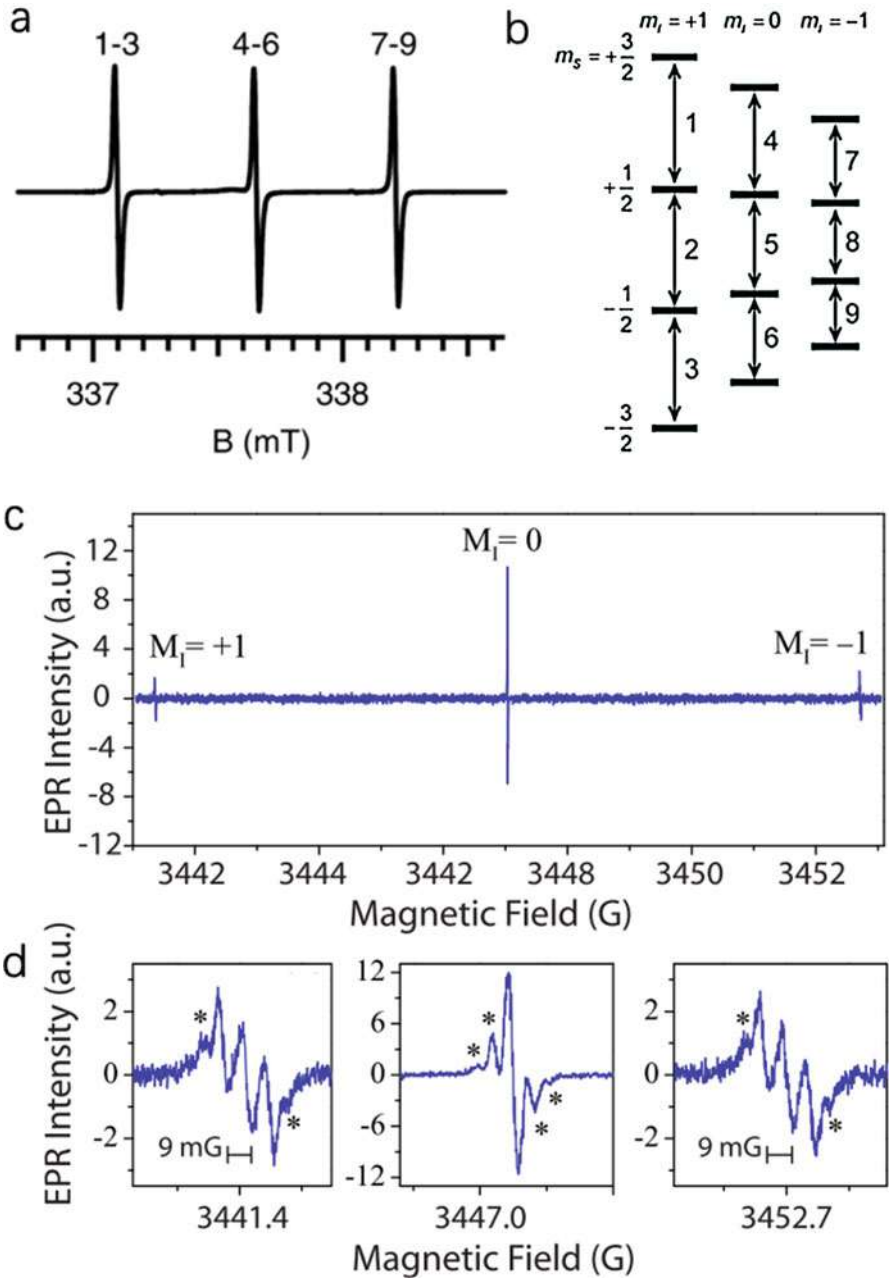

Fig. 5 (**a**) cw-EPR spectrum of N@C_{60} diluted in C_{60} powder. (**b**) Energy diagram and allowed transitions of ^{14}N@C_{60} in high field limit. Figure reproduced from Harneit, W. et al. [23] (**c**) High-resolution EPR measurement of N@C60 in solution with detail of each of triplet signal shown in (**d**). (Figure reproduced from Morton, J. et al. [25])

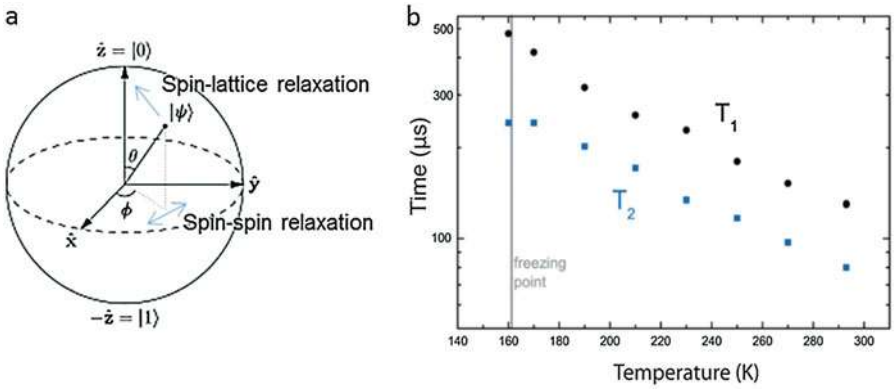

Fig. 6 (**a**) Spin-lattice relaxation and spin-spin relaxation. (**b**) Electron spin relaxation times (T_1 and T_2) of N@C_{60} in CS_2, by measuring the $M_I = 0$ resonance. (Figure reproduced from Morton, J. J. L. et al. [28])

[34]. Compared to other long relaxation electron spin systems (Fig. 7) [35], the long spin relaxation times of ENF are in the desired range for electron spin-based quantum information science studies.

Clock Transitions in a Fullerene-Based Spin System

At a high field limit, where Zeeman effect is the predominate component of the spin Hamiltonian of ENF, the hyperfine term can be treated as a perturbation and only leads its X-band spectrum to split. However, when the magnetic field is considerably smaller, the eigenstate of the spin Hamiltonian will no longer be defined by m_S, and the energy level of the spin system will not have a linear relationship with respect to the magnetic field. When ^{15}N is the nuclei, a magnetic field independent clock transition can be constructed. Similar clock transitions have been observed in atomic H, Rb, and Cs and lead to atomic clock applications. Therefore, it has been proposed that, by utilizing the long spin relaxation time of ENF, a fullerene-based spin system might also provide us with a clock application [36, 37]. There are three benefits of using an encapsulated atom rather than a free atom. The first one is the possibility of scaling up the atomic number without introducing undesired atom collisions or bonding. This is beneficial in the clock signal intensity. The second one is the confinement of the fullerene cage will exclude the problem of Doppler effect which is otherwise tackled by laser cooling [38]. The third one is that no power-hungry vacuum system is required as opposed to *classical* atomic clocks. The first experimental observation of the clock transition of N@C_{60} has been reported using a low-field EPR setup to directly read the transition in a specially designed parallel mode. The frequency of the clock transition has been measured to be 39 MHz [37], which is considerably small than those reported for H or alkali metal atoms. This is due to the small HFC in $^{15}N@C_{60}$, using $^{31}P@C_{60}$ which has larger HFC would be

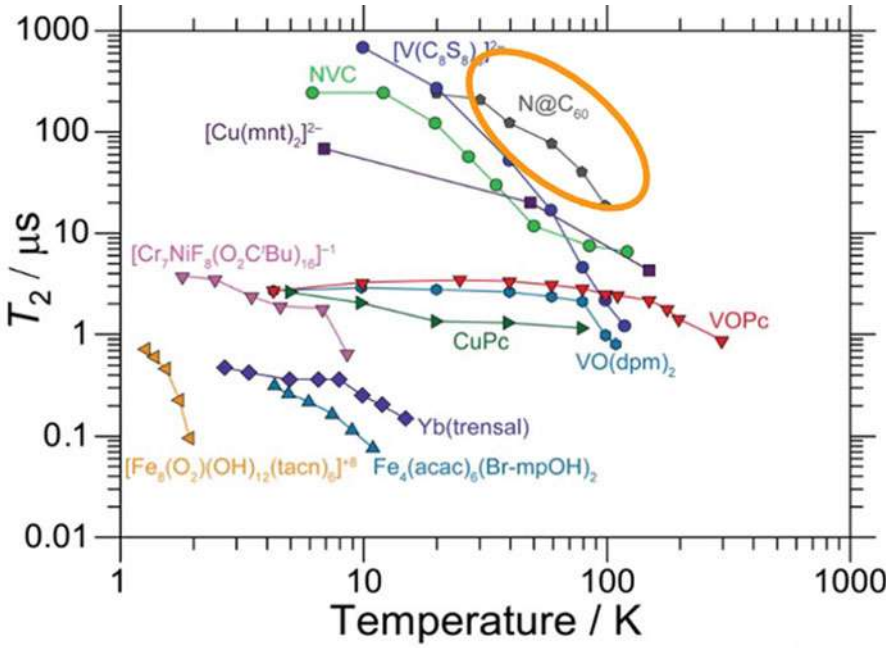

Fig. 7 T_1 and T_2 versus temperature for different spin qubit candidates. (Figure reproduced from Moreno-Pineda E. et al. [35])

more preferred. In order to implement a real clock, technique challenges such as how to polarize the spin state at a low field and how to mitigate molecular vibration in solid state still need more investigation (Fig. 8).

Chemical Functionalization

Chemical Reactivity of ENF

The fullerene acts not only as the container of the electron spin of the endohedral atom, but it also provides the possibility of chemical functionalization, so that new functional groups could be introduced to the ENF system to expend its functionality. Widely used fullerene reactions, such as Bingel reaction and Prato reaction, are compatible with the endohedral system.

Benefiting from the mild room temperature condition which is preferential due to the limited thermal stability of ENF, the Bingel reaction was the first method of chemical functionalization applied to N@C_{60} and P@C_{60} [2, 13, 39–41]. Contradictory spin retention ratios after a Bingel reaction were reported in different early papers [2, 41]. The feasibility of using a Bingel reaction to functionalize ENF was

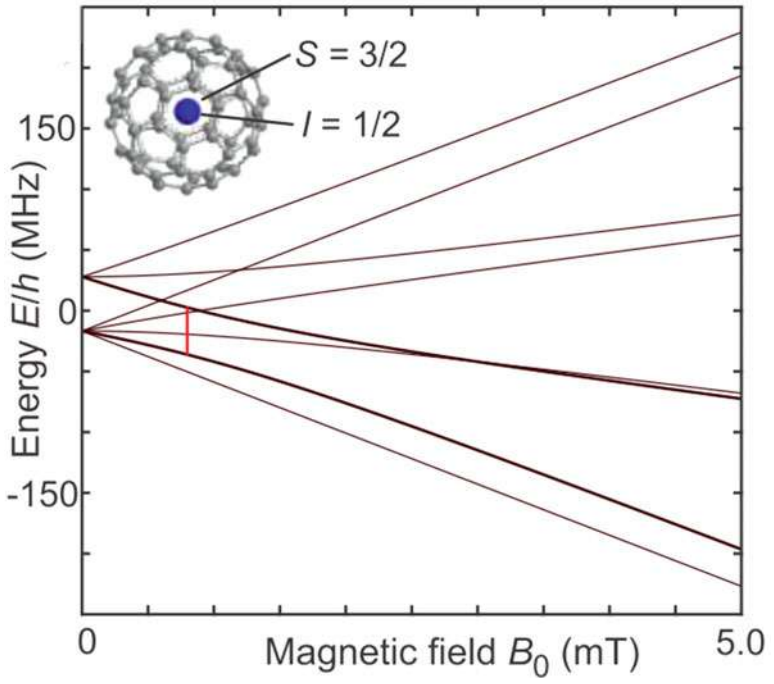

Fig. 8 Simulated energy levels of $^{15}N@C_{60}$ as a function of magnetic field. The clock transition is denoted by a vertical red line. Inset: molecular structure, labelled with electron (S) and nuclear (I) spins. (Figure reproduced from Harding R. et al. [37])

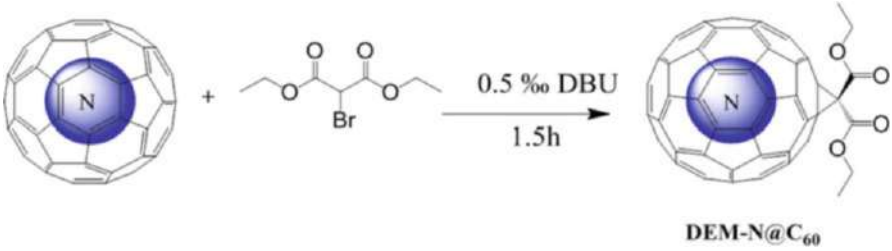

Fig. 9 Reaction scheme of a quantitative study on the spin signal loss during a Bingel reaction

analyzed by adjusting the reaction conditions of a Bingel reaction shown in Fig. 9, and spin signal loss during the reaction was studied quantitatively.

It has been found that the spin retention ratio after a Bingel reaction is highly dependent on two parameters. One is the mole ratio between the base and malonate, and the other is the concentration of base added. It was shown that diluted DBU base with stoichiometric ratio will only lead to negligible spin loss (6%), whereas a much more significant spin-loss ratio (60%) occurs if the usual fourfold excess of DBU is added. Applying pure DBU will lead to a rapid decrease in spin signal at the

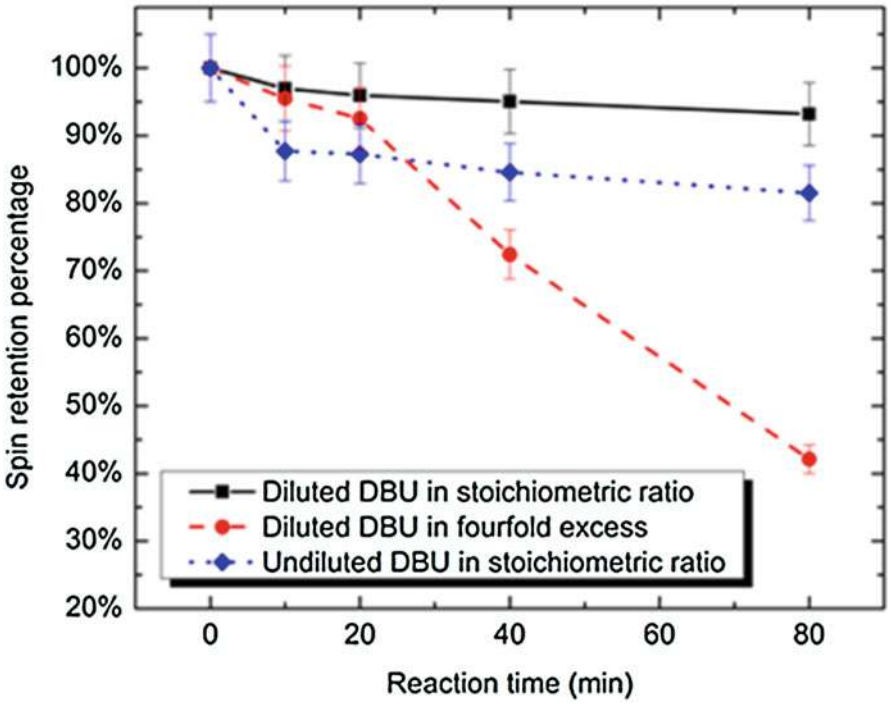

Fig. 10 Different evolutions on the spin retention ratio when repeating the reaction using different amounts or concentrations of DBU

beginning of the reaction, resulting in a final spin-loss ratio of 18%, compared with the value of 6% achieved using dilute DBU. The extra spin loss due to usage of the concentrated base could be correlated with a local excess of DBU arising from a non-uniform mixture between different reagents at the initial stage of the reaction (Fig. 10).

The above quantitative analysis suggests that a direct interaction between DBU and the ENF molecule or its derivatives is the fundamental cause of the spin loss. When the mole ratio is stoichiometric, the reaction will proceed smoothly with a typical Bingel reaction mechanism [42], and all DBU is converted to its conjugate acid. However, if there is more DBU than halomalonate, the excess base can directly react with the fullerene or fullerene derivatives to form dissociated diradicals (Fig. 11), which has been reported during a Bingel reaction with an excessive amount of DBU [43], as well as when reacting C_{60} with DBU directly [44]. Since the dissociated diradical experiences a long lifetime before finally combining to form a zwitterion and precipitating, there is sufficient time for ENF decomposition to take place during the dissociated diradical stage.

Direct interaction between DBU and ENF has experimentally proved that the formation of zwitterion is the fundamental cause of the spin loss (Fig. 12). The typical spin signal of N@C_{60} was completely suppressed by the fullerene anion

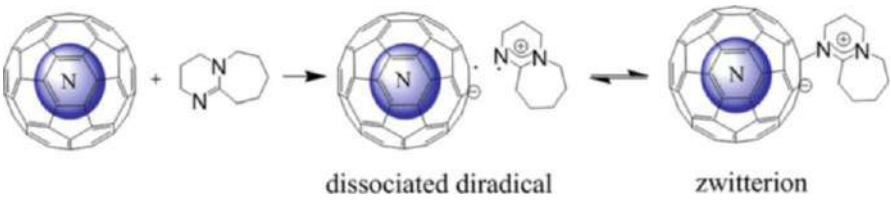

Fig. 11 Direct interactions between DBU and ENF, which form a dissociated diradical and zwitterion

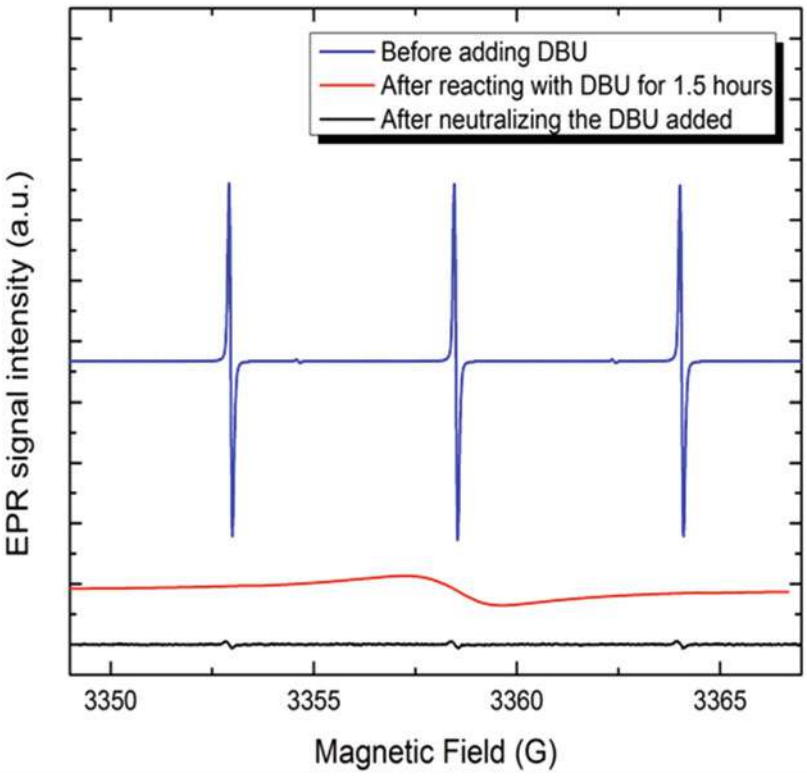

Fig. 12 Significant influence of DBU on the spin signal of $N@C_{60}$

signal at first. After adding acid to neutralize the DBU, almost no spin signal was recovered. This means the endohedral system has irreversibly decomposed. And therefore, to conduct Bingel reaction with ENF, it is preferred to use diluted base in stoichiometric ratio.

Prato reaction has the advantage of abundant choice of aldehyde/ketone, and different mono-pyrrolidine derivatives of $N@C_{60}$ (Fig. 13) have been reported

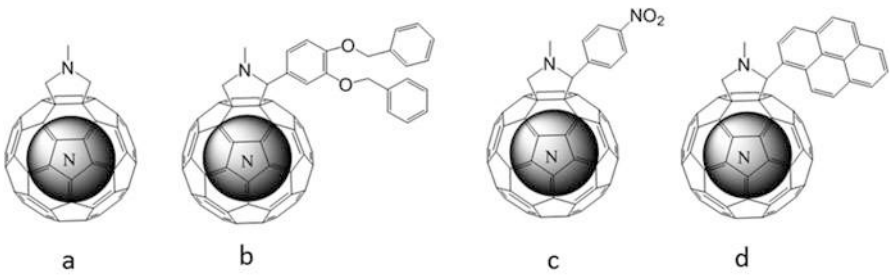

Fig. 13 Mono-pyrrolidine derivatives of N@C_{60} reported in the literature (**a**) [45], (**b**) [45], (**c**) [46], and (**d**) [47]

previously [45–47]. With appropriate reagents the reaction takes place rapidly, but the reaction still requires heating to around 110 °C, which is undesirable given the low thermal stability of ENF [3]. A quantitative study on the spin retention ratio (the intensity of the signal of N@C_{60} after a reaction divided by that before a reaction) for derivative c was reported to be ca. 73%, which means the reaction condition during a Prato reaction is to some extent compatible with the limited stability of ENF.

Apart from the Prato and Bingel reactions, other N@C_{60}-related reactions are shown in Fig. 14, but there are more obstacles needed to be overcome for these chemical functionalization methods to be useful. Two Diels-Alde reactions of N@C_{60} were also reported [45]. The reaction yield and the spin retention ratio were found to be suitable for the endohedral system. However, the drawback lies in the retro-reaction of a D-A reaction. It may cause decomposition of adducts, as well as the undesired tautomerization between different adduct isomers. In addition, compared with the Prato reaction, the less commercial availability of different dienes compared with azomethine ylide precursors leads to difficulties of preparing reagents for a desired molecular structure. A photochemical reaction has been utilized to link a disilirane with the N@C_{60} [48], but a sharp decrease of the spin signal was observed in the product. Apart from the lower photochemical reactivity of N@C_{60}, the decomposition of N@C_{60} may also contribute to the loss of the spin signal. Direct dimerization of N@C_{60} was performed [49], which claimed that no spins were lost by utilizing a mechanochemical method [50]. Nevertheless, the poor thermal stability [51] of C_{120} itself seriously limits the feasibility of synthesizing measurable amount of product. The N@C_{60} oxide has also been studied [52]. Although pure products were separated and characterized by HPLC and EPR spectroscopy, respectively, N@C_{60} oxide was found to be thermally unstable. A new spin signal would gradually replace the spin signal of N@C_{60} when heated at 100 °C. Dimerization and polymerization of N@C_{60}O at this temperature were proposed to be the reason of the instability, as the intermediate state of the dimerization and polymerization reactions might facilitate the decomposition.

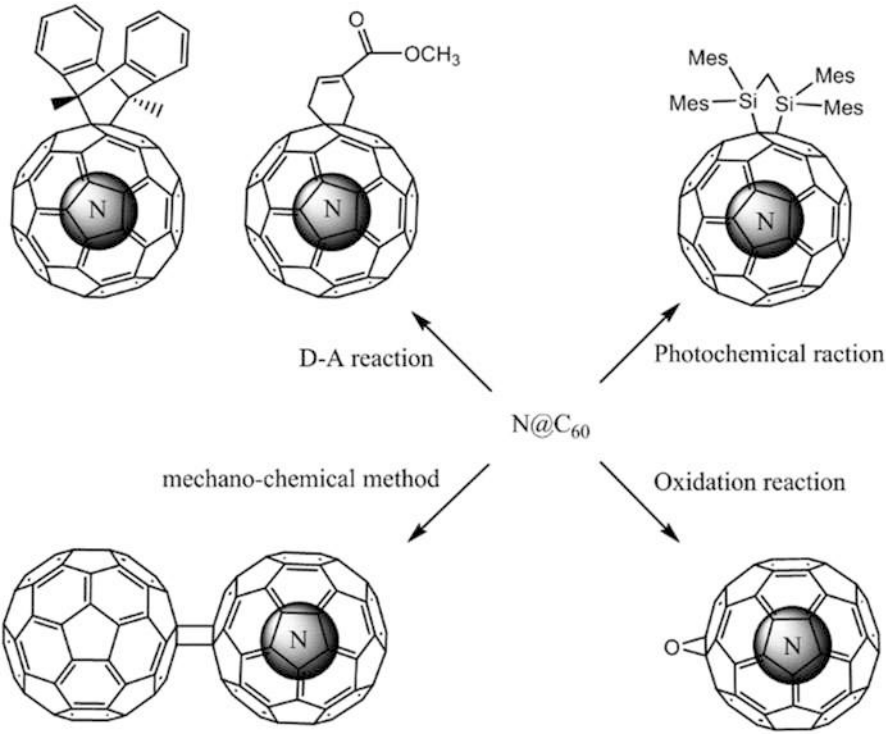

Fig. 14 Other reactions that have been reported with N@C_{60}. Diels-Alde reaction products [45], photochemical reaction product [48], mechanochemical dimerization product [49], and oxidant [52] of N@C_{60}

Characterization of ENF Derivatives

Due to the difficulty of obtaining pure ENF, every reported ENF derivative was a mixture of an ENF derivative and the corresponding empty-cage fullerene derivative. Since conventional structural characterization techniques cannot directly detect the ENF derivative, all studies reviewed in this section conducted structural characterization on the empty-cage fullerene derivatives in the mixture, instead. To prove the presence of the ENF derivatives in the product mixtures, researchers [2, 39, 45–47, 49, 52] further focused on the change of the cw-EPR signal of the reaction product. A small zero-field splitting (ZFS) effect was found to be a common spin feature of ENF derivatives compared to the pristine ENF and was normally used as the characteristic feature to prove the successful chemical functionalization of ENF [2, 39, 45–47, 49, 52]. Limited literature on the chemical functionalized P@C_{60} did not manage to resolve a zero-field spitting pattern [40]. Apart from the appearance of ZFS, it was reported that the triplet HFC peaks became unequal for some ENF derivatives. While researchers initially assigned it to the anisotropy of HFC [46], the

significant increase of the middle peak might also be introduced by an unknown impurity formed during the chemical functionalization reaction. A similar impurity signal overlapping the middle peak has also been reported in other different derivatives [45, 49, 52]. The spin multiplicity of the impurity signal has been determined by pulsed EPR nutation experiments to be 1/2, which is different from that of N@C_{60} [45]. Therefore, zero-field splitting is still the only conclusive evidence for the presence of ENF derivatives.

To measure ZFS, the sample must be in the solid state, because the fast tumbling of the molecule in solution will average the traceless $\boldsymbol{D}$ sensor to zero. The strength of the ZFS is quantified by a traceless second-order tensor $\boldsymbol{D}$, which could be expressed as a diagonal matrix in its eigenframe with elements being $D_{xx} = -D/3 + E$, $D_{yy} = -D/3 - E$, and $D_{zz} = 2D/3$, where D and E are the ZFS parameters representing the axial and the non-axial component of the tensor. The magnitude of the ZFS is heavily affected by the symmetry of the molecule, as it is caused by angle-dependent factors including spin-spin dipolar coupling and spin-orbit coupling [53]. A non-distorted N@C_{60} has no ZFS, but less symmetrical molecules such as N@C_{60} derivatives and a N@C_{70} have a barely detectable intrinsic ZFS effects. In addition to the ZFS introduced by chemical functionalization, in some cases, matrix distortion of the molecular symmetry also introduces a measurable non-intrinsic ZFS effect [54, 55]. Fortunately, the matrix distortion effects from common solvents for fullerenes, such as toluene or CS_2, were found to be negligible [45]. Hence, the intrinsic ZFS of a ENF derivative is normally measured in its frozen solution.

Table 2 lists different N@C_{60} derivatives and their intrinsic ZFS parameters. A positive relationship between the axial parameter D and the ring size of the addend could be found. According to MM2 simulation and DFT simulations, a larger addend ring size has a more pronounced influence on the cage symmetry in the axial direction (Fig. 15). Therefore, more permanent distortions of the endohedral electronic distribution are obtained with larger ring sizes. This explains the positive relationship between the magnitude of D and the size of the ring. No clear trend of the rhombic term of the ZFS could be extracted, but all reported ENF derivatives showed E smaller than 1 MHz, which means the non-axial component of the ZFS effect is not significant.

Table 2 Different simulated ZFS parameters reported in the literature

Derivative type	Ring size attached to the cage	[D, E]/MHz
Diels-Alde reaction product	6	[16.2,0.4][45]
Prato reaction product	5	[16.4, 0.4][45], [17.2, 0.6][45], [16.75, 0.93][47], ,[16.1, 0.7][56], [17.0, 0.8][46],
Dimerization product	4	[14, 0.56][49]
Bingel reaction product	3	[9.15, 0.45][2], [8.6, 0.45][41]
Oxidization product	3	[6.6, 0.5][52]

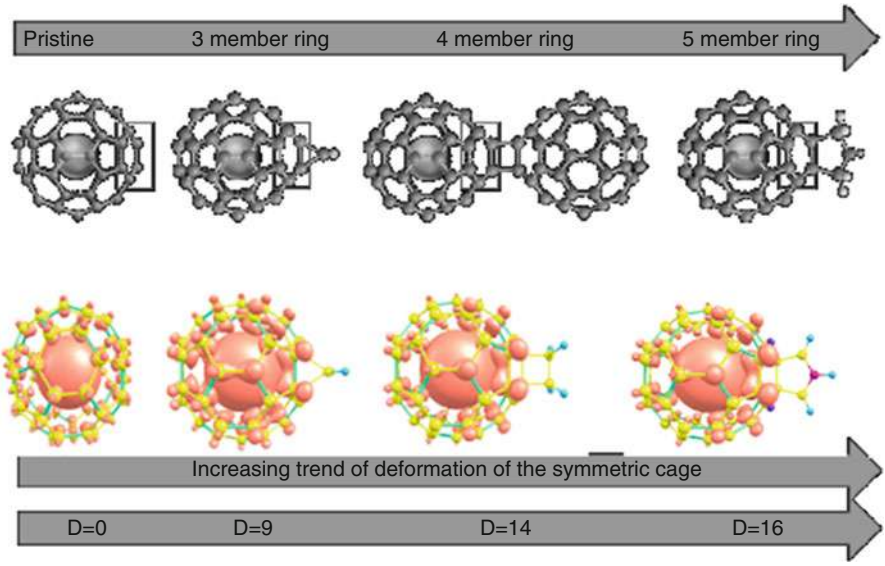

Fig. 15 Relationship between the D value and the symmetry breaking effect of both cage and SOMO configuration caused by exohedral rings with different sizes adding on the cage

Amphiphilic ENF

Using Bingel reactions, β-cyclodextrin-C_{60} derivatives have been reported in the literature to make C_{60} soluble in a wide range of polar solvents [57, 58]. In contrast to the surface modification with groups directly added on the fullerene cage (e.g., fullerenol by multi-hydroxylation of fullerene) [59], which has problems with regioselectivity [60] and spin compatibility, the mono-addition of the Bingel reaction is a more promising approach to make ENFs amphiphilic.

As Fig. 16 shows, mono-functionalization using a Bingel reaction was utilized to integrate N@C_{60} with β-CD. The novel malonate was designed to introduce 40 methoxy groups, which modify the molecular surface. Compared to ordinary β-CD terminated with hydroxyl groups, the methylation makes the molecular surface compatible with not only water but also polar organic solvents.

Benefiting from the polar solvent compatibility of ENF, using the sharp spin signal of ENF to detect other radicals in bio-environments is a highly promising topic. For the proof of concept, copper concentration-dependent cw-EPR signal of β-CD-N@C_{60} in acetone has been demonstrated (Fig. 17a), following a similar dependency reported in toluene solution [61, 62]. By fitting with a set of Lorentzian derivative peaks, the peak-to-peak linewidths of each set of spin signals were determined and compared in Fig. 17b. The magnitude of the broadening effect was plotted against the concentration of Cu^{2+} (Fig. 17c), showing a linear relationship. The dependency was consequently estimated to be 0.0026 mT/mM in the

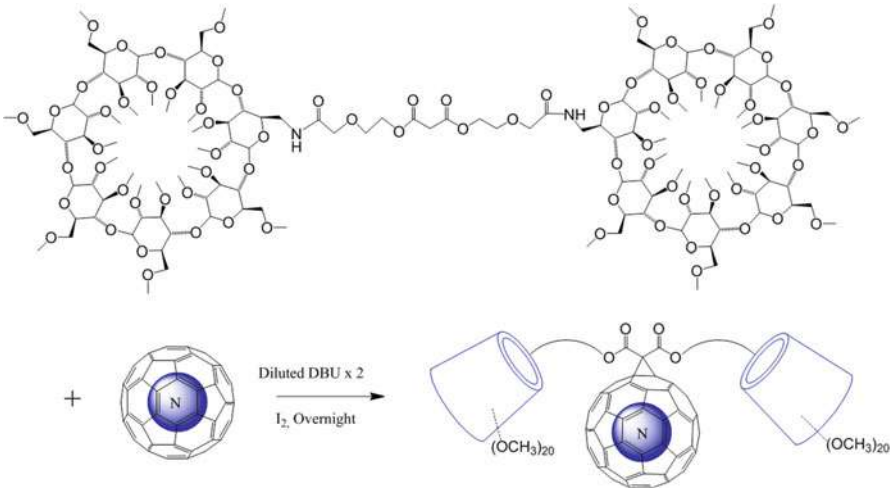

Fig. 16 Bingel reaction synthesizing an amphiphilic ENF, β-cyclodextrin-N@C_{60}

millimolar concentration range. To demonstrate the same experiment in aqueous solution, aggregation of the ENF still needs to be addressed.

Covalently Assembled ENF Spins

Microscopic assembly of spin is required for spin quantum applications and enables a large Hilbert space for information processing. This could be obtained in various dimensions with different molecular engineering technologies. While the 2D [63–69] and 1D [70, 71] arrays of ENF are more promising regarding scalability, they also still suffer from difficulties, such as low spin compatibilities [3] and undesired spin-active impurities. [72] Covalent linkage approach to chemically assembling ENF form spin dyads and dimers is of particular interest.

The protocol of the Prato reaction with ENF is relatively well developed. Thus, ENF dimers have been synthesized using Prato reactions with the organic bridges being an azobenzene group (Fig. 18a) [56], a phenyl group (Fig. 18b) [73], and oligo (p-phenyleneethynylene) groups (Fig. 18c, d) [74], respectively. Since obtaining pure ENF is time-consuming and expensive, all these dimer studies were using N@C_{60}/C_{60} mixtures and normally yielded a half-filled dimer (an ENF dimerized with an empty cage) mostly. Nevertheless, the double-filled dimer (two ENFs dimerized) can be formed using the same reaction condition by starting from high-purity ENF.

An effective way to avoid using 100% pure ENF is link ENF with a hetero-spin system which has 100% spin content. The resulting product showed significant electron spin dipolar coupling according to EPR spectra, which is the experimental evidence of the ENF spin being covalently assembled.

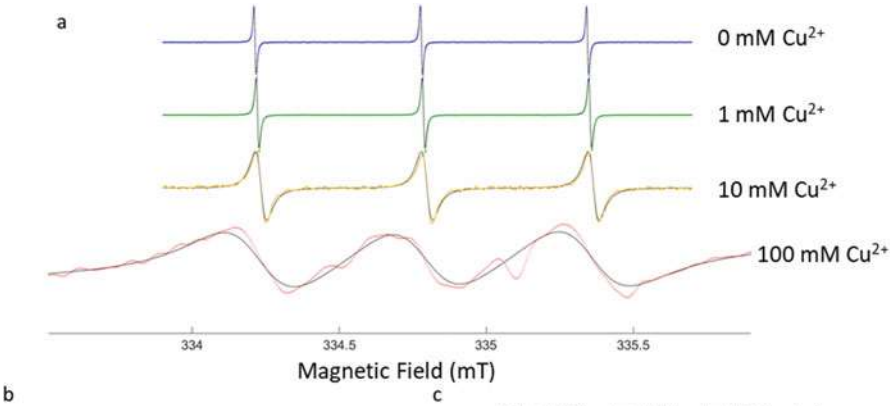

b

[Cu(II)] (mM)	LW_{pp} (mT)	ΔLW_{pp} (mT)
0	0.006829	0
1	0.009191	0.002363
10	0.037787	0.030958
100	0.265757	0.258928

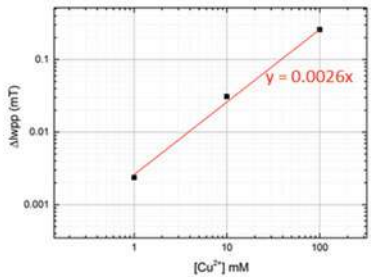

Fig. 17 (**a**) cw-EPR signal comparison of β-CD-N@C_{60} dissolved in acetone with different amounts of Cu^{2+}. (**b**) Simulated peak-to-peak Lorentzian linewidth for the spin signal of β-CD-N@C_{60}, depending on Cu^{2+} concentration. (**c**) Broadening effect of the nitrogen spin signal depending on Cu^{2+} concentration.

A pair of ENF-porphyrin dyads was synthesized to study the spin coupling with ENF in a qualitative manner (Fig. 19) [61], and it was shown that copper (II) tetraphenylporphyrin (TPP) can suppress the EPR signal of N@C_{60} through intramolecular dipolar coupling with a strength of 27.0 MHz [61]. By comparing nitrogen spin signal of CuTPP- and H2TPP-linked ENF dyads (Fig. 19a, 1 N and 2 N), the first one observes a dramatic spin signal intensity difference (Fig. 19b). It has been attributed to the linewidth broadening resulting from a dipolar coupling.

Considering the significant signal-suppressing effect in this closely linked dyad, a longer distance between two spin centers, and hence a smaller coupling strength, is necessary to quantitatively study the spin coupling. Three different ENF-phthalocyanine dyads (Fig. 20) were synthesized.

With the tuned spin distance, more information can be obtained by comparing the solid-state spectra of pristine N@C_{60}, N@C_{60}–1-ZnPc, N@C_{60}–1-CuPc, and N@C_{60}–2-CuPc (Fig. 21). The solid-state cw-EPR spectrum of pristine N@C_{60} only shows three HFC peaks, which exist in all spectra (indicated by blue arrows). In comparison, N@C_{60}–1-ZnPc, which has a lower molecular symmetry, shows characteristic broad ZFS side peaks (marked by red arrows). The spectra of N@C_{60}–1-CuPc and N@C_{60}–2-CuPc in the nitrogen spin region are different from that of

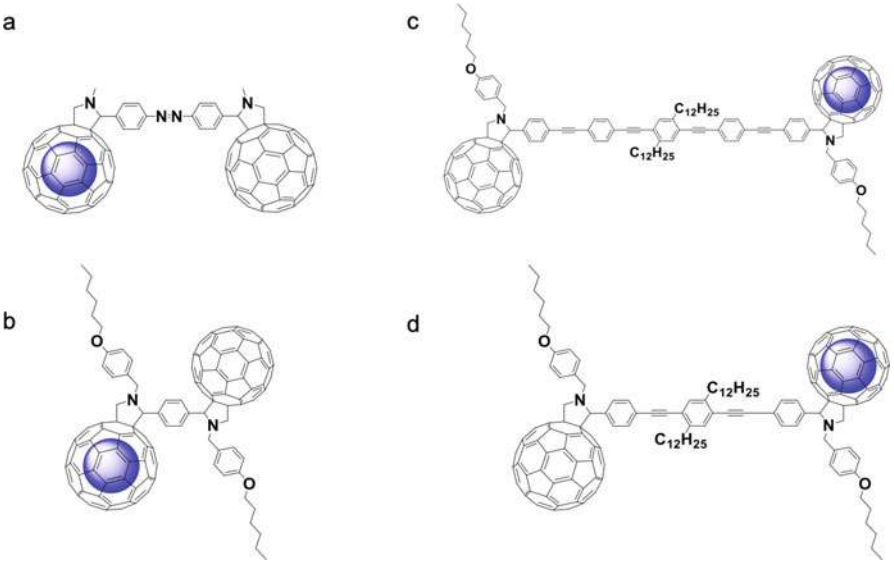

Fig. 18 (**a**) Half-filled dimer with an azobenzene group [56]. (**b**) Half-filled dimer with a phenyl group [73]. (**c**) Half-filled dimer with a long oligo(p-phenyleneethynylene) group [74]. (**d**) Half-filled dimer with a short oligo(p-phenyleneethynylene) group [74]

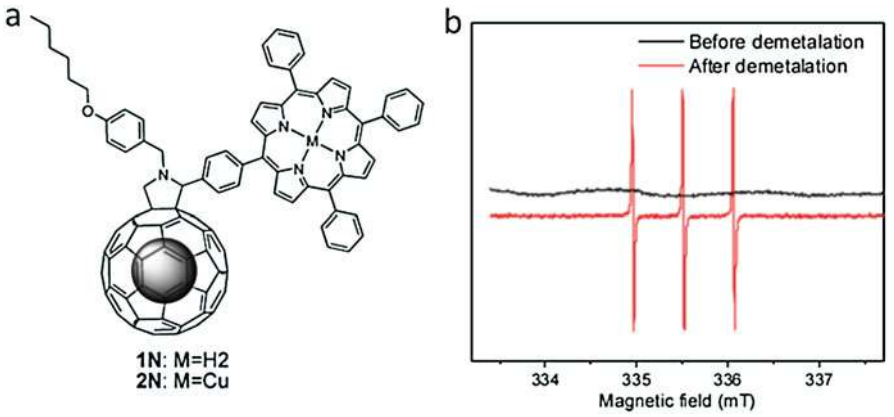

Fig. 19 (**a**) N@C_{60}–MTPP dyads, where M = Cu or H_2. (**b**) Comparison of the nitrogen spin signal before and after converting CuTPP to H_2TPP. Figure reproduced from Liu. G. et al. [61]

N@C_{60}–1-ZnPc (see fine features marked by green arrows in Fig. 21), despite of their nearly identical structure and electron configuration in the fullerene moiety. The spectrum of N@C_{60}–1-CuPc shows stronger dipolar coupling effect as it has more obvious splitting with shoulder peaks emerging next to the HFC peaks. The spectrum of N@C_{60}–2-CuPc with weaker dipolar coupling shows broadened HFC peaks

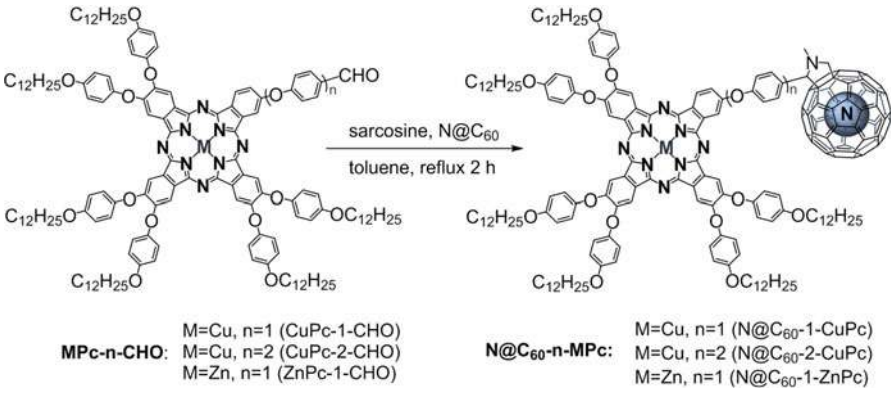

Fig. 20 Synthesis of N@C_{60}–n-MPc dyads. **M** represents the copper or zinc ion, and **n** stands for the number of the phenoxy groups in the bridging unit

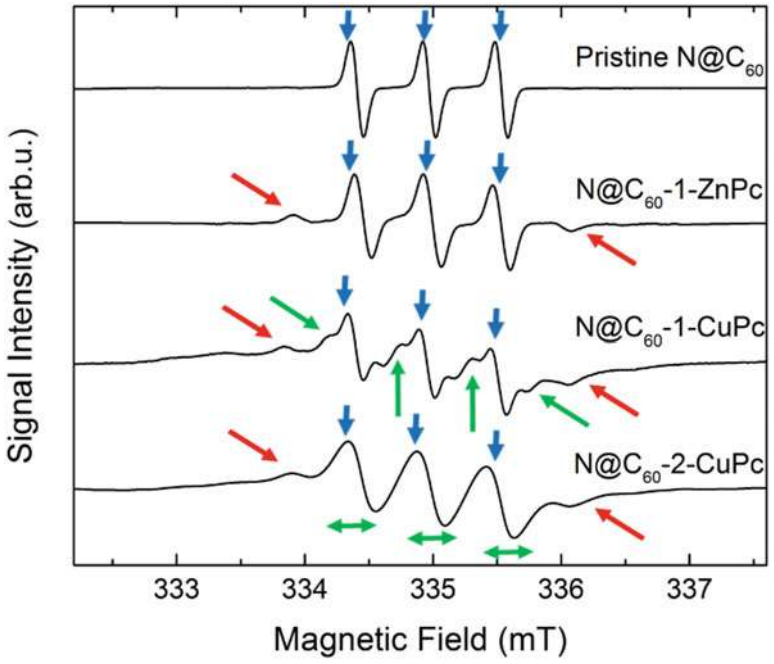

Fig. 21 Solid-state cw-EPR spectra (nitrogen spin region) for pristine N@C_{60}, N@C_{60}–1-ZnPc, N@C_{60}–1-CuPc, and N@C_{60}–2-CuPc, respectively. The peaks of HFC and ZFS are labelled with blue and red arrows, respectively. The dipolar coupling features, such as fine shoulder peaks and line-broadening, are marked with green arrows

only. The extent of the splitting is proportional to the coupling strength [75], and the dipolar coupling strength is reciprocally proportional to the cube of the spin-spin distance Fig. 22a. According to the calculated spin density distributions and

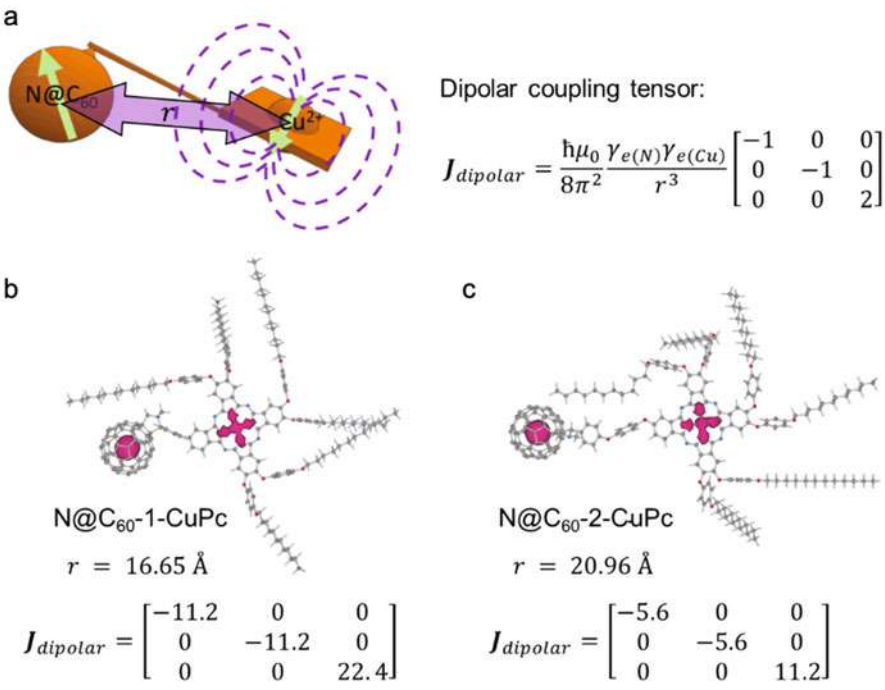

Fig. 22 (**a**) Illustration and equation of the electron spin dipolar coupling depending on spin separation. (**b**, **c**) The spin density distributions of the di-electron-spin systems in their corresponding preferential configurations (contour levels are 1×10^{-3} e/au), on the basis of which the electron spin distances and dipolar coupling strength were calculated

preferential configurations for the dyads (Fig. 22band c), theoretical estimations suggest that the separations between the spin centers are 16.65˚A (N@C_{60}–1-CuPc) and 20.96˚A (N@C_{60}–2-CuPc), respectively. Therefore, the coupling strength for N@C_{60}–1-CuPc (11.2 MHz) is twice as much as for N@C_{60}–2-CuPc (5.6 MHz), which explains the splitting variation in their spectra. With intramolecular spin coupling achieved by ENF, it is the first step towards coherent spin manipulation with the expanded spin density matrix, to perform spin entanglements for quantum information processing.

Conclusions

Endohedral nitrogen fullerenes (ENFs) represent a remarkable class of molecular structures where free atoms can be manipulated while *incarcerated* inside a carbon cage, while at the same time retaining the unique electronic properties of the free atom.

In this chapter the synthesis, properties, and chemical functionalization of ENFs have been summarized highlighting the significant progress that has been achieved

over the last two decades. It is now possible to synthesize and isolate (with relatively high purities) macroscopic amounts of ENFs. Known chemical motifs have been applied, and a plethora of ENF adducts have been successfully synthesized and characterized, including the first ever double-filled ENF dimer system. Results confirmed the extremely long-lived electron spin lifetimes for ENFs in both the pristine and functionalized molecules. This property is unique among other fullerenes and most other spin-active molecules. Hence, a number of applications have been proposed for ENFs, from quantum information processing and atomic clocks all the way to molecular sensors. These research topics are still relatively new; nevertheless, considerable progress has been achieved including a number of significant "firsts." The relevant progress has been reviewed in this chapter. In the near future, there is good reason to believe that further progress towards addressing the formidable challenges remaining will bring one or more applications based on ENFs to fruition.

References

1. Murphy TA, Pawlik T, Weidinger A, Höhne M, Alcala R, Spaeth JM (1996) Phys Rev Lett 77: 1075
2. Dietel E, Hirsch A, Pietzak B (1999) J Am Chem Soc 121:2432
3. Waiblinger M, Lips K, Harneit W, Weidinger A, Dietel E, Hirsch A (2001) Phys Rev B 64(15): 159901
4. Suetsuna T, Dragoe N, Harneit W, Weidinger A, Shimotani H, Ito S, Takagi H, Kitazawa K (2002) Chem A Eur J 8(22):5079
5. Nikawa H, Araki Y, Slanina Z, Tsuchiya T, Akasaka T, Wada T, Ito O, Dinse KP, Ata M, Kato T, Nagase S (2010) Chem Commun 46(4):631
6. Jakes P, Dinse KP, Meyer C, Harneit W, Weidinger A (2003) Phys Chem Chem Phys 5(19): 4080
7. Kanai M, Porfyrakis K, Briggs GAD, Dennis T (2004) J S Chem Commun 40(2):210
8. Mauser H, van Eikema Hommes NJR, Clark T, Hirsch A, Pietzak B, Weidinger A, Dunsch L (1997) Angew Chemie Int Ed 36(24):2835
9. Plakhutin BN, Breslavskaya NN, Gorelik EV, Arbuznikov AV (2005) J Mol Struct THEOCHEM 727(1–3 SPEC. ISS):149
10. Lu X (2005) Chen, Z. Chem Rev 105(10):3643
11. Farrington, B. J. Ph.D. thesis, Oxford University, 2013
12. Zhou, S. Ph.D. thesis, Oxford University, 2017
13. Pietzak B, Waiblinger M, Murphy TA, Weidinger A, Hohne M, Dietel E, Hirsch. A (1997) Chem Phys Lett 4(November):259
14. Ito S, Shimotani H, Takagi H, Dragoe N (2008) Fullerenes Nanotub Carbon Nanostruct 16(3): 206
15. Cho SC, Kaneko T, Ishida H, Hatakeyama R, Cho SC, Kaneko T, Ishida H, Hatakeyama R (2015) J Appl Phys 117:123301
16. Huang H, Ata M, Ramm M (2002) Chem Commun 38(18):2076
17. Ata M, Huang H, Akasaka T (2004) J Phys Chem B 108:4640
18. Hawkins JM, Lewis TA, Loren SD, Meyer A, Heath JR, Shibato Y, Saykally RJ (1990) J Org Chem 55(26):6250
19. Gasper MP, Armstrong DW (1995) J Liq Chromatogr 18(6):1047
20. Liu X, Zuo T, Dorn H (2017) C J Phys Chem C 121(7):4045
21. Plant SR, Porfyrakis K (2014) Analyst 139:4519

22. Wakahara T, Matsunaga Y, Katayama A, Maeda Y, Kako M, Akasaka T, Okamura M, Kato T, Choe Y, Kobayashi K, Nagase S, Huang H, Ata M (2003) Chem Commun 39(23):2940
23. Harneit W, Huebener K, Naydenov B, Schaefer S, Scheloske M (2007) Phys Status Solidi 244 (11):3879
24. Weidinger A, Waiblinger M, Pietzak B, Murphy TA (1998) Appl Phys A Mater Sci Process 66(3):287
25. Morton, J. J. L. Ph.D. thesis, Oxford University, 2005
26. Benjamin SC, Ardavan A (2006) J Phys Condens Matter 18(21):S867
27. Morton JJL, Tyryshkin AM, Ardavan A, Porfyrakis K, Lyon SA, Briggs GAD (2005) J Chem Phys 122(17):174504
28. Morton JJL, Tyryshkin AM, Ardavan A, Porfyrakis K, Lyon SA, Briggws GAD (2006) J Chem Phys 124(1):14508
29. Morton JJL, Tyryshkin AM, Ardavan A, Porfyrakis K, Lyon S a, Briggs GAD (2007) Phys Rev B 76:085418
30. Weil JA, Bolton JR (2007) Electron paramagnetic resonance: elementary theory and practical applications, 2nd edn. Wiley
31. Schweiger, Arthur, Jeschke G (2001) Principles of Pulse Electron Paramagnetic Resonance. Oxford University Press
32. Brown RM (2011) Coherent transfer between electron and nuclear spin qubits and their decoherence properties. Oxford University
33. Zadrozny JM, Niklas J, Poluektov OG, Freedman DE (2015) ACS Cent. Sci 1(9):488
34. Knapp C, Dinse KP, Pietzak B, Waiblinger M, Weidinger A (1997) Chem Phys Lett 272(July):433
35. Moreno-Pineda E, Godfrin C, Balestro F, Wernsdorfer W, Ruben M (2018) Chem Soc Rev 47: 501–513
36. Porfyrakis K, Laird E (2017) A IEEE Spectr 54(12):34
37. Harding RT, Zhou S, Zhou J, Lindvall T, Myers WK, Ardavan A, Briggs GAD, Porfyrakis K, Laird E (2017) A Phys Rev Lett 119(14):1
38. Camparo J (2007) Phys Today 60(11):33
39. Lips K, Waiblinger M, Pietzak B, Weidinger A (2000) Phys Status Solidi 177(1):81
40. Scheloske M, Naydenov B (2006) Isr J Chem 46:407
41. Hörmann F, Hirsch A, Porfyrakis K, Briggs GAD (2011) European J. Org Chem 2011(1):117
42. Diederich F, Isaacs L, Philp D (1994) Chem Soc Rev 23:243
43. Hörmann F, Hirsch A (2013) Chem A Eur J 19(9):3188
44. Skiebe A, Hirsch A, Klos H, Gotschy B (1994) Chem Phys Lett 220:138
45. Franco L, Ceola S, Corvaja C, Bolzonella S, Harneit W, Maggini M (2006) Chem Phys Lett 422 (1–3):100
46. Zhang J, Morton JJL, Sambrook MR, Porfyrakis K, Ardavan A, Briggs G (2006) A D Chem Phys Lett 432(4–6):523
47. Liu G, Khlobystov AN, Ardavan A, Briggs GAD, Porfyrakis K (2011) Chem Phys Lett 508(4):187
48. Wakahara T, Kato T, Miyazawa K, Harneit W (2012) Carbon NY 50(4):1709
49. Goedde B, Waiblinger M, Jakes P, Weiden N, Dinse KP, Weidinger A (2001) Chem Phys Lett 334(February):12
50. Komatsu K, Wang GW, Murata Y, Tanaka T, Fujiwara K (1998) J Org Chem 63:9358
51. Zhang J, Porfyrakis K, Sambrook MR, Ardavan A, Briggs G (2006) A D J Phys Chem B 110(34):16979
52. Jones MAG, Britz DA, Morton JJL, Khlobystov AN, Porfyrakis K, Ardavan A, Briggs G (2006) A D Phys Chem Chem Phys 8(17):2083
53. Radford HE, Evenson KM (1968) Phys Rev 168(1):70
54. Naydenov B, Spudat C, Harneit W, Süss HI, Hulliger J, Nuss J, Jansen M (2006) Chem Phys Lett 424(4–6):327
55. Yang J, Feng P, Sygula A, Harneit W, Su J, Du J (2012) Phys Lett A 376(21):1748
56. Zhang J, Porfyrakis K, Morton JJL, Sambrook MR, Harmer J, Xiao L, Ardavan A, Briggs G (2008) A D J Phys Chem C 112(8):2802

57. Samal S, Geckeler KE (2000) Chem Commun 13:1101
58. Liu Y, Zhao YL, Chen Y, Liang P, Li L (2005) Tetrahedron Lett 46(14):2507
59. Semenov KN, Charykov NA, Keskinov VN (2011) J Chem Eng Data 56(2):230
60. Zhang G, Liu Y, Liang D, Gan L, Li Y (2010) Angew Chemie Int Ed 49(31):5293
61. Liu G, Khlobystov AN, Charalambidis G, Coutsolelos AG, Briggs GAD, Porfyrakis K (2012) J Am Chem Soc 134(4):1938
62. Zhou S, Yamamoto M, Briggs GAD, Imahori H, Porfyrakis K (2016) J Am Chem Soc 138(4): 1313
63. Deak DS, Porfyrakis K, Castell MR (2007) Chem Commun 43(28):2941
64. del Gimenez-Lopez MC, Gardener JA, Shaw AQ, Iwasiewicz-Wabnig A, Porfyrakis K, Balmer C, Dantelle G, Hadjipanayi M, Crossley A, Champness NR, Castell MR, Briggs GAD, Khlobystov AN (2010) Phys Chem Chem Phys 12(1):123
65. Diaconescu B, Yang T, Berber S, Jazdzyk M, Miller G, Tománek D, Pohl K (2009) Phys Rev Lett 102(5):056102
66. Deak DS, Silly F, Porfyrakis K, Castell MR (2006) J Am Chem Soc 128(43):13976
67. Silly F, Shaw AQ, Porfyrakis K, Briggs GAD, Castell MR (2007) Appl Phys Lett 91:253109
68. Wei Y, Reutt-Robey JE (2011) J Am Chem Soc 133(39):15232
69. Raisanen MT, Slater AG, Champness NR, Buck M (2012) Chem Sci 3(1):84
70. Simon F, Kuzmany H, Rauf H, Pichler T, Bernardi J, Peterlik H, Korecz L, Fülöp F, Jánossy A (2004) Chem Phys Lett 383(3–4):362
71. Khlobystov AN, Britz DA, Wang J, O'Neil SA, Poliakoff M, Briggs GAD (2004) J Mater Chem 14(19):2852
72. Rice WD, Weber RT, Leonard AD, Tour JM, Arepalli S, Berka V, Tsai A, Kono J (2012) ACS Nano 6(3):2165
73. Plant SR, Jevric M, Morton JJL, Ardavan A, Khlobystov AN, Briggs GAD (2013) Porfyrakis. K Chem Sci 4(7):2971
74. Farrington BJ, Jevric M, Rance GA, Ardavan A, Khlobystov AN, Briggs GAD (2012) Porfyrakis. K Angew Chemie Int Ed 51(15):3587
75. Banham JE, Baker CM, Ceola S, Day IJ, Grant GH, Groenen EJJ, Rodgers CT, Jeschke G, Timmel CR (2008) J Magn Reson 191:202

Lithium Endohedral Fullerenes

21

Y. Ma and Y. Matsuo

Contents

Y. Ma
Hefei National Laboratory for Physical Sciences at the Microscale, University of Science and Technology of China, Hefei, Anhui, P. R. China
e-mail: ars@mail.ustc.edu.cn

Y. Matsuo (✉)
Department of Mechanical Engineering, School of Engineering, The University of Tokyo, Tokyo, Japan

Department of Chemical System Engineering, Graduate School of Engineering, Nagoya University, Nagoya, Japan
e-mail: yutaka.matsuo@chem.material.nagoya-u.ac.jp; matsuo@photon.t.u-tokyo.ac.jp

X. Lu et al. (eds.), *Handbook of Fullerene Science and Technology*,
https://doi.org/10.1007/978-981-16-8994-9_31

Abstract

Endohedral lithium-containing fullerene, Li@C_{60}, was the first endohedral metallo [60]fullerene that was isolated and structurally determined. This molecule was formed by the reaction of accelerated Li ion derived from Li ion plasma with negative bias in a vacuum chamber with C_{60} continuously deposited on a substrate. Li@C_{60} was chemically oxidized after the synthesis and was first isolated in a pure cation salt ($[Li^+@C_{60}]X^-$) form. The lithium ion-encapsulating fullerene has a high electron affinity because of the electrostatic field of the inner lithium ion, and it easily accepts electrons. Utilizing this strong electron-accepting function, charge-transfer properties and reactions with nucleophiles have been investigated. Neutral lithium-encapsulating fullerene ($Li@C_{60} = Li^+@C_{60}^{\bullet -}$) obtained by electrochemical or chemical reduction has also been isolated, and it has been elucidated to be a monomer in an *ortho*-dichlorobenzene solution and a dimer in a solid. Terahertz absorption and dielectric behavior of $[Li^+@C_{60}]X^-$ were studied associated with the movement of the inner lithium ions in the fullerene cage.

Keywords

Endohedral metallofullerenes · Fullerene derivatives · Lithium ion · Electron-accepting property · Electrochemistry · Electron transfer · Charge transfer · Chemical reduction · Radical anion · Superatoms

Introduction

The past decades have witnessed the prosperous development in the research field of fullerene and its tremendous availabilities in photovoltaics and biology. Lithium ion-encapsulated fullerene, as a unique member of endohedral fullerene cluster with the exactly the same size as empty [60]fullerene, was first obtained from the collision between fullerene and lithium beam and then scaled up from designed apparatus using lithium plasma-fullerene colliding mechanism. The successful complete isolation of lithium ion-encapsulated fullerene was realized via reacting with one-electron oxidant, tris (4-bromophenyl) ammoniumyl hexachloroantimonate, to afford the stable cation $SbCl_6$ salt of $[Li@C_{60}]^+$. Thus, the subsequent series of research upon characterization and chemical reaction were taken by utilizing different cation forms of Li@C_{60} with corresponding counter anion. Li@C_{60} was found to possess greater reactivity by comparing the energy level from empty [60]fullerene, derived from the encapsulated lithium ion. Thus, tremendous efforts have been applied to transplant classic fullerene reaction on Li@C_{60}, and from a kinetic study of the control group, deep comprehension into the role as encapsulated Lewis acid was figured out. Then the instinct neutral form of Li@C_{60} was acquired by chemical and electrochemistry method; the Li@C_{60} was further applied as both p-type and n-type dopant in perovskite solar cells with enhanced stability and power conversion efficiency (PCE). This chapter selectively discusses the Li@C_{60}

following a comprehensive flow, covering the origin, chemical reactions, and ultimately the application of Li@C_{60}. The content of this chapter aims at providing perspective comprehension arise from proven result that will help scholars get further insides into Li@C_{60}.

Synthesis and Characterization of Li@C_{60}

Synthesis of Li@C_{60}

Endohedral metallofullerene was first isolated in 1993 [1, 2], and then its internal structure was reported in 1995 [3]. At that time, the fullerene shell of the endohedral metallofullerene was not C_{60} but a larger shell of C_{80} or C_{82}, and the existence of the encapsulation interaction between of fullerene shell and metal can only be confirmed by its mass spectrum after synthesis; although purification methods such as extraction were reported, pure isolation was not achieved. The most common method for synthesizing metal-encapsulated fullerenes is by sublimation of metal-containing carbon rods under arc discharge. This process could consequently yield metal-encapsulated fullerenes with various cages mixed with empty fullerenes since the method somehow lacks pertinence. Separately, there is another method called ion implantation in which metal ions are included by colliding metal ions with C_{60} in the gas phase or thin film. In particular, encapsulation formed by this method has been specifically studied for metals that could easily form ions in gas phase, such as alkali metal ions [4–7]. Based on established precedent research, a synthesis method toward synthesizing Li endohedral fullerene was first realized in the gas phase by reacting Li ion beams with a mixture of C_{60} and C_{70} vaporized at about 340 °C by Anderson et al., and the encapsulation products were roughly determined by mass spectrometry [8]. Then Campbell et al. further developed ion beam irradiation method employing deposition of the C_{60} thin film, not in the gas phase, and successfully reported the synthesis of endohedral Li@C_{60} with a visible amount for the first time [9, 10].

Finally, the scaled-up production of Li@C_{60} to commercially available level was developed by Ideal Star, Inc., a Japanese venture company [11]. After generating advantages from the previous method and with the intention to improve reaction efficiency by keeping on providing consistent Li source as well as C_{60} source, they designed an apparatus as shown in Fig. 1. They employed Li plasma as the Li source generator because of their superiority in providing high density Li ion. The Li vapor was generated from the left oven and ionized on the rhenium hot plate; at the same time when bearing over 2500 °C degree temperature, electrons emitted from the hot plate and the Li^+ plasma were formed. Then Li^+ plasma moves to the right area of the figure along with the magnetic field and reacted with C_{60} when it reached the right side of the apparatus where there was a continuous thermal deposition process of C_{60} thin film. This method could enable to supply grams scales of Li@C_{60} crude product.

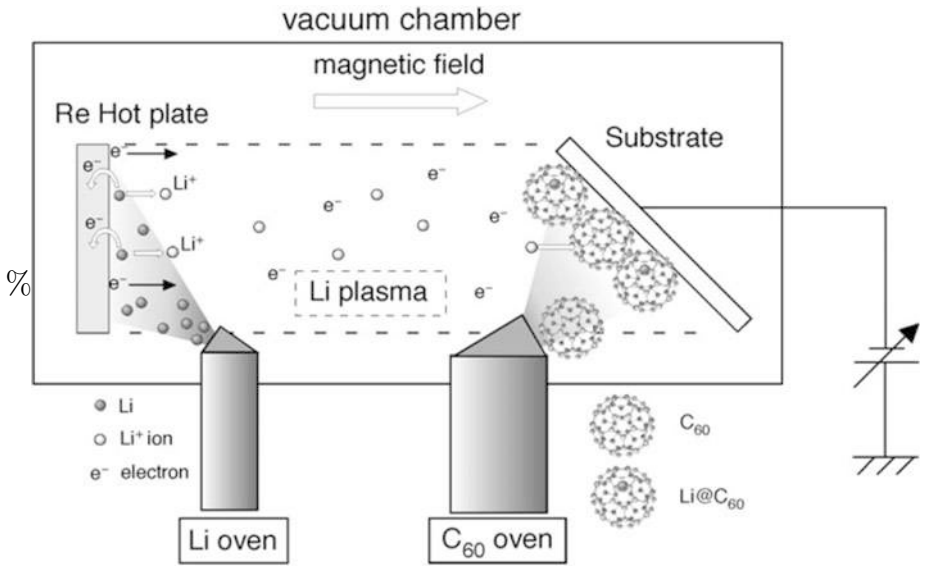

Fig. 1 Illustration of the production apparatus for endohedral fullerene containing Li

Purification of $Li@C_{60}$

Achieving fully isolation and characterization of endohedral metallofullerene has always been an intricate issue concerning scientists for decades because of the coexistence of numerous empty analogues during synthesis, which makes it difficult to obtain purified endohedral metallofullerene in considerable yields. As for $Li@C_{60}$, purification barrier increased due to the formation of dimers and trimers, which is because of the strong charge-transfer interaction between the singly occupied molecular orbital (SOMO) of $Li@C_{60}$ and lowest unoccupied molecular orbital (LUMO) of C_{60}. The precedent efforts including purification method using HPLC or solvent extraction have all been attempted but only yield around 90% purity according to inductively coupled plasma optical emission spectrometry (ICP-OES) detection. In order to prevent the binding of empty fullerenes, isolation of $Li@C_{60}$ by oxidation was performed. The mixture containing $Li@C_{60}$ was treated with a chemical one-electron oxidant, tris (4-bromophenyl) ammoniumyl hexachloroantimonate, to afford the stable cation $SbCl_6$ salt of $[Li@C_{60}]^+$. This $Li@C_{60}SbCl_6$ was then purified by repeated extraction and recrystallization, but the resulting yield is not high. However, since $SbCl_6$ salt is not very stable against moisture, purification by ion exchange columns using the oxidized solution was developed, in which more stable $PF6^-$ was used as the counter anion.

Characterization of $Li@C_{60}$

With the fully purified $Li@C_{60}$ salt in hand, the characterization was performed to get better comprehension on the basic chemical and physical properties of $Li@C_{60}$. In the liquid ^7Li NMR measurement, $[Li@C_{60}]^+$ is observed as a sharp singlet peak

at around −11 ppm. This chemical shift has a considerable high magnetic field shift for Li species. The upfield shifts are explained by strong magnetic shielding effect from fullerene's π-electron conjugated system, which can also be observed in the case of other endohedral fullerenes like $H_2@C_{60}$ (5.98 ppm upfield relative to free H_2) [12], $^3He@C_{60}$ (6.4 ppm upfield relative to free ^3He) [13], and $^{129}Xe@C_{60}$ (8.89 ppm upfield relative to free ^{129}Xe) [14]. Theoretical calculation of Li^+ also predicted that the chemical shift of Li^+ encapsulated in C_{60} shell was expected to be in lower magnetic field than the scenario when Li^+ coordinated to water. In UV-vis absorption spectrum (300–800 nm) in *o*-dichlorobenzene, there is almost no difference between $[Li@C_{60}]PF_6$ and C_{60}. This result indicates that the relative energy difference between the frontier orbitals of the C_{60} shell undergoing electronic transition could hardly be affected by the inclusion of Li^+.

The absolute energy level of the C_{60} cage is greatly affected by the encapsulation of Li^+. This was clarified by measurement of cyclic voltammograms (CVs) and differential pulse voltammograms (DPVs) in *o*-dichlorobenzene. In CV, $[Li@C_{60}]^+$ shows five reversible reduction waves, indicating its electrochemical stability. The corresponding wave was also observed in DPV (Fig. 2). The observed results show that the first to fourth reduction waves observed at C_{60} are all shifted to the oxidation side for about 0.5–0.7 V. The fifth reduction wave is observed in $[Li@C_{60}]^+$, and the first oxidation wave is observed in C_{60}. From the results thus obtained, $[Li@C_{60}]^+$ can be understood by the following structure; as shown as $Li^+@C_{60}$, this molecule has a structure in which Li ions are encapsulated in neutral C_{60}. The electronic structure of the outer C_{60} is almost the same as that of the neutral C_{60}, but its absolute energy level is greatly reduced (about 0.5–0.7 eV) by the encapsulated Li^+ electrostatic potential. C_{60} is known to have a higher electron affinity than other hydrocarbons, but $Li^+@C_{60}$ has improved electron-accepting ability. This greatly affects the chemical reactivity and charge-transfer properties shown in the following sections. Henceforth, the cation of $Li@C_{60}$ is described as $Li^+@C_{60}$.

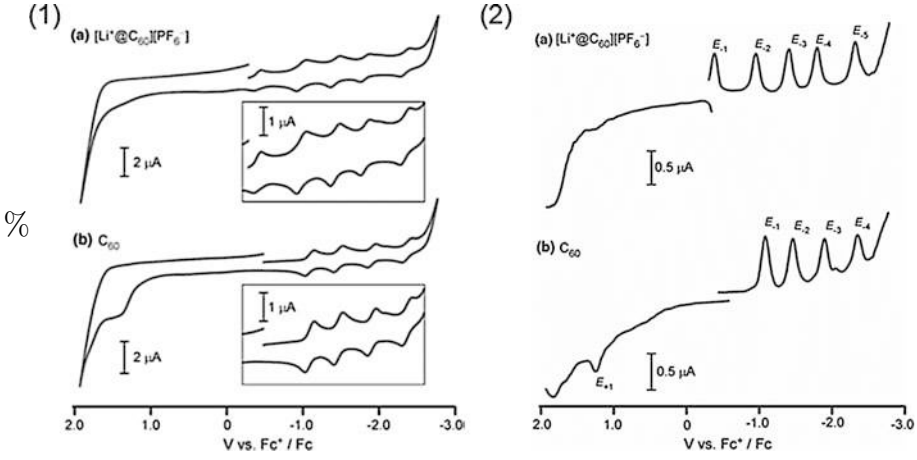

Fig. 2 CVs (1) and DPVs (2) of a. $[Li^+@C_{60}]PF_6^-$ and b. C_{60} in *o*-DCB

Chemical Reactivity and Modifications of $Li^+@C_{60}$

Counter Anion Exchange for $Li^+@C60$

[60]Fullerene, with its low polarity brought from its perfect symmetry structure, has always been notorious for its low solubility in normal organic solvent, which limits the general means to undergo chemical modification on its cage. As mentioned above, the encapsulated Li^+ tends to shift a heavy influence on the overall electron affinity of $Li^+@C_{60}$, and thus $Li^+@C_{60}$ has a relatively higher reactivity than its empty analogue. To note, so far the $Li@C_{60}$-involved chemical modifications have all employed $Li^+@C_{60}$ salt as reactant. Being a salt, the counter anion could exert a dramatic influence on the solubility on the very compound by affecting the overall size as well as the polarity. At the beginning stage of investigating the chemical reaction with $Li^+@C_{60}$, scientists used $Li^+@C_{60}PF_6^-$, which was treated as the most basic in current production, and yielded plenty of inspiring results [15–18]. However, the solubility of $Li^+@C_{60}PF_6^-$ was still relatively similar with that of C_{60}, and yet the scope of the available solvent hasn't changed at all. In this regard, researchers brought up the idea by exchanging this PF_6^- anion for another anion. After screening a variety of possible counter anion candidates including bis(trifluoromethylsulfonyl)imide (NTf_2^-, $N(SO_2CF_3)_2^-$), tetrakis{3,5-bis(trifluoromethyl)phenyl}borate (TFPB$^-$, B$\{C_6H_3(CF_3)_2\}_4^-$), trifluoromethanesulfonate (OTf$^-$), and bistrifluoromethanesulfonimide (TFSI$^-$) salts, TFSI$^-$ was selected as the ideal counter anion for $Li^+@C_{60}$ [19]. There are two methods for exchanging counter ions from PF_6^-, the one using the difference in salt solubility and the other using an anion exchange column.If the solubility of the resulting salt is dramatically higher than that of $Li^+@C_{60}PF_6^-$, anion exchange can be performed by simple mixing. The first method for synthesizing $Li^+@C_{60}$ can be operated by reacting the corresponding anion-containing alkali metal salts with $Li^+@C_{60}PF_6^-$ in dichloromethane, because of the limited solubility of alkali PF_6^- slats in dichloromethane. Therefore, those slats which could be generated from this method should have a superior solubility than $Li^+@C_{60}PF_6^-$. The results show only TFSI, (Sec. 3.3) NTf_2, and TFPB salt (Sec. 3.4) can be prepared by this method. On the other hand, the salt OTf$^-$ has a similar solubility to $Li^+@C_{60}PF_6^-$ when $Li^+@C_{60}$ salt is used. In this case, it is necessary to use an anion exchange column. The anion exchange column containing trimethylammonium unit as the cation part is packed with OTf$^-$, and PF_6^- can be replaced by passing $Li^+@C_{60}PF_6^-$ solution through it. The solubility of $Li^+@C_{60}$ salt changes dramatically due to anion exchange, and $Li^+@C_{60}TFSI^-$ and $Li^+@C_{60}TFPB^-$ showed more than ten times higher solubility in all solvents than PF_6 salt. In particularly, TFSI salts are not so expensive, and LiTFSI, a synthetic reagent, is also not so expensive and is often used in recent years as highly soluble salts. Consequently, using TFSI$^-$ as the counter anion for $Li^+@C_{60}$ makes a watershed for the chemical modification research.

Accompanied with the selectively used counter anion, there is also a continuant change of the purification and reaction monitoring for the post reaction procedure. HPLC was used to monitor the reaction and purify the product since normally the reaction is limited to mg level. At the time when $Li^+@C_{60}PF_6^-$ was generally used,

the researchers applied the suitable HPLC system with the Buckyprep column (Nacalai Tesque), a sophisticatedly used column in fullerene chemistry, and to enlarge the compound peak, researchers added an adequate amount of tetra(*n*-butyl)ammonium hexafluorophosphate (*n*-Bu_4NPF_6) as supporting electrolyte. In the mobile phase, the existence of supporting electrolyte enables a steady distance between $Li^+@C_{60}$ cation and the corresponding PF_6^- counter anion and thus prevents the tailing or uncertainty retention time because of the vague fraction. Obviously, the n-Bu_4NPF_6 electrolyte couldn't be dissolved in the normal solvent for fullerene derivatives, and researchers managed to mix the 50 mM *n*-Bu_4NPF_6 acetonitrile (MeCN) solution and chlorobenzene with the ratio of 5:95 as the eluent for analysis HPLC and chlorobenzene, 1,2-dichloroethane, and MeCN (50:35:15 v/v/v) containing saturated Me_4NPF_6 for preparative HPLC.

Afterward, when the $Li^+@C_{60}PF_6^-$ counter anion was replaced by much higher soluble $Li^+@C_{60}TFSI^-$, there was a change of the eluent condition together with the type of column employed. LiTFSI is a commonly used electrolyte in electrochemistry with considerable low price, and surprisingly $Li^+@C_{60}TFSI^-$ shows a more intensified peak with less concentrated supporting electrolyte in the case of LiTFSI. Using LiTFSI as supporting electrolyte can not only decrease the amount of consumed chemicals but also keep consistent the same counter anion existing in the mobile phase. Researchers successfully established another HPLC system referring to the abovementioned benefits by using a cation-ion exchange column with a mixture of 15:85 chlorobenzene and MeCN eluent containing 5 mM LiTFSI. The increased ratio of MeCN also helps to decrease the column pressure from over 13 mPa to around 5 mPa. After elution of the desired product, acetonitrile was removed by vacuum evaporation to precipitate excess LiTFSI.

Chemical Modification for $Li^+@C60$

As mentioned above, the synthesis of $Li@C_{60}$ seems to have overcome the drawbacks of C_{60} cluster's low solubility and the purification issue concerning endohedral fullerene field. As a result, $Li@C_{60}$ starts to draw numerous attentions from a variety of research area and thought to have potential for electronic and biological devices. To realize this potential, chemical modification shall be applied on the pristine $Li@C_{60}$ in order to get a versatile platform for corresponded applications.

Thanks to the bloomsome in the fullerene chemistry during recent decades, they have yielded plenty of matured methods to functionalize C_{60} in which $Li@C_{60}$ can refer. To note, even though $Li@C_{60}$ has similar size as normal fullerene, the reactivity is enhanced a lot in the case $Li@C_{60}$ because the encapsulated Li cation effectively affects its electron affinity and shifted the LUMO energy level to −4.3 eV. Appropriate changes in the reaction conditions need to be made in the synthesis route of $Li@C_{60}$ derivatives. We will describe the reported synthesis of $Li@C_{60}$ derivatives such as methanol fullerenes, D-A reaction, organometallic complex, supramolecule, etc. in this section.

Li@[6,6]-phenyl-C_{61}-butyric acid methyl ester (PCBM) is the first reported Li@C_{60} derivatives because of its well-known empty analogue, PCBM, the most intensely used commercially available fullerene derivatives in photovoltaic field [17]. At first, researchers attempted to follow the synthesis according to the reported route developed by Hummelen et al. The reaction of $Li^+@C_{60}PF_6^-$ with pre-mixed solution of tosyl hydrazone (PhC = (NNHTs)$CH_2CH_2CH_2CO_2Me$) and NaOMe did not afford the desired product, and the HPLC showed the reaction gave a complicated peak, indicating the formation of multi adducts or other byproduct. Specifically, the reaction finished within seconds under room temperature, rather than reacting for hours during heating at over 70 °C in empty fullerene case. Researchers attributed this phenomenon to the high reactivity brought by the encapsulated Li cation. To solve this problem, researchers tried to lower the reaction rate by changing the reaction route by using diazoalkane (PhC = (NN)$CH_2CH_2CH_2CO_2Me$), which could be readily prepared by pretreatment of tosyl hydrazone with KO^{t}Bu to obtain tosyl hydrazone salt PhC = (NNKTs)$CH_2CH_2CH_2CO_2Me$, instead of tosyl hydrazine and successfully afforded the desired Li^+@PCBM product in 30% isolated yield (Fig. 3).

Inspired by the successful synthesis of Li^+@PCBMPF_6^-, researchers obtained similar fullerene clusters like $Li^+@C_{61}Ph_2TFSI^-$ and $[Li^+@C_{60}$(fluoreno)]$TFSI^-$ obeying the modified synthesis route [20, 21]. Characterization of their chemical and physical properties also shows that their intriguing properties differ from the empty analogues.

All the three Li@C_{60} derivatives afford single crystal in fairly good quality. This is because Li@C_{60} salts contain ionic parts and result in high crystallinity. Via vapor

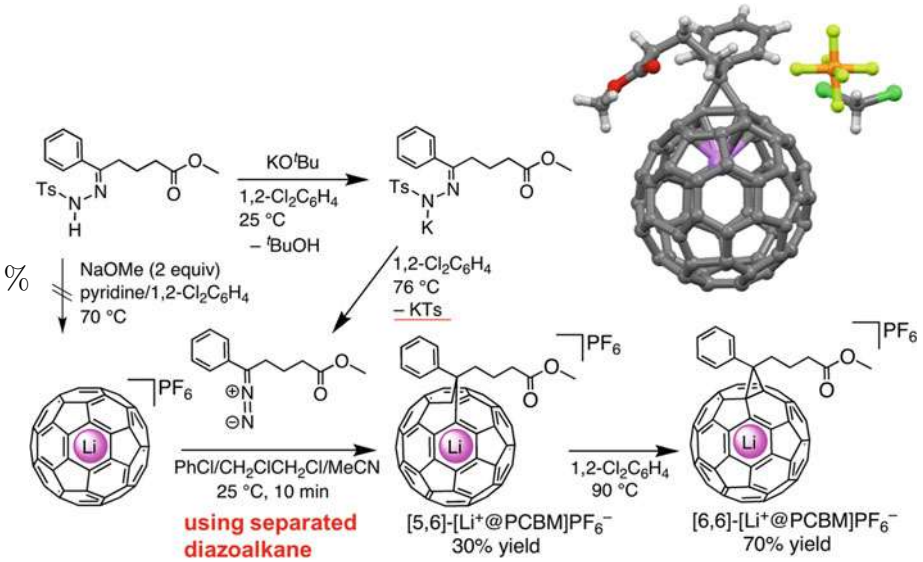

Fig. 3 Schematic illustration of the synthesis route toward Li^+@PCBMPF_6^-

deposition method, the gradual accumulation of less polar solvents like diethyl ether can case electrostatic interaction between their cationic and anionic parts. Especially, for the first time, researchers grew the single crystals of the [5,6]- and [6,6]- $Li^+@C_{61}Ph_2TFSI^-$. In common, when methanol fullerene is prepared, there will be two isomers, [5,6]- and [6] structure, mainly named after the conjunction position where the adduct is located [22, 23]. Compared with [5, 6] structure, [6] structure is more thermodynamically stable, and usually people will roughly heat the [5, 6] structure under high temperature to utilize the fully transformed [6] structure compound for further usage. That inevitably leads to the lack of knowledge for [5, 6] structure; actually there is no report of obtaining the single crystal for any of the [5, 6] structure fullerene compound even though numerous [6] structure fullerene derivatives have been unambiguously determined by X-ray analysis. For $Li^+@C_{61}Ph_2TFSI^-$ researchers successfully obtained single crystal for both [5,6]- and [6,6]-methanol fullerene derivatives for the first time. Theoretical calculation was performed according to the single-crystal data, and the results showed the relative Gibbs energies of [5,6]- $Li^+@C_{61}Ph_2TFSI^-$ is 8.05 kcal/mol higher than those of [6,6]- $Li^+@C_{61}Ph_2TFSI^-$, where there is 1.31 kcal/mol lower than that of the empty analogue, suggesting that the encapsulate Li^+ can help stabilize [5, 6] structure. This also helps explain the facts that [5,6]- $Li^+@C_{61}Ph_2TFSI^-$ can be completely isolated and thus obtain single crystal in good quality.

Intriguingly, from the single-crystal data of all the three $Li@C_{60}$ derivatives mentioned above, we notice that the motion of the encapsulated Li cation can be affected by the adducted function group. For pristine $Li^+@C_{60}PF_6^-$, the Li cation locates right ender the six-membered ring at 22 K, while $Li^+@PCBMPF_6^-$ keeps its Li^+ position at 93 K under the [6,6]-bond. In the case of $[Li^+@C_{60}(fluoreno)]TFSI^-$, Li^+ position was found to take the occupancy at three different positions (0.31/0.38/0.30) at 93 K with even frequency, indicating that the through-space interaction caused by the rigid structure of the fluoreno moiety can decrease Li^+ localizability. The position differences arising from these molecules offer hints for researchers that by changing $Li@C_{60}$ adducts via chemical reactions, interesting research topic including ferromagnetism study by adding outside cage metal complex and physical research focusing on manage motion change in crystal structure can be introduced (Fig. 4).

Considering the enhanced electron-accepting ability endowed by encapsulated Li^+, the $Li^+@C_{60}$ is hoped to have better correlation when forming transition metal complex, under which circumstances, empty fullerene electron-rich metal fragment complex yet cannot be obtained with considerable yield. Watanabe et al. successfully used transition metals like iridium and platinum to afford the first example of $Li^+@C_{60}$ metal complex [24]. As expectation, the $Li^+@C_{60}$ metal complex was formed within several minutes with quantitative yield in *o*-DCB solution. Infrared spectra shows that for the normal fullerene complex solution, there is a coexistence of the $[IrCl(CO)(PPh_3)_2]$ and $[(\eta^2\text{-}C_{60})IrCl(CO)(PPh_3)_2]$ that can be signed as CO stretching bands signal at 1964 cm^{-1} and 2011 cm^{-1}, respectively [25]. On the contrary, there is only one CO stretching band signal that appears at 2025 cm^{-1},

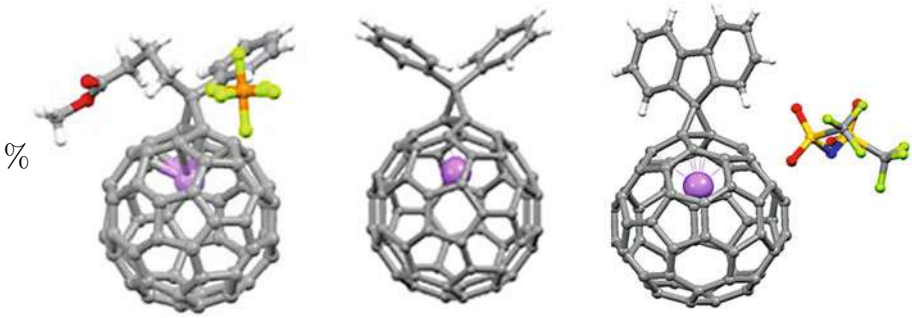

Fig. 4 Crystal structure of Li-encapsulated fullerene derivatives

implying stronger interaction and stability in the case of the Li@C_{60} complex. Moreover, the upshift of the corresponding complex peak signal means that Ir center shifts more π backdonation Li^+@C_{60}. In addition, with the affection of the complex, the encapsulated Li^+ motion got similar change as consistent with the aforementioned feature. Instead of laying under the six-membered ring, the Li^+ is attracted near to the Ir center with similar Li-C distance of Li^+@PCBMPF_6^- (Fig. 5).

Synthesis and characterization of the iridium and platinum complexes of Li^+@C_{60} verified our hypothesis about the motion of the encapsulated Li^+ from the outside cage affection and demonstrate the first example of Li^+@C_{60} complex. Afterward, encouraged by this work, Ueno et al. successfully employed the Li^+@C_{60} ⊂ [10]CPP·X^-, as a new type of ionic supramolecule with unusual charge-transfer interaction between the two molecules [26]. CPP-fullerene supramolecule complex has been obtained with the widely studied trend of the CPP chemistry including C_{60} ⊂ [10]CPP, C_{70} ⊂ [10]CPP, and C_{70} ⊂ [10]CPP. Specifically, La@C_{82} ⊂ [11]CPP was found to have strong intramolecular charge-transfer phenomenon. Inspired by the previous study, the Li^+@C_{60} ⊂ [10]CPP·X^- (X = NTF_2. TFPB) was successfully obtained by simply mixing the Li^+@C_{60} solution and [10]CPP in room temperature. The formation was first confirmed by the downshift of [10]CPP signal and upshift of Li^+@C_{60} signal by ^{1}H NMR spectrum and further unambiguously visualized by analyzing its single-crystal structure. The crystal structure of Li^+@C_{60} ⊂ [10]CPP·$TFPB^-$ exhibited a 1:1 complexation of the Li^+@C_{60} cation and the [10]CPP ring, while the whole cationic complex was formed along with an ionic crystal with TFPB. The [10]CPP ring surrounds the C_{60} center with distance of 6.87 ± 0.14 Å and 6.89 ± 0.11 Å, the electrostatic interaction within the overall cationic moiety causes the Li^+ − [10]CPP distance smaller than the Li^+ $TFPB^-$ distance. Despite the impact of the [10]CPP shifts on the Li^+@C_{60}, Li^+@C_{60} also exerts a strong influence on the outside ring from the strong charge transfer. The photoluminescence excitation (PLE) measurements and the steady-state and time-resolved photoluminescence (PL) measurements showed similar results between the Li^+@C_{60} ⊂ [10]CPP·NTF_2^-, C_{60} ⊂ [10]CPP, and [10]CPP. Yet the Li^+@C_{60} ⊂ [10]CPP·NTF_2^- shows a shorter PL lifetime of 2.5 ns than 4.3 ns displayed from the samples of [10]

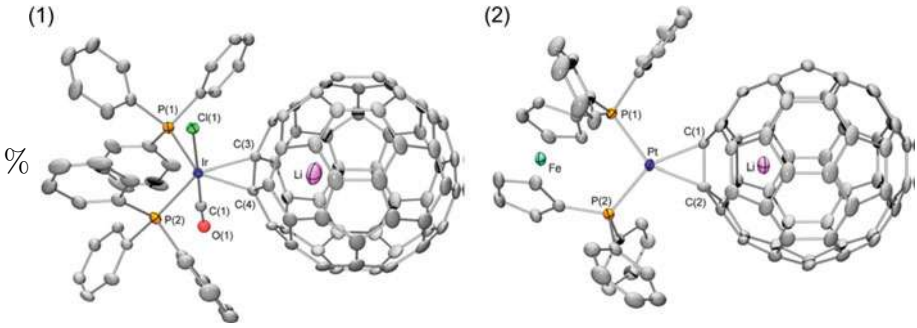

Fig. 5 Crystal structure of (1) [{η^2-(Li^+@C^{60})}IrCl(CO)(PPh_3)$_2$] (cationic part) and (2) [{η^2-(Li^+@C^{60})}Pt(dppf)] (cationic part)

CPP, which indicates that in the cationic complex of Li^+@C_{60} and [10]CPP ring, the cation is no longer mainly localized on the Li^+ but delocalized on the surrounding [10]CPP ring and make the complex the first example of a CPP-based ionic donor-acceptor supramolecule (Fig. 6).

Besides the aforementioned examples of chemical modification on Li^+@C_{60}, researchers also tried to obtain Li^+@C_{60} derivatives including Li^+@$C_{60}O^-(OH)_7$ through hydroxylation and [Li^+@$C_{60}(C_6H_8)$]$TFPB^-$ through Diels-Alder reaction [27, 28]. These works show Li^+@C_{60}, as an emerging type of materials, not only have potential to be a versatile platform undergoing classic fullerene reaction with higher yield and reactivity, but also enables researchers to find more availabilities apart surpass in known fullerene derivatives due to the cationic moiety and the charge transfer given by the encapsulated Li^+. Overall, we believe that chemical modification of Li^+@C_{60} will continue to play an important role in the development of the emerging technology of Li^+@C_{60} and even carbon clusters as novel functionalized materials, and they are expected to be applied in different research fields in electrochemistry, supramolecule chemistry, as well as device fabrication.

Kinetic Study of Li^+@C_{60}-Involved Reaction

Kinetic Study on Diels-Alder Reaction

In the above section, we illustrate the chemical modification of Li^+@C_{60} derivatives and observe the extremely high reactivity of Li^+@C_{60} compared with their empty analogues. For example, the Diels-Alder reaction of Li^+@C_{60} and cyclopentadiene took place within seconds, which was too fast to determinate the rate constant. In order to find out the intrinsic factor that triggered the rapid conversion and to quantitatively demonstrate the superior reactivity of Li^+@C_{60}, Ueno et al. did the kinetic study on the Diels-Alder reaction and proved the encapsulated Li^+ can functionalize as Lewis acid catalyst [27].

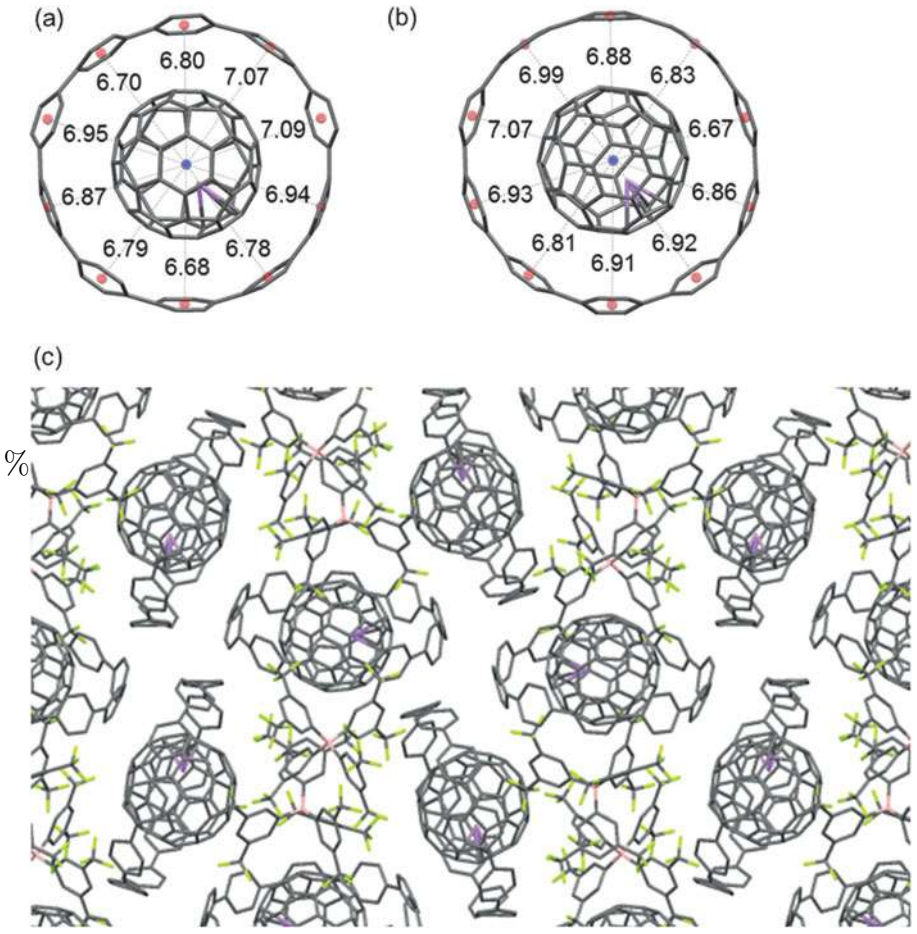

Fig. 6 Crystal structure of $Li^+@C_{60} \subset$ [10]CPP·$TFPB^-$. (**a**, **b**) Crystallographically independent structures were found, with slightly different distances between centroids of $Li^+@C_{60}$ and [10]CPP. c Packing structure

The Diels-Alder reaction is one of the most intensified studied reactions in chemistry field and also has been well-studied to synthesize fullerene derivatives. Yet the fullerene-involved Diels-Alder reaction experiences an equilibrium which limits the yield. Theoretically, Diels-Alder reaction rate can be enhanced by two factors (1) the energy gap between the HOMO of the diene and the LUMO of the dienophile and (2) the existence of Lewis acid catalyst. Considering the observed acceleration in the $Li^+@C_{60}$-involved reaction, the lowered LUMO energy that arose from the encapsulated Li^+ has already been verified, which substantially meets the demand of (1). As for (2), even if Li^+ salts are well-known to work as Lewis acid catalyst, there is no heteroatom on the $Li^+@C_{60}$ moiety to coordinate. Besides, the

other neutral endohedral fullerenes such as He@C_{60}, H_2@C_{60}, and H_2@C_{70} are not reported to enhance reactivity of the Diels-Alder reaction.

For this kinetic study, researchers first synthesized and characterized the DA adduct of Li^+@C_{60} and 1,3-cyclohexadiene instead of previously reported cyclopentadiene. The reaction finished within seconds, and no retro-reaction took place, which is different from the reaction equilibrium of its empty analogue experiences. The reactions were performed under the same conditions except for varying temperatures. The concentration changes over time were monitored by high-performance liquid chromatography (HPLC) (Fig. 7). After analyzing the concentration-time dependence, logarithmic was selected to determine the reaction order. The natural logarithm of **1a** consumption ratio depicted a strong linear time dependence, which suggested that it's a pseudo-first-order, regarding the excess amount of cyclohexadiene added to the reaction system. The calculated k_2 ratio from Arrhenius plots (Li^+@C_{60} vs C_{60} at 303 K) revealed that the DA reaction of [Li^+@C_{60}](PF_6^-) had a dramatically increased rate constant of over 2400-fold faster than the reaction of empty C_{60}. Next, the activation energy E_a, activation enthalpy $\Delta H^{\ddagger}$, activation entropy $\Delta S^{\ddagger}$, and activation Gibbs free energy $\Delta G^{\ddagger}$ were computed from Arrhenius plots (ln k vs $1/T$) and Eyring plots (ln(k/T) vs $1/T$) on the basis of the following equations, respectively:

$$\ln k = -E_a/RT + \ln A$$

$$\ln (k/T) = -H^{\ddagger}/RT + \left[\ln (k_B/h) + S^{\ddagger}/R\right]$$

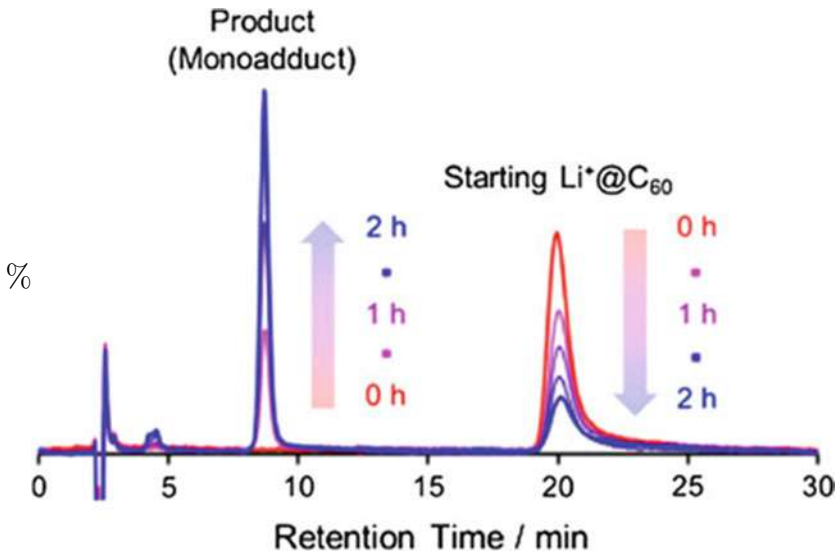

Fig. 7 Illustration of concentration change of Diels-Alder reaction monitored by HPLC

where k is the rate constant, T is the temperature, R is the gas constant, ln A is a constant, k_b is the Boltzmann constant, and h is the Planck constant. The results show that there is no entropy difference between these two reactions, suggesting the reactions undergo the same mechanism. The effect of the encapsulated Li^+ is exhibited from the activation energy where $[Li^+@C_{60}](PF_6^-)$ has a 24 kJ mol^{-1} lowered energy than that of the reaction of empty C_{60} (46.2 kJ mol^{-1} vs 70.4 kJ mol^{-1}). The decreased reaction barrier is therefore attributed to the strengthened FMO interactions, a well-known effect of Lewis acid intermediate. Thus the $[Li^+@C_{60}](PF_6^-)$-involved Diels-Alder reaction is recognized as a rare case of Lewis acid-promoted reaction where it happens in intramolecular and without the participation of a heteroatom to coordinate with. In addition, the output of the theoretical calculation at the M06-2X/6-31G(d) level agrees quite well with the experimental results. What's more, the calculation toward the intermediate reactant complexes (RCs) and transition states imply that in the transition state, C_6H_8 approaches to $Li^+@C_{60}$ from the Li^+ side, which indicates that the inner Li^+ of $Li^+@C_{60}$ is capable to stabilize the transition state through the static effect. Since the size of empty C_{60} and $Li^+@C_{60}$ is completely the same, it would also be an ideal model to quantitatively discuss the electronic effects when sheltering the disturbance from steric effect in Diels-Alder reaction (Fig. 8).

The kinetic study's results substantiate the capacity of the encapsulated lithium ion to lower the LUMO level of $Li^+@C_{60}$ and rationalize the catalytic effect of the

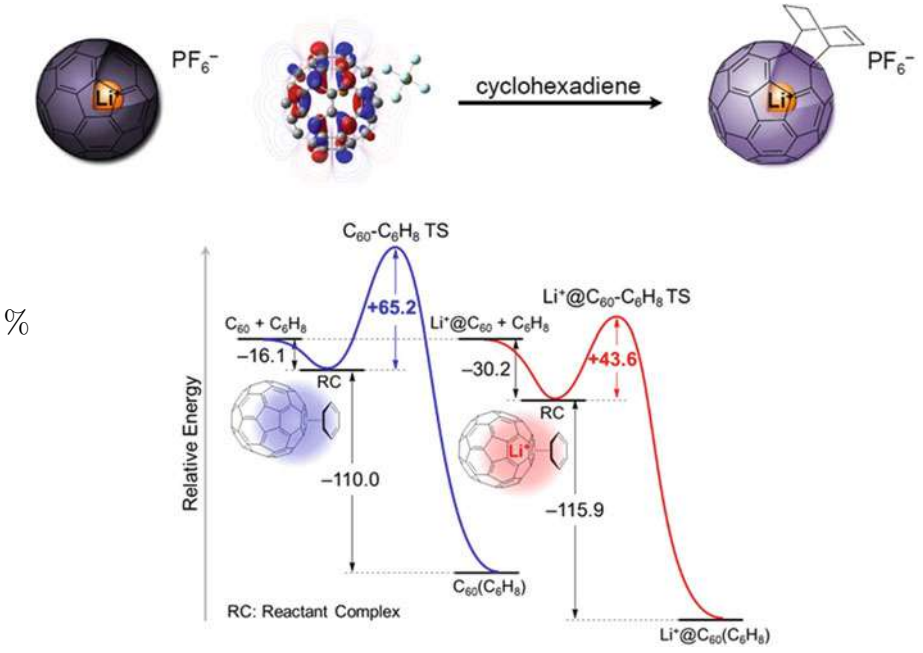

Fig. 8 Energy profiles (in kJ/mol) for the Diels-Alder reaction of empty C60 (blue) and $Li^+@C_{60}$ (red) with 1,3-cyclohexadiene (C_6H_8) calculated by DFT (M06-2X/6-31G(d))

encapsulated Li^+ as Lewis acid catalyst. However, question still remains on how superior the encapsulated Li^+ can act than the normal Li^+ salts since direct comparison cannot be down on the Diels-Alder reaction model, because there is no promotion of Diels-Alder reaction from the Li^+ salts. To quantitatively compare the catalytical effect of the confined Li^+ is relative to the unconfined Li^+. Research has been taken recently to use the reaction concerning conversion from [5,6]- to [6,6]-Li^+@PCBM, since (1) a detailed kinetic study of this reaction has not yet been conducted and (2) the promotion of this reaction from Lewis acid catalyst has been well demonstrated in the literature [43]. Thus, the transformation from [5,6]- to [6,6]-Li^+@PCBM, including that of empty PCBM with external Li^+, was kinetically investigated, and the activation energy E_a and other kinetic parameters were also precisely determined (Tables 1 and 2).

The reaction was found to follow the first-order rule, and the transformation rate of [5,6]-Li^+@PCBM (333 x 10^{10} M^{-1} s^{-1}) was demonstrated to be ca. 700 times greater than that of empty PCBM (0.456 x 10^{10} M^{-1} s^{-1}). The E_a for the transformation of [5,6]- to [6,6]-Li^+@PCBM (100.8 kJ mol^{-1}) is 57.4 kJ mol^{-1} lower than that of empty PCBM (158.2 kJ mol^{-1}), which sustains the relatively higher reaction barrier of this intramolecular reaction. Compared with the case of Diels-Alder reaction, where there is no obvious change of the activation entropy $\Delta S^{\ddagger}$, there is drastic decrease of the reaction disorder. It can be explained that in the transition state, the Li^+ can perfectly pair with the negative charge on the C_{60} cage, while the positive charge on the carbon atom of the intermediate could interact with the counter anion, and both two effects could restrain the reaction disorder. The addition of external Li^+ salts to the empty PCBM system further realized the quantitative comparison. With the addition of LiTFSI salt, as shown in Fig. 9, a first-order dependence was observed within a certain range. Then the catalytical effect of external Li^+ was saturated, yet the overall rate constant enhancement still cannot outweigh than that of the single Li^+ inside the cage. The results further demonstrate that the encapsulated Li^+ accelerates

Table 1 First-order rate constants for isomerization from [5,6]- to [6,6]-Li + −encapsulated and empty PCBM

[5, 6]– to [6]–[Li^+@PCBM]TFSI–		[5, 6]– to [6]–empty PCBM	
Temp. [K]	$10^6 k_1$ [$M^{-1}S^{-1}$]	Temp. [K]	$10^6 k_1$ [$M^{-1}S^{-1}$]
361	2.312	442	3.182
370	5.950	449	6.252
378	11.03	453	8.604
384	17.50	458	14.16
		463	22.60
423	333[a]	423	0.456[a]

Table 2 Activation parameters for isomerization from [5,6]- to [6,6]-Li + −encapsulated and empty PCBM

3000	E_a kJ mol^{-1}	$\Delta H^{\ddagger}$ kJ mol^{-1}	$\Delta S^{\ddagger}$ J mol^{-1}	$\Delta G^{\ddagger}$ [a] kJ mol^{-1}
Li^+@PCBM	100.8	97.68	−83.4	128.5
Emp. PCBM	158.2	154.4	−4.98	156.6

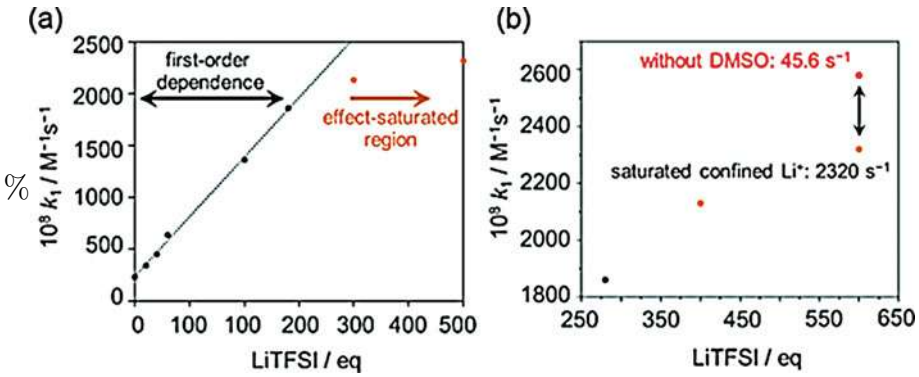

Fig. 9 (**a**) Concentration-dependent acceleration effect by externally added LiTFSI for isomerization of [5,6]-empty PCBM at 423 K. (**b**) Expanded view of (**a**) in low concentration range

the reaction more efficiently owing to the higher effective charge resulting from the steric protection by the C_{60} cage.

From the above-mentioned kinetic studies on the reaction of $Li^+@C_{60}$, it can be concluded that $Li^+@C_{60}$ has unmatched advantages than the normal Li^+ Lewis acid catalyst, with the help of the shelter of the heteroatomless fullerene cage could offer well protection for the Li^+ from been poisoned by forming strong ion pairing with counter anions and solvation and consequently hinder the Lewis acidity. The exploration of $Li^+@C_{60}$ is expected to help in the design of new Lewis acid-catalyzed reactions with very high efficiency.

Neutral Li@C60, $Li^+@C_{60}^{\bullet-}$

Neutralization of Li^+C_{60} Through Electrochemistry

So far, all the knowledge of $Li@C_{60}$ we have discussed are referring to item $Li^+@C_{60}$, the salt form of $Li@C_{60}$ arising from the oxidation during purification of crude $Li@C_{60}$. Undeniably, the successful separation of $Li^+@C_{60}$ salt helps to provide a versatile platform for utilizing this very material with more convenience than normal metal-encapsulated fullerene owing to the superior solubility and purity of $Li^+@C_{60}$. Yet the fact is that the sincere $Li@C_{60}$ has not been obtained and this pity also make $Li@C_{60}$ a fuzzy member of the family of endohedral metallofullerenes (EMFs) (Fig. 10) [29–32]. Besides, even though the salt form of $Li@C_{60}$ brings enhanced solubility of $Li@C_{60}$, there are problems brought by the giant counter anion including the unstable feature and the intermolecular disturbance by the stereo effect. Together with the increased depth insight of the intrinsic $Li^+@C_{60}$, researchers got down to study the reduction reaction from $Li^+@C_{60}$ to $Li@C_{60}$.

Neutralization of Li^+C_{60} through electrochemistry made the first step toward the synthesis of neutral $Li@C_{60}$. In the pioneer work done in 2013, researchers

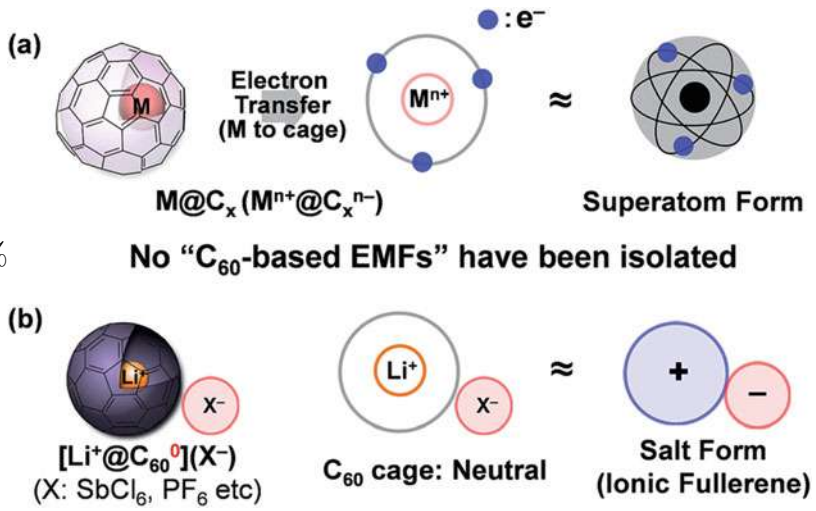

Fig. 10 Illustration of electronic states of a. a general endohedral metallofullerene M@C_x and b. lithium ion-containing fullerene $[Li^+@C_{60}]X^-$

confirmed the existence of neutral Li@C_{60} around the cathode when applying constant current on the $Li^+C_{60}PF_6^-$ *o*-DCB solution in an H-shaped cell through electrochemistry reduction [33]. Even though the $Li^+@C_{60}^{\cdot-}$ was characterized by UV-vis-NIR and ESR spectroscopy, respectively, the formed $Li^+@C_{60}^{\cdot-}$ could not be obtained because of the similar solubility of $Li^+C_{60}PF_6^-$ and $Li^+@C_{60}^{\cdot-}$ in *o*-DCB. Then the final step toward isolation of $Li^+@C_{60}^{\bullet-}$ was accomplished in 2016 when researchers employed $Li^+@C_{60}TFSI^-$ DCM solution instead of $Li^+C_{60}PF_6^-$ *o*-DCB solution as the reaction system, since the TFSI counter anion can drastically increase the solubility of $Li^+@C_{60}$ in DCM where $Li^+@C_{60}^{\bullet-}$ maintains poor solubility [34] (Fig. 11). It can be observed by naked eyes that as reaction proceeds, the purple solution gradually became colorless along with the deposition of the reduced compound on the surface of the cathode area. Furthermore, researchers acquired the single crystal of $Li^+@C_{60}^{\bullet-}$ for the first time by using NiOEP ($OEP2^-$ = octaethylporphyrin dianion), a common crystallizing agent for endohedral fullerenes. The co-crystal clearly indicates that the $Li^+@C_{60}^{\bullet-}$ exists as dimer. It conforms to the known feature of occurring equilibrium of the fullerene radical anion and its dimer form in the solution phase and solid phase, respectively. There is also similar well-known precedence in the literature. The analysis of single-crystal data shows that in the dimer form, the Li^+ is laying near the C2 atom, resulting from the attraction of the excess electron on the 6:6 bond. The approach of Li^+ not only causes the Li–C2 distance to be 2.20(1) Å at 100 K, which is shorter than that of the pristine $Li^+@C_{60}$ (2.344(6) Å), but also helps to further stabilize the anionic C_{60} cage bonded by the single C–C bond in the $Li^+@C_{60}$ (Fig. 11).

Even though the bulk synthesis of neutral $Li^+@C_{60}$ was successfully achieved by electrochemical reduction, the method itself has quite a lot of drawbacks including

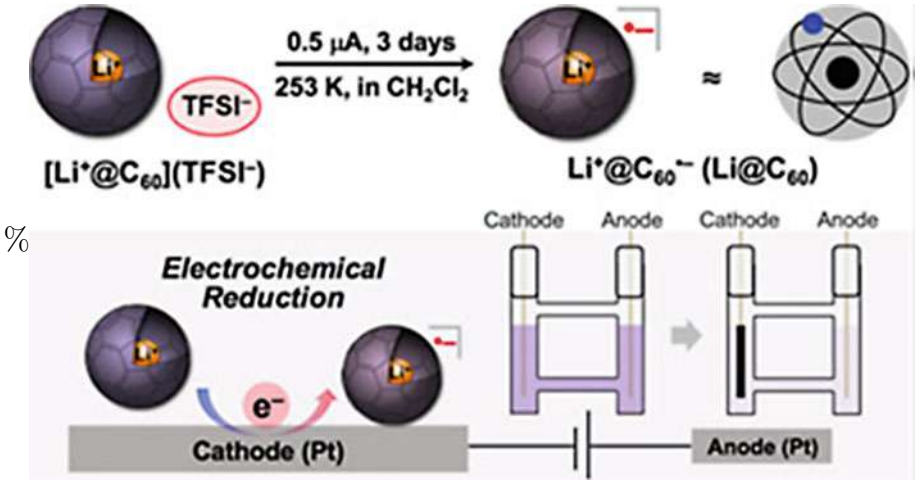

Fig. 11 Schematic illustration of the electrochemical reduction to synthesize Li@C_{60}

relatively high cost, long reaction time, and small scale restrained by the volume of H-shaped cell. To enlarge the reaction dimensions, researchers realized changing the reduction method from electrochemical reduction to chemical reduction and increasing the reaction while shortening the reaction duration. Ideally, the reductant should have first oxidation potential right between first and second reduction potential of $Li^+@C_{60}$, which is known to be −0.32 V and − 0.95 V. Thus, decamethylferrocene (Fc*) with the first reduction potential of −0.59 V was then chosen as the chemical reductant [35]. Surprisingly, the pure Li@C_{60} immediately appears as black powder as soon as decamethylferrocene was added in the reaction system. The characterization of the purified samples obtained by chemical reduction also indicated the dimeric existence of neutral Li@C_{60} (Fig. 12).

Although the neutral Li@C_{60} reveals drawbacks like low solubility and dimerization, it has been well-adapted into applications like photovoltaics which will be discussed in the next section. The neutralization of Li@C_{60} derivatives is also promising to afford product with better solubility and less dimer with the steric effect by adduct function groups which is worth expecting in the coming future.

Device Application of $Li^+@C_{60}$

Endohedral Fullerenes in Photovoltaics

In confront to resource depletion as well as environmental pollution, solar cells, one of the cutting-edge renewable energy, keep receiving attentions from academic field and have yielded a wealth of progress in efficient industrial production [36]. Fullerenes, owing to their adjustable lowest unoccupied molecular orbital (LUMO) and

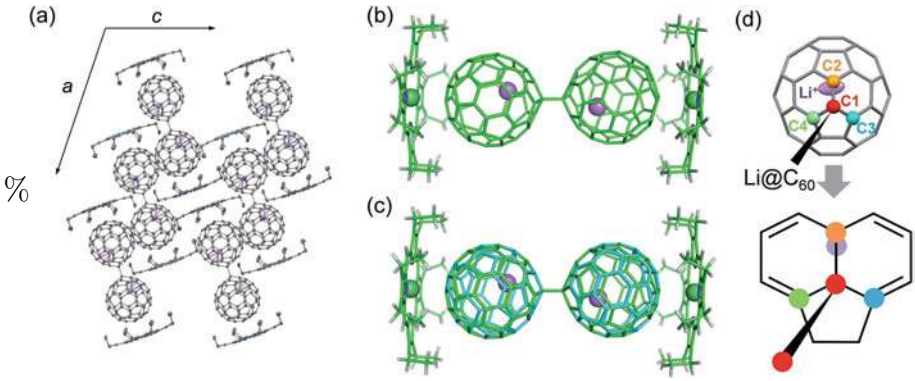

Fig. 12 Illustration of crystal structure of the co-crystal of $Li^{+}@C_{60}^{\cdot-}$ and Ni(OEP)

their intrinsic high electron charge-transfer ability auxiliary for singlet exciton dissociation at the donor-acceptor interfaces as a n-type semiconductor, have been widely employed in the active layer in the organic solar cells (OSCs) and bulk heterojunction (BHJ) polymer solar cells (PSCs). Among the enormous efforts that intend to design the competitive fullerene-employed solar cells, the only existed case to use endohedral fullerenes in the literature is reported by Dress and co-workers [37]. A series of C_{80} endohedral cluster trimetallic nitride endohedral fullerene (TNEFs) derivatives with PCBM-alike structure of $Lu_3N@C_{80}$-PCBX with X = M (methyl), B (butyl), H (hexyl), or O (octyl) end groups on the substituents are synthesized and used as acceptors in BHJ solar cells. $Lu_3N@C_{80}$-PCBX exhibits similar charge mobility compared to C_{60}-PCBM (4.0×10^{-4} for $Lu_3N@C_{80}$-PCBX versus 1.4×10^{-4} cm^2 V^{-1} s^{-1} for C_{60}-PCBM). Since $Lu_3N@C_{80}$-PCBX also possesses similar solubility and miscibility with C_{60}-PCBM, it can be blended with poly(3-hexylthiophene) (P3HT) as the activate layer in the OSCs.

Thus, OSCs with acceptor of $Lu_3N@C_{80}$-PCBX and empty catalogue C_{60}-PCBM and P3HT as donor were fabricated and compared. The $Lu_3N@C_{80}$-PCBX employed devices show a high open-circuit voltage (V_{OC}) of 890 mV and a *power conversion efficiency* (PCE) of 4.2%, which shows an improvement of 280 mV and 0.8% in contrast to employed C_{60}-PCBM devices. To note, the C_{80} fullerene derivatives used as acceptors are known to have potentially high V_{OC}, and the obtained V_{OC} has achieved the highest V_{OC} record for a P3HT/fullerene device. However, the improvement of PCE is limited since there is a drop of *short-circuit current density* (J_{SC}), which compensates for the significantly improved V_{OC}. Intriguingly, Moritz and co-workers successfully figured out that there are triplet excitons formed on the polymer chain, indicating that the intermolecular electron transfer from encapsulated cation to carbon cage of the $Lu_3N@C_{80}$-PCBX acceptor can cause the electron back transfer (EBT) phenomenon to P3HT donor. Even though the abovementioned OSCs with endohedral fullerenes have drawn insights into designing new efficient photovoltaics, there was no further precedent of OSCs applying endohedral fullerenes in consequence of barriers including full synthesis

and characterization of corresponding endohedral fullerenes derivatives, not to mention the relatively high price of C_{70} and C_{80} fullerene clusters.

$Li^+@C_{60}$ as P-Dopant in Perovskite Solar Cells

Since 2,2′,7,7′-tetrakis-(*N*,*N*-di-*p*-methoxyphenylamine)-9,9′-spirobifluorene (spiro-OMeTAD) was first employed as organic hole transporting material (HTM) for solid-state, dye-sensitized solar cells (ssDSCs) in 1998 by Bach and co-workers [38], it has received tremendous efforts from scientist. Furthermore, it has already became the most widely used hole transporting material of lead halide perovskite solar cells (PSCs), which is the most intensified studied topic in the realm of photovoltaics in the recent decade. Since Spiro-OMeTAD is infamous for its low solubility and conductivity, the mixing of Spiro-OMeTAD with p-dopant bis(trifluoromethylsulfonyl) imide (LiTFSI) is inevitably needed, which also brings problems of instability arising from the penetration of Li^+ to perovskite layer and the uncontrolled oxidization extent of spiro-MeOTAD [39]. To overcome the drawbacks of the LiTFSI-doped spiro-MeOTAD layer, and to solve the practical feasibility of PSCs, researchers employed $Li^+@C_{60}TFSI^-$ in place of LiTFSI as the p-type dopant as well as antioxidant and made the first example of using endohedral fullerenes in PSCs [40].

The overall PCE of $Li^+@C_{60}TFSI^-$-doped PSCs is 13.1% in comparison to 17.0% of LiTFSI-doped reference. Unlike the case of reference when PCE reaches peak quickly and undergo a continuant decrease, the $Li^+@C_{60}TFSI^-$-doped PSCs exhibit longer soaking duration and sevenfold stability than the reference. When using more stable mixed $(FAPbI_3)_{0.85}(MAPbBr_3)_{0.15}$-based PSCs, the PCE increased to 16.8% in confront to 18.5% of reference with tenfold higher stability. The improved stability indicates controlled protection derivatives from the addition of $Li^+@C_{60}TFSI^-$. To note, the actual functionalized compound in the general HTM layer is the oxidized spiro-MeOTAD indirectly oxidized by LiTFSI, which means oxygen is needed to be included in the system while simultaneously causing uncontrolled reaction level. As we have discussed above, $Li^+@C_{60}TFSI^-$ could go through one electron transfer from reductant and ultimately became neutral $Li^+@C_{60}^{\bullet-}$, which is confirmed by the UV-vis spectrum at around 500 nm and 1035 nm, respectively, which are assigned of spiro-MeOTAD$^{\bullet+}$TFSI$^-$ and $Li^+@C_{60}^{\bullet-}$. The existence of $Li^+@C_{60}^{\bullet-}$ means in situ oxidation of spiro-MeOTAD could take place without the presence of oxygen and water. Besides, the formed $Li^+@C_{60}^{\bullet-}$ is also able to work as antioxidant to gain further protection for the HTM layer and secure the stability of PSCs. In addition, with the protection of the carbon cage encompassing Li^+, the enlarged dopant size prohibits the penetration of p-dopant downward and poisons the perovskite layer. The whole oxidation mechanism could be illustrated as follows:

1. spiro-MeOTAD + $[Li^+@C_{60}]TFSI^- \rightleftarrows$ spiro-MeOTAD$^{\bullet+}$TFSI$^-$ + $Li^+@C_{60}^{\bullet-}$,
2. $Li^+@C_{60}/Li^+@C_{60}^{\bullet-} + O_2$ or $O_2^{\bullet-} \rightarrow Li^+@C_{60}O_xO^-$.

The proposed mechanism is further sustained by time-resolved microwave conductivity (TRMC) and long-term stability tests. Both measurements show long-scale stability for $Li^+@C_{60}TFSI^-$-doped PSCs. By further analyzing the practical state of the reaction, researchers found that the amount of $[Li^+@C_{60}]TFSI^-$ added in the pre-mixed HTL solution was actually saturated, while the solubility of $Li^+@C_{60}^{\bullet-}$ was impaired after losing the counter anion, thus suggesting the reaction (1) would first shift right and then reach the equilibrium. Ideally it would afford the best device performance if an appropriate reaction extent could be determined. Then researchers performed UV-vis experiment to trace the stirring solution with reaction time from 0 h to 10 h (Fig. 13) [41]. The results indicated the concentration of $Li^+@C_{60}^{\bullet-}$ reached its summit after 2 h and then decreased by transforming to $Li@C_{60}$ dimer or polymer while there was an increase of spiro-MeOTAD$^{\bullet+}TFSI^-$ over time, as a result of the continuance consuming of $Li^+@C_{60}^{\bullet-}$. Then HTL solution with various reaction times was used to fabricate perovskite solar cells with a carbon nanotube (CNT) electrode, which can efficiently prevent metal ion migration and induce an encapsulation effect. Conforming with the long soaking duration the previous study showed, the best device performance was turned out to be 17.2% given by the pre-mixed solution after stirring for 2 h, 0.3% higher than the reference (ITO/SnO_2/[(phenethylamine) (PEA))$_2PbI_4]_1$[(formamidinium (FA))$_{0.97}Cs_{0.03}PbI_3]_{59}$ (2D-3D $FACsPbI_3$)/CNT). The triggered factor brought to achieving first reference surpass result of $[Li^+@C_{60}]TFSI^-$-doped PSCs can be attributed to (1) the function of CNT electrode as a filtrate to exclude the $[Li^+@C_{60}]TFSI^-$ precipitate and build steady charge flow for hole transportation as reflection of the high V_{oc} of 1.09 V in confront to previous 1.01 V and (2) the optimization of the redox time for the reaction between $[Li^+@C_{60}]TFSI^-$ and spiro-MeOTAD. Aside from the improved PCE, the combination merit brought by antioxidant $[Li^+@C_{60}]TFSI^-$ and CNT electrode gave the 1100 h stability under constant illumination in a severe condition (60 °C, 70% humidity) as detected by long-term stability measurement.

$Li^+@C_{60}$ as ETL in Perovskite Solar Cells

Apart from being utilized as p-type dopant in the HTL, $Li@C_{60}$ was also employed as ETL in PSCs [42]. Solution processed pristine fullerenes such as C_{60} and C_{70} has been well demonstrated as ETL in PSCs and exhibited merits like small hysteresis in the *J–V* curves, simple fabrication methods, and better device stability than metal oxides material. Yet the low conductivity of fullerene layer restrained further use of C_{60} in PSCs. To overcome this barrier, researchers managed to use neutral $Li@C_{60}$-doped C_{60} layer and achieved better PSC performance. The size of $Li@C_{60}$ is completely same as the pristine C_{60}, which enables the mixture to form uniform layer without causing distortion of crystallinity. The neutral $Li@C_{60}$ was prepared by chemical reduction as mentioned in the previous section. In order to make neat layer by solution process, *o*-DCB was chosen as the solvent owing to its mild solubility for fullerene derivatives, and particle size distribution suggested $Li@C_{60}$ induced a 120 nm size aggregation to the C_{60} solution. The film made from solution

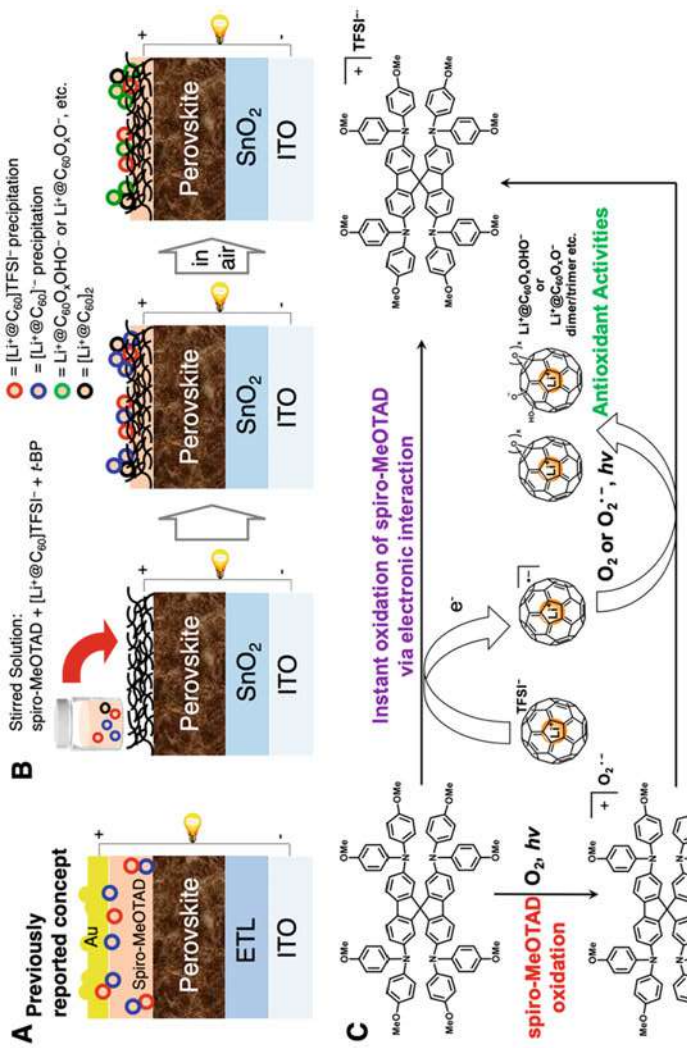

Fig. 13 Schematic illustration of (**a**) structure of $Li^+@C_{60}TFSI^-$-doped PSCs. (**b**) Structure of $Li^+@C_{60}TFSI^-$-doped PSCs with CNTs used as the top electrode. (**c**) Reaction mechanism of spiro-MeOTAD where $Li^+@C_{60}TFSI^-$ is used instead of Li^+TFSI^-

process showed high uniformity and conductivity, which has a 0.12 eV rise in Fermi level, and index Li@C_{60} played the role as n-type dopant. The inverted structure PSCs (ITO/poly(3,4-ethylenedioxythiophene)polystyrene sulfonate (PEDOT:PSS)/$CH_3NH_3PbI_3$/C_{60}:Li@C_{60}/Au) was fabricated and showed a 3.51% PCE improvement from 4.67% of the pristine C_{60} reference to 8.18% of Li@C_{60}-added C_{60} devices. There was a drastic increase in J_{sc} and fill factor along with a decrease in series resistance (R_S) as reflection to the enhanced ETL conductivity.

To briefly summarize, the intensified production of Li-encapsulated fullerene-containing PSCs represents a milestone that the study on basic property of Li-encapsulated fullerene has in turn yielded outcome in cutting-edge applications. The intriguing characteristic of Li-encapsulated fullerene endows its tremendous availabilities to be used both as n-type dopant as the neutral form and p-type dopant as cation form, while both scenarios tend to harvest considerable improvement in PCE as well as provide new intrinsic knowledge of PSCs. However, even the primary stage of applying Li-encapsulated fullerene in PSCs has afforded pretty good results, limited solubility of *o*-DCB or CB for both Li@C_{60} and Li^+@C_{60} prevents gaining better device performance of these materials. Perhaps using chemical modified Li-encapsulated fullerene derivatives could solve the problem. In the case of empty fullerenes, the adducts on the fullerene cage could bring lowered J_{sc} and fill factor because of the weakened electron transporting ability. In the Li@C_{60}-added case, it has been proven that the increased conductivity by doping could lead to better J_{sc} and fill factor, which is promising to further explore the availability of Li-encapsulated fullerene-containing PSCs.

Conclusion and Prospects

To summarize the conclusion of this chapter, we have introduced the development of Li@C_{60} in the past decade from its origin to application in the field of photovoltaics. The research upon Li@C_{60} was sporadic until the scaled-up production process was developed in 2012; and from when, there was a boost in study to reveal the basic property, to synthesize Li@C_{60} derivatives through chemical modification, and to apply them in the perovskite solar cells; and in turn that research has yielded ample comprehension of Li@C_{60}. The unconventional form of Li@C_{60} as a cationic salt offered itself puissant capacity in the chemical reaction, derived from the lowered LUMO level brought by the encapsulated lithium ion and the superior ability to get fully isolated and characterized as salt. To some extent, these advantages are conducive to not only rapidly expose the physical properties of Li^+@C_{60} including single-crystal structure, charge-transfer ability, and electron transfer ability but also offer a versatile platform for chemists to obtained corresponded Li^+@C_{60} derivatives. Moreover, due to the relative mild size of lithium ion, the size of Li^+@C_{60} is perfectly accordant to the empty [60]fullerene, which help researchers to directly compare the cationic feature endowed by the inside lithium ion. Surprisingly, the study proved a rare case of lithium Lewis acid catalyst that could functionalize even if the substrate does not have a heteroatom to coordinate. The strengthened

catalytical effect from the confined Li^+ shows that the disengaged outer one was then quantitatively discussed. However, even though the research toward cationic $Li^+@C_{60}$ has brought precious knowledge for fullerene chemistry and even basic chemistry, it was treated as a real member of the family of EMFs only since researchers managed to obtain neutral $Li@C_{60}$ through reduction methods. Still, the synthesis toward neutral $Li@C_{60}$ or $Li@C_{60}$ derivatives was via the reduction from the corresponded $Li^+@C_{60}$, due to the low solubility and the dimerization trend of neutral $Li@C_{60}$. Therefore, more efforts are expected to be taken for getting deeper insides into this topic. We also illustrated the application of $Li^+@C_{60}$ and $Li@C_{60}$ as p-type dopant for Spiro-OMeTAD in HTL and n-type dopant for PCBM as ETL in perovskite solar cells. The two novel materials have both boosted the PCE and stability individually, owing to their antioxidant property and enhanced conductivity, respectively. Apart from being employed in photovoltaics, $Li@C_{60}$ is also anticipated as a promising material in biological fields. Hence, we hope by composing this chapter that $Li@C_{60}$, as an emerging novel material, could appear into the sight of scholars in the different research fields and offer a referable understanding for them.

References

1. Shinohara H, Yamaguchi H, Hayashi N, Sato H, Ohkohchi M, Ando Y, Saito Y (1993) Isolation and spectroscopic properties of scandium fullerenes ($Sc_2@C_{74}$, $Sc_2@C_{82}$, and $Sc_2@C_{84}$). J Phys Chem 97(17):4259–4261. https://doi.org/10.1021/j100119a004
2. Kikuchi K, Suzuki S, Nakao Y, Nakahara N, Wakabayashi T, Shiromaru H, Saito K, Ikemoto I, Achiba Y (1993) Isolation and characterization of the metallofullerene LaC_{82}. Chem Phys Lett 216(1):67–71. https://doi.org/10.1016/0009-2614(93)E1269-M
3. Takata M, Umeda B, Nishibori E, Sakata M, Saito Y, Ohno M, Shinohara H (1995) Confirmation by X-ray diffraction of the endohedral nature of the metallofullerene $Y@C_{82}$. Nature 377(9):46–49. https://doi.org/10.1038/377046a0
4. Chai Y, Guo T, Jin C, Haufler RE, Chibante LPF, Fure J, Wang L, Alford JM, Smalley RE (1991) Fullerenes with metals inside. J Phys Chem 95(20):7564–7568. https://doi.org/10.1021/j100173a002
5. Christian JF, Wan Z, Anderson SL (1992) $O^+ + C_{60}{\cdot}C_{60}O^+$ production and decomposition, charge transfer, and formation of $C_{59}O^+$. Chem Phys Lett 199(3):373–378. https://doi.org/10.1016/0009-2614(92)80134-W
6. Christian JF, Wan Z, Anderson SL (1992) Nitrogen ion (N+) + C_{60} fullerene reactive scattering: substitution, charge transfer, and fragmentation. J Phys Chem 96(26):10597–10600. https://doi.org/10.1021/j100205a006
7. Wan Z, Christian JF, Anderson SL (1992) $Ne^+ + C_{60}$: collision energy and impact parameter dependence for endohedral complex formation, fragmentation, and charge transfer. J Chem Phys 96(8):3344–3347. https://doi.org/10.1063/1.461931
8. Wan ZM, James F, Christian JF, Basir Y, Anderson SL (1993) Collision of alkali ions with C_{60}/C_{70}: insertion, thermionic emission, and fragmentation. J Chem Phys 99(07):5858–5870. https://doi.org/10.1063/1.465939
9. Tellgmann R, Krawez N, Lin S-H, Hertel IV, Campbell EEB (1996) Endohedral fullerene production. Nature 382(8):407–408. https://doi.org/10.1038/382407a0

10. Campbell EEB, Tellgmann R, Krawez N, Hertel IV (1997) Production and LDMS characterisation of endohedral alkali fullerene films. J Phys Chem Solids 58(11):1763–1769. https://doi.org/10.1016/S0022-3697(97)00063-2
11. Okada H, Komuro T, Sakai T, Matsuo Y, Ono Y, Omote K, Yokoo Y, Kawachi K, Kasama Y, Ono S, Hatakeyama R, Kaneko T, Tobita H (2012) Preparation of endohedral fullerene containing lithium (Li@C_{60}) and isolation as pure hexafluorophosphate salt ([Li^+@C_{60}][PF_6^-]). RSC Adv 2(28):10624–10631. https://doi.org/10.1039/c2ra21244g
12. Komatsu K, Murata M, Murata Y (2005) Encapsulation of molecular hydrogen in fullerene C_{60} by organic synthesis. Science 307(5707):238–240. https://doi.org/10.1126/science.1106185
13. Saunders M, Cross RJ, Jimenez-Vazquez HA, Shimshi R, Khong A (1996) Noble gas atoms inside fullerenes. Science 271(5256):1693–1697. https://doi.org/10.1126/science.271.5256.1693
14. Syamala MS, Cross RJ, Saunders M (2002) 129Xe NMR spectrum of xenon inside C60. J Am Chem Soc 124(21):6216–6219. https://doi.org/10.1021/ja012676f
15. Aoyagi S, Nishibori E, Sawa H, Sugimoto K, Takata M, Miyata Y, Kitaura R, Shinohara H, Okada H, Sakai T, Ono Y, Kawachi K, Yokoo K, Ono S, Omote K, Kasama Y, Ishikawa S, Komuro T, Tobita H (2010) A layered ionic crystal of polar Li@C_{60} superatoms. Nat Chem 2(6):678–683. https://doi.org/10.1038/nchem.698
16. Aoyagi S, Sado Y, Nishibori E, Sawa H, Okada H, Tobita H, Kasama Y, Kitaura R, Shinohara H (2012) Rock-salt-type crystal of thermally contracted C_{60} with encapsulated lithium cation. Angewandte Chem Int Edition 51(14):3377–3381. https://doi.org/10.1002/anie.201108551
17. Matsuo Y, Okada H, Maruyama M, Sato H, Tobita H, Ono Y, Omote K, Kawachi K, Kasama Y (2012) Covalently chemical modification of lithium ion-encapsulated fullerene: synthesis and characterization of [Li^+@PCBM]PF_6^-. Org Lett 14(14):3784–3787. https://doi.org/10.1021/ol301671n
18. Kawakami H, Okada H, Matsuo Y (2013) Efficient Diels-Alder addition of cyclopentadiene to lithium ion encapsulated [60]fullerene. Org Lett 15(17):4466–4469. https://doi.org/10.1021/ol4020046
19. Okada H, Matsuo Y (2014) Anion exchange of Li^+@C_{60} salt for improved solubility. Fullerenes Nanotubes Carbon Nanostruct 22(1):262–268. https://doi.org/10.1080/1536383X.2013.812639
20. Okada K, Kawakami H, Aoyagi S, Matsuo Y (2017) Crystallographic structure determination of both [5,6]- and [6,6]-isomers of lithium-ion-containing diphenylmethano[60]fullerene. J Org Chem 82(11):5868–5872. https://doi.org/10.1021/acs.joc.7b00730
21. Ueno H, Okada H, Aoyagi S, Matsuo Y (2017) Synthesis and crystal structure of Li^+@Fluoreno[60]fullerene: effect of encapsulated Lithium ion on electrochemistry of Spiroannelated fullerene. J Org Chem 82(21):11631–11635. https://doi.org/10.1021/acs.joc.7b01893
22. Hummelen JC, Knight BW, LePeq F, Wudl F (1995) Preparation and characterization of Fulleroid and Methanofullerene derivatives. J Org Chem 60(2):532–538. https://doi.org/10.1021/jo00108a012
23. Janssen RAJ, Hummelen JC, Wudl F (1995) Photochemical fulleroid to methanofullerene conversion via the di-. pi.-methane (Zimmerman) rearrangement. J Am Chem Soc 117(1):544–545. https://doi.org/10.1021/ja00106a068
24. Watanabe T, Itoh MF, Komuro T, Okada H, Sakai T, Ono Y, Kawachi K, Kasama Y, Tobita H (2014) Iridium and platinum complexes of Li^+@C_{60}. Organometallics 33(3):608–611. https://doi.org/10.1021/om4008899
25. Balch AL, Catalano VJ, Lee Balch AL, Catalano VJ, Lee JW (1991) Accumulating evidence for the selective reactivity of the 6-6 ring fusion of fullerene, C60. Preparation and structure of (.eta.2-C60)Ir(CO)Cl(PPh3)2.cntdot.5C6H6. Inorg Chem 30(21):3980–3981. https://doi.org/10.1021/ic00021a003
26. Ueno H, Nishihara T, Segawa Y, Itami K (2015) Cycloparaphenylene-based ionic donor-acceptor supramolecule: isolation and characterization of Li^+@C_{60} ⊂ [10] CPP. Angewandte Chem Int Edition 54(12):3707–3711. https://doi.org/10.1002/anie.201500544

27. Ueno H, Kawakami H, Nakagawa K, Okada H, Ikuma N, Aoyagi S, Kokubo K, Matsuo Y, Oshima T (2014) Kinetic study of the Diels–Alder reaction of $Li^+@C_{60}$ with cyclohexadiene: greatly increased reaction rate by encapsulated Li^+. J Am Chem Soc 136(31):11162–11167. https://doi.org/10.1021/ja505952y
28. Ueno H, Kokubo K, Kwon E, Nakamura Y, Ikuma N, Oshima T (2013) Synthesis of a new class of fullerene derivative $Li^+@C_{60}O^-(OH)_7$ as a "cation-encapsulated anion nanoparticle". Nanoscale 5(6):2317–2321. https://doi.org/10.1039/C3NR33608E
29. Shinohara H (2000) Endohedral metallofullerenes. Rep Prog Phys 63(6):843–892. https://doi.org/10.1088/0034-4885/63/6/201
30. Popov AA, Yang S, Dunsch L (2013) Endohedral Fullerenes. Chem Rev 113(8):5989–6113. https://doi.org/10.1021/cr300297r
31. Johnson RD, de Vries MS, Salem J, Bethune DS, Yannoni CS (1992) Electron paramagnetic resonance studies of lanthanum-containing C_{82}. Nature 355(1):239–240. https://doi.org/10.1038/355239a0
32. Nagase S, Kobayashi K (1994) The ionization energies and electron affinities of endohedral metallofullerenes MC_{82} (M = Sc, Y, La): density functional calculations. J Chem Soc Chem Commun 1(24):1837–1838. https://doi.org/10.1039/c39940001837
33. Ueno H, Kokubo K, Nakamura Y, Ohkubo K, Ikuma N, Moriyama H, Fukuzumi S, Oshima T (2013) Ionic conductivity of $[Li^+@C_{60}](PF_6^-)$ in organic solvents and its electrochemical reduction to $Li^+@C_{60}^{\cdot-}$. Chem Commun 49(67):7376–7378. https://doi.org/10.1039/c3cc43901a
34. Ueno H, Aoyagi S, Yamazaki Y, Ohkubo K, Ikuma N, Okada H, Kato T, Matsuo Y, Fukuzumi S, Kokubo K (2016) Electrochemical reduction of cationic $Li^+@C_{60}$ to neutral $Li^+@C_{60}^{\cdot-}$: isolation and characterisation of endohedral [60]fulleride. Chem Sci 7(9):5770–5774. https://doi.org/10.1039/c6sc01209d
35. Okada H, Ueno H, Takabayashi Y, Nakagawa T, Vrankić M, Arvanitidis J, Kusamoto T, Prassides K, Matsuo Y (2019) Chemical reduction of $Li^+@C_{60}$ by decamethylferrocene to produce neutral $Li^+@C_{60}^{\cdot-}$. Carbon 153(7):467–471. https://doi.org/10.1016/j.carbon.2019.07.028
36. Lo PS, Mayumi K (2017) Toward an integrated assessment of the performance of photovoltaic power stations for electricity generation. Appl Energy 186:167–174. https://doi.org/10.1016/j.apenergy.2016.05.102
37. Ross RB, Cardona CM, Guldi DM, Sankaranarayanan SG, Reese MO, Kopidakis N, Peet J, Walker B, Bazan GC, Van Keuren E, Holloway BC, Drees M (2009) Endohedral fullerenes for organic photovoltaic devices. Nat Mater 8(2):208
38. Bach U, Lupo D, Comte P, Moser JE, Weissortel F, Salbeck J, Spreitzer H, Gratzel M (1998) Solid-state dye-sensitized mesoporous TiO_2 solar cells with high photon-to-electron conversion efficiencies. Nature 395(10):583–585. https://doi.org/10.1038/26936
39. Abate A, Leijtens T, Pathak S, Teuscher J, Avolio R, Errico ME, Kirkpatrik J, Ball JM, Docampo P, McPherson I, Snaith H (2013) Lithium salts as "redox active" p-type dopants for organic semiconductors and their impact in solid-state dye sensitized solar cells. Phys Chem Chem Phys 15(7):2572–2579. https://doi.org/10.1039/C2CP44397J
40. Jeon I, Ueno H, Seo S, Aitola K, Nishikubo R, Saeki A, Okada H, Boschloo G, Maruyama S, Matsuo Y (2018) Lithium-ion endohedral fullerene ($Li^+@C_{60}$) dopants in stable perovskite solar cells induce instant doping and anti oxidation. Angewandte Chem Int Edition 57(17):4607–4611. https://doi.org/10.1002/anie.201800816
41. Jeon I, Shawky A, Lin H-S, Seo S, Okada H, Lee J-W, Pal A, Tan S, Anisimov A, Kauppinen EI, Yang Y, Manzhos S, Maruyama S, Matsuo Y (2019) Controlled redox of Lithium-ion endohedral fullerene for efficient and stable metal electrode-free perovskite solar cells. J Am Chem Soc 141(42):16553–16558. https://doi.org/10.1021/jacs.9b06418
42. Ueno H, Jeon I, Lin H-S, Thote A, Nakagawa T, Okada H, Izawa S, Hiramoto M, Daiguji H, Maruyama S, Matsuo Y (2019) $Li@C_{60}$ endohedral fullerene as a supraatomic dopant for C_{60}

electron-transporting layers promoting the efficiency of perovskite solar cells. Chem Commun 55(79):11837–11118. https://doi.org/10.1039/C9CC06120G

43. Ma Y, Ueno H, Okada H, Manzhos S, Matsuo Y (2020) Solvation-Free Li+ Lewis Acid Enhancing Reaction: Kinetic Study of [5,6]-Li+@PCBM to [6,6]-Li+@PCBM. Org Lett 22(18):7239–7243. https://doi.org/10.1021/acs.orglett.0c02570

Part V

Nanostructures of Fullerenes and Metallofullerenes

Self-Assembled Aggregates of Fullerenes

22

Takatsugu Wakahara and Kun'ichi Miyazawa

Contents

Abstract

Recently, self-assembled nano- and microsized aggregates of fullerenes have been attracting increasing attention in the fields of chemistry, physics, and materials science, because their properties can vary significantly from those of the corresponding macrosized bulk systems. Fullerene aggregates with

T. Wakahara (✉)
Research Center for Functional Materials, National Institute for Materials Science, Ibaraki, Japan
e-mail: Wakahara.Takatsugu@nims.go.jp

K. Miyazawa
Department of Industrial Chemistry, Faculty of Engineering, Tokyo University of Science, Tokyo, Japan
e-mail: miyakuni@rs.tus.ac.jp

X. Lu et al. (eds.), *Handbook of Fullerene Science and Technology*,
https://doi.org/10.1007/978-981-16-8994-9_17

low-dimensionality structures, such as fullerene nanowiskers, fullerene nanosheets, and fullerene cubes which can be prepared by liquid–liquid interfacial precipitation, are important for fabricating various optoelectronic and nanoelectronic devices. Fullerenes form a wide variety of donor–acceptor complexes with different classes of organic and organometallic donors. These complexes show a diverse spectrum of physical properties, including metallic conductivity, photoconductivity, and unusual magnetic properties. Therefore, the construction of self-assembled aggregates of nano- and microsized fullerene–donor complexes has emerged as a promising alternative to create multifunctional nanomaterials. This chapter reviews some recent development on the preparation, structure, and properties of the self-assembled aggregates of fullerenes and their donor complexes and presents interesting nano- and microstructures built using fullerenes.

Keywords

Fullerene · Fullerene nanowhisker · Fullerene nanosheet · LLIP · Donor–acceptor complex · CT · FET · Ambipolar

Introduction

Owing to their unique physical and chemical properties, the fullerene – an allotrope of carbon – has shown tremendous potential as a building block for new materials. Figure 1 displays the models of typical C_{60} and C_{70} fullerene molecules. Recently, self-assembled aggregates of fullerenes such as nanowhiskers, nanotubes, nanorods, nanowires, and nanosheets have attracted increasing interest because of their unique chemical and physical properties and their potential application in the fields of materials and medical sciences [1–3]. The unique properties of such fullerenes are a result of their high symmetry and the presence of novel π-conjugated systems. In addition, these low-dimensionality fullerene aggregates can be used to fabricate various optoelectronic and nanoelectronic devices.

Fullerenes form a wide variety of donor–acceptor (D–A) complexes with different classes of organic and organometallic donors [4]. These complexes show a

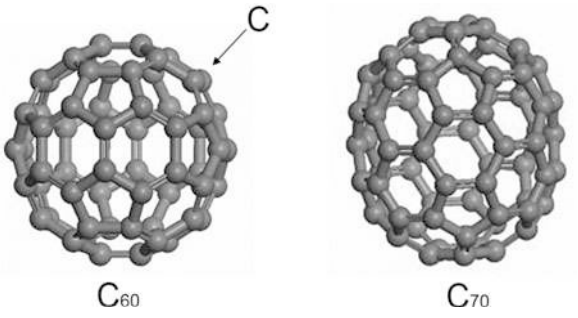

Fig. 1 Models of C_{60} and C_{70} molecules

diverse spectrum of physical properties, including metallic conductivity, photoconductivity, and unusual magnetic properties. Self-assembled aggregates of these fullerene–donor complexes are also being explored as active elements in organic field-effect transistors (FETs) [5].

This chapter reviews various self-assembled aggregates of pristine fullerenes and their donor complexes. This chapter covers not only empty fullerenes such as C_{60} and C_{70} but also endohedral metallofullerenes [6], which can be used to produce novel self-assembled aggregates with unique structures and properties that are normally not observed in empty fullerenes. It also discusses the increasing research on the self-assembled aggregates of fullerenes and their application in the fields of FETs, solar cells, and sensors. In this chapter, the fullerene aggregates are classified based on their structural dimensions, i.e., as one-dimensional (1D; nanowhiskers, nanotubes, nanorods, and nanowires), two-dimensional (2D; nanosheets), and three-dimensional (3D; cubes) structures. This chapter has been organized as follows. First, the construction and properties of the self-assembled aggregates of fullerenes are briefly summarized. Fullerenes are known to act as good electron acceptors. They are combined with electron donors such as porphyrins to construct self-assembled aggregates of fullerene–donor complexes. Hence, this chapter primarily focuses on the fabrication of self-assembled aggregates of fullerene–donor complexes. Finally, it summarizes the physical properties, including the mechanical, optical, and electronic properties, of these fullerene aggregates.

Self-Assembled Aggregates of Fullerenes

Fullerene molecules form various 1D, 2D, and 3D morphologies by self-assembly. Various methods for preparing fullerene in the gas and liquid phases have been discussed in this chapter.

The vacuum sublimation method is useful for preparing pure C_{60} millimeter-sized single crystals [7]. Carbon suit was produced using a direct current arc discharge between two high-purity graphite electrodes in a 0.2 atm helium atmosphere. A powder containing C_{60} and C_{70} was extracted in a boiling toluene using Soxhlet extractor, and a C_{60} powder with a purity of a least 99.5% was obtained using liquid column chromatography. The purified C_{60} powder (~ 10 mg) was placed at the closed end of a quartz tube with a length of 50 cm and a diameter of 1 cm. The tube was evacuated down to 10^{-5} Torr, and then heated to 200 °C to remove solvents. The end of the tube containing the C_{60} powder was heated up to 500 °C, and the sublimed C_{60} was then transported and deposited to the colder side of the furnace at 100–150 °C [7]. This process was repeated to purify the C_{60} powder, which was finally heated in a quartz tube at 500 °C for half an hour and cooled down to room temperature in about four hours. This procedure produced C_{60} crystals as large as $0.5 \times 0.5 \times 0.5$ mm^3. The obtained pure C_{60} crystals, as shown in Fig. 2, had a face-centered cubic (fcc) structure with a lattice constant of $a = 1.42$ nm [7].

C_{60} crystals can be grown in an organic solution of C_{60} molecules to form solvated crystals. By slowly evaporating a m-xylene solution of C_{60}, Ramm et al.

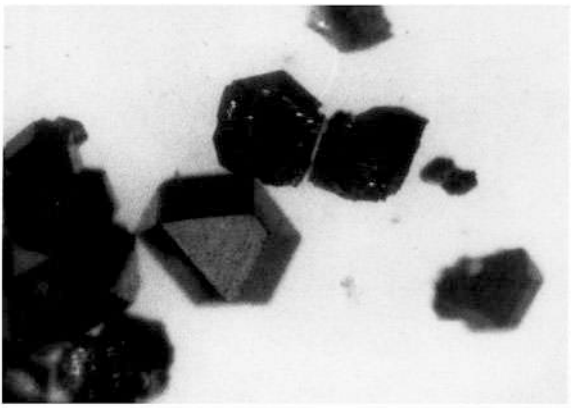

Fig. 2 Average morphology of a C_{60} crystal. (Reprinted with permission from [7])

obtained black C_{60} crystals with hexagonal prisms containing m-xylene molecules. The hexagonal crystals showed lattice constants of a = 2.34 nm and c = 1.00 nm with a space group of $P6_3$ at 20 K and 100 K [8].

Among the various methods developed to prepare fullerene crystals in the liquid phase, the liquid–liquid interfacial precipitation (LLIP) method has been widely used to synthesize 1D, 2D, and 3D fullerene crystals [9]. In the LLIP method, the mutual diffusion of fullerenes in a poor solvent such as isopropyl alcohol (IPA) and a fullerene-saturated toluene solution is utilized to form fullerene nuclei at the liquid–liquid interface.

One-Dimensional Aggregates of Fullerenes

Some examples of 1D materials are whiskers, wires, rods, and tubes, and they are classified as fibers. Although the terminologies of rods and wires do not specify the atomic structure, a whisker is a fibrous material with a crystalline structure. Various forms of whiskers such as those comprising metals, ceramic, and organic molecules have been synthesized. Fullerene nanowhiskers (FNWs) are thin whiskers of diameter <1000 nm [1]. Fullerene nanotubes are tubular FNWs. FNWs are composed of different types of fullerenes such as C_{60}, C_{70}, endohedral fullerenes (also called endofullerenes), and fullerene molecules with functional groups. FNWs are sometimes also called "fullerene nanorods" or "fullerene nanowires." Yosida synthesized C_{60} fullerene whiskers as follows [10]. Opposed two carbon rods with 6 mm in diameter were evaporated by an arc under partial helium atmosphere of ~0.2 bar using a power supply of 40 V and 80 A, and a sootlike material was deposited onto a stainless shield surrounding the rods. The sootlike material was extracted using Soxhlet extractor with boiling benzene. The obtained browned solution was evaporated to yield brown-black crystalline materials. Using column chromatography, a pure fraction containing C_{60} (99.8%) was obtained. C_{60} whiskers were grown by

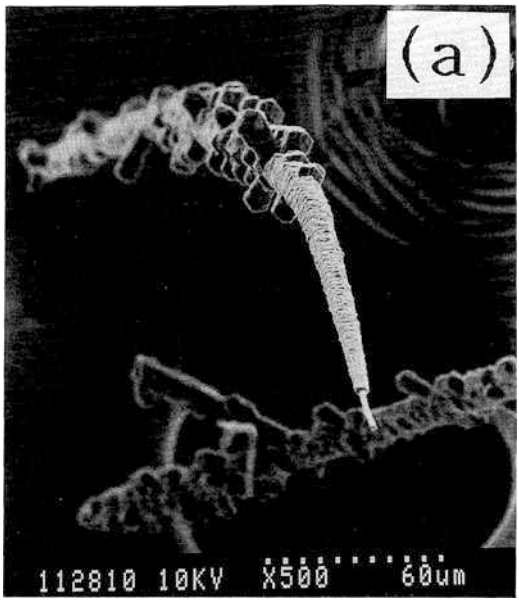

Fig. 3 C_{60} needle-like crystals prepared by evaporating a 95 wt% hexane–5 wt% benzene solution of C_{60}. (Reprinted with permission from [10])

following ways. (1) A solution of ~10 mg C_{60} in 500 mL of solvent containing 95 wt% hexane and 5 wt% benzene was evaporated at 80 °C over 3 days. (2) A solution of ~20 mL with a C_{60} concentration similar to (1) was evaporated at room temperature for 3 days. The C_{60} whiskers fabricated by the process of (1) showed a length of ~300μm and a cross-section of ~60 × 60μm^2, while the C_{60} whiskers fabricated by the process of (2) exhibited a length of ~7 mm, and a diameter of ~15μm. The C_{60} whiskers synthesized at room temperature exhibited rugged surfaces and C_{60} microcrystals along their growth axis (Fig. 3).

Similar to the needle-like crystals reported by Yosida [10], needle-like crystals of C_{60} with diameters of 100–200μm and lengths of >1 mm were fabricated by a sublimation method by evaporating C_{60} at 1173 K under an argon gas flow (Fig. 4) [11]. The fabrication process was as follows. Firstly, 1 g of C_{60} fullerene was set on a silicon substrate located at the center of the heated section of a furnace, and was annealed at 1173 K for one hour. During the annealing, to prevent the oxidizing of fullerene, 0.5 L of argon per minute was flowed through the furnace to remove the oxygen in the air. The needle-like C_{60} crystals, called fullerene finned-nanopillars (FFNPs), have planar crystals along the growth direction.

The LLIP method has the following advantages [1]:

1. The synthesis can be conducted at room temperature in air using simple apparatuses such as glass bottles and refrigerators.
2. Various elements can be doped into the FNWs in solution.

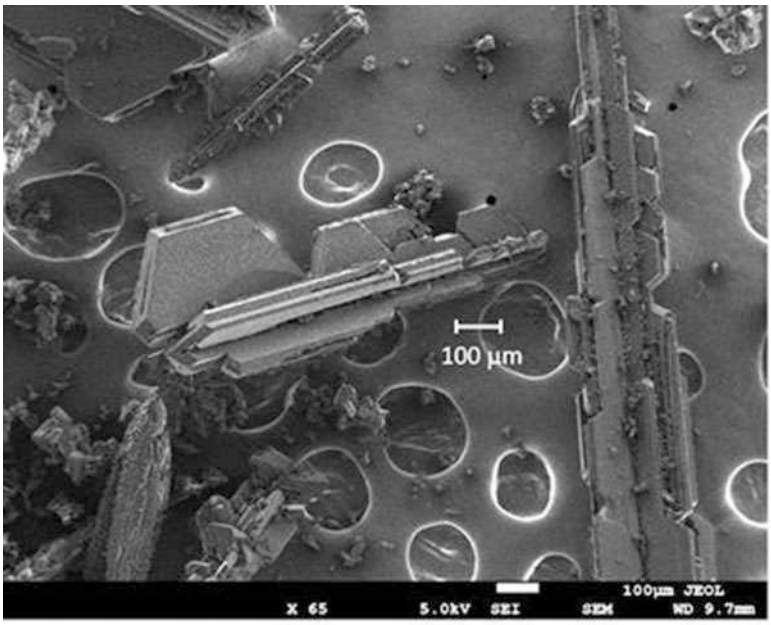

Fig. 4 SEM images of needle-like C_{60} crystals obtained by annealing at 1173 K for 1 h under an argon gas flow of 0.5 L/min. (Reproduced with permission from [11])

3. Multicomponent FNWs composed of different types of fullerene molecules can be synthesized.
4. The diameter of FNWs can be varied by using the appropriate solvent species and composition, growth temperature, and other factors that influence the nucleation and growth of fullerene embryo crystals.
5. Both the FNWs and fine 2D and 3D crystals of fullerene molecules can be synthesized.

As described previously, the LLIP method utilizes the mutual diffusion between a poor solvent of fullerenes, such as IPA, and a good solvent saturated with fullerene. An example of a typical good solvent for fullerenes is toluene. For example, in the synthesis of C_{60}FNWs (or C_{60}NWs), an aliquot of a C_{60}-saturated toluene solution is poured into a transparent glass bottle. Transparent bottles are generally used with the LLIP method, as the growth of C_{60}FNWs is assisted by visible light. Next, a suitable amount of IPA is gently and gradually added to the solution to prepare a liquid–liquid interface. Then, the glass bottle is capped and placed in an incubator and left to stand at temperature of <25 °C. The interdiffusion of toluene and IPA occurs and the liquid–liquid interface becomes supersaturated with C_{60}, resulting in the nucleation of C_{60}FNWs. This supersaturated state is maintained during the mutual diffusion of IPA and toluene and it enhances the growth of C_{60}FNWs. This procedure is called the "static LLIP method." This method can be conducted either by layering a poor

solvent onto a good solvent or vice versa, which can be combined through various methods such as manual mixing and mixing through ultrasonication and injection of a liquid [12–15]. The use of ultrasonication or injection allows rapid mixing of both good and poor solvents, forming fine fullerene nuclei that grow into various shapes. These LLIP methods are collectively known as the "dynamic LLIP method (dLLIP method)."

The size of the initial nuclei of FNWs is influenced by the degree of supersaturation of the fullerene solution, which is determined by the mixing ratio of both good and poor solvents [14]. In the dLLIP process, the mixing between the good solvent and the poor solvent can be performed either manually or ultrasonically. As a result, microscopic liquid–liquid interfaces form between the fullerene solution and the poor solvent of fullerene. The supersaturated solutions cause rapid nucleation of fine fullerene crystals, resulting in the formation of granular, 1D, and 2D fullerene crystal morphologies. The formation of such fullerene crystals depends on the growth kinetics, which in turn are governed by the degree of supersaturation, solvent species, and temperature.

An example of the dLLIP method for the preparation of C_{60}FNWs using benzene and IPA is shown by Miyazawa, Yoshitake, and Tanaka [16]. First, the C_{60} powder was dissolved in benzene to obtain a C_{60}-saturated benzene solution at room temperature. This solution was then stored at 5 °C in an incubator. Next, the C_{60}-saturated benzene solution (14 mL) was transferred to a transparent glass bottle and IPA (14 mL) was gently added to it to form a liquid–liquid interface. The glass bottle was then ultrasonicated for several seconds in an ultrasonic water bath and then stored at 5 °C to grow C_{60}FNWs. Figure 5 shows a transmission electron microscopy (TEM) image of the synthesized C_{60}FNWs and their diameter distribution. The diameter of the C_{60}FNWs was 79 ± 24 nm (mean ± SD). Figure 6 shows a high-resolution TEM (HRTEM) image of a synthesized C_{60}FNW (Fig. 6a). A total of $1\bar{1}1$ and $2\bar{2}0$ spots are indexed to the fcc structure of C_{60}. The inset of Fig. 6b shows a $(1\bar{1}1)$ lattice plane spacing of 0.85 nm. The fast Fourier transformation (FFT) spots

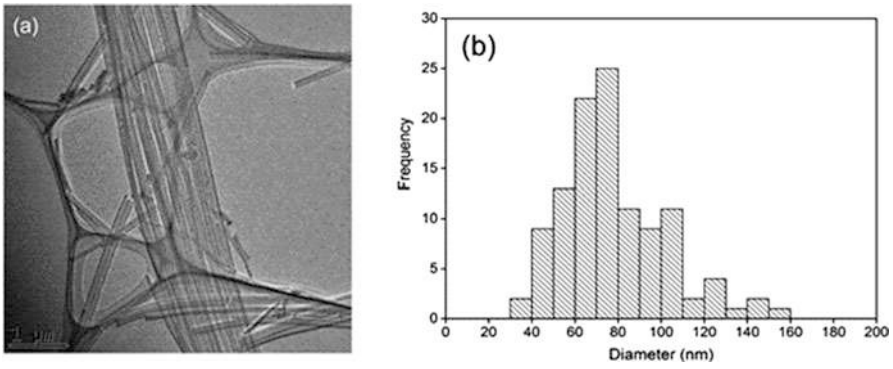

Fig. 5 (**a**) Bright-field TEM image of C_{60}FNWs synthesised by the dLLIP method using a C_{60}-saturated benzene solution and IPA. (**b**) Histogram showing the diameter distribution of 112 synthesised C_{60}FNWs. (Reprinted with permission from [16])

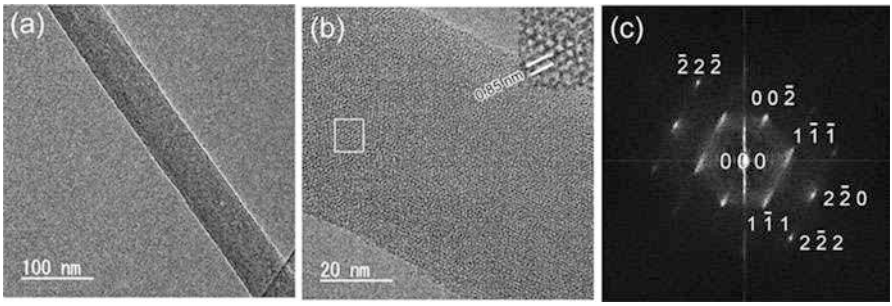

Fig. 6 (**a**) Bright-field TEM image of an as-synthesised C_{60}FNW with a diameter of 64 nm, (**b**) HRTEM image of part of the C_{60}FNW in (**a**). An enlarged HRTEM image of the rectangular area in (**b**) is shown in the inset. (**c**) FFT pattern for the HRTEM image of (**b**). (Reprinted with permission from [16])

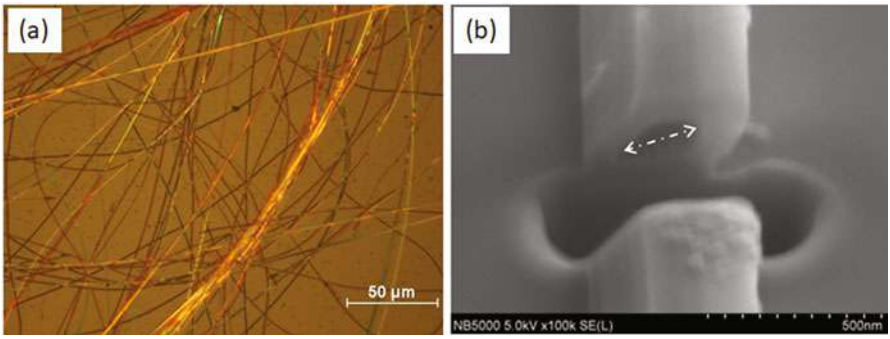

Fig. 7 (**a**) Optical microscopy image of C_{60} fullerene nanotubes. (**b**) Cross-sectional SEM image of a C_{60} fullerene nanotube. (Reprinted with permission from [17])

show streaked images that are elongated perpendicular to the growth axis direction. The streaked FFT spots suggest the presence of a high density of (111) planar faults parallel to the growth axis of the C_{60}FNW.

Figure 7a shows an optical microscopy image of tubular C_{60}FNWs, i.e., C_{60} fullerene nanotubes (C_{60}FNTs) [17]. The C_{60}FNTs are synthesized by a dLLIP method using a C_{60}-saturated pyridine solution and IPA. The typical synthesis procedure is as follows. A C_{60}-saturated pyridine solution was prepared and stored at 5 °C, and then exposed to UV rays (302 nm; UVM-57). A ninefold volume of excess IPA was slowly layered on top of the C_{60}-saturated pyridine solution to form a liquid–liquid interface. The mixture was sonicated for 1 min, shaken ten times by hand to obtain a homogeneous precipitation of the embryo crystals of C_{60}, and further sonicated using an ultrasonic bath for 1 min. The resulting mixture was placed in an incubator at 5 °C. The results showed that the impurity water in pyridine hinders the growth of C_{60}FNTs.

As described above, the growth of C_{60}FNWs is influenced by various factors such as time, temperature, light, solvent species, the ratio between good and poor

solvents, and the content of impurity in water [14]. Previous studies have shown that desolvation of C_{60} molecules from the solvent molecules on the crystal surface is the rate-limiting step in the growth of C_{60}FNWs in C_{60}-saturated toluene and IPA [18].

Using the C_{60}FNWs synthesized by the dLLIP method, Takeya et al. successfully fabricated superconductive C_{60}FNWs by doping them with K [15, 19]. The K-doped C_{60}FNWs with a composition of $K_{3.3}C_{60}$ exhibited a T_c of 17 K, a shielding volume fraction as high as 80%, and a critical current density J_c of more than 3×10^5 A cm^{-2} at 50 kOe, although the shielding volume fraction of the K-doped C_{60} crystal powder was less than 1%. The high shielding volume fraction in K-doped C_{60}FNWs will help realize light, flexible, and recyclable superconducting carbon cables. Rb-doped C_{60}FNWs showed a T_c of 26 K [15]. Because Rb is an abundant alkali metal similar to copper, lead, or zinc, lightweight Rb-doped C_{60}FNWs are expected to find use in various superconducting applications such as motor cars, cables for power delivery, and wind generators.

Figure 7 shows FNWs comprising $Sc_3N@C_{80}$ molecules [20]. The $Sc_3N@C_{80}$ FNWs were synthesized using a static LLIP method. A saturated solution of $Sc_3N@C_{80}$ in toluene was prepared. Approximately 2 mL of this saturated solution was poured into a 10-mL glass bottle, and 6 mL of IPA was slowly added to obtain a liquid–liquid interface. The mixture was left to stand at 20 °C for 5 min and then stored at 5 °C for 24 h to grow $Sc_3N@C_{80}$ FNWs. Based on this report, various endohedral metallofullerenes aggregates such as $Sc_3N@C_{78}$ microspindles [21], $Lu_2@C_{82}$ nanorods [22], and $Tb_3N@C_{80}$ cubes [23] were reported recently (Fig. 8).

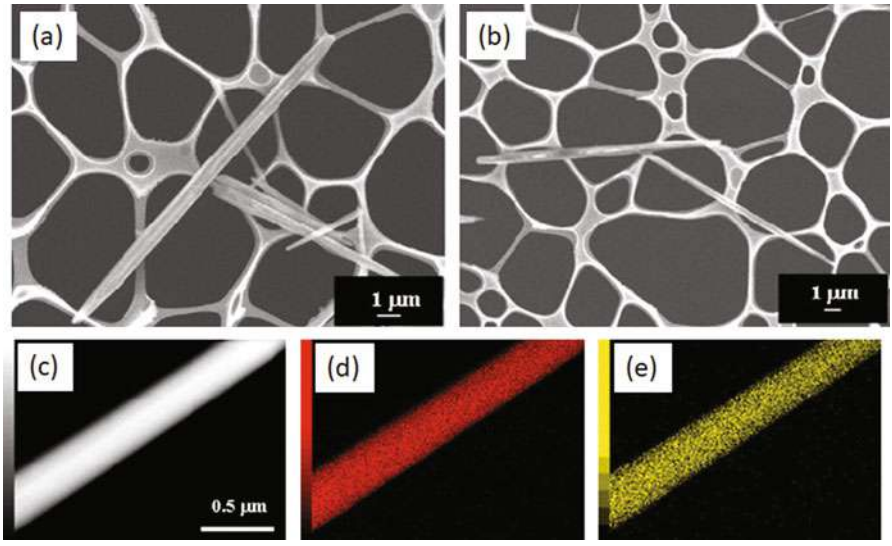

Fig. 8 (**a** and **b**) SEM images of $Sc_3N@C_{80}$ nanowhiskers prepared using toluene. (**c**) STEM image of a $Sc_3N@C_{80}$ nanowhisker. STEM mapping images of (**d**) carbon and (**e**) Sc of a $Sc_3N@C_{80}$ nanowhisker. (Reprinted with permission from [20])

Size control of FNWs is essential for practical applications. Wakahara et al. [24] reported that the diameter of C_{60}FNWs varied with the size of the glass bottles used in dLLIP synthesis. When the total volume of the solution was constant, a linear relationship was observed between the area of the liquid–liquid interface and the diameter of a C_{60}FNW.

Changes in the lengths and diameters of C_{60}FNWs upon varying the solution volume were also examined for the dLLIP process. After the initial formation of a liquid–liquid interface by layering an equal amount of IPA on a C_{60}-saturated toluene solution in a glass bottle, the solution was manually mixed by shaking 30 times. The bottles were then stored in an incubator at 15 °C for 8 days to obtain well-grown C_{60}FNWs. The results showed that the mean lengths and diameters of C_{60}FNWs increase with increasing bottle size [25].

Two-Dimensional Aggregates of Fullerenes

Fullerene nanosheets are 2D aggregates. Various forms of fullerene nanosheets have been synthesized. Wang et al. [26] obtained C_{60} nanosheets with a thickness of $<$250 nm by evaporating a m-xylene solution of C_{60} on glass or silicon substrates. The C_{60} nanosheets showed an fcc structure. Sathish et al. [27] synthesized C_{60} nanosheets by the LLIP method using CCl_4 as the good solvent and IPA, ethanol, and methanol as the poor solvent at 5 °C (Fig. 9). The diameter of the synthesized C_{60} nanosheets varied from ~7.5μm with IPA, ~2.5μm with ethanol, and 500 nm with methanol. Shrestha et al. [28] synthesized porous hexagonal sheets of C_{60} by an LLIP method using a mixture of CCl_4 and benzene as the good solvent and IPA as the poor solvent. They showed that the porosity and electrochemically active surface area of the hexagonal nanosheets could be flexibly controlled by varying the mixing fraction of CCl_4 in benzene.

Nanosheets composed of $Sc_3N@C_{80}$ with thicknesses ranging from 250–400 nm were also successfully fabricated by the LLIP method using IPA and a CS_2 solution of $Sc_3N@C_{80}$ (Fig. 10a) [20]. The HRTEM image and the electron diffraction pattern in Fig. 10b show that $Sc_3N@C_{80}$ has a simple cubic structure with a lattice constant of 1.04 nm.

Three-Dimensional Aggregates of Fullerenes

Various 3D fullerene crystals have been synthesized to date. Nakanishi et al. [29] synthesized a C_{60} derivative consisting of a π-conjugated sp^2-carbon fullerene moiety and three sp^3-C_{16} alkyl chains. They also fabricated fullerene solids with a hollow spherical structure with an average diameter of 250 nm using C_{60} derivative molecules in a mixture of 2-propanol and toluene [29]. In addition to spherical fullerene solids, cone-shaped solids comprising C_{60} derivatives with a diameter of ~1μm were also obtained. The cone-shaped objects were obtained by dispersing the C_{60} derivatives into a 1:1 H_2O/THF mixture. Tan et al. [12] synthesized bipyramidal

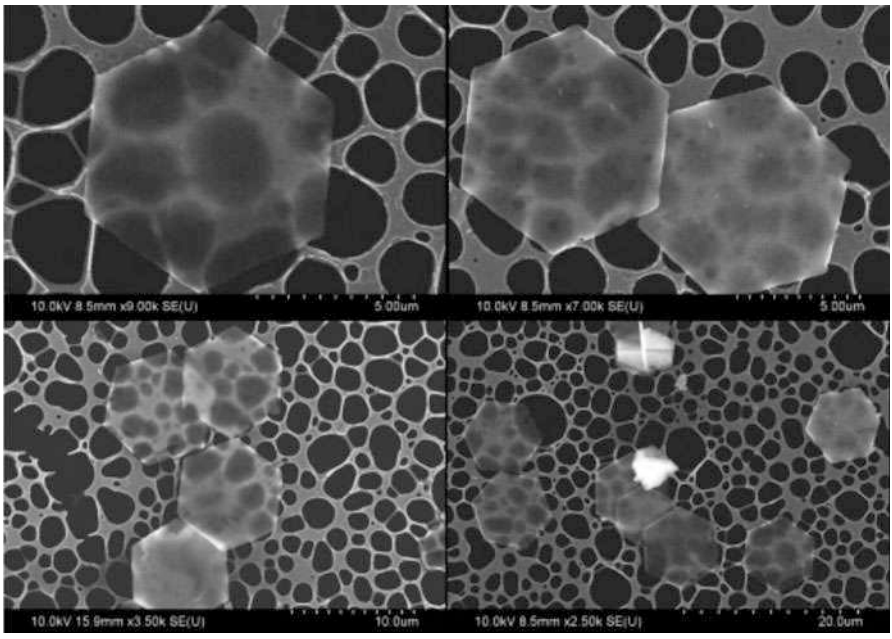

Fig. 9 SEM images of C_{60} nanosheets prepared at the CCl_4 and IPA interface. (Reprinted with permission from [27])

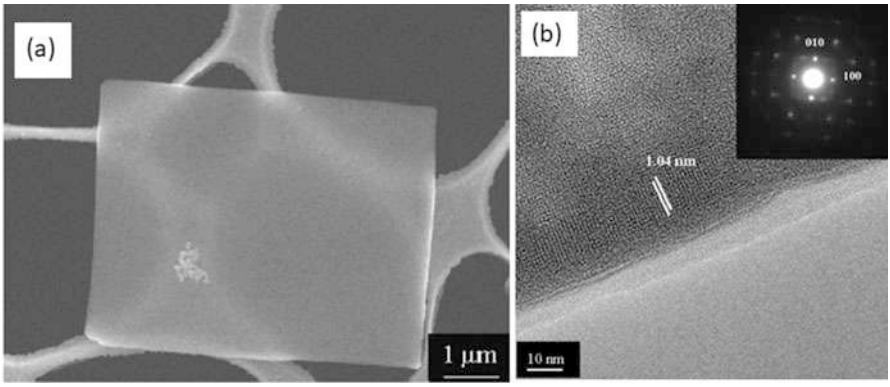

Fig. 10 (**a**) SEM image of a $Sc_3N@C_{80}$ nanosheet. (**b**) HRTEM image of $Sc_3N@C_{80}$ nanosheet. The inset is the selected-area electron diffraction pattern of $Sc_3N@C_{80}$ nanosheet. (Reprinted with permission from [20])

and disc-shaped hcp single C_{60} microcrystals. The bipyramidal C_{60} microcrystals with a 12-face morphology were formed by a reprecipitation method at room temperature. In this method, 0.8 mL of CS_2 solution of C_{60} (0.3 mM) is rapidly injected into 80 mL of ethanol under vigorous magnetic stirring. To form

disc-shaped C_{60} microcrystals, 1.6 mL of p-xylene solution of C_{60} (3 mM) is quickly injected into 80 mL of 1-propanol under vigorous magnetic stirring.

Olmstead et al. [30] first synthesized cubic crystals of dark red $C_{60}(Ag(NO_3))_5$ aggregates using an LLIP method, which involved the diffusion of a silver nitrate solution in ethanol into a C_{60} solution in benzene. In $C_{60}(Ag(NO_3))_5$ aggregates, Ag (NO_3) molecules form a zeolite-like network with round cavities occupied by C_{60} molecules. Shrestha et al. [31] also synthesized tens of micron-sized $C_{60}(AgNO_3)_5$ cubic crystals by an LLIP method using benzene or toluene solutions saturated with C_{60} and 1-butanol or 2-propanol solutions saturated with $AgNO_3$ (Fig. 11a). When the synthesized cubic crystals of $C_{60}(AgNO_3)_5$ were washed with 1-butanol at 5 °C, "bucky cubes" with surfaces covered with fine C_{60} needle-like crystals (C_{60}FNWs) were obtained (Fig. 11b).

Recently, Hou et al. [32], instead of using the LLIP solution method, synthesized $C_{60}(AgNO_3)_5$ aggregates by directly soaking $AgNO_3$ crystals in a C_{60}-saturated toluene solution. This method produced cuboid crystals of $C_{60}(AgNO_3)_5$. Cube-shaped C_{70} crystals were synthesized by the dLLIP method using mesitylene as a good solvent for C_{70} and IPA as a poor solvent for C_{70} [33]. The synthesized crystals comprised C_{70}·$(mesitylene)_2$. Their crystal structure had a simple cubic unit cell with a lattice constant of 10.47 Å at 90 K and 10.59 Å at room temperature. The C_{70} cube crystals emitted remarkably higher photoluminescence with wavelengths of 660–710 nm than that emitted by C_{70} powder.

Cube-shaped crystals made of fullerene can also be prepared using the dLLIP method. Bairi et al. [34] synthesized cube-shaped crystals of C_{70} using mesitylene and tert-butyl alcohol (TBA) as the good and poor solvents for C_{70}, respectively. The size of the cube-shaped C_{70} crystals was $\sim 3.4 \pm 0.4\mu m$. These crystals had open holes of 1-μm diameter on their surfaces (Fig. 12a). Such cube-shaped C_{70} crystals can capture graphitic carbon particles inside these holes (Fig. 12b).

The holes of the cube-shaped C_{70} crystals have a greater capturing ability for graphitic carbon particles than for resin particles. Hence, cube-shaped C_{70} crystals with open holes interact more strongly with graphitic carbon particles containing sp^2

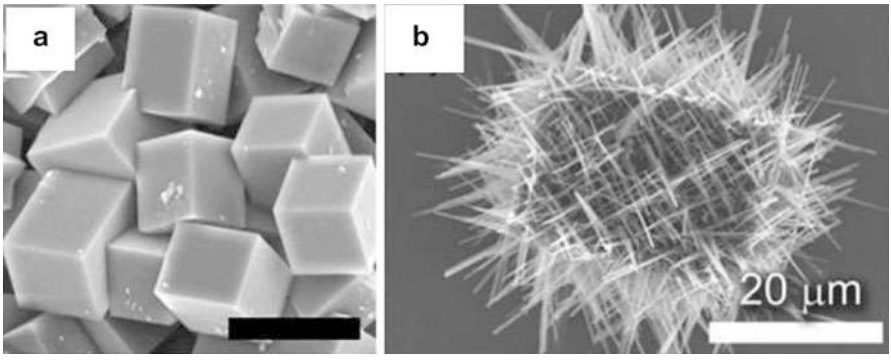

Fig. 11 (**a**) SEM image of the cubic crystals of $[C_{60}(AgNO_3)_5]$. Scale bar 20μm. (**b**) SEM image of a bucky cube. (Reprinted with permission from [31])

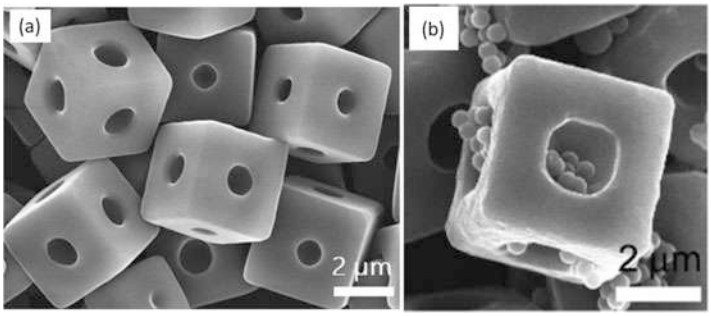

Fig. 12 Cube-shaped C_{70} crystals with (**a**) open holes and (**b**) the holes containing the captured graphitic carbon particles. (Reprinted with permission from [29])

carbon atoms with conjugated π electrons through π − π interactions than the resin particles with a lower sp^2 character than that of graphitic carbon. This selective property of C_{70} crystals with open holes can be used for controlled release of drugs, cosmetics, pigments, protecting biologically active species, and removing pollutants. Bairi et al. [35] also synthesized mesoporous crystalline fullerene cubes (MCFSs) of C_{70} by drop-casting the cube-shaped C_{70} crystals in mother liquor onto a silicon wafer and drying them at 80 °C. The produced mesoporous MCFSs exhibited intense photoluminescence, which is at least ~15 times greater than that of pristine C_{70}.

In addition to cube-shaped C_{60} and C_{70} crystals, cube-shaped microcrystals of C_{78} were also synthesized by an LLIP method using a trimethylbenzene solution of C_{78} and IPA [36]. By changing the concentration of C_{78} in TMB and by keeping the TMB:IPA solvent ratio at 1:8, C_{78} microcubes with average sizes of 5.7, 3.0, and 1.8μm were obtained. The cube-shaped microcrystals of C_{78} displayed enhanced photocurrent densities and PL properties compared to that of the C_{78} powder.

Self-Assembled Aggregates of Fullerene–Donor Complexes

Recently, self-assembled aggregates of D–A nano- and microcomplexes have received much attention in chemistry, physics, and materials science, because of their attractive properties that are not generally found in aggregates comprising single components only [37, 38]. Because fullerenes are good electron acceptors, they can form various D–A complexes with different classes of organic and organometallic donors. These complexes possess a wide range of physical properties, including metallic, photoconductive, and unusual magnetic properties. Konarev et al. have prepared various types of bulk systems from fullerene–donor complexes and determined their structures by X-ray analysis [4]. However, there are very few such reports on the preparation of self-assembled aggregates of nano- and micro-sized fullerene–donor complexes. In 2009, Wakahara et al. reported 2D aggregates of fullerene–donor complexes – C_{60}/ferrocene (Fc) nanosheets, which shows a strong charge-transfer (CT) absorption band in the NIR region [34]. They also

reported C_{60}/cobalt porphyrin nanosheets, another example of 2D aggregates of fullerene–donor complexes; these nanosheets show ambipolar CT characteristics [5]. Various self-assembled aggregates of fullerene–donor complexes have been prepared based on these results. In this section, we describe recent developments on the self-assembled aggregates of fullerene–donor complexes.

One-Dimensional Aggregates of Fullerene–Donor Complexes

In 2016, Wang et al. synthesized 1D aggregates of C_{60} and corannulene by simple evaporation [39] (Fig. 13). The toluene solution of corannulene–C_{60} was dropped onto the substrates and the solute was evaporated to prepare high-quality nanowires. The bowl-shaped geometry of corannulene makes it an ideal receptor for binding fullerenes through concave–convex π–π interactions. This geometric effect, concave–convex π–π interactions, and van der Waals (vdW) forces are the driving forces for the formation of these supramolecular assemblies. Interestingly, corannulene exhibits a strong interaction with C_{60} but not with C_{70}, because corannulene, a part of C_{60}, has a suitable size only for C_{60}. The crystal structure of the aggregate also results in a strong interaction between C_{60} and corannulene.

Recently, Cao et al. fabricated 1D aggregates of C_{60} and imide-fused corannulene derivatives [40]. This 1D aggregate was prepared by the phase transfer of MeOH into an o-dichlorobenzene solution of C_{60} and imide-fused corannulene derivatives. This imide-fused corannulene derivative has two mesomers (isomers **1** and **2**, Fig. 14), which can convert into each other in solution at room temperature and exhibit a 1:1 ratio in their single crystals. X-ray crystal analysis showed that the 1D aggregate has a segregated packing motif with alternating molecular layers of C_{60} and imide-fused corannulene derivatives, as shown in Fig. 14. Interestingly, only isomer 2 was observed in the 1D aggregate, indicating that isomer **1** completely converts into isomer **2** because the binding energy between **2** and C_{60} is higher than that between **1** and C_{60}.

Four types of 1D aggregates composed of fullerene and porphyrin–C_{60}/H_2TPP [41], C_{60}/ZnTPP [41], C_{70}/CoTMPP [42], and C_{60}/3,5-TPP [43] – have been reported in recent years. In 2018, 1D aggregates of C_{60} and 5,10,15,20-tetraphenylporphyrins (H_2TPP, ZnTPP) with high aspect ratios were prepared by a

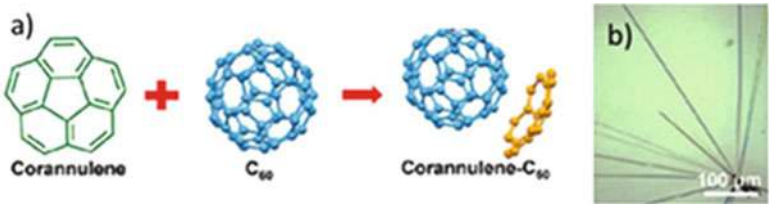

Fig. 13 (**a**) Cocrystallization of corannulene and C_{60}. (**b**) Optical image of 1D C_{60} /corannulene nanocrystals. (Reprinted with permission from [39])

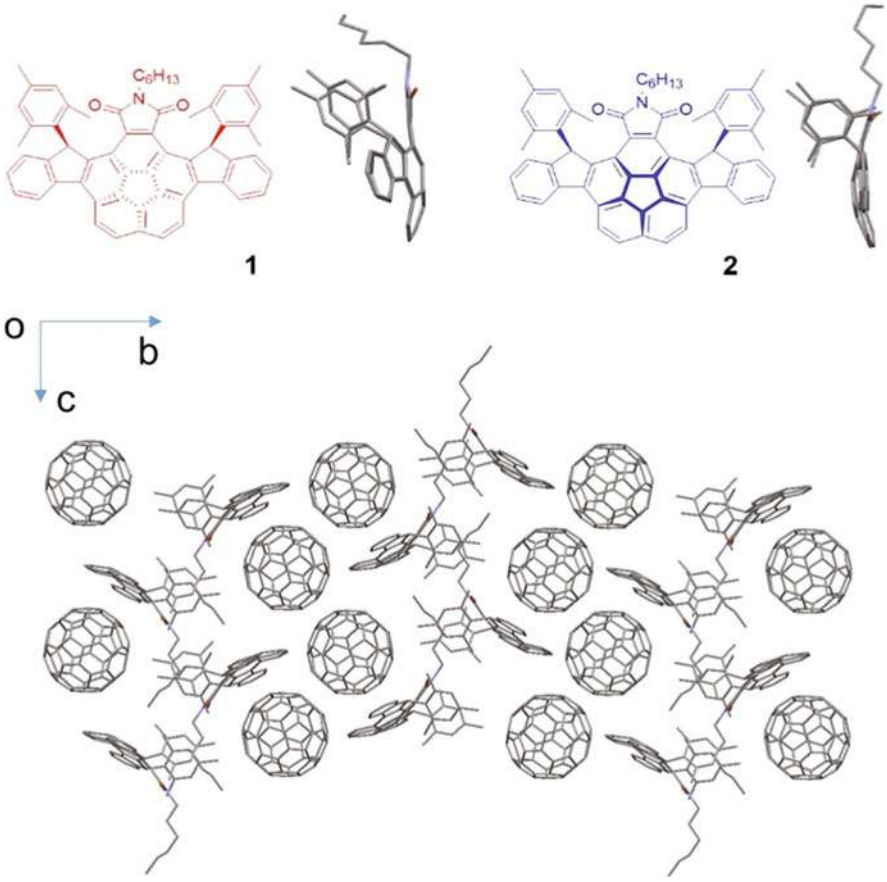

Fig. 14 Molecular structures of **1** and **2**, and cocrystal packing motif (solvent and hydrogen atoms are omitted for clarity) of **2**@C_{60} complex. (Reprinted with permission from [40])

simple drop-casting a m-xylene solution of H_2TPP/ZnTPP and C_{60} (1:1) on various substrates [41]. Interestingly, the central Zn^{2+} in the tetraphenyl porphyrin enables a strong D–A CT interaction in the 1D aggregate.

A highly conductive and thermally stable 1D aggregate composed of C_{70} and 5,10,15,20-tetrakis(4-methoxyphenyl)porphyrinato cobalt (CoTMPP) was successfully obtained by the reprecipitation method [42]. This 1D aggregate has a 2:1 ratio of $2C_{70}$·CoTMPP to form 1D microneedles. Notably, the resultant C_{70}-CoTMPP 1D aggregates exhibit semimetallic behavior at room temperature. These results are also supported by theoretical calculations.

Recently, Wakahara et al. reported the preparation of 1D aggregates of C_{60} and 5,10,15,20-tetrakis(3,5-dimethoxyphenyl)porphyrin (3,5-TPP) [43]. These 1D aggregates have NIR light-sensing abilities, despite the fact that the molecule of each component individually does not exhibit any NIR light-sensing properties.

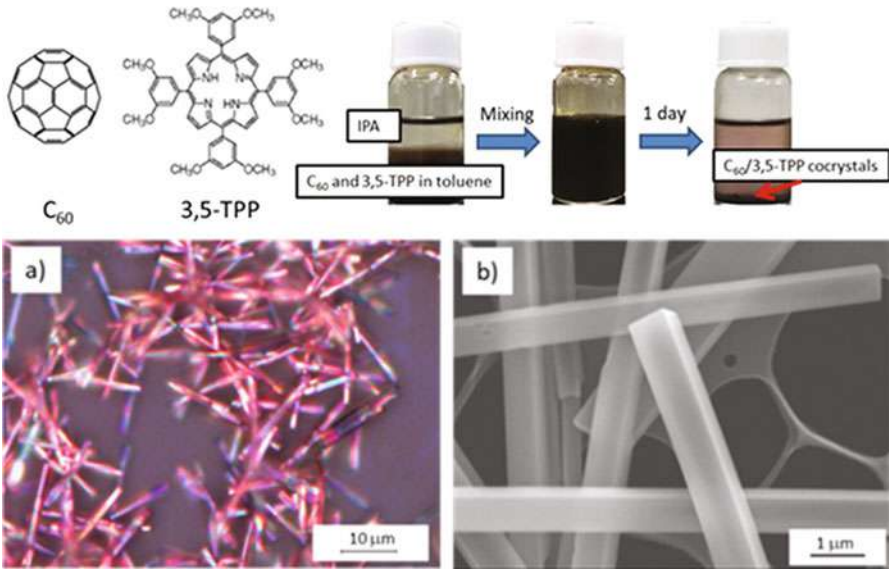

Fig. 15 (**a**) Optical microscopy image and (**b**) SEM image of C_{60}/3,5-TPP cocrystals. (Reprinted with permission from [43])

Micrometer-sized rectangular columnar 1D aggregates of C_{60} and 3,5-TPP were produced by a simple LLIP method. Figure 15 shows the optical microscopy and scanning electron microscopy (SEM) images of the prepared dark-colored precipitate. These images reveal that these crystals are rectangular columns with the average dimensions of 14μm × 1.45μm.

Two-Dimensional Aggregates of Fullerene–Donor Complexes

Fc is a very important donor because of its strong electron-donating ability and high stability under redox conditions. Therefore, 2D aggregates formed by combining fullerene and Fc are expected to have fascinating properties. A C_{60}/Fc complex in the crystalline state was first reported by Crane et al. in 1992 [44]; they determined the crystal structure by assuming that the C_{60} molecules were motionless. They inferred that Fc does not fully donate its electron to C_{60} and that the contribution of the weak intermolecular CT interaction to the stability of the hybrid is very small. However, the electronic properties of the hybrid are still not clear.

In 2009, Wakahara et al. [45] developed a method to synthesize a large quantity of C_{60} nanosheets of size ~9μm by an LLIP method using a toluene solution of C_{60} containing Fc and IPA (Fig. 16a). Figure 16b shows a unit cell of Fc-doped C_{60} nanosheets comprising $C_{60}(Fc)_2$, where the unit cell has a triclinic crystal structure with lattice parameters of a = 10.094(5), b = 10.528(4), c = 11.306(3) Å, α = 95.29(3), β = 90.65(3), and y = 118.47(4)° at 296 K [45]. The C_{60}

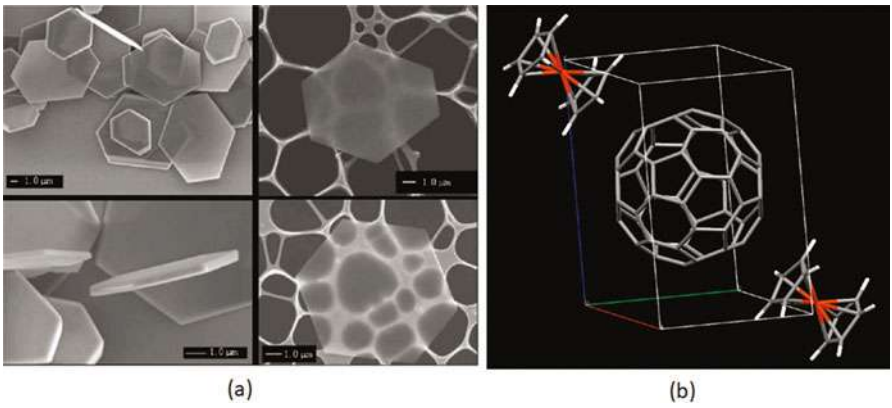

Fig. 16 (**a**) SEM images and (**b**) unit cell model of C_{60} nanosheets containing ferrocene molecules. (Reprinted with permission from [45])

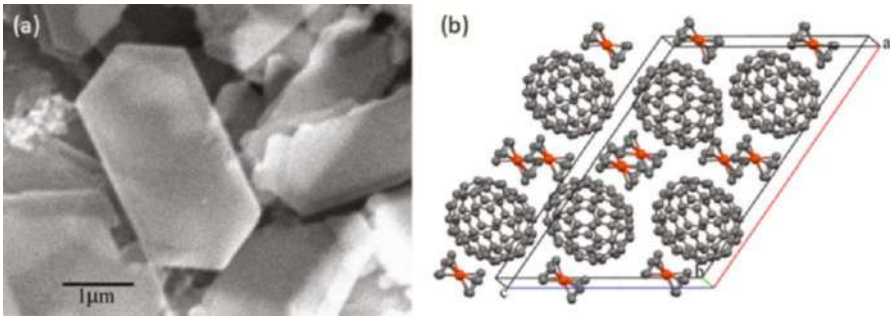

Fig. 17 (**a**) SEM image of C_{70} nanosheets containing ferrocene molecules. (**b**) Packing arrangement of C_{70} and ferrocene molecules in monoclinic C_{70} nanosheets. (Reprinted with permission from [46])

nanosheets containing Fc molecules showed a strong CT band at 782 nm, indicating the presence of D–A interactions in the nanosheets.

In addition to C_{60} nanosheets, C_{70} nanosheets have also been successfully synthesized by an LLIP method using a toluene solution of C_{70} containing Fc and IPA [46]. The obtained C_{70} nanosheets had a composition of $C_{70}(Fc)_2$ with a monoclinic structure with lattice constants of $a = 27.15$ Å, $b = 10.21$ Å, $c = 19.25$ Å, and $\beta = 121.73°$. Figure 17 shows an SEM image of C_{70} nanosheets containing Fc molecules and their unit cell model. The average size of the C_{70} nanosheets was 4.6 ± 3.0μm and the thickness was 250–500 nm. The Fc molecules can be removed by heating the C_{70} nanosheets at 200 °C for 3 h [46].

In 2012, Wakahara et al. reported the preparation of novel 2D aggregates of C_{60}-CoTMPP using an LLIP method [5]. Its structure is in sharp contrast to that of 1D aggregates formed from C_{70} and CoTMPP discussed above [42]. The 2D aggregates have a tetragonal morphology with a size range of 5–10μm; they also tend to stack

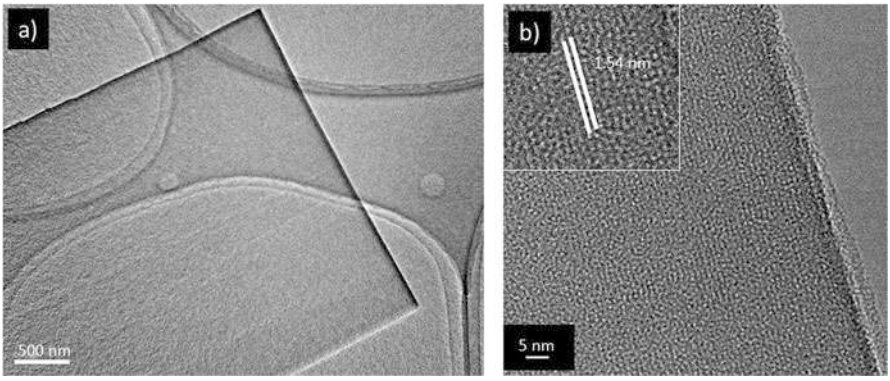

Fig. 18 (**a**) TEM and (**b**) HRTEM images (inset: magnified image) of a single C_{60}/3,5-TMPP nanosheet. (Reprinted with permission from [5])

over each other. The thickness of the 2D aggregates was ~50–200 nm, as determined by AFM measurements. The crystal structure of the 2D aggregates of C_{60}-CoTMPP was determined by X-ray diffraction (XRD). Their XRD pattern is considerably different from that of the C_{60} powder, but identical to that of CoTMPP·C_{60}(1:1) prepared in the presence of excess Fc [47] (Fig. 18).

In 2013, Zhang et al. prepared the 2D aggregates of fullerene–sulfur-bridged annulene by a simple solution process [48]. The sulfur-bridged annulene, meso-diphenyltetrathia [22]-annulene [1, 2] (DPTTA), is a porphyrin-like planar aromatic macrocycle with 22 π electrons and displays superior hole-transport properties than that exhibited by porphyrins. They prepared 2D aggregates using this DPTTA as an electron donor instead of a porphyrin. The 2D aggregates of C_{60} − DPTTA and C_{70} − DPTTA crystals suitable for X-ray crystallography were obtained by slow evaporation of solutions containing equimolar C_{60} or C_{70} and DPTTA in chlorobenzene. The molecular structures and stacking patterns of the 2D aggregates are shown in Fig. 19. A 2D segregated alternating layer structure was observed in the 2D aggregates of both C_{60} − DPTTA and C_{70} − DPTTA crystals, showing that π − π attractions, vdW forces, and polar electrostatic interactions are the driving forces for the formation of 2D aggregates.

Three-Dimensional Aggregates of Fullerene–Donor Complexes

In 2011, Wei et al. reported the fabrication of C_{60}/tetracene hybrid flower-like microstructures from nanoplates [49] by the following growth mechanisms. First, disc-like nanocrystals of tetracene of approximately 5-nm diameter were prepared, which were then used as seeds for the growth of C_{60} molecules at their periphery driven by directional CT interactions. Finally, the 5-nm tetracene discs were embedded in a polycrystalline C_{60} matrix to obtain the composite nanoplate structures, which could interconnect with each other and form the final flower-like microstructures. Complete quenching of tetracene fluorescence was also observed in these microstructures, suggesting a highly efficient electron transfer from tetracene to C_{60} (Fig. 20).

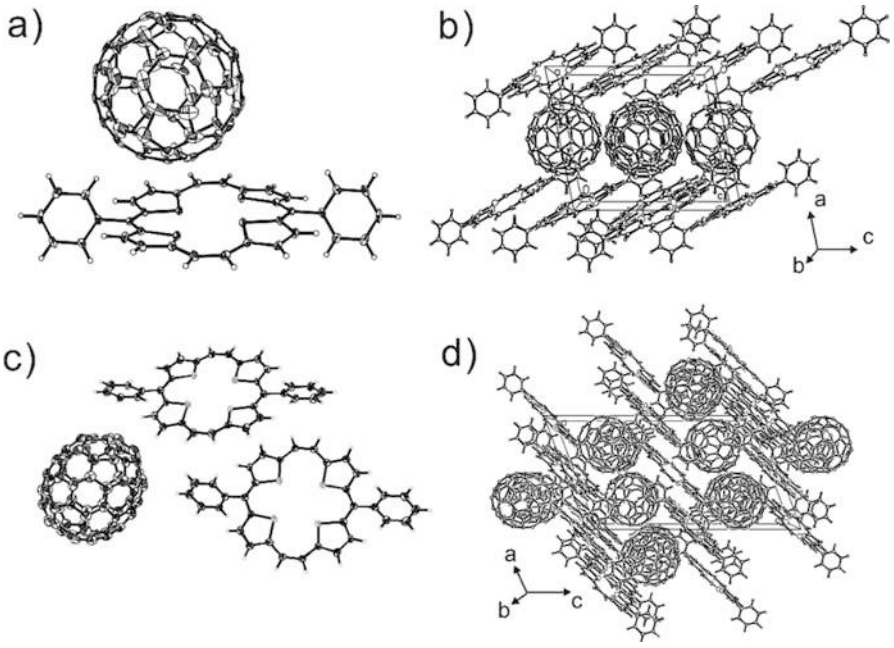

Fig. 19 (**a**, **c**) ORTEP drawings and (**b**, **d**) stacking patterns of (**a**, **b**) C_{60} and (c, d) C_{70}/sulfur-bridged annulene crystals. (Reprinted with permission from [48])

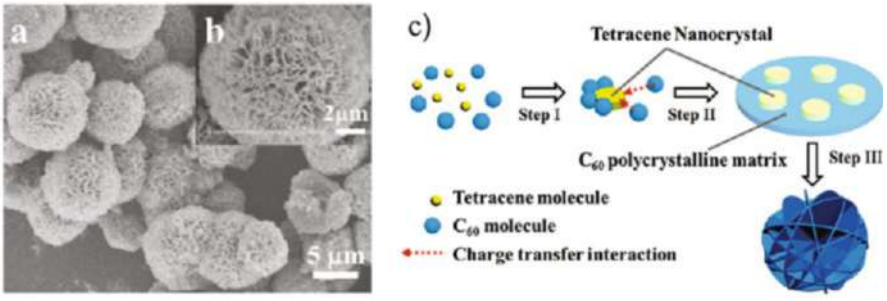

Fig. 20 (**a**) SEM image, (**b**) magnified SEM image, and (**c**) schematic illustration of the formation process of C_{60} flower-like microstructures. (Reprinted with permission from [49])

Physical Properties of Self-Assembled Aggregates of Fullerenes and Their Donor Complexes

Mechanical Properties of Self-Assembled Aggregates of Fullerenes

Self-assembled aggregates of fullerenes have attracted increasing interest owing to their optical and electrical properties. However, molecular crystals such as crystalline fullerenes are generally fragile or brittle because of their weak vdW interactions.

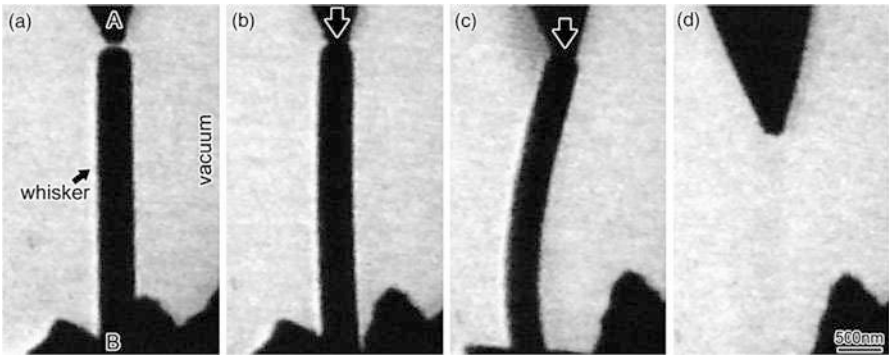

Fig. 21 Time-sequential series of bright-field images of compressive deformation of C_{60}FNWs. The tip of the cantilever (**a**) and the plate (**b**) are observed in the top and bottom of the image, respectively. The diameter of the nanowhisker is 420 nm and the length is 7.3μm. The bright region is a vacuum. (Reprinted with permission from [50])

For practical applications of these fullerene aggregates, it is important to understand their mechanical properties.

Asaka et al. reported in situ observation of the compressive deformation of individual crystalline C_{60}FNWs by transmission electron microscopy (TEM) [50]. They showed that a C_{60}FNW of 420 nm diameter, synthesized by an LLIP method using toluene and IPA, was bent elastically up to a curvature radius of 7.0μm, corresponding to a strain of 0.03. The Young's modulus of the C_{60}FNWs was found to be 28 ± 5 GPa, corresponding to 140%–340% times that of other C_{60} crystalline films and plates (Fig. 21).

Recently, Funamori et al. reported large elastic deformation of C_{60}FNWs grown by the LLIP method using toluene, m-xylene, and mesitylene as the good solvent [51]. The elastic properties of these C_{60}FNWs were examined by bending deformation. They showed that the bending behavior strongly depends on the type of solvent used in the preparation of C_{60}FNWs. The C_{60}FNWs prepared using m-xylene or mesitylene exhibit large elastic deformation, whereas those fabricated using the toluene/IPA interface are brittle, showing no large deformation in air. The large elastic deformation can be attributed to the solvated structure or the solvent in the crystals, which plays a crucial role in the interlocking and buffering of molecules for bending deformation (Fig. 22).

These results indicate that C_{60}FNWs have good mechanical properties and can be utilized for fabricating flexible components of various nanometer-sized carbon composites.

Optical Properties of Self-Assembled Aggregates of Fullerenes and Their Donor Complexes

To investigate the nature of the self-assembled aggregates of fullerene and their complexes, their electronic structure was probed using optical absorption spectroscopy. Wakahara et al. [24] measured the absorption spectra of C_{60}FNWs of various

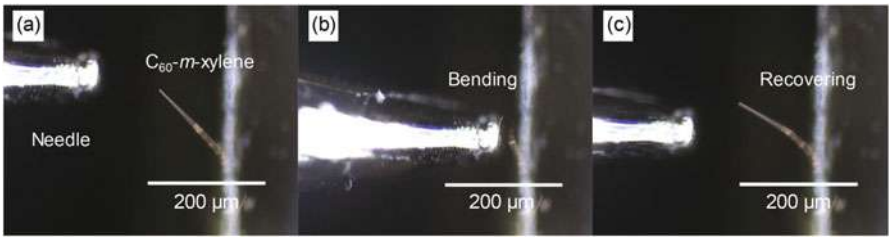

Fig. 22 Time-sequential pictures of typical elastic deformation for air-dried C_{60}-m-xylene, which was dried for 24 h in air. (**a**) The straight sample before applying a stress. (**b**) Large bending deformation under an applied mechanical stress. (**c**) Subsequent elastic recovery for bending after the stress was withdrawn. Scale bar represents 200μm. (Reprinted with permission from [51])

diameters dispersed in toluene/IPA using a UV-Vis-NIR spectroscope equipped with an integrating sphere in order to eliminate the scattering of the monitor light (Fig. 23). When the average C_{60}FNW size is increased, the absorption bands in the visible region (at 500 and 600 nm) broadened with an increase in the absorption in the NIR region, suggesting an increase in the interaction among C_{60} units within each C_{60}FNW. Indeed, the smallest C_{60}FNWs showed spectra similar to that of the C_{60} molecular particles aggregated with minimum interaction. Note that the extinction spectrum measured without an integrating sphere for large C_{60}FNWs is different from those of smaller C_{60}FNWs; that is, the intensity in the wavelength region longer than 600 nm increases, probably because of the high scattering of the monitor light.

Figure 24 shows the diffuse reflectance spectra of the C_{60}/Fc nanosheets and C_{60} powder [45]. The extra spectrum is obtained by subtracting the normalized C_{60} spectrum from the spectrum of the C_{60}/Fc nanosheets, which can be attributed to the CT band of C_{60}/Fc nanosheets with the absorption maxima at 782 nm, because CT interactions between C_{60} and Fc have been frequently reported in solution and liquid crystalline. Interestingly, the disappearance of the 782-nm band when the nanosheets were heated to 150 °C confirms that the band is a CT band. The CT transition energy corresponding to the maximum at 782 nm is estimated to be 1.59 eV. To understand the CT band in more detail, we carried out theoretical calculations for C_{60}/Fc nanosheets. We performed structural optimization of the $C_{60}(Fc)_2$ crystal by considering the unit cell structure determined by XRD in this study. The relaxed geometry is shown in Fig. 16b and is consistent with the structure reported based on the XRD analysis of a single crystal. The nearest distance between the C_5H_5 ring of Fc and the pentagonal face of C_{60} was calculated to be 3.23 Å; the eclipsed Fc was displaced by 1.23 Å with respect to the pentagonal center. The highest occupied molecular orbital (HOMO) mainly consists of Fe 3d orbitals of the two Fc molecules, while the triply degenerated lowest unoccupied molecular orbital (LUMO) mainly comprises the t_{1u} orbitals of C_{60} and a small part of the Fe 3d orbitals of the two Fc molecules. Thus, the electronic transition from the HOMO to LUMO is responsible for the CT excitation. At the DFT Kohn–Sham level, the intramolecular valence excitations in Fc and C_{60} were calculated to be 2.4 and 1.6 eV, respectively, which is consistent with the experimental absorption edges of approximately 500 and 700 nm. The ST method and (TD)-DFT-MLR scheme afforded CT excitation energy values of 1.005

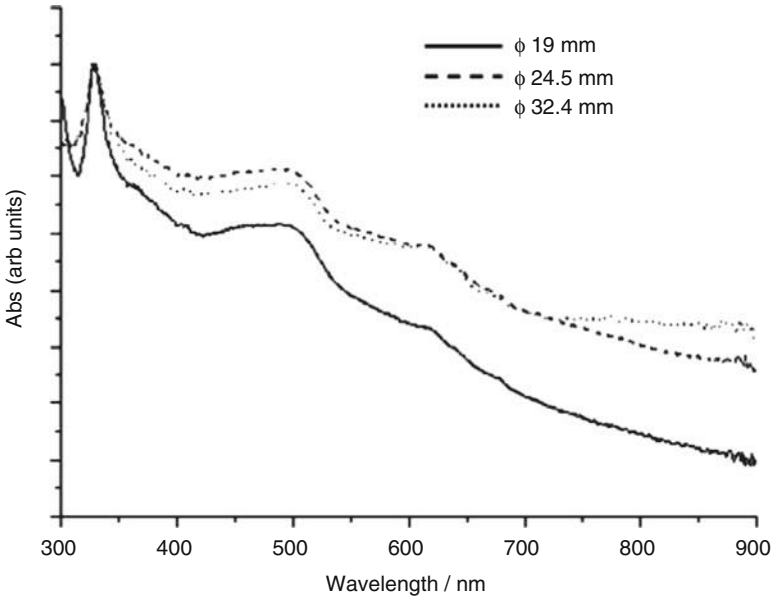

Fig. 23 UV–Vis–NIR absorption spectra of suspended C_{60}FNWs in a mixture of toluene and IPA measured with an integrating sphere. C_{60}FNWs were prepared at the toluene /IPA interface using glass bottles of different sizes. (Reprinted with permission from [24])

and 1.016 eV, respectively, which can be reasonably assigned to the broad absorption with a peak at around 800 nm and an edge at 1000 nm in the diffuse reflectance spectra of the nanosheets. The presence of the CT band supports the ground-state electron D–A interactions in the nanosheets.

Apart from the ground-state characterization, it is also important to understand the excited-state electron D–A interactions. Wang et al. reported the time-resolved transient absorption spectra of C_{70}/(metallo)porphyrin nanosheets in the solid state recorded upon femtosecond excitation at 532 nm [52]. The transient absorption measurements confirmed rapid charge separation, leading to the formation of the one-electron reduced form of C_{70} and the one-electron oxidized form of the (metallo)porphyrins.

Electrical Properties of Self-Assembled Aggregates of Fullerenes and Their Donor Complexes

In 2003, Miyazawa et al. reported the electrical conductivity of C_{60}FNWs, prepared by a simple LLIP method [42]. C_{60}FNWs of $<10\mu m$ diameter possess higher conductivity than that of bulk C_{60} crystals, and the conductivity of C_{60}FNWs increases with decreasing diameter, suggesting that the arrangement of C_{60} molecules in C_{60}FNWs depends on the diameter. Lucyszyn et al. also reported a relatively

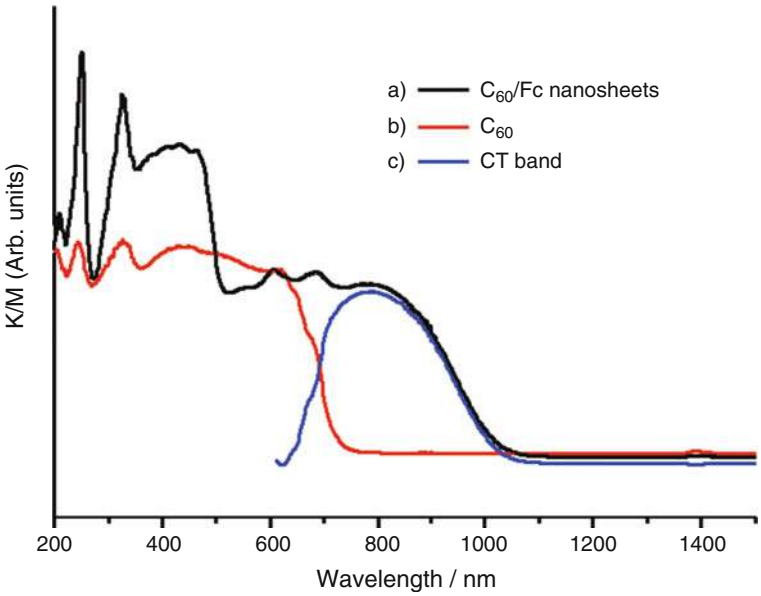

Fig. 24 Diffuse reflectance UV-vis-NIR spectra (K/M: Kubelka–Munk function) of (**a**) C_{60}/Fc nanosheets, (**b**) pristine C_{60} powder, and (**c**) subtracted spectrum (a – b). Spectra a and b are normalized at 610 nm. (Reprinted with permission from [45])

high conductivity (low resistivity of 3 Ωcm) for a small-diameter C_{60}FNW (650 nm) using four-point probe measurements [53] (Figs. 25 and 26).

C_{60} is a promising material for n-channel organic field-effect transistors (FETs) because of its high electron mobility of up to 6 $cm^2\ V^{-1}\ s^{-1}$, as observed for C_{60} thin-film FETs [56]. Therefore, it is interesting to measure the CT properties of C_{60}FNWs with fewer structural defects, because the charge carrier mobility of single-crystal devices is much higher than that of thin-film FETs. Ochiai et al. were the first to fabricate FETs based on C_{60}FNWs and investigate their electrical properties [55]. The C_{60}FNW FETs exhibited n-channel normally on properties; their carrier mobility was estimated to be 2×10^{-2} $cm^2/V\ s$ under vacuum conditions at room temperature. In 2012, Bao et al. reported a solution processing method to grow large arrays of aligned C_{60} 1D single crystals [57]. They fabricated bottom-gate, top-contact FETs using these aligned C_{60} 1D single crystals. Well-aligned C_{60} 1D single crystals show electron mobilities as high as 11 $cm^2\ V^{-1}\ s^{-1}$. These results indicate that the C_{60} 1D single crystals are promising candidates for realizing high-mobility organic FETs (Fig. 27).

Many papers have reported on transistors employing self-assembled aggregates such as C_{60}FNWs. A distinct characteristic of almost all of these transistors is that they transport only a single carrier type, either holes (p-type) or electrons (n-type). Therefore, simultaneous or selectable transport of electrons and/or holes (ambipolar charge transport) remains a highly desirable characteristic to be achieved, because it

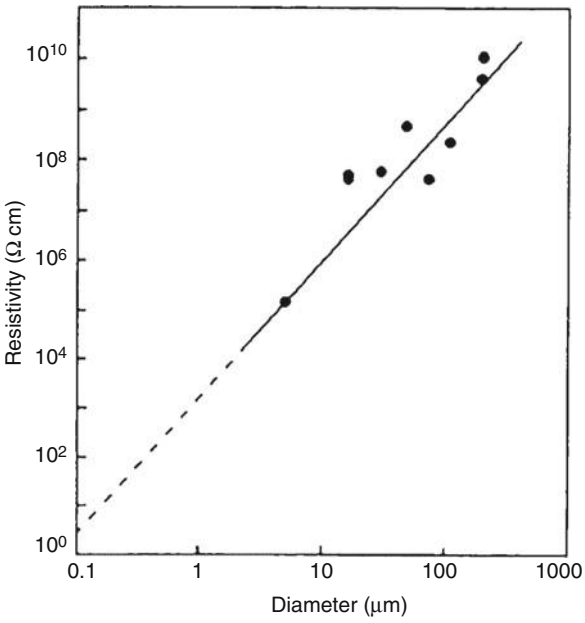

Fig. 25 Electrical resistivity of C_{60} FNWs as a function of diameter. (Reprinted with permission from [54])

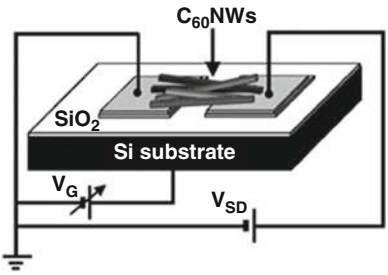

Fig. 26 Schematic illustration of the structure of the C_{60} FNW-FET device. Approximately 50 C_{60} FNWs bridge the two electrodes in the device. (Reprinted with permission from [55])

could help design better performing electronic circuits and demonstrate bifunctional organic devices such as light-emitting and light-sensing transistors. To date, however, very little work has been performed to establish self-assembled aggregates with ambipolar transport properties. In 2012, Wakahara et al. [5] successfully constructed 2D self-assembled aggregates comprising 1:1 C_{60}/CoTMPP using a simple LLIP method as mentioned above. To investigate the charge transport properties of such C_{60}/CoTMPP nanosheets, bottom-gate, bottom-contact FETs employing gold source–drain electrodes and SiO_2 as the gate dielectric were fabricated. The characteristic V-shaped transfer curves with one arm indicating electron transport (n-type) and the other indicating hole transport (p-type) were obtained for C_{60}/CoTMPP nanosheet-based FETs. The C_{60}/CoTMPP nanosheets exhibit ambipolar transport characteristics with nearly balanced hole/electron mobilities. This observation is in

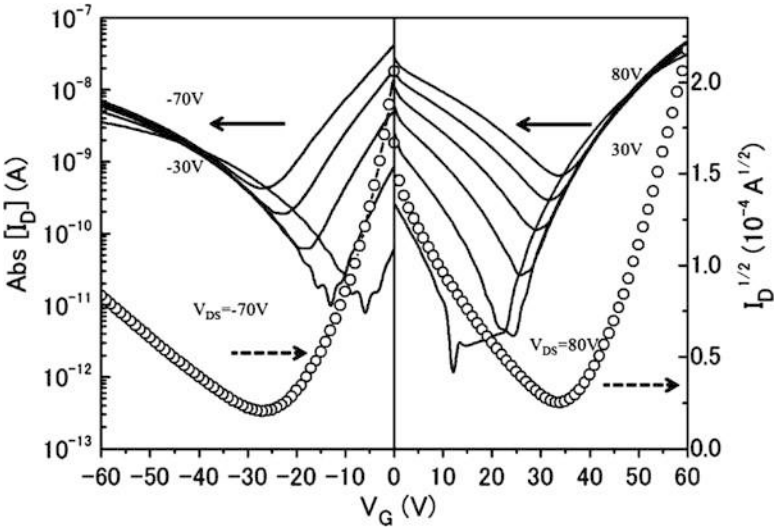

Fig. 27 Transfer characteristics of C_{60}/CoTMPP nanosheets in the dark for positive and negative gate biases. Solid lines show the drain current vs gate voltage for various VDS, and open symbols show the square root of the drain current (right vertical axis). (Reprinted with permission from [5])

sharp contrast to the earlier reported observations on C_{60}FNW-based FETs that showed only n-type behavior [55, 57] as mentioned above. The present results show that single cocrystals containing suitable D − A molecules can be made ambipolar, an important characteristic that could be used to develop improved materials and devices. The crystal structure of CoTMPP·C_{60} (1:1) (zigzag chain of C_{60} spheres with vdW "caps" of CoTMPP) was reported by Konarev et al. [58]. The CoTMPP is located between two C_{60} molecules while forming zigzag chains. It could therefore be argued that the zigzag chains of the C_{60} spheres and CoTMPP are responsible for the balanced electron/hole transport observed in the nanosheets. Following this report, various FETs based on the self-assembled aggregates of fullerene–donor complexes have been reported [41, 48]. However, not all self-assembled aggregates of fullerene–donor complexes exhibit ambipolar transport characteristics. The transfer characteristics of the transistor based on 1D aggregates of C_{60} and 3,5-TPP [43] are shown in Fig. 28, which reveals that the C_{60}/3,5-TPP cocrystal-based FETs display characteristic n-type transfer curves, in sharp contrast to the reported observations for C_{60}/CoTMPP nanosheet-based FETs.

To determine the relationship between the CT properties and molecular arrangement in a cocrystal, the crystal structure of the C_{60}/3,5-TPP cocrystal was determined by single-crystal XRD at 113 K. The C_{60}/3,5-TPP cocrystal prepared by the LLIP method was found to fit the $P2_1/c$ space group with the following unit cell parameters: a = 13.9823(4) Å, b = 22.3768(6) Å, c = 19.3193(5) Å, and β = 103.1050(10)°. The composition of the cocrystal is [(3,5-TPP)·$(C_{60})_2$·$(toluene)_4$]; it contains a C_{60}/(3,5-TPP)/C_{60}] unit in which two C_{60} molecules

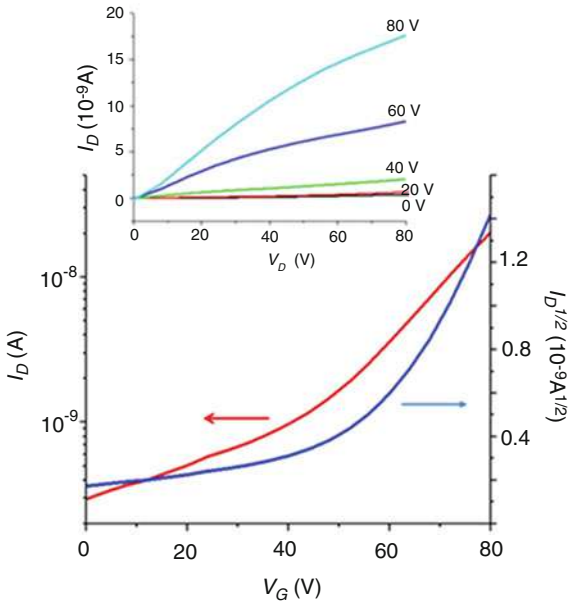

Fig. 28 Transfer (I_D–V_G) characteristics of C_{60}/3,5-TPP cocrystals in the dark (drain voltage [V_D]) = 80 V). The red curve displays drain current (I_D) as a function of gate voltage (V_G), and the blue curve shows the square root of I_D (right vertical axis). Inset: Output characteristics (I_D vs. V_D) at various values of V_G (0 to 80 V; 20 V increments). (Reprinted with permission from [43])

assemble above and below the 3,5-TPP molecular plane (Fig. 29c), which hinders hole transport from one porphyrin to the neighboring porphyrin. Four toluene molecules were located near the C_{60} moieties to fill the crystal interstices (Fig. 29b). Conversely, C_{60} molecules are arranged in 2D sheets that render effective electron transport from one C_{60} molecule to a nearby C_{60} molecule. These structural characteristics support the n-type transport characteristic of C_{60}/3,5-TPP cocrystals.

C_{60} − porphyrin dyads undergo electron transfer under optical excitation. To investigate whether such a process occurs within the self-assembled aggregates of fullerene–donor complexes, Wakahara et al. measured the transistor characteristics under visible-light illumination. Interestingly, all C_{60}/CoTMPP nanosheet-based FETs were found to be photoresponsive, although the sensitivity was not high [5]. A possible reason for this phenomenon could be the fast excited-state deactivation of porphyrin by efficient spin−orbit coupling through the central Co ion. Figure 30 shows the output characteristics of a C_{60}/3,5-TPP-cocrystalphototransistor determined at a fixed V_G of 80 V when illuminated with 660-nm light of different intensities (E_{light}) [45]. This result reveals that the channel current (I_D) of the device increases with increasing light intensity, which is indicative of a strong photoresponse. The C_{60}/3,5-TPP cocrystals absorb appreciably at 660 nm, primarily because of both the component bands and the CT band. The photosensitivity (P_{max}) of C_{60}/3,5-TPP cocrystals at 660 nm (0.05 mW/cm^2) was 4.5, which is much higher than that of the C_{60}/CoTMPP cocrystals. The metal-free 3,5-TPP exhibits a longer excited state than that of CoTMPP. Therefore, the higher sensitivity of C_{60}/3,5-TPP cocrystals may arise from the long lifetime of the 3,5-TPP excited state.

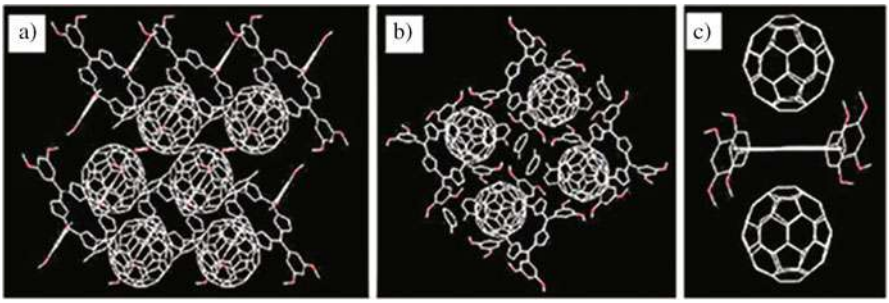

Fig. 29 (**a**) Crystal structure of a C_{60}/3,5-TPP cocrystal, (**b**) $[C_{60}/(toluene)_2/(3,5\text{-TPP})]_4$ unit structure, and c) $[C_{60}/(3,5\text{-TPP})/C_{60}]$ unit structure. (Reprinted with permission from [43])

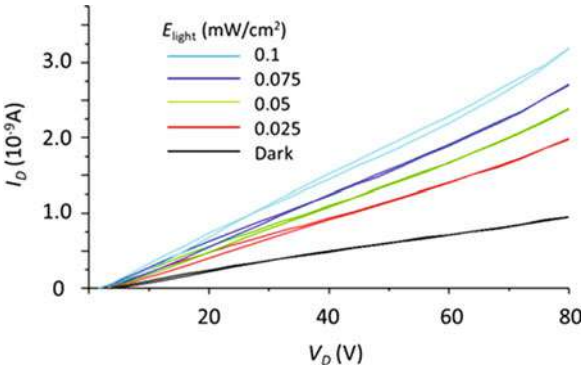

Fig. 30 Output characteristics of a C_{60}/3,5-TPP-cocrystal phototransistor determined at a fixed V_G of 80 V when illuminated with 660-nm light of different intensity (E_{light}). (Reprinted with permission from [43])

Figure 31 shows output curves from the C_{60}/3,5-TPP-cocrystal phototransistor illuminated by different LEDs at constant E_{light}. Clear device photoresponses were observed when illuminated in the 810–450 nm region, while at 940 nm, the photoresponse was very weak and similar to that in the dark. Because neither C_{60} nor 3,5-TPP absorbs at wavelengths longer than 800 nm, the photoresponse at 810 nm is due to excitation of the CT absorption band. This result confirms that it is possible to produce novel D–A cocrystals with NIR light-sensing properties through the self-assembly of molecules that individually do not show any NIR light-sensing property. In fact, a C_{60} NW-based phototransistor did not show any photoresponse to light at wavelengths longer than 780 nm.

Using these fullerene aggregates, which have unique electronic properties, some applications have been reported recently. Wakahara et al. [59] reported the preparation of composite films of nanoporous C_{60}FNWs (Fig. 32) instead of C_{60} molecules because the C_{60}FNWs are known to exhibit high electron mobility. The nanoporous C_{60}FNWs were then mixed with conjugated polymers, poly[2-methoxy-5-(3′,7′-dimethyl-octyloxy)-1,4-phenylene-vinylene] (MDMO-PPV) and poly (3-hexylthiophene (P3HT)). Thus, the nanoporous C_{60}FNWs were expected to be efficient new blend components. They also fabricated photovoltaic devices using

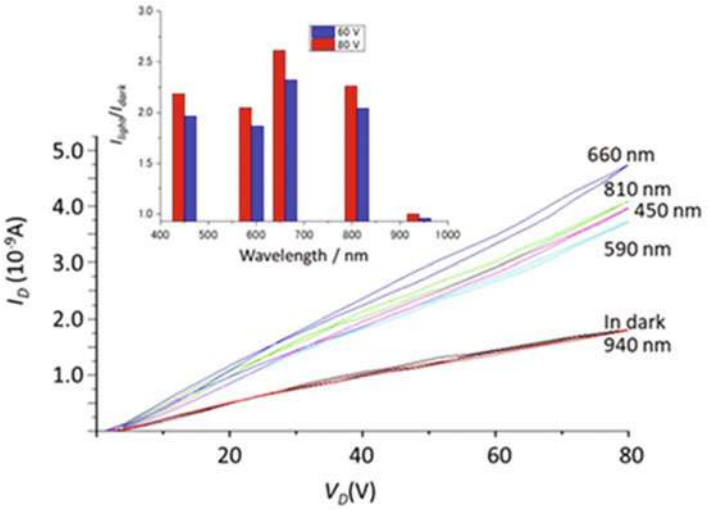

Fig. 31 Wavelength dependence of the output characteristics of a C_{60}/3,5-TPP-cocrystal phototransistor determined at a fixed V_G of 80 V when illuminated with different LEDs (E_{light} = 0.1 mW/cm^2). Inset: I_{light}/I_{dark} at different wavelengths calculated at V_D = 60 V and 80 V. (Reprinted with permission from [43])

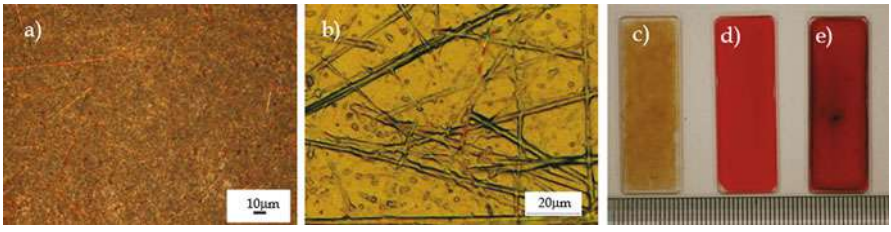

Fig. 32 Optical microscopy images of (**a**) C_{60}FNWs and (**b**) C_{60}FNW-(MDMO-PPV) composite films. Photographs of composite films on glass plates (38 × 13 mm) (**c**) C_{60}FNWs, (**d**) MDMO-PPV, and (**e**) C_{60}FNW -(MDMO-PPV). (Reprinted with permission from [59])

nanoporous C_{60}FNW –(conjugated polymer) composite films. Their results indicated that the physical properties (high surface area and small diameter) of the nanoporous C_{60}FNWs are important for the fabrication of functional C_{60}FNW OPVs.

Wakahara et al. reported the preparation of modified GC electrodes using nanoporous C_{60}FNWs to study the electrochemical oxygen reduction reaction (ORR) [60]. It was found that C_{60}FNWs are active catalysts for O_2 reduction in aqueous solution, whereas pristine C_{60} powders do not show any such activity. The porous and conductive features of C_{60}FNWs play important roles in electrochemical ORP.

Recently, Tsukagoshi et al. reported a principle experiment on a fullerene nanowire to drive a single fullerene switch in a two-terminal configuration [61].

A fullerene C_{60} nanowire exhibited negative differential resistance (NDR) and two-state resistance switching generated by local polymerization and depolymerization among the C_{60} molecules.

Conclusions

This chapter summarized the recent progress on the preparation, structures, and properties of self-assembled aggregates of fullerenes and their donor complexes. Self-assembled aggregates of fullerenes with various forms and compositions were obtained by slow evaporation, reprecipitation, and LLIP methods, and some of their physical and chemical properties were clarified. These self-assembled aggregates of fullerenes have been shown to have unique optoelectronic properties such as diameter-dependent conductivities, very high electron mobility, and a good photoresponse to UV-visible light. These results indicate that the self-assembled aggregates of fullerenes are promising candidates for realizing high-mobility organic devices.

The self-assembled aggregates of fullerene–donor complexes that combine fullerene with donor molecules usually exhibit attractive properties not shown by materials consisting of only fullerene, including CT absorption in NIR, ambipolar charge transport, and NIR light-sensing properties. In addition, these self-assembled aggregates of fullerene–donor complexes have the advantages of tunable composition, adjustable molecular arrangement, and intermolecular interactions within their solid states. These studies have shown that self-assembled aggregates of fullerene–donor complexes can lead to new research fields in organic semiconductors.

However, the basic mechanism for the preparation of self-assembled aggregates of fullerenes and fullerene–donor complexes is still unclear. Therefore, it is important to understand the growth process of the aggregates for successful material design. Importantly, the methods used to prepare these aggregates are very simple and can be applied not only to fullerenes but also to other carbon-based materials. The successful preparation of self-assembled aggregates of fullerenes and fullerene–donor complexes with unique electronic and optical characteristics using a very simple solution method can be viewed as an important stepping stone for the fabrication of novel nanometer-scale devices.

References

1. Miyazawa K (2009) Synthesis and properties of fullerene nanowhiskers and fullerene nanotubes. J Nanosci Nanotechnol 9(1):41–50. https://doi.org/10.1166/jnn.2009.J013
2. Shrestha LK, Ji QM, Mori T, Miyazawa K, Yamauchi Y, Hill JP, Ariga K (2013) Fullerene nanoarchitectonics: From zero to higher dimensions. Chem Asian J 8(8):1662–1679. https://doi.org/10.1002/asia.201300247
3. Xu T, Shen W, Huang W, Lu X (2020) Fullerene micro/nanostructures: controlled synthesis and energy applications. Mater Today Nano 11:100081. https://doi.org/10.1016/j.mtnano.2020.100081

4. Konarev DV, Lyubovskaya RN, Drichko NV, Yudanova EI, Shul'ga YM, Litvinov AL, Semkin VN, Tarasov BP (2000) Donor-acceptor complexes of fullerene C_{60} with organic and organometallic donors. J Mater Chem 10(4):803–818. https://doi.org/10.1039/a907106g
5. Wakahara T, D'Angelo P, Miyazawa K, Nemoto Y, Ito O, Tanigaki N, Bradley DDC, Anthopoulos TD (2012) Fullerene/cobalt porphyrin hybrid nanosheets with ambipolar charge transporting characteristics. J Am Chem Soc 134(17):7204–7206. https://doi.org/10.1021/ja211951v
6. Lu X, Feng L, Akasaka T, Nagase S (2012) Current status and future developments of endohedral metallofullerenes. Chem Soc Rev 41(23):7723–7760. https://doi.org/10.1039/C2CS35214A
7. Verheijen MA, Meekes H, Meijer G, Raas E, Bennema P (1992) Growth and morphology of C_{60} crystals. Chem Phys Lett 191:339–344. https://doi.org/10.1016/0009-2614(92)85311-W
8. Ramm M, Luger P, Zobel D, Duczek W, Boeyens JCA (1996) Static disorder in hexagonal crystal structures of C_{60} at 100 K and 20 K. Cryst Res Technol 31(1):43–53. https://doi.org/10.1002/crat.2170310111
9. Miyazawa K, Kuwasaki Y, Obayashi A, Kuwabara M (2002) C_{60} nanowhiskers formed by the liquid –liquid interfacial precipitation method. J Mater Res 17(1):83–88. https://doi.org/10.1557/jmr.2002.0014
10. Yosida Y (1992) Scanning electron-microscope images of C_{60} whiskers. Jpn J Appl Phys 31(4B):L505–L507. https://doi.org/10.1143/jjap.31.l505
11. Onishi T, Tsukamoto T, Oya T (2020) Simple annealing process for producing unique one-dimensional fullerene crystal named fullerene finned-micropillar. Sci Rep 10(1):19270. https://doi.org/10.1038/s41598-020-76252-6
12. Tan Z, Masuhara A, Ohara S, Kasai H, Nakanishi H, Oikawa H (2013) Facile deposition of gold nanoparticles on C_{60} microcrystals with unique shapes. J Nanopart Res 15(11):2029. https://doi.org/10.1007/s11051-013-2029-z
13. Miyazawa K, Ringor C (2008) Platinum chloride deposition into C_{60} nanotubes. Mater Lett 62(3):410–413. https://doi.org/10.1016/j.matlet.2007.05.069
14. Miyazawa K, Hotta K (2010) The effect of solvent ratio and water on the growth of C_{60} nanowhiskers. J Cryst Growth 312(19):2764–2770. https://doi.org/10.1016/j.jcrysgro.2010.06.020
15. Miyazawa K (2015) Synthesis of fullerene nanowhiskers using the liquid–liquid interfacial precipitation method and their mechanical, electrical, and superconducting properties. Sci Technol Adv Mater 16(1):013502. https://doi.org/10.1088/1468-6996/16/1/013502
16. Miyazawa K, Yoshitake M, Tanaka Y (2018) Characterization of platinum nanoparticles deposited on C_{60} fullerene nanowhiskers. Surf Eng 34(11):846–851. https://doi.org/10.1080/02670844.2017.1396779
17. Mahdaoui D, Hirata C, Omri N, Wakahara T, Abderrabba M, Miyazawa K (2018) Optimization of the liquid–liquid interfacial precipitation method for the synthesis of C_{60}nanotubes. Bull Mater Sci 41(6):165. https://doi.org/10.1007/s12034-018-1665-4
18. Hotta K, Miyazawa K (2008) Growth rate measurement of C_{60} fullerene nanowhiskers. Nano 3(5):355–359. https://doi.org/10.1142/s1793292008001192
19. Takeya H, Miyazawa K, Kato R, Wakahara T, Ozaki T, Okazaki H, Yamaguchi T, Takano Y (2012) Superconducting fullerene nanowhiskers. Molecules (Basel, Switzerland) 17(5):4851–4859. https://doi.org/10.3390/molecules17054851
20. Wakahara T, Nemoto Y, Xu M, Miyazawa K, Fujita D (2010) Preparation of endohedral metallofullerene nanowhiskers and nanosheets. Carbon 48(12):3359–3363. https://doi.org/10.1016/j.carbon.2010.05.026
21. Zhang R, Zhang L, Xia J, Lu X (2019) Controllable synthesis of $Sc_3N@C_{78}$ microspindles with excellent electrophotonic properties. ACS Appl Energy Mater 2:1489–1493. https://doi.org/10.1021/acsaem.8b02078

22. Shen W, Zhang L, Zheng S, Xie Y, Lu X (2017) $Lu_2@C_{82}$ Nanorods with enhanced photoluminescence and photoelectrochemical properties. ACS Appl Mater Interfaces 9:28838–28843. https://doi.org/10.1021/acsami.7b05180
23. Wu J, Zhu X, Guan Y, Wang Y, Jin F, Guan R, Liu F, Chen M, Tian Y, Yang S (2019) From cubes to dice: solvent-regulated morphology engineering of endohedral fullerene microcrystals with anomalous photoluminescence enhancement. Angew Chem Int Ed 58:11350–11354. https://doi.org/10.1002/anie.201905151
24. Wakahara T, Miyazawa K, Nemoto Y, Ito O (2011) Diameter-controlled growth of fullerene nanowhiskers and their optical properties. Carbon 49(14):4644–4649. https://doi.org/10.1016/j.carbon.2011.06.041
25. Miyazawa K, Hirata C, Wakahara T (2014) Influence of solution volume on the growth of C_{60} nanowhiskers. J Cryst Growth 405:68–72. https://doi.org/10.1016/j.jcrysgro.2014.07.036
26. Wang L, Liu BB, Liu DD, Yao MG, Yu SD, Hou YY, Zou B, Cui T, Zou GT, Sundqvist B, Luo ZJ, Li H, Li YC, Liu J, Chen SJ, Wang GR, Liu YC (2007) Synthesis and high pressure induced amorphization of C_{60} nanosheets. Appl Phys Lett 91(10). https://doi.org/10.1063/1.2768634
27. Sathish M, Miyazawa K (2007) Size-tunable hexagonal fullerene (C_{60}) nanosheets at the liquid−liquid interface. J Am Chem Soc 129(45):13816–13817. https://doi.org/10.1021/ja076251q
28. Shrestha LK, Yamauchi Y, Hill JP, Miyazawa K, Ariga K (2013) Fullerene crystals with bimodal pore architectures consisting of macropores and mesopores. J Am Chem Soc 135(2):586–589. https://doi.org/10.1021/ja3108752
29. Nakanishi T, Schmitt W, Michinobu T, Kurth DG, Ariga K (2005) Hierarchical supramolecular fullerene architectures with controlled dimensionality. Chem Commun 48:5982–5984. https://doi.org/10.1039/b512320h
30. Olmstead MM, Maitra K, Balch AL (1999) Formation of a curved silver nitrate network that conforms to the shape of C_{60} and encapsulates the fullerenetstructural characterization of $C_{60}\{Ag(NO_3)\}_5$. Angew Chem Int Ed 38(1–2):231–233. https://doi.org/10.1002/(SICI)1521-3773(19990115)38:1/2<231::AID-ANIE231>3.0.CO;2-5
31. Shrestha LK, Sathish M, Hill JP, Miyazawa K, Tsuruoka T, Sanchez-Ballester NM, Honma I, Ji Q, Ariga K (2013) Alcohol-induced decomposition of Olmstead's crystalline Ag(i)–fullerene heteronanostructure yields 'bucky cubes'. J Mater Chem C 1(6):1174–1181. https://doi.org/10.1039/c2tc00449f
32. Hou Y, Pan Y, Dong C, Nie B (2020) Direct transformation of $AgNO_3$ complex encapsulated fullerene (C_{60}) microcrystals on solid silver nitrate crystals without organic ligands. Appl Organomet Chem 34(12):e5978. https://doi.org/10.1002/aoc.5978
33. Park C, Yoon E, Kawano M, Joo T, Choi HC (2010) Self-crystallization of C_{70} cubes and remarkable enhancement of photoluminescence. Angew Chem Int Ed 49(50):9670–9675. https://doi.org/10.1002/anie.201005076
34. Bairi P, Minami K, Hill JP, Ariga K, Shrestha LK (2017) Intentional closing/opening of "real-hole-in-cube" fullerene crystals with microscopic recognition properties. ACS Nano 11(8):7790–7796. https://doi.org/10.1021/acsnano.7b01569
35. Bairi P, Tsuruoka T, Acharya S, Ji Q, Hill JP, Ariga K, Yamauchi Y, Shrestha LK (2018) Mesoporous fullerene C_{70} cubes with highly crystalline frameworks and unusually enhanced photoluminescence properties. Mater Horiz 5(2):285–290. https://doi.org/10.1039/c7mh00954b
36. Jannatun N, Chen N, Yu P, Shen W, Lu X (2021) Three-dimensional cubic and dice-like microstructures of higher fullerene C_{78} with enhanced photoelectrochemical and photoluminescence properties. Chem Eur J 27(1):348–353. https://doi.org/10.1002/chem.202003476
37. Sun LJ, Zhu WG, Yang FX, Li BL, Ren XC, Zhang XT, Hu WP (2018) Molecular cocrystals: design, charge transfer, and optoelectronic functionality. Phys Chem Chem Phys 20(9):6009–6023. https://doi.org/10.1039/c7cp07167a

38. Zhang J, Jin JQ, Xu HX, Zhang QC, Huang W (2018) Recent progress on organic donor-acceptor complexes as active elements in organic field-effect transistors. J Mater Chem C 6(14): 3485–3498. https://doi.org/10.1039/c7tc04389a
39. Wang Y, Li Y, Zhu W, Liu J, Zhang X, Li R, Zhen Y, Dong H, Hu W (2016) Co-crystal engineering: A novel method to obtain one-dimensional (1D) carbon nanocrystals of corannulene-fullerene by a solution process. Nanoscale 8(32):14920–14924. https://doi.org/10.1039/c6nr05001h
40. Lu RQ, Wu S, Bao YH, Yang LL, Qu H, Saha M, Wang XY, Zhuo YZ, Xu BB, Pei J, Zhang H, Weng WG, Cao XY (2018) Cocrystallization of imide-fused corannulene derivatives and C_{60}: Guest-induced conformational switching and 1:1 segregation packing. Chem Asian J 13(19): 2934–2938. https://doi.org/10.1002/asia.201801086
41. Goudappagouda GM, Kulkarni GU, Babu SS (2018) One-dimensional porphyrin-fullerene (C_{60}) assemblies: Role of central metal ion in enhancing ambipolar mobility. Chem Eur J 24(30):7695–7701. https://doi.org/10.1002/chem.201800197
42. Zheng S, Zhong J, Matsuda W, Jin P, Chen M, Akasaka T, Tsukagoshi K, Seki S, Zhou J, Lu X (2018) Fullerene/cobalt porphyrin charge-transfer cocrystals: excellent thermal stability and high mobility. Nano Res 11(4):1917–1927. https://doi.org/10.1007/s12274-017-1809-7
43. Wakahara T, Nagaoka K, Nakagawa A, Hirata C, Matsushita Y, Miyazawa K, Ito O, Wada Y, Takagi M, Ishimoto T, Tachikawa M, Tsukagoshi K (2020) One-dimensional fullerene/porphyrin cocrystals: near-infrared light sensing through component interactions. ACS Appl Mater Interfaces 12(2):2878–2883. https://doi.org/10.1021/acsami.9b18784
44. Crane JD, Hitchcock PB, Kroto HW, Taylor R, Walton DRM (1992) Preparation and charaterization of C_{60}(ferrocene)$_2$. J Chem Soc Chem Commun 24:1764–1765. https://doi.org/10.1039/c39920001764
45. Wakahara T, Sathish M, Miyazawa K, Hu C, Tateyama Y, Nemoto Y, Sasaki T, Ito O (2009) Preparation and optical properties of fullerene hybrid hexagonal nanosheets and large-scale production of fullerene hexagonal nanosheets. J Am Chem Soc 131(29):9940–9944. https://doi.org/10.1021/ja901032b
46. Osonoe K, Kano R, Miyazawa K, Tachibana M (2014) Synthesis of C_{70} two-dimensional nanosheets by liquid-liquid interfacial precipitation method. J Cryst Growth 401:458–461. https://doi.org/10.1016/j.jcrysgro.2013.12.056
47. Imahori H, Ueda M, Kang S, Hayashi H, Hayashi S, Kaji H, Seki S, Saeki A, Tagawa S, Umeyama T, Matano Y, Yoshida K, Isoda S, Shiro M, Tkachenko NV, Lemmetyinen H (2007) Effects of porphyrin substituents on film structure and photoelectrochemical properties of porphyrin composites electrophoretically deposited on nanostructured SnO_2 electrodes. Chem Eur J 13(36):10182–10193. https://doi.org/10.1002/chem.200700446
48. Zhang J, Tan J, Ma Z, Xu W, Zhao G, Geng H, Di Ca HW, Shuai Z, Singh K, Zhu D (2013) Fullerene/sulfur-bridged annulene cocrystals: two-dimensional segmented heterojunctions with ambipolar transport properties and photoresponsivity. J Am Chem Soc 135(2):558–561. https://doi.org/10.1021/ja310098k
49. Wei L, Wu Y, Wang L, Fu H, Yao J (2011) Supramolecular synthesis of fullerene/tetracene hybrid flower-like microstructures of nanoplates via charge-transfer interactions. J Phys Chem C 115(44):21629–21634. https://doi.org/10.1021/jp206155q
50. Asaka K, Kato R, Yoshizaki R, Miyazawa K, Kizuka T (2007) Fracture surface and correlation of buckling force with aspect ratio of C_{60} crystalline whiskers. Diam Relat Mater 16:1936–1939. https://doi.org/10.1016/j.diamond.2007.08.005
51. Funamori Y, Suzuki R, Wakahara T, Ohmura T, Nakagawa E, Tachibana M (2020) Large elastic deformation of C_{60} nanowhiskers. Carbon 169:65–72. https://doi.org/10.1016/j.carbon.2020.07.061
52. Wang B, Zheng S, Saha A, Bao L, Lu X, Gudi DM (2017) Understanding charge transfer characteristics in crystalline nanosheets of fullerene/(metallo)porphyrin crystals. J Am Chem Soc 139(30):10578–10584. https://doi.org/10.1021/jacs.7b06162

53. Larsson M, Kjelstrup-Hansen J, Lucyszyn S (2019) DC characterization of C_{60} whiskers and nanowhiskers. ECS Trans 2(12):27–38. https://doi.org/10.1149/1.2408950
54. Miyazawa K, Kuwasaki Y, Hamamoto K, Nagata S, Obayashi A, Kuwabara M (2003) Structural characterization of C_{60} nanowhiskers formed by the liquid/liquid interfacial precipitation method. Surf Interface Anal 35(1):117–120. https://doi.org/10.1002/sia.1506
55. Ogawa K, Kato T, Ikegami A, Tsuji H, Aoki N, Ochiai Y, Bird JP (2006) Electrical properties of field-effect transistors based on C_{60} nanowhiskers. Appl Phys Lett 88(11). https://doi.org/10.1063/1.2186519
56. Anthopoulos TD, Singh B, Marjanovic N, Sariciftci NS, Ramil AM, Sitter H, Colle M, de Leeuw DM (2006) High-performance n-channel organic field-effect transistors and ring oscillators based on C_{60} fullerene films. Appl Phys Lett 89(21). https://doi.org/10.1063/1.2387892
57. Li H, Tee BCK, Cha JJ, Cui Y, Chung JW, Lee SY, Bao Z (2012) High-mobility field-effect transistors from large-area solution-grown C_{60} single crystals. J Am Chem Soc 134(5):2760–2765. https://doi.org/10.1021/ja210430b
58. Konarev DV, Kovalevsky AY, Li X, Neretin IS, Litvinov AL, Drichko NV, Slovokhotov YL, Coppens P, Lyubovskaya RN (2002) Synthesis and structure of multicomponent crystals of fullerenes and metal tetraarylporphyrins. Inorg Chem 41(14):3638–3646. https://doi.org/10.1021/ic0113121
59. Wakahara T, Miyazawa K, Ito O, Tanigaki N (2016) Preparation of composite films of a conjugated polymer and C_{60}NWs and their photovoltaic application. J Nanomat 2016. https://doi.org/10.1155/2016/2895850
60. Wakahara T, Sathish M, Miyazawa K, Ito O (2015) Electrochemical characterization of catalytic activities of C_{60} nanowhiskers to oxygen reduction in aqueous solution. Fullerenes, Nanotubes, Carbon Nanostruct 23(6):509–512. https://doi.org/10.1080/1536383x.2013.868441
61. Umeta Y, Suga H, Takeuchi M, Zheng S, Wakahara T, Naitoh Y, Tsukagoshi K (2021) C_{60}-nanowire two-state resistance switching based on fullerene polymerization/depolymerization. ACS Appl Nano Mater 4(1):820–825. https://doi.org/10.1021/acsanm.0c03144

Supramolecular Chemistry of Fullerenes

23

Takeharu Haino and Takehiro Hirao

Contents

Abstract

The globular shape of fullerenes characterizes their unique chemical and physical properties, which have led to the development of container molecules capable of extracting specifically sized fullerenes from raw fullerene mixtures. Calixarenes, cyclodextrins, bisporphyrin clefts, curved macrocycles, and molecular clefts were initially discovered to behave as fullerene host molecules. Extensive work on supramolecular fullerene chemistry has been directed toward nanoscience. Nanometric fullerene organizations and supramolecular fullerene polymers are examples. This chapter mainly addresses the supramolecular chemistry of calix[5]arene-based containers with a focus on the historical overview of the development of fullerene host molecules through nonpolar supramolecular interactions. The supramolecular complexation of calix[5]arenes with fullerene families, selective extraction of higher fullerenes, fullerene sensing, allosteric fullerene hosts, combinatorial screening of fullerene hosts, and encapsulation of C_{120} are described. In addition, supramolecular fullerene polymers with structural variations are documented. It is also shown that a C_{60}•biscalix[5]arene host-guest

T. Haino (✉) · T. Hirao
Graduate School of Advanced Science and Engineering, Hiroshima University, Hiroshima, Japan
e-mail: haino@hiroshima-u.ac.jp

X. Lu et al. (eds.), *Handbook of Fullerene Science and Technology*,
https://doi.org/10.1007/978-981-16-8994-9_36

complex acts as a supramolecular cross-linker and a shape transformer for linear polymers.

Keywords

Calixarene · Macrocycles · Porphyrin · Cyclodextrin · Cycloparaphenylene · Supramolecular polymer · Supramolecular polymer hybrid · π-π stacking · van der Waals interaction · Hydrophobic interaction

Introduction

In 1985, fullerenes were first introduced as new members of the carbon allotrope family by Kroto, Kurl, and Smalley [1]. The practical amount of fullerene production, developed using vaporization of graphite in arc plasma by Krätschmer et al., greatly accelerated fullerene science [2]. The spherical geometries of fullerenes consist of sp^2-hybridized carbon atoms with convex extended π-surfaces; therefore, fullerenes show an excellent electron-accepting ability. The unique electronic structures of fullerenes offer a rich variety of opportunities to develop various functional derivatives for use in, e.g., supercapacitors, hydrogen storage, solar cells, and biological applications, which are of prime scientific interest in fullerene science.

Large-scale production of fullerenes using chemical vapor deposition (CVD) [3, 4] and benzene flame synthesis [5–7] obviously increased their scientific value. Raw fullerene mixtures mainly contain C_{60} and C_{70} with small amounts of other higher fullerenes. Although the separation of C_{60} and C_{70} has matured by complexation [8], sublimation [9, 10], and chromatographic methods using stationary phases [11–13], the efficient separation of fullerene isomers remains tricky. Supramolecular chemistry offers a potential alternative to selectively extract fullerenes from raw fullerene mixtures. It has been a great endeavor to construct molecular containers capable of hosting fullerenes in supramolecular chemistry. A lack of polar functionality in fullerenes limits the noncovalent interactions that can be utilized for a host-fullerene association. Thus, supramolecular chemists have focused on developing host molecules that capture fullerenes by host-guest interactions, relying on weak π-π stacking, donor-acceptor, hydrophobic, and van der Waals interactions. Host molecules require certain complementarity in terms of size, shape, and electronic structure to the exterior of fullerenes to gain sufficient intermolecular interaction energy between hosts and fullerenes. Macrocyclic molecules are often employed through the preorganization concept.

Host-Guest Chemistry of Fullerenes

The first discovery of fullerene hosts was reported in water. Azacrown macrocycles possessing lipophilic side chains were first introduced by Ringsdorf et al. [14] C_{60} and C_{70} were encapsulated within the macrocyclic cavities at the air-water interface

to yield stable monolayers. γ-Cyclodextrins (CD) were reported to be potential hosts for fullerenes [15, 16]. Host-guest complexation between C_{60} and γ-CD occurs at the toluene-water interface. A C_{60} molecule in toluene is extracted into water to form the host-guest complex C_{60}•γ-CD_2 in water, where a C_{60} molecule is located within the cavity surrounded by two γ-CD molecules facing each other. The host-guest complexation between p-tert-butylcalix[8]arene (C8A) and C_{60} is best known among the host-guest complexes reported so far. Atwood [17] and Shinkai [18] took advantage of host-guest complexation for C_{60} separation from raw fullerene mixtures (Fig. 1). When p-tert-butylcalix[8]arene was simply added into a toluene solution of raw fullerene mixtures, the calix[8]arene-C_{60} complex was selectively precipitated. Dissolving the host-guest complex into chloroform liberated C_{60} as a precipitate. Cyclotriveratrylene (CTV) forms the host-guest complex with C_{60} [19]. The 1:1 CTV-C_{60} complex shows beautiful shape complementarity between the convex exterior of C_{60} and the concave interior of CTV in the solid state. An effective stacking interaction is found between the CTV aromatic rings and the C_{60} surface, which most likely results in a certain attractive energy. The recent review article by Martín et al. summarizes the π-π interaction-directed host-guest complexation of fullerenes [20].

A porphyrin ring possesses an electron-rich aromatic surface that generates effective stacking interactions with fullerene surfaces [21]. Reed and Boyd et al. demonstrated that bisporphyrin cleft (BP) molecules are good receptors for fullerenes (Fig. 2) [22, 23]. The binding ability of bisporphyrin BP for C_{60} was influenced by variation of metal cations at the porphyrin centers, increasing in the order of Fe(II) < Pd(II) < Zn(II) < Mn(II) < Co(II) < Cu(II) < 2H. H_2BP showed the best binding for C_{60}. Aida's macrocyclic porphyrin dimer ZnMBP provides a more rigid cavity where C_{60} is encapsulated with a binding constant of 6.7×10^5 L mol^{-1} [24]. Various metal cations can be installed instead of Zn at the center of the porphyrin rings, which varies for the affinity of the fullerenes. Extremely high selectivity for fullerenes such as C_{96} was established by using a zinc-centered cyclic porphyrin host and establishing a remarkably high binding constant of 3.0×10^7 L mol^{-1}. Higher fullerenes were separated by using ZnMBP from raw fullerene mixtures mainly containing C_{60} and C_{70} [25]. The allosteric fullerene host molecule ABP was developed using a bisporphyrin structure [26]. The two porphyrin units are connected with a rotatable single bond, which prefers to adopt an anti-conformation due to the intramolecular pyridine-Zn coordination bonds. A C_{60}

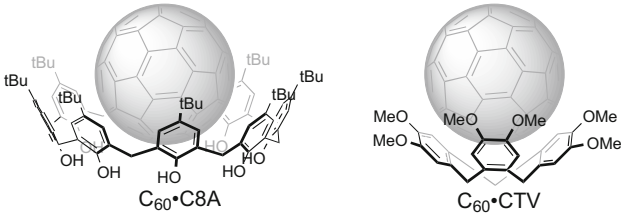

Fig. 1 The host-guest complexes of C_{60}•C8A and C_{60}•CTV

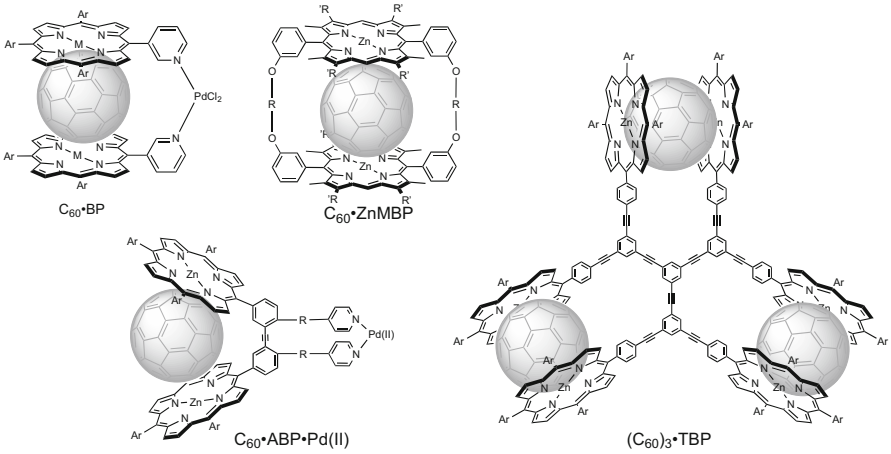

Fig. 2 The host-guest complexes of C_{60}•BP and C_{60}•ZnMBP

molecule is not accessible to the anti-conformation due to a lack of a binding space. The anti-conformation turned into the syn conformation upon palladium complexation, resulting in the bisporphyrin cleft ABP•Pd(II). A C_{60} molecule was accommodated within the binding space between the two porphyrin units. The dendritic hexaporphyrin host TBP is another type of allosteric porphyrin-based fullerene host [27]. The three sets of bisporphyrin cleft units are conformationally coupled. TBP captures a C_{60} molecule at each bisporphyrin cleft unit, which shows a fairly high binding constant of 1.4×10^8 L^3 mol^{-3} with a Hill coefficient of 2.8. Therefore, the multiple fullerene binding is highly cooperative. Accordingly, the first and second fullerene binding processes preorganize the rest of the cleft units, which encourages the subsequent fullerene binding processes to form $(C_{60})_3$•TBP. Recently, Nitschke et al. developed a self-assembled porphyrin-based cuboctahedron that encapsulated two molecules of C_{60} or C_{70}. The binding events were highly regulatable in terms of cooperativity by using various counteranions [28]. A tetrathiafulvalene-calix[4]pyrrole is an electron-rich aromatic ring that can become an allosteric fullerene host. A cone shape for calix[4]pyrrole was induced by anion complexation at the center of calix[4]pyrrole, which produced complementary cavities where C_{60} and C_{70} were encapsulated in a cooperative manner [29]. Rosarin is known to be one of the porphyrin analogs and contains three meso-aryl-linked bipyrrole units. A C_{60} molecule can fit within the cavity of rosarin to produce a 1:1 host-guest complex [30].

Curved hydrocarbon surfaces are potentially useful for fullerene encapsulation. Corannulenes (CR) are curved aromatic rings that are complementary to the exterior of C_{60}; however, a limited van der Waals interaction between C_{60} and CR (X = H) produced a host-guest complex in the gas phase (Fig. 3) [31]. Polarizable sulfur atoms at the periphery of a CR (X = S-Ar) molecule facilitate host-guest complexation with a binding constant of 1420 L mol^{-1} in CS_2 [32]. It is obvious that the

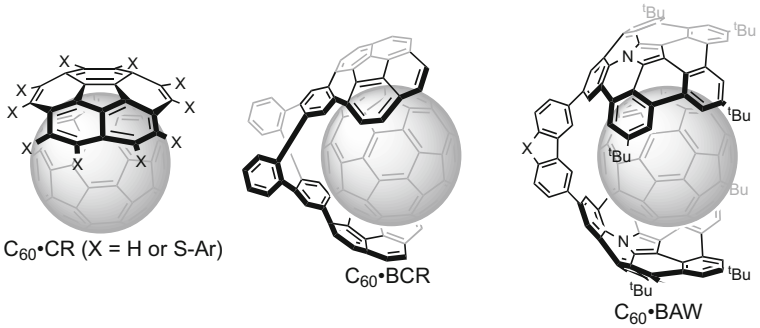

Fig. 3 Host-guest complexes of C_{60}•CR, C_{60}•BCR, and C_{60}•BAW

convex cavity of CR is extended with sulfur atoms, enhancing the intermolecular van der Waals interaction. A face-to-face arrangement of two CR units is efficient in integrating weak van der Waals interactions between CR and C_{60}. Sygula et al. developed a molecular cleft (BCR) possessing two corannulene units in a face-to-face manner. The cavity surrounded the C_{60} exterior with perfect shape complementarity, which resulted in the formation of a host-guest complex in solution and in the solid state. The curved anthracene units of exTTF connected with an isophthalate bridge generate a complementary cavity in which C_{60} is accommodated [33]. π-Extended azacorannulene was recently introduced as a new member of curved π-systems, named azabuckybowl, which embeds one nitrogen atom. The concave basic molecular surface generates effective contact with C_{60} [34]. Azabuckybowl units are linked with aromatic linkers, giving rise to molecular tweezers (BAW) [35]. Two azabuckybowl units are organized in a face-to-face fashion. The resulting cavity greatly enhances fullerene binding to C_{60} and C_{70} with effective π-π stacking interactions. Dipyrrolylbenzodiazepines possess curved, electron-rich aromatic surfaces. The hydrogen-bonded macrocyclic form captures C_{60} in the solid state [36]. Twisted perylene diimide units were installed within a macrocyclic structure, which provide the cavity for fullerene binding. C_{70} shows better binding than C_{60} within the cavity [37]. Wu reported that a bowl-shaped carbon nanobelt possessing a fully conjugated aromatic system hosted C_{70} over C_{60} [38].

Macrocyclic aromatic rings have obvious potential for fullerene encapsulation by gaining intermolecular van der Waals interactions. [6]-Cycloparaphenyleneacetylene (CPPA) was first introduced as a fullerene host molecule by Kawase and Oda et al. (Fig. 4) [39]. The large cavity of [6]CPPA is surrounded by aromatic walls, which possess a diameter of 1.3 nm. The complementary cavity provides an effective π-π interaction with C_{60}. The host-guest complex [6]CPPA•C_{60} was formed with a binding constant of 1.6×10^4 L mol^{-1}. The interior of [9]CPPA is complementary to the exterior of [6]CPPA; thus, the host-guest complex [9]CPPA•[6]CPPA was stably formed in chloroform solution. The host-guest complex [6]CPPA•C_{60} still has the ability to bind within [9]CPPA to form the onion-type ternary

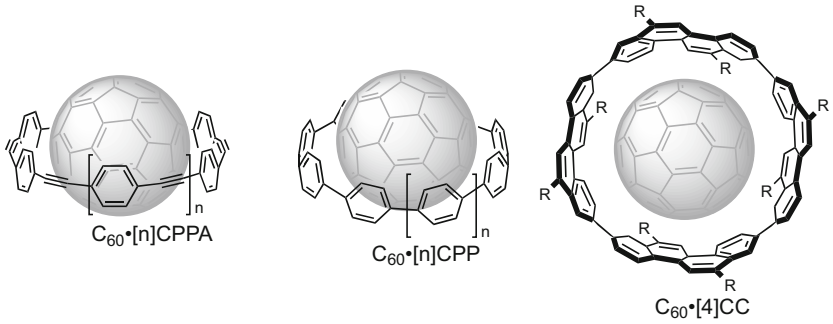

Fig. 4 Macrocyclic hosts

complex [9]CPPA•[6]CPPA•C_{60}. Yamago et al. reported that [10]cycloparaphenylene (CPP) selectively encapsulated C_{60} with an internal cavity surrounded by ten aromatic rings. C_{60} complexation is quite sensitive to the CPP ring size. When C_{60} was added into a mixture of [8–12]CPP, the host-guest complex [10]CPP•C_{60} was exclusively formed with an unusually high binding constant of 2,790,000 L mol^{-1} [40]. C_{70} prefers to bind within the cavities of [10]- and [11]CPP with association constants of 84,000 and 150,000 L mol^{-1}, respectively, despite a difference in ring sizes [41]. C_{70} is located within the [10]CPP ring, where the pseudo-C_{5v} axis of C_{70} passes through the center of the ring, which gains an effective intermolecular π-π stacking interaction. In contrast, C_{70} accepts the standing orientation within the [11]CPP ring, where the principal axis of C_{70} is oriented vertical to the C_{11v} axis of the [11]CPP ring, which results in slight deformation of the ring with an effective intermolecular π-π stacking interaction. These conformational characteristics rationalize the size preference in C_{70} binding. [11]CPP also encapsulates various higher fullerenes and endohedral metallofullerenes [42, 43]. [4]Cyclochrysenylene (CC) provides a remarkably effective intermolecular π-π stacking interaction with C_{60}, resulting in a log Ka value of 12.3 in benzene solution [44]. An anthracene cyclic hexamer possesses a huge cavity where C_{60} is encapsulated through CH/π interactions [45]. The unique supramolecular structure was named "Nano-Saturn."

Calixarenes have been recognized as potential host molecules capable of capturing various guest molecules. As already mentioned, calix[8]arene was discovered to be a potential host molecule for fullerenes. However, the cavity is not complementary to the exteriors of C_{60} and C_{70}. The strained conformation of calix[8]arene appears to complex with two C_{60} molecules [46]. Calix[6]arene also encapsulates C_{60} in a 1:1 ratio with an association constant of 100 L mol^{-1} [47]. In contrast, calix[6]arene forms cocrystals with two molecules of C_{60} or C_{70} [48]. The strained conformation of calix[6]arene provides two complementary cavities where C_{60} and C_{70} are accommodated. A homooxacalix[3]arene, a member of the calixarene family, cannot interact with C_{60}. However, metal coordination-directed dimerization results in the homooxacalix[3]arene dimeric capsule that encapsulates the C_{60}

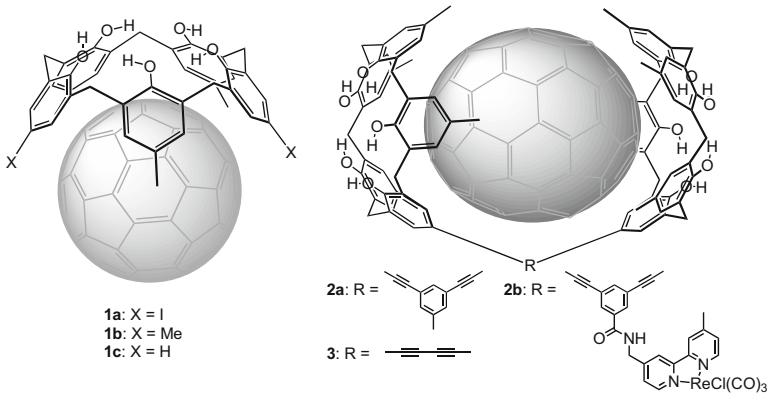

Fig. 5 Fullerene containers **1a-c**, **2**, and **3** based on calix[5]arene

molecule within the cavity with an association constant of 54 L mol^{-1} [49]. Ogoshi et al. reported that pillar[10]arene selectively encapsulates C_{60} within the cavity [50].

The small members of the series are calix[4]arene and calix[5]arene, which possess symmetric and cone-shaped cavities due to the intramolecular cyclic hydrogen bonding of the phenolic hydroxyl groups (Fig. 5). The most complementary cavity of calix[5]arenes for C_{60} was introduced by Fukazawa et al. [51] The effective van der Waals and stacking interactions effectively facilitate the host-guest complexation of calix[5]arene and C_{60}. Calix[5]arenes **1a-c** encapsulate C_{60} to organize host-guest complexes C_{60}•**1a-c** in solution. The association constants are influenced by the para-substituents (Table 1). Polarizable iodine enhances fullerene encapsulation more than methyl and hydrogen groups. Although **1a** is bound to C_{60} in a ratio of 1:1 in solution, the 2:1 host-guest complex C_{60}•$\mathbf{1a}_2$ is found in the solid state (Fig. 6). The crystal structure shows that the fivefold rotation axes of the hosts pass through the fivefold rotation axis of C_{60} [52]. The calix[5]arenes create effective intermolecular π-π stacking interactions between the aromatic cavities and the exterior of C_{60}. The polarizable iodine groups at the para-positions generate effective contacts to the C_{60} surface, which most likely enhance the van der Waals attraction. Therefore, the van der Waals and π-π stacking interactions primarily direct host-guest complexation. Increasing the size of fullerenes diminishes the binding abilities of **1a,b**. Therefore, C_{60} is the best complement to the interior of the calix[5]arenes over higher fullerenes [53].

The concave cavities were connected with covalent linkages to produce biscalix[5]arenes **2a** and **3**. The wider and more extended guest-binding cavities are shape-complementary to fullerenes, which incredibly improves the binding abilities to fullerenes. The binding ability of C_{60} to **2a** is increased 30 times as large as that to **1a**. The highest fullerene binding is achieved in the host-guest complexation of **2a** with C_{78} with a binding constant of 300,000 L mol^{-1}. The biscalix[5]arene cavity is modified by the structure of the linkers, which results in a significant influence on fullerene binding. The slightly extended cavity of **3** with the butadiyne linkage

Table 1 Association constants (Ka/L mol^{-1}) for **1a-c**, **2**, and **3** in toluene[53]

	K_a/L mol^{-1}				
Host	C_{60}	C_{70}	C_{76}	C_{78}	C_{84}
1a	2100 ± 100	520 ± 60	430 ± 10	310 ± 40	220 ± 30
1b	1670 ± 70	380 ± 30	250 ± 20	150 ± 30	55 ± 3
1c	588 ± 70	310 ± 30	n.d.	n.d.	n.d.
2	68,000 ± 5000	118,000 ± 12,000	200,000 ± 14,000	300,000 ± 50,000	53,000 ± 2000
3	9000 ± 200	91,000 ± 9000	41,700 ± 2000	28,000 ± 3000	36,000 ± 4000

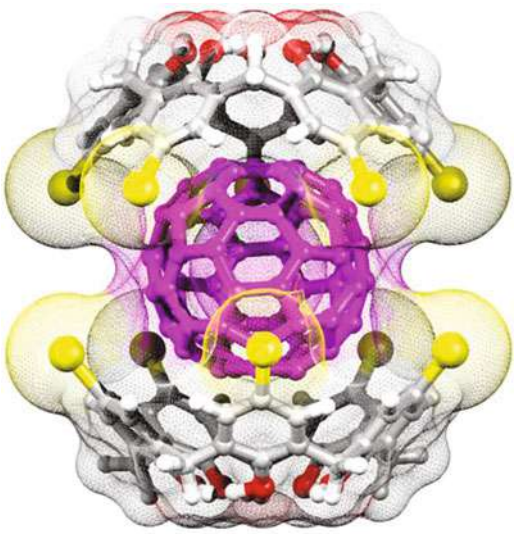

Fig. 6 Crystal structure of host-guest complex C_{60}•**1a**$_2$

reduces the binding ability for all fullerenes. Thus, the tunable cavity shape determines the binding ability for fullerenes.

Fullerene sensors **2b** were constructed by the combination of calix[5]arene units and the luminogenic rhenium complex [54]. The rhenium complex shows an intense emission at 600 nm, which is quenched by fullerene molecules within the cavity due to intramolecular static quenching of host-guest complexes **2b** with C_{60} or C_{70}. The emission quenching is selective for C_{60} and C_{70} over another quencher, anthracene. The apparent quenching rate constants for C_{60}, C_{70}, and anthracene were determined to be 200×10^4 s^{-1}, 120×10^4 s^{-1}, and 11.9×10^4 s^{-1}, respectively, when the concentrations of **2b** and fullerenes were fixed to be 1.0×10^{-5} mol L^{-1} and 5.6×10^{-6} mol L^{-1}, respectively. Thus, sensor **2b** enhances selective fullerene detection to be 17-fold more efficient than anthracene detection. The selective fullerene encapsulation of the biscalix[5]arene unit determines the selectivity and sensitivity of fullerene sensing.

The D_2 symmetric feature of C_{76} results in 19 discrete resonances of nonequivalent carbons, which allows for study of the conformational characteristics of the host-guest complex (Fig. 7). When C_{76} is encapsulated within biscalix[5]arene **2a**, the 19 resonances shift upfield by more than 1 ppm. The carbons at the polar ends show more upfield shifts than the other carbons; thus, the polar ends are located deep inside the calix[5]arene cavities to experience strong shielding effects. Thus, the principal axis of C_{76} is oriented along the pseudo-C_5 axis of **2a** in solution. Selective complexation to higher fullerenes was established by biscalix[5]arene **2a**. However, higher fullerenes cannot be selectively extracted.

A doubly bridged biscalix[5]arene **4** was developed for the separation of higher fullerenes [55]. The more preorganized concave cavity is produced by the

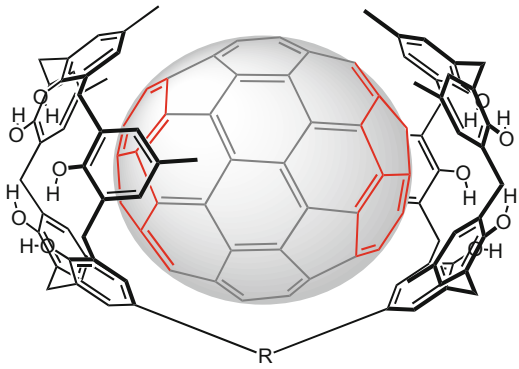

Fig. 7 Plausible conformation of C_{76} within biscalix[5]arene **2a**

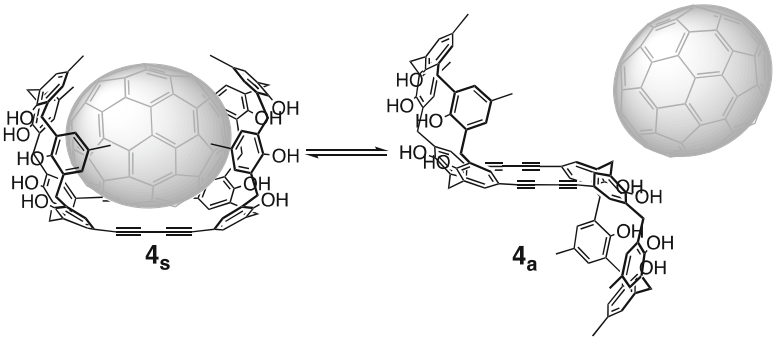

Fig. 8 Schematic illustration of the uptake and release of fullerene by biscalix[5]arene **4**

introduction of two butadiyne linkages that restrict the rotational freedom of the single bonds (Fig. 8). **4** possesses two conformational isomers; the cavity is confined with the two calix[5]arene units of *syn* isomer **4s**, which face one another, and *anti* isomer **4a** bears two calix[5]arene units in an *anti* configuration. The interconversion of the two conformational isomers can be controlled, which results in the direct regulation of the uptake and release of fullerenes. The energetic barrier for the isomerization between **4s** and **4a** is more than 100 kJ mol^{-1}. Thus, **4s** and **4a** are atropisomeric and isolable at room temperature, whereas the isomerization is in equilibrium over 130 °C. Thus, the interconversion between **4s** and **4a** is turned on by heating. In addition, toluene enhances the difference in solubility between **4s** and **4a**. **4a** shows better solubility than **4s** in toluene; therefore, **4s** selectively precipitated out from the solution of the isomeric mixtures. Isolated **4s** effectively encapsulates higher fullerenes even in 1,1,2,2-tetrachloroethane. Good selectivity for higher fullerenes is achieved by **4s**, which suggests that the interior of **4s** is complementary to the exteriors of higher fullerenes (Table 2). **4s** is capable of excluding C_{60} from raw fullerene mixtures.

Table 2 Association constants (Ka/L mol^{-1}) for **4s** and **3** in 1,1,2,2-tetrachloroethane

	K_a/L mol^{-1}	
	4 s	3
C_{60}	9700	1550
C_{70}	29,000	2800
C_{76}	90,000	1850
C_{78}	110,000	2500
C_{84}	20,000	110

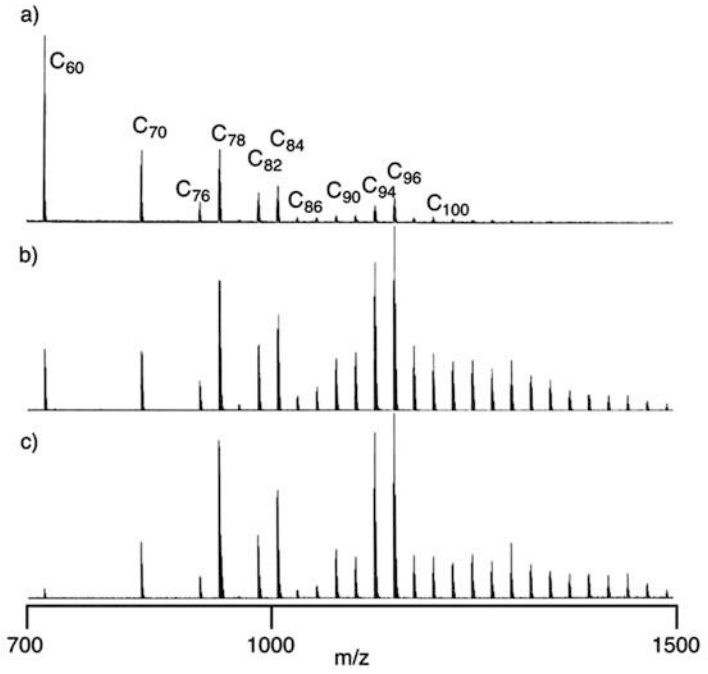

Fig. 9 MALDI-TOF mass spectra for (**a**) fullerene mixtures, (**b**) first extract, and (**c**) second extract through host-guest complexation of **4 s**. Reproduced with permission from Ref. [55]. Copyright 2006 American Chemical Society

Upon elevating the solution temperature to over 60 °C, syn-anti isomerization is accelerated, which suggests that the fullerenes are liberated from **4s** through isomerization to **4a**. A higher fullerene extraction protocol was developed by using **4s** from raw fullerene mixtures consisting of C_{60} (67%), C_{70} (23%), and higher fullerenes (10%) (Fig. 9a). Upon the addition of **4s** solution into a solution of raw fullerene mixtures, the host-guest complexes of **4s** and fullerenes are precipitated and collected by filtration. The precipitates are soluble in 1,1,2,2-tetrachloroethane, which was heated at 100 °C for a while. The fullerenes captured are released into the solution. In the mass spectra shown in Fig. 9b, higher fullerenes are enriched in the

first extract. Repeating the extraction process for the first extracts results in higher fullerene mixtures with the successful exclusion of C_{60} (Fig. 9c).

The regulation of fullerene encapsulation using calix[5]arenes was demonstrated in a cooperative manner. Biscalix[5]arene **5** was developed as an allosteric fullerene host molecule where the two calix[5]arene units were tied with the flexible linker (Fig. 10). The copper ion complexation to the bipyridine units results in the tetrahedral complex **5**•Cu. As a result, the calix[5]arene units are in close proximity to form the complementary cavity for fullerenes. **5** shows the binding abilities for C_{60} and C_{70} with association constants of 98 L mol^{-1} and 250 L mol^{-1}, respectively, in 1,1,2,2-tetrachloroethane. The fullerene binding of **5**•Cu is greatly improved with binding constants of 3800 L mol^{-1} and 950 L mol^{-1} for C_{60} and C_{70}, respectively. C_{60} complexation shows more obvious cooperativity between the presence and absence of copper ions. The hydrogen bonding-directed self-assembly of calix[5]arene **6** results in supramolecular biscalix[5]arene **6•6**, which shows effective binding to C_{60}. The assembly and disassembly of dimeric **6•6** is easily controlled by the addition of trifluoroacetic acid (TFA). Dimeric **6•6** shows a binding constant of 1500 L mol^{-1} for C_{60}, which is diminished by TFA addition. Even though monomeric **6** still shows a binding ability for C_{60} with a binding constant of 450 L mol^{-1}, the cooperative regulation of C_{60} binding was directly monitored by ^{13}C NMR spectroscopy. The ^{13}C signal for C_{60} showed an upfield shift with a complexation-induced chemical shift of −0.82 ppm with the rationale that the C_{60} molecule is located within the two calix[5]arene cavities, enjoying the strong shielding effect of the ten aromatic rings. The TFA addition liberates the C_{60} molecule by disrupting the hydrogen-bonded dimer **6•6**, which results in a downfield shift of the ^{13}C signal. Thus, fullerene binding is regulated by pH regulation.

Dynamic combinatorial supramolecular chemistry is known to be based on equilibrium among library members, where permutation and combination of subunits occur. Therefore, a guest-temptation amplifies a desired member in the dynamic equilibrium of host members. A preferred member of a host library gains a certain stability by complementary guest complexation, which leads to a shift of the equilibrium toward preferred and far from undesired not to participate in guest

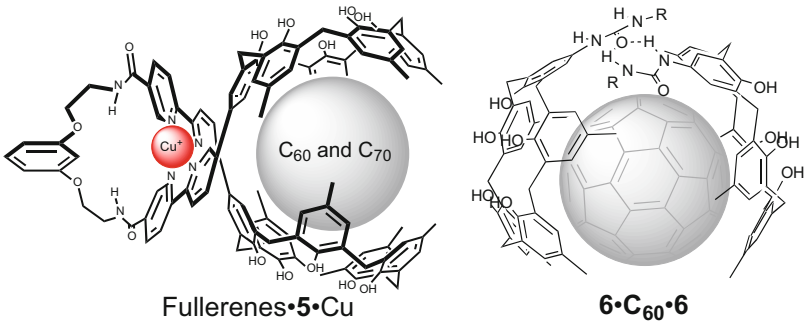

Fig. 10 Allosteric fullerene hosts

complexation. Thus, an amplified member is easily identified in diverse libraries. This dynamic combinatorial library is potentially useful for the discovery of fullerene host molecules [56, 57].

The potential subunits **7a-d** possessing calix[5]arene, benzyl, pyrene, and porphyrin units are mixed together with the silver cation, which results in the permutation-combination-based dynamic library including the ten discrete library members (Fig. 11). Electrospray mass spectrometry allows for the detection of all the library members [**7a-d**•Ag^+•**7a-d**] formed in dynamic equilibrium. The addition of C_{60} into the library results in the formation of four supramolecular complexes C_{60}•[**7a**•Ag^+•**7b-d**]. In contrast, C_{70} binding biases the dynamic equilibrium to form C_{70}•[**7a**•Ag^+•**7d**] and C_{70}•[**7d**•Ag^+•**7d**] complexes. Accordingly, the calix[5]arene unit is required to capture C_{60}, whereas C_{70} prefers to bind to porphyrin-based hosts. The permutation-combination-based dynamic combinatorial library obtained through supramolecular assembly is potentially useful for developing supramolecular fullerene host molecules.

Dumbbell-shaped C_{120}, synthesized by Komatsu et al., carries a cyclobutene ring [58]. Studies of the physical and chemical properties of C_{120} have been hampered due to its poor solubility in solvents. Host-guest chemistry can overcome the low solubility of C_{120} (Fig. 12). Biscalix[5]arene host molecules **2a**, **3**, and **8** have the potential to encapsulate C_{120} to form host-guest complexes [59]. C_{120} shows fair solubility in o-dichlorobenzene. Biscalix[5]arenes **2a**, **3**, and **8** capture C_{120} in a host-guest ratio of 1:1, giving rise to associate constants of 3900 L mol^{-1}, 12,300 L mol^{-1}, and 10,700 L mol^{-1}, respectively. The association constants depend on the linker structures. There are two possible binding modes: conformation A, where both C_{60} units are accommodated within the cavity of the two calix[5]arene units, and conformation B, where one of the C_{60} units is captured within the cavity composed of the two calix[5]arene units (Fig. 13). Molecular calculations for the host-guest complexes suggest that hosts **3** and **8** adopt conformation A upon encapsulating C_{120} to gain effective intermolecular surface contacts,

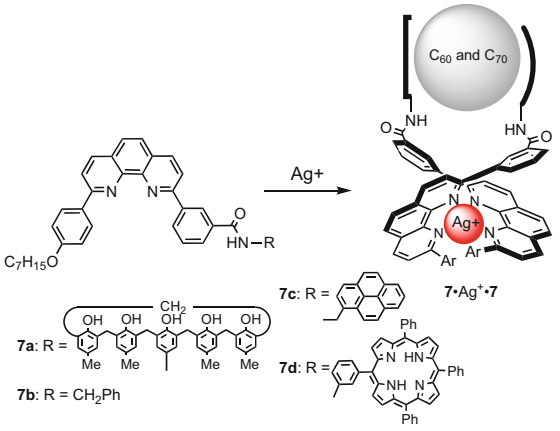

Fig. 11 Dynamic combinatorial library formed via self-assembly of **7a-d** through metal coordination

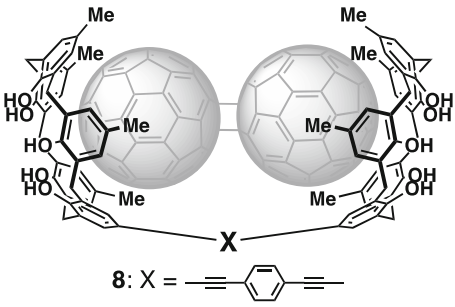

Fig. 12 The host-guest complex of biscalix[5]arene **8** with C_{120}

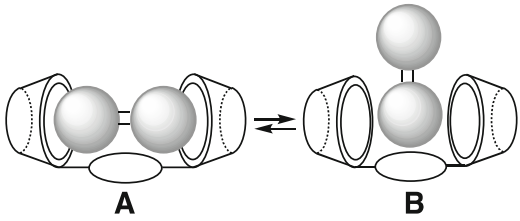

Fig. 13 Possible binding modes for C_{120} binding within biscalix[5]arenes

whereas the cavity of **2a** is too small to fit to the exterior of C_{120}, resulting in conformation B. The complementary cavities of **3** and **8** result in fairly strong binding to C_{120}.

Supramolecular Organization of Fullerenes

Controlling supramolecular fullerene ensembles is crucial in various phases, e.g., solid state, mesophase, and solution. Multiple ensembles of fullerenes in nanometric space can be engineered by manipulating noncovalent interactions, comprising hydrogen-bond, π-π stacking, dipole-dipole, and van der Waals interactions. Initially, nanometric C_{60} organizations were studied through the concept of supramolecular chemistry in the solid state. Cocrystallization of C_{60} and a calix[4]arene has driven the development of a linear array of C_{60} in the solid state [60]. Balch et al. employed the host-guest chemistry of C_{60} to build a C_{60} nanoarray (Fig. 14) [61]. The two phenylethynylbenzene units are located on a C_{60} iridium complex, which results in the complementary cavity. The exterior of C_{60} fits to the cavity, generating π-π stacking interactions. Head-to-tail host-guest complexation occurs in the solid state to form the C_{60} nanoarray. A shuttlecock-like C_{60} assembly was developed by Nakamura et al. [62] The five aromatic tails are attached via a copper-mediated addition reaction on the pentagon of a C_{60} molecule, which give rise to a deeply conical cavity complementary to the exterior of C_{60}. The head-to-tail and convex-concave π-π stacking interaction drives the endless one-dimensional linear order in the hexagonal columnar liquid crystalline phase.

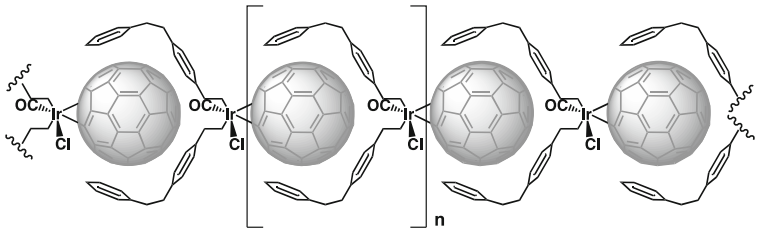

Fig. 14 C_{60} linear array in the solid state

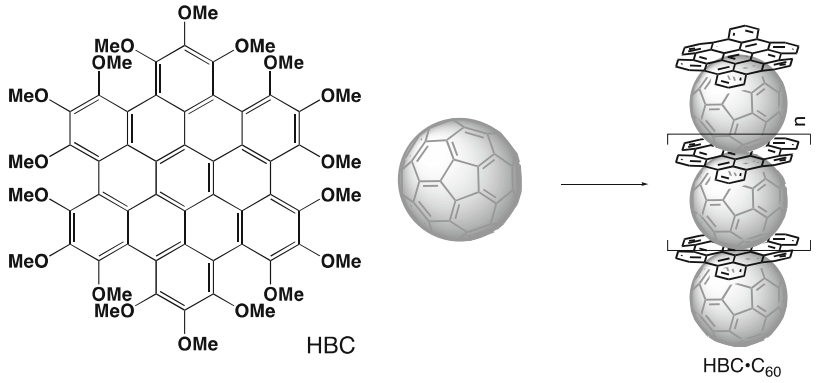

Fig. 15 Alternating linear array of permethoxylated hexa-peri-hexabenzocoronene HBC and C_{60}

Atwood, Barbour, Raston et al. reported that C_{60} cocrystallizes with calix[5]arene to provide structural variation in C_{60} arrangements in the solid state [63]. The self-assembly of C_{60}, calix[5]arene, and toluene produces a multiple molecular organization in a ratio of 1:1:1, resulting in a zigzag C_{60} array, whereas the helical array of C_{60} emerges with *tert*-Butyl-calix[5]arene [64]. A linear C_{60} array was fabricated by the cocrystallization of double-concave permethoxylated hexa-peri-hexabenzocoronene (HBC) with C_{60} (Fig. 15) [65]. Steric congestion at the bay region for HBC results in nonplanar congestion. The alternating orientation of the outer aromatic rings allows HBC to possess two concave faces by adopting a centrosymmetric structure. Thus, both of the faces are complementary to the exterior of C_{60}. The alternatingly arranged columnar packing of HBC-C_{60} is established, where the two C_{60} molecules are located at each face through noncovalent van der Waals and π-π stacking interactions. A tetraphenylprophyrin possessing amide functionalities was dimerized with C_{60} to result in a ternary complex, which facilitates the formation of the higher nanometric C_{60} organization [66]. The linear C_{60} array can form fiber networks that are responsible for gelation.

Naphthalenediimide (NDI) possessing amino acid groups was helically assembled to generate an artificial nanotube through hydrogen bonding interactions (Fig. 16) [67]. The diameter of the nanotube was determined to be 12.4 Å in the crystal structure with the helical structure. The helix turn consists of three NDI units.

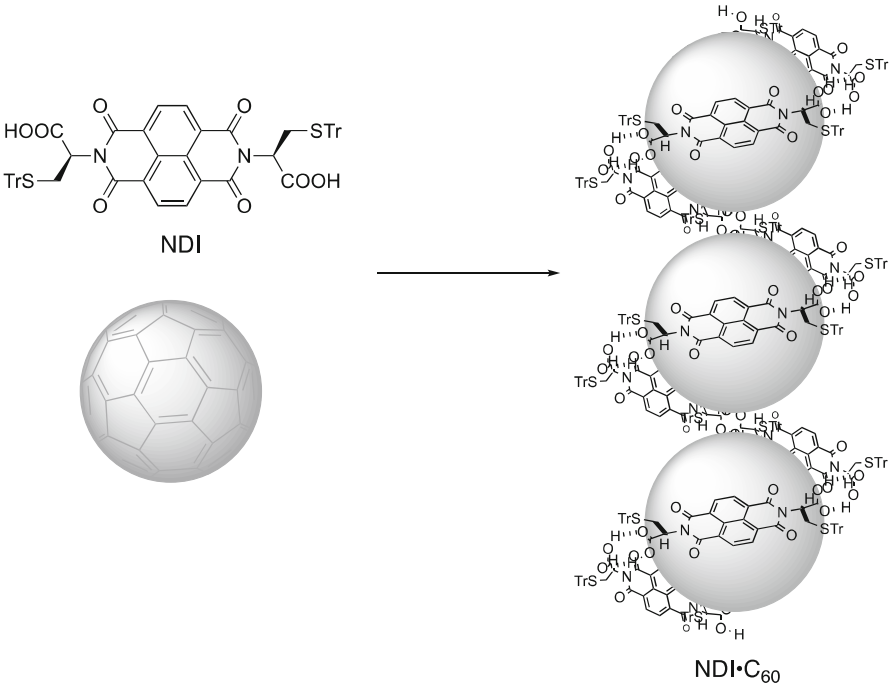

Fig. 16 Guest-induced helical assembly of naphthalenediimide (NDI) with C_{60}

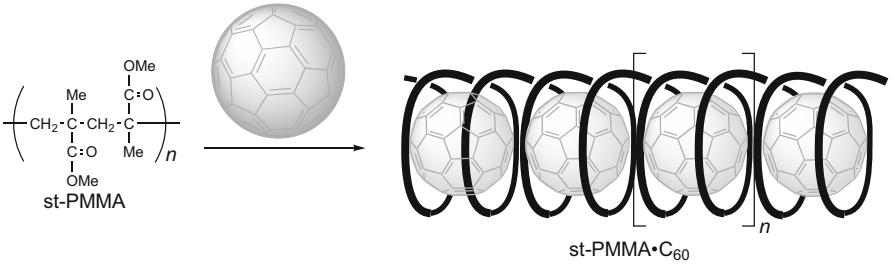

Fig. 17 Encapsulation of C_{60} in the st-PMMA helical cavity

The tubular cavity fits with the exterior of the C_{60} molecule, which is linearly arranged within the tubular structure, where the C_{60} molecule generates close contacts to its neighbors with the C_{60}-C_{60} interaction. In particular, the induced circular dichroism was found at the absorption band of C_{60}, which indicates that the helical nanotube directs the chirality of the C_{60} array.

Kawauchi, Kumaki, Yashima et al. demonstrated that C_{60} is encapsulated within the tubular cavity in the helical conformation of syndiotactic poly(methyl methacrylate) (st-PMMA) (Fig. 17) [68]. The toluene solution of C_{60} gelled in the presence of st-PMMA through the formation of a peapod-like nanostructure, where 86% of

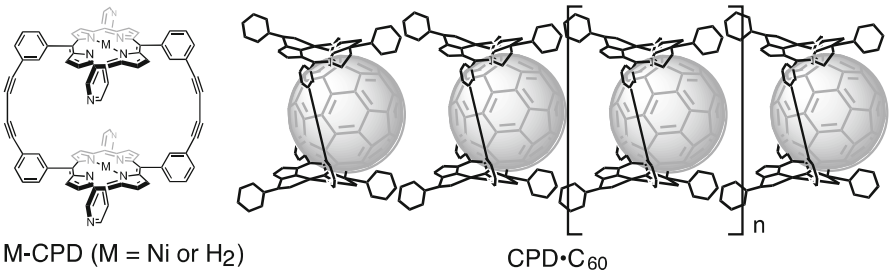

Fig. 18 Encapsulation of C_{60} in the Ni-CPD cavity

the helical cavity is occupied by C_{60} molecules. The linearly aligned C_{60} array was directly observed by transmission electron microscopy. The helical supramolecular structure is chirally directed by the complexation of chiral phenethyl alcohol. The induced chirality was maintained after removal of the alcohol.

The cyclic porphyrin dimer (CPD) was developed by Tani et al. (Fig. 18) [69]. Ni-CPD is a good fullerene host molecule that captures C_{60} within the tubular nanospace of Ni-CPD with a binding constant of 20,000 L mol^{-1} [70]. The single crystal of C_{60}•Ni-CPD shows a remarkable linear polymeric arrangement of C_{60} molecules through the Ni-CPD nanometric tubular channel, which is maintained by the CH/N hydrogen bonds. Anisotropic high electron mobility was observed along the linear C_{60} array passing through the crystallographic b axis. In contrast, the free base cyclic dimer H_2-CPD produced a slightly different single-crystal structure where the C_{60} molecules are arranged in a zigzag array through the crystallographic b axis, generating van der Waals contacts [71]. An anisotropic charge mobility of 0.13 $cm^2\ V^{-1}\ s^{-1}$ was observed along the zigzag channel passing through the b axis. A solar cell was fabricated with C_{60}•CPD, which exhibited photovoltaic activity with a current conversion efficiency of 17%.

Supramolecular Polymerization of Fullerene

Fullerene chemistry has been combined with supramolecular polymer science, which results in synergetic collaboration, offering a brand-new supramolecular fullerene polymer material. Fullerene polymers were initially synthesized through direct polymerization using a [2+2]cycloaddition reaction [72]. There are many chemically equivalent double bonds; thus, dimensionally extended networked polymeric structures lose stereo- and regioregularity. This defect can be compensated by introducing a supramolecular method to construct C_{60}-containing polymers in a dimensionally controlled manner.

C_{60}-Containing supramolecular polymers have been actively studied, where monomer units are connected with complementary noncovalent interactions [73]. Therefore, the formation and dissociation of supramolecular polymers are reversible and stimuli responsive. The size, shape, and dimension of the

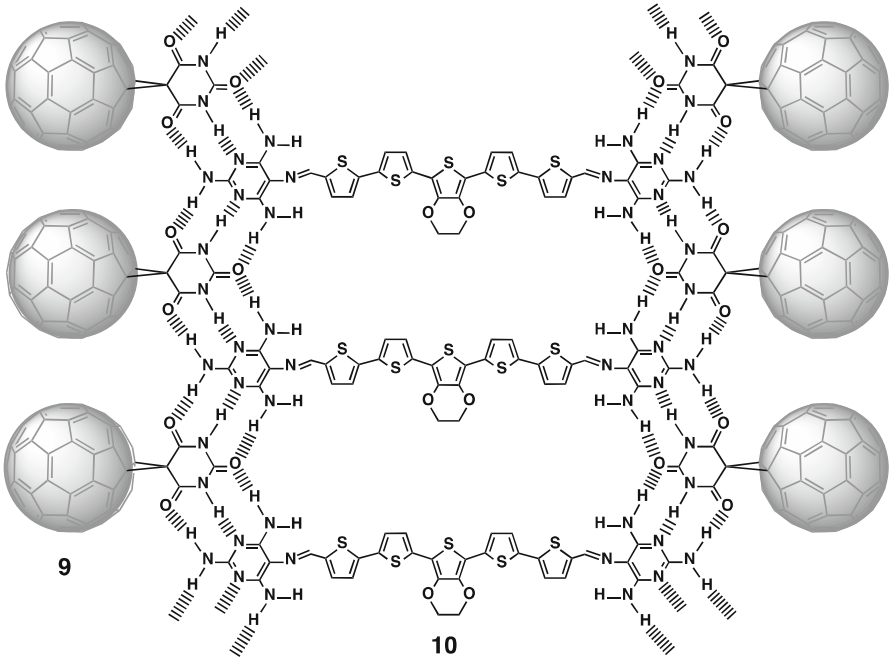

Fig. 19 Hydrogen-bonded supramolecular polymer

supramolecular C_{60} polymers can be governed by external stimuli. Hydrogen bonding is one of the most commonly used methods for realizing supramolecular polymerization. A hydrogen-bonded polymeric C_{60} array was reported by Bassani et al. (Fig. 19) [74, 75]. Barbituric acid-attached C_{60} molecule **9** and pentathienylmelamine **10** were coassembled with multiple hydrogen bonds. The supramolecular organization of the C_{60} molecule and the pentathienylmelamine molecule are maintained with the aid of complementary hydrogen bonding interactions. The phase-separated supramolecular donor-acceptor arrangement was processed into a photovoltaic device, which showed light harvesting with good efficiency in the visible region due to the oligothiophene moiety. Hummelen et al. showed that a hydrogen-bonded supramolecular C_{60} polymer can be built by using C_{60} molecules possessing two ureidopyrimidone (UPy) units. Meijer's UPy group possesses a donor-donor-acceptor-acceptor hydrogen-bonding motif, which forms a hydrogen-bonded dimer with remarkable stability [76]. Therefore, UPy is often utilized for constructing supramolecular polymerization. The complementary quadruple hydrogen bonds facilitate the supramolecular polymerization of the C_{60} molecules where the C_{60} units are linearly arranged.

CD is known to be a potential host molecule for C_{60} in water. CD was utilized for supramolecular polymerization by Liu et al. (Fig. 20) [77]. Water-soluble bisCD host **11** and C_{60} were assembled in an end-to-end fashion. The repeating host-guest

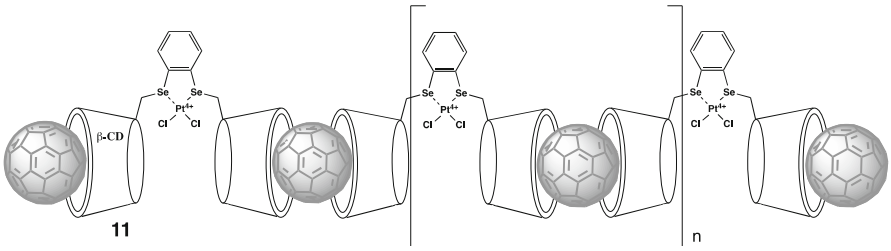

Fig. 20 Supramolecular C_{60} polymer formed via complementary host-guest interactions in water

complexation resulted in the linear supramolecular C_{60} polymer, where the C_{60} molecules were arranged in the supramolecular chain. The desirably aligned supramolecular polymer chains were observed by scanning tunneling microscopy (STM). The length of the supramolecular polymer chain ranged from 150 to 250 nm, which suggested that the polymer chain consists of 60–80 monomer units. A polyrotaxane end-capped with β-CD units was used for supramolecular polymerization [78]. The addition of C_{60} into the polyrotaxane formed the supramolecular C_{60} polymer, which was visualized by STM.

Biscalix[5]arenes are potential fullerene host molecules with high binding constants. Haino et al. reported that the strong "ball-and-socket" interaction takes advantage of the construction of a supramolecular fullerene polymer and network (Fig. 21) [79, 80]. There exist ditopic and tritopic host molecules **12** and **13**: the former possesses two binding pockets, and the latter bears three binding pockets, with each pocket composed of two calix[5]arenes, to encapsulate one C_{60} molecule. Dumbbell-shaped fullerene **14** is ditopic with two C_{60} units. The repeating host-guest complexations between the dumbbell fullerene and the ditopic host or the tritopic host are directed by the ball-and-socket interaction, creating linear or networked supramolecular C_{60} polymers.

The intermolecular associations of ditopic and tritopic hosts **12** and **13** and dumbbell fullerene **14** were examined by ^{1}H NMR spectroscopy. The bridge methylene protons of the calix[5]arene units appear at 4 ppm as a broad resonance because the calix[5]arene shows ring flipping between the cone conformation and its mirror image, which take place at a frequency close to the NMR time scale. When the hosts and the dumbbell fullerene were mixed together, the bridge methylene protons showed AB-quartet-like splitting, indicating that the ring inversion process becomes slower. Evidently, the ball-and-socket interaction raises the energetic barrier of the inversion process.

The size of supramolecular assemblies in solution can be evaluated by diffusion ordered NMR spectroscopy (DOSY). The Stokes-Einstein relation, $D = k_B T/6\pi\eta R$, describes that the hydrodynamic radius (R) of a molecular species is inversely proportional to the diffusion coefficient (D). The degree of polymerization (DP) can be evaluated by the D value of a supramolecular polymer. The diffusion coefficients for **12** and **13** with the dumbbell fullerene decreased upon increasing

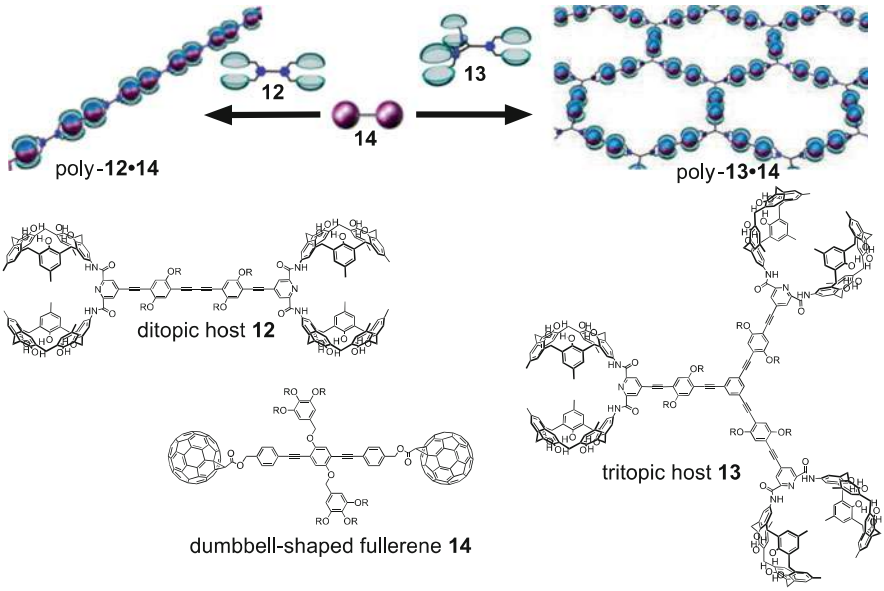

Fig. 21 Schematic representation of the formation of supramolecular linear and networked fullerene polymers and the structures of hosts **12** and **13** and dumbbell fullerene **14**. Reproduced with permission from Ref. [79]. Copyright 2014 Wiley-VCH

the solution concentrations of the mixtures. When all the aggregates in solution are considered to be hydrospherical, the DP values were fairly given to be 83-mer and 151-mer, respectively, at high concentrations; thus, the supramolecular fullerene polymer and network were given in solution.

Scanning electron microscopy was used to visualize the morphologies of the supramolecular polymers (Fig. 22). Thick fibers 100 nm long and 200–500 nm wide were formed by the complexation of **12** and **14**. In contrast, the complexation of **13** and **14** resulted in thick widespread films. The large differences in the morphologies most likely form the dimensions of the host molecules; the supramolecular polymerization between **12** and **14** grows the polymer chain in a linear fashion, whereas the supramolecular networking between **13** and **14** is formed in sheet-like growth. When pristine C_{60} was added to the solutions of the mixtures, the supramolecular polymers were completely disrupted. Accordingly, the C_{60} molecules occupy the biscalix[5]arene cavities, which terminate the complexation of the ditopic and tritopic hosts and dumbbell fullerene; as a result, it is not possible for the supramolecular polymers to grow in the solid state.

Atomic force microscopy (AFM) was used to visualize the supramolecular chains. The nanometric supramolecular polymer fibers from **12** and **14** are highly oriented with an interchain distance of 5.0 nm, which most likely arises from the segregation between the C_{60}-containing polymer chains and the long flexible alkyl side chains. Based on the calculated structure of the oligomer, the chain distance is reasonably persistent to a molecular width of 4.7 nm. Honeycomb supramolecular polymer networks from **13** and **14** were produced with many voids with an average

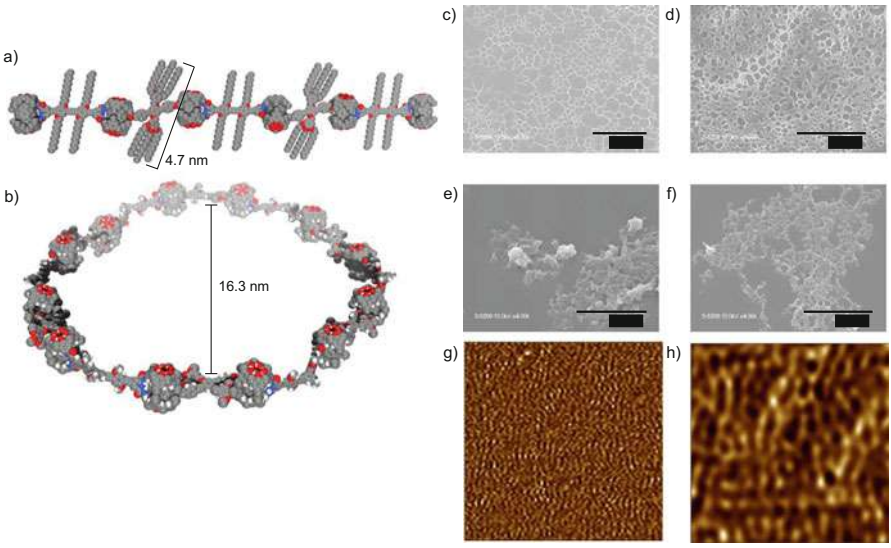

Fig. 22 Calculated structures of (a) linear complex $\mathbf{12}_3$•$\mathbf{14}_2$ and (b) cyclic complex $\mathbf{13}_6$•$\mathbf{14}_6$. SEM images of cast films of (c) a 1:1 mixture of **12** and **14**, (d) a 2:3 mixture of **13** and **14**, (e) a 1:2 mixture of **12** and **14**, and (f) a 2:3 mixture of **13** and **14**. AFM images of cast films of (g) a 1:1 mixture of **12** and **14** (220 nm × 220 nm) and a 2:3 mixture of **13** and **14** (180 nm × 180 nm). Reproduced with permission from Ref. [79]. Copyright 2014 Wiley-VCH

diameter of 14 nm. The modeled macrocyclic ring of the tritopic host and the dumbbell fullerene in a ratio of 6:6 possesses a diameter of 16 nm, which is close to that observed.

Sequence-defined polymer chains composed of three or more kinds of monomers are incredible targets in polymer science. It is quite difficult to construct polymers with perfectly controlled microstructures through a controlled polymerization technique in solution. Self-sorting-directed supramolecular polymerization can be utilized to define the monomer sequence in a copolymerization. In contrast to an AB alternating copolymer, the realization of an ABC-sequence-controlled supramolecular terpolymer is scientifically challenging because of the three pairs of host-guest complexes that exhibit exceptional specificities. Haino et al. demonstrated a supramolecular terpolymer with a controlled ABC sequence in a self-sorting manner (Fig. 23) [81]. A biscalix[5]arene-C_{60} host-guest motif is one of the key supramolecular interactions, which is directed by π-π stacking interactions. A bisporphyrin-TNF complex is driven by donor-acceptor interactions. Hamilton's host-guest complex is formed through multiple complementary hydrogen bonding interactions. Thus, these three host-guest complexes show extremely high orthogonality due to a difference in the nature of the noncovalent interactions. Supramolecular terpolymerization was directed by using a biscalix[5]arene-C_{60} host-guest complex, a bisporphyrin-TNF host-guest complex [82], and Hamilton's host-guest complex [83] in a sequence-controlled manner through self-sorting behavior.

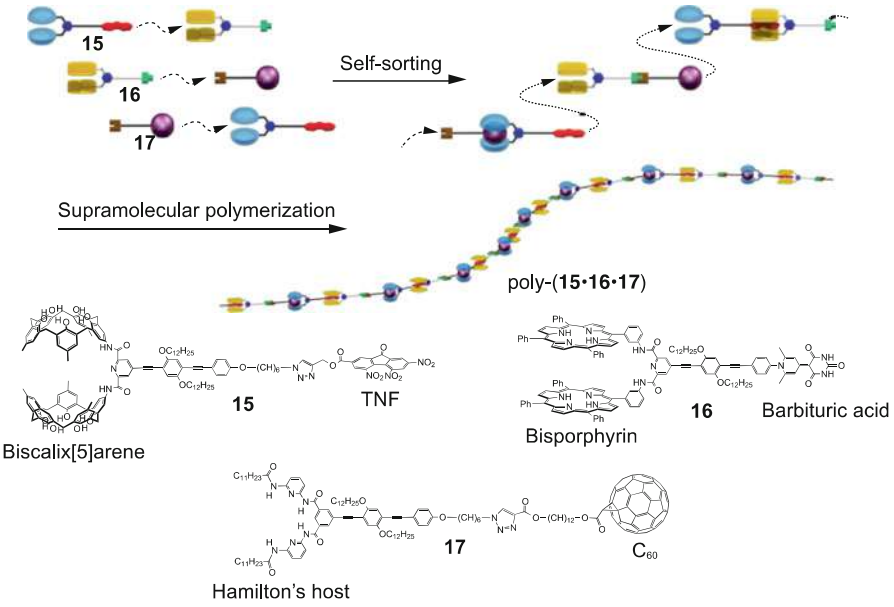

Fig. 23 Supramolecular terpolymerization in a self-sorting manner. Reproduced with permission from Ref. [81]

A mismatched combination of host and guest units are installed into designer monomers **15**, **16**, and **17**, which are not allowed to self-assemble. The intermolecular host-guest complexations among **15**, **16**, and **17** are highly specific; thus, **15**-**16**, **16**-**17**, and **17**-**15** can be selectively formed. Thus, a sequenced controlled supramolecular terpolymer poly-(**15•16•17**) is given in a self-sorting manner.

The sequence of poly-(**15•16•17**) was studied using mass spectrometry. There was one set of trimers, [**15•16•17**]; three sets of tetramers, [**16•17•15•16**], [**15•16•17•15**], and [**17•15•16•17**]; and three sets of pentamers, [**15•16•17•15•16**], [**16•17•15•16•17**], and [**17•15•16•17•15**], in the gas phase. The desired repeating sequence poly-(**15•16•17**) was obviously formed. End-capping studies with C_{60}, 2,4,6-TNF, and barbituric acid (BA) specified the chain termination sites, resulting in C_{60}-**15**-**16**-**17**, C_{60}-**15**-**16** 2,4,6-TNF-**16**, and BA-**16**, which excluded scrambled monomer sequences. The supramolecular terpolymer poly-(**15•16•17**) was proven with the repeating sequence **15**-**16**-**17**.

The formation of supramolecular terpolymer poly-(**15•16•17**) was studied by the DOSY technique in solution (Fig. 24). The *D* values for **15**, **16**, and **17** were consistent throughout the concentration changes; that is, they existed as monomeric forms. In addition, two of **15**, **16**, and **17** were mixed in an equimolar concentration, which resulted in heterodimeric host-guest complexes **15**-**16**, **16**-**17**, and **17**-**15**. The *D* values for **15** with **16**, **16** with **17**, and **17** with **15** decreased by 65%, which suggested that heterodimeric complexes **15**-**16**, **16**-**17**, and **17**-**15** were judiciously produced. A 1:1:1 mixture of **15**, **16**, and **17** showed a remarkable reduction of 85%,

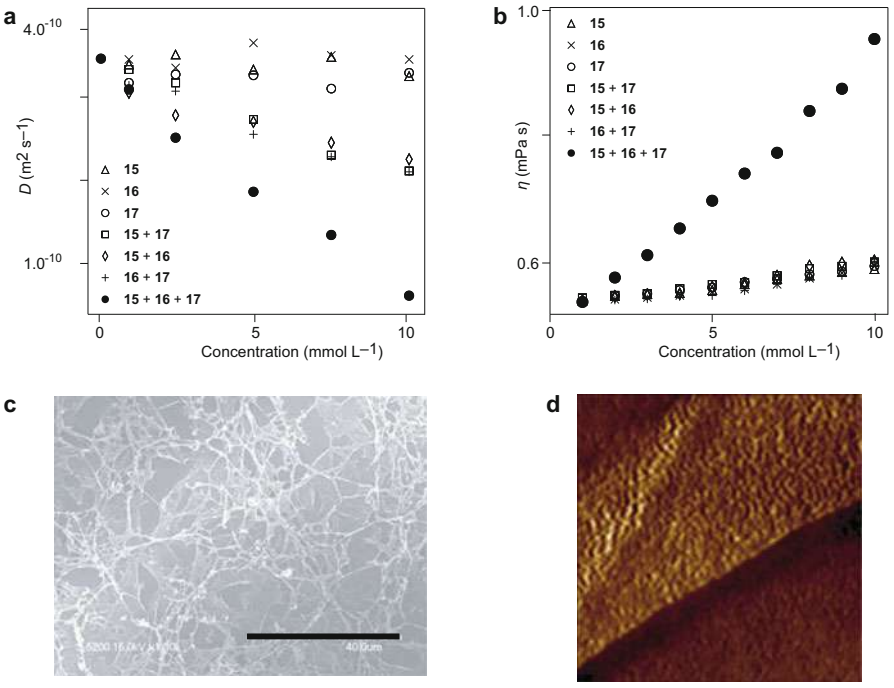

Fig. 24 (**a**) Diffusion coefficients (D). (**b**) Viscosities (η). (**c**) SEM and AFM images of supramolecular terpolymer poly-(**15•16•17**). The scale bar denotes 40μm. d AFM image (200 nm × 200 nm) of a spin-coated film. Reproduced with permission from Ref. [81]

which was attributed to the large polymeric assemblies with a DP of 200-mer. Viscometry was found to be helpful for investigating the macroscopic structure of the polymeric assemblies. The solution viscosities of **15**, **16**, **17**, **15** with **16**, **16** with **17**, and **17** with **15** were not influenced by the concentrations. Increasing the concentration of the 1:1:1 mixture of **15**, **16**, and **17** had a remarkable impact on the solution viscosity. The solution became viscous due to the presence of well-developed polymer chains, which contributed to viscous drag. The supramolecular terpolymer chain poly-(**15•16•17**) is established in a sequence-controlled fashion in solution. The supramolecular polymeric fibers of poly-(**15•16•17**) with sheet-like bundles were observed by scanning electron microscopy (SEM); accordingly, the long, fibrous polymer chains are directed by the iterative self-sorting step-growth supramolecular polymerization of **15**, **16**, and **17**.

The ball-and-socket, donor-acceptor, and hydrogen-bonding interactions drive the *uncommon* ABC sequence of the supramolecular terpolymer. Supramolecular terpolymerization is directional and specific and is directed by the high-fidelity, self-sorting of the three kinds of host-guest motifs. There are many host-guest motifs that show self-sorting behavior. Accordingly, our synthetic methodology offers extensive utilization for building artificial polymers with designed sequences and structural diversity.

Hybrid Materials of Supramolecular Polymers and Conventional Polymers Formed Via C_{60}-Calix[5]arene Complexation

Polymer cross-linking is an essential subject in polymer science. Linear polymer chains are cross-linked with certain covalent bonds, which reduce structural flexibility, resulting in dynamic variation in morphologies and properties associated with molecular weight, chain structure, chain sequence, etc. In general, the covalent cross-linking of polymer chains gives rise to irreversible three-dimensional networks; therefore, the cross-linked network structures and their properties cannot be perfectly restored. The reversible nature has to be implemented into cross-linkages, which presents a great challenge for fabricating recyclable polymer materials. Employing noncovalent interactions can enable one to realize reversible cross-linkages. Supramolecular chemistry offers reversible cross-linking of polymer chains. While a conventional polymer is attached with supramolecular entities, specific host-guest interactions are responsible for the reversible regulation of the noncovalent cross-linking of polymers. The supramolecular complex of biscalix[5]arene-C_{60} shows highly specific molecular recognition, which can be engaged in noncovalent polymer cross-linking (Fig. 25).

C_{60}-appended polyacetylene poly-**18** was used for the study of the supramolecular cross-linking strategy by using ditopic tetrakiscalix[5]arene host **12** possessing two fullerene binding sites [84]. The C_{60} units grafted onto the polyacetylene backbone can be bound with ditopic host **12**, which results in a remarkably stable noncovalent cross-linkage. Upon mixing poly-**18** and host **12**, the elution peak of poly-**18** is shifted in size-exclusion chromatography, and free host **12** is not found until a molar ratio of the binding site of **12** and the C_{60} unit is 1:1 (Fig. 26). In the presence of excess host **12**, unbound host **12** was eluted. Based on the SEC chromatogram, the molecular weight of poly-**18** was increased more than twofold. Of particular note is that pristine C_{60} was not allowed to disrupt the cross-linkage in toluene, even though the noncovalent π-π stacking interaction of a calix[5]arene and C_{60} drives host-guest complexation. The properties of solvents significantly influence the stability of the cross-linkage. Chloroform and *o*-dichlorobenzene are more competitive for host-guest complexation, which interferes with the generation of cross-links.

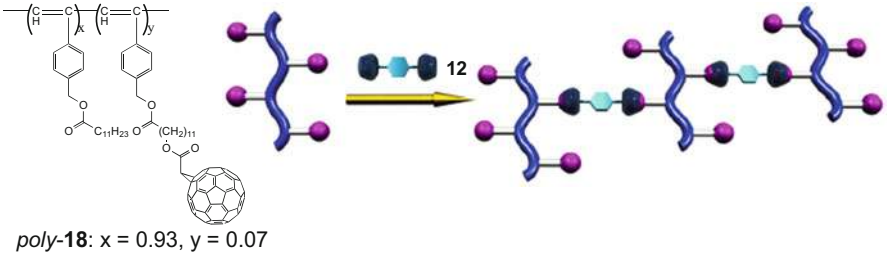

Fig. 25 Supramolecular cross-linking of C_{60}-grafted polyacetylene. Reproduced with permission from Ref. [84]. Copyright 2010 Wiley-VCH

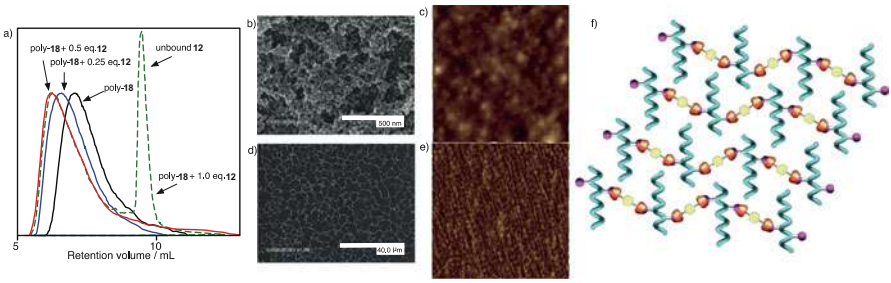

Fig. 26 (**a**) Size-exclusion chromatograms for poly-**18** in the presence of **12** in toluene. (**b**, **c**) SEM and (**d**, **e**) AFM images of thin films of (**b**, **d**) poly-**18** and (**c**, **e**) poly-**18** with **12**. (**f**) Schematic representation of cross-linked polyacetylene. Reproduced with permission from Ref. [84]. Copyright 2010 Wiley-VCH

The solid-phase morphology of poly-**18** is quite sensitive to supramolecular cross-linking with host **12**. Poly-**18** gives rise to agglomerated particles due to the cohesion given by the intermolecular π-π interactions and the immiscible nature of the C_{60} units. The interfullerene interactions are disrupted by the encapsulation of C_{60} units by the biscalix[5]arene cavity. As a result, the polymer chain of poly-**18** is extended through liberation from the aggregated state, leading to a dramatic change in morphology from nanoparticles to widespread fibrillar networks. A highly ordered pyrolytic graphite (HOPG) surface induced a highly oriented polymer alignment for the cross-linked fibrils. The peak-to-peak profile gives rise to a uniform pitch of 19.6 nm. The fairly large interchain distance most likely arises from the interdigitation of the highly aligned polymer side chains, which is shown in Fig. 26.

The physical and chemical properties of polymers vary for polymer structures, encompassing rings, grafts, stars, ladders, etc. However, these preformed polymer structures are not interchangeable due to the irreversible nature of covalent bonds. To manipulate polymer properties, synthetic strategies for fabricating distinctly shaped polymers have been actively studied thus far. Thus, shape transformable polymers with multiple shapes are quite attractive for this purpose. Supramolecular chemistry offers novel methodologies for realizing the shape transformation of polymer chains. Takata et al. demonstrated the elegant shape transformation of polymer chain structures among linear, star, cyclic shapes using a rotaxane unit at the juncture of polymer chains [85]. This shape transformation among these shapes relies on the dynamic nature of a rotaxane structure. Therefore, such shape transformation is regulated by external stimuli.

The host-guest chemistry of a calix[5]arene and C_{60} offers another strategy to create shape-transformable polymers (Fig. 27) [86]. Ditopic host **12** can bind to the C_{60} unit at the terminus polymethylmethacrylate (PMMA) poly-**19**, which results in chain-extended (poly-**19**)$_2$•**12**, whereas tritopic host **13** can be employed to give rise to the star-shaped polymer (poly-**19**)$_3$•**13**.

The association constant between the biscalix[5]arene and the monosubstituted C_{60} molecule is 13,800 L mol^{-1}, which is fairly strong. There is no significant steric

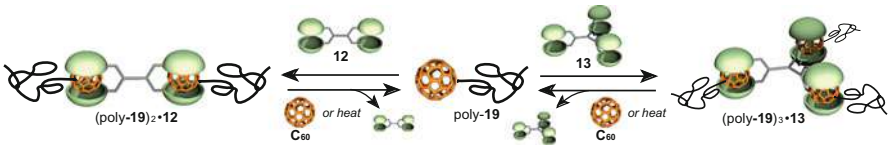

Fig. 27 Schematic representation of shape transformation through host-guest complexation of ditopic and tritopic hosts. Reproduced with permission from Ref. [86]. Copyright 2020 American Chemical Society

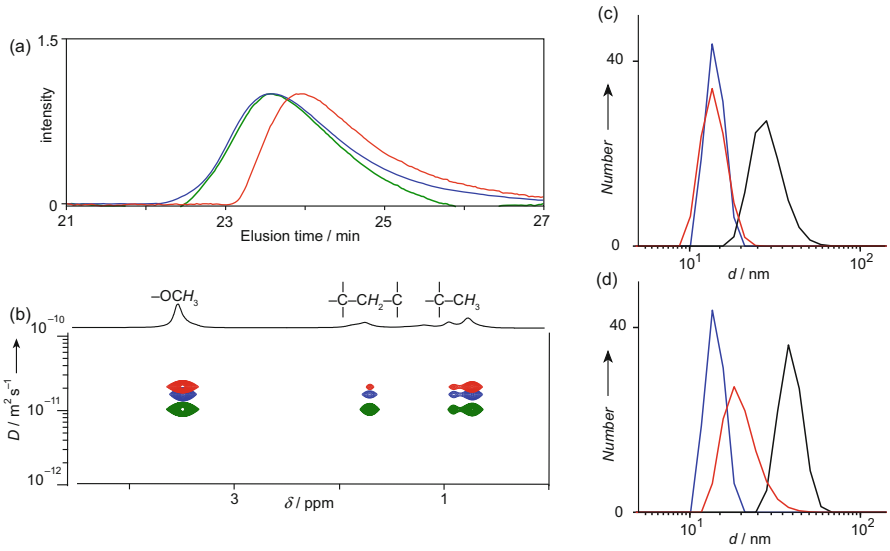

Fig. 28 (**a**) Size-exclusion chromatograms for poly-**19** (red), a 1:2 mixture of poly-**19** and **12** (blue), and a 1:3 mixture of poly-**19** and **13** (green) in toluene. (**b**) 2D DOSY spectra for poly-**19** (red), a 1:2 mixture of poly-**19** and **12** (blue), and a 1:3 mixture of poly-**19** and **13** (green) in chloroform-*d*. (**c**, **d**) Changes in the hydrodynamic diameter of poly-**19** at 25 °C (blue): in the presence of (**c**) **12** or (**d**) **13** (black): equilibrating the mixture at 60 °C (red), as inferred from DLS experiments. Reproduced with permission from Ref. [86]. Copyright 2020 American Chemical Society

influence between the C_{60} substituent and the biscalix[5]arene. The intermolecular associations of poly-**19** with **12** or **13** were studied using SEC and DOSY experiments (Fig. 28). Increasing the hydrodynamic radius of polymers generally results in a short SEC elution time and a small diffusion coefficient. The elution time of poly-**19** becomes faster upon the addition of hosts **12** and **13** in SEC. The diffusion coefficient of poly-**19** is reduced by 19% and 42% upon the addition of **12** and **13**, respectively, indicating that the hydrodynamic radius of poly-**19** is obviously increased by host-guest complexations with **12** and **13** even though the supramolecular polymers (poly-**19**)$_2$•**12** and (poly-**19**)$_3$•**13** are maintained by noncovalent bonds. The shape transformation shows a remarkable impact on the glass transition temperature (T_g) in the bulk. The glass transition for poly-**19** appears at 99.9 °C,

which moves to higher temperatures of 103.9 °C and 107.5 °C for (poly-**19**)$_2$•**12** and (poly-**19**)$_3$•**13**, respectively. The supramolecular shape transformation of poly-**19** was discussed using dynamic light scattering. The hydrodynamic radius of poly-**19** was determined to be 14 nm. The addition of 0.5 equivalents of **12** increased this value to 28 nm, whereas the host-guest complexation of poly-**19** with **13** resulted in a hydrodynamic radius of 38 nm. The complexation of pristine C_{60} completely disrupted the supramolecular polymers (poly-**19**)$_2$•**12** and (poly-**19**)$_3$•**13** to produce poly-**19**•C_{60} with a hydrodynamic radius consistent with that of poly-**19**.

Conclusion

In the three decades that have passed since the discovery of fullerenes, supramolecular chemistry has been used to deal with fullerenes as molecular units for fabricating numerous carbon-based supramolecular structures. Initially, the unique globular structure of C_{60} attracted many chemists to capture it within certain container molecules without using polar interactions. Taking advantage of the effective complementarity of shape with π-π stacking, van der Waals, donor-acceptor, etc., interactions has resulted in successful development of fullerene container molecules. The host-guest chemistry of fullerene has started moving into nanoscience with the development of innovative functions. In this book chapter, we describe a brief history of the development of fullerene host molecules with a special focus on calix[5]arene-based fullerene containers and some supramolecular polymer chemistry for calix[5]arene-C_{60} complexation. The efforts in supramolecular fullerene chemistry shown in this chapter shed light on the bright future for fullerene science through collaboration with supramolecular chemistry.

Cross-References

- ▶ Chemical Reactivity and Addition Pattern on C_{60} and C_{70}
- ▶ Functionalization of Fullerenes: Addition Reactions
- ▶ Preparation, Extraction/isolation From Soot, and Solubility of Fullerenes
- ▶ Self-Assembled Aggregates of Fullerenes

References

1. Kroto HW et al (1985) C60: buckminsterfullerene. Nature (London) 318:162–163
2. Krätschmer W, Lamb LD, Fostiropoulos K, Huffman DR (1990) Solid C60: a new form of carbon. Nature (London) 347:354–358
3. Chow L et al (1995) Fullerene formation during production of chemical vapor deposited diamond. Appl Phys Lett 66:430–432
4. Kleckley S et al (1997) Fullerenes and polymers produced by the chemical vapor deposition method, ACS symposium series, pp 51–60

5. Grieco WJ et al (1998) Fullerenes and PAH in low-pressure premixed benzene/oxygen flames. Symp Combust 27:1669–1675
6. Grieco WJ, Howard JB, Rainey LC, Vander Sande JB (2000) Fullerenic carbon in combustion-generated soot. Carbon 38:597–614
7. Mojica M, Alonso JA, Méndez F (2013) Synthesis of fullerenes. J Phys Org Chem 26:526–539
8. Nagata K, Dejima E (2005) Kikuchi, Y. & Hashiguchi, M. kilogram-scale [60]fullerene separation from a fullerene mixture: selective complexation of fullerenes with 1,8-Diazabicyclo[5.4.0]undec-7-ene (DBU). Chem Lett 34:178–179
9. Yeretzian C et al (1993) Partial separation of fullerenes by gradient sublimation. J Phys Chem 97:10097–10101
10. Diener MD, Alford JM (1998) Isolation and properties of small-bandgap fullerenes. Nature 393: 668–671
11. Scrivens WA, Bedworth PV, Tour JM (1992) Purification of gram quantities of C60. A new inexpensive and facile method. J Am Chem Soc 114:7917–7919
12. Atwood JL, Koutsantonis GA, Raston CL (1994) Purification of C60 and C70 by selective complexation with calixarenes. Nature 368:229–231
13. Darwish AD, Kroto HW, Taylor R, Walton DRM (1994) Improved chromatographic separation of C60 and C70. J Chem Soc, Chemical Communications, pp 15–16
14. Diederich F et al (1992) C60 and C in a basket? - investigations of monolayer and multilayers from Azacrown compounds and fullerenes. Angewandte Chemie Int Edition Eng 31:1599–1602
15. Andersson T et al (1992) C-60 embedded in gamma-Cyclodextrin - a water-soluble fullerene. J Chem Soc Chem Comm:604–606
16. Yoshida ZI, Takekuma H, Takekuma SI, Matsubara Y (1994) Molecular recognition of C60 with γ-cyclodextrin. Angew Chem Int Ed Engl 33:1597–1599
17. Atwood JL, Koutsantonis GA, Raston CL (1994) Purification of C-60 and C-70 by selective complexation with Calixarenes. Nature 368:229–231
18. Suzuki T, Nakashima K, Shinkai S (1994) Very convenient and efficient purification method for fullerene (C-60) with 5,11,17,23,29,35,41,47-Octa-Tert-Butylcalix[8]Arene-49,50,51,52,53,54,55,56-Octol. Chem Lett:699–702
19. Steed JW et al (1994) Ball-and-socket nanostructures - new supramolecular chemistry based on Cyclotriveratrylene. J Am Chem Soc 116:10346–10347
20. Perez EM, Martin N (2015) Pi-pi interactions in carbon nanostructures. Chem Soc Rev 44: 6425–6433
21. Boyd PDW et al (1999) Selective supramolecular porphyrin/fullerene interactions. J Am Chem Soc 121:10487–10495
22. Sun DY et al (2002) Supramolecular fullerene-porphyrin chemistry. Fullerene complexation by metalated “jaws porphyrin” hosts. J Am Chem Soc 124:6604–6612
23. Sun DY et al (2000) Porphyrin-fullerene host-guest chemistry. J Am Chem Soc 122:10704–10705
24. Tashiro K et al (1999) A cyclic dimer of metalloporphyrin forms a highly stable inclusion complex with C-60. J Am Chem Soc 121:9477–9478
25. Shoji Y, Tashiro K, Aida T (2004) Selective extraction of higher fullerenes using cyclic dimers of zinc porphyrins. J Am Chem Soc 126:6570–6571
26. Ayabe M et al (2002) A novel [60]fullerene receptor with a Pd(II)-switched bisporphyrin cleft. Chem Commun:1032–1033
27. Ayabe M et al (2002) A dendritic porphyrin receptor for C-60 which features a profound positive allosteric effect. Angewandte Chemie-International Edition 41:2790–2792
28. Rizzuto FJ, Nitschke JR (2017) Stereochemical plasticity modulates cooperative binding in a (Co12L6)-L-II cuboctahedron. Nat Chem 9:903–908
29. Davis CM et al (2014) Ion-regulated allosteric binding of fullerenes (C-60 and C-70) by Tetrathiafulvalene-calix[4]pyrroles. J Am Chem Soc 136:10410–10417

30. Ke XS et al (2017) Expanded Rosarin: a versatile fullerene (C-60) receptor. J Am Chem Soc 139:4627–4630
31. Becker H et al (1993) Gas-phase ion-molecule reactions of Corannulene, a fullerene subunit. J Am Chem Soc 115:11636–11637
32. Mizyed S et al (2001) Embracing C-60 with multiarmed geodesic partners. J Am Chem Soc 123:12770–12774
33. Pérez EM, Sánchez L, Fernández G, Martín N (2006) exTTF as a building block for fullerene receptors. Unexpected solvent-dependent positive Homotropic cooperativity. J Am Chem Soc 128:7172–7173
34. Yokoi H et al (2015) Nitrogen-embedded buckybowl and its assembly with C-60. Nat Commun 6
35. Takeda M et al (2018) Azabuckybowl-based molecular tweezers as C-60 and C-70 receptors. J Am Chem Soc 140:6336–6342
36. Haketa Y et al (2020) Self-associating curved pi-electronic systems with Electron-donating and hydrogen-bonding properties. J Am Chem Soc 142:16420–16428
37. Barendt TA et al (2020) The green box: an electronically versatile Perylene Diimide macrocyclic host for fullerenes. J Am Chem Soc 142:349–364
38. Lu XF et al (2019) Bowl-shaped carbon Nanobelts showing size-dependent properties and selective encapsulation of C-70. J Am Chem Soc 141:5934–5941
39. Kawase T et al (2003) Complexation of a carbon nanoring with fullerenes. Angewandte Chemie-International Edition 42:1624–1628
40. Iwamoto T et al (2011) Size-selective encapsulation of C-60 by [10]Cycloparaphenylene: formation of the shortest fullerene-peapod. Angewandte Chemie-International Edition 50: 8342–8344
41. Iwamoto T et al (2013) Size- and orientation-selective encapsulation of C70 by Cycloparaphenylenes. Chem A Eur J 19:14061–14068
42. Iwamoto T et al (2014) Partial charge transfer in the shortest possible Metallofullerene peapod, La@C-82 subset of[11]Cycloparaphenylene. Chem Eur J 20:14403–14409
43. Nakanishi Y et al (2014) Size-selective complexation and extraction of endohedral Metallofullerenes with Cycloparaphenylene. Angewandte Chemie-International Edition 53:3102–3106
44. Isobe H, Hitosugi S, Yamasaki T, Iizuka R (2013) Molecular bearings of finite carbon nanotubes and fullerenes in ensemble rolling motion. Chem Sci 4:1293–1297
45. Yamamoto Y, Tsurumaki E, Wakamatsu K, Toyota S (2018) Nano-Saturn: experimental evidence of complex formation of an anthracene cyclic ring with C-60. Angewandte Chemie-International Edition 57:8199–8202
46. Chen XJ et al (2015) Unravelling the structure of the C-60 and p-Bu-t-calix[8]arene complex. Chem Commun 51:11413–11416
47. Araki K et al (1996) Molecular design of calixarene-based host molecules for inclusion of C-60 in solution. Tetrahedron Lett 37:73–76
48. Atwood JL, Barbour LJ, Raston CL, Sudria IBN (1998) C-60 and C-70 compounds in the pincerlike jaws of calix[6]arene. Angewandte Chemie-International Edition 37:981–983
49. Ikeda A et al (1999) Inclusion of [60]fullerene in a homooxacalix[3]arene-based dimeric capsule cross-linked by a Pd-II-pyridine interaction. J Am Chem Soc 121:4296–4297
50. Ogoshi T et al (2014) Conversion from pillar[5]arene to pillar[6-15]arenes by ring expansion and encapsulation of C-60 by pillar[n]arenes with Nanosize cavities. Org Lett 16:2896–2899
51. Haino T, Yanase M, Fukazawa Y (1997) New supramolecular complex of C60 based on calix[5] arene - its structure in the crystal and in solution. Angew Chem Int Ed Engl 36:259–260
52. Haino T, Yanase M, Fukazawa Y (1997) Crystalline supramolecular complexes of C60 with calix[5]arenes. Tetrahedron Lett 38:3739–3742
53. Haino T, Fukunaga C, Fukazawa Y (2007) Complexation of higher fullerenes by calix[5]arene-based host molecules. J Nanosci Nanotechnol 7:1386–1388
54. Haino T et al (2002) Fullerene sensors based on calix[5]arene. Chem Comm:2148–2149

55. Haino T, Fukunaga C, Fukazawa Y (2006) A new calix[5]arene-based container: selective extraction of higher fullerenes. Org Lett 8:3545–3548
56. Haino T, Mitsuhashi H, Ishizu Y, Fukazawa Y (2006) Dynamic combinatorial library for fullerene receptors based on metal-assisted self-assembly. Tetrahedron Lett 47:7915–7918
57. Haino T, Araki H, Yamanaka Y, Fukazawa Y (2001) Fullerene receptor based on calix[5]arene through metal-assisted self-assembly. Tetrahedron Lett 42:3203–3206
58. Wang GW, Komatsu K, Murata Y, Shiro M (1997) Synthesis and x-ray structure of dumb-bell-shaped C-120. Nature 387:583–586
59. Haino T et al (2005) Calix[5]arene-based receptor for dumb-bell-shaped C120. Bull Chem Soc Jpn 78:768–770
60. Barbour LJ, Orr GW, Atwood JL (1901-1902) Supramolecular assembly of well-separated, linear columns of closely-spaced C-60 molecules facilitated by dipole induction. Chem Commun 1998
61. Balch AL, Catalano VJ, Lee JW, Olmstead MM (1992) Supramolecular aggregation of an (eta (2)-C(60)) iridium complex involving phenyl chelation of the fullerene. J Am Chem Soc 114: 5455–5457
62. Sawamura M et al (2002) Stacking of conical molecules with a fullerene apex into polar columns in crystals and liquid crystals. Nature 419:702–705
63. Atwood JL, Barbour LJ, Heaven MW, Raston CL (2003) Controlling van der Waals contacts in complexes of fullerene C-60. Angewandte Chemie-International Edition 42:3254–3257
64. Hubble LJ, Raston CL (2007) Nanofibers of fullerene C-60 through interplay of ball-and-socket supermolecules. Chem Eur J 13:6755–6760
65. Wang ZH, Dotz F, Enkelmann V, Mullen K (2005) "Double-concave" graphene: Permethoxylated hexa-peri-hexabenzocoronene and its cocrystals with hexafluorobenzene and fullerene. Angewandte Chemie-International Edition 44:1247–1250
66. Shirakawa M, Fujita N, Shinkai S (2003) [60]fullerene-motivated organogel formation in a porphyrin derivative bearing programmed hydrogen-bonding sites. J Am Chem Soc 125:9902–9903
67. Pantos GD, Wietor JL, Sanders JKM (2007) Filling helical nanotubes with C-60. Angewandte Chemie-International Edition 46:2238–2240
68. Kawauchi T et al (2008) Encapsulation of fullerenes in a helical PMMA cavity leading to a robust processable complex with a macromolecular helicity memory. Angewandte Chemie-International Edition 47:515–519
69. Nobukuni H, Shimazaki Y, Tani F, Naruta Y (2007) A nanotube of cyclic porphyrin dimers connected by nonclassical hydrogen bonds and its inclusion C-60 in a linear arrangement. Angewandte Chemie-International Edition 46:8975–8978
70. Nobukuni H et al (2009) Anisotropic high Electron mobility and Photodynamics of a self-assembled porphyrin nanotube including C-60 molecules. J Phys Chem C 113:19694–19699
71. Nobukuni H et al (2010) Supramolecular structures and Photoelectronic properties of the inclusion complex of a cyclic Free-Base porphyrin dimer and C-60. Chem Eur J 16:11611–11623
72. Rao AM et al (1993) Photoinduced polymerization of solid C-60 films. Science 259:955–957
73. Haino T (2013) Molecular-recognition-directed formation of supramolecular polymers. Polym J 45:363–383
74. Huang C-H et al (2005) Enhanced photovoltaic response in hydrogen-bonded all-organic devices. Org Lett 7:3409–3412
75. Chu CC et al (2010) Self-assembly of supramolecular fullerene ribbons via hydrogen-bonding interactions and their impact on fullerene electronic interactions and charge carrier mobility. J Am Chem Soc 132:12717–12723
76. Sijbesma RP et al (1997) Reversible polymers formed from self-complementary monomers using quadruple hydrogen bonding. Science 278:1601–1604
77. Liu Y, Wang H, Liang P, Zhang HY (2004) Water-soluble supramolecular fullerene assembly mediated by metallobridged beta-cyclodextrins. Angewandte Chemie-International Edition 43: 2690–2694

78. Liu Y, Yang Y-W, Chen Y, Zou H-X (2005) Polyrotaxane with Cyclodextrins as stoppers and its assembly behavior. Macromolecules 38:5838–5840
79. Hirao T, Tosaka M, Yamago S, Haino T (2014) Supramolecular fullerene polymers and networks directed by molecular recognition between calix[5]arene and C60. Chem A Eur J 20:16138–16146
80. Haino T, Matsumoto Y, Fukazawa Y (2005) Supramolecular Nano networks formed by molecular-recognition-directed self-assembly of Ditopic calix[5]arene and dumbbell [60]fullerene. J Am Chem Soc 127:8936–8937
81. Hirao T, Kudo H, Amimoto T, Haino T (2017) Sequence-controlled supramolecular Terpolymerization directed by specific molecular recognitions. Nat Commun 8:634
82. Haino T, Fujii T, Fukazawa Y (2006) Guest binding and new self-assembly of Bisporphyrins. J Org Chem 71:2572–2580
83. Chang S-K, Hamilton AD (1988) Molecular recognition of biologically interesting substrates - synthesis of an artificial receptor for barbiturates employing six hydrogen-bonds. J Am Chem Soc 110:1318–1319
84. Haino T, Hirai E, Fujiwara Y, Kashihara K (2010) Supramolecular cross-linking of [60] fullerene-tagged Polyphenylacetylene by the host-guest interaction of calix[5]arene and [60] fullerene. Angew Chem Int Ed 49:7899–7903
85. Takata T (2020) Switchable polymer materials controlled by Rotaxane macromolecular switches. ACS Cent Sci 6:129–143
86. Hirao T, Fukuta K, Haino T (2020) Supramolecular approach to polymer-shape transformation via Calixarene-fullerene complexation. Macromolecules 53:3563–3570

Part VI

Applications of Fullerenes and Derivatives

Fullerenes in Photovoltaics

24

H.-S. Lin and Y. Matsuo

Contents

Abstract

Fullerenes are among the most widely used n-type organic semiconducting materials and have been extensively investigated in a variety of applications. Fullerene materials have frequently been used in photovoltaic applications thanks to their excellent electrical properties, which include ultrafast photoinduced charge transfer and low reorganization energy. Accordingly, fullerene materials provide superior performance in both organic solar cells (OSCs) and perovskite solar cells (PSCs) despite playing different roles in these two types of cells. To date, fullerene organic photovoltaics have achieved power conversion efficiency (PCE) reaching 21.3%, up from the PCE of 3.2% reported for the first fullerene derivative photovoltaics in 1995. In OSCs, fullerenes are used as electron

H.-S. Lin · Y. Matsuo (✉)
Department of Mechanical Engineering, School of Engineering, The University of Tokyo, Tokyo, Japan

Department of Chemical System Engineering, Graduate School of Engineering, Nagoya University, Nagoya, Japan
e-mail: linhaosheng@photon.t.u-tokyo.ac.jp; yutaka.matsuo@chem.material.nagoya-u.ac.jp

X. Lu et al. (eds.), *Handbook of Fullerene Science and Technology*,
https://doi.org/10.1007/978-981-16-8994-9_37

acceptors and are mixed with an electron donor to fabricate the active layer of the device. Consequently, the energy level and molecular packing of fullerenes are major concerns and frequent subjects of investigation. In PSCs, on the other hand, a perovskite-structured compound is required in the active layer, so fullerenes are used as electron transport materials or dopants rather than as electron acceptors. For these roles in PSCs, attention shifted to electron carrier mobility, interlayer morphology, and passivation effects. This chapter discusses in depth the recent progress of fullerenes in both OSCs and PSCs from a broad perspective, covering the fundamentals of photovoltaics, fullerene materials design, and advanced techniques that have recently been developed.

Keywords

Fullerenes · Fullerene derivatives · Photovoltaics · Organic solar cells · Perovskite solar cells

Introduction

In organic photovoltaics (OPVs), fullerenes are among the most advantageous and widely used n-type organic semiconducting materials (bandgap = 2.3 eV) [1] because of their ultrafast photoinduced charge transfer [2] and low reorganization energy [3]. Tremendous effort has been devoted to developing various fullerene materials in order to improve the performance of both organic solar cells (OSCs) and perovskite solar cells (PSCs), the latter of which has seen remarkable progress in recent years. The first fullerene derivative used as an electron acceptor in the active layer of OSCs was phenyl-C_{61}-butyric acid methyl ester ($PC_{61}BM$), which gave a power conversion efficiency (PCE) of 3.2% [4]. Since then, dramatic performance gains have been achieved, with PCE reaching 21.3% in PSCs using a fullerene derivative as a surface-modifying overcoat on a SnO_2 electron transport layer (ETL) [5]. The rapid advancement of fullerene OSCs is without doubt linked to the rapid development of fullerene synthetic chemistry, which provides fullerene with various properties that enable better OSC performance. The application of fullerenes in OSCs has long been investigated and has been well covered by a number of interesting review articles [6–9]. This chapter does not duplicate the summaries from these previous reviews or provide an update on the progress of fullerenes in OSCs. Instead, we selected representative examples in order to comprehensively discuss the methodology and mechanisms of fullerenes in OSCs. For clarity, this chapter begins with an introduction to the fundamentals of OSCs and then extended the discussion to deeper aspects such as the molecular design for good fullerene derivatives for OSCs and advanced techniques for the fabrication of fullerene OSCs. Accordingly, the aim of this chapter is to provide a comprehensive understanding of fullerene OSCs and their advanced technology not only for scholars and scientists currently engaged in this field but also for prospective researchers.

Fullerenes in Photovoltaics

Fundamentals of Photovoltaics

Photovoltaics convert light into electricity by using semiconducting materials and are widely regarded as the most sustainable and environmentally friendly energy conversion devices because they operate without generating pollution or emitting greenhouse gases [10]. Typically, both laboratory-scale and industrial-scale photovoltaics consist of three essential components: an active layer, two charge transport layers, and two conductive electrodes (Fig. 1). The active layer, which can be regarded as the core engine in photovoltaics, consists of light-sensitive materials

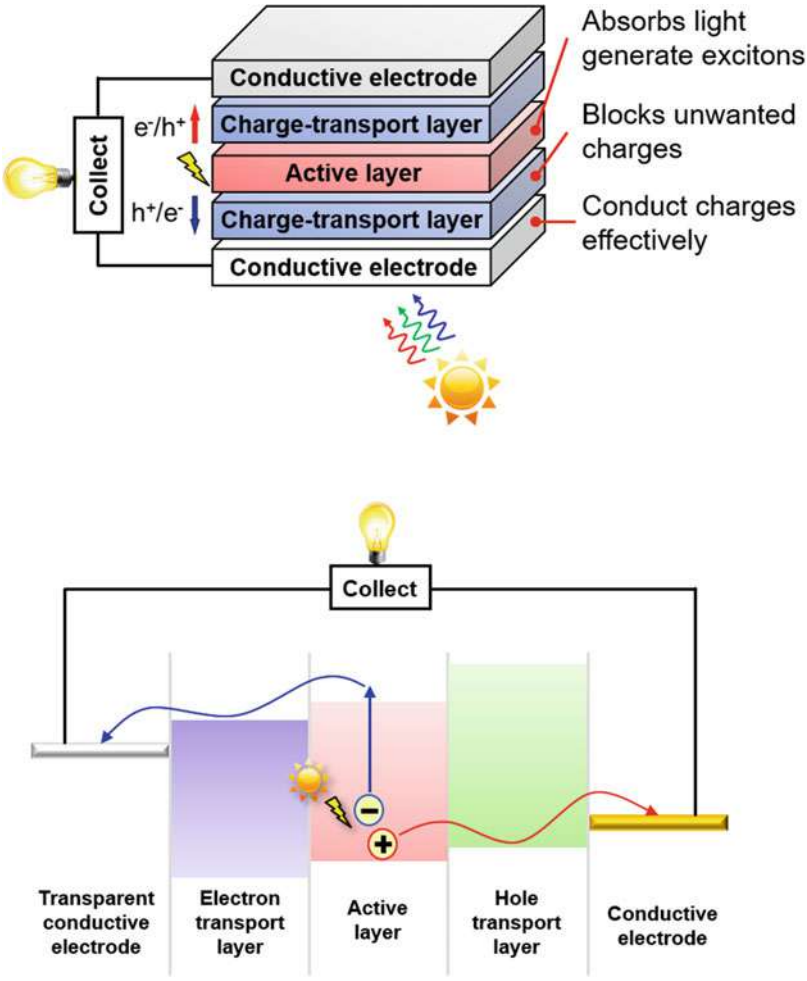

Fig. 1 Illustrations of the structure and operating principle of OSCs

that generate excitons (electron-hole pairs) upon absorbing light. Therefore, the performance of photovoltaics is mainly dependent on the choice of active material, which also determines the type of photovoltaics. For instance, when the active layer is fabricated using an organic electron acceptor/donor pair, the photovoltaics are classified as OSCs. When the active layer is fabricated using organic-inorganic perovskite materials, photovoltaics are classified as PSCs. The active layer is the site of the initial step in photocurrent generation, namely, exciton generation upon light absorption, so a tremendous amount of research has been devoted to developing active layer materials in various ways, such as expanding the light absorption range, enhancing exciton generation, tuning the energy levels of the conduction band (CB) and valence band (VB) to achieve high output voltage, and using dopants or optimizing device fabrication to accelerate charge dissociation and reduce charge recombination. After a first step, the generated excitons dissociate into electrons and holes, which produce photocurrent as they move away from each other. Because the recombination of electrons and holes decreases the photocurrent, charge transport layers are placed above and below the active layer, which are designed to filter out the unwanted charge carriers. In other words, the charge transport layers selectively transport only one type of charge carrier (holes or electrons) and thusly are classified as a hole transport layer (HTL) or an ETL. Notably, although some recent studies have presented novel device structures for HTL-free or ETL-free devices, this does not mean that charge recombination can be ignored. For example, HTL-free devices are designed to have a highly efficient ETL. Because the electrons can be transported with extremely high efficiency and selectivity, the remaining holes can be collected directly by an electrode without the need for an HTL. Without high efficiency and selectivity of the ETL in this example, significant charge recombination would occur and degrade device performance. Finally, the structure is sandwiched by two conductive electrodes, which collect the filtered charges to supply the external circuit. The conductive electrode on the side exposed to light, commonly called the transparent electrode, should be sufficiently transparent to allow for efficient light absorption in the active layer. From the fundamentals of photovoltaics and the intrinsic electron affinity of fullerenes [1–3, 11], it is easy to see that fullerenes are prone to accept electrons and why they are used as electron acceptors in OSCs. In addition, thanks to the ultrafast charge transfer of fullerenes [2], they are being developed as ETLs for PSCs.

For reproducibly evaluating device characteristics of photovoltaics, current-voltage (J–V) curves and corresponding photovoltaic parameters are introduced (Fig. 2) [9]. *Open-circuit voltage* (V_{OC}) is the maximum photovoltage in an OPV and mainly depends on the materials used in the active layer and the energy levels (bandgap, etc.) of the photosensitive materials. *Short-circuit current density* (J_{SC}) is the maximum photocurrent in an OSC and depends on device thickness and coverage of the solar spectrum for light absorption. *Fill factor* (FF) is the ratio of the maximum power output (P_{out}), which is the product of the voltage (V_{mp}) and current density (J_{mp}) at the maximum power output, to the product of V_{OC} and $J_{SC.}$ FF is determined by the charge carrier recombination, charge transport, and impedance in an OPV. *Power conversion efficiency* (PCE) describes the useful output of energy

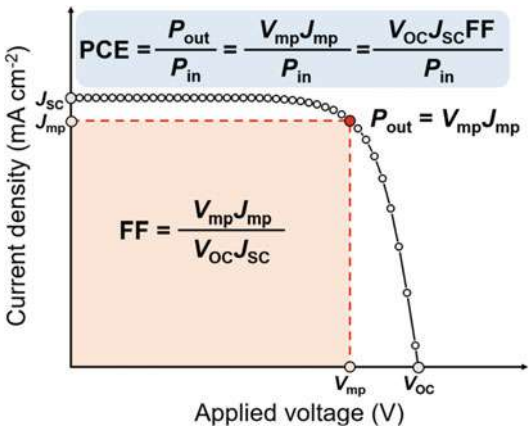

Fig. 2 Illustration of the *J–V* curve and related photovoltaic parameters

conversion and is calculated as the ratio of P_{out} to the power of the incident light (P_{in}). These photovoltaic parameters have been well defined in order to consistently evaluate the device performance in any kind of photovoltaic research, and ongoing efforts are aimed at explaining the correlations of between these photovoltaic parameters and material properties such as energy levels, absorption properties, solid-state packing, and processing conditions [12].

Because OSCs and PSCs have different operating principles, fullerenes play different roles in these two types of cells. In an OSC, fullerenes are conventionally mixed with an organic electron donor material, and together they function as the active layer. By contrast, fullerenes are typically used as an ETL in PSCs without being mixed with other materials. Therefore, the application of fullerenes in OSCs and PSCs will be covered separately in this chapter for discussing the correlations between photovoltaic parameters and the properties of fullerene materials.

Fullerenes in Organic Solar Cells

Introduction to Organic Solar Cells

OSCs are a type of photovoltaic cell in which organic materials are used in the active layer for light absorption to produce electricity from sunlight. Typically, the active layer in OSCs comprises an electron donor (p-type semiconductor) and an electron acceptor (n-type semiconductor). As fullerenes have been well demonstrated to be n-type semiconductors with high electron affinity and ultrafast photoinduced charge separation, they have been widely used as electron acceptors in OSCs. The donor/acceptor pair in an OSC can be regarded as a *p-n* junction to explain the photoelectric conversion mechanism (Fig. 3).

The process of photocurrent generation has four main steps: (1) light absorption and exciton generation; (2) exciton diffusion; (3) charge separation and transport; and (4) charge collection. First, the electron donor material in OSCs absorbs most of the

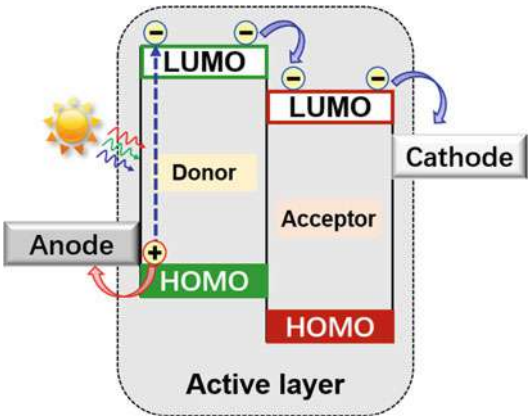

Fig. 3 Schematic illustration of the photoelectric conversion mechanism in the active layer of OSCs

incident sunlight to generate many excitons, which are electron-hole pairs bound by the Coulomb interaction. In chemistry words, the electrons move from the highest occupied molecular orbital (HOMO) of the electron donor material to its lowest unoccupied molecular orbital (LUMO). Second, the excitons diffuse to the interface between electron donor and electron acceptor. Excitons that fail to reach the interface cannot contribute to the photocurrent because of charge recombination. For this reason, photovoltaic materials with a longer exciton diffusion length are generally believed to deliver better performance in OSCs. Third, the excitons dissociate at the interface into separated electrons and holes. This forms a charge separation state. The electrons flow from the LUMO of the electron donor to the LUMO of the electron acceptor at their interface. At this point, the V_{OC} of OSCs is determined by the energy gap between the LUMO of the electron acceptor and the HOMO of the electron donor. V_{OC} (in volts) can be roughly calculated as the difference of two energy levels (in electronvolts): $V_{OC} = \mathrm{LUMO}_{\mathrm{acceptor}} - \mathrm{HOMO}_{\mathrm{donor}}$. Fourth, the electrons flow through the ETL and are collected at the cathode, and the holes flow through the HTL and are collected at the anode. In consideration of this mechanism, much research has been done with the aim of increasing the LUMO level of fullerene derivatives, which can effectively increase PCE by increasing V_{OC} when paired with a given electron donor. A typical strategy for effectively increasing the LUMO level of fullerenes is to disrupt the conjugated π system of pristine C_{60} (60-π system) by functionalization of fullerenes. Examples include the 58-π system of $PC_{61}BM$ [4] and the 56-π systems of indene-C_{60} bisadduct (ICBA) [13] and methano-indene-[60]fullerene (MIF) [14]. However, further disruption of the conjugated π system has so far failed to achieve better PCE despite significantly increasing V_{OC} as a result of the poor morphology of solid-state packing dramatically lowering J_{SC}. In the 20 years following the first report of fullerene OSCs, which had a PCE of 2.9% [4], considerable effort was devoted to the development of fullerene electron acceptors, which successfully improved the PCE to 6.4% in OSCs using poly(3-hexylthiophene) (P3HT):fullerenes as the active layer [15] (Fig. 4). Since then, through further optimization of electron donor

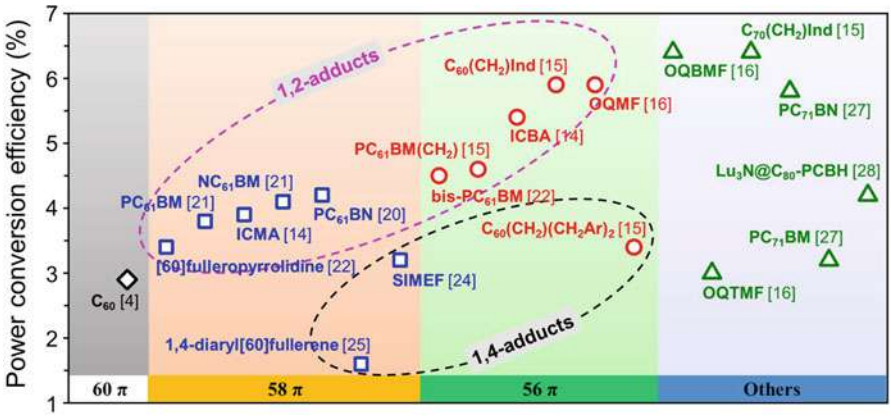

Fig. 4 PCE record plot of OSCs with P3HT:fullerenes as the active layer

materials and device fabrication, the Wang group achieved the current highest PCE of 11.2% in a ternary OSC using poly[(5,6-difluoro-2,1,3-benzothiadiazol-4,7-diyl)-*alt*-(3,3‴'di(2-octyldodecyl)2,2′;5′,2″;5″,2‴'-quaterthiophen-5,5‴'-diyl)] (PffBT4T-2OD):$PC_{71}BM$ as the active layer [16]. This section describes the development of fullerene electron acceptors with different conjugated π system for use in OSCs.

60-π System Acceptors

Pristine [60]fullerene (C_{60}), a soccer ball-shaped molecule, consists of 12 pentagons and 20 hexagons and perfectly complies with the isolated pentagon rule according to Euler's theorem [17]. This I_h symmetrical shape is constructed by carbon atoms with a mixture of sp^2 and sp^3 hybridization. Accordingly, C_{60} has 60 electrons located in its *p*-orbitals forming the 60-π system, which has significant delocalization. In 1995, the Heeger group reported the first [60]fullerene OSC, which had a PCE of 2.9% [4]. They mixed poly(2-methoxy-5-(2′-ethyl-hexyloxy)-1,4-phenylene vinylene) (MEH-PPV) and C_{60} to form the MEH-PPV:C_{60} electron donor/acceptor pair in the active layer of the OSCs (Fig. 5). Owing to the poor solubility of C_{60} in conventional organic solvents such as xylene and 1,2-dichlorobenzene, C_{60} tended to crystalize during film formation, which hindered the application of C_{60} in high concentration in the active layer. To overcome these problems, a series of derivatives with soluble functional groups was developed, among which $PC_{61}BM$ exhibited excellent solubility. At the same time, the V_{OC} of OSCs using $PC_{61}BM$ was significantly increased due to its higher LUMO level. As expected, the PCE of OSC using $PC_{61}BM$ improved to 3.2% because of the increased V_{OC} and improved solubility of this fullerene acceptor. Although these first OSCs using $PC_{61}BM$ did not achieve the high level of performance seen in subsequently developed OSCs using $PC_{61}BM$ as the electron acceptor, which was attributed to the non-optimized structure of the earlier devices, this pioneering research undoubtedly paved the way for later research and development of fullerene electron acceptors for OSCs.

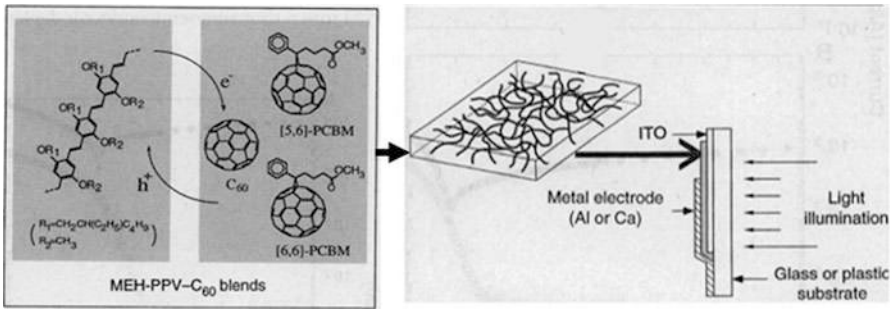

Fig. 5 The first fullerene OSCs with an illustration of the device structure. (This picture is reproduced from Science, https://doi.org/10.1126/science.270.5243.1789 [4])

58-π System Acceptors

From the aforementioned comparison between OSCs using C_{60} and those using $PC_{61}BM$, it is easy to see that increasing the LUMO level of the fullerene electron acceptor can significantly improve PCE. Also, introducing functional groups onto the fullerene cage can be a facile way to efficiently disrupt the π-system of fullerenes. Since the first report of using $PC_{61}BM$ in OSCs, numerous studies have investigated ways of effectively increasing V_{OC} to improve the output performance of OSCs. As a result, many fullerene electron acceptors with a 58-π system have been developed through the mono-addition of various functional groups onto the [60]fullerene cage.

Innumerable modifications of $PC_{61}BM$ have been investigated owing to the high potential for chemical modification of its phenyl ring, its alkyl ester, and even its fullerene cage itself (Fig. 6) [18]. However, most PCBM derivatives have failed to achieve significantly better performance than the $PC_{61}BM$ as an electron acceptor in OSCs. This was not for a lack of trying. There is a large body of research on all aspects of $PC_{61}BM$ derivatives' performance as an electron acceptor, including their energy levels, solubility, morphology, and charge mobility. Here, we focus our discussion on PCBM derivatives that outperformed $PC_{61}BM$ as electron acceptors in the active layer of OSCs. To ensure a fair comparison of all these PCBM electron acceptors, the most frequently used electron donor, namely, P3HT, was selected as the reference electron donor. OSCs using P3HT:$PC_{61}BM$ as the active layer typically exhibit a PCE of around 3.8%, despite some differences in their photovoltaic parameters due to inevitable processing variations. In 2011, the Sharma group successfully developed a PCBM analogue by using in which a 4-nitro-4′-hydroxy-α-cyanostilbene (NHCS) unit replaced the methyl group of $PC_{61}BM$ [19]. When used as an electron acceptor in OSCs with P3HT as the electron donor, this new PCBM analogue ($PC_{61}BN$) produced PCE of 4.2% with all other photovoltaic parameters showing significant improvement. High V_{OC} of 0.86 V was achieved thanks to the increased LUMO level of −5.9 eV (compared with −6.2 eV for $PC_{61}BM$), which was ascribed to the strong electron-withdrawing effect of the NHCS functional group. High J_{SC} of 8.5 mA cm^{-2} was reasonably attributed to the strong absorption by the $PC_{61}BN$ in a range of 250–900 nm, which helped the

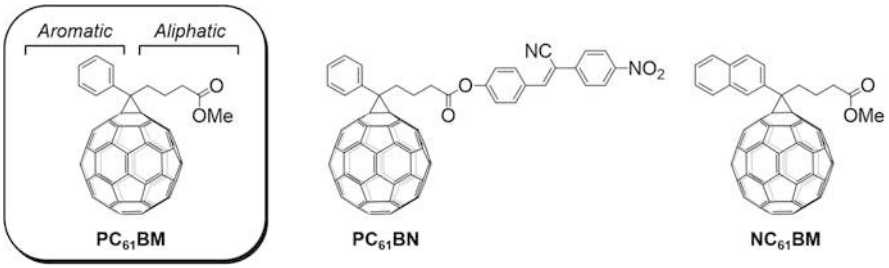

Fig. 6 Chemical modification sites of $PC_{61}BM$ and representative PCBM analogues

active layer generate more excitons leading to greater photocurrent. High FF of 0.58 was achieved as a result of better film quality enabled by the improved solubility of $PC_{61}BN$. Although the performance of photovoltaics is strongly influenced by the materials, fabrication techniques still play an important role in device performance. It is therefore understandable that optimization of processing techniques can further improve OSC performance. When the solvent used to make the P3HT:$PC_{61}BN$ active layer was changed to a mixed acetone/chloroform solvent, PCE improved to 4.6%. In addition to the solvent effect, annealing is also effective for controlling the morphology of the active layer and enhancing the hole and electron mobilities. When the P3HT:$PC_{61}BN$ film prepared from acetone/chloroform was subjected to thermal annealing at 120 °C, PCE significantly increased to 5.3% with marked improvement of J_{SC} from 9.4 mA cm^{-2} to 10.3 mA cm^{-2}. Compared with the non-annealed device, both hole and electron mobilities were dramatically increased by an order of magnitude (hole mobility μ_h from 6.4×10^{-4} cm^2 V^{-1} s^{-1} to 1.2×10^{-3} cm^2 V^{-1} s^{-1}; electron mobility μ_e from 7.4×10^{-4} cm^2 V^{-1} s^{-1} to 1.1×10^{-3} cm^2 V^{-1} s^{-1}). These results demonstrate that optimization of fabrication conditions offers benefits for photovoltaic performance, including more efficient light-harvesting and greater film uniformity. Aside from the modification of the aliphatic part of PCBM, modification of the aromatic part has also been investigated. Hwang's group substituted a naphthalene ring for the phenyl ring to obtain naphthalene C_{61}-butyric acid methyl ester ($NC_{61}BM$) and successfully used it as an electron acceptor in OSCs [20]. The P3HT:$NC_{61}BM$ OSCs outperformed the reference P3HT:$PC_{61}BM$ OSCs, giving a high PCE of 4.1% with significantly improved photovoltaic parameters ($V_{OC} = 0.70$ V, $J_{SC} = 9.1$ mA cm^{-2}, and FF = 0.64). The higher V_{OC} value was derived from the higher LUMO energy level of $NC_{61}BM$ relative to that of $PC_{61}BM$. The higher FF can be explained by the balance of charge carrier mobilities in the P3HT:$NC_{61}BM$ film, which exhibited a hole to electron mobility ratio of $\mu_h/\mu_e = 1.34$. Compared with the μ_h/μ_e ratio of 1.41 for P3HT:$PC_{61}BM$ film, this ratio for the P3HT:$NC_{61}BM$ film was much closer to 1.0, demonstrating well-balanced charge carrier mobility in the P3HT:$NC_{61}BM$ OSCs. However, further modification of phenyl ring by using anthracene or pyrene failed to give better performance than that of $PC_{61}BM$ OSCs. The reasons for this were the low LUMO levels of these PCBM analogues with larger polycyclic aromatic groups

and the poor morphology of the corresponding active layer films. Atomic force microscopy showed that the surface roughness of the P3HT:$PC_{61}BM$ and P3HT:$NC_{61}BM$ films was much lower, which can be interpreted as better interconnection between the P3HT donor and fullerene acceptors. In addition, the cage of $PC_{61}BM$ was modified, changing the conjugated π-system from a 58-π system to a 56-π system, which will be discussed in the following section on 56-π system acceptors.

PCBM derivatives have a characteristic cyclopropane structure that is synthesized by applying 1,3-dipole cycloaddition methodology. Enlightened by this point, researchers have installed other cyclic structures on the [60]fullerene cage by other cycloaddition reactions, such as the Diels-Alder reaction and the Prato reaction, producing various fullerene electron acceptors with a 58-π system (Fig. 7). In 2010, Li, Hou, and co-workers reported the indene-C_{60} monoadduct (ICMA) electron acceptor synthesized by Diels-Alder addition of the indene to C_{60}. When ICMA was applied as the electron acceptor with P3HT as the electron donor, the P3HT:ICMA OSCs exhibited a PCE of 3.9%, which matched the output of P3HT:$PC_{61}BM$ OSCs [13]. Compared with $PC_{61}BM$, ICMA gave a higher V_{OC} value to 0.63 V and a higher FF value of 0.64. Similar to the previously presented examples, the higher V_{OC} value of the P3HT:ICMA OSC was due to the increased LUMO energy level of ICMA. Intriguingly, although the absorption of ICMA was much stronger in the visible region from 400 to 800 nm compared with that of $PC_{61}BM$, J_{SC} of the P3HT:ICMA OSC was dramatically lower. This result was mainly due to poor molecular packing in the solid state because of the indene moiety. Consequently, ICMA OSCs failed to outperform $PC_{61}BM$ OSCs. Taking into consideration the low J_{SC} value of the ICMA OSCs, they further introduced a second indene moiety onto ICMA to form indene-C_{60} bisadduct (ICBA) (Fig. 9). Although the J_{SC} value of P3HT:ICBA OSCs was predictably lower than that of P3HT:$PC_{61}BM$ OSCs, it showed no further decrease compared with P3HT:ICMA OSCs, and both V_{OC} and FF were dramatically higher. As a result, the PCE of the P3HT:ICBA OSCs improved to 5.4%, with an impressively high V_{OC} of 0.84 V and an increased FF of 0.67. As discussed above, fullerene derivatives with a smaller conjugated π-system have a higher LUMO energy level. Therefore, the higher V_{OC} value of P3HT:ICBA OSCs compared with P3HT:IMBA OSCs can undoubtedly be explained by the 56-π system of

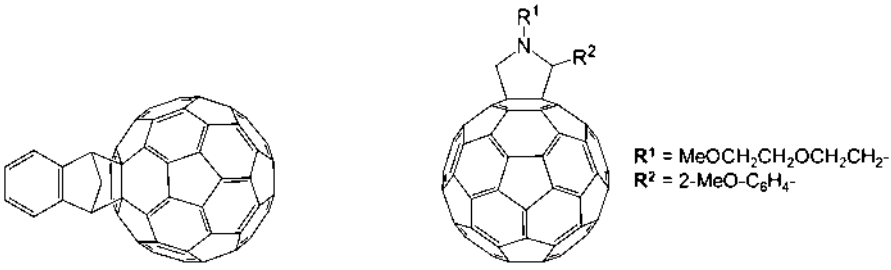

Fig. 7 Cyclo[60]fullerene electron acceptors with a 58-π system

ICBA. In addition to the Diels-Alder reaction, the Prato reaction has been widely used to modify the [60]fullerene cage, attaching a pyrrolidine ring to give various [60]fulleropyrrolidine derivatives. Synthetically speaking, [60]fullerene derivatives with a heterocyclic ring structure are much more amenable to synthesis thanks to the ready availability of starting materials with versatile functional groups. Unfortunately, fullerene derivatives with a heterocyclic ring have generally failed to produce better performance than $PC_{61}BM$ OSCs. Here, the best-performing fullerene derivative with a heterocyclic ring is discussed as an illustrative example, though it did not outperform $PC_{61}BM$ when used in OSCs. In 2010, Itoh's group designed a series of fulleropyrrolidine-imidazolium hybrids. One specifically designed fulleropyrrolidine with R^1 of $MeOCH_2CH_2OCH_2CH_2$- and R^2 of 2-MeO-C_6H_4- exhibited the best performance among these fulleropyrrolidine derivatives [21]. The P3HT: fulleropyrrolidine OSCs showed moderate performance with PCE of 3.4%, V_{OC} of 0.66 V, J_{SC} of 7.85 mA cm^{-2}, and FF of 0.66. Although V_{OC} was significantly increased because of this derivative's higher LUMO energy level, FF did not show much improvement and J_{SC} was markedly worse in comparison with P3HT: $PC_{61}BM$. The reason why the fulleropyrrolidine OSCs performed poorly was that the fulleropyrrolidine derivatives were incompatible with conventional electron donor materials such as P3HT in OSCs. This incompatibility of electron donor/acceptor pair resulted in poor film quality of the active layer, leading to the smaller J_{SC} value. These findings also help explain why more fulleropyrrolidine derivatives are used as an ETL or dopant in PSCs rather than as an electron acceptor in the active layer of OSCs.

Fullerene derivatives have two different addition patterns – the 1,2-addition pattern and the 1,4-addition pattern. Cyclo[60]fullerene derivatives typically have a 1,2-addition pattern. Although there are relatively few examples of applying fullerene derivatives with a 1,4-addition pattern in OSCs compared with cyclo[60] fullerene derivatives, the fullerene 1,4-adducts have nonetheless been investigated in OSCs because they can serve as electron acceptors with a 58-π system (Fig. 8). In

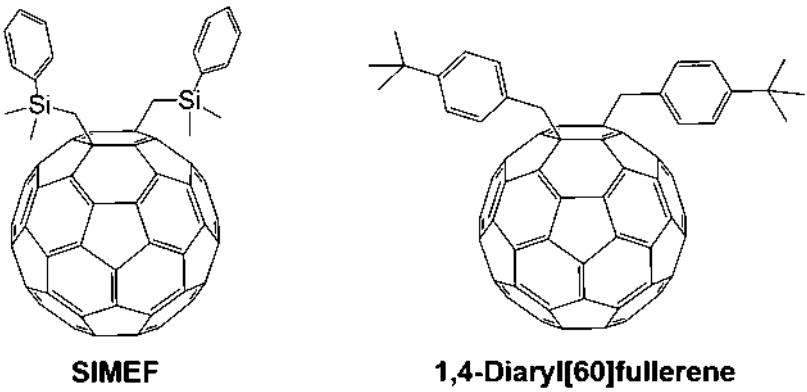

Fig. 8 Fullerene electron acceptors with a 1,4-addition pattern

2009, Matsuo et al. successfully synthesized a fullerene derivative with a 1,4-addition pattern, namely, 1,4-bis(dimethylphenylsilylmethyl)[60]fullerene (SIMEF). They blended tetrabenzoporphyrin with SIMEF to form an electron donor/acceptor pair for the active layer of OSCs [22]. The tetrabenzoporphyrin: SIMEF OSCs exhibited PCE of 5.2%, V_{OC} of 0.75 V, J_{SC} of 10.5 mA cm^{-2}, and FF of 0.65. This excellent device performance arose from the outstanding packing of the SIMEF molecules. They have a columnar fullerene core array that produces high electron mobility and undergoes thermal crystallization that produces better phase separation with electron donors. However, when SIMEF was blended with the conventional electron donor P3HT, it failed to outperform P3HT:$PC_{61}BM$ OSCs [23]. The P3HT:SIMEF OSCs exhibited PCE of 3.2% with V_{OC} of 0.67 V, J_{SC} of 9.2 mA cm^{-2}, and FF of 0.52. Although the V_{OC} value was significantly increased thanks to the higher LUMO energy level of the fullerene 1,4-adducts, neither J_{SC} nor FF contributed to improved performance of OSCs, which could be attributed to incompatibility of P3HT and SIMEF for film formation. In addition, other investigations have shown that fullerene 1,4-adduct OSCs show similarly poor performance compared with $PC_{61}BM$ OSCs. The Nakamura group reported the use of a 1,4-diaryl[60]fullerene derivative as the electron acceptor in OSCs [24]. The P3HT:1,4-diaryl[60]fullerene OSCs gave a much lower PCE of 1.6% compared with the performance of P3HT:$PC_{61}BM$ OSCs, though V_{OC} was significantly increased owing to the high LUMO energy level of the fullerene 1,4-adduct. Consequently, fullerene derivatives with a 1,4-addition pattern have failed to outperform fullerene derivatives with a 1,2-addition pattern, which could also empirically explain why there are few examples of fullerene 1,4-adducts used in OSCs. Indeed, the poor performance of fullerene 1,4-adduct OSCs could be attributable to the poor solid-state packing between fullerene 1,4-adducts and electron donor molecules, as fullerene 1,4-adducts are generally too bulky to interact favorably with the electron donor molecules. Taken together, the results for fullerene derivatives with a 58-π system show that increasing the LUMO energy level can predictably increase V_{OC}. However, this is just one piece of the puzzle. Higher V_{OC} did not necessarily give better overall performance because it was often accompanied by lower J_{SC} and FF as a result of unfavorable molecular packing or morphology. Therefore, the enhancement of PCE requires balancing of all photovoltaic parameters. To accomplish this, subsequent research has sought to increase the LUMO energy level of fullerene electron acceptors without sacrificing the J_{SC} and FF, and this point has emerged as the key consideration in the design of fullerene electron acceptors with much smaller conjugated π systems.

56-π System Acceptors

To prepare fullerene electron acceptors with a 56-π system, the easiest approach would seem to be introducing further functional groups onto the cage of fullerene electron acceptors with a 58-π system. In one such example discussed earlier in this chapter, introduction of a second indene onto ICMA (58-π system) via the Diels-Alder reaction produced ICBA (56-π system), which improved PCE to 5.4% [13]. Nevertheless, simply decreasing the size of the π system has failed to produce

better performance in most cases. Accordingly, further consideration has been given to factors such as molecular packing and film morphology, in order to achieve better performance via well-balanced photovoltaic parameters. Inspired by the advantages of $PC_{61}BM$, Bolm and co-workers introduced an additional phenyl-butyric acid methyl ester group onto the cage of $PC_{61}BM$ to produce bis-$PC_{61}BM$ [25]. They fabricated the active layer by blending P3HT with the synthesized bis-$PC_{61}BM$ and evaluated the performance of the resulting P3HT:bis-$PC_{61}BM$ OSCs. The P3HT:bis-$PC_{61}BM$ OSCs delivered an excellent performance with an externally verified PCE of 4.5%, which was better than the performance of P3HT:$PC_{61}BM$ OSCs. In line with the higher LUMO energy level of fullerene electron acceptors with a 56-π system, the V_{OC} value of the P3HT:bis-$PC_{61}BM$ OSCs increased to 0.73 V, which was 0.15 V higher than that of P3HT:$PC_{61}BM$ OSCs. Notably, J_{SC} was decreased to some extent, but this decrease did not significantly offset the contribution from the increased V_{OC} of the P3HT:bis-$PC_{61}BM$ OSCs through further addition onto fullerene cage. This study clearly demonstrated that P3HT:bis-$PC_{61}BM$ OSCs can give better performance than that of P3HT:$PC_{61}BM$ OSCs. However, the long aliphatic chain of $PC_{61}BM$ definitely increases the size of molecules, which potentially hinders close packing of electron donor molecules. In subsequent work, Matsuo and co-workers designed a small building block to replace the phenyl-butyric acid methyl ester group of $PC_{61}BM$, and used the resulting compound as a fullerene synthetic precursor with a 58-π system [14]. The small building block that they introduced onto the cage of the 58-π fullerene derivative was the methene group (-CH_2-), which produces a cyclopropanated fullerene, namely, methano[60]fullerene ($C_{61}H_2$), that can then be used to synthesize fullerene electron acceptors with a 56-π system. Further introduction of various functional groups onto $C_{61}H_2$ ultimately gave a series of fullerene electron acceptors with a 56-π system. For example, when a phenyl-butyric acid methyl ester group was installed onto $C_{61}H_2$, methano phenyl-C_{61}-butyric acid methyl ester, denoted as $PC_{61}BM(CH_2)$, was successfully obtained. Then, the synthesized $PC_{61}BM(CH_2)$ was used as an electron acceptor in the active layer of OSCs, which showed slightly better performance, with PCE of 4.6%, V_{OC} of 0.73 V, J_{SC} of 9.0 mA cm^{-2}, and FF of 0.71, than P3HT:bis-$PC_{61}BM$ OSCs. Intriguingly, both J_{SC} and FF of P3HT:$PC_{61}BM(CH_2)$ OSCs were significantly improved compared to those of P3HT:bis-$PC_{61}BM$ OSCs, perfectly in line with the concept of smaller substitution group giving better solid-state packing of the donor/acceptor pair. When the less bulky functional group indene was installed onto $C_{61}H_2$, methano-indene-[60]fullerene ($C_{60}(CH_2)$Ind, MIF), denoted as $C_{60}(CH_2)$Ind, was correspondingly obtained. The PCE of P3HT:MIF OSCs dramatically improved to 5.9% with V_{OC} of 0.78 V, J_{SC} of 10.3 mA cm^{-2}, and FF of 0.73. This excellent performance can be conclusively attributed to the good balancing of all the photovoltaic parameters. The increased V_{OC} value was undoubtedly due to the high LUMO energy level of MIF, which has a typical 56-π system. Thanks to the small size of both the methano and indene groups, MIF had close solid-state molecular packing with the electron donor, which is advantageous for forming an active layer with high film quality. However, when the methano group was introduced onto the cage of diaryl[60]fullerene, which has a 1,4-addition pattern, the resulting derivative,

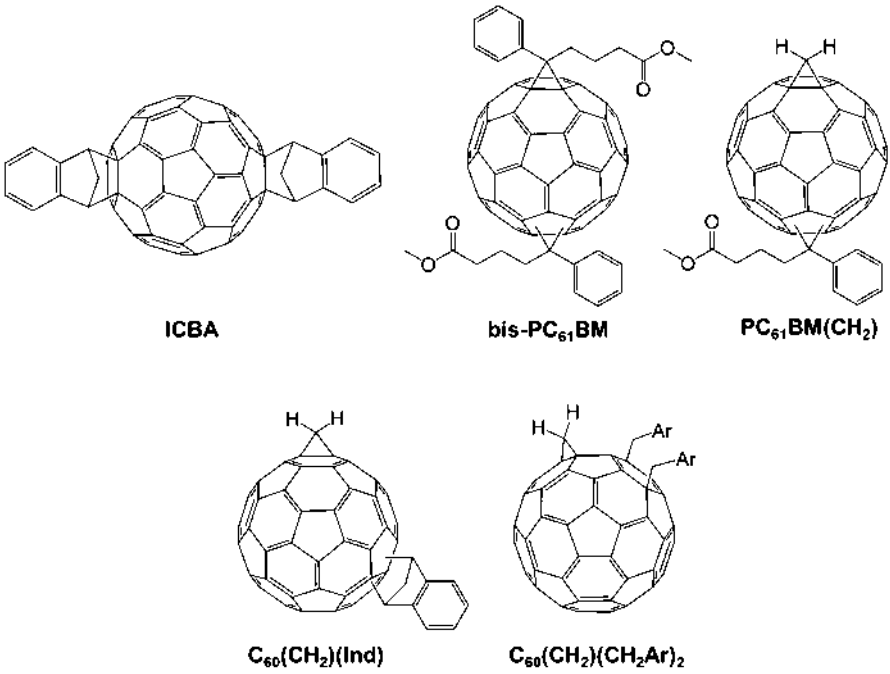

Fig. 9 Fullerene electron acceptors with a 56-π system

denoted as $C_{60}(CH_2)(CH_2Ar)_2$, failed to outperform P3HT:$PC_{61}BM$ in OSCs. The P3HT:$C_{60}(CH_2)(CH_2Ar)_2$ OSCs gave a poor PCE of 3.4% with V_{OC} of 0.82 V, J_{SC} of 7.1 mA cm^{-2}, and FF of 0.58. Although the V_{OC} of $C_{60}(CH_2)(CH_2Ar)_2$ was the highest among all other fullerene electron acceptors with a 56-π system, J_{SC} and FF were substantially decreased, which completely overwhelmed the contribution of the increased V_{OC} and caused the extremely poor performance of the P3HT:$C_{60}(CH_2)(CH_2Ar)_2$ OSCs. This result suggests that fullerene electron acceptors with a 1.4-addition pattern are not good candidates for use in OSCs, owing to their bulky molecule size as mentioned above. This result makes clear why greater attention has been paid to the solid-state molecular packing of donor/acceptor pairs and the morphology of the active layer film in the design of fullerene electron acceptors with smaller conjugated π systems: It is difficult to optimize the structures such that J_{SC} and FF are well balanced with naturally increased V_{OC} that accompanies substitution onto the fullerene cage (Fig. 9).

Other π System Acceptors

All of the abovementioned fullerene electron acceptors with a 58-π or 56-π system are currently the most commercially applicable electron acceptors in OSCs owing to their facile synthesis and satisfactory photovoltaic performance. Other possible strategies for improving the performance of fullerene electron acceptors include further decreasing the size of the conjugated π system by further addition of

substituents or switching to higher fullerenes with different π-systems. However, such fullerene derivatives with other π systems are seldom used in OSCs because they require complicated multistep synthesis or have high cost. Moreover, most research investigating fullerenes with smaller conjugated π system has shown this approach to be counterproductive, owing to the dramatic decreases in J_{SC} and FF. Nevertheless, fullerene derivatives with a further decreased π system could still achieve enhanced performance when less bulky functional groups were installed. In 2014, Ding and co-workers reported a series of fullerene electron acceptors with a further decreased π system that gave improved OSC performance [15]. They first used the Bingel reaction to synthesize the methanofullerenes $C_{60}CH_2$ (58-π system), $C_{60}(CH_2)_2$ (56-π system), and $C_{60}(CH_2)_3$ (54-π system) as starting materials for further derivatization. They introduced the *o*-quino group onto these methano[60]fullerenes to obtain *o*-quinomethano[60]fullerene derivatives. Specifically, $C_{60}CH_2$ was converted to *o*-quinomethane[60]fullerene (OQMF; 56-π system), $C_{60}(CH_2)_2$ to *o*-quinobismethane[60]fullerene (OQBMF; 54-π system), and $C_{60}(CH_2)_3$ to *o*-quinotrimethane[60]fullerene (OQTMF; 52-π system)d. Owing to the structural similarity between OQMF and MIF, the photovoltaic performance of P3HT:OQMF OSCs and P3HT:MIF OSCs was comparable, similar to photovoltaic parameters, with OQMF exhibiting V_{OC} of 0.84 V, J_{SC} of 9.96 mA cm^{-2}, and FF of 0.70. Also, the PCE of P3HT:OQBMF OSCs dramatically improved to 6.4% with V_{OC} of 0.95 V, J_{SC} of 9.67 mA cm^{-2}, and FF of 0.70. Although J_{SC} decreased as expected from the increased molecular size due to the additional addend, it did not significantly overshadow the contribution of the increased V_{OC}. Moreover, the electron mobility of the P3HT:OQBMF active layer film was 1.1×10^{-4} cm^2 V^{-1} s^{-1}, which was comparable to that of P3HT:OQMF active layer film (1.5×10^{-4} cm^2 V^{-1} s^{-1}). Such excellent results can be attributed to the small substituents increasing the LUMO energy level of the fullerene electron acceptor without degrading other photovoltaic parameters. These results demonstrated the utility of the methano group as a building block for effectively increasing V_{OC} to enhance PCE. However, this strategy also has a ceiling. The P3HT:OQTMF OSCs showed a very low PCE of 3.0% even though V_{OC} was further improved to 1.00 V. This poor performance was due to dramatic drops in J_{SC} (5.52 mA cm^{-2}) and FF (0.54). Furthermore, the electron mobility of the P3HT:OQTMF film was much worse (2.2×10^{-5} cm^2 V^{-1} s^{-1}), which can be reasonably ascribed to the poor solid-state packing between P3HT and OQTMF. Thus, from OQMF to OQTMF, multi-addition increased V_{OC} by raising the LUMO level but also increased the molecular size, which adversely affected the solid-state packing of donor/acceptor pairs. The results of this study showed why there are few examples for fullerene electron acceptors with a 52-π system and why there have been no investigations of fullerene electron acceptors with further decreased conjugated π system.

It should be noted that there are more examples of [60]fullerene derivatives used as electron acceptors than of higher fullerenes such as [70]fullerene (C_{70}) and [80] fullerene (C_{80}), which is mainly due to the abundance of C_{60} and the easy synthesis of [60]fullerene derivatives. On a positive note, recent investigations have suggested that higher fullerene derivatives have considerable promise for use in OSCs.

Compared with C_{60}, C_{70} has a much larger conjugated π-system with 70 electrons located at its *p* orbitals. Despite this, the LUMO energy level of C_{70} and C_{60} are similar [1]. Intriguingly, most [70]fullerene derivatives produce even better performance in OSCs than the corresponding [60]fullerene derivatives, which can be explained by the higher solubility and stronger light absorption of the [70]fullerene derivatives. For example, introducing an indene group onto methano[70]fullerene gives methano-indene-[70]fullerene ($C_{70}CH_2$(Ind)), which is a 66-π system [14]. When $C_{60}CH_2$(Ind) is replaced with $C_{70}CH_2$(Ind) in OSCs, the PCE of P3HT:C_{70}(CH_2)(Ind) OSCs improved from 5.9% for P3HT:C_{60}(CH_2)(Ind) OSCs to 6.4%, with V_{OC} of 0.79 V, J_{SC} of 11.1 mA cm^{-2}, and FF of 0.73. It should be noted that all photovoltaic parameters showed similar performance except for the significantly increased J_{SC}, which can be attributed to the strong absorption of C_{70} derivatives in the visible region. As J_{SC} value is positively correlated with the amount of light that is harvested by the active layer, the strong absorption by C_{70} derivatives definitely contributes to the light absorption of active layer, leading to more exciton generation and ultimately higher PCE. By the same token, when PC_{71}BN was synthesized by introducing 4-nitro-4′-hydroxy-*α*-cyanostilbene (NHCS) onto the fullerene cage of C_{70}, it performed better than the corresponding [60]fullerene derivatives, PC_{61}BN [26]. P3HT:PC_{71}BN OSCs achieved a high PCE of 5.8% with a notably enhanced J_{SC} of 11.8 mA cm^{-2} compared with the J_{SC} value of 10.3 mA cm^{-2} for P3HT:PC_{61}BN OSCs. However, the phenyl-butyric acid methyl ester functionalized C_{70} derivative PC_{71}BM did not outperform PC_{61}BM when blended with P3HT to form the active layer in OSCs. P3HT:PC_{71}BM OSCs gave a slightly poorer PCE of 3.2%, with V_{OC} of 0.66 V, J_{SC} of 9.4 mA cm^{-2}, and FF of 0.52, which can be ascribed to incompatible solid-state packing between P3HT and PC_{71}BM. Thus, other electron donor materials were explored, such as PffBT4T-2OD, and PffBT4T-2OD:PC_{71}BM OSCs achieved the current highest PCE of 11.2% for fullerene electron acceptors [16].

All the fullerenes discussed so far have been empty fullerenes, with nothing encapsulated within their inner cages. If additional atoms, ions, or clusters are enclosed within the fullerene cage, another type of fullerene is obtained, namely, endohedral fullerenes. The electrical properties of endohedral fullerenes are usually different from those of empty fullerenes, so several researches have been investigating the application of endohedral fullerenes in OSCs, although few examples have given performance superior to that of empty fullerene in OSCs. In 2009, the Dress group presented the first example of applying an endohedral fullerene derivative in OSCs [27]. Because fullerene derivatives function as the electron acceptor inside the active layer, OSCs typically require a sufficient amount of fullerene derivatives with appropriate properties for film formation. However, non-derivatized endohedral fullerenes generally have extremely low solubility, which hinders the formation of a condensed state of electron acceptor in OSCs. Thus, to enhance solubility, Dress and co-workers introduced phenyl-butyric acid hexyl ester (PCBH) onto lutetium nitride-containing C_{80} ($Lu_3N@C_{80}$) to obtain the endohedral fullerene derivative $Lu_3N@C_{80}$-PCBH, which gave a high PCE of 4.2% with V_{OC} of 0.81 V, J_{SC} of 8.6 mA cm^{-2}, and FF of 0.61. This enhanced efficiency was mainly due to the

significantly increased V_{OC} value of P3HT:$Lu_3N@C_{80}$-PCBH OSCs, which arose from the higher LUMO energy level of $Lu_3N@C_{80}$-PCBH compared with $PC_{61}BM$. Notably, $Lu_3N@C_{80}$-PCBH exhibits good solid-state packing with P3HT and charge carrier mobility similar to that of $PC_{61}BM$. Accordingly, P3HT:$Lu_3N@C_{80}$-PCBH OSCs gave significantly improved PCE without sacrificing J_{SC} and FF. Despite endohedral fullerene electron acceptors showing promising performance in OSCs, the need for sufficient amounts of endohedral fullerenes for film formation has posed a major challenge that has seriously limited their application in OSCs, primarily due to the limited availability and difficulty of handling these materials. However, more endohedral fullerenes have been investigated in perovskite solar cells (PSCs) thanks to the rapid development of fabrication techniques for this type of cell. The active layer in PSCs is, by definition, a perovskite-structured material, but the endohedral fullerenes can be used as a dopant, which requires only trace amounts of material (usually less than 1.0 wt %). Even though very small amount of endohedral fullerenes are used as dopants in PSCs, their impact on PSC performance is huge. Outstanding results have been obtained by applying this doping strategy in all three layers of PSCs, which has greatly broadened the application scope of endohedral fullerenes. The application of endohedral fullerenes as dopants in PSCs will be discussed in detail in the following section (Fig. 10).

To give a brief summary, fullerenes and their derivatives have been widely investigated as electron acceptors in OSCs. For a given electron donor with a particular HOMO energy level, increasing the LUMO energy level of fullerene electron acceptors can increase V_{OC} and thus the PCE of OSCs. Therefore, many functional groups have been designed and introduced onto fullerenes to disrupt their conjugated π system. Empirically, fullerene electron acceptors with a 58-π system, such as $PC_{61}BM$ and ICMA, and those with a 56-π system, such as bis-$PC_{61}BM$, ICBA, and MIF, have demonstrated the best performance among fullerene acceptors in OSCs. Also, these fullerene derivatives are now the most commercially available fullerene electron acceptors owing to their facile synthesis and excellent performance. Although further decrease in the size of the conjugated π system could theoretically give better performance because of the predictable increase in V_{OC}, most examples of this strategy have failed to achieve better performance than that of fullerene electron acceptors with a 58-π or 56-π system. This counterproductive outcome is mainly due to the poor molecular packing and poor electron mobility of fullerene electron acceptors with a smaller π system, and their complicated multistep syntheses seriously limit the applications of these materials in the photovoltaic industry. In addition, fullerene derivatives with a 1,2-addition pattern usually exhibit better performance than 1,4-adducts, which can be reasonably ascribed to the less bulky size of 1,2-adducts compared with 1,4-adducts. Although there is no overarching theory to predict a good fullerene electron acceptor that improves OSC performance, there are some empirical rules and theoretical insights that can serve as a guide for designing potentially good fullerene electron acceptors. For instance, effectively increasing the LUMO energy level of fullerene derivatives by the addition of small size substituents can sufficiently maintain high J_{SC} and FF values while increasing V_{OC} for fullerene OSCs. There is a trade-off among V_{OC}, J_{SC}, and FF that

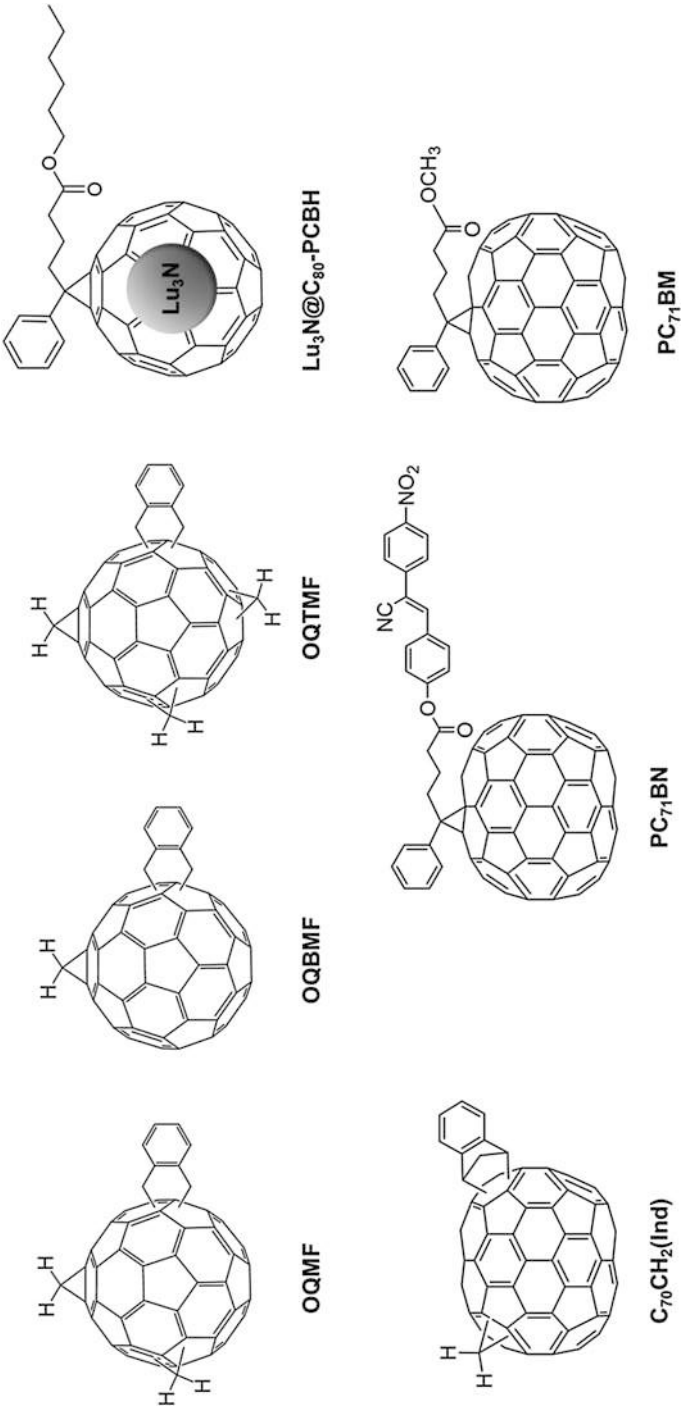

Fig. 10 Fullerene electron acceptors with other π systems

Table 1 Summary of OSCs using fullerenes as electron acceptors in the active layer

Active layer (donor:acceptor)	V_{OC} (V)	J_{SC} (mA cm^{-2})	FF	PCE (%)	Ref.
P3HT:$PC_{61}BM$	0.67	9.2	0.61	3.8	[21]
P3HT:$NC_{61}BM$	0.70	9.1	0.64	4.1	
P3HT:$PC_{61}BN$	0.86	8.5	0.58	4.2	[20]
P3HT:ICMA	0.63	9.7	0.64	3.9	[14]
P3HT:ICBA	0.84	9.7	0.67	5.4	
P3HT:Fulleropyrrolidine	0.66	7.9	0.66	3.4	[22]
Tetrabenzoporphyrin:SIMEF	0.75	10.5	0.65	5.2	[23]
P3HT:SIMEF	0.67	9.2	0.52	3.2	[24]
P3HT:1,4-diaryl[60]fullerene	0.77	4.8	0.57	1.6	[25]
P3HT:Bis-$PC_{61}BM$	0.73	9.6	0.68	4.5	[26]
P3HT:$PC_{61}BM(CH_2)$	0.73	9.0	0.71	4.6	[15]
P3HT:$C_{60}(CH_2)$Ind	0.78	10.3	0.73	5.9	
P3HT: $C_{60}(CH_2)(CH_2Ar)_2$	0.82	7.1	0.58	3.4	
P3HT:$C_{70}(CH_2)$Ind	0.79	11.1	0.73	6.4	
P3HT:OQMF	0.84	9.9	0.70	5.9	[16]
P3HT:OQBMF	0.95	9.7	0.70	6.4	
P3HT:OQTMF	1.00	5.5	0.54	3.0	
P3HT:$PC_{71}BM$	0.66	9.4	0.52	3.2	[27]
P3HT:$PC_{71}BN$	0.82	10.6	0.56	4.9	
PffBT4T-2OD:$PC_{71}BM$	0.79	18.8	0.75	11.2	[17]
P3HT:$Lu_3N@C_{80}$-PCBH	0.81	8.6	0.61	4.2	[28]

must be weighed to realize the best performance of OSCs. In addition, higher fullerene derivatives such as [70]fullerene and its derivatives, including $PC_{71}BN$, $C_{70}(CH_2)$Ind, and $PC_{71}BM$, have been demonstrated to be better electron acceptors in OSCs owing to their strong light absorption in the visible region and excellent solubility compared with [60]fullerene derivatives. Apart from empty fullerenes, endohedral fullerenes, such as $Lu_3N@C_{80}$-PCBH, have also shown excellent performance as electron acceptors in OSCs. However, there are few examples of applying endohedral fullerenes in OSCs, because the limited availability of endohedral fullerenes cannot satisfy the bulk amounts required in OSCs. For quick reference, Table 1 summarizes the performance of the OSCs with fullerene acceptors discussed in this section. Our hope is that this section has provided further guidance and knowledge not only for scholars and scientists currently engaged in the OSC field but also for prospective researchers.

Fullerenes in Perovskite Solar Cells

Introduction to Perovskite Solar Cells

PSCs are currently the most rapidly advancing type of photovoltaics. In the active layer of these cells, a perovskite-structured material such as a hybrid

organic-inorganic lead or a tin halide-based material is used as the light-harvesting material. Since the first PSC was demonstrated in 2009 by the Miyasaka group [28], who obtained a PCE of 3.8%, tremendous efforts have been devoted to this area of research, and the current National Renewable Energy Laboratory (NREL) certified highest PCE record of 25.2% was achieved in 2019. The impressive performance of PSCs is thanks to the many advantageous properties of perovskite materials, such as high absorption coefficients, long charge carrier (electron-hole) diffusion lengths, tunable bandgaps, and very low production costs. In contrast to the light-harvesting materials used in OSCs, which commonly consist of an organic electron donor/acceptor pair, the light-harvesting materials of PSCs are defined by a perovskite structure. Perovskite materials have a characteristic crystal octahedra structure with the general formula ABX_3, which is made up of corner-linked octahedral of X atoms with the B cation at their center, and the A cation between them (Fig. 11a) [29]. The perovskite-structured active layer is the core engine of PSCs, so recent studies have successfully worked to broaden the scope of perovskite materials with various bandgaps (Fig. 11b) [30]. However, the most commonly investigated perovskite materials are still confined to methylammonium lead trihalide ($MAPbX_3$; $CH_3NH_3PbX_3$, where X is a halogen atom such as iodine, bromine, or chlorine) or formamidinium lead trihalide ($FAPbX_3$; $H_2NCHNH_2PbX_3$), primarily because of their facile processing procedures and low cost. In addition, the device architecture of PSCs has also been optimized from the perspective of device engineering. Generally, the device geometry structures is classified into two main types: the normal-type structure, which consists of three layers n-i-p from bottom to top, and the inverted-type structure, which consists of three layers p-i-n from bottom to top. Depending on the materials used for PSCs and the processing conditions for their fabrication, both normal-type and inverted-type structures have been widely utilized. However, this chapter mainly focuses on advanced technology for the application of

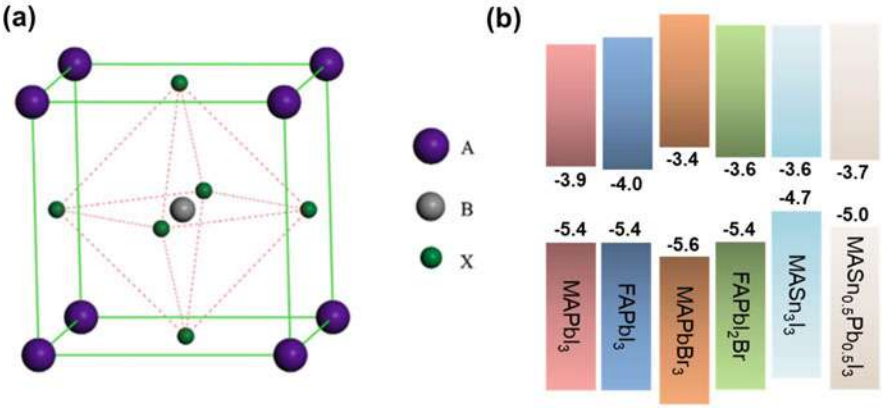

Fig. 11 (**a**) Illustration of the octahedra structure of the perovskite material. (**b**) Summary of energy level diagrams of representative organometal perovskite materials

fullerenes in PSCs, rather than on the development of perovskite materials or device engineering, which have been already reviewed elsewhere [30].

Owing to the intrinsic electron affinity of fullerenes, they have been widely used as electron acceptor materials paired with electron donor materials in OSCs [12]. Moreover, fullerenes are also well known for their remarkable charge-transfer ability, which enables them to serve as ETLs in PSCs. Unlike OSCs, PSCs utilize the high charge-transfer ability of fullerenes, which thus exert a greater influence on J_{SC} and FF in PSCs compared with OSCs. As discussed in regard to OSCs, the installation of more addends on fullerene cage leads to higher V_{OC} in OSCs, but sharply lowers J_{SC} and FF and thus seriously undermines device performance, which can be attributed to poor charge transport ability. Because the charge-transfer ability of fullerenes is recognized as a more important factor for PSCs, pristine C_{60} tended to be used as the ETLs of PSCs rather than multi-adduct fullerenes. Besides being used as ETLs in PSCs, fullerenes have been also studied for their effect on the perovskite layer. For example, during the formation of the perovskite layer, if the perovskite crystal size can be controlled to be larger, then grain boundaries and defects can be reduced to enhance the performance of PSCs. Accordingly, fullerenes have been used as an additive in the perovskite active layer to help reduce grain boundaries and defects to improve PSC performance. Similarly, fullerene derivatives also can be fabricated as a layer under the perovskite layer to serve as a perovskite growth template, which helps the perovskite seeds grow into larger crystals to reduce grain boundaries and defects. In PSCs, such fullerene layers are placed underneath the perovskite layer and deposited above the other ELTs, which are usually metal oxides, and thus are called fullerene overcoat layers. Interestingly, there are more examples of applying endohedral fullerenes in PSCs than in OSCs. This is undoubted because a trace amount of endohedral materials (usually less than 1.0 wt %) can be used as a dopant in PSCs. As fullerene derivatives in PSCs must usually have a low LUMO level to efficiently accommodate the photoelectrons generated from the perovskite layer, fullerene derivatives in these cells usually have a higher π system, such as a 60-π and 58-π system, rather than a further decreased π system. In this section, we mainly discuss recent advances in fullerene materials based on the different application methodologies for fullerenes in PSCs. It should be noted that performance differs among perovskite materials, with some such as $FAPbI_3$ and $MAPbI_{3-x}Cl_x$ often exhibiting better performance because of their strong absorption in the visible region and their wider bandgaps. Thus, to compare the performance of all PSCs on a level playing field, we consider only examples that used $MAPbI_3$ as the active layer in order to focus on the development of fullerene applications in PSCs, which is graphically illustrated in Fig. 12.

Fullerene Electron Transport Layers

As in OSCs, the ETL is also an essential component in PSCs that is used to filter out unwanted holes that may recombine with the electrons and decrease photocurrent output. The conventional electron transport materials used as ETLs in PSCs are metal oxides such as TiO_2, ZnO, SnO_2, and Cs_2CO_3. Although PSCs with metal oxide ETLs usually achieved excellent performance, the use of metal oxides

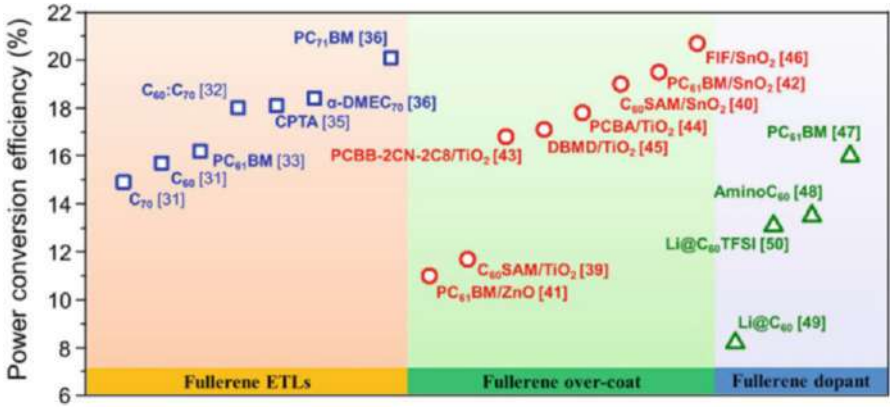

Fig. 12 Plot of PCEs for $MAPbI_3$ PSCs utilizing fullerenes in different ways

commonly results in a number of problems, such as large hysteresis in the *J–V* curves of PSCs, high sintering temperature, and the long time required for ETL fabrication, which obviously limits the practical application of PSCs. Fullerene materials can be effectively used as ETLs to solve these problems, thanks to their low chemical capacitance and fast electron transfer. Additionally, fullerenes can also function as a moisture barrier, which can enhance the long-term stability of PSCs. In this section, we discuss several representative examples of fullerene ETLs that have been used in PSCs (Fig. 13). In 2016, the Yan group reported the first use of thermally deposited C_{60} as an ETL in normal-type PSCs, which had a configuration of fluorine-doped tin oxide (FTO)/C_{60}/$MAPbI_3$/2,2′,7,7′-tetrakis-(*N*,*N*-di-*p*-methoxyphenylamine)-9,9′-spirobifluorene (Spiro-OMeTAD)/Au [31]. The PSCs with thermally deposited C_{60} ETLs showed the best performance among the devices they tested, with PCE of 15.7%, V_{OC} of 1.10 V, J_{SC} of 18.9 mA cm^{-2}, and FF of 0.75, which are attributable to the excellent electron transport ability of C_{60} ETLs. Compared with solution-processed C_{60} ETLs, the thermally deposited C_{60} ETLs can be reproducibly fabricated with an even and uniform surface for better PSC performance. However, when C_{60} ETLs were replaced with C_{70} ETLs, the device performance dramatically declined to a PCE of 14.9% ($V_{OC} = 1.03$ V, $J_{SC} = 18.6$ mA cm^{-2}, and FF = 0.78). This was mainly due to the much strong light absorption of C_{70}, which hindered light absorption by the perovskite layer for generating excitons. Thermal deposition can produce a uniform ETL with better performance in PSCs but is a slow and expensive process, which has limited its application in the photovoltaic industry. Later on, Lin et al. achieved high PCE by spin-coating a C_{60}:C_{70} mixture (9:1 w/w) to fabricate ETLs [32]. A similar normal-type PSC with a device structure of indium tin oxide (ITO)/(C_{60}:C_{70})/$MAPbI_3$/Spiro-OMeTAD/Au was used, which achieved a high PCE of 16.7% with V_{OC} of 1.02 V, J_{SC} of 22.9 mA cm^{-2}, and FF of 0.71, matching the performance of a reference PSC with a thermally deposited C_{60} ETL (PCE = 16.7%, $V_{OC} = 1.01$ V, $J_{SC} = 22.7$ mA cm^{-2}, and FF = 0.72). The main reason why thermally deposited C_{60} ETLs can improve the performance of PSCs is

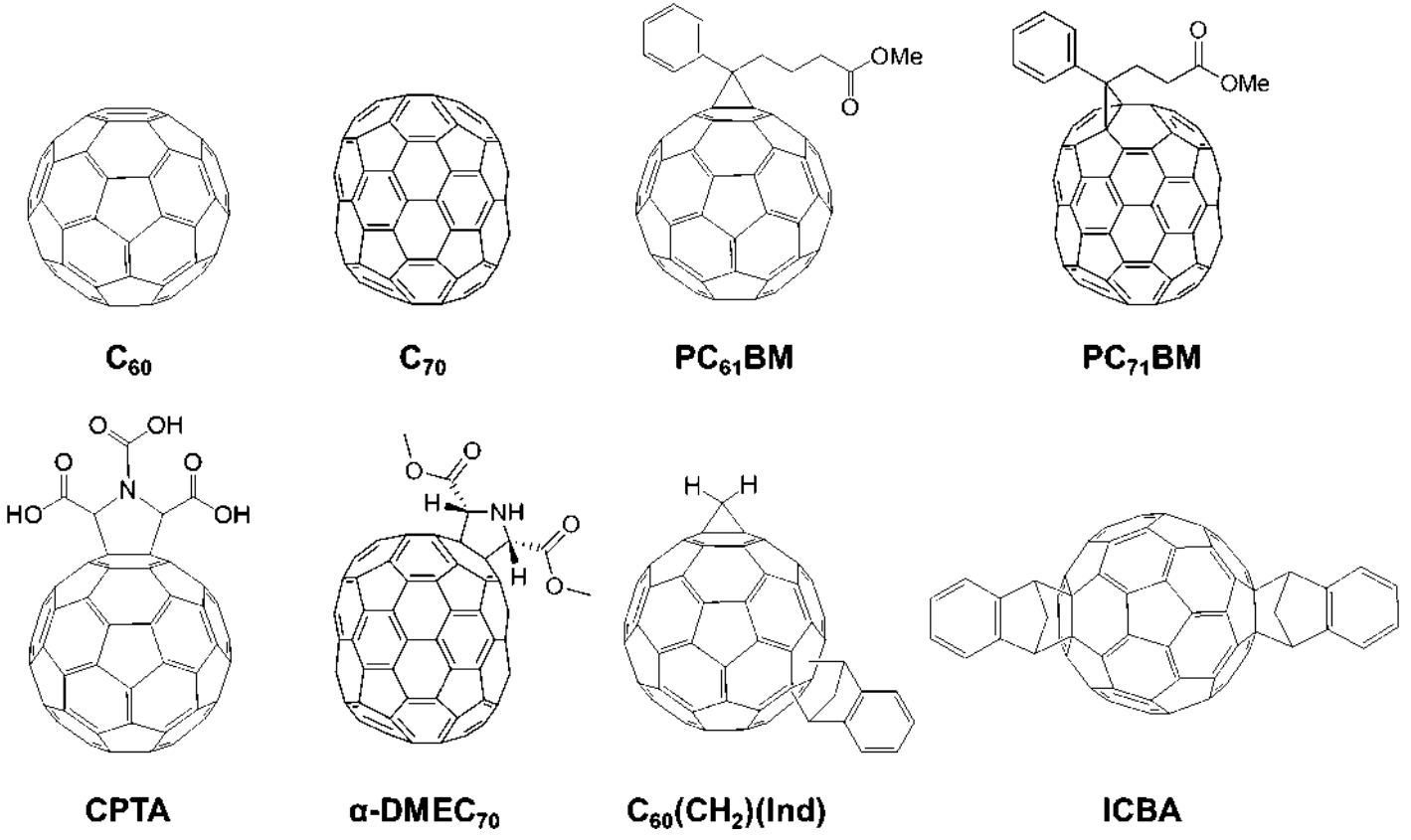

Fig. 13 Fullerenes applied as ETLs in PSCs

that even and uniform ETLs can be formed. Intriguingly, 10 wt % addition of C_{70} to C_{60} ETLs fabricated by spin-coating not only inhibited crystallization of the solution-processed C_{60} ETLs but also produced ETLs as uniform as the thermally deposited ETLs. Moreover, performance could be further improved by a vacuum-drying process to remove residual solvent from the spin-coating process; a vacuum-dry process was studied to remove the solvent residue to further enhance the performance of PSCs with solution-processed C_{60}:C_{70} ETLs. After the vacuum-drying treatment, the solution-processed C_{60}:C_{70} ETLs became denser and absorbed less light, leading to a higher PCE of 18.0% with significant improvement in all other photovoltaic parameters (V_{OC} = 1.03 V, J_{SC} = 24.3 mA cm^{-2}, and FF = 0.73). It should be noted that only pristine fullerenes such as C_{60} and C_{70} can be fabricated by thermal deposition, because fullerene derivatives usually decompose under the high-temperature conditions typically required for thermal deposition.

In addition to the extensive application of pristine fullerenes as ELTs in PSCs, fullerene derivatives have also been widely investigated as ETLs in PSCs. However, all examples of applying fullerene derivatives as ETLs have used a solution-based fabrication method because of the thermal instability of fullerene derivatives. For example, Han, Grätzel, and co-workers reported the use of $PC_{61}BM$ as an ETL in an inverted-type PSC with an architecture of FTO/NiMgLiO/$MAPbI_3$/$PC_{61}BM$/Ti(Nb)O_x/Ag, achieving a PCE of 16.2% with V_{OC} of 1.07 V, J_{SC} of 20.6 mA cm^{-2}, and FF of 0.75 [33]. Notably, the $MAPbI_3$/$PC_{61}BM$ interface was very efficient for electron extraction, resulting in the higher FF observed for this PSC. Additionally, $PC_{61}BM$ is much more soluble than C_{60} in all conventional organic solvents, which allow $PC_{61}BM$ to be formed in a dense uniform film via a simple spin-coating process. As in studies of OSCs, in which $PC_{61}BM$ ETLs were replaced with $PC_{71}BM$ ETLs in PSCs, the performance was further improved. Huang's group mixed three $PC_{71}BM$ stereoisomers together to form an integrated ETL in an inverted-type PSC with a device structure of ITO/poly(3,4-ethylenedioxythiophene) polystyrene sulfonate (PEDOT:PSS)/$MAPbI_3$/$PC_{71}BM$/Ca/Al [34]. The $PC_{71}BM$ PSCs demonstrated the best performance among the devices tested, with PCE of 20.1%, V_{OC} of 1.03 V, J_{SC} of 23.51 mA cm^{-2}, and FF of 0.83. However, this study mainly focused on optimization of the perovskite layer by using different amount of H_2O-doped $MAPbI_3$ to increase crystal size in order to decrease grain boundaries and reduce charge traps. Consequently, the superior characteristics of $PC_{71}BM$ were not discussed in detail, but at the very least PSCs with $PC_{71}BM$ ETLs showed better performance than PSCs with $PC_{61}BM$ ETLs.

Although [60]fulleropyrrolidine derivatives have been demonstrated to perform poorly in OSCs, they have shown considerable promise as electron transport materials in PSCs. The Fang group successfully synthesized a carboxyl-functionalized [60]fullerene, C_{60} pyrrolidine tris-acid (CPTA), and applied it as an ETL in a normal-type PSC with a conventional configuration of ITO/CPTA/$MAPbI_3$/Spiro-OMeTAD/Au [35]. PSCs with solution-processed CPTA ETLs exhibited a promising PCE of 18.4% with V_{OC} of 1.10 V, J_{SC} of 22.06 mA cm^{-2}, and FF of 0.76. Thanks to strong surface interaction between the carboxylic group of CPTA and the top surface of the ITO substrate, the surface roughness of the CPTA-coated ITO was

significantly decreased, becoming even smoother than the surface after $MAPbI_3$ film deposition. In addition, despite the LUMO level of CPTA (−3.91 eV) not being significantly different from that of $PC_{61}BM$, the electron mobility (μ_e) of CPTA ($\mu_e = 5.4 \times 10^{-3}$ cm^2 V^{-1} s^{-1}) was more than twice that of $PC_{61}BM$ ($\mu_e = 2.1 \times 10^{-3}$ cm^2 V^{-1} s^{-1}), which reasonably explains the better performance obtained when CPTA was applied as an ETL in PSCs. The steady-state photoluminescence (PL) quenching spectra showed that the CPTA ETLs had remarkably higher quenching efficiency than $PC_{61}BM$ ETLs. Taken together, these results show that the CPTA ETL was a more efficient charge separator due to its excellent interfacial contact, high electron mobility, and suitable energy band alignment. As in the case of replacing $PC_{61}BM$ with $PC_{71}BM$, PSC performance could be further improved when [60]fulleropyrrolidine ETLs were replaced with [70]fulleropyrrolidines ETLs. In 2017, Echegoyen and co-workers utilized a pure *cis*-*α*-dimethoxy carbonyl [70]fulleropyrrolidine (*α*-$DMEC_{70}$) as the ETL in an inverted-type PSC with a device architecture of ITO/PEDOT:PSS/$MAPbI_3$/*α*-$DMEC_{70}$/Al [36]. The PSCs with pure *α*-$DMEC_{70}$ ETLs exhibited a substantially enhanced PCE of 18.6% with V_{OC} of 1.02 V, J_{SC} of 22.90 mA cm^{-2}, and FF of 0.80. Notably, *α*-$DMEC_{70}$-based PSCs showed both higher J_{SC} and higher FF, which was associated with the higher electron mobility of *α*-$DMEC_{70}$. Also, *α*-$DMEC_{70}$-based PSCs showed a higher charge extraction efficiency, exceeding even that of $PC_{71}BM$-based PSCs. More importantly, when [60]fulleropyrrolidine ETLs were replaced with [70] fulleropyrrolidine ETLs, the PL quenching efficiency surpassed that of the $PC_{61}BM$ ETLs, which apparently contributed to further improvement of PSC performance. In contrast to the limited application of fulleropyrrolidines in OSCs, there are more examples of their successful use in PSCs giving improved performance. This is mainly due to the favorable low LUMO energy level of fulleropyrrolidine derivatives and their excellent electron transport ability. Notably, [70] fullerene derivatives demonstrated better performance than the corresponding [60]fullerene derivatives in both OSCs and PSCs. Thus, it is conceivable that [70] fullerene derivatives can potentially provide more advantages in applications if their limited availability and expensive processing can be addressed.

Aside from pristine fullerenes and fullerene monoadducts, fullerene bis-adducts have also been investigated, but there are only a few examples of favorable results. For example, $C_{60}(CH_2)$(Ind), which performed impressively in OSCs [14], was also studied as the ETL in an inverted-type PSC with a configuration of ITO/NiO/DEA/$MAPbI_3$/$C_{60}(CH_2)$Ind/PN4N/Ag by Yip, Matsuo, and co-workers [37]. PSCs using $C_{60}(CH_2)$Ind showed an increased PCE of 18.1% with V_{OC} of 1.13 V, J_{SC} of 20.4 mA cm^{-2}, and FF of 0.80. Although electron mobility was slightly lower for $C_{60}(CH_2)$(Ind) compared with $PC_{61}BM$, both V_{OC} and FF of PSCs using $C_{60}(CH_2)$(Ind) as the ETL were significantly increased. This was mainly attributed to more effectively suppressed trap-assisted charge recombination in the $C_{60}(CH_2)$(Ind) ETLs. In addition to the substantially enhanced PL quenching efficiency that $C_{60}(CH_2)$(Ind) ETLs provided, there was an obvious blueshift in the PL spectra, which apparently indicated a better passivation effect between the $C_{60}(CH_2)$(Ind) ETL and the perovskite layer. ICBA, another widely used fullerene material in

OSCs, was also investigated as an ETL in an inverted-type PSC with a device architecture of ITO/poly(triaryl amine) (PTAA)/$(FA_{0.83}MA_{0.17})_{0.95}Cs_{0.05}Pb(I_{0.6}Br_{0.4})_3$/ICBA/$C_{60}$/bathocuproine (BCP)/Cu by Huang's group. Considering the higher-lying LUMO energy level of ICBA, they used it as the ETL to boost efficiency by constructing an efficient wide-bandgap PSC. The PSCs with an ICBA ETL exhibited PCE of 18.3% with significantly enhanced V_{OC} of 1.20 V, J_{SC} of 19.7 mA cm^{-2}, and FF of 0.78 [38]. It is interesting that PSCs using both of these fullerene bis-adduct ETLs showed substantially higher V_{OC} values, which could be attributed to their high-lying LUMO energy level. Although it may seem that these satisfactory V_{OC} values of PSCs with fullerene ETLs are enhanced for the same reason as in OSCs, it remains unclear why V_{OC} can be increased by mismatched energy level with conduction band of the perovskite material. In addition, there is lack of subsequent research in which fullerene multi-adducts were used as ETLs in PSCs to achieve high PCE. In addition, both of the fullerene multi-adduct ETLs presented here had lower electron mobility when used as ETLs, which seriously limited further enhancement of performance even though V_{OC} was enhanced. Consequently, there is a strong need for further investigation of the fundamental theory explaining why fullerene multi-adduct ETLs improve PSC performance. For this reason, fullerene monoadducts are still preferred because of their high electron mobility for use as ETLs in PSCs.

Fullerenes as Overcoat Layers

Although much work has gone into developing fullerene ETLs for high-performance PSCs, it is still difficult to exceed the performance of PSCs with metal oxide ETLs, despite the inevitable problem of hysteresis when using metal oxides. Therefore, many groups have looked to the combined use of fullerene ETLs and metal oxide ETLs as a way to achieve hysteresis-free high-performance PSCs. For this purpose, the overcoat methodology was developed, and many fullerene derivatives have been investigated as overcoat materials (Fig. 14). In 2013, considering that the low electron mobility of a compact TiO_2 ETL causes charge recombination at the interface, Snaith's group was the first to use a [60]fulleropyrrolidine derivative as a fullerene overcoat layer on top of the TiO_2 ETL in a normal-type PSC [39]. The applied [60]fulleropyrrolidine was called a [60]fullerene self-assembled monolayer (C_{60}SAM) because it can effectively functionalize the surface of mesoporous TiO_2 or ZnO to enhance the photoinduced electron transfer. In that study, a normal-type PSC was constructed with a device structure of FTO/TiO_2/C_{60}SAM/$MAPbI_{3-x}Cl_x$/Spiro-OMeTAD/Ag, which exhibited a pioneering PCE of 11.7% with V_{OC} of 0.84 V, J_{SC} of 19.6 mA cm^{-2}, and FF of 0.72. This significantly surpassed the performance of the reference device without a C_{60}SAM overcoat layer, which exhibited PCE of 10.2%, V_{OC} of 0.82 V, J_{SC} of 19.4 mA cm^{-2}, and FF of 0.65. Although the performance was significantly improved, it was still far from the level needed for application in PSCs as a result of electron trapping in the C_{60}SAM overcoat film. Subsequently, Yan, Zhao, and co-workers successfully achieved a best PCE of 19.0% by using a C_{60}SAM overcoat in a normal-type PSC with a device architecture of FTO/SnO_2/C_{60}SAM/$MAPbI_3$ + $Pb(SCN)_2$/Spiro-OMeTAD/Au [40]. To avoid electron

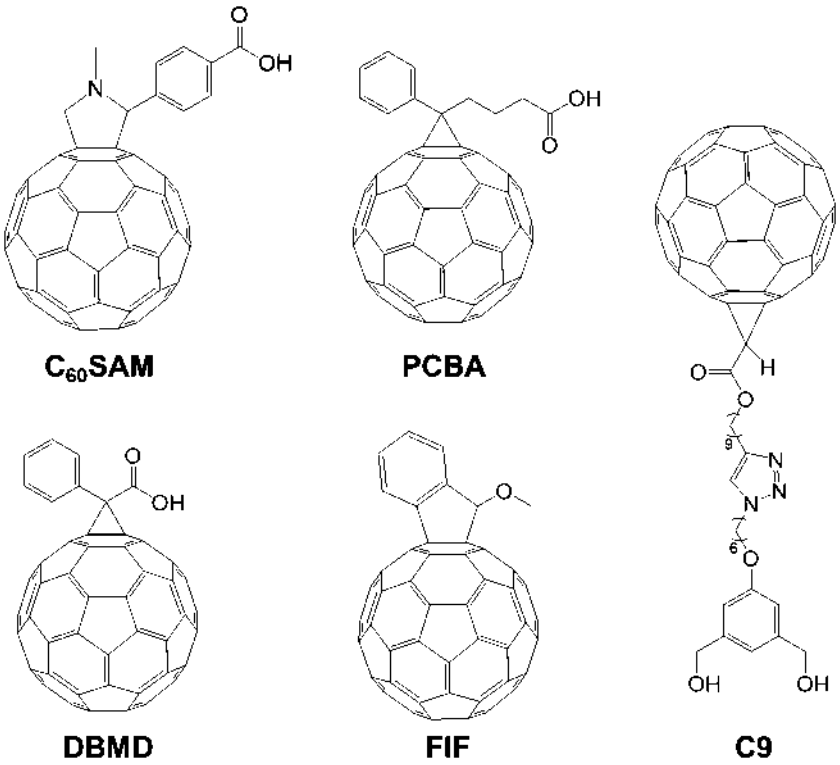

Fig. 14 Fullerenes applied as overcoats on the metal oxide layer in PSCs

trapping like that seen in the previous study, they applied C_{60}SAM as a very thin fullerene overcoat layer onto the top surface of SnO_2, which can both passivate the surface of metal oxide and effectively enhance charge transfer at metal oxide ETLs/perovskite interfaces. Accordingly, all photovoltaic parameters were significantly enhanced with V_{OC} of 1.13 V, J_{SC} of 21.35 mA cm^{-2}, and FF of 0.79. The perovskite film on C_{60}SAM/SnO_2 showed much higher PL quenching efficiency than that on bare SnO_2, clearly demonstrating that the C_{60}SAM overcoat improved electron extraction from the perovskite layer. Notably, the PSCs showed negligible hysteresis, which is compelling evidence for the advantages of combining fullerenes and metal oxides.

PCBM derivatives are other fullerene derivatives that can be used for overcoat to enhance the performance of PSCs. Let us consider the most commercially available PCBM derivative, $PC_{61}BM$, as an example. The successful use of $PC_{61}BM$ as an overcoat in PSCs was successfully demonstrated by Lee's group in 2014 [41]. They deposited $PC_{61}BM$ onto sol-gel ZnO in a normal-type PSC with a device configuration of ITO/ZnO/$PC_{61}BM$/$MAPbI_3$/PTB7-Th/MoO_3/Ag. The PSC with a $PC_{61}BM$ overcoat showed a promising PCE of 11.0% with V_{OC} of 1.03 V, J_{SC} of 15.10 mA cm^{-2}, and FF of 0.71. Both high V_{OC} and high FF were attributed to the more favorable energy-level alignment of $PC_{61}BM$/ZnO at the interfaces, which

were effectively facilitating cascade charge extraction from the $PC_{61}BM$/ZnO film. Although the first PSCs with a $PC_{61}BM$ overcoat outperformed the first ones with a [60]fulleropyrrolidine overcoat, this level of performance was still too low for actual application in the PSC industry. Three years later, Yan and co-workers elegantly utilized $Pb(SCN)_2$-doped $MAPbI_3$ in a $PC_{61}BM$ overcoat PSC with an optimized device structure of FTO/SnO_2/$PC_{61}BM$/$MAPbI_3$ + $Pb(SCN)_2$/Spiro-OMeTAD/Au [42]. The performance of this $PC_{61}BM$ overcoat PSC was further enhanced to a remarkably high PCE of 19.5% with V_{OC} of 1.11 V, J_{SC} of 22.44 mA cm^{-2}, and FF of 0.77, which was reasonably attributed to the large perovskite crystal size and decreased grain boundaries of the doped $Pb(SNC)_2$. $PC_{61}BM$ can be readily applied as a fullerene overcoat on metal oxide ETLs to further enhance the performance of PSCs, owing to its efficient electron extraction capability, and favorable energy-level alignment. Aside from $PC_{61}BM$, other PCBM derivatives elegantly designed for PSCs have been reported. In 2015, Yang, Li, and co-workers successfully synthesized the PCBM analogue [6,6]-phenyl-C_{61}-butyric acid-dioctyl-3,3′-(5-hydroxy-1,3-phenylene)-bis(2-cyanoacrylate) ester (PCBB-2CN-2C8) [43]. To evaluate its performance as an overcoat on a TiO_2 ETL, they utilized a normal-type PSC with a device architecture of ITO/TiO_2/PCBB-2CN-2C8/$MAPbI_{3-x}Cl_x$/Spiro-OMeTAD/Au. The PCBB-2CN-2C8 overcoat device demonstrated a high PCE of 16.8% with V_{OC} of 1.06 V, J_{SC} of 20.68 mA cm^{-2}, and FF of 0.79. Like other fullerene overcoats, the PCBB-2CN-2C8 overcoat enhanced charge extraction from the perovskite layer and also improved the perovskite film quality, increasing the crystal size and reducing grain boundaries through the surface passivation effect. Intriguingly, when the methyl ester in $PC_{61}BM$ was hydrolyzed to its acid form, the resulting [6,6]-phenyl-C_{61}-butyric acid (PCBA) can effectively bond to the surface of a TiO_2 ETL [44]. A normal-type device with the structure FTO/TiO_2/PCBA/$MAPbI_3$/Spiro-OMeTAD/Ag exhibited a substantially improved PCE of 17.8% with V_{OC} of 1.16 V, J_{SC} of 21.38 mA cm^{-2}, and FF of 0.72. The V_{OC} value of the PCBA overcoat device was much larger than that of the $PC_{61}BM$ overcoat device, which was clearly attributable to the much stronger interaction between PCBA and the top surface of TiO_2 effectively reducing the recombination of holes at the TiO_2/perovskite interface. Additionally, PCBA also can improve the perovskite film quality, enabling better performance of the overall device. It is worth noting that more PCBM derivatives have successfully achieved high performance in PSCs compared with the limited number of examples in OSCs, which also suggested that different photovoltaics require fullerene derivatives designed to have different properties.

The three-membered carbon ring in $PC_{61}BM$ is a key structural unit that provides a handle for further synthetic modification. Many groups have utilized this ring to develop various promising fullerene materials for PSCs. In 2016, Bo's group reported a thermo-cleavable fullerene derivative, di-*tert*-butyl methano[60]fullerene-61,61-dicarboxylate (DBMD) [45]. DBMD was applied as a fullerene overcoat on TiO_2 in a normal-type PSC with a device structure of FTO/TiO_2/DBMD/$MAPbI_3$/Spiro-OMeTAD/Ag. The DBMD overcoat device exhibited a PCE of 17.1% with V_{OC} of 1.17 V, J_{SC} of 20.6 mA cm^{-2}, and FF of 0.71. Notably, the V_{OC} value of the device using DBMD was as high as that of devices using other

PCBM derivatives, which clearly show the effectiveness of utilizing the methano building block in PSCs. Later on, the Zhan group demonstrated the highest PCE yet in a PSC with a fullerene overcoat [5]. They designed a long-chain fullerene derivative, called C9, with two hydroxyl groups as anchors for surface modification of the SnO_2 layer. C9 had a suitable LUMO energy level and high electron affinity, which enhanced the extraction of electrons from the perovskite layer and efficiently transferred them to the SnO_2 ETL. Thanks to the elegant introduction of the hydroxyl groups, oxygen vacancies at the SnO_2 surface could be effectively passivated to further improve the electron transport ability of SnO_2. Meanwhile, the C9 overcoat layer efficiently enhanced interfacial charge extraction, thus reducing trap-assisted charge recombination. Moreover, C9 can also function as a perovskite growth template, which substantially improved the quality of perovskite layer by enlarging grain size, reducing grain boundaries, and improving the crystallinity of the film. As a result, a normal-type PSC with a device structure of ITO/SnO_2/C9/$(FAPbI_3)_x(MAPbBr_3)_{1-x}$/Spiro-OMeTAD/Au exhibited a highest PCE of 21.3% with V_{OC} of 1.12 V, J_{SC} of 24.1 mA cm^{-2}, and FF of 0.79.

Interestingly, all fullerene derivatives used in OSCs and PSCs have a cyclic unit in their structure. Notably, cyclo[60]fullerene derivatives with a full-carbon ring structure, such as $PC_{61}BM$, ICBA, MIF, and C9, have outperformed those with a heterocyclic structure, such as [60]fulleropyrrolidine derivatives. However, for cyclo[60]fullerene derivatives with a full-carbon ring structure, only three-membered rings had been reported, with no study investigating cyclo[60]fullerenes with a five-membered carbon ring. The main obstacle was a lack of accessible synthetic methodology for constructing cyclo[60]fullerenes with a five-membered carbon ring. In 2019, Lin, Matsuo, and co-workers successfully developed a fullerene cation-mediated synthetic protocol to produce a series of cyclo[60]fullerenes with a five-membered carbon ring, which were denoted as full-carbon indene[60]fullerenes (FIFs) [46]. They demonstrated the application of FIFs as an overcoat layer in normal-type PSCs with a device structure of ITO/SnO_2/FIF/$MAPbI_3$/Spiro-OMeTAD/Au, achieving a highest PCE of 20.7% with V_{OC} of 1.09 V, J_{SC} of 23.7 mA cm^{-2}, and FF of 0.79. This high performance reflected the excellent properties of FIF. For instance, the ether unit in FIF substantially contributed to the passivation of the perovskite layer, which enhanced both electron extraction from the perovskite layer and the growth of large-crystal perovskite with reduced grain boundaries and reduced electron-trap density. More importantly, although fullerene monoadducts generally have lower electron mobility owing to their increased LUMO energy level compared with the pristine fullerenes, FIF showed no significant decrease in electron mobility compared with that of pristine [60]fullerene. Accordingly, we can conclude that FIF is capable of not only efficient electron extraction from the perovskite layer but also fast transfer of electrons to the SnO_2 ETL.

In general, although only selected examples are discussed in this section, it bears emphasis that all fullerene derivative overcoats on metal oxide ETLs can reproducibly enhance the performance of PSCs with neglectable hysteresis. In contrast to the use of fullerene derivatives as a single ETL in PSCs, the fullerene overcoat strategy

does not require high solubility of the fullerene derivatives because of only a thin layer is applied. However, further consideration is needed of specific aspects, such as functional groups (hydroxyl-, carboxylic-, amino-, etc.) to improve the passivation effect and electron extraction ability. There are still other avenues to explore for fullerene derivative overcoats in PSCs, and this is a promising area of future research.

Fullerenes as Dopants

Recently developed doping methodology has further broadened the scope of applying fullerene materials in PSCs. As the availability of fullerene materials is still limited, especially for endohedral fullerenes, the doping method immediately attracted considerable attention because it requires only trace amounts of fullerene materials for application in PSCs. In an unprecedented development, even trace amounts of fullerene dopants can produce dramatic improvements in PSC performance. Also, the doping strategy can be effectively applied to all three layers: the active layer, the ETL, and the HTL. In this section, we discuss three representative examples selected to demonstrate the application of fullerenes as dopants in PSCs. For instance, $PC_{61}BM$ can also be doped into the perovskite active layer. In 2016, Wu and Chiang presented an inverted-type $PC_{61}BM$-doped PSC with a device structure of ITO/PEDOT:PSS/$PC_{61}BM$-$CH_3NH_3PbI_3$/Ca/$PC_{71}BM$/Al [47]. The PSCs 0.1 wt % $PC_{61}BM$ doping in the active layer demonstrated a significantly increased PCE of 16.0% with V_{OC} of 0.97 V, J_{SC} of 20.2 mA cm^{-2}, and FF of 0.82 compared with the corresponding non-doped PSCs, which exhibited PCE of 11.4% with V_{OC} of 0.95 V, J_{SC} of 16.2 mA cm^{-2}, and FF of 0.73. All photovoltaic parameters were substantially enhanced. The increased J_{SC} value was mainly due to increased light absorption by $PC_{61}BM$-doped perovskite layer, which is resulted from the strong absorption of $PC_{61}BM$ in a range 400–700 nm. The enhanced FF value was achieved through the increased perovskite crystal size and efficient electron transport. Through the effects of doping, the perovskite layer had a larger crystal size, reduced grain boundaries, and decreased electron-trapping sites. In addition, the steady-state PL quenching spectra clearly showed that the 0.1 wt % $PC_{61}BM$-doped perovskite film had much better quenching efficiency than the non-doped perovskite film, demonstrating the improved electron transport in the $PC_{61}BM$-doped perovskite film. However, further increasing the doping concentration to 1.0 wt % $PC_{61}BM$ dramatically undermined device performance, which was ascribed to the poor solubility of $PC_{61}BM$ in the perovskite precursor solution, and the perovskite precursor solution with an overly high $PC_{61}BM$ concentration could not produce a dense perovskite film, and the grain boundaries were larger. Given that $MAPbI_3$ contains an amino group in its structure, many amines have been investigated as dopants in $MAPbI_3$-based PSCs. Recently, Matsuo's group investigated the use of an amino[60]fullerene derivative as a dopant in an inverted-type $MAPbI_3$-based PSC with a device architecture of ITO/PEDOT:PSS/amino[60]fullerene-$MAPbI_3$/C_{60}/BCP/Ag [48]. The fabricated device exhibited slightly improved PCE of 13.5% with V_{OC} of 0.93 V, J_{SC} of 20.2 mA cm^{-2}, and FF of 0.74. As in the study of $PC_{61}BM$-doped PSCs, both J_{SC} and FF were improved by the increased light

absorption of the amino[60]fullerene-doped perovskite film. Therefore, doping the perovskite layer with a trace amount of fullerene derivative can generally realize larger perovskite crystals and enhanced light absorption by the perovskite film to generate more photoelectrons.

Endohedral fullerenes have also been doped into the ETL to enhance PSC performance. In 2019, Matsuo and co-workers reported the application of a Li@C_{60}-doped C_{60} ETL in an inverted-type PSC with a device structure of ITO/PEDOT:PSS/$MAPbI_3$/Li@C_{60}-doped C_{60}/Au [49]. The Li@C_{60}-doped PSC exhibited an improved PCE of 8.2% with V_{OC} of 0.86 V, J_{SC} of 16.7 mA cm^{-2}, and FF of 0.57 compared with a reference PSC that exhibited a PCE of 4.7%. However, the overall device performance was low compared with PSCs in general, which was attributed to the mismatched structure used in the device. Conventionally, the top electrode of a normal-type PSC is composed of Au, which has the lowest work function for collecting holes from the HTL, and the top electrode of an inverted-type PSC is composed of BCP/Ag, which has the highest work function for collecting electrons from the ETL. In this example, however, an Au electrode was mistakenly used in an inverted-type PSC, predictably resulting in low performance. Comparison between the performance of PSC with the Li@C_{60}-doped C_{60} ETL and that of the PSC with the C_{60} ETL nonetheless provides some insights. Doping with Li@C_{60} substantially increased V_{OC}, which was attributed to the better alignment between the Fermi level of the C_{60} ETL and the conductive band of the perovskite layer. Additionally, the steady-state PL quenching spectra clearly showed that the Li@C_{60}-doped C_{60} film had much better quenching efficiency, indicating that Li@C_{60} conclusively enhanced the electron transport ability of the C_{60} film.

Fullerenes are conventionally used as electron acceptors in OSCs and electron transport materials in PSCs. Notably, with the advent of endohedral metallic fullerenes, the electronic properties of fullerene can be significantly modified by the encapsulated metal. Accordingly, cutting-edge studies have recently succeeded in using endohedral fullerenes in the HTL for the first time. In 2018, Jeon, Matsuo, and co-workers reported the first investigation of Li@C_{60}TFSI as a p-dopant in Spiro-OMeTAD to replace the conventional p-dopant LiTFSI in PSCs [50]. The tested PSC with a structure of FTO/C_{60}/$MAPbI_3$/Li@C_{60}TFSI-doped Spiro-OMeTAD/Au exhibited a low PCE of 13.1% (V_{OC} = 0.89 V, J_{SC} = 22.2 mA cm^{-2}, FF = 0.72) compared with the conventional LiTFSI-doped Sprio-OMeTAD with a PCE of 17.0% but achieved stability approximately seven-fold than that of the conventional PSCs. Moreover, when the perovskite layer was replaced by a mixed halide perovskite $(FAPBI_3)_{0.85}(MAPbBr_3)_{0.15}$, the performance substantially improved, giving a PCE of 16.8% with V_{OC} of 1.01 V, J_{SC} of 22.9 mA cm^{-2}, and FF of 0.72, though its performance was still worse than that of a reference device with PCE of 18.5%. However, the stability of the PSC with $(FAPbI_3)_{0.85}(MAPbBr_3)_{0.15}$ was further enhanced to ten-fold than that of reference devices. This high stability of the PSC using Li@C_{60}TFSI as a dopant was ascribed to Li@C_{60}TFSI, serving as an antioxidant to prevent unnecessary oxidation in the device system. Therefore, endohedral metallic fullerenes provide a potentially useful doping strategy for addressing the problem of PSC stability (Fig. 15).

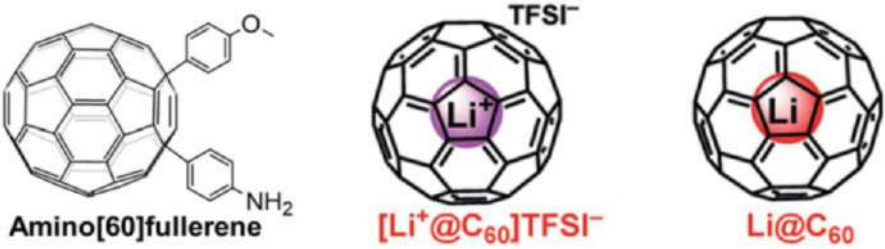

Fig. 15 Fullerenes used as dopants in PSCs

To briefly summarize, fullerene and its derivatives have shown remarkable advantages in the rapidly developing area of PSC research in recent years. In contrast to the limited applications of fullerenes in OSCs, a wide range of applications in PSCs are possible, including as the ETL, as an overcoat on the metal oxide ETL, and as a dopant for improving PSC performance. Among these applications, fullerene overcoats showed by far the best performance, owing to this strategy combining the advantages of both fullerene derivatives and metal oxides. Fullerene and its derivatives are well known for their high electron affinity and extremely fast electron transport, which thus provided hysteresis-free PSCs. Unlike fullerene materials, metal oxides are typically used as ETLs in PSCs because of their impressively fast electron transport, which allows for extremely high PCE but often suffers from the problem of severe hysteresis. Through the overcoating of fullerene materials on metal oxides, PSCs can achieve high PCE with negligible hysteresis. In addition to the doping strategy, fullerenes have been widely studied as single ETLs in PSCs. In particular, pristine fullerenes such as C_{60} and C_{70} are frequently applied in inverted-type PSCs by thermal deposition, primarily due to their compatibility with this facile fabrication process. However, normal-type PSCs seldom use fullerene materials as ETLs, owing to the low PCE provided by fullerene ETLs, so fullerene ETLs have received relatively little attention compared with metal oxide ETLs. Notably, both fullerene overcoats and fullerene ETLs are placed just below the perovskite layer, where they have a clear impact on perovskite crystal growth. Through the good molecular design of passivating functional groups, it is possible to improve work function, enhance electron extraction ability, increase perovskite crystal size, reduce grain boundaries, and lower electron-trap density, leading to better PSC performance. Apart from the two abovementioned approaches, the doping strategy has been established through substantial advances in device engineering. In particular, this strategy broadens the scope of applying endohedral fullerenes in PSCs, because only trace amounts of materials are required, which is a definite advantage considering the limited availability of endohedral fullerenes. Although the doping strategy can effectively enhance the performance of PSCs, it cannot increase the efficiency as much as the other two methods. This is because the core of PSCs is still defined by the perovskite active layer, the ETL, and the HTL and the scope for optimizing the dopants present in trace amounts is still limited. Nevertheless, the doping strategies led to some interesting results. For example, it was found that Li@C_{60}TFSI

functions well as a dopant in the HTL to improve the stability of PSCs. For quick reference, Table 2 provides a summary of the application of fullerenes in PSCs. We hope that this section will serve as a useful reference and guide for the further development of fullerene materials in PSCs.

Challenges and Prospects

To conclude this chapter, we discuss the current challenges and prospects of applying fullerene in the photovoltaic industry. In the past three decades, fullerene chemistry and materials science have rapidly advanced and so has the application of fullerene materials in photovoltaics. However, fullerene materials science is now faced with the most serious challenges in its history. In OSC research, the rapid development of non-fullerene acceptors that have much better performance, with PCEs often exceeding 10% in a single cell, has resulted in a shift away from fullerene research. Consequently, the development of fullerene acceptors in OSCs has suddenly slowed to a crawl. Although non-fullerene electron acceptors in OSCs have shown better performance than fullerene electron acceptors, they have a greater number of practical issues for industrial application, such as complicated synthesis and isolation procedures and poor stability, especially for the low bandgap non-fullerene acceptors. This has inevitably limited their industrial applications in real photovoltaics. Yet, despite the comparatively low PCE of fullerene electron acceptors, their reliable synthesis and high stability have definitely helped fullerene electron acceptors maintain their dominant position in the OSC industry. This shows that in actual practice, the OSC industry requires more than a race to improve PCE, and there is still room for the development of fullerene electron acceptors in applications such as flexible OSCs and wearable devices. In a positive development, the emergence of PSCs has helped fullerene materials return to the forefront of photovoltaic research. Nevertheless, we must temper our excitement, because the challenges facing fullerene applications in PSCs are even greater than those in OSCs. Although PSCs are well known for their impressive PCEs and innumerable researchers have moved into PSC research to chase after ever higher PCEs, when the issue of stability is raised, most PSC researchers are at a loss for words. There are no doubt more opportunities for breakthroughs through the use of fullerene materials in PSCs, but we should remember that not every breakthrough is a higher PCE. It should be emphasized that the strategies for investigating fullerene applications in PSCs cannot simply use the same ideas from OSC research. Doing so would be counterproductive. Although $PC_{61}BM$ showed excellent performance in both OSCs and PSCs, this case is more than likely just a happy coincidence. When $PC_{61}BM$ is used in OSCs and PSCs, it performed well for completely different reasons in each. In OSCs, the LUMO energy level, which relates to V_{OC}, was the most important consideration. In PSCs, on the other hand, the major concern was electron transport ability, which relates to good performance in terms of electron transfer and electron extraction. Generally, increasing the LUMO energy level of the electron acceptor in an OSC leads to an immediate increase in V_{OC}. However, increasing the LUMO

Table 2 Summary of the PSCs using fullerene derivatives

Application method	Device structure	V_{OC} (V)	J_{SC} (mA cm^{-2})	FF	PCE (%)	Ref.
Fullerene ETLs	FTO/**C_{60}**/$MAPbI_3$/Spiro-OMeTAD/Au	1.10	18.9	0.75	15.7	[31]
	FTO/**C_{70}**/$MAPbI_3$/Spiro-OMeTAD/Au	1.03	18.6	0.78	14.9	
	ITO/**C_{60}:C_{70}**/$MAPbI_3$/Spiro-OMeTAD/Au	1.03	24.3	0.73	18.0	[32]
	FTO/NiMgLiO/$MAPbI_3$/**$PC_{61}BM$**/Ti(Nb)O_x/Ag	1.07	20.6	0.75	16.2	[33]
	ITO/PEDOT:PSS/$MAPbI_3$/**$PC_{71}BM$**/Ca/Al	1.03	23.5	0.83	20.1	[34]
	ITO/**CPTA**/$MAPbI_3$/Spiro-OMeTAD/Au	1.10	22.1	0.76	18.4	[35]
	ITO/PEDOT:PSS/$MAPbI_3$/**α-DMEC$_{70}$**/Al	1.02	22.9	0.80	18.6	[36]
	ITO/NiO/DEA/$MAPbI_3$/**$C_{60}(CH_2)$(Ind)**/PN4N/Ag	1.13	20.4	0.80	18.1	[37]
	ITO/PTAA/$(FA_{0.83}MA_{0.17})_{0.95}Cs_{0.05}Pb(I_{0.6}Br_{0.4})_3$/**ICBA/$C_{60}$**/BCP/Cu	1.20	19.7	0.78	18.3	[38]
Fullerene overcoat	FTO/TiO_2/**C_{60}SAM**/$MAPbI_{3-x}Cl_x$/Spiro-OMeTAD/Ag	0.84	19.6	0.72	11.7	[39]
	FTO/SnO_2/**C_{60}SAM**/$MAPbI_3$+$Pb(SCN)_2$/Spiro-OMeTAD/Au	1.13	21.4	0.79	19.0	[40]
	ITO/ZnO/**$PC_{61}BM$**/$MAPbI_3$/PTB7-Th/MoO_3/Ag	1.03	15.1	0.71	11.0	[41]
	FTO/SnO_2/**$PC_{61}BM$**/$MAPbI_3$+$Pb(SCN)_2$/Spiro-OMeTAD/Au	1.11	22.4	0.77	19.5	[42]
	ITO/TiO_2/**PCBB-2CN-2C8**/$MAPbI_{3-x}Cl_x$/Spiro-OMeTAD/Au	1.06	20.7	0.79	16.8	[43]
	FTO/TiO_2/**PCBA**/$MAPbI_3$/Spiro-OMeTAD/Ag	1.16	21.4	0.72	17.8	[44]
	FTO/TiO_2/**DBMD**/$MAPbI_3$/Spiro-OMeTAD/Ag	1.17	20.6	0.71	17.1	[45]
	ITO/SnO_2/**C9**/$(FAPbI_3)_x(MAPbBr_3)_{1-x}$/Spiro-OMeTAD/Au	1.12	24.1	0.79	21.3	[5]
	ITO/SnO_2/**FIF**/$MAPbI_3$/Spiro-OMeTAD/Au	1.09	23.7	0.79	20.7	[46]
Fullerene dopant	ITO/PEDOT:PSS/**$PC_{61}BM$**-$MAPbI_3$/Ca/$PC_{71}BM$/Al	0.97	20.2	0.82	16.0	[47]
	ITO/PEDOT:PSS/**aminoC$_{60}$**-$MAPbI_3$/C_{60}/BCP/Ag	0.93	20.2	0.74	13.5	[48]
	ITO/PEDOT:PSS/$MAPbI_3$/**Li@C$_{60}$**-C_{60}/Au	0.86	16.7	0.57	8.2	[49]
	FTO/C_{60}/$MAPbI_3$/**Li@C$_{60}$TFSI**-Sprio-OMeTAD/Au	0.89	22.2	0.72	13.1	[50]
	FTO/C_{60}/$(FAPbI_3)_{0.85}(MAPbBr_3)_{0.15}$/**Li@C$_{60}$TFSI**-Sprio-OMeTAD/Au	1.01	22.9	0.72	16.8	

energy level of the ETL material in PSCs will raise the barrier to electron transfer from the perovskite layer, which may decrease the efficiency of the ELT and undermine performance. Therefore, the fullerene materials used in OSCs and those used in PSCs should be considered independently. In closing, we hope that this chapter has provided an up-to-date understanding of fullerene photovoltaic applications and clarified their advanced technologies not only for researchers currently engaged in this area but also prospective researchers.

References

1. Rabenau T, Simon A, Kremer RK, Sohmen E (1993) The energy gaps of fullerene C60 and C70 determined from the temperature dependent microwave conductivity. Zeitschrift für Physik B Condensed Matter 90(1):69–72. https://doi.org/10.1007/BF01321034
2. Brabec CJ, Sariciftci NS, Hummelen JC (2001) Plastic solar cells. Adv Funct Mater 11(1):15–26. https://doi.org/10.1002/1616-3028(200102)11:1<15::Aid-adfm15>3.0.Co;2-a
3. Hiroshi I, Kiyoshi H, Tsuyoshi A, Masanori A, Seiji T, Tadashi O, Masahiro S, Yoshiteru S (1996) The small reorganization energy of C60 in electron transfer. Chem Phys Lett 263(3):545–550. https://doi.org/10.1016/S0009-2614(96)01244-4
4. Yu G, Gao J, Hummelen JC, Wudl F, Heeger AJ (1995) Polymer photovoltaic cells: enhanced efficiencies via a network of internal donor-acceptor heterojunctions. Science 270(5243):1789. https://doi.org/10.1126/science.270.5243.1789
5. Liu K, Chen S, Wu J, Zhang H, Qin M, Lu X, Tu Y, Meng Q, Zhan X (2018) Fullerene derivative anchored SnO2 for high-performance perovskite solar cells. Energy Environ Sci 11(12):3463–3471. https://doi.org/10.1039/C8EE02172D
6. Castro E, Murillo J, Fernandez-Delgado O, Echegoyen L (2018) Progress in fullerene-based hybrid perovskite solar cells. J Mater Chem C 6(11):2635–2651. https://doi.org/10.1039/C7TC04302C
7. Collavini S, Delgado JL (2018) Fullerenes: the stars of photovoltaics. Sustain Energy Fuels 2(11):2480–2493. https://doi.org/10.1039/c8se00254a
8. Gatti T, Menna E, Meneghetti M, Maggini M, Petrozza A, Lamberti F (2017) The renaissance of fullerenes with perovskite solar cells. Nano Energy 41:84–100. https://doi.org/10.1016/j.nanoen.2017.09.016
9. Mishra A, Bäuerle P (2012) Small molecule organic semiconductors on the move: promises for future solar energy technology. Angew Chem Int Ed 51(9):2020–2067. https://doi.org/10.1002/anie.201102326
10. Lo Piano S, Mayumi K (2017) Toward an integrated assessment of the performance of photovoltaic power stations for electricity generation. Appl Energy 186:167–174. https://doi.org/10.1016/j.apenergy.2016.05.102
11. Fagan PJ, Calabrese JC, Malone B (1991) The chemical nature of buckminsterfullerene (C60) and the characterization of a platinum derivative. Science 252(5009):1160. https://doi.org/10.1126/science.252.5009.1160
12. Potscavage WJ, Sharma A, Kippelen B (2009) Critical interfaces in organic solar cells and their influence on the open-circuit voltage. Acc Chem Res 42(11):1758–1767. https://doi.org/10.1021/ar900139v
13. He Y, Chen H-Y, Hou J, Li Y (2010) Indene−C60 Bisadduct: a new acceptor for high-performance polymer solar cells. J Am Chem Soc 132(4):1377–1382. https://doi.org/10.1021/ja908602j
14. Matsuo Y, Kawai J, Inada H, Nakagawa T, Ota H, Otsubo S, Nakamura E (2013) Addition of dihydromethano group to fullerenes to improve the performance of bulk heterojunction organic solar cells. Adv Mater 25(43):6266–6269. https://doi.org/10.1002/adma.201302607

15. He D, Du X, Xiao Z, Ding L (2014) Methanofullerenes, C60(CH2)n (n = 1, 2, 3), as building blocks for high-performance acceptors used in organic solar cells. Org Lett 16(2):612–615. https://doi.org/10.1021/ol4035275
16. Li W, Cai J, Cai F, Yan Y, Yi H, Gurney RS, Liu D, Iraqi A, Wang T (2018) Achieving over 11% power conversion efficiency in PffBT4T-2OD-based ternary polymer solar cells with enhanced open-circuit-voltage and suppressed charge recombination. Nano Energy 44:155–163. https://doi.org/10.1016/j.nanoen.2017.12.005
17. Kroto HW (1987) The stability of the fullerenes Cn, with n = 24, 28, 32, 36, 50, 60 and 70. Nature 329(6139):529–531. https://doi.org/10.1038/329529a0
18. Troshin PA, Hoppe H, Renz J, Egginger M, Mayorova JY, Goryachev AE, Peregudov AS, Lyubovskaya RN, Gobsch G, Sariciftci NS, Razumov VF (2009) Material solubility-photovoltaic performance relationship in the Design of Novel Fullerene Derivatives for bulk heterojunction solar cells. Adv Funct Mater 19(5):779–788. https://doi.org/10.1002/adfm.200801189
19. Mikroyannidis JA, Kabanakis AN, Sharma SS, Sharma GD (2011) A simple and effective modification of PCBM for use as an electron acceptor in efficient bulk heterojunction solar cells. Adv Funct Mater 21(4):746–755. https://doi.org/10.1002/adfm.201001807
20. Kim HU, Kim J-H, Kang H, Grimsdale AC, Kim BJ, Yoon SC, Hwang D-H (2014) Naphthalene-, anthracene-, and pyrene-substituted fullerene derivatives as electron acceptors in polymer-based solar cells. ACS Appl Mater Interfaces 6(23):20776–20785. https://doi.org/10.1021/am504939c
21. Matsumoto K, Hashimoto K, Kamo M, Uetani Y, Hayase S, Kawatsura M, Itoh T (2010) Design of fulleropyrrolidine derivatives as an acceptor molecule in a thin layer organic solar cell. J Mater Chem 20(41):9226–9230. https://doi.org/10.1039/C0JM01565B
22. Matsuo Y, Sato Y, Niinomi T, Soga I, Tanaka H, Nakamura E (2009) Columnar structure in bulk heterojunction in solution-processable three-layered p-i-n organic photovoltaic devices using tetrabenzoporphyrin precursor and Silylmethyl[60]fullerene. J Am Chem Soc 131(44):16048–16050. https://doi.org/10.1021/ja9048702
23. Matsuo Y, Ozu A, Obata N, Fukuda N, Tanaka H, Nakamura E (2012) Deterioration of bulk heterojunction organic photovoltaic devices by a minute amount of oxidized fullerene. Chem Commun 48(32):3878–3880. https://doi.org/10.1039/C2CC30262D
24. Zhang Y, Matsuo Y, Li C-Z, Tanaka H, Nakamura E (2011) A scalable synthesis of Methano[60]fullerene and congeners by the oxidative cyclopropanation reaction of silylmethylfullerene. J Am Chem Soc 133(21):8086–8089. https://doi.org/10.1021/ja201267t
25. Lenes M, Wetzelaer G-JAH, Kooistra FB, Veenstra SC, Hummelen JC, Blom PWM (2008) Fullerene bisadducts for enhanced open-circuit voltages and efficiencies in polymer solar cells. Adv Mater 20(11):2116–2119. https://doi.org/10.1002/adma.200702438
26. Singh SP, Kumar CHP, Sharma GD, Kurchania R, Roy MS (2012) Synthesis of a modified PC70BM and its application as an electron acceptor with poly(3-hexylthiophene) as an Electron donor for efficient bulk heterojunction solar cells. Adv Funct Mater 22(19):4087–4095. https://doi.org/10.1002/adfm.201200729
27. Ross RB, Cardona CM, Guldi DM, Sankaranarayanan SG, Reese MO, Kopidakis N, Peet J, Walker B, Bazan GC, Van Keuren E, Holloway BC, Drees M (2009) Endohedral fullerenes for organic photovoltaic devices. Nat Mater 8:208. https://doi.org/10.1038/nmat2379. https://www.nature.com/articles/nmat2379#supplementary-information
28. Kojima A, Teshima K, Shirai Y, Miyasaka T (2009) Organometal halide perovskites as visible-light sensitizers for photovoltaic cells. J Am Chem Soc 131(17):6050–6051. https://doi.org/10.1021/ja809598r
29. Lang L, Yang J-H, Liu H-R, Xiang HJ, Gong XG (2014) First-principles study on the electronic and optical properties of cubic ABX3 halide perovskites. Phys Lett A 378(3):290–293. https://doi.org/10.1016/j.physleta.2013.11.018
30. Chueh C-C, Li C-Z, Jen AKY (2015) Recent progress and perspective in solution-processed interfacial materials for efficient and stable polymer and organometal perovskite solar cells. Energy Environ Sci 8(4):1160–1189. https://doi.org/10.1039/C4EE03824J

31. Zhao D, Ke W, Grice CR, Cimaroli AJ, Tan X, Yang M, Collins RW, Zhang H, Zhu K, Yan Y (2016) Annealing-free efficient vacuum-deposited planar perovskite solar cells with evaporated fullerenes as electron-selective layers. Nano Energy 19:88–97. https://doi.org/10.1016/j.nanoen.2015.11.008
32. Lin H-S, Jeon I, Xiang R, Seo S, Lee J-W, Li C, Pal A, Manzhos S, Goorsky MS, Yang Y, Maruyama S, Matsuo Y (2018) Achieving high efficiency in solution-processed perovskite solar cells using C60/C70 mixed fullerenes. ACS Appl Mater Interfaces 10(46):39590–39598. https://doi.org/10.1021/acsami.8b11049
33. Chen W, Wu Y, Yue Y, Liu J, Zhang W, Yang X, Chen H, Bi E, Ashraful I, Grätzel M, Han L (2015) Efficient and stable large-area perovskite solar cells with inorganic charge extraction layers. Science 350(6263):944. https://doi.org/10.1126/science.aad1015
34. Chiang C-H, Nazeeruddin MK, Grätzel M, Wu C-G (2017) The synergistic effect of H2O and DMF towards stable and 20% efficiency inverted perovskite solar cells. Energy Environ Sci 10(3):808–817. https://doi.org/10.1039/C6EE03586H
35. Wang Y-C, Li X, Zhu L, Liu X, Zhang W, Fang J (2017) Efficient and hysteresis-free perovskite solar cells based on a solution processable polar fullerene Electron transport layer. Adv Energy Mater 7(21):1701144. https://doi.org/10.1002/aenm.201701144
36. Castro E, Zavala G, Seetharaman S, D'Souza F, Echegoyen L (2017) Impact of fullerene derivative isomeric purity on the performance of inverted planar perovskite solar cells. J Mater Chem A 5(36):19485–19490. https://doi.org/10.1039/C7TA06338E
37. Xue Q, Bai Y, Liu M, Xia R, Hu Z, Chen Z, Jiang X-F, Huang F, Yang S, Matsuo Y, Yip H-L, Cao Y (2017) Dual interfacial modifications enable high performance semitransparent perovskite solar cells with large open circuit voltage and fill factor. Adv Energy Mater 7(9):1602333. https://doi.org/10.1002/aenm.201602333
38. Lin Y, Chen B, Zhao F, Zheng X, Deng Y, Shao Y, Fang Y, Bai Y, Wang C, Huang J (2017) Matching charge extraction contact for wide-bandgap perovskite solar cells. Adv Mater 29(26):1700607. https://doi.org/10.1002/adma.201700607
39. Abrusci A, Stranks SD, Docampo P, Yip H-L, Jen AKY, Snaith HJ (2013) High-performance perovskite-polymer hybrid solar cells via electronic coupling with fullerene monolayers. Nano Lett 13(7):3124–3128. https://doi.org/10.1021/nl401044q
40. Wang C, Zhao D, Grice CR, Liao W, Yu Y, Cimaroli A, Shrestha N, Roland PJ, Chen J, Yu Z, Liu P, Cheng N, Ellingson RJ, Zhao X, Yan Y (2016) Low-temperature plasma-enhanced atomic layer deposition of tin oxide electron selective layers for highly efficient planar perovskite solar cells. J Mater Chem A 4(31):12080–12087. https://doi.org/10.1039/C6TA04503K
41. Kim J, Kim G, Kim TK, Kwon S, Back H, Lee J, Lee SH, Kang H, Lee K (2014) Efficient planar-heterojunction perovskite solar cells achieved via interfacial modification of a sol–gel ZnO electron collection layer. J Mater Chem A 2(41):17291–17296. https://doi.org/10.1039/C4TA03954H
42. Ke W, Xiao C, Wang C, Saparov B, Duan H-S, Zhao D, Xiao Z, Schulz P, Harvey SP, Liao W, Meng W, Yu Y, Cimaroli AJ, Jiang C-S, Zhu K, Al-Jassim M, Fang G, Mitzi DB, Yan Y (2016) Employing Lead thiocyanate additive to reduce the hysteresis and boost the fill factor of planar perovskite solar cells. Adv Mater 28(26):5214–5221. https://doi.org/10.1002/adma.201600594
43. Li Y, Zhao Y, Chen Q, Yang Y, Liu Y, Hong Z, Liu Z, Hsieh Y-T, Meng L, Li Y, Yang Y (2015) Multifunctional fullerene derivative for Interface engineering in perovskite solar cells. J Am Chem Soc 137(49):15540–15547. https://doi.org/10.1021/jacs.5b10614
44. Dong Y, Li W, Zhang X, Xu Q, Liu Q, Li C, Bo Z (2016) Highly efficient planar perovskite solar cells via interfacial modification with fullerene derivatives. Small 12(8):1098–1104. https://doi.org/10.1002/smll.201503361
45. Xu Q, Lu Z, Zhu L, Kou C, Liu Y, Li C, Meng Q, Li W, Bo Z (2016) Elimination of the J–V hysteresis of planar perovskite solar cells by interfacial modification with a thermo-cleavable fullerene derivative. J Mater Chem A 4(45):17649–17654. https://doi.org/10.1039/C6TA06143E
46. Lin H-S, Jeon I, Chen Y, Yang X-Y, Nakagawa T, Maruyama S, Manzhos S, Matsuo Y (2019) Highly selective and scalable fullerene-cation-mediated synthesis accessing Cyclo[60]

fullerenes with five-membered carbon ring and their application to perovskite solar cells. Chem Mater 31(20):8432–8439. https://doi.org/10.1021/acs.chemmater.9b02468
47. Chiang C-H, Wu C-G (2016) Bulk heterojunction perovskite–PCBM solar cells with high fill factor. Nat Photonics 10(3):196–200. https://doi.org/10.1038/nphoton.2016.3
48. Yang X-Y, Lin H-S, Jeon I, Matsuo Y (2018) Fullerene-cation-mediated Noble-metal-free direct introduction of functionalized aryl groups onto [60]fullerene. Org Lett 20(11):3372–3376. https://doi.org/10.1021/acs.orglett.8b01295
49. Ueno H, Jeon I, Lin H-s, Thote A, Nakagawa T, Okada H, Izawa S, Hiramoto M, Daiguji H, Maruyama S, Matsuo Y (2019) Li@C60 endohedral fullerene as a supraatomic dopant for C60 electron-transporting layers promoting the efficiency of perovskite solar cells. Chem Commun 55(79):11837–11839. https://doi.org/10.1039/C9CC06120G
50. Jeon I, Ueno H, Seo S, Aitola K, Nishikubo R, Saeki A, Okada H, Boschloo G, Maruyama S, Matsuo Y (2018) Lithium-ion endohedral fullerene (Li+@C60) dopants in stable perovskite solar cells induce instant doping and anti-oxidation. Angew Chem Int Ed 57(17):4607–4611. https://doi.org/10.1002/anie.201800816

Fullerene Derivatives as Antiviral and Anticancer Agents

25

Tomoyuki Ohe and Tadahiko Mashino

Contents

Abstract

Fullerenes represent a new molecular form of carbon that is of interest for the unique chemical and physical properties and may be novel lead compounds for drug discovery. However, one of the major issues that prevents the application of fullerenes in the biomedical field is their poor solubility in water, which is related to their high hydrophobic character. To overcome this issue, hydrophilic groups have been incorporated into the fullerene core. These fullerene derivatives possess inhibitory activities against human immunodeficiency virus (HIV) protease, HIV reverse transcriptase protease, HCV NS5B RNA polymerase, and hepatitis C virus (HCV) NS3/4A protease. Therefore, fullerene derivatives may be used as antiviral agents. In addition, some kinds of fullerene derivatives exhibit antiproliferative activities by inducing apoptosis resulting from the generation of

T. Ohe (✉) · T. Mashino
Faculty of Pharmacy, Keio University, Tokyo, Japan
e-mail: ohe-tm@pha.keio.ac.jp; mashino-td@keio.jp

X. Lu et al. (eds.), *Handbook of Fullerene Science and Technology*,
https://doi.org/10.1007/978-981-16-8994-9_38

reactive oxygen species. In this way, fullerene derivatives have the potential to be new anticancer agents.

Keywords

Fullerene · HIV · HCV · Antiviral · Anticancer

Introduction

In drug discovery, the usage of novel drug scaffolds with unique properties is important, because such structures can lead to breakthrough medicines that can overcome intractable diseases and drug resistance.

Fullerenes were experimentally discovered in 1985 as the third allotropic form of carbon following diamond and graphite [1]. Fullerenes represent a new molecular form of carbon that is of interest for the unique chemical and physical properties associated with the cage-like structure. Fullerenes may be novel lead compounds for drug discovery in the future. However, one of the major issues that prevents the application of fullerenes in the biomedical field is their poor solubility in water, which is related to their hydrophobic character. To overcome this issue, water-soluble groups have been incorporated into the fullerene core [2, 3]. These fullerene derivatives possess a range of pharmacological properties, including anti-proliferative activities and inhibitory effects against various enzymes such as human immunodeficiency virus (HIV) protease, HIV reverse transcriptase (RT), hepatitis C virus (HCV) NS5B RNA polymerase, and HCV NS3/4A protease. Our recent studies on these biological activities of the fullerene derivatives are described in this chapter.

Anti-HIV Activities

The acquired immunodeficiency syndrome (AIDS) epidemic has a substantial impact on the health of many individuals and economy of many countries. AIDS is caused by the HIV, discovered in 1983, that infects and destroys vital cells in the human immune system, such as helper T cells, macrophages, and dendritic cells [4]. Three essential enzymes for the replication of HIV are RT, integrase, and protease, which are targets for major anti-HIV drugs. Currently, antiretroviral therapy (ART), the standard regimen for people living with HIV, provides maintained suppression of viral replication and the maintenance of an acceptable level of immune reconstitution [5]. It is recommended to administer a HIV integrase inhibitor in combination with a nucleoside reverse transcriptase inhibitor (NRTI) backbone as the first-line ART regimen. Despite the general use of the ART regimen, the emergence of multidrug-resistant HIV is still a serious problem for anti-HIV therapy. For this reason, it is a challenge to develop a novel type of anti-HIV drug that is structurally distinct from the pharmaceutical agents currently used.

Inhibition of HIV Protease

HIV protease has a cylindrical substrate-binding site composed of lipophilic amino acid residues. Several molecular modeling studies have suggested that fullerenes are adapted to this binding site because of their hydrophobicity and size. Friedman et al. have synthesized a fullerene derivative 1 (Fig. 1). They showed that the fullerene derivative inhibits HIV protease and has activity against HIV-infected cells in vitro [6, 7]. This fullerene derivative was reported to have no cytotoxicity and, therefore, may be an alternative option as an anti-HIV agent.

Inhibition of HIV Reverse Transcriptase

There are two kinds of HIV-RT inhibitors, NRTIs and non-nucleoside reverse transcriptase inhibitors (NNRTIs). NRTIs are analogs of nucleic acids, and their inhibitory mechanism is caused by their incorporation as substrates in place of nucleic acids. However, NNRTIs (e.g., nevirapine) bind at different sites at the substrate-binding site. The binding of NNRTIs changes the protein structure of the substrate-binding site and results in the inhibition of the RT reaction [8, 9]. In the evaluation of the potential of fullerene derivatives as anti-HIV drugs, the HIV-RT inhibitory activities of pyrrolidinium-type fullerene derivative 2 and proline-type fullerene derivative 3 have been also investigated [10, 11] (Fig. 1). The half-maximal inhibitory concentrations (IC_{50}) of fullerene derivatives 2 and 3 are approximately 1.5 μM and 0.15μM, respectively; thus, these derivatives are more effective than nevirapine ($IC_{50} = 3.5\mu M$) (Table 1).

The incorporation of an additional carboxyl group to fullerene derivative 3 increases the inhibitory activity against HIV-RT. The IC_{50} values of fullerene derivatives 4 and 5 are 0.032μM and 0.029μM, respectively, and are less than that of derivative 3. A docking simulation of HIV-RT and fullerene derivative 4 suggests that this compound can adapt to the binding site of nevirapine [12]. The superimposition of nevirapine and derivative 4 at the binding site of nevirapine reveals that a carboxyl group can be replaced by a hydrophobic group because it overlaps with the methyl group of nevirapine. Therefore, we have synthesized fullerene derivatives 6–11 (Fig. 1), and HIV-RT inhibitory activities have been investigated. Most fullerene derivatives were discovered to have activities comparable to those of 4 (Table 1).

Pyridinium-type fullerene derivatives 12–17 were also synthesized based on the cationic moiety of pyrrolidinium-type fullerene derivative 2 (Fig. 1), which shows relatively weak, but significant, activity [13]. The HIV-RT inhibition activities of all pyridinium-type derivatives are more potent than those of nevirapine, although they are comparable to, or slightly weaker than, those of proline-type derivatives [4–11] (Table 1). The most potent compound, with IC_{50} values under 0.1μM, is derivative 13 which shows an approximately 40-fold greater inhibition activity than nevirapine. These results revealed that cationic derivatives without any carboxyl groups have strong HIV-RT inhibition activity, which indicates that not only anionic fullerene derivatives but also cationic derivatives can potently inhibit HIV-RT. In general,

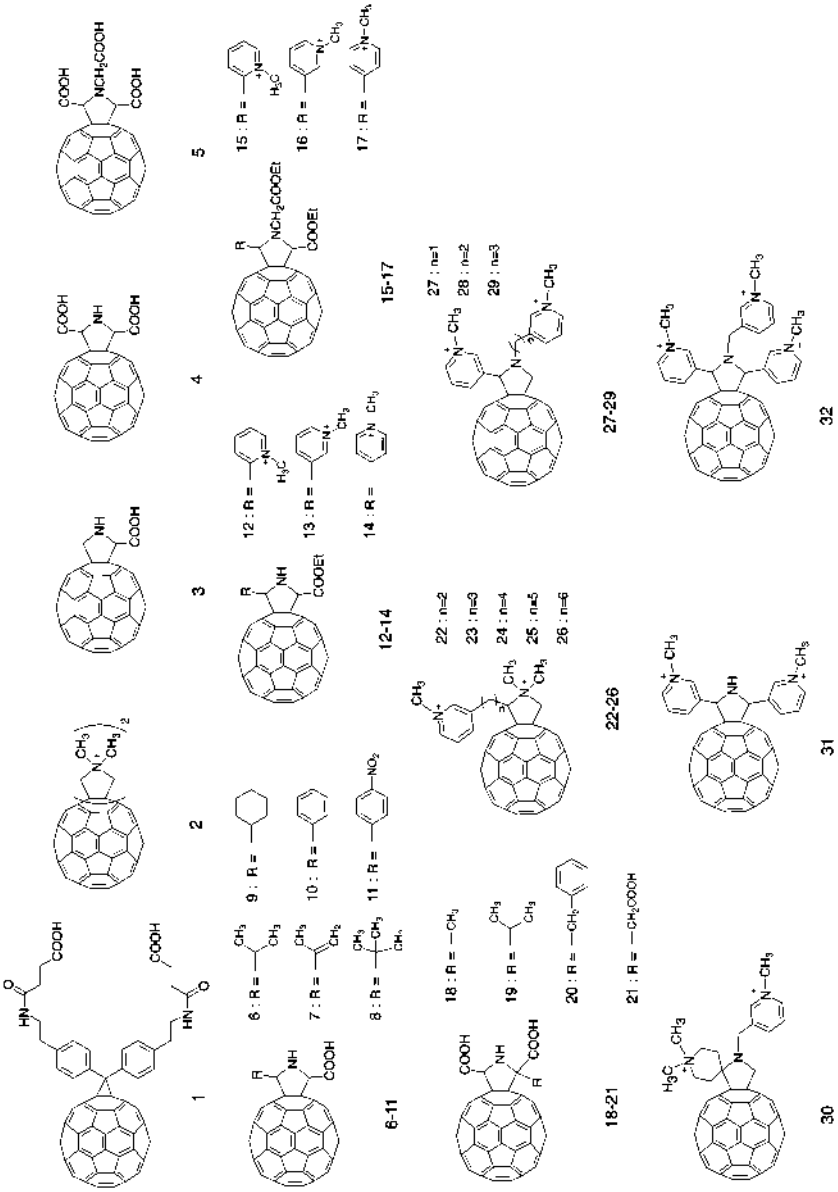

Fig. 1 Chemical structures of fullerene derivatives

Table 1 HIV-RT inhibition activities of fullerene derivatives

Compound	HIV-RT inhibitory activity (IC_{50}, μM)
2	1.4–1.7
3	0.15
4	0.032
5	0.029
6	0.018
7	0.019
8	0.011
9	0.042
10	0.018
11	0.21
12	0.33
13	0.094
14	0.37
15	0.30
16	0.25
17	0.74
Nevirapine	3.5

N.T. not tested

lipophilic, positively charged compounds are facilitated across cell membranes [14]. Therefore, pyridinium-type derivatives would surpass proline-type derivatives in cellular-based assays and in vivo. Our group evaluated a cellular-based assay of these pyridinium-type derivatives and will report the results in the near future.

These fullerene derivatives may be lead compounds for the development of anti-HIV drugs in the future. ART is widely used for HIV-infected patients [5], and the most serious problem of anti-HIV drugs is the emergence of multidrug-resistant HIV. Bulky amino acids, such as tyrosine, tryptophan, and valine, are located at the NNRTI-binding site and are often replaced by smaller amino acids in NNRTI-resistant mutants [15, 16]. In that case, the currently used NNRTIs cannot tightly bind to the binding site. Fullerene derivatives may be able to occupy the binding site, even in the cases of drug-resistant mutants, due to their large size.

Anti-HCV Activities

HCV was identified as a non-A and non-B hepatitis virus in 1989 [17]. HCV infection is one of the most serious public health problems, leading to the development of chronic hepatitis, liver fibrosis, cirrhosis, and hepatocarcinoma. The HCV genome encodes a large precursor polyprotein, which is cleaved by viral or host proteases into three structural proteins and seven non-structural (NS) proteins. Many studies have focused on the discovery of agents that prevent HCV NS proteins (hence, prevent viral replication), and NS3/4A protease, NS5A protein, and NS5B RNA polymerase inhibitors have been recently developed and used clinically

[18]. HCV has become a curable disease with the use of these antiviral agents. However, new antiviral therapeutics are needed in preparation for future pandemics caused by the emergence of drug-resistant HCV strains.

Inhibition of HCV RNA Polymerase

Fullerene derivatives 2 and 4 inhibit NS5B polymerase with IC_{50} values of approximately 0.30μM and 0.29μM, respectively (Table 2), which indicates that these derivatives are weaker than a known selective NS5B inhibitor, VX-222 [10, 11]. Among these derivatives, 4 has strong NS5B inhibitory activity without potential cytotoxicity in the low micromolar range. To improve the inhibitory activities against NS5B, various substituents have been introduced at the methine position of 4 [19] (Fig. 1). The synthesized fullerene derivatives 18–21 significantly inhibit NS5B with IC_{50} values in the submicromolar range (Table 2). The introduction of various substituents on the pyrrolidine ring of 4 appears to have no impact on NS5B inhibitory activity.

Inhibition of HCV Protease

The NS3/4A protease inhibition activities of 4 and 18–21 have been examined [19]. All fullerene derivatives inhibit NS3/4A significantly in the submicromolar range (Table 2); however, the inhibition activities of the derivatives are weaker than those of a clinically used NS3/4A inhibitor, telaprevir. Similar to the results of the NS5B inhibition assay, there is no remarkable difference in the inhibitory activities among these derivatives. These results suggest that the fullerene derivatives inhibit HCV NS3/4A protease, in addition to NS5B polymerase. These fullerene derivatives may be dual inhibitors that act against both NS5B and NS3/4A, although the respective inhibitory activities are weaker than the existing inhibitors. These activities may strongly inhibit HCV replication via a synergistic effect, and fullerene

Table 2 HCV NS5B and NS3/4A inhibition activities of fullerene derivatives

Compound	NS5B polymerase inhibitory activity (IC_{50}, μM)	NS3/4A protease inhibitory activity (IC_{50}, μM)
2	0.24–0.31	N.T.
4	0.29	0.15
18	0.48	0.37
19	0.29	0.87
20	0.26	0.43
21	0.28	0.87
VX-222	0.052	–
Telaprevir	–	0.024

N.T. not tested

derivatives may be used as novel multi-target agents for the treatment of HCV infections in the future.

Antiproliferative Activities

Worldwide, cancer is, or shortly will be, the leading disease-related cause of death in the human population, and it is estimated that there will be over ten million deaths from cancer in 2030 [20]. Although chemotherapy treats many types of cancer effectively, chemotherapy fails in over 90% of patients with metastatic cancer due to multidrug resistance (MDR) [21]. Once tumors acquire MDR, they become resistant to many anticancer drugs at the same time. Therefore, there is an urgent need for a new class of drugs for cancer treatment.

As an application of fullerenes in this field, Gd-metallofullerenol $Gd@C_{82}(OH)_{22}$ has been demonstrated to be highly therapeutic efficacy nanomedicine in inhibiting tumor growth and metastasis via multiple mechanisms [22–24]. This fullerene derivative, due to its unique physicochemical properties and high antineoplastic activities, appears to be the most promising candidate for potential antitumor therapeutic implication.

We also investigate antiproliferative effects of cationic fullerene derivatives without metals. Panels of 39 human cancer cell lines were used to evaluate the antiproliferative activities [25]. It has been demonstrated that the pyrrolidinium-type fullerene derivative 2 and its analogs have relatively potent antiproliferative activity. In addition, further analysis suggests that these fullerene derivatives are expected to be unique anticancer agents with a novel mechanism of action.

Moreover, derivative 2 and its analogs markedly induce apoptosis of tyrosine kinase Janus kinase 2 V617F mutant-induced transformed cells via the inhibition of the c-Jun N-terminal kinase activation pathway [26, 27]. This mutation is observed in the majority of patients with myeloproliferative neoplasms (MPNs); therefore, these fullerene derivatives are potent candidates for the treatment of MPNs.

The antiproliferative mechanism of derivative 2 has been investigated in human promyeloleukemia (HL-60) cells [28]. From the analysis of the cell cycle, derivative 2 leads to apoptosis, as indicated by the appearance of the subG1 phase. The appearance of DNA fragmentation and condensation of nuclear chromatin is also observed on exposure to 2. The activation of the caspase cascade and release of cytochrome c suggest that 2 induces apoptosis in HL-60 cells.

Pretreatment with the typical antioxidant α-tocopherol (vitamin E) completely suppresses the derivative 2-induced cell death. Fluorescent analysis of reactive oxygen species (ROS) using 2',7'-dichlorodihydrofluorescein diacetate demonstrates that 2 induces the intracellular oxidative stress in a dose-dependent manner. These results suggest that the antiproliferative activity of 2 is related to the intracellular generation of ROS.

Thus, derivative 2 may be a potential lead compound for an anticancer agent; however, 2 is not suitable for drug development, because it is a bisadduct fullerene and mixture of multiple regioisomers, which cannot be readily separated due to the

variability of substituent positions on the fullerene cage. To overcome this issue, a set of mono-adduct derivatives 22–32 that contain di- or tri-cation functionalized with pyridinium groups have been synthesized (Fig. 1), and their antiproliferative activities were evaluated using various cancer cell lines [26]. Most derivatives exhibit significant antiproliferative activities (Table 3). The synthesized compounds are potent inhibitors of a drug-resistant cancer cell line, NIH:OVCAR-3 (cisplatin-resistant). In addition, these fullerene derivatives are more potent inhibitors of K562/ADM (doxorubicin-resistant) with overexpressed of P-glycoprotein than doxorubicin.

Furthermore, the antitumor effect of fullerene derivatives in vivo was investigated using a mouse xenograft model [29]. Nude mice were subcutaneously injected with human lung cancer A549 cells and treated with an intraperitoneal injection of derivatives 2, 27, 30, or 31 for 6 days. Nude mice treated with fullerene derivatives exhibit no obvious alterations, including the weight of livers and spleens, which suggests that these compounds show low toxicity in vivo. The time-dependent growth of tumor volume was suppressed by the administration of fullerene derivatives. Especially, the administration of derivative 30 significantly reduced tumor volume and weight.

Considering that derivative 30 has neither a regioisomer nor stereoisomer, strongly inhibits the proliferation of various cancer cell lines including drug-resistant cancer cell lines, and significantly suppresses the tumor growth in xenograft mice models without significant toxicity, 30 may serve as the lead compound for a novel anticancer agent.

Table 3 Antiproliferative activities of fullerene derivatives

	Cell growth inhibition IC_{50} (μM)						
Compound	NIH3T3	HepG2	A549	HeLa	NIH:OVCAR-3	K562	K562/ADM
2	>50	34.0	>50	31.2	28.4	21.1	22.1
22	21.3	7.3	12.0	16.1	9.9	11.3	14.4
23	12.2	10.4	16.2	13.0	11.3	11.4	16.8
24	5.8	7.4	13.1	11.1	10.4	10.8	13.7
25	6.0	5.2	12.6	10.7	10.9	9.4	15.2
26	4.2	5.8	7.1	7.3	8.6	5.4	11.8
27	4.6	0.014	5.7	6.2	7.6	4.2	8.9
28	11.5	6.9	7.0	6.9	6.4	8.9	10.7
29	4.9	4.5	5.1	5.0	7.1	4.9	8.6
30	6.6	4.0	7.4	6.7	7.6	5.4	9.9
31	5.0	0.013	6.4	7.0	8.4	4.6	5.8
32	4.8	0.017	8.8	8.3	10.0	4.6	7.5
Cisplatin	N. T.	N. T.	N. T.	17.3	>100	N. T.	N. T.
Etoposide	1.5	14.0	N. T.	N. T.	N. T.	N. T.	N. T.
Doxorubicin	N. T.	N. T.	0.20	N. T.	N. T.	0.14	15.8

N.T. not tested

Conclusion

Fullerene derivatives are multi-target inhibitors against some enzymes that are essential for the replication of HIV and HCV. The increase in the number of patients with HIV and HCV and the emergence of drug-resistant mutants are serious problems; thus, new antiviral drugs are continuously needed. Fullerene derivatives that have unique molecular structures and properties may be lead compounds for the development of antiviral agents in the future. Moreover, pyrrolidinium and pyridinium fullerene derivatives show antiproliferative activities against various cancer cell lines including drug-resistant cells via a novel mechanism that is likely different from those of existing anticancer drugs. These fullerene derivatives have the potential to be new anticancer agents.

References

1. Kroto HW, Heath JR, O'Brien SC et al (1985) C_{60}: Buckminsterfullerene. Nature 318:162–163
2. Bingel C (1993) Cyclopropanierung von Fullerenen. Chem Ber 126:1957–1959
3. Prato M (1997) [60] Fullerene chemistry for materials science applications. J Mater Chem 7: 1097–1109
4. Barre-Sinoussi F, Chermann JC, Rey F et al (1983) Isolation of a T-lymphotropic retrovirus from a patient at risk for acquired immune deficiency syndrome (AIDS). Science 220:868–871
5. Bartlett JA, Fath MJ, Demasi R et al (2006) An updated systematic overview of triple combination therapy in antiretroviral-naive HIV-infected adults. AIDS 20:2051–2064
6. Friedman SH, DeCamp DL, Sijbesma RP et al (1993) Inhibition of the HIV-1 protease by fullerene derivatives: model building studies and experimental verification. J Am Chem Soc 115:6506–6509
7. Friedman SH, Ganapathi PS, Rubin Y et al (1998) Optimizing the binding of fullerene inhibitors of the HIV-1 protease through predicted increases in hydrophobic desolvation. J Med Chem 41: 2424–2429
8. Cohen KA, Hopkins J, Ingraham RH et al (1991) Characterization of the binding site for nevirapine (BI-RG-587), a nonnucleoside inhibitor of human immunodeficiency virus type-1 reverse transcriptase. J Biol Chem 266:14670–14674
9. Smerdon SJ, Jäger J, Wang J et al (1995) Structure of the binding site for nonnucleoside inhibitors of the reverse transcriptase of human immunodeficiency virus type 1. Proc Natl Acad Sci USA 91:3911–3915
10. Mashino T, Shimotohno K, Ikegami N et al (2005) Human immunodeficiency virus-reverse transcriptase inhibition and hepatitis C virus RNA-dependent RNA polymerase inhibition activities of fullerene derivatives. Bioorg Med Chem Lett 15:1107–1109
11. Nakamura S, Ikegami N, Harada M et al (2006) Synthesis of novel amino acid-type fullerenes and their inhibition activity of HIV reverse transcriptase and HCV RNA polymerase. J Kyoritsu Univ Pharm 1:77–84
12. Nakamura S, Mashino T (2009) Biological activities of water-soluble fullerene derivatives. J Phys Conf Ser 159:012003
13. Yasuno T, Ohe T, Takahashi K et al (2015) The human immunodeficiency virus-reverse transcriptase inhibition activity of novel pyridine/pyridinium-type fullerene derivatives. Bioorg Med Chem Lett 25:3226–3229
14. Yang NJ, Hinner MJ (2015) Getting across the cell membrane: an overview for small molecules, peptides, and proteins. Methods Mol Biol 1266:29–53

15. Kelly TA, Proudfoot JR, McNeil DW et al (1995) Novel non-nucleoside inhibitors of human immunodeficiency virus type 1 reverse transcriptase. 5. 4-Substituted and 2,4-disubstituted analogs of nevirapine. J Med Chem 38:4839–4847
16. Das K, Clark AD Jr, Lewi PJ et al (2004) Roles of conformational and positional adaptability in structure-based design of TMC125-R165335 (etravirine) and related non-nucleoside reverse transcriptase inhibitors that are highly potent and effective against wild-type and drug-resistant HIV-1 variants. J Med Chem 47:2550–2560
17. Choo QL, Kuo G, Weiner AJ et al (1989) Isolation of a cDNA clone derived from a blood-borne non-A, non-B viral hepatitis genome. Science 244:359–362
18. Götte M, Feld JJ (2016) Direct-acting antiviral agents for hepatitis C: structural and mechanistic insights. Nat Rev Gastroenterol Hepatol 13:338–351
19. Kataoka H, Ohe T, Takahashi K et al (2016) Novel fullerene derivatives as dual inhibitors of Hepatitis C virus NS5B polymerase and NS3/4A protease. Bioorg Med Chem Lett 26:4565–4567
20. Gibbs JB (2000) Mechanism-based target identification and drug discovery in cancer research. Science 287:1969–1973
21. Goldman B (2003) Multidrug resistance: can new drugs help chemotherapy score against cancer? J Natl Cancer Inst 95:255–257
22. Liu Y, Chen C, Qian P et al (2015) Gd-metallofullerenol nanomaterial as non-toxic breast cancer stem cell-specific inhibitor. Nat Commun 6:5988
23. Kang SG, Zhou G, Yang P et al (2012) Molecular mechanism of pancreatic tumor metastasis inhibition by $Gd@C_{82}(OH)_{22}$ and its implication for de novo design of nanomedicine. Proc Natl Acad Sci USA 109:15431–15436
24. Chen C, Xing G, Wang J et al (2005) Multihydroxylated $[Gd@C_{82}(OH)_{22}]_n$ nanoparticles: antineoplastic activity of high efficiency and low toxicity. Nano Lett 5:2050–2057
25. Mashino T, Nishikawa D, Takahashi K et al (2003) Antibacterial and antiproliferative activity of cationic fullerene derivatives. Bioorg Med Chem Lett 13:4395–4397
26. Funakoshi-Tago M, Nagata T, Tago K et al (2012) Fullerene derivative prevents cellular transformation induced by JAK2 V617F mutant through inhibiting c-Jun N-terminal kinase pathway. Cell Signal 24:2024–2034
27. Funakoshi-Tago M, Tsukada M, Watanabe T et al (2014) Effect of chemical modification on the ability of pyrrolidinium fullerene to induce apoptosis of cells transformed by JAK2 V617F mutant. Int Immunopharmacol 20:258–263
28. Nishizawa C, Hashimoto N, Yokoo S et al (2009) Pyrrolidinium-type fullerene derivative-induced apoptosis by the generation of reactive oxygen species in HL-60 cells. Free Radical Res 43:1240–1247
29. Yasuno T, Ohe T, Ikeda H et al (2019) Synthesis and antitumor activity of novel pyridinium fullerene derivatives. Int J Nanomedicine 14:6325–6337

Potential of Fullerenes for Photodynamic Therapy Application

26

Yoko Yamakoshi

Contents

Abstract

Since the initial reports on $^1O_2$ generation from C_{60} and C_{70} by Foote in 1991 and photo DNA cleavage activity of water-soluble C_{60} derivative by Nakamura in 1993, many studies have been reported on the use of fullerenes (C_{60} and C_{70}) in

Y. Yamakoshi (✉)
Laboratorium für Organische Chemie, ETH Zürich, Zürich, Switzerland
e-mail: yamakoshi@org.chem.ethz.ch

X. Lu et al. (eds.), *Handbook of Fullerene Science and Technology*,
https://doi.org/10.1007/978-981-16-8994-9_39

photodynamic therapy (PDT). The advantages of fullerenes as photosensitizers (PSs) in PDT include high quantum yield in the generation of reactive oxygen species (ROSs) and a relatively long excitation wavelength; but one major disadvantage for medical use is insolubility in water. In this chapter, the important photophysical properties of C_{60} and C_{70}, the preparation of water-soluble materials, and their application to PDT are outlined.

Keywords

Photosensitizer (PS) · Water-soluble fullerenes · Singlet oxygen ($^1O_2$) · Superoxide radical anion ($O_2^{\bullet -}$) · Visible light · Type I electron transfer pathway · Type II energy transfer pathway · Photodynamic therapy (PDT) · Photodynamic inactivation (PDI)

Introduction

Since the first report on the detection of C_{60} was published in 1985, an enormous number of studies on the physicochemical properties of fullerenes have been reported due to their unique, cage-like aromatic frameworks. In addition to their beautiful symmetrical chemical structures, their fully conjugated structures attracted attention in the fields of physics and electrochemistry. Early studies of fullerenes reported their unique electrochemical properties such as reversible redox reactions (up to six electrons for C_{60}), small HOMO-LUMO gap, and photosensitivity, which led to later studies on nanoscale conductive devices, molecular transistors, and photovoltaics. These researches on the fullerene-based materials became possible by the effort on the large-scale synthesis of fullerenes by Krätschmer's electronic arc method reported in 1990 [36] and, more recently, by the combustion method [35, 61]. The developments of the chemical conversion methods of fullerenes further enabled these researches for the preparation of desired fullerene derivatives on demand.

Compared to the application of fullerenes in electronic device research areas, studies on their bioapplications were slower to emerge. This was mainly because of the insolubility of fullerenes in water or other water-miscible solvents, hampering the possibility of biological assays especially in in vitro systems, where it is required to prepare the homogeneous aqueous solutions of compounds to be tested. To address this problem, water-soluble complexes and derivatives of fullerenes have been prepared, partially by taking advantages of a variety of chemical reactions of fullerenes and to allow their biological activities to be tested.

In this chapter, water-soluble C_{60} and C_{70} materials will be discussed together with their photoinduced biological activities, mainly related to the photodynamic therapy (PDT). In addition, the mechanism of their photobiological activities and the generations of responsible chemical species, such as reactive oxygen species (ROSs) generated via both *type II* energy transfer and *type I* electron transfer pathways, will be described (Fig. 1).

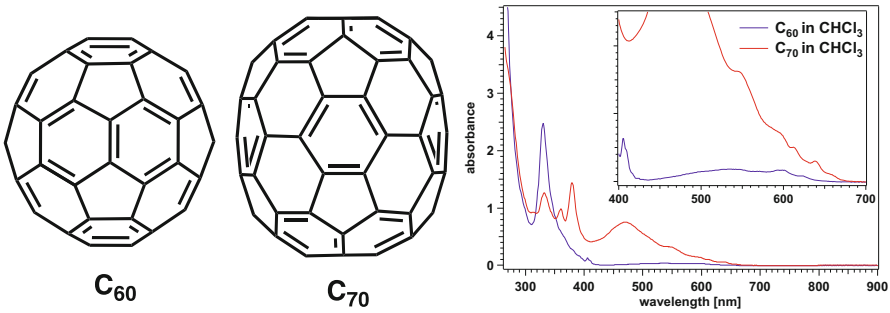

Fig. 1 Structures of C_{60} and C_{70} and UV-vis spectra in $CHCl_3$ (normalized as 40 μM solutions)

General Concept of Photodynamic Therapy (PDT) and Advantage in Use of Fullerenes

Photodynamic Therapy

Photodynamic therapy (PDT) is a clinical process involving a **photosensitizer** (PS), molecular oxygen, and **light** that together generate **reactive oxygen species** (ROSs). PDT is used in the clinical cases such as (1) **inactivation of microorganisms and virus** (sometimes called as photodynamic inactivation; PDI) and (2) **treatment of the malignant cells such as cancers**. While prior applications of PDT (or PDI) have a long history in the clinic targeting many infectious microorganisms, it has been recently considered to be an important method to treat the new types of antibiotic-resistant bacteria that were formed by the repeated use of general antibiotics. A similar situation is found in the case of antiviral treatments [65]. Since PDT (PDI) offers a new antibacterial and antivirus mechanism involving a physical process (light), it is different from the existing antibiotics working through biological pathways; PDT may be a new useful alternative in antimicrobial and antiviral treatments. In the latter cases for the treatment of malignant cells (e.g., cancers) in the body, one of the most important challenges is a selective damage of the diseased tissues, in contrast to the normal tissue. Through the use of PDT involving PS molecules that are nontoxic in the absence of light, it is possible to selectively damage the cells in the targeting malignant tissues by focused light irradiation, enabling one to switch on or off the cytotoxicity of the photosensitizers on demand. The addition of targeting moieties, which provide **selective affinity to the diseased tissues**, will make the treatment more efficient.

Figure 2 illustrates the concept of PDT treatment of malignant tumors. The initial step is to inject a PS molecule to the patient's body. The PS molecules will spread in the body with a good biodistribution, ideally with increased accumulation in the target diseased tissue to provide enough concentration of PS. For instance, macromolecular materials are sometimes used as PSs as they are thought to have better accumulation in tumors (and other inflammatory tissues) with leaky vascular system

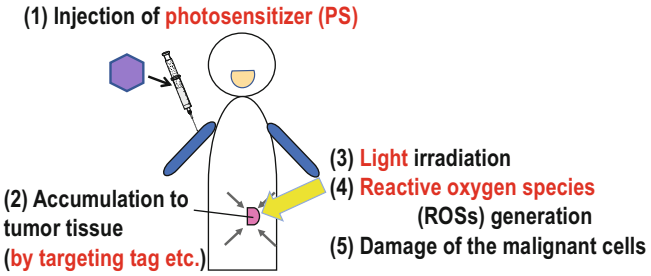

Fig. 2 Illustration of photodynamic therapy (PDT) of malignant tumors including (1) injection of PS, (2) delivery to diseased tissue, (3) irradiation of light, (4) generation of ROS, and (5) damage of malignant cells

based on the enhanced permeation and retention (EPR) theory. Furthermore, tumor-targeting moieties (e.g., folic acid to bind to the folic acid receptor overexpressed in the malignant tumors) are known to accelerate the delivery of PS to the targeting diseased organs. At the time point when the target tissue contains the highest concentration of PS molecules, they will be irradiated with light at the site of the diseased tissue to switch on the generation of reactive oxygen species (ROSs) from the PS. These ROSs will damage the malignant cells, where the PS molecules are accumulated. To monitor the timing of light irradiation, it would be helpful to have molecular designs that include an **imaging probe**, such as MRI contract agents, together with the PS moiety to allow to see the real-time biodistribution of the PS molecules (theranostics).

Photoexcitation of Photosensitizers (PSs) and Generation of Reactive Oxygen Species (ROSs)

As described above, the photoexcitation of PS molecules is an important process in PDT, and the proper choice of PS is key to a successful PDT system. Figure 3 shows a simplified Jablonski's photoexcitation diagram for the generation of ROSs from the PSs. Upon photoirradiation, PS in a singlet ground state (S_0) is excited to a singlet excited state (S_1). The S_1 is converted to triplet excited state (T_1) through intersystem crossing (ISC). The T_1 transfers the electron or energy to oxygen molecules to generate (1) superoxide radial anion (O_2•$^-$) and subsequently hydroxyl radial (•OH) via **electron transfer pathway (*type I*)** or (2) singlet oxygen ($^1O_2$) via the **energy transfer pathway (*type II*)**. The generated ROSs will damage biomolecules in the cells causing cell death. While both types of ROSs are efficient to cause the damage of tissues where the PSs are accumulated, it is important to know the mechanism in the generation of ROSs (*type I* or *II*) for the molecular design of more effective PSs in PDT.

Important considerations in the choice of PDT-PSs are listed as follows. First, the used PS should be **nontoxic in the absence of light**, while **efficiently generating the ROSs** in the presence of light with high quantum yields (ROS generation should be switchable in the presence/absence of light). This will avoid unnecessary damage

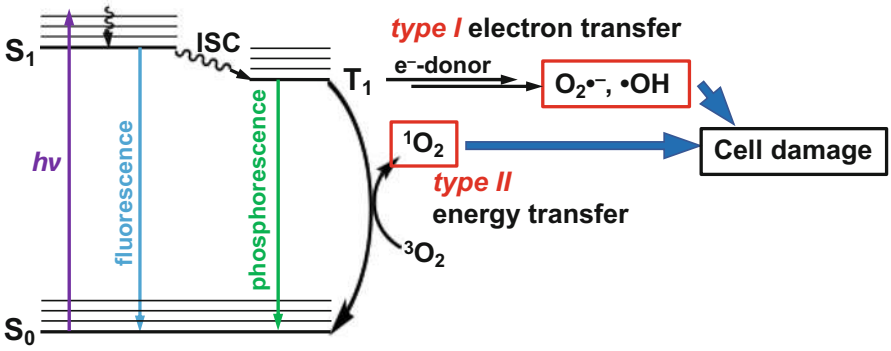

Fig. 3 Simplified Jablonski diagram of photoexcitation reaction and subsequent ROS generation for the cell damage

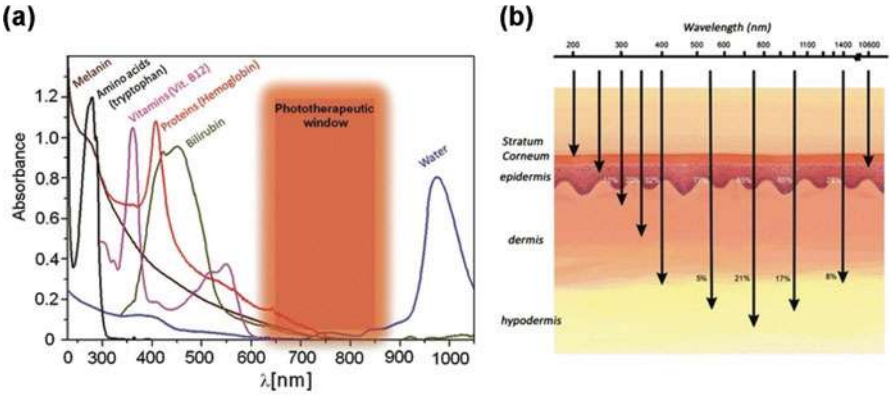

Fig. 4 Phototherapeutic window (**a**) [20] and wavelength-dependent light penetration to the skin (**b**) [13]. (Figures were adopted from *Photochem. Photobiol. Sci.* 2015, *14*, 1765 (**a**) and *Chem. Commun.* 2017, *53*, 12857 (**b**))

of the cells, when they are not irradiated. Second, it is better to use **light in the visible region** to efficiently irradiate the light to excite PS molecules in vivo. Figure 4a shows the phototherapeutic window; the best wavelength for PDT does not overlap with the absorbance of abundant molecules in the body [20]. It is known that the use the light with the wavelength inside of the phototherapeutic window (600–850 nm) will provide efficient excitation of the PS in vivo. Similarly, Fig. 4b shows the depth of light penetration as a function of the wavelength. In the wavelength range of 550–1000 nm, the light can reach into the hypodermis through the skin to efficiently excite the PS molecules in the tissue [13]. In addition, longer wavelengths of light are less harmful in the absence of PS and can avoid undesired damages of normal tissues. Furthermore, **selective delivery of PS** to the diseased tissue in vivo will increase the efficiency of the PDT treatment.

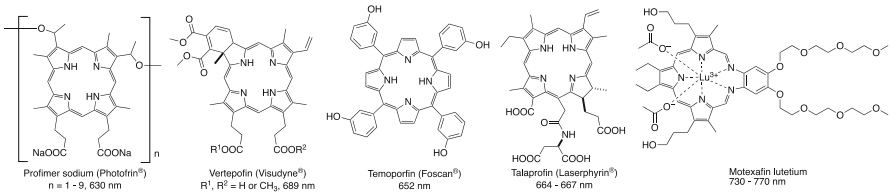

Fig. 5 Examples of PSs for PDT, which were clinically approved or are under clinical trial, with excitation wavelength. Porfimer sodium is the first FDA-approved and long-standing PDT-PS. Verteporfin, temoporfin, and taraporfin were approved in the USA, EU, and Japan, respectively

Most of the PSs, which were clinically approved or are under the clinical trials, are porphyrin-related compounds (Fig. 5). In the first generation, a polymeric porphyrin derivative, porfimer sodium (Photofrin®), has been used as the first FDA-approved PDT-PS. Second-generation PSs include other porphyrin-related compounds, such as verteporfin, temoporfin, and motexafin lutetium, with somewhat longer excitation wavelength (Fig. 5). A third generation that includes targeting delivery system is currently under development [11].

Basic Photophysical Property of Fullerenes

The use of fullerenes as PSs in PDT has been contemplated since the early 1990s. Initially, early studies on photoinduced reactions of fullerenes were intensively reported by Foote and co-workers. In their first study in 1991 [4], they reported the photoexcitation of C_{60} from singlet ground state ($^1C_{60}$) to singlet excited state ($^1C_{60}$*) that was efficiently converted to $^3C_{60}$* by subsequent intersystem crossing (ISC). While the phosphorescence generation by the decay of $^3C_{60}$* was observed, the very little fluorescence by the decay of $^1C_{60}$* was detected, indicating the evidence of ISC proceeded efficiently (see also Fig. 3). This triplet excited state of C_{60} ($^3C_{60}$*) was shown to transfer the energy to molecular oxygen ($^3O_2$) to produce singlet oxygen ($^1O_2$) (**type II energy transfer reaction**). The quantum yield of $^1O_2$ generation was quantitative in benzene and benzonitrile solutions and shown by Nagano to be higher than the other photosensitizers such as methylene blue, rose bengal, and eosin (see in section "$^1O_2$ Generation from C60 in Organic Solvents and Water") [48]. A similar situation was observed in C_{70}, providing almost quantitative quantum yield of $^1O_2$ generation [3] (Table 1).

Alternatively, photoinduced **electron transfer (type I) reaction** (Fig. 6) was reported almost simultaneously. An initial study by Krusic and co-workers in 1991 documented the generation of $C_{60}^{\bullet-}$ detected by ESR under photoirradiation in the presence of electron donor (di-4-butylperoxide) [37]. Slightly thereafter, Foote and co-workers reported the conversion from $^3C_{60}$* to $C_{60}^{\bullet-}$ via one-electron transfer in the presence of electron donor (amines) [5]. They estimated the redox potential (first reduction potential) of $^3C_{60}$* to be $E_1 = +1.41$ V (vs SCE in benzonitrile, calcd.) that was much higher than the one of $^1C_{60}$ ($E_1 = -0.42$ V vs SCE in benzonitrile),

Table 1 Photophysical properties of C_{60} and C_{70}

	S-S absorption [nm]	τ (singlet)	T-T absorption [nm]	τ (triplet)	Φ_T	Φ_{1O2}
C_{60}	530, 920	1.3 ns	400, 740	0.7 ns	~1	0.96
C_{70}	570, 660, ~740, ~900	135 μs	400, 525, 575, 960	110.8 ms	~1	0.9

τ lifetime, Φ_T quantum yield of triplet state generation, Φ_{1O2} quantum yield of $^1O_2$ generation

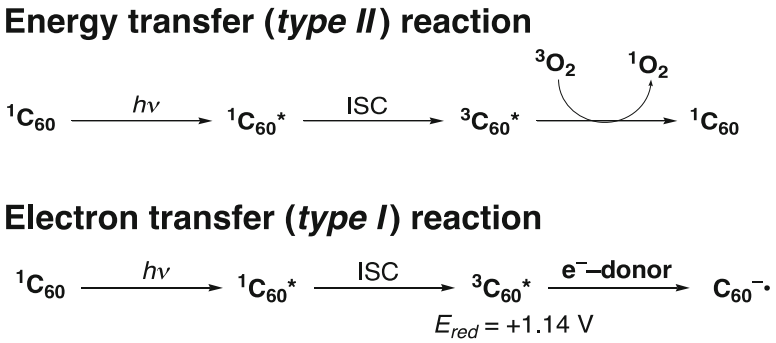

Fig. 6 Photoreaction of C_{60} via energy **type II energy transfer** and **type I electron transfer** pathways

rationalizing the efficient electron transfer reaction under photoirradiation proceeded quantitatively. This *type I* reaction leads to the generation of ROSs such as $O_2•^-$ and •OH by electron transfer reaction and subsequent Fenton reaction (see section "$O_2•^-$and •OH Generation in Aqueous Solution of Pristine C60/PVP Complex") [69, 70]. Interestingly, C_{70} showed a much longer lifetime of the triplet state (135 μs), in comparison to C_{60} (1.3 ns). Taken together with its more intensive absorption in the visible region (see absorption spectra of C_{60} and C_{70} in Fig. 1), C_{70} seems to be better suited as a photosensitizer and more suitable for use in PDT.

These studies on the photoreactions of C_{60} and C_{70}, which can be proceeded by the **irradiation of visible light** in a longer wavelength region and **produce the ROSs** in the extremely high quantum yields, led fullerenes to be considered as ideal compounds for PDT-PSs. However, there was a critical problem in the use of fullerenes as PDT-PS – the **insolubility of fullerenes** in water or water-miscible solvents. This hampered biological studies, and medicinal applications of fullerenes were considerably delayed compared to the other fullerene-related research areas such as material science.

Water-Soluble Fullerenes

Solubility of C_{60}

Fullerenes are not soluble in water or other polar solvents due to their hydrophobic surface, suppressing the biological studies on these molecules. As shown in Fig. 7, C_{60} is quite soluble in apolar solvents such as CS_2 and aromatic organic solvents

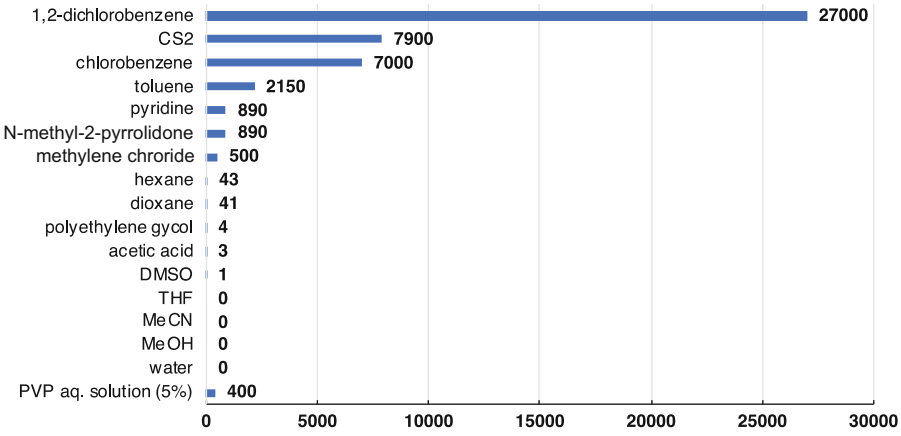

Fig. 7 Solubility of C_{60} in various solvents (μg/mL, at room temperature) [55, 58]

including toluene, chlorobenzenes, and pyridine. But they are scarcely soluble in water and water-miscible polar solvents such as alcohols, DMF, DMSO, and dioxane, which can be used in biological tests. Therefore, it is necessary to prepare **water-soluble materials** in order to subject fullerenes to biological assays. To address this, many approaches to solubilize fullerenes by covalent functionalization or non-covalent complexations have been pursued.

Water-Soluble Derivatives of C_{60} in Early Studies

The high chemical reactivity of C_{60} is beneficial for the preparation of useful derivatives. A variety of chemical reactions, including nucleophilic addition, cycloaddition, hydrogenation, oxidation, halogenation, and radical addition, are available as suitable choices of functionalization. In 1993, two landmark studies of chemical functionalization of C_{60} to prepare the **first water-soluble C_{60} derivatives** were reported independently by the groups of Nakamura and Wudl (Fig. 8) [57, 62].

Compound **1** was synthesized by cycloaddition of C_{60} with trimethylenemethane biradical [53] and found to induce DNA cleavage and cytotoxicity under visible light irradiation [62]. The selectivity in the DNA cleavage occurred in G-selective manner, and the active species involved in this activity appears to be $^1O_2$. Compound **2** was prepared by the cycloaddition of C_{60} with diphenylazomethane to provide the so-called methanofullerene derivative with a cyclopropane adduct. This molecule showed interesting HIV-1 protease inhibition activity by binding into the hydrophobic cleft of the homodimeric enzyme, as suggested by the computational docking study. Following these initial studies, a variety of water-soluble C_{60} derivatives were reported as listed in Fig. 9 [15, 49].

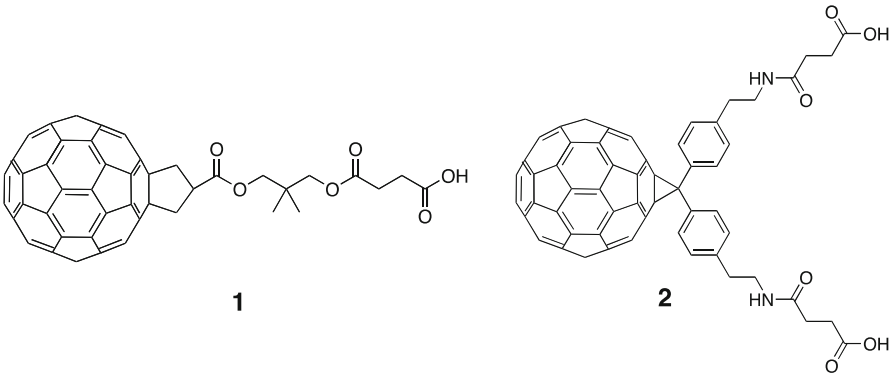

Fig. 8 Water-soluble C_{60} derivatives of 1st generation. Compound 1 with photoinduced DNA cleaving activity [62] and compound 2 with HIV-1 proteinase inhibiting activity [57]

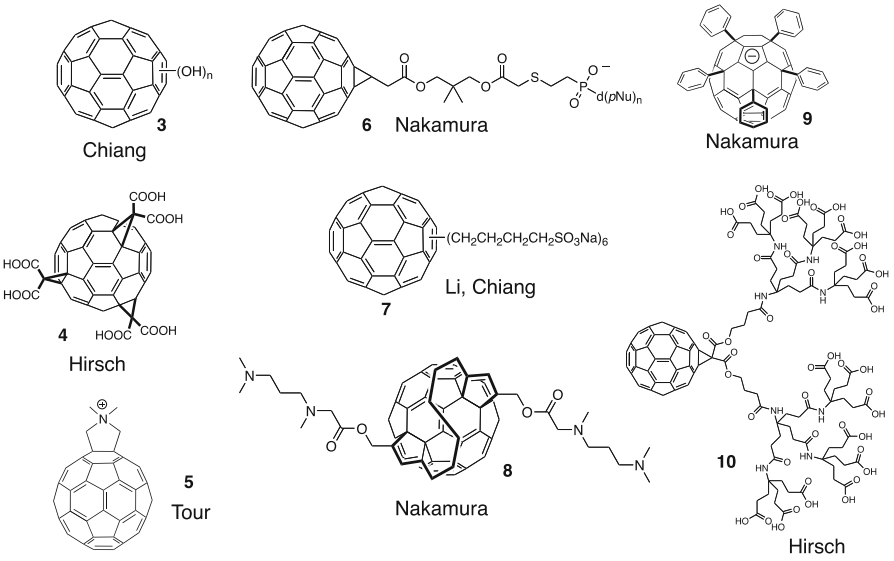

Fig. 9 Structures of water-soluble C_{60} derivatives in early studies

Bingel-Hirsch Reaction in the Preparation of Bioactive Derivatives

For the preparation of bioactive fullerene derivatives, the approaches with **two key reactions** – Bingel-Hirsch reaction and Prato reaction – are often used. The initial study of **Bingel reaction** in 1993 reported the cyclopropanation reaction of C_{60} and C_{70} with a bromo derivative of diethyl malonate in the presence of base (NaH or DBU) to provide **11** (Fig. 10) [12]. This reaction was further developed by Hirsch (**Bingel-Hirsch reaction**) using in situ generation of monohalomalonate, which

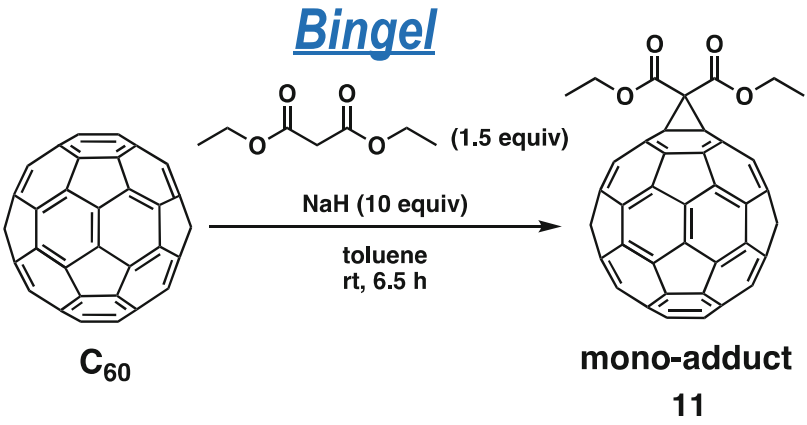

Fig. 10 Bingel cyclopropanation of C_{60} [12]. *Reagents and conditions:* NaH (10 equiv), bromomalonate diethylester (1.5 equiv), toluene, rt, 6.5 h, 45%. Reaction occurs on [6,6]-junction

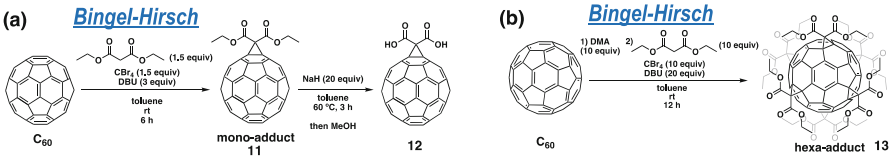

Fig. 11 Bingel-Hirsch reaction of C_{60} with the monohalomalonate generated in situ [18]. *Reagents and conditions:* (**a**) $CH_2(COOEt)_2$ (1.5 equiv), CBr_4 (1.5 equiv), DBU (3 equiv), toluene rt, 6 h, 57%; (**b**) (i) DMA (10 equiv), (ii) $CH_2(COOEt)_2$ (10 equiv), CBr_4 (10 equiv), DBU (20 equiv), toluene, rt. 12 h, 45%

reacted with C_{60} to provide the cycloadduct (57%) (Fig. 11a) [18]. The addition was observed only at the [6,6]-junction, which has a shorter bond length. The obtained Bingel-Hirsch adducts bearing ethyl esters were deprotected to provide acid derivatives using NaH under an anhydrous condition [38]. The acid derivatives with at least three addition sites (with six acid moieties in total, compound **4** in Fig. 9) were thoroughly soluble in water and showed antioxidant activity [66].

Very interestingly, in the presence of excess amounts of reagents, multiple adducts (up to six additions) were obtained in a regioselective manner (Fig. 11b, **13**). Using this beautifully symmetric addition pattern, a variety of biomaterials were prepared including an amphiphilic molecule with dendrimer structures of alkyl chains (buckysomes) (**14** in Fig. 12a) [17] and a unique hexa-glycosylated compound (sugar balls) using C_{60} as a platform molecule for the attachment of multiple sugar moieties (in total 16) that showed antiviral activity (**15** in Fig. 12b) [31].

The Bingel-Hirsch reaction generally proceeds in a high yield, although some question the stability of the cyclopropane adducts, which sometimes undergo decarboxylation, presumably due to the strained cyclopropane structure. This reaction is often used as a key step in the synthesis of bioactive fullerenes by taking advantage of excellent yields in the adduct formation. Especially in the synthesis of water-soluble

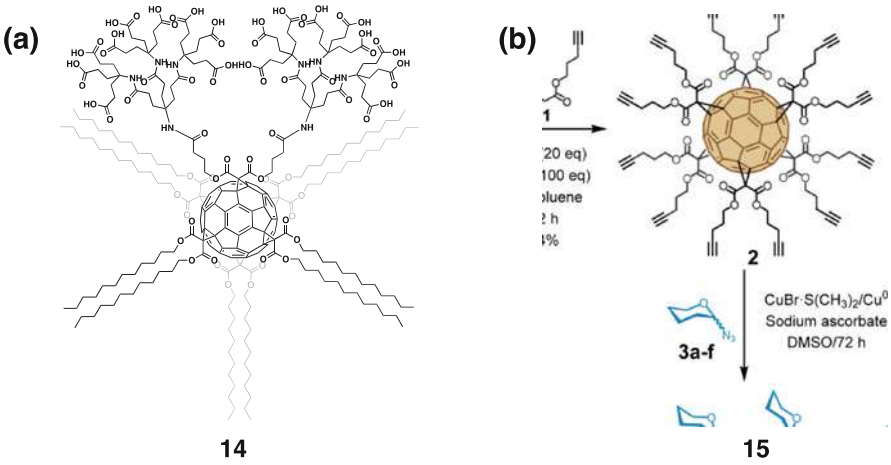

Fig. 12 Bioactive C_{60} derivatives with regioselectively obtained hexa-substitution; (**a**) amphiphilic nano-carrier (buckysome) **14** [17] and (**b**) multivalent glycosylated C_{60} **15**, which inhibits Ebola virus infection [31]. (The figure was adopted from *J. Am. Chem. Soc.* **2017,** *139* (17), 6018–6025 (**b**))

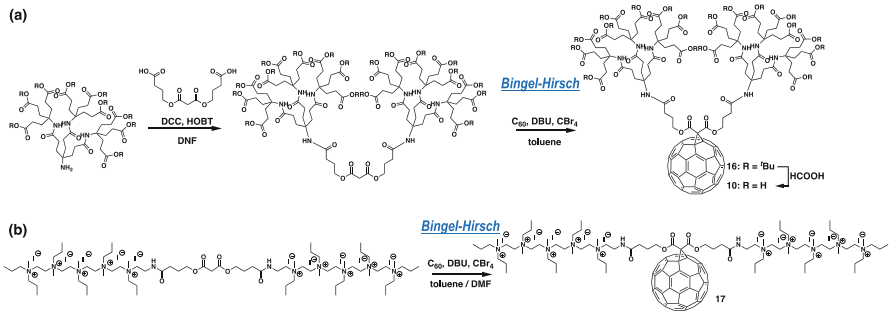

Fig. 13 Synthesis of bioactive fullerenes using the Bingel-Hirsch cyclopropanation. (**a**) Synthesis of highly water-soluble dendrofullerene **10** [16]. *Reagents and conditions in the Bingel-Hirsch reaction:* dendritic malonate (1.0 equiv), DBU (1.1 equiv), CBr_4 (1.0 equiv), toluene, 29%. (**b**) Synthesis of decacationic C_{60} decaiodide **17** [64]. *Reagents and conditions:* decacationic malonate (1.0 equiv), C_{60} (1.5 equiv), CBr_4 (1.3 equiv), DBU (2.8 equiv), toluene-DMF (5:1), under N_2, rt, 10 h, 65%

fullerene materials, which involves a difficulty in the purification of the products, this reaction has been often used at the later steps in the synthetic schemes. For instance, as shown in Fig. 13a, in the synthesis of highly water-soluble dendrofullerene **10** by Hirsch, the Bingel-Hirsch reaction was used in the second to the last step to provide the protected precursor **16** of final product. In the presence of 1.0 equiv of malonate derivative, the product **16** was synthesized in a good yield (29%) leading a deprotected water-soluble acid derivative **10** successfully [16]. The obtained dendrofullerene (**10** in Fig. 13a) showed antioxidant property similar to the tri-malonate derivative (**4** in Fig. 9). Using the same strategy, Hamblin and Ching recently synthesized

decacationic C_{60} derivative (Fig. 13b, **17**) using the Bingel-Hirsch reaction in the last step in the presence of excess C_{60} in a yield of 65% [64]. The synthesized cationic molecule **17** was highly water-soluble and shows the ROS generation and PDI activity against Gram-positive *Saccharomyces aureus* and Gram-negative *Escherichia coli* under illumination of LED (365 nm) (see ▶ Chap. 10, "Functionalization of Fullerenes: Addition Reactions").

Water-Soluble Derivatives by the Prato Reaction

In 1993, Prato and co-workers reported 1,3-dipolar cycloadditions of azomethine ylides to C_{60} (**Prato reaction**, Fig. 14a) [43]. The azomethine ylides were easily accessible by in situ decarboxylation of azazolidine-5-one formed from *N*-methylglycine and formaldehyde. The reaction proceeded in a good yield (41%) to provide a **fulleropyrrolidine** derivative **15** possessing a stable 5-membered pyrrolidine moiety on a [6,6]-junction and showed good solubility in many organic solvents. Through the combination of appropriate amino acids and aldehydes, fulleropyrrolidine derivatives having a variety of substituents, including biologically interesting moieties, can be synthesized (R^1, R^2, and R^3 in Fig. 14b) [21]. Furthermore, fulleropyrrolidine derivatives with secondary free amine ($R^1 = H$), which are available from the reaction with natural amino acids and aldehydes, can be used as good starting materials for the addition of bioactive moieties (Fig. 14c). For example, dimethyl fulleropyrrolidine **19**, formed from the reaction with L-alanine and acetoaldehyde, showed good solubility in many organic solvents (such as chloroform, DMF, toluene, etc.). The solubility of fulleropyrrolidine with R1 = R2 = R3 =

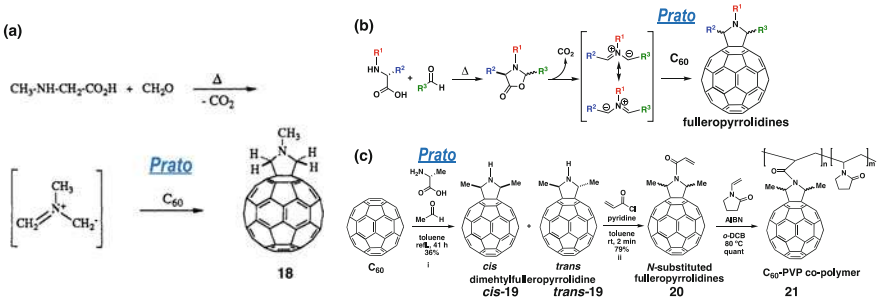

Fig. 14 Addition of azomethine ylides to C_{60} (Prato reaction). (**a**) Initial study by Prato to provide *N*-methyl fulleropyrrolidine **18** [43]. *Reagents and conditions: N*-methylglycine (2 equiv), paraformaldehyde (5 equiv), toluene, reflux, 2 h, 41% (82% conversion yield). (Figure adapted from *J. Am. Chem. Soc.* **1993**, *115*, 9798). (**b**) General scheme for the Prato reactions with an *N*-substituted amino acid and an aldehyde to provide fulleropyrrolidines. While the starting amino acids usually have a stereo center, the obtained product contains the mixture of *cis* and *trans* isomers as the intermediate azomethine ylides are achiral. (**c**) The synthesis of dimethylfulleropyrrolidine **19** with secondary amine and further addition of functional group [32]. *Reagents and conditions:* (i) L-alanine (2.0 equiv), acetoaldehyde (5.0 equiv), toluene, reflux, under N_2, 41 h, 36% (67% conversion yield, *cis*:*trans* (77:23) by NMR); (ii) acryloyl chloride (10 equiv), toluene-pyridine (90:10 v/v), under N_2, rt, 2 min, 79%

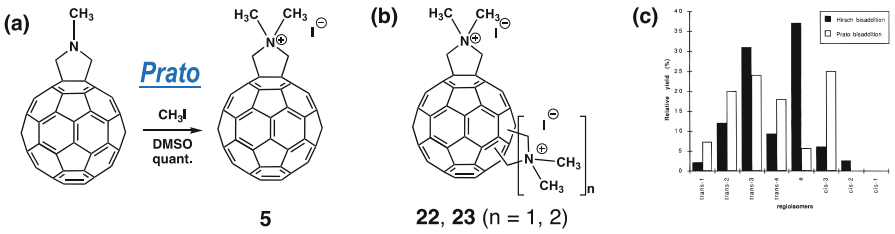

Fig. 15 Cationic fulleropyrrolidine **5** and poly adducts **22** and **23** with water solubility. (**a**) The mono-substituted *N,N*-dimethylfulleropyrrolidine **5** soluble in DMSO initially reported by Tour [19]. (**b**) The poly-substituted fulleropyrrolidine adducts **22**, **23** soluble in water. (**c**) Regioselectivity in the generation of bis-adducts by Bingel-Hirsch reaction and Prato reaction [42]. (Figure adapted from *J. Org. Chem.* **1996,** *61* (14), 4764 (**c**))

H is very low in many solvents, and it is better to have some alkyl group (e.g., Me) in R2 and R3 to make secondary amine (R1 = H) for the further substitution. It is used as a versatile starting material for coupling with acid chlorides for the addition of functional groups by a quick and efficient reaction [32]. Figure 14c shows an example of the preparation of *N*-substituted fulleropyrrolidine **20**, which was used in the AIBN-mediated radical polymerization reaction with *N*-vinylpyrrolidone to provide a water-soluble C_{60}-PVP copolymer **21**.

Utilizing the pyrrolidine moiety, cationic fulleropyrrolidine materials were prepared for bioapplications. Following the initial report by the Tour group on *N,N*-dimethyfulleropyrrolidine derivative **5** with quaternary ammonium cation, which was soluble in DMSO and slightly soluble in water (Fig. 15a) [19], several groups reported *N,N*-dimethylfulleropyrrolidine derivatives with multiple cationic groups (Fig. 15b, **22**–**23**) that showed bioactivities such as anti-HIV activity [14] and respiratory chain inhibition [44]. Unlike the Bingel-Hirsch reaction, the multiple Prato reaction proceeded with reduced regioselectivity in the bis-addition reaction (Fig. 15c) [42].

Due to the good solubility and high stability of pyrrolidine moieties, fulleropyrrolidine derivatives can be used for multistep reactions. Recently, Yamakoshi and co-workers reported fulleropyrrolidine **24** as a versatile starting material for the productions of a variety of fullerene biomaterials (Fig. 16) [6]. The deprotection reaction of *t*-butyl ester group was carried out under acidic condition, without affecting the C_{60} carbon cage, to give a bis-carboxylic acid **25**. This acid derivative was used for conjugation with PEG groups to provide a water-soluble derivative **26** or used for solid-phase peptide synthesis to provide a C_{60}-peptide conjugate **27** [8]. Alternatively, a cyclic anhydride derivative **28** was obtained from **24** and can be converted into mono-functionalized C_{60}-poly(vinylpyrrolidone) (PVP) **29** [7].

Water-Soluble Complexes

Instead of synthesizing water-soluble derivatives, it is possible to prepare water-soluble fullerene materials by forming complexes. In addition to obviating the need for chemical functionalization, an advantages in use of such water-soluble

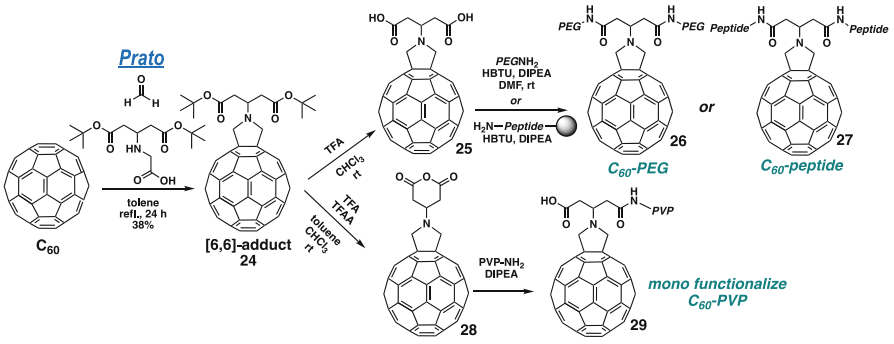

Fig. 16 Prato addition of C_{60} to provide a ^{t}Bu-protected bis-carboxylic acid derivative **24** as a versatile intermediate for the production of a variety of water-soluble/bioactive C_{60} derivatives. Compound **24** can be converted to bis-acid **25** by deprotection under acidic condition or the anhydride **28**. Compound **25** was a useful starting material for PEGylation and solid-phase peptide synthesis to provide water-soluble derivatives **26** or C_{60}-peptide conjugates **27**. Compound **28** was used for the preparation of unsymmetric (mono-functionalized) C_{60} derivatives such as **29**

complexes is that the biological activities of intact and pristine fullerenes can be studied. An initial study by Wennerström in 1992 was the preparation of 2:1 complex of C_{60} with γ-cyclodextrin (γ-CD) **30**, which provided an aqueous solution with **0.08 mM** (Fig. 17a) [2]. Yoshida performed the detailed NMR study on the complexation structure [72]. Recent work by Ikeda showed lipid nanoparticle-incorporated C_{60}@γ-CD [28] or *N,N*-dimethyl fulleropyrrolidine@γ-CD system exhibiting an excitation wavelength of 610 nm to generate $^{1}O_2$ [30]. A similar bi-cap complexation of C_{60} was prepared using calixarenes **31** (Fig. 17b). Following the initial study by Raston and co-workers for the formation of C_{60}@calix[6 or 8]arene complex **31ab** in toluene [9], a water-soluble 1:2 complex of C_{60} and water-soluble cationic oxacalix[3]arene **32** was reported by Shinkai to provide **0.5 mM** aqueous solution and showing photo DNA cleavage (Fig. 17b) [27]. Yamakoshi and co-workers have investigated the complexation of C_{60} or C_{70} with a water-soluble nontoxic polymer, poly(vinylpyrrolidone) (PVP) **33** (Fig. 17c), providing water-soluble C_{60}/PVP and C_{70}/PVP complexes with concentrations of **0.56** and **0.24 mM**, respectively [68]. These complexes showed photo DNA cleavage in the presence of an e-donor (Fig. 17c), with a mechanism involving ROS generation mechanism [69, 70]. The details are described in detail in section "$O_2^{\bullet-}$ and •OH Generation in Aqueous Solution of Pristine C60/PVP Complex."

ROS Generation from Fullerenes

$^{1}O_2$ Generation from C_{60} in Organic Solvents and Water

As described in section "Basic Photophysical Property of Fullerenes," the generation of $^{1}O_2$ from fullerenes was initially reported by Foote in 1991 (Fig. 1) [3, 4]. A more detailed study of $^{1}O_2$ generation ability of C_{60} was performed by Nagano in 1994

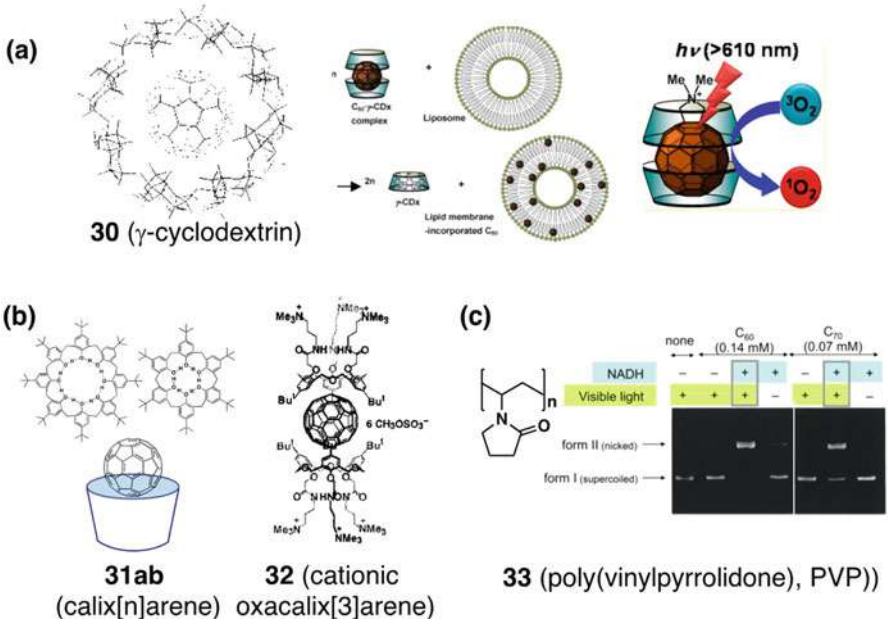

Fig. 17 (**a**) Water-soluble complex of C_{60} with γ-CD **30** (C_{60}@γ-CD): initial study by Wennerström [2], lipid incorporated C_{60}@γ-CD [28], and *N,N*-dimethylfulleropyrrolidine@γ-CD by Ikeda [30]. (**b**) C_{60}@calixarene complexes: initial report by Raston on complex of C_{60} with calix [8 or 6]arene **31ab** (C_{60}@)calix[8 or 6]arene) formed in toluene [9] and water-soluble 1:2 complex of C_{60} with oxacalix[3]arene **32** (C_{60}@oxacalix[3]arene) by Shinkai [27]. (**c**) Structure of poly (vinylpyrrolidone) (PVP) **33**, solubilizing agent for C_{60} and C_{70} [68] and photo DNA cleaving activities of C_{60}/PVP or C_{70}/PVP complexes [68, 69]. (The figures were adopted from *J. Chem. Soc., Chem. Comm.* **1992,** (8), 604–606; *Org. Biomol. Chem.* **2005,** *3* (16), 2907–2909; *ACS Med. Chem. Lett.* **2013,** *4* (8), 752–756 (**a**); *Chem. Commun.* **1999,** (15), 1403–1404 (**b**))

[48]. They compared the amount of $^1O_2$ generation from several PSs, including C_{60}, based on the specific emission at 1268 nm, corresponding to the generation of $^1O_2$, as measured by NIR spectrometer (Fig. 18a). As shown in Fig. 18b, C_{60} showed a significant emission at 1268 nm under the irradiation of laser (514.5 nm) in both benzene and benzonitrile solvents. The quantum yield of $^1O_2$ generation by C_{60} was shown to be much higher than the other PSs (Table 2). These results established the high potential of C_{60} as a PS for PDT.

Interestingly, the amount of $^1O_2$ generation from C_{60} derivatives was lower in comparison to the pristine C_{60}. Nagano determined the $^1O_2$ generation of epoxide and diethylmalonate Bingel adducts of C_{60} in CS_2 by NIR spectroscopy [25]. The addition of functional groups caused a decrease of $^1O_2$ generation in comparison to pristine C_{60}, in a manner dependent on the number of adducts. In the case of fullerene epoxides, the relative numbers of I/ε for mono-, bis-, tris-, tetra-, and penta-adduct were 0.74, 0.11, 0.22, 0.06, and 0.03, respectively, relative to C_{60} (1.00). Similarly, in the case of diethylmalonate adducts, the I/ε were 0.77 (mono), 0.53 or 0.59 (bis), 0.40 or 0.52 (tris). From these results, it was suggested that it is better to have the

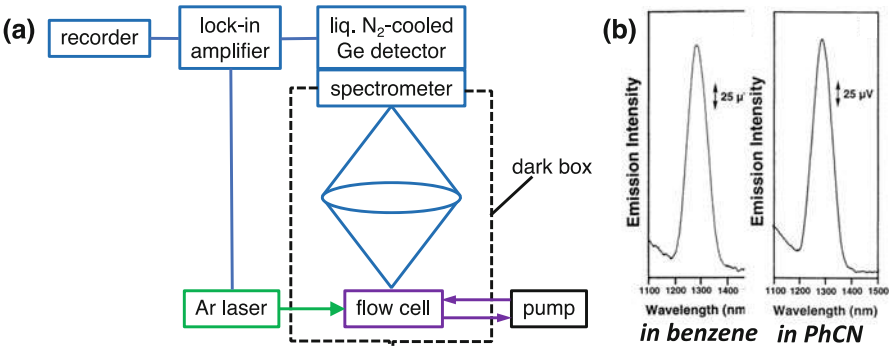

Fig. 18 (**a**) Schematic design of NIR spectrometer for the detection of $^1O_2$ emission [48]. (**b**) NIR $^1O_2$ luminescence emission spectrum of C_{60} in benzene and benzonitrile

Table 2 Comparison of relative emission intensities at 1268 nm [48]

PSs	$OD_{514.5}$	$\varepsilon_{514.5}$	Emission at 1268 nm (I)*	I/ε	I/ε (relative)
Methylene blue	0.0283	2830	485	0.1713	4.3
Rose bengal	0.2729	27290	2680	0.0982	2.5
Eosin	0.5471	54710	2160	0.0394	1.0
C_{60}	0.0074	740	350	0.4729	12.0

*Measured in benzene/MeOH solution, with 10 μM solution, and excited with Ar laser light at 514.5 nm (200 mW)

least possible amount of functionalization on the fullerene carbon cage to preserve sufficient $^1O_2$ generation.

The $^1O_2$ generation from pristine C_{60} was studied in water using C_{60}/PVP complex [70]. Although the efficient generation of $^1O_2$ from pristine C_{60} was observed in organic solvents even in the presence of PVP, there was no generation of $^1O_2$ observed in aqueous solutions of C_{60}/PVP by NIR spectrometer. No $^1O_2$ generation from C_{60}/PVP aqueous solution was further confirmed by an ESR study using a spin-trapping agent (4-oxo-TEMP) for $^1O_2$ (Fig. 19). As shown in Fig. 19a, C_{60}/PVP aqueous solution did not show significant signal corresponding to $^1O_2$ adduct of 4-oxo-TEMP, in comparison to the positive standard experiment using rose bengal (Fig. 19b). This was in line with the results in photo DNA cleavage test using standard pBR322 plasmid, revealing that the DNA cleavage by C_{60}/PVP or C_{70}/PVP complex was not observed in the absence of NADH (Fig. 17c), indicating that non-$^1O_2$-related mechanism was involved in the photoinduced DNA cleavage by pristine fullerenes in aqueous solution.

O_2•– and •OH Generation in Aqueous Solution of Pristine C_{60}/PVP Complex

As described in section "Photoexcitation of Photosensitizers (PSs) and Generation of Reactive Oxygen Species (ROSs)," in general, two photoreaction pathways, *type I*

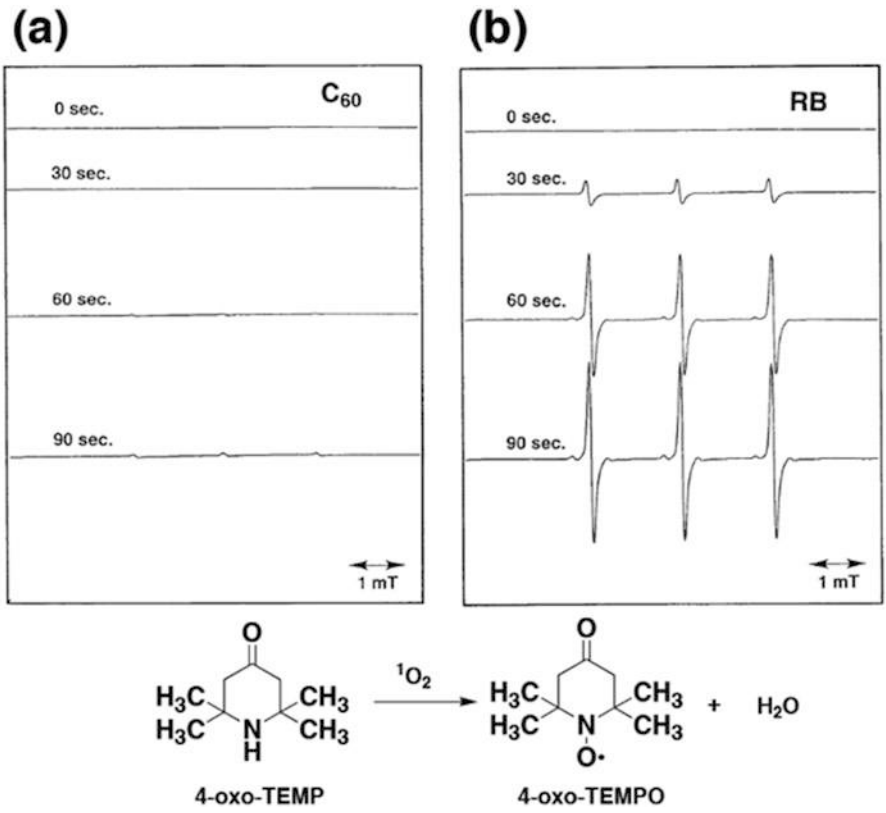

Fig. 19 X-band ESR spectra of 4-oxo-TEMP adduct of $^1O_2$ generated in C_{60}/PVP aqueous solution (**a**) and positive control experiment with rose bengal (**b**) under irradiation with a 300 W photoreflector lamp

electron transfer and *type II* energy transfer, can be involved in the photoexcitation of PSs. Since $^1O_2$ generation via the *type II* energy transfer pathway was not detected in aqueous C_{60}/PVP or C_{70}/PVP complex solutions above (Fig. 19), it was postulated that *type I* electron transfer reaction can be a key pathway in the photoreaction of pristine C_{60} or C_{70} in aqueous solution. A key intermediate ROS in *type I* pathway, O_2•$^-$, was sought by ESR method using DMPO or DEPMPO as a spin-trapping reagent [69, 70]. As shown in Fig. 20a, the generation of O_2•$^-$ was clearly observed only in the presence of C_{60}, NADH, and light as the specific signals corresponding to the O_2•$^-$ adduct of DMPO (DMPO-OOH). With an experiment using DEPMPO as a spin-trapping reagent, which produces a more stable O_2•$^-$ adduct (DEPMPO-OOH), the O_2•$^-$ generation was observed in a photoirradiation time-dependent manner (Fig. 20b). Furthermore, efficient •OH generation, which acts as the main ROS in the oxidative cleavage of DNA, was detected by ESR using DMPO as a spin-trapping agent.

Taken together, the results support the hypothesis that C_{60}/PVP complex generated $^1O_2$ in the apolar organic solvents via energy transfer pathway. In contrast, it

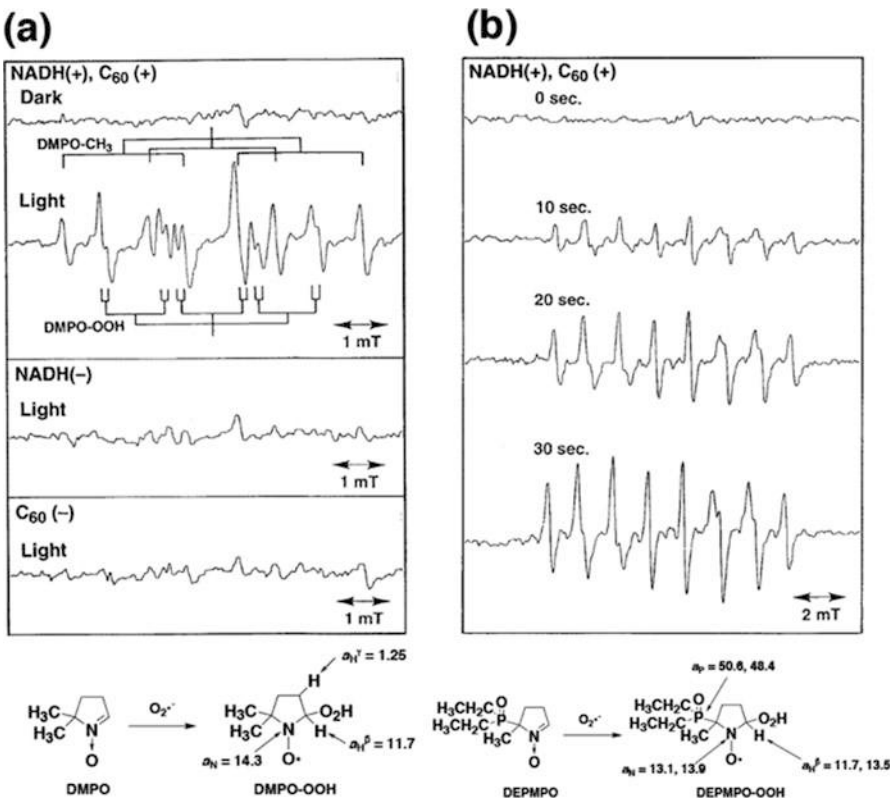

Fig. 20 X-band ESR spectra of DMPO adduct (**a**) and DEPMPO adduct (**b**) with $O_2\bullet^-$ generated in C_{60} aqueous solution under irradiation with a 300 W photoreflector lamp

produces more toxic $O_2\bullet^-$ and •OH in polar aqueous solution in the presence of electron donor via an electron transfer pathway under visible light irradiation (Fig. 21). To confirm that this phenomenon – preferred electron transfer pathway in polar solvent – can be observed as general matter in many water-soluble C_{60} materials, Yamakoshi and co-workers tested the ROS generation patterns in other water-soluble C_{60} by ESR spin-trapping methods as described in section "Comparison of ROS Generation from Water-Soluble C_{60} Complexes and Derivatives in Aqueous Solution."

Comparison of ROS Generation from Water-Soluble C_{60} Complexes and Derivatives in Aqueous Solution

Four types of water-soluble materials, C_{60}/PVP (**33**) complex, C_{60}-PVP conjugate (**34**), C_{60}@γ-CD (**30**), and $C_{60}(C(COOH)_2)_3$ (**4**), were used to compare for their ROS generation (Table 3) [71]. A macromolecular C_{60}-PVP conjugate was prepared

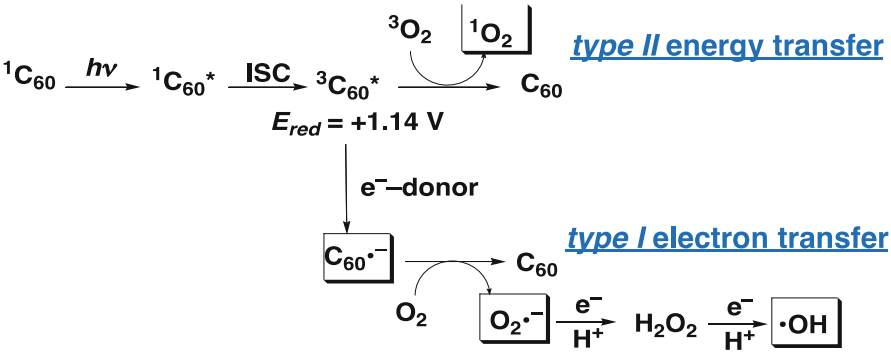

Fig. 21 Scheme for the generation of $^1O_2$ by *type II* energy transfer pathway *or* O_2•⁻ and •OH by *type I* electron transfer pathway

Table 3 ROS generation from water-soluble C_{60} materials [71]

PVP(ca. 40 kDa)			
C_{60}/PVP (**33**)	C_{60}-PVP (**34**)	C_{60}@γ-CD (**30**)	C_{60}(C(COOH)$_2$)$_3$ (**4**)

run	C_{60} materials	Types of the materials		$^1O_2$	O_2•⁻
1	C_{60}/PVP	Macromolecule	Complex	–	++
2	C_{60}-PVP	Macromolecule	Derivative	++	++
3	C_{60}@γ-CD	Small molecule	Complex	+	+++
4	C_{60}(C(COOH)$_2$)$_3$	Small molecule	Derivative	+++	(•CH_3)*

*Mechanism in the generation of •CH_3 remains unclear

by end-cap polymerization of C_{60} and *N*-vinylpyrrolidone in the presence of AIBN [50]. Bi-cap-type C_{60}@γ-CD and C_{60} tris-Bingel-Hirsch type carboxylic acid derivative (C_{60}(C(COOH)$_2$)$_3$), were prepared based on the previous studies (see sections "Water-Soluble Complexes" and "Water-Soluble Derivatives by the Prato Reaction"). The ROS generations were investigated by ESR methods using 4-oxo-TEMP and DEPMPO as spin-trapping reagents for the detections of $^1O_2$ and O_2•⁻, respectively. The results are summarized in Table 3. All of the water-soluble C_{60} materials showed the generation of either $^1O_2$ or O_2•⁻ under visible light irradiation. While C_{60}/PVP complex generated only O_2•⁻, generation of both $^1O_2$ and O_2•⁻ was observed from C_{60}-PVP conjugate, which used the same type of water-soluble polymer (PVP). The difference between C_{60}/PVP and C_{60}-PVP was only the interaction of C_{60}, and PVP was non-covalent or covalent. Taken together, the fact that more efficient generation of O_2•⁻ was observed in C_{60}@γ-CD complex involving the pristine C_{60} while $^1O_2$ generation was observed from the carboxylic acid derivative,

it appears that chemical functionalization may affect the type of generated ROSs under photoirradiation.

Use of Fullerenes in Photodynamic Therapy (PDT)

Photoinduced Biological Activities of Fullerenes In Vitro

As described above in section "ROS Generation from Fullerenes," efficient ROS generation from a variety of water-soluble fullerene derivatives and complexes were observed, indicative of a vast potential for the use of fullerenes as PDT-PSs. Accordingly, a number of studies of PDT applications of fullerenes have been reported. As a preliminary study for PDT, in vitro photocytotoxicity studies were carried out by several groups. Early studies included photocytotoxicity tests of water-soluble C_{60} derivatives (compounds **4** and **10** in Fig. 9) by Boehm, Hirsch, and Moussa in 2002 using Jurkat cells [54]. In the absence of light, tris-malonate-adduct **4** showed little cytotoxicity, while dendritic monoadduct **10** inhibited cell growth. Both molecules showed photocytotoxicity, with **4** being much more efficient than **10**, which was in a good agreement with the $^1O_2$ generation quantum yield from these derivatives. Hamblin compared the cytotoxicity of two types of water-soluble C_{60} derivatives, neutral **35**–**37** and cationic **21**–**23** (Fig. 22), using mouse cancer cell lines (J774, LLC, and CT26) [46]. Both types of C_{60} derivatives showed the efficient ROS generation via both *type I* and *type II* pathways. Consistent with the results by Nagano (section "$^1O_2$ Generation from C60 in Organic Solvents and Water") on the $^1O_2$ generation from poly-substituted C_{60} derivatives [25], the effectiveness of PS in **35**–**37** and **21**–**23** was inversely proportional to the numbers of substituents. Among these, compound **21** showed the highest activity in photocytotoxicity assay.

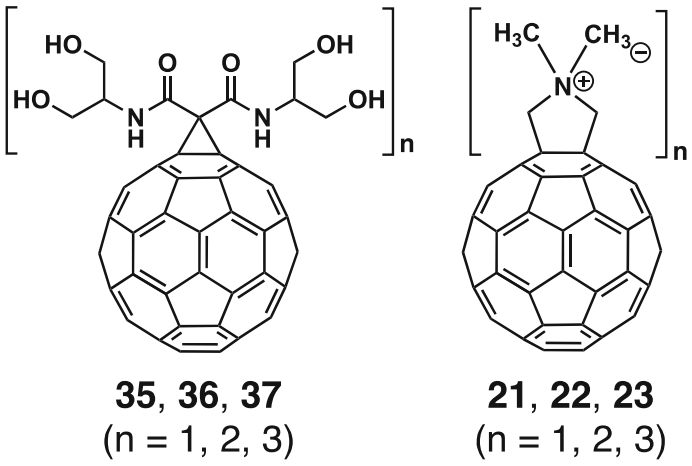

Fig. 22 C_{60} derivatives for photocytotoxicity study by Hamblin

A separate study using C_{60}@γ-CD complex **33** reported photocytotoxicity in human keratinocytes [73].

As described in section "Basic Photophysical Property of Fullerenes," the use of **C_{70}** as a PS has advantages due to the longer lifetime of the triplet state (Table 1). Furthermore, the absorption intensity of pristine C_{70} in visible region is much higher than pristine C_{60} (Fig. 1), offering one more advantage for the use of C_{70}. Accordingly, water-soluble C_{70} derivatives were prepared and tested for their photocytotoxicity. Ikeda used γ-CD complex of C_{60} and C_{70} and studied their photocytotoxicity on Hela cells [29]. Due to the faster incorporation of C_{70} into cell membranes, C_{70}@γ-CD showed better photodynamic effect. Shu, Fang, and Wang reported on the photocytotoxicity of polymalonate derivatives (bis-, tris-, and tetra-adducts) of C_{60} (Fig. 23, **38, 4, 39**) and C_{70} (Fig. 23, **40–42**) using Hela cells [40]. In comparison to the C_{60} derivatives **38**, **4**, and **39**, C_{70} derivatives **40-42** caused cell death more efficiently under visible light (400–700 nm) irradiation due to their better absorption of light causing *type II* $^1O_2$-induced necrosis, revealing membrane blebbing in the cells. Based on this result, they attached an aptamer to the tris-malonate of C_{70} **41** to provide an enhanced effect on tumor cells (A549) [41]. Hamblin further explored water-soluble C_{70} and $C_{80}O$ (Fig. 23, **43, 44, 45, 46**) with covalently attached electron-donating deca-tertiary amine chains [59]. They studied photocytotoxicity of these molecules using Hela cells under irradiation of a variety of lights such as UVA, blue, green, white, and red. The cytotoxicity was observed in $C_{80}O$ derivatives more efficiently than C_{70} especially under the irradiation of the light with shorter wavelength by the generation of •OH via the *type I* pathway. In addition, fullerene-porphyrin conjugates (Fig. 23, **47**, **48**) were reported to have photodynamic effect to human carcinoma cell line [1] and tumor cells (A549) [23]. C_{60}-porphyrin conjugate **47** was used in a liposomal vesicle system and showed the photoinduced charge-separation to cause either *type I* or *type II*

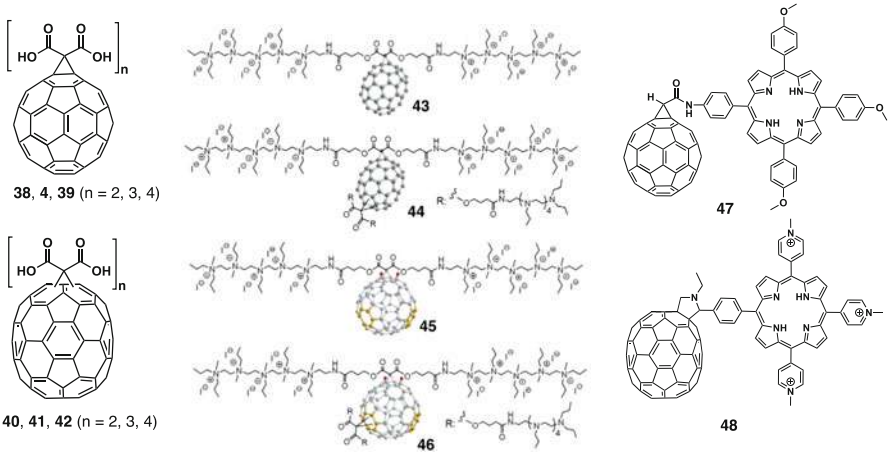

Fig. 23 C_{60}, C_{70}, and $C_{80}O$ derivatives reported for their photocytotoxicity. (The figures for compounds **43-46** were adopted from *Nanomed. Nanotechnol. Biol. Med.* **2013,** *9* (4), 570–579)

photodynamic activity to Hep2 cell line. More water-soluble C_{70}-porphyrin conjugate **48** formed liposomal nanostructures by itself in the aqueous phase and showed increase absorption coefficient and longer lifetime of triplet state (211 μs), providing an increased photodynamic effect under the hypoxia condition using A549 cell lines.

In Vivo PDT Early Studies and Recent Progress

The promising photodynamic effect of fullerene materials observed during in vitro studies using cell lines above (section "Photoinduced Biological Activities of Fullerenes In Vitro") encouraged researchers to pursue in vivo studies. Early trials for in vivo PDT by Ikada in 1997 described the preparation of macromolecular water-soluble C_{60}-PEG conjugates (Fig. 24, **49**) prepared from C_{60} and PEG-amine derivatives and in vivo studies [60]. Although the detailed structural characterization of C_{60}-PEG materials used in this study was not completely clear, they observed significant tumor suppression effect by C_{60}-PEG in a manner more efficient than clinically approved porfimer sodium (Photofrin®) on subcutaneous tumors under the irradiation of halogen lamp (400–505 nm). Later, the same group prepared a conjugate of C_{60}-PEG with Gd(DTPA) chelate with a theranostic approach by combining PDT and MRI [39]. They successfully imaged tumors enhanced with accumulated C_{60}-PEG-Gd(DTPA) conjugate, largely due to their EPR effect of macromolecular materials ca. after 24 hours of post-injection. The effect of PDT was better when the light irradiation was performed in sync with highest concentration of C_{60}-PEG-Gd(DTPA) conjugate localized to the tumor tissues (with the highest enhancement by MRI).

A PDT study with more active targeting was reported in 2010 by Otake and co-workers using a glucose tag to target a glucose receptor overexpressed in tumor tissue [51]. They synthesized C_{60}-glucose conjugates (Fig. 24, **50**) and subjected them to in vitro photocytotoxicity assay and in vivo PDT test using melanoma-bearing mouse models. Significant apoptotic photoinduced cytotoxicity, caused by $^1O_2$, was observed in several cancer cell lines, and suppression of tumor in vivo was observed by the irradiation of UVA. Hamblin has reported PDT study of

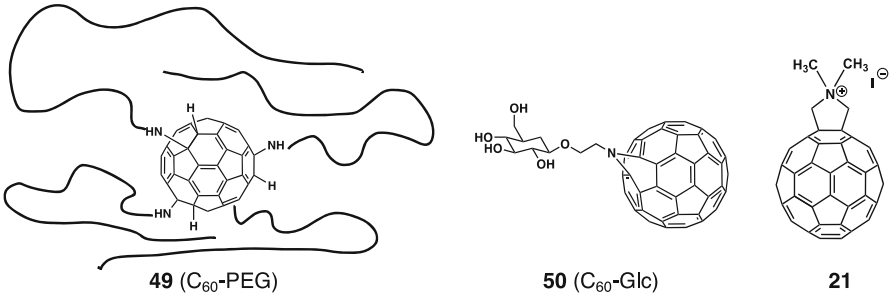

49 (C_{60}-PEG) **50** (C_{60}-Glc) **21**

Fig. 24 C_{60} derivatives used for in vivo PDT studies

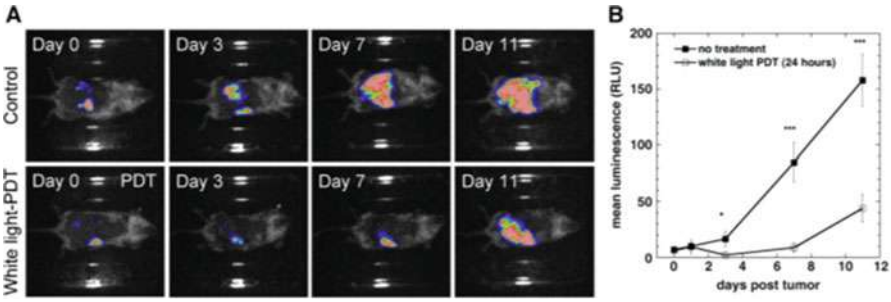

Fig. 25 Hamblin's in vivo PDT study of compound **21** on mouse model with CT26-Luc tumors observed by bioluminescence imaging (**a**) and quantitative analysis (**b**). (The figures were adopted from *Nanomed.: Nanotechnol. Biol. Med.* **2011,** *7*(6), 965–974)

N,N-dimethylfulleropyrrolidine (Fig. 24, **21**) complexed with Cremophor (a solubilizing reagent commonly used in PDT-PSs which are often insoluble in water) solubilized in 5% dextrose solution [47]. In a preliminary in vitro test using CT26-Luc (luciferase expressing carcinoma cell line) cells under white light, compound **21** showed higher PDT activity in comparison to porfimer sodium (Photofrin®). Furthermore, the in vivo study clearly showed the suppression in CT26-Luc tumor-growing model mice administrated with compound **21** and subjected to the white light irradiation, as observed by bioluminescence imaging (Fig. 25), and afforded a longer survival interval.

Recent in vivo PDT studies reported nanoparticle-type fullerene materials with multiple functions in combination with imaging modalities. Zhang reported a nanocomposite of PEGylated fullerene and iron oxide for both MRI and PDT and subjected to the in vivo study [56]. Shu prepared a conjugate of tris-malonate derivative of C_{70} and chlorin e6 (Ce6) as a NIR imaging probe as a theranostic agent with NIR and PDT functions [24]. The obtained conjugate formed nanovesicle type of the material with enhanced cellular uptake and further more efficient cytotoxicity only under light irradiation (660 nm laser) in vitro on A549 cells. Further in vivo studies were carried out with xenograft Balb/c mice bearing with 4T1-luc (luciferase expressing breast cancer cell line). The mice administrated with C_{70}-Ce6 conjugate were treated with 660 nm laser irradiation for 4 h and 15 days. As observed in bioluminescence imaging and by the ex vivo study of the tumor with hematoxylin-eosin staining, the tumor was significantly suppressed after treatment. Interestingly, the activities of the C_{70}-Ce6 conjugate were higher than the C_{70} tris-malonate adduct or the Ce6 moiety alone (Fig. 26).

Photodynamic Inactivation (PDI) Studies

As described above in section "Photodynamic Therapy" photodynamic inactivation (PDI) of microorganisms has a longer history in comparison to general PDT as a therapeutic approach for cancer. Especially for the treatment of the infectious

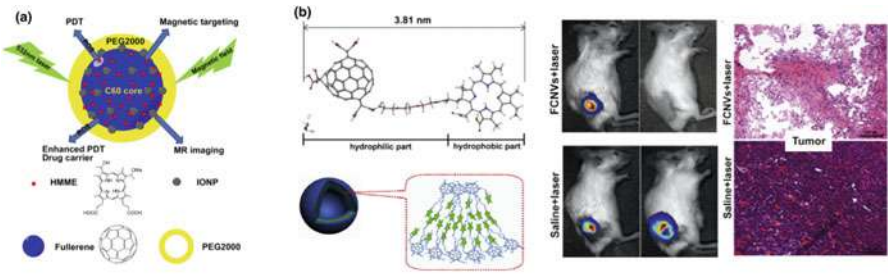

Fig. 26 Theranostic fullerene materials used in in vivo studies. (**a**) C_{60} and iron oxide nanocomposite for MRI-PDT by Zhang. (**b**) An amphiphilic conjugate of C_{70} tris-malonate and chlorin 6 to form vesicles for NIR-PDT by Shu. (The figures were adopted from *Biomaterials* **2013,** *34* (37), 9666–9677 and *Biomaterials* **2016,** *103*, 75–85)

wounds – often observed on the surface of the body – PDI using light can work efficiently. Based on the ROS generation from fullerenes, it was reasonable to expect that fullerene would show antibacterial activities under photoirradiation. An initial study was reported by Käsermann in 1997 on the inactivation of the enveloped viruses, Semliki Forest virus (SFV) and vesicular stomatitis virus (VSV) [34]. Using a C_{60} suspension and under irradiation with short arc mercury lamp in the presence of saturated O_2, PDI activity was clearly observed on both strains of virus. Yamakoshi et al. have reported a primitive but promising result in 2003 on the photoinduced antimicrobial activity of water-soluble C_{60}/PVP complex [33]. Under aerobic condition where *Bacillus subtilis* PCI219 can grow efficiently, C_{60}/PVP showed significant suppress in the bacteria growing in the presence of the white light.

Hamblin has been intensively and systematically investigating the use of fullerene for PDI of infectious diseases. They initially used C_{60} derivatives (Fig. 22, **35**-**37**, **21**-**23**) and probed their PDI activity on a Gram-negative bacterium (*Staphylococcus aureus*), two Gram-negative bacteria (*Escherichia coli* and *Pseudomonas aeruginosa*), and a fungus (*Candida albicans*). The results showed that cationic derivatives **22** and **23** showed sufficient PDI activity (more than 99% of microorganisms were killed) after 10 min of incubation followed by white light irradiation. Importantly, the mammalian cells were undamaged under the same condition, and the activity was better than a widely used dye, toluidine blue O. Since it appears that the increased number of cationic charges and decreased hydrophobicity of the C_{60} derivative was advantageous in PDI [45], they synthesized water-soluble deca-cationic C_{60} derivative **17** (Fig. 13) and subjected to the PDI study together with its analogous molecule of C_{70} derivative **43** (Fig. 23) on Gram-positive *S. aureus* and Gram-negative *E. coli* under white light irradiation [63]. While both compounds **17** and **43** revealed significant PDI on both bacteria, the efficiency was higher in C_{70} derivative **43**, which generated •OH under photoirradiation, damaging the less permeable Gram-negative bacteria cell wall. Finally, the in vivo PDI studies were carried using C_{70} mono- or bis-adducts **43** and **44** (Fig. 23) on infected model mouse contaminated with

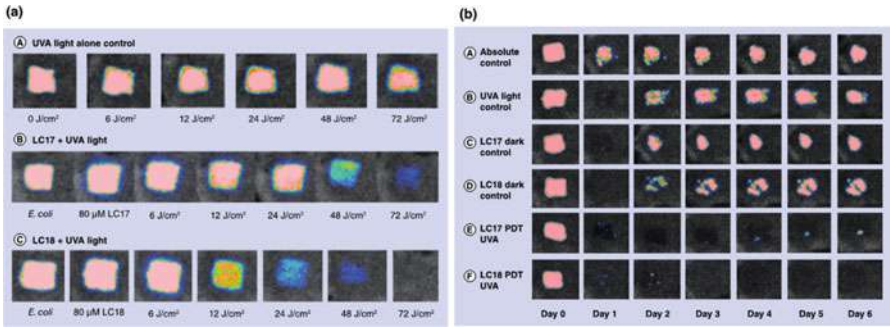

Fig. 27 Bioluminescence images of burn infection model with *E. coli* (a) and *A. baumannii* (b) in the presence of compound **43** (LC17) or **44** (LC18) irradiated with UVA light. (Figures were adopted from *Nanomedicine-Uk* **2014,** *9* (2), 253–266)

Gram-negative *E. coli* or *Acinetobacter baumannii* [26]. Figure 27 shows recovery from burn infection model images by bioluminescence. Recovery from burn infection was observed to be significantly better in the presence of compounds **43** and **44** on *E. coli*-infected model (a) in comparison to the control UVA-irradiated model. Figure 27b shows the growing back of the bacteria (*A. baumannii*) after PDT treatment with or without **43** or **44**. It was clearly shown that in the presence of UVA and compound **43** or **44**, bacterial growth was completely suppressed, while the bacteria, once suppressed by UVA or the compounds alone under dark condition, grew back 2 days after treatments.

Summary and Perspectives

The biological application of fullerenes at first seemed to be difficult due to their insolubility in many solvents, especially in water. Owing to the development of chemical reactions of fullerenes, it became possible to prepare water-soluble derivatives, which can be subjected to biological tests. Although compared to the pristine C_{60} and $C_{70,}$ which are highly efficient photosensitizers that produce ROS in extremely high quantum yields, these derivatives possess somewhat different properties for ROS generation. However, they preserve sufficient photosensitivity to operate in biological systems under PDT-relevant light irradiation in the PDT window. Furthermore, by transformations on the fullerene cores, it became possible to attach imaging probe and disease-targeting tags in their structures.

One of the important concerns in PDT application of fullerenes is ensuring that they are nontoxic. Especially when the toxicity risk of carbon nanotubes became a topic in the scientific community [52], the toxicity of C_{60} and C_{70} was discussed intensively. However, there is no clear evidence of toxicity of both fullerenes in the in vivo studies initially reported by Nakamura using ^{14}C-labeled water-soluble C_{60} derivative [67] and further intensive studies by Moussa [10, 22] using pristine C_{60}.

Since it is hard to confirm that a compound is nontoxic (in comparison to confirming that a compound is toxic), careful and systematic investigation on the toxicity of fullerenes still needs to be carried out.

References

1. Alvarez MG, Prucca C, Milanesio ME, Durantini EN, Rivarola V (2006) Photodynamic activity of a new sensitizer derived from porphyrin-C60 dyad and its biological consequences in a human carcinoma cell line. Int J Biochem Cell Biol 38(12):2092–2101. https://doi.org/10.1016/j.biocel.2006.05.019
2. Andersson T, Nilsson K, Sundahl M, Westman G, Wennerstrom O (1992) C-60 embedded in gamma-cyclodextrin – a water-soluble fullerene. J Chem Soc Chem Comm 8:604–606. https://doi.org/10.1039/c39920000604
3. Arbogast JW, Foote CS (1991) Photophysical properties of C-70. J Am Chem Soc 113(23):8886–8889. https://doi.org/10.1021/ja00023a041
4. Arbogast JW, Darmanyan AP, Foote CS, Rubin Y, Diederich FN, Alvarez MM, Anz SJ, Whetten RL (1991) Photophysical properties of C60. J Phys Chem-Us 95(1):11–12. https://doi.org/10.1021/j100154a006
5. Arbogast JW, Foote CS, Kao M (1992) Electron-transfer to triplet C-60. J Am Chem Soc 114(6):2277–2279. https://doi.org/10.1021/ja00032a063
6. Aroua S, Schweizer WB, Yamakoshi Y (2014) C-60 pyrrolidine bis-carboxylic acid derivative as a versatile precursor for biocompatible fullerenes. Org Lett 16(6):1688–1691. https://doi.org/10.1021/ol500363r
7. Aroua S, Tiu EGV, Ayer M, Ishikawa T, Yamakoshi Y (2015) RAFT synthesis of poly (vinylpyrrolidone) amine and preparation of a water-soluble C-60-PVP conjugate. Polym Chem-UK 6(14):2616–2619. https://doi.org/10.1039/c4py01333f
8. Aroua S, Tiu EGV, Ishikawa T, Yamakoshi Y (2016) Well-defined amphiphilic C-60-PEG conjugates: water-soluble and thermoresponsive materials. Helv Chim Acta 99(10):805–813. https://doi.org/10.1002/hlca.201600171
9. Atwood JL, Koutsantonis GA, Raston CL (1994) Purification of C-60 and C-70 by selective complexation with calixarenes. Nature 368(6468):229–231. https://doi.org/10.1038/368229a0
10. Baati T, Bourasset F, Gharbi N, Njim L, Abderrabba M, Kerkeni A, Szwarc H, Moussa F (2012) The prolongation of the lifespan of rats by repeated oral administration of [60] fullerene. Biomaterials 33(19):4936–4946. https://doi.org/10.1016/j.biomaterials.2012.03.036
11. Baskaran R, Lee J, Yang SG (2018) Clinical development of photodynamic agents and therapeutic applications. Biomater Res 22:25. https://doi.org/10.1186/s40824-018-0140-z
12. Bingel C (1993) Cyclopropylation of Fullerenes. Chem Ber-Recl 126(8):1957–1959. https://doi.org/10.1002/cber.19931260829
13. Bolze F, Jenni S, Sour A, Heitz V (2017) Molecular photosensitisers for two-photon photodynamic therapy. Chem Commun 53(96):12857–12877. https://doi.org/10.1039/c7cc06133a
14. Bosi S, Da Ros T, Spalluto G, Balzarini J, Prato M (2003a) Synthesis and anti-HIV properties of new water-soluble bis-functionalized[60]fullerene derivatives. Bioorg Med Chem Lett 13(24):4437–4440. https://doi.org/10.1016/j.bmcl.2003.09.016
15. Bosi S, Da Ros T, Spalluto G, Prato M (2003b) Fullerene derivatives: an attractive tool for biological applications. Eur J Med Chem 38(11-12):913–923. https://doi.org/10.1016/j.ejmech.2003.09.005
16. Brettreich M, Hirsch A (1998) A highly water-soluble dendro[60]fullerene. Tetrahedron Lett 39(18):2731–2734. https://doi.org/10.1016/S0040-4039(98)00491-2
17. Brettreich M, Burghardt S, Bottcher C, Bayerl T, Bayerl S, Hirsch A (2000) Globular amphiphiles: membrane-forming hexaadducts of C-60. Angew Chem Int Edit 39(10):1845. https://doi.org/10.1002/(Sici)1521-3773(20000515)39:10<1845::Aid-Anie1845>3.0.Co;2-Q

18. Camps X, Hirsch A (1997) Efficient cyclopropanation of C-60 starting from malonates. J Chem Soc Perk T 1(11):1595–1596. https://doi.org/10.1039/a702055d
19. Cassell AM, Asplund CL, Tour JM (1999) Self-assembling supramolecular nanostructures from a C(60) derivative: nanorods and vesicles. Angew Chem Int Ed Engl 38(16):2403–2405. https://doi.org/10.1002/(sici)1521-3773(19990816)38:16<2403::aid-anie2403>3.0.co;2-j
20. Dabrowski JM, Arnaut LG (2015) Photodynamic therapy (PDT) of cancer: from local to systemic treatment. Photoch Photobio Sci 14(10):1765–1780. https://doi.org/10.1039/c5pp00132c
21. DaRos T, Prato M, Novello F, Maggini M, Banfi E (1996) Easy access to water-soluble fullerene derivatives via 1,3-dipolar cycloadditions of azomethine ylides to C-60. J Org Chem 61(25):9070–9072. https://doi.org/10.1021/jo961522t
22. Gharbi N, Pressac M, Hadchouel M, Szwarc H, Wilson SR, Moussa F (2005) [60]Fullerene is a powerful antioxidant in vivo with no acute or subacute toxicity. Nano Lett 5(12):2578–2585. https://doi.org/10.1021/nl051866b
23. Guan MR, Qin TX, Ge JC, Zhen MM, Xu W, Chen DQ, Li SM, Wang CR, Su HM, Shu CY (2015) Amphiphilic trismethylpyridylporphyrin-fullerene (C-70) dyad: an efficient photosensitizer under hypoxia conditions. J Mater Chem B 3(5):776–783. https://doi.org/10.1039/c4tb01314j
24. Guan MR, Ge JC, Wu JY, Zhang GQ, Chen DQ, Zhang W, Zhang Y, Zou TJ, Zhen MM, Wang CR, Chu TW, Hao XJ, Shu CY (2016) Fullerene/photosensitizer nanovesicles as highly efficient and clearable phototheranostics with enhanced tumor accumulation for cancer therapy. Biomaterials 103:75–85. https://doi.org/10.1016/j.biomaterials.2016.06.023
25. Hamano T, Okuda K, Mashino T, Hirobe M, Arakane K, Ryu A, Mashiko S, Nagano T (1997) Singlet oxygen production from fullerene derivatives: effect of sequential functionalization of the fullerene core. Chem Commun 1:21–22. https://doi.org/10.1039/a606335g
26. Huang LY, Wang M, Dai TH, Sperandio FF, Huang YY, Xuan Y, Chiang LY, Hamblin MR (2014) Antimicrobial photodynamic therapy with decacationic monoadducts and bisadducts of [70] fullerene: in vitro and in vivo studies. Nanomedicine-Uk 9(2):253–266. https://doi.org/10.2217/nnm.13.22
27. Ikeda A, Hatano T, Kawaguchi M, Suenaga H, Shinkai S (1999) Water-soluble [60]fullerene-cationic homooxacalix[3]arene complex which is applicable to the photocleavage of DNA. Chem Commun 15:1403–1404. https://doi.org/10.1039/a903872h
28. Ikeda A, Sato T, Kitamura K, Nishiguchi K, Sasaki Y, Kikuchi J, Ogawa T, Yogo K, Takeya T (2005) Effcient photocleavage of DNA utilising water-soluble lipid membrane-incorporated [60]fullerenes prepared using a [60]fullerene exchange method. Org Biomol Chem 3(16):2907–2909. https://doi.org/10.1039/b507954c
29. Ikeda A, Matsumoto M, Akiyama M, Kikuchi J, Ogawa T, Takeya T (2009) Direct and short-time uptake of [70]fullerene into the cell membrane using an exchange reaction from a [70] fullerene-gamma-cyclodextrin complex and the resulting photodynamic activity. Chem Commun 12:1547–1549. https://doi.org/10.1039/b820768b
30. Ikeda A, Iizuka T, Maekubo N, Aono R, Kikuchi J, Akiyama M, Konishi T, Ogawa T, Ishida-Kitagawa N, Tatebe H, Shiozaki K (2013) Cyclodextrin complexed [60]fullerene derivatives with high levels of photodynamic activity by long wavelength excitation. Acs Med Chem Lett 4(8):752–756. https://doi.org/10.1021/ml4001535
31. Illescas BM, Rojo J, Delgado R, Martin N (2017) Multivalent glycosylated nanostructures to inhibit ebola virus infection. J Am Chem Soc 139(17):6018–6025. https://doi.org/10.1021/jacs.7b01683
32. Iwamoto Y, Yamakoshi Y (2006) A highly water-soluble C-60-NVP copolymer: a potential material for photodynamic therapy. Chem Commun 46:4805–4807. https://doi.org/10.1039/b614305a
33. Kai Y, Komazawa Y, Miyajima A, Miyata N, Yamakoshi Y (2003) [60]Fullerene as a novel photoinduced antibiotic. Fuller Nanotub Car N 11(1):79–87. https://doi.org/10.1081/Fst-120018664
34. Kasermann F, Kempf C (1997) Photodynamic inactivation of enveloped viruses by buckminsterfullerene. Antivir Res 34(1):65–70. https://doi.org/10.1016/S0166-3542(96)01207-7

35. Komatsu N, Ohe T, Matsushige K (2004) A highly improved method for purification of fullerenes applicable to large-scale production. Carbon 42(1):163–167. https://doi.org/10.1016/j.carbon.2003.10.009
36. Kratschmer W, Lamb LD, Fostiropoulos K, Huffman DR (1990) Solid C-60 – a new form of carbon. Nature 347(6291):354–358. https://doi.org/10.1038/347354a0
37. Krusic PJ, Wasserman E, Parkinson BA, Malone B, Holler ER, Keizer PN, Morton JR, Preston KF (1991) Electron-spin-resonance study of the radical reactivity of C60. J Am Chem Soc 113(16):6274–6275. https://doi.org/10.1021/ja00016a056
38. Lamparth I, Hirsch A (1994) Water-soluble malonic-acid derivatives of C-60 with a defined 3-dimensional structure. J Chem Soc Chem Comm 14:1727–1728. https://doi.org/10.1039/c39940001727
39. Liu J, Ohta S, Sonoda A, Yamada M, Yamamoto M, Nitta N, Murata K, Tabata Y (2007) Preparation of PEG-conjugated fullerene containing Gd3+ ions for photodynamic therapy. J Control Release 117(1):104–110. https://doi.org/10.1016/j.jconrel.2006.10.008
40. Liu QL, Guan MR, Xu L, Shu CY, Jin C, Zheng JP, Fang XH, Yang YJ, Wang CR (2012) Structural effect and mechanism of C70-carboxyfullerenes as efficient sensitizers against cancer cells. Small 8(13):2070–2077. https://doi.org/10.1002/smll.201200158
41. Liu QL, Xu L, Zhang XJ, Li N, Zheng JP, Guan MR, Fang XH, Wang CR, Shu CY (2013) Enhanced photodynamic efficiency of an aptamer-guided fullerene photosensitizer toward tumor cells. Chem-Asian J 8(10):2370–2376. https://doi.org/10.1002/asia.201300039
42. Lu Q, Schuster DI, Wilson SR (1996) Preparation and characterization of six bis(N-methylpyrrolidine)-C-60 isomers: magnetic deshielding in isomeric bisadducts of C-60. J Org Chem 61(14):4764–4768. https://doi.org/10.1021/jo960466t
43. Maggini M, Scorrano G, Prato M (1993) Addition of azomethine ylides to C-60 – synthesis, characterization, and functionalization of fullerene pyrrolidines. J Am Chem Soc 115(21):9798–9799. https://doi.org/10.1021/ja00074a056
44. Mashino T, Usui N, Okuda K, Hirota T, Mochizuki M (2003) Respiratory chain inhibition by fullerene derivatives: hydrogen peroxide production caused by fullerene derivatives and a respiratory chain system. Bioorg Med Chem 11(7):1433–1438. https://doi.org/10.1016/s0968-0896(02)00610-7
45. Mizuno K, Zhiyentayev T, Huang L, Khalil S, Nasim F, Tegos GP, Gali H, Jahnke A, Wharton T, Hamblin MR (2011) Antimicrobial photodynamic therapy with functionalized fullerenes: quantitative structure-activity relationships. J Nanomed Nanotechnol 2(2):1–9. https://doi.org/10.4172/2157-7439.1000109
46. Mroz P, Pawlak A, Satti M, Lee H, Wharton T, Gali H, Sarna T, Hamblin MR (2007) Functionalized fullerenes mediate photodynamic killing of cancer cells: Type I versus Type II photochemical mechanism. Free Radical Bio Med 43(5):711–719. https://doi.org/10.1016/j.freeradbiomed.2007.05.005
47. Mroz P, Xia YM, Asanuma D, Konopko A, Zhiyentayev T, Huang YY, Sharma SK, Dai TH, Khan UJ, Wharton T, Hamblin MR (2011) Intraperitoneal photodynamic therapy mediated by a fullerene in a mouse model of abdominal dissemination of colon adenocarcinoma. Nanomed-Nanotechnol 7(6):965–974. https://doi.org/10.1016/j.nano.2011.04.007
48. Nagano T, Arakane K, Ryu A, Masunaga T, Shinmoto K, Mashiko S, Hirobe M (1994) Comparison of singlet oxygen production efficiency of C-60 with other photosensitizers, based on 1268-Nm emission. Chem Pharm Bull 42(11):2291–2294
49. Nakamura E, Isobe H (2003) Functionalized fullerenes in water. The first 10 years of their chemistry, biology, and nanoscience. Accounts Chem Res 36(11):807–815. https://doi.org/10.1021/ar030027y
50. Oriana S, Aroua S, Sollner JO, Ma XJ, Iwamoto Y, Yamakoshi Y (2013) Water-soluble C60- and C70-PVP polymers for biomaterials with efficient (1)O2 generation. Chem Commun (Camb) 49(81):9302–9304. https://doi.org/10.1039/c3cc45501g
51. Otake E, Sakuma S, Torii K, Maeda A, Ohi H, Yano S, Morita A (2010) Effect and mechanism of a new photodynamic therapy with glycoconjugated fullerene. Photochem Photobiol 86(6):1356–1363. https://doi.org/10.1111/j.1751-1097.2010.00790.x

52. Poland CA, Duffin R, Kinloch I, Maynard A, Wallace WAH, Seaton A, Stone V, Brown S, MacNee W, Donaldson K (2008) Carbon nanotubes introduced into the abdominal cavity of mice show asbestos-like pathogenicity in a pilot study. Nat Nanotechnol 3(7):423–428. https://doi.org/10.1038/nnano.2008.111
53. Prato M, Suzuki T, Foroudian H, Li Q, Khemani K, Wudl F, Leonetti J, Little RD, White T, Rickborn B, Yamago S, Nakamura E (1993) [3+2] and [4+2] cycloadditions of C60. J Am Chem Soc 115(4):1594–1595. https://doi.org/10.1021/ja00057a065
54. Rancan F, Rosan S, Boehm F, Cantrell A, Brellreich M, Schoenberger H, Hirsch A, Moussa F (2002) Cytotoxicity and photocytotoxicity of a dendritic C-60 mono-adduct and a malonic acid C-60 tris-adduct on Jurkat cells. J Photoch Photobio B 67(3):157–162. https://doi.org/10.1016/S1011-1344(02)00320-2
55. Ruoff RS, Tse DS, Malhotra R, Lorents DC (1993) Solubility of C-60 in a variety of solvents. J Phys Chem-Us 97(13):3379–3383. https://doi.org/10.1021/j100115a049
56. Shi JJ, Yu XY, Wang L, Liu Y, Gao J, Zhang J, Ma R, Liu RY, Zhang ZZ (2013) PEGylated fullerene/iron oxide nanocomposites for photodynamic therapy, targeted drug delivery and MR imaging. Biomaterials 34(37):9666–9677. https://doi.org/10.1016/j.biomaterials.2013.08.049
57. Sijbesma R, Srdanov G, Wudl F, Castoro JA, Wilkins C, Friedman SH, Decamp DL, Kenyon GL (1993) Synthesis of a fullerene derivative for the inhibition of HIV enzymes. J Am Chem Soc 115(15):6510–6512. https://doi.org/10.1021/ja00068a006
58. Sivaraman N, Dhamodaran R, Kaliappan I, Srinivasan TG, Rao PRV, Mathews CK (1992) Solubility of C-60 in organic-solvents. J Org Chem 57(22):6077–6079. https://doi.org/10.1021/jo00048a056
59. Sperandio FF, Sharma SK, Wang M, Jeon S, Huang YY, Dai TH, Nayka S, de Sousa SCOM, Chiang LY, Hamblin MR (2013) Photoinduced electron-transfer mechanisms for radical-enhanced photodynamic therapy mediated by water-soluble decacationic C-70 and C84O2 fullerene derivatives. Nanomed-Nanotechnol 9(4):570–579. https://doi.org/10.1016/j.nano.2012.09.005
60. Tabata Y, Murakami Y, Ikada Y (1997) Photodynamic effect of polyethylene glycol-modified fullerene on tumor. Jpn J Cancer Res 88(11):1108–1116. https://doi.org/10.1111/j.1349-7006.1997.tb00336.x
61. Takehara H, Fujiwara M, Arikawa M, Diener MD, Alford JM (2005) Experimental study of industrial scale fullerene production by combustion synthesis. Carbon 43(2):311–319. https://doi.org/10.1016/j.carbon.2004.09.017
62. Tokuyama H, Yamago S, Nakamura E, Shiraki T, Sugiura Y (1993) Photoinduced biochemical-activity of fullerene carboxylic-acid. J Am Chem Soc 115(17):7918–7919. https://doi.org/10.1021/ja00070a064
63. Wang M, Huang L, Sharma SK, Jeon S, Thota S, Sperandio FF, Nayka S, Chang J, Hamblin MR, Chiang LY (2012) Synthesis and photodynamic effect of new highly photostable decacationically armed [60]- and [70]fullerene decaiodide monoadducts to target pathogenic bacteria and cancer cells. J Med Chem 55(9):4274–4285. https://doi.org/10.1021/jm3000664
64. Wang M, Maragani S, Huang LY, Jeon S, Canteenwala T, Hamblin MR, Chiang LY (2013) Synthesis of decacationic [60]fullerene decaiodides giving photoinduced production of superoxide radicals and effective PDT-mediation on antimicrobial photoinactivation. Eur J Med Chem 63:170–184. https://doi.org/10.1016/j.ejmech.2013.01.052
65. Wiehe A, O'Brien JM, Senge MO (2019) Trends and targets in antiviral phototherapy. Photoch Photobio Sci 18(11):2565–2612. https://doi.org/10.1039/c9pp00211a
66. Witte P, Beuerle F, Hartnagel U, Lebovitz R, Savouchkina A, Sali S, Guldi D, Chronakis N, Hirsch A (2007) Water solubility, antioxidant activity and cytochrome C binding of four families of exohedral adducts of C60 and C70. Org Biomol Chem 5(22):3599–3613. https://doi.org/10.1039/b711912g
67. Yamago S, Tokuyama H, Nakamura E, Kikuchi K, Kananishi S, Sueki K, Nakahara H, Enomoto S, Ambe F (1995) In-vivo biological behavior of a water-miscible fullerene – C-14 labeling, absorption, distribution, excretion and acute toxicity. Chem Biol 2(6):385–389. https://doi.org/10.1016/1074-5521(95)90219-8

68. Yamakoshi YN, Yagami T, Fukuhara K, Sueyoshi S, Miyata N (1994) Solubilization of fullerenes into water with polyvinylpyrrolidone applicable to biological tests. J Chem Soc Chem Comm 4:517–518. https://doi.org/10.1039/c39940000517
69. Yamakoshi Y, Sueyoshi S, Fukuhara K, Miyata N (1998) center dot OH and O-2(center dot-) generation in aqueous C-60 and C-70 solutions by photoirradiation: an EPR study. J Am Chem Soc 120(47):12363–12364. https://doi.org/10.1021/ja9823969
70. Yamakoshi Y, Umezawa N, Ryu A, Arakane K, Miyata N, Goda Y, Masumizu T, Nagano T (2003) Active oxygen species generated from photoexcited fullerene (C-60) as potential medicines: O-2(-center dot) versus O-1(2). J Am Chem Soc 125(42):12803–12809. https://doi.org/10.1021/ja0355574
71. Yamakoshi Y, Aroua S, Nguyen TM, Iwamoto Y, Ohnishi T (2014) Water-soluble fullerene materials for bioapplications: photoinduced reactive oxygen species generation. Faraday Discuss 173:287–296. https://doi.org/10.1039/c4fd00076e
72. Yoshida ZI, Takekuma H, Takekuma SI, Matsubara Y (1994) Molecular recognition of C-60 with gamma-cyclodextrin. Angew Chem Int Ed Engl 33(15-16):1597–1599. https://doi.org/10.1002/anie.199415971
73. Zhao B, Bilski PJ, He YY, Feng L, Chignell CF (2008) Photo-induced reactive oxygen species generation by different water-soluble fullerenes (C) and their cytotoxicity in human keratinocytes. Photochem Photobiol 84(5):1215–1223. https://doi.org/10.1111/j.1751-1097.2008.00333.x

Soft Materials

27

Kentaro Tashiro

Contents

Abstract

This chapter picked up some selected examples of soft materials of fullerenes and the related compounds reported in no earlier than 1993. These representative examples include (1) polymers containing covalently linked fullerenes in their main chain or at their pendant positions; (2) non-covalent blends of fullerenes and other organic or inorganic polymers; (3) covalently modified fullerene derivatives as the forms of, e.g., donor–fullerene dyads, dendrimers with the fullerene core, or amphiphilic fullerene derivatives; and (4) mixtures of fullerenes and another molecule that can form their supramolecular complexes. The resultant polymers and molecules as well as blends mostly exhibited particular self-assembling or nanostructure-forming behavior, affording various macroscopic forms such as liquid crystals, vesicles, membranes, films, gels, etc. By taking advantage of the unique structural features together with the particular chemical and physical properties of fullerene, they work not only as photovoltaic, charge carrier transporting, or photocatalytic materials but also for some biomedical or separation applications.

K. Tashiro (✉)
International Center for Materials Nanoarchitectonics (MANA), National Institute for Materials Science (NIMS), Tsukuba, Japan
e-mail: TASHIRO.Kentaro@nims.go.jp

X. Lu et al. (eds.), *Handbook of Fullerene Science and Technology*,
https://doi.org/10.1007/978-981-16-8994-9_40

Keywords

Polymer · Blend · · Liquid crystal · Amphiphile · Vesicle · Membrane · Film · Gel · Dendrimer · Dyad

Introduction

Fullerenes intrinsically tend to form non-soft crystalline assemblies because of their spherical shape composed of rigid carbon frameworks. Therefore, it is generally necessary to modify their structures or hybridize with other compounds to design soft materials of fullerenes. The resultant materials can be classified into two categories, i.e., traditional polymer and molecule-based materials. The former contains polymeric components with the distribution of molecular weight, while the latter was originally based on a relatively small molecule having the unique molecular weight. Although the molecular size in the latter category nowadays sometimes reaches to the range for macromolecules because of the development of synthetic technology for them, there is still a clear gap between these two categories in terms of the structural design philosophy of the materials. Therefore, this chapter aims to describe selected topical examples of the soft materials of fullerenes with their classification according to the concept of structural design strategy adopted but not by the type of the resultant properties of the materials or the direction of the applications. This is expected to be an efficient way to highlight the key points of the described works from the synthetic point of view, hopefully allowing the new challenges with the similar design concepts by the following researchers in the related fields. Because of the same reason, the structures of the compounds that played the main role in each research work are shown in the figures as detailed as possible. It is clear that even among the limited numbers of the research works selected in this chapter, the conceptually common particular structural motifs, namely, donor–fullerene dyads, dendrimers with the fullerene core, and amphiphilic fullerene derivatives, repeatedly appear. This can be understood as the natural consequence of the efforts of the accompanied researchers to make use of the unique structural features together with the particular chemical and physical properties of fullerenes for the engineering of soft materials.

Main Text

Polymeric Materials with the Distribution of Molecular Weight

Covalent Polymers

Main Chain Polymers

While the polymers containing fullerenes at their main chain have been the attractive synthetic targets as theoretically it is the best way to maximize the content of fullerenes in the polymers, their examples via the one-pot polymerization followed

by the certain levels of the structural characterization are not so ample because of the occurrence of more than three numbers of the reactions at the same fullerene moiety that eventually affords cross-linked, insoluble products. A generally applicable solution for this issue is the usage of sterically demanding chemical species to attack fullerenes so that the possible number of reactions per fullerene can be limited. One of the earliest successful examples along with this concept was reported in 2000 by Geckeler et al., where bis(*p*-aminophenyl) ether included in *ß*-cyclodextrin was coupled with C_{60} to achieve their alternating copolymerization (**1**, Fig. 1) [1]. The cyclodextrin moiety played the essential roles not only to make the diamine bulkier enough but also give satisfactory high water solubility to the resultant polymers, allowing their solution-phase characterizations such as absorption and NMR spectroscopies. The resultant polymer was found to behave as a scavenger for a living free radical such as 1,1-diphenyl-2-picrylhydrazyl and cleave DNA under photoirradiation, suggesting the potentials for the biological and biomedical applications. Another type of fullerene main chain polymer (**2**, Fig. 2), which is soluble in common organic solvents, was prepared via the reaction between relatively bulky 1,4-bis(methylcyclohexyl ether)-2,5-dibromomethyl benzene and C_{60} by applying the chemistry of copper-catalyzed atom transfer radical addition [2]. The products showed a broad endothermic melting peak around 297 °C in the differential scanning calorimetry (DSC) profile, while the fullerene content in them were calculated to be

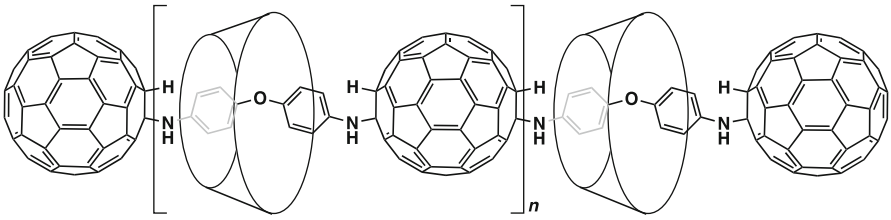

Fig. 1 Molecular structure of polymer **1**

Fig. 2 Molecular structure of polymer **2**

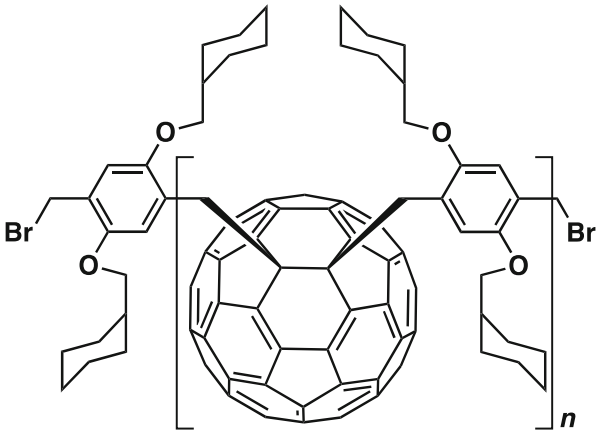

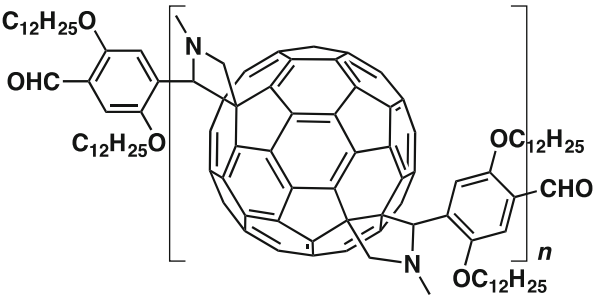

Fig. 3 Molecular structure of polymer **3**

62 weight percent from their thermogravimetric analysis (TGA) data. These polymers were mixed with poly(3-hexylthiophene) (P3HT), and their potentials for the fabrication of photovoltaic devices were examined, where the trace of the surface state of the blends through annealing by means of tapping-mode atomic force microscopy (AFM) unveiled the presence of particular nano-structuralization in the material unprecedented in the case of the blends of P3HT with [6,6]-phenyl-C61-butyric acid methyl ester (PCBM). More recently, a sterically controlled azomethine ylide cycloaddition, a metal-free reaction for fullerenes, was successfully applied for the synthesis of main chain fullerene polymers with their molecular weights up to 24,300 g mol^{-1} that corresponds to the repeating unit number of 19 (**3**, Fig. 3) [3]. Further structural characterizations including modelling studies on the obtained polymers indicated that they are composed of regio-irregularly di-substituted fullerene moieties with a majority of *trans*-3 isomers. The polymers showed a sign of decomposition around 350–400 °C in their TGA profiles possibly due to the loss of the alkyl side chains. Their DSC profiles up to 180 °C exhibited only featureless curves, suggesting that the obtained polymers afforded an unstructured amorphous form, while the presence of the disorder-order transition upon heating was not completely excluded.

Pendant Polymers

As the fullerene moiety does not need to join into the polymerization reaction, the preparation of fullerene-pendant polymers can readily avoid the occurrence of problematic cross-linking reactions between fullerene moieties by the judicious choice of the type of polymerization reaction. Due to this high flexibility in the design of monomer structures, several examples of the fullerene-pendant polymers have been reported so far. For example, π-conjugated enyne polymers bearing pendant C_{60} moieties (**4**, Fig. 4) have been obtained by means of a palladium-catalyzed acetylene–iodobenzene cross-coupling reaction by expecting that the resultant polymers would be able to play the role as a covalently linked donor–acceptor bulk heterojunction, where the polymer main chain and pendant fullerenes serve the donor and acceptor, respectively [4]. In fact, the photo-induced absorption spectroscopy on the polymer thin film indicated the migration of photo-generated opposite charges to different sites in the film, suggesting that the material behaves as

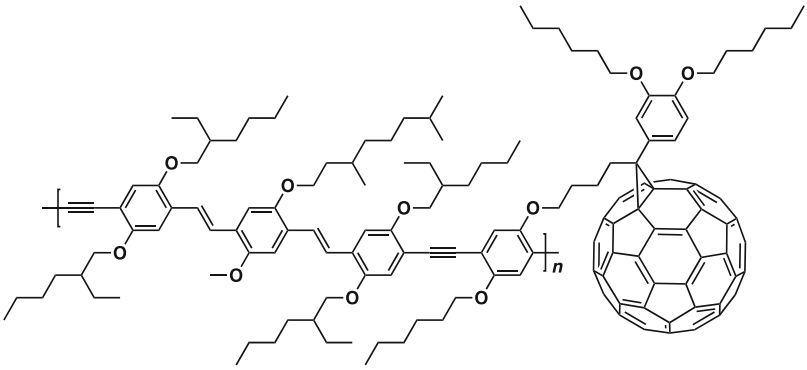

Fig. 4 Molecular structure of polymer **4**

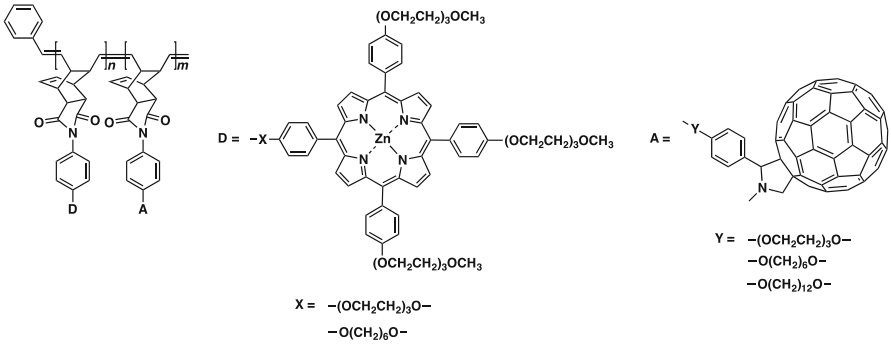

Fig. 5 Molecular structure of block copolymer **5**

a heterojunction. As another approach for the construction of heterojunction, block copolymers bearing both of the donor and acceptor pendant moieties were designed, where the two types of diene monomers attached with a zinc porphyrin or fullerene moiety were polymerized in a stepwise fashion by using the methodology of living ring-opening metathesis polymerization (**5**, Fig. 5) [5]. Scanning as well as transmission electron microscopy (SEM and TEM) demonstrated the successful segregation of the domains having the width of 5–6 nm composed of multiple donor or acceptor moieties, which allowed the cast polymer films to display a good photoconductivity with the ambipolar charge-transporting property. The hole and electron mobility values in the largest cases, evaluated by the current-mode time-of-flight (TOF) technique, were 3.7×10^{-2} and 3.0×10^{-3} $cm^2\ V^{-1}\ s^{-1}$, respectively. Being motivated to see the structural and electronic effects of fullerenes on a helix-forming, π-conjugated polymer, the optically active form of polyphenylacetylene was also merged with C_{60}, through the rhodium-catalyzed copolymerization of fullerene-appended and non-appended phenylacetylene monomers (**6**, Fig. 6) [6]. Since the fullerene non-appended monomer used was bearing an optically active (*R*)-[(1-phenylethyl)carbamoyl]oxy substituent, the resultant polyphenylacetylene

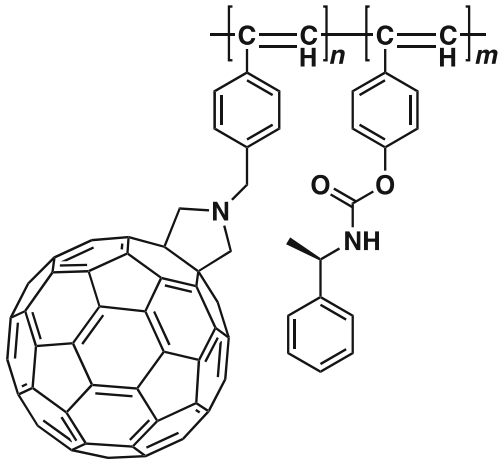

Fig. 6 Molecular structure of copolymer **6**

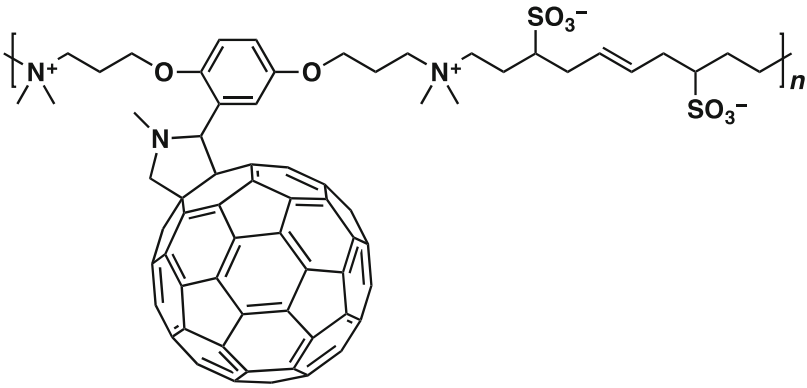

Fig. 7 Molecular structure of polymer **7**

exhibited intense circular dichroism (CD) signals in the π-conjugated main-chain absorption region below 500 nm. Variable-temperature (VT) CD spectroscopy down to −80 °C together with the tapping-mode AFM on the polymers suggested that they are able to adopt a helical conformation even in the presence of bulky pendant groups, where their helix sense is assumed to be controlled to be left-handed. While all of the polymer main chains in **4**–**6** are hydrophobic in nature as is the case of fullerenes, covalent linkage of ionic polymers and fullerene pendants also produced intriguing properties. One of the recent representative examples was prepared by the nucleophilic ring-opening reaction of a bis-sultone with a fullerene derivative bearing two tertiary amine groups, which afforded zwitterionic polymers containing sulfonate/ammonium functionalities (**7**, Fig. 7) [7]. Co-existence of fullerene and ionic polymer main chain structures in the same molecule, where the former and latter are friendly with organic *n*-type semiconductors and metal electrode surfaces,

respectively, made it as the excellent cathode interlayer material for the organic photovoltaics, as demonstrated by the significant improvement of the power conversion efficiency (PCE) of the device containing [6,6]-phenyl-C_{71}-butyric acid methyl ester as the *n*-type semiconductor from 2.75% to 10.74% by its integration into the setup.

End-Attached Polymers

The third approach to make polymers containing covalently linked fullerene moieties is the functionalization of polymer terminals with fullerenes. While this approach is disadvantageous for the preparation of polymers with a high fullerene content, it is advantageous to control the position of fullerene moieties in the polymer structure. As a representative combination of the donor and acceptor, P3HT having two formyl functionalities at its ends was reacted with C_{60} to make the fullerene-P3HT-fullerene configuration (**8**, Fig. 8) [8]. The fullerene weight content in the product was assumed to be 19% by means of NMR spectroscopy. In spite of the presence of spherically shaped fullerene moieties that could potentially inhibit the stacking interactions between P3HT moieties, the resultant polymers were found to preserve the capability to form an ordered self-assembled structure as P3HT has, which was proved by DSC, small- and wide-angle X-ray scattering, and AFM. Another example of the polymers bearing fullerenes at their ends can be found among polymer amphiphiles, where the multiply surface-functionalized hydrophilic fullerene bearing terminal alkyne groups was tethered with one or two polystyrene chains by using the Huisgen 1,3-dipolar cycloaddition known as the click reaction (**9**, Fig. 9) [9]. Since the polystyrene chain length was able to be precisely controlled by means of atom transfer radical polymerization technique, the structural modification of **9** became flexible enough to allow the systematic studies on the relationship between the molecular and assembled structures of this type of polymer amphiphiles. In fact, these amphiphiles were found to self-assemble into spherical micelles, cylinders, or bilayer vesicles dependent on the parameters such as

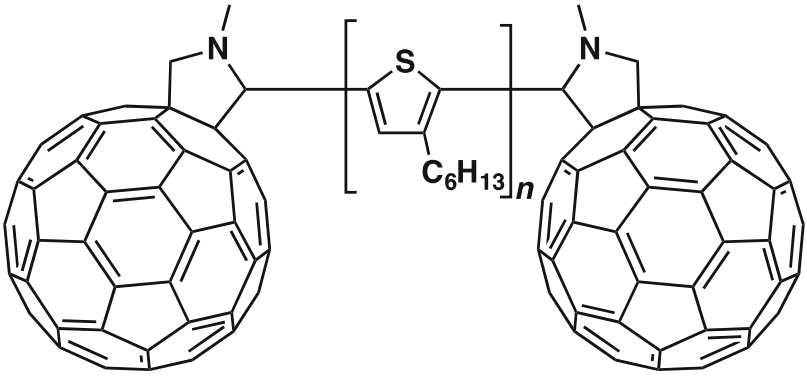

Fig. 8 Molecular structure of polymer **8**

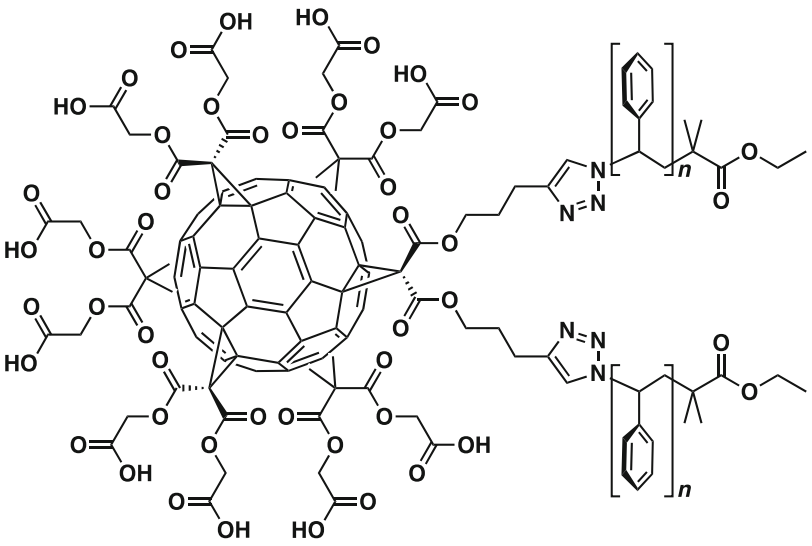

Fig. 9 Molecular structure of polymer amphiphile **9**

molecular shape, concentration, and polystyrene chain length, as revealed through the characterizations by TEM and light scattering experiments.

Blends with the Polymers

Binary Blends

Since the discovery of fullerenes in 1985, particularly after the report of arc-discharge method by Krätchmer and Huffman that allows the supply of the visible quantity of fullerenes to the researchers, their biological and biomedical activities have always been the attractive research subjects. Such situations prompted synthetic chemists to design various types of charged fullerene derivatives that are soluble in water or semi-aqueous solvent conditions to allow their hybridization with biopolymers. In 1998, Tour et al. reported C_{60}-*N*,*N*-dimethylpyrrolidinium compound (**10**, Fig. 10) whose cationic charge on the pyrrolidinium nitrogen was expected to work for the electrostatic interactions with the negatively charged phosphate moieties in DNA strands [10]. In fact, mixing of plasmid DNA and iodide salt of **10** caused the compaction of the DNA, which was visualized by TEM without any staining of the sample due to the accumulation of fullerenes around the DNA through the anion exchange on **10**. Not only the helical polymers in nature but also those among synthetic polymers were found to form complexes with fullerenes. Yashima et al. found that syndiotactic poly(methyl methacrylate) (st-PMMA), a well-known helix-forming polymer, encapsulates fullerenes (Fig. 11) [11]. While st-PMMA alone forms physical gels in aromatic solvents with the encapsulation of solvent molecules in the inner space of the polymer helix, replacement of these trapped solvent molecules with fullerenes by their complexation made the gel thermally more stable, as its melting temperature showed a clear increase. Although

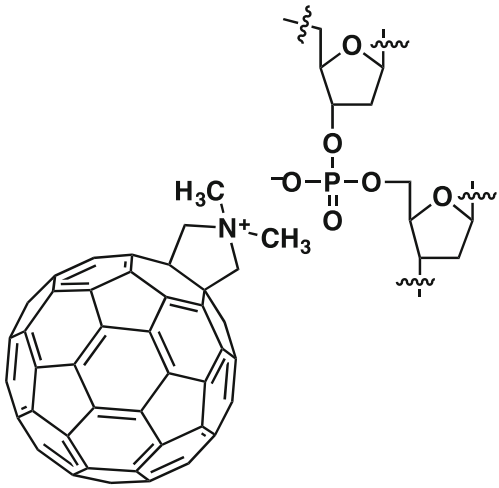

Fig. 10 Molecular structure of cationic fullerene **10** that forms an ion pair with a phosphate in DNA

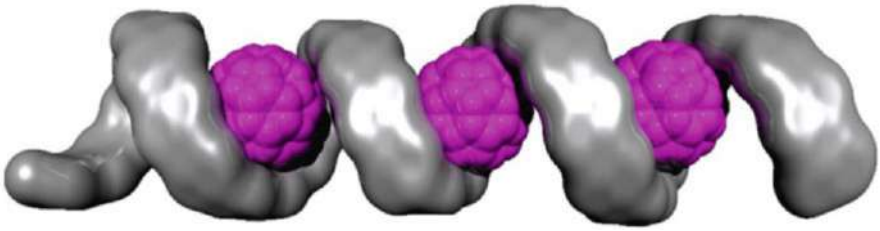

Fig. 11 Schematic representation of the supramolecular complex of syndiotactic poly(methyl methacrylate) and C_{60}

the helical conformation of st-PMMA in the absence of fullerenes was disrupted in the film state after the removal of the solvent from the gel, the polymer-fullerene complexes preserved the conformation even after forming dry film, as demonstrated by DSC, polarized optical microscopy (POM), X-ray diffractometry (XRD), and AFM. The encapsulation phenomenon that took place through an induced-fit mechanism was later applied for the selective extraction of C_{70} from its mixtures with C_{60} and the enrichment of higher fullerenes from the commercially available carbon soot containing C_{60}, C_{70}, and higher fullerenes [12]. Moreover, by taking advantage of the controllability of the helix sense of st-PMMA by using an enantiomer of chiral liquid as the solvent, optically active st-PMMA with an excess single-handed helix, prepared by using (*R*)- or (*S*)-1-phenylethylamine, was subjected to the complexation with the chiral fullerene mixtures containing racemic C_{76}, C_{84}, C_{86}, C_{88}, C_{90}, C_{92}, C_{94}, and C_{96}, which allowed to afford fractions enriched in one of the enantiomer of those chiral fullerenes. For the separation of fullerenes, cross-linked porphyrin polymers were also found to work, where commercially available protoporphyrin disodium salt **11** was allowed to react with a mixture of trimethylol propane **12** and 1,6-hexanediol under acidic conditions (Scheme 1) [13]. The resultant insoluble

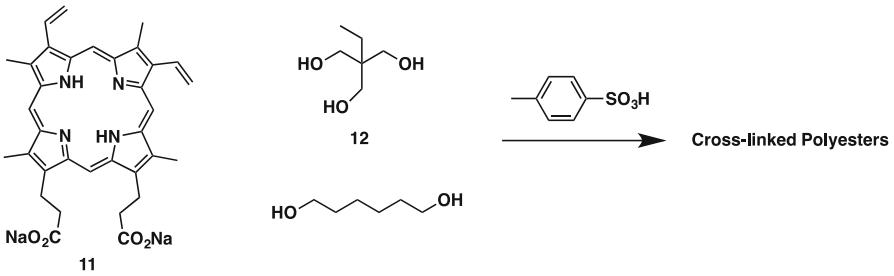

Scheme 1 Synthesis of porphyrin polymers cross-linked via ester bonds

polymers embedded in a toluene solution of the soluble portion of the carbon soot selectively adsorbed higher fullerenes, allowing their enrichment from 10% to 34% through one adsorption–desorption cycle on the carbon soot. Imprinting of one of the higher fullerenes C_{78} at the polymerization step to optimize the pore size of the polymers for them improved the degree of the enrichment up to 79%, while the similar but more heavily cross-linked polymers as obtained from the same porphyrin monomer and **12** without using 1,6-hexanediol rather enriched C_{60}, indicating the tunability of the selectivity of the polymers toward targeted fullerenes.

Ternary Blends

Examples of the ternary blends with fullerene can been found in the attempts to design photo-responsive electrodes by their surface modification. Ikeda and Shinkai et al. applied the layer-by-layer approach for the construction of a film composed of the layered donor and acceptor on an anion-coated indium–tin oxide (ITO) electrode, where (1) hexacationic homooxacalix[3]arene-C_{60} 2:1 complex and (2) anionic polymers bearing porphyrin or zinc porphyrin pendant groups were deposited in a stepwise fashion by using their electrostatic interactions as the driving force (Fig. 12) [14]. Because of the electron transfer from the photo-excited porphyrin or zinc porphyrin to C_{60} to the ITO electrode, dipped in a Na_2SO_4 aqueous solution, stable anodic photocurrent was observed under the irradiation with monochromatic visible light in the presence of ascorbic acid as the sacrificial electron donor in the electrolyte solution. Supramolecular hybridization of fullerene and porphyrin or its zinc complex has been also achieved on the gold nanoparticles [15]. In this particular system, the surface of the gold nanoparticle was firstly covered with the thiol-appended porphyrin or zinc porphyrin monolayer via the sulfur–gold bond formation, to which C_{60} or C_{70} was further hybridized through its supramolecular insertion between the neighboring non- or zinc metallated porphyrin moieties by using the attractive interaction operative between them as the driving force (Fig. 13). The resultant ternary blend, after their solvent-triggered clusterization, was deposited on a nanostructured SnO_2 film electrode surface by using an electrophoretic method and subjected to the characterization of its photochemical and photo-electrochemical properties, where the photo-electrochemical cell using the blend with one of the non-metallated porphyrins afforded PCE of 1.5% as the best performance.

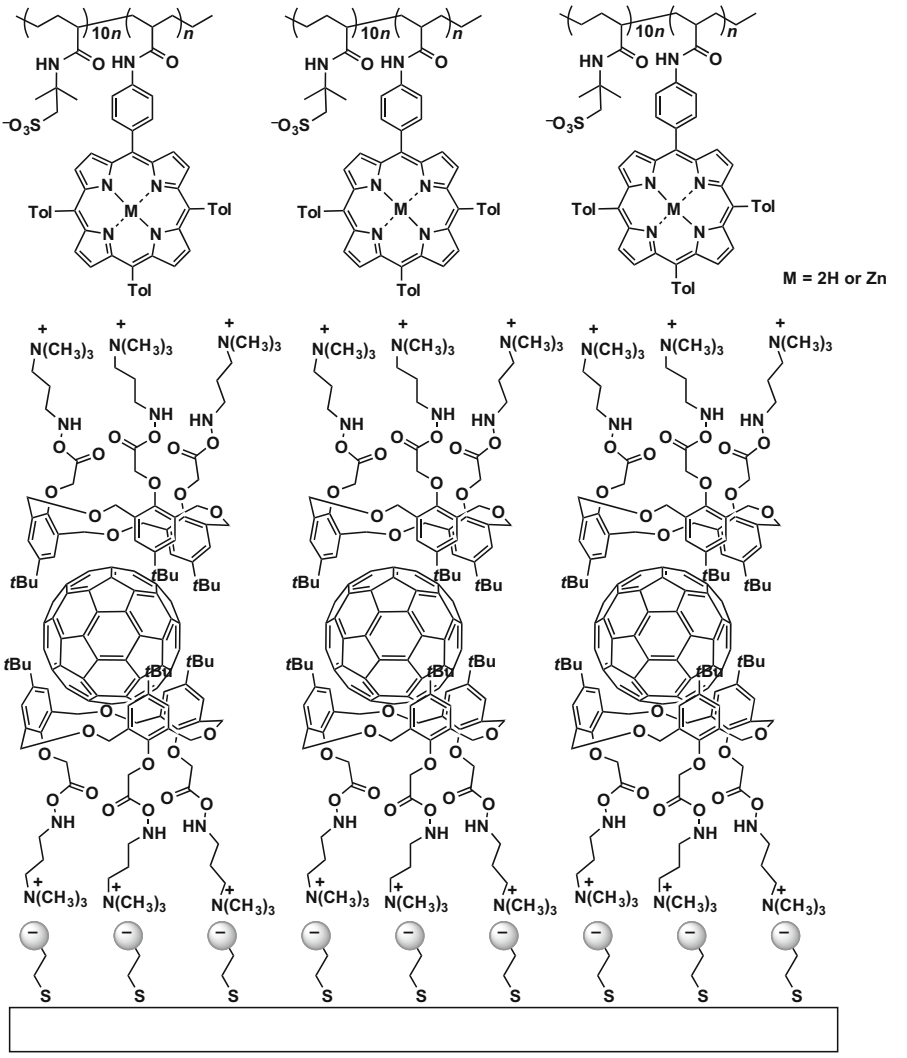

Fig. 12 Schematic representation of the electrode surface modified with hexacationic homooxacalix[3]arene-C_{60} 2:1 complex and anionic polymers bearing porphyrin or zinc porphyrin pendant group

Materials with Unique Molecular Weight Components

Covalent Derivatives

Long-Alkylated Derivatives

Introduction of long alkyl chains covalently into the fullerene moiety has been a widely adopted molecular design strategy to obtain the soft materials of fullerenes by

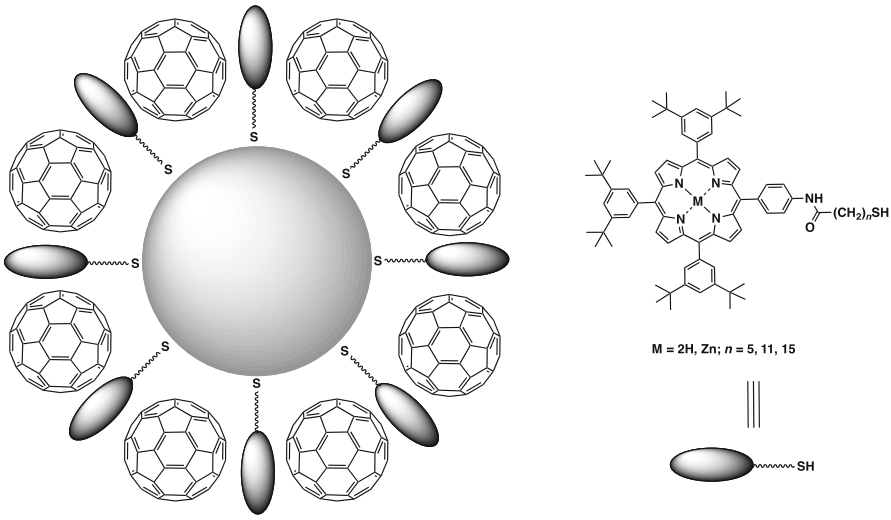

Fig. 13 Schematic representation of the ternary blends of gold nanoparticle, thiol-appended porphyrin or zinc porphyrin, and C_{60}

Fig. 14 Molecular structure of fullerene lipid **13**

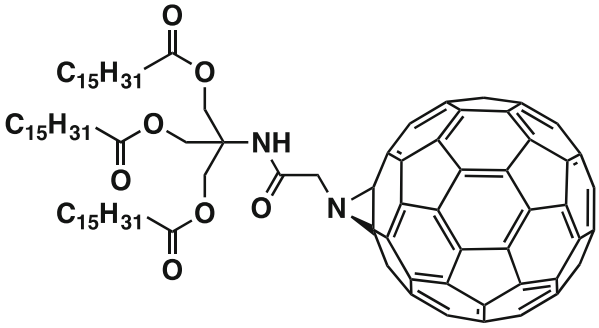

expecting the merge of temperature or solvent-dependent self-assembling behaviors of the long-alkylated molecules and particular properties of fullerenes. In 1996, Nakashima et al. reported a fullerene derivative with a lipid-like substituent bearing three C_{15} alkyl chains (**13**, Fig. 14) [16]. Casting a chloroform solution of **13** at room temperature afforded a film, in which the molecule was found to form multibilayer membrane structures as proved by its diagnostic XRD pattern. DSC and VT-IR studies on the film revealed that the elevation of the temperature caused a phase transition at 35. 2 °C, which was followed by another subphase transition occurring at 47 °C. The latter transition was accompanied with the blue shifts of the UV absorptions of the fullerene due to the smaller electronic interactions between fullerene moieties at the more fluid phase located above that temperature. As another approach, C_{60} was covalently modified with six pairs of C_{12} or C_{18} alkyl chains

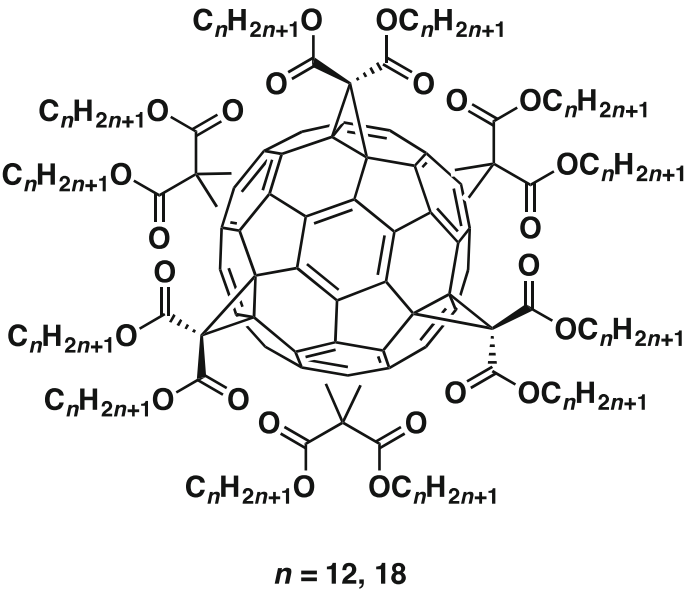

Fig. 15 Molecular structure of lipo-fullerene **14**

linked to the malonate substituents to afford so-called lipo-fullerene having T_h symmetry (**14**, Fig. 15), which was mixed with 1,2-dipalmitoyl-*sn*-glycero-3-phosphocholine (DPPC) to see the effects of that fullerene on the multilamellar vesicles composed of DPPC [17]. Although their mixtures containing up to 25 mol% of **14** showed no sign of their macroscopic segregation, the presence of **14** affected scarcely on the phase transition behavior of DPPC, which suggested the occurrence of their microscopic segregation. In fact, freeze fracture electron microscopy allowed to visualize the rod-like assembly of **14** in the bilayer of DPPC, which made the bilayer more tolerant against the deformation under the application of magnetic field. Alkylation of fullerene works not only to make fullerene-containing lipids but also for the design of liquid crystalline (LC) fullerenes. Fulleropyrrolidines with a site-specifically multi-alkoxylated phenyl group were found to form mesomorphic lamella phases at temperatures over 40 °C dependent on the substitution pattern and chain length (C_{16} or C_{20}) of the substituents (**15**, Fig. 16) [18]. Due to the possible formation of 2D layers of the fullerene moiety in the lamella phases, **15** preserved its intrinsic redox activity as a molecule even after the formation of LC assemblies. This feature allowed the material to work for the electron transportation, where the mobility was evaluated to be 3×10^{-3} cm^2 V^{-1} s^{-1} by the TOF technique. While the molecular structure is somewhat more elaborated, alkyl-functionalized fullerenes containing a *trans*-azobenzene unit, yet non-isomerizable into its *cis* form, in the molecular structure (**16**, Fig. 17) also formed 2D layers of fullerene moiety in their smectic LC phases in a wide temperature range including room temperature [19]. Evaluation of the electron mobility by means of the space-charge-limited current method afforded the highest value of 2.7×10^{-3} cm^2 V^{-1} s^{-1}, which is

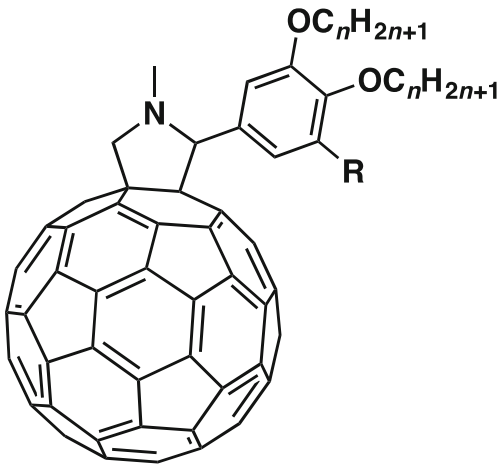

Fig. 16 Molecular structure of liquid crystalline fullerene **15**

R = OC_nH_{2n+1} or H

***n* = 16, 20**

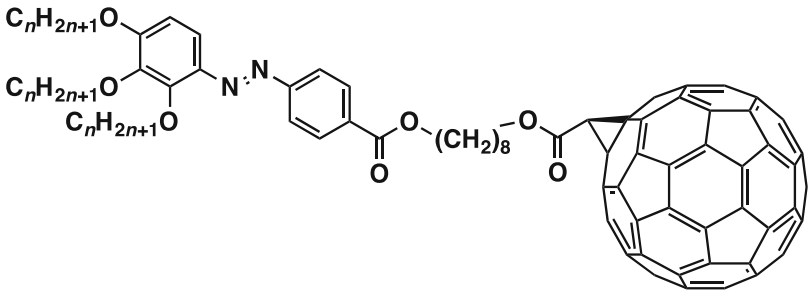

***n* = 4, 7, 8, 9, 12**

Fig. 17 Molecular structure of liquid crystalline fullerene **16**

comparable with the value obtained from PCBM even the fullerene content in **16** is only as low as around 50%. Corannulene composed of a single 5-membered ring surrounded by fused 5 benzene rings, known as a partial structure of fullerene, was also decorated with 30 dodecyl chains at the periphery to achieve its first liquid crystallization (**17**, Fig. 18) [20]. With the assists of ten amide as well as sulfur moieties also located in the substituents for the self-assembly, resultant molecule **17** successfully formed a hexagonal columnar mesophase from −10 to 154 °C, where a representative fan texture was observed under POM. Application of the AC electric field of 15 $V\mu m^{-1}$ to the LC phase at 125 °C caused the gradual disappearance of the

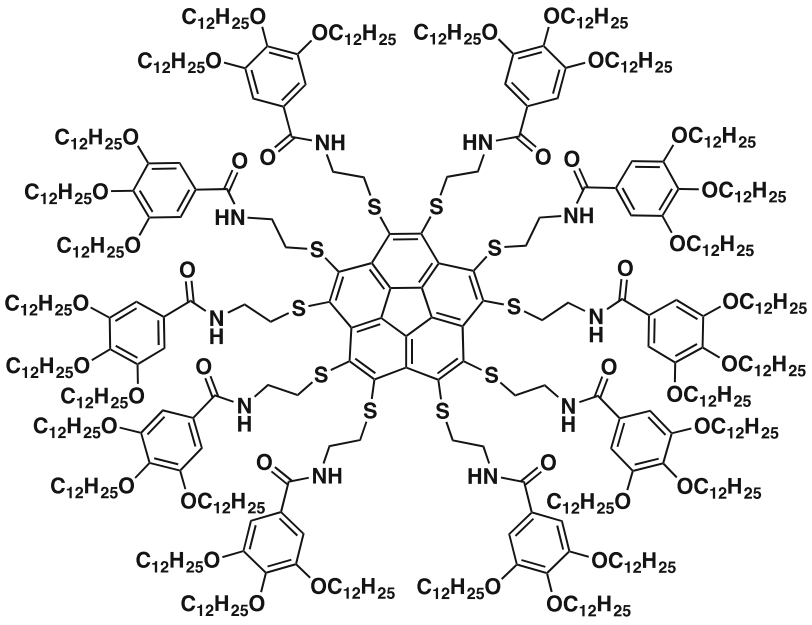

Fig. 18 Molecular structure of liquid crystalline corannulene **17**

birefringent image, demonstrating that the columnar assemblies of this LC corannulene were homeotropically aligned to the electrode surface (Fig. 19). The observed responsive nature of the LC to the application of electric field is most likely due to the presence of relatively large dipole moment of the supramolecular polar column composed of multiple amide functionalities and bowl-shaped corannulene moieties in **17**.

Dyads

As C_{60} serves as the excellent electron acceptor and *n*-type semiconductor, numerous examples of covalently linked donor–fullerene dyads have been designed so far. Georgakilas, Pellarini, and Prato et al. reported a series of amphiphilic fullerene derivatives having a positively charged ammonium functionality, among which a porphyrin–fullerene dyad molecule (**18**, Fig. 20) was found to exclusively form nano-tubular assemblies reaching 30 nm in diameter and 500 nm in length under aqueous conditions as observed by TEM [21]. The morphology of the assembled dyad was completely different from those obtained from a reference fullerene that lacks the porphyrin moiety, indicating the important role of the fullerene–porphyrin and porphyrin–porphyrin intermolecular interactions to form the observed tubular structures with the higher structural integrity. Another amphiphilic fullerene–porphyrin dyad bearing four triethyleneglycol chains at the one side of the porphyrin moiety, after the metallation of the porphyrin moiety with zinc ion (**19**, Fig. 21), formed micro-vesicles with the averaged diameter of 100 nm in mixtures of THF and

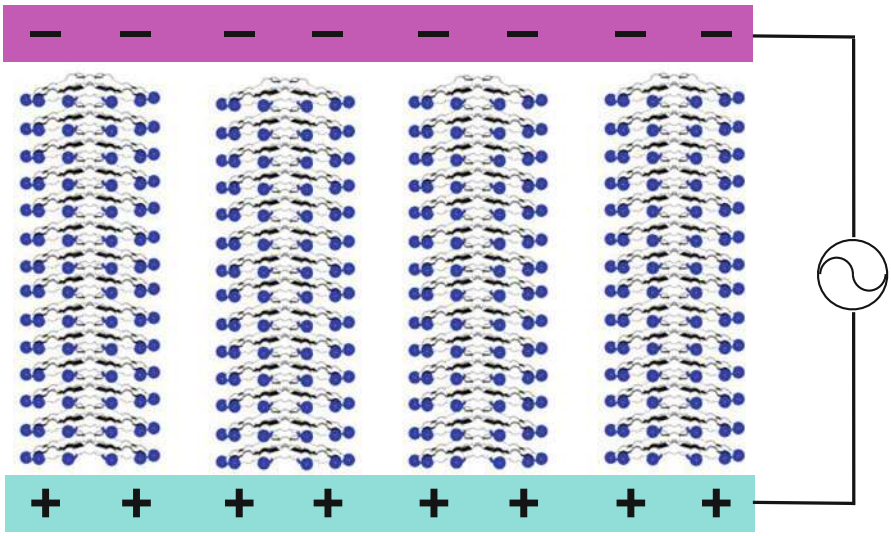

Fig. 19 Schematic representation of the homeotropic alignment of the columnarly assembled **17** in response to the application of AC electric field

Fig. 20 Molecular structure of amphiphilic dyad **18**

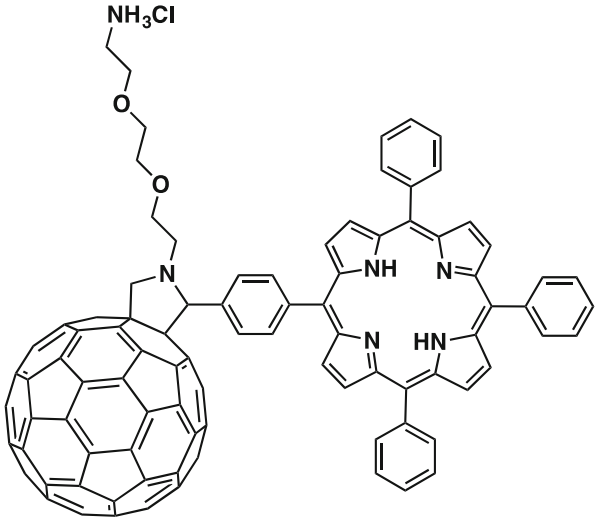

water [22]. Since the absorption spectrum of the vesicle showed the sign of fullerene–zinc porphyrin supramolecular interaction, their interdigitation to afford multilamellar vesicular membrane was suggested. In contrast to the lipid-based analogues, the resultant vesicular structures were highly tolerant against surfactants such as Triton X-100 and exhibited slow release of the encapsulated guest molecules from the interior space, indicating a feature of membranes composed of rigid π-electronic

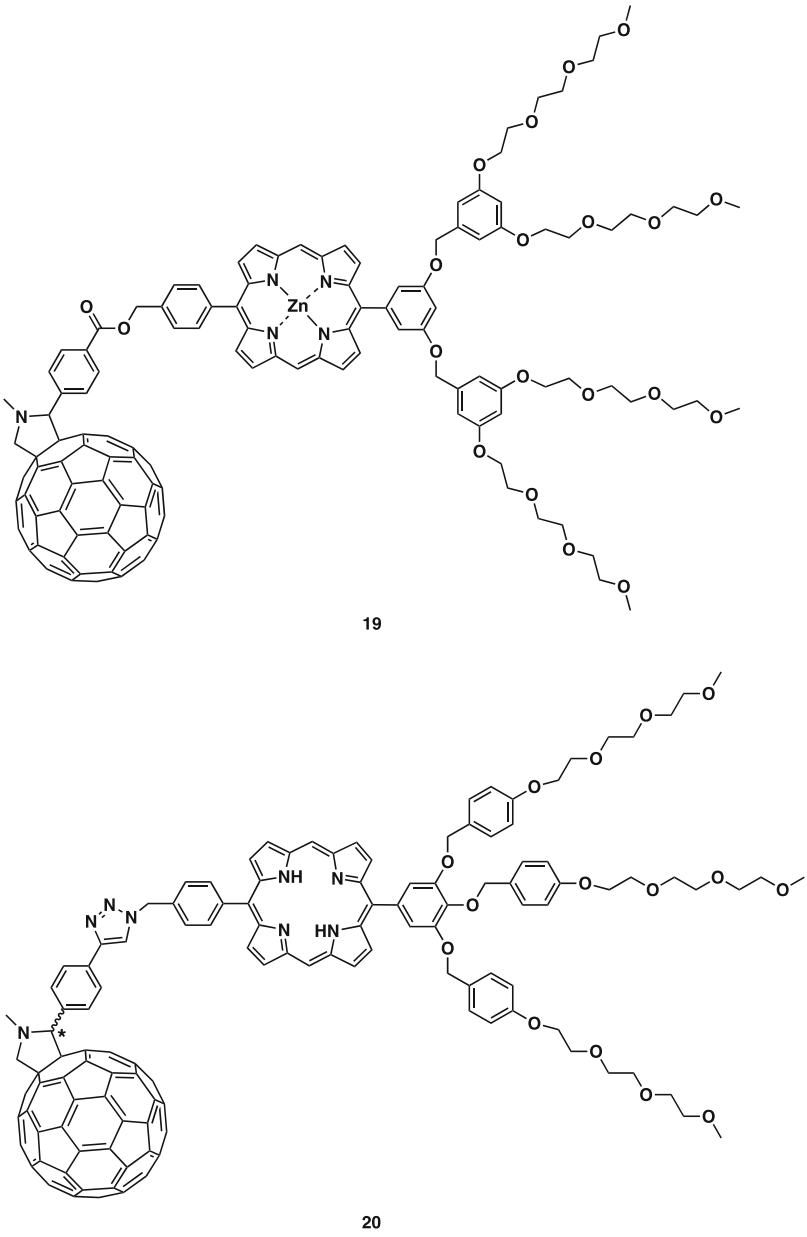

Fig. 21 Molecular structures of amphiphilic dyads **19** and **20**

molecular structures. Following researches on the self-assembling behavior of the analogous dyad systems revealed that the subtle change in a molecular structural parameter drastically changes not only the morphology of the resultant assemblies but also their physical properties. One of the representatives can be seen in the self-

assembly of a chiral dyad that possesses a stereogenic center at a carbon in the pyrrolidine ring (**20**, Fig. 21) [23]. While the slow diffusion of methanol into a CH_2Cl_2 solution of a racemic mixture of the dyad afforded submicrometer-sized spherical objects, assembly of one of its enantiomers under the identical conditions resulted in the formation of nanofibers up to 10μm in length. Because of their morphological as well as molecular packing differences, the photoconduction properties of the latter assemblies were much superior than that of the former, where the electron and hole TOF mobility values for the nanofibers (0.14 and 0.10 $cm^2\ V^{-1}\ s^{-1}$, respectively) are much superior than those of nanospheres (not observed and $1.5 \times 10^{-4}\ cm^2\ V^{-1}\ s^{-1}$, respectively). Although fullerene is intrinsically a hydrophobic molecule, its multiply hydroxylated form called fullerenol can serve as a hydrophilic moiety in the amphiphilic dyads. Very recently, a series of dyads composed of fullerenol and relatively hydrophobic dyes such as acridine yellow G (**21-Y**, Fig. 22), neutral red (**21-R**), and toluidine blue O (**21-B**) having different peak top position at 445, 530, and 629 nm, respectively, were prepared to form vesicular structures where the five dye moieties per fullerenol were expected to be located at the inner part of the membrane with their intermolecular interdigitation [24]. The vesicles obtained from the mixture of two types of dyads **21-Y** and **21-B** bearing different dyes showed a better performance in oxygen reduction to produce superoxide under visible light irradiation than the reference vesicles composed of either of the two dyads, while intramolecular mixing of these two dyes did not achieve the similar improvement of the photochemical activity. Moreover, they also worked as the photocatalyst for CO_2 reduction to afford formic acid in the presence of ascorbic acid as the sacrificial electron donor. While the amphiphilic molecular design as seen in **18**–**21** is a one of the highly effective strategies to construct bilayer structures with the segregation of donor and acceptor moieties by overcoming the heteroselective interaction operative between donors and acceptors, use of metal–metal interaction could be an alternative approach as that interaction is intrinsically homoselective. This idea was experimentally tested by using an organometallic dyad composed of

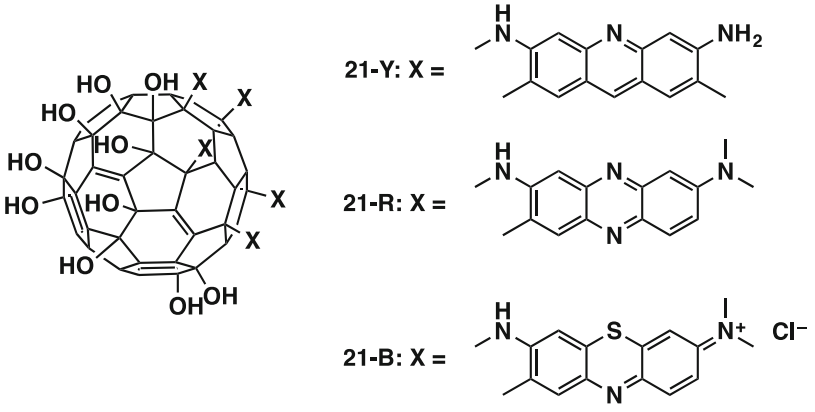

Fig. 22 Molecular structures of amphiphilic dyads **21**

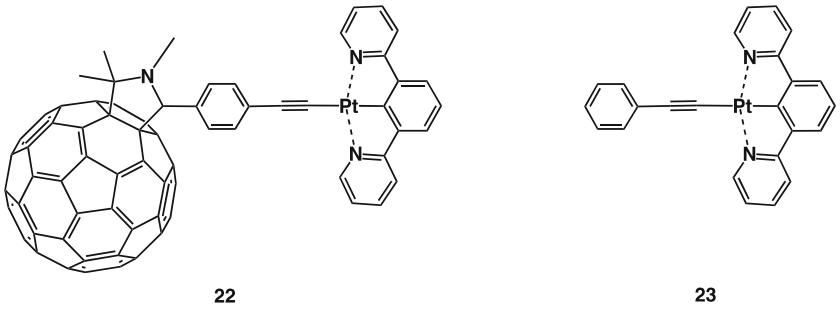

Fig. 23 Molecular structures of dyad **22** and its reference **23**

cyclometalated organoplatinum(II) complex and fullerene as the donor and acceptor, respectively (**22**, Fig. 23) [25]. While the self-assembly of **22** resulted in the formation of multilayered structure composed of the segregated donor and acceptor 2D sheets, its co-assembly with the corresponding organoplatinum(II) complex that lacks fullerene (**23**, Fig. 23) afforded the targeted bilayer as an exfoliated analogue of the multilayers of **22**. The bilayer showed better performance in its photoconduction behavior than the multilayer on a field-effect transistor setup, where the former transported both of the photogenerated holes and electrons while the latter exhibited only the sign of electron transportation.

A variety of donor moieties have been covalently linked to fullerenes for the design of LC materials, where the selected representative examples of them are thiophene oligomer (Fig. 24) [26], phthalocyanine zinc complex (Fig. 25) [27], phenylene ethynylene oligomer (Fig. 26) [28], and oligophenylenevinylene (Fig. 27) [29]. When a dyad composed of the linearly linked thiophene hexamer and fullerene was modified with two lipophilic side wedges (**24**$_{\mathbf{lip}}$, Fig. 24) or the combination of lipophilic and hydrophilic wedges (**24**$_{\mathbf{amp}}$) at the terminals, both molecules formed similar smectic A mesophases in temperature ranges from less than 20 to over 100 °C, where the thiophene hexamer and fullerene moieties were most likely homosegregated. However, their response upon photoirradiation was quite different, where the liquid crystal of amphiphilc dyad **24**$_{\mathbf{amp}}$ was much more photoconductive than that of lipophilic analogue **24**$_{\mathbf{lip}}$. Since flash photolysis time-resolved microwave conductivity measurements on these two materials suggested that the behavior of photogenerated charge carriers in a nanoscale distance up to 10 nm in them was not so different except for the longer lifetime of the carriers in the former assembly, the superiority of LC **24**$_{\mathbf{amp}}$ was ascribed to the smaller number of trapping sites in that material due to the formation of more uniform, defectless 2D layers of the donor and acceptor moieties in that assembly. In the case of a hydrophobic dyad of phthalocyanine zinc complex and fullerene (**25**, Fig. 25) [27], the strong π-stacking interactions homoselectively operative between the phthalocyanine zinc complex moieties were assumed to play a key role to achieve the segregation of donor and acceptor moieties. As the fullerene moiety of **25** locates around the columnar assembly of the phthalocyanine zinc complex moiety to afford

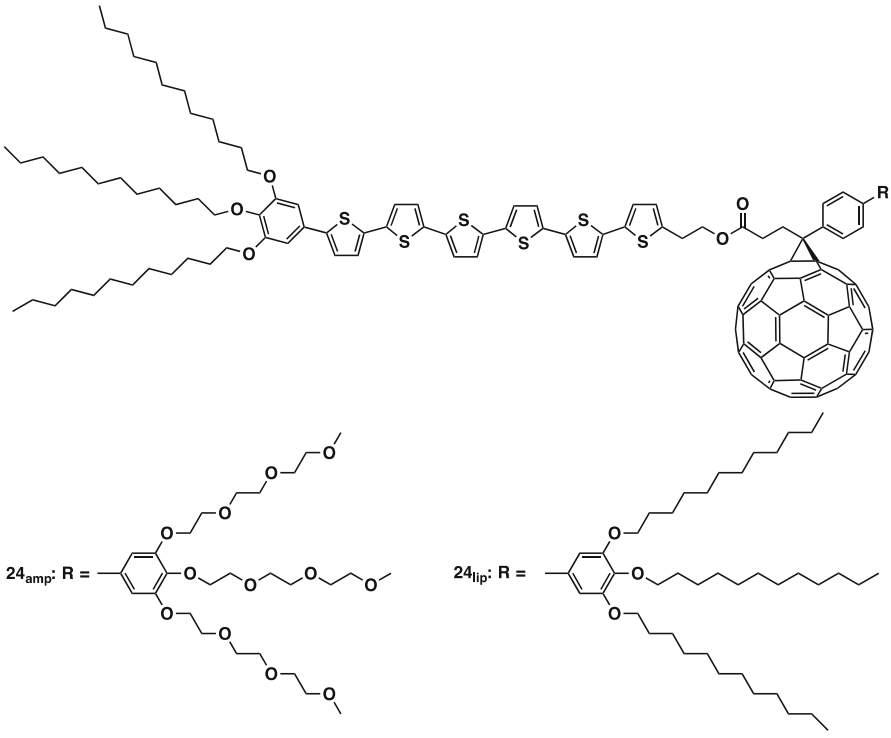

Fig. 24 Molecular structures of liquid crystalline dyads bearing amphiphilic $\mathbf{24_{amp}}$ and hydrophobic $\mathbf{24_{lip}}$ wedges

a donor–acceptor bicontinuous structure, the material had the ambipolar charge transportation capability with the electron and hole mobility values of 0.11 and 0.26 $cm^2\ V^{-1}\ s^{-1}$, respectively, as evaluated by the time-of-flight method after the heating–cooling treatment on the material to afford a glassy LC state at 25 °C. Although the usage of fullerenes other than C_{60} and C_{70} for the engineering of soft materials has been quite limited due to their scarcity, a LC dyad composed of phenylene ethynylene oligomers and tri-yttrium nitride encapsulated C_{80} ($Y_3N@C_{80}$) (**26**, Fig. 26) was reported in 2013 [28] by taking advantage of its relatively high production yield as an endohedral metallofullerene. While $Y_3N@C_{80}$ played the role as the energy acceptor as similar to C_{60} for the photo-excited phenylene ethynylene oligomer moieties, a clear difference between the dyads with $Y_3N@C_{80}$ and C_{60} was observed in their emission properties, where the quantum yield of the fullerene emission of the former (8%) was much higher than that of the latter (0.03%) at 25 °C. DFT calculation suggested that the endohedral configuration of $Y_3N@C_{80}$ leads to the long lifetime of the excited state by inhibiting deactivation pathways possible for C_{60}. While the linkage of fullerene to a mesogenic component mostly destabilizes the LC phase of the parent mesogen as the spherically- shaped fullerene moiety tends to behave as the structural impurity

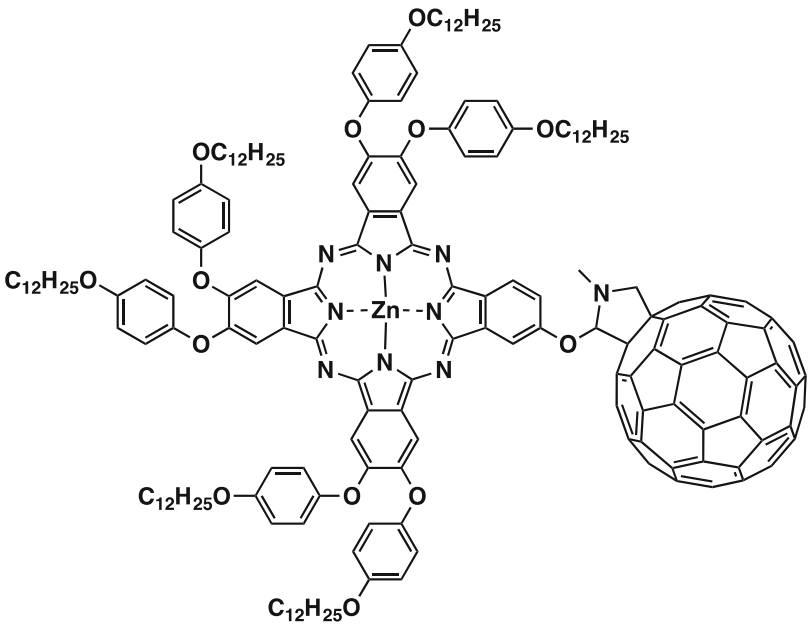

Fig. 25 Molecular structure of liquid crystalline dyad **25**

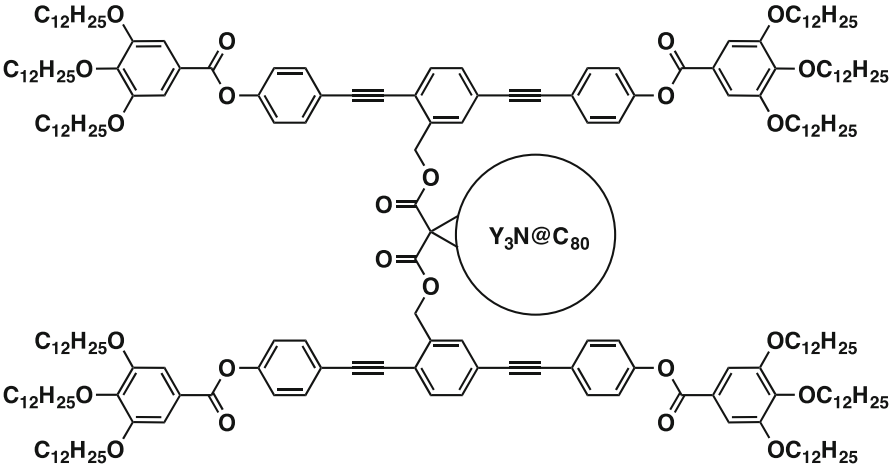

Fig. 26 Molecular structure of liquid crystalline dyad **26**

for the ordering of the mesogenic moiety, there are some exceptional cases where it oppositely stabilizes the LC phase. When one arm of a triply branched oligophenylenevinylene mesogen was modified with a fullerene moiety (**27$_1$**, Fig. 27) [29], the phase transition temperature to become isotropic melt from the LC phase increased by more than 70 °C. As the rigid mesogen framework could afford large void space

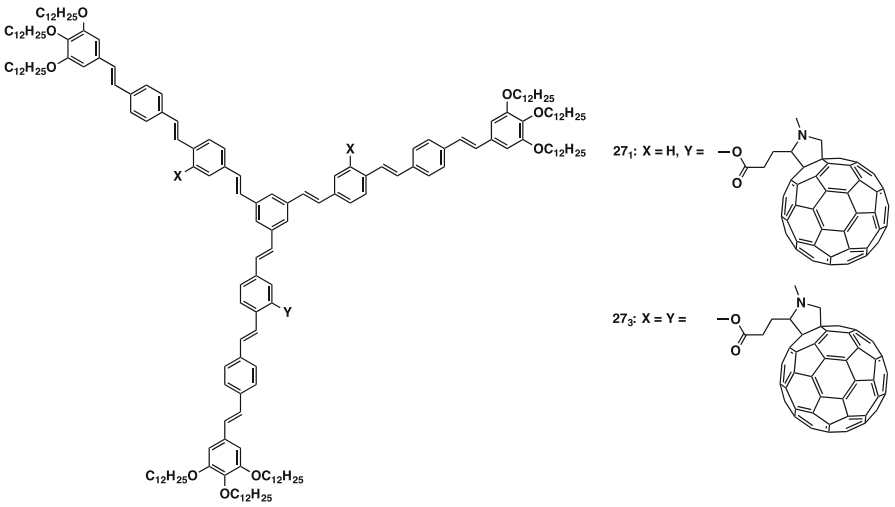

Fig. 27 Molecular structures of liquid crystalline dyad $\mathbf{27_1}$ and non-liquid crystalline $\mathbf{27_3}$

in its assembly, the attached fullerene presumably works to stabilize the mesophase by filling that void space, as suggested by the modeling studies based on the XRD data. This assumption was also supported by the fact that the parent LC phase of fullerene non-appended mesogen was stabilized thermally by adding an analogous but non-LC compound bearing three fullerene moieties ($\mathbf{27_3}$, Fig. 27), where the optimized mesogen to fullerene ratio in the mixture was found to be one.

Dendrimers

Design of dendrimers containing fullerene moieties in their structure has been an extensively attempted research subject in the last quarter century by aiming the merge of two "rising starts" in the chemistry to provide macromolecules with the unique molecular weight and the well-defined molecular structure. The first example has been reported in 1993 as the collaboration of two research groups headed by Fréchet and Wudl, where a 6–6 bridged methano-fullerene carrying two phenolic functionalities was coupled with two Fréchet-type poly(aryl ether) dendron bromides to afford an isolable macromolecule having the core of a carbon nanocluster with a unique exact mass of 7685 (**28**, Fig. 28) [30]. As described in the corresponding manuscript, one of the main aims to link the fullerene core with dendritic wedges is to efficiently control the solubility of fullerenes. Hirsch et al. replaced a pair of C_{12} alkyl chains of a previously reported lipo-fullerene (**14**, Fig. 15) with two hydrophilic poly-amide dendrons bearing multiple carboxylic acids at the periphery to afford a globular amphiphile ($\mathbf{29_{ester}}$, Fig. 29) that exhibited a melting behavior at 186 °C [31]. Freeze fracture as well as cryo-electron microscopy revealed that the amphiphile preferentially forms the double-layer membranes to afford sub-micrometer-scale spherical and cylindrical structures in phosphate buffer at pH 7.4. In the following trials, an analogous amphiphile was designed by

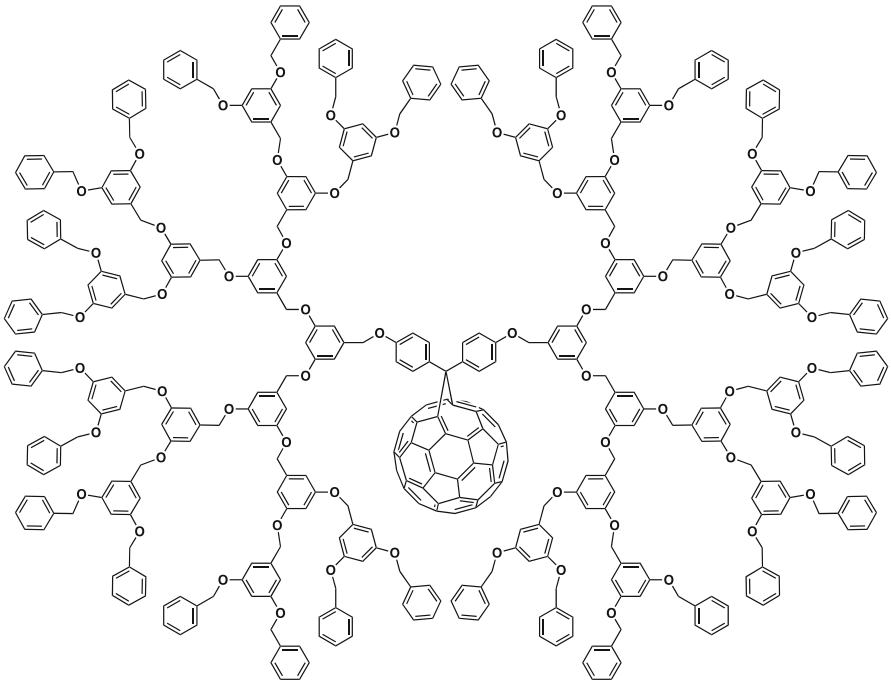

Fig. 28 Molecular structure of dendrimer **28**

replacing the two ester bonds of the malonate substituent for the attachment of the dendritic wedges with the more rigid amide linkages (**29**$_{\mathbf{amide}}$ Fig. 29) [32]. Being different from previous amphiphile **29**$_{\mathbf{ester}}$, newly obtained **29**$_{\mathbf{amide}}$ showed a pH-dependent self-assembling behavior, where its partially deprotonated form at pH value of 7.2 in phosphate buffer predominantly formed rod-shaped aggregates having a double-layer ultrastructure with a diameter of 65 ± 5 Å. When the pH value was increased to around 9 by using borate buffer to fully deprotonate the carboxylic acid functionalities at the dendrimer surface, globular micelles with a diameter of 85 ± 10 Å were observed exclusively. Through the modeling studies on the 3D density map reconstructed from the electron cryogenic microscopic data, the micelle structure was proposed to be a perpendicularly interlocked two U-shaped smaller assemblies composed of four molecules of **29**$_{\mathbf{amide}}$ in each. Another type of dendrimer-attached amphiphilic fullerene derivatives were prepared by achieving the multi-point coupling of hydrophilic dendrons to the fullerene core by means of click reaction (**30**, Fig. 30), where the rigid spherical carbon framework of the fullerene moiety, instead of the flexible long alkyl chains in **29**, was expected to play the role for the hydrophobic interactions [33]. Among the three prepared dendrofullerenes having 4, 8, or 16 carboxylic acid functionalities at the surface, **30**$_8$ with 8 acid groups was found to form more well-defined assemblies such as multi-layered vesicles or nanorods in THF or its mixtures with water, respectively, than the other two, suggesting that the structural balance between the hydrophilic

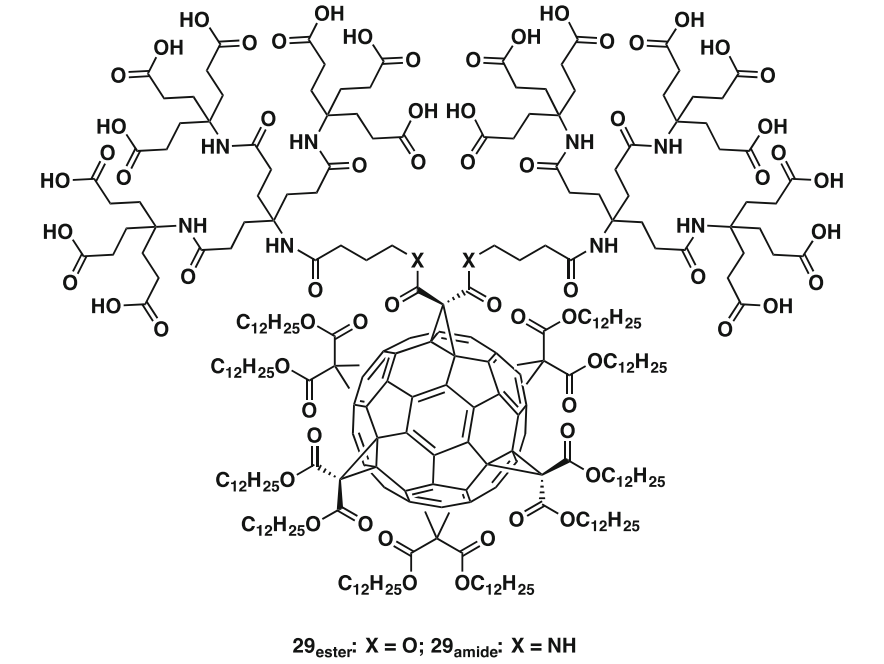

Fig. 29 Molecular structures of amphiphilic dendrimers **29**

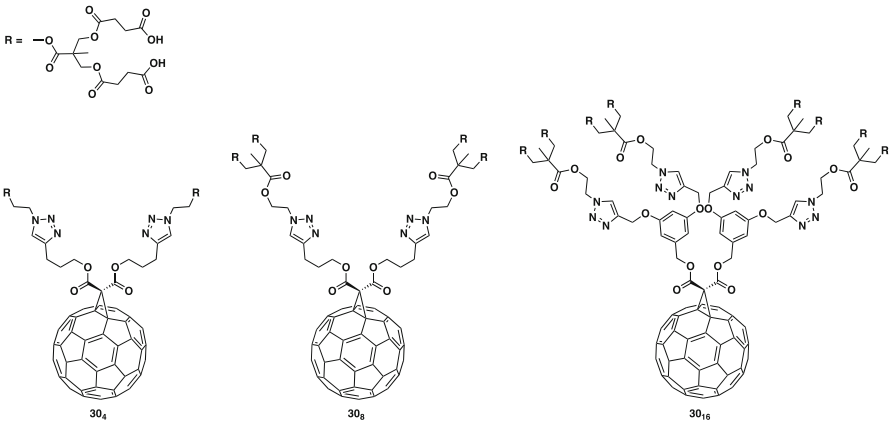

Fig. 30 Molecular structures of amphiphilic dendrimers **30**

and hydrophobic moieties in $\mathbf{30}_8$ is more suitable for the controlled self-assembly. Since a dendritic wedge can also serve as the self-assembling unit by accumulating multiple mesogens or alkyl chains at its periphery, a variety of the fullerene derivatives bearing self-assembling dendrimers have been synthesized to thoroughly investigate their assembled structures and phase transition behavior. For example,

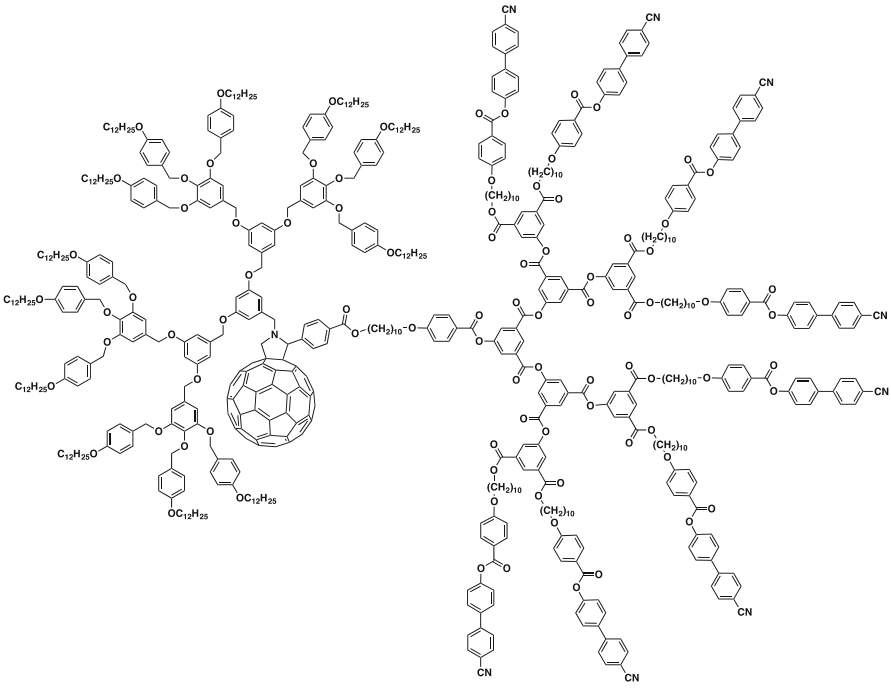

Fig. 31 Molecular structure of liquid crystalline dendrimer **31**

a series of Janus-type LC fullerodendrimers such as **31** (Fig. 31) possessing two types of dendrons that tend to form different mesophase structures, i.e., lamellar and columnar, were designed to clarify the relationship between their molecular and LC structures, where their supramolecular organization was found to be controlled by (1) the adequacy of the cross-sectional area of the dendrons, (2) microscopic segregation of the dendrimers, (3) core deformation of the dendrimers, and (4) the intradendron dipolar interactions between the cyanobiphenyl groups [34]. As their fullerene-free analogues exhibited the similar mesomorphic properties to the corresponding fullerodendrimers, it was concluded that fullerene moiety in these cases does not influence the type of mesophase formed. In the following trial by one of the same research groups who conducted the studies on **31**, all of the four diastereoisomers of fulleropyrrolidine derivatives containing two stereogenic centers were isolated, where each of them was then coupled with a nematic dendron (**32**, Fig. 32) to seek the possibility to induce mesoscopic chirality in the LC materials [35]. As expected, all of fulleropyrrolidine derivatives **32** displayed chiral nematic phases containing supramolecular helicoidal organizations as proved by CD and POM. Through the POM observations on the natural textures of the resultant LC materials, the helix sense in those supramolecular assemblies was found to be dominantly controlled by the chirality at one of the two asymmetric carbons in the fulleropyrrolidine moiety. When multiple dendrimers are needed to be linked to a single fullerene, steric repulsions between them often inhibited the smooth progress

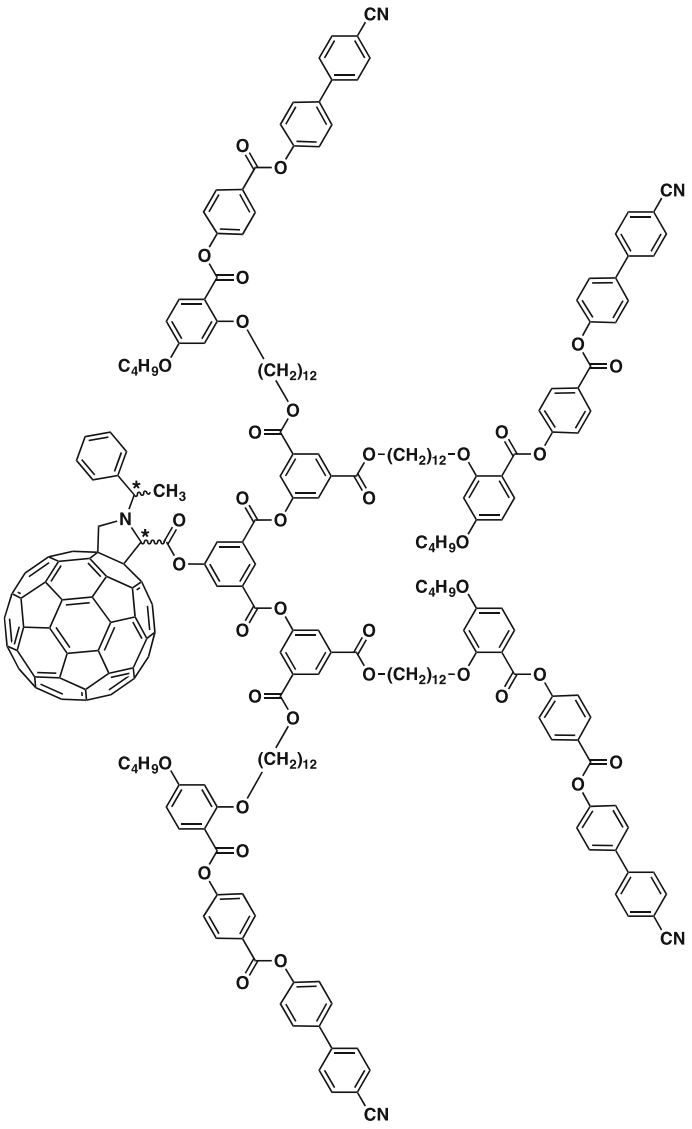

Fig. 32 Molecular structures of liquid crystalline dendrimers **32**

of the reaction to reach the targeted structures. A fullerene hexakis adduct with a T_h-symmetry is a suitable precursor to address this issue as the reaction sites are symmetrically distributed around the fullerene so that the steric hindrance between dendrimers can be minimized. Based on this idea, a T_h-symmetric fullerene hexakis adduct bearing 12 terminal alkyne units was subjected to the click chemistry-mediated coupling reaction with azide-terminated Percec-type self-assembling dendrons to successfully prepare a dodeca-dendronized fullerene (**33**, Fig. 33)

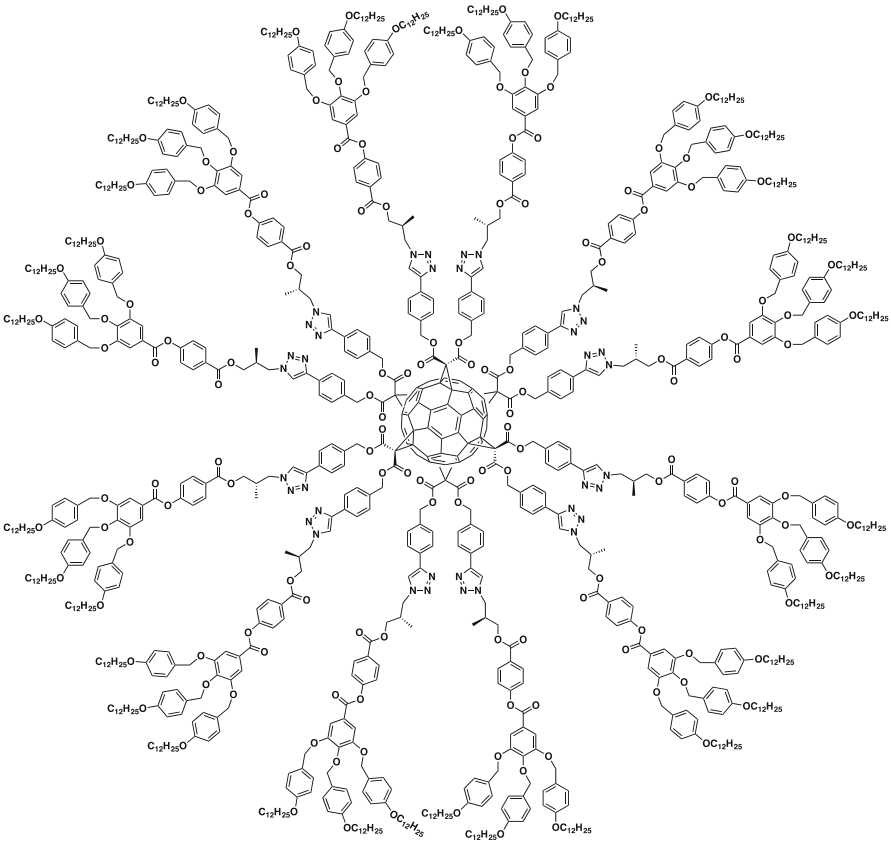

Fig. 33 Molecular structure of liquid crystalline dendrimer **33**

[36]. Although the molecule was intuitively expected to adopt a globular shape to afford cubic, tetragonal, and quasicrystalline phases, it actually formed a 2D columnar hexagonal phase of *p6mm* symmetry by most likely adopting a disk-shaped conformation, suggesting the preorganization of the dendrons via the intramolecular inter-dendron π–π and van der Waals interactions. Being inspired by the results of the molecular-level structural analysis on the natural photosynthesis system, light-harvesting functions in dendritically oriented multi-chromophore systems have been extensively studied, where one of the intriguing findings was the efficient funneling of absorbed light energy into the core position of the dendrimers. In order to make use of the harvested light energy to trigger a chemical reaction as the next step to mimic the natural system, C_{60} was linked with a dendritic zinc porphyrin heptamer at its focal point (**34**, Fig. 34) as the electron acceptor for the photo-induced electron transfer from the neighboring zinc porphyrin moiety [37]. Steady-state as well as time-resolved photochemical studies on the array system revealed that, compared with the reference array systems composed of less numbers of zinc porphyrin

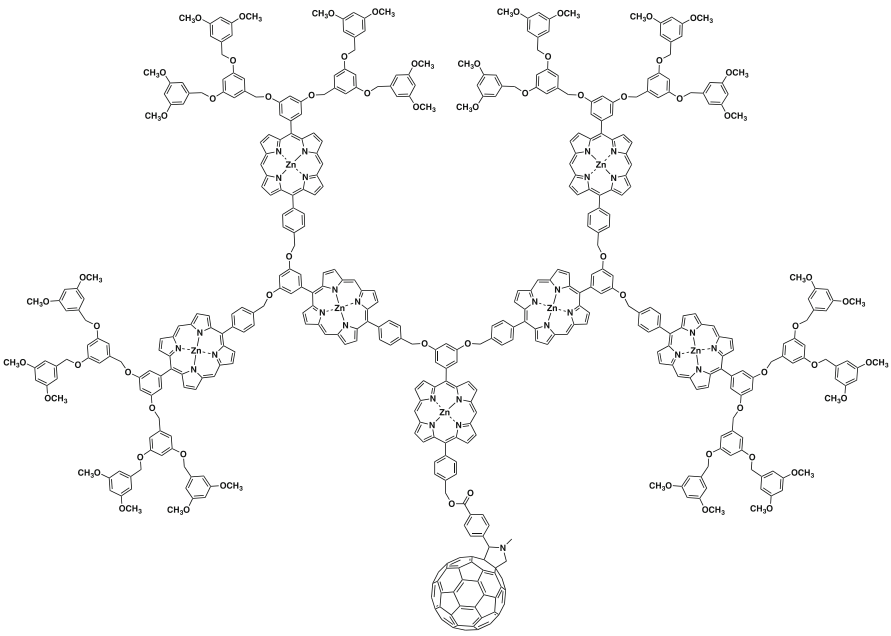

Fig. 34 Molecular structure of dendrimer **34**

moiety, the heptamer-bearing system achieved the retardation of the back-electron transfer from the photo-generated fullerene anion to the co-produced zinc porphyrin cation radical, the latter of which can be distant from the fullerene moiety through the hole migration into the zinc porphyrin moieties at the dendrimer periphery.

While the structural merge of fullerenes and dendrimers in most cases has been achieved by locating the fullerene moiety at the core of the molecule as shown in Figures 28–34, there have been some trials that integrated multiple fullerenes at the dendrimer periphery. A pioneering work was reported by Armaroli, Gross, and Nierengarten et al. in 1999, where 16 fullerene *cis*-2 bis-adducts, as the largest case, covered a copper(I) bis-phenanthroline core (**35**, Fig. 35) [38], while the appreciable ground-state electronic interactions between these two kinds of redox active moieties were not observed. Electrochemical studies on the compounds having the dendrimers of different generation by means of cyclic and steady-state voltammetry revealed that the individual fullerenes in all cases behave as the independent redox centers, while the copper(I) bis-phenanthroline core, as is usually observed for the redox active cores in dendrimers, becomes less responsive toward the metal centered oxidation along with the increase of the size of dendritic wedges. The fullerene-appended dendrimers with carboxylic acid (**G*n*H**, Fig. 35), used as the synthetic intermediates for the coupling with the phenanthroline core, were later subjected to the attempts of the Langmuir–Blodgett (LB) film preparation as their structures looked suitable for preventing the irreversible aggregation of fullerene moieties that is critical for the fabrication of LB films [39]. In fact, all of the three

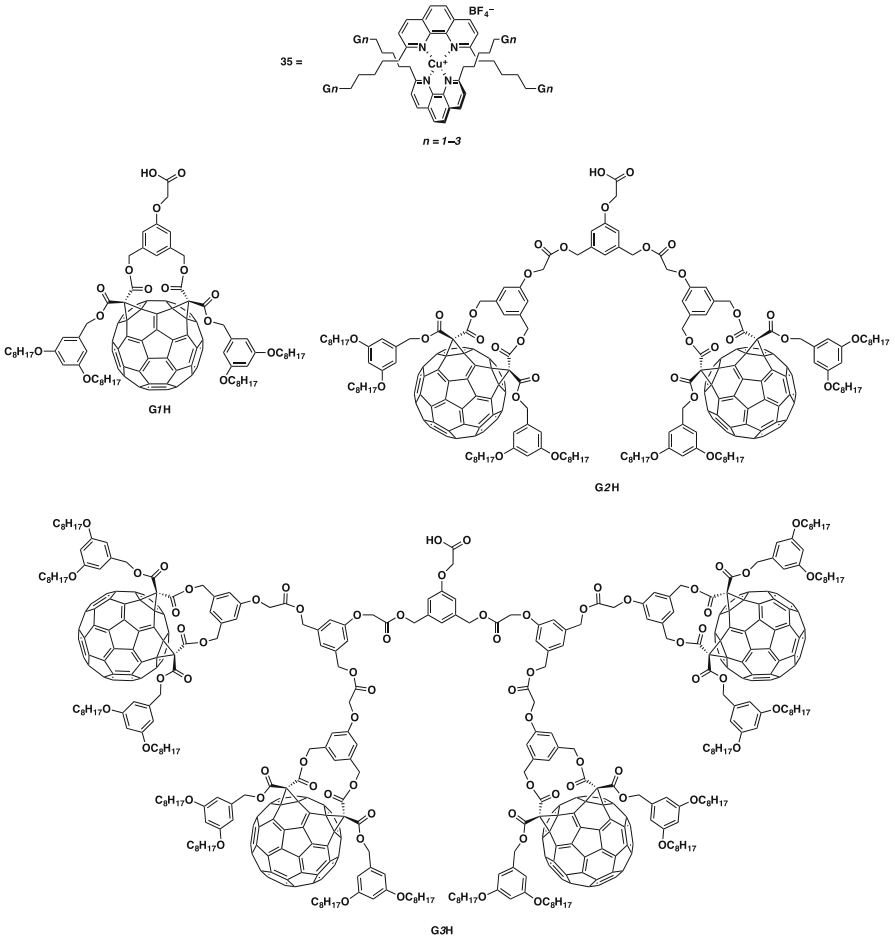

Fig. 35 Molecular structures of dendrimers **35** and **G*n*H**

tested dendrimers exhibited the reversible compression/decompression behavior at the air–water interface and formed stable LB films, some of which were also transferable onto a substrate covered with a monolayer of octadecyltrichlorosilane to afford their monolayers as well as the multilayers with their controllable thickness. As the hybrid of centrally and peripherally oriented fullerene-containing structures, a giant globular molecule with the diameter of some nm, composed of 13 hexakis adducts of C_{60} covered with overall 120 carbohydrate units (**36**, Fig. 36), was successfully constructed by making use of the two well-established synthetic technologies, i.e., (1) the finely tunable structural design of the hexakis adducts of C_{60} and (2) highly efficient azide–terminal alkyne coupling by means of click chemistry [40]. Because of its structural feature as a relatively compact yet highly multivalent carbohydrate compound, the mannosylated molecule (**36**) named as "superball" was

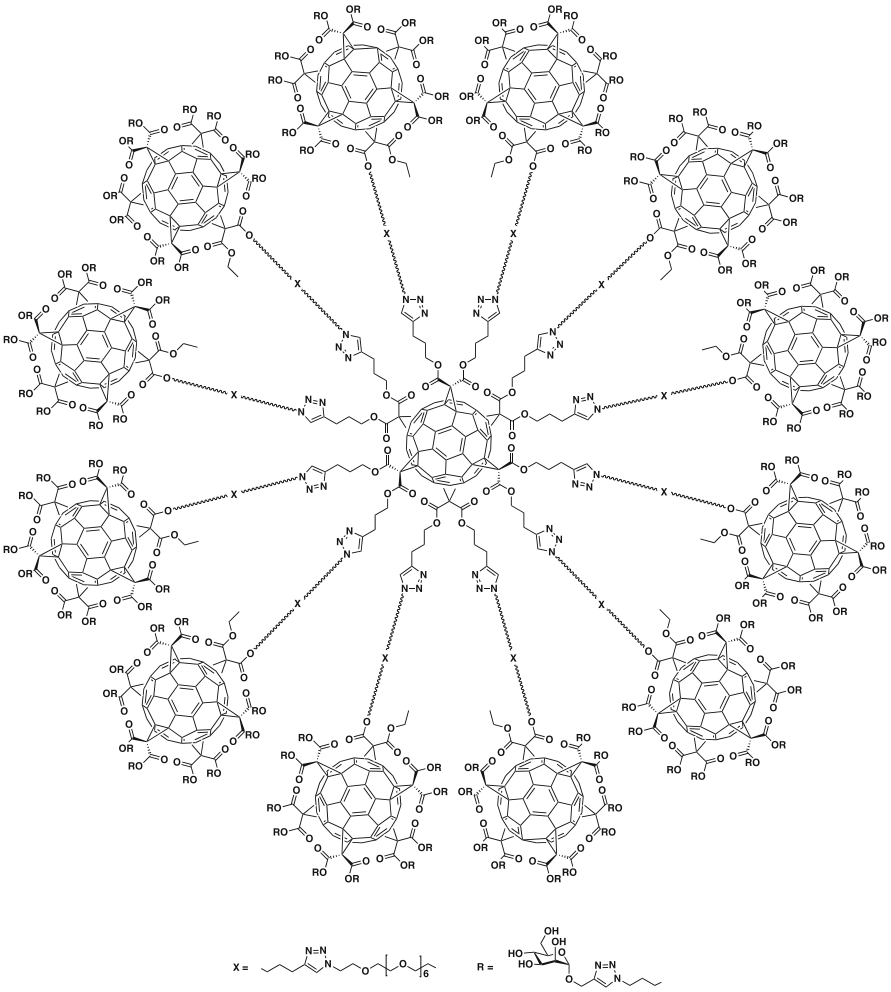

Fig. 36 Molecular structure of dendrimer **36**

found to behave as a potent inhibitor in a model of Ebola virus infection with the half-maximum inhibitory concentration (IC_{50}) in the subnanomolar range, which was claimed even as 18-fold more potent than the previously reported huge virus-like particles covered with a great number (1620) of mannose units after normalizing their IC_{50} values with the mannose unit number.

Conical-Shaped Derivatives

Nakamura et al. developed an organocopper-based synthetic methodology to attach five aromatic groups to one pentagon of C_{60}, which allows to prepare a series of conical-shaped fullerene derivatives (**37**, Fig. 37) with high yields. These fullerene derivatives can adopt two different forms, i.e., the structures possessing either of the

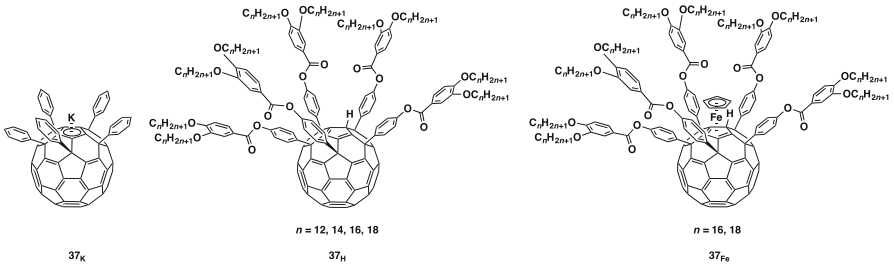

Fig. 37 Molecular structures of conical-shaped fullerenes **37**

stable hydrocarbon anion or the corresponding hydrophobic cyclopentadiene upon their protonation, where the self-assembly of the corresponding amphiphilic and hydrophobic derivatives resulted in the formation of vesicles and liquid crystals, respectively. For example, dissolution of potassium salt of pentaphenyl fullerene ($\mathbf{37_K}$) into water was found to afford spherical bilayer vesicles with a radius of 17 nm at a critical aggregation concentration of less than submicromolar order, as determined by laser light scattering techniques as well as AFM [41]. The vesicles preserved its size in a wide molecular concentration range of $\mathbf{37_K}$ from millimolar to submicromolar order, indicating that the structure is thermodynamically highly preferable in water. Evaluation of the permeability coefficient of water across the bilayer membrane of $\mathbf{37_K}$ at various temperatures, as determined by investigating the effect of paramagnetic ion on the relaxation time of water molecules encapsulated in the vesicles, revealed that the membrane of the fullerene amphiphile possesses a negative temperature-dependent permeability due to the large entropy barrier, which is entirely different from the water permeation through a lipid bilayer membrane that occurs more readily at higher temperature [42]. These observations highlighted the contrasting nature of the bilayer membranes made of fullerene and lipid where the former is more rigid and crystalline, while the latter is more dynamic and open for water permeation. Though the cyclopentadienide anion of the conical-shaped fullerene amphiphiles is relatively stable due to the delocalization of the negative charge toward the residual 50-π electron system of the fullerene moiety, its neutralization upon protonation can leave a hydrophobic cavity surrounded by the five aromatic substituents. When the structure of these substituents was properly modified by adding another aromatic moiety, that cavity became deep enough to efficiently interact with the convex-shaped fullerene hemisphere surface to afford columnar assemblies of the conical-shaped fullerenes as demonstrated by single X-ray crystallography [43]. This molecular design strategy together with the further introduction of long alkyl chains of 12, 14, 16, and 18 carbons at the aromatic substituents successfully yielded thermotropic and lyotropic LC materials composed of the hexagonally packed polar columns of so-called nano-shuttlecock ($\mathbf{37_H}$, Fig. 37) as finely characterized by DSC, POM, and VT-XRD. The pure organic conical-shaped fullerene structure was later modified by the metallation with cyclopentadienyliron dicarbonyl dimer to afford a “buckyferrocene” as a fusion of fullerene and ferrocene by sharing one of their pentagons, whose synthetic protocol was then applied for the

design of mixed fullerene/ferrocene mesogens (**37$_{Fe}$**, Fig. 37) [44]. Although the hydrophobic cavity of a conical-shaped buckyferrocene is shallower than its precursor and the sign of weaker intermolecular stacking interaction was observed as expected, it was concluded that the former bearing sufficiently long alkyl chains still forms a columnar stacking structure to afford LC assembly, where its liquid crystallinity was preserved even after the chemical oxidation of the integrated ferrocene moiety into ferrocenium state.

Bent-Shaped Derivatives

Bent-shaped molecules that form LC assemblies have attracted attentions due to their potential as ferroelectric and nonlinear optical materials with a switching function. The key point for these applications is to realize the spontaneous non-zero macroscopic polarization in the materials through the sophisticated control on the assembled structure. To see the effects of the incorporation of fullerene in the molecular structure on the supramolecular organization, C_{60} moiety was linked with one or two bent-shaped mesogenic units (**38**, Fig. 38) [45]. One of these molecules bearing two bent mesogens (**38$_2$**) was found to form a smectic C polar mesophase at temperatures over 57 °C, whose polar character was evidenced by the observation of spontaneous polarization value of around 60 nC cm^{-2} and the presence of second harmonic generation activity at room temperature without the application of an electric field. Moreover, the direction of the polarization in that LC material was switched by applying a triangular-wave electric field, indicating the re-orientation of the molecule in the assembly.

Non-covalent Blends

Blends with Dendrimers

Merge of the sciences of fullerenes and dendrimers through their supramolecular blending is an attractive approach in that the three-dimensional π-conjugation over the carbon framework of fullerene could be perfectly preserved as it does not require any covalent structural modifications on fullerenes that inevitably cause the partial destruction of the conjugation. To achieve the smooth mixing of fullerenes and dendrimers without their homo-segregation, π-conjugated moieties affinitive to fullerenes were employed in the core or periphery of the dendrimers. One of the suitable structural motifs is a cyclic dimer of porphyrin which was found to include fullerenes with quite high binding constants even in a good solvent for fullerenes such as 1,2-dichlorobenzene (ODCB). By taking advantage of this finding, a rigid cyclodimeric form of porphyrin encapsulated within the two Fréchet-type dendrons (**39**, Fig. 39) was designed to form the 1:1 inclusion complexes with C_{60} or C_{70} in various organic solvents such as THF, toluene, CH_2Cl_2, and ODCB as confirmed by various spectroscopic methods including electrospray ionization mass spectrometry [46]. Due to the high compatibility of the attached dendrimers with commodity polymers, the mixture of atactic PMMA and the 1:1 complex of **39** with C_{60} afforded optical microscopically homogeneous cast film (Fig. 40a), while in the absence of **39** under otherwise identical conditions a heterogeneous film containing the heavily

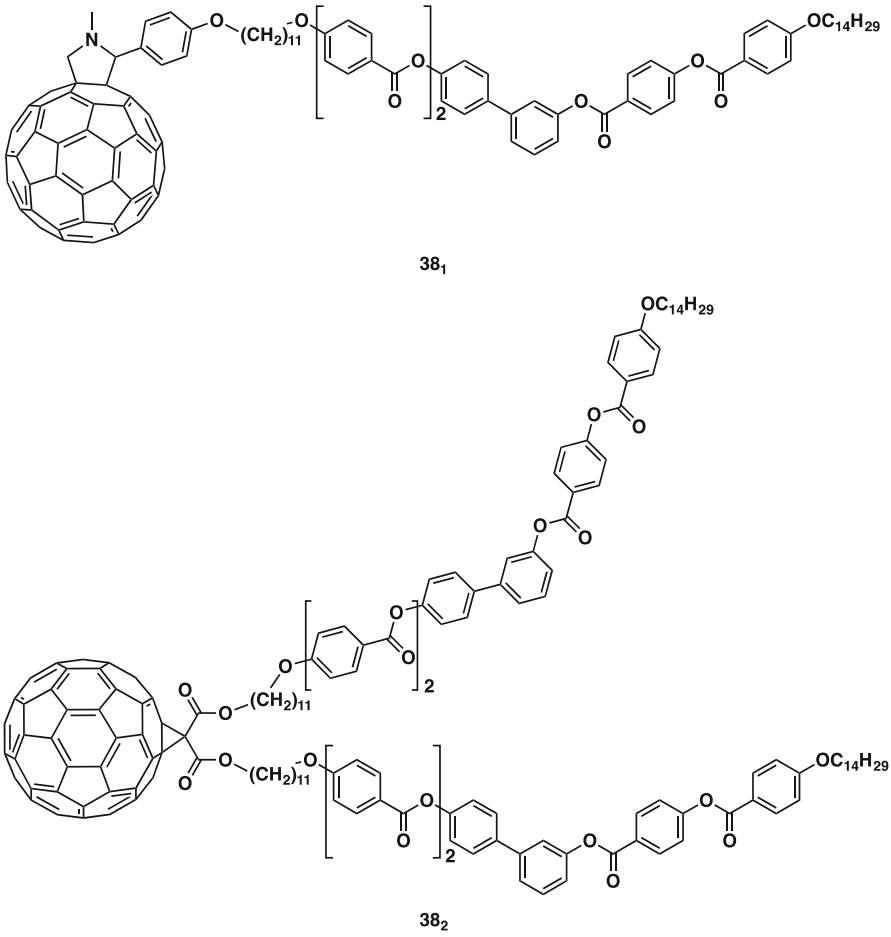

Fig. 38 Molecular structures of bent-shaped LC fullerenes **38**

aggregated fullerene domains resulted (Fig. 40b). Although the affinity of a monomeric porphyrin to fullerenes is generally too weak to detect their interaction in solution absorption spectroscopically, monomeric porphyrin **40** wrapped with phenylene-based rigid four dendritic substituents (Fig. 41) exhibited a clear spectral change in solution, demonstrating the trapping of one molecule of C_{60} into a void space surrounded by the porphyrin core and the rigid dendrimer frameworks [47]. Since the dendrimer periphery was decorated with multiple C_{12} alkyl chains, **40** formed a rectangular columnar mesophase at the temperature range from 39 to 110 °C, while the presence of stoichiometric amount of C_{60} altered the mesophase structure to provide a thermally more tolerant columnar LC phase with its clearing temperature of 250 °C. Another π-conjugated motif integrated in dendrimers for the complexation with fullerenes is π-extended tetrathiafulvalene (exTTF) developed by Martín et al., which was located at the periphery of a poly(aryl ester) dendrimer

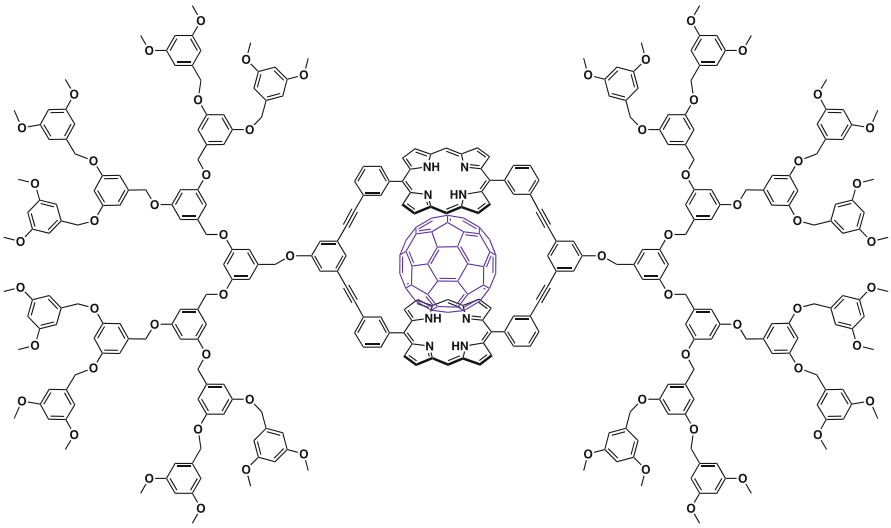

Fig. 39 Molecular structure of supramolecular complex of **39** and C_{60}

(**41**, Fig. 42) [48] by expecting that the two exTTF moieties having the curved aromatic surface sandwich one molecule of fullerene to afford multi-fullerene complexed hybrids. In organic solvents such as $CHCl_3$, the dendrimer bearing 24 exTTF units tended to form aggregates that possess a narrow distribution of hydrodynamic radius around 120 nm, as evaluated by their dynamic light scattering profiles. Because of this aggregation, dendrimer **41** showed a positive allosterism at its complexation with fullerene in solution as demonstrated by the observation of a sigmoidal feature in its titration profile with C_{60}.

Blends with Low Molecular Weight Organic Gelators

Addition of fullerenes into organogels was found to alter the morphology and mechanical properties of the assembly of the gelators if their molecular structure contained an affinitive moiety toward fullerenes. A porphyrin derivative bearing in total eight amide functionalities at the aromatic substituents (**42**, Fig. 43) for its self-assembly was designed to form gels in aromatic solvents such as benzene [49]. Addition of C_{60} up to 0.5 equivalent of gelator **42** clearly improved the thermal stability of the gels, as evidenced by the marked increase of the gel-to-sol phase-transition temperature from 79 to 120 °C. SEM as well as TEM on the xerogels revealed that the original sheet-like morphology of the assembled gelator was changed into the fibrous one in the presence of C_{60}. With the supports by means of IR spectroscopy and XRD, the formation of fibrous morphology in the presence of C_{60} was ascribed to the supramolecular 2:1 complexation of **42** and fullerene, followed by the one-dimensional aggregation of that sandwich-like complex via the amide–amide hydrogen-bonding interactions between **42**. Another system composed of an isomeric mixture of photo-dimerized anthracene derivative (**43**, Fig. 44) afforded

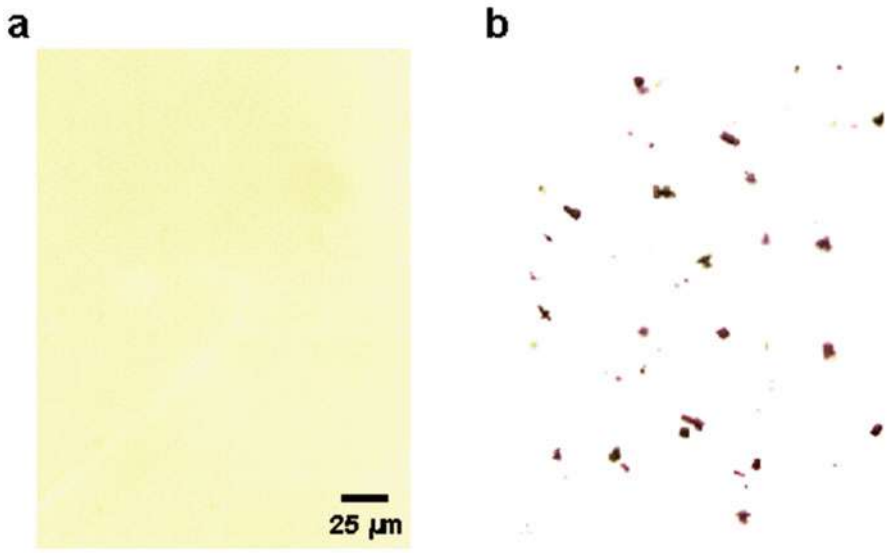

Fig. 40 Optical microscopic images of atactic PMMA cast films mixed with (**a**) C_{60}/**39** and (**b**) C_{60}

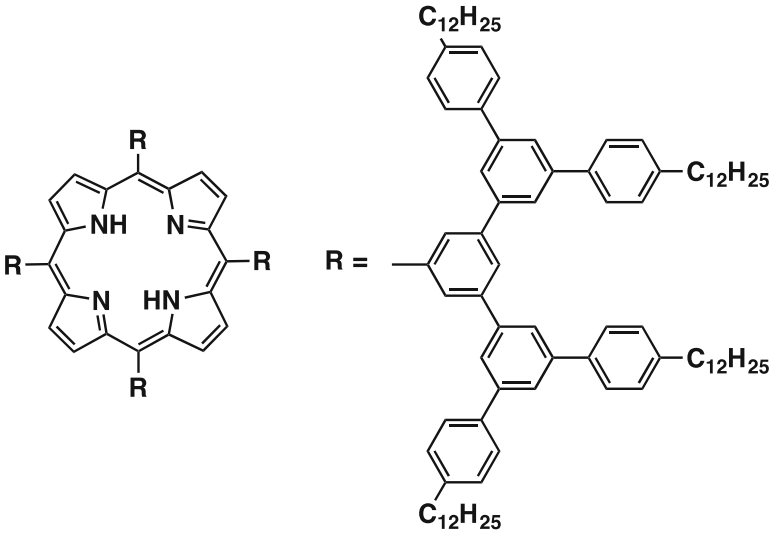

Fig. 41 Molecular structure of LC dendrimer **40**

thixotropic gels in hydrocarbons such as decalin [50]. The rheological properties of the gel were responsive to the co-existence of fullerenes such as C_{60} and C_{70}, where the crossover point between the storage and loss moduli shifted toward higher-frequency regions upon addition of fullerenes, demonstrating that the dynamic nature of the gel was enlarged by the dope of fullerene. Moreover, the thixotropic

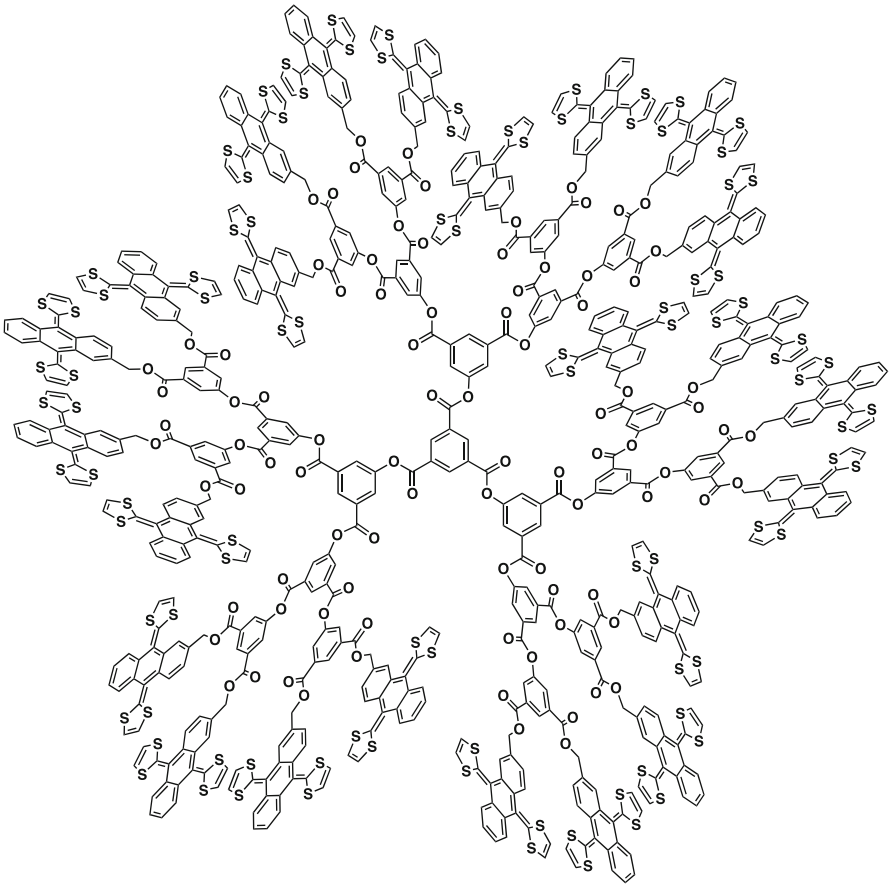

Fig. 42 Molecular structure of dendrimer **41**

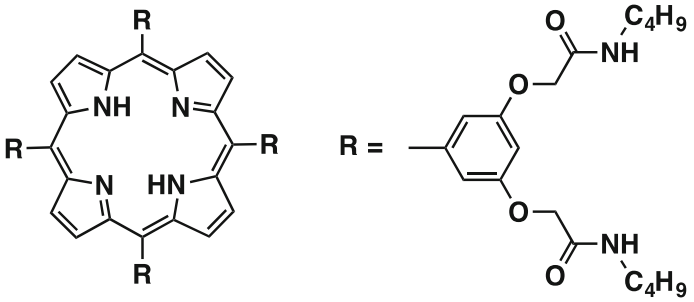

Fig. 43 Molecular structure of gelator **42**

behavior of the gel was enhanced by the presence of these fullerenes, achieving faster recovery of the storage modulus after the gel destruction by the application of sheer stress, possibly due to the interactions between fullerenes and concave-shaped

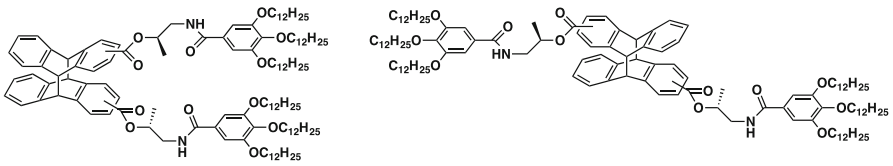

Fig. 44 Molecular structures of gelator **43**

dimerized anthracene moieties of **43**. Observation of the more significant effects of C_{70} than that of C_{60} supports this assumption as generally the former fullerene shows stronger interaction to the aromatic moieties.

References

1. Samal S, Choi BJ, Geckeler KE (2000) The first water-soluble main-chain polyfullerene. Chem Commun:1373–1374
2. Hiorns RC, Cloutet E, Ibarboure E, Vignau L, Lemaitre N, Guillerez S, Absalon C, Cramail H (2009) Main-chain fullerene polymers for photovoltaic devices. Macromolecules 42:3549–3558
3. Ramanitra HH, Silva HS, Bregadiolli BA, Khoukh A, Combe CMS, Dowland SA, Bégué D, Graeff CFO, Dagron-Lartigau C, Distler A, Morse G, Hiorns RC (2016) Synthesis of main-chain poly(fullerene)s from a sterically controlled azomethine ylide cycloaddition polymerization. Macromolecules 49:1681–1691
4. Ramos AM, Rispens MT, van Duren JKJ, Hummelen JC, Janssen RAJ (2001) Photoinduced electron transfer and photovoltaic devices of a conjugated polymer with pendant fullerenes. J Am Chem Soc 123:6714–6715
5. Charvet R, Acharya S, Hill JP, Akada M, Liao M, Seki S, Honsho Y, Saeki A, Ariga K (2009) Block-copolymer-nanowires with nanosized domain segregation and high charge mobilities as stacked p/n heterojunction arrays for repeatable photocurrent switching. J Am Chem Soc 131:18030–18031
6. Nishimura T, Takatani K, Sakurai S, Maeda K, Yashima E (2002) A helical array of pendant fullerenes on an optically active polyphenylacetylene. Angew Chem Int Ed 41:3602–3604
7. Liu Y, Sheri M, Cole MD, Emrick T, Russell TP (2018) Combining fullerenes and zwitterions in non-conjugated polymer interlayers to raise solar cell efficiency. Angew Chem Int Ed 57:9675–9678
8. Boudouris BW, Molins F, Blank DA, Frisbie CD, Hillmyer MA (2009) Synthesis, optical properties, and microstructure of a fullerene-terminated poly(3-hexylthiophene). Macromolecules 42:4118–4126
9. Yu X, Zhang WB, Yue K, Li X, Liu H, Xin Y, Wang CL, Wesdemiotis C, Cheng SZD (2012) Giant molecular shape amphiphiles based on polystyrene−hydrophilic [60]fullerene conjugates: Click synthesis, solution self-assembly, and phase behavior. J Am Chem Soc 134:7780–7787
10. Cassell AM, Scrivens WA, Tour JM (1998) Assembly of DNA/fullerene hybrid materials. Angew Chem Int Ed 37:1528–1530
11. Kawauchi T, Kumaki J, Kitaura A, Okoshi K, Kusanagi H, Kobayashi K, Sugai T, Shinohara H, Yashima E (2008) Encapsulation of fullerenes in a helical PMMA cavity leading to a robust processable complex with a macromolecular helicity memory. Angew Chem Int Ed 47:515–519
12. Kawauchi T, Kitaura A, Kawauchi M, Takeichi T, Kumaki J, Iida H, Yashima E (2010) Separation of C_{70} over C_{60} and selective extraction and resolution of higher fullerenes by syndiotactic helical poly(methyl methacrylate). J Am Chem Soc 132:12191–12193

13. Tashiro K (2006) Summary report of NEDO Industrial Technology Research Grant Program (Grant for Young Researchers): 04A23003
14. Ikeda A, Hatano T, Shinkai S, Akiyama T, Yamada S (2001) Efficient photocurrent generation in novel self-assembled multilayers comprised of [60]fullerene-cationic homooxacalix[3] arene inclusion complex and anionic porphyrin polymer. J Am Chem Soc 123:4855–4856
15. Hasobe T, Imahori H, Kamat PV, Ahn TK, Kim SK, Kim D, Fujimoto A, Hirakawa T, Fukuzumi S (2005) Photovoltaic cells using composite nanoclusters of porphyrins and fullerenes with gold nanoparticles. J Am Chem Soc 127:1216–1228
16. Murakami H, Watanabe Y, Nakashima N (1996) Fullerene lipid chemistry: Self-organized multibilayer films of a C_{60}-bearing lipid with main and subphase transitions. J Am Chem Soc 118:4484–4485
17. Hetzer M, Bayerl S, Camps X, Vostrowsky O, Hirsch A, Bayerl TM (1997) Fullerenes in membranes: Structural and dynamic effects of lipophilic C_{60} derivatives in phospholipid bilayers. Adv Mater 9:913–917
18. Nakanishi T, Shen Y, Wang J, Yagai S, Funahashi M, Kato T, Fernandes P, Möhwald H, Kurth DG (2008) Electron transport and electrochemistry of mesomorphic fullerenes with long-range ordered lamellae. J Am Chem Soc 130:9236–9237
19. Hu Y, Wu KY, Zhu T, Shen P, Zhou Y, Li X, Wang CL, Tu Y, Li CY (2018) Unique supramolecular liquid-crystal phases with different two-dimensional crystal layers. Angew Chem Int Ed 57:13454–13458
20. Miyajima D, Tashiro K, Arakawa F, Takezoe H, Kim J, Kato K, Takata M, Aida T (2009) Liquid crystalline corannulene responsive to electric field. J Am Chem Soc 131:44–45
21. Georgakilas V, Pellarini F, Prato M, Guldi DM, Melle-Franco M, Zerbetto F (2002) Supramolecular self-assembled fullerene nanostructures. Proc Natl Acad Sci U S A 99:5075–5080
22. Charvet R, Jiang DL, Aida T (2004) Self-assembly of a π-electronic amphiphile consisting of a zinc porphyrin–fullerene dyad: Formation of micro-vesicles with a high stability. Chem Commun:2664–2665
23. Hizume Y, Tashiro K, Charvet R, Yamamoto Y, Saeki A, Seki S, Aida T (2010) Chiroselective assembly of a chiral porphyrin-fullerene dyad: photoconductive nanofiber with a top-class ambipolar charge-carrier mobility. J Am Chem Soc 132:6628–6629
24. Kunkel M, Sutter S, Polarz S (2019) Molecular semiconductor surfactants with fullerenol heads and colored tails for carbon dioxide photoconversion. Angew Chem Int Ed 52:15620–15625
25. Sato S, Takei T, Matsushita Y, Yasuda T, Kojima T, Kawano M, Ohnuma M, Tahsiro K (2015) Coassembly-directed fabrication of an exfoliated form of alternating multilayers composed of a self-assembled organoplatinum(II) complex−fullerene dyad. Inorg Chem 54:11581–11583
26. Li WS, Yamamoto Y, Fukushima T, Saeki A, Seki S, Tagawa S, Masunaga H, Sasaki S, Takata M, Aida T (2008) Amphiphilic molecular design as a rational strategy for tailoring bicontinuous electron sonor and acceptor arrays: Photoconductive liquid crystalline oligothiophene-C_{60} dyads. J Am Chem Soc 130:8886–8887
27. Hayashi H, Nihashi W, Umeyama T, Matano Y, Seki S, Shimizu Y, Imahori H (2011) Segregated donor–acceptor columns in liquid crystals that exhibit highly efficient ambipolar charge transport. J Am Chem Soc 133:10736–10739
28. Toth K, Molloy JK, Matta M, Heinrich B, Guillon D, Bergamini G, Zerbetto F, Donnio B, Ceroni P, Felder-Flesch D (2013) A strongly emitting liquid-crystalline derivative of $Y_3N@C_{80}$: Bright and long-lived near-IR luminescence from a charge transfer state. Angew Chem Int Ed 52:12303–12307
29. Lehmann M, Hügel M (2015) A perfect match: Fullerene guests in star-shaped oligophenylenevinylene mesogens. Angew Chem Int Ed 54:4110–4114
30. Wooley KL, Hawker CJ, Fréchet JMJ, Wudl F, Srdanov G, Shi S, Li C, Kao M (1993) Fullerene-bound dendrimers: Soluble, isolated carbon clusters. J Am Chem Soc 115:9836–9837
31. Brettreich M, Burghardt S, Böttcher C, Bayerl T, Bayerl S, Hirsch A (2000) Globular amphiphiles: Membrane-forming hexaadducts of C_{60}. Angew Chem Int Ed 39:1845–1848
32. Burghardt S, Hirsch A, Schade B, Ludwig K, Böttcher C (2005) Switchable supramolecular organization of structurally defined micelles based on an amphiphilic fullerene. Angew Chem Int Ed 44:2976–2979

33. Muñoz A, Illescas BM, Sánchez-Navarro M, Rojo J, Martín N (2011) Nanorods versus nanovesicles from amphiphilic dendrofullerenes. J Am Chem Soc 131:16758–16761
34. Lenoble J, Campidelli S, Maringa N, Donnio B, Guillon D, Yevlampieva N, Deschenaux R (2007) Liquid-crystalline Janus-type fullerodendrimers displaying tunable smectic-columnar mesomorphism. J Am Chem Soc 129:9941–9952
35. Campidelli S, Bourgun P, Guintchin B, Furrer J, Stoeckli-Evans H, Saez IM, Goodby JW, Deschenaux R (2010) Diastereoisomerically pure fulleropyrrolidines as chiral platforms for the design of optically active liquid crystals. J Am Chem Soc 132:3574–3581
36. Guerra S, Iehl J, Holler M, Peterca M, Wilson DA, Partridge BE, Zhang S, Deschenaux R, Nierengarten JF, Percec V (2015) Self-organisation of dodeca-dendronized fullerene into supramolecular discs and helical columns containing a nanowire-like core. Chem Sci 6:3393–3401
37. Choi MS, Aida T, Luo H, Araki Y, Ito O (2003) Fullerene-terminated dendritic multiporphyrin arrays: "Dendrimer effects" on photoinduced charge separation. Angew Chem Int Ed 42:4060–4063
38. Armaroli N, Boudon C, Felder D, Gisselbrecht JP, Gross M, Marconi G, Nicoud JF, Nierengarten JF, Vicinelli V (1999) A copper(I) bis-phenanthroline complex buried in fullerene-functionalized dendritic black boxes. Angew Chem Int Ed 38:3730–3733
39. Felder D, Gallani JL, Guillon D, Heinrich B, Nicoud JF, Nierengarten JF (2000) Investigations of thin films with amphiphilic dendrimers bearing peripheral fullerene subunits. Angew Chem Int Ed 39:201–204
40. Muñoz A, Sigwalt D, Illescas BM, Luczkowiak J, Rodríguez-Pérez L, Nierengarten I, Holler M, Remy JS, Buffet K, Vincent SP, Rojo J, Delgado R, Nierengarten JF, Martín N (2016) Synthesis of giant globular multivalent glycofullerenes as potent inhibitors in a model of Ebola virus infection. Nat Chem 8:50–57
41. Zhou S, Burger C, Chu B, Sawamura M, Nagahama N, Toganoh M, Hackler UE, Isobe H, Nakamura E (2001) Spherical bilayer vesicles of fullerene-based surfactants in water: A laser light scattering study. Science 291:1944–1947
42. Isobe H, Homma T, Nakamura E (2007) Energetics of water permeation through fullerene membrane. Proc Natl Acad Sci U S A 104:14895–14898
43. Sawamura M, Kawai K, Matsuo Y, Kanie K, Kato T, Nakamura E (2002) Stacking of conical molecules with a fullerene apex into polar columns in crystals and liquid crystals. Nature 419:702–705
44. Matsuo Y, Muramatsu A, Kamikawa Y, Kato T, Nakamura E (2006) Synthesis and structural, electrochemical, and stacking properties of conical molecules possessing buckyferrocene on the apex. J Am Chem Soc 128:9586–9587
45. Vergara J, Barberá J, Serrano JL, Ros MB, Sebastián N, de la Fuente R, López DO, Fernández G, Sánchez L, Martín N (2011) Liquid-crystalline hybrid materials based on [60] fullerene and bent-core structures. Angew Chem Int Ed 50:12523–12528
46. Nishioka T, Tashiro K, Aida T, Zheng JY, Kinbara K, Saigo K, Sakamoto S, Yamaguchi K (2000) Molecular design of a novel dendrimer porphyrin for supramolecular fullerene/dendrimer hybridization. Macromolecules 33:9182–9184
47. Kimura M, Saito Y, Ohta K, Hanabusa K, Shirai H, Kobayashi N (2002) Self-organization of supramolecular complex composed of rigid dendritic porphyrin and fullerene. J Am Chem Soc 124:5274–5275
48. Fernández G, Sánchez L, Pérez EM, Martín N (2008) Large exTTF-based dendrimers. Self-assembly and peripheral cooperative multiencapsulation of C_{60}. J Am Chem Soc 130:10674–10683
49. Shirakawa M, Fujita N, Shinkai S (2003) [60]Fullerene-motivated organogel formation in a porphyrin derivative bearing programmed hydrogen-bonding sites. J Am Chem Soc 125:9902–9903
50. Dawn A, Shiraki T, Ichikawa H, Takada A, Takahashi Y, Tsuchiya Y, Lien LTN, Shinkai S (2011) Stereochemistry-dependent, mechanoresponsive supramolecular host assemblies for fullerenes: A guest-induced enhancement of thixotropy. J Am Chem Soc 134:2167–2171

Superconductivity

28

Katsumi Tanigaki

Contents

Abstract

A molecule of C_{60} discovered as a new type of carbon has high symmetry and a large hollow inside. The crystal forming from this molecule consists of five- and triple-fold degeneracy in the valence and the conduction band. Various exotic properties are expected from this molecule and its derived crystals. Actually, very intriguing metallicity and superconductivity with high critical temperature are observed in these 30 years, the latter of which surpasses the superconducting critical temperature of organic superconductors and beyond the limit of the conventional Bardeen-Cooper-Schrieffer (BCS) theory. In this chapter, the history and advancement of the C_{60} superconductivity is reviewed.

Keywords

C_{60} · Fullerides · Metallicity · Superconductivity · High Tc · Carrier doping · BCS theory · Non-BCS theory

K. Tanigaki (✉)
Beijing Academy of Quantum Information Sciences (BAQIS), Beijing, China

Advanced Institute of Materials Research, Tohoku University, Sendai, Japan
e-mail: katsumitanigaki@baqis.ac.cn; katsumi.tanigaki.c3@tohoku.ac.jp; tanigaki@m.tohoku.ac.jp

X. Lu et al. (eds.), *Handbook of Fullerene Science and Technology*,
https://doi.org/10.1007/978-981-16-8994-9_42

Introduction

C_{60} is a member of a series of molecules, carbon polyhedra C_n (fullerenes). They geometrically follow Euler's theorem, $V-E+F=2$ applied to a convex polyhedron, where V, E, and F are the numbers of vertices, edges, and faces in a polyhedron. Hitherto, a family of similar polyhedra, such as C_{70}, C_{76}, and C_{82}, is also discovered. Especially, C_{82} is nearly a round high symmetric fullerene next to C_{60}, while C_{70} and C_{76} show a little bit elongated shape leading to a lower symmetry of a molecule. The evidence of C_{60} was spectroscopically given when Kroto, Smalley, and Hoffmann proposed its existence in 1895 by mass spectrometry. The spectrum with the mass number of 720 was only the indication of C_{60} as an interstellar molecule experimentally given in laser ablation experiments in a laboratory. Materials scientists did not pay much attention to this new finding in the beginning because this was not a real material which one can have in his/her hand. Such a situation was greatly changed after the discovery of macroscopic production of C_{60} by an arc-discharge vaporization of carbon rods under a He atmosphere, together with extraction of C_{60} and C_{70} from the produced soot using organic solvents and their crystallization, reported by Krätchmer in 1990. This large-yield production provided a very unique chance to scientists for exploring metallicity and superconductivity from these novel molecular solids. A vast number of experiments were made immediately to search for intriguing physical properties.

One of the most attractive things for C_{60} was its high symmetry leading to a nearly isotropic three-dimensional solid as shown in Fig. 1. Various organic

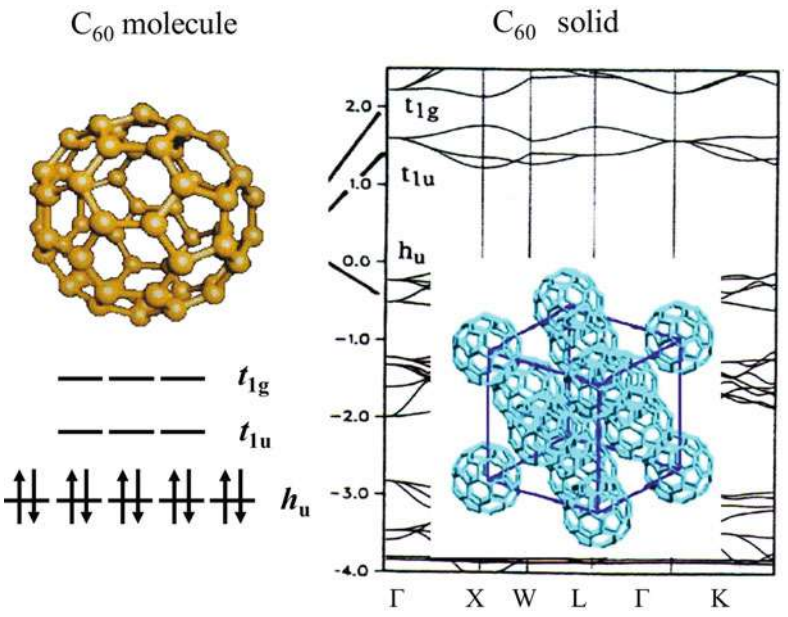

Fig. 1 Molecular orbitals of C_{60} and the derived band structure of C_{60} solid

molecules had been synthesized in the past already in order to search for synthetic metals with high conductivity in organic compounds and superconductivity with high critical temperature (T_c) based on a fused carbon network comprising of a six-membered aromatic ring system as well as linear-long-chain poly-acetylenes according to the highly conductive polymers discovered by Heeger, Shirakawa, and MacDiarmid. The problem, however, has been the instabilities caused by the low dimensionality. Seeing the high symmetry of the molecular structure and its crystal structure of C_{60}, it would have been natural that many scientists expected various novel properties to appear from C_{60} with their large anticipations. Before the large-scale production of C_{60} and its related molecules, theorists had already started to calculate what kind of properties could be observed from these molecules. We indeed encountered for the wonderful time when we were able to make experiments to see what occurs in the early of 1990. We know presently what has happened in these 30 years in electronic properties of fullerenes, such as C_{60}, C_{70}, C_{76}, etc. Highly conducting compounds were synthesized and superconductors with high critical temperature (T_c) were realized in C_{60}.

Coming back to the history of superconductivity, the phenomenon was experimentally first discovered by Kamerlingh Onnes in 1991 for mercury (Hg) [1] as shown in Fig. 2. The intrinsic microscopic understanding of the mechanism was established by Bardeen, Cooper, and Schrieffer in 1957, being known as the BCS theory in terms of the phonon-mediated Cooper-pairing of electrons [2]. For a long time, scientists had believed that the limit of T_c will exist around below 30 K because no remarkable advancements had been made for a long time after the discovery of superconductivity, which scientists called as the BCS limit of the conventional superconductors.

The situation, however, greatly changed when the high T_c superconductors, which surpass the conventional BCS limit and reach 140 K to date, were found in cuprates by Bednorz and Muller in 1986 [3]. The T_c found in cuprates is far beyond the BCS limit and the electron correlations giving a Mott insulator with a half band filling seemed to play an important role in the formation of the superconducting paired electrons. A tremendous number of studies were triggered to search for other superconductors with the non-BCS mechanism. When the superconductivity was found beyond 30 K in C_{60} in 1991 [4], various discussions have started as to whether the superconductivity mechanism is BCS or non-BCS. A new iron pnictide superconductor was found by Kamihara and Hosono in 2006 [5] and its T_c was located above 50 K, and further enthusiastic discussions have started on the superconducting mechanism of whether this is either phonon-mediated BCS or electron-correlation-mediated non-BCS.

Very recently, some of hydrogen-associated compounds have shown a T_c surpassing those of cuprates as reported by Drozdov et al. in 2015 [6] and subsequently other groups. They are coming very close to or near room temperature importantly within the context of the purely phonon-mediated BCS mechanism. Regarding the symmetry of superconductivity, the conventional superconductors were s-wave symmetry with a full energy gap opening. On the other hand, in the case of cuprate superconductors, however, d-wave symmetry with gap-closed nodes was proposed.

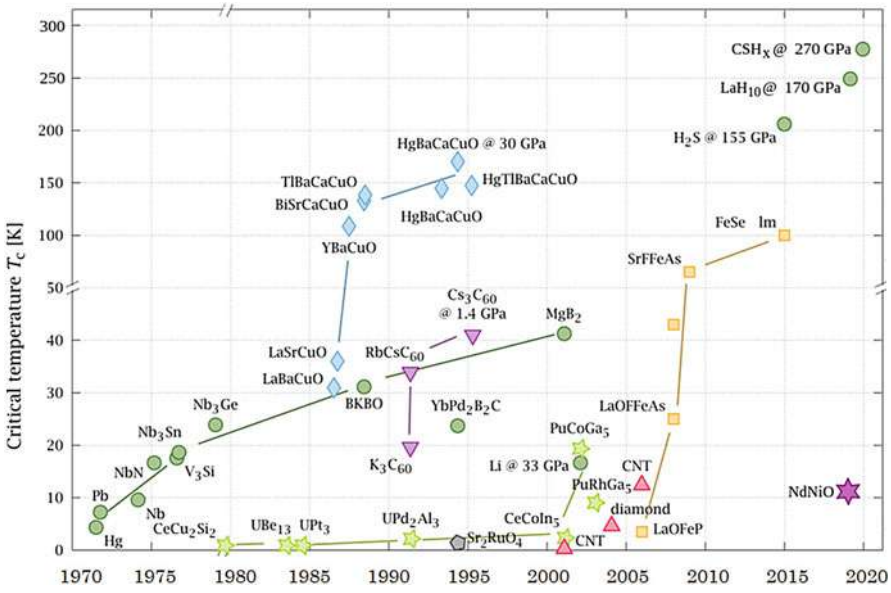

Fig. 2 Superconductivity (Wikipedia: https://en.wikipedia.org/wiki/Superconductivity): Superconducting critical temperature (T_c) in the history with the discovery of new superconductors. After the elementary superconductors, compound superconductors were searched. A surprising change in T_c upgrade was made in cuprate superconductors, and non-BCS mechanism associated with electron correlations has been discussed. Some organic superconductors were found in a similar period, the T_c of which became beyond the BCS limit by the T_c of C_{60} superconductors. The discovery of Fe pnictide superconductors provided scientific discussions on the superconductivity mechanism between the phonon-mediated and electron-correlation-mediated electron pairing. The discovery of the highest T_c in hydrogen-associated compounds under high pressure within the formalism of purely phonon-mediated conventional BCS superconductivity mechanism is giving continuous debates on the superconductivity mechanism for high T_c

This has recently been reclaimed to be s-wave symmetry and continuous scientific arguments have been under the debate. A variety of discussions on the mechanism of high T_c superconductivity have still been continuing.

Here, I review the progress of the superconductivity of fullerenes mainly focusing on C_{60} in these 30 years and describe the present understanding of the mechanism of superconductivity for C_{60}.

History of Finding Superconductivity in C_{60}

Metallicity and superconductivity of C_{60} were discovered by the research members of Bell Telephone Laboratory in 1991 [4, 8]. Since the C_{60} molecule and its crystal are in three-dimensionally high symmetry, high temperature superconductivity was expected from the viewpoint of the history of superconductivity in organic molecules, which was realized for $(TMTSF)_2PF_6$ by Jerome in 1980 [7]. Since instability

of low-dimensional organic crystals is one of the essential problems occurring in the stage of adding other elements or molecules in the donor-acceptor-type organic complexes for introducing carriers into a solid, a three-dimensional high symmetry in C_{60} solids was very attractive in a scope of realizing not only a stable metal but also a superconductor with high T_c. Such an attempt was made successfully in 1991 using a combination of C_{60} with a potassium element (K) as an intercalant for making a metal with high resistivity of 100 Ωcm by Haddon et al. [8] and subsequently a superconductivity with an onset of T_c of 18 K was reported by Hebbard et al. [4] for the stoichiometric K_3C_{60}. A finding of metallic and superconducting K_3C_{60} triggered immediately various studies for making further experimental progresses and theoretical studies for understanding the mechanism. The crystal structure was determined to be the unique face-centered cubic (fcc) with including a rotational disorder of C_{60} molecules on the residing site in a unit cell by Stephenes et al. [9].

Subsequent studies of alkali metal–intercalated C_{60} fullerides provided an increase in T_c from 18 K of K_3C_{60} [4] to 28 K of Rb_3C_{60} by Rosseinsky et al. [10] and to 33 K of $RbCs_2C_{60}$ by Tanigaki et al. [11], the last of which has been the highest record of T_c at ambient room pressure to date as shown in Fig. 3. The relationship between the T_c and the cell parameter in A_3C_{60} has become the intensive debates for scientists [12]. An unstable Cs_3C_{60} was successfully stabilized to both

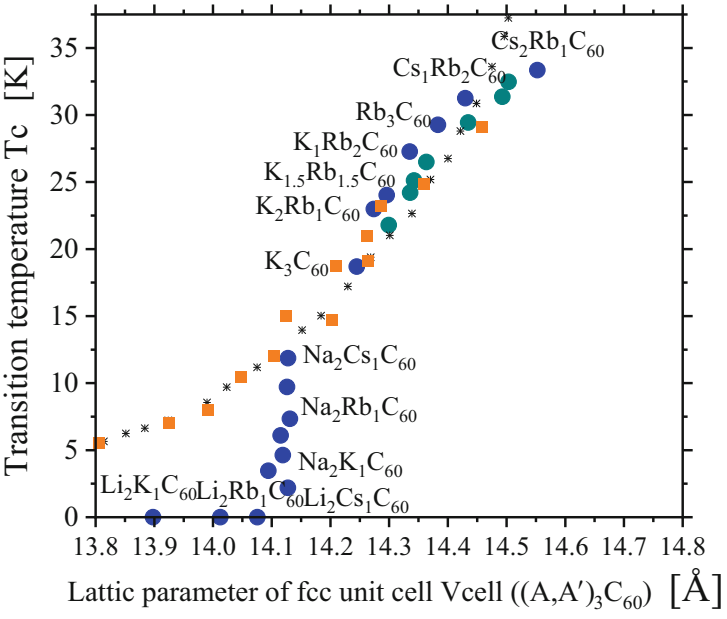

Fig. 3 Relationship between Tc and cell parameter of A_3C_{60} superconductors. Blue filled circles are experimental data carried out in our laboratory (see references [11, 12]), green filled circles are the experimental data reported from the researchers in Bell laboratories [4, 10], and the filled squares in orange are the T_c of Rb_3C_{60} and K_3C_{60} under hydrostatic pressure

fcc and A15 in 2008 by the collaborative studies of Rosseinsky and Prassides et al. [13], but its intrinsic property was a Mott insulator under ambient pressure. This group searched for the superconductivity under high pressure and found superconductivity of 35 K for fcc Cs_3C_{60} and 38 K for A15 Cs_3C_{60} [14], which have become the new record in high T_c of C_{60} superconductors under high pressure. The situation seems to be reminiscent of the history of cuprate superconductors although the T_c upgrades were made by carrier tuning in the case of cuprates, whereas the progress was made in the cell-size control in the case of C_{60} fullerides. The expanded $Cs_xRb_{3-y}C_{60}$ was synthesized in the early stage of the research, but the observed decrease in T_c was interpreted in terms of the instability of the crystal phase [15]. Considering the Mott insulating states, the effect of cell expansion was studied by Iwasa et al. [16] also in the early stage of research, but clear discussions were difficult due to the distortion of the crystal structure.

Considering a large molecular size of C_{60} with the carbon network, a large hollow space inside is almost the same as or larger than that of the interstitial space existing among C_{60} molecules. Therefore, a C_{60} molecule itself intriguingly can accommodate one or multiple other elements inside the carbon-truncated icosahedron, such as $Li^+@C_{60}{}^{1-}$, $La^{3+}@C_{60}{}^{3-}$, and $Ar@C_{60}$. The efforts to make a large mass production of these endohedral fullerenes were made, but a few experiments were successful in macroscopic productions for carrying out meaningful physical properties. A report can be found that $K_3(Ar@C_{60})$ shows a superconductivity [17], but its T_c is reported to be lower than that of K_3C_{60}. Even though $Li@C_{60}$ was successfully and macroscopically produced by tremendous efforts, the isolated endohedral molecule exists only in a solution, and complex bonded solids can result to be solidified after evaporation of the solvents [18]. Unfortunately, neither metallic nor superconductivity was reported. Synthetic chemical synthesis successfully produced $C_{59}N$ by replacing a carbon atom by nitrogen N in a C_{60} molecule. Since this molecule corresponds to one-electron addition to the C_{60} t_{1u}-derived band, it is intriguing to see what electronic properties can be observed. However, due to the formation of a $(C_{59}N)_2$ dimer caused by the instability of the molecule, an insulating property is reported without any intriguing electronic states [19]. Although a $(NC_{59})_2$ dimer can be re-separated to a molecular form of $C_{59}N$ when alkali metal of K is added, the stable solid was reported to be an insulating $K_6(C_{59}N)$ without superconductivity [20]. Some reports suggest that C_{70} can be metallic when they are intercalated. However, no firm experimental evidences were reported that show a fact that any higher fullerenes show metallic and superconducting when other elements were intercalated as far as I can recognize in the literatures reported so far.

Updated Phases of Alkali, Alkaline-Earth, and Rare-Earth Metal Intercalated C_{60} Fullerides

Since a C_{60} solid has three important molecular orbital-derived bands (fivefold degenerate h_u valence band, the lowest t_{1u}- and the second lowest t_{1g}-derived conduction bands with threefold degeneracy), these bands can accommodate

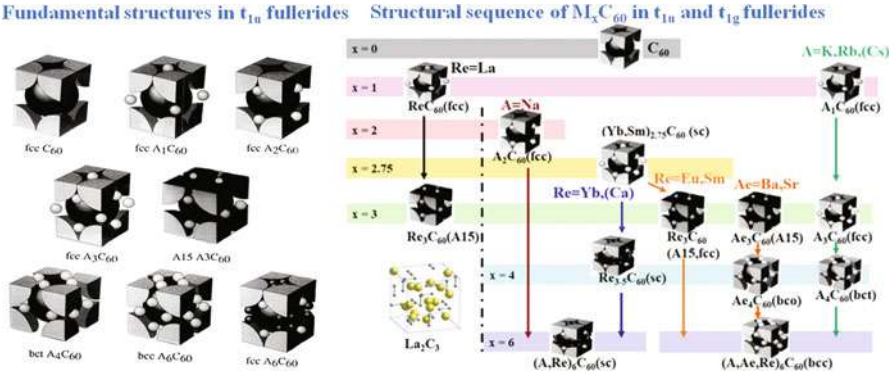

Fig. 4 Structural sequences found in t_{1u} fullerides and the modified structure sequence in t_{1u} and t_{1g} fullerides with alkali-metal, alkaline-earth metal, and rare-earth metal elements as the intercalants

electrons or holes to be itinerant. From the viewpoint of crystal structure, we can see both octahedral (O) and tetrahedral (T) interstitial spaces in a unit cell in the case of an fcc unit cell composed of C_{60} molecules, and therefore the full stoichiometry can be $A(O)B(T)_2C_{60}$, where A and B denote the intercalant elements [21] as displayed in Fig. 4. Therefore, when a monovalent alkali-metal (A) atom is accommodated to all sites in the unit cell, an fcc A_3C_{60} stoichiometric compound is made which corresponds to the half filling t_{1u}-band-associated structure. Since the crystal structure can be valid depending on the accommodated number of intercalant elements from face-centered cubic (fcc) A_1C_{60}, either fcc or A15 A_3C_{60}, to body-centered tetragonal (bct) A_4C_{60} to body-centered cubit (bcc) A_6C_{60}, the band filling can be modulated from 1 to 6 in the case of t_{1u}-associated band as shown in Fig. 5. When divalent alkaline-earth metals (E) are used in place of alkali-metals (A), the higher t_{1g}-associated band can also be partly or fully occupied. Therefore, two types of metallic and superconducting phases are produced, t_{1u}-associated and t_{1g}-associated phases, depending on the elements employed such as monovalent alkali-metal A, divalent alkaline-earth metal E, and other rare-earth metal R with either divalent or trivalent as well as upon their occupation numbers.

Metallic and superconducting t_{1u}-associated band compounds are based on the nearly pure triply degenerate t_{1u}-derived bands and a good metallic and superconducting phase appears only for half-occupied $(A,A')_3C_{60}$ stoichiometric compounds as shown in Fig. 6. A relatively bad metallic phase forms in monovalent and pentavalent band filling of the t_{1u}-derived band upon the odd/even number of band filling per C_{60}, such as $A^+C_{60}^-$ and $A^{1+}E^{2+}{}_2C_{60}^{5-}$, but these valence state compounds do not show superconductivity. Superconductivity in the t_{1u}-associated band only appears exactly or very near the trivalent stoichiometric $(A,A')^-{}_3C_{60}^{3-}$ compounds. On the other hand, t_{1g}-derived band–associated superconductivity appears with spreading over a wide valence state. This is considered to be due to the hybridization between the t_{1g}-derived band of C_{60} and the orbitals of intercalant

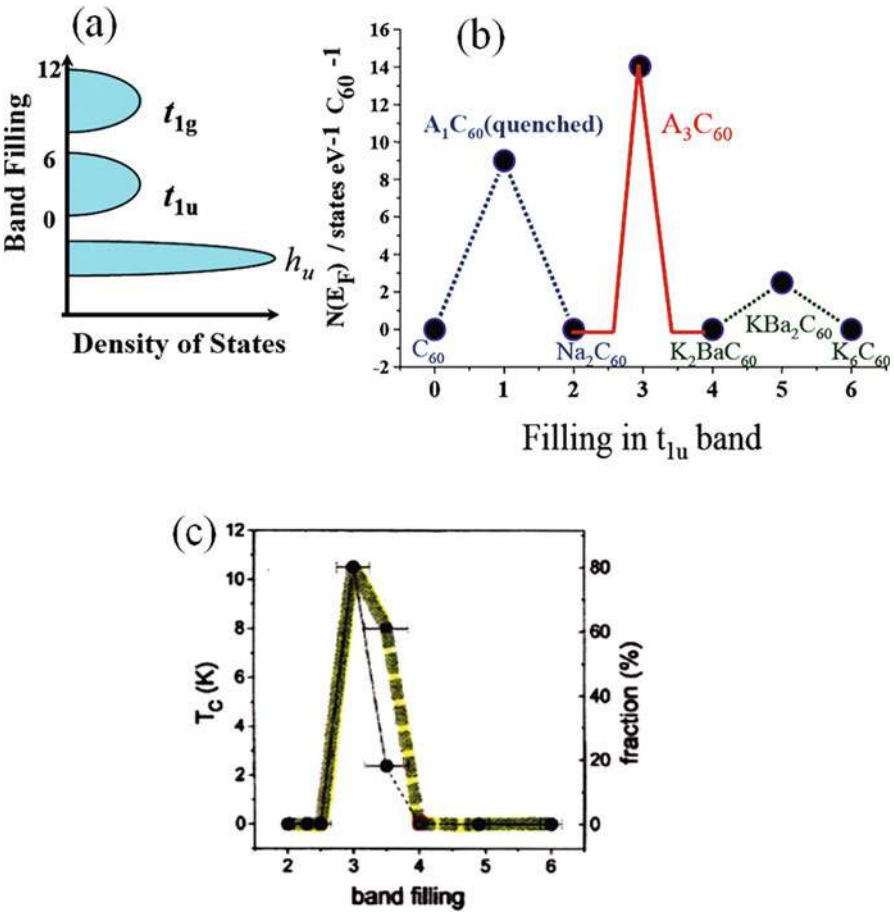

Fig. 5 (**a**) Important three bands in C_{60} solids: t_{1u} and t_{1g} conduction band and h_u valence band. (**b**) Fullerides existing in the t_{1u}-derived band with various valence states. An odd-even effect on the metallicity is generally recognized. (**c**) Superconductivity occurs at the half-filled band with three electron occupation per C_{60} in the small band filling regime of t_{1u}-associated fullerides. The superconductivity only occurs at trivalent states of C_{60} with the half-filled state, being confirmed by experiments using alkali-metal (A) and alkaline-earth metal (E) binary $(A, E)_3C_{60}$ [34] or $LixCsC_{60}$ [33]

elements of E and/or R. Electron correlations such as the on-site Coulomb repulsion U as well as the exchange interaction J become weaker than those in the case of pure t_{1u}-derived bands and a metallic system is produced in a wide range of band filling in the case of t_{1g}. Superconductivity is reported for various valence states in the case of t_{1g}-derived band–associated compounds as shown in Figs. 7 and 8.

Kortan et al. reported Ca_xC_{60} [22] in the early stage of the C_{60} superconductors. The structure is reported to be most probably a primitive cubic structure. Due to the

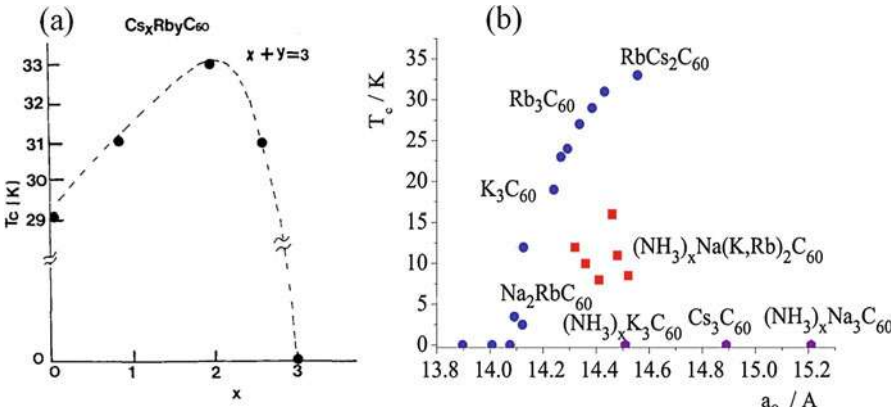

Fig. 6 (**a**) A_3C_{60} with Na, K, Rb, and Cs intercalated shows superconductivity with an increase in T_c with cell parameter, but T_c disappears in the small cell parameter reason for Li_2KC_{60}, Li_2RbC_{60}, and Li_2CsC_{60} and in the large cell parameter region such as Cs_3C_{60}. The reason of missing in T_c for $Li_2(K,Rb,Cs)C_{60}$ is the insufficient carrier transfer to C_{60}, leading away from trivalent half filling of C_{60}^{3-}. T_c of $Li_2Cs_3C_{60}$ is recovered to when excess amount of Li is introduced to the half filling [33]. (**b**) The cell-expanded fullerides with intercalation of ammonium (NH_3) show superconductivity with lower T_c [16]. The reason would be due to the lower symmetry of structural distortion. Cs_3C_{60} did not show superconductivity at this time and was interpreted in terms of instability of the crystal [15]. High-quality Cs_3C_{60} can be synthesized as the Mott insulator and be confirmed to be superconducting [13, 14]

relatively small cation size of Ca^{2+} intercalant element compared to the tetrahedral and the octahedral spaces to be formed among C_{60} molecules in a cell, the Ca_xC_{60} crystal is very unstable and the intrinsic superconducting phase was not successfully determined. Compared with Ca, other alkaline-earth metals form more stable fullerides and the body-centered cubic (bcc) A_6C_{60} phases were originally proposed to be superconducting with $Tc = 4$ K for Sr_6C_{60} and $Tc = 6.5$ K for Ba_6C_{60} as the subsequent studies by Kortan et al. [23]. It has been confirmed later that the true superconducting phases are the body-centered orthorhombic (bco) with the stoichiometry of A_4C_{60} fullerides [24], the structure of which was determined clearly by synchrotron X-ray diffractions later [25]. It was thus of paramount importance to know the bcc phases as to whether they are metallic or not. Theoretically it has been predicted that N_{EF} of Sr_6C_{60} is larger than that of Ba_6C_{60} [26], being contradictory to the unit cell volume between two alkaline-earth fullerides that the former is smaller than the latter. Such a behavior was drastically different from what is predicted theoretically and found experimentally in fcc metallic and superconducting A_3C_{60} fullerides as described earlier, in which the conduction band is derived from the t_{1u}-derived band. The bcc Ba_6C_{60} and Sr_6C_{60} fullerides are not superconducting, although they are metallic. Of particular importance is the fact that the observed DOS values are the opposite to what has established in the case of fcc $(A,A')_3C_{60}$, where A and A′ are Li, Na, K, Rb, Cs, and their mixtures. This would presumably be related to the fact that while electron transfer from the alkali metals to C_{60} is

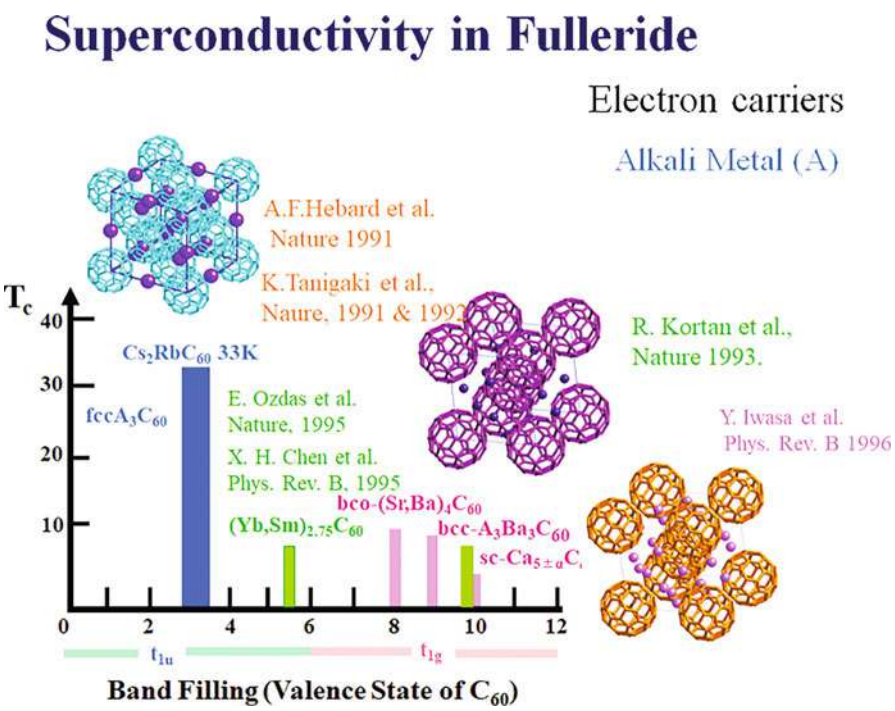

Fig. 7 Relationship between T_c and band filling in C_{60} superconductors. The highest T_c can be found in a half-filled C_{60} stoichiometry in the t_{1u}-derived band

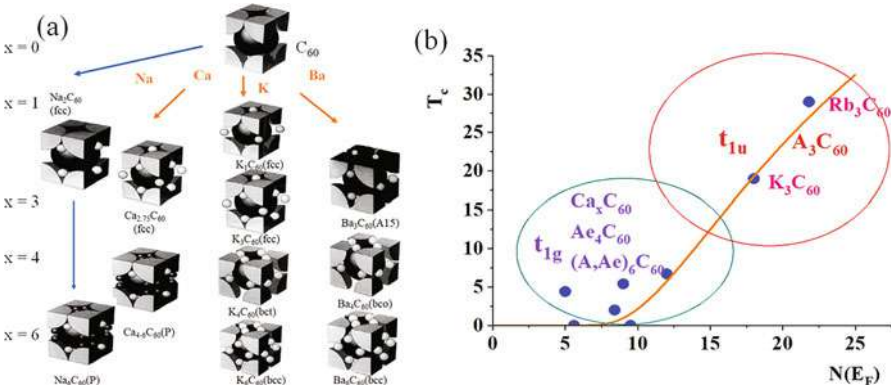

Fig. 8 (**a**) Structural sequence for C_{60} fullerides with the intercalants of Na, Ca, K, and Ba. (**b**) T_c as a function of density of states $N(E_F)$ [States/C_{60}-mol]. The superconductors in the t_{1g}-derived band have lower density of states and show the lower T_c than those in the t_{1u}-derived band

essentially complete in the case of alkali metals, strong hybridization of the Ba/Sr and C_{60} orbitals leads to incomplete charge transfer that is sensitive to the extent of orbital mixing in the case of t_{1g}-derived band.

For R_xC_{60} with intercalant elements of rare-earth metals, many of the fullerides were not stable and were difficult to synthesize. Ozdas made his intensive efforts to produce Yb_xC_{60} and reported that $Yb_{2.75}C_{60}$ shows superconductivity with the site vacancy [27]. When Yb elements fully occupy until the stoichiometry of three in C_{60}, the divalent Yb^{2+} element will give a situation of the full t_{1u} band occupation and accordingly no metallic and superconducting states can occur. Therefore, it is intriguing to recognize, if this could correct experimentally, that a vacancy gives a unique situation that superconductivity can appear besides the half-filled band situation in t_{1u}-derived band. In other scientific viewpoints, this corresponds to the fact that a hole-doped t_{1u} band superconductor is realized in the site-vacant $Yb_{2.75}C_{60}$ with superlattice structure. Afterward, more careful studies were made for divalent Yb and Sm intercalated C_{60} in two research groups. Both groups concluded that a site-vacant $R_{2.75}C_{60}$ is produced for both Yb and Sm, but however the latter does not show any superconductivity while the former is superconducting. It is noted that the interpretations as to why $Sm_{2.75}C_{60}$ is not superconducting is different between the two groups [28, 29].

In the case of trivalent rare-earth metals, the appearance of superconductivity with $Tc = 12$ K in C_{60} was reported when it is intercalated with La. La was intercalated by the pioneering work of Kortan et al. [30], being similar to the situation of the divalent alkaline-earth metal elements (E = Ca, Sr, and Ba) and divalent rare-earth metal elements (R = Eu, Yb, and Sm). La_xC_{60} was the first situation where superconductivity can be found when the trivalent elements were used. Furthermore, the superconducting transition temperature T_c of 12 K was relatively high among rare-earth metal C_{60} fullerides, the *Tc*'s of which generally range from 6 to 8 K. However, the fraction of this superconducting phase was too small to determine the real superconducting phase at that time, as was reported in the original report [30]. Afterward, further experiments have led to a success in achieving superconductivity with a fraction of around 10% with *Tc* of 12 K. High-resolution X-ray diffraction studies, unfortunately, provided a conclusion that the real superconducting phase with *Tc* of 12 K made from La-C_{60} should be ascribed to a carbide but not to the C_{60} fullerides [31]. This is the first situation where one encountered as a fact that the superconductivity found from C_{60} is not coming from the C_{60} fullerides. The two superconducting phases were proven to be possible as LaC_x carbides, the both of which are most likely related to the same stoichiometric La_2C_3 phase.

After finding of the first reports on conductivity and superconductivity in C_{60} fullerides [4, 8], a variety of alkali and alkaline-earth metal-doped C_{60} fullerides have been discovered by the tremendous efforts of scientists in their pioneering experiments [10–31]. The experiments, however in early of 1990, were very difficult to make the final confirmation and conclusions about the structure, and it needed more time to make sure which structure is the intrinsic superconducting phase. In contrast to the t_{1u}-derived band–associated C_{60} fullerides, the t_{1g}-derived band–associated fullerides show a markedly different situation as shown in Fig. 8. The change in properties upon the odd-even stoichiometries observed in the t_{1u}-associated fullerides, for example, seeing a simplified situation in the t_{1u} C_{60} fullerides (Fig. 3), is no longer observed in the t_{1g}-associated ones. The studies on

the C_{60} fullerides extended from alkali-metals (A), alkaline-earth (E) to rare-earth metals (R) with divalent (Ca, Yb, Sm, and Eu) or trivalent (La) valence states needed lots of time to know the details about their structure and physical properties. Although they have gradually been clarified and come to the better understanding, to be honest I am still puzzled sometimes whether we were able to know all the nature of these superconductivities.

The Mechanism of Superconductivity

As described in the history of superconductivity, the superconducting critical temperature (T_c) in C_{60} started with the discovery for K_3C_{60} with 18 K [4], it was immediately raised to 28 K in Rb_3C_{60} [10] with a lattice expansion, being further increased to 31 K in $Rb_2Cs_1C_{60}$ until up to $Rb_1Cs_2C_{60}$ [11, 12]. The important experimental results were the evidence that the T_c rises by following the simple sequential order according to the total cell volume of A_3C_{60} $V_{cell}(A^+{}_3C_{60}{}^{3-})$ with corresponding to the ionic radius of the intercalant alkali-metals (A) employed in the case of the t_{1u}-associated band. Noted is the fact that superconductivity arising from the t_{1g}-associated band, with more higher band filling than six electrons, is lower in T_c and their values do not greatly change compared to those found in t_{1u}-associated band, see Fig. 8. In the early time of studies, the T_c was also found to be lowered when the crystal cell shrinks to be smaller with replacing K or Rb by the smaller alkali metal of Na, such as Na_2RbC_{60} (Tc = 3.5 K) and Na_2KC_{60} (Tc = 2.5 K) [12]. Since the density of states at the Fermi level increases monotonically with an increase in cell volume parameter, a little bit simple expectation was given in the early stage based on the original phonon-mediated Bardeen-Cooper-Schrieffer theory (BCS), where the high frequency phonons play an important role [35, 36]. However, when a conventional free-electron model is applied to estimate the density of states at the Fermi-level $D(E_F)$, $D(E_F)$ deduces with an expansion of the cell volume $V(A_3C_{60})$ and T_c reduces with an increase in V (A_3C_{60}), giving the opposite conclusion to the experimental data. Consequently, the band narrowing for tuning the $D(E_F)$ was pointed out in order to provide the interpretations. Many band calculations performed based on local density approximation (LDA) and density functional theory (DFT) clearly showed such phenomenon [32]. This is a similar consequence obtained in many molecular organic metals and superconductors, where the strength of overlap transfer integrals is strongly modulated by the distance among molecules.

The two problems, however, at least had been to be clarified as the essential problems for further understanding in the future. One is the fact that electron-phonon interactions are the retarded effects and, therefore, the highest limit should be constrained to the phonon frequency, for giving the effective attractive force for the electron Cooper pairing. This should especially be considered for the relatively slow velocity of itinerant electrons in such a case as a molecular system with small transfer integrals. Another is the electron repulsion energy (U), which is much larger than that of the bandwidth (W). Many band calculations and photoemission spectroscopic studies showed that on-site Coulomb electron-electron repulsion energy U

is as large as 1.0–1.5 eV compared to the relatively narrow bandwidth of c.a. 0.5 eV. These suggest that A_3C_{60} can be in a Mott insulating state.

From the standard estimates of the bandwidth W and the on-site electron repulsion U in the case of A_3C_{60}, the ratio of U/W becomes larger than 1 and a band gap is opened to be insulating. Experimental data based on photoelectron spectroscopy gives the firm evidence of large U in the case of C_{60} crystals. However, electrical transports as well as magnetic measurements by SQUID or NMR experiments provide the evidence of a metallic behaviors at high temperatures and a superconducting transition at low temperatures. Therefore, a possibility had been discussed that A_3C_{60} is not in the stoichiometric and the band is not in the half occupation. Such nonstoichiometric situation makes A_3C_{60} metallic, being reminiscent of that of cuprates. Noted is also the difference in the comparison with Fe superconductors with having also high T_c, that Fe pnictides are generally still in the metallic regime due to orbital-selective behaviors thanks to the five d multibands. However, careful experiments by changing the composition of $A_{3-x}A'_xC_{60}$ provided the firm conformation that the metallic $A_{3-x}A'_xC_{60}$'s are always in the stoichiometric $(A,A')_3C_{60}$ and metallicity can be observed in the trivalent stoichiometry and superconductivity arises from its Fermi surface. The same conclusion was given for by the experiments for Li_xCsC_{60} [33]. Because of the small cation size of Li^+ element, the x can be changed from two to a higher number in the stable Li_nCsC_{60}; metallic properties as well as superconductivity arises only when the three electrons are provided from the n number of Li and one Cs to C_{60}. The situation was carefully studied using $A_xE_{3-x}C_{60}$ by employing the combinations of alkali-metal A and alkaline-earth E metal elements by Yildrium et al. [34], and it was proven that the experiments provide the clear evidence that trivalent $(C_{60})^{3-}$ is essential for giving rise to metallic Fermi surfaces and superconductivity.

Gunnarsson and coworkers provided a theoretical explanation considering the degeneracy in the band structure [37, 38]. The discussion on the critical value of U/W for a Mott-Hubbard transition was made for a system without orbital degeneracy, while the conduction band derived from the t_{1u} orbitals of C_{60} has a threefold degeneracy. They provided the estimates that the hopping among these multibands gives a screening from the electron repulsion and change the criterium of the Mott-Hubbard transition to be from $E_G = U\text{-}W$ in the single band to $E_G = U\text{-}\sqrt{N}W$ in the case of a band with N degeneracy. This interpretation gave the very important thought for the explanation on the A_3C_{60} electronic properties as to why the metallic properties can be obtained in spite of the larger U than W.

The story of metallicity and superconductivity had been unchanged for a while and the highest T_c was left for a long time without any improvement until the experiments are made for high-quality Cs_3C_{60} under high pressure by the collaborative research between Prassides and Rosseinsky [13, 14]. The unstable fcc and A15 Cs_3C_{60} crystal phase were successfully synthesized using a mono-methyl ammonium solution. Although the synthesized Cs_3C_{60} as the mixture of fcc and A15 phases is insulating, it showed superconductivity with a maximum T_c of 38 K under hydrostatic pressure. The experiments showed for the first time that superconductivity exists near the Mott insulator boundary. Seeing back the history

again, experiments with lattice expansion targeting for the Mott insulator boundary were attempted by Iwasa et al. using ammoniation of $(A,A')_3C_{60}$ [16], but the superconductivity in the vicinity of the Mott boundary was not found most probably due to the lattice distortion. Various careful experiments have been made continuously on the fcc Cs_3C_{60} and the A15 Cs_3C_{60} as well as a series of $Rb_{3-x}Cs_xC_{60}$ residing in the expanded lattice regime by Prassides and the collaborative research teams [13, 14]. Seeing the history, $Rb_{x-3}Cs_xC_{60}$ with expanded lattice residing in the Mott region was synthesized in the early stage of C_{60} superconductivity, but, however, unfortunately a decrease in T_c was recognized and ascribed to the lattice instability [15].

The new experimental evidences showed that a relatively high T_c, beyond or close to the BCS limit, arises under the high pressure in the near phase boundary of Mott insulators for both fcc and A15 Cs_3C_{60} at $T_c = 35$ K and 38 K, respectively. The new experimental data making similar experiments for $Rb_{3-x}Cs_xC_{60}$ series showed that A_3C_{60} displays a $V_{cell}(A_3C_{60})$-T_c phase diagram (Fig. 9), being similar to nonconventional superconductors, such as cuprates and pnictides. However, a high T_c is importantly realized in a s-wave superconducting state, being different from those cuprates and Fe pnictides. Many scientists have the common understanding that the Mott physics on strong electron correlations and pure BCS formalism on phonon-mediated s-wave superconductivity are generally incompatible, and therefore a vast of fundamental questions about the mechanism of the superconductivity were raised for A_3C_{60}. It is noted that the symmetry of superconductivity has been still under intensive debates among scientists, for example, S(++) or S(+−) for Fe pnictides, and d-wave or s-wave even for cuprates.

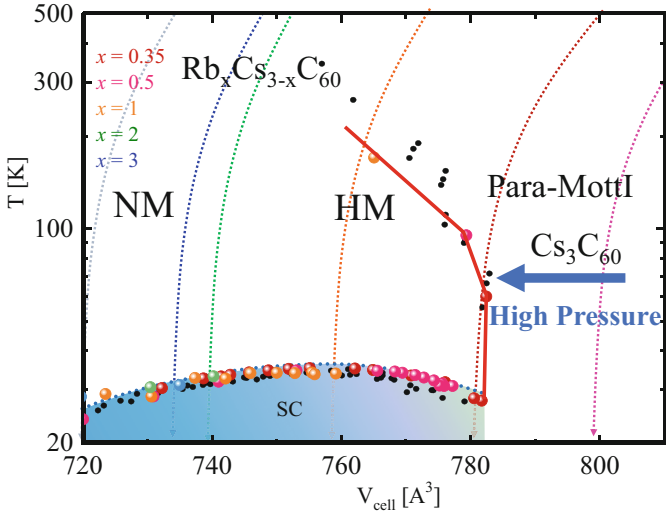

Fig. 9 The phase diagram in C_{60} superconductors in the fcc $(A,A')_3C_{60}$. The high T_c can arise in the boarder of Mott insulators. Cs_3C_{60} with fcc or A15 show the highest Tc of 35 K and 38 K, respectively, under high pressure in the series of C_{60} superconductor family [13, 14]. A superconducting dome can be recognized in a similar fashion to that of cuprates

From the viewpoint of theory in order to understand the superconducting mechanism, a new important interpretation was given by Cappone and Tossatti [39–42]. They pointed out that the intramolecular interactions with the coexistence of a strongly repulsive Coulomb interaction (U) and a small effectively negative exchange interaction (J) are very important, the latter of which is made as a consequence by a subtle energy balance between the parallel and the antiparallel electron spin ordering with the Jahn-Teller electron-phonon interactions. This unusual situation of the negative J leads to a formation of up- and down-spin paired electrons on a molecule, which is not anticipated considering the general Hund rule coupling among the threefold degenerate orbitals in a C_{60} molecule. Consequently, the two electron spins among the three residing in the three degenerate t_{1u} orbitals are antiparallelly coupled in one orbital with leaving one electron spin of $S = 1/2$ in another orbital inside a C_{60} molecule via the Jahn-Teller interactions, and this becomes the most stable electronic ground state in A_3C_{60}. Such paired electronic states can be stabilized during the time scale of Jahn-Teller distortion under many configurations which are equally stabilized within the constraints by the high symmetry of C_{60} crystal. These paired electrons transfer intermolecularly to other orbitals with keeping the paired state, forming the coherent superconducting Cooper paired electronic states to open a gap with s-wave symmetry. This mechanism leads A_3C_{60} to an unconventional high T_c superconductor. The superconductivity mechanism can be benefited from both the strong electron correlations (U) and electron-phonon interactions (V_{e-ph}), the former of which is generally considered to work for preventing phonon-mediated superconducting mechanism. The interplay between electron correlations and electron-phonon interactions can be categorized in a proposed superconductivity theory of Sudo-Kondo mechanism [44, 45]. The recent sophisticated ab initio band calculations based on DFT-DMFT made by Nomura, Arita, and Cappone [42, 43] provide the further firm understandings of this scenario. An occurrence in superconductivity adjacent to the Mott insulating boundary is reminiscent of the cuprates as well as Fe pnictide, where the symmetry of the order parameter is understood to be different under the present understandings, *d*-wave for cuprates and S(++)/S(+−) for Fe pnictides. In the case of A_3C_{60} superconductors, the superconductivity occurs in the *s*-wave symmetry, although it has been believed to be sensitive and fragile to the strong electron correlations.

It is noted that T_c observed under high pressure shows a difference between fcc and A15 Cs_3C_{60} to a small extent, the former being $Tc = 35$ K and the latter being 38 K. From the viewpoint of crystal structural symmetry, C_{60} molecules align to the same direction in the A15 phase, while C_{60} molecules are aligned in the case of fcc into the several directions under the symmetry constraints and fcc Cs_3C_{60} is a frustrated system with a triangular lattice into the (111) direction. At low temperature, an antiferromagnetic state has been observed for both fcc and A15 system [13, 14] with the remarkably large different Neel temperature T_N between the two systems. In the A15 systems, being less frustrated than the fcc, the antiferromagnetic long-range order at around 46 K [13, 14] is reported, whereas the magnetic instability in the fcc is drastically suppressed to 5 K. Even below the T_N, the observed antiferromagnetic order is not perfectly long-range ordered and is in a glass-like

ordered magnetic state. A simple interpretation can be made that the small difference in T_c between fcc and A15 Cs_3C_{60} will be explained in terms of the change in density of states at E_F due to the C_{60} orientational modulations.

Epilogue

When we look the history of superconductivity back, the limit of T_c below 40 K in the conventional formalism of the purely phonon-mediated BCS superconductors has frequently been pointed out. The important difference between unconventional (non-BCS) and conventional (BCS) has always been one of the most important frontier scientific issues in superconductivity. Recently, optical excitation experiments on K_3C_{60} reported an existing transient high T_c state with greatly higher than that of the synthesized A_3C_{60} [46, 47]. It seems important to see whether such a transient state can be stabilized in the ground states of materials. As for the hole-doped C_{60} superconductors, no advancements were achieved although a higher T_c than that in the electron-doped regime can be expected theoretically. We can find an unfortunate misconduct about the hole-doped story [48, 49]. When we discuss the superconductivity issues, we need correct experiments and arguments based on the crystal structure, electrical transport, and magnetic Meissner effect. In the long history of superconductivity, it seems that we have learned a lot. Thanks to the unique structure as well as the electronic properties of C_{60} and its related materials, the intriguing superconductivity has given scientists a variety of wonderful scientific contents that we have been less experienced before. The T_c of C_{60} superconductors, however, will not greatly increase in the future considering the present mechanism. In the case of C_{60} superconductors, I feel that we have come very close to the final understanding. On the other hand, a possibility has recently been shown that room temperature superconductivity for hydrogen compounds can be realized [50], surprisingly in the framework of the conventional BCS mechanism. It is interesting to see how the situation proceeds in the next 10 years.

Cross-References

- ▶ Lithium Endohedral Fullerenes
- ▶ Structural Characteristics of Fullerenes
- ▶ Structures and Properties of Endohedral Metallofullerenes

References

1. Kamerlingh Onnes H (2010) Further experiments with liquid helium. D. On the change of electric resistance of pure metals at very low temperatures. The disappearance of the resistance of mercury. Comm Phys Lab Univ Leiden; No. 122b, 1911.; Dirk van Delft, Peter Kes, the discovery of superconductivity. Phys Today 63:38–43. https://doi.org/10.1063/1.3490499
2. Bardeen J, Cooper LN, Schrieffer JR (1957) Microscopic theory of superconductivity. Phys Rev 106:162–164. https://doi.org/10.1103/PhysRev.106.162; Bardeen J, Cooper LN, Schrieffer JR

(1957) Theory of superconductivity. Phys Rev 108:1175–1204. https://doi.org/10.1103/PhysRev.108.1175
3. Bednorz JG, Müller KA (1986) Possible high Tc superconductivity in the Ba−La−Cu−O system. Z Phys B 64:189–193. https://doi.org/10.1007/BF01303701. S2CID 118314311
4. Hebard F, Rosseinsky MJ, Haddon RC, Murphy DW, Glarum SH, Palstra TTM, Ramirez AP, Kortan AR (1991) Superconductivity at 18 K in potassium-doped C_{60}. Nature 350(6319):600. https://doi.org/10.1038/350600a0
5. Kamihara Y, Hiramatsu H, Hirano M, Kawamura R, Yanagi H, Kamiya T, Hosono H (2006) Iron-based layered superconductor: LaOFeP. J Am Chem Soc 128(31):10012–10013. https://doi.org/10.1021/ja063355c
6. Drozdov P, Eremets MI, Troyan IA, Ksenofontov V, Shylin SI (2015) Conventional superconductivity at 203 kelvin at high pressures in the sulfur hydride system. Nature 525. https://doi.org/10.1038/nature14964
7. Jérome D, Mazaud A, Ribault M, Bechgaard K (1980) Superconductivity in a synthetic organic conductor $(TMTSF)_2PF_6$. J Phys Lett 41(4):95–98. https://doi.org/10.1051/jphyslet:0198000410409500
8. Haddon RC, Hebard AF, Rosseinsky MJ, Murphy DW, Duclos SJ, Lyons KB, Miller B, Rosamilia JM, Fleming RM, Kortan AR, Glarum SH, Makhija AV, Muller AJ, Eick RH, Zahurak SM, Tycko R, Dabbagh G, Thiel FA (1991) Conducting films of C_{60} and C_{70} by alkali-metal doping. Nature 350(6316):320–322
9. Stephens P, Mihaly L, Lee P et al (1991) Structure of single-phase superconducting K_3C_{60}. Nature 351:632–634. https://doi.org/10.1038/351632a0
10. Rosseinsky MJ et al (1991) Superconductivity at 28K in $RbxC_{60}$. Phys Rev Lett 66:2830–2832
11. Tanigaki K, Ebbesen TW, Saito S, Mizuki J, Tsai JS, Kubo Y, Kuroshima S (1991) Superconductivity at 33 K in $Cs_xRb_yC_{60}$. Nature 352(6332):222–223. https://doi.org/10.1038/352222a0
12. Tanigaki K, Hirosawa I, Ebbesen TW, Mizuki J, Shimakawa Y, Kubo Y, Tsai JS, Kuroshima S (1992) Superconductivity in sodium- and lithium-containing alkali-metal fullerides. Nature 356:419–421. https://doi.org/10.1038/356419a0
13. Ganin Y, Takabayashi Y, Jeglič Y, Arčon D, Potočnik A, Baker PJ, Ohishi Y, McDonald MT, Tzirakis MD, McLennan A, Darling GR, Takata M, Rosseinsky MJ, Prassides K (2010) Polymorphism control of superconductivity and magnetism in Cs_3C_{60} close to the Mott transition. Nature 466:221–225. https://doi.org/10.1038/nature09120
14. Zadik RH, Takabayashi Y, Klupp G, Colman RH, Ganin AY, Potočnik A, Jeglič P, Arčon D, Matus P, Kamarás K, Kasaharam Y, Iwasa Y, Fitch AN, Ohishi Y, Garbarino G, Kato K, Rosseinsky MJ, Prassides K (2015) Optimized unconventional superconductivity in a molecular Jahn-Teller metal. Sci Adv 1:e1500059. https://doi.org/10.1126/sciadv.1500059
15. Tanigaki K (1993) Structure and properties of alkali-doped C_{60}. Mater Sci Eng 19:135–140. https://doi.org/10.1016/0921-5107(93)90178-P
16. Iwasa Y, Takenobu T (2003) Superconductivity, Mott Hubbard states, and molecular orbital order in intercalated fullerides. J Phys Condens Matter 15(13):R495–R519. https://doi.org/10.1088/0953-8984/15/13/202
17. Takeda Y, Yokoyama S, Ito T, Miyazaki H, Shimotani K, Yakigaya T, Kakiuchi H, Sawa H, Takagi K, Kitazawa N (2006) Dragoe, superconductivity of doped $Ar@C_{60}$. Chem Commun (Camb) 28:912–914. https://doi.org/10.1039/b514974f
18. Aoyagi S, Nishibori E, Sawa H, Sugimoto K, Takata M, Miyake Y, Kitaura R, Shinohara H, Okada H, Sakai T, Ono Y, Kawachi K, Yokoo K, Ono S, Omote K, Kasama Y, Ishikawa S, Kumuro T, Tobita H (2010) A layered ionic crystal of polar $Li@C_{60}$ superatoms. Nat Chem 2:678–683. https://doi.org/10.1038/nchem.698
19. Brown CM, Cristofolini L, Kordatos K, Prassides K, Bellavia C, González R, Wudl F, Cheetham AK, Zhang JP, Andreoni W, Curioni A, Fitch AN, Pattison P (1996) On the crystal structure of azafullerene $(C_{59}N)_2$. Chem Mater 8:2548–2550. https://doi.org/10.1021/Cm960354I
20. Prassides K, Hummelen JC, Andreoni W, Giannozzi P, Beer E, Bellavia C, Cristofolini L, González R, Lappas A, Murata Y, Malecki M, Srdanov V, Wudl F (1996) Isolation, structure,

and electronic calculations of the heterofullerene salt $K_6C_{59}N$. Science 271:1833–1835. https://doi.org/10.1126/Science.271.5257.1833
21. Fleming RM, Ramirez AP, Rosseinsky MJ, Murphy DW, Haddon RC, Zahurak SM, Makhija AV (1991) Relation of structure and superconducting transition temperatures in A_3C_{60}. Nature 352:787–788. https://doi.org/10.1038/352787a0
22. Kortan R, Kopylov N, Glarum S, Gyorgy EM, Ramirez AP, Fleming RM, Thiel FA, Haddon RC (1992) Superconductivity at 8.4 K in calcium-doped C_{60}. Nature 355:529–532. https://doi.org/10.1038/355529a0
23. Kortan R, Kopylov N, Glarum S, Gyogry EM, Ramirez AP, Zhou O, Thiel FA, Trevor PL, Haddon RC (1992) Superconductivity in barium fulleride. Nature 360:566–568. https://doi.org/10.1038/360566a0
24. Gogia B, Kordatos K, Suematsu H, Tanigaki K, Prassides K (1998) Electronic states of Ba_6C_{60} and Sr_6C_{60} fullerides. Phys Rev B 58:1077. https://doi.org/10.1103/PhysRevB.58.1077
25. Brown M, Taga S, Gogia B, Kordatos K, Margadonna S, Prassides K, Iwasa Y, Tanigaki K, Fitch AN, Pattison P (1999) Structural and electronic properties of the noncubic superconducting fullerides A'_4C_{60} ($A' = Ba,Sr$). Phys Rev Lett 1999(83):2258–2261. https://doi.org/10.1103/PhysRevLett.83.2258
26. Saito S, Oshiyama A (1993) Electronic states of Ba_6C_{60} and Sr_6C_{60} fullerides. Phys Rev Lett 71:121. https://doi.org/10.1103/PhysRevLett.71.121
27. Özdaş E, Kortan AR, Kopylov N, Ramirez AP, Siegrist T, Rabe KM, Bair HE, Schuppler S, Citrin PH (1995) Superconductivity and cation-vacancy ordering in the rare-earth fulleride $Yb_{2.75}C_{60}$. Nature 375:126–129. https://doi.org/10.1038/375126a0
28. Arvanitidis J, Papagelis K, Margadonna S, Prassides K, Fitch AN (2003) Temperature-induced valence transition and associated lattice collapse in samarium fulleride. Nature 425:599. https://doi.org/10.1038/nature01994
29. Akada M, Hirai T, Takeuchi J, Yamamoto T, Tanigaki K (2006) Superconducting phase sequence in RxC_{60} fullerides (R=Sm and Yb). Phys Rev B 73:094509. https://doi.org/10.1103/PhysRevB.73.094509
30. Kortan R, Kopylov N, Ozdas E (1996) Proceedings of ECS meeting. Fullerenes 3:423–428
31. Akada M, Hirai T, Takeuchi J, Hiroshiba N, Kumashiro R, Yamamoto T, Tanigaki K (2005) Superconducting phase made from C_{60} doped with La. Phys Rev B 72:132505. https://doi.org/10.1103/PhysRevB.72.132505
32. Saito S, Oshiyama A (1991) Cohesive mechanism and energy bands of solid C_{60}. Phys Rev Lett 66:2637. https://doi.org/10.1103/PhysRevLett.66.2637
33. Kosaka M, Tanigaki K, Prassides K, Margadonna S, Lappas A, Brown C (1999) Superconductivity in Li_xCsC_{60} fullerides. Phys Rev B 59:R6628–R6630. https://doi.org/10.1103/PhysRevB.59.R6628
34. Yildirim T, Barbedette L, Fischer JE, Lin CL, Robert J, Petit P, Palstra TTM (1996) Tc vs carrier concentration in cubic fulleride superconductors. Phys Rev Lett 77:167. https://doi.org/10.1103/PhysRevLett.77.167
35. Schluter M, Lannoo M, Needels M, Baraff GA, Tománek D (1992) Electron-phonon coupling and superconductivity in alkali-intercalated solid. Phys Rev Lett 68:526–529. https://doi.org/10.1103/PhysRevLett.68.526
36. Varma M, Zaanen J, Raghavachari K (1991) Superconductivity in the fullerenes. Science 254:989–992. https://doi.org/10.1126/science.254.5034.989
37. Gunnarsson O, Koch E, Martin RM (1998) Superconductivity in doped C_{60} compounds. In: Kresin VZ (ed) Pair correlations in many-fermion systems. Springer, Boston. https://doi.org/10.1007/978-1-4899-1555-9_10
38. Gunnarsson O (1997) Superconductivity in fullerides. Rev Mod Phys 69:575. https://doi.org/10.1103/RevModPhys.69.575
39. Capone M, Fabrizio M, Castellani C, Tosatti E (2009) Modeling the unconventional superconducting properties of expanded A_3C_{60} fullerides. Rev Mod Phys 81:943–958. https://doi.org/10.1103/RevModPhys.81.943
40. Capone M, Fabrizio M, Castellani C, Tosatti E (2002) Strongly correlated superconductivity. Science 296:2364–2366. https://doi.org/10.1126/science.1071122

41. Capone M, Fabrizio M, Castellani C, Tosatti E (2004) Strongly correlated superconductivity and pseudogap phase near a multiband Mott insulator. Phys Rev Lett 93:047001. https://doi.org/10.1103/PhysRevLett.93.047001
42. Nomura Y, Sakai S, Capone M, Arita R (2015) Unified understanding of superconductivity and Mott transition in alkali-doped fullerides from first principles. Sci Adv 1:e1500568. https://doi.org/10.1126/sciadv.1500568
43. Nomura Y, Arita R (2015) Ab initio downfolding for electron-phonon-coupled systems: constrained density-functional perturbation theory. Phys Rev B 92:245108. https://doi.org/10.1103/PhysRevB.92.245108
44. Suhl H, Matthias BT, Walker LR (1959) Bardeen-Cooper-Schrieffer theory of superconductivity in the case of overlapping bands. Phys Rev Lett 3:552–554. https://doi.org/10.1103/PhysRevLett.3.552
45. Kondo J (1963) Superconductivity in transition metals. Prog Theor Phys 29:1–9. https://doi.org/10.1143/PTP.29.1
46. Mitrano M, Cantaluppi A, Nicoletti D, Kaiser S, Perucchi A, Lupi S, Di Pietro P, Pontiroli D, Riccò M, Clark SR, Jaksch D, Cavalleri A (2016) Possible light-induced superconductivity in K_3C_{60} at high temperature. Nature 530:461–464. https://doi.org/10.1038/nature16522
47. Buzzi M, Jotzu G, Nicoletti D, Mitrano M, Pontiroli D, Riccò M, Perucchi A, Di Pietro P, Cavalleri A (2018) Pressure tuning of light-induced superconductivity in K_3C_{60}. Nat Phys 14:837–841. https://doi.org/10.1038/s41567-018-0134-8
48. Gunnarsson O (2000) C_{60} – the hole story. Nature 408:528–529. https://doi.org/10.1038/35046179
49. Many papers have already been retrieved from many scientific journals. An article related to the scientific misconduct can be found in https://link.springer.com/article/10.1023/A:1023402605160
50. Snider N, Dasenbrock-Gammon R, McBride M, Debessai H, Vindana K, Vencatasamy KV, Lawler A, Salamat RP (2020) Dias, room-temperature superconductivity in a carbonaceous sulfur hydride. Nature 586:373. https://doi.org/10.1038/s41586-020-2801-z

Part VII

Formation Mechanism of Fullerenes/ Metallofullerenes

Formation Mechanism of Fullerenes/ Metallofullerenes

29

Ryan A. Crichton and Jianyuan Zhang

Contents

Abstract

The formation mechanism of fullerenes and metallofullerenes has been an intriguing question for chemists, physicists, and astronomers. Different mechanisms with various precursors, including small carbon fragments, polyaromatic hydrocarbons, and graphene, have been proposed and studied. Meanwhile, the discovery of multiple structural links among metallofullerene cage structures also suggests many fullerene and metallofullerene cages share the same stream of precursors. Understanding the formation of fullerenes and metallofullerenes will provide critical insights.

Keywords

Fullerene · Metallofullerene · Mechanism · Top-down · Bottom-up · Graphene · Interstellar · Carbon vapor · Stardust

R. A. Crichton · J. Zhang (✉)
Department of Chemistry and Chemical Biology, Rutgers, The State University of New Jersey, Piscataway, NJ, USA
e-mail: r.crichton@rutgers.edu; jy.zhang@rutgers.edu

X. Lu et al. (eds.), *Handbook of Fullerene Science and Technology*,
https://doi.org/10.1007/978-981-16-8994-9_44

Introduction

As early as the 1960s–1970s, researchers have speculated the possibility of three-dimensional delocalization of π-electrons in a conjugated molecule [1–5]. Inspired by seeing a corannulene structure on the cap of a football (soccer ball), Osawa conjectured the possible structure of the spherical carbon cage, later known as C_{60} [2], but the concept was published in Japanese [1] and was only translated to English much later. Sumio Iijima directly observed and identified extremely small, spherical structures in graphitized carbon black with electron microscopy [6]. The hypothetical football-shaped molecule was present in the MS data by a team from Exxon Mobile in 1984, together with many other carbon clusters, from the products of laser-irradiated graphite, but the authors made no mention of a possible structure of these molecules [7]. The 1985 paper "C_{60}: Buckminsterfullerene" by Kroto, Curl, and Smalley et al. [8] marked the official birth of fullerenes, when the authors discovered C_{60} molecules in the soot created by vaporizing carbon in a helium atmosphere, and named them after the American architect Buckminster Fuller. This chapter later led to the Nobel Prize in Chemistry awarded to these three key authors in 1996.

Following the initial discovery, many important studies discussing the production, stability, spectroscopy, and size of fullerenes were performed [9–14] based on miniscule quantities of samples, generally produced with laser ablation of graphite. The production of macroscopic quantities, or rather a "visible amount," of fullerenes was achieved by Krätschmer, Huffman, and collaborators [15, 16], which marked the success of the effort that was once described as "search for the yellow vial" by Smalley and Curl [17].

The new synthetic method involves evaporation of graphite rods with high heat (>1300 °C) and extraction of the soluble content in the resulting soot with organic solvents (benzene, carbon disulfide, etc.). The experimental setup was later developed into the "Krätschmer-Huffman generator," or "K-H generator" (Fig. 1), in which graphite rods are evaporated by an electric arc in low-pressure (~100 torr) helium atmosphere. The arc discharge method can provide high temperature

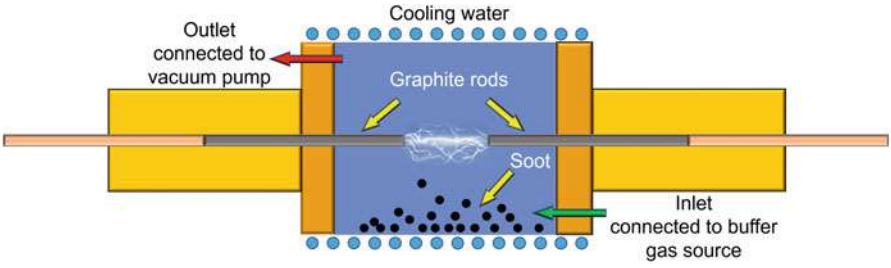

Fig. 1 Schematic depiction of a Krätschmer-Huffman reactor for macroscale synthesis of fullerenes. The generated soot contains mainly not only amorphous carbon, but also aromatic molecules, carbon nanotubes, fullerenes, and other carbon nanomaterials. Metallofullerenes can be synthesized with the same apparatus by drilling one graphite electrode hollow and packing metal sources in the cavity

efficiently, with the center of the plasma well above 2000 °C. The system is cooled by condensing water, generating a temperature gradient in the chamber where various fullerenes are formed. In the past three decades, many iterations of the K-H generator have been developed; however, still to this day, the arc discharge method remains the best method to scale up fullerene synthesis (the other candidate is the flame method [18], another effective production approach, but it generates persistent byproducts, so the products may not be appropriate for certain applications, such as biomedicines).

Despite great success in the continued engineering of the K-H type generators that can produce fullerene products in tons annually, there is a lack of understanding of exactly how the fullerenes are formed in the arc discharge process due to the hot, closed, and inhomogeneous system.

At the dawn of fullerene work, metallofullerenes were discovered as a by-product in mass-spectroscopy [19]. Although it was generally believed that the metal ions were encapsulated inside the fullerene cage, the endohedral nature of metallofullerenes was not confirmed by direct experimental evidence until 10 years later, by the synchrotron X-ray diffraction of $Y@C_{82}$ by Shinohara and coworkers [20] (the structure was updated in 2009 by Akasaka et al. to show the cage symmetry and the location of the endohedral Y atom [21]). Therefore, the phrase endohedral metallofullerene (EMF) is somewhat interchangeable with the single word "metallofullerene" in many literatures. Metallofullerenes are formed under similar conditions with empty fullerenes with the presence of transition metals (mostly rare earth). As of today, the most successful scale-up production of metallofullerenes is also achieved via the arc discharge process, with tweaks to optimize the yield of metallofullerenes. A mass-spectral analysis of empty fullerenes and metallofullerenes of the same number of carbon atoms (84) produced in the same arc discharge synthesis with ^{13}C-enriched graphite rods showed identical isotopic distributions, which suggests they are formed via the same mechanism [22]. On the other hand, due to the presence of the endohedral metal ions that transfer electrons to the cage, metallofullerene cages bear negative formal charges, which often lead to different cage structures compared to empty fullerenes (neutral cages). For example, due to the charge transfer of six electrons from the M_3N cluster to the cage [23], $M_3N@I_h$-C_{80} EMFs are formed in high yields in the electric arc conditions, although the I_h-C_{80} cage was never discovered as an empty fullerene structure [24]. Other notable examples are that many unconventional cages, such as those not following the isolated-pentagon-rule (IPR) [25], were found in metallofullerenes [26, 27] (although the reported cage structure of $Sc_2@C_{66}$ in ref. [26] was later corrected by Akasaka et al. [28]), which would not otherwise survive as empty cage fullerenes. In this regard, understanding the formation of metallofullerenes not only is meaningful by its own right, i.e., improving the yield of metallofullerenes, but also provides critical clues for the formation mechanism of all fullerenes, as the metallofullerenes, in some ways, can be viewed as the survived intermediates to reveal the formation path.

There are numerous papers using experimental or theoretical approaches to directly or indirectly probe, deduce, conjecture, infer, or intuit the formation

mechanism of fullerenes and metallofullerenes. In this chapter, we will introduce these efforts, with an emphasis on more recent work.

The "Bottom-Up" and "Top-Down" Formations

In the 1990s, the formation mechanisms of fullerenes and metallofullerenes had been proposed in two hypotheses – the "bottom-up" formation theory, and the "top-down" formation theory, as shown in Fig. 2. In general, the bottom-up hypothesis states that, in the synthetic process, graphite is first completely vaporized into atoms or C_2 units,

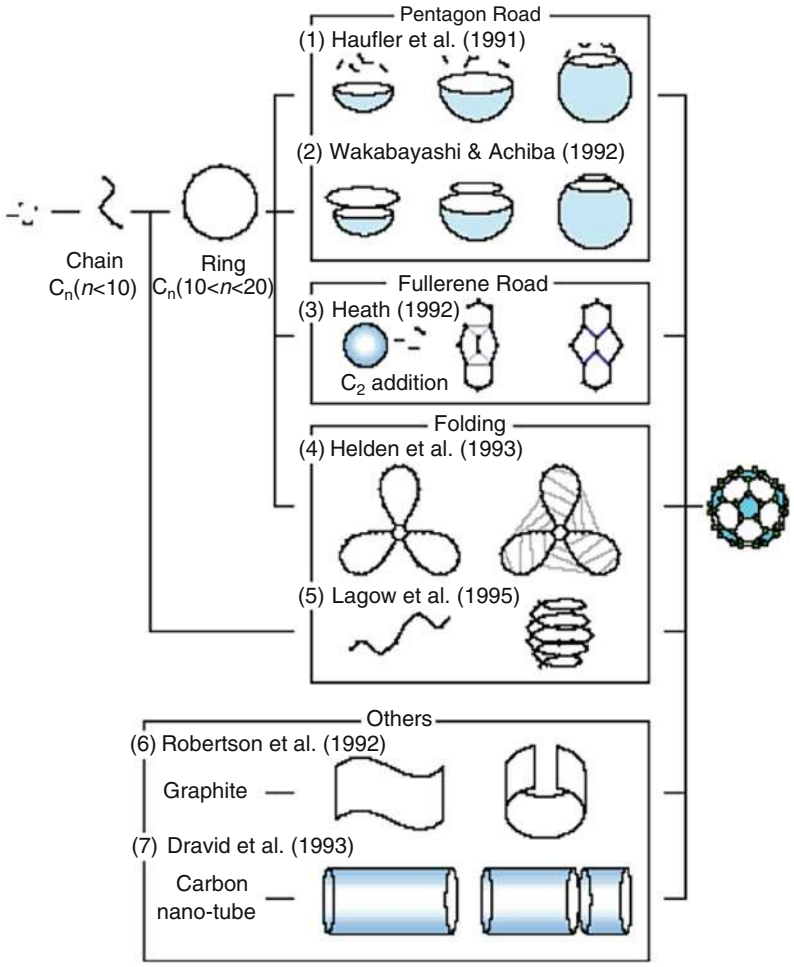

Fig. 2 Illustration showing the hypothetical fullerene formations. (Reprinted (adapted) with permission from ref. [37]. Copyright © 2006 American Chemical Society)

and then fullerene emerges from the constant reactions of carbon fragments and C_2 units until complete termination. Within the bottom-up system, there are two major subtheories: pentagon road [29–31], closed network growth/fullerene road [32], among others (folding [33, 34], etc.). The "top-down" theory is more relevant to the likely condition of the outer space formation of fullerenes [35]. It states that within interstellar or experimental mimics, fullerenes can be formed from large carbonaceous structures, such as graphene and polyaromatic hydrocarbons (PAHs). Due to the nature of the dangling bonds on graphene/PAHs and the high temperature, they warp and eventually roll up, forming large fullerenes, and then decay into energetically favorable smaller fullerenes via C_2 or small chain ejections until stable molecules are reached [36, 37]. These two theories seem to be, and were once considered, mutually exclusive, but there is increasing belief that they can coexist and compete in different conditions.

The Bottom-Up Theory

Pentagon Road

The "pentagon road" was explicitly described in an article from *Scientific American* by Curl and Smalley [17]. Here they framed the model as growing from small linear carbon chains, which eventually form into graphene-like sheets or PAHs. From this stage, the dangling bonds of the sheets/PAHs become the site of high reactivity and generate pentagons and hexagons to reduce this energy as an open bowl is formed [11, 14, 38, 39]. In this process, fused pentagons should be avoided due to the energy punishment, which is the foundation of the IPR in the pentagon road theory. With more C_2 joining the structure, above a certain size, the rearrangement of the bonding pattern will drastically reduce the dangling bonds and eventually form IPR structures of high symmetry, such as C_{60} – the most abundant species in the fullerene family and the smallest IPR cage, C_{70}, the second smallest IPR cage, and others. The driving force of the bottom-up growth is the energy released from the reduction of dangling bonds and the closure of a fullerene cage. A key paper walking around this idea – abet it more toward soot particles – was performed by the fullerene discoverers [11]. They studied the remarkable stability of the formed fullerenes against NO, H_2, CO, SO_2, O_2, and NH_3. The overall conclusion was that the resistive molecule (C_n, $n > 40$) must be spherical and not an open PAH system as a spherical structure will maximize the number of carbon-carbon bonds.

Soon after, Curl and Smalley et al. studied the photophysics of fullerenes and related ions [13]. They noticed the fragmentation pattern of two sets of clusters: one set C_n, $n < 32$ and the other C_m, $m > 32$. The striking difference was that for $n < 32$, the MS recorded pattern matching a C_3 loss versus the C_2 loss was observed in $m > 32$. This result hinted the $n < 32$ are possibly PAHs, and $m > 32$ are more likely spherical. Also, there was a gap in the MS for both sets between 24 and 30 as the number of carbons. These results are revisited by Smalley a couple of years later [31], where he described a crucial step in the process, annealing. Annealing will allow the IPR structures to be more prominent, and this explains the reason that laser

ablation fails to synthesize C_{60} in macroscopic quantities. There is insufficient time for the clusters to cool slowly and form the more/most stable product; thus, this version of laser ablation makes the kinetically favorable products.

The pentagon road mechanism can explain many experimental observations in the early days of fullerene research. However, a weakness of the mechanism is that the "bowls" of pentagons and hexagons with daggling bonds are very high in energy. Works from Bowers et al. showed evidence that pentagon road is less likely than the "fullerene road," [40, 41] discussed in the next section.

Fullerene Road

The "fullerene road," also described as "closed network growth," works as follows: The graphite rod is vapored and leads to huge amount of small carbon fragments, primarily C_2, that quickly react with each other and become linear chains. As these linear chains form PAHs and grow further, they eventually reach and exceed a critical threshold (~28) [42]; they then form closed networks, i.e., small fullerenes, instead of staying as "open bowls." These small carbon cages (less than 60 carbon atoms) inevitably contain fused pentagons, which continue to grow into the more stable fullerenes such as C_{60} and C_{70} via C_2 incorporation and Stone-Wales transformation (SWT, where the central bond in a pyracylene motif rotates 90 degrees, Fig. 3) [10].

A clear advantage of the "fullerene road" over the "pentagon road" is that the closed fullerenes are less energetic than open bowls with daggling bonds on the periphery. Moreover, Bowers et al. showed experimentally that there was no cuplike fullerene precursor in their ion chromatography data [40, 41]. However, something to note, these cuplike precursors have chance of being extremely short-lived with lifetimes less than what can be detected in chromatography.

The most notable work on the closed network growth mechanism is a series of papers by Dunk, Marshall, Kroto, and collaborators [43–50]. Their fundamental tool in the investigation was Fourier transform ion cyclotron resonance mass spectrometry (FT-ICR-MS) that can directly analyze the vapor generated by a laser-ablated graphite (Fig. 4a). The growth of C_{60} was studied first [43]. Fullerene C_{60} sample was primarily desorbed into this carbon vapor under the flow of helium and allowed to react with the carbon vapor, containing presumably mainly atomized C_2 and small carbon clusters. Using C_{60} as a source without carbon vapor (Fig. 4b), there is no presence of higher fullerenes detected by the MS, while low-abundance smaller peaks (C_{58}, C_{56}, etc.) were observed but likely due to the fragmentation of C_{60}.

Fig. 3 Illustration of a Stone-Wales transformation

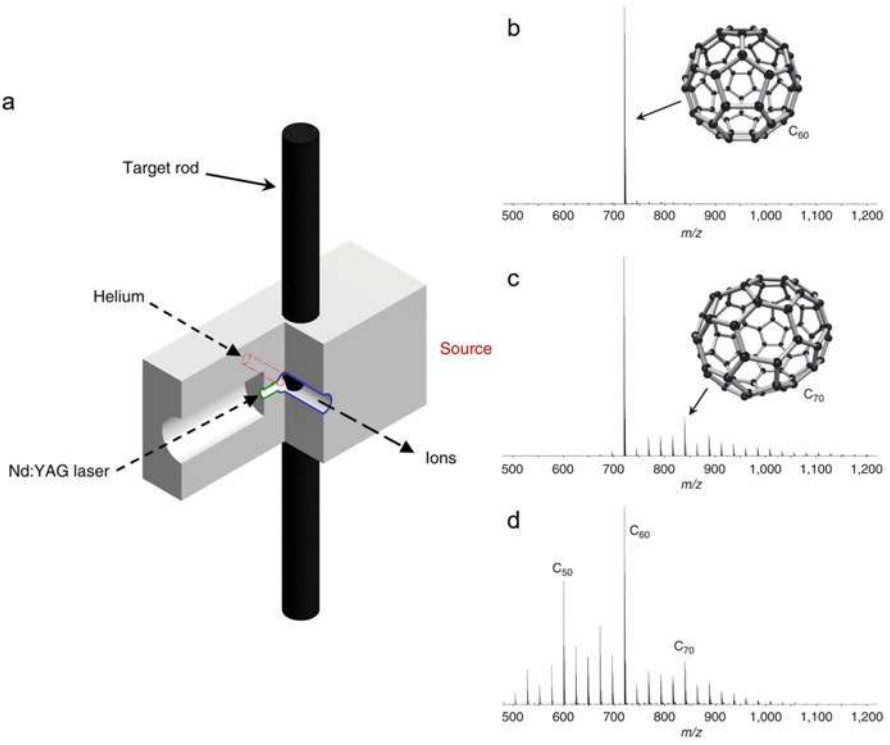

Fig. 4 FT-ICR-MS study of fullerene growth: (**a**) schematic illustration of the FT-ICR-MS setup; (**b**) MS of the laser-irradiated C_{60} without carbon vapor; (**c**) MS of the laser-irradiated C_{60} with carbon vapor, under low helium flow insufficient for direct fullerene formation; and (**d**) MS of the laser-irradiated C_{60} with carbon vapor, with high helium flow that allows for direct fullerene formation. (Reprinted with permission from ref. [43]. Copyright © 2012, Nature Publishing Group)

However, when C_{60} reacted with applied carbon vapor, a distribution of higher fullerenes C_{62} – ~C_{100} was observed in the mass-spec (Fig. 4c), in addition to the C_{60} peak. The helium pressure applied here is lower than what was required to generate fullerenes directly from laser ablation of a graphite rod, so the higher peaks observed here are mainly due to the fullerene growth from C_{60}. For comparison, higher helium pressure that met the requirements of fullerene synthesis would generate a wide distribution of peaks corresponding to the full range of carbon numbers (~42 – ~84, Fig. 4d). More convincing evidence was provided by a beautiful isotopic experiment that used ^{13}C-labeled graphite rod and natural abundance C_{60} to perform the same experiment, in which generated mass spectral distribution of C_{62}, C_{64}, C_{66}, etc. centered at $^{12}C_{60}{}^{13}C_2$, $^{12}C_{60}{}^{13}C_4$, $^{12}C_{60}{}^{13}C_6$, etc., respectively. In other words, regardless of the number of carbon atoms, 60 of them are mainly ^{12}C, while the rest are dominantly ^{13}C. This observation is only consistent with C_{60} growth, rather than direct fullerene formation from laser vaporization of the graphite rod.

Although the growth process was monitored by mass-spectroscopy and there was no experimental confirmation of the structures corresponding to each peak, the higher peak of C_{70} in Fig. 4c suggests that these peaks were likely to be closed cages, because open-cage alternatives cannot explain the preferred mass corresponding to C_{70}, the second most abundant fullerene specie only after C_{60} found in most laboratory syntheses. A possible growth pathway was also proposed based on quantum chemical modeling detailed in the paper.

Finally, the authors demonstrated similar growth for higher fullerenes C_{76}, C_{78}, C_{84}, and metallofullerene $La_2@C_{80}$, which showed the growth process is universally applicable to many known fullerenes and metallofullerenes. In a later work, monometallic EMF $Pr@C_{82}$ was shown to grow in a similar fashion [47]. Moreover, this approach was proven successful in synthesizing heterofullerenes via atom exchange, when C_{60} and C_{70} were exposed to boron vapor [46].

The FT-ICR-MS technique also enabled the observation of various monometallic EMFs, many of which are too unstable to be observed in solid state or in solution, from laser-ablation of metal-doped graphite rods. Smallest stable fullerene cages stabilized by metal encapsulation, C_{28}, were detected in the forms of $Ti@C_{28}$, $Zr@C_{28}$, and $U@C_{28}$ in the mass spectra [44]. Moreover, $Na@C_{60}$ and $Na@C_{70}$ were successfully synthesized along with PAHs to create new candidate cosmic molecules within the diffuse interstellar bands (DIBs) resulting from supernovae [45]. Furthermore, a broad survey of metallofullerene synthesis with more than 80 elements including Group I, II, III, and transition metals revealed that the size and charge (valence) of the metal ions would favor different cage sizes in their experimental conditions [47]. Due to the extremely reactive nature of these $M@C_{2n}$ EMFs, the intermediates in the formation process were not isolated or structurally characterized with approaches other than mass spectra; however, additional experimental work was performed to suggest the endohedral nature of these species. Many $M@C_{60}$ molecules were isolated after formation in the ICR cell by stored waveform inverse Fourier transform (SWIFT) excitation and then thermally excited in ultrahigh vacuum by sustained off resonance irradiation collision induced dissociation (SORI-CID). All excited molecules showed loss of C_2 in the MS (i.e., MC_{58}), but none of them showed loss of the metal ion, which suggests $M@C_{2n}$ instead of metal-associated to open structures because in the latter case, the loss of metal ion should have been more readily observed than the loss of C_2. The closed network growth process is theoretically modeled and validated by density functional theory (DFT) and Car–Parrinello molecular dynamics (CPMD) approaches using $Ti@C_{2n}$ as examples [49].

The ultimate challenge in this approach is to synthesize clusterfullerenes, which was conquered by Dunk in collaboration with Echegoyen and Poblet et al. in 2017 [50]. By vaporizing doped graphite rods containing metal (Sc or Y) oxide and solid nitrogen sources (e.g., melamine), the authors successfully observed $Sc_3N@C_{2n}$ and $Y_3N@C_{2n}$ nitride clusterfullerenes (trimetallic nitride templated, TNT, and EMFs) among other traditional EMFs. Key members of the M_3N species were isolated with the SWIFT approach and further characterized by

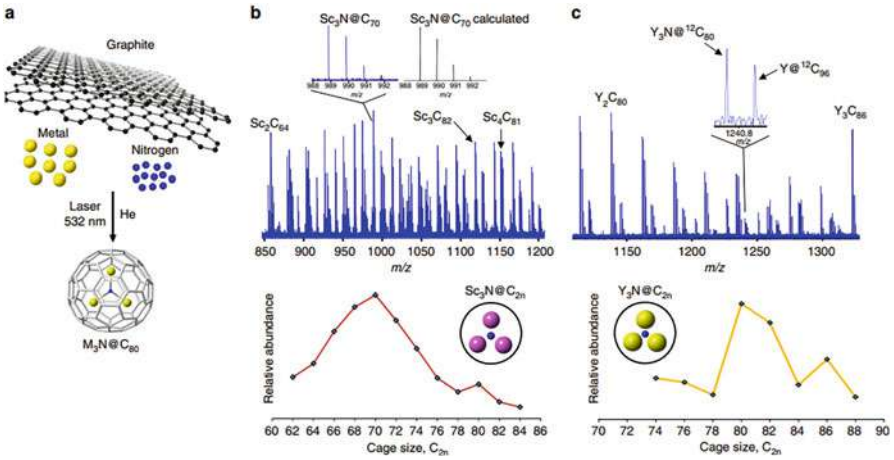

Fig. 5 Clusterfullerenes from laser-ablated doped graphite: (**a**) schematic for clusterfullerenes formed from a mixture of graphite, metal oxide, and melamine (nitrogen source) in this work. FT-ICR-MS for (**b**) $Sc_3N@C_{2n}$ and (**c**) $Y_3N@C_{2n}$ data (top) and formation distributions (bottom). (Reprinted with permission from ref. [50]. Copyright © 2017, The Author(s))

the SORI-CID mass spectra. If there were any remaining doubts regarding whether the MS peaks in the abovementioned work are (at least mainly) resulted by closed-cages, they should be cleared by the compelling evidence that the well-established high-yield nitride clusterfullerene $M_3N@C_{2n}$ species are seen (and SWIFT-isolated) in high yields in this study (Fig. 5), together with other multi-metal species, but very little single-metal or all-carbon species. Based on the absence of high-yield C_{60}, it was argued that the nucleation of cage surrounding an M_3N cluster started at larger cages (62 for Sc, 74 for Y). Growing from the smallest number, Sc covered a cage size from C_{62} to C_{84}, with $Sc_3N@C_{68}$, $Sc_3N@C_{70}$, and $Sc_3N@C_{72}$, being the highest abundance species (Fig. 5b). $Sc_3N@C_{80}$, the dominant metallofullerene product in arc discharge conditions, showed a "bump" in the yield map but not as high as many smaller-size family members. On the other hand, Y covered a midrange cage size from C_{74} to C_{88}, with $Y_3N@C_{80}$ the most abundant product. Importantly, with lower laser fluence (~ 5 mJ), the size distribution for Sc reduced to C_{62} to ~C_{74}, which suggests in the experimental condition, smaller Sc_3N clusterfullerenes formed before the larger ones, supporting the cage growth mechanism. Meanwhile, we note that the experimental conditions are very different from the arc discharge condition, suggested by the absence of C_{60}, C_{70}, and $Sc_3N@C_{80}$, three dominant products produced in the electric arc.

The studies were followed by using pure $Sc_3N@C_{68}$ and $M_3N@C_{80}$ as starting materials, paired with the FT-ICR-MS technique. Without carbon vapor, $Sc_3N@C_{68}$ was ablated with laser and generated a mass-spectrum dominated by the starting material $Sc_3N@C_{68}$, but within the resulting new peaks, those corresponding to larger EMFs, $Sc_3N@C_{70}$ and $Sc_3N@C_{72}$, are more abundant than smaller ones,

$Sc_3N@C_{66}$ and $Sc_3N@C_{64}$. The authors interpreted the result as a suggestion that growth is the preferred process compared to shrinkage, even at low-carbon vapor concentration. When carbon vapor was applied, $Sc_3N@C_{68}$ showed the growth into a family of larger EMFs, $Sc_3N@C_{2n}$ (C_{2n} = 70–94), which was consistent with the results from empty cage and traditional metallofullerenes [43, 47]. Very notably, computational analysis has revealed global pathways from D_3-C_{68} cage into the high-symmetry I_h-C_{80} cage stepwise, going through low-energy isomers that were formed via a series of C_2 insertions and SWTs (Fig. 6). Meanwhile, a pathway that consists of only C_2 insertion, no SWT, and leads to another high-symmetry C_{80} cage, D_{5h}-C_{80}, was also revealed by theoretical approach (bottom half, Fig. 6d).

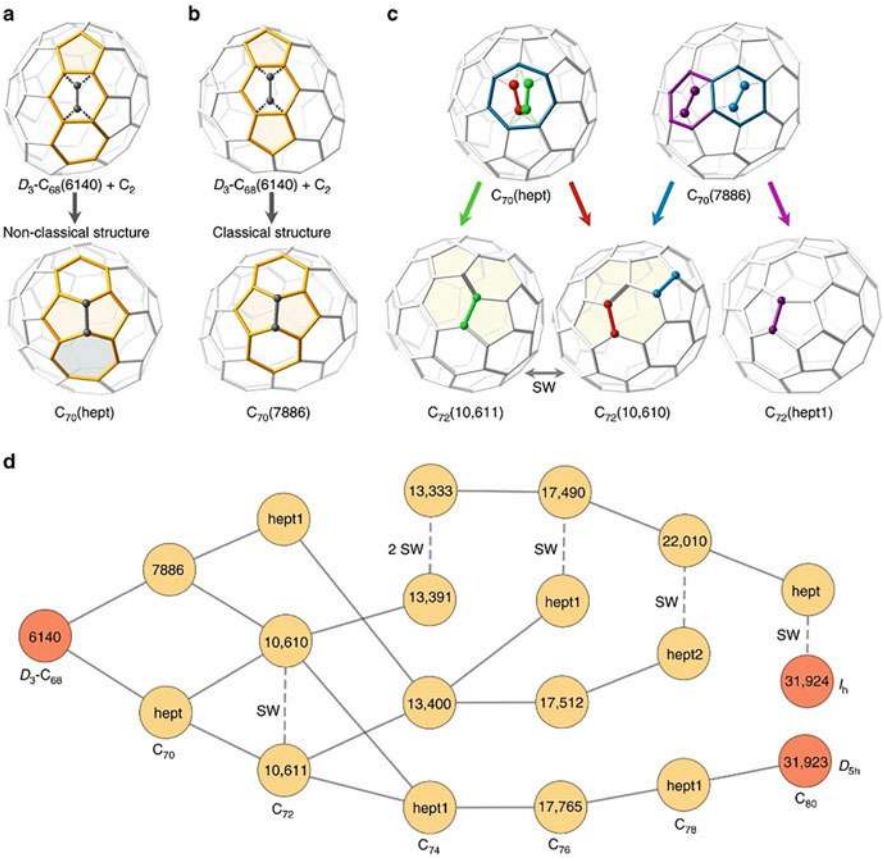

Fig. 6 Pathway from lower-symmetry D_3-C_{68} to high-symmetry cages (I_h-C_{80} and D_{5h}-C_{80}) via (non)-classical cages. D_3-C_{68} can grow (**a**) nonclassical heptagon cage, C_{70}(hept) or (**b**) a classic C_{70}(7886), having only hexagons and pentagons via C2 insertion; (**c**) from C_{70} to C_{72} (bottom-up transformation) is most likely to result in one of the following cages: C_{72}(10611), C_{72}(10610), and C_{72}(hept1); and (**d**) from those C_{72} isomers, reaction paths to high-symmetry C_{80} cages, I_h-C_{80} and D_{5h}-C_{80}, involve C_2 insertion reactions and a couple of SWRs. (Reprinted with permission from ref. [50]. Copyright © 2017, The Author(s))

In summary, various bottom-up formation mechanisms were proposed by experimental and theoretical approaches. Two key subtheories, the "pentagon road," which suggests pathways via various open bowls, and the "fullerene road," which suggests the growth via a series of closed networks with C_2 insertions, are described. As of now, there is more evidence (both experimental and theoretical) for the fullerene road subtheory, which are highlighted by the work of Dunk et al. in the recent decade.

The Top-Down Theory and Shrinking of Giant Fullerenes

While the bottom-up formation theory has witnessed significant developments, particularly with the in-depth understanding of the presenting species in high-concentration of carbon vapor conditions, it did not solve all the puzzles regarding fullerene and metallofullerene formation, especially when all conditions are concerned. There are also a few clues that suggest fullerenes and metallofullerenes would form via a top-down mechanism that starts with the warp and wrap of graphene or PAHs and then close into large networks, i.e., "giant fullerenes," which shrink into more stable, smaller fullerenes.

First, fullerenes can form in interstellar and circumstellar environments [35] where the density of carbonaceous building blocks are many orders of magnitude lower than terrestrial environments, e.g., air on Earth [51], which is nowhere close to the sufficient level to allow for the assembly of large carbon molecules. A recent work mimicked the stardust formation in circumstellar envelops (CSEs) in a bottom-up pathway and detected prevalently aliphatic molecules that are known to form in bottom-up process, but very little aromatic molecules, and no fullerenes [52].

Second, the formation of metallofullerenes with large clusters, such as M_3N, M_2C_2, or even larger ones up to 7 atoms (e.g., $Sc_4O_3@I_h$-C_{80} [53]), cannot start from small, closed networks like $C_{30–60}$. If formed via bottom-up mechanism, the starting point of cage closure has to be larger, as suggested by researchers (e.g., C_{62} for Sc_3N, 74 for Y_3N) [50], prior to which it should be assumed an open-cage pentagon road growth. Then, it seems an acknowledgment that fullerenes and metallofullerenes are formed via different pathways: Under 60 carbon atoms, closed network growth (fullerene road) is favored for empty fullerenes [43], while open-bowl growth (pentagon road) is favored for clusterfullerenes, which contradicts the long-time belief that fullerenes and metallofullerenes have the same formation mechanism. Furthermore, it is a myth why C_{60} is bypassed, and why there are "magic numbers" for the starting point of clusterfullerenes (e.g., 62, 74). In the context of clusterfullerenes, the "shrinkage of giant fullerenes" is more attractive.

Third, the most abundant fullerenes, C_{60} and C_{70}, are on the lower end of fullerene size distribution. From the early attempt [54] to recent studies [55] that extracted giant fullerenes of C_{100}-C_{250}, it is almost certain that significantly more giant fullerenes once existed than those were extracted and characterized. These giant fullerenes may be related to a shrinkage process in the fullerene formation.

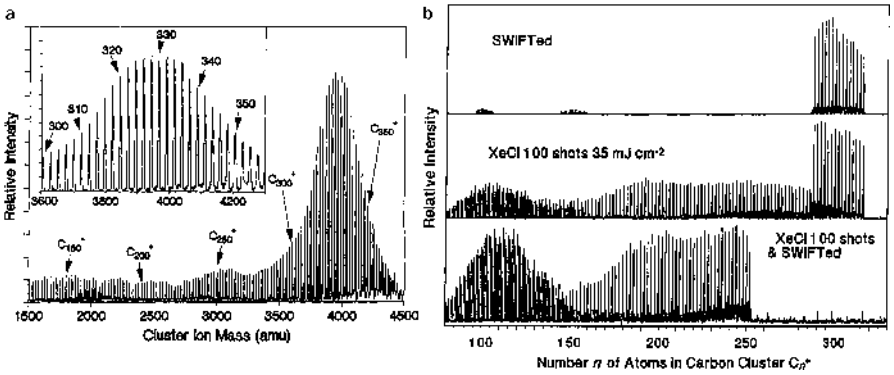

Fig. 7 Mass spectra of large carbon cages from laser-ablated graphite rod: (**a**) MS of a family of large carbon clusters with hundreds of carbon atoms, generated by laser ablation of graphite. (Reprinted from ref. [56] with permission. Copyright © 1991, Springer-Verlag. (**b**) (top) selected MS of C_n^+ fullerenes, n = 288–316. (middle) MS after 100 shots of a XeCl excimer laser. (bottom) same as the middle but all fullerene clusters above 252 were removed via ICR before arriving at the MS. Reprinted by permission from Springer Nature, ref. [57], Copyright © 1991)

The initial proposal of "top-down" mechanism also dates to the early stage of fullerene research. With the same FT-ICR-MS technique, Smalley et al. detected a family of MS peaks consisting of hundreds of carbon atoms (Fig. 7a) [56], using a different setup but similar principle with Dunk and Kroto et al. [43], from laser-ablated graphite. Furthermore, in another work by Smalley et al., the authors isolated the species between C_{288} and C_{316}, and further irradiated with laser at fluence 35 mJ•cm^{-2} [57]. Smaller C_{2n} species were generated by the stronger laser and were isolated again with SWIFT (Fig. 7b). Smalley argued these experiments provide important evidence for a "shrink-wrap" process that a sequential shrinking happened to giant fullerenes when more C_2 left the cage [31]. To some extent, these results provide a "top-down" counterpart to the series of FT-ICR-MS work by Dunk et al., suggesting that exact combination of experimental parameters is key in the mass-spectral study of products from laser-ablated graphite. On the other hand, the top-down mass-spectral studies were not as well-developed as the later bottom-up growth studies, because it only showed the shrinking of giant fullerenes (hundreds of carbon atoms) to smaller, but still large species, yet was able to connect these giant fullerenes to lab-isolated fullerenes such as C_{60}.

These large carbon cluster peaks and the process of giant fullerene shrinkage were rationalized by a series of works, nicely presented by Irle and Morokuma et al. with quantum mechanical molecular dynamics (QM/MD) simulations [37] and the references therein. Within these studies, the authors considered the key factors known to fullerene formation, including temperature, cooling rate, carbon vapor concentrations, and carbon fragmentation types, and examined the theory by matching these factors with known experimental results, with an emphasis on the high yield of C_{60}. It was argued that fullerene formation consists of both "size-up" and "size-down" components. In the "size-up" process, large carbon chains (e.g., polyynes) nucleate

and form ring structures, which can consume more C_2 or small carbon fragments to grow and then get annealed into giant fullerenes. Some of these giant "fullerenes" may still have imperfect structures, such as large openings (> 6 membered rings) or small carbon tails, i.e., they are not "real" fullerenes of closed cage consisting only pentagons and hexagons. Formed at high temperature and continued to be exposed to heat (both from environment and the released energy from exothermic ring closure), the excited "hot giants" are experiencing violent motions, which would occasionally set free C_2 units, i.e., C_2 ejections (extrusions). These C_2 ejections are not universally equally probable on the surface of a giant fullerene; rather, they tend to be concentrated on a specific part of the giant fullerenes, such as the areas with high curvatures. The pop-out events were estimated to be fast at the beginning, on the order of one carbon atom per picosecond. When the giant fullerenes cool off, and the cages become more spherical, the ejection would slow down and eventually stop, to end the shrinking process and give the final fullerenes. During the shrinking process, heat annealing would also cause fullerenes to isomerize into more stable isomers. Curl et al. later suggested the C_2 swap between fullerenes is a key driving force for the shrinking [58].

A very important update by the same group suggested that the carbon vapor concentration is a critical factor dictating the competition of two opposite processes, C_2 insertion and C_2 ejection [59]. In the earlier modeling of the "shrinkage of hot giants," the environment was treated as a vacuum, so only the "size-down" process would happen. However, this is very different from laboratory conditions for fullerene and metallofullerene synthesis. With carbon vapor present, fullerene cages can either capture or eject C_2, with the following preference: Larger giant fullerenes (> ~100 cage carbons) tend to shrink whereas smaller fullerenes (< ~100 cage carbons) tend to grow. Meanwhile, understandably, high concentrations of free carbon fragments (including C_2, and other small building blocks) in the surrounding will increase the net growth rate, while lack of such would increase the net shrinking rate. If we combine this understanding with the prior study [37] that assumed "size-up" and then "size-down," in which the "size-up" process would consume all small carbon fragments and afterward the "size-down" is the only viable route, maybe a mix of the two processes in the presence of small carbon fragments (that are consumed by both nonfullerene carbon clusters and giant fullerenes) would better fit the experimental reality. Additionally, the critical role of the concentration/density of carbon fragments may be the foundation of different findings under different conditions, i.e., bottom-up growth in carbon vapor conditions, while top-down shrinkage in interstellar or TEM (see below) conditions. In terms of the electric-arc reaction, a detailed understanding of the carbonaceous vapor concentration, zone of fullerene formation, temperature, and cooling rate is important to understand the fullerene and metallofullerene formation.

A direct support of the top-down mechanism was provided by the curling and closure of graphitic materials. In 1992, Ugarte reported that carbon soot particles and tubular graphitic structures responded to strong electron beam (e-beam) and gradually curled into spherical and semispherical structures, directly observed with high-resolution electron microscopy [60]. After the discovery of graphene, a much better

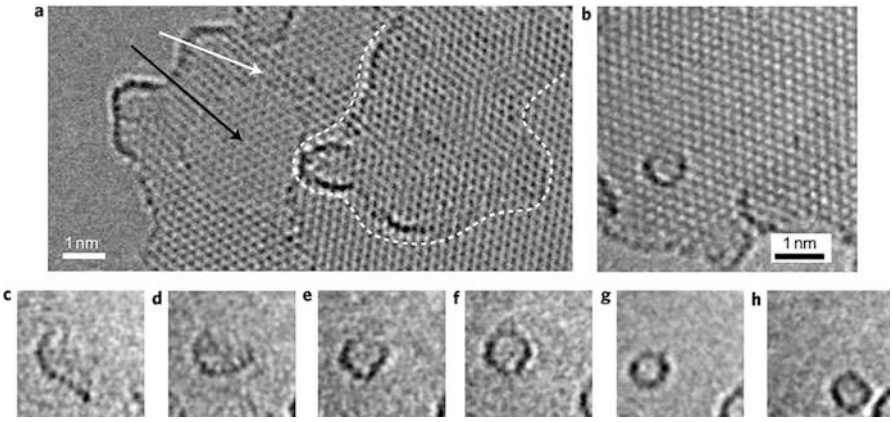

Fig. 8 TEM transformation of graphene flake to fullerene: (**a**) the black arrow points to the bilayer graphene support film/substrate; the white arrows point to a monolayer of graphene on the support film; and the dashed white lines trace a graphene island with notable curved edges; (**b**) final product from the graphene wrapping, a formed fullerene on a monolayer of graphene; and (**c–h**) show the sequence of the transformation that graphene flake undergoes to become a fullerene. (Reprinted by permission from Springer Nature: Nature Chemistry, ref. [36], Copyright © 2010)

platform for such experiments, the transformation was achieved with single-layer graphene using much more advanced TEM techniques by Chuvilin et al. (Fig. 8) [36].

In this challenging experiment, the authors disperse graphene from graphite via grinding and ultrasonication in ethanol and film transfer to the holey carbon grid. Then, much time was taken to locate ideal area, where e-beam was applied on a strip of graphene on a double-layer graphene substrate. The e-beam provided the energy required to break a graphene flake; however, the flake needs to be of appropriate size (50–100 atoms) to avoid significant penalty for curvature. Under the applied condition, the graphene strip was seen to gradually transform into a spherical structure (Fig. 8b). The typical sequence of transformation was broken down as shown in Fig. 8c–h that the graphene flake gradually changed shape under the influence of the e-beam. Based on the TEM images, the authors quantum chemically modeled a matching pathway for the transformation. The e-beam target graphene flake would curl and wrap to form a spherical structure, without the involvement of any small carbon fragments. This is a key difference from the "shrinkage of hot giant" mechanism as the transformation from graphene flake to fullerene was direct, without a "size-up" phase.

These TEM images provide compelling evidence for the graphene-to-fullerene transformation and are one of the best direct visualizations of fullerene formation ever reported. However, it is important to note that, while the e-beam irradiation provides an analogue of the hot temperature in the laser condition or the electric arc, in TEM there is no significant concentration of C_2 or small carbon fragments, which is very different from most other laboratory fullerene-synthetic methods. The top-down formation of fullerenes observed under TEM proves that it is a viable

mechanism but does not suggest it is the major mechanism in electric arc or laser. On the contrary, the work by Dunk et al. described above suggested that in the carbon vapor from laser ablation of graphite, the bottom-up is the major, if not the only, mechanism.

On the other hand, although not matching laboratory synthetic conditions, the TEM observation of direct transformation from graphene to fullerene has significant meaning in the astrochemical formation of fullerenes. Due to the scarcity of atoms in outer space (both CSE and interstellar media, ISM), it is difficult to meet the required concentration of small carbonaceous building blocks, in a reasonable timescale, to realize efficient bottom-up synthesis of large and complex molecules like fullerenes. While it is still an open question, top-down formation of cosmic fullerenes [35] has been an essential theory by astrophysicists [61–64] because it fits better to the current understanding of elementary environments in the outer space.

A very valuable recent work by MartÍn-Gago et al. employed a specialized and groundbreaking ultrahigh vacuum apparatus, called the "Stardust," to mimic the circumstellar environments, and investigate the molecular formation processes with an array of in situ approaches, including spectroscopic and mass spectrometry. As shown in Fig. 9, the "Stardust" apparatus (lower part of the figure) consists of three zones: the aggregation zone, where the optical emission spectroscopy (OES) is performed and hydrogen is introduced; the expansion area, where quadrupole mass-spectroscopy (QMS) is performed and sample is taken out for ex situ studies; and the analysis area, where the temperature-programmed desorption (TPD) is performed. The three zones have different distance (d) from a graphite target, vaporization of which creates the simulation of the CSE of a carbon-rich asymptotic giant branch (AGB) star (upper part of the figure). Carbon atoms and hydrogen molecules are common precursors in the outer atmospheres of evolved carbon-rich stars, based on the estimated density of the atoms, but scaled up a few orders of magnitude higher than the actual dust nucleation zones, which allows reactions taking hundreds of years or longer in the actual CSE to be accelerated, and investigated on laboratory timescales. The feeding of carbon atoms and hydrogen molecules would simulate the bottom-up reactions in the AGB envelop, but without larger building blocks, top-down processes could not happen. One key advantage of the Starburst setup over the traditional flame method is the reactants are "purer," as they do not already contain all sorts of large and small hydrocarbon molecules. After the authors tried many different experimental parameters including a broad range of hydrogen densities, they found many expected bottom-up products, including carbon particles, clusters, aliphatic carbon chains, and quantitively reproduced ethylene and acetylene, but only trace amounts of aromatic molecules, and no fullerenes were detected. This result is very different from previous experiments in flames where aromatic molecules are readily formed.

Although it is a negative result for fullerene formation, this work provides strong indications for a top-down mechanism: While cosmic bottom-up formation of fullerenes [65] cannot be excluded, its more likely site is at the inner layers of the envelop of carbon-rich stars. However, even though the Stardust used significantly

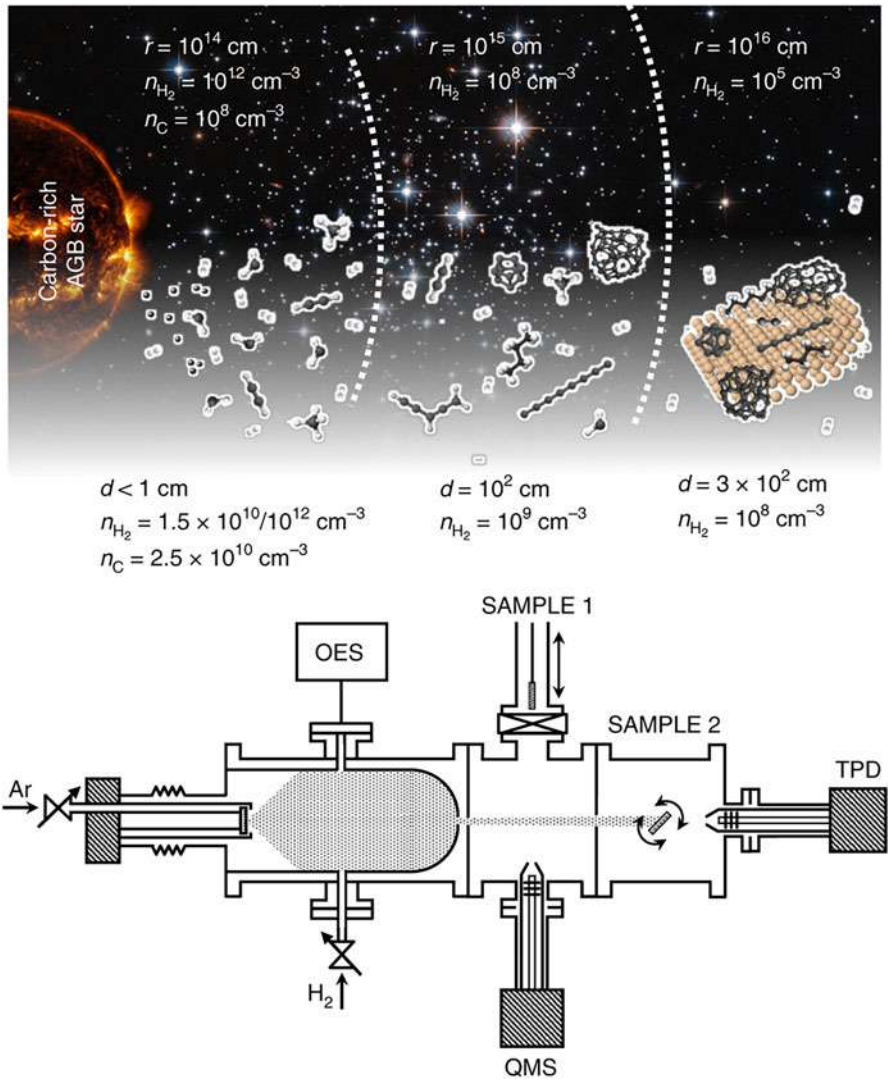

Fig. 9 Replicating cosmological carbon species/Stardust: top image: representation of the CSEs of a carbon-rich AGB star and highlighting the differences in carbon species based on distance from the star; bottom image: Stardust machine schematic, which can produce a well-controlled simulation environment for stardust formation. (Reprinted by permission from Springer Nature: Nature Astronomy, ref. [52], Copyright © 2019)

higher carbon densities, which is more favorable for bottom-up synthesis, no fullerene and only minute amounts of aromatic molecules were detected. This work suggests the cosmic origins of fullerenes, and other aromatic molecules, are more complicated than a direct built-up process and require further careful studies. Meanwhile, it should be noted that the recreated conditions in Stardust are typical,

but not exhaustive, for the whole CSE. Other factors, such as strong irradiation (energetic photons) and stellar winds, are also important in the molecular transformations.

Structural Relation of Metallofullerene Cages

Although there are different proposals of the fullerene formation mechanisms, it is a consensus that fullerenes are formed from carbonaceous precursors that reorganize into cages with optimum structures. This theory is self-evident: Out of 1813 possible isomers of C_{60} fullerene that only contains hexagons and pentagons, only 1 following the IPR (i.e., no fused pentagons) has been found experimentally. The same can be said for C_{70} that 1 out of 8149 possible isomers is detected. Overall, only a small number of pristine fullerenes (please note here, "pristine fullerene" is defined as a carbon allotrope of closed networks, without exohedral or endohedral addition of any other elements) were discovered out of thousands of times more mathematical possibilities, and these isomers all follow the IPR (which avoid the energetic punishment of a pentalene motif) and tend to have high symmetry (which have more even distributions of curvature, can be viewed as converging points of different precursors). Clearly, formation of fullerenes is not a random process. There must have been significant and extensive reorganizations leading to the observation of isolated fullerene molecules today.

Within different versions of formation mechanism, there are various structural descriptions of these carbonaceous fullerene precursors. On the other hand, despite the starting point of fullerene formation (C_2, small carbon fragments, graphene, PAH, etc.), the immediate precursors should be "fullerene-like," i.e., other fullerenes, non-IPR fullerenes, nonclassical fullerenes (cages with large openings, > 7 membered rings), open bowls that are almost closed, or cages with small tails, and they may be larger, smaller, or similar in size compared to the final products. Studying these fullerene-like precursors is important for mechanistic understanding. Even if they do not reveal the distant origin of the formation process, they still have close impact on the final product distribution. Like how paleontologists deduce biological evolutions with the information provided by fossils, chemists study reaction mechanisms via stabilized intermediates. For fullerenes, these "fossils" can be metallofullerenes (technically not fullerenes as they are not a carbon allotrope) with "special cages" – cages that would not survive if not for the extra stabilization from a metal cluster. Close examinations of the structural relations among these molecules, and known fullerenes and metallofullerenes, would be meaningful in three ways:

1. Two related structures may be the reactant and product in a direct transformation.
2. While related structures discovered in the same synthetic system may not have direct transformations between them, they may be from the same stream of precursors.

3. Related structures discovered in different synthetic systems (for example, Sc vs Gd metal source, N_2 vs no N_2) may reveal possible common pathways but ended up in different forms of final products due to varied stabilization factors.

In this part of the chapter, we describe various findings of these special structures and their relation to other fullerenes and metallofullerenes.

The traits of a "good" fullerene final product would be high-symmetry, IPR-following cages, and the opposite of a preferable product ("bad" fullerene) that is unlikely to survive would be a low-symmetry, non-IPR cage. A non-IPR cage with no symmetry (C_1) was experimentally discovered by Olmstead, Balch, and Dorn et al. in two metal carbide metallofullerenes, $M_2C_2@C_1(51383)$-C_{84} (M = Gd, Y) [22]. Such a cage would not have survived without the right stabilization, from an M_2C_2 cluster. In other words, if the $C_1(51383)$-C_{84} cage was formed as an empty fullerene, or a metallofullerene other than the metal carbide type, such as a nitride clusterfullerene, it would transform into other cages. The authors found the cage consisted of a "hot half" (with unstable structural features) and a "cold half" (with stable structure features), and within 2–3 simple steps on the "hot half," i.e., direct ejection of C_2, or SWTs, the C_{84} cage can transform into many known cage structures for traditional metallofullerenes and cluster metallofullerenes, as shown in Fig. 10. These cages have "better" features for a stable cage, such as higher symmetry or IPR-obeyance, and collectively would account for the majority yield of solvent-extracted metallofullerenes [$M_3N@I_h(7)$-C_{80}, $M_2C_2@C_{3v}(8)$-C_{82}, $M_3N@D_{5h}(6)$-C_{80}, $M_3N@C_s(39663)$-C_{82}, etc.]. With the assumption that the product selectivity in fullerene synthesis is a process of gaining stability and symmetry, the more stable, higher symmetry structures, e.g., $I_h(7)$-C_{80}, would be the later product, and the non-IPR, and lower symmetry structures, e.g., $C_1(51383)$-C_{84}, would be the earlier precursor. Therefore, the structural relation shown in Fig. 10 implies a "top-down" process. However, it is important to note that these conceptual transformations are not experimentally realized (and there is a fundamental challenge for experimental realization: Isolated EMFs are not good study objects because they are already stabilized by respective clusters, and one cluster cannot transform into another cluster anyway). Hence, the "top-down" process was only stated as an implication, and "bottom-up" or reversible processes are also possible, for the described transformations. Rather, this work provided the relation among a large selection of metallofullerene cages and suggested their formations are likely related to a group of common or structural similar precursors.

One of the three proposed possible heptagon-containing intermediates in Fig. 10 (in brackets) was experimentally found, as the first heptagon-containing fullerene cage directly from electric arc synthesis reported by Olmstead, Balch, and Popov et al. based on the unambiguous single-crystal structure of a mixed-metal nitride clusterfullerene $LaSc_2N@C_s$(hept)-C_{80} [66]. The structure of the heptagon-containing C_{80} cage (Fig. 11) is related to the most abundant I_h-C_{80} cage by only one SWT (Fig. 11b). Further, removal of one C_2 unit from the cage would result in the known $C_2(22010)$-C_{78} cage (Fig. 11c) found in many trimetallic nitride clusterfullerenes. Meanwhile, removal of the C_2 fragment from $C_{3v}(8)$-C_{82} cage

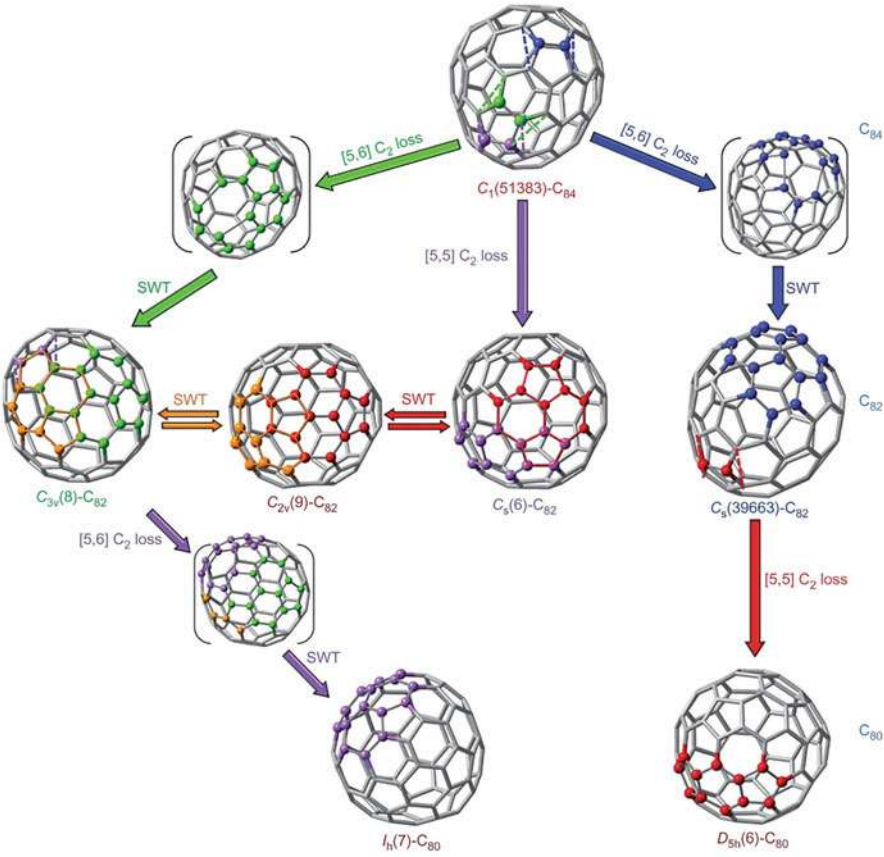

Fig. 10 A fullerene cage rearrangement scheme starting with $C_1(51383)$-C_{84} cage toward higher symmetry, IPR products. (Reprinted by permission from ref. [22], Copyright © 2013, Nature Publishing Group)

would lead to the C_s(hept)-C_{80} cage. This cage is an experimental realization of a proposed structure in Fig. 10, bottom left corner, intermediate between the $C_{3v}(8)$-C_{82} and $I_h(7)$-C_{80}. On the other hand, while this work proved the existence of such a cage, it did not reveal the direction of the transformation (from C_{82} or C_{80}). Theoretical calculation suggests that the $LaSc_2N@C_s$(hept)-C_{80} is even more stable than the $LaSc_2N@D_{5h}(6)$-C_{80} EMF, which is typically the second most abundant C_{80} cage in the trimetallic nitride EMF family. The heptagon cage is likely a kinetical product, trapped due to its exceptional stability. The isolation and characterization of $LaSc_2N@C_s$(hept)-C_{80} provided strong evidence that $C_{3v}(8)$-C_{82}, $I_h(7)$-C_{80}, and $C_2(22010)$-C_{78} are close relatives that may transform into each other in the electric arc, or formed by common precursors.

A few years later, another important heptagon-containing metallofullerene $Sc_2C_2@C_s$(hept)-C_{88} was discovered by Olmstead, Balch, Poblet, and Echegoyen

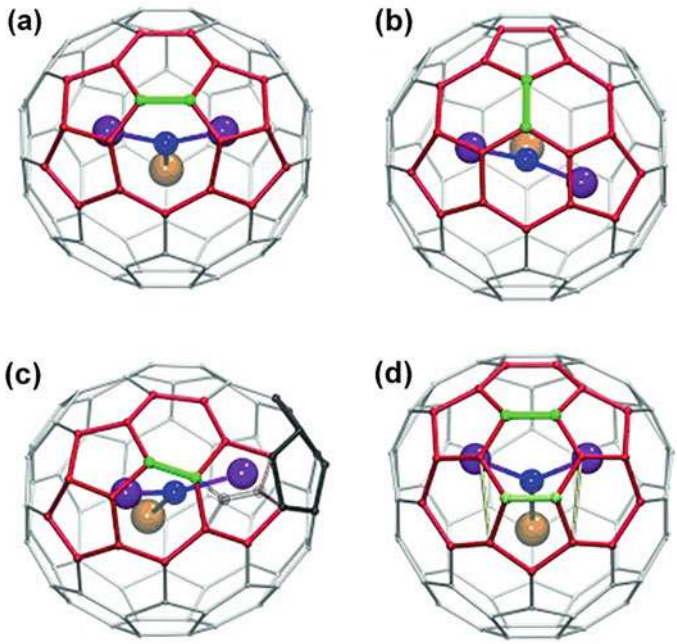

Fig. 11 Structures of $LaSc_2N@C_{80}$ isomers and related cages: (**a**) $LaSc_2N@C_s$(hept)-C_{80}; (**b**) $LaSc_2N@I_h$-C_{80}; the adjacent hexagons and pentagon to the heptagon are in red; the SWR of 7/5–6/6 C-C bond is light green; (**c**) $LaSc_2N@C_{78}$ with the C_2(22010) cage can be formed from $LaSc_2N@C_s$(hept)-C_{80} (**a**) via a C_2 removal; position of the removed fragment is shown as "ghost" atoms, and the second pentagon pair in C_2(22010)-C78 formed after removal of the C_2 fragment is highlighted in black; and (**d**) $LaSc_2N@C_{3v}$(8)-C_{82} can be converted to $LaSc_2N@C_s$(hept)-C_{80} (**a**) via a C_2 removal (yellow lines); Sc magenta, La orange, and N blue. (Reprinted from ref. [66] with permission. Copyright © 2014, WILEY-VCH Verlag GmbH & Co.)

et al., which is also a kinetically trapped product directly from the Krätschmer−Huffman arc-discharge reactor [67]. Interestingly, this cage only differs from the earlier reported $Sc_2C_2@C_{2v}$(9)-C_{86} carbide EMF [68] by one C_2 unit. The authors examined all possible route for a C_2 insertion from $Sc_2C_2@C_{2v}$(9)-C_{86} and found that $Sc_2C_2@C_s$(hept)-C_{88} is the lowest energy product among all possibilities. Computational studies showed that the formation of $Sc_2C_2@C_s$(hept)-C_{88} is likely to be the result of a C_2 insertion from $Sc_2C_2@C_{2v}$(9)-C_{86}. The authors also theoretically investigated similar transformations, between $LaSc_2N@C_2$(22010)-C_{78} and $LaSc_2N@C_s$(hept)-C_{80} (see above), as well as $Sc_2S@C_2$(7892)-C_{70} and $Sc_2S@C_2$(10528)-C_{72}. In each pair, the latter is a result of direct C_2 insertion of the former via an energetically feasible pathway established with theoretical methods (Fig. 12).

Also based on metal carbide EMFs, Lu et al. demonstrated the structural relations between two new large EMFs in their report, $La_2C_2@C_s$(574)-C_{102} and $La_2C_2@C_2$(816)-C_{104} [69]. The former has an "ideal" tubular shape, i.e., in an elongated structure, the pentagons are located at the "ends," while the hexagons

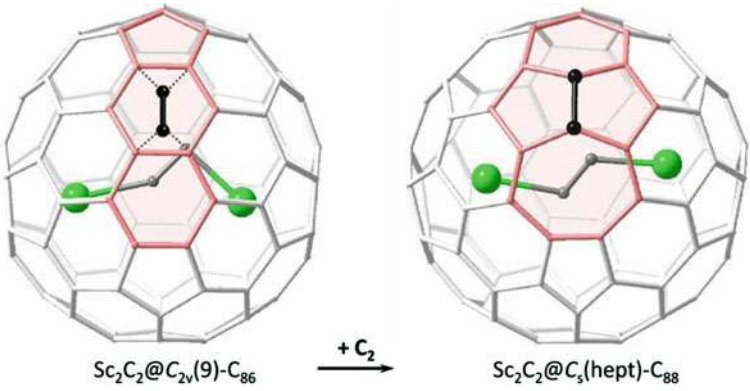

Fig. 12 Structural relationship between $Sc_2C_2@C_{2v}(9)$-C_{86} and $Sc_2C_2@C_s(hept)$-C_{88} by a C_2 insertion. (Reprinted with permission from ref. [67]. Copyright © 2016 American Chemical Society)

are located in the middle (like carbon nanotubes), while the latter does not represent an "ideal" carbon nanotube analogue, with pentagons in the middle region (shown in pink in Fig. 13). The authors examined the structure relation between the two cages and found high degrees of similarity between the two. Additionally, the authors also found the structural relation between $C_2(816)$-C_{104} and two other characterized metallofullerene cages, $D_5(450)$-C_{100} and $D_{3d}(822)$-C_{104}, both of which have "ideal" tubular structures (Fig. 13). Although these transformation pathways proposed by the authors contain many steps and may be deemed "too complicated", we note that the "stepwise model" (including C_2 insertion/extrusion and SWT) only adding/deleting/moving two carbon atoms at a time is not the reality in the high temperature arc discharge condition. It is entirely possible that multiple carbon atoms or rings move in a concerted process, provided that there is an appropriate driving force. The authors argued that the overall similarity among these cages suggested a "top-down" formation process from a nonideal cage to other tubular cages. In this context, it showed that not only the "undesirable" structural features of a fullerene cage, i.e., non-IPR, low symmetry, but also the "undesirable" features for carbon nanotube, i.e., pentagons in a belt of hexagons, can be the driving force of cage rearrangement, at least for tubular structural motifs.

The broad structural relation among a large group of metal oxide clusterfullerenes was nicely summarized by RodrÍguez-Fortea, Chen, and Poblet et al. in a short review [70]. For Sc_2O EMFs between 70 and 84 carbon atoms, the authors presented the X-ray crystallographically characterized EMFs, $Sc_2O@C_2(7892)$-C_{70}, $Sc_2O@T_d(19151)$-C_{76}, $Sc_2O@C_{2v}(24107)$-C_{78}, $Sc_2O@D_{3h}(24109)$-C_{78}, $Sc_2O@C_{2v}(31922)$-C_{80}, $Sc_2O@C_s(39715)$-C_{82}, $Sc_2O@C_{3v}(39718)$-C_{82}, and theoretically predicated most stable isomers for a given cage size, $Sc_2O@C_s(10528)$-C_{72}, $Sc_2O@D_{3h}(14246)$-C_{74}, $Sc_2O@C_2(13333)$-C_{74}, $Sc_2O@C_{2v}(51575)$-C_{84}, and $Sc_2O@C_1(51580)$-C_{84}, in the same figure (Fig. 14a), and demonstrated how they can convert to each other with C_2 insertions and SWTs (Fig. 14b), which is a

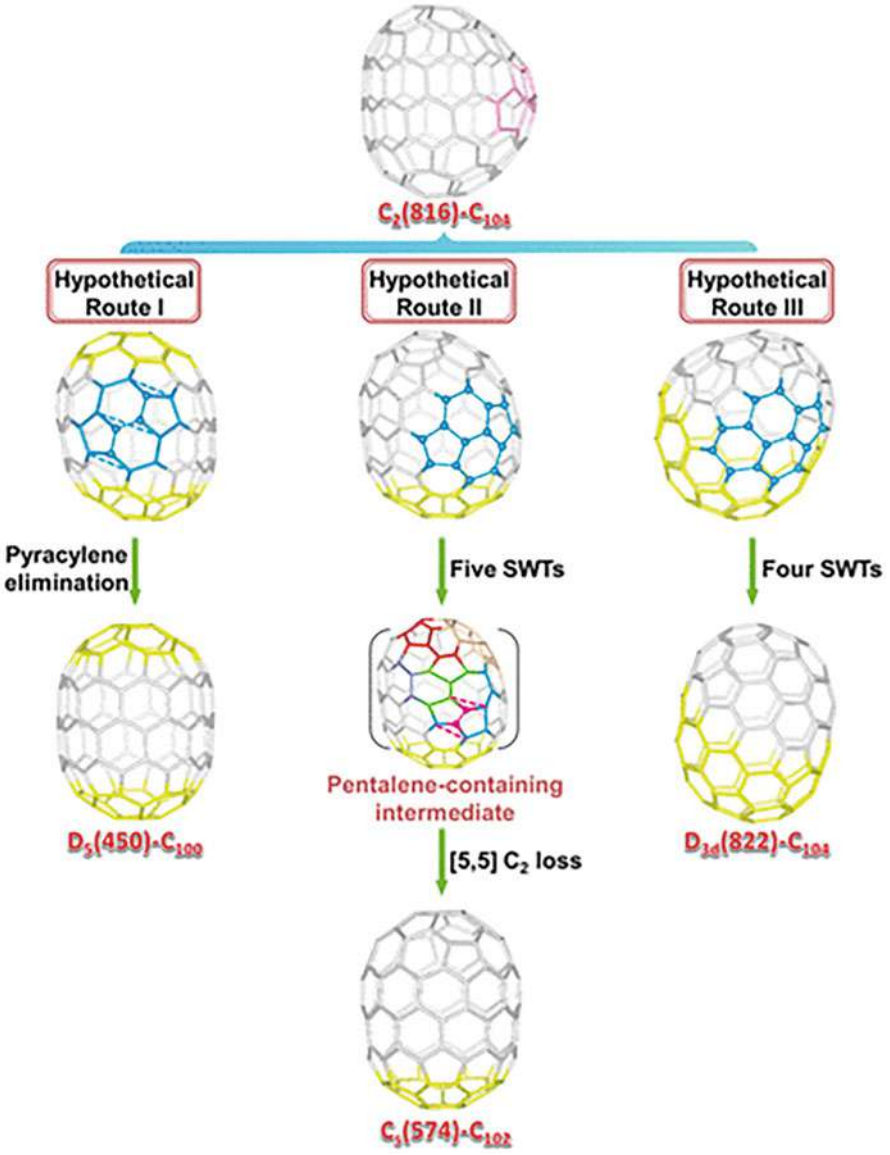

Fig. 13 Structural relation map of $C_2(816)$-C_{104} to three ideal tubular fullerene cages, $D_5(450)$-C_{100}, $C_s(574)$-C_{102}, and $D_{3d}(822)$-C_{104}. The blue atoms signify the beginning of SWT. The yellow atoms are unchanged caps. Multiple colors are used to assist in visualization of the process. (Reprinted with permission from ref. [69]. Copyright © 2016 American Chemical Society)

comprehensive expansion of the earlier proposed structural relation among $Sc_2O@C_{2n}$ (n = 38–40) [71]. The systematic relationships among these cages are strong revelation that the family of metal oxide EMFs may be from the same stream of common or relevant precursors.

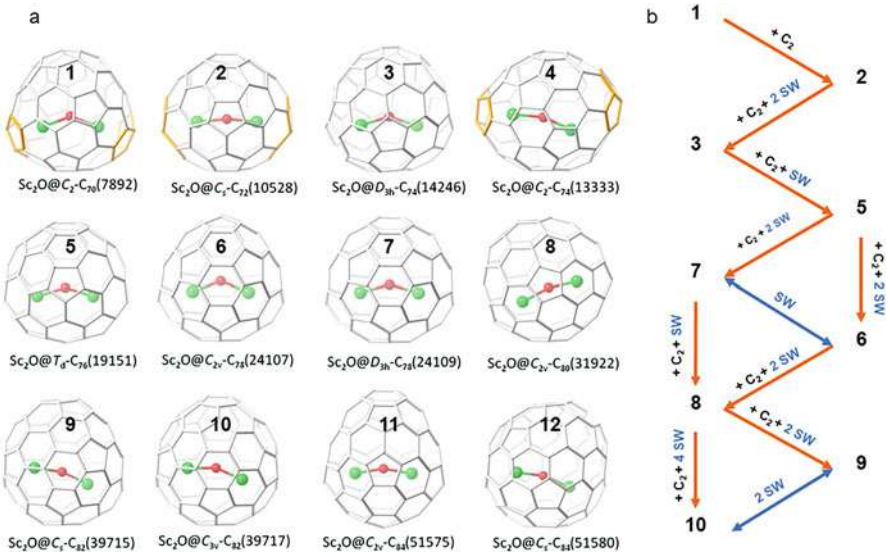

Fig. 14 The X-ray crystallographically characterized EMFs, or theoretically predicted most abundant EMFs, with a Sc_2O cluster inside cages between C_{70} and C_{84}. These structures are shown in (**a**), and their relations are shown in (**b**). (Reprinted with adoption from ref. [70] with permission © 2017 Elsevier B.V. All rights reserved)

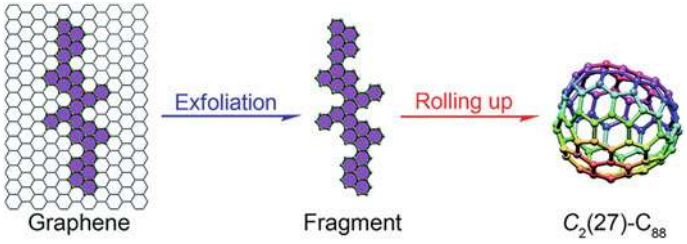

Fig. 15 Hypothetical formation of $C_2(27)$-C_{88} from a strip of graphene. (Used with permission of Royal Society of Chemistry from ref. [72], Copyright © 2019; permission conveyed through Copyright Clearance Center, Inc.)

Similar structural relations were also found in traditional metallofullerenes as well – not only for cluster metallofullerenes. With the crystallographic study of four new Eu monometallic EMFs, Eu@C_2(27)-C_{88}, Eu@C_1(7)-C_{86}, Eu@C_2(13)-C_{84}, and Eu@C_2(11)-C_{84}, Lu et al. found these four EMF cages have structural connections in a large swath of other EMF cages [72]. Additionally, they showed that the $C_2(27)$-C_{88} can be viewed as the result of a hypothetical transformation directly from a small piece of graphene (Fig. 15). This discovery added crucial insight to the top-down formation mechanism that it may not require giant fullerene cages of hundreds of carbon atoms, and a direct "roll" or "wrap" self-assembly a graphene stripe is a possible alternative, at least for empty fullerenes and small-encapsulant (e.g., monometallic) EMFs.

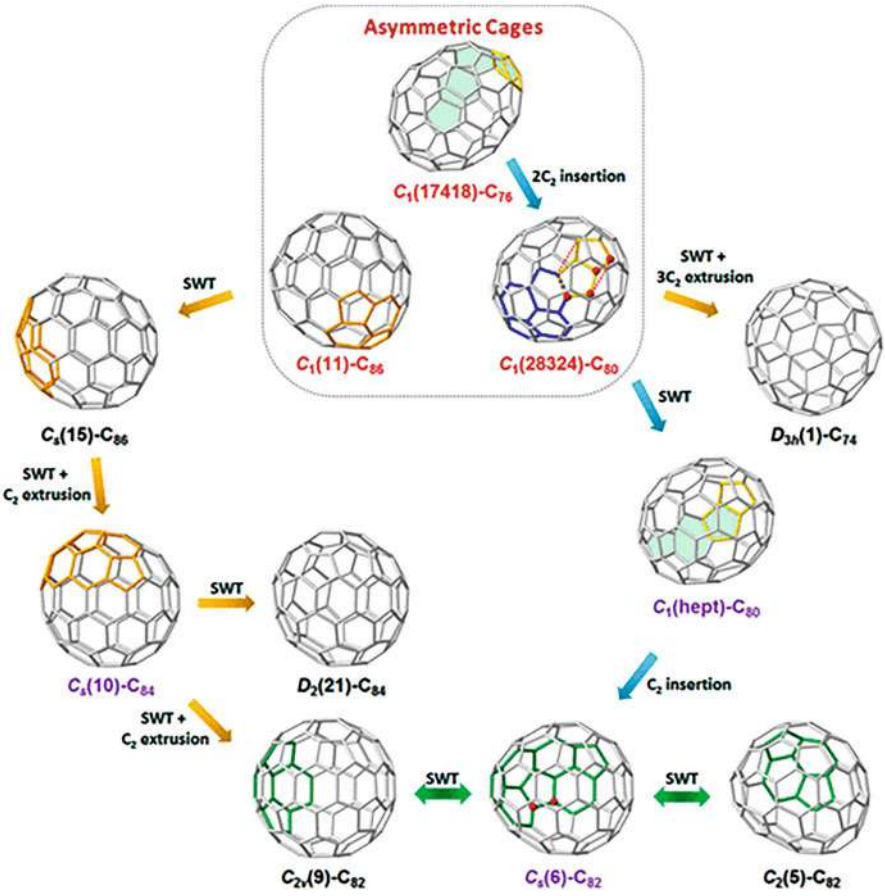

Fig. 16 Fullerene map showing both top-down and bottom-up routes. The top-down processes are indicated by orange arrows, while the bottom-up processes are indicated by blue arrows. Minor products are in purple. The fused pentagons in the cage are yellow. The orange, blue, and green atoms indicate the beginning of the top-down process, the bottom-up process, and the SWT interconversion, respectively. (Reprinted with permission from ref. [73]. Copyright © 2020 American Chemical Society)

The study of uranium EMFs expanded the scope of metal ions in metallofullerenes to include actinide elements. The discovery of three new mono-uranium U@D_2(21)-C_{84}, U@C_s(15)-C_{86}, and U@C_1(11)-C_{86} metallofullerenes helped establish a systematic interconversion map for all mono-uranium metallofullerenes, as shown in Figure 16 [73]. The authors suggested that in electric arc, C_2 ejection, C_2 insertion, and SWTs can coexist. This discovery is another strong evidence that metallofullerenes of the same encapsulated metal ion(s) or cluster may be from a common stream of structurally relevant, and interconverting, precursors, and those relatively stable intermediates will be trapped and become the eventually characterized products. Interestingly, in the same work, the authors also identified

hypothetical transformation routes directly from a small piece of graphene to either $C_1(11)$-C_{86} or $C_1(17418)$-C_{76}, which echoed the "graphene wrap-up" formation theory for Eu@$C_2(27)$-C_{88}.

Concluding Remarks

After over three decades since the discovery of fullerenes, an unambiguous, detailed mechanism that can account for fullerene and metallofullerene remains an open challenge. In situ monitoring and direct intermediate isolation of fullerene formation are nearly impossible, primarily due to the extreme conditions of their formation, from the over 2000 °C temperature in the electric arc generators to the cosmic rays in circumstellar envelops. However, the studies described in this chapter have given a reasonable picture of fullerene and metallofullerene formation, with the following key aspects:

1. In laser-ablated graphite conditions, the carbon vapor concentration is high; fullerenes and metallofullerenes can form from "bottom-up assembly." When fullerene and metallofullerene molecules are exposed to carbon vapor, they can undergo closed network growth likely via stepwise C_2 insertions.
2. In circumstellar and interstellar environments, where carbon atom density is several orders of magnitude lower than air on Earth, fullerenes (and metallofullerenes, if any) are likely formed from integral structures like large PAHs.
3. Theoretical studies showed that C_2 insertion is more energetically favorable than the reverse process, i.e., C_2 ejection [49]. Therefore, C_2 insertion deserves primary consideration in fullerene cage interconversion. However, it is possible, and even probable, that both processes coexist in the extremely energetic condition of fullerene and metallofullerene formation.
4. In reversible reactions of C_2 insertion/ejection, two factors are very important that may dictate which direction is more favorable: C_2 concentration (broadly, carbon density) and temperature [37, 59]. High carbon concentration would increase fullerene growth rate, while low carbon concentration would increase fullerene shrinkage rate. Meanwhile, high temperature is required for "hot giant" fullerene shrinkage due to its energetic requirement.
5. In arc discharge conditions, the formation of fullerene cages can be complicated, depending on the materials (carbon) and temperature gradient of the particular experimental setup. Moreover, helium flow also plays an essential role because it influences cooling and the direct collision between helium molecules and carbon species [74].
6. Fullerenes and metallofullerenes are formed in the same pathway. Metallofullerenes cages can be viewed as stabilized intermediates in fullerene synthesis. The discovery of many structural relations among metallofullerene cages revealed the likely common set of precursors of many cages.

The formation of fullerenes and metallofullerenes is still undoubtedly an intriguing question. Further understanding of their formation in electric arc will facilitate the optimization of their synthetic conditions, and thereby make significantly cheaper fullerenes and metallofullerenes. Meanwhile, it is possible to tune the synthetic conditions to change the product distributions for certain types of cages. On the other hand, further understanding of their formation in outer space will help recognize and map the flow of carbon element in the universe. This is vital for understanding the origin of life on Earch, and seeking other carbon-based planet and cosmic life. Complete revelation of fullerene and metallofullerene formation mechanism will need the joint effort of chemists, physicists, and astrophysicists worldwide, on both experimental and theoretical fronts.

Cross-References

- ▶ Fullerenes Violating the Isolated Pentagon Rule
- ▶ Our Road to Fullerenes: A Personal Account
- ▶ Preparation, Extraction/Isolation from Soot, and Solubility of Fullerenes
- ▶ Structures and Properties of Endohedral Metallofullerenes
- ▶ Theoretical Predictions of Fullerene Stabilities

References

1. Osawa E (1970) Superaromaticity. Kagaku 25:854–863. https://ci.nii.ac.jp/naid/10021261422/en/
2. Ōsawa E, Kroto HW, Fowler PW et al (1993) The evolution of the football structure for the C_{60} molecule: a retrospective. Philos Trans R Soc A 343(1667):1–8. https://doi.org/10.1098/rsta.1993.0035
3. Schultz HP (1965) Topological organic chemistry. Polyhedranes and Prismanes. J Org Chem 30(5):1361–1364. https://doi.org/10.1021/jo01016a005
4. Shinohara H (2000) Endohedral metallofullerenes. Rep Prog Phys 63(6):843–892. https://doi.org/10.1088/0034-4885/63/6/201
5. Bochvar D, Galpern E (1973) Hypothetical systems-carbododecahedron, s-icosahedrone and carbo-s-icosahedron. Dokl Akad Nauk SSSR 209(3):610–612
6. Iijima S (1980) Direct observation of the tetrahedral bonding in graphitized carbon black by high resolution electron microscopy. J Cryst Growth 50(3):675–683. https://doi.org/10.1016/0022-0248(80)90013-5
7. Rohlfing EA, Cox DM, Kaldor A (1984) Production and characterization of supersonic carbon cluster beams. J Chem Phys 81(7):3322–3330. https://doi.org/10.1063/1.447994
8. Kroto HW, Heath JR, O'Brien SC, Curl RF, Smalley RE (1985) C_{60}: Buckminsterfullerene. Nature 318(6042):162–163. https://doi.org/10.1038/318162a0
9. Klein DJ, Schmalz TG, Hite GE, Seitz WA (1986) Resonance in C_{60} buckminsterfullerene. J Am Chem Soc 108(6):1301–1302. https://doi.org/10.1021/ja00266a032
10. Stone AJ, Wales DJ (1986) Theoretical studies of icosahedral C_{60} and some related species. Chem Phys Lett 128(5):501–503. https://doi.org/10.1016/0009-2614(86)80661-3
11. Zhang QL, O'Brien SC, Heath JR et al (1986) Reactivity of large carbon clusters: spheroidal carbon shells and their possible relevance to the formation and morphology of soot. J Phys Chem 90(4):525–528. https://doi.org/10.1021/j100276a001

12. Iijima S (1987) The 60-carbon cluster has been revealed. J Phys Chem 91(13):3466–3467. https://doi.org/10.1021/j100297a002
13. O'Brien SC, Heath JR, Curl RF, Smalley RE (1988) Photophysics of buckminsterfullerene and other carbon cluster ions. J Chem Phys 88(1):220–230. https://doi.org/10.1063/1.454640
14. Schmalz TG, Seitz WA, Klein DJ, Hite GE (1988) Elemental carbon cages. J Am Chem Soc 110(4):1113–1127. https://doi.org/10.1021/ja00212a020
15. Krätschmer W, Lamb LD, Fostiropoulos K, Huffman DR (1990) Solid C_{60}: a new form of carbon. Nature 347(6291):354–358. https://doi.org/10.1038/347354a0
16. Krätschmer W, Fostiropoulos K, Huffman DR (1990) The infrared and ultraviolet absorption spectra of laboratory-produced carbon dust: evidence for the presence of the C_{60} molecule. Chem Phys Lett 170(2):167–170. https://doi.org/10.1016/0009-2614(90)87109-5
17. Curl RF, Smalley RE (1991) Fullerenes. Sci Am 265(4):54–63. http://www.jstor.org/stable/24938758
18. Howard JB, McKinnon JT, Makarovsky Y, Lafleur AL, Johnson ME (1991) Fullerenes C_{60} and C_{70} in flames. Nature 352(6331):139–141. https://doi.org/10.1038/352139a0
19. Heath JR, O'Brien SC, Zhang Q et al (1985) Lanthanum complexes of spheroidal carbon shells. J Am Chem Soc 107(25):7779–7780. https://doi.org/10.1021/ja00311a102
20. Takata M, Umeda B, Nishibori E et al (1995) Confirmation by X-ray diffraction of the endohedral nature of the metallofullerene $Y@C_{82}$. Nature 377(6544):46–49. https://doi.org/10.1038/377046a0
21. Lu X, Nikawa H, Feng L et al (2009) Location of the yttrium atom in $Y@C_{82}$ and its influence on the reactivity of cage carbons. J Am Chem Soc 131(34):12066–12067. https://doi.org/10.1021/ja905001w
22. Zhang JY, Bowles FL, Bearden DW et al (2013) A missing link in the transformation from asymmetric to symmetric metallofullerene cages implies a top-down fullerene formation mechanism. Nat Chem 5(10):880–885. https://doi.org/10.1038/nchem.1748
23. Campanera JM, Bo C, Poblet JM (2005) General rule for the stabilization of fullerene cages encapsulating trimetallic nitride templates. Angew Chem Int Ed 44(44):7230–7233. https://doi.org/10.1002/anie.200501791
24. Sun M-L, Slanina Z, Lee S-L, Uhlík F (1995) AM1 computations on seven isolated-pentagon-rule isomers of C_{80}. Chem Phys Lett 246(1):66–72. https://doi.org/10.1016/0009-2614(95)01084-M
25. Kroto HW (1987) The stability of the fullerenes C_n, with $n = 24, 28, 32, 36, 50, 60$ and 70. Nature 329(6139):529–531. https://doi.org/10.1038/329529a0
26. Wang C-R, Kai T, Tomiyama T et al (2000) C_{66} fullerene encaging a scandium dimer. Nature 408(6811):426–427. https://doi.org/10.1038/35044195
27. Stevenson S, Fowler PW, Heine T et al (2000) A stable non-classical metallofullerene family. Nature 408(6811):427–428. https://doi.org/10.1038/35044199
28. Yamada M, Kurihara H, Suzuki M et al (2014) $Sc_2@C_{66}$ revisited: an endohedral fullerene with scandium ions nestled within two unsaturated linear triquinanes. J Am Chem Soc 136(21):7611–7614. https://doi.org/10.1021/ja5035649
29. Dinadayalane TC, Leszczynski J. (2017) Fundamental structural, electronic, and chemical properties of carbon nanostructures: graphene, fullerenes, carbon nanotubes, and their derivatives. In: Handbook of computational chemistry, pp 1175–1258. https://doi.org/10.1007/978-94-007-0711-5_22
30. Maruyama S, Yamaguchi Y (1998) A molecular dynamics demonstration of annealing to a perfect C_{60} structure. Chem Phys Lett 286(3):343–349. https://doi.org/10.1016/S0009-2614(98)00103-1
31. Smalley RE (1992) Self-assembly of the fullerenes. Acc Chem Res 25(3):98–105. https://doi.org/10.1021/ar00015a001
32. Hammond GS, Kuck VJ (1992) Fullerenes: synthesis, properties, and chemistry of large carbon clusters. Conference: 201. American Chemical Society (ACS) national meeting, Atlanta, GA (United States), 14–19 Apr 1991; Related Information: ACS symposium series 481. United States: Washington, DC (United States); American Chemical Society; 1992: Medium: X; Size: 209 p

33. von Helden G, Hsu MT, Gotts N, Bowers MT (1993) Carbon cluster cations with up to 84 atoms: structures, formation mechanism, and reactivity. J Phys Chem 97(31):8182–8192. https://doi.org/10.1021/j100133a011
34. Lagow RJ, Kampa JJ, Wei H-C et al (1995) Synthesis of linear acetylenic carbon: the "*sp*" carbon allotrope. Science 267(5196):362–367. https://doi.org/10.1126/science.267.5196.362
35. Cami J, Bernard-Salas J, Peeters E, Malek SE (2010) Detection of C_{60} and C_{70} in a young planetary nebula. Science 329(5996):1180–1182. https://doi.org/10.1126/science.1192035
36. Chuvilin A, Kaiser U, Bichoutskaia E, Besley NA, Khlobystov AN (2010) Direct transformation of graphene to fullerene. Nat Chem 2(6):450–453. https://doi.org/10.1038/nchem.644
37. Irle S, Zheng G, Wang Z, Morokuma K (2006) The C_{60} formation puzzle "solved": QM/MD simulations reveal the shrinking hot Giant road of the dynamic fullerene self-assembly mechanism. J Phys Chem B 110(30):14531–14545. https://doi.org/10.1021/jp061173z
38. Slanina Z, Zahradnik R (1977) Calculations of absolute values of equilibrium and rate constants. 9. MINDO/2 study of equilibrium carbon vapor. J Phys Chem 81(24):2252–2257. https://doi.org/10.1021/j100539a011
39. Pitzer KS, Clementi E (1959) Large molecules in carbon vapor. J Am Chem Soc 81(17):4477–4485. https://doi.org/10.1021/ja01526a010
40. von Helden G, Gotts NG, Bowers MT (1993) Experimental evidence for the formation of fullerenes by collisional heating of carbon rings in the gas phase. Nature 363(6424):60–63. https://doi.org/10.1038/363060a0
41. von Helden G, Gotts NG, Bowers MT (1993) Annealing of carbon cluster cations: rings to rings and rings to fullerenes. J Am Chem Soc 115(10):4363–4364. https://doi.org/10.1021/ja00063a065
42. Shvartsburg AA, Hudgins RR, Dugourd P, Gutierrez R, Frauenheim T, Jarrold MF (2000) Observation of "stick" and "handle" intermediates along the fullerene road. Phys Rev Lett 84(11):2421–2424. https://doi.org/10.1103/PhysRevLett.84.2421
43. Dunk PW, Kaiser NK, Hendrickson CL et al (2012) Closed network growth of fullerenes. Nat Commun 3(1):855. https://doi.org/10.1038/ncomms1853
44. Dunk PW, Kaiser NK, Mulet-Gas M et al (2012) The smallest stable fullerene, M@C_{28} (M = Ti, Zr, U): stabilization and growth from carbon vapor. J Am Chem Soc 134(22):9380–9389. https://doi.org/10.1021/ja302398h
45. Dunk PW, Adjizian J-J, Kaiser NK et al (2013) Metallofullerene and fullerene formation from condensing carbon gas under conditions of stellar outflows and implication to stardust. Proc Natl Acad Sci U S A 110(45):18081. https://doi.org/10.1073/pnas.1315928110
46. Dunk PW, Rodríguez-Fortea A, Kaiser NK, Shinohara H, Poblet JM, Kroto HW (2013) Formation of heterofullerenes by direct exposure of C_{60} to boron vapor. Angew Chem Int Ed 52(1):315–319. https://doi.org/10.1002/anie.201208244
47. Dunk PW, Mulet-Gas M, Nakanishi Y et al (2014) Bottom-up formation of endohedral monometallofullerenes is directed by charge transfer. Nat Commun 5:8. https://doi.org/10.1038/ncomms6844
48. Dunk PW, Niwa H, Shinohara H, Marshall AG, Kroto HW (2015) Large fullerenes in mass spectra. Mol Phys 113(15–16):2359–2361. https://doi.org/10.1080/00268976.2015.1046963
49. Mulet-Gas M, Abella L, Dunk PW, Rodríguez-Fortea A, Kroto HW, Poblet JM (2015) Small endohedral metallofullerenes: exploration of the structure and growth mechanism in the Ti@C_{2n} (2n = 26–50) family. Chem Sci 6(1):675–686. https://doi.org/10.1039/C4SC02268H
50. Mulet-Gas M, Abella L, Cerón MR et al (2017) Transformation of doped graphite into cluster-encapsulated fullerene cages. Nat Commun 8(1):1222. https://doi.org/10.1038/s41467-017-01295-9
51. Abergel A, Arab H, Compiègne M et al (2010) Evolution of interstellar dust with Herschel. First results in the photodissociation regions of NGC 7023. A&A 518:L96. https://doi.org/10.1051/0004-6361/201014643

52. Martínez L, Santoro G, Merino P et al (2020) Prevalence of non-aromatic carbonaceous molecules in the inner regions of circumstellar envelopes. Nat Astron 4(1):97–105. https://doi.org/10.1038/s41550-019-0899-4
53. Mercado BQ, Olmstead MM, Beavers CM et al (2010) A seven atom cluster in a carbon cage, the crystallographically determined structure of $Sc_4(\mu_3\text{-}O)_3@I_h\text{-}C_{80}$. Chem Commun 46(2): 279–281. https://doi.org/10.1039/B918731F
54. Shinohara H, Sato H, Saito Y, Takayama M, Izuoka A, Sugawara T (1991) Formation and extraction of very large all-carbon fullerenes. J Phys Chem 95(22):8449–8451. https://doi.org/10.1021/j100175a010
55. Koenig RM, Tian H-R, Seeler TL et al (2020) Fullertubes: cylindrical carbon with half-fullerene end-caps and tubular graphene belts, their chemical enrichment, crystallography of pristine C_{90}-D_{5h}(1) and C_{100}-D_{5d}(1) fullertubes, and isolation of C_{108}, C_{120}, C_{132}, and C_{156} cages of unknown structures. J Am Chem Soc 142(36):15614–15623. https://doi.org/10.1021/jacs.0c08529
56. Maruyama S, Anderson LR, Smalley RE (1990) Direct injection supersonic cluster beam source for FT-ICR studies of clusters. Rev Sci Instrum 61(12):3686–3693. https://doi.org/10.1063/1.1141536
57. Maruyama S, Lee MY, Haufler RE, Chai Y, Smalley RE (1991) Thermionic emission from giant fullerenes. Z Phys D - Atoms, Molecules and Clusters 19:409–412. https://doi.org/10.1007/bf01448340
58. Curl RF, Lee MK, Scuseria GE (2008) C_{60} buckminsterfullerene high yields Unraveled. J Phys Chem A 112(46):11951–11955. https://doi.org/10.1021/jp806951v
59. Saha B, Irle S, Morokuma K (2011) Hot Giant fullerenes eject and capture C_2 molecules: QM/MD simulations with constant density. J Phys Chem C 115(46):22707–22716. https://doi.org/10.1021/jp203614e
60. Ugarte D (1992) Curling and closure of graphitic networks under electron-beam irradiation. Nature 359(6397):707–709. https://doi.org/10.1038/359707a0
61. Berné O, Tielens AGGM (2012) Formation of buckminsterfullerene (C_{60}) in interstellar space. Proc Natl Acad Sci U S A 109(2):401–406. https://doi.org/10.1073/pnas.1114207108
62. Micelotta ER, Jones AP, Cami J, Peeters E, Bernard-Salas J, Fanchini G (2012) The formation of cosmic fullerenese from arophatic clusters. Astrophys J 761(1):35. https://doi.org/10.1088/0004-637x/761/1/35
63. Zhen J, Castellanos P, Paardekooper DM, Linnartz H, Tielens AGGM (2012) Laboratory formation of fullerenes from PAHs: top-down interstellar chemistry. Astrophys J 797(2):L30. https://doi.org/10.1088/2041-8205/797/2/l30
64. Berné O, Montillaud J, Joblin C (2015) Top-down formation of fullerenes in the interstellar medium. A&A 577:A133. https://doi.org/10.1051/0004-6361/201425338
65. Cherchneff I, Le Teuff YH, Williams PM, Tielens AGGM (2000) Dust formation in carbon-rich Wolf-Rayet stars. I. Chemistry of small carbon clusters and silicon species. Astron Astrophys 357:572–580
66. Zhang Y, Ghiassi KB, Deng Q et al (2015) Synthesis and structure of $LaSc_2N@C_s$(hept)-C_{80} with one heptagon and thirteen pentagons. Angew Chem Int Ed 54(2):495–499. https://doi.org/10.1002/anie.201409094
67. Chen C-H, Abella L, Cerón MR et al (2016) Zigzag Sc_2C_2 carbide cluster inside a [88]fullerene cage with one heptagon, $Sc_2C_2@C_s$(hept)-C_{88}: a kinetically trapped fullerene formed by C_2 insertion? J Am Chem Soc 138(39):13030–13037. https://doi.org/10.1021/jacs.6b07912
68. Chen C-H, Ghiassi KB, Cerón MR et al (2015) Beyond the butterfly: $Sc_2C_2@C_{2v}$(9)-C_{86}, an endohedral fullerene containing a planar, twisted Sc_2C_2 unit with remarkable crystalline order in an unprecedented carbon cage. J Am Chem Soc 137(32):10116–10119. https://doi.org/10.1021/jacs.5b06425
69. Cai W, Li F-F, Bao L, Xie Y, Lu X (2016) Isolation and crystallographic characterization of $La_2C_2@C_s$(574)-C_{102} and $La_2C_2@C_2$(816)-C_{104}: evidence for the top-down formation mechanism of fullerenes. J Am Chem Soc 138(20):6670–6675. https://doi.org/10.1021/jacs.6b03934

70. Abella L, Wang Y, Rodríguez-Fortea A, Chen N, Poblet JM (2017) Current status of oxide clusterfullerenes. Inorg Chim Acta 468:91–104. https://doi.org/10.1016/j.ica.2017.05.040
71. Hao Y, Tang Q, Li X et al (2016) Isomeric $Sc_2O@C_{78}$ related by a single-step stone–wales transformation: key links in an unprecedented fullerene formation pathway. Inorg Chem 55(21): 11354–11361. https://doi.org/10.1021/acs.inorgchem.6b01894
72. Bao L, Yu P, Pan C, Shen W, Lu X (2019) Crystallographic identification of $Eu@C_{2n}$ ($2n = 88$, 86 and 84): completing a transformation map for existing metallofullerenes. Chem Sci 10(7):2153–2158. https://doi.org/10.1039/C8SC04906H
73. Cai W, Alvarado J, Metta-Magaña A, Chen N, Echegoyen L (2020) Interconversions between uranium mono-metallofullerenes: mechanistic implications and role of asymmetric cages. J Am Chem Soc 142(30):13112–13119. https://doi.org/10.1021/jacs.0c04888
74. Qian H-J, Wang Y, Morokuma K (2017) Quantum mechanical simulation reveals the role of cold helium atoms and the coexistence of bottom-up and top-down formation mechanisms of buckminsterfullerene from carbon vapor. Carbon 114:635–641. https://doi.org/10.1016/j.carbon.2016.12.062

Index

X. Lu et al. (eds.), *Handbook of Fullerene Science and Technology*,
https://doi.org/10.1007/978-981-16-8994-9

N